Lecture Notes in Civil Engineering

Hoang-Hung Tran-Nguyen
Henry Wong
Frederic Ragueneau
Cuong Ha-Minh *Editors*

# Proceedings of the 4th Congrès International de Géotechnique – Ouvrages – Structures

## CIGOS 2017, 26–27 October, Ho Chi Minh City, Vietnam

Springer

# Lecture Notes in Civil Engineering

Volume 8

**Lecture Notes in Civil Engineering** (LNCE) publishes the latest developments in Civil Engineering - quickly, informally and in top quality. Though original research reported in proceedings and post-proceedings represents the core of LNCE, edited volumes of exceptionally high quality and interest may also be considered for publication. Volumes published in LNCE embrace all aspects and subfields of, as well as new challenges in, Civil Engineering. Topics in the series include:

- Construction and Structural Mechanics
- Building Materials
- Concrete, Steel and Timber Structures
- Geotechnical Engineering
- Earthquake Engineering
- Coastal Engineering
- Hydraulics, Hydrology and Water Resources Engineering
- Environmental Engineering and Sustainability
- Structural Health and Monitoring
- Surveying and Geographical Information Systems
- Heating, Ventilation and Air Conditioning (HVAC)
- Transportation and Traffic
- Risk Analysis
- Safety and Security

More information about this series at http://www.springer.com/series/15087

Hoang-Hung Tran-Nguyen
Henry Wong · Frederic Ragueneau
Cuong Ha-Minh
Editors

# Proceedings of the 4th Congrès International de Géotechnique – Ouvrages –Structures

CIGOS 2017, 26–27 October,
Ho Chi Minh City, Vietnam

Springer

*Editors*
Hoang-Hung Tran-Nguyen
University of Technology
Ho Chi Minh City
Vietnam

Frederic Ragueneau
University of Paris-Saclay
Cachan Cedex
France

Henry Wong
University of Lyon
Vaulx-en-Velin
France

Cuong Ha-Minh
University of Paris-Saclay
Cachan Cedex
France

ISSN 2366-2557 ISSN 2366-2565 (electronic)
Lecture Notes in Civil Engineering
ISBN 978-981-10-6712-9 ISBN 978-981-10-6713-6 (eBook)
DOI 10.1007/978-981-10-6713-6

Library of Congress Control Number: 2017954899

© Springer Nature Singapore Pte Ltd. 2018
This work is subject to copyright. All rights are reserved by the Publisher, whether the whole or part of the material is concerned, specifically the rights of translation, reprinting, reuse of illustrations, recitation, broadcasting, reproduction on microfilms or in any other physical way, and transmission or information storage and retrieval, electronic adaptation, computer software, or by similar or dissimilar methodology now known or hereafter developed.
The use of general descriptive names, registered names, trademarks, service marks, etc. in this publication does not imply, even in the absence of a specific statement, that such names are exempt from the relevant protective laws and regulations and therefore free for general use.
The publisher, the authors and the editors are safe to assume that the advice and information in this book are believed to be true and accurate at the date of publication. Neither the publisher nor the authors or the editors give a warranty, express or implied, with respect to the material contained herein or for any errors or omissions that may have been made. The publisher remains neutral with regard to jurisdictional claims in published maps and institutional affiliations.

Printed on acid-free paper

This Springer imprint is published by Springer Nature
The registered company is Springer Nature Singapore Pte Ltd.
The registered company address is: 152 Beach Road, #21-01/04 Gateway East, Singapore 189721, Singapore

# Preface

Following the success of the CIGOS (Congrès International de Géotechnique - Ouvrages -Structures) conferences in 2010, 2013 and 2015, the Fourth international conference CIGOS Vietnam 2017 has expanded beyond the collaboration of scientists between France and Vietnam, to an international level. CIGOS Vietnam 2017 was held in Ho Chi Minh City University of Technology, which is one of the best universities in Vietnam. About 130 technical papers were reviewed carefully, and many outstanding professors from over 20 countries delivered keynote lectures during the conference. The proceedings of CIGOS Vietnam 2017 published by Springer issued the latest research achievement and exchanged ideas among worldwide researchers and professional engineers in the civil engineering arena.

The conference covered six topics which discussed recent findings in civil engineering as follows :

1 Advanced modelling of structure
2 Materials for construction
3 Geotechnics for environment and energy
4 Innovative design and methods
5 Water treatment and environment
6 Case studies (Tunnel, Nuclear Power Plant, etc.)

We acknowledge all the contributors for the high-quality papers, the international advisory members and the organizing committee for their dedicated work and a great collaboration, and the sponsors for their generous support. Finally, we would like to thank all the invited speakers and participants who made the CIGOS Vietnam 2017 a unique international event.

By the editors of the CIGOS Vietnam 2017

Hoang-Hung Tran-Nguyen
Henry Wong
Frédéric Ragueneau
Cuong Ha-Minh

# Organization

## Organizing Committee

### Chairmen

| | |
|---|---|
| Ha Minh, Cuong | ENS Paris-Saclay & Association of Vietnamese Scientists and Experts (AVSE), France |
| Herve-Secourgeon, Guillaume | Ecole Spéciale des Travaux Publics (ESTP), France |
| Mai, Thanh Phong | Ho Chi Minh City University of Technology (HCMUT), Vietnam |
| Ragueneau, Frédéric | École Normale Supérieure Paris-Saclay (ENS), France |

### Organizing Team

| | |
|---|---|
| Benboudjema, Farid | ENS Paris-Saclay, France |
| Bui, Le Khanh | ESTP Paris, France |
| Do, Tuan Anh | Ecole Polytechnique, France |
| Duong, Trong Vinh | GCMM & Semofi, France |
| Le, Minh Quan | ENS Paris-Saclay, France |
| Le, Van Nhat | GCMM & UVSQ, France |
| Luu, Xuan Loc | HCMUT, Vietnam |
| Ngo, Van Trang | ESTP Paris, France |
| Nguyen, Duy Hung | FAYAT Group, France |
| Nguyen, Khanh Son | HCMUT, Vietnam |
| Nguyen, Hai Nam | ENS Paris-Saclay, France |
| Nguyen, Thanh Son | GCMM & ENS Paris-Saclay, France |
| Nguyen, Thuong Anh | GCMM & ESTP Paris, France |

| | |
|---|---|
| Nguyen, Tien Long | Tractebel, France |
| Nguyen, Van Linh | GCMM & SETEC Lyon, France |
| Nguyen, Van Ngan | GCMM & Egis, France |
| Rouzaud, Christophe | ESTP Paris, France |
| Tran, Cong Danh | HCMUT, Vietnam |
| Tran, Ngoc Tien Dung | CARE-Rescif, HCMUT, Vietnam |
| Tran Nguyen, Hoang Hung | HCMUT, Vietnam |
| Tran, Thanh Danh | Open Univ., Vietnam |

## Scientific Committee

### Chairman

| | |
|---|---|
| Wong, Henry | École Nationale des Travaux Publics de l'État, France |

### Members

| | |
|---|---|
| Azenha, Miguel | Minho Univ., Portugal |
| Beakou, Alexis | IFMA/SIGMA Clermont, France |
| Benboudjema, Farid | ENS Cachan, France |
| Benson, Craig H. | Univ. of Virginia, USA |
| Boutillon, Laurent | Vinci Construction, France |
| Bredy Tuffe, Patricia | ESTP, France |
| Bui, Ha | Monash Univ., Australia |
| Bui, Quoc Bao | Savoie Mont Blanc Univ., France |
| Bui, Tuan Anh | Nante Univ., France |
| Bui, Xuan Thanh | HCMUT, Vietnam |
| Colin, Johan | ESTP, France |
| Collin, Frédéric | Liege Univ., Belgium |
| Darquennes, Aveline | ENS Paris-Saclay, France |
| Do, Quang Minh | HCMUT, Vietnam |
| Drogui, Patrick | INRS, Canada |
| Edil, Tuncer B. | Univ. of Wisconsin-Madison, USA |
| Fukagawa, Ryoichi | Ritsumeikan Univ. Japan |
| Ghorbel, Elhem | Cergy-Pontoise Univ., France |
| Gourdon, Rémy | INSA Lyon, France |
| Herve-Secourgeon, Guillaume | EDF, France |
| Huynh, Khoa | NGI, Norway |
| Huynh, Quoc Vu | HBCR, Vietnam |

| | |
|---|---|
| Indraratna, Buddhima | Wollongong Univ., Australia |
| Kitazume, Masaki | Tokyo Tech, Japan |
| Lanos, Christophe | IUT/INSA Rennes, France |
| Le, Trung Chon | HCMUT, Vietnam |
| Leo, Chin | Western Sydney Univ., Australia |
| Liang, Robert Y. | Univ. of Akron, USA |
| Luong, Duc Long | HCMUT, Vietnam |
| Luong, Van Hai | HCMUT, Vietnam |
| Nemery, Julien | Grenoble-INP, France |
| Nguyen, Frédéric | Liege Univ., Belgium |
| Nguyen, Giang | Adelaide Univ., Australia |
| Nguyen, Minh Tam | HCMUT, Vietnam |
| Nguyen, Phuoc Dan | HCMUT, Vietnam |
| Nguyen, Tan Phong | HCMUT, Vietnam |
| Nguyen, Trung Kien | HCMUTE, Vietnam |
| Nguyen, Xuan Hung | HUTECH, Vietnam |
| Otani, Jun | Kumamoto Univ., Japan |
| Pham, Cao Hung | Univ. of Sydney, Australia |
| Pham, Duc Chinh | VAST Hanoi, Vietnam |
| Phan, Thi San Ha | HCMUT, Vietnam |
| Poh, Leong Hien | National University of Singapore |
| Proust, Gwénaëlle | Univ. of Sydney, Australia |
| Ragueneau, Frédéric | ENS Cachan, France |
| Ranzi, Gianluca | Sydney Univ., Australia |
| Rouzaud, Christophe | ESTP, France |
| Santhanam, Manu | Madras Inst. India |
| Sechet, Philippe | Grenoble-INP, France |
| Skatulla, Sebastian | Univ. of Cape Town, South Africa |
| Takahashi, Hiroshi | Tohoku Univ., Japan |
| Takebayashi, Hiroshi | Kyoto University, Japan |
| Tanaka, Hitoshi | Tohoku Univ., Japan |
| Tang, Anh Minh | ENPC, France |
| Torrenti, Jean-Michel | Ifsttar, France |
| Tran, Ba Viet | IBST, Vietnam |
| Tran, Ngoc Tien Dung | HCMUT, Vietnam |
| Tran Nguyen, Hoang Hung | HCMUT, Vietnam |
| Tran, The Truyen | UTC, Vietnam |
| Tran, Tuan Anh | HCMC Open Univ., Vietnam |
| Tran, Van Mien | HCMUT, Vietnam |
| Vu, Xuan Hong | Lyon 1 Univ., France |
| Wahab, Magd Abdel | Ghent Univ., Belgium |
| Zhou, Annan | RMIT Melbourne, Australia |

## Sponsors

### Gold Sponsor

FECON

*Listen to the Earth, conquer the height*

### Silver Sponsor

SHMZ
SHIMIZU VIETNAM CO., LTD.

JFE

BM
BM Windows

TRƯỜNG ĐẠI HỌC KIẾN TRÚC

XÂY DỰNG
ĐẠI HỌC

SOMETHING
VIETNAM

STRUCTURES VIETNAM
together @ VINCI

## Organizers

ASSOCIATION OF VIETNAMESE SCIENTISTS AND EXPERTS
HỘI KHOA HỌC VÀ CHUYÊN GIA VIỆT NAM

école
normale
supérieure
paris—saclay

ESTP
PARIS
L'ÉCOLE DES GRANDS PROJETS

Mécanique et Matériaux
Génie Civil
GCMM

BK
TP.HCM

## Supporter

AFGC

CARE Rescif
Trung tâm châu Á nghiên cứu về nước
Centre Asiatique de Recherche sur l' Eau

# Contents

**Keynote Lectures**

**A Review of Recycled Aggregates (RAP and RCA) as Unbound Base Course Material for Sustainable Highway Construction** . . . . . 3
Tuncer B. Edil

**Effective Slab Width for Evaluating Ultimate Seismic Capacities of Reinforced Concrete Buildings** . . . . . 15
Toshimi Kabeyasawa and Toshikazu Kabeyasawa

**From 3-D to 1-D Generalised and Cosserat Continua for Structural Dynamics - Energy-Momentum Methods** . . . . . 30
Carlo Sansour, Tien Long Nguyen, and Mohammed Hjiaj

**Recent Developments in Design for Structural Stability** . . . . . 41
Gregory J. Hancock

**Advanced Modelling of Structures (AMS)**

**A Numerical Modeling of RC Beam-Column Joints Compared to Experimental Results** . . . . . 59
Q.-B. Bui, B. Sentosa, and T.-H. Duong

**Application of a Newly Puzzel Shaped Crestbond Rib Shear Connector in Composite Beam Using Opposite T Steel Girder: An Experimental Study** . . . . . 68
Duy Kien Dao, Duc Vinh Bui, Thi Hai Vinh Chu, and Van Phuoc Nhan Le

**Application of the THIN-WALL-2 V2.0 Program for Analysis of Thin-Walled Sections Under Localised Loading** . . . . . 78
Van Vinh Nguyen, Gregory J. Hancock, and Cao Hung Pham

**Bending Resistance of Steel-Bar Reinforced Concrete Beam with Extreme Compression Zones Using High-Performance Composite** . . . . . 89
Duy-Liem Nguyen and Duy-Ngo Tong

**Bolt-Loosening Detection in Steel Column Connections Using Impedance Responses** . . . . . 100
Duc-Duy Ho, Trung-Hieu Nguyen, and Quang-Huy Le

**Crack Propagation Analysis in Concrete Dams Based on the eXtended Finite Element Method** . . . . . 111
Giang Vo Thi Tuyet and Trong Nguyen Vo

**Experimental Study of Hybrid Walls with Several Fully Encased Steel Sections** . . . . . 120
Van Toan Tran and Quang Huy Nguyen

**Failure Analysis of a Cold-Rolled Steel Tensile Specimen Using a Damage-Plasticity Model** . . . . . 131
Bac V. Mai, Giang D. Nguyen, Cao Hung Pham and Gregory J. Hancock

**Finite Strain Plasticity Formulations for Dynamic Beams With and Without Rotational Degrees of Freedom** . . . . . 142
Tien Long Nguyen, Carlo Sansour, and Mohammed Hjiaj

**Fuzzy Linear Elastic Dynamic Analysis of 2-Dimensional Semi-rigid Steel Frame with Fuzzy Fixity Factors** . . . . . 152
Thanh Viet Tran, Quoc Anh Vu, and Xuan Huynh Le

**Incorporation of Measured Geometric Imperfections into Finite Element Models for Cold-Rolled Aluminium Sections** . . . . . 161
Ngoc Hieu Pham, Cao Hung Pham, and Kim J.R. Rasmussen

**Micromechanical Model for Describing Intergranular Fatigue Cracking in an Innovative Solder Alloy** . . . . . 172
Van-Nhat Le, Lahouari Benabou, and Quang-Bang Tao

**Modelling the Static Interaction Between a Shallow Foundation and Soil Base Using Contact Conditions** . . . . . 181
H.T. Tai Nguyen, T. Hang Nguyen, and N. Hung Nguyen

**Numerical Analysis of Hybrid Walls Using FEM** . . . . . 191
Van Toan Tran

**Numerical Simulations of Cold-Rolled Aluminium Alloy 5052 Channel Sections in Stub Column Tests** . . . . . 202
Le Anh Thi Huynh, Cao Hung Pham, and Kim J.R. Rasmussen

**Numerical Studies of Composite Steel-Concrete Columns Under Fire Conditions Including Cooling Phase** . . . . . 213
Thi Binh Chu and Quang Vinh Truong

**On the Finite Element Modeling of the Screwed Connections of Cold-Formed Steel** . . . . . 224
Minh Toan Huynh, Cao Hung Pham, and Gregory J. Hancock

**Redistribution of Moment at Beam-Column Joints in RC Structures: Comparison Between an Experimental Study and Eurocode 2** . . . . . 233
B. Sentosa, Q.-B. Bui, J.-P. Plassiard, O. Plé, P. Perrotin, and H. Purnomo

**Shear Resistance Behaviors of a Newly Puzzle Shape of Crestbond Rib Shear Connector: An Experimental Study** . . . . . 243
Thi Hai Vinh Chu, Van Phuoc Nhan Le, Duy Kien Dao, Thanh Hai Nguyen, and Duc Vinh Bui

**Simulation of Reinforced Concrete Short Shear Walls Subjected to Seismic Loading** . . . . . 254
Khuong Le Nguyen, Ba Tam Truong, and Minh Quyen Cao

**Strength Capacity of Steel Piles Filled with Concrete at Pile Top** . . . . . 263
Moeko Matoba, Mutsuki Sato, Toshiharu Hirose and Yoshihiro Kimura

**Systematic Analysis of the Concept of Equivalent Linear Behavior in Seismic Engineering** . . . . . 273
Thuong Anh Nguyen, Pierre Labbé, Jean-François Semblat, and Guillaume Hervé

**Tensioning Process Update for Cable Stayed Bridges** . . . . . 283
Jose Antonio Lozano-Galant, Dong Xu, and Jose Turmo

**The Roles and Effects of Friction in Cohesive Zone Modelling: A Thermodynamics-Based Formulation** . . . . . 288
Giang D. Nguyen and Ha H. Bui

**Materials For Construction (MFC)**

**A Review on Immobilisation of Toxic Wastes Using Geopolymer Technique** . . . . . 299
Tran Huyen Vu and Mien Van Tran

**Additional Carbon Dependent Electrical Resistivity Behaviors of High Performance Fiber-Reinforced Cementitious Composites** . . . . . 310
Duy-Liem Nguyen, Thi-Ngoc-Han Vuong, and Tri-Thong Nguyen

**An Experimental Study on Earthen Materials Stabilized by Geopolymer** . . . . . 319
Q.-B. Bui, E. Prud'homme, A.-C. Grillet, and N. Prime

**Analysis Behavior of Reinforcement in a Reinforced Concrete Beam Using Steel Slag Replacing Crushed-Stone Aggregate** . . . . . 329
Anh-Thang Le, Trong-Quang Hoang, and Tat-Thanh Nguyen

**Application of Empirical Models to Optimizing Concrete Pumpabiltity** . . . . . 338
Tien-Tung Ngo, Chanh-Trung Mai, El-Hadj Kadri, and Abdelhak Kaci

**Behavior of Concrete-Filled Hybrid Large Rupture Strain FRP Tubes Under Cyclic Axial Compression** . . . . . 346
Monika Nain, Mohanad M. Abdulazeez, and Mohamed A. ElGawady

**Chemical Shrinkage Characteristics of Binder Pastes in Ultra High Performance Concrete Made from Different Types of Cement** . . . . . 354
Quoc Si Bach

**Chloride Binding Ability and Anti-corrosion Properties of Supersulfated Cement in Seawater/Sand Mixing Concrete** . . . . . 367
Khanh Son Nguyen, Anh Toan Nguyen-Phung, Hong Thai Le, Thanh Tri Ho, Tri Huynh Nguyen-Ngoc, Soon Poh Yap, Nobuhiro Chijiwa, and Nobuaki Otsuki

**Correlation Between Resilient Modulus and Permanent Deformation During a Large Scale Model Experiment of Unbound Base Course** . . . . . 377
Makhaly Ba

**Correlations Between DCP Penetration Index and Properties of Pavement Layer Materials** . . . . . 385
Suppakorn Wachiraporn, Auckpath Sawangsuriya and Wilailak Sramoon

**Crumb Rubber as a Sustainable Aggregate in Chip Seal Pavement** . . . . 392
Ahmed A. Gheni and Mohamed A. ElGawady

**Development of Geopolymer-Based Materials from Coal Bottom Ash and Rice Husk Ash with Sodium Silicate Solutions** . . . . . 402
Hoc Thang Nguyen, Trung Kien Pham, and Michael A.B. Promentilla

**Development of New Type of Screwed Pile with Large Bearing Capacity and Ecological Driving Method "Tsubasa Pile™"** . . . . . 411
Marina Kawai, Kazuomi Ichikawa, and Kenji Kono

**Durability of Polyester-Based GFRP Subjected to Hybrid Environmental and Mechanical Loads** . . . . . 426
Song Wang and Mohamed ElGawady

**Effect of Manufacturing Process on Material Properties at the Corners of G450 Cold-Formed Steel Channel Sections** . . . . . 434
Huu Nam Trinh, Gwénaëlle Proust, and Cao Hung Pham

**Effect of Pre-compressive Stress on Chloride Permeability of Concrete Used Anti-permeable Admixture** . . . . . 442
The Truyen Tran, Xuan Tung Nguyen, and Xuan Ba Ho

**Effect of Thermal-Humid Media on Durability of CFRP-Wrapped Reinforced Concrete Columns** . . . . . 448
Van Mien Tran and Dong Viet Phuong Tran

**Effective Design of Flexible Pavement on Treated Expansive Soil** . . . . . 459
Raju Sarkar, Ankur Mudgal, Ritesh Kurar, and Varun Gupta

**Experimental Approach to Identify the Thermomechanical Behaviour of a Textile Reinforced Concrete (TRC) Subjected to High Temperature and Mechanical Loading** . . . . . 471
Tala Tlaiji, Xuan Hong Vu, Emmanuel Ferrier, and Amir Si Larbi

**Experimental Study on the Thermo-Mechanical Behavior of Hand-Made Carbon Fiber Reinforced Polymer (H-CFRP) Simultaneously Subjected to Elevated Temperature and Mechanical Loading** . . . . . 484
Phi Long Nguyen, Xuan Hong Vu, and Emmanuel Ferrier

**Fresh Properties and Early Compressive Strength of Alkali-Activated High Calcium Fly Ash Paste** . . . . . 497
Eslam Gomaa, Simon Sargon, Cedric Kashosi and Mohamed ElGawady

**Hygric and Thermal Insulation Properties of Building Materials Based on Bamboo Fibers** . . . . . 508
Dang Mao Nguyen, Anne-Cécile Grillet, Thi My Hanh Diep, Thi Vi Vi Do, Chi Nhan Ha Thuc, and Monika Woloszyn

**Investigation on the Blended Cement Mixture of Sintered Clinker of Calcium Sulfoaluminate Cement and Granulated Blast Furnace Slag** . . . . . 523
Khanh Son Nguyen, Tuan Nghia Le, Anh Quyen Nguyen-Thi, Anh Toan Nguyen-Phung, Tri Huynh Nguyen-Ngoc, and Quang Minh Do

**Numerical Tool for the Evaluation of the Hygrothermal Performance of a Hemp-Lime Concrete** . . . . . 533
S. Moissette, M. Bart, Y. Aït Oumeziane, C. Lanos, F. Collet and S. Prétot

**Seismic Performance of Hollow-Core Composite Columns Under Cyclic Loading** . . . . . 544
Mohanad M. Abdulazeez and Mohamed A. ElGawady

**Semi-flexible Material: The Sustainable Alternative for the Use of Conventional Road Materials in Heavy-Duty Pavement** . . . . . 552
T. Nhan Tran, H.T. Tai Nguyen, K. Son Nguyen, and N.T. Huynh Nguyen

**Shear Behavior of High Performance Concrete Beams Using Digital Image Correlation Technique** . . . . . 560
Touhami Tahenni, Mohamed Chemrouk, and Thibaut Lecompte

**Study on Effect of Cornsilk Fiber in Cemented Soil Stabilization** . . . . . 571
Khiem Quang Tran, Tomoaki Satomi, and Hiroshi Takahashi

**Study on Strength of Modified Sludge Produced By Fiber-Cement Stabilized Soil Method Using Several Kinds of Fiber Materials** . . . . . 580
Thanh Nga Duong, Tomoaki Satomi, and Hiroshi Takahashi

**Synergic Effects of Activation Routes of Ground Granulated Blast-Furnace Slag (GGBS) Used in the Precast Industry** . . . . . 588
Martin Cyr and Ludovic Andre

**The Flow Response of Reinforced Earth Structures Utilized Fine-Grained Poorly Draining Materials as Backfill** . . . . . 598
D. Bui Van, A. Chinkulkijniwat, S. Horpibulsuk, S. Yubonchit, A. Udomchai, I. Limrat, A. Le Tuan, H. Pham Tien, and O. Kennedy

**Using a Spray Test to Study the Surface Erosion of Geomaterials Application on Construction Material of Soil-Cement Mixtures in Le Havre, France** . . . . . 610
Van-Nghia Nguyen and Said Taibi

**Using Wastes from Thermal Power Plants for Manufacturing of Low Strength Construction Materials** . . . . . 617
Quoc-Bao Bui, Minh-Tung Tran, and Duc-Hien Le

**Geotechnics for Environment and Energy (GEE)**

**3D Electrical Resistivity Tomography of Karstified Formations Using Cross-Line Measurements** . . . . . 627
Maurits Van Horde, Thomas Hermans, Gael Dumont, and Frédéric Nguyen

**A Case Study of a Long-Duration Thermal Response Test in Borehole Heat Exchangers** . . . . . 637
Georgia Radioti, Benjamin Cerfontaine, Robert Charlier, and Frederic Nguyen

**An Elastoplastic Model for Soils Exhibiting Particle Breakage** . . . . . 644
Vu P.Q. Nguyen and Mamoru Kikumoto

**Application of a Cyclic Accumulation Model UDCAM to FE Analyses of Offshore Foundations** . . . . . 656
Huynh Dat Vu Khoa and Hans Petter Jostad

**Assessment of Multiple Geophysical Techniques for the Characterization of Municipal Waste Deposit Sites** . . . . . 668
Gael Dumont, Tanguy Robert, Nicolas Mark, and Frédéric Nguyen

**Seismic Cone Testing Using Seafloor Drill Technology** . . . . . 677
D.H. Doan, P. Looijen, and A.G. Cooper

**Conductive Heat Transfer Analysis of Energy Pile** . . . . . 685
Tri Van Nguyen, Anh Minh Tang, and Jean-Michel Pereira

**Effect of Site Parameters on Dynamic Impedance of Bridge Piles Subjected to Seismic Loading** . . . . . 694
Muhammad Tariq A. Chaudhary

**Effects of Operating Parameters of the NSV System on Field Soilcrete Characteristics in the Mekong Delta, Vietnam** . . . . . 704
Hoang-Hung Tran-Nguyen, Chau Dac Truong, and Khang Thien Truong

**Effects of Pore-Water Chemistry on the Behaviour of Unsatuarted Clays** . . . . . 716
X. Lei, H. Wong, A. Fabbri, A. Limam, and Y.M. Cheng

**Influence of Microcracking of Host Rock on the Hydromechanical Responses of Underground Structures: Constitutive Modeling and Numerical Simulations** . . . . . 726
T.A. Bui, H. Wong, and F. Deleruyelle

**Jet Grouting Mitigating Settlement of Bridge Approaching Embankments of Tam Bang and Vam Dinh Bridges** . . . . . 736
Hoang-Hung Tran-Nguyen and Chuong Hong Quach

**Laboratory Study of Local Clay-Pile Friction Evolution for Large Numbers of Cycles** . . . . . 746
Rawaz Dlawar Muhammed, Jean Canou, Jean-Claude Dupla, and Alain Tabbagh

**Numerical Modelling of Desiccation Cracking of Clayey Soil by Using Cohesive Fracture Method** . . . . . 756
Thi Dong Vo, Amade Pouya, Sahar Hemmati, and Anh Minh Tang

**Pneumatic Flow Mixing Method for Beneficial Use of Dredged Soil** . . . 765
M. Kitazume

**Rigid Retaining Walls Interacting with Unsaturated Soils in Axial Symmetry** . . . . . 775
Thanh Vo and Adrian Russell

**Sanding Onset for Offshore Depleted Using Critical Drawdown Pressure: A Case Study for Well X Cuulong Basin in Vietnam** . . . . . 786
Tu An Bui, Van Hung Nguyen, Tien Trung Duong, Hai Linh Duong, Huu Truong Nguyen, and Minh Hoang Truong

**Soil Stabilization by Using Alkaline-Activated Ground Bottom Ash Coupled with Red Mud** . . . . . 800
My Quoc Dang, Young-sang Kim, and Tan Manh Do

**Thermal Conductivity of Controlled Low Strength Material (CLSM) Made with Excavated Soil and Coal Ash** . . . . . 808
Tan Manh Do, Young-sang Kim, My Quoc Dang, and Ngan Thi Tuyet Vu

**Undrained Behavior of Macau Marine Clay with Various Strain Rates and Different Stress Histories** . . . . . 816
Shengshen Wu, Thomas Lok, and Annan Zhou

**Innovative Design and Methods (IDM)**

**A New Formula for the Shear Strength of Exterior RC Beam-Column Joints Using Headed Bars** . . . . . 829
Minh Tung Tran, Minh Tien Nguyen, and Quoc Bao Bui

**A Probabilistic Explicit Cracking Model for Steel Fibres Reinforced Concretes (SFRC)** . . . . . 840
Pierre Rossi and Jean-Louis Tailhan

**Achieving Robustness of Structures Is Key to Resilience** . . . . . 850
Paul Smith

**BATIPACK®: An Innovative and Ecologic Building Process** . . . . . 860
N. Matiere and Q.H. Ung

**Experimental Investigation of Bond-Dependent Coefficient of Glass Fiber Reinforced Polymer Bars** . . . . . 868
Thuy Duong Tran, Manh Hung Nguyen, and Trung Hieu Nguyen

**Experimental Research on Flexural Strengthening of Two-Way Reinforced Concrete Slabs Using Carbon Fiber Reinforced Polymer Sheets** . . . . . 878
Manh Hung Nguyen, Thuy Duong Tran, and Trung Hieu Nguyen

**Image Processing in the Characterization of Crack Propagation in Cold-Formed Steel Samples** . . . . . 885
Daniel Dias-da-Costa, Cao Hung Pham, and Gregory J. Hancock

**Impact of Measurement Errors in Inverse Analysis** . . . . . 894
Jun Lei, Jose-Antonio Lozano-Galant, Maria Nogal, Dong Xu, and Jose Turmo

**Improving the Understanding of Tunnel Excavation Under Pressure Using a Small-Scale EPBS Model** . . . . . 905
N. Berthoz, D. Branque, and D. Subrin

**Influence of Boundary Conditions on the Behavior of Infilled Frames** . . . . . 914
Quoc Khanh Le Dinh and Thanh Cong Bui

**In-Plane Behavior of Seismically Damaged Clay Masonry Walls Repaired with External TRC** . . . . . 925
Thi-Loan Bui, Xuan-Huy Nguyen, and A. Si Larbi

**Potential of Periodic Networks for Seismic Isolation of Sites** . . . . . 935
Ali Bougressi, Nouredine Bourahla, and Mohamed Anis Doufene

**Quantitatively Analysing Holistic Risk and Testing the Accident Coping Strategies** . . . . . 945
Paul Smith

**Review of Direct Strength Method of Design for Cold-Formed Steel Structures with Holes with a Focus on Shear** . . . . . 954
Song Hong Pham, Cao Hung Pham, and Gregory J. Hancock

**The Need for a Holistic Approach to Address Future Emerging Risks** . . . . . 964
Paul Smith

**Transmissibility Based Operational Modal Analysis in Presence of Harmonics** . . . . . 972
Van-Dong Do, Thien-Phu Le, and Alexis Beakou

**Unibridge®: A New Concept in Prefabricated Modular Bridge** . . . . . 981
N. Matiere, Q.H. Ung, and P.A. Nicolaudie

**Water Treatment and Environment (WTE)**

**A Modified Model for the Prediction of Bioclogging in Saturated Porous Media** . . . . . 991
Hoang Lam Pham, Philippe Sechet, and Zhujun Huang

**Modelling of Pollutant Diffusion in Unsaturated Double-Porosity Medium by a Multiscale Method** . . . . . 1000
T.D. Tran Ngoc, Q. Pham Minh, H. Ly Minh, T. Tran Van, and Thong Nguyen

**On the Use of Foam for the in Situ Remediation of Polluted Heterogeneous Soils** . . . . . 1009
H. Bertin, E. Del Campo Estrada, and O. Atteia

**Optimization of Decolorization and COD Removal from Textile Wastewater Using Electro Fenton Process** . . . . . 1017
Duc Dat Duc Nguyen, Thi Thuy Nguyen, and Tan Phong Nguyen

**Parameter Study on Remediating Cr(VI) in Water Using Activated Charcoal** . . . . . 1027
Alfa-Sika Mande Seyf-Laye, Tchakala Ibrahim, Djaneye-Boundjou Gbandi, and Chen Honghan

**Processes Causing Strong Acidic Groundwaters in and Around the Mekong Delta Area** . . . . . 1037
Quang-Khai Ha, Seunghyun Choi, and Kangjoo Kim

**Removal of Cd(II) from Aqueous Solutions Using Red Mud/Graphene Composite** . . . . . 1044
Xuan Linh Ha, Ngan Hanh Hoang, Thi Trang Nhung Nguyen, Thi Thuy Nguyen, Thanh Hai Nguyen, Van Thanh Dang, and Nhat Huy Nguyen

**Studies on the Photocatalytic Activity of Metal Oxide and Their Composite for Dye Degradation Application** . . . . . 1053
Tchakala Ibrahim, Kodom Tomkouani, M. Vedhanayagam, Alfa-Sika Mande Seyf-Laye, K.J. Sreeram, Bawa L. Moctar, and Djaneye-Boundjou Gbandi

**Treatment of Domestic Wastewater from Small Cities on Vertical Flow Constructed Wetlands (VFCWs)** . . . . . 1066
R. Gourdon, M. Kania, M. Gautier, B. Kim, and P. Michel

**Treatment of Slaughterhouse Wastewater by Intermittent Cycle Extended Aeration System (ICEAS)** . . . . . 1074
Duc Tiep Nguyen and Tan Phong Nguyen

**Urban Stormwater Management by Green Infrastructure: Design and Comparison of Three Scenarios** . . . . . 1084
Jean-Luc Bertrand-Krajewski and Pauline Herrero

**Case Studies (CS)**

**Behavior of Prestressed Concrete Self-stabilizing Floating Fuel Storage Tanks** . . . . . 1097
D. Jiang, K.H. Tan, K.C.G. Ong, S. Heng, J. Dai, B.K. Lim and K.K. Ang

**Current Concerns on Durability of Concrete Used in Nuclear Power Plants and Radioactive Waste Repositories** . . . . . 1107
Quoc Tri Phung, Norbert Maes, and Diederik Jacques

**Innovating a New Kind of Modular Reactor Power Station Design** . . . . 1122
Paul Smith

**Nuclear Civil Engineering Towards the Simplification and Digitalisation** . . . . . 1134
Nguyen-Hoang Bui, Pascal Charles, and Hervé Blieck

**Soil-Structure Interaction Under Multiple Static Loads Using a Flexibility Matrix of Soil: Case Study of a Nuclear Power Plant** . . . . . 1142
V.-N. Nguyen, P.-L. Regazzoni, D. Pham Thi Anh, S. Erlicher, S. Reynaud, and D. Allagnat

**Tunnel Muck Recycling for Road Construction – A Case Study in Vietnam** . . . . . 1153
Thu-Hang Tran and Minh-Long Le

**Author Index** . . . . . 1165

# Keynote Lectures

# A Review of Recycled Aggregates (RAP and RCA) as Unbound Base Course Material for Sustainable Highway Construction

Tuncer B. Edil(✉)

University of Wisconsin-Madison, Madison, WI, USA
tbedil@wisc.edu

**Abstract.** This paper presents a review of unbound recycled materials, specifically recycled asphalt pavement (RAP) and recycled concrete aggregate (RCA), as road base course for sustainable highway construction. A total of fifteen recycled materials were collected for characterization and testing from across the USA. Compaction characteristics and resilient moduli of these samples were determined and predictive equations were derived. Test sections were constructed using recycled materials in the granular base layers at the MnROAD test facility. Large-Scale Model Experiments (LSME) replicating field-scale conditions were also conducted and scalability of various scale modulus measurements was investigated. When compared to conventional base course, RAP and RCA experienced higher modulus. Discussion includes mechanical and durability characteristics, and leaching behavior. Sustainability evaluation of material alternatives in a project is described.

**Keywords:** Base course aggregate · Recycled asphalt pavement · Recycled concrete aggregate · Modulus · Durability · Leachate · Sustainability

## 1 Introduction

This paper presents a review of unbound recycled materials, specifically recycled asphalt pavement (RAP) and recycled concrete aggregate (RCA), as road base course for sustainable highway construction based on a comprehensive research conducted on the subject (Edil et al. 2012). RAP and RCA are the two most common recycled construction materials used as base course (Fig. 1). RAP is produced by removing and reprocessing the hot mix asphalt layer of existing asphalt pavement (Guthrie et al. 2007; FHWA 2008). RAP particles are coated with asphalt and its most value added use is in production of hot mix asphalt (HMA) with the benefit of reducing the fresh asphalt content; however, its use as unbound recycled aggregate in base course is extensive. There is some ambiguity regarding the nomenclature involved in the production of RAP. Full depth reclamation (FDR) refers to the removal and reuse of the HMA and the entire base course layer; and recycled pavement material (RPM) refers to the removal and reuse of either the HMA and part of the base course layer or the HMA, the entire base course layer and part of the underlying subgrade implying a mixture of pavement layer materials (Guthrie et al. 2007, Edil et al. 2012). Unless specified, these

© Springer Nature Singapore Pte Ltd. 2018
H. Tran-Nguyen et al. (eds.), *Proceedings of the 4th Congrès International de Géotechnique - Ouvrages -Structures*, Lecture Notes in Civil Engineering 8,
DOI 10.1007/978-981-10-6713-6_1

three distinct recycled asphalt materials are collectively referred to as RAP. RAP is typically produced through milling operations, which involves the grinding and collection of the existing HMA, and FDR and RPM are typically excavated using full-size reclaimers or portable asphalt recycling machines (FHWA 2008, Guthrie et al. 2007). RAP can be stockpiled, but is most frequently reused immediately after processing at the site. Typical aggregate gradations of RAP are achieved through pulverization of the material, which is typically performed with a rubber-tired grinder.

**Fig. 1.** Recycled asphalt pavement (RAP) and recycled concrete aggregate (RCA).

The production of RCA involves crushing structural or pavement concrete to a predetermined gradation. Fresh RCA typically contains a high amount of debris and reinforcing steel, and it must be processed to remove this debris prior to reuse (FHWA 2008). One of the value-added applications is use of RCA as a base course material although it can be used in constructing working platforms over soft subgrade and drainage medium as well as aggregate in concrete production. Depending on the crushing methods, the particle size distribution of an RCA can have a wide variability; with a lower particle density and greater angularity than would normally be found in more traditional virgin base course aggregates. Residual mortar and cement paste are typically found on the surface of the RCA, as well as contaminants associated with construction and demolition debris. The self-cementing capabilities of RCA are an interesting secondary property. The crushed material exposes un-hydrated concrete that can react with water, potentially increasing the strength and durability when used as unbound base course for new roadway construction. It follows that service life could also be extended as a result of these properties.

A survey of the state departments of transportation was conducted in the USA to better define the state of practices involving the use, storage, and testing of materials used as granular base course in roadway applications (i.e. RAP and RCA) (Edil et al. 2012). RCA was the most commonly used material, followed by RAP and recycled pavement material, RPM. However, when RAP and RPM combined accounts for a higher frequency and quantity of use than RCA. RAP and RCA are more commonly stockpiled before use while RPM is more commonly used immediately. The most common test used for specification with recycled materials is Grain Size Analysis.

To evaluate aggregate quality, the most common tests were: the California Bearing Ratio test to evaluate aggregate strength, LA Abrasion for toughness, and the Sulfate Soundness test for durability. From the survey, it was apparent that there is limited data for structural properties of RAP and RCA (i.e. no resilient modulus tests are performed routinely). The literature implied that RAP and RCA have higher resilient moduli than natural aggregate; however, a lack of in-depth studies on characterizing RAP and RCA compositionally and mechanically was indicated.

## 2 Characteristics of RAP and RCA

To identify the characteristics of RAP and RCA typically available in different parts of the country, samples were obtained from eight states: California (CA), Colorado (CO), Michigan (MI), Minnesota (MN), New Jersey (NJ), Ohio (OH), Texas (TX), and Wisconsin (WI) covering a geographically diverse area. A conventional base course meeting the Class 5 gradation standard of the Minnesota Department of Transportation was used as a control and comparison material as well as a 50/50 RCA/Class 5 blend. These materials were characterized with respect to grain size distribution, fines content, asphalt content (RAPs), mortar content (RCAs), specific gravity, absorption, and impurities. The materials, although obtained form 8 different states, had reasonably consistent properties.

### 2.1 Physical Properties

Washed sieve analyses were performed according to ASTM D 422 and specific gravity ($G_s$) and absorption tests were conducted according to AASHTO T 85. Asphalt content was determined via ASTM 6307. Materials were classified according to the Unified Soil Classification System (USCS) (ASTM D 2487). The modified Proctor compaction test (ASTM D 1557) was performed to determine the optimum moisture content ($w_{opt}$) and maximum dry unit weight ($\gamma_{dmax}$). Physical properties of the recycled materials are summarized in Table 1.

**Table 1.** Physical properties of RCA and RAP/RPM

| Properties | RCA Average (range) | RAP/RPM Average (range) |
|---|---|---|
| %Fines | 5.05 (2.01–12.8) | 0.92 (0.4–1.8) |
| %Gravel | 46.19 (32–69) | 38.38 (32–51) |
| Cu | 24.60 (8–45) | 9.80 (7–17) |
| Specific gravity | 2.31 (2.2–2.4) | 2.38 (2.34–2.57) |
| Absorption (%) | 5.52 (5.5–6.9) | 1.84 (0.6–3.0) |
| Asphalt content (%) | – | 5.9 (4.7–7.1) |
| Mortar content (%) | 50 (37–65) | |
| Classification | SP, GP, GW | SP, SW, GW |
| | A-1-a, A-1-b | A-1-a, A-1-b |

Fines content was 3–4% for RCAs except two samples and lower for RAPs, i.e., 1–2%. The mortar content was about 50% with small variation for the RCA samples and the asphalt content was about 5% with small variations for the RAP samples. The most distinguishing physical characteristics were the grain size with some samples coarser and others finer. Most samples had grain size distributions within the bounds for RCA and RAP given in the literature. A new standard developed by ASTM (D 8038 Standard Practice for Reclamation of Recycled Aggregate Base (RAB) Material) provides guidance for processing RAP and RCA as a quality base aggregate. Table 2 gives the grading requirements for aggregate base including RCA and RAP according to ASTM D 8038.

**Table 2.** Aggregate grading requirements for RAB (ASTM D 8038)

| | Design range (percentage passing by mass) | | Tolerances (percentage passing by mass) | |
|---|---|---|---|---|
| Sieve sizes (mm) | Bases | Subbases | Bases | Subbases |
| 50.0 | 100 | 100 | −2 | −3 |
| 37.5 | 95–100 | 90–100 | ±5 | ±5 |
| 19.0 | 70–92 | | ±8 | |
| 9.5 | 50–70 | | ±8 | |
| 4.75 | 35–55 | 30–60 | ±8 | ±10 |
| 0.60 | 12–25 | | ±5 | |
| 0.075 | 0–8 | 0–12 | ±3 | ±5 |

## 2.2 Deleterious Materials

The amount of deleterious materials present in RCA and RAP varied amongst the source of the materials. The most predominant impurities for RCA were asphalt aggregate, aggregate with plastic fibers, brick, and wood chips. Geotextiles and pavement markings were the predominant type of impurity in RAP. The average impurity content was 1% for RCA and 0.2% for RAP, indicating that recycling industry has developed sufficient controls. The effect of brick content on the resilient modulus and compaction of RCA was investigated at 0, 10, 20, and 30% brick by mass (Edil et al. 2012). No apparent trends were observed between modulus and brick content of RCA, but a decrease in plastic strain was observed with increased brick content. An increase in optimum moisture content and decrease in dry unit weight was observed in RCA mixed with brick at 30% compared to 0% brick. This was attributed to brick having higher absorption and lower specific gravity and density than RCA. ASTM D8038 limits deleterious materials to be no more than 1% by mass in RAB, however, brick content is allowed up to 20% by weight in RCA.

## 3 Compaction Characteristics

The compaction characteristics were also determined using the modified Proctor test. Maximum dry unit weight (MDU) varies within a narrow range of 19.4 to 21.5 kN/m$^3$ for RAP at optimum moisture contents (OMC) of 5.2 to 8.8% and 19.4 to 20.9 kN/m$^3$ for RCA at OMC of 8.7 to 11.8%. Figure 2 shows the trend of MDU versus OMC for RAP and RCA samples. The OMC of RAP was lower than RCA since asphalt coatings reduce the amount of water required to achieve MDU by preventing the water from reaching the individual particles of the material. RCA has high absorption capacity due to the porous nature of the cement paste portion. Therefore, the amount of water required to achieve the MDU for RCA is higher than for natural aggregate and RAP. Stepwise regression was performed by using multiple linear regressions to

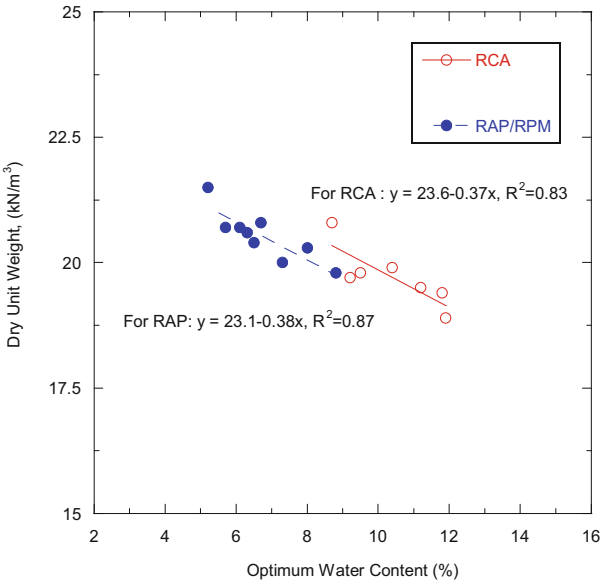


**Fig. 2.** Maximum dry unit weight versus optimum moisture content

**Table 3.** Correlations between compaction characteristics and index properties

| Materials | Compaction characteristics | Correlation equations | $R^2$ |
|---|---|---|---|
| RCA | $w_{opt}$ (%) | −0.064 * $C_u$ + 0.763 * Absorption (%) + 7.749 | 0.65 |
| | $\gamma_{dmax}$ (kN/m$^3$) | −0.373 * $w_{opt}$ (%) + 23.575 | 0.67 |
| RAP | $w_{opt}$ (%) | −0.0626 * $C_u$ − 1.349 * Absorption (%) + 9.844 | 0.92 |
| | $\gamma_{dmax}$ (kN/m$^3$) | −0.398 * $w_{opt}$ (%) + 23.264 | 0.70 |

develop correlations (models) to predict the compaction characteristics (OMC and MDU) of RCA and RAP based on their gradation characteristics as shown in Table 3 (Bozyurt et al. 2012). OMC correlates significantly with the uniformity coefficient and percent moisture absorption and MDU correlates with OMC for both RAP and RCA.

# 4 Modulus

## 4.1 Laboratory Resilient Modulus

Resilient modulus of the samples was measured on specimens at OMC and 95% modified Proctor MDU in accordance with NCHRP 1-28a (2004). The MEPDG model with 5 parameters were fitted to the test data. A summary resilient modulus (SMR) was calculated from the fitted equations at a stress level representative of the base course layer. For base course, the summary resilient modulus (SRM) corresponds to the $M_r$ at bulk stress of 208 kPa and octahedral shear stress of 48.6 kPa, as suggested in Section 10.3.3.9 of NCHRP 1-28a (2004). A comparison of SRM indicated that RAP/RPM has the highest SRM of the recycled materials evaluated. RCA has slightly lower SRM in comparison to RAP/RPM, while Class 5 aggregate has the lowest SRM. Stepwise regression was performed by using multiple linear regressions to develop correlations (models) to predict SRM of RCA and RAP based on their physical and moisture content as shown in Table 4 (Bozyurt et al. 2012). SRM is significantly correlated with $D_{30}$ and moisture content, i.e., OMC for RCA. The correlation for RAP involved other variables such as grain size characteristics (percent fines, $D_{60}$), asphalt content, specific gravity and percent absorption. Blending recycled materials with natural aggregate result in intermediate modulus between the moduli of the two materials.

**Table 4.** Correlations between compaction characteristics and index properties

| Materials | Resilient modulus (MPa) | Correlation equations | $R^2$ |
|---|---|---|---|
| RCA | $SMR_{INT}$ | $14683.478 - (36.764 * D_{30}) - (72.719 * w_{opt})$ | 0.89 |
| RAP | $SMR_{INT}$ | $_2268.783 - (285.884 * \text{Fines } \%) + (628.742 * \text{AC } \%) + (201.107 * D_{60}) - (483.158 * G_s) - (58.243 * \text{Absorption } \%)$ | 0.99 |

Note: AC = Asphalt content

## 4.2 Scalability of Modulus from Laboratory to Field

To verify the scalability of laboratory modulus to field conditions both Large-Scale Model Experiment (LSME), a large prototype-scale test developed for simulating the performance of pavement sections in a laboratory setting (Edil et al. 2012), and field

testing at MNROAD field test facility were conducted on the RAP, RCA, Class 5 aggregate, and RCA-Class 5 blend samples that were used in the base course of the MNROAD field test sections. The pavement sections, or parts of them, were loaded cyclically in the LSME to simulate field traffic loads and the resilient modulus was back calculated from the recorded response. The moduli obtained from the LSME testing were compared to the resilient moduli determined using bench-scale laboratory resilient modulus tests and the moduli from the field tests using falling weight deflectometer (FWD). FWD tests were conducted at the MnRoad facility on pavement with base course material of RAP, RCA, and a 50/50 blend of RCA/Class 5, and Class 5 aggregate to determine deflection and resilient modulus from 2009 to 2012. The back calculated moduli are given in Fig. 3, which indicate an order of stiffness similar to the one indicated by the laboratory resilient modulus tests as did the moduli from LSME. All other pavement layers except HMA (i.e. base, subbase, and subgrade) retained a relatively constant stiffness regardless of temperature. Resilient modulus has not displayed any deterioration over 4 years of observation. The scalability of the laboratory results to field conditions was addressed by adjusting the resilient modulus to reflect a comparable stress-state and strain level. The recycled granular material tested in the LSME is sensitive to layer thickness, indicating that the resilient modulus of the material is sensitive to varying strain levels as well as stress levels. After applying corrections for stress-state and strain level, the resulting low-strain moduli for FWD, LSME and bench-scale tests were determined and found to be of the same magnitude within a reasonable amount of variance as shown in Fig. 4 thus indicating the scalability of laboratory modulus to operating field modulus although the directly obtained moduli from the three methods have different values.

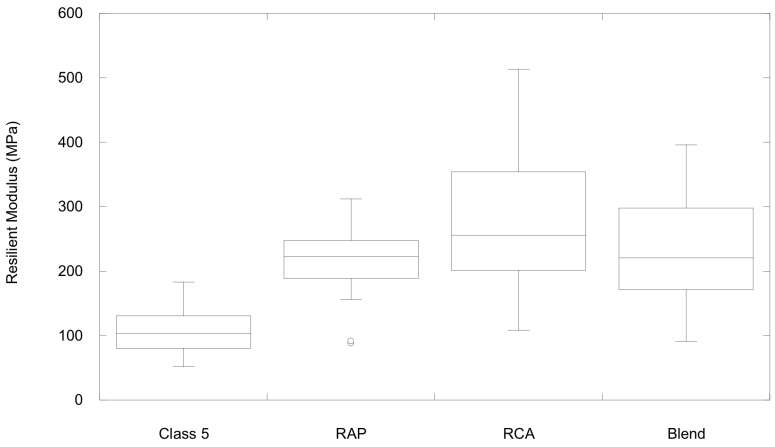


**Fig. 3.** Field modulus for all base materials

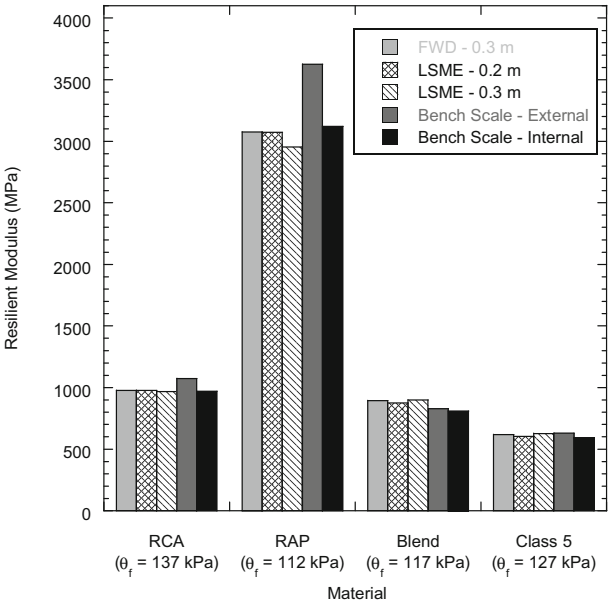


**Fig. 4.** Low-strain elastic modulus at field bulk stress (θf) for RAP, RCA, blended RCA/Class 5, and Class 5 from different test methods

## 5 Effect of Climatic Conditions

The mechanical properties of RAP and RCA were also evaluated under different climatic conditions. The effects of freeze-thaw cycling on resilient modulus, wet/dry cycling on particle degradation, and the effects of temperature on resilient modulus were all evaluated. For the freeze-thaw cycles, a decrease in stiffness was observed in RAP after five cycles and further decrease was observed at 10 and 20 cycles. Class 5 aggregate (the control) saw a decrease in stiffness with increasing freeze-thaw cycles, but overall a lower percentage of decrease than RAP. The RCA specimens saw a decrease in stiffness after the first five freeze-thaw cycles, but then an increase in stiffness after 10 and 20 freeze-thaw cycles. Overall, both RAP and RCA had higher stiffness than Class 5 regardless of the number of freeze-thaw cycles.

To evaluate the effects of temperature on resilient modulus of RAP and RCA, specimens were tested using NCHRP 1-28a protocols at 7, 23, 35, and 50 °C (Soleimanbeigi et al. 2015). Essentially no decrease in SRM was observed in the RCA and natural aggregate specimens tested, but a decrease of approximately 30% was observed in the RAPs tested between the 23 and 35 °C temperatures as shown in Fig. 5. An increase in strain rate and cumulative plastic strain with temperature was also observed in all RAPs, but was not present in the natural aggregates or RCA specimens.

Micro-Deval and particle size distribution tests were conducted on RAP, RCA, and natural aggregate after 5, 10, and 30 wet/dry cycles and no apparent trend was found between particle degradation and wet/dry cycling of the material (Edil et al. 2012).

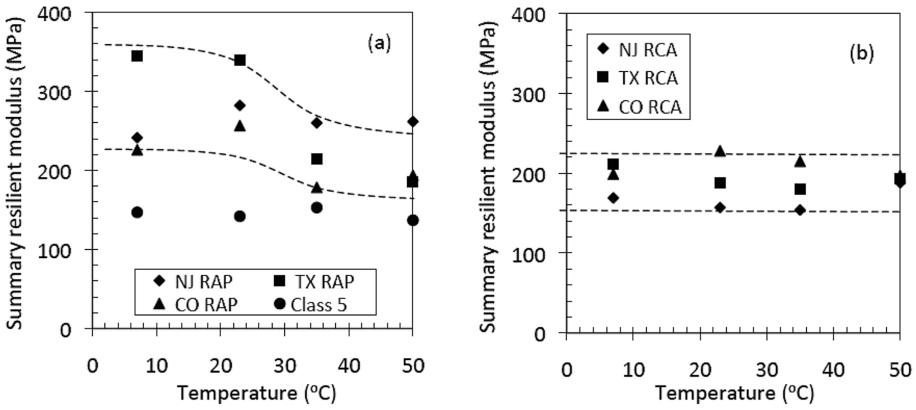


**Fig. 5.** Variation of summary resilient modulus with temperature for RAP (a) and RCA (b) (Soleimanbeigi et al. 2015).

## 6 Hydraulic Properties

The hydraulic properties of RAP and RCA were investigated by determining their unsaturated hydraulic conductivities and also generating their soil-water characteristic curves (SWCCs) fitted with the van Genuchten and Mualem-van Genuchten models (Nokkaew et al. 2012, 2014). All materials had high drainage capacities. RAP had the best drainage capacity due to the hydrophobic nature of the asphalt coating while RCAs tended to have the best ability to retain water because of its hydrophilic cement mortar. It was found that increasing the gravel content decreased the air entry pressure in recycled and natural aggregates while increasing the fines content increased the air entry pressure.

## 7 Leaching Characteristics

Samples of RCA and RAP were tested in the laboratory to determine their pH and leaching characteristics (Chen et al. 2013). Additionally, lysimeters were placed under the base course including RCA and RAP in the field test sections and leachate samples were collected periodically to track the effluent pH and released metals during the base course service life in the field. Although the MNROAD site showed a consistently neutral pH (6.6 to 8.0 l) for RCA which is different than that observed in the laboratory column leaching tests using the same RCA and 4 other RCA materials (pH = 10.8 to 12.5) and as well as at another test site, the Madison field site, where pH = 12.9. The reasons are not known for this observation. As, Cr, Pb, and Se exceeded the maximum contaminant levels (MCLs) for the USEPA drinking water standard both at the Madison field site and in the laboratory column leaching tests on RCA. However, the MNROAD site concentrations of As, Pb, and Se for RCA were observed to exceed the corresponding MCL only once or twice and the leaching behaviors were similar to that of Class 5 aggregate. As and Cr appear to be mainly sourced from the cement mortar based on the acid digestion results. The oxyanions (As, Se, and Cr) should be given

more attention to as they demonstrate enhanced leaching in a highly alkaline environment. For RAP, concentrations of As, Se and Sb were slightly higher than the corresponding USEPA groundwater maximum contaiminant level (MCL), otherwise the RAP leachate indicated no predicted risk. Brown et al. (2015) conducted indirect analyses that assess the field conditions more realistically at a point of compliance (POC) such as at the right of way of the road (e.g., 20 m from the center line) using the field lysimeter data obtained directly under the roadway as input to a hydrologic modeling software (WiscLEACH by Li et al. 2006). These analyses imply that trace element elution from roadways employing recycled materials demonstrate no risk, no additional risk, or no predicted risk to the surrounding surface and drinking water quality and the use of recycled materials are considered to be suitable beneficial reuse applications with respect to water quality.

## 8 Assessment of Sustainability

Assessment of sustainability involves the life cycle assessment (LCA) of the environmental benefits and the life cycle cost analysis (LCCA). LCA involves determining a variety of sustainability metrics (e.g., energy consumption, GHG emissions, water use, hazardous waste generation, etc.) associated with production of construction materials, their transportation to the construction site, and construction itself. These determinations can be made using available database programs such as the PaLATE model (Horvarth 2004). LCCA evaluates life cycle cost of design alternatives including the initial construction and maintenance based on service life. A convenient computer code named RealCost can be used for this purpose (FHWA 2004). Service life is a crucial part of this analysis and materials with higher modulus typically result in a longer service life for the same thickness of pavement layers.

A rating system for sustainable highway construction, named Building Environmentally and Economically Sustainable Transportation-Infrastructure-Highways, BE$^2$ST-in-Highways$^{TM}$ was developed to provide a quantitative methodology for rating the benefits of sustainable highway construction (Lee et al. 2013). The methodology is grounded in quantitative and auditable metrics so that a transparent linkage exists between the project rating and the sustainable practices employed in construction. This rating system can be employed by the highway construction industry and agencies to quantitatively evaluate sustainable practices and to incorporate sustainable elements into projects.

The BE$^2$ST-in-Highways$^{TM}$ system evaluates sustainability of a highway project in terms of a quantitative difference between a reference design and proposed alternative design(s). Thus, the reference highway design must be defined realistically. A conventional design approach in which sustainability concepts are not incorporated explicitly can be used as a reference design. An example is shown in Fig. 6. LCA and LCCA analyses for the designs shown in Fig. 6 indicated 20% reduction in $CO_2$ emissions, 16% reduction in energy consumption, and 21% savings in life cycle costs as a result of using the alternative recycled materials design. If recycled materials are also incorporated in the HMA layer (e.g., 15% RAP and 5% recycled asphalt shingles, RAS) the environmental and cost savings would further increase (Lee et al. 2010). The analysis assumes that the service life of conventional and alternative designs can be

based on an international roughness index (IRI) prediction made with the Mechanistic Empirical Pavement Design Guide (M-EPDG) program (NCHRP 2009) and that rehabilitation occurs at the end of the predicted service life.

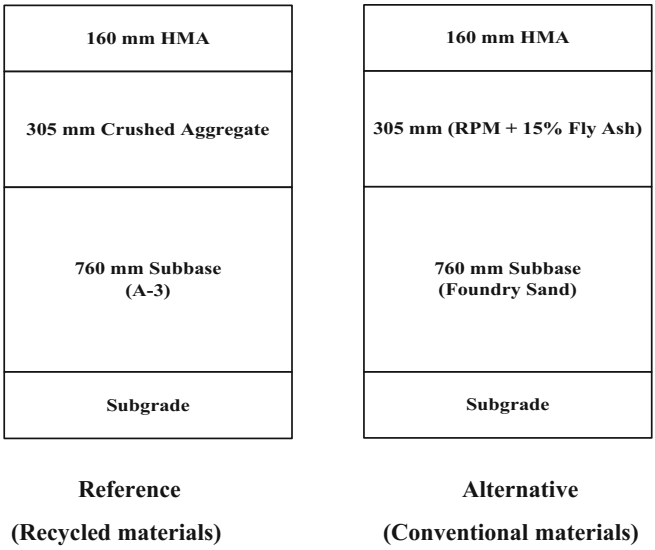


**Fig. 6.** Schematic of two designs

## 9 Conclusions

The extensive investigation undertaken on RCA and RAP indicate that these materials are suitable for unbound base course applications. They show equal or superior performance characteristics compared to natural aggregates in terms of stiffness, freeze-thaw and wet-dry durability, and toughness. Their typical compositional and mechanical properties and their variability are defined in this study providing a basis for design considerations. Their relative differences from natural aggregate such as temperature sensitivity, plastic deformations, and water absorption and retention characteristics are also well established.

1. It is imperative that industry-wide sustainable construction practices be adopted and recycled materials play a significant role in earthen construction where large quantities of materials are used such as in roadway construction.
2. Benefits of recycled materials include reduction in greenhouse gas emissions, energy, natural resources, and cost.
3. Wise use of recycled materials may create longer lasting structures and reduction in cost however their specific aspects need to be considered such as temperature sensitivity of RAP and high pH of RCA leachate.
4. Conducting quantitative analyses using appropriate sustainability metrics to assess alternatives involving recycled materials is imperative.

**Acknowledgements.** The information and ideas presented were developed through numerous projects involving many associates and students, too long to list here. Prof. Craig H. Benson and the Recycled Materials Resource Center are acknowledged.

## References

Bozyurt, O., Tinjum, J.M., Son, Y.H., Edil, T.B., Benson, C.H.: Resilient modulus of recycled asphalt pavement and recycled concrete aggregate. In: GeoCongress 2012, pp. 3901–3910. ASCE, GSP No. 225, Oakland (2012)

Brown, B., Bradshaw, S., Edil, T., Benson, C.: Leaching from roadways stabilized with fly ash: data assessment and synthesis. Paper presented at the 2015 World of Coal Ash (WOCA) Conference, Nashville, TN (2015). http://www.flyash.info/2015/011-brown-2015.pdf

Chen, J., Tinjum, J.M., Edil, T.B.: Leaching of Alkaline Substances and Heavy Metals from Recycled Concrete Aggregate Used as Unbound Base Course. Transp. Res. Rec.: J. Transp. Res. Board **2349**, 81–90 (2013)

Edil, T.B, Tinjum, J.M., Benson, C.H.: Recycled unbound materials. TPF-5 (129) Final Report. MNDOT, MN, USA (2012)

FHWA: User Guideline for Byproducts and Secondary Use Materials in Pavement Construction. FHWA-RD-97-148, VA, USA (2008)

FHWA: Life Cycle Analysis RealCost User Manual. VA, USA (2004)

Guthrie, S.W., Cooley, D., Eggett, D.L.: Effects of reclaimed asphalt pavement on mechanical properties of base materials. J. Transp. Res. Board, 44–52 (2007). NRC, No. 2005, Washington, D.C.

Horvath, A.: Pavement Life-cycle Assessment Tool for Environmental and Economic Effects (PaLATE) User Manual (2004). http://rmrc.wisc.edu

Lee, J.C., Edil, T.B., Tinjum, J.M., Benson, C.H.: Use of $BE^2ST$ in-highways for green highway construction rating in wisconsin. In: Green Streets and Highways. American Society of Civil Engineers, T&DI, (CD-ROM) (2010)

Lee, J.C., Edil, T.B., Benson, C.H., Tinjum, J.M.: Building environmentally and economically sustainable transportation infrastructure: green highway rating system. J. Constr. Eng. Manag. **130**(12), A4013006:1–10 (2013)

Li, L., Benson, C., Edil, T., Hatipoglu, B.: WiscLEACH: a model for predicting groundwater impacts from fly-ash stabilized layers in roadways. In: DeGroot, D., DeJong, J., Frost, J., Baise, L. (eds.) Geotechnical Engineering in the Information Technology Age. ASCE (2006)

NCHRP: Laboratory Determination of Resilient Modulus for Flexible Pavement Design. NCHRP Research Results Digest (2004)

NCHRP: Mechanistic-Empirical Design of New & Rehabilitated Pavement Structures Version 1.00. NCHRP (2009). http://www.trb.org/mepdg/software.html

Nokkaew, K., Tinjum, J.M., Benson, C.H.: Hydraulic properties of recycled asphalt pavement and recycled concrete aggregate. In: GeoCongress, pp. 1476–1485. ASCE, Oakland (2012)

Nokkaew, K., Tinjum, J.M., Likos, W.J., Edil, T.B.: Effect of matric suction on resilient modulus for compacted recycled base course in postcompaction state. J. Transp. Res. Board, (2433), 68–78 (2014). Paper No. 05-1395, National Research Council, Washington D.C.

Soleimanbeigi, A., Shedivy, R.F., Tinjum, J.M., Edil, T.B.: Climatic effect on resilient modulus of recycled unbound aggregates. Road Mater. Pavement Des., 1–18 (2015). doi:10.1080/14680629.2015.1060250

# Effective Slab Width for Evaluating Ultimate Seismic Capacities of Reinforced Concrete Buildings

Toshimi Kabeyasawa[1(✉)] and Toshikazu Kabeyasawa[2]

[1] Earthquake Research Institute, University of Tokyo, Tokyo, Japan
kabe@eri.u-tokyo.ac.jp
[2] Metropolitan University of Tokyo, Tokyo, Japan
tosikazu@tmu.ac.jp

**Abstract.** A series of static and seismic loading tests of reinforced concrete frame assemblies were conducted in 2010, 2012, 2013 and 2014 to identify the effects of slab for evaluation of seismic capacities of reinforced concrete buildings as part of national research projects for review of the technical standards on seismic design practices in Japan. Two-fifth or half scale seven specimens were tested representing three-dimensional reinforced concrete beam-yielding frames with floor slab. A special loading set-up was invented and used to simulate the boundary conditions of the medium-story frame so that the axial elongation of the beams would not be constrained by the reaction supports consisting of pin-fixed and pin-roller. It was generally found from the series of tests and analyses that the slab reinforcing bars were increasing almost uniformly through the whole slab width and was fully effective to the flexural strength of the beams at around one percent story drift. The observed and calculated beam strengths with the full width of slab was much higher than those with the effective slab reinforcing bars assumed in the current design practice.

**Keywords:** Slab · Effective width · Beam · Reinforced concrete · Seismic design

## 1 Introduction

The seismic performance of reinforced concrete buildings in Japan shall be verified through a standard design procedure in two phases by checking the serviceability in the first phase and the safety in the second phase in accordance with the Building Standard Law of Japan, pertinent regulations and design code of practice. The ultimate lateral load carrying capacity is checked against the demand which is equivalent to the response under a very rare event based on static pushover analysis taking inelastic deformation capacities and the collapse mechanism into account. An overall and ductile beam-yielding collapse mechanism is to be selected mostly for medium- to high-rise reinforced concrete buildings, where the effects of the floor slabs are significant in the evaluation of the beam ultimate flexural strengths. A series of static and seismic loading tests of reinforced concrete frame assemblies were planned and conducted in 2010, 2012, 2013 and 2014 to identify the effects of slab as part of national research projects for review of the technical standards on seismic design practices in Japan.

© Springer Nature Singapore Pte Ltd. 2018
H. Tran-Nguyen et al. (eds.), *Proceedings of the 4th Congrès International de Géotechnique - Ouvrages -Structures*, Lecture Notes in Civil Engineering 8,
DOI 10.1007/978-981-10-6713-6_2

Three specimens in the first series of 2010 were two-fifth scale three-dimensional reinforced concrete beam-yielding frames with floor slab consisting of four columns and two frames in both directions. The high strength materials were used representing high-rise buildings. A special loading set-up was invented and used to simulate the boundary conditions of the medium-story frame so that the axial elongation of the beams would not be constrained by the reaction supports at the columns. One of the two specimens was repaired and tested again in 2012 to verify the seismic performance after repair. Three specimens tested in 2013 and two in 2014 using normal strength materials to represent medium-rise reinforced concrete frame buildings with different parameters. The damage patterns as well as the lateral resistances of the frames in various inter-story drift ratios were investigated considering the contributions of the slab to the beam resistance to reconsolidate the current design practice. Here are reported in this paper an outline and backgrounds of the test series, the test results in 2013, new findings from the serial tests and analyses, and design implications derived from the test series, such as effective slab widths for analytical modelling and evaluating ultimate strength of beams in seismic design in relation with drift responses.

## 2 Effective Slab Widths in Design and Tests

The effective slab width in the elastic analysis for the first phase design is prescribed in the AIJ guidelines [1] as approximately one tenth of the beam longitudinal length, as shown in Fig. 1(a). The effective slab width is evaluated mainly to derive the equivalent stiffness of T-beam section in the frame model for linear analysis, while the effects of slab reinforcing bars on the flexural strength is normally neglected during the first phase design. On the other hand, the effective slab width is taken as a constant length of 1.0 m on each side of the beam for the pushover analysis in the second phase design [2], as shown in Fig. 1(b). The slab reinforcing bars within the effective width may be taken into account for the evaluation of the ultimate flexural strengths of the beams. However, only the slab reinforcing bars in the upper chord have been counted in practice when the slab is in tension neglecting the slab bars in the lower chord because the anchorage lengths of the lower chord bars have been regarded as insufficient to develop the full tensile strength in accordance with the normal practice of construction details.

The standard assumptions for the effective slab width described as above have been used commonly in analytical models and strength evaluation, not only for static analyses of low and medium rise buildings in the two design phases, but also for time-history response analyses of high rise buildings.

(a) Effective slab width for the first phase design (b) Effective slab width for the second phase design

**Fig. 1.** Effective slab width for beams in the Japanese seismic design code of practice

The assumptions above on the effective slab widths, especially those for the second phase evaluation, seemed to be conservative because most of past tests on beams with slab or one column sub-assemblage tests performed in 1980s or early 1990s [3–6] showed much higher effects on the beam flexural strengths at the ultimate deformations. However, the effective widths observed in the tests were gradually increasing with the inelastic drift amplitudes to attain wider widths so that the design practices have still been maintained as above. On the other hand, the effectiveness of slabs have also been examined through recent laboratory tests on full-scale building structures under static, pseudo-dynamic, or dynamic loading [7–10], where the measured overall capacities were close to those calculated by assuming the full span slab width in most cases. It should be noted that the conservative evaluation on the effective slab widths may not always be safe from the viewpoint of ensuring flexural failure mode and/or beam yielding mechanism in the structure. Therefore, it is important to take in account a probable effective slab width in the seismic design calculations, especially, in the assurance design to estimate beam shear and column actions in the overall beam yielding mechanism. Not only the ultimate strength but also the hysteretic relations of the beam-slab component could be different from the current models for time-history response analysis. Therefore, the seismic performance of the beams with floor slabs need be further verified through realistic tests and analyses.

## 3 New Method of Testing Beam-Column Assembly with Slab

Based on the review of past test research, a new loading method of testing frame assembly with slab was planned and applied to validate the effectiveness of the floor slab on the beam in the current design evaluation including frame analyses. In the first 2010 project, a thirty-story building was selected as a proto-type design for the test specimens. The two-fifth scale specimens were designed and constructed, as shown in Fig. 2(a) and in the attached photo, representing part of interior frames with floor slab in a middle story of the proto-type building. Four columns from lower mid-height to upper mid-height and the beams with floor slab of one span and two half spans in each direction were extracted.

A series of three-dimensional frame tests were carried out under static cyclic lateral loading to investigate the hysteretic behavior with the contribution of the slab in the beam-yielding frames. A special loading set-up was invented to be used for the frame assembly. The four columns were loaded laterally and independently at mid-height of upper story and supported at mid-height of lower story with pin-fixed and pin-roller so that axial elongation of the beams and the slab would not be constrained by the lateral forces, as shown in Fig. 2(b). Also, special consideration was made with respect to the boundary conditions at the mid-height columns so that the axial elongations in the beams were not constrained.

Beam resistance including the slab might be different at interior and exterior beams. It is expected at the interior beams that axial elongation would occur due to cracking, as shown in Fig. 2(b), so that the slab reinforcement could be effective simultaneously with the beam reinforcement over the full width of slab as the reaction of the beam compressive force. On the other hand, the effectiveness of the slab at the exterior beam would occur at larger deformation due to the boundary condition at the end.

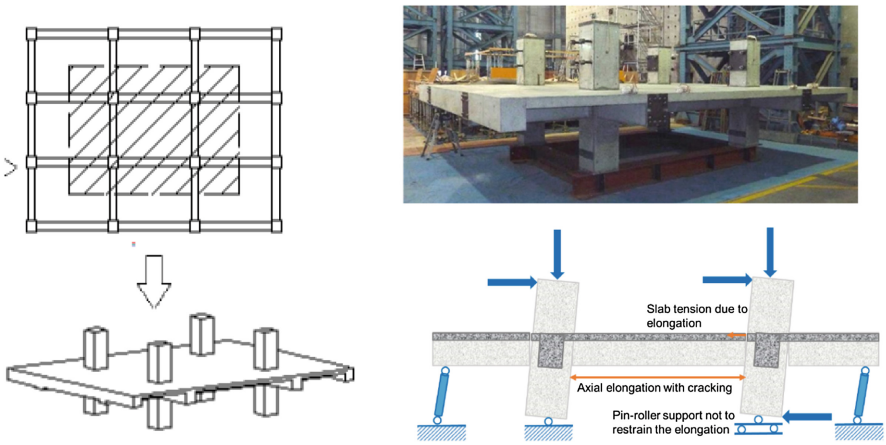


(a) Assembly model with floor slab (b) New loading system and mechanism allowing axial elongation

**Fig. 2.** Assembly model and loading method representing part of floor in multi-story frame with expected mechanism

Two specimens were tested in the first 2010 test series with the only difference being the slab reinforcement ratios. The detailed test results and the problem in the testing method have been discussed in Japanese [11], while the test results and the contribution of the slab to the beam resistance are outlined here with the calculated strengths.

## 4 Frame Test with Slab

### 4.1 Slab Assembly Specimen

The specimens were reduced by two-fifth scale from the sections and reinforcement details of the original design of the thirty-story proto-type building to make the reinforcement diameter and spacing as equivalent as possible. Two specimens, No. 1 and No. 2, were constructed and tested, where the slab reinforcement ratios were varied. The common geometric sizes of the specimen are shown in Fig. 3(a). The height of the specimen was 2010 mm with 1085 mm upper columns and 925 mm lower columns measured from the center of the beam, though the story height was 1360 mm between the lower to the upper mid-height for loading. In the longitudinal direction, the center-to-center middle span length was 3200 mm, while the center-to-end half-span was 1600 mm. In the transverse direction, the center-to-center middle span was 2500 mm, while the center-to-end half-span was 1250 mm. The column sectional dimensions were 400 mm by 400 mm. The width of the main beams was 300 mm and a depth of 360 mm in two directions. The transverse beams of 220 mm by 290 mm were placed for loading at the two ends assuming the inflection point at the middle of the continuous beam span in both directions. The slab thickness was 100 mm.

The reinforcement details are shown in Fig. 3(b). Deformed bars with the diameter of 6 mm (D6) and the nominal yield strength of 295 MPa (SD295) were placed at the

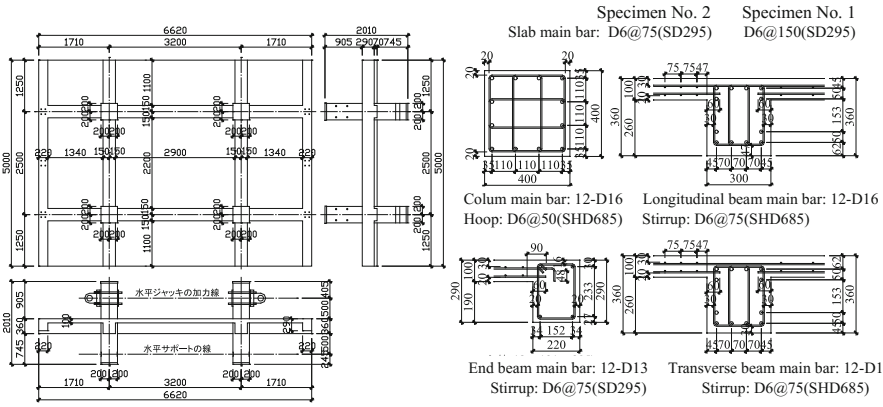


(a) Geometry of the specimens

(b) Reinforcement details in columns and beams

**Fig. 3.** Design of the specimen No. 1 and No. 2 in the first test series

spacing of 150 mm and 75 mm at both upper and lower chords (2-D6@150 and 2-D6@75) in both directions, for the specimen No. 1 and No. 2, respectively. The main bars of the columns were 12-D16 (SD490) with the gross sectional ratio of 1.51% and the column hoops were 4-D6@50 (SHD685). The beams had 6-D16 at the top and 6-D16 at the bottom (SD490) as main bars with the gross sectional ration of 2.23%, both arranged in two layers as shown in the figure. The stirrups in the beams were D6@50 (SHD685). The main bars of the columns and beams were welded to the steel plates at the ends. The concrete was cast in three stages, consisting of: (1) lower columns and joints, (2) beams and slabs, and (3) upper columns. The construction joints were placed about 75 mm away from the column faces with wire mesh.

## 4.2 Material Properties

Material tests were conducted at the date of testing. Relatively high strength materials were used for both steel and concrete in the specimen to represent the design of the proto-type high-rise building. The actual material properties from the tests are shown in Table 1. D16 bars used as the longitudinal reinforcement for beams and columns had a distinct yield plateau region in the stress-strain results, while the yield plateau of the D6 bars used as the reinforcements of slabs and hoops were not apparent.

**Table 1.** Material properties of concrete and reinforcing steel bars

| Concrete | | | | | Steel bars | | | | | |
|---|---|---|---|---|---|---|---|---|---|---|
| Concrete cast part of the specimen | Nominal strength | Comp. strength | Strain at strength | Elastic modulus | Nominal diameter | Nominal strength | Yield strength | Yield strain | Elastic modulus | Max. strength |
| | $N/mm^2$ | $N/mm^2$ | $(\times 10^{-6})$ | $N/mm^2$ | | | $N/mm^2$ | $(\times 10^{-6})$ | $N/mm^2$ | $N/mm^2$ |
| Lower column | Fc60 | 74.6 | 3016 | 35530 | D16 | SD490 | 550.2 | 3277 | 204990 | 707.9 |
| Beam and slab | Fc48 | 58.7 | 2730 | 31420 | D6 | SD295 | 371.5 | 3981 | 185907 | 541.4 |
| Upper column | Fc48 | 56.0 | 2549 | 31170 | D6 | SHD685 | 712.8 | 5840 | 186305 | 910.1 |

### 4.3 Loading Methods

The loading setup is illustrated in Fig. 4(a) and an overview photo is shown in Fig. 4 (b). The two columns on the south side were supported with pin ends assuming the inflection points as mid-height of lower columns, while the two columns on the north side were supported with pin-roller ends, so that the axial deformations would not be restrained by the axial forces caused by the beam and slab elongation increasing with the inelastic deformations. The transverse beams at both ends of the outside half-spans were supported in the vertical direction with the pin-end jacks and the load cells simulating the inflection points at the mid-span. H-shaped steel beams of 200 mm by 200 mm size were appended to increase the stiffness and strength at the top of both end beams additionally. A constant axial load of 990 kN was applied at each top of the four columns using vertical actuators with pin-connected to the column at the bottom end and roller support at the top end of the actuators, which could move freely by four 2-D roller supports attached to two big steel beams on the top. Seismic loads were applied to the tops of the columns using four jacks and to the pin roller supports at north side were also loaded by two jacks. The pin supports were fixed to the concrete base.

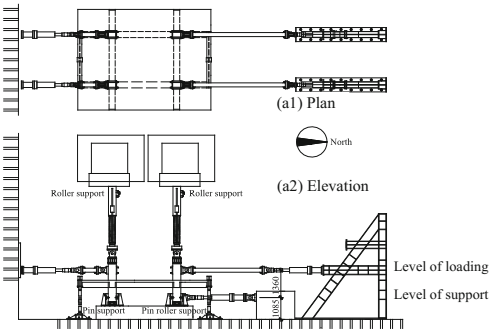


(a) Plan and elevation of loading set up

(b) Structural testing laboratory, Building Research Institute, Tsukuba

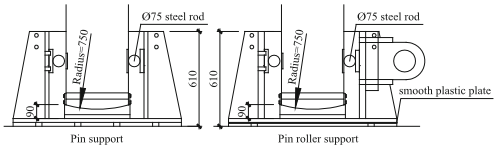


(c1) Pin support (c2) Pin roller support

(c) Details of pin support and pin-roller support

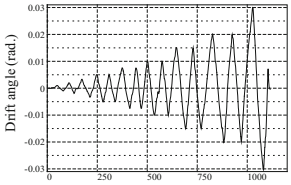


(d) History of loading in story drift ratio for No. 2

**Fig. 4.** Loading methods

The details of the pin and pin roller supports at the column bases are shown in Fig. 4(c). The steel footing of pin support was fixed on the foundation, while the steel footing of pin roller support was just placed on a smooth plastic plate so that transversal movement was allowed. Steel rods of 75 mm diameter welded on the steel footing were

attached to the column faces to apply horizontal force or reactions. Two smooth steel curve face plates with a radius of 750 mm were manufactured. One was connected to the column bottom, and another one was just put under it and could move freely with the rotation of column. However, during the test these supports did not work as well as anticipated due to unexpected movement in larger cyclic deformations and the friction or precision of manufacture, by which eccentric reaction of axial load occurred. The correction method of these errors is described in details elsewhere [11].

To simulate the vertical loads of high-rise buildings in testing, an axial force of 990 kN was applied to each column and kept constant automatically by the four vertical actuators. The averaged compressive stress in the column section was 0.084 times the concrete strength corresponding ten stories in the upper level. Then static lateral cyclic forces were applied with six lateral oil jacks. The south jacks and the north jacks were operated independently. The north jacks of upper and lower stories were operated to keep the same level but in the opposite directions by the common oil pressure, while the story drift angles of the south columns were synchronized to those of the north columns controlled manually through the instantaneous feedback data from the lateral displacement gauges at the upper and lower loading level of each column. Number of cyclic loading was selected as common with the other component tests in the project. Enough large numbers, such as ten times of cyclic load reversals in 0.5 and 1.0% story drift angles, were selected based on the simulation of the responses of high rise buildings under design long period of motion with long duration. However, the first specimen showed sufficient ductile behavior in flexural even under ten repetitions of cyclic loading. Therefore, for the second specimen reported here was loaded in accordance with the history shown in Fig. 4(d) consisting of two cycles at each peak drift. The maximum drift was amplitudes of 0.06 rad for the first specimen, while terminated at 0.03 rad for the second specimen by observing the damage levels regarded as nearly the reparable limit state. Then the second specimen here was repaired and tested again in the ERI laboratory in the next year.

### 4.4 Instrumentations

Local deformations and strains in reinforcement were measured by displacement gauges and wire strain gauges as dense as possible. Lateral displacements of each column were measured at the top and the bottom of loading levels, also at the floor level, from which lateral deflection of columns and overall elongations were derived. Local axial deformations, or elongations, rotations were measured on the surfaces of slab and beams and also on the column side faces using displacement gauges and sliding pipes with universal joints at each end. Relatively dense measurement was planned at the slab surface at the critical sections to drive slab effects by the distribution of axial elongations at the sections. The strains were measured on the reinforcement in the beam and the slab not only at the critical sections but also at points away from the critical sections.

# 5 Test Results on Bare Specimens

## 5.1 Observed Cracks

The crack pattern observed in the east beam side of the specimen No. 2 at the 1/200 cycle and 1/100 cycle are shown in Fig. 5(a) and (b), respectively. At the 1/100 cycle, cracks were observed on the column side faces above the joints, and the number and width of cracks increased with the increasing of story drift. However, no cracks were found on the column side faces below the joints during the entire test. The cracking of the column was minor due to high axial load and high flexural strength.

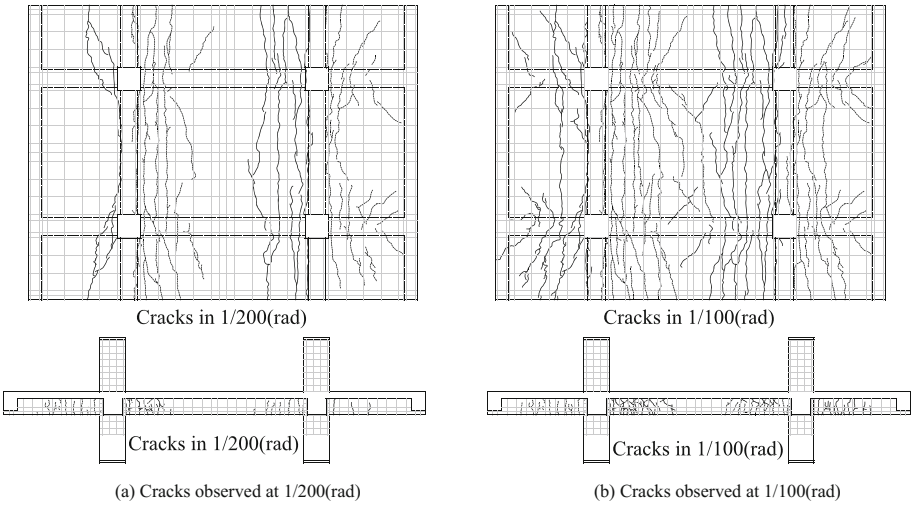


**Fig. 5.** Cracks at the story-drift angle of 1/200 (rad) and 1/100 (rad) of specimen No. 2

Cracking of the slab observed on the top face at the peak of the 2/1000 cycle. The initial cracks on the slab face immediately penetrated to the whole width of slab and the cracking could also be observed at the bottom face. The cracks on the inner span were perpendicular to the longitudinal beams or parallel to the transverse beams, while the cracks on the on the outer half-spans were inclined, as shown in the figures. On the other hand, the cracks on the slab that propagated into the inner beams tended to incline vertically, while relatively vertically parallel in the outer span beams. These might be because of the boundary conditions and associated resistance mechanisms, which were different between the inner and outer spans.

## 5.2 Local Deformations and Strains

Distributions of the longitudinal elongations in the inner span measured on the slab surface of the south half span and the west half region are shown in Fig. 6. The

elongations are shown as unit length in mm at each negative peak drift when the slab is in tension. Maximum elongation was observed at the location of the beam and relatively smaller at the edge or at the center of slab, though 80% even at the edge, which may be regarded as nearly uniform distribution across the critical section. This is also the case through the transition from elastic to inelastic response, which indicates that the slab reinforcement could be uniformly effective at full span to the yield and ultimate strength of beam.

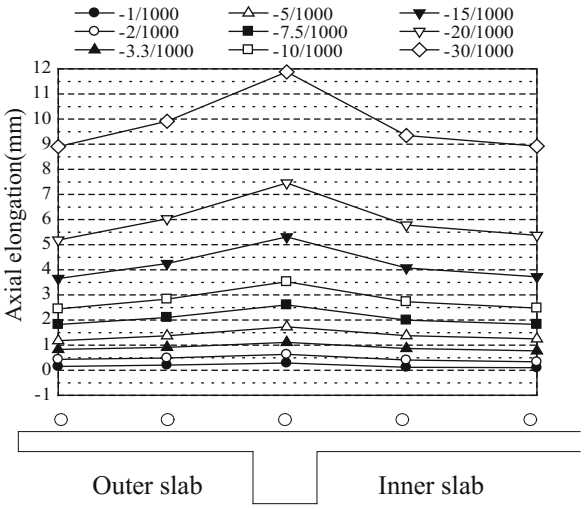


**Fig. 6.** Distributions of axial deformations on the slab for south and west half span of the inner beam (No. 2)

Strains in the slab reinforcement at the critical sections of the inner span beam were measured at three different locations at the distance of 0 mm, 150 mm and 300 mm inside from the critical section at the column face line, 50 mm apart from the side face of the transverse beams. The slab reinforcement started to yield at a story drift of 1/300 rad. The yielding was also observed in the lower chord slab reinforcement, although it has been neglected in design due to an insufficient anchorage length of 10d. The strain and stress distributions measured at 150 mm apart from at the critical section for peak drifts are shown in Fig. 7(a) and (b), respectively. It may be concluded that most of the slab reinforcement attained near yield stress (371 N/mm$^2$) almost uniformly at the critical section until a story drift of 1/100.

The observation and measurement for local deformations and strains indicated that the slab reinforcement could probably be working at stress levels close or equal to the yield stress of the steel material along the critical section with the full span width even around the yielding deformation of the beams.

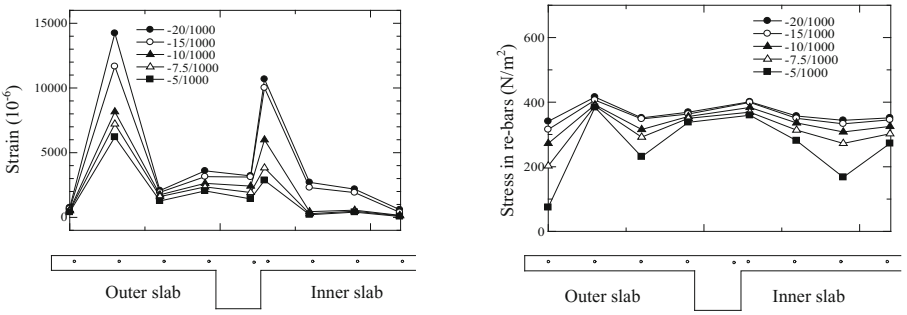


(a) Measured strains (b) Stress distributions derived from measured strains

**Fig. 7.** Strains and stresses in the slab reinforcement at the critical sections of the inner span beam at peak drifts (No. 2)

### 5.3 Evaluation of Overall Hysteresis and Beam Strengths

The overall hysteretic response for story shear force vs. story drift ratio are shown in Fig. 8. The shear force is the sum of the lateral shear forces of the four columns directly derived from the load cells at the column tops. The calculated strengths are also shown in the figure, which considers the additional base moment. The moments at the bases are estimated from the measured deflections of the columns which remained in elastic region, and were subtracted from the measured lateral resistance by the load cells, to identify the actual resistance of the specimen or the beam strength. The method has been reported in detail elsewhere. In cases of the tests in the following series from 2012 to 2014, the details at the base supports were improved so that the base moments in the columns were negligible small and above correction became unnecessary.

The ultimate strength calculated by the code specified design procedure of phase II is 1217 (kN) for the specimen No. 1 and 1264 (kN) for the specimen No. 2, shown with dotted lines in the figure, where the design effective slab width of 400 mm as two-fifth scale specimen is assumed, which corresponds to 1.0 m for full scale on one side slab as illustrated in Fig. 1(b). In this case, only the upper chord slab reinforcing bars within the effective width are considered. In both cases, the measured material yield strengths

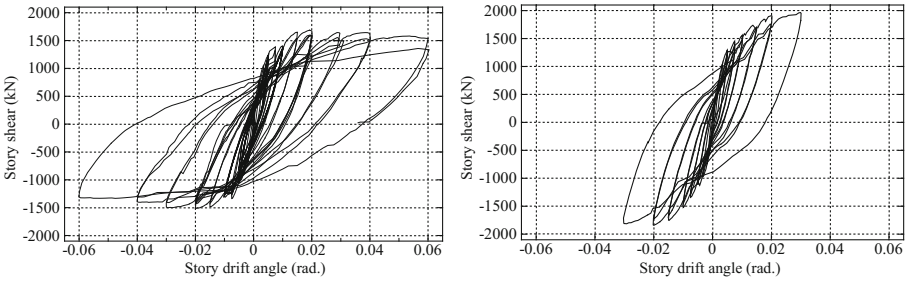


(a) Specimen No. 1 (b) Specimen No. 2

**Fig. 8.** Hysteresis relations of overall story shear and story drift

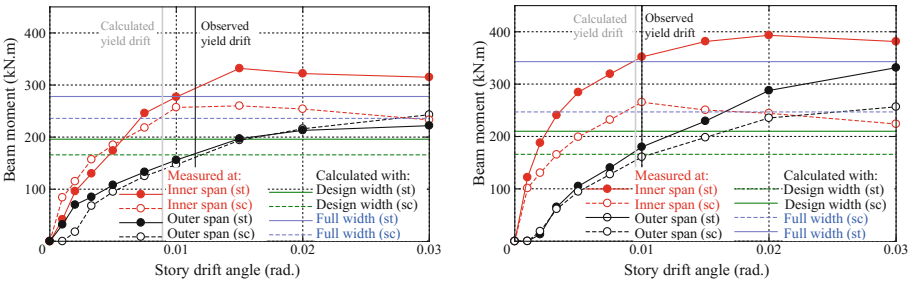


(a) Specimen No. 1 (b) Specimen No. 2

**Fig. 9.** Measured and calculated flexural resistances at the beam critical sections

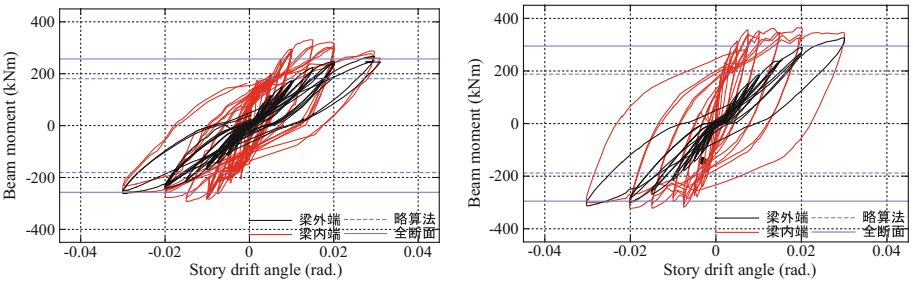


(a) Specimen No. 1 (b) Specimen No. 2

**Fig. 10.** Hysteretic relations of beam sections at inner ends and at outer ends

are used as shown in Table 1. The observed resistances of both specimens exceeded the code specified calculation above even at less than 1/200 story drift. The measured maximum capacities of the frame exceeded the code calculation by more than 1.5 times at around the drift of 3/100 rad.

The flexural strengths were calculated by assuming the full width of the slab and compared with the measured moments at the four critical sections of the beams. The measured moments were statically identified as the moment diagram from the applied lateral forces measured with the load cells. The initial skeletons are shown in Fig. 9 and the hysteretic relations with the overall story drift in Fig. 10. The measured moment resistance at the critical section in the positive loading direction shown with four lines with circles in Fig. 9 as show with: (1) the red solid line shows the moment at the inner span with the slab in tension, (2) the red dashed line shows the moment at the inner span with the bottom edge in tension, (3) the black solid line shows the moment at the outer span with the slab in tension and (4) the black dashed line shows the moment at the outer span with the bottom edge in tension.

On the other hand, the calculated flexural strengths of the beams with slab are also shown in both cases of the design width calculation and the full width calculation. The design width calculation is based on the design equation and only by using the upper slab reinforcement within the design effective width, which are shown with black lines

in the figure for both bending directions with the slab in tension (solid lines) and the bottom edge in tension (dashed lines). The full width calculation is based on flexural theory assuming linear strain distribution for the full span width of the slab concrete with all of the slab reinforcing bars into account, namely the full effective slab width of 1050 mm on one side for two-fifth scale specimen, as shown with blue lines in the figure. It should be noted by comparing these that the full width calculation is much higher than the design calculation not only in the slab tension direction but also in the slab compression, which is 1.5 times the code calculation. It was found from the calculation that this is because the lower chord slab reinforcing bars and the second row beam upper main bars are also effective in the direction of slab compression bending.

It should also be noted that the resistance at the inner span apparently increases rapidly in relation with the drift than that at the outer span. The moment at the inner span with the slab in tension attained the calculated strength at the drift of 1/100 rad, and also the moment at the inner span with the bottom edge tension exceeded the calculated moment. On the other hand, the moments at the outer span ends increased gradually. In particular, the moment with the slab in tension was much smaller at 1/100, although it finally reached close to the calculated strength at the drift of 3/100 rad.

It was estimated this might be partially due to the insufficient support conditions at the end of the outer slab. The transverse steel beams were placed on and beneath the outer span end, by which axial reaction forces were transferred to the transverse beams and the longitudinal beam ends. The beams were supported with one vertical jack and load cell at each end of outer span. The two jacks were not working with oil pressure but just used as pin support rod initially tightened up by torque wrench. However, the pin-connection devices at both ends of the supporting jacks had some looseness. Also the jack was placed only at the center of whole span so that the stiffness of the transverse beams also might have been insufficient to fix the vertically displacement at the end of longitudinal beams. These insufficient details were revised in the succeeding test series from 2012 to 2014.

## 6 Test on Repaired Specimen

### 6.1 Methods of Repair

The test series on the frame assemblies with slab was interrupted after the East Japan earthquake, March 11, 2011. Due to the long period of the earthquake motion, vibration of long duration and moderate damages to high rise reinforced concrete buildings were observed incidentally, even in far source areas. High rise building should be designed as repairable, even after very rare motions. However the test on repaired members using high strength materials were few so that experimental verification of seismic performance would be significant. The specimen No. 2, which had been loaded up to the maximum drift of 0.03 rad, was repaired as planned and tested in 2012 during the interval to the next series. The residual lateral drifts and the constant axial load on the columns were return to zero for repair work, where epoxy resin was injected into the cracks and polymer cement mortar was placed at cover concrete spalling off. The repaired specimen was subjected to similar drift history with the same

loading method, from which the stiffness, strength and hysteretic energy dissipation were obtained and compared with those of the bare specimen.

Residual cracks exceeding width of 0.2 mm were repaired with epoxy resin of low viscosity level, while medium velocity level was used for cracks exceeding 1.0 mm for the beams, slabs and columns of the specimen No. 2. The maximum residual widths of cracks at slabs,beams and columns before repairing were 4.0 mm, 1.4 mm and 0.6 mm, respectively. The total number and length of the repaired cracks were 1287 and 488 m, respectively. Compressive strength after one week was 76 N/mm$^2$ for low velocity epoxy and 79 N/mm$^2$ for medium viscosity epoxy. Crushing parts such as lower chord at the critical sections of the longitudinal beams were replaced with polymer cement mortar (PCM). Spalling of concrete was checked by hammering test and taken off in advance. The repaired area using PCM was 0.3 m$^2$ in total. The compressive strength of PCM after one week was 42.5 N/mm$^2$, while the repair test was done after 15 days of repairing.

## 6.2 Overall Hysteresis Relations of the Repaired Specimen

The hysteretic relations of the specimen No. 2 were compared before and after repaired as shown in Fig. 11(a) with red line before and black line after repair. The stiffness reduction factor at each cycle of loading was calculated by comparing with the stiffness of the bare hysteretic relations as shown in Fig. 11(b). The initial stiffness of the repaired specimen was reduced to about 60% of the bare specimen, while increasing with the drift level, and the stiffness reduction ratio recovered up to about 90% or more in the larger drift level over 0.01 rad. The skeleton of the story shear after repair was close to that of the bare specimen in positive loading, while a bit lower in negative direction. The reduction of stiffness and hysteretic energy dissipation capacity due to repeated cyclic loading were similar to those of the bare specimen.

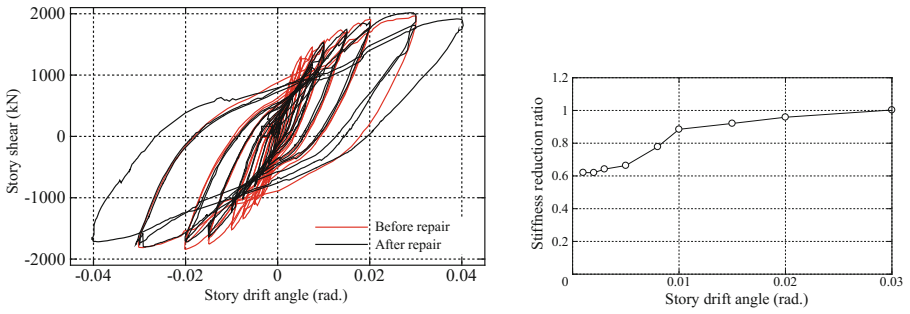


(a) Hysteresis relations before and after repair

(b) Stiffness reduction ratio after repair from bare specimen

**Fig. 11.** Hysteretic relations of the specimen No. 2 before and after repair and stiffness reduction ratio after repair

## 6.3 Hysteresis Relations of Beam End Moment and Story Drift

Hysteresis relations of inner span beam ends and outer span beam ends are shown in Fig. 12(a) and (b), respectively, both compared for the bare specimen and the repaired

specimen. Although the stiffness was reduced less the story drift of 0.01 rad, comparable levels in strength and hysteretic energy are observed between the bare and the repaired specimens after the cyclic loading of 0.01 rad. Therefore, it may be concluded that the initial stiffness recovery was 60% while the reduction of the seismic performance was small after the larger drift level at 1/100 rad and over.

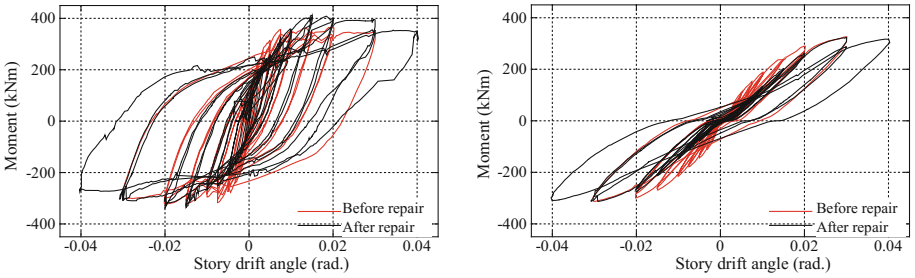


(a) Hysteresis relations of inner span beam ends

(b) Hysteresis relations of outer span beam ends

**Fig. 12.** Hysteresis relations of beam moment and story drift before/after repair, averaged for both ends

## 7 Conclusions

A series of frame assembly tests were conducted to investigate the effective slab width when calculating the ultimate strengths of beams in reinforced concrete buildings. The test results of a specimen is reported and discussed in detail, from which the following conclusions may be drawn:

(1) The observed crack patterns, densely measured local deformations and strains in slab reinforcement strongly indicated that the slab reinforcing bars would be effective with close to or equal to the yield stress along the full span width of the critical section, even at around the yielding deformation of the beams at the story drifts of 1/100 rad and over, especially at the inner span ends.

(2) The measured flexural strengths of the inner beam ends in both directions exceeded at the drift of 1/100 rad the full width calculation by assuming the full effective slab width and all of the reinforcement based on flexural theory, which are much higher than those by the design width calculation, especially in the direction of slab compression bending, in case the lower chord slab reinforcing bars and the second row beam upper main bars are also effective.

(3) The effectiveness of slab in relation to the story drift was obviously influenced by the boundary conditions of the specimen and loading. Cracks in the inner span the beam elongations produced straight cracks on the slab in parallel to the transverse beam, while the cracks in the outer span were inclined perpendicular to the radiating forces from the reaction points. The findings on the slab effectiveness at the inner beams are clearly dependent on the new loading system on the frame assembly that allowed the axial elongation of beams.

(4) The initial stiffness of the repaired specimen recovered up to 60% to that of the bare specimen, while the reduction of the seismic performance such as strength and hysteretic energy was small after the larger drift level around 1/100 rad and over.

**Acknowledgments.** This research was funded as part of national research projects for the consolidation of the Building Standard Law of Japan in 2010. The frame tests were conducted at the Large Size Experiment Laboratory of Building Research Institute, Tsukuba, supported by many related researchers with ERI, BRI, NILIM and Ohbayashi-Gumi LTD. Contributions of Deng Xuan, formerly with ERI, are gratefully acknowledged.

## References

1. Architectural Institute of Japan: Article 8: Basics of structural analysis. AIJ Standard for Structural Calculation of Reinforced Concrete Structures, 63–64 (2009). AIJ (in Japanese)
2. Building Center of Japan: Guidelines for Structural Standard Requirements on Buildings, 620–663 (2007). BCJ (in Japanese)
3. Suzuki, N., Otani, S., Kobayashi, Y.: Three-dimensional beam-column subassemblages under bidirectional earthquake loadings. In: Proceedings of the Eighth World Conference on Earthquake Engineering, vol. 6, pp. 453–460. Prentice-Hall, San Francisco (1984)
4. Joglekar, M., et al.: Full scale tests of beam-column joints. US-Japan Research: Earthquake Effects on Reinforced Concrete Structures, Publication SP-ACI84, 271–304 (1988). ACI
5. French, C.W., Boroojerdi, A.: Contribution of R.C. floor slabs in resisting lateral loads. J. Struct. Eng. **115**(1), 1–18 (1989). ASCE
6. Qi, X., Pantazopoulou, S.J.: Response of RC frame under lateral loads. J. Struct. Eng. **117** (4), 1167–1188 (1991). ASCE
7. Kabeyasawa, T., Shiohara, H., Otani, S.: U.S.-Japan cooperative research on R/C full-scale building test, part 5 discussion on dynamic response system. In: Proceedings of the Eighth World Conference on Earthquake Engineering, vol. 6, pp. 627–634. Prentice-Hall, San Francisco (1984)
8. Kabeyasawa, T., Kabeyasawa, T., Matsumori, T., Kabeyasawa, T., Kim, Y.: Full-scale dynamic collapse tests of three-story reinforced concrete buildings on flexible foundation at E-Defense. In: Proceedings of the 14th World Conference on Earthquake Engineering, Beijing, China, S15-002-8 pp. IAEE (2008)
9. Kabeyasawa, T., Kabeyasawa, T., Matsumori, T., Kim, Y., Kabeyasawa, T.: Full-scale 3-D shake table tests on reinforced concrete building structures at E-Defense. In: Proceedings of ConMat 2009, 4th International Conference on Construction Materials, Performance, Innovations and Structural Implications, Nagoya, pp. 1–16. JCI (2009)
10. Nagae, T., Tahara, K., Fukuyama, K., Matsumori, T., Shiohara, H., Kabeyasawa, T., Kono, S., Nishiyama, M., Moehle, J.P., Wallace, J.W., Sause, R., Ghannoum, W.M.: Test results of four-story reinforced concrete and post-tensioned concrete buildings: the 2010 E-Defense shaking table test. In: Proceedings of 15th World Conference on Earthquake Engineering 1 (No. 3870)-10 pp. IAEE, Lisbon (2012)
11. Kabeyasawa, T., Kabeyasawa, T., Xuan, D., Fukuyama, H.: Frame test on effects of slab to beam strength in reinforced concrete buildings. J. Struct. Eng. **61B**, 103–110 (2015). Architectural Institute of Japan (in Japanese)

# From 3-D to 1-D Generalised and Cosserat Continua for Structural Dynamics - Energy-Momentum Methods

Carlo Sansour(✉), Tien Long Nguyen, and Mohammed Hjiaj

Civil Engineering Department, Institut National des Sciences Appliques de Rennes, 20 Avenue des Buttes de Coesmes, 35708 Rennes, France
{carlo.sansour,mohammed.hjiaj}@insa-rennes.fr, tienlongng@yahoo.com

**Abstract.** A unified access to dynamics of structures is presented. It is based on the idea of a Cosserat continuum which can be three, two- or one-dimensional. In the three dimensional case we can capture scale effects relevant to failure and stress singularities. In the two- and one-dimensional cases we arrive at shell and rod theories derived under the same umbrella. The development of stable energy-momentum integration schemes is key to capture the dynamics for large simulation times. Examples are presented to underline the suggested methodology. The formulations can be extended to capture anisotropies of fibre reinforced materials as well as for coupled systems.

**Keywords:** Shells · Rods · Scale effects · Cosserat continua · Structural dynamics · Energy-momentum methods

## 1 Introduction

Generalised continua are characterised by extra degrees of freedom beyond a displacement field, by assigning to every point of the continuum a displacement vector and, in addition, further fields characterizing the continuum under consideration. Within Cosserat continua it is a rotation tensor which is taken as a further kinematical quantity enhancing the degrees of freedom of the system. The material response of a body to an external stimuli is a corresponding stress field and an extra couple stress field. Correspondingly, the field equations are richer in nature. In the three-dimensional case, generalised continua provide a scale effect otherwise absent in a classical continuum. These scale effects are highly relevant to capture defects, fracture, shear bands and the like, that is whenever information from the micro scale is necessary to better capture the physics of the problem at hand, see [1–3] for a general account and some examples.

On the other hand, Cosserat continua provide a direct approach to derive shell and rod theories [4], which essentially are dimensionally reduced theories of three-dimensional continua. The three-dimensional continuum is modelled from the very beginning as one- or two-dimensional generalised continuum. Since the

© Springer Nature Singapore Pte Ltd. 2018
H. Tran-Nguyen et al. (eds.), *Proceedings of the 4th Congrès International de Géotechnique - Ouvrages -Structures*, Lecture Notes in Civil Engineering 8,
DOI 10.1007/978-981-10-6713-6_3

framework is the same whatever the dimension of the continuum is, we have a unified concept to derive one-, two- or three-dimensional theories providing means for one and the same approach in all three cases.

In addition to the theoretical framework, the non-linear dynamics of geometrically exact shells and rods where the whole non-linearity is taken into account is another important field of research. At the heart of the issue are robust integration schemes which can be used for long term simulations and run stable also for high non-linear deformations.

The concept of energy-momentum methods is central with regard to the mechanical integrator. Motivated by the above facts, the authors suggested an energy-momentum method which has the most important feature of being independent of the configuration space as well as of the kind of the non-linearities retained in the strain-displacement relations. Accordingly, the method applies equally to shell and rod formulations including a rotation tensor or not. First applications of the method was carried out in [5–7].

## 2 Strain Tensors of the Cosserat Continuum

### 2.1 Preliminaries

Let $\mathcal{B} \subset \mathbb{R}^3$, where $\mathbb{R}$ denotes the real numbers, be a three-dimensional manifold defining a material body. For $\mathbf{X} \in \mathcal{B}, \mathbf{x}$ is its counterpart at the current configuration. Let further $\vartheta^i,\ i = 1, 2, 3$ be general curvilinear coordinate charts in $\mathcal{B}$, which we choose to be attached to the body (convected). The covariant base vectors are $\mathbf{G}_i = \partial\mathbf{X}/\partial\vartheta^i$ and $\mathbf{g}_i = \partial\mathbf{x}/\partial\vartheta^i$. Here and in what follows Latin indices take the values $1, 2$ or $3$. The *Riemannian* metric in either configuration is given by $G_{ij} = \mathbf{G}_i \cdot \mathbf{G}_j$ and $g_{ij} = \mathbf{g}_i \cdot \mathbf{g}_j$ respectively, where scalar products of vectors are denoted by a dot. The determinants of the metrics are denoted by $G$ and $g$ respectively; their inverse as usual by $G^{ij}$ and $g^{ij}$ respectively. Further, we consider a Cartesian frame denoted by $\mathbf{e}_i$ and define the quantities $c_{ij} = \mathbf{G}_i \cdot \mathbf{e}_j, \mathbf{G}_i = c_{ij}\mathbf{e}_j, \mathbf{e}_i = c_{ji}\mathbf{G}^j$. Note that the matrix $c_{ij}$ is not symmetric. The basic permutation tensor is defined as

$$e^{ijk} = e_{ijk} = \begin{cases} +1 & \text{for odd permutations of } i, j, k \\ -1 & \text{for even permutations of } i, j, k \end{cases} \tag{1}$$

The deformation gradient $\mathbf{F}$ is defined as $\mathbf{F} = \mathbf{g}_i \otimes \mathbf{G}^i$. Introducing the displacement field $\mathbf{u} = \mathbf{x} - \mathbf{X}$ and denoting partial derivatives by a comma we get $\mathbf{g}_i = \mathbf{G}_i + \mathbf{u}_{,i}, \mathbf{F} = (\mathbf{G}_i + \mathbf{u}_{,i}) \otimes \mathbf{G}^i$.

### 2.2 The Three-Dimensional Case

In the contrary to a classical continuum, the *Cosserat* continuum, which is the simplest possible continuum of a wide class of generalised continua, is characterized by the fact that to every point of the continuum displacements as well as

rotations are assigned. That is, attached with every point of the *Cosserat* continuum are the degrees of freedom of a rigid body. Since the rotation field is considered independent, the strain measures of the continuum are not fully described by one strain tensor alone. A further strain tensor is needed to describe the independent change of the rotation. Let $\mathbf{R} \in SO(3)$ be a rotation tensor which fulfils the relation $\mathbf{R}\mathbf{R}^T = \mathbf{1}$. One has $\mathbf{R}^T\mathbf{R}_{,i} + \mathbf{R}_{,i}^T\mathbf{R} = \mathbf{0}$, from which we infer that $\mathbf{R}^T\mathbf{R}_{,i} \in so(3)$, the tangent space of $SO(3)$ consisting of the skew-symmetric tensors. In order to get explicit formula, the parametrisation of the rotation tensor $\mathbf{R}$ is carried out with the help of the exponential map as follows [1]

$$\mathbf{R} = \mathbf{1} + \frac{\sin|\boldsymbol{\gamma}|}{|\boldsymbol{\gamma}|}\boldsymbol{\Gamma} + \frac{1-\cos|\boldsymbol{\gamma}|}{|\boldsymbol{\gamma}|^2}\boldsymbol{\Gamma}^2, \tag{2}$$

with $\boldsymbol{\Gamma} = -\boldsymbol{\Gamma}^T$ and $\boldsymbol{\gamma}$ being its corresponding axial vector. With $\mathbf{k}_i$ we refer to the axial vector of the skew-product $\mathbf{R}^T\mathbf{R}_{,i}$. One may derive the relation

$$\mathbf{k}_i = \frac{\sin|\boldsymbol{\gamma}|}{|\boldsymbol{\gamma}|}\boldsymbol{\gamma}_{,i} + \frac{1-\cos|\boldsymbol{\gamma}|}{|\boldsymbol{\gamma}|^2}\boldsymbol{\gamma}_{,i}\times\boldsymbol{\gamma} + \left(\frac{1}{|\boldsymbol{\gamma}|} - \frac{\sin|\boldsymbol{\gamma}|}{|\boldsymbol{\gamma}|^2}\right)\frac{(\boldsymbol{\gamma}\cdot\boldsymbol{\gamma}_{,i})}{|\boldsymbol{\gamma}|}\boldsymbol{\gamma} \tag{3}$$

relating $\mathbf{k}_i$ to $\boldsymbol{\gamma}$, the eigenvector of $\mathbf{R}$.

With the rotation tensor $\mathbf{R} \in SO(3)$ being independent from the deformation gradient, the strain measures are then defined to be the first *Cosserat* strain tensor and the second *Cosserat* strain tensor:

$$\mathbf{U} := \mathbf{R}^T\mathbf{F}, \qquad \mathbf{K} := -\mathbf{k}_i \otimes \mathbf{G}^i. \tag{4}$$

## 3 Shell Theory with Drilling Rotations

To derive a shell theory we just need to restrict the dimension of the continuum to two, that is to a surface denoted here by $\mathcal{M}$, [4]. First, we let $\vartheta^\alpha, \alpha = 1,2$ be coordinate charts in $\mathcal{M}$, which we choose again to be attached to the surface (convected). The covariant base vectors are $\mathbf{G}_\alpha = \partial\mathbf{X}/\partial\vartheta^\alpha$ and $\mathbf{g}_\alpha = \partial\mathbf{x}/\partial\vartheta^\alpha$ at the reference surface the normal vector is defined by $\mathbf{N} = 1/\sqrt{G}\, e^{\alpha\beta 3}\mathbf{G}_\alpha \times \mathbf{G}_\beta$, where it is always understood that $\mathbf{N} \equiv \mathbf{G}_3$. The components $B_{\alpha\beta}$ of the curvature tensor $\mathbf{B} = B_{\alpha\beta}\mathbf{G}^\alpha \otimes \mathbf{G}^\beta$ are then given by $B_{\alpha\beta} = -\mathbf{N}_{,\alpha}\cdot\mathbf{G}_\beta$. The *Riemannian* metric in either configuration is given by $G_{\alpha\beta} = \mathbf{G}_\alpha\cdot\mathbf{G}_\beta$ and $g_{\alpha\beta} = \mathbf{g}_\alpha\cdot\mathbf{g}_\beta$ respectively. The deformation gradient is completely determined by (the two maps) $\mathbf{F} = \mathbf{g}_\alpha \otimes \mathbf{G}^\alpha$ which, with the displacement field $\mathbf{u} = \mathbf{x} - \mathbf{X}$, can be written in the form $\mathbf{F} = (\mathbf{G}_\alpha + \mathbf{u}_{,\alpha}) \otimes \mathbf{G}^\alpha$.

In the two-dimensional case there exist two skew-symmetric products $\mathbf{R}^T\mathbf{R}_{,\alpha}$ with two corresponding axial vectors $\mathbf{k}_\alpha$:

$$\mathbf{k}_\alpha = \frac{\sin|\boldsymbol{\gamma}|}{|\boldsymbol{\gamma}|}\boldsymbol{\gamma}_{,i} + \frac{1-\cos|\boldsymbol{\gamma}|}{|\boldsymbol{\gamma}|^2}\boldsymbol{\gamma}_{,\alpha}\times\boldsymbol{\gamma} + \left(\frac{1}{|\boldsymbol{\gamma}|} - \frac{\sin|\boldsymbol{\gamma}|}{|\boldsymbol{\gamma}|^2}\right)\frac{(\boldsymbol{\gamma}\cdot\boldsymbol{\gamma}_{,\alpha})}{|\boldsymbol{\gamma}|}\boldsymbol{\gamma}. \tag{5}$$

With the geometric quantities $c_{ij}$ defined earlier as well as the components of $\mathbf{u}$ and $\boldsymbol{\gamma}$: $\mathbf{u} = u_k\mathbf{e}_k, \quad \boldsymbol{\gamma} = \gamma_k\mathbf{e}_k$, explicitly the following relations can then be derived:

$$\begin{aligned}\mathbf{U}-\mathbf{1} &= \Big\{c_{\beta k}\,u_{k,\alpha}+(c_{\alpha k}+u_{k,\alpha})c_{\beta j}\\ &\quad\times\left[\frac{\sin|\boldsymbol{\gamma}|}{|\boldsymbol{\gamma}|}\,e_{ijk}\,\gamma_i+\frac{1-\cos|\boldsymbol{\gamma}|}{|\boldsymbol{\gamma}|^2}\,(\gamma_k\gamma_j-\gamma_i\gamma_i\delta_{jk})\right]\Big\}\,\mathbf{G}^\beta\otimes\mathbf{G}^\alpha\\ &\quad+\Big\{c_{3k}u_{k,\alpha}+(c_{\alpha k}+u_{k,\alpha})c_{3j}\\ &\quad\times\left[\frac{\sin|\boldsymbol{\gamma}|}{|\boldsymbol{\gamma}|}\,e_{ijk}\,\gamma_i+\frac{1-\cos|\boldsymbol{\gamma}|}{|\boldsymbol{\gamma}|^2}\,(\gamma_k\gamma_j-\gamma_i\gamma_i\delta_{jk})\right]\Big\}\,\mathbf{N}\otimes\mathbf{G}^\alpha \qquad (6)\\ \mathbf{K} &= -c_{\beta k}\left(\frac{\sin|\boldsymbol{\gamma}|}{|\boldsymbol{\gamma}|}\,\gamma_{k,\alpha}+\frac{1-\cos|\boldsymbol{\gamma}|}{|\boldsymbol{\gamma}|^2}\,e_{ijk}\gamma_{i,\alpha}\gamma_j\right.\\ &\qquad\left.+\frac{|\boldsymbol{\gamma}|-\sin|\boldsymbol{\gamma}|}{|\boldsymbol{\gamma}|^2}\,|\boldsymbol{\gamma}|_{,\alpha}\gamma_k\right)\mathbf{G}^\beta\otimes\mathbf{G}^\alpha\\ &\quad-c_{3k}\left(\frac{\sin|\boldsymbol{\gamma}|}{|\boldsymbol{\gamma}|}\,\gamma_{k,\alpha}+\frac{1-\cos|\boldsymbol{\gamma}|}{|\boldsymbol{\gamma}|^2}\,e_{ijk}\gamma_{i,\alpha}\gamma_j+\frac{|\boldsymbol{\gamma}|-\sin|\boldsymbol{\gamma}|}{|\boldsymbol{\gamma}|^2}\,|\boldsymbol{\gamma}|_{,\alpha}\gamma_k\right)\mathbf{N}\otimes\mathbf{G}^\alpha \qquad (7)\end{aligned}$$

## 4 The Rod Formulation

The counterpart of the two-dimensional case is the one-dimensional one. By restricting the dimension of the continuum to just one and following exactly the same steps as in the three- and two-dimensional cases one ends up with one tangent vector given by $\mathbf{G}_1=\partial\mathbf{X}/\partial\vartheta^1$ or $\mathbf{g}_1=\partial\mathbf{x}/\partial\vartheta^1$, respectively, as well as the deformation gradient given by the one map $\mathbf{F}=\mathbf{g}_1\otimes\mathbf{G}^1$. Analogously, their exist only one skew-symmetric product $\mathbf{R}^T\mathbf{R}_{,1}$ with one axial vector given by

$$\mathbf{k}_1=\frac{\sin|\boldsymbol{\gamma}|}{|\boldsymbol{\gamma}|}\boldsymbol{\gamma}_{,1}+\frac{1-\cos|\boldsymbol{\gamma}|}{|\boldsymbol{\gamma}|^2}\boldsymbol{\gamma}_{,1}\times\boldsymbol{\gamma}+\left(\frac{1}{|\boldsymbol{\gamma}|}-\frac{\sin|\boldsymbol{\gamma}|}{|\boldsymbol{\gamma}|^2}\right)\frac{(\boldsymbol{\gamma}\cdot\boldsymbol{\gamma}_{,1})}{|\boldsymbol{\gamma}|}\boldsymbol{\gamma}. \qquad (8)$$

Further, we have $\mathbf{F}=(\mathbf{G}_1+\mathbf{u}_{,1})\otimes\mathbf{G}^1$. The strain measures of the *Cosserat* curve now read:

$$\mathbf{H}=\mathbf{R}^T\mathbf{F}-\mathbf{1}=\mathbf{R}^T(\mathbf{G}_1+\mathbf{u}_{,1})\otimes\mathbf{G}^1-\mathbf{G}_1\otimes\mathbf{G}^1,\qquad \mathbf{K}=-\mathbf{k}_1\otimes\mathbf{G}^1. \qquad (9)$$

Explicitly, one has

$$\begin{aligned}\mathbf{H} &= \Big\{c_{nk}\,u_{k,1}+(c_{1k}+u_{k,1})c_{nj}\\ &\quad\times\left[\frac{\sin|\boldsymbol{\gamma}|}{|\boldsymbol{\gamma}|}\,e_{ijk}\,\gamma_i+\frac{1-\cos|\boldsymbol{\gamma}|}{|\boldsymbol{\gamma}|^2}\,(\gamma_k\gamma_j-\gamma_i\gamma_i\delta_{jk})\right]\Big\}\,\mathbf{G}^n\otimes\mathbf{G}^1 \qquad (10)\\ \mathbf{K} &= -c_{nk}\left(\frac{\sin|\boldsymbol{\gamma}|}{|\boldsymbol{\gamma}|}\,\gamma_{k,1}+\frac{1-\cos|\boldsymbol{\gamma}|}{|\boldsymbol{\gamma}|^2}\,e_{ijk}\gamma_{i,1}\gamma_j\right.\\ &\qquad\left.+\frac{|\boldsymbol{\gamma}|-\sin|\boldsymbol{\gamma}|}{|\boldsymbol{\gamma}|^2}\,|\boldsymbol{\gamma}|_{,1}\gamma_k\right)\mathbf{G}^n\otimes\mathbf{G}^1 \qquad (11)\end{aligned}$$

## 5 The Lagrangian and Hamilton's Principle

Let us postulate the existence of a kinetic energy as a quadratic function in the following form

$$T = \frac{1}{2}\int_{\mathcal{B}} (\rho_{ref}\boldsymbol{v}\cdot\boldsymbol{v} + \boldsymbol{\Theta}\boldsymbol{\omega}\cdot\boldsymbol{\omega})d\Sigma. \tag{12}$$

In the last expression we have $\boldsymbol{v} = \dot{\mathbf{u}}, \boldsymbol{\Theta}$ a positive definite tensor of the second order and $\boldsymbol{\omega}$ the angular velocity, and $\rho_{ref}$ denote an adequately defined density.

We assume further the existence of an internal potential $\psi$ according to

$$\psi_{int}(\mathbf{U},\mathbf{K}) = \int_{\mathcal{B}} \rho_{ref}\psi_{int}(\mathbf{U},\mathbf{K})d\Sigma \tag{13}$$

The force tensor and the couple tensor are then given as

$$\mathbf{n} := \rho_{ref}\frac{\partial\psi_{int}(\mathbf{U},\mathbf{K})}{\partial\mathbf{U}} \qquad \mathbf{m} := \rho_{ref}\frac{\partial\psi_{int}(\mathbf{U},\mathbf{K})}{\partial\mathbf{K}}. \tag{14}$$

By definition, they are not symmetric in general.

Accordingly the Lagrangian reads

$$\mathcal{L} = T - \psi_{int}. \tag{15}$$

Starting from Hamilton's principle we have

$$\delta\int_{t_0}^{t_1}\mathcal{L}dt + \int_{\mathcal{B}}\mathbf{p}\cdot\delta\mathbf{u} + \mathbf{M}\cdot\mathbf{w}d\Sigma + \int_{\partial\mathcal{B}}\mathbf{p}\cdot\delta\mathbf{u} + \mathbf{M}\cdot\mathbf{w}d\Sigma = 0, \tag{16}$$

where $\mathbf{p},\mathbf{M}$ are some external forces and moments, and $\mathbf{w}$ being a virtual linear rotation vector. Using Eqs. (12)–(15):

$$\begin{aligned}
&\int_{\mathcal{B}}(\rho_{ref}\boldsymbol{v}\cdot\delta\boldsymbol{v} + \boldsymbol{\Theta}\boldsymbol{w}\cdot\delta\boldsymbol{w})d\Sigma \\
&-\int_{\mathcal{B}}\left(\rho_{ref}\frac{\partial\psi_{int}(\mathbf{U},\mathbf{K})}{\partial\mathbf{U}} : \delta\mathbf{U} + \rho_{ref}\frac{\partial\psi_{int}(\mathbf{U},\mathbf{K})}{\partial\mathbf{K}} : \delta\mathbf{K}\right)d\Sigma \\
&+\int_{\mathcal{B}}(\mathbf{p}\cdot\delta\mathbf{u} + \mathbf{l}\cdot\delta\mathbf{w})d\Sigma + \int_{\partial\mathcal{B}}(\mathbf{p}_s\cdot\delta\mathbf{u} + \mathbf{l}_s\cdot\delta\mathbf{w})ds = 0.
\end{aligned} \tag{17}$$

## 6 Time Integration- the Energy-Momentum Scheme

Let us be given two time steps $n$ and $n+1$ with all kinematical fields and velocities are known at step $n$. With $\boldsymbol{\Omega}$ as angular velocity skew-symmetric tensor, the axial vector of which is $\boldsymbol{\omega}$ as well as $\mathbf{W}$ being the corresponding virtual linear rotation the axial vector of which is $\mathbf{w}$, within the time interval $\Delta T$, we consider the following approximations

$$\dot{\mathbf{u}}_{n+\frac{1}{2}} = \frac{\mathbf{u}_{n+1}-\mathbf{u}_n}{\Delta T}, \quad \boldsymbol{\Omega}_{n+\frac{1}{2}} = \frac{\mathbf{W}}{\Delta T}. \tag{18}$$

$$\mathbf{R}_{n+\frac{1}{2}} = \mathbf{R}_n\exp(\frac{1}{2}\Delta T\boldsymbol{\Omega}_{\frac{1}{2}}), \quad \mathbf{R}_{n+1} = \mathbf{R}_n\exp(\Delta T\boldsymbol{\Omega}_{\frac{1}{2}}). \tag{19}$$

These expressions define a midpoint rule for time integration. One can show that the momentum and angular momentum are conserved under this scheme. As to energy conservation, the fundamental idea of making the integration scheme independent of the configuration space rests on the observation that the coupling of the strain field to the kinematic field can be achieved without restoring directly to the relations in Eq. (4), [5–7]. To this goal we consider the strain velocity field defined with the help of Eq. (4) as follows. Now, instead of defining the strain field within the interval $\Delta T$ by means of the relations (4), we consider the following definitions of strains

$$\mathbf{U}_{n+\frac{1}{2}} = \mathbf{U}_n + \frac{\Delta T}{2}\dot{\mathbf{U}}_{n+\frac{1}{2}}, \qquad \mathbf{K}_{n+\frac{1}{2}} = \mathbf{K}_n + \frac{\Delta T}{2}\dot{\mathbf{K}}_{n+\frac{1}{2}}. \tag{20}$$

According to these definitions of strains, which are at the heart of the new integration method, the kinematical relations in Eq. (4) are dropped in defining the strain fields. Instead, the strain field is defined by means of a corresponding strain-velocity field. Accordingly, the kinematical relations (4) are not used to define the strains themselves but to define the corresponding velocities. Let us recall the definition of the first and second Cosserat deformation tensors: $\mathbf{U} = \mathbf{R}^T\mathbf{F}$ and $\mathbf{K} = -\mathbf{k}_i \otimes \mathbf{G}^i$, where $\mathbf{k}_i$ is the axial vector of the antisymmetric quantity $\mathbf{R}^T\mathbf{R}_{,i}$. From these definitions the following strain velocities are derived

$$\dot{\mathbf{U}} = \dot{\mathbf{R}}^T\mathbf{F} + \mathbf{R}^T\dot{\mathbf{F}} = -\mathbf{R}\boldsymbol{\Omega}\mathbf{R}^T\mathbf{U} + \mathbf{R}^T\dot{\mathbf{F}} \tag{21}$$

$$\dot{\mathbf{K}} = -\mathbf{R}^T\boldsymbol{\omega}_{,\alpha} \otimes \mathbf{G}^\alpha. \tag{22}$$

Specifically one has

$$\begin{aligned}\dot{\mathbf{U}}_{n+\frac{1}{2}} &= (\dot{\mathbf{R}}^T\mathbf{F})|_{n+\frac{1}{2}} + (\mathbf{R}^T\dot{\mathbf{F}})|_{n+\frac{1}{2}} \\ &= -\mathbf{R}_n^T \exp\left(\frac{-\Delta\mathbf{W}}{2}\right)\frac{\Delta\mathbf{W}}{\Delta T}\mathbf{F}_{n+\frac{1}{2}} + \dot{\mathbf{F}}_{n+\frac{1}{2}}\end{aligned} \tag{23}$$

and

$$\dot{\mathbf{K}}_{n+\frac{1}{2}} = \mathbf{R}_n^T \exp\left(\frac{-\Delta\mathbf{W}}{2}\right)\frac{\Delta\mathbf{W}_{,\alpha}}{\Delta T} \otimes \mathbf{G}^\alpha. \tag{24}$$

The formulation of the midpoint rule for the strain measures can then achieve the desired result.

## 7 Numerical Examples

### 7.1 Cantilever Beam

A very thin cantilever beam depicted in Fig. 1, and subjected to an external force at the tip of the beam. The loading history is presented in Fig. 2, where

$P_0 = 1E7\,\mathrm{N}, t_0 = 0.2\,\mathrm{s}$. The Elastic modulus $E = 0.2e12\,\mathrm{Pa}$, the density $\rho = 48831\,\mathrm{kg/m^3}$. The length of the beam $L = 3\,\mathrm{m}$. The cross section area $A = 0.1\,\mathrm{m}^2$, the moment of inertia $I = 8.330E-5\,\mathrm{m}^4$. The Poisson's ratio $\nu = 0.3$. We run the calculation for 1 million time steps with $\Delta T = 1E-3\,\mathrm{s}$ and the beam model has 15 linear elements.

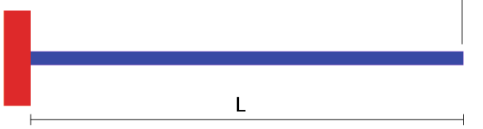


**Fig. 1.** Cantilever beam

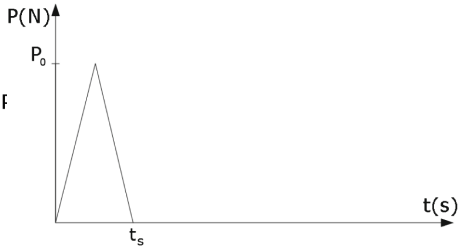


**Fig. 2.** Loading history

Figures 3 and 4 plot the horizontal and vertical displacement of the tip of the beam respectively for the first 5 s. The maximum value of the displacement ≈2.5 m compared to the length of the beam shows the very high non-linearity of the problem. One can see that by using the enhanced strain method presented in [.....], the beam model doesn't suffer from any locking phenomena. We have run this example for 1 million time steps and no instabilities have been observed. The resolution is stable and the conservation of energy is shown in Fig. 5, even when zooming in, the value of total energy is perfectly conserved. Some motions of the beam are captured in Fig. 6.

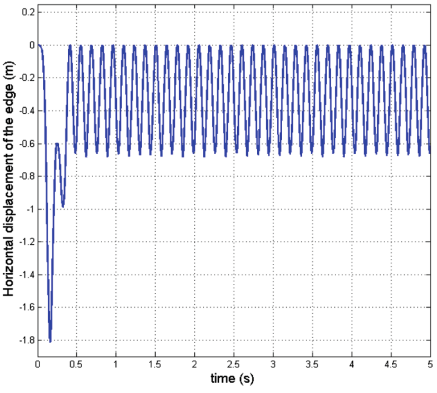


**Fig. 3.** Horizontal displacement of the tip

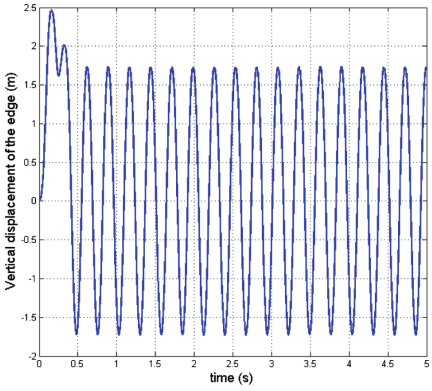


**Fig. 4.** Vertical displacement of the tip

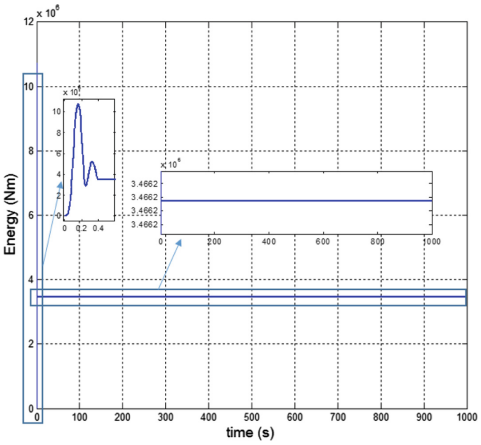


**Fig. 5.** Energy history

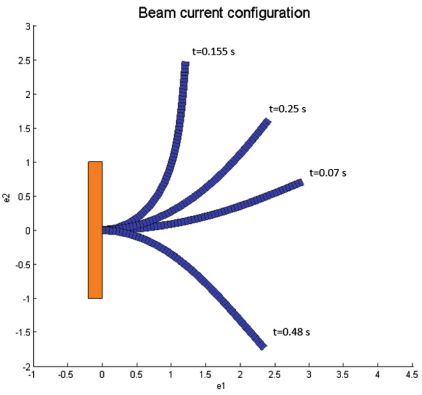


**Fig. 6.** Beam motions

### 7.2 Flying Beam

To prove not only the conservation of the total energy but also the one of the momentum and the angular momentum in highly nonlinear system, we consider a slender beam without any support. The beam is subjected to an external moment at the first tip and external force at the other, Fig. 7. The loading history is depicted in Figs. 8 and 9, where $P_0 = 7E6\,\mathrm{N}, M_0 = 4.5E5\,\mathrm{Nm}$ and $t_0 = 0.2\,\mathrm{s}$. The beam length $L = 3\,\mathrm{m}$. The Elastic modulus $E = 0.55e11\,\mathrm{Pa}$, the density $\rho = 48E3\,\mathrm{kg/m^3}$. The cross section area $A = 0.07\,\mathrm{m}^2$, the moment of inertia $I = 2.8583E-5\,\mathrm{m}^4$. The Poisson's ratio $\nu = 0.3$. We run the calculation for 1 million time steps using 20 linear elements with $\Delta T = 1E-4\,\mathrm{s}$.

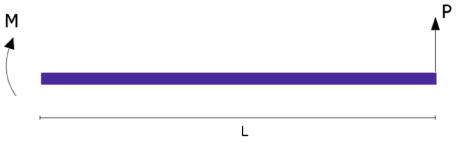


**Fig. 7.** Flying beam

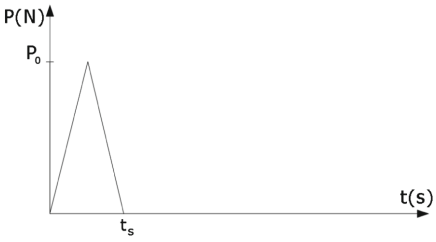


**Fig. 8.** Force loading history

Figure 10 shows the displacement of the first edge of the beam, one can see that the displacement is extremely large until $14E3\,\mathrm{m}$. In Fig. 14, some beam deformations are captured, the beam does exhibit also very large deformations for the whole process until one million time steps. The calculation remains stable and accurate. The total energy is perfectly conserved, Fig. 11. The conservation of the momentum and the angular momentum when external moment and external force vanish are illustrated in Figs. 12 and 13.

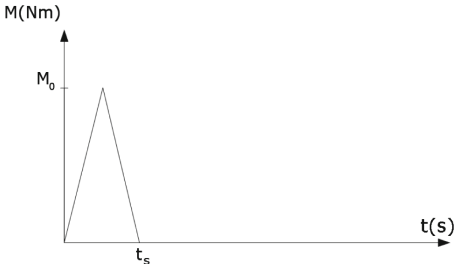


**Fig. 9.** Moment loading history

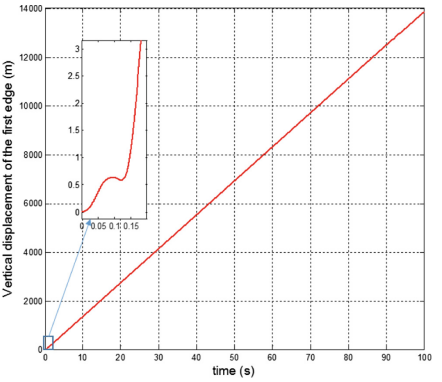


**Fig. 10.** Displacement of the first edge

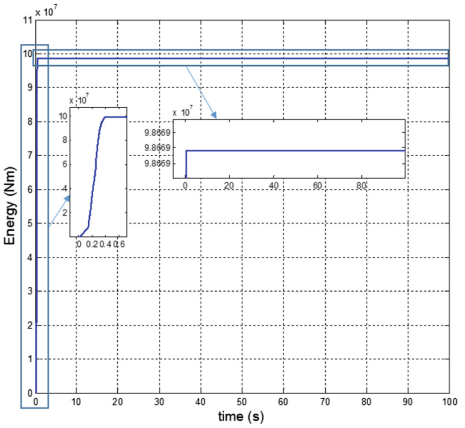


**Fig. 11.** Energy history

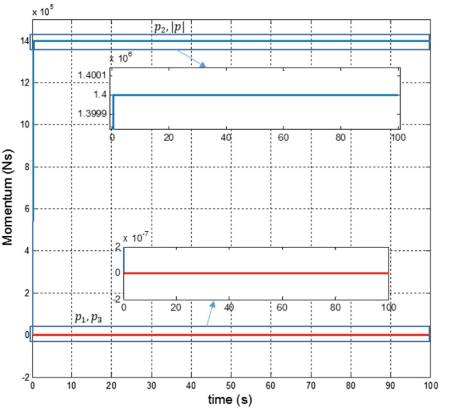


**Fig. 12.** Momentum history

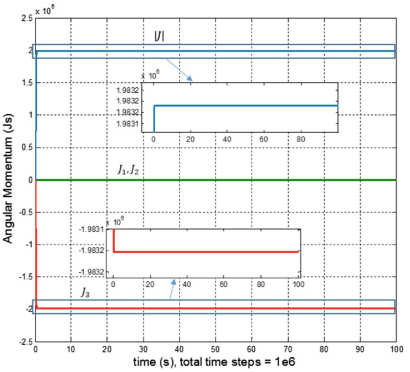


**Fig. 13.** Angular momentum history

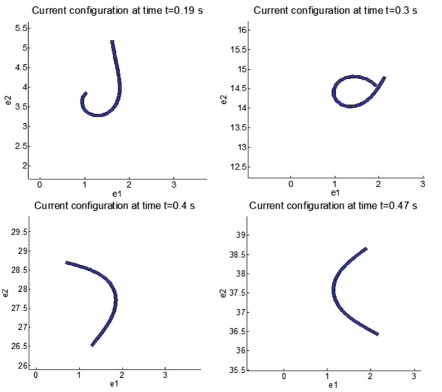


**Fig. 14.** Beam motions

### 7.3 Shallow Arch

To show the performance of this formulation for curved-type beams, we study a shallow arch subjected to dynamic loading, Fig. 15. The arch is clamped at one end and articulated to a movable support and it's loaded by a distributed force on one third of the arch first half. The loading history is depicted in Fig. 16, where $q_0 = 1E6\,\mathrm{N/m}, t_0 = 0.6\,\mathrm{s}$. The radius $R = 20\,\mathrm{m}, \phi = \pi/6$. The Elastic modulus $E = 0.2e12\,\mathrm{Pa}$, the density $\rho = 7850\,\mathrm{kg/m^3}$. The cross section area $A = 0.4\,\mathrm{m^2}$, the moment of inertia $I = 0.0053\,\mathrm{m^4}$. The Poisson's ratio $\nu = 0.3$. We run the calculation for 1 million time steps using 30 elements with $\Delta T = 1E-3\,\mathrm{s}$. The displacement of the mid point and of the second edge are plotted in Figs. 17 and 18. Figure 19 records the total energy history and shows clearly the conservation after removing the external force at a high level of accuracy for the whole time. Some snap shots illustrate the deformation of the arch in Fig. 20.

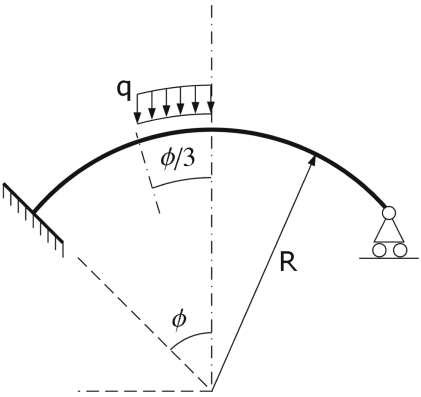


**Fig. 15.** Shallow arch

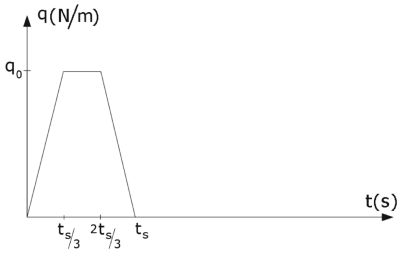


**Fig. 16.** Loading history

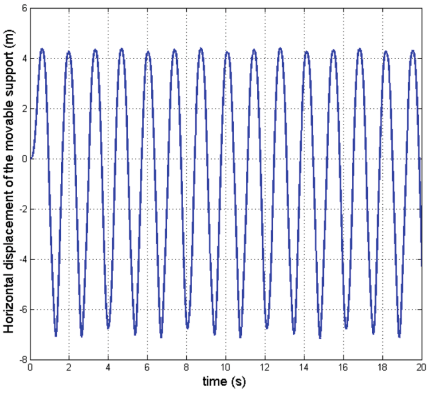


**Fig. 17.** Horizontal displacement of the movable support

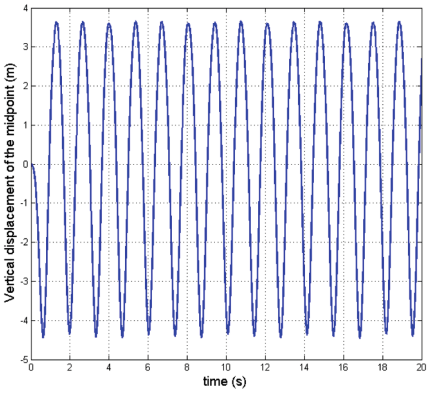


**Fig. 18.** Vertical displacement of the midpoint

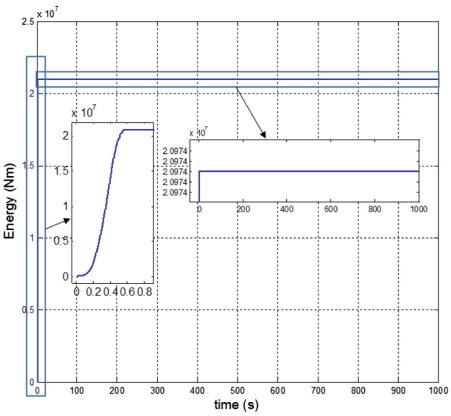


**Fig. 19.** Energy history

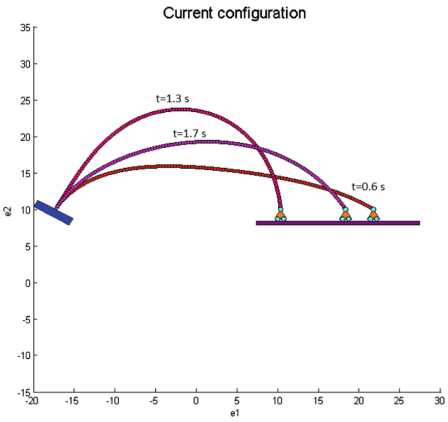


**Fig. 20.** Arch motions

## 8 Conclusion

In this paper we have presented a powerful methodology to derive three-, two- and one-dimensional theories of continua within the same framework. Moreover, a method was presented to integrate the dynamic equations of motion for these continua which preserves the momentum, angular momentum as well as the energy for Hamiltonian systems. The integration scheme is powerful, can be applied to whatever the non-linearities of the system are and is stable. The method has been successfully applied to shells and rods as well as to structures under impact.

## References

1. Sansour, C., Skatulla, S.: Approaches to generalized continua. In: Sansour, C., Skatulla, S. (eds.) Generalized Continua and Dilocation Theory: Theoretical Concepts Computational Methods and Experimental Verification. Springer, Vienna (2012). doi:10.1007/978-3-7091-1222-9_2
2. Sansour, C., Skatulla, S., Zbib, H.: A formulation for the micromorphic continuum at finite inelastic strains. Solids Struct. **47**, 1546–1554 (2010)
3. Skatulla, S., Sansour, C.: A formulation of a Cosserat-like continuum with multiple scale effects. Comput. Mater. Sci. **67**, 113–122 (2013)
4. Sansour, C., Bednarczyk, H.: The Cosserat surface as a shell model, theory and finite-element formulation. Comput. Methods Appl. Mech. Eng. **120**, 1–32 (1995)
5. Sansour, C., Wriggers, P., Sansour, J.: Nonlinear dynamics of shells: theory, nite element formulation, and integration schemes. Nonlinear Dyn. **13**, 279–305 (1997)
6. Sansour, C., Wriggers, P., Sansour, J.: On the design of energy-momentum integration schemes for arbitrary continuum formulations. Applications to classical and chaotic motion of shells. Int. J. Numer. Methods Eng. **60**, 2419–2440 (2004)
7. Sansour, C., Nguyen, T.L., Hjaij, M.: An energy-momentum method for in-plane geometrically exact Euler-Bernoulli beam dynamics. Int. J. Numer. Methods Eng. **102**, 99–134 (2015)

# Recent Developments in Design for Structural Stability

Gregory J. Hancock(✉)

School of Civil Engineering, University of Sydney, Sydney, NSW, Australia
gregory.hancock@sydney.edu.au

**Abstract.** The potential for structural instability in metal structures has been known since the famous paper of Leonard Euler in 1744 on column buckling. The constant challenge has been the desire to turn the excellent research worldwide in the area into design rules and specifications such as the Eurocodes, American Specifications, Japanese, Chinese and Australian Standards. New methods of stability analysis and design such as the Direct Strength Method (DSM) in the AISI S100 Specification and the Australian/New Zealand Standard AS/NZS 4600 for Cold-Formed Steel Structures have unified stability design across a range of buckling modes such as local, distortional and overall (Euler) buckling. Further, Advanced Analysis methods (often called GMNAI) which use the Finite Element Method (FEM) are being standardized for routine design of structural systems. The paper reviews these new methods, and their incorporation in design standards and specifications.

**Keywords:** Structural instability · Direct Strength Method · Advanced analysis standards and specifications buckling

## 1 Introduction

The area of structural stability especially metal structures has attracted considerable interest for nearly 300 years. As structures have become higher and longer, and their components thinner, structural stability has increased in importance, especially as many structures have failed by instability. Petroski (1992) in his acclaimed book "To Engineer is Human" clearly sets out the challenges in his chapter "Engineering as Hypothesis". In this he quotes from The Structural Engineer, the official journal of the British Institution of Structural Engineers, which says:

"Structural engineering is the science and art of designing and making, with economy and elegance, buildings, bridges, frameworks, and other similar structures so that they can safely resist the forces to which they may be subjected."

The key statement here is "safely resist the forces". In designing structures against failure, there are two main modes of failure. These are structural instability often with material yielding, and material fracture. Many failures are a result of the first mode, what we now call inelastic buckling or geometric and material nonlinear structural response. More recently, the term Geometric and Material Nonlinear Analysis with Imperfections (GMNAI) has been used to describe the analyses used to study these

© Springer Nature Singapore Pte Ltd. 2018
H. Tran-Nguyen et al. (eds.), *Proceedings of the 4th Congrès International de Géotechnique - Ouvrages -Structures*, Lecture Notes in Civil Engineering 8,
DOI 10.1007/978-981-10-6713-6_4

phenomena. So there are actually three significant components in the study of structural instability. These are:

Geometric nonlinear response (Change of geometry),
Material yielding (Material plasticity), and
The effect of structural imperfections (Geometric and residual stresses).

Design methods used by structural engineers to design against structural instability must adequately account for all three phenomena. The Structural Stability Research Council (SSRC) of the USA has published 6 editions of its guide "Guide to Stability Design Criteria for Metal Structures", the latest edition edited by Ziemian (2010). In the introduction to the guide, it is stated:

"The history of column theory goes back to the work of the Swiss mathematician Leonard Euler, who in 1744 published his famous column formula. The theoretical developments since then represent some of the finest achievements in applied mechanics".

The method by which design engineers account for structural instability is by prescriptive design rules in structural design standards. These include the American Institute of Steel Construction AISC 360 (2013), Eurocode 3 Part 1.1 (2005) and the Australian Standard AS4100 (1998) for hot-rolled structural members, and American Iron and Steel Institute Specification AISI S100 (2016), Eurocode 3 Part 1.3 (2006) and the Australian/New Zealand Standard for Cold-Formed Steel Structural Members AS/NZS 4600 (2005). As the author of this paper is a member of the AISI Specification Committee, and Chair of the Australian Standards committees, this paper will be mainly focused on recent developments in American Specifications and Australian Standards.

## 2 Member Buckling Modes

The member buckling modes depend upon the nature of the actions applied to the members. These may be:

(i) Compression
(ii) Bending
(iii) Shear
(iv) Localised loading

For each of these actions, the modes may be classified into three types as follows:

(i) Local buckling (short half-wavelength)
(ii) Distortional buckling (intermediate half-wavelength)
(iii) Global buckling such as flexural or flexural-torsional (long half-wavelength)

The first 3 action types can be considered using a uniform stress scenario where the compression, bending moment or shear force are considered uniform along the length of the member producing uniform stresses. The 4$^{th}$ action type usually results in non-uniform stress and a localised mode of failure at the loading point or closely adjacent. To demonstrate each of these scenarios, the recently developed computer

program THIN-WALL-2 Version 1.0 (Nguyen et al. 2015) is applied to study the stability of a lipped channel section. This program considers sections with simply supported boundary conditions. The relationship between the theory for uniform loading and for localised loading is given in Hancock and Pham (2015). A more recent version of this program THIN-WALL-2 Version 2.0 which considers general boundary conditions is described in a separate paper (Nguyen et al. 2017a) in this conference.

## 2.1 Compression

The buckling load factor versus buckle half-wavelength and buckling modes for a 200 mm deep 2.0 mm thick lipped channel in pure compression of 10 kN are shown in Fig. 1. The signature curve is a plot of the buckling stress or buckling load factor under a given action type against the half-wavelength of the buckle. The local buckle minimum occurs at about 160 mm, the distortional buckle minimum at 700 mm and the flexural-torsional buckle does not reach a minimum so is drawn at 2000 mm. The local buckle is confined mainly to the web, the distortional buckle involves both the web, flanges and lip, and the flexural buckle involves undistorted deformation of the whole section. Note also that the buckling load factor for local buckling is 8.05 which is well below the distortional buckling load factor of 14.7.

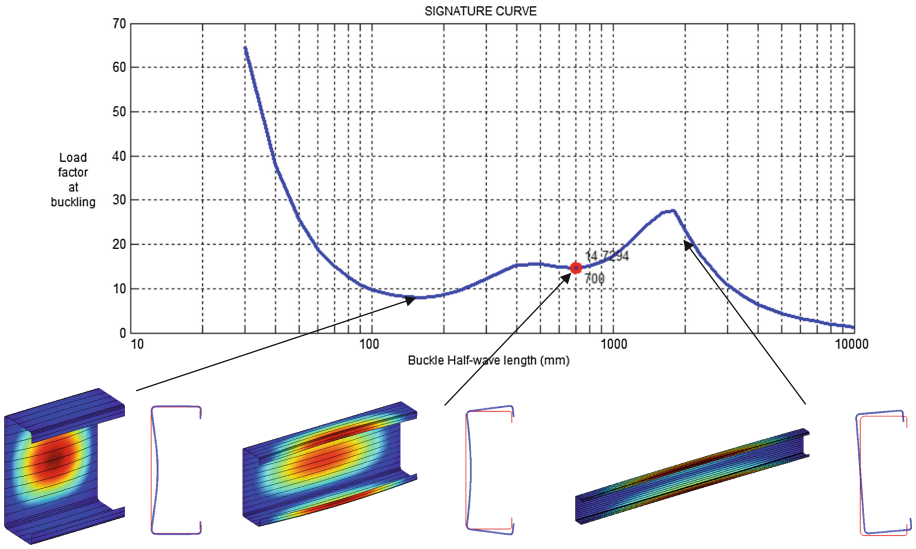


**Fig. 1.** Buckling load factor versus buckle half-wavelength for a lipped channel in compression (N = 10 kN): local, distortional and flexural-torsional modes

## 2.2 Bending

The buckling load factor versus buckle half-wavelength and buckling modes for the 200 mm deep 2.0 mm thick lipped channel in pure bending of 4 kN.m are shown in

Fig. 2. The local buckle minimum occurs at about 100 mm, the distortional buckle minimum at 700 mm and the flexural-torsional buckle is drawn at 3000 mm. The local buckle is confined mainly to the compression portion of the web and the flange, the distortional buckle involves mainly the compression flange and lip, and the flexural-torsional buckle involves undistorted deformation of the whole section with the compression flange moving sideways. The buckling load factor for local buckling is 6.07 which is well above the distortional buckling load factor of 4.56. So the change of action results in a change of buckling mode at shorter half wavelengths.

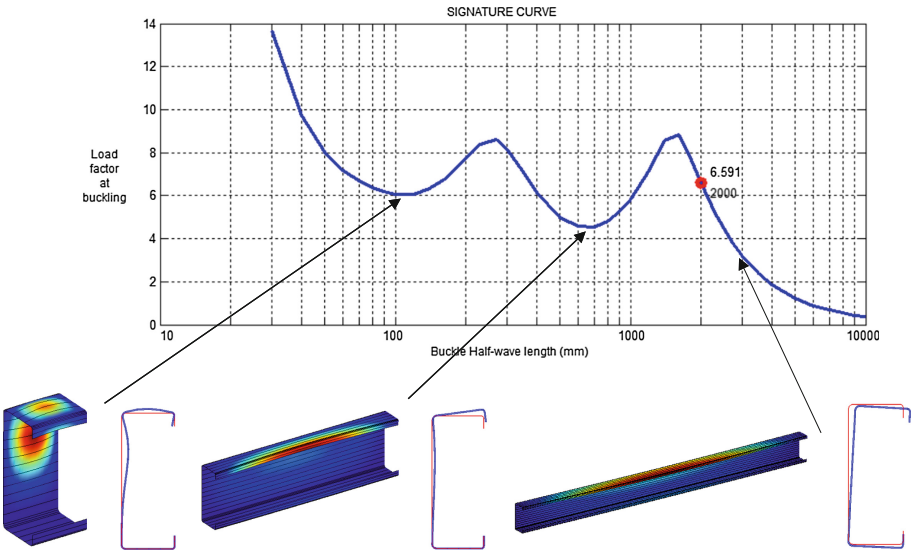


**Fig. 2.** Buckling load factor versus buckle half-wavelength for lipped channel in bending (M = 4 kN.m): local, distortional and flexural-torsional modes

## 2.3 Shear

The buckling load factor versus buckle half-wavelength and buckling mode for the 200 mm deep 2.0 mm thick lipped channel in pure shear of 10 kN are shown in Fig. 3. The local buckle minimum occurs at about 200 mm. There is no distortional buckle minimum and the flexural-torsional buckle is somewhat unrealistic for pure shear due to the long length at which it occurs. The local buckle is confined mainly to the web with the buckle diagonal as a result of the shearing action. There are no nodal lines perpendicular to the section in this buckling mode. The buckling load factor for local buckling is 4.82 which is below that for compression of the same load magnitude at 8.05.

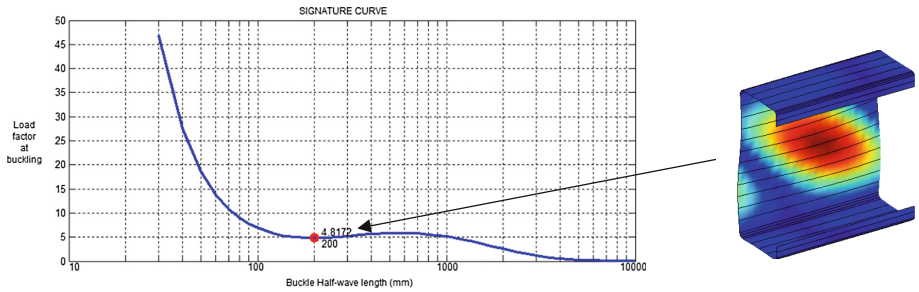


**Fig. 3.** Buckling load factor versus buckle half-wavelength for lipped channel in pure shear (V = 10 kN): local mode only shown

### 2.4 Localised Loading

The localised buckling mode for a line load of 100 kN/m along the flange-web corner junction of length 100 mm at the centre of a simply supported span of 1000 mm is shown in Fig. 4. The applied load is therefore 10 kN similar to the compression in 2.1 and shear in 2.4. There is no signature curve in this case as the loading is not uniform along the length of the sections due to its local nature. The load factor at buckling is 3.25 which is less than either the compression or shear loads indicating the difficulty these types of sections have under localised loading. The buckling mode is mainly in the top of the web under the load although the flange and lip help to spread this load as shown in Fig. 4.

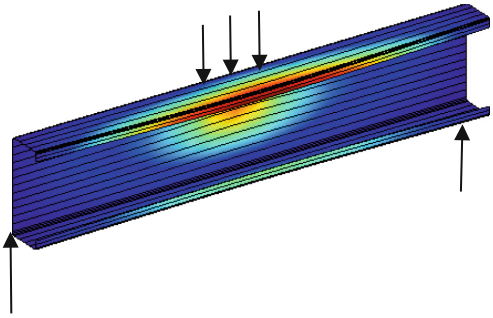

**Fig. 4.** Buckling mode for lipped channel under localised loading of 10 kN over 100 mm

## 3 Member Strengths Using the Direct Strength Method (DSM)

The Direct Strength Method (DSM) of design was developed by Schafer and Pekoz (1998) based on earlier research by the author (Hancock et al. 1994) on the distortional buckling mode. The method uses the signature curve described above to calculate the

local buckling load ($N_{ol}$), the local buckling moment ($M_{ol}$), the distortional buckling load ($N_{od}$), the distortional buckling moment ($M_{od}$), the shear local buckling load ($V_{cr}$) as the minimum points in Figs. 1, 2 and 3 above. In the case of localised loading, a buckling load of $P_{cr}$ is proposed. The method also requires a yield load as the second input variable as described below. The DSM for compression and bending is incorporated in AISI (2016) and Standards Australia (2005) and for shear in AISI (2016) and the proposed revision of Standards Australia (2005) under development. A consistent and simplified DSM for localised loading has been proposed by Nguyen et al. (2017b) based on research by Natário at el. (2016). A new proposal for combined compression and bending has been made by Torabian et al. (2014) but not yet incorporated in design standards and specifications. It should be noted that actions rather than stresses are used in the DSM method of design.

The DSM strength for a given structural member in compression, bending and/or shear is simply the least of the values computed from Sect. 3.1 Local buckling, Sect. 3.2 Distortional buckling and Sect. 3.3 Global buckling following. This section of the paper will firstly summarize the basic DSM equations for compression, bending and shear. It will then discuss the interaction of modes and how they are incorporated as well as recent research on mode interaction. The influence of holes is also covered. The proposed extensions to the DSM for combined bending and compression, and localised loading will be explained in Sect. 4.

### 3.1 Basic Local Buckling Strength Equations

For compression

$$N_{cl} = N_y \quad \text{for } \lambda_l \leq 0.776 \tag{1}$$

$$N_{cl} = \left(1 - 0.15\left(\frac{N_{ol}}{N_y}\right)^{0.4}\right)\left(\frac{N_{ol}}{N_y}\right)^{0.4} N_y \quad \text{for } \lambda_l > 0.776 \tag{2}$$

$$\text{where } \lambda_l = \sqrt{\frac{N_y}{N_{ol}}} \tag{3}$$

$$\text{and } N_y = A.f_y \tag{4}$$

The local buckling load $N_{ol}$ is shown in Fig. 1 based on the applied load and buckling load factor for local buckling (10 * 8.05 = 80.5 kN in the example above)
For bending

$$M_{bl} = M_y \quad \text{for } \lambda_l \leq 0.776 \tag{5}$$

$$M_{bl} = \left(1 - 0.15\left(\frac{M_{ol}}{M_y}\right)^{0.4}\right)\left(\frac{M_{ol}}{M_y}\right)^{0.4} M_y \quad \text{for } \lambda_l > 0.776 \tag{6}$$

$$\text{where } \lambda_l = \sqrt{\frac{M_y}{M_{ol}}} \tag{7}$$

$$\text{and } M_y = Z.f_y \tag{8}$$

The elastic local buckling moment $M_{ol}$ is shown in Fig. 2 based on the applied moment and buckling load factor for local buckling (4 * 6.07 = 24.3 kN.m in the example above). Equations are also given in AISI (2016) for inelastic reserve in local buckling and are being included in Standards Australia (2005).

For shear without tension field action (TFA)

$$V_n = V_y \quad \text{for } \lambda_v \leq 0.776 \tag{9}$$

$$V_n = 0.815\sqrt{V_{cr}V_y} \text{ for } 0.815 < \lambda_v \leq 1.227 \tag{10}$$

$$V_n = V_{cr} \text{ for } \lambda_v > 1.227 \tag{11}$$

$$\text{where } \lambda_v = \sqrt{\frac{V_y}{V_{cr}}} \tag{12}$$

$$\text{and } V_y = 0.6A_w f_y \tag{13}$$

For shear with tension field action (TFA)

$$V_n = V_y \quad \text{for } \lambda_v \leq 0.776 \tag{14}$$

$$V_n = \left(1 - 0.15\left(\frac{V_{cr}}{V_y}\right)^{0.4}\right)\left(\frac{V_{cr}}{V_y}\right)^{0.4} V_y \quad \text{for } \lambda_v > 0.776 \tag{15}$$

The elastic local buckling shear load $V_{cr}$ is shown in Fig. 3 based on the applied shear and buckling load factor for local buckling (10 * 4.82 = 48.2 kN.m in the example above).

### 3.2 Basic Distortional Buckling Strength Equations

For compression

$$N_{cd} = N_y \qquad \text{for } \lambda_d \leq 0.561 \tag{16}$$

$$N_{cd} = \left(1 - 0.25\left(\frac{N_{od}}{N_y}\right)^{0.6}\right)\left(\frac{N_{od}}{N_y}\right)^{0.6} N_y \quad \text{for } \lambda_d > 0.561 \tag{17}$$

$$\text{where } \lambda_d = \sqrt{\frac{N_y}{N_{od}}} \tag{18}$$

and $N_y$ is given by Eq. 4 above

The distortional buckling load $N_{od}$ is shown in Fig. 1 based on the applied load and buckling load factor for distortional buckling (10 * 14.7 = 147 kN in the example above)

For bending

$$M_{bd} = M_y \quad \text{for } \lambda_d \leq 0.673 \tag{19}$$

$$M_{bd} = \left(1 - 0.22\left(\frac{M_{od}}{M_y}\right)^{0.5}\right)\left(\frac{M_{od}}{M_y}\right)^{0.5} M_y \quad \text{for } \lambda_l > 0.673 \tag{20}$$

$$\text{where } \lambda_d = \sqrt{\frac{M_y}{M_{od}}} \tag{21}$$

and $M_y$ is given by Eq. 8 above.

The distortional buckling moment $M_{od}$ is shown in Fig. 2 based on the applied moment and buckling load factor for local buckling (4 * 4.56 = 18.24 kN.m in the example above). Equations are also given in AISI (2016) for inelastic reserve in distortional buckling and are being included in Standards Australia (2005).

### 3.3 Global Buckling Strength Equations

For compression

Elastic global buckling loads ($N_{oc}$) are given by the traditional equations in AISI (2016), British Standard (2006) and Standards Australia (2005). They are not summarized here as they are well known and include flexural (Euler) buckling and flexural-torsional buckling. The equations depend on whether the sections are doubly symmetric (I-sections), mono-symmetric (channel and hat sections), point-symmetric (Z-sections), or asymmetric (non-equal angles). The strength equations in AISI (2016) and Standards Australia (2005) in the notation of Standards Australia are given by:

$$N_{ce} = \left(0.658^{\lambda_c^2}\right) N_y \quad \text{for } \lambda_c \leq 1.5 \tag{22}$$

$$N_{ce} = \left(\frac{0.877}{\lambda_c^2}\right) N_y \quad \text{for } \lambda_c > 1.5 \tag{23}$$

$$\text{where } \lambda_c = \sqrt{\frac{N_y}{N_{oc}}} \tag{24}$$

and $N_y$ is given by Eq. 4 above

For bending

Elastic global buckling moments ($M_o$) are given by the traditional flexural-torsional buckling equations in AISI (2016), British Standard (2006) and Standards Australia (2005). They are not summarized here as they are well known. The equations depend

on whether the sections are doubly symmetric (I-sections), mono-symmetric (channel and hat sections), point-symmetric (Z-sections), or asymmetric (non-equal angles). The strength equations in AISI (2016) and Standards Australia (2005) in the notation of Standards Australia (2005) are given by:

$$M_{be} = M_y/\lambda_c^2 \quad \text{for } M_o < 0.56M_y \tag{25}$$

$$M_{be} = \frac{10}{9}M_y\left(1 - \frac{10M_y}{36M_0}\right) \text{for } 2.78\,M_y \geq M_o \geq 0.56M_y \tag{26}$$

$$M_{be} = M_y \quad \text{for } M_o > 2.78M_y \tag{27}$$

and $M_y$ is given by Eq. 8 above
Inelastic reserve in bending for flexural-torsional buckling can be accounted for using:

$$M_{be} = M_p - \left(M_p - M_y\right)\left(\frac{\sqrt{\frac{M_y}{M_o}} - 0.23}{0.37}\right) \leq M_p \quad \text{for } M_o < M_y \tag{28}$$

$$\text{where } M_p = \text{plastic moment} = S_f f_y \tag{29}$$

### 3.4 Interaction of Local and Global Buckling

Based on the proposals of Schafer (AISI 2006), the interaction of local and global buckling in compression is accounted for by substituting $N_{ce}$ from Eqs. 22 and 23 for $N_y$ in Eqs. 1–3. This approach is known as the unified approach (Pekoz 1987). Similarly, the interaction of local and flexural-torsional buckling in bending is accounted for by substituting $M_{be}$ from Eqs. 25–28 for $M_y$ in Eqs. 5–7.

### 3.5 Interaction of Local and Distortional Buckling

The original proposals of Schafer (AISI 2006) did not include the interaction of local and distortional buckling and so are not incorporated in AISI (2016) and Standards Australia (2005). However, considerable research has taken place in recent years in this area as it is believed that significant interaction may occur in some cases. The most recent summary of this research for compression members including design proposals is given by Martins et al. (2016). Earlier experimental research was performed by Yang and Hancock (2004) and Yap and Hancock (2011) on high strength steel sections with flange and web stiffeners.

### 3.6 Interaction of Local, Global and Distortional Buckling

As for the interaction of local and distortional buckling, interaction of local, distortional and global buckling is not included in the current design standards and specifications.

There is also less research on these modes of interaction. The best summary of research to date is given in Santos et al. (2014) for simple lipped channels where both numerical and experimental research has been performed.

### 3.7 Influence of Holes on the DSM Design Method

There has been considerable research on the influence of holes on the DSM design equations. For columns, the work of Moen and Schafer (2011) has been used in the DSM equation in AISI (2016) and is being used in the current revisions of Standards Australia (2005). The basic approach is to include the effect of the holes in the calculation of the elastic buckling loads $N_{ol,}$ $N_{od}$ *and* $N_{oc.}$ In addition, the stub column strength cannot exceed the net section strength $N_{ynet} = A_{net} f_y$. A similar approach has been used for beams except that the net section strength is now $M_{ynet} = Z_{net} f_y$.

For shear, the calculation of the elastic local buckling load has been detailed in Pham (2017) and this can be used in the DSM shear equations. However, the use of $V_{ynet} = 0.6A_{net} f_y$ can lead to unconservative solutions for sections with large holes. A proposal based on the Vierendeel model is given in Pham et al. (2017a). Another paper at this conference by Pham et al. (2017b) gives more detail on the DSM method of design including holes with a particular focus on shear.

### 3.8 Combined Compression and Bending

Until recently, there had been very little research on the DSM method for combined compression and bending. The method used in AISI (2016) and the proposed revisions to Standards Australia (2005) rely on a simple linear interaction equation as given by:

$$\frac{N^*}{\phi_c N_c} + \frac{M_x^*}{\phi_b M_{bx}} + \frac{M_y^*}{\phi_b M_{by}} \leq 1.0 \tag{30}$$

where $N^*$is the design axial compression and $M_{bx}^*, M_{by}^*$ are the design bending moments about the x- and y-axes of the gross section respectively including the second order moments as discussed later in Sect. 5 of this paper. The design capacities are simply those described in detail in Sects. 3.1–3.3 above. Recent research by Torabian et al. (2014) has proposed a new method accounting for the direct inclusion of compression and bending in both buckling analyses, yield and plasticity analyses. This new proposal is discussed in detail in Sect. 4.2 of this paper.

### 3.9 Combined Bending and Shear

Significant experimental and numerical research on combined bending and shear was performed by Pham and Hancock (2012) leading to design rules in AISI (2016) and the proposed revisions to Standards Australia (2005). They are based on the interaction equations already existing in AISI (2016) and Standards Australia (2005). The major problem with combined bending and shear is that it has to take account of the Tension Field Action (TFA) evident in the test programs. The DSM shear equations have two separate approaches both including and not including TFA as described in Sect. 3.1

above. This makes development of advanced rules for the inclusion of combined bending and shear more difficult because of the need to produce interaction in the post-buckling range in shear.

## 4 Recent Developments in the Direct Strength Method (DSM)

The methodology described in Sect. 3 above has already been incorporated in specifications and standards. This section of the paper describes recent research which will be considered for inclusion in new editions of AISI (2016) and Standards Australia (2005).

### 4.1 Localised Loading

Localised loading of the type shown in Fig. 4 requires a DSM design methodology for its inclusion in AISI (2016) and Standards Australia (2005). The approach proposed by Natário et al. (2016) has been extended and simplified by Nguyen et al. (2017b). The methodology is the same as for all DSM equations where a buckling load ($P_{cr}$) and a yield load ($P_y$) are computed. In the case of the buckling load, the program THIN-WALL 2 Version 2.0 described in a separate paper at this conference (Nguyen et al. (2017b)) can be used. The yield load requires a consideration of plastic mechanism models as demonstrated in Fig. 5. As the localised load is normally eccentric from the web of the section as a result of the rounded corners, then the failure mechanism will be a primary yielding mechanism with $P_y$ given by Eq. 31.

$$P_y = \frac{M_p}{\gamma r}\left(N_{m1} + \left(\frac{D}{D-h}\right)N_{m2}\right) \tag{31}$$

$$\text{where } M_p = \frac{f_y t^2}{4} = \text{plastic moment per unit length} \tag{32}$$

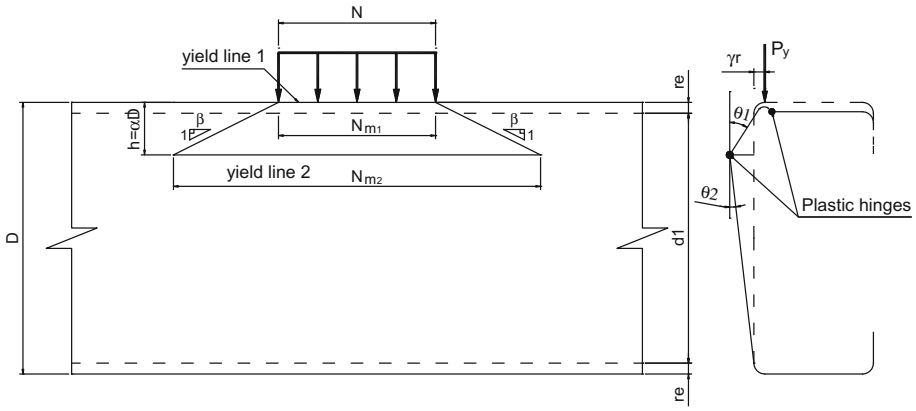


**Fig. 5.** Plastic mechanism model for the Interior One Flange (IOF) loading case.

Similar models have been produced for the Interior Two Flange (ITF), Exterior One Flange (EOF) and Exterior Two Flange (ETF) loading cases in Nguyen (2017).

The DSM equations for localised loading consist of two Eqs. 33 and 34 to predict the strength $P_n$. The first gives the inelastic capacity and is analogous to Eq. 28 where capacity beyond first yield at low slenderness can be accounted for. The second is of a similar format to the DSM yield equations for compression and bending.

$$\frac{P_n}{P_y} = \left[1 + \left(1 - \frac{\lambda}{\lambda_0}\right)(k_4 - 1)\right] \quad \text{for } \lambda \leq \lambda_o \tag{33}$$

$$\frac{P_n}{P_y} = k_1 \left[1 - k_2 \left(\frac{P_{cr}}{P_y}\right)^{k3}\right] \left(\frac{P_{cr}}{P_y}\right)^{k3} \quad \text{for } \lambda > \lambda_0 \tag{34}$$

$$\text{where } \lambda = \sqrt{\frac{P_y}{P_{cr}}} \tag{35}$$

$$\text{and } \lambda_0 \text{ is the sectional slenderness when } \frac{P_n}{P_y} = 1.0 \tag{36}$$

The coefficients and exponents $k_1$, $k_2$ *and* $k_3$ are calibrated against experimental data and are given in Nguyen et al. (2017b). Values of $k_3$ of 0.4, 0.4, 0.6 and 1.0 for the IOF, EOF, ITF and ETF loading cases respectively imply different post-buckling behavior. The coefficient $k_4$ is a mechanism strengthening effect coefficient and has been chosen as 1.8 based on experimental data.

### 4.2 Combined Compression and Bending

A new methodology for combined compression and bending has recently been produced by Torabian et al. (2014). The method considers the buckling interaction, the yield surface and the plastic surface under combined actions rather than combining the actions through linear interaction equations as in Eq. 30. The positions in this 3D space shown in Fig. 6 can be computed from the combined actions. The non-dimensional distance to a surface is described by the parameter β so that the DSM equations for compression and bending in Sects. 3.1, 3.2 and 3.3 can be computed as a function of β.

By reformulating the methodology this way including appropriate plastic surfaces, substantial increases in design capacity for combined actions can be achieved. To demonstrate the nature of the revised equations, the local buckling equations for compression and bending given by Eqs. 1–8 can be reformulated as a function of β as follows:

$$\beta_{cl} = \beta_y \quad \text{for } \lambda_l \leq 0.776 \tag{37}$$

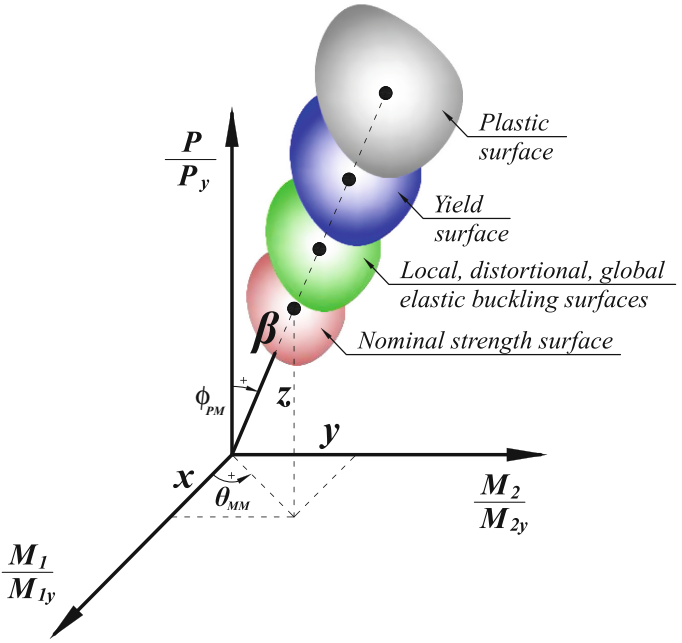


**Fig. 6.** Normalized $P$-$M_1$-$M_2$ space and conceptual strength surfaces (Torabian et al. (2014))

$$\beta_{cl} = \left(1 - 0.15\left(\frac{\beta_{ol}}{\beta_y}\right)^{0.4}\right)\left(\frac{\beta_{ol}}{\beta_y}\right)^{0.4}\beta_y \quad \text{for } \lambda_l > 0.776 \tag{38}$$

$$\text{where } \lambda_l = \sqrt{\frac{\beta_y}{\beta_{ol}}} \tag{39}$$

The term $\beta_{ol}$ represents the non-dimensional local buckling action under combined compression and bending and the term $\beta_y$ represents non-dimensional yield action under combined compression and bending. The term $\beta_{cl}$ is the non-dimensional local strength for the beam-column relative to $\beta_y$ in the 3D space shown in Fig. 6.

## 5 System Structural Analysis

Methods of system structural analysis have traditionally been either first order elastic, second order elastic or plastic. The first order elastic, also referred to as linear elastic (LA), assumes the structures are analyzed in their un-deformed shapes. Consequently the design equations in standards and specifications need to account for structural deformations both within the members (P-δ) and of the joints of the structure (P-Δ). Recently, second order elastic analysis methods, also referred to as geometric nonlinear analysis (GNA), which account for structural deformations have been developed and

included in commercial software and design standards and specifications. When these methods are used, then design equations such as Eq. 30 can be used to compute the strengths without the need for moment amplification. Recently, advanced analysis methods, also referred to as geometric and material nonlinear analysis with imperfections (GMNAI) have been developed. These commonly use Finite Element Method (FEM) packages. The methods must consider all of the following:

(a) Flexural, shear and axial member deformations, and connection deformations that contribute to displacements of the structure;
(b) Second-order effects arising from displacements of the structure and its members;
(c) Geometric imperfections, comprising:
   - frame imperfections (out-of-plumbness),
   - member imperfections (out-of straightness), and
   - cross-sectional imperfections (distortions of cross-section);
(d) Stiffness reductions due to axial forces and inelasticity including the effect of residual stresses and partial yielding of the cross-section;
(e) Stiffness reductions due to cross-section deformations or local and distortional deformations;
(f) Uncertainty in system, member, and connection stiffness and strength.

For the strength and stability limit states, the revisions to AS/NZS 4600 (Standards Australia 2005) require the frame to support the factored limit states actions multiplied by $1/\phi$, where values of $\phi$ are given for prequalified frames. For steel storage racks, $\phi = 0.9$ and for pitched roof portal frames, $\phi = 0.85$. Connections are required to have adequate strength and ductility to ensure the structure fails within the members. The new methodology is based on the research of Cardoso et al. 2015).

## 6 Conclusions

Structural instability is one of the key limit states in structural design. With the advent of more complex structural systems and structural members, including high strength cold-formed steel sections, the need for advanced computer methods increases. Two of the key developments are the Direct Strength Method (DSM) of design of cold-formed steel sections, and advanced analysis of structural systems. This paper reviews the recent developments in these areas including the inclusion in structural design standards and specifications in Australia and North America. Two key developments in the DSM are design under localised loading, and beam-column design. For structural systems, the methods have progressed from linear elastic and second order elastic analysis to advanced analysis which is a type of geometric material nonlinear analysis with imperfections (GMNAI) which can be performed using Finite Element Method (FEM) software to produce direct designs without reference to particular member design rules. However, these methods still require the connections to be independently designed until sufficiently reliable FEM models of connections can be developed and validated.

**Acknowledgements.** The author is grateful to Professor Ben Schafer, Johns Hopkins University for the provision of Fig. 6.

## References

AISC. Specification for Structural Steel Buildings. ANSI/AISC 360-13, Chicago, Illinois (2013)

AISI. Direct Strength Method (DSM) design guide. AISI CF06-1, June, Washington, D.C. (2006)

AISI. North American Specification for the Design of Cold-Formed Steel Structural Members. AISI S100-2016, Washington, D.C. (2016)

British Standard. Eurocode 3 – Design of steel structures – Part 1.1 General rules and rules for buildings, BS EN 1993-1-1:2005 (2005)

British Standard. Eurocode 3 – Design of steel structures – Part 1.3 General rules – Supplementary rules for cold-formed members and sheeting, BS EN 1993-1-3:2006 (2006)

Cardoso, F.S., Rasmussen, K.J.R., Zhang, H.: System reliability-based criteria for design of cold-formed portal frames by advanced analysis. Paper Presented at International Eight International Conference on Advances in Steel Structures, Lisbon, Portugal, July 2015

Hancock, G.J., Kwon, Y.B., Bernard, E.S.: Strength design curves for thin-walled sections undergoing distortional buckling. J Constr. Res. **31**, 169–186 (1994)

Hancock, G.J., Pham, C.H.: Relationship between the semi-analytical finite strip methods for buckling analysis of thin-walled sections under uniform loading and localised loading. Paper Presented at the Eighth International Conference on Advances in Steel Structures, Lisbon, Portugal (2015)

Martins, A.D., Camotim, D., Dinis, P.B.: Behaviour and DSM design of stiffened lipped channel columns undergoing local-distortional interaction. Thin-Walled Struct. **101**, 181–208 (2016)

Moen, C.D., Schafer, B.W.: Direct strength method of design for cold-formed steel columns with holes. J. Struct. Eng. ASCE **137**(5), 559–570 (2011)

Natário, P., Silvestre, N., Camotim, D.: Direct strength prediction of web crippling failure of beams under ETF loading. Thin-Walled Struct. **98**, 360–374 (2016)

Nguyen, V.V.: Direct strength method for design of cold-formed steel sections under localised loading. Ph.D. thesis, University of Sydney (2017)

Nguyen, V.V., Hancock, G.J., Pham, C.H.: Development of the THIN-WALL-2 program for buckling analysis of thin-walled sections under generalised loading. Paper Presented at the Eighth International Conference on Advances in Steel Structures, Lisbon, Portugal (2015)

Nguyen, V.V., Hancock, G.J., Pham, C.H.: Application of the THIN-WALL-2 program for analysis of thin-walled sections under localised loading. Paper Presented at CIGOS 2017, Ho Chi Minh City, Vietnam (2017a)

Nguyen, V.V., Hancock, G.J., Pham, C.H.: New developments in the direct strength method (DSM) for design of cold-formed steel sections under localised loading. Paper Presented at Eurosteel 2017, Copenhagen, Denmark (2017b)

Pekoz, T.: Development of a unified approach to the design of cold-formed steel members. American Iron and Steel Institute Research report CF87-1, Washington, D.C. (1987)

Petroski, H.: To Engineer is Human. Vintage Books, New York (1992)

Pham, C.H.: Shear buckling of plates and thin-walled channel sections with holes. J. Constr. Res. **128**, 800–811 (2017)

Pham, C.H., Hancock, G.J.: Direct strength design of cold-formed C-sections in shear and combined actions. J. Struct. Eng. ASCE **138**(6), 759–768 (2012)

Pham, S.H., Pham, C.H., Hancock, G.J.: A direct strength method (DSM) of design for channel sections in shear with square and circular web holes. J. Struct. Eng. ASCE **04017017**, 1–8 (2017a)

Pham, S.H., Pham, C.H., Hancock, G.J.: Review of direct strength method of design for cold-formed steel structures with holes with a focus on shear. Paper Presented at CIGOS 2017, Ho Chi Minh City, Vietnam (2017b)

Santos, E.S., Dinis, P.B., Batista, E.M., Camotim, D.: Local-distortional-global interaction: experimental and numerical investigation. Paper Presented at Twenty Second International Specialty Conference on Cold-Formed Steel Structures, St. Louis, Missouri, USA (2014)

Schafer, B.W., Pekoz, T.: Direct strength prediction of cold-formed steel members using numerical elastic buckling solutions. Paper Presented at Fourteenth International Specialty Conference on Cold-Formed Steel Structures, St. Louis, Missouri, USA (1998)

Standards Australia. AS4100 Steel Structures. Standards Australia, Sydney (1998)

Standards Australia. AS/NZS 4600:2005 Cold-Formed Steel Structures. Standards Australia/Standards New Zealand (2005)

Torabian, S., Zheng, B., Schafer, B.W.: Development of a new beam-column design method for cold-formed steel lipped channel members. Paper Presented at Twenty Second International Specialty Conference on Cold-Formed Steel Structures, St. Louis, Missouri, USA (2014)

Yang, D., Hancock, G.J.: Compression tests of high strength steel columns with interaction between local and distortional buckling compression. J. Struct. Eng. ASCE **130**(12), 1954–1963 (2004)

Yap, D.C.Y., Hancock, G.J.: Experimental study of high strength cold-formed stiffened web C-sections in compression. J. Struct. Eng. ASCE **137**(2), 162–172 (2011)

Ziemian, R.: Guide to Stability Design Criteria for Metal Structures, 6th edn. Wiley, New Jersey (2010)

# Advanced Modelling of Structures (AMS)

# A Numerical Modeling of RC Beam-Column Joints Compared to Experimental Results

Q.-B. Bui[1(✉)], B. Sentosa[2], and T.-H. Duong[1]

[1] Sustainable Developments in Civil Engineering Research Group, Faculty of Civil Engineering, Ton Duc Thang University, Ho Chi Minh City, Vietnam
buiquocbao@tdt.edu.vn
[2] Université Savoie Mont Blanc, LOCIE – CNRS UMR 5271, Chambéry, France

**Abstract.** Beam-column joints are commonly considered critic regions for RC frames subjected to earthquake. That is why assessing the beam-column joint capacity is an important topic, especially for structures constructed before the modern seismic design codes, or for buildings in post-seismic situations. Among the in-situ structural assessment methods, the vibrational testing is currently mentioned. The authors have developed an analytical method to assess the damage evolution of a structure in function of its dynamic characteristics. The method consists of two main steps and the first one necessitates a robust model which can reproduce the static behavior of the studied structure. For this purpose, the authors try and assess the relevancy of existing numerical models to choose the most relevant for the second step. This paper presents an assessment of the CDP (Concrete Damage Plasticity) model implemented in the Abaqus software. First, an experimental study on a RC beam-column frames is presented. Unloading-reloading cycles were performed during the tests and the displacement fields were recorded by using the image correlation technique. The experimental data are used to assess the relevancy of the CDP model, but these data can be useful also for the further studies to verify and improve the accuracy of the numerical or analytical models.

**Keywords:** Reinforced concrete · Beam-column frame · Experiment · Abaqus modelling

## 1 Introduction

The seismic behaviour of reinforced concrete (RC) buildings can be affected by the performance of beam-column joints involved in the failure mechanism, especially in typical existing buildings. So, the assessment of the beam-column joint performance is an important topic, for existing structures and especially for post-seismic structures. A structural evaluation is needed to decide if a any retrofitting is requested. Among the in-situ structural assessment methods, the non-destructive method using vibrational measurements (by accelerometers or velocimeters) is currently mentioned (Boutin et al. 2005; Brownjohn 2003; Bui et al. 2014; Volant et al. 2002).

© Springer Nature Singapore Pte Ltd. 2018
H. Tran-Nguyen et al. (eds.), *Proceedings of the 4th Congrès International de Géotechnique - Ouvrages -Structures*, Lecture Notes in Civil Engineering 8,
DOI 10.1007/978-981-10-6713-6_5

From the dynamic characteristics measured by vibrational tests, several approaches were proposed in the literature to establish the relationship between the dynamic characteristics and the structure's health (Boutin et al. 2005; Chang et al. 2003; Fang et al. 2008; Maas et al. 2012). However, the proposed approaches enable to diagnose a structure on a global scale (the whole structure), while the damage assessment at a local scale (each element of the structure and the beam-column joints) remains to be explored (Bui et al. 2014; Maas et al. 2012). The authors have recently developed an analytical method which can use results for the vibrational measurements to identify the structural damages at the element scale, and especially for beam-column joints.

The method consists of two main steps. In the first step, the displacements of some specific points on the structure (corresponding to the principal mode shapes) and the actual stiffness (the stiffness corresponds to the damaged structure) should be relevantly determined. To obtain these information, the authors have chosen to use the numerical approach (FEM) and seeked a numerical model which could reproduce finely the structural behavior at the element's scale.

For the beam-column joint modelling, conventional approaches consider only beam and column flexibility, although joints can provide a significant contribution also to the overall frame deformability (DeRisi et al. 2016). Although several experiments have already been carried out in the literature at the RC beam-column frame level, the number of experiments is still modest comparing to the important number of parameters which affect the joint behaviour: interior joint, exterior joint, stiffness ratio between beam and column, steel reinforcement type, semi-rigid connections… (Bui et al. 2014; Haselton et al. 2008; Metelli et al. 2015; Omidi and Behnamfar 2015; Sharma et al. 2011). That is why additional experimental studies in this topic is interesting for the scientific community, to improve the existing models.

In this context, the presents first an experimental study on an RC beam-column frame structure, which provides additional experimental data for the further models. Unloading-reloading cycles were performed during the tests and the displacement fields were recorded by using the DIC (Digital Image Correlation) technique. Then, the obtained experimental results are used to assess the CDP (Concrete Damage Plasticity) model implemented in the Abaqus software (Abaqus 2012). The cracking is evaluated by using the Equivalent Plastic Straint (PEEQT) model.

## 2 Experiment

### 2.1 Materials and Structure Investigated

The structure studied is a beam-column RC structure having H-form (two columns and one beam, Fig. 1). The cross-sections of the beam and columns are (0.2 m × 0.2 m) and (0.2 m × 0.25 m), respectively.

The RC frame structure was fixed and the ends of the columns by steel jacks (Fig. 2). Then, the RC frame was loaded at the beam's mid-span by an actuator (maxi capacity of 300 kN), via a steel box placed on the beam (Fig. 2). The actuator was controlled in displacement (0.1 mm/min). The displacements were measured at the same time by displacement sensors (Fig. 2) and by the DIC (digital image correlation)

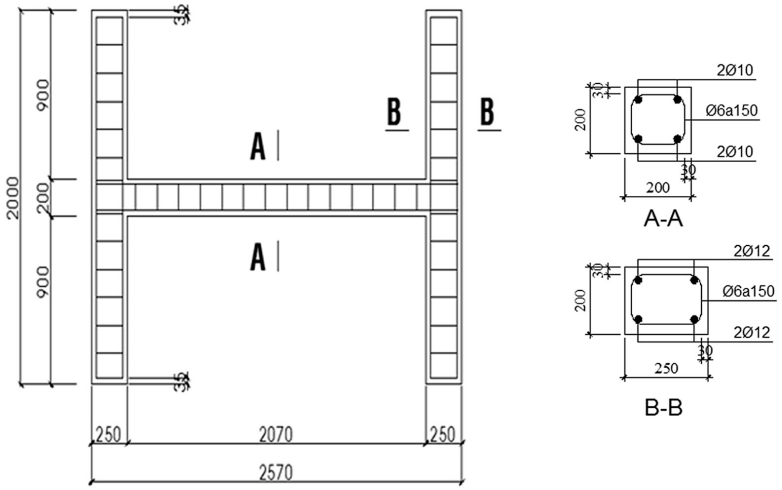


**Fig. 1.** Beam-column RC structure studied, dimensions in mm.

technique (Vacher et al. 1999). The use the DIC technique, two cameras (16 MPixels) were installed and recorded the test. After a data processing, the displacement fields (on whole structure tested) could be determined. To obtain better results with the DIC technique, RC beam-column structure was sprayed with black paint to have random points on its surface. Accelerometers (uniaxial and triaxial) were also installed on the structure to measure the dynamic characteristics and their relationship with the damage evolution; however, in this paper, due to the limited space, dynamic results will not be presented.

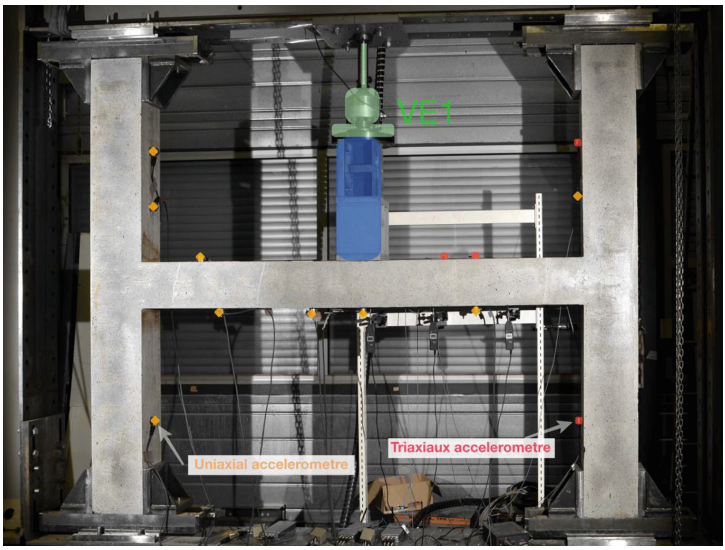


**Fig. 2.** Experimental model.

Concrete used was an industrial concrete "*béton pro 350*" of VICAT, which is similar to a C30/37 following Eurocode 2 Aydin et al. (2016). Three cylindrical specimens (16 cm-diameter and 32 cm-height) were manufactured (Fig. 3) for uniaxial compression tests to determine the compressive strength and the Young's modulus.

**Fig. 3.** Cylindrical specimens during the curing (at the left) and after the paint spraying for DIC (at the right).

## 2.2 Experimental Results

Uniaxial compression tests on cylindrical specimens gave results of 38.55 MPa for the mean compressive strength, 33.98 GPa for the Young's modulus and 0.217% for the strain corresponding to the maximal stress.

For the test on the beam-column structure, loading and unloading cycles were performed during the tests, in order to assess the performance of the numerical models in the case of cyclic loadings. The results are illustrated on Fig. 4: on the left, the experimental relationship between the force and the displacement at the beam's mid-span, with the "moments" of the cracks' apparition, corresponding to the crack numbers illustrated in Fig. 3 on the right. The crack apparition was captured by the DIC technique.

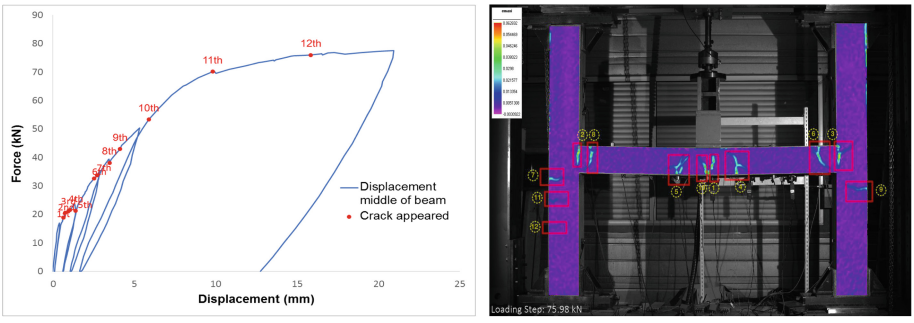


**Fig. 4.** Left: experimental relationship between the force and the displacement at the beam's mid-span. Right: crack apparition during the experiment.

# 3 Finite Element Modeling

## 3.1 RC Frame Model on Abaqus

Abaqus software was used for the present study, due to its robustness in the solving of complex problems. Solid elements were used for concrete parts and beam elements were used for steel reinforcement rods. The numerical model of the RC frame structure is shown in Fig. 5. The steel box was modelled at the beam mid-span, as in the experiment, and the loading was applied on this steel box.

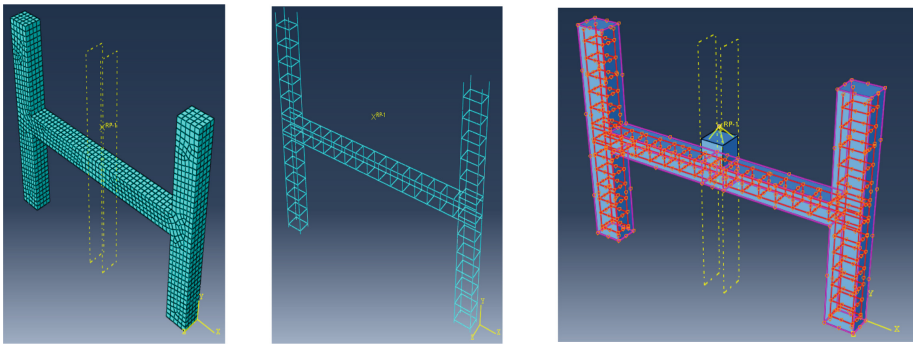

**Fig. 5.** Concrete, reinforcement steel rods and the entire RC frame structure modelled in Abaqus.

## 3.2 Material Characteristics

The compressive characteristics of the concrete (compressive strength, Young's modulus, stress-strain relationship) were determined from the tests on cylindrical specimens. Uniaxial compression tests on cylindrical specimens gave results of 38.55 MPa for the mean compressive strength, 33.98 GPa for the Young's modulus and 0.217% for the strain corresponding to the maximal stress. The tensile behavior of concrete was determined following the empirical relationships provided in *Eurocode 2* (2004). The stress-strain relationship of the steel was taken following the manufacturer data (steel S500B following Eurocode 2).

The characteristics of concrete and steel used for the numerical study are presented in Fig. 6. The CDP (Concrete Damage Plasticity) model was used to model the concrete behavior. Parameters used for this model are taken following values recommended in Aydin et al. (2016), after analyzing several studies existing in the literature (Cho et al. 2013; Hamid et al. (2012)Tejaswini and Raju 2015; Yusu and Muharrem 2015). It is important to note that these studies only investigated on RC beams and not yet on beam-column frame structures. So, an assessment on the relevancy of the proposed parameters for the case of RC beam-column frame is interesting (Table 1).

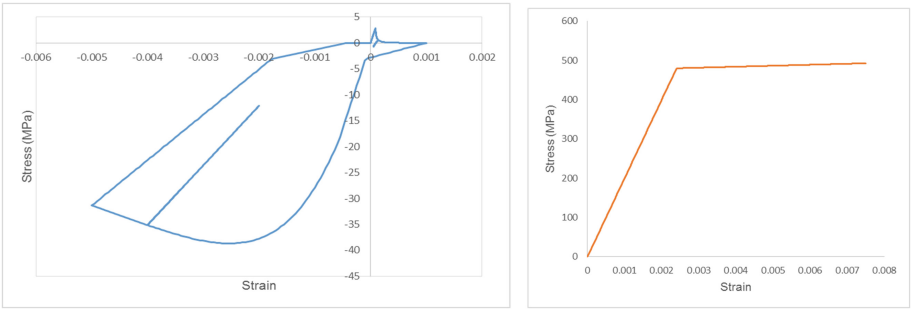


**Fig. 6.** Stress-strain relationships of concrete (left) and steel (right) used for the numerical model.

**Table 1.** Parameters used for concrete (CDP model).

| Parameter | Value | Description |
|---|---|---|
| $\psi$ | 56 | Dilation angle |
| e | 0.1 | Eccentricity |
| $f_{b0}/f_{c0}$ | 1.16 | The ratio of initial equibiaxial compressive yield stress to initial uniaxial compressive yield stress |
| K | 0.667 | The ratio of the second stress invariant on the tensile meridian |
| $\mu$ | 0.0001 | Viscosity parameter |

### 3.3 Numerical Results

The structure was also loaded in the model by a displacement control as in the case of the experiment. The result about the relationship between the force applied and the displacement of are presented in Fig. 7, on the left. The results shows that the

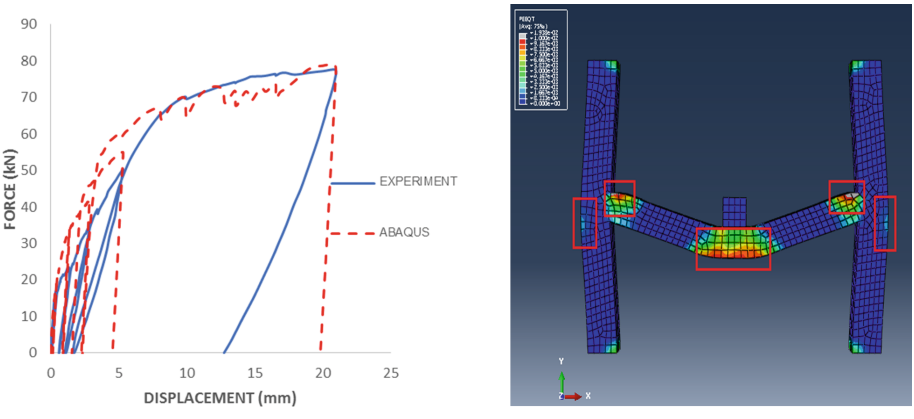


**Fig. 7.** Left: load – displacement curves at the beam's mid-span, obtained from the experiment and the modelling. Right: locations of the cracks in the numerical model at the maximal load.

numerical model could reproduce the global form of the force-displacement curve and the maximal load was captured. However, the cyclic effects were not well reproduced: the slopes of the unloading-reloading cycles in the numerical model was higher than that of the experiment; and the hysteresis phenomenon in the unloading-reloading cycles could not be reproduced by the model. This could come from the parameters and the model used. Further studies on this will be performed.

The cracking evolution could be visualized by using the PEEQT model in Abaqus and is presented in Fig. 7 (on the right) and Fig. 8, in which the twelve cracks appeared are respectively illustrated. By comparing the results in these figures with the experimental results (Fig. 4, on the right), it is observed that the cracking was well reproduced in the model in term of order of apparition, location of cracks and the force value

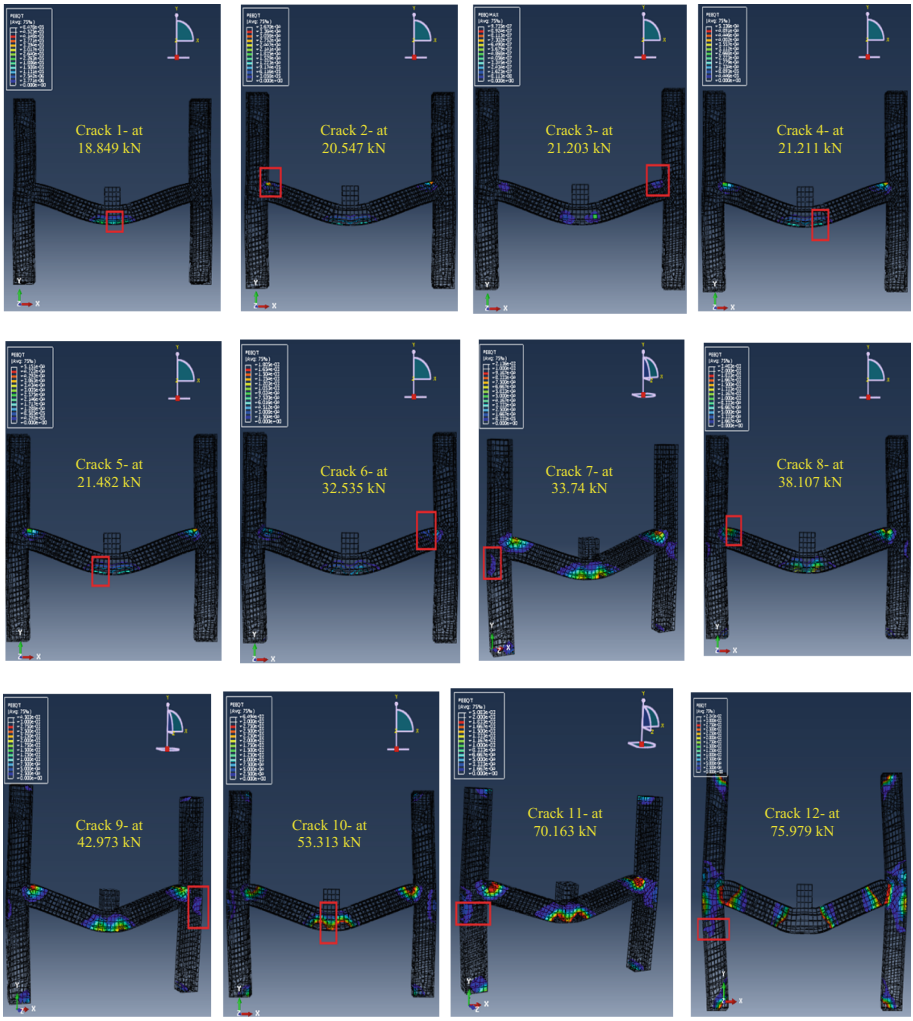


**Fig. 8.** Cracking evolution observed in the numerical model.

corresponding to each crack. The model could not precisely reproduce the real forms of the cracks observed in the experiment. However, this point can be improved by using the XEFM (Extend Finite Element Method) implemented in Abaqus.

If the results obtained by the model used in the present study are compared with that obtained by another model using the multi-fiber beams in CAS3 M code and the LaBorderie's model for concrete (that study was also carried out by the same authors, Sentosa et al. 2016), the results show that the LaBorderie multifiber model provided better results for the unloading-reloading cycles. However, visualizing of the cracking evolution is easier in Abaqus with the model used, which provides interesting information to verify the relevancy of the studied numerical model.

## 4 Conclusions

This paper presents an experimental and a numerical study on the behavior of a RC beam-column frame structure. Firstly, the experiment was performed on an H-form RC frame structure with several loading-unloading cycles. Displacement fields during the test were recorded by the DIC technique which enabled to visualize the cracking evolution.

For the numerical model, solid elements and the Concrete Damage Plasticity model were used for the concrete; the classical elasto-plastic model was used for the steel reinforcement rebars. The results showed that the model could reproduce the global behavior of the experimental test: global force-displacement curve, ultimate load, cracks apparition (location and order of apparition). However, the model could not reproduce correctly the unloading-reloading cycles (slopes and the hysteresis behavior). That means that the model investigated can be used for the case of static loadings. For the case of cyclic loading (earthquake for example), an improvement of the model is necessary and this will be the objective of the further studies.

## References

ABAQUS: ABAQUS Analysis User's Manual. ABAQUS Inc., Providence (2012)

Aydin, D., Hankan, O., Gokhan, D.: 3D nemerical modeling of RC deep beam behaviour by nonlinear finete element analysis. Disaster Sci. Eng. **2**(1), 13–18 (2016)

Boutin, C., Hans, S., Ibraim, E., Roussillon, P.: In situ experiments and seismic analysis of existing buildings. Part II: seismic integrity threshold. Earthq. Eng. Struct. Dyn. **34**, 1531–1546 (2005)

Brownjohn, J.M.W.: Ambient vibration studies for system identification of tall building. Earthq. Eng. Struct. Dyn. **32**, 71–95 (2003)

Bui, Q.B., Hans, S., Boutin, C.: Dynamic behaviour of an asymmetric building: experimental and numerical studies. Case Stud. Nondestr. Test. Eval. **2**, 38–48 (2014a)

Bui, Q.B., Mommessin, M., Perrotin, P., Plassiard, J.P., Plé, O.: Assessing local-scale damage in reinforced concrete frame structures using dynamic measurements. Eng. Struct. **79**, 22–31 (2014b)

Sentosa, B., Bui, Q.B., Plassiard, J.P., Plé, O., Perrotin, P., Purnomo, H.: Redistribution of moment at beam-column joints in RC structures: comparison between an experimental study and Eurocode 2. Submitted to CIGOS 2017, Ho Chi Minh City, Vietnam (2016)

Chang, P.C., Flatau, A., Liu, S.C.: Review paper: health monitoring of civil infrastructure. Struct. Health Monit. **2**, 257–267 (2003)

Chao, Z., Peng, C., Yixiang, C., Jianbo, J.: Using finite element software to similation fracture behavior of three-point bending beam with initial crack. J. Softw. **8**(5), 1145–1150 (2013)

DeRisi, M.T., Ricci, P., Verderame, G.M.: Modelling exterior unreinforced beam-column joints in seismic analysis of non-ductile RC frames. Earthq. Eng. Struct. Dyn. (2016) doi:10.1002/eqe.2835

Eurocode 2: Design of concrete structures - EN 1992, European Committee for Standardization (2004)

Fang, S.E., Perera, R., Roeck, G.D.: Damage identification of a reinforced concrete frame by finite element model updating using damage parameterization. J. Sound Vib. **313**, 544–559 (2008)

Hamid, S., Mahdi, S., Amir, H.A., Mohammad, A., Ali, S.: Evaluation of reinforced concrete beam behaviour using finite element analysis by ABAQUS. Sci. Res. Essays **7**(21), 2002–2009 (2012)

Haselton, C.B., Liel, A.B., Lange, S.T., Deierlein, G.G.: Beam-Column Element Model Calibrated for Predicting Flexural Response Leading to Global Collapse of RC Frame Buildings. Pacific Earthquake Engineering Research Center, PEER 2007/03, 152 p., May 2008

Maas, S., Zürbes, A., Waldmann, D., Waltering, M., Bungard, V., De Roeck, G.: Damage assessment of concrete structures through dynamic testing methods. Part 1- Laboratory tests. Eng. Struct. **34**, 351–362 (2012)

Metelli, G., Messali, F., Beschi, C., Riva, P.: A model for beam–column corner joints of existing RC frame subjected to cyclic loading. Eng. Struct. **89**, 79–92 (2015)

Omidi, M., Behnamfar, F.: A numerical model for simulation of RC beam-column connections. Eng. Struct. **88**, 51–73 (2015)

Sharma, A., Eligehausen, R., Reddy, G.R.: A new model to simulate joint shear behavior of poorly detailed beam–column connections in RC structures under seismic loads Part I: exterior joints. Eng. Struct. **33**, 1034–1051 (2011)

Tejaswini, T., Raju, M.V.R.: Analysis of RCC Beams using ABAQUS. Int. J. Innov. Eng. Technol. **5**, 248–252 (2015)

Vacher, P., Dumoulin, S., Morestin, F., Mguil-Touchal, S.: Bidimensional strain measurement using digital images. Proc. Inst. Mech. Eng. Part C: J. Mech. Eng. Sci. **213**, 811–817 (1999)

Volant, P., Orbovic, N., Dunand, F.: Seismic evaluation of existing nuclear facility using ambient vibration test to characterize dynamic behavior of the structure and microtremor measurements to characterize the soil: a case study. Soil Dyn. Earthq. Eng. **22**, 1159–1167 (2002)

Yusu, S., Muharrem, A.: Defining parameters for concrete damage plasticity model. Challlenge J. Struct. Mech. **1**(3), 149–155 (2015)

# Application of a Newly Puzzel Shaped Crestbond Rib Shear Connector in Composite Beam Using Opposite T Steel Girder: An Experimental Study

Duy Kien Dao[1], Duc Vinh Bui[2], Thi Hai Vinh Chu[3], and Van Phuoc Nhan Le[2(✉)]

[1] Department of Civil Engineering, Pusan National University, Geumjeong-Gu, Busan, Korea
kiendaoduy@gmail.com
[2] Department of Civil Engineering, Ho Chi Minh City University of Technology, District 10, Ho Chi Minh City, Vietnam
{vinhbd, lvpnhan}@hcmut.edu.vn
[3] Faculty of Civil Engineering, MienTrung University of Civil Engineering, Tuy Hoa City, Phu Yen, Vietnam
chuthihaivinh@muce.edu.vn

**Abstract.** The shear connector is the most important part of a composite beam and promotes a composite action between a steel beam and concrete slab. This paper presents the experiment results of three large-scale composite beams with a newly puzzle shaped crestbond rib shear connector. The behavior of this shear connector was investigated and the results were correlated with those obtained from the push-out-test specimens. Four-point-bending load testing was carried out on steel-concrete composite beam models to consider the effects of the concrete strength, number of transverse rebars in the crestbond and the width of the concrete slab. The results of large scale experimental test include of: the deflection, ultimate load, strains of the concrete, steel beam and Perfobond connectors; the relative slip between the steel beam and the concrete slab at the end of the beams; and the relative failure mechanism. The results showed that the general behavior of a steel-concrete composite beam using Perfobond shear connectors was similar to that of a steel-concrete composite beam using conventional shear connectors such as head stud shear conector. The newly puzzle shaped crestbond shear connectors showed satisfactory performance, and could be considered for application in composite structures.

**Keywords:** Crestbond rib shear connector · Concrete-steel composite beam · Composite behavior · Shear resistance · Opposite steel beam

## 1 Introduction

There are lots of studies on behavior of these two well-known shear connectors [1]. Several modifications are proposed for Perfobond shear connectors up to date [2–6]. A Perfobond shear connector is a typical rigid shear connector. It consists of a flat steel

© Springer Nature Singapore Pte Ltd. 2018
H. Tran-Nguyen et al. (eds.), *Proceedings of the 4th Congrès International de Géotechnique - Ouvrages -Structures*, Lecture Notes in Civil Engineering 8,
DOI 10.1007/978-981-10-6713-6_6

pale with holes, and its shear resistance strength is provided by the concrete end bearing, concrete dowel resistance of the holes, and rebar penetrating the holes. The existence of open holes can create an advantage in placing reinforcing bars though the holes. The open holes of crestbond rib shear connectors were designed to be able to obtain two crestbond ribs when cutting a steel rib [7, 8]. It is welded along the length of a steel beam at the interface of the concrete slab and top flange of the steel beam. However, there are relatively few studies on crestbond rib shear connectors compared to those on Perfobond ribs, and various parameters were not considered [9]. Lorence *et al.* [10–12] proposed a new type of crestbond where the steel connector constitutes an integral part of the steel part of the composite beam, which is subjected, apart from the local longitudinal shear acting between the steel and concrete, to the global effects of bending and axial loading. The stress criteria describing a composite dowel's behavior must be established and involve much more than the pure load-bearing capacity criteria used at present. Test procedures combining the concept of the load-bearing capacity of the concrete part of the connector and the elasticity of its steel part lead to the efficient design of composite structures. The opened holes made the assembly of the concrete slab steel reinforcement easier.

For this reason, a newly puzzle shaped crestbond rib connector with a "ʊ" shape was proposed by Chu *et al*. [13]. To reduce the stress concentration on steel dowel, the steel-dowel and dowel-root were redesigned more circular, and the dowel-core is lager. Its shear resistance and composite behaviors were examined in a push-out test. Six push-out test specimens were fabricated and five main parameters were considered in the push-out test to evaluate the effects of shear resistance parameters such as the dimensions of the crestbond rib, transverse rebars in the crestbond dowel, concrete strength, rebar strength, dowel action on the shear strength. A design equation was proposed based on the test results. However, its applicability to a composite beam as a shear connector was not examined. In this study, therefore, static loading tests were conducted on a composite beam with a newly puzzle shaped crestbond rib. Three full-size steel-concrete composite beams with this shear connector were fabricated to compare the composite behaviors in relation to the transverse reinforcement and concrete compressive strength. Based on loading tests, their structural behaviors such as their loading capacities, deflections, relative slips, crestbond rib strains, and failure mechanisms were quantitatively investigated.

## 2 Experimental Program

### 2.1 Material Properties

To examine the material properties of the concrete, concrete cube and cylinder specimens were fabricated at the same time as the concrete slab for each beam was cast. The ratios of 0.52 and 0.34 of Water/Cement (W/C) were applied to fabricate the concrete B25 and B40, respectively. The material properties of the concrete, steel beam, and crestbond rib are dertermined. The yield strength and ultimate strength of the transverse and longitudinal rebars were 250 MPa and 390 MPa, respectively.

## 2.2 Test Specimens

To examine the applicability and composite behaviors of the puzzle shaped crestbond rib in composite beams under monotonic loading, three full-size composite beams were prepared (B1, B2, and B3). Each composite beam had a 4000 mm of length and a concrete slab that was 120 mm thick and 600 mm wide. Specially, cross section of B2 is chamfered to compare the ability to work with B1, and the cross section area of B1, B2, B3 were same. Two longitudinal rebars with a diameter of 12 mm were installed in this concrete slab. An opposite T beam with a height of 264 mm and flange width of 200 mm was used. For the shear connector, a continuous crestbond rib shear connector with a height of 70 mm and a thickness of 8 mm was attached to the top flange of the steel H beam, as shown in Fig. 1.

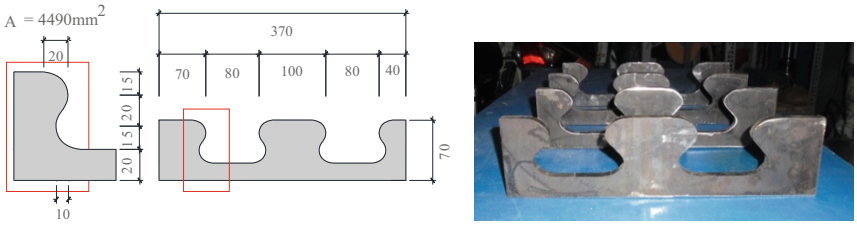


**Fig. 1.** Dimensions of crestbond connector used [13]

For the transverse rebars in the crestbond holes, composite beam specimens B1, B2 and B3 used two transverse rebars passing through each of the crestbond holes, as shown in Fig. 2. A 12-mm rebar was used as the transverse rebar for the crestbond rib holes. The compressive strength of the concrete slab was considered as the main parameter. The concrete material properties of composite beam specimens B2 and B3 were changed to 39.9 MPa and 50.4 MPa, respectively. The sectional and material characteristics of each composite beam specimen are summarized in Table 1.

## 2.3 Test Setup

A hydraulic jack was used to apply a load to the composite beam with the newly puzzle shaped crestbond rib. To apply a four-point-bending moment to the composite beam specimen, two lateral steel transfer beams were placed at distances of 350 mm from the mid-span. To measure the relative slip at the composite interface, deflection, and strain distributions of the composite beam, strain gauges and linear variable displacement transducers (LVDTs) were installed as shown in Fig. 3. Accordingly, these are the positions to determine the failure of crestbond rib, concrete slab, and steel beam that maximum stress is occurred.

First, the composite beam specimens were loaded to 40% of the predicted failure load and then unloaded. Then, this load level was repeated 25 times to eliminate friction between the concrete slab and the steel beam. Finally, loading tests were conducted at loads increasing toward the ultimate load, $P_{max}$. These tests were terminated after decreasing the load back to 90% of $P_{max}$.

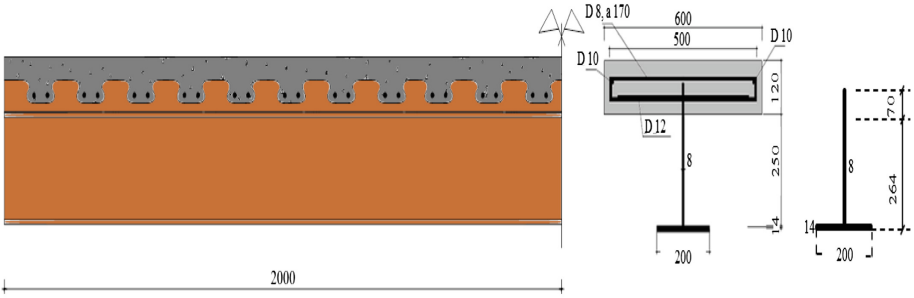


Composite beam specimen B1

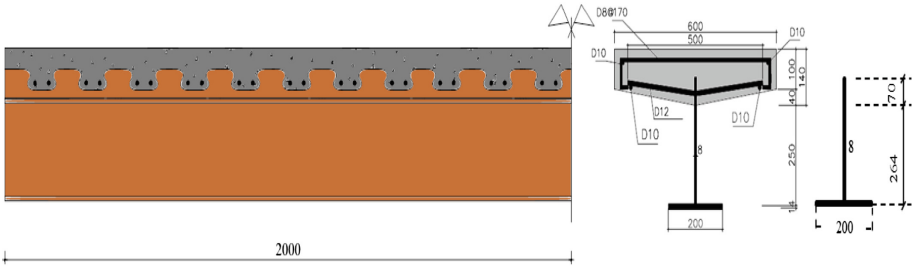


Composite beam specimen B2

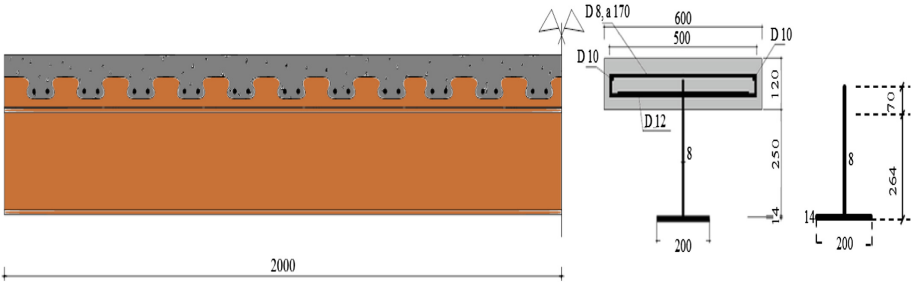


Composite beam specimen B3

**Fig. 2.** Dimensions of composite beam specimen

**Table 1.** Composite beam specimens

| | | Concrete slab | | Steel beam | No. of transverse reinforcement | Note |
|---|---|---|---|---|---|---|
| | Grade | Compressive strength $f_c$ | Section (H × W) | | | |
| | | MPa | mm | | | |
| B1 | C30 | 39.9 | 120 × 600 | ↕264 × 200 | 2 | All holes |
| B2 | C30 | 39.9 | (100–140) × 600 | ↕264 × 200 | 2 | All holes |
| B3 | C40 | 50.4 | 120 × 600 | ↕264 × 200 | 2 | All holes |

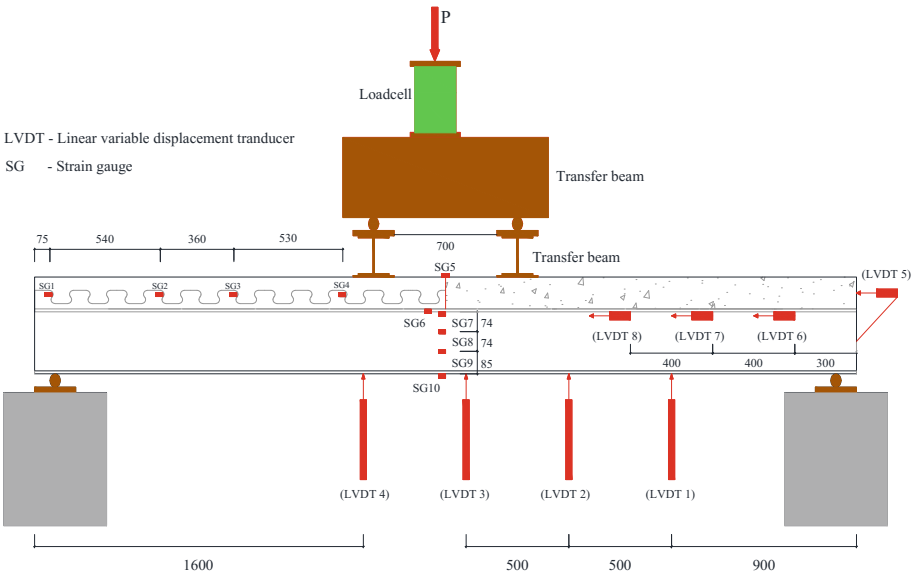


**Fig. 3.** Test schematic and arrangement of instruments.

## 3 Results And Discussion

### 3.1 Load-Displacement Relationships and Load-Deflection Relationships

To examine the structural behaviors of composite beam specimens with the newly puzzle shaped crestbond rib, their load-displacement and load-deflection relationships were compared using four LVDTs placed at locations that were 0.8 m, 1.3 m, 1.9 m, and 2.25 m from the right end of the composite beam, named LVDT1 to LVDT4, respectively. Figure 4 compares the curves of the load vs. deflection at the mid-spans of

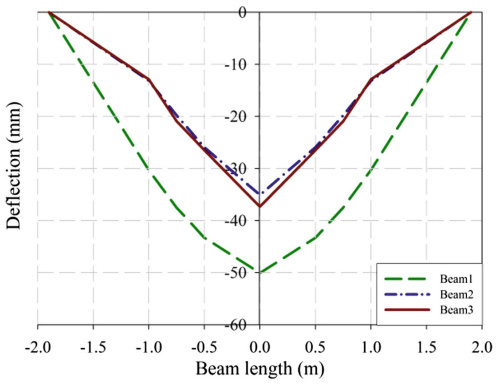


**Fig. 4.** Comparison of maximum load vs. deflection at mid-span curves of beams B1, B2, and B3

the three beams. The deflection at the mid-span of beam B1 is the highest, whereas that of beam B2 and B3 is same. This is reasonable because the flexural stiffness of beam B2 was the highest among these beams. The deflection of beam B1 was 42.7% and 34.1% increased than that of beam B2, and B3, respectively. This also shows that the concrete compressive strength and the shape of cross section significantly affect the behavior of concrete-steel composite beams using the newly puzzle shaped crestbond rib shear connectors.

### 3.2 Load-Relative Slip at Composite Interface

To measure the relative slip between the concrete slab and the ↕ beam, four LVDTs were installed at distances of 0 m, 0.3 m, 0.7 m, and 1.1 m from the end of the beam. At location of ultimate load, the relative slip between the concrete slab and the steel girder of beam B1 was 18.1% greater than that of beam B2. This result is likely due to the different shape of cross section. In previous research, Chu *et al.*, the ductility of the connectors depended on the concrete strain. Therefore, the concrete part enclosing the steel bars decreases when the transverse reinforcement is increased. Because failure of the concrete occurs more quickly, the ductility of the connectors decreases.

The relative slip between the concrete slab and the steel girder of beam B3 was the smallest because the stiffness of the concrete slab was greater. This delayed the failure of the concrete in the connection and resulted in increases in the ductility and shear resistance of the Perfobond connector, which caused a lower relative slip between the concrete slab and the steel girder of beam B3. A comparison of the relative slips of the beams is shown in Fig. 5.

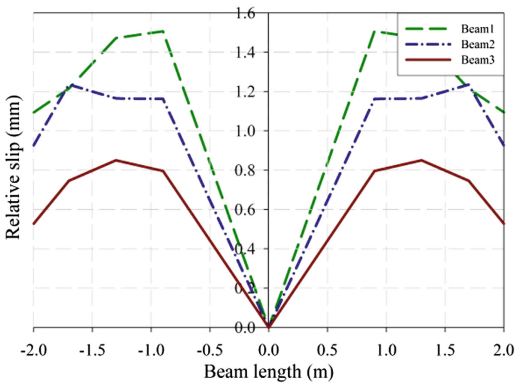


**Fig. 5.** Comparison of maximum load vs. relative slip at mid-span curves of beams B1, B2, and B3.

### 3.3 Strain of Concrete Slab

The strain of the concrete slab was observed by strain gauges attached at the top and bottom of the concrete slab, named SG5 and SG6. Figure 6 shows the load-strain curves recorded at the top (left side) and bottom (right side) of the concrete slab. At low

loading, both surfaces of the concrete slab were in compression. With increasing load, the bottom surface became gradually supported in tension. In beam B3, the compressive region lasted longer because the concrete slab of this beam was made of C40, with a compressive strength greater than that of beams B1 and B2.

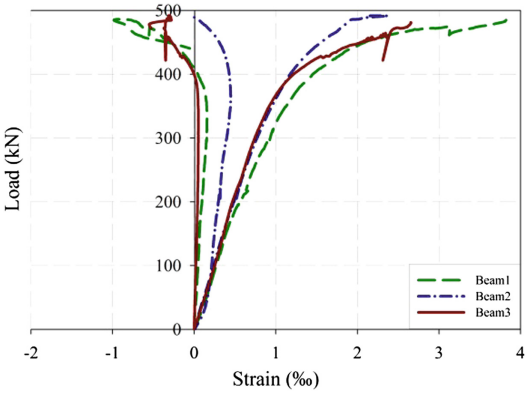


**Fig. 6.** Load-strain relationships of concrete slabs

### 3.4 Strain of H Beam and Strain of Newly Puzzle Shaped Crestbond Rib

The steel strain was recorded by strain gauges attached at the mid-span sections of the steel girders. Strain gauges SG7 and SG10 were attached at the top and bottom flanges of the steel girders, and SG8 and SG9 were attached at the webs of the steel girders. The strain results are simply shown in Fig. 7(a). The strain of the steel beam increases in proportion to the distance from the neutral axis to the tensile fibers. At the mid-span section, the strain of the steel girder reached the plastic yield level at the outer fiber, while the strain at the inner fibers near the centroid axis of the beam was still small at the time of beam failure.

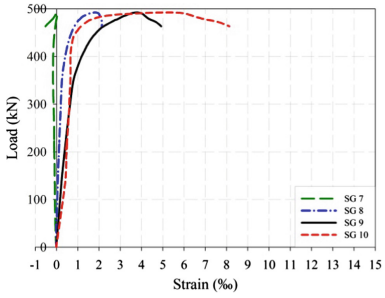


(a) Load–strain relationships of H beam

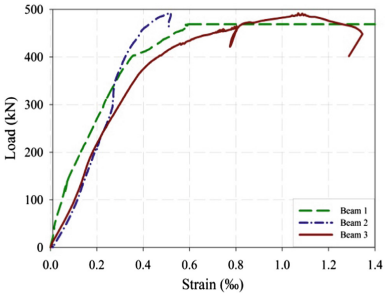


(b) Comparison of beams at SG3

**Fig. 7.** Strain of H beam (a) and Strain of newly puzzle shaped crestbond rib (b)

Strain gauges SG1 to SG4 were attached to the Perfobond shear connectors in order to investigate the Perfobond strains at different positions. The relative slip between the steel girder and the concrete slab increased as the load increased. The Perfobond strain was rather small, and the Perfobond was in compression, as shown in Fig. 7(b). Perfobond steel has a plastic strain of 1.8‰, while the maximum measured strain was 1.3‰, which means that no failure occurred at the Perfobond. Figure 7(b) shows that the neutral axis (the line passing through the points where the strain equaled zero) in beam B3 is insider of the concrete slab than the zero lines in beams B1 and B2. This resulted in a greater compressive strain of the crestbond in beam B3 at the position where the strain gauge was attached, in comparison to those in beams B1 and B2.

### 3.5 Failure Mode of Composite Beam with Newly Puzzle Shaped Crestbond Rib

Failures occurred only in the concrete slab and steel girder, with no failure occurring in the Perfobond shear connectors. This is entirely consistent with the strain results for the concrete slab and steel girder, as illustrated in Fig. 8. The strains in the steel girder and concrete slab exceeded 1.8‰ and 2.0‰, respectively, while the maximum Perfobond strain only reached 1.3‰, as mentioned above. The results also showed that the neutral axis was lower in beam B1, and B2 than in beams B3, even though B3 was made of higher-strength concrete. This is because the concrete strength of beam B3 was higher than those of beams B1 and B2, which resulted in a decrease in the hardness of the concrete slab. The neutral axis in beam B1, B2 was very close to the upper fiber of the steel girder, whereas the zero line in beams B3 was far from the upper fiber of the steel girder. It is assumed that the concrete compressive strength considerably affected the capacity and strain of the steel-concrete composite beams.

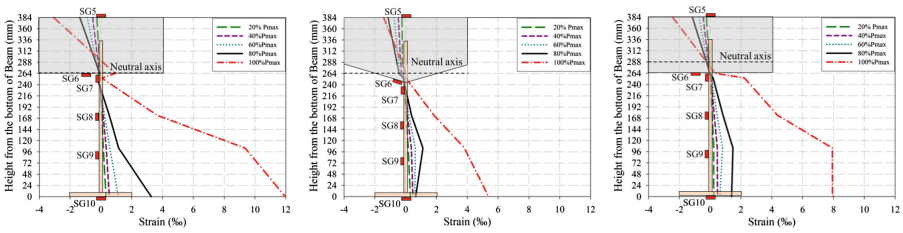


(a) Composite beam B1 (b) Composite beam B2 (c) Composite beam B3

**Fig. 8.** Failure modes of composite beam specimens

Figure 8 shows that only the neutral axis of beam B1, and B2 was located correctly, based on its designation, while the neutral axes of beams B3were located in the concrete slab. This phenomenon could have occurred because the concrete strengths of test beams B3 higher than the designated concrete strength, and the steel plate of the crestbond helped to improve the compressive strength of the concrete slab.

### 3.6 Effect of Shape of Cross Section of Concrete Slab on Behavior of Composite Beam Using Newly Puzzel Shape of Crestbond Crib

The effect of cross section of concrete slab on behavior of composite beam using newly puzzle shaped crestbond rib was simply described in Fig. 8. The results indicated that the change of cross section of Beam 2 was significant to reduce of 30% displacement and 22.3% relative slip in comparison with that of Beam 1. Simultaneously, the stiffness of Beam 2 was higher than Beam 1. Therefore, this study proposed a modified cross section in design, the compression area of concrete slab should be increased, and the reduction of area at the edge.

## 4 Conclusions

In this study, static loading tests of three full-size steel-concrete composite beams with newly puzzle shaped crestbond rib shear connector were carried out to examine the applicability of these connectors in composite beams, and to evaluate the effects of the transverse reinforcement and concrete compressive strength on the behaviors of composite beams with them. Therefore, the loading capacity, deflections, relative slips, strains of the crestbond ribs, and failure mechanisms of composite beams with the newly puzzle shaped crestbond ribs were quantitatively investigated. The following conclusions can be drawn:

(i) The compressive strength of the concrete considerably influenced the behavior of the steel-concrete composite beam. Increasing the compressive strength enhanced the load capacity and decreased the deflection of the beam.
(ii) The ductility of the connector depended on the concrete strain. The concrete part enclosing the steel bars decreased when the transverse reinforcement was increased, the concrete failed more quickly, and the ductility of the connector decreased.
(iii) Failures occurred only in the concrete slab and steel girder, with no failure occurring in the Perfobond shear connectors. Therefore, the thickness of the newly puzzle shaped crestbond rib shear connectors will be reduced in the next experiment.
(iv) The newly puzzle shaped crestbond rib shear connectors could be used as shear connectors, and should be considered for application in a composite bridge, which utilizes a large number of steel beams.

**Acknowledgments.** This study has been supported in part by HOANG VINH Technology Research and Construction Consultants (HOANG VINH TRCC) in Vietnam.

## References

1. Shariati, A., et al.: Various types of shear connectors in composite structures: a review. Int. J. Phys. Sci. **7**(22), 2876–2890 (2012)

2. Kim, S.H., et al.: Y-type perfobond rib shear connectors subjected to fatigue loading on highway bridges. J. Constr. Steel Res. **122**, 445–454 (2016)
3. Kim, S.H., et al.: Shear resistance characteristic and ductility of Y-type perfobond rib shear connector. Steel Compos. Struct. **18**(2), 497–517 (2015)
4. Rodrigues, J.P.C., Laím, L.: Experimental investigation on the structural response of T, T-block and T-Perfobond shear connectors at elevated temperatures. Eng. Struct. **75**, 299–314 (2014)
5. Kim, S.-H., et al.: Behavior of composite girder with Y-type perfobond rib shear connectors. J. Constr. Steel Res. **103**, 275–289 (2014)
6. Kim, S.-H., et al.: End-bearing resistance of Y-type perfobond rib according to rib width-height ratio. J. Constr. Steel Res. **103**, 101–116 (2014)
7. Seidl, G.: Precobeam-prefabricated enduring composite beams based on innovative shear transmission. Final Report RFSR-CT-2006-00030 (2011). (http://bookshop.europa.eu)
8. Seidl, G.: Prefabricated enduring composite beams based on innovative shear transmission–Final Report RFSR-CT-2006-00030. sl: Eur. Comm. (2011)
9. Chromiak, P., Studnicka, J.: Shear connector for composite beam. Taylor and Francis Group (2006)
10. Lorenc, W., Kubica, E., Kożuch, M.: Testing procedures in evaluation of resistance of innovative shear connection with composite dowels. Arch. Civ. Mech. Eng. **10**(3), 51–63 (2010)
11. Lorenc, W., Kożuch, M., Rowiński, S.: The behaviour of puzzle-shaped composite dowels—Part I: Experimental study. J. Constr. Steel Res. **101**, 482–499 (2014)
12. Lorenc, W., Kożuch, M., Rowiński, S.: The behaviour of puzzle-shaped composite dowels—Part II: Theoretical investigations. J. Constr. Steel Res. **101**, 500–518 (2014)
13. Chu, T.H.V., et al.: Resistance behaviors of a newly puzzle shape of crestbond rib shear connector: an experimental study. Steel Compos. Struct. **21**(5), 1157–1182 (2016)

# Application of the THIN-WALL-2 V2.0 Program for Analysis of Thin-Walled Sections Under Localised Loading

Van Vinh Nguyen[1,2], Gregory J. Hancock[1], and Cao Hung Pham[1(✉)]

[1] The University of Sydney, Sydney, NSW, Australia
{vanvinh.nguyen, gregory.hancock, caohung.pham}@sydney.edu.au
[2] University of Transport and Communications, Hanoi, Vietnam

**Abstract.** The Finite Strip Method (FSM) has been developed for pre-buckling and buckling analyses of thin-walled sections under localised loading for general end boundary conditions. The theory is included in the THIN-WALL-2 V2.0 program which has been developed at the University of Sydney using a MATLAB graphical interface, Visual Studio C++ computational engines and a FSM module. The paper describes the application of the THIN-WALL-2 V2.0 program in analysis of thin-walled sections under the four localised loading cases namely IOF (Interior one-flange loading), EOF (End one-flange loading), ITF (Interior two-flange loading) and ETF (End two-flange loading). A linear analysis is required for pre-buckling analysis to determine the pre-buckling modes and the membrane stresses of structural members subjected to localised loading. These stresses are then used in the buckling analysis to get the buckling load and the buckling modes of the structural members.

**Keywords:** Thin-walled sections · Localised load · Pre-buckling analysis · Buckling analysis · Finite Strip Method · THIN-WALL-2

## 1 Introduction

The development of the Direct Strength Method (DSM) for design of cold-formed steel sections as specified in the North American Specification for the Design of Cold-Formed Steel Structural Members AISI S100-2012 (2012) and the Australian/New Zealand Standard AS/NZS 4600:2005 (2005) requires the ability to compute the elastic buckling loads of thin-walled sections including overall (Euler), distortional and local modes. Li and Schafer (2010) developed the CUFSM computer program for the buckling analysis of thin-walled members under compression and bending. The program is based on the Constrained Finite Strip Method (cFSM) developed by Ádány and Schafer (2014a) and (Ádány and Schafer 2014b). Another computer program THIN-WALL was developed by Papangelis and Hancock (1994) which is also used for analysis of thin-walled sections under compression and bending. This program is based on the Semi-Analytical Finite Strip Method (SAFSM) of analysis developed by Cheung (1976) and then applied to the buckling of thin-walled sections under compression and bending by Plank and Wittrick (1974). Currently, both of these programs

© Springer Nature Singapore Pte Ltd. 2018
H. Tran-Nguyen et al. (eds.), *Proceedings of the 4th Congrès International de Géotechnique - Ouvrages -Structures*, Lecture Notes in Civil Engineering 8,
DOI 10.1007/978-981-10-6713-6_7

are not available for analysis of thin-walled sections under localised loading. An alternative approach based on Generalised Beam Theory (GBT) has been recently developed by D. Camotim and his colleagues in a program namely GBTWEB (Natário et al. 2015). The latest version of this program allows for arbitrary cross-sections, and arbitrary loadings. More recently, Nguyen et al. (2015) developed the THIN-WALL-2 V1.0 program for analysis of thin-walled sections under uniform stresses due to compression, bending and shear force and localised loading with simply supported boundary condition.

This paper introduces a new development of the THIN-WALL-2 V2.0 program used for analysis of thin-walled sections under generalised loading. In addition, an overview about the Finite Strip Method (FSM) used to develop the program is given. The paper also gives a comparison between the three versions of the THIN-WALL program to assess the new development. Finally, a detailed description about Version 2.0 of the THIN-WALL-2 program in analysis of thin-walled sections under localised loading is provided.

## 2 Finite Strip Method-Brief Overview

The Finite Strip Method is an effective method for the static, stability, post-buckling and vibration analyses of thin-walled structures. In this method, in order to give compatibility between strips, the longitudinal harmonic series are chosen to satisfy the boundary conditions at the longitudinal ends of strips of structural members. In this case the FSM is known as the Semi-Analytical Finite Strip Method (SAFSM). In another case, the local spline functions are used instead of the harmonic series functions in the longitudinal direction to account for different boundary conditions. This is known as the Spline Finite Strip Method (SFSM).

The SAFSM analysis implemented in the THIN-WALL-2 program uses two different versions of the SAFSM buckling analysis. The first is **bfinst7.cpp** (Hancock and Pham 2012) for uniform loading which uses complex mathematical functions with no end constraints and so shear modes and the signature curve associated with shear are included as well as those associated with bending and compression. The second is **bfinst10.cpp** (Hancock and Pham 2015) for localised loading which assumes simply supported end boundary conditions and arbitrary loading. The theory including displacement functions used in the buckling analyses is described in detail in (Hancock and Pham 2015). Also, the theory is included in Version 1.0 of the THIN-WALL-2 program (Nguyen et al. 2015) for analysis of thin-walled sections under localised loading with simply supported boundary condition.

The FSM has been developed for analysis of thin-walled sections under localised loading for general end boundary conditions as described in (Nguyen et al. 2016a) and (Nguyen et al. 2016b). This theory is included in Version 2.0 of the THIN-WALL-2 program as described in this paper.

# 3 The THIN-WALL-2 V2.0 Program Outline

## 3.1 Domain of Application

The THIN-WALL-2 V2.0 program is written to define input data using a Graphical User Interface (GUI) to perform pre-buckling and buckling analyses of thin-walled sections under generalised loading. The loading may contain uniform stress and localised loading. The GUI is then used to display the results of the analyses. It is also possible to use this program to perform a cross-section analysis to generate the section properties. The cross-sections can be formed from different shapes includes open and closed sections or mixed sections.

## 3.2 Code Structure

The THIN-WALL-2 V2.0 program contains the GUI which calls three programs: bfinst7.cpp, bfinst10.cpp which are written using C++ computer language and the FSM module which is written by Matlab. The bfinst7.cpp program as described in (Pham et al. 2014) and (Hancock and Pham 2015) is used in a Uniform Stress module where the main functions are a cross-section analysis, a stress analysis and a buckling analysis of thin-walled sections under uniform stress. The bfinst10.cpp program is used in a Localised Loading module for both analysis of thin-walled sections under localised loading with both end simply supported boundary condition as described in (Hancock and Pham 2015). The FSM module is used for analyses of thin-walled sections under localised loading with general end boundary conditions.

The program sequence in THIN-WALL-2 V2.0 is shown in Fig. 1. In the first step, the user defines the input data such as materials, element types, sections and the restraints. The second step includes two types of analysis of a structural member under loads. The first type is the analysis of a structural member under uniform stress. In this case, the user defines the half-wavelengths and assigns the uniform loads such as compression, bending and shear before running the section analysis, the stress analysis and the buckling analysis. The second type is the analysis of a structural member under localised loading. The user defines the series terms number, the boundary conditions and assigns the localised loading before running the pre-buckling analysis and the buckling analysis. In the final step, the results from the analyses are displayed on the main window of THIN-WALL-2 V2.0 and exported to data files.

## 3.3 Comparison Between THIN-WALL-2 V2.0 with Previous Versions

The THIN-WALL-2 V2.0 program is developed by expanding the functions of the THIN-WALL and THIN-WALL-2 V1.0 programs. This expansion refers to the extension of THIN-WALL-2 V2.0 to pre-buckling and buckling analyses of thin-walled sections under generalised loading such as uniform stress or localised loading with general boundary condition compared to only uniform compression and bending in THIN-WALL and only simply supported boundary condition for localised

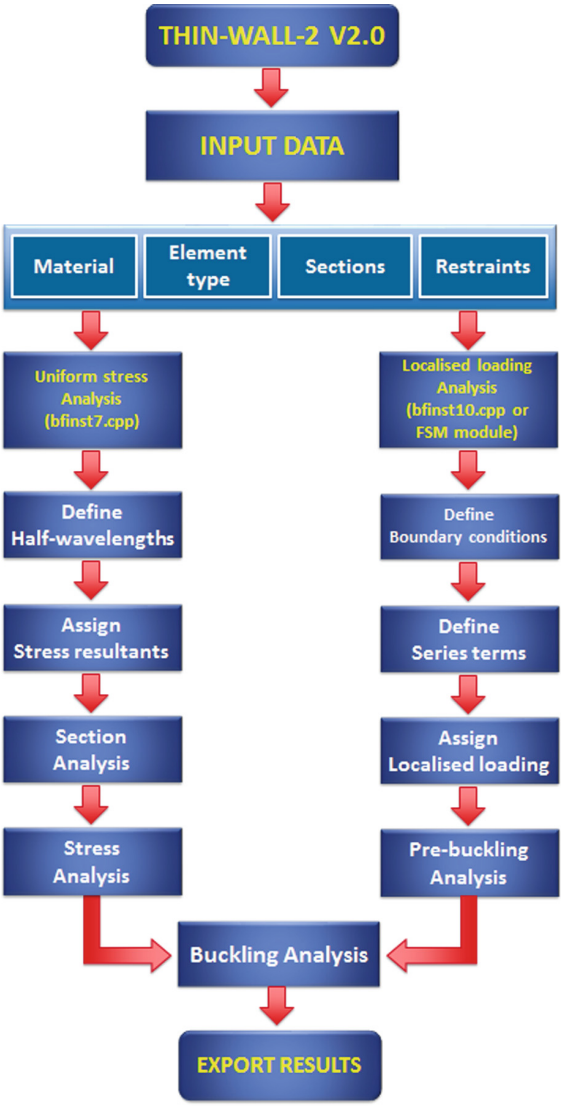


**Fig. 1.** Sequence of THIN-WALL-2 V2.0

loading analysis in THIN-WALL-2 V1.0. In addition, the new version improves the quality of some features related to the graphical interface. Table 1 shows a comparison among three versions of the THIN-WALL program, making it possible to assess the new developments.

**Table 1.** Comparison of THIN-WALL versions

| Features | | THIN-WALL | THIN-WALL-2 V1.0 | THIN-WALL-2 V2.0 |
|---|---|---|---|---|
| Modeling | Material | Limited number of materials Isotropic material Corrugated webs | Unlimited number of materials Isotropic material | Unlimited number of materials Isotropic or orthotropic materials |
| | Element type | One element type | Many element types | Many element types |
| | Cross-section geometry | Default and general section types | Default and general section types | Default and general section types |
| | Boundary condition | One "standard" of end supports (S-S) | 2 "standards" of end supports (Free to deform for uniform loading and simply supported boundary condition for localised loading) | 6 "standards" of end supports (Free to deform for uniform loading and general end boundary conditions for localised loading) |
| | Restraint | Restraint by X, Y, Z axes and rotation by Z axis | Restraint by X, Y, Z axes and rotation by Z axis | Restraint by X, Y, Z axes and rotation by Z axis |
| Loading | Static loading | Uniform compression (N) and bending (M) | Uniform compression (N), bending (M), shear (V) or localised loading (2 load cases IOF and ITF) | Uniform compression (N), bending (M), shear (V) or localised loading (4 load cases IOF, EOF, ITF and ETF) |
| Analysis | Cross-section analysis | Available | Available | Available |
| | Pre-Buckling analysis | – | Available | Available |
| | Buckling analysis | Available | Available | Available |
| Results | Deformation modes | One section | All sections | All sections |
| | Deformation shapes | 2D view | 2D and 3D views | 2D and 3D views |
| | Stress | $\sigma_x$ stress due to N or M | $\sigma_x$, $\sigma_y$ and $\tau_{xy}$ stresses due to N, M, V and localised loading | $\sigma_x$, $\sigma_y$ and $\tau_{xy}$ stresses due to N, M, V and localised loading |
| | Export data and report | Available | Not available | Available |
| Support | Introduction | Available | Not available | Available |
| | Tutorial | Available | Not available | Available |
| Other | Cross-section templates | 17 | 9 | 9 |
| | General section | Available | Available | Available |
| | Save/load data | Available | Available | Available |
| | Changing font style | Available | Not available | Available |
| | Changing unit | – | Not available | Available |
| | Output files type | *.txt (text file) | *.txt and *.xls files (text and excel files) | *.txt and *.xls files (text and excel files) |

# 4 Analysis of Thin-Walled Sections Under Localised Loading Using THIN-WALL-2 V2.0

## 4.1 Define Materials, Element Types, Sections and Series Terms Number

Before a computer analysis of a thin-walled section can be commenced, the materials, element types and geometry of the cross-section must be described to the computer as described in (Nguyen et al. 2015). In addition, in the pre-buckling and buckling analyses of a structural member under localised loading, THIN-WALL-2 V2.0 performs the analyses with multiple series terms to get the most accurate results. In general, 15 series terms are required to get the accurate buckling load factor as described in (Nguyen et al. 2016b).

## 4.2 Assign Boundary Conditions and Restraint Conditions

Boundary condition refers to the support condition at the ends of the structural member for use in the localised loading analyses using the Localised Loading module. By assigning the boundary condition for each end of the strips of the structural member, there are six possible different combinations of boundary such as both ends simply supported (SS), one end simply supported and one end clamped (SC), one end simply supported and one end free (SF), both ends clamped (CC), one end clamped and one end free (CF) and both ends free (FF).

In order to avoid the lateral buckling of the structural member under localised loading, restraints are applied along the member. There are four degree of freedom for each node, thus the user can fix the nodal translation such as $D_x$, $D_y$, $D_z$ in the $X,Y,Z$ directions and the nodal rotation about the $Z$ axis as described in (Nguyen et al. 2015).

## 4.3 Assign Localised Loading

There are four localised loading cases such as the IOF, ITF, EOF and ETF as shown in Fig. 2.

The user selects the Localised Transverse Loads option from the Assign/Localised Loading menu, then Fig. 3 appears to define the localised loading. Firstly, the user selects a loading case by clicking on one of the four Load buttons, so that the loading case is displayed in the Load View panel. Secondly, the user inputs the length of the beam ($L$), the load length ($n$) and the load position. The user can select the relative assign or the absolute assign to define the position of loading on the beam. In addition, the value of loading must be input into the Load Value panel in the middle of this table. Finally, the user defines the applied loading points by selecting nodes in the Applied Loading Points table on the right side of this window.

In the analysis of a beam under the IOF load case, the both ends simply supported boundary condition is assigned for the beam to match up with the practical boundary condition applied for the beam in experiments as shown in Fig. 2(a). In addition, the localised load is applied on the top flange of the beam with interior locations. For the

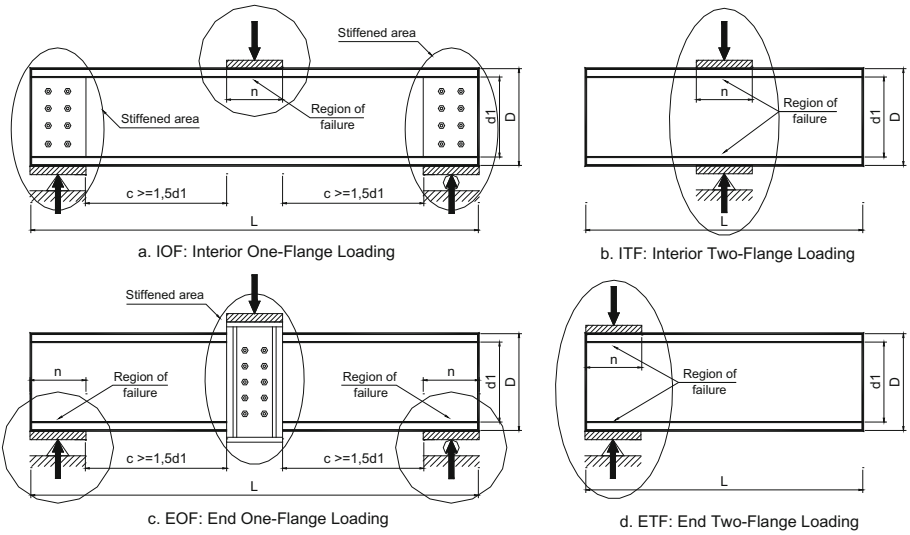


**Fig. 2.** Localised loading cases

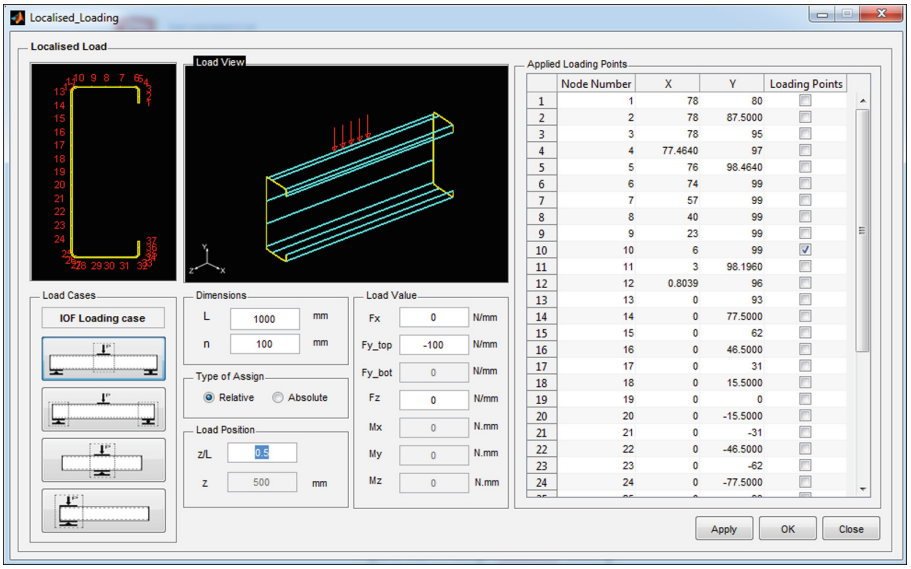


**Fig. 3.** Assign localised loading

ITF load case as shown in Fig. 2(b), the boundary condition is selected similar to the IOF load case; however, the localised loads are applied at both sides of the beam with interior locations.

In the experiment of the beam under the EOF load case as shown in Fig. 2(c), the load is applied in the interior of the beam at a stiffened loading point in order to prevent failure around this area. With this loading condition, reactions appear at the ends of the beam which leads to web crippling. Thus, in the analysis, the beam length is taken as half of the original beam length from the experiment as shown in Fig. 2(c) and the Clamped-Free (CF) is assigned for the beam. The localised load is applied at the end of the bottom flange. For the ETF load case, the Simply-Free (SF) is assigned to the beam. Also, the longitudinal restraints are applied at the applied loading points to prevent the movement of the beam in the longitudinal directions. The beam length is equal to the original length of the beam as shown in Fig. 2(d). The localised loads are applied at the end of the both flanges.

### 4.4 Running Analysis

The Analysis window appears as shown in Fig. 4 when the user selects the Analysis option from the Analysis menu or the Analysis button on the Analysis bar. From this window, the user can select the analysis type with suitable loading. In order to run the analyses of thin-walled sections under localised loading, the user selects the Localised Loading option. With regard to the main code of the analysis, if the user selects BFINST10 option, the Localised Loading module is called to run the bfinst10.cpp engine for analyses of structural members under localised loading with both ends simply supported boundary condition. If the user selects the FSM option, the Localised Loading module is called to run the FSM module for analyses of structural members under localised loading with general end boundary conditions. The user can select running pre-buckling analysis only or both pre-buckling and buckling analyses.

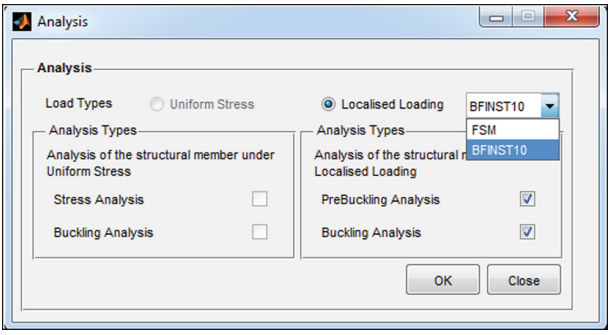


**Fig. 4.** Running analysis

### 4.5 Export the Results

After running, the results are exported which includes the pre-buckling modes (deflections) and the pre-buckling stresses as shown in Fig. 5. These stresses will be used in the buckling analysis to get the buckling modes as shown in Fig. 6 and buckling loads ($P_{cr}$). The results can be exported to different data files by the Report function of the program.

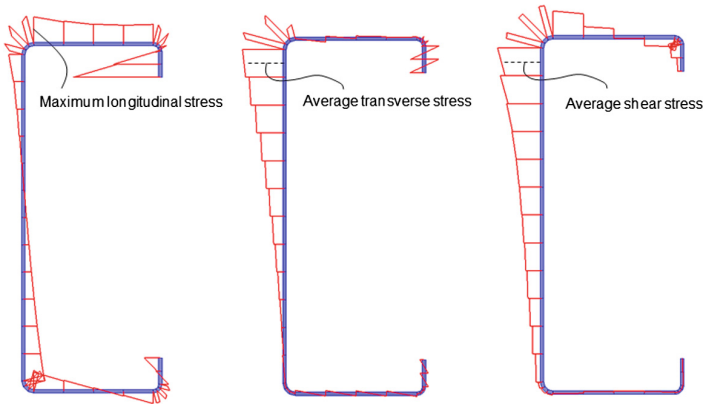


(a) Longitudinal (0.5L) (b) Transverse (0.5L) (c) Shear Stresses (0.45L)

**Fig. 5.** Pre-buckling stresses

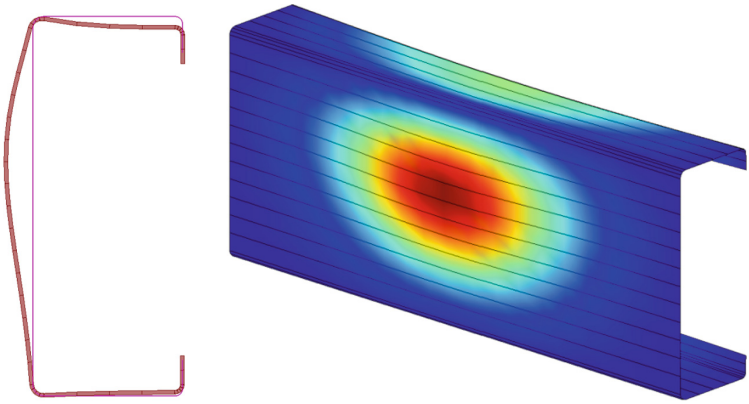

**Fig. 6.** Buckling modes in 2D and 3D views

## 5 Conclusions

This paper provides a presentation of the THIN-WALL-2 V2.0 program which is based on the FSM. This third release extends the domain of application of the first one THIN-WALL (Papangelis and Hancock 1994) and the second one THIN-WALL-2 V1.0 (Nguyen et al. 2015). It is possible to use this program to analyse structural members under uniform compression, bending and shear or localised loading. The structural members may be made from isotropic or orthotropic materials. In addition, with the general section module, THIN-WALL-2 V2.0 can be used to define and analyse all types of sections such as open sections, closed sections and mixed sections. The program can be used effectively in both pre-buckling and buckling analyses of

structural members under all localised load cases with general end boundary conditions.

Finally, the GUI module which is included in THIN-WALL-2 V2.0 shows an improvement of this program in displaying the results from the analyses. The buckling modes and shapes are displayed in both 2D and 3D views, thus the user can understand the working of the structural member clearly.

**Acknowledgements.** Funding provided by the Australian Research Council Discovery Project Grant DP110103948 has been used to perform this project. The first author is sponsored by scholarships provided by VIED 911 scheme from Vietnamese Government and supplemental scholarship from School of Civil Engineering, the University of Sydney.

## References

Ádány, S., Schafer, B.W.: Generalized constrained finite strip method for thin-walled members with arbitrary cross-section: primary modes. Thin-Walled Struct. **84**, 150–169 (2014a)

Ádány, S., Schafer, B.W.: Generalized constrained finite strip method for thin-walled members with arbitrary cross-section: secondary modes, orthogonality, examples. Thin-Walled Struct. **84**, 123–133 (2014b)

Australian/New Zealand Standard AS/NZS 4600:2005. Cold-Formed Steel Structures. Standards Australia/Standards New Zealand (2005)

Cheung, Y.K.: Finite Strip Method in Structural Analysis. Pergamon Press Inc, New York, NY (1976)

Hancock, G.J., Pham, C.H.: Direct strength method of design for shear of cold-formed channel sections based on a shear signature curve. In: Proceedings, 21st International Specialty Conference on Cold-Formed Steel Structures, St Louis, Missouri, USA, pp. 207–221 (2012)

Hancock, G.J., Pham, C.H.: Buckling analysis of thin-walled sections under localised loading using the semi-analytical finite strip method. Thin-Walled Struct. **86**, 35–46 (2015)

Hancock, G.J., Pham, C.H.: Relationship between the semi-analytical finite strip methods for buckling of thin-walled sections under uniform and localised loading. In: 8th International Conference on Advances in Steel Structures. Lisbon, Portugal, p. 20 (2015)

Li, Z., Schafer, B.W.: Buckling analysis of cold-formed steel members with general boundary conditions using CUFSM:conventional and constrained finite strip methods. In: 20th International Specialty Conference on Cold-Formed Steel Structures, Saint Louis, Missouri, USA, p. 15 (2010)

Natário, P., et al.: GBTWEB, GBT-based code for web buckling analysis of members under localised loads (2015)

Nguyen, V.V., et al.: Development of the THIN-WALL-2 program for buckling analysis of thin-walled sections under generalised loading. In: 8th International Conference on Advances in Steel Structures, Lisbon, Portugal, p. 20 (2015)

Nguyen, V.V., et al.: Analyses of thin-walled sections under localised loading for general end boundary conditions - Part 1: Pre-buckling. In: CCFSS2016, Baltimore, Maryland, USA, p. 20 (2016a)

Nguyen, V.V., et al.: Analyses of thin-walled section under localised loading for general end boundary conditions - Part 2: Buckling. In: CCFSS 2016, Baltimore, Maryland, USA, p. 20 (2016b)

North American Specification for the Design of Cold-Formed Steel Structural Members AISI S100-2012 American Iron and Steel Institute (AISI) (2012)

Papangelis, J.P., Hancock, G.J.: Computer analysis of thin-walled structural members. Comput. Struct. **56**(1), 157–176 (1994)

Pham, S.H., et al.: Direct strength method of design for shear including sections with longitudinal web stiffeners. Thin-Walled Struct. **81**, 19–28 (2014)

Plank, R.J., Wittrick, W.H.: Buckling under combined loading of thin, flar-walled structures by a complex finite strip method. Int. J. Numer. Meth. Eng. **8**, 323–339 (1974)

# Bending Resistance of Steel-Bar Reinforced Concrete Beam with Extreme Compression Zones Using High-Performance Composite

Duy-Liem Nguyen(✉) and Duy-Ngo Tong

Ho Chi Minh City University of Technology and Education,
Ho Chi Minh City, Vietnam
liemnd@hcmute.edu.vn, tongduyngol987@gmail.com

**Abstract.** This study performed on composited beam using normal concrete joined cement-based strain-hardening composite (CSHC). The bending resistances of composited beams are provided with a new approach as follows: CSHC is placed in extreme compressive zone at top of simple beam whereas normal concrete is placed in the lower part of beam. The models and equations are suggested for various cases of steel reinforcing bar to useful predict bending resistance of beam. Also, an experimental program is conducted to generally evaluate bending resistance of the investigated beams. The moment capacity and stiffness of the composited beam are clearly improved with the increase of CSHC thickness.

**Keywords:** High-performance · Composited beam · Bending resistance · Moment capacity · Section analysis

## 1 Introduction

Much research has been reported various approaches to practically apply advanced or so-called high performance materials which can resist cruelly mechanical and environmental loads such as earthquake, impact, blast and marine corrosion. Cement-based strain-hardening composite (CSHC), e.g., ultra-high performance fiber reinforced concrete (UHPFRC) or high performance fiber reinforced cementitious composite (HPFRCC), recently has been considered as a very promising construction material owing to its very high resistance and durability in comparison with normal concrete (Graybeal and Davis (2008); Naaman and Reinhardt (2006); Nguyen et al. (2013, 2014a, 2015); Song et al. (2015); Park et al. (2012); Wille et al. (2011)). Specially, one of the most advanced properties of CSHC is strain-hardening or deflection-hardening performance accompanied with multiple micro-cracks which result high ductility, large energy absorption capacity as well as superior crack resistance (Nguyen et al. (2013, 2015); Song et al. (2015); Park et al. (2012)).

Nontheless, CSHC is much expensive than that of normal concrete at present (Špak et al. (2016)) and this becomes a main hindrance for widely application of CSHC. To remedy the such hindrance, a developed beam using normal concrete joined with CSHC is proposed. The composited beam is hoped to minimize the construction cost

© Springer Nature Singapore Pte Ltd. 2018
H. Tran-Nguyen et al. (eds.), *Proceedings of the 4th Congrès International de Géotechnique - Ouvrages -Structures*, Lecture Notes in Civil Engineering 8,
DOI 10.1007/978-981-10-6713-6_8

owing to the reduction of CSHC amount used whereas it can still produce a significant enhancement of bending resistances.

In previous study (Nguyen (2017a)), the moment capacities of composited beams using CSHC in extreme tension zone was reported with section analysis. This study is the next step to investigate bending resistance of steel-bar reinforced concrete beam with extreme compression zones using CSHC. The objective of this study is to analytically determine bending resistance of composite beam when CSHC is placed in extreme compressive zone at top of a simple beam and normal concrete is placed in the lower of that beam. Beside, the authors conducted an experimental test to preliminarily evaluate bending resistance of investigated composite beams.

## 2 Analytical Study

### 2.1 Proposed Models of Materials

Normal concrete, CSHC and steel are modeled and shown in Figs. 1 and 2. The compressive and direct tensile behavior of CSHC are shown in Figs. 1(a, b), respectively. Figure 2(a) shows the stress versus strain relationship of normal concrete while Fig. 2(b) provides that of steel reinforcing bar under uniaxial load. The stress $\sigma_1$ and $\sigma_2$ of CSHC can be found using interpolation method from strain value $\varepsilon_1$ and $\varepsilon_2$, respectively, illustrated in Fig. 1(a).

The applied load transfers across the interface between normal concrete and CSHC differently according to connection method, i.e., the different connections between CSHC and normal concrete lead to different composite behaviors (Ju et al. (2014)). In this study, the investigated beams would be designed with small-spacing stirrups, as described in Fig. 3(a), for the purpose of providing fully composite behavior between two materials conjointly. The fully composite behavior would produce the best bending performance (Ju et al. (2014)).

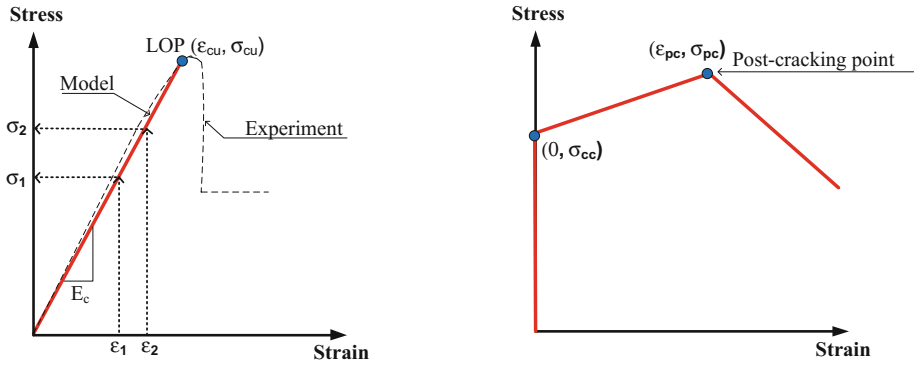


(a) Compressive behavior of CSHCs

(b) Direct tensile behavior of CSHCs

**Fig. 1.** Simplified model of axial stress versus strain responses of CSHCs (Nguyen et al. (2017b); Shin et al. (2015))

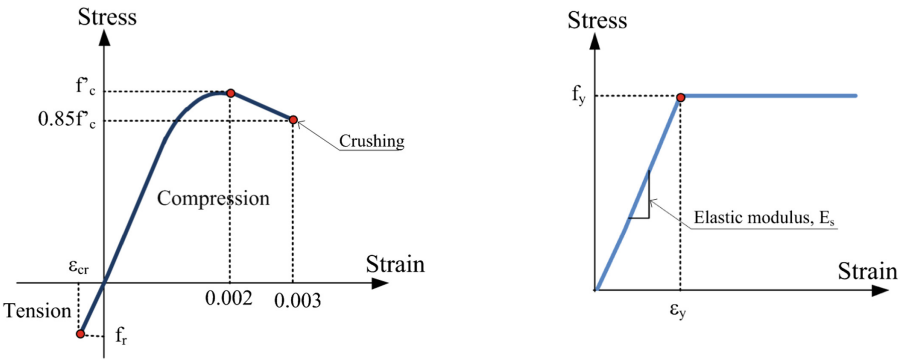


**Fig. 2.** Modeling stress versus strain response of normal concrete and steel reinforcing bar under uniaxial loading (Ju et al. (2014))

## 2.2 Analysis Methodology

The basic assumptions for the analysis are as follows:

- Concrete and CSHC is a homogeneous and isotropic material;
- The shear connection at the interface (bonding at interface) between composite components is continuous and constant along the longitudinal direction of the member;
- The section remains in plane during loading;
- Separation in a vertical direction does not occur.
- Resistance of concrete in tensile zone is negligible.

A simple beam with rectangular section having depth $h$, width $b$ and single tensile steel layer was analyzed under positive moment. Figure 3(c) shows the simplification of compressive CSHC block as a trapezoid while compressive concrete block as a triangle. Location of neutral axis ($NA$), determined by $c = kh$, curvature of beam ($\Phi$) and nominal moment capacity ($M_n$) are obtained using the equilibriums of horizontal forces and moments at section, as provided in Eqs. (1–3).

$$\sum C_i = \sum T_i \tag{1}$$

$$M_n = \sum T_i \cdot y_{Ti} + \sum C_i \cdot y_{Ci} \tag{2}$$

$$\Phi = \varepsilon_{ts}/(d - c) = \varepsilon_{cu}/c = 0.0035/c \tag{3}$$

where $y_{Ti}$, $y_{Ci}$ is the distance from $NA$ to equivalent tensile force $T_i$ and to equivalent compressive force $C_i$, respectively; $\Phi$ is the curvature corresponded with moment $M_n$, whereas $\varepsilon_{cu}$ is the strain at the top of beam.

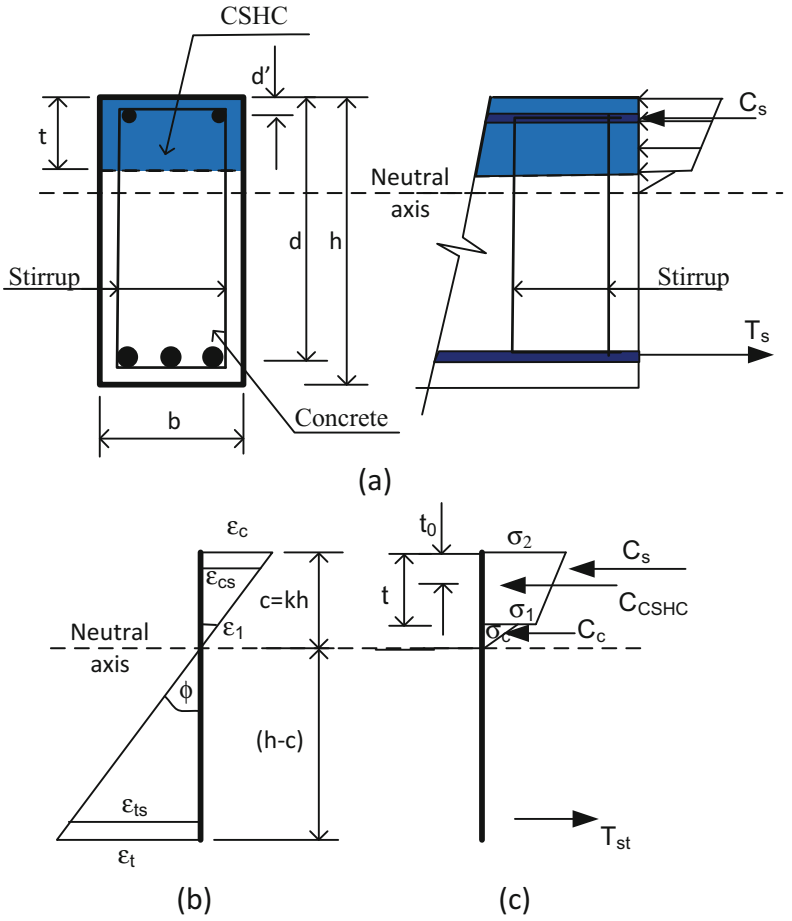


**Fig. 3.** Distribution of stress, strain and steel force along the depth of section when CSHC is placed in extreme compression zone

## 3 Analysis Result

Figure 3 provides the distribution of the stress, strain and steel force along the depth of section with only tensile steel bar when CSHC is placed in extreme compression zone at beam top and normal concrete is placed in the lower of beam. Based on the reported compressive behavior of CSHC (Nguyen and Kim (2014b); Shin et al. (2015)), the top strain, $\varepsilon_{cu}$, is proposed to be equal to 0.0035 at the ultimate stage, this value is also suitable with recommendation of RILEM TC 162-TDF (2003). The top strain, $\varepsilon_{cu}$, is equal to 0.0035 at the ultimate stage while the tensile strain in the extreme tensile steel, $\varepsilon_{ts}$, can be changed according to failure types (ACI 318-02 (2002)), illustrated in Fig. 4 as follows:

- Compression-controlled sections are either balanced or overreinforced ($\varepsilon_{ts} \leq 0.002$).
- Transition sections are somewhat underreinforced ($0.002 < \varepsilon_{ts} < 0.005$).
- Tension-controlled sections are significantly underreinforced ($\varepsilon_{ts} \geq 0.005$).

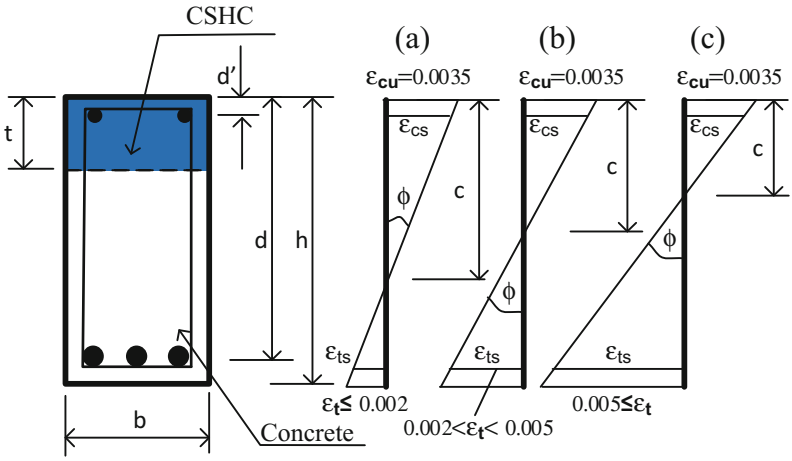


**Fig. 4.** Tensile steel strain condition with CSHC placed in compressive zone: (a) Compression-controlled section, (b) Transition section and (c) Tension-controlled section

A beam containing both tensile and compressive steel can be analytically described under beam 1 in addition to beam 2, as shown in Fig. 5. To avoid brittle failure resulting catastrophic collapse of constructions, the beams would be designed to be either tension-controlled, or in the transition zone between tension-controlled and compression-controlled, i.e., beam has underreinforced section. For a rectangular cross-section, the analytical derivation is given with three cases as follows:

- Singly reinforced section with no compressive steel (or compressive steel is negligible compared with tensile steel);
- Doubly reinforced section with compressive steel in plastic deformation;
- Doubly reinforced section with compressive steel in elastic deformation.

To reach the limit strain 0.0035 at extreme compressive strain, the amount of steel reinforcing bar must be satisfied Eq. (4), and Table 1 used for this case. Contrary to this condition, the extreme strain is not equal to 0.0035 and it has been interpolated.

$$A_s f_y > \frac{1}{2}(\sigma_1 + \sigma_2)tb = (1 - \frac{t}{2c})f'_{HPFRCC}.t.b \tag{4}$$

Example: Considering a simple beam with depth h = 40 cm (d = 35 cm), width b = 20 cm, at beam bottom, steel reinforcement in tension includes 3 bars with diameter of 25 mm ($A_s = 14.73$ cm$^2$), $f_y = 400$ MPa; normal concrete has compressive strength $f'_c = 20$ MPa, CSHC is HPFRCC having compressive strength of $f'_{HPFRCC} = 80$ MPa and its thickness of 5 cm on the top of beam. Based on Table 1, the predicted moment capacity of composited beam is 224.21 kN.m while this beam with no HPFRCC (using all normal concrete) will produce a moment of 155.14 kN.m only. The enhancement of moment capacity is more than 44%.

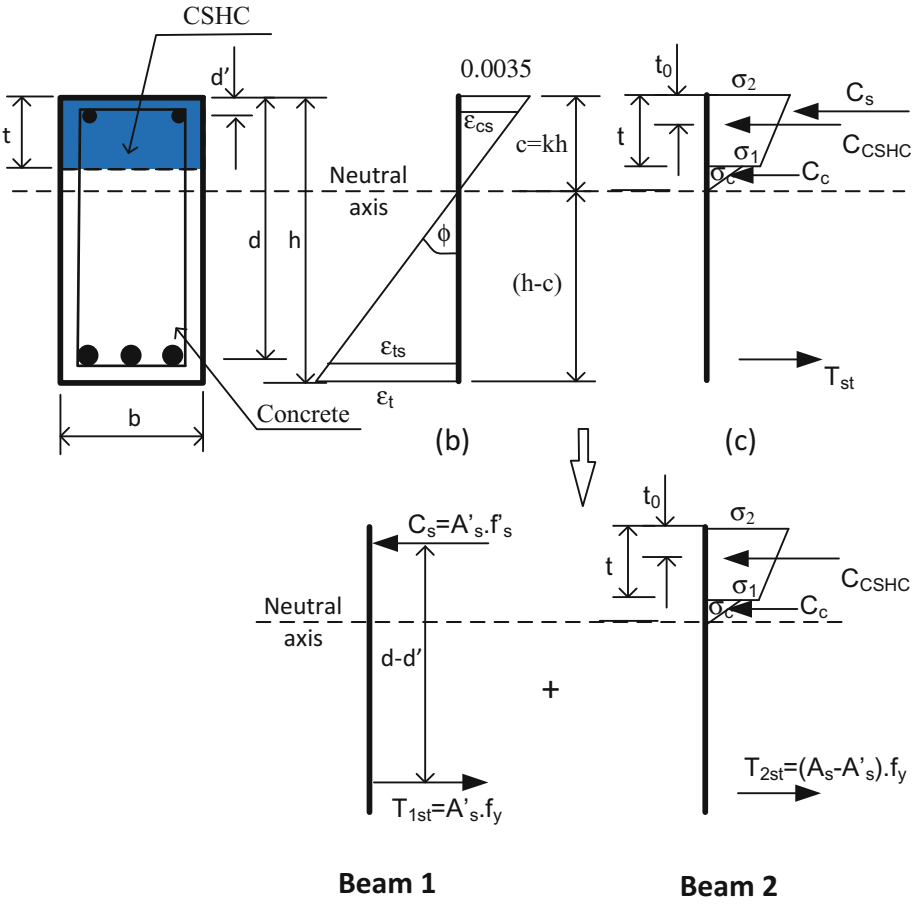


**Fig. 5.** Strain and equivalent stress distribution of doubly reinforced section

## 4 Experiment

### 4.1 Materials and Specimen Preparation

The compressive strength of normal concrete is 20 MPa while that of CSHC (using HPFRCC in this research) is 80 MPa. The composition of the HPFRCC matrix is provided in Table 2. Figures 6(a, b) show the hybrid fibers and their properties are summarized in Table 3. The hybrid fibers are used 2.0% volume content as follows: 1.5% macro-steel hooked and 0.5% micro-steel smooth fibers. HPFRCC was placed in the extreme top of beam whereas normal concrete was placed in the lower zone of beam. Four specimen types were prepared in the experimental program as follows: having same dimension (width × depth × span length) 150 × 150 × 450 $mm^3$ but different thickness of HPFRCC as follows: 0 mm (no HPFRCC - beam 1), 50 mm (beam 2), 100 mm (beam 3) and 150 mm (no normal concrete - beam 4). Figure 7(c)

**Table 1.** Equations of section analysis when CSHC is placed in extreme compression zone

| Analysis case | Equation of the $M_n$ and neutral axis $c$ | Checking |
|---|---|---|
| (C1) Singly reinforced section with no compressive steel | $\frac{1}{2}(\sigma_1+\sigma_2)tb+\frac{1}{2}\sigma_c(c-t)b=A_sf_y$<br>or $c=\frac{2A_sf_y-(\sigma_1+\sigma_2)tb+\sigma_ctb}{\sigma_cb}$<br>$M_n=A_sf_yd+\frac{(\sigma_1+\sigma_2)}{2}tb\left(\frac{2\sigma_1+\sigma_2}{\sigma_1+\sigma_2}\right)\frac{t}{3}$<br>$+\frac{1}{2}\sigma_c(c-t)b\frac{(c+2t)}{3}$<br>Where $A_s$, $f_y$ are the area and yield strength of mild steel tension reinforcement, respectively; $t, t_0$ are the thickness and distance from centroid of CSHC stress block to beam top, respectively<br>The strain of CSHC block:<br>$\varepsilon_1=\frac{0.0035}{c}(c-t)$ and $\varepsilon_2=0.0035$ | $\varepsilon_{ts}=\frac{0.0035}{c}(d-c)$ or<br>$\varepsilon_{ts}=0.0035\,(d/c-1)$<br>- Condition for an underreinforced beam:<br>$\varepsilon_{ts}>0.002$ or<br>$c/d<\frac{0.0035}{(0.0035+0.002)}=0.636$, at this condition, the tensile steel stress $f_{ts}=f_y$.<br>- Condition for beam producing tension-controlled section:<br>$\varepsilon_{ts}>0.005$ or<br>$c/d<\frac{0.0035}{(0.0035+0.005)}=0.412$.<br>- Condition for NA occurring in normal concrete zone: $t<c$ |
| (C2) Doubly reinforced section with compressive steel in plastic deformation | $\frac{1}{2}(\sigma_1+\sigma_2)tb+\frac{1}{2}\sigma_c(c-t)b+A_s^{'}f_y=A_sf_y$<br>or $c=\frac{2(A_s-A_s^{'})f_y-(\sigma_1+\sigma_2)tb+\sigma_ctb}{\sigma_cb}$<br>$M_n=A_s^{'}f_y(d-d^{'})+(A_s-A_s^{'})f_yd$<br>$+\frac{(\sigma_1+\sigma_2)}{2}tb\left(\frac{2\sigma_1+\sigma_2}{\sigma_1+\sigma_2}\right)\frac{t}{3}+\frac{1}{2}\sigma_c(c-t)b\frac{(c+2t)}{3}$<br>Where $A_s$, $A_s^{'}$ are the area of mild steel tension and compression reinforcement, respectively while $f_y$ is the yield strength of mild steel; $t, t_0$ are the thickness and distance from centroid of CSHC stress block to beam top, respectively. | - Checking whether compressive steel stress $f_s^{'}=f_y$:<br>$d^{'}/c\le(1-\frac{f_y}{(0.035\times200000)}=(1-f_y/700)$<br>,<br>- Checking whether tensile steel stress $f_{ts}=f_y$:<br>$c/d<0.636$.<br>- Condition for beam producing tension-controlled section: $c/d<0.412$<br>- Condition for NA occurring in normal concrete zone: $t<c$ |
| (C3) Doubly reinforced section with compressive steel in elastic deformation | $\frac{1}{2}(\sigma_1+\sigma_2)tb+\frac{1}{2}\sigma_c(c-t)b$<br>$+E_sA_s^{'}(1-d^{'}/c)0.0035=A_sf_y$ or<br>$\sigma_cc^2+[(\sigma_1+\sigma_2)tb-\sigma_ctb+0.007E_sA_s^{'}-2A_sf_y]c$<br>$-(0.007E_sA_s^{'}d^{'})=0$<br>$M_n=A_sf_yd-E_sA_s^{'}(1-d^{'}/c)0.0035d^{'}$<br>$+\frac{(\sigma_1+\sigma_2)}{2}tb\left(\frac{2\sigma_1+\sigma_2}{\sigma_1+\sigma_2}\right)\frac{t}{3}+\frac{1}{2}\sigma_c(c-t)b\frac{(c+2t)}{3}$<br>Where $E_s$ is modulus of elasticity of steel bar | - Checking compresive steel in elastic deformation by condition of $d^{'}/c>(1-f_y/700)$<br>- Checking tensile steel stress in plastic deformation $f_{ts}=f_y$ by condition of $c/d<0.636$.<br>- Condition for beam producing tension-controlled section: $c/d<0.412$<br>- Condition for NA occurring in normal concrete zone: $t<c$ |

**Table 2.** Composition of mortar matrix of HPFRCC

| Cement (Type 3) | Silica fume | Silica sand | Fly ash | Superplas-ticizer | Water |
|---|---|---|---|---|---|
| 0.80 | 0.07 | 1.00 | 0.20 | 0.04 | 0.26 |

shows the photos of specimen formwork before placing. The tested beams using steel reinforcement includes 2 bars in tension with diameter of 12 mm ($A_s$ = 2.26 cm$^2$, $t_0$ = 25 mm), and 2 bars in compression with diameter of 6 mm ($A_s'$ = 0.57 cm$^2$,

a) Macro-steel hooked fibers

b) Micro-steel smooth fibers

c) Specimen formwork

**Fig. 6.** Photos of fibers and formwork used

**Table 3.** Properties of steel fibers

| Fiber type | Micro-steel smooth fiber | Macro-steel hooked fiber |
|---|---|---|
| Product origin | Vietnam | Vietnam |
| Diameter (mm) | 0.2 | 0.5 |
| Length (mm) | 13 | 35 |
| Aspect ratio (Length/Diameter) | 65 | 70 |
| Tensile strength (MPa) | >1200 | >2500 |
| Section shape | Circular, smooth | Circular, hooked |

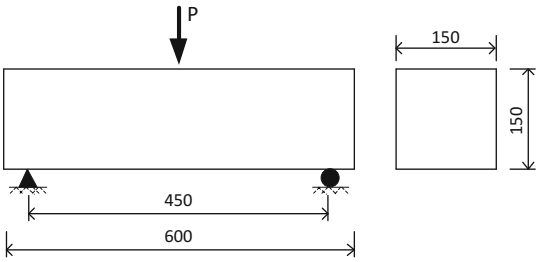


a) Geometry of the bending specimen

b) Test setup

**Fig. 7.** Bending test setup

$d'$ = 25 mm), $f_y = f'_y$ = 400 MPa. With a small steel amount embedded in compressive zone, the tested beams can be classified with singly reinforced section, i.e., no compressive steel.

### 4.2 Test Setup and Procedure

All specimens were tested using three-point bending test (3PBT). The geometry of the bending specimen and test setup are shown in Fig. 7. The speed of loading during the test was 1 mm/min for all specimens. The load and deflection were measured by UTM machine. The moment resistance under 3PBT is computed using Eq. (5) and the curves of moment versus deflection of tested beams can be simply obtained. In the curve of moment versus deflection, two key points indicating bending resistance are identified as follows: the limit of proportionality (LOP), and the modulus of rupture (MOR). The LOP is defined in this research as the limit of the linear elastic region due to first cracking while the MOR is defined as the point where the maximum moment occurs.

$$M = \frac{PL}{4} \tag{5}$$

where $L$ is span length and $P$ is the applied load.

## 5 Experimental Result and Discussion

Figure 8 shows the moment versus deflection responses of investigated beams while Table 4 shows bending resistances at LOP and MOR in addition to predicted moment capacity. Generally, as the thickness of HPFRCC increases, the bending resistances of beam enhance in both moment at LOP and MOR. However, the deflection capacity at LOP has opposite trend, i.e., there is a reduction in deflection capacity at LOP with the increase of HPFRCC thickness. Besides, the deflection capacity of beam at MOR shows unclear trend. As shown in Fig. 8, the stiffness of beam is ranked as follows: beam 4 > beam 3 > beam 2 > beam 1, i.e., the stiffness of beam enhances with the increase of HPFRCC thickness.

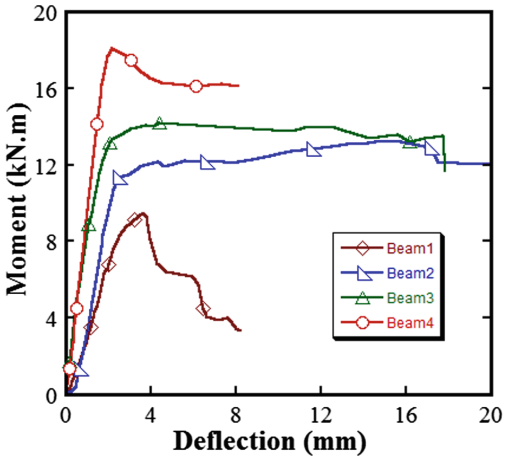


**Fig. 8.** Moment versus deflection responses of investigated beams

**Table 4.** Bending resistances of investigated beams

| Beam No. | At LOP | | At MOR | | Predicted moment capacity (kN.m) |
|---|---|---|---|---|---|
| | Moment (kN.m) | Deflection (mm) | Moment (kN.m) | Deflection (mm) | |
| Beam 1 | 8.45 | 2.61 | 9.45 | 3.64 | 9.70 |
| Beam 2 | 11.34 | 2.43 | 13.22 | 16.27 | 14.83 |
| Beam 3 | 13.31 | 2.17 | 14.21 | 4.37 | 16.35 |
| Beam 4 | 16.19 | 1.67 | 18.07 | 2.19 | 18.25 |

## 6 Conclusion

Some conclusions can be drawn from analytical analyses and experimental test as follows:

(1) The proposed models and equations are basically similar to traditional reinforcement concrete but more complex. This analytical procedure is very useful to predict bending resistance of composited beam.
(2) The enhanced moment capacity and stiffness of the composited beam are clear as thickness of CSHC increases.
(3) The analytical results are in good agreement with the experimental results. However, a further study is needed with many specimens tested to obtain more reliable data.
(4) The composited beam is hoped to be economical and highly resistant since only small amount of CSHC used in extreme compressive zone.

**Acknowledgments.** This research was supported by Ho Chi Minh city University of Technology and Education (Vietnam). The opinions expressed in this paper are those of the authors and do not necessarily reflect the views of the sponsors.

## References

ACI 318-02. Building code requirements for structural concrete (2002)

Graybeal, B., Davis, M.: Cylinder or cube: strength testing of 80 to 200 MPa (11.6 to 29 ksi) ultra-high-performance-fiber-reinforced concrete. ACI Mater. J. **105**(6), 603–609 (2008)

Ju, H., Lee, D.H., Cho, H.C., Kim, K.S., Yoon, S., Seo, S.Y.: Application of hydrophilic silanol-based chemical grout for strengthening damaged reinforced concrete flexural members. Materials **7**, 4823–4844 (2014). doi:10.3390/ma7064823

Naaman, A.E., Reinhardt, H.W.: Proposed classification of HPFRC composites based on their tensile response. Mater. Struct. **39**, 547–555 (2006)

Nguyen, D.L., Kim, D.J., Ryu, G.S., Koh, K.T.: Size effect on flexural behavior of ultra-high-performance hybrid fiber-reinforced concrete. Compos. Part B **45**, 1104–1116 (2013)

Nguyen, D.L., Ryu, G.S., Koh, K.T., Kim, D.J.: Size and geometry dependent tensile behavior of ultra-high-performance fiber-reinforced concrete. Compos. Part B **58**, 279–292 (2014a)

Nguyen, D.L., Kim, D.J.: Compressive behavior of ultra-high-performance fiber-reinforced concretes with steel fiber. In: KCI Conference, Jeju, pp. 945–946 (2014b)

Nguyen, D.L., Song, J., Manathamsombat, C., Kim, D.J.: Comparative electromechanical damage-sensing behavior of six strain-hardening steel-fiber-reinforced cementitious composites under direct tension. Compos. Part B **69**, 159–168 (2015)

Nguyen, D.L.: Flexural behavior of two-cement-based-material composite beam. In: Proceedings of the 11th South East Asean Technical University Consortium Symposium, (ISSN of abstract 1882-5796, ISSN of full paper 2186-7631), Ho Chi Minh, Viet Nam, OS06-53, p. 152 (2017a)

Nguyen, D.L., Thai, D.K., Kim, D.J.: Direct tension-dependent flexural behavior of ultra-high-performance fiber-reinforced concretes. J. Strain Anal. Eng. Des. **52**(2), 121–134 (2017)

RILEM TC 162-TDF. Test and design methods for steel fibre reinforced concrete – σ-ε design method. Mater. Struct./Matériaux Constr. **36**, 560–567 (2003)

Shin, K.J., Jang, K.H., Choi, Y.C., Lee, S.C.: Flexural behavior of HPFRCC members with inhomogeneous material properties. Materials **8**, 1934–1950 (2015). doi:10.3390/ma8041934

Špak, M., Kozlovská, M., Struková, Z., Bašková, R.: Comparison of conventional and advanced concrete technologies in terms of construction efficiency. Adv. Mater. Sci. Eng. **2016**, Article ID 1903729, 6 p. (2016). http://dx.doi.org/10.1155/2016/1903729

Song, J., Nguyen, D.L., Manathamsombat, C., Kim, D.J.: Effect of fiber volume content on electromechanical behavior of strain-hardening steel-fiber-reinforced cementitious composites. J. Compos. Mater. (2015). doi:10.1177/0021998314568169

Wille, K., Kim, D.J., Naaman, A.E.: Strain hardening UHP-FRC with low fiber contents. Mater. Struct. **44**, 583–598 (2011)

Park, S.H., Kim, D.J., Ryu, G.S., Koh, K.T.: Tensile behavior of ultra-high performance hybrid fiber reinforced concrete. Constr. Build. Mater. **34**(2), 172–184 (2012)

# Bolt-Loosening Detection in Steel Column Connections Using Impedance Responses

Duc-Duy Ho[1(✉)], Trung-Hieu Nguyen[2], and Quang-Huy Le[2]

[1] Faculty of Civil Engineering, Ho Chi Minh City University of Technology, VNU – HCM, Ho Chi Minh City, Vietnam
hoducduy@hcmut.edu.vn

[2] Faculty of Civil Engineering, Ho Chi Minh City University of Transport, Ho Chi Minh City, Vietnam
trghieu.nguyen@gmail.com, lequanghuyl992@gmail.com

**Abstract.** This study has been motivated to evaluate the practicality of numerical simulation of impedance monitoring for bolt-loosening detection in steel column connection. In order to achieve the objective, the following approaches are implemented. Firstly, the theory of electro-mechanical (E/M) impedance responses and impedance-based damage monitoring method are outlined. Secondly, the feasibility of numerical simulation of impedance monitoring is verified for several pre-published experimental examples on steel beams, cracked aluminum beams, and aluminum round plates. Undamaged and damaged steel and aluminum beams are simulated to compare to experimental impedance responses. An aluminum round plate with PZT patch in center is simulated to investigate sensitive range of impedance responses. Finally, numerical simulation of the impedance-based damage monitoring is performed for a steel column connection in which connection bolts are damaged. From the numerical simulation test, the applicability of the impedance-based monitoring to the target steel column connection can be evaluated.

**Keywords:** Electro-mechanical impedance · PZT sensor · Damage detection · Numerical simulation · Steel column connection · Bolt-loosening

## 1 Introduction

During service life of civil structures, the occurrence of damages is inevitable. If the damages are not detected timely, they will cause catastrophic incidents for the safety of not only self-structures but also the humans. One of the promising ways to guarantee the structural safety and integrity is to enact structural health monitoring (SHM) in a regular periodic manner and to detect critical damage in its early stage [1, 2]. Recently, impedance-based damage monitoring technologies have been widely used in SHM applications [3–9]. The impedance-based SHM methods are useful to detect damage in critical local members.

In this study, the practicality of numerical simulation of impedance monitoring for bolt-loosening detection in steel column connections is evaluated. Firstly, impedance-based SHM method is briefly outlined. Secondly, feasibility verification of

© Springer Nature Singapore Pte Ltd. 2018
H. Tran-Nguyen et al. (eds.), *Proceedings of the 4th Congrès International de Géotechnique - Ouvrages -Structures*, Lecture Notes in Civil Engineering 8,
DOI 10.1007/978-981-10-6713-6_9

numerical impedance simulation by using several examples such as steel and aluminum beams, aluminum round plate. Undamaged and damaged steel and aluminum beams are simulated to compare to experimental impedance responses. An aluminum round plate with PZT patch in center is simulated to investigate sensitive range of impedance responses. Finally, a numerical simulation of steel column connection is carried out to evaluate the applicability of the proposed SHM method. A bolted connection in steel column is simulated to detect bolt-loosening.

## 2 Impedance-Based SHM

The electro-mechanical (E/M) impedance response is based on the coupling of mechanical and electrical characteristics [3]. As shown in Fig. 1, the host structure is described as the effects of mass, stiffness, damping, and boundary condition. The PZT (Lead Zirconate Titanate) patch is modeled as a short circuit powered by a harmonic voltage or current. When a PZT patch is surface-bonded to a structure, the electrical admittance (the inverse of E/M impedance) of the patch is a combined function of the mechanical impedance of the host structure and that of the piezoelectric patch. The mechanical impedance of the host structure is a function of mass, stiffness and damping. Therefore, any changes in dynamic characteristics of the structure could be represented in the change in E/M impedance.

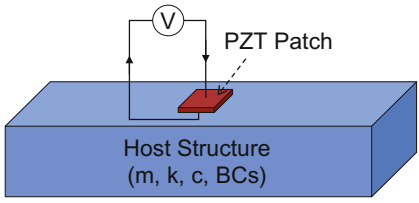


**Fig. 1.** E/M interaction between piezoelectric patch and host structure.

In order to quantify the change in impedance signatures due to structural damage, root mean square deviation (RMSD) of impedance signatures is used [4]

$$RMSD(Z, Z^*) = \sqrt{\sum_{i=1}^{N} [Z^*(\omega_i) - Z(\omega_i)]^2 \Big/ \sum_{i=1}^{N} [Z(\omega_i)]^2} \quad (1)$$

where $Z(\omega_i)$ and $Z^*(\omega_i)$ are the impedance signatures measured before and after damage for the $i^{th}$ frequency, respectively; and $N$ denotes the number of frequency points in the sweep. The RMSD is larger than 0 if damage, and vice versa.

## 3 Feasibility Verification of Numerical Simulation

In order to demonstrate the applicability of the impedance-based SHM method, numerical simulations are carried out on aluminum and steel structures. COMSOL Multiphysics 4.0 software which is efficient for E/M impedance simulation was employed to estimate models. Steel and aluminum beams and an aluminum round plate were simulated to compare to experiments and to diagnosis occurrence of cracks. In the finite element (FE) models, solid element was used for host structure, and piezoelectric element was used for PZT patch.

### 3.1 Uncracked Steel Beams

Four uncracked steel beams which are different from dimensions were simulated to compare to experimental results from [10], as shown in Fig. 2. A thin 7-mm square PZT 5-A patch was boned on each beam. The distance from left end of beam to PZT patch was 40 mm. A voltage 2 V was applied to PZT patch. The beams' properties and PZT patch's properties are same as [10]. In the experiment, impedance signals measured by HP 4194A Impedance Analyzer was performed in the 1−30 kHz range. The boundary conditions of beams were free. Figure 3 shows the FE model of the beams.

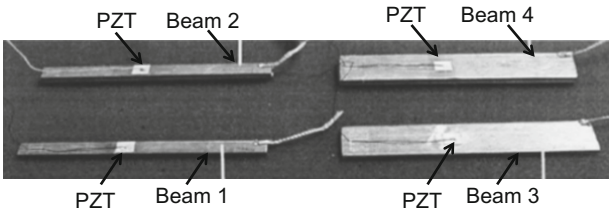


**Fig. 2.** Experimental specimens [10].

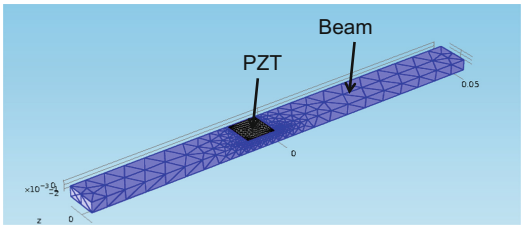


**Fig. 3.** FE model of steel beams.

The comparisons between FE model and experiment are showed in Fig. 4. The resonant frequencies increase proportionally to the thick of beam. The numerical impedance responses are good match with the experimental ones. The differences of resonant frequency are 0.1−5.1%. Therefore, COMSOL is reliable software for simulation of E/M impedance responses.

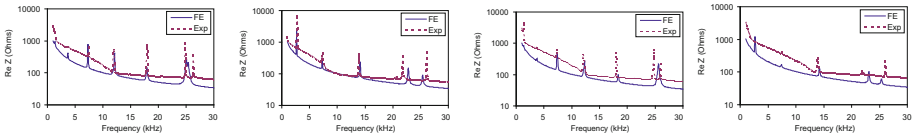


(a) Beam 1 (b) Beam 2 (c) Beam 3 (d) Beam 4

**Fig. 4.** Real impedance: simulation vs experiment.

### 3.2 Cracked Aluminum Beam

In this section, a FE model of an aluminum beam was made to detect the occurrence of crack. The beam's dimensions were 1000 × 20 × 2 mm; the boundary conditions were free. A thin 1000 × 10 × 0.5-mm PZT patch was bond on beam at location 62.5 mm from left end. Crack was cut at center with two depths of 3 mm and 6 mm (Fig. 5). A voltage 0.5 V was applied to PZT patch. The beam's properties and PZT patch's properties are as [11]. Figure 6 shows the FE model of the beam.

**Fig. 5.** Aluminum beam [11].

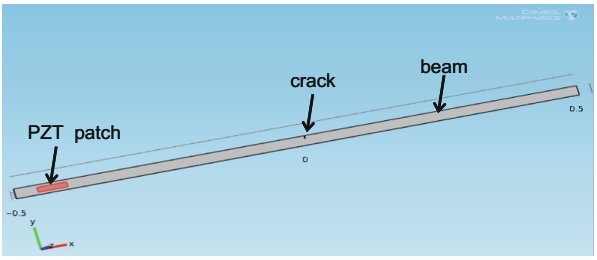


**Fig. 6.** FE model of cracked aluminum beam.

Figure 7 shows the real impedance responses for uncracked and cracked conditions. The real impedance signatures shift to the left side when the crack size increases from 0−6 mm. These results are very similar to ones from [11]. A little difference may cause by bonding layer which did not consider in FE model. In order to evaluate this effect, the RMSD of impedance signatures was computed by Eq. (1). From the results shown in Fig. 8, it is observed that the RMSD of impedance tends to increase as the crack size increases. As a result, the occurrence of cracks was successfully detected by using RMSD of impedances.

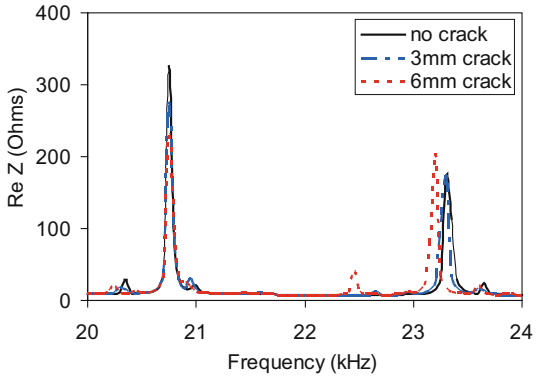


**Fig. 7.** Real impedances of aluminum beam.

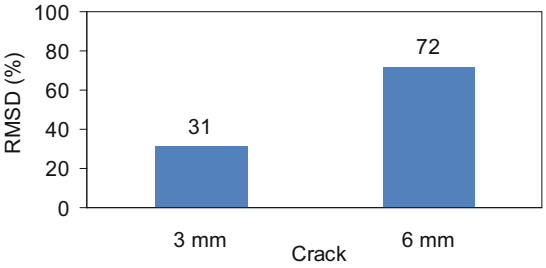


**Fig. 8.** RMSD vs crack size.

### 3.3 Round Aluminum Plate

A round aluminum plate was simulated to diagnosis of cracks and to investigate sensitive range of impedance responses. The FE models of five plates were simulated the same to the experiments from [6]. The diameter of each plate was 100 mm and the thickness was 0.8 mm. Each plate was bonded a 7-mm diameter PZT patch at its center. Group 0 was uncracked; groups 1−4 were cracked with decreasing distance from the PZT patch. A 10-mm circumferential slit was used to simulate the crack. The radial positions 40, 25, 10, and 3 mm from the PZT patch were considered. In the experiment, the plates were placed on foam for free boundary conditions, as shown in Fig. 9. A voltage 1.5 V was applied to each PZT patch. The plates' properties and PZT patch's properties are same as [6]. The impedance signatures were measured by HP 4194 A Impedance Analyzer for three frequency ranges: 10−40 kHz, 10−150 kHz, and 300−450 kHz. Figure 10 shows the FE model of the plates.

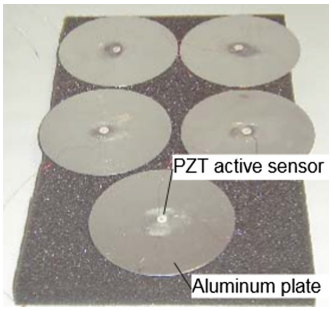


**Fig. 9.** Round aluminum plate [6].

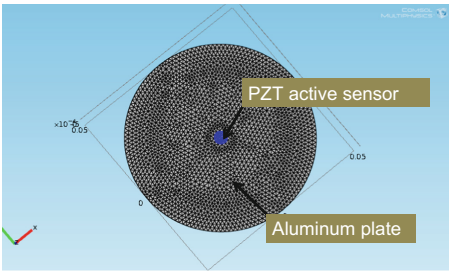


**Fig. 10.** FE model of round aluminum plate.

As shown in Fig. 11, the numerical and experimental impedances are well agreement. The errors of resonant frequencies are less than 10%. The numerical peak frequencies shift to left side in comparison to experimental ones. Figure 12 shows the real impedance responses for numerical simulations (Group 0−Group 4). An appropriate frequency range should be selected to get reliable SHM results. In this study, frequency

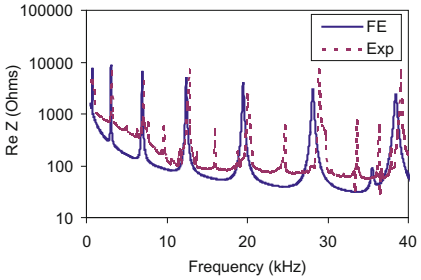


**Fig. 11.** Real impedance of Group 0: simulation vs experiment.

range 300−450 kHz was selected to computed RMSD of impedance signatures by Eq. (1). As shown in Fig. 13, it is observed that the RMSD of impedance increases as the crack distance decreases. The results are similar to experiments from [6].

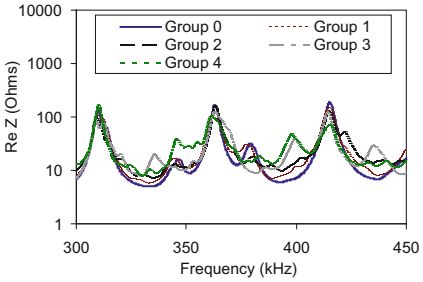


**Fig. 12.** Simulation impedance signatures.

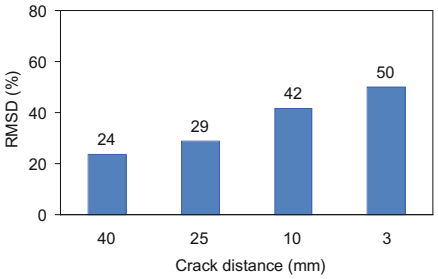


**Fig. 13.** RMSD vs crack distance.

## 4 Impedance-Based Bolt-Loosening Monitoring for Steel Column Connection

After successful verification of the feasibility of impedance's numerical simulations, in this study, a bolted connection in steel column was simulated to monitor the bolt-loosening issue. For steel structures, bolted connections are widely used and bolt-loosening is an important target for SHM. The connection which used to connect two sections of H-330 × 220 × 8× 10 mm included two plates of 470 × 220 × 10 mm, four stiffeners of 220 × 70 × 8 mm, four stiffeners of 220 × 100 × 8 mm, and eight bolts of M18. Material properties of steel were defined as modulus of elasticity $E$ = 200 GPa, mass density $\rho$ = 7850 kg/m$^3$, Poisson's ratio $v$ = 0.33, and damping

coefficient $\zeta = 0.01$. A 20 × 20 × 0.2-mm PZT-5A patch was bonded at each bolt. Material properties of PZT patch were defined as modulus of elasticity $E = 67$ GPa, mass density $\rho = 7750$ kg/m$^3$, Poisson's ratio $v = 0.31$, and damping coefficient $\zeta = 0.023$. A voltage 5 V was applied to each PZT patch. The FE model is shown in Fig. 14. Bolt-loosening of each bolt was simulated at three levels 10%, 25%, and 50%. The bolt-loosening scenarios are listed in Table 1. The fastener tension forces were calculated from the corresponding torque [12]. In the FE model, the bolt-loosening levels were simulated by reducing the assigned forces on corresponding washers, as shown in Fig. 14(c). The impedance signatures were analyzed in range 1−12 kHz with increment step of 200 Hz. Figure 15 shows the real impedance signatures of PZT1 and PZT2. Figure 16 shows the displacement of structure under applied voltage on PZT patches. The displacement gets high value at the bolts; it proves that the PZT patches are sensitive enough to detect the bolt-loosening. The RMSD of impedance signatures computed by Eq. (1) for frequency range 3−7 kHz are shown in Fig. 17 and summarized in Table 2.

**Table 1.** Bolt-loosening scenarios

| Level | Torque (kNm) | Fastener tension force (kN) | Assigned force (kN/m$^2$) |
|---|---|---|---|
| 0% | 172E−3 | 69 | 217E3 |
| 10% | 155E−3 | 62 | 196E3 |
| 25% | 129E−3 | 52 | 163E3 |
| 50% | 86E−3 | 35 | 109E3 |

Level 0% = Undamage; Assigned force = Fastener tension force/Area of washer

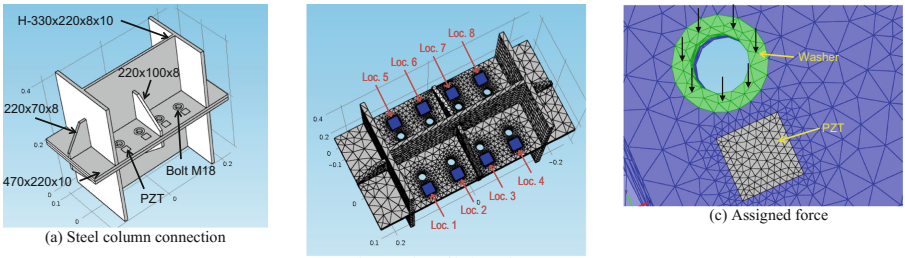


(a) Steel column connection

(b) Location of bolts and PZTs

(c) Assigned force

**Fig. 14.** FE model of steel column connection.

The RMSD index is highest at the corresponding bolt-loosening. When the level of damage increases, the RMSD increases. Due to the sensitivity of PZT patches bonding near loose bolt, the corresponding RMSD indices are not equal 0; however, these values are much less than the RMSD index at damaged location. Additionally, the stiffness of H-columns and stiffeners also effect to the sensing of PZT patches on connection. In summary, the bolt-loosening issue in the bolted connection in steel column was successfully detected by using impedance responses.

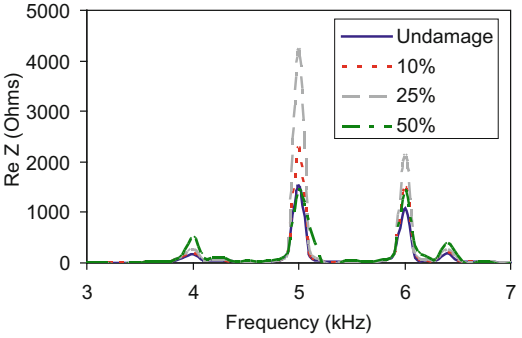


**Fig. 15.** Real impedance signatures.

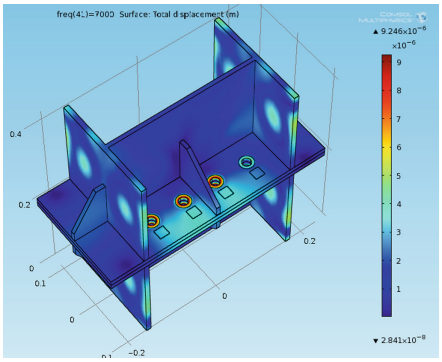


**Fig. 16.** Deformed shape of steel column connection.

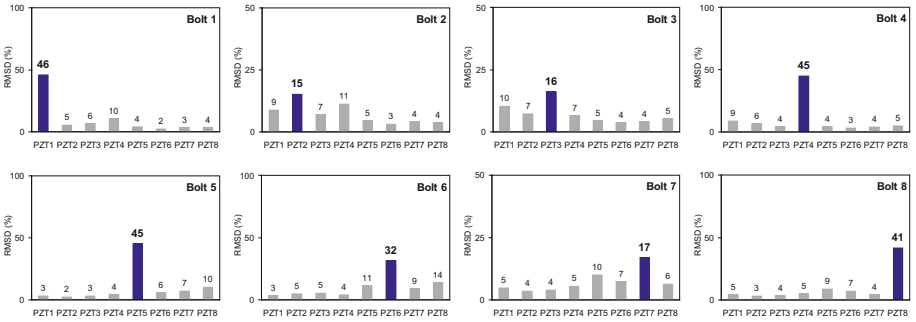


**Fig. 17.** RMSD vs bolt-loosening 10%.

**Table 2.** RMSD vs bolt-loosening

| *Bolt 1-loosening* | | | | | | | | |
|---|---|---|---|---|---|---|---|---|
| Level | **PZT1** | PZT2 | PZT3 | PZT4 | PZT5 | PZT6 | PZT7 | PZT8 |
| 10% | **46** | 5 | 6 | 10 | 4 | 2 | 3 | 4 |
| 25% | **151** | 15 | 17 | 24 | 9 | 5 | 9 | 9 |
| 50% | **48** | 38 | 35 | 41 | 18 | 9 | 18 | 17 |
| *Bolt 2-loosening* | | | | | | | | |
| Level | PZT1 | **PZT2** | PZT3 | PZT4 | PZT5 | PZT6 | PZT7 | PZT8 |
| 10% | 9 | **15** | 7 | 11 | 5 | 3 | 4 | 4 |
| 25% | 23 | **38** | 18 | 26 | 11 | 7 | 11 | 9 |
| 50% | 46 | **166** | 37 | 44 | 20 | 12 | 21 | 18 |
| *Bolt 3-loosening* | | | | | | | | |
| Level | PZT1 | PZT2 | **PZT3** | PZT4 | PZT5 | PZT6 | PZT7 | PZT8 |
| 10% | 10 | 7 | **16** | 7 | 5 | 4 | 4 | 5 |
| 25% | 24 | 19 | **38** | 16 | 11 | 9 | 11 | 13 |
| 50% | 43 | 38 | **160** | 30 | 22 | 20 | 22 | 24 |
| *Bolt 4-loosening* | | | | | | | | |
| Level | PZT1 | PZT2 | PZT3 | **PZT4** | PZT5 | PZT6 | PZT7 | PZT8 |
| 10% | 9 | 6 | 4 | **45** | 4 | 3 | 4 | 5 |
| 25% | 21 | 17 | 11 | **95** | 10 | 8 | 10 | 12 |
| 50% | 37 | 34 | 23 | **54** | 20 | 16 | 20 | 23 |
| *Bolt 5-loosening* | | | | | | | | |
| Level | PZT1 | PZT2 | PZT3 | PZT4 | **PZT5** | PZT6 | PZT7 | PZT8 |
| 10% | 3 | 2 | 3 | 4 | **45** | 6 | 7 | 10 |
| 25% | 8 | 5 | 8 | 10 | **125** | 16 | 18 | 23 |
| 50% | 15 | 10 | 17 | 19 | **56** | 40 | 38 | 41 |
| *Bolt 6-loosening* | | | | | | | | |
| Level | PZT1 | PZT2 | PZT3 | PZT4 | PZT5 | **PZT6** | PZT7 | PZT8 |
| 10% | 3 | 5 | 5 | 4 | 11 | **32** | 9 | 14 |
| 25% | 10 | 7 | 10 | 10 | 22 | **40** | 20 | 25 |
| 50% | 18 | 12 | 20 | 20 | 45 | **158** | 41 | 44 |
| *Bolt 7-loosening* | | | | | | | | |
| Level | PZT1 | PZT2 | PZT3 | PZT4 | PZT5 | PZT6 | **PZT7** | PZT8 |
| 10% | 5 | 4 | 4 | 5 | 10 | 7 | **17** | 6 |
| 25% | 11 | 9 | 10 | 13 | 24 | 20 | **38** | 15 |
| 50% | 22 | 19 | 21 | 25 | 43 | 41 | **161** | 29 |
| *Bolt 8-loosening* | | | | | | | | |
| Level | PZT1 | PZT2 | PZT3 | PZT4 | PZT5 | PZT6 | PZT7 | **PZT8** |
| 10% | 5 | 3 | 4 | 5 | 9 | 7 | 4 | **41** |
| 25% | 11 | 8 | 9 | 13 | 21 | 18 | 12 | **89** |
| 50% | 21 | 16 | 19 | 24 | 38 | 36 | 25 | **63** |

## 5 Conclusions

Bolt-loosening in steel column connection were successfully detected by using impedance responses. The following conclusions have been drawn from the results: (1) numerical simulations of E/M impedance responses were well estimated; (2) the impedance responses were good agreement between numerical results and experimental ones; (3) the damages were accurately diagnosed by using impedance-based SHM method. Numerical results show that impedance responses are potential for damage monitoring in real structures.

**Acknowledgments.** This research is funded by Bach Khoa University - VNU-HCM, under grant number T-KTXD-2016-92.

## References

1. Doebling, S.W., Farrar, C.R., Prime, M.B.: A summary review of vibration-based damage identification methods. Shock Vib. Dig. **30**(2), 91–105 (1998)
2. Farrar, C.R.: "Historical overview of structural health monitoring". In: Lecture Notes on Structural Health Monitoring Using Statistical Pattern Recognition, Los Alamos Dynamics, Los Alamos, NM (2001)
3. Liang, C., Sun, F.P., Rogers, C.A.: Coupled electro-mechanical analysis of adaptive material systems-determination of the actuator power consumption and system energy transfer. J. Intell. Mater. Syst. Struct. **5**, 12–20 (1994)
4. Sun, F.P., Chaudhry, Z., Liang, C., Rogers, C.A.: Truss structure integrity identification using PZT sensor-actuator. J. Intell. Mater. Syst. Struct. **6**, 134–139 (1995)
5. Park, G., Sohn, H., Farrar, C., Inman, D.: Overview of piezoelectric impedance-based health monitoring and path forward. Shock Vib. Dig. **35**, 451–463 (2003)
6. Giurgiutiu, V., Zagrai, A.: Damage detection in thin plates and aerospace structures with the electro-mechanical impedance method. Struct. Health Monit. **4**(2), 99–118 (2005)
7. Min, J., Park, S., Yun, C.B., Song, B.: Development of a low-cost multifunctional wireless impedance sensor node. Smart Struct. Syst. **6**(5–6), 689–709 (2010)
8. Kim, J.T., Park, J.H., Hong, D.S., Park, W.S.: Hybrid health monitoring of prestressed concrete girder bridges by sequential vibration impedance approaches. Eng. Struct. **32**, 115–128 (2010)
9. Ho, D.D.: "Multi-scale smart sensing of vibration and impedance for structural health monitoring of cable-stayed bridge". Ph.D. dissertation, Pukyong National University, Korea (2012)
10. Giurgiutiu, V., Zagrai, A.N.: Embedded self-sensing piezoelectric active sensors for online structural identification. ASME J. Vib. Acoust. **124**, 116–125 (2002)
11. Liu, X., Jiang, Z.: "Design of a PZT patch for measuring longitudinal mode impedance in the assessment of truss structure damage". Smart Mater. Struct. **18**, Article ID 125017 (2009)
12. Nassar, S.A., Barber, G.C., Zuo, D.: Bearing friction torque in bolted joints. Tribology Trans. **48**, 69–75 (2005)

# Crack Propagation Analysis in Concrete Dams Based on the eXtended Finite Element Method

Giang Vo Thi Tuyet(✉) and Trong Nguyen Vo

Ho Chi Minh City University of Technology, Ho Chi Minh City, Vietnam
{tuyetgiang.vo,nguyenvotrong}@hcmut.edu.vn

**Abstract.** In this paper, crack propagation in concrete dams is investigated using the eXtended Finite Element Method (X-FEM). The implementation of the crack model is undertaken through the development of a sub-program coded for this study. In order to simulate crack propagation, two level set functions are developed to represent a moving interface. The discontinuity of displacement due to the crack is introduced by a generalized Heaviside function and the addition of the asymptotic fields near the crack tip in order to improve the accuracy in elastic fracture mechanics. A validation example is presented to demonstrate the analysis procedure and capacities of the model. The results obtained show that the proposed model enables an accurate calculation of the Stress Intensity Factors (SIFs) and performs well for predicting crack trajectories. Finally, this work is applied to analyze and predict the fracture response in concrete dams and to evaluate the dam safety against cracking.

**Keywords:** Crack propagation · Concrete dams · eXtended Finite Element Method (X-FEM) · Stress Intensity Factors (SIFs)

## 1 Introduction

The study of cracking in concrete dams has focused on two principal issues: the constitutive model for cracking and its numerical implementation. For crack configurations with the Finite Element Method (FEM), the crack needs to conform to the mesh and with crack advancement, remeshing algorithms are required. This task results in a practical disadvantage of the method. With the Boundary Element Method (BEM), only the boundary of the domain under consideration needs to be discretized. Nevertheless, compared to the FEM, the main drawback of this method is that special techniques are required to deal with non-linear problems or non-homogenous media.

X-FEM's major advantage is that it represents the crack without explicitly meshing it [1]. This method of crack propagation allows many steps of crack propagation to be performed using a single mesh and enables a more accurate calculation of the stress intensity factors and the strain energy release rate around the crack front. The Level Set Method (LSM) is the numerical scheme developed by Osher and Sethian [2] to track the evolution of interfaces and shapes. To describe a crack, two level set functions are required [3]. They are updated at each propagation step to produce the new crack geometry.

© Springer Nature Singapore Pte Ltd. 2018
H. Tran-Nguyen et al. (eds.), *Proceedings of the 4th Congrès International de Géotechnique - Ouvrages -Structures*, Lecture Notes in Civil Engineering 8,
DOI 10.1007/978-981-10-6713-6_10

In this paper, an algorithm where the X-FEM is coupled with the LSM is described to study crack propagation in concrete dams. The discontinuity of displacement due to the crack is introduced by a generalized Heaviside function and the addition of the asymptotic fields near the crack tip in order to improve the accuracy in elastic fracture mechanics.

The remainder of this paper is organized as follows. In the next section, the general descriptions of the X-FEM and LSM as well as the criteria of propagation are given. The numerical simulation results for a fatigue propagation in a pre-cracked concrete dam scale model appear in Sect. 3 with the discussions. And finally, in Sect. 4, some conclusions and prospects are provided.

## 2 Numerical Techniques

### 2.1 Basics of Level Set Method and X-FEM

In the LSM, the interface is represented as the zero level set of a function of one higher dimension. To describe a crack, two level set functions are required. The normal level set (lsn) represents the signed distance to the crack surface and the tangent level set (lst) represents the distance to the crack front.

The X-FEM allows modelling the crack growth without having to modify the original mesh. In cracking, the discontinuity of displacement due to the crack is introduced by a generalized Heaviside function and the addition of the asymptotic fields near the crack tip in order to improve the accuracy in elastic fracture mechanics. The formula used for the displacement approximation $u^h(x)$ at point $x$ is given in Eq. (1). The first term is the standard one (continuous). The second term brings the discontinuity of displacement for the elements crossed by the crack (Heaviside enrichment) and the third term brings the singularities for the elements around the crack tip (asymptotic enrichment). Figure 1a shows a representation of a crack with additional degrees of freedom for enriched elements. Note that the crack passes through the elements and that the crack is not explicitly meshed [4].

$$u^h(x) = \sum_{i \in N_n(x)} a_i \Phi_i(x) + \sum_{j \in N_n(x) \cap K} b_j \Phi_j(x) H(lsn(x)) + \sum_{k \in N_n(x) \cap L} \sum_{\alpha=1}^{4} c_k^\alpha \Phi_k(x) F^\alpha(lsn(x), lst(x)) \tag{1}$$

where:

- $\boldsymbol{a_i}$ are the traditional displacement degrees of freedom associated with node $i$,
- $\Phi_i$ is the linear shape function of node $i$, $\boldsymbol{b_j}$ are the enriched degrees of freedom associated with node $j$,
- $c_k^\alpha$ are the enriched degrees of freedom associated with node $k$.

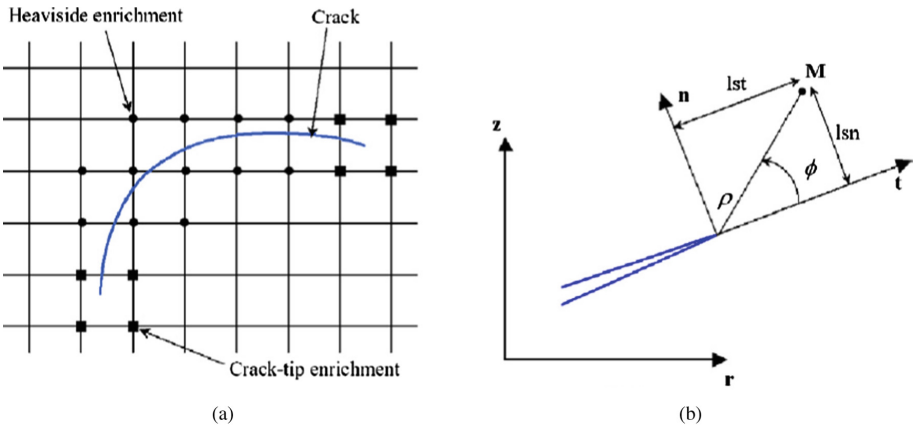


**Fig. 1.** A representation of a crack with additional degrees of freedom for enriched elements (circle symbols represent the elements enriched by the Heaviside function and square symbols represent the elements enriched by the singular functions) (a), global Cartesian coordinate system (r, z), local Cartesian coordinate system (n, t), local polar coordinate system ($\rho$, $\varphi$) and representation of the level sets (b).

The function $H(x)$ is a Heaviside function, which is discontinuous across the crack surface. Consider an element that is crossed by the crack, H(lsn(x)) = 1 for the nodes located on the side where lsn(x) > 0, whereas H(lsn(x)) = –1 for those located on the other side where lsn(x) < 0. Only one layer of elements is enriched. Note that a geometrical (fixed area) enrichment can also be done.

The expressions of the function $F^{\alpha}$, $\alpha$ = 1.4, are the following [5]:

$$F = \left\{ \begin{array}{l} \sqrt{\rho}\,\sin\frac{\phi}{2}, \sqrt{\rho}\,\cos\frac{\phi}{2}, \\ \sqrt{\rho}\,\sin\frac{\phi}{2}\sin\phi, \sqrt{\rho}\,\cos\frac{\phi}{2}\sin\phi \end{array} \right\} \tag{2}$$

The local polar co-ordinates ($\rho$, $\phi$) can be expressed in terms of the level sets at the crack tip as (see Fig. 1b):

$$\rho = \sqrt{lsn^2 + lst^2}\,;\ \phi = \tan^{-1}\left(\frac{lst}{lsn}\right) \tag{3}$$

Two types of crack tip element enrichment are shown in Fig. 2. For the topological enrichment, only one crack tip element is enriched (Fig. 2a). For the geometrical enrichment, all elements around the crack tip within a circle of radius $r_{max}$ are enriched (Fig. 2b). Note that the number of enriched elements increases when the mesh is refined [4].

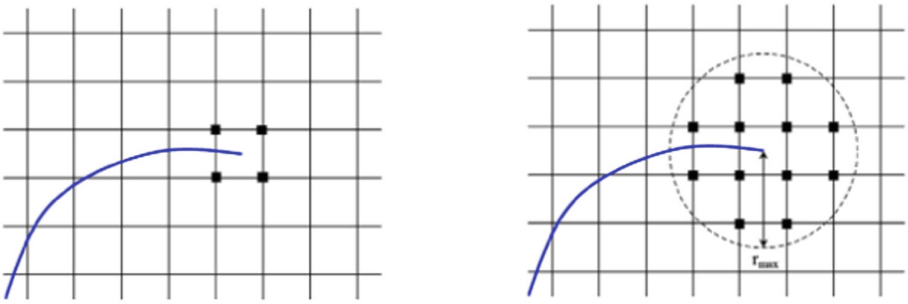

(a) (b)

**Fig. 2.** Crack tip elements for topological enrichment and geometrical enrichment.

### 2.2 Criteria of Propagation – The Maximum Hoop Stress Criterion

Erdogan and Sih [6] proposed the maximum hoop stress criterion. The maximum hoop stress criterion assumes that the crack will propagate where the hoop stress $\sigma_{\theta\theta}$ is maximized. Near the crack front, a good approximation of the hoop stress field is given by Eq. (4).

$$\sigma_{\theta\theta} = \frac{1}{\sqrt{2\pi r}} \cos\left(\frac{1}{2}\theta\right)\left[K_I \cos^2\left(\frac{1}{2}\theta\right) - \frac{3}{2}K_{II}\sin\theta\right] \tag{4}$$

The angle of propagation is deduced by differentiating the Eq. (4) and is given in Eq. (5).

$$\theta = 2\tan^{-1}\left(\frac{1}{4}\left(\frac{K_I}{K_{II}} - sign(K_{II})\sqrt{\left(\frac{K_I}{K_{II}}\right)^2 + 8}\right)\right) \tag{5}$$

where $K_I$, $K_{II}$ are the values of the stress intensity factors.

The computation of the energy release rate G is done using the G-theta method [7]. This method is based on domain integrals and Lagrangian derivation of the potential energy, with respect to a virtual crack extension velocity field θ. To compute the stress intensity factors, the G-theta method is extended with the bilinear form of the energy release rate [5]. In two dimensions, only one field θ is needed.

## 3 Numerical Example

In order to implement the crack model, we develop a sub-program code using the X-FEM in Code_Aster [8], an open source finite element software package developed by EDF R&D since 1989. A 2D numerical example is chosen to demonstrate the capacities of our algorithm and the robustness of the X-FEM/Level Set Method coupling for crack growth simulation in concrete dams.

This example reproduces a fatigue propagation in a pre-cracked concrete dam scale model (of a 96-m-high gravity dam) where the experimental measurements obtained by Carpintieri et al. [9] and the numerical results obtained by other methods (FEM [9] and Boundary Element Method (BEM) [10]) are available for comparison. The hydraulic load was generated by means of servo-controlled actuator with a 2000 kN capacity and applied onto the upstream side of the model specimen [9]. This force was distributed into four concentrated loads whose intensities increase with depth. Figure 3 illustrates the model dimensions, the equivalent hydraulic loads and the position of the crack. Also, for the purpose of comparison with experimental results and numerical ones obtained by other methods, the initial crack is located on the up-stream side and at a quarter of the dam, with the initial length of 15 cm. This crack is represented implicitly and independently of the mesh by the normal and the tangential level sets.

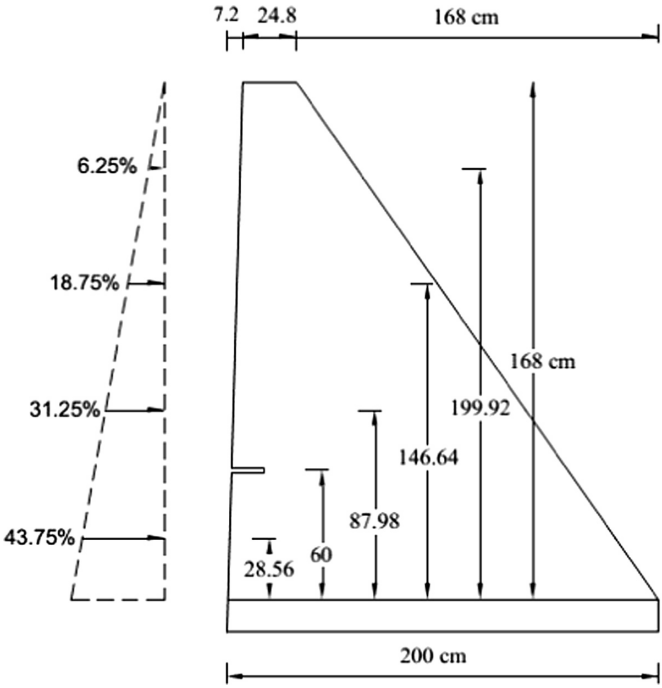


**Fig. 3.** Dam model, equivalent hydraulic loads and position of the crack.

The Young modulus is equal to 35700 MPa and the Poisson ratio is 0.1. The mesh used for the calculation is composed of 62128 triangles. The maximum mesh size is 1 cm. The mesh is refined in the area near the crack front (the distance is evaluated by the values of the level sets) at each propagation step in order to ensure an accurate SIF computation. It should be noted that the crack is not meshed during the X-FEM computations. The maximum growth size is set to be 4 cm.

For each propagation step, an iterative process is used to ensure that complete convergence was obtained. Convergence is defined as a solution of which the results for SIFs congregate to a single value through this process and the oscillation of the results stabilizes within the given refined meshes.

The propagation of crack consists in updating the level sets and determining the new crack front. The flowchart for a Code_Aster model with X-FEM crack propagation is presented in Fig. 4.

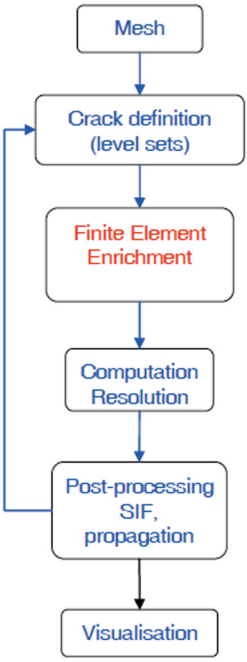


**Fig. 4.** Flowchart for Code_Aster model with X-FEM crack propagation.

Simulations are performed for 23 iterations of crack growth. The total computational time is 21 s. It is much lower than the ones required by the resolution of the Hamilton-Jacobi equations, by classic approaches or by other methods.

Figure 5 shows the level sets of the functions representing the crack and the crack tip after 23 propagation steps. These results are similar to those of [9] (the shaded area represents the crack front across the dam width in experiments and the "Ref. [8]" crack trajectory is determined by a cohesive crack model using a finite element code) and those of [10] (the simulated BEM crack trajectory) (Fig. 6). Reasonable agreement is observed between the X-FEM/Level Set Method coupling and these other methods.

In Fig. 7, the stress intensity factors $K_I$ and $K_{II}$ are plotted as functions of propagation steps. It can be seen that the $K_I$ values at the crack tip increase with the increase of crack growth length and the $K_{II}$ values are much smaller than the $K_I$ values. The crack propagation is non-steady and mode-I is the main form of crack propagation. Note that

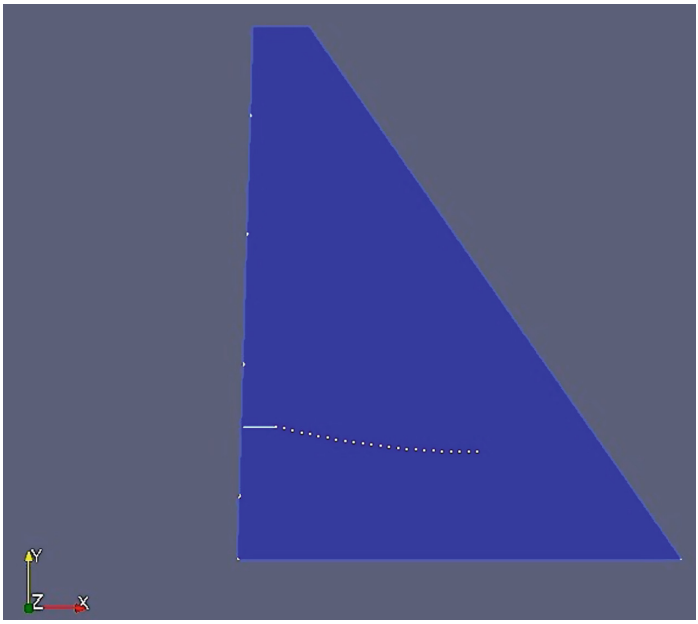


**Fig. 5.** Crack propagation path with the X-FEM/Level Set Method coupling.

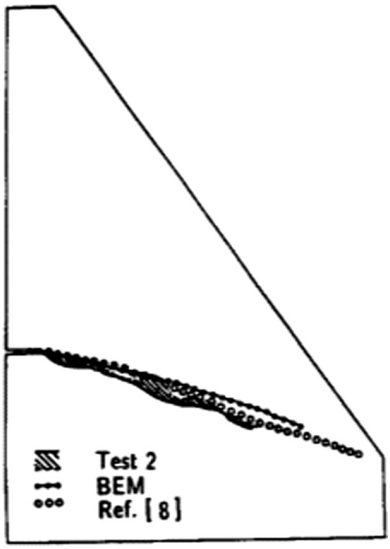


**Fig. 6.** Crack propagation path in experiments and with FEM and BEM [9, 10].

the $K_{II}$ can be a small positive or negative value as the crack propagates, depending on the chosen crack growth size. This can be explained by the fact that the direction for the next time step is determined by the $K_I$ and $K_{II}$ values of the previous step.

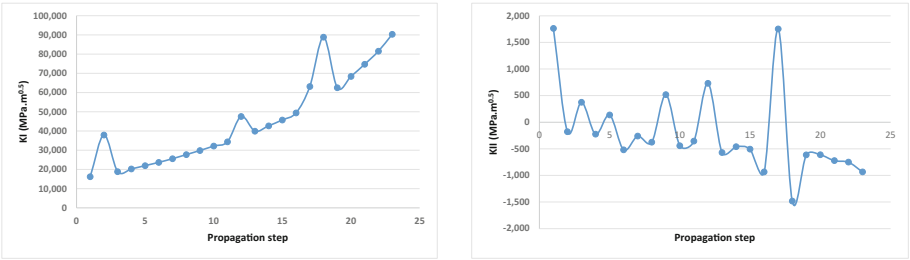


**Fig. 7.** The SIFs as functions of propagation steps.

## 4 Conclusions

In this paper, an algorithm where the X-FEM is coupled with the LSM is described to study crack propagation in concrete dams. X-FEM's major advantage is that it represents the crack without explicitly meshing it. To reduce the computational time and increase the robustness of the update calculations, the crack tip location and the crack shape are determined by two level set functions whose values are calculated based on geometrical considerations only.

The results obtained show that the proposed method allows many steps of crack propagation to be performed and enables an accurate calculation of the Stress Intensity Factors (SIFs). The total computational time is much lower than the ones required by the resolution of the Hamilton-Jacobi equations, by classic approaches or by other methods. This shows a good feature of the algorithm presented in this paper.

This work contributes to the better understanding of crack propagation behavior in concrete dams. Further work to model crack propagation in full-scale concrete dams is ongoing.

**Acknowledgments.** This research is funded by HCMC University of Technology under Grant Number T-KTXD-2016-76. The collaboration with the Modelling and Simulation Centre (MASC) at The University of Manchester for the study of crack propagation is greatly appreciated [11].

## References

1. Moës, N., Dolbow, J., Belytschko, T.: A finite element method for crack growth without remeshing. Int. J. Number Methods Eng. **46**, 131–150 (1999)
2. Osher, S., Sethian, J.A.: Fronts propagating with curvature dependent speed: algorithms based on Hamilton-Jacobi formulations. J. Comput. Phys. **79**, 12–49 (1988)
3. Stolarska, M., Chopp, D.L., Moës, N., Belytschko, T.: Modelling crack growth by level sets in the extended finite element method. Int. J. Numer. Methods Eng. **51**, 943–960 (2001)
4. Tran, V.X., Geniaut, S.: Development and industrial applications of X-FEM axisymmetric model for fracture mechanics. Eng. Fract. Mech. **82**, 135–157 (2012)
5. Geniaut, S., Galenne, E.: A simple method for crack growth in mixed mode with X-FEM. Int. J. Solids Struct. **49**, 2094–2106 (2012)

6. Erdogan, F., Sih, G.C.: On the crack extension in plates under plane loading and transverse shear. J. Basic Eng.-Trans. ASME **85**, 519–527 (1963)
7. Destuynder, P., Djaoua, M., Lescure, S.: Some remarks on elastic fracture mechanics. J. Méc. Théor. Appl. **2**, 113–135 (1983)
8. Code_Aster website. http://www.code-aster.org
9. Carpintieri, A., Valente, S.V., Ferrara, G., Imperato, A.L.: Experimental and numerical fracture modelling of a gravity dam. In: Bazant, Z.P. (ed) Fracture Mechanics of Concrete Structures, Elsevier Appl Sci, 351–360 (1992)
10. Chahrour, A.H., Ohtsu, M.: Crack growth prediction in scaled down model of concrete gravity dam. Theor. Appl. Fract. Mech. **21**(1), 29–40 (1994)
11. Vo, T.T.G., Martinuzzi, P., Tran, V.X., McLachlan, N., Steer, A.: Modelling 3D crack propagation in ageing graphite bricks of advanced gas-cooled reactor power plant. In: Paper Presented at the 23rd International Conference on Structural Mechanics in Reactor Technology (SMiRT-23), Manchester, United Kingdom, 10–14 August 2015 (2015)

# Experimental Study of Hybrid Walls with Several Fully Encased Steel Sections

Van Toan Tran[1(✉)] and Quang Huy Nguyen[2]

[1] Thuy loi University, Hanoi, Vietnam
tranvantoan@wru.vn
[2] European University of Bretagne – INSA Rennes, Rennes, France
quang-huy.nguyen@insa-rennes.fr

**Abstract.** Hybrid reinforced concrete steel (RCS) frames consisting of reinforced concrete (RC) column and steel (S) are used frequently in practice for mid-to-high-rise buildings. RCS frames possess several advantages from structural, economical and construction view point compare to either traditional RC or steel frames. One of the most important elements in RCS frames is the composite shear wall consisting of several steel sections encased in reinforced concrete. Regarding the RC walls reinforced by more than one steel profile, namely "Hybrid" wall, although number of researchers have focused on its various aspects, they are currently not covered by standards because they are neither reinforced concrete structures in the sense of Eurocode 2 (1992) or ACI-318 (2005) nor composite steel-concrete structures in the sense of Eurocode 4 (1994) or AISC-2010 (2010). An experimental study on the static behavior of hybrid walls with several embedded steel profiles subjected to combined shear and bending is presented. Six hybrid walls with different types of the structural steel-concrete connection and reinforcement detailing are tested. The specimens exhibited ductility behavior. The experimental results indicate that the load bearing capacity of the hybrid specimens considerably grows, as result of the encased steel profiles. The specimens with shear connectors (i.e. headed studs, stiffeners) were more ductile in terms of displacement ductility than the ones without connectors.

**Keywords:** Hybrid wall · Shear connection · Design method · Static test · Steel-concrete · Profile · Steel section

## 1 Introduction

Nowadays, hybrid reinforced concrete steel (RCS) frames consisting of reinforced concrete (RC) column and steel (S) are used frequently in practice for mid to high-rise buildings. RCS frames possess several advantages from structural, economical and construction view points compared to either traditional RC or steel frames. As described by Griffis (1986) RCS frames effectively combine structural steel and reinforced concrete members to their best advantage. From construction view point, these systems are usually built by first erecting a steel skeleton, which allows the performance of different construction tasks along the height of the building.

© Springer Nature Singapore Pte Ltd. 2018
H. Tran-Nguyen et al. (eds.), *Proceedings of the 4th Congrès International de Géotechnique - Ouvrages -Structures*, Lecture Notes in Civil Engineering 8,
DOI 10.1007/978-981-10-6713-6_11

Regarding the RC walls reinforced by more than one steel profile, namely "hybrid" wall, although number of researchers have focused on its various aspects, they are currently not covered by standards because they are neither reinforced concrete structures in the sense of Eurocode 2 (2004) or ACI-318 (2005) nor composite steel-concrete structures in the sense of Eurocode 4 (2005) or AISC-2010 (2010). Gaps in knowledge are mostly related to the problem of force transfer between concrete and embedded steel profiles, a situation in which it is neither known how to combine the resistances provided by bond, by stud connectors and by plate bearings, nor how to reinforce the transition zones between classical reinforced concrete and concrete reinforced by steel profiles. This paper introduces experimental study of hybrid walls with several embedded steel profiles (Van-Toan 2015). Six hybrid walls with different types of the structural steel-concrete connection and reinforcement detailing are tested. The experimental results will be the basis for developing a design method to analysis some main behaviors such as load bearing capacity, relation of load and displacement or strain and stress distributions of the hybrid walls reinforced by more than one steel profile.

## 2 Experimental Program

### 2.1 Description of Test Specimens

The experimental program consists of seven 2:3 scale wall specimens whose one is RC wall (served as reference specimen) and six others are composite wall with three encased steel profiles. All specimens had the same size, geometry and longitudinal reinforcing bar arrangements. The primary differences between seven specimens were the type of the structural steel-concrete connection and the stirrup spacing. Details evaluated in the test include the contributions of the steel profiles, shear studs, stiffeners, bond and stirrup spacing to the bending and shear resistance. Figure 1 shows the design details of all the seven specimens of hybrid walls. All specimens consisted of RC wall that had 5 m length, 25 × 90 cm rectangular cross-section and were reinforced with eight 20 mm diameter vertical reinforcing bars (Grade B). The horizontal reinforcement consisting of 14 mm and 6 mm reinforcing bars was made in form of stirrups. The reinforcing bar arrangement is the same in all specimens except the stirrup spacing which was 200 mm in A-RC, BW, CW and DW specimens and 100 mm in BW-HC, CW-HC and DW-HC specimens. All hybrid wall specimens were reinforced by three embedded HEB100.

### 2.2 Test Setup

The test setup is shown in Fig. 2. The third-point flexural beam test configuration was adopted to evaluate the resistance of specimens to combined bending and shear without axial force. Specimens were loaded at the mid-length by two hydraulic actuators (1500 kN capacity each). The actuators were operated in displacement control, with each actuator having the same displacement at any instant of time. Pinned boundary conditions at the each end of the specimens were simulated by two supports as shown

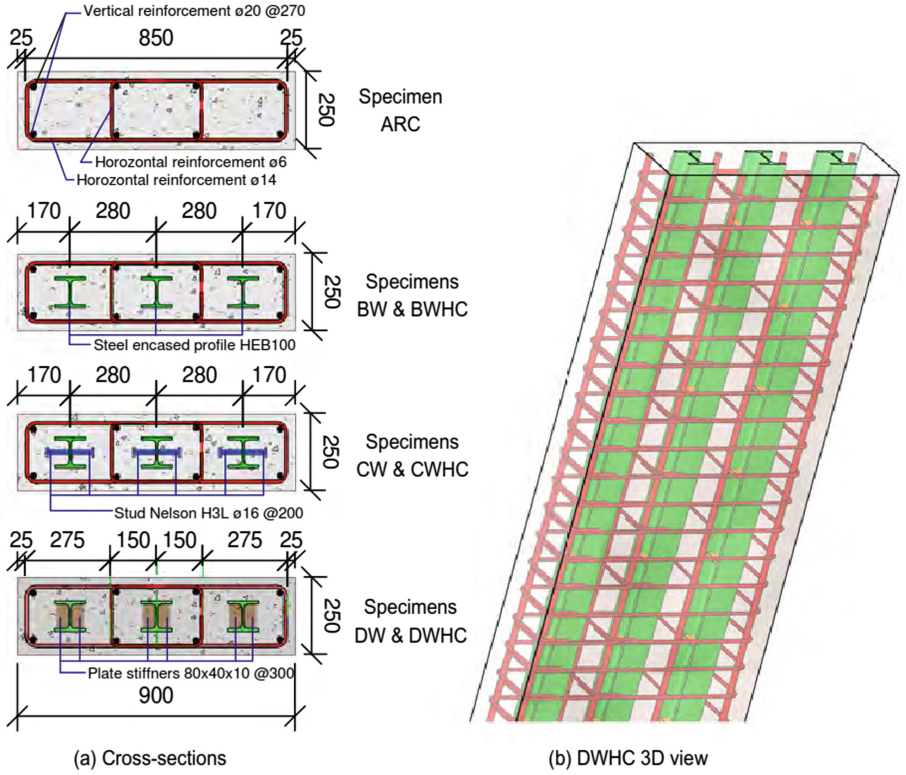


**Fig. 1.** Details of the test specimens

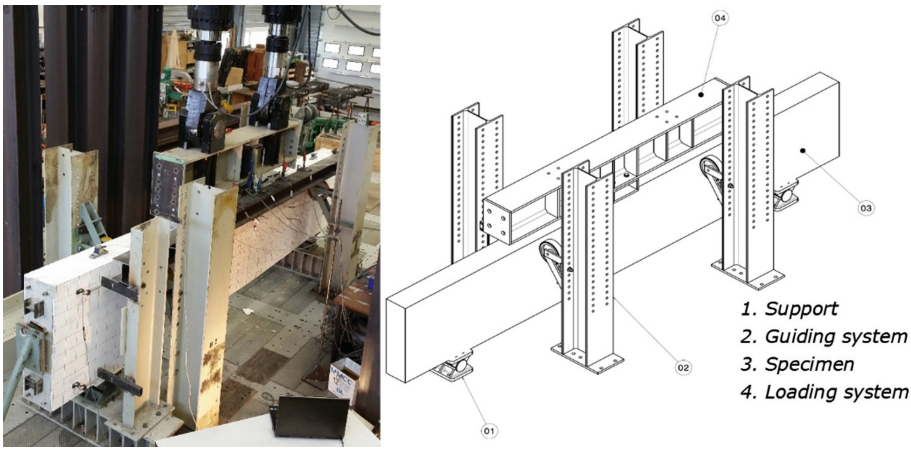


**Fig. 2.** Test setup

in Fig. 3. No restraint was provided against rotation along any axis. PTFE plates were placed between supports and specimen in order to avoid the friction and to allow the specimen deform freely in the horizontal direction. A transverse brace system was used in order to avoid out-of-plan displacement of the specimens.

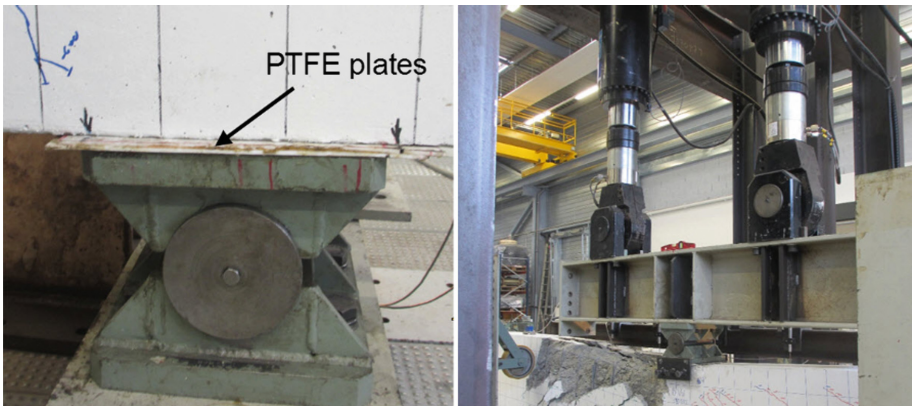


**Fig. 3.** Pinned support and loading system

### 2.3 Loading Procedure

All specimens were tested under statically increasing vertical loads. The loading was performed with displacement control through 4 steps: *First step* - Initial cycles-three cycles with an amplitude 0.2 mm and displacement speed of 0.01 mm/s, *Second step* - Monotonic loading up to a displacement of 25 mm with a speed of 0.01 mm/s, *Third step* - Monotonic loading from 25 mm displacement up to 50 mm with a speed of 0.02 mm/s and *Forty step* - Monotonic loading from 50 mm displacement up to 100 mm with a speed of 0.04 mm/s.

It was decided that each load increment of 100 kN was followed by a few minutes of stop to record the crack development in the specimens. All cracks were detected and marked with numerical order and loading value.

### 2.4 Instrumentation

Several different instruments were used in the testing of the specimens. The arrangement of the instrumentation is presented in Fig. 4. During the loading, the test results were recorded every second. The data acquisition devices include: *5 LVDT* placed along the specimen length (2 at middle), measuring the deflection shape, *5 LVDT* measuring the slips at the interface concrete-steel profile, *2 LVDT* measuring the horizontal displacements at the specimen end, *2 inclinometers* (devices that measure changes in angle) measuring the rotations at specimen's ends, *2 concrete strain gauges* pasted to the top concrete surface, *22 strain gauges* pasted to the reinforcement steel and *9 strain gauge rosettes* $0^o$–$45^o$–$90^o$ pasted to steel profiles.

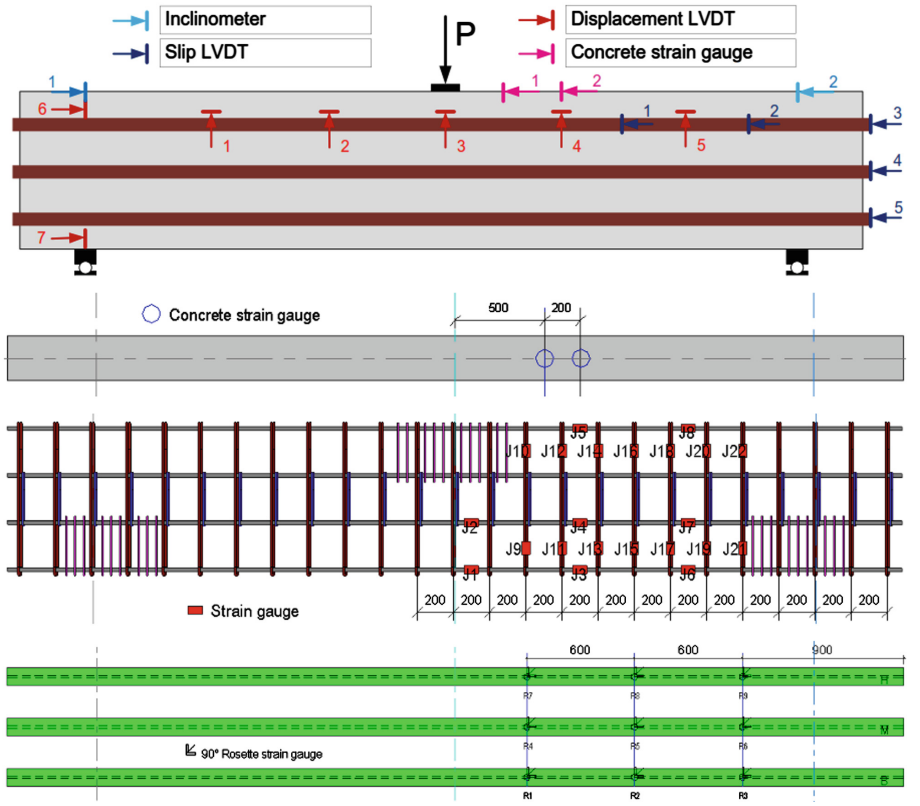


**Fig. 4.** Detailed arrangement of measuring devices

## 2.5 Material Properties

The designed concrete quality was C30 according to Eurocode 2 (2004), the reinforcement S500 steel and structural steel S460. The experimental results related to the steel properties are given in Table 1. At age of 28 days and on the day of the tests, the average cube strength and Young modulus of concrete had the values presented in Table 2.

**Table 1.** Structural and reinforcing steel properties

| Steel name | No of samples | $f_y$ (MPa) | $f_u$ (MPa) | $E_s$ (GPa) |
|---|---|---|---|---|
| HEB100 | 6 | 462.65 | 583.50 | 214.45 |
| Steel rebar $\varphi$20 | 4 | 383.91 | 542.62 | 210.74 |
| Steel rebar $\varphi$14 | 4 | 633.26 | 656.34 | 207.46 |

**Table 2.** Concrete properties

| Specimen | N° of samples | $f_{cm}$ (MPa) at age of 28 days | $f_{cm}$ (MPa) on the day of the tests | $E_{cm}$ (MPa) |
|---|---|---|---|---|
| A-RC | 3 | 22.99 | 24.61 | 30,179 |
| BW-HC | 3 | 22.99 | 26.04 | 30,862 |
| BW | 3 | 31.50 | 31.50 | 31,341 |
| CW | 3 | 27.67 | 32.00 | 31,328 |
| CW-HC | 3 | 27.67 | 31.63 | 31,194 |
| DW | 3 | 27.67 | 32.73 | 31,563 |
| DW-HC | 3 | 27.67 | 31.30 | 31,149 |

# 3 Experimental Results

## 3.1 Behavior of Test Specimens Until Failure

As a general conclusion, the all hybrid specimens had similar behavior. Flexure-dominant behavior which was expected according to design prediction was observed. It is noted that all specimens had a small aspect ratio of 2.08 resulting in the significant effect of transversal shear. Among the 7 test specimens, only A-RC specimen was failed in pure flexure. The other specimens were failed more or less in combined flexural-shear with domination of bending failure. A general view of specimens at failure stage is presented in Fig. 5.

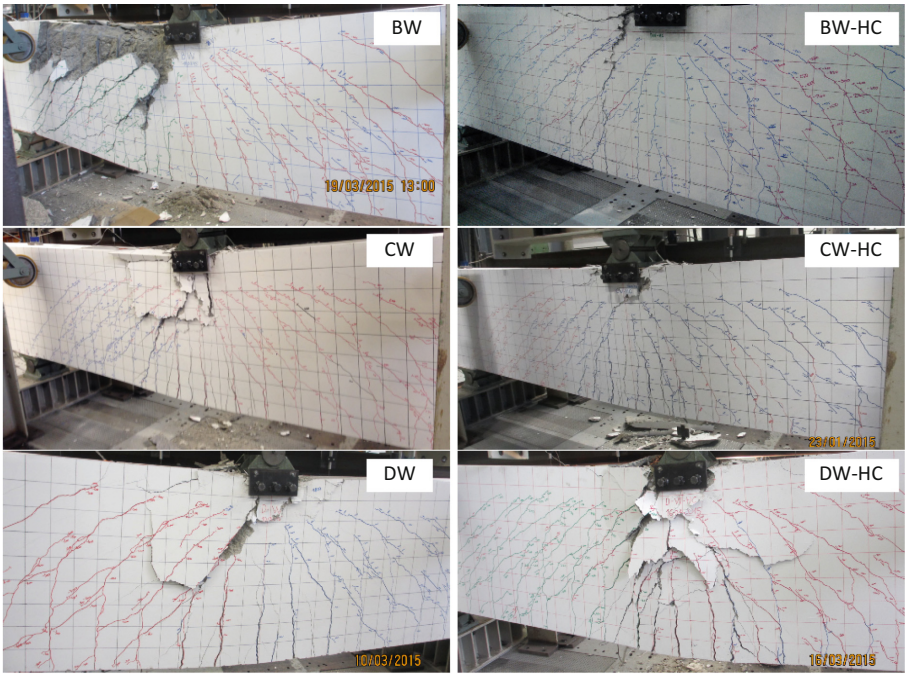


**Fig. 5.** Specimens at failure stage

According to the observation during the tests, the flexural-shear failure behavior of the hybrid specimens can be described by three phases as follows: *Phase 1 - pure flexural behavior:* The first flexural crack rapidly occurs at the mid-span then other flexural cracks emerge when loading increases; *Phase 2 - flexural-shear behavior:* The flexural crack at the mid-span almost stay the same while other formerly flexural cracks and new cracks continue to grow up. The direction of these cracks tends to be inclined to the loading point. These cracks are termed as flexural-shear cracks since they are originated by bending moment and later influenced by both flexure and shear while propagating; And *Phase 3 - shear behavior:* The flexural-shear cracks seem not to grow up any more. However, there appear cracks with inclined angle of about 45° at the tips of the flexural-shear cracks or there appear pure shear cracks in the web of specimens.

A stable applied load versus displacement behavior was observed in all seven specimens. Figure 6 presents the load versus displacement at mid-span curves for all specimens. It was observed that ductile failure took place gradually with the widening of the critical flexural cracks. Its can be seen that the specimens with shear connectors had more ductile behavior than the ones without connectors.

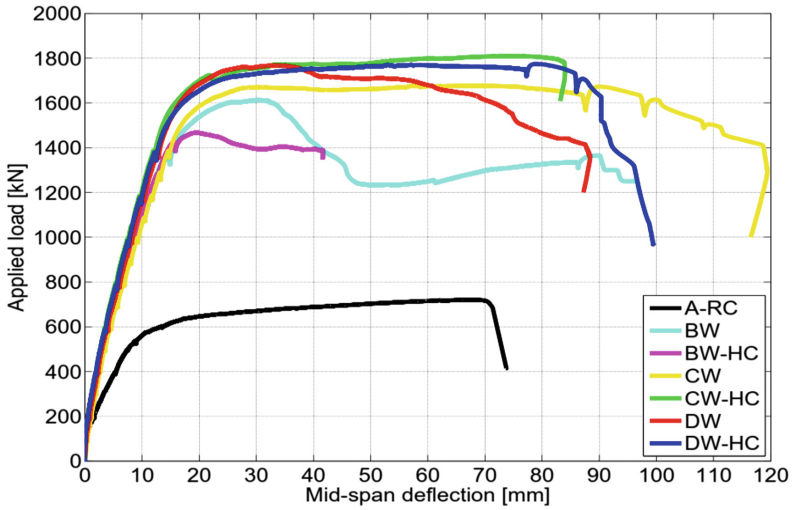


**Fig. 6.** Load-displacement at mid-span curves for all specimens

### 3.2 Discussion About the Global Response

In Table 3 is presented the correspondence between the forces and the displacements at different characteristic points from the tests, which are: As - The yielding point of the first longitudinal reinforcement layer, Bs - The yielding point of the second longitudinal reinforcement layer, Cs - The yielding point of stirrups, Ds - The yielding point of the lower encased steel profile, Fs - The ultimate load capacity of the specimen and Ys - The yielding of the specimen.

**Table 3.** Forces and displacements at different characteristic points

| Specimens | Yielding point As | | Yielding point Bs | | Yielding point Cs | | Yielding point Ds | | Maximum load point Fs | | Yielding point Ys | | Failure mode |
|---|---|---|---|---|---|---|---|---|---|---|---|---|---|
| | $F_{As}$ (kN) | $\Delta_{As}$ (mm) | $F_{Bs}$ (kN) | $\Delta_{Bs}$ (mm) | $F_{Cs}$ (kN) | $\Delta_{Cs}$ (mm) | $F_{Ds}$ (kN) | $\Delta_{Ds}$ (mm) | $F_{Fs}$ (kN) | $\Delta_{Fs}$ (mm) | $F_{Ys}$ (kN) | $\Delta_{Ys}$ (mm) | |
| A-RC | 352 | 4.3 | 519 | 8.2 | – | – | – | – | 721 | 66.9 | 557 | 7.9 | Flexural |
| BW | 820 | 6.1 | 1226 | 11.8 | 1302 | 12.9 | 1410 | 15.7 | 1613 | 30.0 | 1241 | 12.5 | Flexural & Shear |
| BW-HC | 880 | 7.0 | 1281 | 12.6 | – | – | 1423 | 15.4 | 1568 | 19.6 | 1173 | 11.3 | Flexural & Shear |
| CW | 898 | 7.9 | 1402 | 15.1 | – | – | 1455 | 15.9 | 1678 | 57.2 | 1428 | 16.4 | Flexural & Shear |
| CW-HC | 977 | 7.3 | 1526 | 14.0 | – | – | – | – | 1809 | 76.6 | 1490 | 14.6 | Flexural & Shear |
| DW | 924 | 7.4 | 1610 | 16.9 | – | – | 1436 | 13.5 | 1768 | 33.6 | 1467 | 15.3 | Flexural & Shear |
| DW-HC | 778 | 5.6 | 1299 | 11.1 | – | – | 1363 | 12.0 | 1774 | 78.8 | 1459 | 14.5 | Flexural & Shear |

The yielding points As, Bs, Cs and Ds are determined using the date collection from the strain gauges and rosettes whilst the yielding point Ys is determined based on the general yielding method as shown in Fig. 7 (Griffis 1986). Elastic behavior line with initial tangent stiffness intersects the horizontal line passing the peak strength at point A. Vertical line passing the point A intersects the load-displacement envelope curve at point B. Secant line passing the point O and the point B intersects the horizontal peak strength line at the point B. A vertical line passing the point B intersects the envelope curve at the point D which is the yielding point of the hybrid walls.

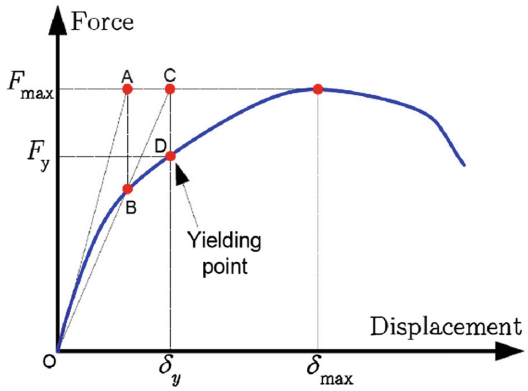


**Fig. 7.** General yielding point method by Zhang X (2015)

The strength of the specimens was defined in terms of load bearing capacity and represents the maximum applied vertical force. The absolute values of the load bearing capacity are presented in Table 3. The maximum load bearing capacity of the hybrid specimens was attained by CW-HC and DW-HC specimens, whilst the minimum is attained by BW-HC specimen. For BW, CW and DW specimens, which were realized using a concrete of 1.3 times compressive strength from the compressive strength of A-RC specimen, the difference in load bearing capacity is about between 2.2 and 2.4 times (see Figs. 6 and 8). This highlights the important contribution of three encased steel profiles on the load bearing capacity.

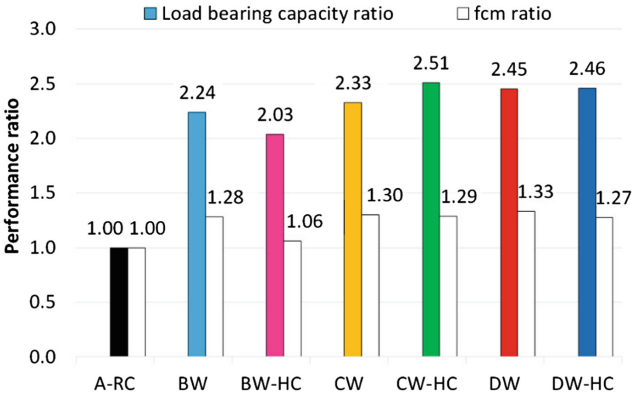


**Fig. 8.** The normalized load bearing capacity of the specimens

It can be noticed that the cracking displacement is almost the same for tested specimen group BW, CW, DW and group BW-HC, CW-HC, DW-HC excepting A-RC specimen. For instant, the first yielding point As of specimen BW appeared at a displacement of 6.1 mm, but it can be noticed that the cracking force is comparable with the cracking forces of the other hybrid specimens. The displacement corresponding to the specimen's yielding (Yielding point Ys) has almost the same values for all tested hybrid specimens, but some differences appear in terms of corresponding forces.

### 3.3 Discussion About the Local Response

During the experimental tests, the strains at different point on rebars, on steel profiles and on concrete were measured using strain gauges and rosettes. The locations of the strain gauges, of the strain gauge rosettes attached on the horizontal and vertical rebars, on the steel profiles and on the concrete for each test specimens are shown in Fig. 4. From there, stresses are calculated from the strains using linear elastic theory.

It is recalled that the locations of the strain gauge J1, J2, J3, J4, J6 and J7 attached on the horizontal rebars were in the regions of the wall which were subjected to tension. On the contrary, the locations of the strain gauge J5 and J8 attached on the horizontal

rebars were in the compressive region of the wall. Similarly, the locations of the strain gauges J9–J22 attached on the stirrups were in the regions of the wall which were subjected to tension.

Figure 9 shows the applied load versus stresses in longitudinal reinforcement. It can be observed that for all specimens the yielding stress was logically reached at the first reinforcement layer (J1 and J3) then at the second layer.

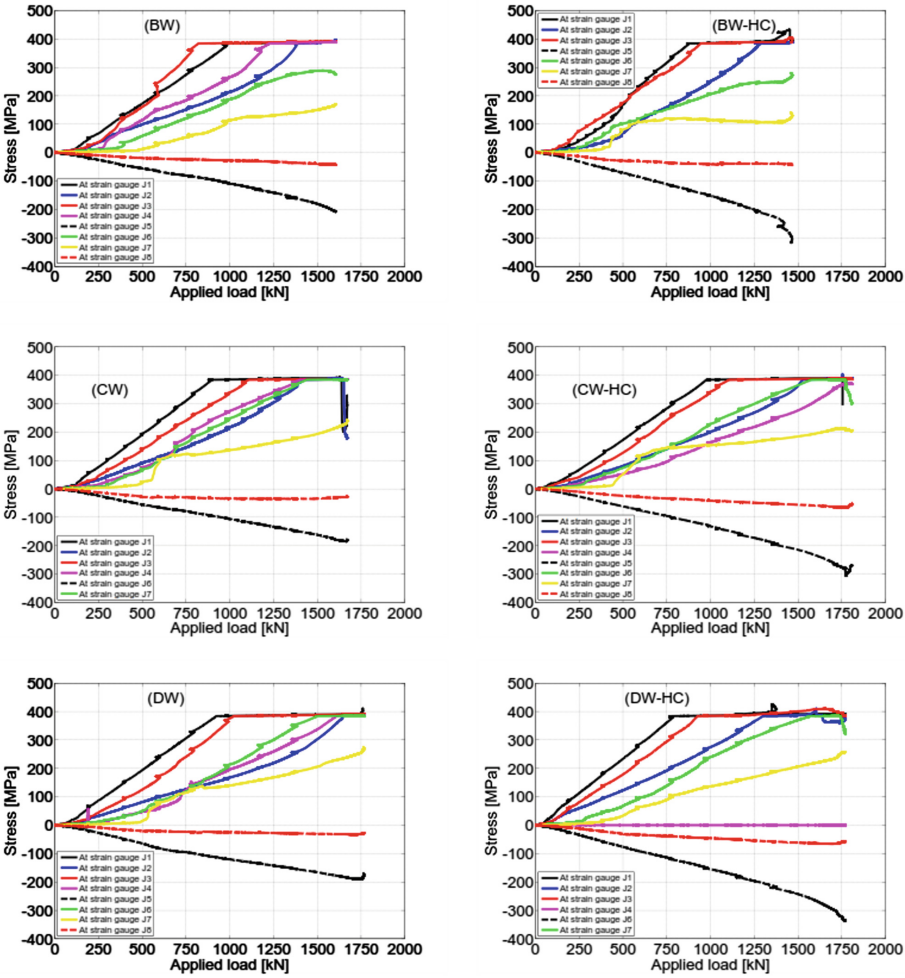


**Fig. 9.** Applied load versus stresses in longitudinal reinforcement

## 4 Conclusions

In this paper, an experimental study on the behavior of hybrid walls subjected to combined shear and bending has been presented. Based on the experimental results tested, we have some following conclusions:

Specimens showed very good behavior absorbing shear forces and bending moment as well. The load bearing capacity of the specimens considerably grows, as the result of the encased steel profiles. Except the pure RC specimen which was failed by bending, the six composite specimens had a similar failure mode which was identified as flexural-shear failure mode: yielding of the longitudinal rebars followed by yielding of steel profile then concrete crushing by shear effect;

For six hybrid specimens, the load bearing capacity was very close. The load-displacement experimental curves indicate that they had almost the same behavior until the applied reached about 70% of the load bearing capacity. The specimens with shear connectors (i.e. headed studs, stiffeners) were more ductile in terms of displacement ductility than the ones without connectors;

The concrete confinement made by mean of stirrups in BW-HC, CW-HC and DW-HC specimens does not significantly increase the specimen's load bearing capacity. In other words, the concrete may be already well confined with the number of stirrups placed in BW, CW and DW specimens.

Further experimental studies need to be conducted to extend the range of the test data for the basis for proposing a design model.

**Acknowledgements.** The authors gratefully acknowledge financial support by the European Commission (Research Fund for Coal and Steel) through the project SMARTCOCO (SMART COmposite COmponents: concrete structures reinforced by steel profiles) under grant agreement RFSR-CT-2012-00039.

## References

ACI: ACI-318 - Building code requirements for reinforced concrete, USA (2005)

ACI: AISC2010 - Specification for structural steel buildings, USA (2010)

EN 1992-1-1: Eurocode 2 - Design of concrete structures - Part 1: General rules and rules for buildings. CEN, Brussels (2004)

EN 1992-1-1: Eurocode 3 - Design of concrete structures - Part 1: General rules and rules for buidings. CEN, Brussels (2004)

EN 1994-1-1: Eurocode 4 - Design of composite steel and concrete structures - Part 1.1: General rules and rules for buildings. CEN, Brussels (2005)

Griffis, L.: Some design considerations for composite-frame structures. Eng. J. **23**(2), 59–64 (1986)

Zhang, X.: Experimental seismic behavior of innovative composite shear walls. J. Constr. Steel Res. **116**(218–232), 2015 (2015)

Van-Toan, T.: Etude numérique et expérimentale des murs en béton armé renforcés par plusieurs profilés métalliques totalement enrobés, Thèse, Insa de Rennes, 2015 (2015)

# Failure Analysis of a Cold-Rolled Steel Tensile Specimen Using a Damage-Plasticity Model

Bac V. Mai[1(✉)], Giang D. Nguyen[2], Cao Hung Pham[1], and Gregory J. Hancock[1]

[1] The University of Sydney, Sydney, New South Wale, Australia
{vanbac.mai, caohung.pham, gregory.hancock}@sydney.edu.au
[2] The University of Adelaide, Adelaide, South Australia, Australia
g.nguyen@adelaide.edu.au

**Abstract.** This paper presents preliminary results on the formulation of a damage-plasticity model and its applications for the failure analysis of cold-rolled high strength steels. The model is based on von Mises plastic theory combined with a damage criterion to capture both hardening and softening responses. The proposed constitutive model is calibrated against available experimental data and implemented into the ABAQUS finite element (FE) package for the failure analysis in a tensile test of cold-formed steel (CFS). Both the experimental overall response of the member and its fracture pattern can be predicted, showing the potentials of the model in structural applications. In addition, both advantages and disadvantages of the model are discussed with proposals for further improvements.

**Keywords:** Damage-plasticity · Constitutive modelling · Cold-rolled steel

## 1 Introduction

Cold-rolled high strength steel (HSS) materials to AS 1397-2001 (Standards Australia 2001) are being widely applied in engineering structures because they possess a higher strength and are more durable and lighter than the traditional hot rolled steels. However, the cold-rolling technique also results in several challenges. One of them is known as ductility reduction arising in the cold-rolling process which may lead to a premature failure of the material under stress. Although there have been many studies conducted for this material failure, most of them are based on experiments (Teh and Clements 2012; Hancock and Rogers 1998) and to the best of our knowledge research works on the development of constitutive models for cold-rolled steel (CRS) and their structural applications are still limited. For this reason, a full understanding of the ductile fracture behavior in conjunction with the development of an appropriate model for the cold-rolled steel are always necessary. The model can be applied to a practical design such as the prediction of the load-bearing capacity and failure mode of bolted steel connections. This is because the capacity of this connection is controlled by the plastic-damage behavior of the metal at a local area which the failure is initiated.

© Springer Nature Singapore Pte Ltd. 2018
H. Tran-Nguyen et al. (eds.), *Proceedings of the 4th Congrès International de Géotechnique - Ouvrages -Structures*, Lecture Notes in Civil Engineering 8,
DOI 10.1007/978-981-10-6713-6_12

The experimental observations show that HSS also undergoes a considerable amount of plastic deformation prior to a material separation. This behavior is considered as a ductile damage. From the microstructural viewpoint, a process of nucleation, growth and coalescence of voids in the material has been adopted to describe the area reduction and material softening. This effect can be described as a damage accumulation that is incorporated into the constitutive behavior. Also, a failure mode of a specimen made by CRS under a tensile load was observed (Teh and Clements 2012) in which the material degradation can be governed by the stress triaxiality and the level of plastic deformation. However, these mechanisms have not been investigated by a numerical study.

Damage modelling for ductile materials has been studied for a long time. The damage growth may depend on stress, strain and the level of plastic deformation. Early formulations considered that a fracture is simply assumed to occur when the equivalent plastic strain reaches a critical level (Bjorklund 2012). Although the assumption is convenient, the experimental observations show that using a constant plastic strain for the fracture is insufficient, as stress or strain alone are not adequate to capture the onset and evolution of a ductile fracture process. Significant effects of stress triaxiality on the failure process have been shown in several studies (Gurson 1977; McClintock 1968; Rice and Tracey 1969). In addition, the effect of the third stress invariant, Lode angle, has also been observed and taken into account in the modelling of metal failure (Bai and Wierzbicki 2008; Wen and Mahmoud 2016; Xue 2008). Essentially, all these features (triaxiality and Lode angle dependence of failure) should appear in a model devoted to modelling metal failure, in conjunction with the modelling of ductile hardening and softening processes using plasticity theory and damage mechanics, respectively.

The aim of this study does not include all the features discussed above. It focus on investigating a simple but effective approach combining damage mechanics and plasticity theory for the modelling of ductile failure. In this approach a coupled damage-plasticity model is adopted (Nguyen et al. 2015). In the model, a Von Mises plasticity model with nonlinear hardening rule is used, and enhanced with a damage criterial based on the equivalent plastic strain to capture the softening process. Stress return algorithm is developed for the implementation of the model in ABAQUS and a 3D example of ductile failure is used to demonstrate the model capabilities. In addition, the future development of the model are proposed.

## 2 Formulation of the Damage-Plasticity Model

### 2.1 Enhanced Damage-Plasticity Model

The constitutive equation of stress-strain-damage relationship is given by:

$$\boldsymbol{\sigma} = (1 - D)\mathbf{C} : (\boldsymbol{\varepsilon} - \boldsymbol{\varepsilon}^{p}) \tag{1}$$

In the formulation, $\boldsymbol{\sigma}$, $\boldsymbol{\varepsilon}$ and $\boldsymbol{\varepsilon}^{\mathrm{p}}$ are the stress, total strain and plastic strain tensors respectively; $\mathbf{C}$ is the isotropic elastic stiffness tensor while $D$ is used to present the damage accumulation.

For the present study, the von Mises criterion is adopted, and the yield function $y_p$ taking into account damage effects is written as:

$$y_p = \sqrt{\frac{3}{2}\boldsymbol{\sigma}' : \boldsymbol{\sigma}'} - (1 - D)F(\varepsilon_p) = 0 \tag{2}$$

Isotropic hardening is employed. In Eq. (2), $\boldsymbol{\sigma}'$ is the deviatoric stress tensor and $\varepsilon_p$ is the equivalent plastic strain. The first term of the yield function is equivalent stress or von Mises stress. The second term is a complex function controlling both hardening and softening regions. In this term, $F(\varepsilon_p)$ can be considered as a function governing the pre-peak hardening process while $D$ is a parameter controlling damage-softening response $(0 \leq D < 1)$. For the hardening curve, a power law proposed by Chaboche (1989) is adopted, i.e.:

$$F(\varepsilon_p) = k + A\left(1 - e^{-B\varepsilon_p}\right) \tag{3}$$

According to the selected function, the hardening process is a function of the equivalent plastic strain ($\varepsilon_p$). In the formulation, $k$ represents for the yield stress, the sum of $A$ and $k$ plays a role as an ultimate stress while $B$ controls the shape of the hardening curve. For the softening-damage progress, the damage evolution law is defined as:

$$D = 1 - e^{-q\left(\varepsilon_p - \varepsilon_{p0}\right)^n} \tag{4}$$

Here, damage growth (i.e., $D$) depends on the effective plastic strain ($\varepsilon_p$). It is activated when the effective plastic strain reaches its threshold ($\varepsilon_{p0}$) which plays the role of a damage threshold. Some recent studies show that this damage enhancement is also controlled by the stress state including the stress triaxiality and the Lode angle (Xue 2008). The treatment in this study is however limited to the case that the damage evolution is independent of the stress state and effects of Lode angle will be considered in our future work. Thus, it is assumed that it only depends on the plastic strain or the stored energy as given in the Lemaitre's studies (Lemaitre 1986). The softening process is governed by two parameters $q$ and $n$. The link between essential work of fracture and these parameters will be presented in the next part.

The associated flow rule is employed:

$$\mathrm{d}\boldsymbol{\varepsilon}^p = d\lambda \frac{\partial y_p}{\partial \boldsymbol{\sigma}} = d\lambda\, \mathbf{a} \tag{5}$$

The accumulated plastic strain rate is obtained as:

$$\mathrm{d}\varepsilon_p = \sqrt{\frac{2}{3}\mathrm{d}\boldsymbol{\varepsilon}^p : \mathrm{d}\boldsymbol{\varepsilon}^p} = d\lambda\sqrt{\frac{2}{3}\mathbf{a} : \mathbf{a}} \tag{6}$$

## 2.2 Model Behavior

The model behavior and its link with the calibration parameters are briefly presented. According to Nguyen et al. (2015), the non-essential work to the rupture ($w_p$) is separated from the essential work of rupture ($w^*_{nt}$) as shown in Eqs. (7 and 8). These parts are illustrated in Fig. 1 and their formulations are rewritten as (Nguyen et al. 2015):

$$w_p = \int_0^{\varepsilon_{p0}} \mathrm{F}(\varepsilon_p)\delta\varepsilon_p = (k+A)\varepsilon_{p0} - \frac{A}{B}(1 - e^{-B\varepsilon_{p0}}) \tag{7}$$

$$w^*_{nt} = \int_{\varepsilon_{p0}}^{\infty} \frac{(\mathrm{F}(\varepsilon_p))^2}{2E}\frac{\partial D}{\partial \varepsilon_p}\mathrm{d}\varepsilon_p + \int_{\varepsilon_{p0}}^{\infty} [1 - D]\mathrm{F}(\varepsilon_p)\mathrm{d}\varepsilon_p \tag{8}$$

In this study, a practical approach to calibrate the damage-softening parameters is proposed and applied to a 3-dimensional simulation. The focus is on Eq. (8), $w^*_{nt}$ is the volumetric fracture energy. It is calculated by dividing a surface energy ($w_{nt}$) for a value of elemental characteristic length (h). While the surface energy is an experimental value (Korsunsky and Kim 2005; Nguyen et al. 2015), the characteristic length depends on the finite element size. For a first-order 3D element, for example, it can roughly be approximated as a cubic root of the element volume. The use of this value taken from the ABAQUS subroutine's estimation (UMAT) allows a reduction in computational efforts. The relationship between the post-peak parameters $q$, $n$ and the volumetric fracture energy is illustrated in Eq. (8) through the damage parameter $D$. When the experimental energy is known, these parameters can be determined via this integration. An integration calculation and bisection algorithms are written and combined in FORTRAN environment for the determination of $q$ given the element characteristic length in ABAQUS.

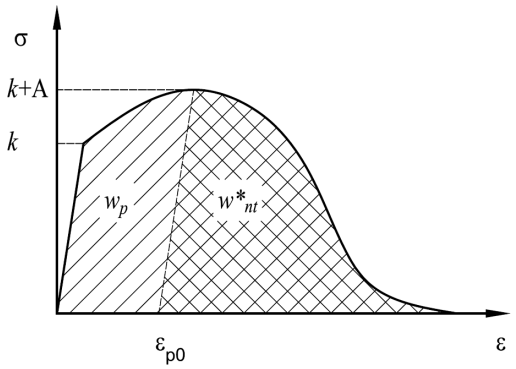


**Fig. 1.** Non-essential and essential work of fracture

An examination of a calibration for damage softening parameters is firstly discussed. All elastic and plastic hardening parameters must be known, for example, $E$ = 210000, $v$ = 0.3, $k$ = 500 MPa, $A$ = 200 MPa, $B$ = 25, $\varepsilon_{p0}$ = 0.1. Then, an experimental value of essential work, $w_{nt}$ = 181.5 N.mm/mm$^2$ and the element characteristic length taken from UMAT information (CELENT) $h$ = 3.0 mm are assumed. The volumetric fracture energy, $w^*_{nt} = w_{nt}/h$ = 60.5 N.mm/mm$^3$ is then computed. For simplicity, n = 2 is kept and thus the integration in Eq. (8) becomes a function of only variable $q$. By using the bisection method for several steps, $q$ = 74.84 is estimated.

### 2.3 Implementation Algorithm

Equations (1–6) define the damage-plasticity model. These equations allow the establishment of the proposed model in the FE algorithm. This task requires a stress return algorithm to solve the nonlinear system. Particularly, during a strain increment, the algorithm must take a trial stress state back into a new state, which satisfies the yield criterion. In this research, a semi-implicit algorithm is adopted. Figure 2 illustrates the algorithm in which a starting point X is assumed to be known. During an increment, point C lying on the new yield surface has to be determined. The predictor for C depends on trial point B, which lies outside the yield surface.

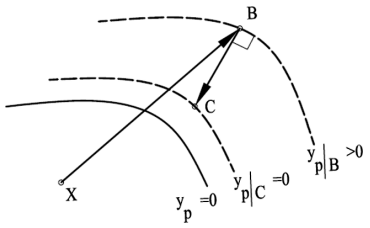


**Fig. 2.** A backward-Euler procedure

For this operator, the first order Taylor expansion of the yield function in Eq. (2) is applied for the point B:

$$y_p\big|_C = y_p\big|_B + \frac{\partial y_p}{\partial \boldsymbol{\sigma}} : d\boldsymbol{\sigma} + \frac{\partial y_p}{\partial D} dD + \frac{\partial y_p}{\partial \varepsilon_p} d\varepsilon_p \tag{9}$$

It is noted that all terms in Eq. (9) are computed at a trial point B. Using only plastic and damage parts of the incremental stress, which are taken from an increment of stress in Eq. (1), i.e.,

$$d\boldsymbol{\sigma} = \boldsymbol{\sigma}_C - \boldsymbol{\sigma}_B = -(1-D)\mathbf{C} : d\boldsymbol{\varepsilon}^p - \frac{\boldsymbol{\sigma}}{1-D} dD = -d\lambda\,(1-D)\mathbf{C} : \mathbf{a} - \frac{\boldsymbol{\sigma}}{1-D} dD \tag{10}$$

From Eq. (10), by substituting into Eq. (9), one obtains:

$$y_p\big|_C = y_p\big|_B + \mathbf{a} : \left[-d\lambda\,(1-D)\mathbf{C} : \mathbf{a} - \frac{\boldsymbol{\sigma}}{1-D}dD\right] + F(\varepsilon_p)dD - (1-D)\frac{\partial F(\varepsilon_p)}{\partial \varepsilon_p}d\varepsilon_p \tag{11}$$

Obviously, value $y_p\big|_C$ of the yield function at point C should vanish. Using the flow rule in Eq. (5) and the accumulated plastic strain in Eq. (6), the plastic multiplier is computed as:

$$d\lambda = \frac{y_p\big|_B}{(1-D)\left[\mathbf{a} : \mathbf{C} : \mathbf{a} + \frac{\partial F(\varepsilon_p)}{\partial \varepsilon_p}\sqrt{\frac{2}{3}\mathbf{a} : \mathbf{a}}\right]} \tag{12}$$

Once multiplier dλ has been evaluated in Eq. (12), the incremental plastic strain and incremental equivalent strain can be obtained from Eqs. (5) and (6). The damage and its rate are computed from Eq. (4) and its derivation.

Finally, the new stress state (point C) can be obtained as in Eq. (10). In general, this point does not precisely lie on the yield surface, thus it requires some more iterations to take it back to the yield surface. For a simple scheme, the procedure can be iterated until a new stress state satisfies the yield criterion.

### 2.4 Parametric Study

This part presents the influence of the parameters on the model response at a local integration or elemental level. A numerical simulation of a uniaxial tensile test is examined. All parameter values are assumed as: $E$ = 210000, $v$ = 0.3, $k$ = 500 MPa, $A$ = 200 MPa, $B$ = 25, $\varepsilon_{p0}$ = 0.1. The capability of the proposed model is discussed.

The influence of the parameters on the model response are shown in Fig. 3. For post-peak response, parameter $k$ plays a role as a yield stress threshold while sum of $k$ and $A$ is an ultimate stress. For the softening response, it is controlled by a combination of the plastic and the damage functions. When the three hardening parameters are determined, the two damage-softening parameters $q$ and $n$ must be calibrated. The introduction of the essential and non-essential works of fracture is enhanced for the task and is demonstrated in the model behavior. With a given value of the volumetric

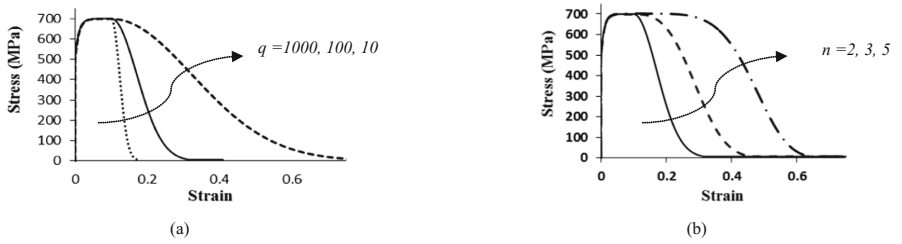


**Fig. 3.** Model responses (a) Effects of parameter $q$ ($n$ = 2), (b) Effects of parameter $n$ ($q$ = 100)

fracture energy, obtained from the experimentally given essential work of fracture and a length scale, parameter $q$ can be found by Eq. (8) with respect to a given value of $n$. The link of the essential work and these parameters is temporarily ignored, so the effect of these two parameters are directly presented in this part.

Both pre- and post-peak responses provide an accurate and flexible behavior. The equivalent stress precisely reflects the von Mises criterion in the hardening period while the responses are flexible in the softening one. This allows the model to capture a wide arrange of post-peak responses.

## 3 Numerical Validation of a Tensile Experiment

The model is adopted to predict the structural behavior and damage growth of a tensile specimen made of CFS G450 (Standards Australia 2001). The experiment was carried out in the School of Civil Engineering, University of Sydney. The geometry, boundary condition (BC) and mesh are illustrated in Fig. 4. For the sake of symmetry, half of the specimen is simulated. The FE discretization employs 8-node hexagonal elements (C3D8) and a full integration is utilized.

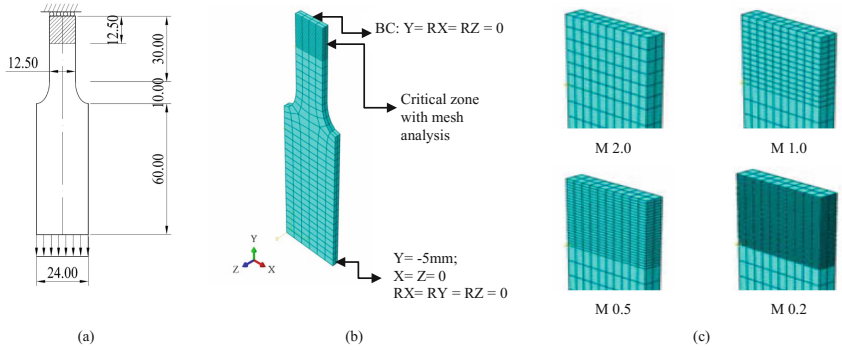


**Fig. 4.** Tensile specimen (a) Geometry, (b) Finite element (M 0.5) and boundary condition, (c) Different meshes in the critical zone

**The hardening parameters** are simply estimated based on the experimental data of G450 steel specimen and are listed in Table 1. The threshold strain is directly determined at the peak load. These parameters are kept constant during the flowing analysis. From the analysis of the parameter study, $n = 2$ is selected for the whole analysis so that the only remaining parameter $q$ is calibrated.

**Table 1.** Material properties of the high strength steel G450

| E | $v$ | $k$ (MPa) | $A$ (MPa) | $B$ | $\varepsilon_{p0}$ |
|---|---|---|---|---|---|
| 210000 | 0.3 | 515.0 | 85.0 | 25.0 | 0.07 |

**A mesh sensitivity study** is conducted and in this study, the mesh size is varied in a critical area (12.5 mm) along the length of simulated specimen (Fig. 4a). While the element sizes are fixed along the specimen thickness and width in this region, only the change in the dimension along the specimen's length is considered. This dimension is employed to present for the elemental mesh size in the critical region (Fig. 4c). For instance, M2.0 denotes an elemental length of 2.0 mm.

Figure 5 presents the load-displacement curves corresponding to the different mesh sizes with the same the essential work ($w_{nt}$ = 300.0 N.mm/mm$^2$). Three mesh groups are classified. A coarse mesh is M2.0 while a "strongly fine mesh" is M0.1. Medium and fine meshes are between M0.5 and M0.2. For the coarse mesh, the softening branch mainly depends on a few critical elements where large displacement and localization occur. For the strongly fine mesh, the localization happens in random patterns and critical elements are uncertain. The reason may be related to an inappropriate estimation of the element's characteristic length, which depends on the elements' "bad" geometry. A divergent response in the softening region can be seen in these cases. In contrast, the medium or fine meshes provide close paths. In this case, a fair dependence of the post-peak response is observed. The load-displacement curves are likely to be more ductile with finer meshes because of the enrichment of the fracture energy. This asserts that the approach works reasonably well for an appropriate of mesh size.

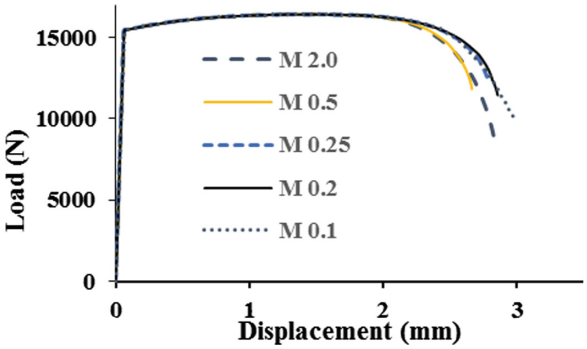


**Fig. 5.** Load-displacement curves verse different mesh sizes ($w_{nt}$ = 300.0 N.mm/mm$^2$)

From the authors' point of view, the smearing of the surface energy over the characteristic length for all elemental sizes are not appropriate. However, this way is a common adaptation and avoids the complex establishment of the effective length. It is accompanied with an arrangement of mesh size which is acceptable.

**The damage-softening parameters'** calibration is based on the fracture energy. Only the parameter $q$ is calibrated because $n$ = 2 is kept. The essential work of necking and tearing is assumed here due to lack of current experimental data and its scatter (Korsunsky and Kim 2005). Three different values of the energy are given. Using the same mesh size (M0.2) as the above mesh analysis, the characteristic length of elements in the critical zone taken from ABAQUS/UMAT are constant (0.6676 mm) and the parameter $q$ controlling the softening are calculated based on Eq. 8. With the same hardening parameters in Table 1, the set of softening parameters is listed in Table 2.

**Table 2.** Model parameter corresponding to a value of $w_{nt}$

| Parameter | $w_{nt}$ = 300.0 (N.mm/mm$^2$) |
|---|---|
| $n$ | 2 |
| $q$ | 1.398 |

As observed in Fig. 6, the numerical responses with different values of the essential work are compared with the experimental result. The changed value of fracture energy is reflected in the structural responses. The higher value of $w_{nt}$ makes the plastic plateau last longer and softening process milder. This gives sense/meaning to the essential work. Furthermore, the experimental curve bounded by the experimental ones is another advantage of the model. Three-dimension strain localization can be captured via the simulation. This natural behavior is a mode of tensile deformation when the

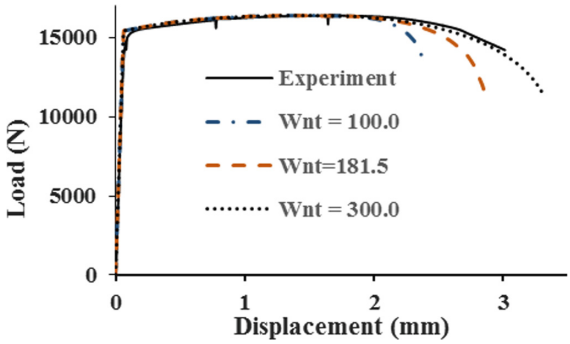


**Fig. 6.** Load-displacement curves verse different energies (M0.2)

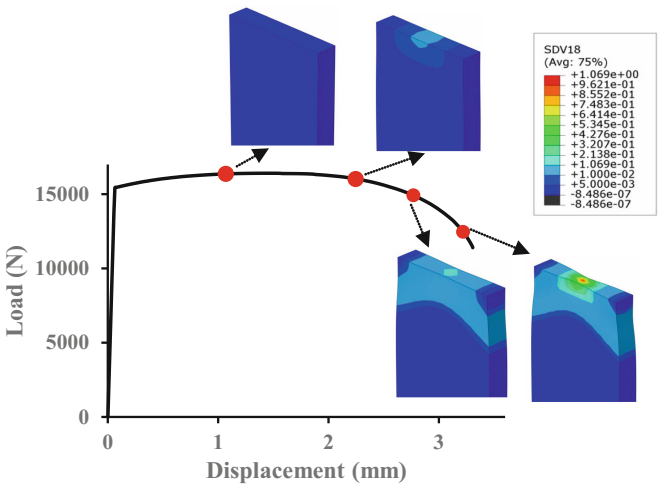


**Fig. 7.** Structural response and damage patterns using mesh M0.2 and $w_{nt}$ = 300.0 Nmm/mm$^2$

material effective area is reduced, which is accompanied with damage growth. This process boosts the necking concentration in a particular region until rupture. A whole failure process can be seen in Fig. 7. Some points are marked in a structural response and their counterparts of damage contours are illustrated (Fig. 7). Initially, plastic deformation occurs over the whole specimen before reaching the peak load. After that the activation of damage causes localization of deformation and a decrease in the load bearing capacity occurs. As a consequence, the rapid increase in the equivalent plastic strain accompanies the sharp growth in the damage process.

## 4 Conclusions

Based on the results presented in this paper, significant advantages of the proposed model are demonstrated. Firstly, all the model parameters can be calibrated from experiment results, which provides a more practical model. Secondly, the whole structural response including the softening behavior according to a material degradation are predicted. Finally, a simple regularization technique ensures the mesh independency of the numerical results, although further investigation for better regularization is still needed. The present study is a preliminary step towards better capturing the ductile fracture of cold-rolled steels for structural applications. Some proposals for further development in the model are also discussed. The lack of an experimental value of fracture energy is the first disadvantage. Besides, the damage threshold, which is solely based on the plastic strain at peak load without considering the effects of stress triaxiality, is not appropriate for every case. In this sense, the improvements can be the enhancement of stress triaxiality and/or the Lode angle, in conjunction with better model calibration with experimental results for improved numerical predictions.

**Acknowledgments.** Financial supports from Vietnamese Government and School of Civil Engineering, University of Sydney to the first author are gratefully acknowledged. Giang D. Nguyen thanks the Australian Research Council for support through project FT140100408.

## References

Bai, Y., Wierzbicki, T.: A new model of metal plasticity and fracture with pressure and Lode dependence. Int. J. Plast **24**, 1071–1096 (2008)

Bjorklund, O.: Modelling of failure in high strength steel sheets. Ph.D. dissertation, Linkoping University (2012)

Chaboche, J.L.: Constitutive equations for cyclic plasticity and cyclic viscoplasticity. Int. J. Plast **5**, 247–302 (1989)

Gurson, A.L.: Continuum theory of ductile rupture by void nucleation and growth: part I—yield criteria and flow rules for porous ductile media. J. Eng. Mater. Technol. **99**, 2–15 (1977)

Hancock, G.J., Rogers, C.A.: Bolted connection tests of thin G550 and G300 sheet steels. J. Struct. Eng. **124**(7), 798–808 (1998)

Korsunsky, A.M., Kim, K.: Determination of essential work of necking and tearing from a single tensile test. Int. J. Fract. **132**, 37–44 (2005)

Lemaitre, J.: Local approach of fracture. Eng. Fract. Mech. **25**, 523–537 (1986)

McClintock, F.A.: A criterion for ductile fracture by the growth of holes. J. Appl. Mech. **35**, 363–371 (1968)

Nguyen, G.D., Korsunsky, A.M., Belnoue, J.P.H.: A nonlocal coupled damage-plasticity model for the analysis of ductile failure. Int. J. Plast **64**, 56–75 (2015)

Rice, J.R., Tracey, D.M.: On the ductile enlargement of voids in triaxial stress fields∗. J. Mech. Phys. Solids **17**, 201–217 (1969)

Standards Australia: Steel sheet and strip- hot-dip zinc-coated or aluminium/zinc-coated, AS 1397-2001, Sydney, Australia (2001)

Teh, L.H., Clements, D.D.A.: Block Shear Capacity of Bolted Connections in Cold-Reduced Steel Sheets. J. Struct. Eng. **138**(4), 459–467 (2012)

Wen, H., Mahmoud, H.: New model for ductile fracture of metal alloys. I: monotonic loading. J. Eng. Mech. **142**, 04015088 (2016)

Xue, L.: Constitutive modeling of void shearing effect in ductile fracture of porous materials. Eng. Fract. Mech. **75**, 3343–3366 (2008)

# Finite Strain Plasticity Formulations for Dynamic Beams With and Without Rotational Degrees of Freedom

Tien Long Nguyen[1(✉)], Carlo Sansour[2,3], and Mohammed Hjiaj[2]

[1] Tractebel Engineering, ENGIE, 5 Rue du 19 Mars 1962, 92622 Gennevilliers, France
tien-long.nguyen@tractebel.engie.com
[2] Civil Engineering Department, Institut National des Sciences Appliques de Rennes, INSA de Rennes, 20 Avenue des Buttes de Coesmes, 35708 Rennes, France
[3] Faculty of Engineering, University of Nottingham, Nottingham NG7 2RD, UK

**Abstract.** In this paper, we developed a finite strain multiplicative elasto-plasto-dynamic formulation for Euler-Bernoulli and Timoshenko-type beam. The relations are formulated in an inertial frame approach. The multiplicative decomposition of the deformation gradient and the logarithmic strain measure are used. The exponential map for material evolution equations, as well as the derivative forms is given. In an attempt to deliver a stable time integration scheme for this non-linear beams in the context of finite strain elasto-dynamics, we made use of the concept of the energy-momentum method recently developed by the authors for geometrically exact Euler-Bernoulli and Timoshenko-type elastic beams. One example of finite strain elasto-plastic beam deformation is presented.

**Keywords:** Temperature · Stones · Bricks

## 1 Introduction

In today's structural dynamical engineering problems, the structural members can undergo very large elasto-plastic deformations. The issue of finite strain plasticity has received great interest over the last decades. Its applications in structural engineering can be found in Lee (1969); Healy et al. (1992); Sansour et al. (1997) amongst the others. The classical Bernoulli beam has the advantage of having a displacement-only formulation and so reduces the pointwise number of degrees of freedom. However, their expressions for the strain-displacement relation and for its inertial terms are often very complex. The main difficulties of Timoshenko beams in the context of finite strain plasto-dynamics, is the combination of the concept of multiplicative decomposition of the deformation gradient into elastic and plastic parts and the use of the logarithmic strain with the enforcement of plane stress with the use of the full 3D-material law. Beside the kinematics, the time integration scheme is also an issue, since the commonly used time-stepping algorithms such as Newmark's method, the classical midpoint rule Newmark (1959) are not stable for the non-linear regimes. The energy-momentum

© Springer Nature Singapore Pte Ltd. 2018
H. Tran-Nguyen et al. (eds.), *Proceedings of the 4th Congrès International de Géotechnique - Ouvrages -Structures*, Lecture Notes in Civil Engineering 8,
DOI 10.1007/978-981-10-6713-6_13

methods are known as the best to provide stable time integration scheme Nguyen et al. (2017); Sansour et al. (2015). The central idea of our integration scheme is the use of velocity field to define the deformations as well as the rotations. The outline of the paper is as follows: The next section is dedicated to the beam kinematic descriptions, the constitutive model including the kinematics of finite strain plasticity as well as the elastic and plastic constitutive laws. The dynamic equations and the spatial discretisation are given in Sects. 3 and 4, respectively. Section 4 deals with the time integration scheme and the local integration. One example is given in Sect. 5 in order to demonstrate the excellent performance of the method.

## 2 Kinematics and Strain Measure of Elastic and Inelastic Body

Let's consider the reference configuration $\mathbf{B} \subset \mathbb{R}^3$ of a body at time $t_0$ in a 3D Euclidean space, with $\mathbb{R}$ denoting the real numbers. We consider a Cartesian coordinate system of bases $\mathbf{e}_i, i = 1, 2, 3$. The placement of any point on $\mathbf{B}$ is defined by the position vector denoted by $\mathbf{X}$. A motion of $\mathbf{B}$ is a one-to-one map $\varphi(\mathrm{t})$, with t denoting the time, $\varphi(\mathrm{t}) : \mathbf{B} \rightarrow \mathbf{B}_\mathrm{t}$. For $\mathbf{X} \in \mathbf{B}$, we have $\mathbf{x} = \varphi(\mathbf{X})$ as the position vector in the actual configuration. We define the deformation gradient $\mathbf{F} = \partial\mathbf{x}/\partial\mathbf{X}$. All center points of the rod cross sections define the center line, which is assumed to be smooth. We consider also an arc length parameterization of this line at the reference configuration denoted by $s$. We want to restrict ourselves to the plane $\mathbf{e_1} - \mathbf{e_2}$. A further suitable convected curvilinear coordinate system defined by the triple $s, z, x_3$ and attached to the body is also considered, with $z$ being the coordinate in the normal direction. Let's define $\mathbf{X}_0$ as the position vector of the center line at the reference configuration, one can write $\mathbf{X}(\mathrm{s}, \mathrm{z}) = \mathbf{X}_0(\mathrm{s}) + \mathrm{z}\mathbf{N}(\mathrm{s})$, where $\mathbf{N}$ is the normal vector in the cross section. For our Timoshenko-like beam, we introduce a rotation tensor of our cross section which is assumed to be rigid, this rotation tensor defines rotations in the $\mathbf{e}_1 - \mathbf{e}_2$ plane:

$$\mathbf{R} = \cos\gamma(\mathbf{e}_1 \otimes \mathbf{e}_1 + \mathbf{e}_2 \otimes \mathbf{e}_2) - \sin\gamma(\mathbf{e}_1 \otimes \mathbf{e}_2 - \mathbf{e}_2 \otimes \mathbf{e}_1),$$

where $\gamma$ is the rotation angle of the cross section. According to the beam assumption, cross section deforms in a plane but it allows to have shear deformation for Timoshenko-type beam and is perpendicular to the center line for Euler-Bernoulli beam. The position vector in the actual configuration can be characterised as follows:

$$\mathbf{x} = \mathbf{X}(\mathrm{s}) - \mathrm{z}\mathbf{N}(\mathrm{s}) + \mathbf{u}(\mathrm{s}) + \mathrm{z}\mathbf{R}\mathbf{N} = \mathbf{X}_0(\mathrm{s}) + \mathbf{u}(\mathrm{s}) + \mathrm{z}\mathbf{R}\mathbf{N}.$$

The reference configuration local bases $\mathbf{G}_1 = \mathbf{X}_{,\mathrm{s}} = \mathbf{X}_{0,\mathrm{s}} + \mathrm{z}\mathbf{N}_{,\mathrm{s}}$, $\mathbf{G}_2 = \mathbf{N}$ and $\mathbf{G}_3 = \mathbf{e}_3$, where a comma denotes the derivative. The corresponding tangent vectors in the actual configuration are defined as $\mathbf{g}_1 = \mathbf{x}_{,\mathrm{s}} = \mathbf{X}_{0,\mathrm{s}} + \mathbf{u}_{,\mathrm{s}} + \mathrm{z}(\mathbf{R}\mathbf{N})_{,\mathrm{s}}$, $\mathbf{g}_2 = \mathbf{x}_{,\mathrm{z}} = \mathbf{R}\mathbf{N}$ and $\mathbf{g}_3 = \mathbf{e}_3$. As a result, we obtain the right Cauchy deformation tensor which is defined as $\mathbf{C} = \left(\mathbf{g}_\mathrm{i} \cdot \mathbf{g}_\mathrm{j}\right)\mathbf{G}^\mathrm{i} \otimes \mathbf{G}^\mathrm{j}$.

In an explicit form, the following expressions hold (Fig. 1)

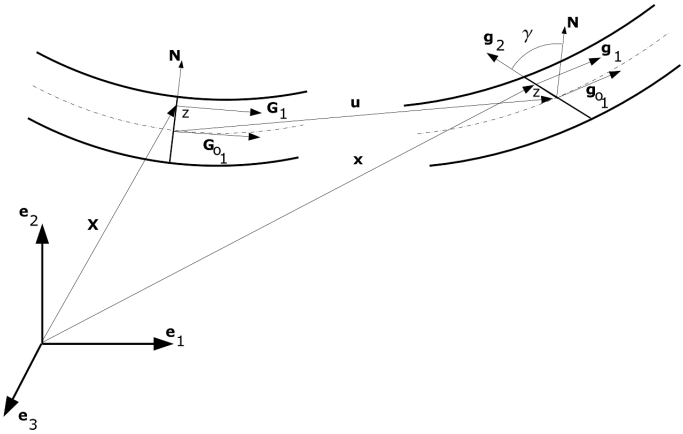


**Fig. 1.** Kinematic of beam element

$$C_{11} = \left(\mathbf{X}_{,s} - z\mathbf{N}_{,s} + \mathbf{u}_{,s} + z(\mathbf{RN})_{,s}\right) \cdot \left(\mathbf{X}_{,s} - z\mathbf{N}_{,s} + \mathbf{u}_{,s} + z(\mathbf{RN})_{,s}\right),$$
$$C_{12} = C_{21} = \mathbf{g}_1 \cdot \mathbf{g}_2 = \left(\mathbf{X}_{,s} - z\mathbf{N}_{,s} + \mathbf{u}_{,s} + z(\mathbf{RN})_{,s}\right) \cdot (\mathbf{RN}).$$
$$C_{22} = C_{33} = 1, C_{23} = C_{32} = C_{31} = C_{13} = 0.$$

Note that for Euler-Bernoulli beams, we obtain also $C_{12} = C_{21} = 0$.

To describe the equations of finite strain plasticity, starting point is the multiplicative decomposition of the deformation gradient $\mathbf{F} = \mathbf{F}_e\mathbf{F}_p$, Lee (1969), which motivates the introduction of the two following Cauchy-Green-type deformation tensors: $\mathbf{C}_e := \mathbf{F}_e^T\mathbf{F}_e, \mathbf{C}_p := \mathbf{F}_p^T\mathbf{F}_p$. Let introduce the spatial velocity gradient $\mathbf{l}$ defined by $\mathbf{l} = \dot{\mathbf{F}}\,\mathbf{F}^{-1}$. Beside the spatial velocity gradient, let's introduce the pull-back of the mixed spacial velocity gradient to the reference configuration given by $\mathbf{L} = \mathbf{F}^{-1}\mathbf{l}\mathbf{F} = \mathbf{F}^{-1}\,\dot{\mathbf{F}}$. The corresponding relation is of the form $\mathbf{L} = \mathbf{F}_p^{-1}\mathbf{L}_e\mathbf{F}_p + \mathbf{L}_p, \mathbf{L}_e \equiv \dot{\mathbf{F}}_e\mathbf{F}_e^{-1}$, $\mathbf{L}_p \equiv \dot{\mathbf{F}}_p\mathbf{F}_p^{-1}$, Sansour et al. (1997). Let's consider $\tau$ as the Kirchhoff stress tensor. The expression of the internal power holds: $\mathcal{W} = \boldsymbol{\tau} : \mathbf{l}$, where a double dot refers to the scalar product of two tensors. The later relation can be rewritten by using the material stress tensors as $\mathcal{W} = \frac{1}{2}\mathbf{S} : \dot{\mathbf{C}} = \boldsymbol{\Xi} : \mathbf{L}$, with $\mathbf{S}$ as the second Piola-Kirchhoff tensor and the tensor $\boldsymbol{\Xi}$ as a mixed variant pull-back of the Kirchhoff tensor $\boldsymbol{\Xi} = \mathbf{CS}$, $\boldsymbol{\Xi} = \mathbf{F}^T\boldsymbol{\tau}\mathbf{F}^{T-1}$.

- *Elastic constitutive model and the stored energy function*

In the context of finite strains, the use of the logarithmic strain measure is essential which is defined as follows $\boldsymbol{\alpha} = \ln \mathbf{C}_e, \mathbf{C}_e = \exp \boldsymbol{\alpha}$. The definition of $\exp \boldsymbol{\alpha}$ gives $\mathbf{C}_e = \exp \boldsymbol{\alpha} = \mathbf{1} + \boldsymbol{\alpha} + \frac{\boldsymbol{\alpha}^2}{2!} + \frac{\boldsymbol{\alpha}^3}{3!} + \cdots$. Our material is assumed to be elastically isotropic. The above expression together with the fact that $\mathbf{C_e}$ and $\boldsymbol{\alpha} = \ln \boldsymbol{\alpha}$ are symmetric, accordingly $\frac{\partial \psi_e}{\partial \boldsymbol{\alpha}} = \mathbf{C}_e \frac{\partial \psi_e}{\partial \mathbf{C}_e}$. We assume to have a linear elastic relation and our free energy is of the form $\rho\psi_e = \frac{1}{8}\left(K_b - \frac{2}{3}G\right)\mathrm{tr}^2\overline{\boldsymbol{\alpha}} + \frac{1}{4}\mathrm{tr}\left(\overline{\boldsymbol{\alpha}}^2\right)$, where $K_b$ and $G$ are the bulk modulus and the shear modulus, respectively. Thus, $K_b = \frac{E}{3(1-2\nu)}$ and $G = \frac{E}{2(1+\nu)}$ with $E$ being Young modulus and $\nu$ Poission's ratio. Accordingly, $\boldsymbol{\Xi}$ receives its final form $\boldsymbol{\Xi} = \frac{1}{2}\mathrm{K_b tr}\overline{\boldsymbol{\alpha}}^{\mathbf{T}}\mathbf{1} + \mathrm{G\ dev}\overline{\boldsymbol{\alpha}}^{\mathbf{T}}$, with dev as the devatoric and $\overline{\boldsymbol{\alpha}}^T = \ln\left(\mathbf{C}\mathbf{C}_\mathrm{p}^{-1}\right)$ is the transpose of $\overline{\boldsymbol{\alpha}}$. Due to the properties of the pull-back to the reference configuration, although $\boldsymbol{\Xi}$ is physically equivalent to the Kirchhoff stress tensor as they have the same invariants, $\boldsymbol{\Xi}$ is unsymmetric and the same is true for $\overline{\boldsymbol{\alpha}}$.

- *Plastic constitutive model*

Our material is assumed to be of the isotropic hardening type meaning that the center of the yield surface remains at the origin. The yield condition is written using von Mises-type criterion as follows

$$f = \sqrt{3J_2(\boldsymbol{\Xi})} - \left(\sigma_y - Y\right) \leq 0,$$

where $\sigma_y$ is the material yield strength. $\boldsymbol{\Xi}$ and $\mathbf{L}_\mathrm{p}$ are also conjugate. The standard assumption of maximum dissipation provides that with Kuhn-Tucker conditions which read $\mathbf{L}_\mathrm{p} = \dot{\lambda}\frac{\partial \mathrm{f}}{\partial \boldsymbol{\Xi}}, \dot{\lambda} \geq 0$, $\dot{\beta} = \dot{\lambda}\frac{\partial \mathrm{f}}{\partial \mathbf{Y}} = \dot{\lambda}$, where $\dot{\lambda}$ stands for the plastic multiplier. From the latter together with the plane stress conditions, we end up with the direct form of $\mathbf{L}$p

$$\mathbf{L}_\mathrm{p} = \dot{\lambda}\begin{bmatrix} \frac{\Xi_{11}}{\sqrt{3\mathrm{J2}}} & \frac{3}{2}\frac{\Xi_{21}}{\sqrt{3\mathrm{J2}}} & 0 \\ \frac{3}{2}\frac{\Xi_{12}}{\sqrt{3\mathrm{J2}}} & -\frac{1}{2}\frac{\Xi_{11}}{\sqrt{3\mathrm{J2}}} & 0 \\ 0 & 0 & -\frac{1}{2}\frac{\Xi_{11}}{\sqrt{3\mathrm{J2}}} \end{bmatrix},$$

which defines the plastic rate as the function of the stress and the plastic multiplier.

## 3 Dynamic Equations and the Finite Element Formulation

The virtual work principal in dynamics reads

$$\int_V \rho\ddot{\mathbf{x}} \cdot \delta\mathbf{x}\mathrm{dV} + \int_\mathrm{V} \frac{1}{2}\mathbf{S} : \delta\mathbf{C}\mathrm{dV} - \int_\mathbf{L} \mathbf{q}(\mathrm{s}) \cdot \delta\mathbf{u}(\mathrm{s})\mathrm{ds} - \sum_{\mathrm{i}=1}^{\mathrm{N}} \mathbf{P}_\mathrm{i} \cdot \delta\mathbf{u}_\mathrm{i} - \sum_{\mathrm{j}=1}^{\mathrm{M}} \mathrm{M_j}\delta\boldsymbol{\gamma}_\mathrm{j} = \mathbf{0},$$

where $V$ is the volume, $L$ is the length of the beam, $\mathbf{q}(\mathrm{s})$ is the distributed external force, $\mathbf{P}_\mathrm{i}$, $\mathrm{i} = 1, \ldots, \mathrm{N}$ and $\mathbf{u}_\mathrm{i}$ are the concentrated forces and the corresponding displacements, respectively, $M_j, j = 1, \ldots, M$ and $\gamma_j$ are concentrated external moments and the corresponding rotation angles respectively. Let's define $\mathbf{n} = \mathbf{RN}$. Take the integral over $z$ for the two first terms the above equation, it follows

$$\int_L \rho A \ddot{\mathbf{u}} \cdot \delta\mathbf{u}\mathrm{d}s + \int_\mathbf{L} \rho \mathrm{I} \ddot{\mathbf{n}} \cdot \frac{\partial \mathbf{n}}{\partial \gamma} \delta\gamma \mathrm{d}s + \int_\mathrm{V} \frac{1}{2}\mathbf{S} : \delta\mathbf{C}\mathrm{d}V - \int_\mathbf{L} \mathbf{q}(\mathrm{s}) \cdot \delta\mathbf{u}(\mathrm{s})\mathrm{d}s - \sum_{\mathrm{i}=1}^{\mathrm{N}} \mathbf{P}_\mathrm{i} \cdot \delta\mathbf{u}_\mathrm{i} - \sum_{\mathrm{j}=1}^{\mathrm{M}} \mathrm{M}_\mathrm{j} \delta\gamma_\mathrm{j} \; = \; \mathbf{0},$$

where $A$ is the cross section area, $I$ is the moment of inertia. In order to avoid locking phenomena in the case of Timoshenko-type beams, we employ here the enhanced strain method. Accordingly, the strain itself is enhanced.

- *Finite element formulation for Euler-Bernoulli beams*

Given the fact that second derivatives are present in the dynamic equation (a result of the Bernoulli hypothesis), the finite element formulation must exhibit continuous first derivatives. Hence, we resort, within a finite element context to interpolation functions defined by cubic Hermite polynomials. Consider a 2D beam element of length $l$ having two nodes $(I, II)$. At each node the degrees of freedom are $u_1, u_2, u_1', u_2'$ which describe the displacement and their derivatives. For the displacement field the interpolations, at the element level read $\mathbf{u} = \mathbf{N} \cdot \mathbf{U}, \mathbf{u}_{,\mathrm{s}} = \mathbf{N}_{,\mathrm{s}} \cdot \mathbf{U}, \mathbf{u}_{,\mathrm{ss}} = \mathbf{N}_{,\mathrm{ss}} \cdot \mathbf{U}$,

$$\mathbf{u} = \mathbf{N} \cdot \mathbf{U}, \mathbf{u}_{,\mathrm{s}} = \mathbf{N}_{,\mathrm{s}} \cdot \mathbf{U}, \mathbf{u}_{,\mathrm{ss}} = \mathbf{N}_{,\mathrm{ss}} \cdot \mathbf{U}$$

where

$$\mathbf{N} = \begin{pmatrix} \tilde{N}_1 & 0 & \tilde{N}_2 & 0 & \tilde{N}_3 & 0 & \tilde{N}_4 & 0 \\ 0 & \tilde{N}_1 & 0 & \tilde{N}_2 & 0 & \tilde{N}_3 & 0 & \tilde{N}_4 \\ 0 & 0 & 0 & 0 & 0 & 0 & 0 & 0 \end{pmatrix}, \quad \mathbf{U} = \begin{pmatrix} \mathrm{u}_1^{\mathrm{I}} \\ \mathrm{u}_2^{\mathrm{I}} \\ \mathrm{u}_1^{\prime\mathrm{I}} \\ \mathrm{u}_2^{\prime\mathrm{I}} \\ \mathrm{u}_1^{\mathrm{II}} \\ \mathrm{u}_2^{\mathrm{II}} \\ \mathrm{u}_1^{\prime\mathrm{II}} \\ \mathrm{u}_2^{\prime\mathrm{II}} \end{pmatrix}$$

with $\tilde{N}_1 = \frac{\zeta^3}{4} - \frac{3\zeta}{4} + \frac{1}{2}, \tilde{N}_2 = \frac{l\zeta^3}{8} - \frac{l\zeta^2}{8} - \frac{l\zeta}{8} + \frac{l}{8}, \tilde{N}_3 = \frac{-\zeta^3}{4} + \frac{3\zeta}{4} + \frac{1}{2}, \tilde{N}_4 = \frac{l\zeta^3}{8} + \frac{l\zeta^2}{8} - \frac{l\zeta}{8} - \frac{l}{8}$, $\zeta = [-1, 1]$.

- *Finite element formulation for Timoshenko-type beams*

To solve the dynamic equation within a finite element context, we resort to linear interpolation functions which are completely sufficient as only $C^0$ continuity is necessary. Let's consider a two-node beam element of length $l$. The nodes are denoted I

and II. The degrees of freedom are $u_1^I, u_2^I, u_1^{II}, u_2^{II}, \gamma^I, \gamma^{II}$. Let's call $\mathbf{\Theta}$ as the nodal degree of freedom vector, one has

$$\mathbf{\Theta} = \begin{bmatrix} \mathrm{u}_1^{\mathrm{I}} \\ \mathrm{u}_2^{\mathrm{I}} \\ \gamma^{\mathrm{I}} \\ \mathrm{u}_1^{\mathrm{II}} \\ \mathrm{u}_2^{\mathrm{II}} \\ \gamma^{\mathrm{II}} \end{bmatrix}.$$

The interpolation matrix for the degrees of freedom reads:

$$\mathbf{N} = \begin{bmatrix} N_1 & 0 & 0 & N_2 & 0 & 0 \\ 0 & N_1 & 0 & 0 & N_2 & 0 \\ 0 & 0 & 0 & 0 & 0 & 0 \end{bmatrix}, N_1 = \frac{1}{2} - \frac{\zeta}{2}, N_2 = \frac{1}{2} + \frac{\zeta}{2},$$

with $\zeta = [-1, 1]$. One has $\mathbf{u}(\mathrm{s}) = \begin{bmatrix} \mathrm{u}_1 \\ \mathrm{u}_2 \\ 0 \end{bmatrix} = \mathbf{N}\mathbf{\Theta}, \mathbf{u}_{,\mathrm{s}}(\mathbf{s}) = \mathbf{N}_{,\mathrm{s}}\mathbf{\Theta}$. The interpolation vector for the rotation has the following form: $\mathbf{W} = [\,0 \quad 0 \quad N_1 \quad 0 \quad 0 \quad N_2\,]$, $\gamma(s) = \mathbf{W}\mathbf{\Theta}, \boldsymbol{\gamma}_{,\mathrm{s}}(\mathrm{s}) = \mathbf{W}_{,\mathrm{s}}\mathbf{\Theta}$.

## 4 Time Integration and Local Integration

Assuming that at time step $n$, all kinematical fields and velocities are known, we need to find these quantities for time step $n+1$. Consider $\xi$ to be a scalar which defines any position within the time interval $\Delta T$, with $0 \leq \xi \leq 1$. Given the strain fields, $\gamma$ and the enhanced fields at time $n$, those quantities at step $n+\eta$ are then defined as follows:

$$C_{11}|_{n+\eta} = C_{11}|_n + \eta \Delta T \dot{C}_{11\,n+\frac{1}{2}}, C_{12}|_{n+\eta} = C_{12}|_n + \eta \Delta T \dot{C}_{12\,n+\frac{1}{2}},$$
$$C_1|_{n+\eta} = C_1|_n + \eta \Delta T \dot{C}_{1\,n+\frac{1}{2}}, C_2|_{n+\eta} = C_2|_n + \eta \Delta T \dot{C}_{2\,n+\frac{1}{2}}.$$

Specifically for $\eta = \frac{1}{2}$, the relations hold

$$C_{11\,n+\frac{1}{2}} = C_{11}|_n + \frac{1}{2}\Delta T \dot{C}_{11\,n+\frac{1}{2}}, C_{12\,n+\frac{1}{2}} = C_{12}|_n + \frac{1}{2}\Delta T \dot{C}_{12\,n+\frac{1}{2}},$$
$$C_1|_{n+\frac{1}{2}} = C_1|_n + \frac{1}{2}\Delta T \dot{C}_{1\,n+\frac{1}{2}}, C_2|_{n+\frac{1}{2}} = C_2|_n + \frac{1}{2}\Delta T \dot{C}_{2\,n+\frac{1}{2}}.$$

The development of the formulation as well as the proof for elastic case are presented in Sansour et al. (2015) and Nguyen et al. (2017). The local integration starts with the construction of a so-called trial state where the material is supposed to deform elastically. Then, the yield condition at the trial step is checked and a projection to the yield surface is carried out to obtain the corresponding stress and strain at the real state.

## 5 Numerical Example

In this example a Shallow arch subjected to a cyclic dynamic load is considered, Fig. 2. The loading history is depicted in Fig. 3 with $P_0 = 3.5E7$ N, $t_0 = 0.2$ s. The arch parameters are as follows: the elastic modulus $E = 0.3E11$ Pa, the density $\rho = 7850\ \mathrm{kg/m^3}$, the radius $R = 20$ m and $\Phi = \frac{\pi}{6}$, Poisson's ratio $v = 0.3$. The cross section is rectangular with the thickness $h = 2$ m and the width $b = 1$ m. The elasto-plastic constitutive law is isotropic hardening with the yield strength $\sigma_y = 235E5$ Pa, the plastic modulus $H = E/20$. We run the calculation for 100.000 time steps with $\Delta T = 1E - 3s$ using 30 elements. The integration over the element is carried out using 6 Gauss's points with respect to $z$ and 6 Gauss's points with respect to $s$.

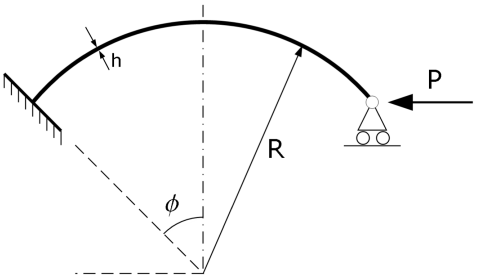


**Fig. 2.** Shallow arc

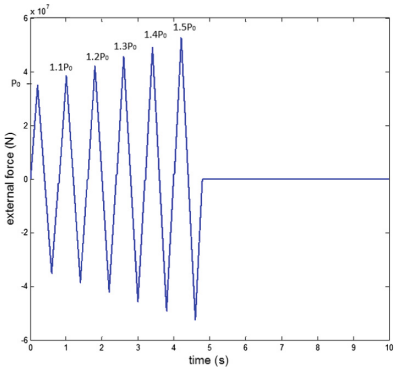


**Fig. 3.** Loading history

The displacement of the movable support and the arch midpoint for the first 50 s are illustrated in Figs. 4 and 5, respectively. The arch turns into a regular motion quickly after removing the external load. The time integration is stable until the end of the process. No degradations or instabilities of displacement have been observed. The total energy as well as the dissipation are plotted in Fig. 6 is clearly demonstrated. The material point of the arch top fiber at the midspan is examined. Figure 7 plots the yield

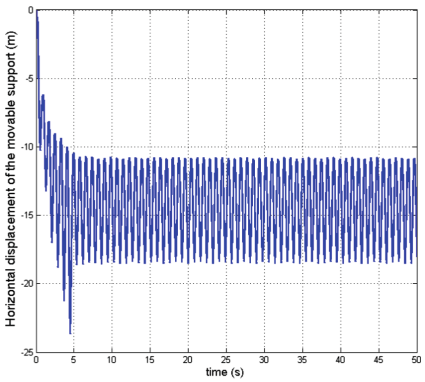


**Fig. 4.** Horizontal displacement of the movable support

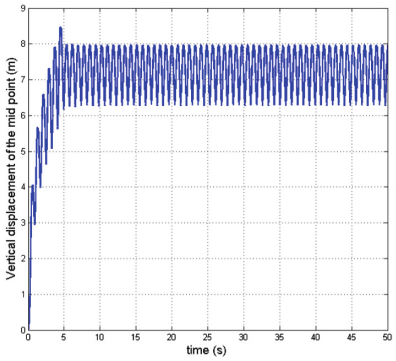


**Fig. 5.** Vertical displacement of the midpoint

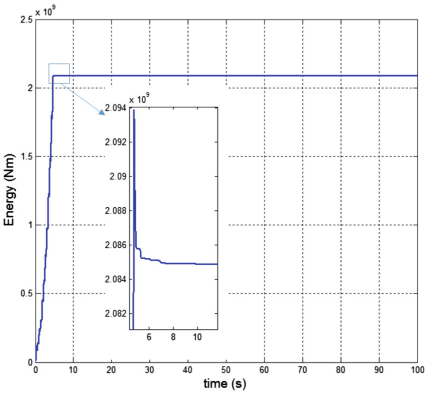


**Fig. 6.** Energy history

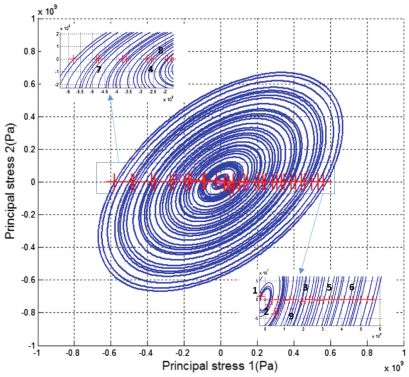


**Fig. 7.** Stress and yield surface

**Table 1.** State values

| State | t (s) | X1 (Pa) | X2 (Pa) | ep11 | ep12 |
|---|---|---|---|---|---|
| 1 | 0.239 | −1.96E7 | 8.25E6 | −7.04E-4 | 0.0012 |
| 2 | 0.339 | 2.175E7 | −1.36E7 | −0.0012 | 0.0047 |
| 3 | 1.936 | 2.11E8 | −8.87E5 | 0.0628 | 0.0113 |
| 4 | 2.337 | −2.57E8 | 1.03E6 | 0.073 | 0.01 |
| 5 | 2.798 | 3.35E8 | 1.12E4 | 0.114 | 0.0128 |
| 6 | 3.667 | 4.58E8 | −4.281E5 | 0.172 | 0.012 |
| 7 | 4.024 | −4.75E8 | −3.55E5 | 0.12 | 0.013 |
| 8 | 12.7 | 4.803E8 | −2.853E5 | 0.2042 | 0.0119 |
| 9 | 13.2 | −2.79E8 | −5.24E5 | 0.1695 | 0.0123 |

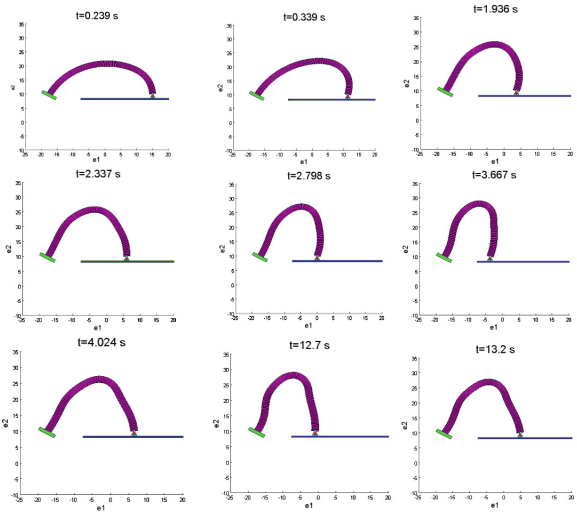


**Fig. 8.** Beam motions

surface mostly when the plastic state occurs (some selected points are plotted) and two representative elastic states when the arch has regular displacement. One can observe that the characteristics of the isotropic hardening law are well captured. The values of principal stresses as well as the corresponding strains of the selected points in Fig. 7 are represented in Table 1. In which one can see that the point experiences very large axial strains (maximum 20.4%) and still small shear deformations. The principal stress in the second direction at some states (for example state 1, 2) are quite large compared to the one in the first direction. Some arch motions are recorded in Fig. 8, overall very large deformations are observed.

## 6 Conclusions

A finite strain multiplicative elasto-plasto-dynamic formulation for Euler-Bernoulli and Timoshenko-type beam presented in this paper. The multiplicative decomposition of the deformation gradient as well as the logarithmic strain measure is well incorporated. The exponential map for material update is provided. Within the idea of our energy-momentum method for elastic case, a stable time integration scheme for these non-linear beams in the context of finite strain plasto-dynamics is provided. Via the numerical example, one can show the large deformations, the non-negative dissipation of the time integration scheme. A fully three-dimensional formulation is currently developed.

## References

Healy, B.E., Dodds Jr., R.H.: A large strain plasticity model for implicit finite element analyses. Comput. Mech. **9**, 95–112 (1992)

Lee, E.H.: Elastic–plastic deformation at finite strains. J. Appl. Mech. **36**, 1–6 (1969)

Newmark, N.M.: A method of computation for structural dynamics. ASCE J. Eng. Mech. Div. **85** (EM3), 67–94 (1959)

Nguyen, T.L., Sansour, C., Hjiaj, M.: Long-term stable time integration scheme for dynamic analysis of planar geometrically exact Timoshenko beams. J. Sound Vibr. **396**, 144–171 (2017)

Sansour, C., Wriggers, P., Sansour, J.: Nonlinear dynamics of shells: theory finite element formulation, and integration schemes. Nonlinear Dyn. **13**, 279–305 (1997)

Sansour, C., Nguyen, T.L., Hjiaj, M.: An Energy-momentum method for in-plane geometrically exact Euler-Bernoulli beam dynamics. Int. J. Numer. Meth. Eng. **102**, 99–134 (2015)

Simo, J.C., Tarnow, N.: The discrete energy-momentum method. Conserving algorithms for nonlinear elastodynamics. J. Appl. Math. Phys. **43**, 757–792 (1992)

# Fuzzy Linear Elastic Dynamic Analysis of 2-Dimensional Semi-rigid Steel Frame with Fuzzy Fixity Factors

Thanh Viet Tran[1(✉)], Quoc Anh Vu[2], and Xuan Huynh Le[3]

[1] Duy Tan University, Danang, Vietnam
ttviet05@gmail.com
[2] Ha Noi Architectural University, Hanoi, Vietnam
anhquocvu@gmail.com
[3] National University of Civil Engineering, Hanoi, Vietnam
lxhuynhllkcxd@gmail.com

**Abstract.** This paper proposes a fuzzy finite element procedure for dynamic analysis of planar steel frame structures with fuzzy input parameters. The fixity factors of beam – column and column – base connections, loads, mass per unit volume and damping ratio are modeled as triangular fuzzy numbers. The Newmark-β numerical integration method is applied to determine the displacement of the linear dynamic equilibrium equation system. The α-level optimization using the Differential Evolution (DE) involving integrated finite element modeling is proposed to apply in the fuzzy structural dynamic analysis. The efficiency of proposed methodology is demonstrated through example problem relating to for the twenty-story, four-bay portal steel frame.

**Keywords:** Steel frame · Fuzzy connection · Fuzzy structural dynamic · Differential evolution algorithm

## 1 Introduction

In the dynamic analysis of steel frame structures with semi-rigid connections, rigidity of the connection (or fixity factor of the connection), loads, mass per unit volume, and damping ratio have a significant influence on the time-history response of steel frame structure [3, 8, 10, 11]. In practice, however, many parameters like worker skill, quality of welds, properties of material and type of the connecting elements affect the behavior of a connection, and this fixity factor is difficult to determine exactly. Therefore, in a practical analysis of structures, a systematic approach is needed to include the uncertainty in the joints behavior and the fixity factor of a connection modeled as the fuzzy number is reasonable [7]. In addition, the uncertainty of input parameters such as the external forces, mass per unit volume and damping ratio are also described in form of the fuzzy numbers.

In recent years, the fuzzy static analysis, and the fuzzy stability analysis for planar steel frame structures with the fuzzy connections have been reported [5–7, 14]. However, the fuzzy dynamic analysis for determining the fuzzy time-history response

© Springer Nature Singapore Pte Ltd. 2018
H. Tran-Nguyen et al. (eds.), *Proceedings of the 4th Congrès International de Géotechnique - Ouvrages -Structures*, Lecture Notes in Civil Engineering 8,
DOI 10.1007/978-981-10-6713-6_14

by using exact approach has been limited. For the rigid frame, Tuan *et al*. (2015) presented an approach by using Response Surface Method (RSM) for fuzzy free vibration analysis of linear elastic structure in which response surfaces (surrogate functions) in terms of complete quadratic polynomials are presented for model quantities and all fuzzy variables are standardized [13]. The usage of the RSM shows that this approach has effectiveness for the complex structural problems with a large number of fuzzy variables. However, the RSM is only suitable for problems which all fuzzy variables are modeled as symmetric triangular fuzzy numbers. For the problems with non-symmetric triangular fuzzy numbers, the fuzzy structural analysis must use another approach. Anh *et al*. presented an optimization algorithm for fuzzy analysis by combining the Differential Evolution (DE) with the α-level optimization [1]. DE is a global optimization technique, which combines the evolution strategy and the Monte Carlo simulation, and is simple and easy to use [4, 12].

In this paper, the fuzzy displacement - time dependency of planar steel frame structure is determined in which the fixity factor, loads, and mass per unit volume are described in the form of triangular fuzzy numbers. A procedure is based on finite element model by combining the α-level optimization with the Differential Evolution algorithm (DEa). The Newmark-β average acceleration numerical integration method is applied to determine the displacements from the linear dynamic equilibrium equation system of the finite element model. A twenty-floor, four-bay portal steel frame structure is considered. The deterministic results of the proposed algorithms are also compared with ones of the SAP2000 software.

## 2 Finite Element with Linear Semi-rigid Connection

The linear dynamic equilibrium equation system is given as following

$$[M]\{\ddot{u}\} + [C]\{\dot{u}\} + [K]\{u\} = \{P(t)\} \tag{1}$$

where $\{\ddot{u}\}$, $\{\dot{u}\}$, and $\{u\}$ are the vectors of acceleration, velocity, and displacement respectively; $[M]$, $[C]$, and $[K]$ are the mass, damping, and stiffness matrices respectively; $\{P(t)\}$ is the external load vector. The viscous damping matrix $[C]$ can be defined as

$$[C] = \alpha_M[M] + \beta_K[K] \tag{2}$$

where $\alpha_M$ and $\beta_K$ are the proportional damping factors which defined as

$$\alpha_M = \xi\frac{2\omega_1\omega_2}{\omega_1 + \omega_2}; \beta_K = \xi\frac{2}{\omega_1 + \omega_2} \tag{3}$$

where $\xi$ is the damping ratio; $\omega_1$ and $\omega_2$ are the natural radian frequencies of the first and second modes of the considered frame, respectively.

In this study, a the frame element with linear semi-rigid connection is shown in Fig. 1, with $E$ - the elastic modulus, $A$ - the section area, $I$ - the inertia moment, $m$ - the mass per unit volume, $k_1$ and $k_2$ - rotation resistance stiffness at connections.

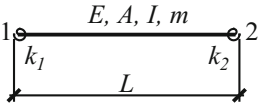


**Fig. 1.** Frame element with linear semi-rigid connection

The element stiffness matrix - $[K^{el}]$ and the mass matrix - $[M^{el}]$ of the frame are given as following [2]:

$$\left[K^{el}\right] = \begin{bmatrix} \frac{EA}{L} & & & & & \\ 0 & k_{22} & & & symmetric & \\ 0 & k_{32} & k_{33} & & & \\ -\frac{EA}{L} & 0 & 0 & \frac{EA}{L} & & \\ 0 & k_{52} & k_{53} & 0 & k_{55} & \\ 0 & k_{62} & k_{63} & 0 & k_{65} & k_{66} \end{bmatrix} \tag{4}$$

where

$$k_{22} = k_{55} = -k_{52} = \frac{12EI}{L^3}\frac{(s_1 + s_2 + s_1 s_2)}{(4 - s_1 s_2)}; k_{32} = -k_{53} = \frac{6EI}{L^2}\frac{s_1(s_2 + 2)}{(4 - s_1 s_2)} \tag{5a}$$

$$k_{33} = 2k_{63} = \frac{12EI}{L}\frac{s_1}{(4 - s_1 s_2)}; k_{62} = -k_{65} = \frac{6EI}{L^2}\frac{s_2(s_1 + 2)}{(4 - s_1 s_2)}, k_{66} = \frac{12EI}{L}\frac{s_2}{(4 - s_1 s_2)} \tag{5b}$$

and

$$\left[M^{el}\right] = \frac{mAL}{420(4 - s_1 s_2)^2}\begin{bmatrix} 140(4 - s_1 s_2)^2 & & & & & \\ 0 & m_{22} & & & symmetric & \\ 0 & m_{32} & m_{33} & & & \\ 70(4 - s_1 s_2)^2 & 0 & 0 & 140(4 - s_1 s_2)^2 & & \\ 0 & m_{52} & m_{53} & 0 & m_{55} & \\ 0 & m_{62} & m_{63} & 0 & m_{65} & m_{66} \end{bmatrix} \tag{6}$$

where

$$m_{22} = 16\left(140 - 49s_2 + 8s_2^2\right) + 4s_1^2\left(32 - 55s_2 + 32s_2^2\right) + 4s_1\left(224 - 328s_2 + 50s_2^2\right);$$
$$m_{33} = 4L^2 s_1^2\left(32 - 31s_2 + 8s_2^2\right) \tag{6a}$$

$$m_{55} = 64\left(35 + 14s_2 + 2s_2^2\right) + 4s_1^2\left(32 - 50s_2 + 32s_2^2\right) - 4s_1\left(196 - 328s_2 + 55s_2^2\right);$$
$$m_{66} = 4L^2 s_2^2\left(32 - 31s_2 + 8s_1^2\right) \tag{6b}$$

$$m_{32} = 2Ls_1\left(32\left(7 - 5s_2 + s_2^2\right) + s_1\left(64 - 86s_2 + 25s_2^2\right)\right) \tag{6c}$$

$$m_{52} = 1120 - 56s_2 - 128s_2^2 + 2s_1\left(-28 - 184s_2 + 5s_2^2\right) + 2s_1^2\left(-64 + 5s_2 + 41s_2^2\right) \tag{6d}$$

$$\begin{aligned} m_{53} &= Ls_1\left(4\left(98 - 25s_2 - 16s_2^2\right) - s_1\left(128 + 38s_2 - 55s_2^2\right)\right); \\ m_{63} &= L^2 s_1 s_2(64s_2 - 124 + s_1(64 - 31s_2)) \end{aligned} \tag{6e}$$

$$m_{65} = -2Ls_2\left(224 + 64s_2 + s_1^2(32 + 25s_2) - 2s_1(80 + 43s_2)\right) \tag{6f}$$

where $s_i = Lk_i/(3EI + Lk_i)$ denote the fixity factor of semi-rigid connection at the boundaries ($i$ = 1, 2).

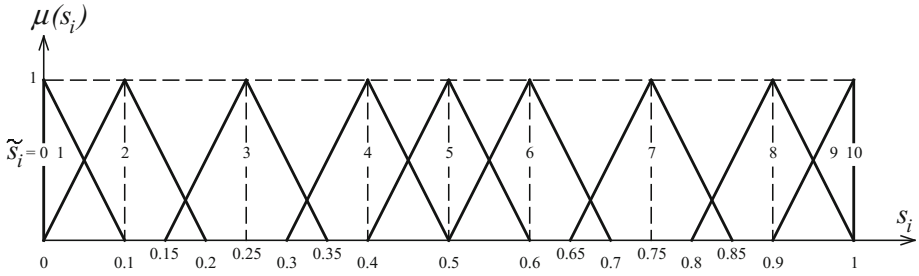


**Fig. 2.** Membership functions of fuzzy fixity factors.

In Eq. (1), when fixity factors of connections, external loads, mass per unit volume and damping ratio are given by fuzzy numbers, the displacements of joints are also the fuzzy numbers. In steel structures, the common fuzzy connections can be defined by linguistic terms as shown in Fig. 2. Eleven linguistic terms are assigned numbers from 0 to 10 ($\tilde{s}_i = 0, 1, \ldots 10$) [7].

In the classical finite element method (FEM), in Eq. (1), the displacement-time dependency of the joints is determined by solving the linear dynamic equilibrium equation system. The Newmark-β method has been chosen for the numerical integration of this equation system because of its simplicity [9]. The fuzzy displacement is determined by the fuzzy finite element method (FFEM) using the a-cut strategy with the optimization approaches. FFEM is an extension of FEM in the case that the input quantities in the FEM are modeled as fuzzy numbers. In this study, an optimization approach is presented in the next sections: the differential evolution algorithm (DEa).

## 3 Procedure for Fuzzy Structural Analysis

### 3.1 Linear Elastic Dynamic Analysis Algorithm

The Newmark-β average acceleration method is based on the solution of an incremental form of the equations of motion. For the equations of motion (1), the incremental equilibrium equation is:

$$[M]\{\Delta\ddot{u}\} + [C]\{\Delta\dot{u}\} + [K]\{\Delta u\} = \{\Delta P\} \tag{7}$$

where $\{\Delta\ddot{u}\}$, $\{\Delta\dot{u}\}$, and $\{\Delta u\}$ are the vectors of incremental acceleration, velocity, and displacement respectively; $\{\Delta P\}$ is the external load increment vector. The displacement of the joint at each time step is determined by this algorithm of linear elastic dynamic analysis.

### 3.2 α-Level Optimization Using Differential Evolution Algorithm (DEa)

For fuzzy structural analysis, the α-level optimization is known as a general approach in which all the fuzzy inputs are discretized by the intervals that are equal α-levels. The output intervals are then searched by the optimization algorithms. The optimization process is implemented directly by the finite element model and the goal function is evaluated many times in order to reach to an acceptable value. In this study, the output intervals are the displacement intervals at each time step, and the solution procedure is proposed by combining the Differential Evolution algorithm (DEa) with the α-level optimization. DEa which is a population-based optimizer, which is suggested by Storn and Price [12]. The DEa has shown better than the genetic algorithm (GA) and is simple and easy to use.

## 4 Numerical Illustration

The example is considered by fuzzy elastic dynamic analysis a twenty-story, four-bay linear semi-rigid portal steel frame subjected to fuzzy loads $\tilde{P}(t)$ concentrated at joints as shown in Fig. 3. The elastic modulus is $E = 210 \times 10^6$ kN/m$^2$, damping ratio $\xi = 0.05$. Fuzzy terms were considered to be triangular fuzzy numbers with 20% absolute spread [15]. The fuzzy mass per unit volume of the columns and the beams are $\tilde{m}_1 = (7.85, 0.785, 0.785)$ and $\tilde{m}_2 = (50, 5, 5)$ (included load dead from slab), respectively. The fuzzy fixity factor at column base is $\tilde{s}_1 = 9$. The fuzzy fixity factor at the ends of beams from story 1 to story 4 is $\tilde{s}_2 = 8$, from story 5 to story 8 is $\tilde{s}_3 = 7$, from story 9 to story 14 is $\tilde{s}_4 = 6$, and from story 9 to story 14 is $\tilde{s}_5 = 5$. The fuzzy loads are: $\tilde{P}(t) = \tilde{P}\sin(\pi t)$ $(0 \leq t \leq 2$ s), and $\tilde{P}(t) = 0$ $(t > 2$ s), in which $\tilde{P} = (40, 4, 4)$. The section properties used for analysis of the frame are shown in Table 1.

A time step $\Delta t$ of 0.05 s is chosen in the dynamic analysis. Since the fuzzy fixity factor at column base is the non-symmetric triangular fuzzy number, the fuzzy displacement is determined by using the α-level optimization in combination with the DEa

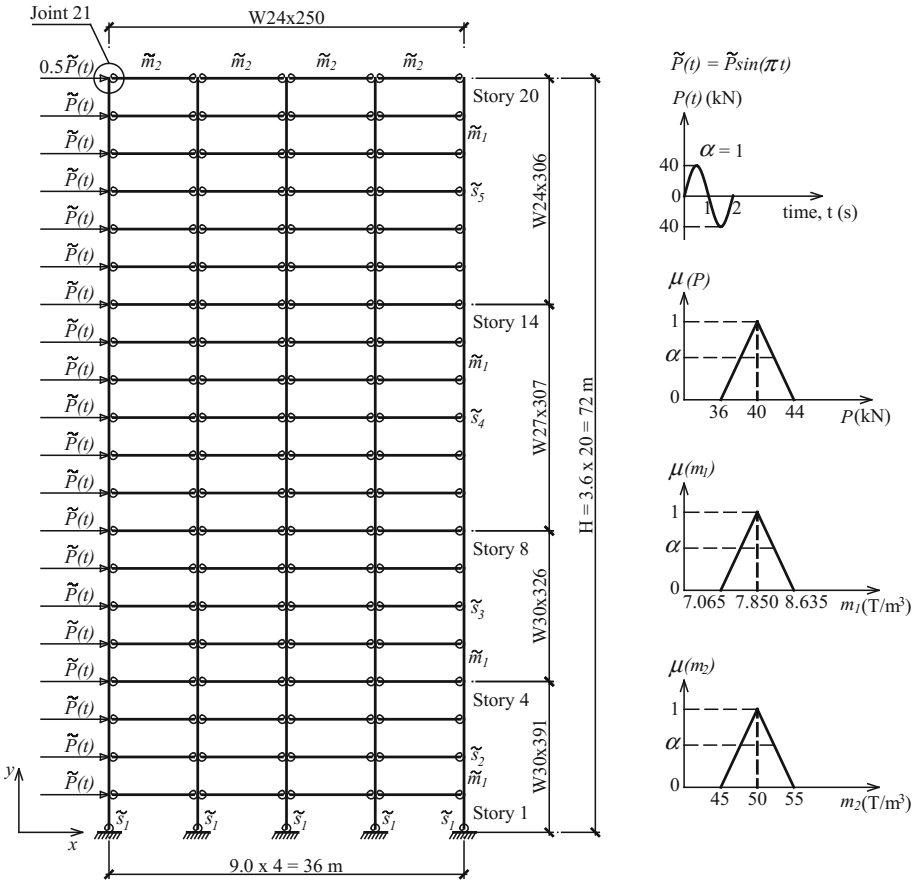


**Fig. 3.** Portal steel frame with fuzzy input parameters.

**Table 1.** Section properties used for analysis of the portal steel frame

| Member | Section | Cross-section area, $A$ ($m^2$) | Moment of inertia, $I$ ($m^4$) |
|---|---|---|---|
| Column ($1^{st}$ to $4^{th}$ story) | W30x391 | 7.35E−02 | 8.616E−03 |
| Column ($5^{th}$ to $8^{th}$ story) | W30x326 | 6.17E−02 | 6.993E−03 |
| Column ($9^{th}$ to $14^{th}$ story) | W27x307 | 5.82E−02 | 5.453E−03 |
| Column ($15^{th}$ to $20^{th}$ story) | W24x306 | 5.79E−02 | 4.454E−03 |
| Beam ($1^{st}$ to $20^{th}$ story) | W24x250 | 4.74E−02 | 3.534E−03 |

which is programmed in MATLAB. The parameters for DE are: the $NP = 50$, $F = 0.5$, $C_r = 0.9$. The optimization process is stopped after 40 iterations.

The time dependency of the displacement (at the central input values) in $x$ direction at joint 21 of this frame up to $t = 20$ s is plotted in Fig. 4, and match well with that of the SAP2000 software. With the fuzzy result for the displacement-time dependency up

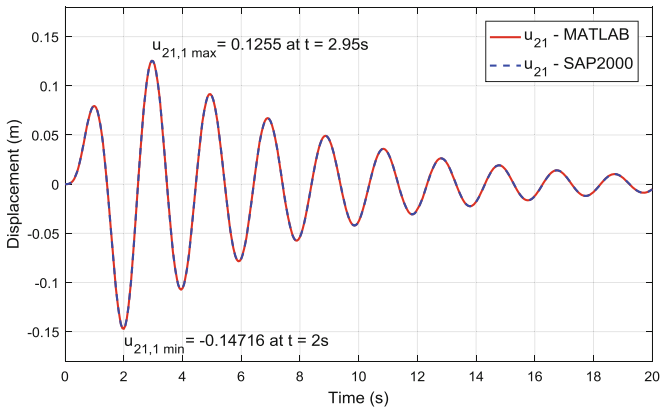


**Fig. 4.** Time-displacement response at joint 21 in $x$ direction of the twenty-story frame in MATLAB and SAP2000.

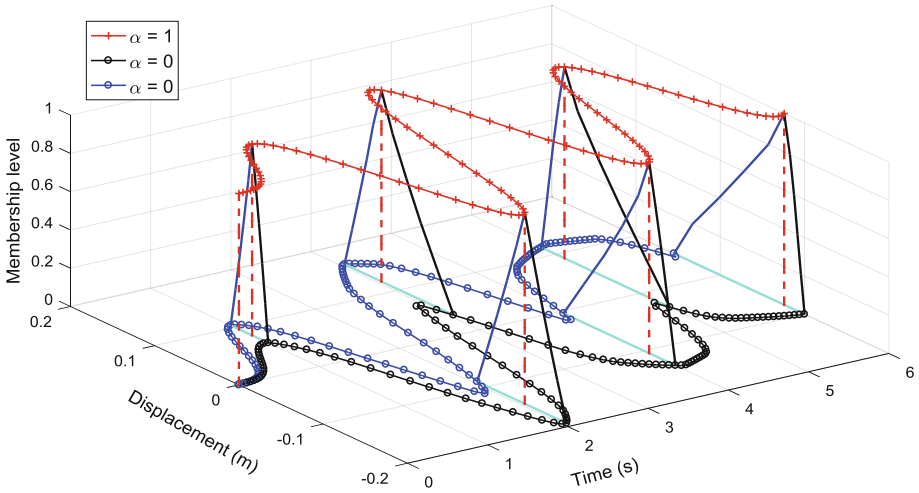


**Fig. 5.** Fuzzy displacement-time response at joint 21 in $x$ direction of the twenty-story frame.

to $t$ = 6.0 s of the joint 21 in $x$ direction of that frame, Fig. 5 shows the fuzzy displacement-time response and the membership function of fuzzy displacement at different times in 3D-axis; Fig. 6 shows the envelope of fuzzy displacement and the values: $\inf(u_{21,0\ \min}) = -0.1938$ m at $t$ = 2.05 s and $\sup(u_{21,0\ \max}) = 0.1651$ m at $t$ = 3.05 s; and Fig. 7 shows the membership function of fuzzy displacement and the displacement (at central value) from the SAP2000 software, with $t$ = 1.00, 2.05, 3.05, 4.00, 5.00, and 6.00 s. This Fig. 7 shows a significant difference between the shape of the fuzzy displacement membership functions at the different times.

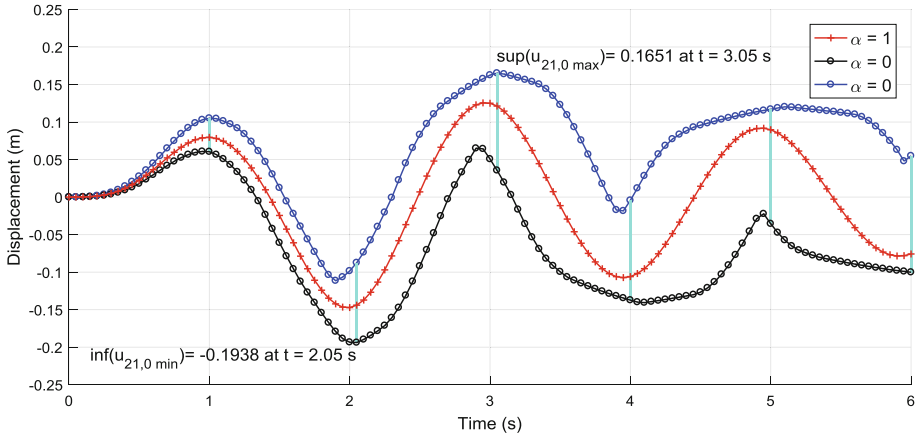


**Fig. 6.** Envelope of Fuzzy displacement at joint 21 in *x* direction of the twenty-story frame.

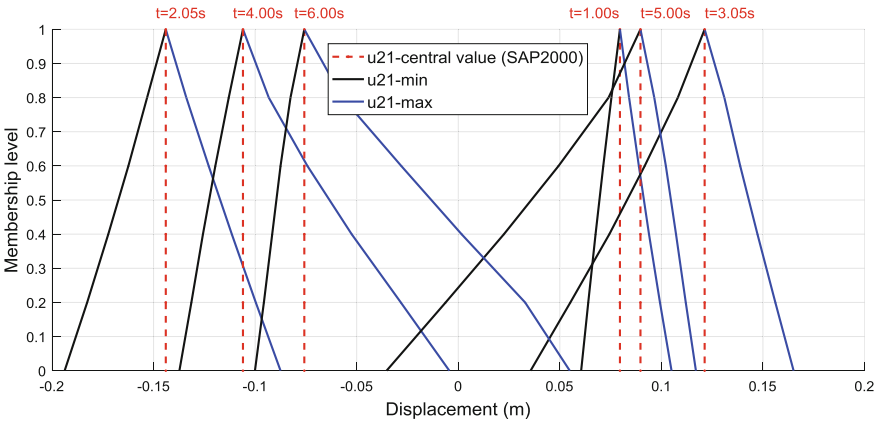


**Fig. 7.** The membership function of Fuzzy displacement at joint 21 in *x* direction at different times of the twenty-story frame.

## 5 Conclusions

A fuzzy dynamic analysis procedure is proposed for the linear elastic semi-rigid steel frame dynamic analysis with the input triangular fuzzy numbers. The fuzzy finite element analysis based on the Differential Evolution (DE) in combination with the α-level optimization, in which the Newmark-β average acceleration method is applied to determine the deterministic displacement. The fuzzy input parameters such as fixity factors of connections, external forces, mass per unit volume, and damping ratio have significant influence on the time dependency of the fuzzy displacement. The numerical examples illustrated that this procedure is applied efficiently. The deterministic results are also compared with ones of the SAP2000 software. However, using simple linear

elastic semi-rigid connection model is suitable for the structural system assumed that its displacement is small. As the displacement is large, it is necessary to include geometric nonlinearity and fuzzy initial geometric imperfections into advanced fuzzy dynamic analysis of steel frames, this may be subject of studies in the future.

## References


1. Anh, H.P., Thanh, X.N., Hung, V.N.: Fuzzy structural analysis using improved differential evolution optimization. In: International Conference on Engineering Mechanic and Automation (ICEMA 3), Hanoi, pp. 492–498, 15–16 October 2014
2. Anh, Q.V., Hien, M.N.: Geometric nonlinear vibration analysis of steel frames with semi-rigid connections and rigid zones. Vietnam J. Mech. VAST **25**(2), 122–128 (2003). doi:10.15625/0866-7136/25/2/6584
3. Chan, S.L., Chui, P.P.T.: Nonlinear Static and Cyclic Analysis of Steel Frames with Semi-rigid Connections. Elsevier, Amsterdam (2000)
4. Efrén, M.M., Margarita, R.S., Carlos, A.C.: Multi-objective optimization using differential evolution: a survey of the state-of-the-art. Soft Comput. Appl. (SCA) **1**(1), 173–196 (2013)
5. Huynh, X.L., Anh, T.D.: Stability analysis of planar frame structure with uncertain input quantities modeled as triangular fuzzy numbers (in Vietnamese). In: Vietnam Proceeding of Solid Mechanics (XXI), pp. 529–541 (2013)
6. Huynh, X.L., Anh, T.D.: Determining critical load of planar frame structure with input quantities modeled as triangular fuzzy numbers using α-level optimization algorithm (in Vietnamese). In: Vietnam Proceeding of Engineering Mechanics (2014)
7. Keyhani, A., Shahabi, S.M.R.: Fuzzy connections in structural analysis. MECHANIKA **18** (4), 380–386 (2012). ISSN 1392-1207. http://www.mechanika.ktu.lt/index.php/Mech/article/download/2329/1786
8. Lui, E.M., Lopes, A.: Dynamic analysis and response of semi-rigid frames. Eng. Struct. **19** (8), 644–654 (1997)
9. Newmark, N.M.: A method of computation for structural dynamic. J. Eng. Mech. Div. ASCE **85**, 67–94 (1959)
10. Nguyen, P.C.: Advanced analysis for three-dimensional semi-rigid steel frames subjected to static and dynamic loadings. Thesis of Doctor of Philosophy, Sejong University (2014)
11. Nguyen, P.C., Kim, S.E.: Advanced analysis for planar steel frames with semi-rigid connections using plastic-zone method. Steel Compos. Struct. **21**(5), 1121–1144 (2016). doi:10.12989/scs.2016.21.5.1121
12. Storn, R., Price, K.: Differential evolution – a simple and efficient adaptive scheme for global optimization over continuous spaces. In: International Computer Science Institute, Berkeley (1995). http://www.icsi.berkeley.edu/~storn/TR-95-012.pdf
13. Tuan, H.N., Huynh, X.L., Anh, H.P.: A fuzzy finite element algorithm based on response surface method for free vibration analysis of structure. Vietnam J. Mech. VAST **37**(1), 17–27 (2015). doi:10.15625/0866-7136/37/1/3923
14. Viet, T.T., Anh, Q.V., Huynh, X.L.: Fuzzy analysis for stability of steel frame with fixity factor modeled as triangular fuzzy number. Adv. Comput. Des. **2**(1), 29–42 (2017). doi:10.12989/acd.2017.2.1.029
15. Wang, L.-X.: A Course in Fuzzy Systems and Control. Prentice-Hall, Upper-Saddle River (1997)

# Incorporation of Measured Geometric Imperfections into Finite Element Models for Cold-Rolled Aluminium Sections

Ngoc Hieu Pham(✉), Cao Hung Pham, and Kim J.R. Rasmussen

The University of Sydney, Sydney, NSW, Australia
{ngochieu.pham, caohung.pham,
kim.rasmussen}@sydney.edu.au

**Abstract.** Geometric imperfections have a significant effect on both buckling and strength capacities of structural members. It is essential to accurately measure the geometric imperfections for finite element simulation especially for thin-walled sections. This paper presents the procedure to measure and incorporate geometric imperfections into finite element models using ABAQUS software package with the focus of attention for cold-rolled aluminium sections. Laser scanners are firstly used to measure geometric imperfections along high-precision tracks while recording the distances to corresponding points on the surface of specimen. The measurement lines are located around the cross-section. Subsequently, a MATLAB code is developed to incorporate the measured imperfection magnitudes into a perfect mesh of the finite element model. The Fourier series approximation is used in the longitudinal direction along measurement lines while the linear interpolation is used for flanges, lips and web in the transverse direction.

**Keywords:** Geometric imperfections · Finite element models · Cold-rolled aluminium sections

## 1 Introduction

Aluminium alloy structures have been used increasingly in bridges, building walls (Szumigala and Polus 2015) due to its excellent corrosion resistance, high strength to weight ratio and convenience in transportation, extrusion and assembly. The conventional way to produce aluminium alloy is extrusion. In Australian, the guidelines for the design of aluminium structures AS1664.1 (Australian Standard 1997) are premised on research of extruded sections. In recent years, BlueScope Lysaght (2015) has used rollers of steel sections to roll-form successfully aluminium sections with dimensional tolerances to AS/NZS 1734 (Australian Standard 1997). In comparison with extrusion method, roll-forming method is more cost effective, and enhances strength of aluminium alloy. The issue of the cold-rolled aluminium section is sensitive to buckling which is significantly affected by geometric imperfections. The geometric imperfections are caused by unavoidable disturbances during production, transportation and assembly processes causing imperfect straight of real dimensions of members. Thus, the incorporation of geometric imperfections needs to be considered in analyzing cold-rolled aluminium sections.

© Springer Nature Singapore Pte Ltd. 2018
H. Tran-Nguyen et al. (eds.), *Proceedings of the 4th Congrès International de Géotechnique - Ouvrages -Structures*, Lecture Notes in Civil Engineering 8,
DOI 10.1007/978-981-10-6713-6_15

Geometric imperfections can be divided into global and sectional imperfections. Global imperfections are represented by initial twists and initial deflections whereas the sectional imperfections include displacements of plate elements. For channel sections, overall imperfections are presented by three values $(G_1, G_2, G_3)$ as shown in Fig. 1 where $G_G, G_2$ and $G_3$ are bow, camber and twist of a member respectively. The sectional imperfections comprise two values $(d_1, d_2)$ as also shown in Fig. 1 where $d_1$ is the plate out of flatness, and $d_2$ is the plate out of straightness.

Due to the effect of imperfections, buckling process occurs gradually in lieu of the abruption from pre-buckling, buckling to post-buckling in perfect members, which results in the unclear buckling point. For example, a plate is compressed between two rigid frictionless platens and its relationship between the compressive load and the transverse deflection is shown in Fig. 2. Although being quite far from curve of the perfect plate in the pre-buckling period, the response of the imperfect plate approaches that of the perfect plate in the post-buckling period.

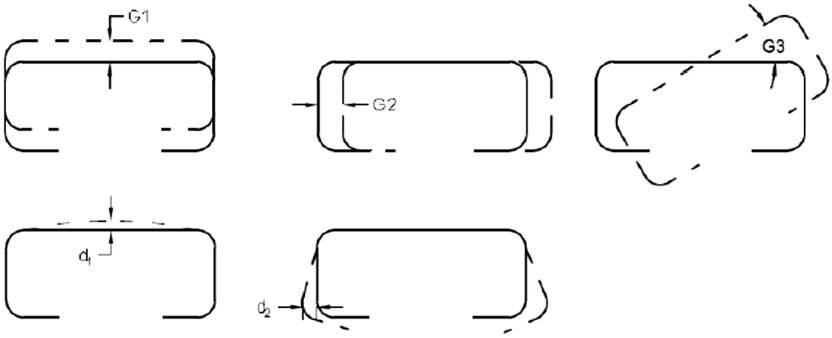


**Fig. 1.** Representative values for overall and sectional imperfections.

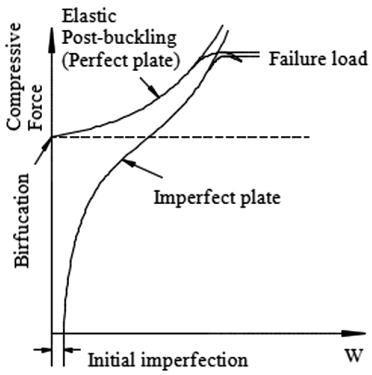


**Fig. 2.** Load-deflection relationship of a compression plate.

Several methods were proposed to measure geometric imperfections. Dat and Pekoz (1980) and Mulligan (1983) used a dial gauge to provide a global member out-of-straightness at the middle of the web with reference to a straight line between ends of the specimen. The specimen lied on a plane surface, and a dial gauge was used to measure the elevation of various points of the specimens as described in Fig. 3(a). This device was also used to measure local initial imperfection. It includes a ground bar, and fixed and movable support points, where the latter is established at a constant distance from the top of the bar as shown in Fig. 3(b). This device measured the out-of-flatness of stiffened and edge-stiffened elements, as referenced to their longitudinal edges. The local initial imperfection was calculated based on measurements taken with and without the ground bar using an independent 0.001-inch dial gauge. For distortional imperfection, a perfectly square ground bar was set up in Fig. 3(c) to measure the deviations of the flange element from a right angle established off of the corner of the web. Similarly, the imperfection was calculated from 0.001-inch dial gauge measurements taken with and without the square ground bar. Dat and Pekoz (1980) also used an alternative method to measure long specimens as shown in Fig. 4. The specimen was rested horizontally, and a telescope was placed approximately ten feet away to measure along the specimen axis. An optical micro-meter mounted at the end of telescope can be rotated. The imperfection was measured by determining the angular deviation of the optical micrometer compared to a fixed reference point. The dead weight deflections were also accounted for by subtracting or adding to the initial deflections depending on the direction of the initial deflections. In general, measurements just focused on a few sparse points and global out of straightness characters. Subsequently, Young (1997) employed transducers attached on an aluminium frame to measure five isolated longitudinal lines along a specimen, and used three transducers to measure the initial deflection and initial twist of the specimen as shown in Fig. 5. With the increasing of measurement lines, Young (1997) was able to access both global deviations and cross-section imperfections of a channel section. Based on Young (1997)'s idea, Becque (2008) and Niu (2013) used laser scanners instead of transducers to measure geometric imperfections of five and seven lines around a channel cross-section respectively as shown in Fig. 6, and provided much finer scale imperfection measurements. MCAnallen et al. (2014) provided non-contact techniques to take 3D measurements such as photogrammetry. In terms of photogrammetry method, sets of photos are taken from multiple viewpoints around the specimen, and then the commercial software is used to identify all the targets as shown in Fig. 7. MCAnallen et al. (2014) used ringed automatically detected (RAD) targets and dot targets to complete the photogrammetry process of making targets, identifying camera locations, referencing targets, and using an optimization algorithm to process a 3D point cloud. In addition, Zhao et al. (Zhao and Schafer 2014, 2016; Zhao *et al.* 2015, 2016) constructed a high-throughput and high-accuracy laser measurement platform for complicated structural geometries as shown in Fig. 8. The measuring rig consisted of three major components: laser scanner, rotary stage, and linear stage. Installed on the rotary stage, the laser could move around the circle to any desired scanning angle. The rotary stage was attached on a frame that could drive the laser along the longitudinal direction of the specimen. The laser imperfection measurement rig can collected full-field 3D

point clouds of the specimen. Later, the measurement point clouds were converted into operational 3D models for imperfection estimation.

Aluminium is a soft and lightweight material. Cold-rolled aluminium alloys members contain significantly large imperfections. Based on the method of Becque (2008) and Niu (2013), this paper presents the laser scanner method in measuring geometric imperfections as described in Sect. 2.

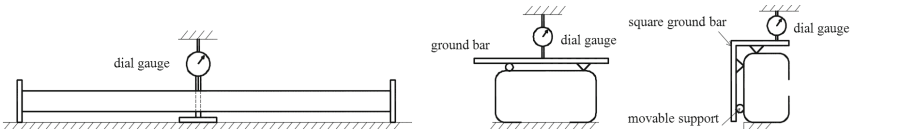


a) global member out of straightness b) local initial imperfection c) distortional initial imperfection

**Fig. 3.** Measuring imperfections using a dial gage (Mulligan 1983)

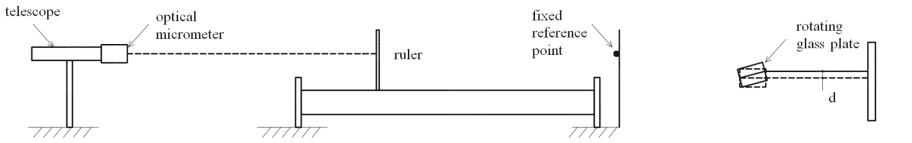


a) Set up b) Detail of optical micrometer

**Fig. 4.** Measuring imperfections using a telescope (Dat and Pekoz 1980)

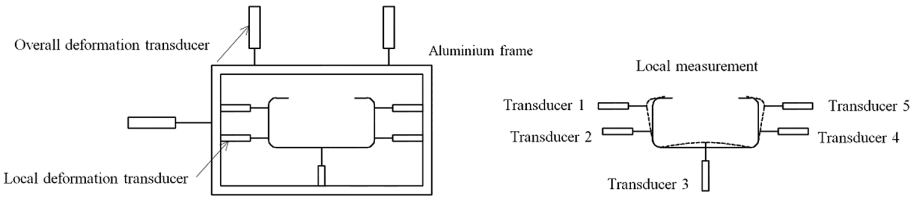


**Fig. 5.** Measuring imperfections using transducers (Young 1997)

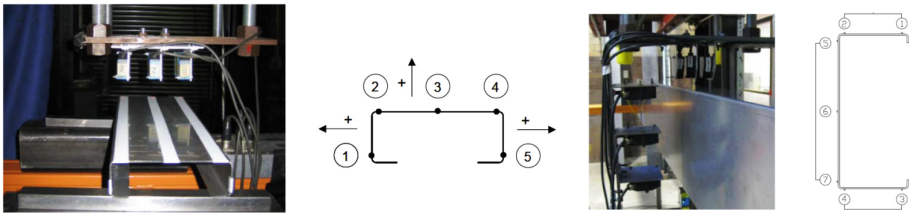


a) Becque's imperfection rigs (Becque 2008) b) Niu's imperfection rigs (Niu 2013)

**Fig. 6.** Measuring imperfections using laser scanners

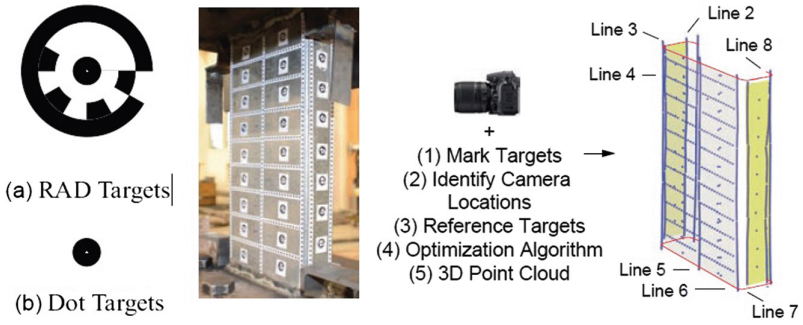


**Fig. 7.** Photogrammetry process (MCAnallen et al. 2014)

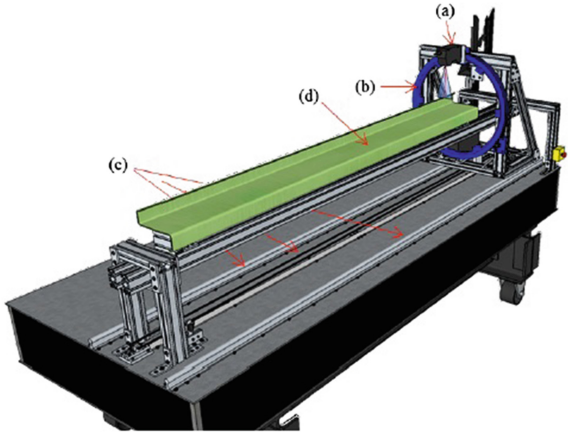


**Fig. 8.** Laser-based imperfection measurement platform (Zhao et al. 2014)

## 2 Measured Geometric Imperfections

### 2.1 Imperfection Measuring Rigs

The imperfection measuring rigs are shown in Fig. 9. They include two high precision bars attached on a rigid frame and a trolley was hung and ran along the bars. Laser devices attached to the trolley measure the distances to the surfaces of test specimens while the trolley moves along the bars with a constant speed. All measurement data are recorded at points whose distance is 1 mm. The locations of nine imperfection measurement lines along the longitudinal direction of specimens are shown in Fig. 10. To keep away from the edge and corner region, as well as to allow room for the laser devices, the measurement lines are offset 10 mm from the edges. While the global imperfections are measured through lines (3), (4), (6) and (7), the sectional imperfections are obtained through the remaining lines. Lines (1), (2), (8) and (9) capture distortional imperfections of two flanges whereas line (5) captures local imperfections of the web. Compared to seven measurement laser lines of Niu (2013), nine measurement laser lines in this paper should access imperfections more thoroughly in two lips of the channel sections.

**Fig. 9.** Measuring rigs

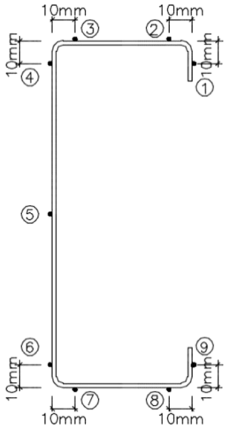


**Fig. 10.** Measurement line Locations

## 2.2 Sketching Two Cross-Sections at the Edges

Two end cross-sections of the specimen are labeled as A and B. Laser scanners run from Section A to Section B. The cross-sections at two ends are not perfect. It is necessary to account for those non-perfect cross-sections in analysis models. These

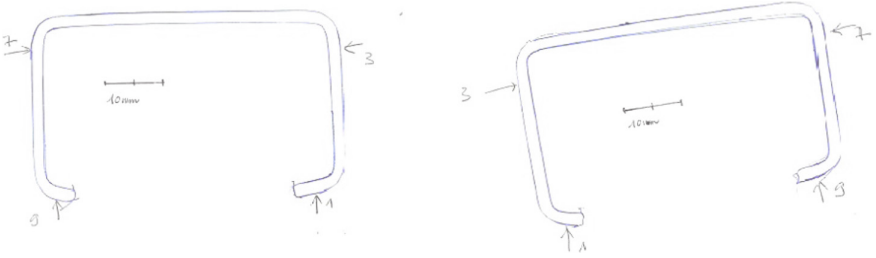

a) Section A b) Section B

**Fig. 11.** Non-perfect cross-sections

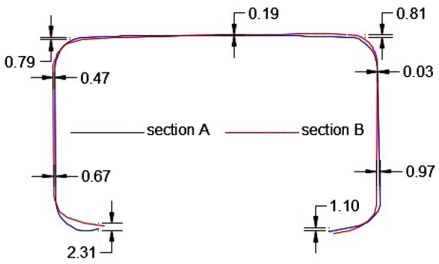


**Fig. 12.** Compare the difference between two cross-sections

cross-sections are firstly sketched on papers as shown in Fig. 11, and are subsequently redrawn in AutoCAD. The next step is to compare the difference between two cross-sections of end cross-sections based on the initial twist. The initial twist is determined by using imperfections data of lines (4) and (6). Cross-section (B) is compared to cross-section (A) through nine points to determine nine values as shown in Fig. 12. Those values are used for the processing method as described in Sect. 3.

## 3 Processing Method

After measuring imperfections, raw results of an imperfection line include data of separate points along the length of a specimen. In order to introduce this data into numerical models, each discrete data line is converted into Fourier series as given in Eqs. (1) and (2).

$$f(x) = \sum_{n=1}^{\infty} K_n sin\frac{\pi nx}{L}\,(With\,0 < x < L) \tag{1}$$

$$K_n = \frac{2}{L}\int_0^L f(x)sin(\frac{\pi nx}{L})dx\,(n = 1, 2, 3, \ldots, \infty) \tag{2}$$

The number of terms in Eq. (1) for each specimen length was chosen to encompass short half wave lengths which are more influential to local buckling behavior. Typically, number of series terms ranging from 20–35 is used for different specimen length, and depends on the ratio of the length of specimen and a half wave length of local buckling of that section (Becque 2008; Niu 2013). For example, the specimen (AC10030-2000C-1) requires 25 terms in the imperfection line expression. A typical imperfection taken from the line (5) of specimen AC10030-2000C-1 as shown in Fig. 13, the Fourier expression curve fits very well with the measured imperfection line. In order to account for the difference between two cross-sections at two end cross-sections of specimens, values $(a_i)$ in Fig. 12 are transformed into linear equations expressed in Eq. (3) to capture the initial twist of the specimen. Hence, imperfections lines are expressed by combinations of Fourier series f(x) and linear equations g(x) as described in Eq. (4). A MATLAB code (1) is created to determine the coefficients $K_n$

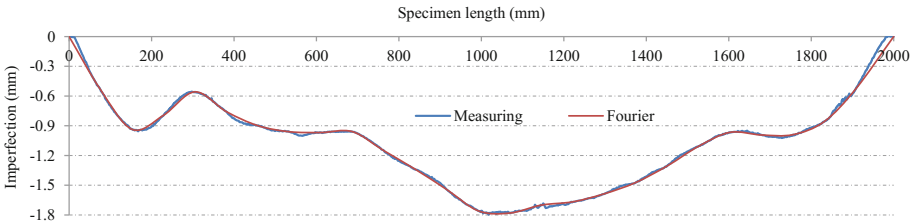


**Fig. 13.** Fourier expression curve and actual imperfection line (5) of the specimen AC10030-2000C-1

of measurement lines based on measured data. Fourier series f(x) and linear equations g(x) are introduced into a MATLAB code (2) to incorporate imperfections into finite element models as described in Sect. 4.

$$g(x) = (\pm)\frac{a_i}{L}x(with\,0 < x < L) \tag{3}$$

$$F(x) = \sum_{n=1}^{\infty} K_n sin\frac{\pi nx}{L}(\pm)\frac{a_i}{L}x\,(With\,0 < x < L) \tag{4}$$

## 4 Incorporation Imperfections into Finite Element Models

To incorporate imperfections into Finite Element (FE) models, two end cross-sections (A and B) of the real specimen are sketched on papers and subsequently transferred into AutoCAD. The cross-section (A) measured at the beginning of measuring process is used as the original cross-section. After being imported into ABAQUS by using the command "File>Import/Sketch", the original cross-section is extruded to create the perfectly straight specimen as shown in Fig. 14(a).

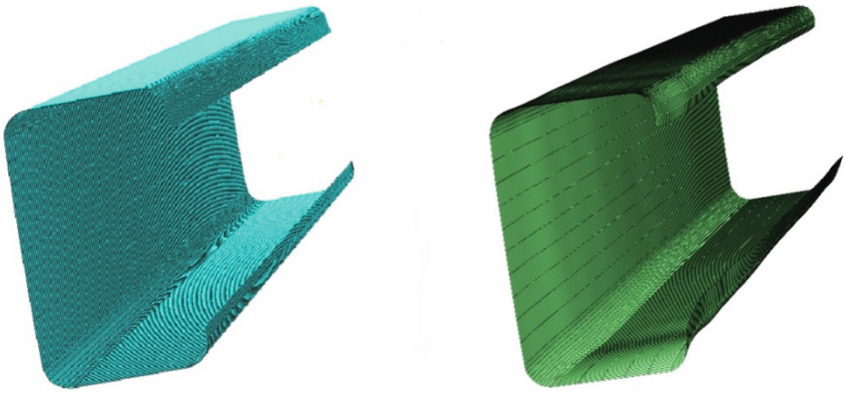

a) b)

**Fig. 14.** The perfect specimen (a) and the imperfect specimen (b)

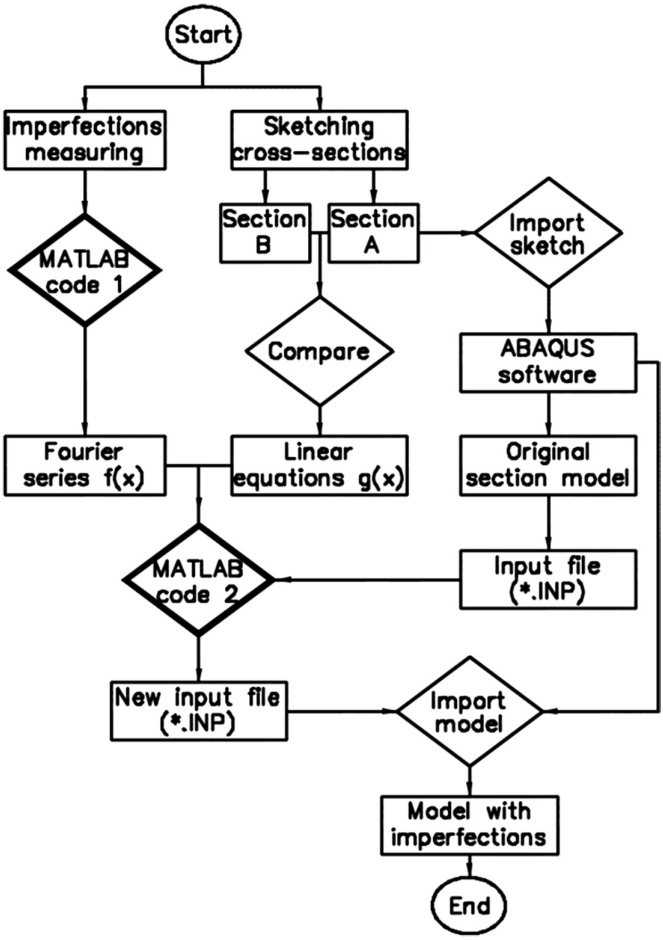


**Fig. 15.** The procedure to incorporate geometric imperfections into finite element models

With an input file (*.INP) exported from an original model in ABAQUS/Standard – Version 6.14 (2014), the coordinates of all nodes in this input file are reproduced by using a MATLAB code (2). This code can introduce Fourier series curves into nodes along reading lines and interpolate the co-ordinates of intermediate nodes. In addition, the difference between two end cross-sections (A and B) is considered to determine the changes of local, distortional imperfection between two end cross-sections in association with initial twist rotation of the specimen. Subsequently, the new input file is imported into ABAQUS by using the command "File>Import/Model". Figure 14(b) shows an example of the actual imperfections of the specimen AC10030-2000C-1 after incorporating into the finite element model. In comparison with Fig. 14(a), (b) shows the changes of local imperfections of the web, distortional imperfections of the flanges as well as initial twist of two end cross-sections. The procedure to incorporate geometric imperfections into finite element models is summarized in the flowchart format in Fig. 15.

## 5 Conclusion

This paper provides various methods to measure geometric imperfections of the cold-formed sections. While methods using a dial gauge or transducers typically measure a few sparse points and global out-of straightness characterization, non-contacts methods described in this paper using laser scanners or photogrammetry provide more accurate data in measuring geometric imperfections. With more data collected, geometric imperfections are therefore studied more thoroughly.

The paper also presents the procedure to introduce geometric imperfections into ABAQUS models. Two MATLAB codes are created for implementing this procedure. This first code is used to convert the discrete data of imperfection lines into Fourier series. The second code aims to introduce Fourier series into reading points, and then interpolate the coordinates of intermediate nodes.

**Acknowledgments.** Funding provided by the Australian Research Council Linkage Research Grant LP140100563 between BlueScope Lysaght and the University of Sydney has been used to perform this research. The authors would like to thank Permalite Aluminum Building Solutions Pty Ltd for the supply of the test specimens and financial support for the project. The first author is sponsored by the scholarship provided by Australian Awards Scholarships (AAS) scheme from Australian Government.

## References

AS/NZS 1664.1:1997. Australian/New Zealand Standard Part 1: Limit state design aluminium structures. Standards Australia, Sydney (1997)

AS/NZS 1734: 1997. Australian/New Zealand Standard: Aluminium and aluminium alloys-Flat sheet, coiled sheet and plate. Standards Australia, Sydney (1997)

ABAQUS/Standard. ABAQUS/CAE User's Manual. Dassault Systemes Simulia Corp, Providence, RI, USA (2014)

Becque, J.: The interaction of local and overall buckling of cold-formed stainless steel columns. Dissertation, University of Sydney (2008)

BlueScope Lysaghts. Perlimate - Aluminium Rollformed Purlin Solutions. Permilate Aluminium Building Solutions Pty Ltd, Eagle Farm Qld 4009, Australia (2015)

Dat, D.T., Pekoz, T.P.: The strength of cold-formed steel columns. Department of Structural Engineering Report, Library 110, Ithaca, NY, Cornell University (1980)

Mulligan, G.P.: The influence of local buckling on the structural behavior of singly symmetric cold-formed steel columns. Dissertation, Cornell University (1983)

MCAnallen, L.E., Padilla-Llano, D.A., Zhao, X., Moen, C.D., Schafer, B.W., Eatherton, M.R.: Initial geometric imperfection measurement and characterization of cold-formed steel C-section structural members with 3D non-contact measurement techniques. In: Proceeding of the Annual Stability Conference Toronto (2014)

Niu, S.: The interaction of cold-formed stainless steel beams. Dissertation, University of Sydney (2013)

Szumigala, M., Polus, L.: Applications of aluminium and concrete composite structures. Procedia Eng. 108, 544–549 (2015)

Young, B.: The behaviour and design of cold-formed channel columns. Dissertation, University of Sydney (1997)

Zhao, X., Schafer, B.W.: Laser scanning to develop three-dimensional fields for the precise geometry of cold-formed steel members. Recent research and development in cold-formed steel design and construction (2014)

Zhao, X., Tootkaboni, M., Schafer, B.W.: Development of a laser-based geometric imperfection measurement platform with application to cold-formed steel construction. Exp. Mech. **55**, 1779–1790 (2015)

Zhao, X., Schafer, B.W.: Measured geometric imperfections for Cee, Zee, and built-up cold-formed steel members. In: Jwei-Wen Yu International Specialty Conference on Cold-Formed Structures, pp. 73–87 (2016)

Zhao, X., Tootkaboni, M.P., Schafer, B.W.: High fidelity imperfection measurements and characterization for cold-formed steel members. In: Proceeding of the 7th International Conference on Coupled Instabilities in Metal Structures (2016)

# Micromechanical Model for Describing Intergranular Fatigue Cracking in an Innovative Solder Alloy

Van-Nhat Le[1(✉)], Lahouari Benabou[1], and Quang-Bang Tao[2]

[1] LISV, University of Versailles Saint Quentin-en-Yvelines, 45 avenue des Etats-Unis, 78035 Versailles, France
levannhat.vn@gmail.com, lahouari.benabou@uvsq.fr
[2] Da Nang University of Technology, Da Nang, Vietnam
tqbang@dut.udn.vn

**Abstract.** Fatigue of solder joints remains one of the critical concerns in thermo-mechanical reliability of high-power electronic systems. Several semi-empirical fatigue models based on effective material properties at macro-scale already exist, but have shown some limitations for providing accurate lifetime prediction of solder joints in the scale of microelectronic packages. Therefore, there is a need to enrich the existing approaches by a description of the failure mechanisms at the microstructure scale, taking into account some important features of the alloy. In this study, a 3D microstructure-informed model for reproducing the intergranular fatigue crack in the solder joint is developed. The submodeling technique has been applied in order to only investigate the critical zone of the solder joint. A global model of the whole module is first simulated to obtain the inputs for a submodel focused on the zone of interest where failure is expected to develop. The submodel simultaneously makes use of the cohesive zone and the crystal plasticity theories to represent decohesion at grain boundaries and plastic slips in the grains of the solder joint, respectively. Simulations of repeated thermo-mechanical loading on the package demonstrate how cracking occurs at grain boundaries in the solder joint of the submodel. In addition, it is shown that the crack propagation rate is almost constant during the whole loading time. This suggests an ability of the present approach to give a fatigue lifetime estimate for the entire solder joint by extrapolating some specific computed quantities from the local model.

**Keywords:** Fatigue fracture · Innovative soldering alloy · Crystal plasticity · Cohesive zone model · Finite element modeling

## 1 Introduction

The Insulated-Gate Bipolar Transistor (IGBT), a power electronic device, is increasingly applied to answer demands of electrical energy management in transport systems (Lu et al. 2009). A description of a typical IGBT power module is illustrated in Fig. 1. It can be seen that the module contains a certain number of materials with different coefficients of thermal expansion; which results in the appearance of stresses during the

© Springer Nature Singapore Pte Ltd. 2018
H. Tran-Nguyen et al. (eds.), *Proceedings of the 4th Congrès International de Géotechnique - Ouvrages -Structures*, Lecture Notes in Civil Engineering 8,
DOI 10.1007/978-981-10-6713-6_16

thermal loading and, thus, the possibility of different types of failure modes such as wire bonding fracture (Celnikier et al. 2011), substrate delamination, chip metallization degradation, and particularly solder joints fatigue (Benabou et al. 2014). In this paper, we focus on the solder joint fatigue due to its key role in the thermo-mechanical reliability of electronic packages.

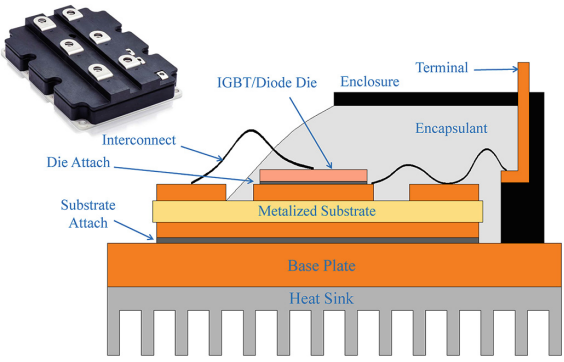


**Fig. 1.** Schematic of an IGBT power module.

To date, the Tin-Silver-Copper (SAC) alloys have become the dominant choice in power module industries for replacing the former Tin-Lead alloys due to potential environmental concerns associated with the toxicity of lead. Prediction of fatigue lifetime of the newly-developed alloys is extremely difficult due to the complexity of their microstructure. Observations show that the SAC solder experiences a brittle fracture mode with occurrence of an intergranular cracking path (Beyer et al. 2014). Although several previous studies dealt with solder joint fatigue lifetime predictions, this subject still needs to be developed. Several phenomenological models of fatigue already exist and are simply fitted to match experimental thermal/mechanical cyclic test data. The weakness of such semi-empirical approaches is that they are strongly related to the specific conditions of material characterization (size of samples, testing conditions, etc.) and that they are limited to a mere macroscopic description by completely ignoring issues like the scale at which the solder alloys are used in the microelectronic packages, namely in the form of extremely thin layers of the order of a few grains. Therefore, constitutive macroscopic laws, such as that of Anand (Anand 1985), do not possess the ability to describe the microscopic anisotropy of the alloys at this small scale and, thus, can prove very limited for the design of solder joints against fatigue.

The objective of this paper is to provide a numerical methodology for reproducing initiation and propagation of intergranular fatigue cracking in a solder joint embedded in a global model of a power module. A micromechanical finite element model, coupling crystal plasticity (CP) with cohesive zone model (CZM), is developed to account for the anisotropy and plastic slips in the grain structure on the one hand, and failure at grain boundaries on the other. Due to excessive computational requirements

for simulating the whole polycrystalline microstructure of the solder layer, the sub-modeling technique has been employed in order to only investigate the critical zone of the solder joint. The global model of the power module has been first modeled, using bulk elements with the corresponding macroscopic constitutive laws, to find the joint critical zone, as well as the boundary conditions needed for the submodel. The identified critical zone is then refined in the submodel by being reconstructed with its crystalline microstructure including grains and grain boundaries. In this step, both CP and CZM constitutive laws are used for describing the behavior of the polycrystalline alloy under fatigue fracture. In addition, viscous regularization is applied to improve the convergence of the CZM.

## 2 Crystal Plasticity Model

### 2.1 Constitutive Equations

The initial CP model of Asaro (Asaro 1983) gives the ability to follow the most active slip systems, calculate the shear rate for each one of them, and obtain the total plastic deformation. The plastic slip rate can be expressed as follows (Hutchinson 1976):

$$\dot{\gamma}^{(\alpha)} = \dot{\gamma}_0 . \left( \frac{\tau^{(\alpha)}}{g^{(\alpha)}} \right)^n \operatorname{sgn}(\tau^{(\alpha)}) \tag{1}$$

where $\dot{\gamma}_0$ is the reference strain rate, n is the rate sensitivity exponent, and $\tau^{(\alpha)}$ and $g^{(\alpha)}$ are the resolved shear stress and the slip system strain hardness for the $\alpha th$ slip system, respectively.

This CP model is implemented for FCC systems into the widely used commercial FE software ABAQUS through the user-defined material subroutine (UMAT) of Huang (Huang 1991). The subroutine has been adapted in this work to the BCT system of the tin-based solder alloy.

### 2.2 Microstructure of the Solder Alloy

Lead-free solders contains mostly tin, usually more than 95%. Therefore, the behavior of the alloy depends mainly on the properties of tin crystals. For the sake of simplicity, the solder material is assumed in the simulation to be only made of tin grains. Previous investigations (Darbandi et al. 2014), showed that the anisotropy of tin is characterized by six independent elastic moduli presented in Table 1.

**Table 1.** Elastic constants (GPa) of Tin used in numerical analysis (Darbandi et al. 2014).

| $C_{11}$ | $C_{12}$ | $C_{13}$ | $C_{33}$ | $C_{44}$ | $C_{66}$ |
|---|---|---|---|---|---|
| 72.3 | 59.4 | 35.8 | 88.4 | 22.0 | 24.0 |

### 2.3 Identification of Parameters for CP

Several mean field models, based on the theory of homogenization of polycrystalline aggregates, were developed in the past and are still widely used for parameter identification of crystal plasticity, such as the models of Berveiller-Zaoui and the $\beta$-rule, for example. The Berveiller-Zaoui model has been used in this study according to the procedure described in (Benabou et al. 2014); this model does not require any additional parameters for the adjustment of the scale transition scheme and shows a good agreement in the case of radial monotone loading. The identification process is done in 2 steps: (i) a pre-identification is first carried out by using the mean field model to fit the experimental global response of the material under uniaxial tension, (ii) a FE analysis is then conducted to validate and calibrate the material parameters of the CP model. The calibrated parameters are reported in Table 2 and are found to be in good agreement with recent results on lead-free solder characterization (Bieler anf Telang 2009).

**Table 2.** Identified values of the crystal plasticity parameters.

| Crystal plasticity parameters | | | | | |
|---|---|---|---|---|---|
| $h_0$ $(MPa)$ | $\tau_s$ $(MPa)$ | $\tau_0$ $(MPa)$ | $\dot{\gamma}_0$ $(s^{-1})$ | q | n |
| 6000 | 16.0 | 10.5 | 0.001 | 1.4 | 15.75 |

## 3 Modelling of Decohesion at Grain Boundaries

### 3.1 Theory

The CZM approach was used in this work to represent the intergranular fatigue cracking in the solder joint. Details on the constitutive equations of the model have been discussed in a previous study (Benabou et al. 2013), in which a global damage variable is incorporated in order to explicitly reproduce the irreversible damage under cyclic loading. Evolution of the damage variable is given as:

$$\dot{d} = \frac{(1-d)k_n^+}{G_c^m - G_0^m} \langle \delta \rangle \left\langle \dot{\delta} \right\rangle \tag{2}$$

where $k_n^+$ is the undamaged normal stiffness of the interface and $\delta$ its effective opening during loading, and $G_0^m$ and $G_c^m$ are the initial mixed-mode damage threshold and the mixed-mode fracture energy, respectively. The traction-separation law of the cohesive elements has been implemented in the UEL subroutine of ABAQUS.

### 3.2 Material Parameters

The input parameters for the CZM includes the stiffness $k_x$, the damage threshold energy density $G_0^x$ and the fracture energy density $G_c^x$ for each particular mode $x$ ($x$ = I, II or III). The initial tensile and shear stiffnesses of the cohesive elements can be derived from the elastic and shear modulus of the solder bulk material:

$$k_n = \frac{E}{t_{cz}} \quad and \quad k_t = \frac{G}{t_{cz}} \tag{3}$$

where $E$ and $G$ are the elastic young and shear moduli of the bulk element, and $t_{cz}$ is the fictitious thickness of the cohesive element. The elastic constants of the solder, which are here assumed independent of temperature for simplicity, are $E$ = 41000 MPa and $G$ = 15070 MPa (Motalab et al. 2012). The damage threshold energy density, $G_0^x$, and the fracture energy density, $G_c^x$, for mode $x$, are two decisive parameters in determining the evolution of the intergranular cracks. These fracture energies can be measured by experiments, but there is no efficient method to do this, particularly at the microstructure scale. In this paper, the grain boundary fracture energy in mode-I is determined based on the surface energy, $\gamma_s$, and the grain boundary energy, $\gamma_{GB}$ following an approach presented in (Simonovski and Cizelj 2013). For tin element, the surface energy is taken as $\gamma_s = 0.709 \times 10^{-3}\text{mJ/mm}^2$ with a ratio of $\gamma_{GB}/\gamma_S = 0.24$. Fracture energies in the tangential modes (II and III) have been assumed equal to that of mode-I, e.g. $G_c^{II} = G_c^{III} = G_c^I$. All the CZM parameters used in the FE analysis are reported in Table 3. With regard to the damage threshold energy density, $G_0^x$, the value is expected to be very small in the case of solder alloys. Since this parameter does not significantly influence the final lifetime prediction, its value is chosen equal to 2% of the fracture energy density $G_c^x$.

**Table 3.** Estimated parameters for the CZM approach.

| $t_{cz}$ (mm) | E (MPa) | G (MPa) | $G_c^I$ (mJ/mm) | $G_c^{II} = G_c^{III}$ (mJ/mm) | $\mu$ |
|---|---|---|---|---|---|
| 0.01 | 41000 | 15070 | 0.0014 | 0.0014 | 0.0001 |

## 4 Finite Element Simulation

### 4.1 Numerical Methodology

Simulation of the IGBT module is done according a two-step procedure illustrated in Fig. 2. Firstly, the global model is built based on the real geometry of the power module whose components are given their distinct thermo-mechanical properties. Due

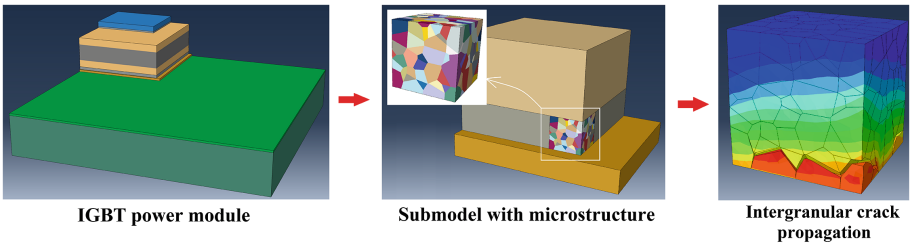


**Fig. 2.** Numerical methodology for studying crack propagation in the solder joint.

to the symmetry in the 3D geometry, only one-fourth of the model is considered, resulting in a substantial reduction of the model size. The visco-plastic behaviour of the solder alloy is governed by the classical Anand law (Anand 1985). The model parameters estimated by Motalab et al. (Motalab et al. 2012) are taken in our work. Concerning the properties of the other materials used in the power module (silicon chip, copper substrate, aluminum base plate), they are assumed to behave elastically with temperature-dependent properties.

The global model of the IGBT module is simulated under thermal loading with cycles of 5700 s and temperature range from 10 °C to 80 °C (thermal shocks). The critical zone in the solder layer is where energy dissipation is the highest in the stabilized cycle. This region and its vicinity will be modeled more accurately in the submodel. The nodal displacements at the border of the detailed zone, obtained during the stabilized cycle, are also stored to serve as boundary conditions in the submodel.

Secondly, the submodel is generated by keeping a smaller region of the IGBT global model, comprising the critically loaded region of the solder joint and its vicinity made of the materials coming into contact with the zone of interest. The latter, located in the corner of the solder layer, is approximated by a cubic part (Fig. 2) which is modeled by a grain microstructure made of crystals and grain boundaries. The submodel is loaded during 150 thermal cycles so that intergranular cracking can occur in the polycrystalline aggregate. Fatigue behaviour of the solder joint is finally investigated using results obtained on the refined submodel, giving the ability to do extrapolation of some predicted quantities over the whole solder layer when cyclic stabilization is reached.

### 4.2 Results of Simulation

Figure 3 shows the grain boundary damage evolution for some of the 150 loading cycles. Most of the early damage initiates at the intersection of grain boundaries with the external surface of the model. A smaller fraction of damage initiation is found inside the model, mostly at the triple lines. This occurrence damage within the material may be explained by the increase of normal stresses in the cohesive zone elements located at the triple lines. This can be caused by the use of triangular prism cohesive elements as this is not the case when rectangular prism cohesive elements are employed (Shawish et al. 2013). However, the application of rectangular prism elements is not possible here since it requires a conformal mesh between the grain boundaries and the grains. Another observation is that the dominant damage nucleation occurs in the same

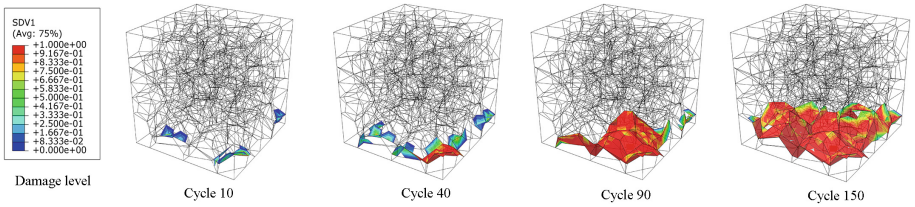


**Fig. 3.** Intergranular damage evolution during the loading cycles.

critical zone as where deformation is the highest in the global model. Thus, the present microscopic modeling of the solder joint has the ability to reproduce the fatigue crack initiation at the corner of the layer near the bottom interface, as well as its propagation from outside to inside by following an almost horizontal plane path. Such a numerical result is corroborated by previous experimental studies of this type of failure (Perpina et al. 2012).

In Fig. 4, the total number of damaged cohesive elements is plotted as function of the number of cycles. The shape of the curve shows that an interesting correlation exists between damage and the number of loading cycles, which can be approximated by a second-order polynomial evolution trend. The quadratic function, obtained by data fitting, is used to establish a fatigue criterion as follows. The cohesive element mesh size being almost uniform in the model, the average damaged area is then a linear function of the number of damaged elements. This suggests that the damaged area is a quadratic function of the number of cycles. Once this quadratic relation between the crack area and the number of cycles is soundly established based on longer simulations, lifetime of the whole solder joint can be predicted by a simple extrapolation of the obtained quantities in the local model.

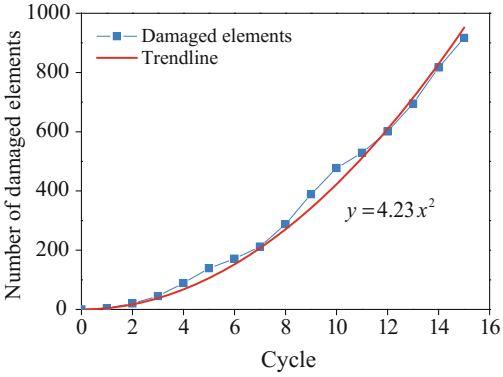


**Fig. 4.** Damaged cohesive elements versus the cycle numbers.

## 5 Conclusions

In this work, a numerical methodology is proposed for reproducing the intergranular fatigue crack in the critical zone of the solder joint. The submodelling technique has been used to reduce the computational cost of the simulations. The global model of the power module is fist simulated with the bulk material properties of all the components to find both the critical zone in the solder joint and the boundary conditions to be applied to the submodel of the module. In the submodel, the solder joint is reconstructed at grain structure level using a crystal plasticity model for the grains and cohesive elements for the grain boundaries. The parameters for crystal plasticity of the lead-free solder are calibrated using the Berveiller-Zaoui transition rule to fit tensile test

data, while the cohesive zone parameters are obtained using some assumptions on the stiffness of the interface and its energy. It was demonstrated that the developed methodology could successfully reproduce the intergranular crack initiation and propagation in the solder joint during fatigue loading. Damage initiates at intersections of grain boundaries at the external surface. The dominant crack develops from the corner of the solder layer near the bottom interface and propagates towards the interior, in accordance with previous experimental observations. Another interesting result obtained in this work is the nearly stable crack propagation rate through the grain boundaries of the solder alloy during the thermal loading cycles. This suggests that the global fatigue lifetime of the solder joint can be predicted by simple extrapolation from quantities obtained in the local model.

## References


Anand, L.: Constitutive equations for hot-working of metals. Int. J. Plast. **1**, 213–231 (1985)

Asaro, R.J.: Crystal plasticity. J. Appl. Mech. **50**, 921–934 (1983)

Benabou, L., Le, V.N., Sun, Z., Pougnet, P., Etgens, V.: Effects of voids on thermal-mechanical reliability of lead-free solder joints. In: MATEC Web of Conferences, vol. 12, p. 4026 (2014). doi:10.1051/matecconf/20141204026

Benabou, L., Sun, Z., Dahoo, P.R.: A thermo-mechanical cohesive zone model for solder joint lifetime prediction. Int. J. Fatigue **49**, 18–30 (2013). doi:10.1016/j.ijfatigue.2012.12.008

Beyer, H., Sivasubramaniam, V., Hajas, D., Nanser, E., Brem, F.: Reliability improvement of large area soldering connections by antimony containing lead-free solder. In: PCIM Europe 2014, pp. 1–8 (2014)

Bieler, T.R., Telang, A.U.: Analysis of slip behavior in a single shear lap lead-free solder joint during simple shear at 25 °C and 0.1/s. J. Electron. Mater. **38**(12), 2694–2701 (2009). doi:10.1007/s11664-009-0909-x

Celnikier, Y., Benabou, L., Dupont, L., Coquery, G.: Investigation of the heel crack mechanism in Al connections for power electronics modules. Microelectron. Reliab. **51**(5), 965–974 (2011). doi:10.1016/j.microrel.2011.01.001

Darbandi, P., Lee, T., Bieler, T.R., Pourboghrat, F.: Crystal plasticity finite element study of deformation behavior in commonly observed microstructures in lead free solder joints. Comput. Mater. Sci. **85**, 236–243 (2014). doi:10.1016/j.commatsci.2014.01.002

Huang, Y.: A User-Material Subroutine Incorporating Single Crystal Plasticity in the ABAQUS Finite Element Program. Division of Applied Sciences, Harvard University (1991)

Hutchinson, J.W.: Bounds and self-consistent estimates for creep of polycrystalline materials. Proc. R. Soc. A: Math. Phys. Eng. Sci. **348**(1652), 101–127 (1976). doi:10.1098/rspa.1976.0027

Lu, H., Bailey, C., Yin, C.: Design for reliability of power electronics modules. Microelectron. Reliab. **49**(9–11), 1250–1255 (2009). doi:10.1016/j.microrel.2009.07.055

Motalab, M., Cai, Z., Suhling, J.C., Lall, P.: Determination of Anand constants for SAC solders using stress-strain or creep data. In: Intersociety Conference on Thermal and Thermomechanical Phenomena in Electronic Systems, ITHERM, pp. 910–922 (2012). doi:10.1109/ITHERM.2012.6231522

Perpina, X., Navarro, L., Jorda, X., Vellvehi, M.: Reliability and lifetime prediction for IGBT modules in railway traction chains. In: Reliability and Safety in Railway, pp. 193–222 (2012). doi:10.5772/2660

Shawish, S.E., Cizelj, L., Simonovski, I.: Modeling grain boundaries in polycrystals using cohesive elements: qualitative and quantitative analysis. Nucl. Eng. Des. **261**, 371–381 (2013). doi:10.1016/j.nucengdes.2013.01.023

Simonovski, I., Cizelj, L.: Cohesive element approach to grain level modelling of intergranular cracking. Eng. Fract. Mech. **110**, 364–377 (2013). doi:10.1016/j.engfracmech.2013.05.011

# Modelling the Static Interaction Between a Shallow Foundation and Soil Base Using Contact Conditions

H.T. Tai Nguyen(✉), T. Hang Nguyen, and N. Hung Nguyen

Department of Civil Engineering, Thu Dau Mot University,
Thu Dau Mot City, Binh Duong Province, Vietnam
{tainht, hangnt, hungnn}@tdmu.edu.vn

**Abstract.** The displacement of foundation due to the deformation of soil base has a significant effect on the internal forces and reactions resulted from an analysis of building structure. However, this effect is generally not properly considered, causing eventual large errors in structural analysis and design. In this work, the authors aim to model the interaction between a shallow foundation and soil base by using contact conditions to analyse the building structure which is simultaneously exerted by the external loading and deformation of soil base. The internal forces and reactions obtained with this analysis are compatible with the deformation of soil base—namely, the displacements of foundations are exactly the consolidated settlements of the soil base and the internal forces caused by the unequal settlement are also included in the results. Because of the nonlinearities of the contact conditions and the soil characteristics, the discrete equations resulted from the finite element discretization are nonlinear, which can be solved by Newton-Raphson scheme with the aid of tangent stiffness matrices.

**Keywords:** Building structures · Static foundation–soil interaction · Contact conditions

## 1 Introduction

In civil engineering, the static analysis and design of a building structure is decomposed into two separate stages: structural analysis and foundation design. With this kind of procedure, the influence of the settlement on the behaviour of the superstructure is not yet considered, causing eventual large errors in structural analysis and design.

In the literature, the simple (or linear) Winkler's model has long time been used as a remedy for the lack of foundation–soil base interaction (Hain and Lee 1974; Lee and Brown 1972). In Vietnam, the problem of foundation–soil base interaction was firstly discussed in the book of Dang (1999), where the building structure and its continuous spread footing were simultaneously modelled using plane frame elements and Winkler's springs. The stiffness of the spring is defined as the ratio of reaction force

© Springer Nature Singapore Pte Ltd. 2018
H. Tran-Nguyen et al. (eds.), *Proceedings of the 4th Congrès International de Géotechnique - Ouvrages -Structures*, Lecture Notes in Civil Engineering 8,
DOI 10.1007/978-981-10-6713-6_17

over displacement. Its value is related to the modulus of subgrade reaction of the soil base $k_s$ which can be determined by an in situ plate loading test, a consolidation test, a triaxial test or a CBR test as discussed in (Bowles 1988; Dutta and Roy 2002; Terzaghi and Peck 1957; Verruijt 2001). By using the Winkler's model, the gained internal forces seem to be closer to the real behaviour of the building structure. However, the Winkler's model has some limitations as follows. Firstly, the vertical displacement at a node depends only on the reaction force applied to this node; secondly, the soil base is assumed to behave as a liquid; and thirdly, the spring stiffness is a constant. Moreover, the evaluation of the modulus of subgrade reaction is relatively difficult. Its value depends not only on the soil stiffness but also on the geometry and the stiffness of the plate. Although several attempts have been made to overcome these shortcomings by using a nonlinear modulus of subgrade reaction (Chandra et al. 1987; Witczak et al. 1995) or using an improved version of Winkler's model where individual springs are connected together, the displacement field calculated with this approach does not match the settlement of the soil base.

Another alternative is to model the whole building structure by using frame element and the soil base around it by using plane finite element, where a non-linear behaviour of the soil base can be considered by using a modulus of elasticity depending on stress level (Noorzaei et al. 1993; Shoaei et al. 2015). For a more sophisticated modelling, the infinite plane element is used to define the semi-infinite soil base media (Viladkar et al. 1991). The interface between the structure and the soil base can be modelled by using contact conditions or treated with the aid of some special techniques as summarised in (David et al. 2015). The analysis takes much more memory and time than a classical calculation, where only frame element is used. Therefore, a frame-based modelling coupled with a simple static foundation–soil base interaction is needed and is the main objective of this paper. The sought formulation adds a foundation–soil base interaction laws into the classical formulation of the frame–based finite element modelling, which should fulfil the following conditions: (i) the vertical displacement of the foundation must be exactly the consolidated settlement of the soil base, (ii) the resultant of the net foundation pressure that causes the settlement and the reaction forces that apply to the building structure must be exactly balanced. While the dynamic interaction is an interesting topic, it is out of the scope of this study and will not be discussed hereafter.

## 2 Modelling the Interaction Between a Shallow Foundation and Soil Base

Let $\mathbf{u}$ be the vector of nodal displacements of the building structure, $\mathbf{f_p}$ the vector of normal (soil base) reaction forces acting upon a foundation of the building structure. Let $\mathbf{S}$ denote the vector of foundation settlements. One can represent the interaction between the building structure and soil base by a relationship between the displacements of foundation and normal reaction forces of soil base by a function of $R(u, p) = 0$ (see also Fig. 1). Let $e$ be the void ratio at a point of the soil base and $\sigma$ the vertical normal stress at that point. There is a relationship between $e - \sigma$ named the pressure-void ratio curve, which can be determined by laboratory tests. In most cases,

one can assimilate this curve by using a polynomial function of $\sigma$—namely, $e = \sum_{i=0}^{n} a_i \cdot \sigma^i$ where $a_i$ are fitting coefficients. The relationship between the vertical displacement of a foundation and the normal reaction force can be described by the following normal contact condition Eq. (1). The interested readers are invited to consult the works of Laursen (2003), Wriggers (2006) and Le van and Nguyen (2009) for more detailed presentations on contact problem.

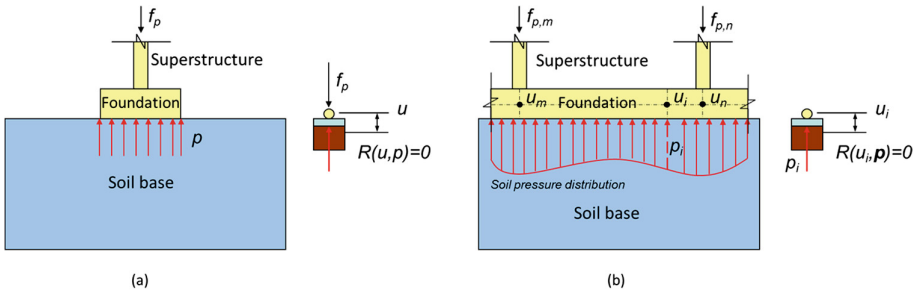


**Fig. 1.** Static foundation–soil base interaction model. (a) Isolated footing. (b) Spread footing.

$$\begin{cases} \text{If } u \le 0, \text{ there is contact between foundation and soil, } f_p \ge 0 \\ \text{If } u > 0, \text{ there is not contact, } f_p = 0 \end{cases} \tag{1}$$

If there is contact, the vertical displacement of foundation must equal the settlement. In case of no contact occurred, the normal reaction force must be zero. The following equation is equivalent to the statement in Eq. (1)

$$\begin{cases} s + u = 0, \text{ if } u \le 0 \\ p = 0, \text{ if } u > 0 \end{cases} \tag{2}$$

where $s \ge 0$ is the settlement, $p = f_p/(\text{area of foundation})$ is the average normal contact pressure. According to the Vietnam Building Code TCXD 45-78, the settlement can be calculated by

$$s = \sum_i \frac{e_{i1}(\sigma_{bt}) - e_{i2}(\sigma_{gl}(p) + \sigma_{bt})}{1 + e_{i1}(\sigma_{bt})} \Delta z_i \tag{3}$$

where $\sigma_{bt}$, $\sigma_{gl}$ are the normal stress resulted from the self-weight of soil and the effective normal stress caused by the net foundation pressure at $i^{th}$ sub-layer, respectively; and $\Delta z_i$ is the thickness of $i^{th}$ sub-layer. Interested readers can refer to the books of soil mechanics, e.g. (Bowles, 1988; Terzaghi and Peck, 1957; Verruijt, 2001) for more comprehensive presentations on this issue. Substituting Eq. (3) into Eq. (2) results in the following static foundation–soil base interaction law (Nguyen and Nguyen, 2012)

$$\begin{cases} \sum\limits_i \frac{e_{i1}(\sigma_{bt}) - e_{i2}(\sigma_{gl}(p) + \sigma_{bt})}{1 + e_{i1}(\sigma_{bt})} \Delta z_i + u = 0, \text{ if } u \leq 0 \\ p = 0, \text{ if } u > 0 \end{cases} \tag{4}$$

The normal contact condition (4) is written for the interaction of an isolated footing and its soil base. The extension of Eq. (4) to the interactions of a spread footing or a raft footing and their soil base can be made in a straightforward manner. Combining Eq. (4) with the local equilibrium equation, the material constitutive law and the limit conditions results in the strong formulation of the structure-foundation-soil base interaction problem as follows:

- Local equilibrium equation

$$div\boldsymbol{\sigma} + \rho\mathbf{f} = 0 \tag{5}$$

  where $\boldsymbol{\sigma}$ is Cauchy stress tensor, $\rho$ is density mass and $\mathbf{f}$ is body force;
- Deformation-displacement relation

$$\boldsymbol{\varepsilon} = \frac{1}{2}(\mathbf{grad}.\mathbf{u} + \mathbf{grad}^T.\mathbf{u}) \tag{6}$$

  where $\boldsymbol{\varepsilon}$ is linear strain tensor and **grad** is gradient operator;
- Material behaviour law $\boldsymbol{\sigma} = function(\boldsymbol{\varepsilon})$;
- Limit conditions

$$\begin{cases} \mathbf{u} = \overline{\mathbf{u}} \text{ on Dirichlet boundary } (S_u) \\ \boldsymbol{\sigma}.\mathbf{n} = \overline{\boldsymbol{\sigma}} \text{ on Neumann boundary } (S_t) \end{cases} \tag{7}$$

  where $\overline{\mathbf{u}}$ and $\overline{\boldsymbol{\sigma}}$ are the prescribed displacement and traction, respectively; and $\mathbf{n}$ is the outward unit normal vector;
- Interaction conditions: on the boundary $S_c = S \backslash S_u \cup S_t$

$$\begin{cases} \sum\limits_i \frac{e_{i1}(\sigma_{bt}) - e_{i2}(\sigma_{gl}(p) + \sigma_{bt})}{1 + e_{i1}(\sigma_{bt})} \Delta z_i + u_i = 0, \text{ if } u_i \leq 0 \\ p = 0, \text{ if } u_i > 0 \end{cases} \tag{8}$$

  where $(\boldsymbol{\sigma}.\mathbf{n}).\mathbf{n} = p$. The Eqs. from (5) to (7) are of classical continuum mechanics. The interested readers may consult (Sadd 2005; Timoshenko and Goodier 1951) for a complete presentation.

## 3 Finite Element Implementation

Within the limits of small deformations and elastic behaviour, the discretization of the local equilibrium equation is classical and gives rise to (Crisfield 1997; Zienkiewicz and Taylor 2000)

$$\mathbf{R}_u(\mathbf{u},\mathbf{p}) = \mathbf{K}.\mathbf{u} - \mathbf{F} - \mathbf{F}_p = \mathbf{0} \tag{9}$$

While the stiffness matrix $\mathbf{K}$ and the vector of nodal forces $\mathbf{F}$ are classical terms, the new term $\mathbf{F}_p$ is a result of the interaction of structure and soil, which is named as the vector of contact forces and is calculated by $\left(\mathbf{F}_p\right)_i = p_i \times (\text{area of } i^{th} \text{ foundation})$. Without loss of generality, let us assume that all foundations are circular and the value of vector $\mathbf{F}_p$ is $\left(\mathbf{F}_p\right)_i = \pi r_i^2.p_i$ where $r_i$ is the radius of $i^{th}$ foundation. The finite element discretization of Eq. (8) can be performed in a similar manner and gives rise to

$$\{\mathbf{R}_p(\mathbf{u},\mathbf{p})\}_i = \begin{cases} \sum\limits_k \frac{e_{k1}(\sigma_{bt}) - e_{k2}(\sigma_{gl}(p_i) + \sigma_{bt})}{1 + e_{k1}(\sigma_{bt})} \Delta z_k + \mathcal{L}_{ji} u_j = 0, \text{ if } \mathcal{L}_{ji} u_j \le 0 \\ p_i = 0, \text{ if } \mathcal{L}_{ji} u_j > 0 \end{cases} \tag{10}$$

where $\mathcal{L}$ is a connection matrix such that $\mathcal{L}_{ij} = 1$ if the displacement $u_i$ is related to the normal pressure $p_j$, $\mathcal{L}_{ij} = 0$ elsewhere. The nonlinear equation system formed by Eqs. (9)–(10) can be resolved iteratively by the Newton-Raphson scheme with the aid of the tangent stiffness matrices determined as follows (Crisfield 1997). Let us assume that $\mathbf{R}_u(\mathbf{u},\mathbf{p})$ and $\mathbf{R}_p(\mathbf{u},\mathbf{p})$ are differentiable (or at least piecewise differentiable). The values of $\mathbf{R}_u$, $\mathbf{R}_p$ at the i$^{th}$ iteration can be estimated using the Taylor's decomposition and by forcing the value of these vectors to be zero, one has

$$\begin{cases} \mathbf{K}_{uu}.\Delta\mathbf{u} + \mathbf{K}_{up}.\Delta\mathbf{p} = -\mathbf{R}_u^{i-1}(u,p) \\ \mathbf{K}_{pu}.\Delta\mathbf{u} + \mathbf{K}_{pp}.\Delta\mathbf{p} = -\mathbf{R}_p^{i-1}(u,p) \end{cases} \tag{11}$$

where the superscript $i$ of the a term at i$^{th}$ iteration is neglected for the sake of brevity and the tangent stiffness matrices are those following:

$$\mathbf{K}_{uu} \equiv \frac{\partial \mathbf{R}_u}{\partial \mathbf{u}} = \mathbf{K};\ [\mathbf{K}_{up}]_{ij} \equiv \frac{\partial R_{ui}}{\partial p_j} = \pi \mathcal{L}_{ij}.r_j^2 \text{ (no summation)} \tag{12}$$

$$[\mathbf{K}_{pu}]_{ij} \equiv \frac{\partial R_{pi}}{\partial u_j} = \begin{cases} \mathcal{L}_{ji}, \text{ if } \mathcal{L}_{ji} u_j \le 0 \\ 0, \text{ if } \mathcal{L}_{ji} u_j > 0 \end{cases};\ [\mathbf{K}_{pp}]_{ij} = \begin{cases} \frac{\partial}{\partial p_j} \sum\limits_0^{h_{gl}} \frac{e_{i1} - e_{i2}(\sigma(p_i))}{1 + e_{i1}} \Delta z, \text{ if } \mathcal{L}_{ij} u_i \le 0 \\ = \delta_{ij}, \text{ if } \mathcal{L}_{ij} u_i > 0 \end{cases} \tag{13}$$

## 4 Numerical Results

This section shows the calculation results carried out on the basis of the previous formulation. The results are compared with the solution of Winkler's model or that resulted from a classical analysis for validation purpose. All numerical results have been obtained using a homemade finite element code developed under the Matlab environment.

### 4.1 2-D Frame on Isolated Footing

In this example, we consider a two-span two-story plane frame related to the soil base by 3 isolated footings. All spans have the same width of 5 m and all stories have the same height of 3.5 m. The nodes numbered 1, 2 and 3 are related to the soil base using the foundation–soil base interaction model as illustrated in Fig. 2(a). The properties of the material are $E = 3 \times 10^{10}\mathrm{N/m^2}$, $v = 0.2$. All beams and columns have the same cross sections with dimensions $0.2\,\mathrm{m} \times 0.4\,\mathrm{m}$. A uniform distributed load of $39250\,\mathrm{N/m}$ and two concentrated loads of 78500 N are applied perpendicularly to each beam as indicated in Fig. 2(a).

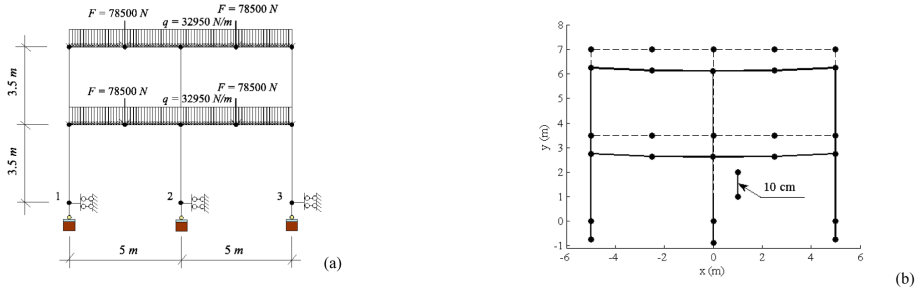


**Fig. 2.** 2-D frame structure on isolated footings. (a) Initial configuration. (b) Deformed configuration.

All the footings are assumed to have circular shape. The diameters of the end footings and the central footing are 2.2 m and 2.6 m, respectively. The soil characteristics are those following: weight per unit volume $\gamma = 18000\mathrm{N/m^3}$; pressure-void ratio curve $e = -(4 \times 10^{-9}).\sigma^3 + (4 \times 10^{-6}).\sigma^2 - 0.0012\sigma + 0.8308$.

The calculation results are summarized as follows. The displacement of the end footings is −0.073816 m and that of the central footing is −0.086667 m. The normal reaction forces are 316725.7626 N at the end footings and 465548.4749 N at the central footing. With these normal reaction forces in hand, we used the Eq. (3) to calculate the settlements and found that the settlements are equal to the displacements of footings to the 7th digit. The discrete equation system is accurately rendered.

It can be seen that two bending moment diagrams represented in Fig. 3 are quite different. Generally, the bending moment (in absolute value) calculated with the proposed method is greater than that calculated with the classical method. Interestingly, the hogging moment of the beam is highest at the locations of the end columns instead of at the central column location—namely, the hogging moments at the central column location increase about 2.5 times compared to those obtained with the classical calculation whereas the hogging moments at the location of the end columns increase about 1.5 times. The sagging moments at the middle of spans are almost unchanged. This observation can be explained by the fact that the central footing settles more than the end footings by a value of 0.012851 m. This unequal settlement causes the

additional part to the bending moment in the beams. This is also the reason that the normal force of the central column decreases while those of the end columns increase compared to those obtained with the classical calculation as can be seen in Fig. 4.

**Fig. 3.** Bending moment diagram of a 2-D frame on isolated footings. (a) Calculation with the proposed model. (b) Classical calculation.

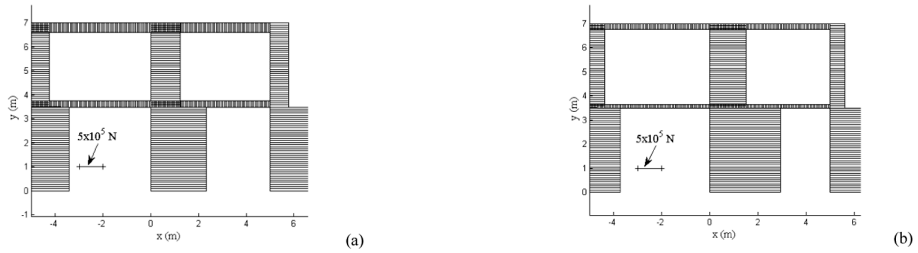


**Fig. 4.** Normal force diagram of a 2-D frame on isolated footings. (a) Calculation with the proposed model. (b) Classical calculation.

### 4.2 2-D Frame on Spread Footing

In this example, we consider a two-span two-story plane frame lying on a spread footing as shown in Fig. 5. The widths of spans are 3 m and 5 m, respectively, and all the stories have the same height of 3.5 m. In order to assess the efficient of the proposed model, an extreme loading are considered so that there will be a partial loss of contact between the foundation and soil base as indicated in Fig. 5(a). All beams and columns have the same cross sections with dimensions 0.2 m × 0.2 m while the spread footing has a cross section of an inverse T with dimensions: 0.3 m in height, 1 m in width and 0.2 m in thickness.

The structure, the footing and the soil base have the same properties of material as those in the previous example. In order to analyse the behaviour of the structure and the footing simultaneously with the deformation of the soil base, a foundation–soil base interaction model was assigned to each node of the spread footing as shown in Fig. 5(a). Moreover, tangential contact conditions were checked at every node of the spread footing using the penalty method as follows:

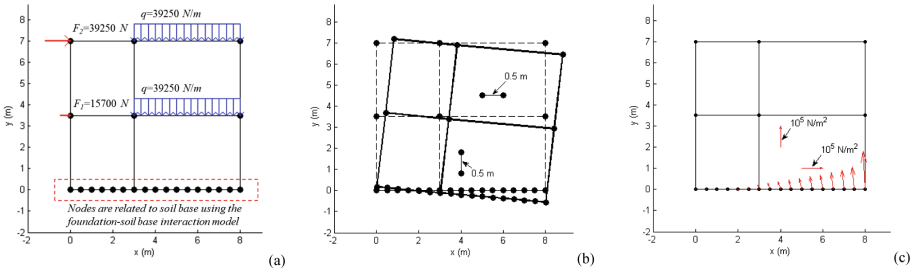


**Fig. 5.** 2-D frame structure on a spread footing. (a) Initial configuration. (b) Deformed configuration. (c) Soil base reaction pressure.

$$\begin{cases} \cdot \text{ if } u \le 0, \begin{cases} f_s = \varepsilon_T.\Delta u_T, & \text{if } \varepsilon_T.\Delta u_T \le \mu.p + a_T \text{ (stick)} \\ f_s = \mu.p + a_T \text{ (slip)} \end{cases} \\ \cdot \text{ if } u > 0, f_s = 0 \end{cases} \tag{14}$$

where $f_s$ is tangential contact pressure, $\varepsilon_T = 10^6 \text{N/m}^3$ is a penalty coefficient, $\Delta u_T$ is the horizontal displacement of a node at the foundation and $\mu = 0.3$; $a_T = 10^3 \text{N/m}^2$ are friction coefficient and adhesion between the foundation and soil base. It is worth noted that the settlement of the soil base at a point depends on the soil base reaction pressure not only at that point but also at the other remaining points. The calculation results are summarized as follows.

The spread footing is lifted up by a distance of 0.0886 m at the leftmost node and settles 0.2832 m at the rightmost node. The average settlement of the foundation is therefore 0.0973 m and the inclination of the building is 3.28°. The distribution of soil base reaction pressure acting upon the spread footing is drawn in Fig. 5(c). It can be seen that the contact pressure is equal to zero at the four leftmost nodes where no contact occurs while the contact pressure has the highest values at the rightmost nodes.

It can be proved that the resultant of the reaction pressure is equilibrated by the external loading and the gained settlement of the footing is in good agreement with that resulted from an analytical calculation (0.0918 m) using the average value of soil base pressure. The discrete equation system is again accurately rendered. The bending moment diagrams obtained with the proposed model, the classical calculation and that resulted from the calculation using Winkler's model are drawn (at the same scale) in Fig. 6. It can be observed that the partial loss of contact does not have a significant effect on the bending diagrams of the building structure including the spread footing beam. This can be explained by the fact that the differences between the settlements are small because of the better load transfer capacity of the spread footing. However, there is still a relative difference in the bending moment diagram of the spread footing beam—namely, the hogging moment obtained with the proposed model is slightly smaller than that obtained with the Winkler's model while the sagging moment is slightly higher.

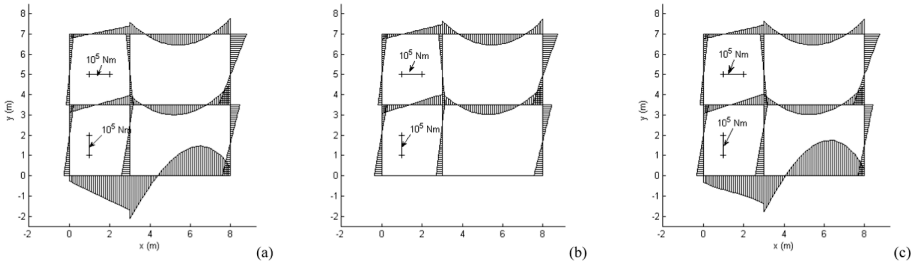


**Fig. 6.** Bending moment diagram of a 2-D frame on a spread footing. (a) Calculation with the proposed model. (b) Classical calculation. (c) Calculation with the Winker model

## 5 Conclusions

The proposed model proves to be efficient in modelling the static interaction between a shallow foundation and the soil base. From the various results in the earlier section, the deformation of the soil base has an influence on the behaviour of the building structures including the footing beam. The effect of foundation–soil base interaction is more significant when isolated footings are used. Although the deformation of soil base does not affect much the behaviour of the superstructure lying on a spread footing, it still has an influence on the behaviour of the footing beam. The new point of the method proposed in this paper is that the soil characteristics are considered in the calculation of the building structure, which gives rise to the followings distinguished characteristics when compared to either the classical calculation or the Winkler's model: (i) the vertical displacements of the foundation are exactly the settlements of the soil base and (ii) the internal forces resulted from the unequal settlement are included in the analysis result.

## References

Bowles, J.E.: Foundation Analysis and Design. McGraw-Hill, Singapore (1988)

Chandra, S., Madhav, M.R., Iyengar, N.G.R.: A new model for nonlinear subgrades. Math. Model. **8**, 513–518 (1987). doi:10.1016/0270-0255(87)90635-X

Crisfield, M.A.: Nonlinear Finite Element Analysis of Solids and Structures. Wiley, New York (1997)

Dang, T.: Finite element method for the simultaneous calculation of frame structure and foundation. The Publisher of Science and Engineering, Hanoi (1999). (in Vietnamese)

Shoaei, M.D., Huat, B.B.K., Jaafar, M.S., Alkarni, A.: Soil-framed structure interaction analysis - a new interface element. Lat. Am. J. Solids Struct. **12**(2), 226–249 (2015). doi:10.1590/1679-78251130

Dutta, S.C., Roy, R.: A critical review on idealization and modeling for interaction among soil–foundation–structure system. Comput. Struct. **80**, 1579–1594 (2002). doi:10.1016/S0045-7949(02)00115-3

Hain, S.J., Lee, I.K.: Rational analysis of raft foundation. J. Geotech. Eng. Div. **100**, 843–860 (1974). ASCE

Laursen, T.A.: Computational Contact and Impact Mechanics: Fundamentals of Modeling Interfacial Phenomena in Nonlinear Finite Element Analysis. Springer, Berlin (2003)

Le van, A., Nguyen, T.T.H.: A weighted residual relationship for the contact problem with Coulomb friction. Comput. Struct. **23–24**, 1580–1601 (2009). doi:10.1016/j.compstruc.2009.08.013

Lee, I.K., Brown, P.T.: Structure foundation interaction analysis. J. Struct. Div. **98**, 1413–1431 (1972). ASCE

Nguyen, H.T.T., Nguyen, K.T.: A simple model for calculation of superstructure-soil interaction. In: Nguyen, X.H., Nguyen, T.T., Chau, D.T. (ed.) Proceeding of the International Conference on Advances in Computational Mechanics, Ho Chi Minh City (2012)

Noorzaei, J., Godbole, P.N., Viladkar, M.N.: Non-linear soil-structure interaction of plane frames-a parametric study. Comput. Struct. **49**(3), 561–566 (1993). doi:10.1016/0045-7949(93)90058-L

Sadd, M.H.: Elasticity: Theory, Application and Numeric. Elsevier Butterworth-Heinemann, Burlington (2005)

Terzaghi, K., Peck, R.B.: Mécanique des sols appliquées aux travaux publics et au bâtiment. Dunod, Paris (1957)

David, T.K., Krishnamoorthy, R.R., Mohamed Jais, I.B.: Finite element modelling of soil-structure interaction. J. Teknologi **79**(3), 59–63 (2015)

Timoshenko, S.P., Goodier, J.N.: Theory of Elasticity. McGraw-Hill, New York (1951)

Verruijt, A.: Soil mechanics. Delft University of Technology, Delft (2001)

Viladkar, M.N., Godbole, P.N., Noorzaei, J.: Soil-structure interaction in plane frames using coupled finite-infinite elements. Comput. Struct. **39**(5), 535–546 (1991). doi:10.1016/0045-7949(91)90062-Q

Witczak, M.W., Xicheng, Q., Mirza, M.W.: Use of nonlinear subgrade modulus in AASHTO design procedure. J. Transp. Eng. **121**(3), 273–282 (1995). doi:10.1016/0148-9062(95)99680-v. ASCE

Wriggers, P.: Computational Contact Mechanics. Springer, Berlin (2006)

Zienkiewicz, O.C., Taylor, R.L.: The Finite Element Method. Butterworth-Heinemann, Boston (2000)

# Numerical Analysis of Hybrid Walls Using FEM

Van Toan Tran(✉)

Thuyloi University, Hanoi, Vietnam
tranvantoan@wru.vn

**Abstract.** The article presents the numerical study dealing with the behavior and the real load bearing capacity of hybrid walls by Abaqus software. Especially identify the bearing capacity behavior of the composite steel-concrete walls with several fully encased steel profiles (hybrid walls) while the materials were yielded until failure. Structural hybrid steel-concrete walls, material constitutive law for steel and concrete, load schematic, element types, numerical solution controls, interactions, steel-concrete bond, composite behavior and mechanical contact, … will be described in detail. It is expected that nonlinear FEM analysis can give more details on behavior as well as on shear and bending resistance mechanisms until failure of the hybrid walls. The nonlinear FEM analysis able to predict well specimen strength, maximum displacement, strains and stress distribution, crack pattern and failure modes. The reliability of this method was evaluated by comparing the analysis results with the experimental results.

**Keywords:** Numerical analysis · Hybrid wall · Profile · Connection · Simple bending · Plastic · Failure

## 1 Introduction

Nowadays, finite element method (FEM) is widely adopted as a potential numerical method to investigate the behavior of composite steel-concrete structures because of many achieved advances in numerical techniques, material models and computer performance. Especially some various concrete models and sophisticated contact elements have been implemented in commercial FEM packages that make modeling and analysis become much easier.

One of the most FEM software used nowadays is ABAQUS software. Abaqus has several built-in models to predict the behavior of materials as well as the provision to add user defined models. The program offers a wide range of options regarding element types, material behavior and numerical solution controls, as well as graphic user interfaces, auto-meshes, sophisticated post-processors and graphics to speed the analyses (David et al. 2012).

In this article, this commercial software is employed to develop reliable three-dimensional finite element model for the hybrid steel-concrete wall specimens of the experimental program. It is expected that nonlinear FEM analysis can give more details on behavior as well as on shear and bending resistance mechanisms until failure of test specimens in our experimental program. The nonlinear FEM analysis capable of predicting well specimen strength, maximum displacement, crack pattern and failure modes.

© Springer Nature Singapore Pte Ltd. 2018
H. Tran-Nguyen et al. (eds.), *Proceedings of the 4th Congrès International de Géotechnique - Ouvrages -Structures*, Lecture Notes in Civil Engineering 8,
DOI 10.1007/978-981-10-6713-6_18

## 2 Description of Wall Test Specimens

The experimental program consists of six 2:3 scale wall specimens are composite wall with three encased steel profiles (hybrid wall). All specimens had the same size, geometry and longitudinal reinforcing bar arrangements. The primary differences between six specimens were the type of the structural steel-concrete connection and the stirrup spacing. Details evaluated in the test include the contributions of the steel profiles, shear studs, stiffeners, bond and stirrup spacing to the bending and shear resistance. Figure 1 shows the design details of all the six specimens of hybrid walls. All specimens consisted of RC wall that had 5 m length, 25 × 90 cm rectangular cross-section and were reinforced with eight 20 mm diameter vertical reinforcing bars (Grade B). The horizontal reinforcement consisting of 14 mm and 6 mm reinforcing bars was made in form of stirrups. The reinforcing bar arrangement is the same in all specimens except the stirrup spacing which was 200 mm in BW, CW and DW specimens and 100 mm in BW-HC, CW-HC and DW-HC specimens. Moreover, they had additional three HEB100 which were totally encased into the concrete with shear stud connectors between the concrete and the steel profiles for the CW and CW-HC specimens (50 × 3 Nelson S3L16-75 mm, 200 mm spacing), with stiff connectors

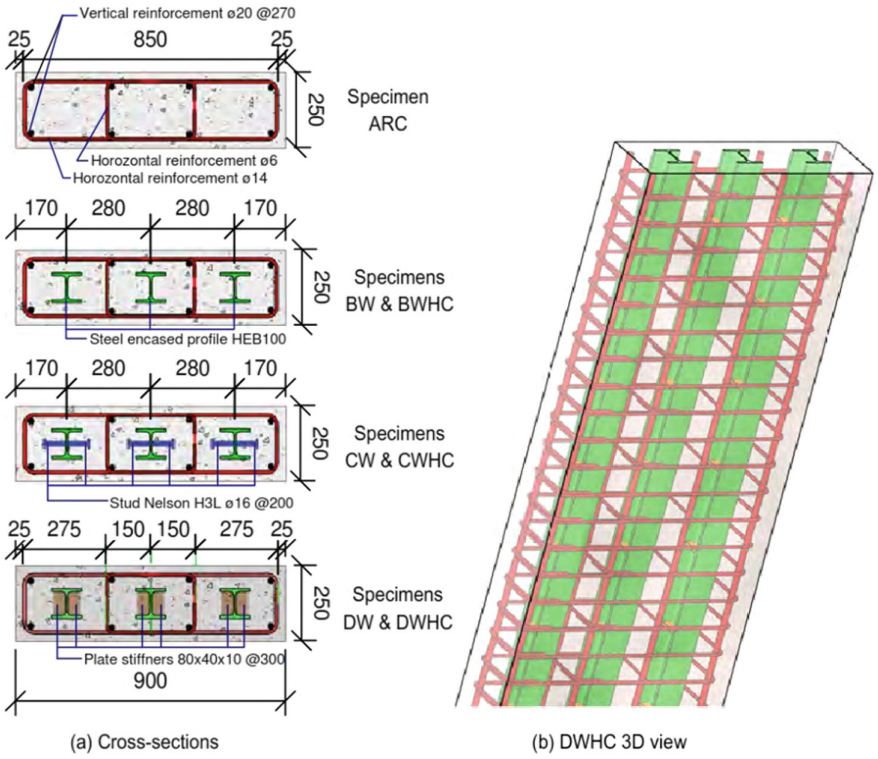


**Fig. 1.** Details of the test specimens

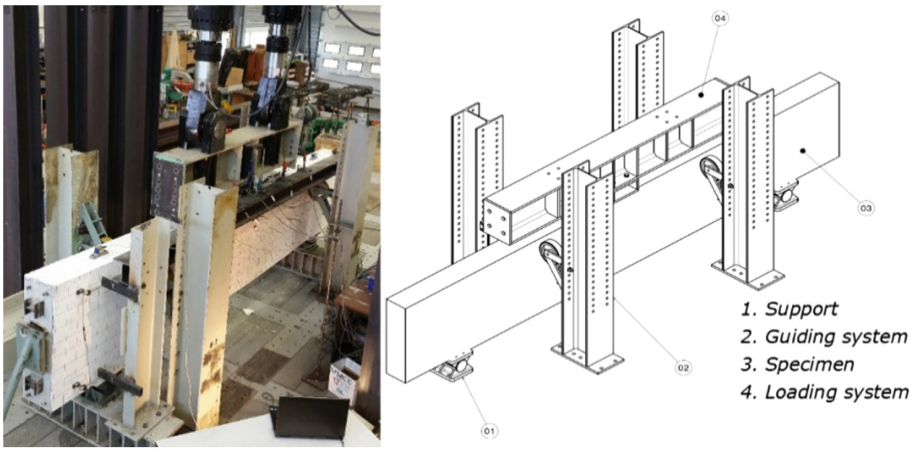


**Fig. 2.** Test setup

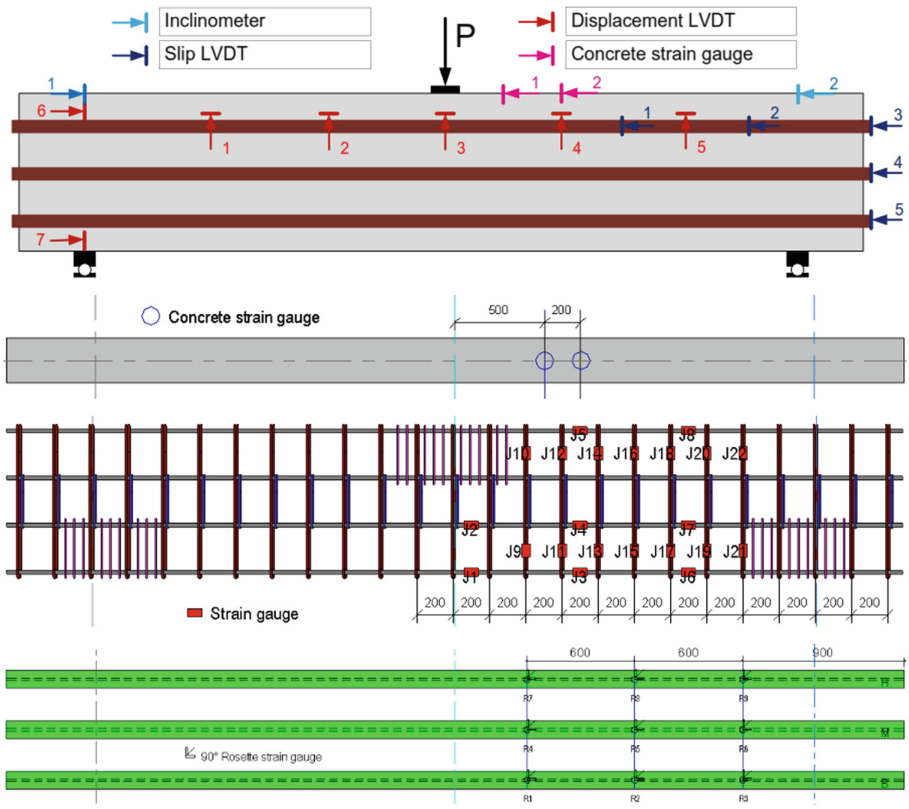


**Fig. 3.** Detailed arrangement of measuring devices

between the concrete and the steel profiles for the DW and DW-HC specimens (30 × 3 plate stiffeners, 10 mm thickness, 300 mm spacing) and without connectors for the BW and BW-HC specimens.

In the test, the solution of keeping the walls in simple cantilever form is not possible for the test setup to be shown in Fig. 2. The third-point flexural beam test configuration was adopted to evaluate the resistance of specimens to combined bending and shear without axial force. Specimens were loaded at the mid-length by two hydraulic actuators (1500 kN capacity each). The actuators were operated in displacement control, with each actuator having the same displacement at any instant of time. Pinned boundary conditions at each end of the specimens were simulated by two supports. No restraint was provided against rotation along any axis.

Several different instruments were used in the testing of the specimens. The arrangement of the instrumentation is presented in Fig. 3. The data acquisition devices include: *5 LVDT* placed along the specimen length (2 at middle), measuring the deflection shape, *5 LVDT* measuring the slips at the interface concrete-steel profile, *2 LVDT* measuring the horizontal displacements at the specimen end, *2 inclinometers* (devices that measure changes in angle) measuring the rotations at specimen's ends, *2 concrete strain gauges* pasted to the top concrete surface, *22 strain gauges* pasted to the reinforcement steel and *9 strain gauge rosettes 0°–45°–90°* pasted to steel profiles.

## 3 Finite Element Model

We have simulated 3D models for 6 hybrid walls (namely BW, BW-HC, CW, CW-HC, DW, DW-HC as described above) in the Abaqus software. Due to the symmetry of the specimen geometry and loading, in order to save the calculation time, only half of the specimen was modeled as shown in Fig. 4. Four components of specimen (concrete, rebars, steel profile and connector) are modeled separately and assembled to make a complete specimen model.

### 3.1 Type of Finite Elements

The hybrid walls proposed for finite element modeling embody situations of material discontinuity, yielding, stress concentration, contact and composite behavior. These complex 3D phenomena are reproduced by adopting hexahedra solid elements (David et al. 2012), which are used to model majority of the parts of the specimens. Exception is the ordinary reinforcement in the concrete walls, where truss elements are used. In ABAQUS, the finite elements C3D8 (8 nodes) and C3D20 (20 nodes) are continuum stress/displacement 3D solid finite elements of first and second order, respectively, either with reduced or full integration. The 8-node element with reduced integration is chosen for the general numerical simulations. A sensitivity analysis is performed with respect to the element type to check the required mesh density for application. For this purpose, the second order element (C3D20R) with reduced integration is used to obtain the "correct" solution. The truss element (T3D2) used to model the ordinary reinforcement is a 2-node linear 3D truss element that can only transmit axial forces.

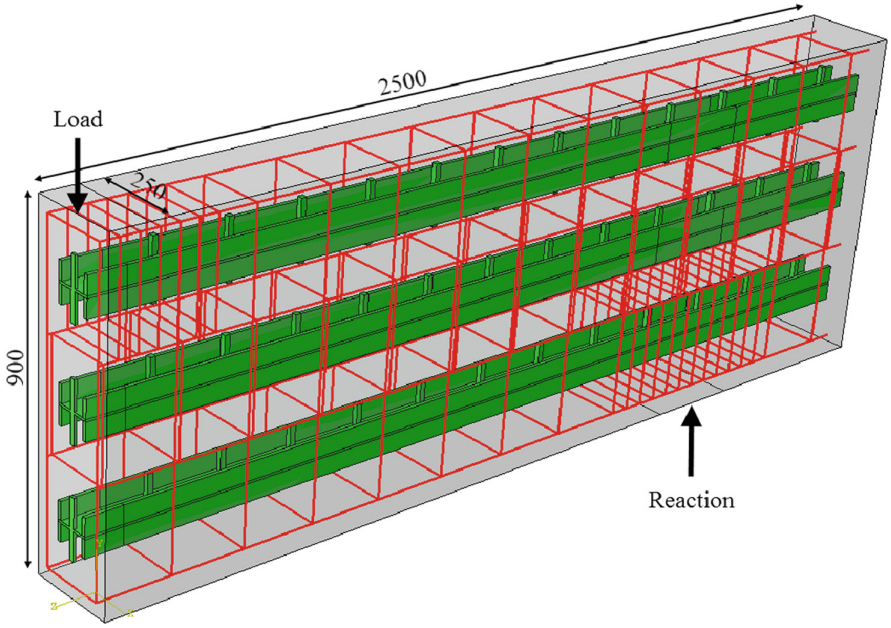


**Fig. 4.** Model of a half hybrid wall specimens

### 3.2 Finite Element Mesh

Figure 5 shows the meshing of the FE model for the concrete wall, rebar, steel wall and headed studs. The element size is 0.025 m for the elements of concrete wall, steel profiles, reinforcement bars and shanks of the shear connectors, plate stiffeners and 0.005 m for a head of the shear connectors. The head and the stud of the connectors are approximated by a hexagon.

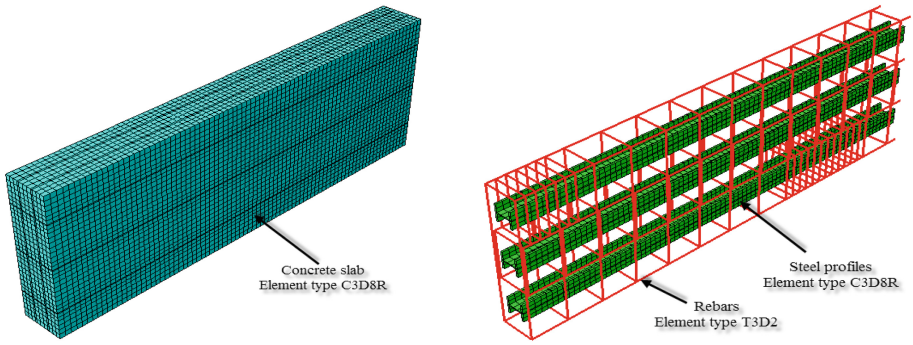


**Fig. 5.** Finite element type and mesh

### 3.3 Constitutive Laws and Mechanical Properties

The constitutive laws used to model the mechanical behavior of the different materials and interactions considered include five types: Concrete Damage Plasticity for the concrete slab and Isotropic Material for the structural steel, the rebars and connectors. The Concrete Damage Plasticity was chosen because it is simpler to model and more stable for the numeric calculation.

**Table 1.** Material parameter of CDP model for concrete of $f_{cm}$ = 30 MPa

| **Density** | | **Parameters of Concrete Damaged Plasticity model** | | |
|---|---|---|---|---|
| P (tonne/mm$^3$) | 2.4x10$^{-9}$ | Dilation angle | | 38° |
| Elasticity | | Eccentricity | | 0.1 |
| E (MPa) | 33346 | $f_{b0}/f_{c0}$ | | 1.16 |
| ν | 0.2 | K | | 0.67 |
| | | Viscosity Parameter | | 0.0001 |
| **Compressive behavior** | | **Tensile behavior** | | |
| Yield stress (MPa) | Inelastic strain | Yield stress (MPa) | Displacement (mm) | Damage |
| 12.80 | 0 | 2.870 | 0 | 0 |
| 19.40 | 0.00016 | 2.428 | 0.0225 | 0.492 |
| 24.37 | 0.00037 | 1.706 | 0.0662 | 0.802 |
| 28.86 | 0.00066 | 1.192 | 0.1084 | 0.904 |
| 30.00 | 0.00102 | | | |
| 28.41 | 0.00156 | | | |
| 23.77 | 0.00219 | | | |
| 16.27 | 0.00291 | | | |

The Stress-Displacement curve is defined by Lubliner et al. (1989) and by Lee and Fenves (1988) according to (David et al. 2012). For the five constitutive parameters ($\psi$ – dilatation angle; $\varepsilon$ – flow potential eccentricity; $f_{b0}/f_{co}$ – ratio of initial equibiaxial compressive yield stress to initial compressive yield stress; $k$ – ratio of second stress invariant on the tensile meridian; $\mu$ – viscosity parameter) required to complete the definition of the constitutive model, no information was available from the experimental tests and therefore default values (David et al. 2012; José et al. 2013) were used (see Table 1). Design concrete class is the C30 (Eurocode 2 2004; Eurocode 4 2005).

### 3.4 Relation for Steel Profiles and Rebars and Connectors Behavior

To model the behavior of structural steel and reinforcement, the classical isotropic material law that implements the von Mises plasticity model (isotropic yielding) is used. For the generality of the steel parts, an elasto-plastic behavior with hardening is assumed. For the steel profiles and rebars, the true stress–strain ($\sigma_{true} - \varepsilon_{true}$) material curve available from the experimental tests is considered.

The steel profile and the steel plate stiffener grade are S460. The steel longitudinal rebar class, the steel stirrups class and the steel shear stud class are S500B (Eurocode 2 2004; Eurocode 4 2005; ACI-318 2005; AISC2010 2010). The material behavior was considered as bilinear stress-strain diagram with hardening until $\varepsilon_{lim} = 0.05$. And their detailed values are presented in Table 2.

**Table 2.** Structural and reinforcing steel strenghts

| Item | $f_y$ (MPa) | $f_u$ (MPa) | $f_u/f_y$ | E (GPa) | Applying |
|---|---|---|---|---|---|
| HEB100 | 462.7 | 583.5 | 1.26 | 214.45 | Profiles, plate stiffener |
| ϕ20 mm bars | 383.91 | 542.62 | 1.41 | 210.74 | Longitudinal rebar |
| ϕ14 mm bars | 633.26 | 656.34 | 1.04 | 207.46 | Stirrups class, shear stud |

### 3.5 Steel Reinforcement-Concrete Interaction

In ABAQUS, the 3D modeling of reinforced concrete may be performed using steel rebar (truss element (2-nodes)), steel profile, steel shear stud, steel plate stiffener (solid (continuum) element (8-nodes)) and all ordinary reinforcement embedded or not in the concrete. Due to the importance of the steel profiles and connectors reinforced in the hybrid wall, they are modeled with 3D solid elements. Therefore, modeling the interaction with perfect bond leads to excessive stresses in concrete and stiffer response of the reinforcement. Contact with cohesive behavior may be considered to model the bond behavior in the reinforcement–concrete interface. The contact and interface stresses are treated using the "hard" contact model with frictional behavior. In the "hard" contact: (i) pressure is transmitted when nodes of slave surface contact the master surface; (ii) no penetration is allowed; (iii) no limit to the pressure is assumed when the surfaces are in contact. The frictional behavior is guaranteed by the stiffness (penalty) method and the sliding conditions between bodies are reproduced with the classical isotropic Coulomb friction model. For more detailed information reference is given to (David et al. 2012; José et al. 2013).

In order to reduce the modeling time, the "real" bond behavior is only applied in regions around the steel profiles–concrete slab interface with the coefficient of friction between the steel and the concrete is assumed to be 0.45. The test BW and BW-HC the specimens were carried out without shear connectors welded to the encased steel profiles allowing however achieving the full bending resistance of the element without any apparent problem related to longitudinal shear, like slippage between concrete and steel profile. Therefore, the perfect bond is simulated for these 2 specimens. Moreover, the perfect bond model is applied in all the other parts of these reinforcement bars and for all ordinary reinforcement.

### 3.6 Boundary Conditions

For the application of the support conditions, all the nodes at the support location (concrete reaction surface) in the opposite direction of loading are restricted from moving in the Y direction to resist the flexion load. All the nodes of the concrete wall, steel profile flanges and the rebar web, that lie on the opposite symmetry surface are restricted due to symmetry from moving in the Z direction and rotating in the Y and Z direction. All the concrete nodes and steel profile flange nodes that lie on the perpendicular to symmetry surface, are restricted from moving in the X direction and rotating in the Y and Z direction.

### 3.7 Application of the Load

A deformation controlled load is applied at the mid-span of the hybrid wall, i.e. above the concrete load surface on the symmetrical surface as shown in Fig. 4. Load can be applied using the arc length method. An initial increment of displacement is given on the data line and the initial load proportionality factor is assigned to this initial increment using the automatic incremental scheme.

## 4 Numerical Analyse Results

The analysis results are compared with the experimental results. The load bearing capacity analysis and failure modes have been investigated.

### 4.1 Load-Deflection Response

The load-displacement curves obtained from the FE model for all test specimens are compared to the experimental ones in Fig. 6. It can be observed that the numerical load-deflection behavior resembles the experimental behavior reasonably well. The numerical response is the load up to failure. It can be noticed that the stiffness of the elements obtained in the numerical analysis is higher that the stiffness obtained in the experimental tests. This difference appears firstly to the different material pattern (homogeneous in case of numerical analysis and inhomogeneous in the experimental tests) and secondly due to the different way in simulating the connection between steel profiles and concrete surrounding.

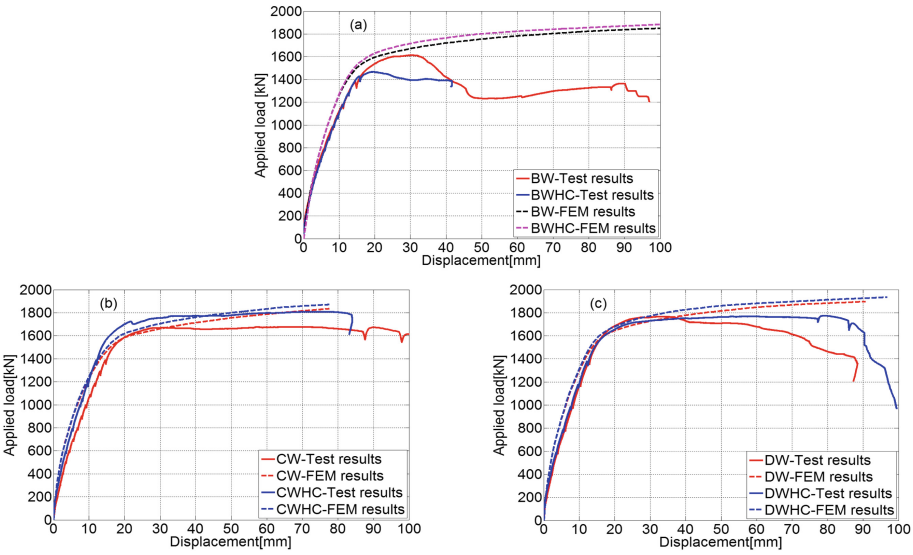


**Fig. 6.** Numerical - experimental comparison of load-displacement curves

**Table 3.** Comparative study of the load bearing capacity

| Specimen | $\Delta_{Fs}$ (mm) | Experimental | Numerical | $\frac{F_{Fs}^{Num}}{F_{Fs}^{Exp}}$ |
|---|---|---|---|---|
| | | $F_{max}^{Exp}$ (kN) | $F_{max}^{Num}$ (kN) | |
| BW | 30.0 | 1613.4 | 1730.5 | 1.07 |
| BW-HC | 19.6 | 1567.5 | 1690.4 | 1.08 |
| CW | 57.2 | 1677.9 | 1780.8 | 1.06 |
| CW-HC | 76.6 | 1809.2 | 1870.7 | 1.03 |
| DW | 33.6 | 1767.6 | 1747.2 | 0.99 |
| DW-HC | 78.8 | 1774.2 | 1910.7 | 1.08 |

Nevertheless, the values of the load bearing capacities of the elements obtained in the experimental tests (Van-Toan and Quang-Huy 2017) and those obtained in the numerical analysis are very close (1 ÷ 8% difference). Table 3 shows the load bearing capacities of the test specimens predicted by the FE model in comparison with those from the experiment (The load bearing capacity is maximum load obtained in the experimental or is load obtained in the numerical corresponding to the displacement of the experimental).

### 4.2 Crack Pattern

Figure 7 illustrates the tensile damage distribution in the concrete at two deflection level 60 mm. Note that the concrete model adopted for FEM is a continuous model therefore the cracking can not be reproduced in the discrete way as can be seen in the experiment. However, by analyzing the distribution of the tensile damage variable one can have an idea about the crack pattern at different load level. It can be observed that initial the specimens were principally damaged by flexion eect at mid-span region, after that the concrete "struts" were formed in the regions in between steel profiles. The concrete struts between upper and middle profiles were more pronounced in BW and BW-HC specimens than the other specimens. It should be noted that in the FE model of BW and BW-HC specimens the steel profiles were embedded in concrete. That means that full interaction between steel profile and concrete was assumed. Therefore the slip is prevented in BW and BW-HC specimens and that explains why the concrete between upper and middle profiles was more mobilized in tension. In other words, by preventing the slip the concrete struts are totally anchored therefore the shear effect is more active. It also explains the fact that in BW and BW-HC specimens the concrete region after the support is not damaged. In contrast, in other specimens the slip is not prevented therefore one can see the effect of the longitudinal shear which is locally active at the connector location and that makes the concrete region after the support damaged as can be seen in Fig. 7.

It can be observed in the right part of Fig. 7 and that at 60 mm of deflection the concrete damaged by shear is more pronounced, especially in BW specimen. One can see clearly the concrete struts in the region at the middle between load point and support. By regarding the direction of the tensile damaged zone one can say that the angle of the concrete struts is about 45°. This numerical observation confirms what has been observed in the experiment.

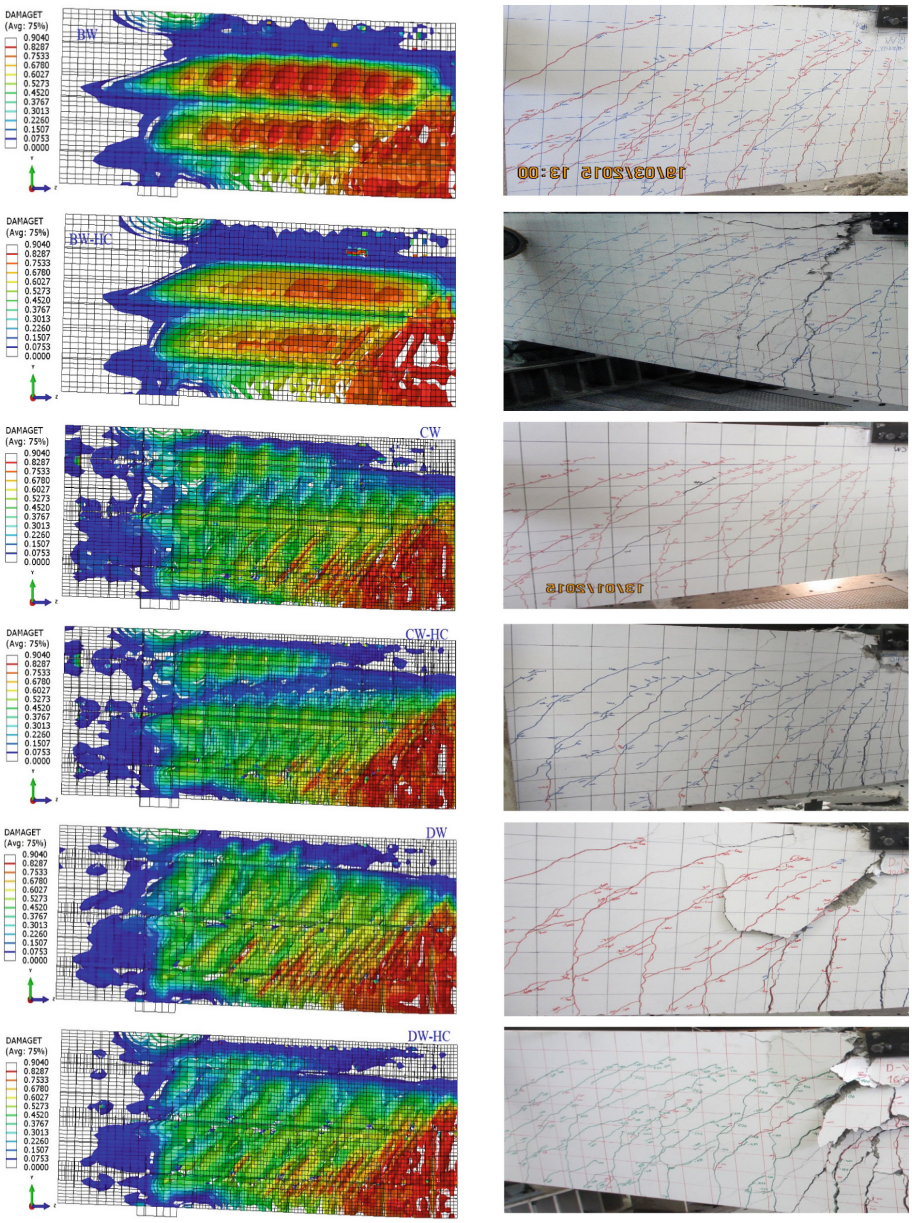


**Fig. 7.** Comparative of crack pattern in the concrete at deflection level 60 mm

The concrete confinement effect can be noticed by comparing the damage zone of BW specimen with the one of BWHC specimen. As can be seen, the concrete is indeed less damaged in the specimens where a double number of stirrups were placed to make the concrete confinement.

## 5 Conclusion

A 3D FE model has been developed in Abaqus Software to investigate the nonlinear behavior of hybrid wall. The results of the numerical analysis show that some main behaviors of the studied hybrid wall specimens such as load bearing capacity, relation of load and displacement predicted by FE model are in good agreement with test results. The developed FE model can be eventually used in the future works to perform a parametric study or to propose a design method on hybrid walls.

**Acknowledgements.** The authors gratefully acknowledge financial support by the European Commission (Research Fund for Coal and Steel) through the project SMARTCOCO (SMART COmposite COmponents: concrete structures reinforced by steel profiles) under grant agreement RFSR-CT-2012-00039.

## References

Van-Toan, T.: Etude numérique et expérimentale des murs en béton armé renforcés par plusieurs profilés métalliques totalement enrobés, Thèse, Insa de Rennes (2015)

EN 1992-1-1. Eurocode 2 - Design of concrete structures - Part 1: General rules and rules for buildings, CEN, Brussels (2004)

EN 1994-1-1. Eurocode 4 - Design of composite steel and concrete structures - Part 1.1: General rules and rules for buildings, CEN, Brussels (2005)

ACI. ACI-318 - Building code requirements for reinforced concrete, USA (2005)

ACI. AISC2010 - Specification for structural steel buildings, USA (2010)

Van-Toan, T., Quang-Huy, N.: Experimental study of hybrid walls with several fully encased steel sections. In: International Conference of the CIGOS 2017, Ho Chi Minh (2017)

David, H., et al.: ABAQUS standard user's manual Version 6.12.1, USA (2012)

Jankowiak, T., Lodygwoski, T.: Identification of parameters of concrete damage plasticity constitutive model. Found. Civil Environ. Eng. **6**, 53–62 (2005)

Girao Coelho, A., Simoes da Silva, L., Bijlaard, F.: Numerical evaluation of the behaviour of the T-Stub. J. Struct. Eng. **132**(6), 918–928 (2006)

Eligehausen, R., Popov, E., Bertero, V.: Local bond stress–slip relationship of deformed bars under generalized excitations. Report No. UCB/EERC-83/23, Earthquake Engineering Centre, University of California, Berkeley (1983)

José, H., Luís, S., Isabel, B.: Numerical modeling of composite beam to reinforced concrete wall joints - Part I: calibration of joint components. Eng. Struct. **52**, 747–761 (2013)

# Numerical Simulations of Cold-Rolled Aluminium Alloy 5052 Channel Sections in Stub Column Tests

Le Anh Thi Huynh(✉), Cao Hung Pham, and Kim J.R. Rasmussen

School of Civil Engineering, The University of Sydney,
Sydney, NSW 2006, Australia
{leanhthi.huynh, caohung.pham,
kim.rasmussen}@sydney.edu.au

**Abstract.** The paper describes finite element analyses using the program ABAQUS 6.14 of cold-rolled alluminium alloy 5052 channel sections in stub column tests. Aluminium structural members have been used considerably in not only roof systems but also primary load-bearing components due to such advantages as superior corrosion resistance, light weight, ease of maintenance, constructability and recyclability. While the majority of aluminum structural applications are formed by extrusion, recently, aluminum Z- and C- sections have been successfully cold-formed from aluminium coil using existing rollers for cold-formed steel sections. The results of nonlinear analysis by the finite element method (FEM) depend on the measured input parameters such as the material properties, actual initial geometric imperfections and forming-induced residual stresses. The paper summaries the results of the finite element nonlinear simulations of the stub column tests on channel sections performed at the University of Sydney. The FEM results are compared and calibrated against the tests. The effect of the measured input parameters is also discussed thoroughly.

**Keywords:** Aluminium alloys 5052 · Cold-rolled channel sections · Section capacity · Residual stress

## 1 Introduction

The use of aluminium structural members has risen dramatically in primary load-bearing components due to their advantages such as lightweight, superior corrosion resistance, ease of maintenance, constructability and recyclability. The majority of aluminum structural applications are formed by extrusion (Feng *et al.* 2006; Su *et al.* 2015; Zhu and Young 2006; Zhu 2006).

In Australia, aluminum structural solutions, well-known as PERMALITE® (Permalite 2010), consists of aluminum cladding and structural C- and Z-sections. In the past, these C- and Z-sections were produced by extrusion and were frequently fabricated overseas. In recent years, successful trials have been undertaken to cold-roll aluminum coil into C- and Z-sections as shown in Fig. 1. By using the existing rollers for cold-formed steel sections, the trials have demonstrated the possibility to roll-form aluminum sections to within acceptable dimensional tolerances.

© Springer Nature Singapore Pte Ltd. 2018
H. Tran-Nguyen et al. (eds.), *Proceedings of the 4th Congrès International de Géotechnique - Ouvrages -Structures*, Lecture Notes in Civil Engineering 8,
DOI 10.1007/978-981-10-6713-6_19

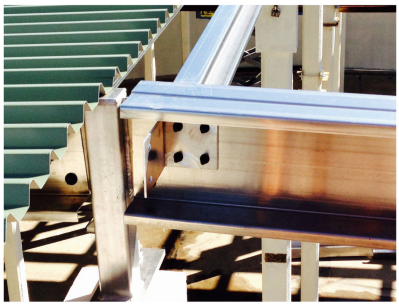

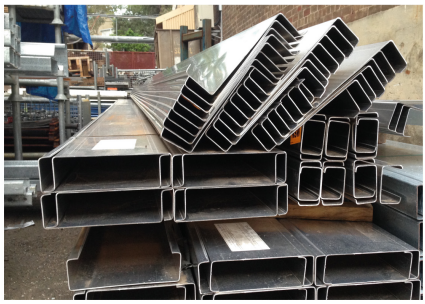

**Fig. 1.** Cold-rolled C- and Z-section (Permalite 2010)

In current Australian Standards, guidelines for the design of aluminium structures are formally available in AS/NZS1664.1:1997 (1997). These guidelines are premised on research on extruded sections and do not allow the increase in strength produced by cold-forming to be accounted for. To date, there are no design guidelines for these types of cold-rolled aluminium structural members. This has opened the door for not only Australian companies but for cold-formed steel/stainless steel manufacturing companies worldwide to commercialize cold-rolled aluminium structural sections. The main innovation is that the roll-forming is a new way of producing aluminium structural sections, which has the potential to lead to strength enhancement compared to extrusion and is a more cost effective method of production.

The experimental programs (Huynh *et al.* 2016a, b) have been recently performed at the University of Sydney to investigate the mechanical properties and ultimate strengths of cold-rolled aluminium alloy 5052 channel stub columns. The initial geometric imperfection and the measurement of residual stress have been thoroughly studied. The paper presents the finite element (FE) modeling and analysis of the experimental aluminium channels in stub column tests. The effect of such input parameters as initial geometric imperfection, mechanical properties at corner areas and residual stresses have been investigated in the models. Experiment data from Huynh *et al.* (2016a, b) was utilized to evaluate the performance of the FE model.

## 2 Finite Element Simulation

### 2.1 General

A detail FE model has been developed to study the structural behavior of cold-rolled aliminium alloy 5052 channel section in stub column test. The commercially available software package ABAQUS/Standard, Version 6.14-1(ABAQUS/Standard 2014). In the first step, the initial imperfection and measured residual stresses were incorporated into a perfect FE model. The second step was a nonlinear analysis using the modified Riks method (Riks 1972, 1979).

## 2.2 Material Properties

The measured stress-strain curves based on tensile coupon tests of the flat portion and corner areas from Huynh *et al.* (2016a) were incorporated in the model. Typical stress-strain curves of C40030 coupons are shown in Fig. 2 and the mean values of coupon tests of all tested sections are included in Table 1. In order to obtain realistic results from the FE nonlinear analyses, plastic strains were incorporated in the material definition. In the plastic analysis, the static engineering stress-strain curves obtained from tensile coupon tests were converted to true stress vs logarithmic true plastic strain curves. The true stress $\sigma_{true}$ and true plastic strain $\varepsilon_{true}$ were calculated using Eqs. (1) and (2) as follows:

$$\sigma_{true} = \sigma(1+\varepsilon) \tag{1}$$

$$\varepsilon_{true} = \ln(1+\varepsilon) - \sigma_{true}/E \tag{2}$$

where $\sigma$ and $\varepsilon$ are the measured engineering stress and strain respectively obtained from the tensile coupon tests.

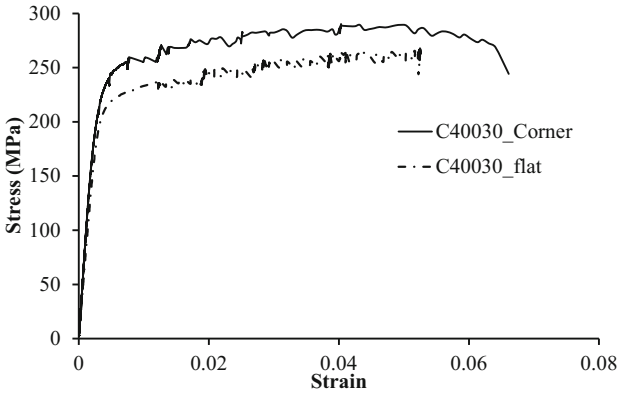


**Fig. 2.** Typical stress-strain curves of C40030 coupons

**Table 1.** Material properties from tensile coupon tests

| Coupon | Position | $\sigma_{0.2}$ MPa | $\sigma_u$ MPa | $E_o$ GP |
|---|---|---|---|---|
| C10030 | Flat | 220 | 267 | 69.3 |
| C25025 | Flat | 215 | 262 | 69.7 |
| C40030 | Flat | 220 | 268 | 69.9 |
| C10030 | Corner | 244 | 290 | 70.1 |
| C25025 | Corner | 248 | 292 | 71.2 |
| C40030 | Corner | 240 | 282 | 70.5 |

### 2.3 Test Rig Configuration and Specimen Boundary Conditions

The experimental program comprised a total of twelve tests conducted in the J.W. Roderick Laboratory for Materials and Structures at the University of Sydney. All tests were performed in the 2000 kN capacity DARTEC testing machine using a servo-controlled hydraulic ram. Figure 3 shows dimensions of three chosen cross sections. A photo of test set-up is shown in Fig. 4. The test specimen was placed vertically between two fixed ends. Two ends of specimen were milled to ensure the load is applied uniformly across sections. Initially, the DARTEC loading ram was moved slightly downwards to apply a small load to the specimen. This caused the spherical head to rotate slightly until full contact between the end plate and the

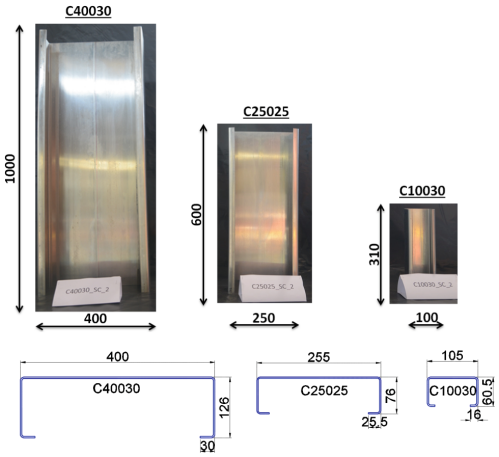


**Fig. 3.** Dimension of stub column test

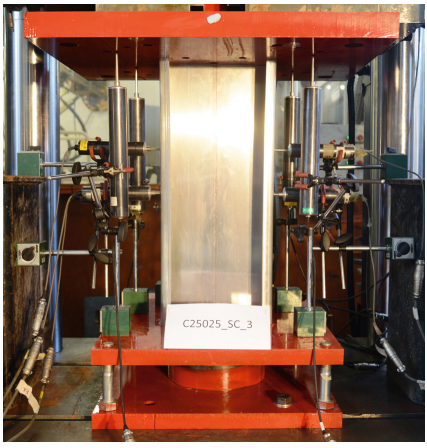


**Fig. 4.** Test set-up for cold-rolled aluminium stub column test

specimen was achieved. Four bolts installed at the four corners of the two bearing plates were subsequently adjusted to lock the two plates into a fixed position (see Fig. 4). This set-up ensures that load was applied concentrically and uniformly between two fixed ends as per the guidelines of the Structural Stability Research Council (Ziemian 2010).

### 2.4 Initial Geometrical Imperfection

Similarly to cold-formed steel structures, initial geometric imperfections have a significant effect on the load carrying capacity of thin-walled aluminium structures. It is therefore necessary to accurately measure the actual initial imperfections prior to testing. The arrangement for the imperfection measurement of each specimen is shown in Fig. 5, in which nine lasers measuring devices travel along high-precision tracks while recording the distance to nine corresponding points on the surface of the specimen. The measurement lines are located around the cross-section as also shown in Fig. 5. The laser transducers were programmed to take readings about every 2 mm along the length of the specimen. Each laser transducer had a reading range of approximately 10–25 mm. Based on data from the laser readings, the imperfection magnitude values are directly inputted into the node numbers of the entire perfect straight specimen created by the finite element model. The imperfection magnitudes are obtained using a Fourier series approximation longitudinally and linear or quadratic interpolation transversely. Figure 7 shows specimen in ABAQUS before and after imperfection input (Fig. 6).

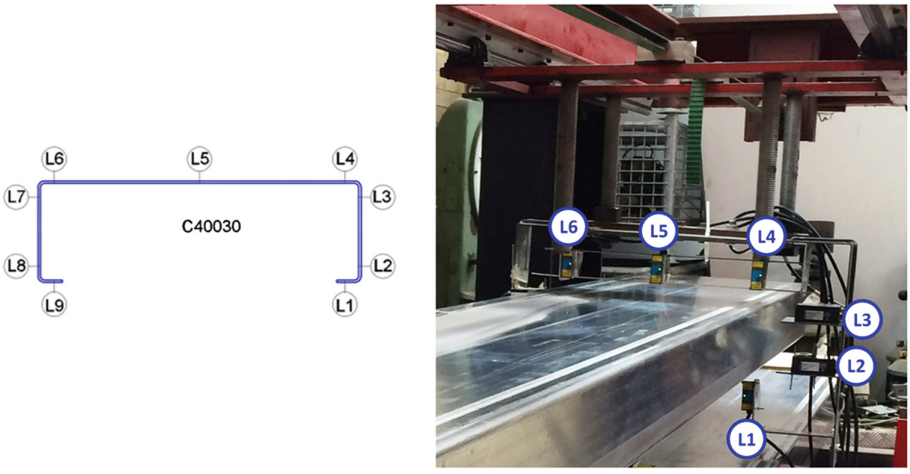


**Fig. 5.** Imperfection measurement lines and rig

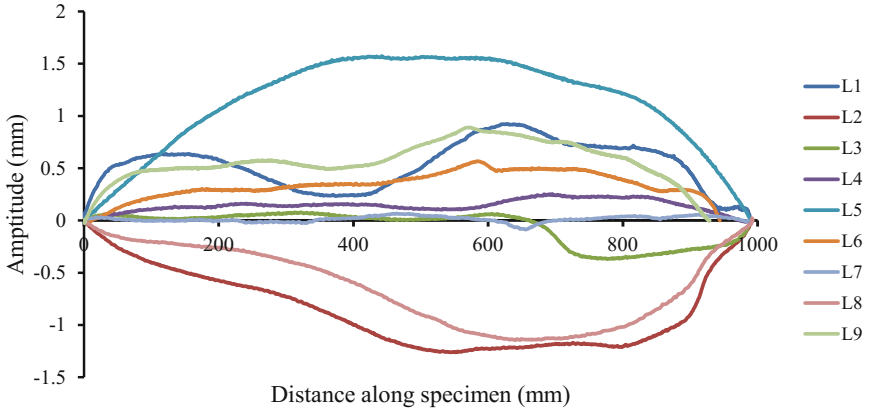


**Fig. 6.** Measured imperfection of C40030_SC4, using Fourier series

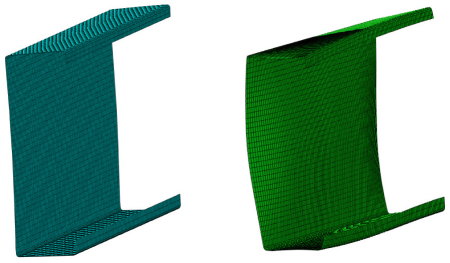

(a) No Imperfection (b) With Imperfection

**Fig. 7.** Finite element before and after input measured imperfection C40030

## 2.5 Residual Stresses

Figure 8 shows the experiment and result data from the residual stress measurement of a C25025 cold-rolled aluminium section performed in Huynh *et al.* (2016a). The measured residual stress profile was incorporated in the FE model to investigate effect of residual stress on the column strength of cold-rolled aluminium alloy 5052 stub column. It is worth noting that while the material properties obtained from the flat and corner coupon tests in Huynh *et al.* (2016a) have already included the bending residual stress effect, only membrane residual stress was included in the FE model in this study. The distribution of residual stress of C25025 section was shown in Fig. 8c. The measured membrane residual stresses were included in the finite element model using ABAQUS (*INITIAL CONDITIONS, TYPE = STRESS) parameter. The stub column FE model was partitioned into strips which have same widths with those cut from the specimen for residual stress measurement.

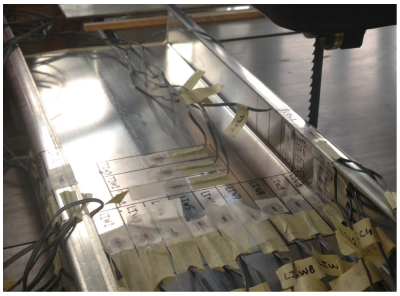

(a) Sectioning of specimen C25025

(b) C25025 after cut

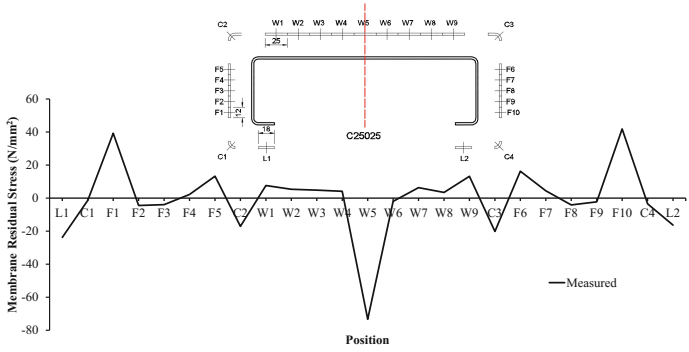


(c) Membrane residual stress distribution C25025

**Fig. 8.** Typical specimen C25025 for sectioning method to measure initial residual stress

### 2.6 Element Mesh

The aluminium cold-rolled channels were modeled using the 4-node shell element with reduced integration, type S4R, available from the ABAQUS element library. This shell element uses three translational and three rotational degrees of freedom at each node. The element accounts for finite membrane strains and arbitrarily large rotations. Therefore, it is suitable for large strain analyses and geometrically nonlinear problems. The top and bottom plates at the two ends were generated in ABAQUS using 3D-deformable solid elements and were assigned standard steel properties. Contact between nodes of the cross-section and the surfaces of the top and bottom bearing plates were incorporated to obtain realistic failure modes.

## 3 Comparisons of Test Loads with Finite-Element Modelling

Figure 9 shows the load vs end shorting curves of the representative tests for three cross sections (C10030, C25025 and C40030). As seen in Fig. 9, the loads increase linearly up to approximately 41 kN for C25025 and 45 kN for C40030 respectively where local buckling occurs mainly in the web. Subsequently, the slopes of the load vs end shortening curves change due to local buckling and the loads keep increasing up to

the peak load 119.9 kN for C25025 and 182.7 kN for C40030. For stocky C10030 sections, the load increases linearly up to approximately 120 kN followed by nonlinear behavior up to the peak load at about 135 kN with no distinct local buckling point.

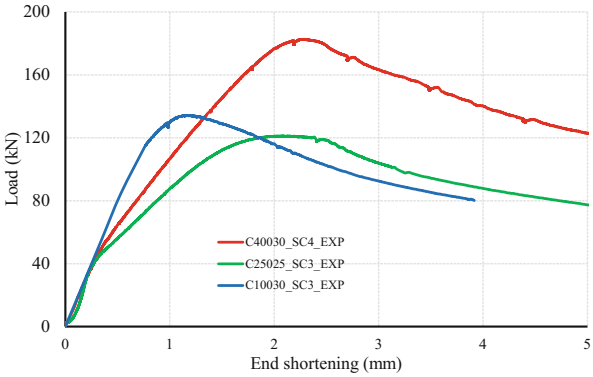


**Fig. 9.** Load vs end shortening curve experiment

The load vs end shortening curves for the C40030_SC4 test (——) and the ABAQUS results without geometric imperfections (– – –), with geometric imperfection (—○—) and with both imperfection and residual stress (– · –) are illustrated in Figs. 10 and 11. Excellent agreement between the predicted FE curve and the experimentally recorded curve was achieved. As clearly seen in Fig. 11, when including residual stress in FE, the curve lies slightly lower and closer to the experiment curve. This fact shows that both initial imperfections and residual stresses in the sections affect behavior and ultimate strength of the cold-rolled aluminium channel sections in stub column tests.

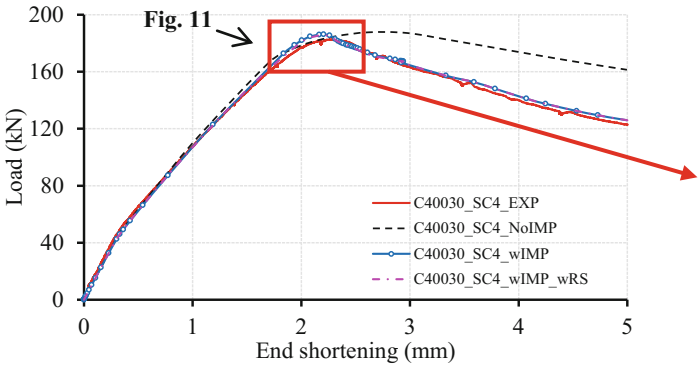


**Fig. 10.** Load vs end shortening finite element

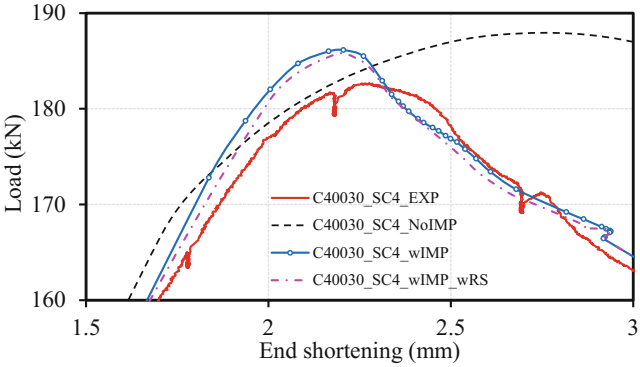


**Fig. 11.** Zoom out from Fig. 10

It is also interesting to note that while the flanges and lips of all C10030 and C25025 sections move inwards as shown in Figs. 12a and b, those of C40030 sections move in two different ways (2 inwards and 2 outwards) (see Figs. 12c and d). Figure 12 displays the comparison failure mode shapes of tests and corresponding ABAQUS modes. The explanation for this fact is that initial geometric imperfections influence flange and lip movement and failure mode shapes.

(a) C10030_SC3 (inward)

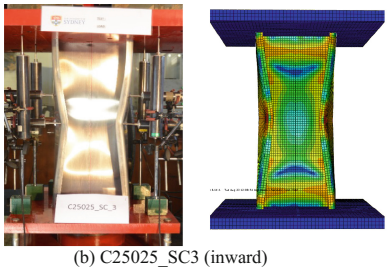

(b) C25025_SC3 (inward)

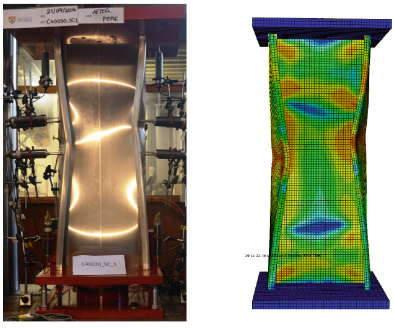

(c) C40030_SC1 (inward)

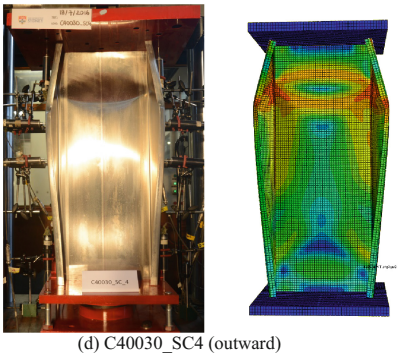

(d) C40030_SC4 (outward)

**Fig. 12.** Comparison between failure mode shapes of tests and ABAQUS Models

Table 2 summaries the ultimate strength results of the 12 stub column tests on cold-rolled aluminium channel sections. Also included in Table 2 are two different predicted FE peak loads. While the first FE load ($P_{wIMP}$) only included the initial geometric imperfection in the analysis, the latter ($P_{wImp_wRS}$) took into account both initial imperfection and residual stress. It can be seen in Table 2 that the initial imperfection affects both ultimate strengths and buckling mode shapes (movement of flanges and lips). However, the effect of the residual stress on the ultimate loads is not significant.

**Table 2.** Test and ABAQUS-FEM results

| Specimen | Length | Test | | ABAQUS-FEM | | | | $\frac{P_{EXP}}{P_{wIMP}}$ | $\frac{P_{EXP}}{P_{wIMP_wRS}}$ |
|---|---|---|---|---|---|---|---|---|---|
| | (mm) | $P_{EXP}$ (kN) | Flange movement | $P_{wImp}$ (kN) | Flange movement | $P_{wImp_wRS}$ (kN) | Flange movement | | |
| C10030_SC1 | 310 | 130.9 | Inward | 138.6 | Inward | 138.4 | Inward | 0.944 | 0.946 |
| C10030_SC2 | 310 | 136.6 | Inward | 140.1 | Inward | 139.2 | Inward | 0.975 | 0.981 |
| C10030_SC3 | 310 | 134.3 | Inward | 139.0 | Inward | 137.5 | Inward | 0.966 | 0.977 |
| C10030_SC4 | 310 | 137.0 | Inward | 137.2 | Inward | 136.0 | Inward | 0.999 | 1.007 |
| C25025_SC1 | 600 | 119.6 | Inward | 118.7 | Inward | 117.7 | Inward | 1.008 | 1.016 |
| C25025_SC2 | 600 | 116.0 | Inward | 119.6 | Inward | 119.1 | Inward | 0.970 | 0.974 |
| C25025_SC3 | 600 | 121.2 | Inward | 119.9 | Inward | 119.4 | Inward | 1.011 | 1.015 |
| C25025_SC4 | 600 | 118.2 | Inward | 125.2 | Inward | 124.8 | Inward | 0.944 | 0.947 |
| C40030_SC1 | 1000 | 172.1 | Inward | 177.4 | Inward | 177.1 | Inward | 0.970 | 0.972 |
| C40030_SC2 | 1000 | 170.1 | Outward | 172.1 | Outward | 172.0 | Outward | 0.988 | 0.989 |
| C40030_SC3 | 1000 | 176.8 | Inward | 186.4 | Inward | 186.0 | Inward | 0.948 | 0.951 |
| C40030_SC4 | 1000 | 182.7 | Outward | 186.1 | Outward | 185.6 | Outward | 0.982 | 0.984 |

## 4 Conclusion

The paper describes the numerical investigation using geometrically and materially non-linear FE analysis to simulate the behavior of cold-rolled aluminium alloy 5052 channel sections in stub column tests. The simulations using the FE program ABAQUS were compared with and calibrated against 12 stub column tests. The FE study was conducted to investigate the effect of such input parameters as mechanical properties of flat and corner areas, initial geometric imperfection and residual stress. The ABAQUS results were generally in good agreement with the experimental values. The FE results also show that the effect of initial geometric imperfection is sensitive to the ultimate strengths and buckling modes shapes. Further, the effect of residual stress on the behavior and strengths of the stub channel columns was found not significant in the ultimate loads. ABAQUS can therefore be used for further investigation to design and optimize cold-rolled aluminium sections.

**Acknowledgments.** Funding provided by the Australian Research Council for Linkage Project Grant LP140100563 between BlueScope Permalite and the University of Sydney has been used to perform this research. The authors would like to thank Permalite Aluminum Building Solutions Pty Ltd for the supply of the test specimens and financial support for the project.

## References

ABAQUS/Standard. ABAQUS/CAE User's Manual. Dassault Systemes Simulia Corp, Providence, RI, USA (2014)

AS/NZS1664.1:1997. Australian/New Zealand Standard ® Part 1: Limit state design Aluminium structures (1997)

Feng, R., et al.: Experimental investigation of aluminum alloy stub columns with circular openings. J. Struct. Eng. **141**(11), 1–10 (2006)

Huynh, L.A.T., et al.: Mechanical properties of cold-rolled aluminium alloy 5052 channel sections. In: 8th International Conference on Steel and Aluminium Structures, Hong Kong, China (2016a)

Huynh, L.A.T., et al.: Stub column tests and finite element modelling of cold-rolled aluminium channel section. In: 8th International Conference on Steel and Aluminium Structures, Hong Kong, China (2016b)

Permalite. (2010). http://permalite.com.au/

Riks, E.E.: The application of Newton's method to the problem of elastic stability. J. Appl. Mech. **39**, 1060–1066 (1972)

Riks, E.E.: An incremental approach to the solution of snapping and buckling problems. Int. J. Solids Struct. **15**, 529–551 (1979)

Su, M., et al.: Continuous beams of aluminum alloy tubular cross sections. I: tests and FE model validation. J. Struct. Eng. **141**(1991), 1–7 (2015)

Zhu, J.H., Young, B.: Aluminum alloy circular hollow section beam-columns. Thin-Walled Struct. **44**, 131–140 (2006)

Zhu, J.-H.: Behaviour and design of aluminium alloy structural members. Thesis - University of Hong Kong, Pokfulam, Hong Kong (2006)

Ziemian, R.D.: Guide to Stability Design Criteria for Metal Structures, 6th edn. Wiley, New York (2010)

# Numerical Studies of Composite Steel-Concrete Columns Under Fire Conditions Including Cooling Phase

Thi Binh Chu[1(✉)] and Quang Vinh Truong[1,2]

[1] Hanoi Architectural University, Hanoi, Vietnam
chuthibinh.hau@gmail.com, tqvinhduy@gmail.com
[2] The University of Fire Fighting and Prevention, Hanoi, Vietnam

**Abstract.** This work presents an analysis of the behaviour of composite steel-concrete columns under natural fires which include cooling phase. Thermo-mechanical numerical simulations based on the non-linear finite element method are conducted using the parametric fire model of Eurocodes to represent the natural fires. Results show that structural failure of the composite columns during or after the cooling phase of a fire is a possible event. The duration of heating phase (DHP) leading to the failure of structures during or after the cooling phase is always lower than the fire resistance of structures exposed to heating phase only. Parametric studies have been done to show the relationships between DHP and some major parameters such as load ratio, slenderness of column, eccentricity of load. This work enhances the understanding of the structural behaviour under natural fires.

**Keywords:** Natural fire · Steel concrete columns · Performance based design · Cooling phases

## 1 Introduction and Scope

When a structural member is exposed to natural fire, its load bearing capacity decreases during the heating phase of the fire, but it also decreases after the maximum gas temperature is attained. As a consequence, structural failure may occur during or after the cooling phase. This delayed decrease in load bearing capacity may be caused by the combination of various phenomena, such as:

- the delayed temperature increase in the sections, due to thermal inertia;
- the non-recovery or additional loss of material properties during cooling;
- the built-up and reversal of thermal forces in a structure subjected to heating - cooling (e.g. tensile forces in connections).

The possibility of structural collapse during or after the cooling phase has first been examined by Gernay and Franssen who introduced a standard measure, noted DHP, to characterize the ability of structural members to resist a natural fire (Gernay and Franssen 2015). DHP is defined as the minimum exposure time to standard ISO fire (ISO 834-1 1999) (followed by cooling phase in accordance with the Eurocode

© Springer Nature Singapore Pte Ltd. 2018
H. Tran-Nguyen et al. (eds.), *Proceedings of the 4th Congrès International de Géotechnique - Ouvrages -Structures*, Lecture Notes in Civil Engineering 8,
DOI 10.1007/978-981-10-6713-6_20

parametric fire model (EN 1991-1-2 2002)) that will eventually result in the failure of the structural component, even if the fire stops thereafter.

The objective of this research is to conduct numerical analyses of composite steel-concrete columns subjected to natural fires in order to verify that the possibility of structural collapse during or after the cooling phase exists for those structural elements and, if so, to identify which parameters affect the duration of heating phase (DHP) indicator. The studied columns consist of a steel profile embedded in concrete encased in a steel tube.

## 2 Computational Models of Composite Columns Exposed to Fire

Using program SAFIR (Franssen 2005), - a non linear finite element software developed at the University of Liege Belgium for the simulation of thermal and structural behavior under ordinary and fire conditions - the analysis of a structure exposed to fire consists of two steps. The first step involves predicting the temperature distribution inside the structural members, referred to as "thermal analysis". The second step, named "structural analysis", is carried out in order to determine the mechanical response of the structure due to the thermal effects, since the load is usually assumed to remain constant during the fire. The validation of SAFIR code has been done in some studies (Talamona et al. 2003; Binh et al. 2010)

### 2.1 Fire Model

The adopted model for the natural fires is the parametric fire model from Eurocode EC1 (EN 1991-1-2 2002). It is chosen to set the value of the factor Γ at 1.0 in the model, which makes the heating phase of the time-temperature curve of this natural fire model approximates the standard ISO curve. Hence, the only varying parameter in the natural fire model is the duration of the heating phase DHP. Figure 1 shows the

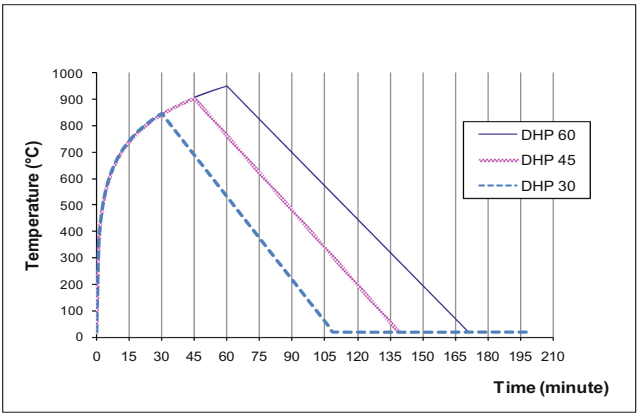


**Fig. 1.** Eurocode parametric fire model for natural fire

time-temperature curves for different values of DHP. Curve DHP 60 expresses the natural fire with 60 min of heating phase.

## 2.2 Heat Transfer Analysis

In beam elements incorporated a frame, a uniform temperature is assumed over the height of the single element. Thus, thermal analysis can be reduced to a two-dimensional problem of transient heating. A two-dimensional thermal FE analysis is conducted for the heated member using a fiber discretization of the cross-section, see Fig. 2 representing one of the composite section analyzed in this study. The discretization for plane sections of different shapes is possible by using triangular and/or quadrilateral elements. For each element the material can be defined separately. Any material can be analyzed provided its physical properties at elevated temperatures are known. The variation of material properties with temperature can be considered.

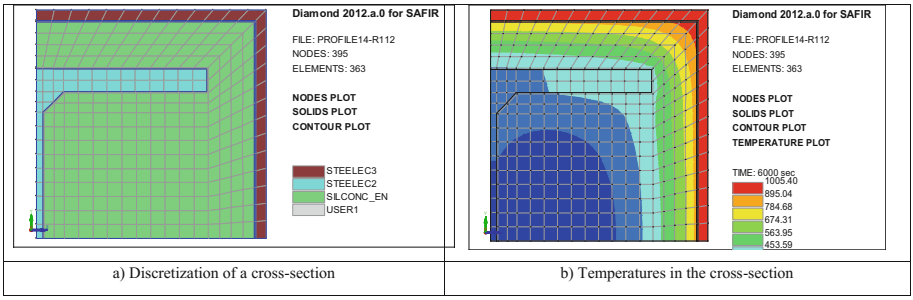


a) Discretization of a cross-section

b) Temperatures in the cross-section

**Fig. 2.** Column cross-sections (1/4 of the section by symmetry)

The local equation describing conduction in solid materials has the form of Eq. 1 in a Cartesian system of coordinates.

$$k\left(\frac{\partial^2 T}{\partial x^2}+\frac{\partial^2 T}{\partial y^2}+\frac{\partial^2 T}{\partial z^2}\right)+Q-C\rho\frac{\partial T}{\partial t}=0 \tag{1}$$

where

k: Thermal conductivity;
T: Temperature;
x, y, z: Coordinates;
Q: Internally generated heat
C: Specific heat;
ρ: Specific mass density;
t: Time

The thermal properties of steel and concrete in the heating phase are taken from Eurocodes EC4 (EN 1994-1-2 2005). Where concrete is used, siliceous concrete is

chosen, with a density of 2400 kg/m$^3$ and a water content of 48 kg/m$^3$. The emissivity is taken as 0.7 and the coefficient of convection between concrete and the air is 35 W/m$^2$K.

### 2.3 Structural Analysis

The program can be used to study the behaviour of two and three-dimensional structures. SAFIR accommodates various elements for different idealizations, several calculation procedures and various materials. The elements include the 2-D SOLID elements, 3-D SOLID elements, BEAM elements, SHELL elements and TRUSS elements. The time-temperature evolution in each fiber results from the previously conducted thermal analysis. The structural analysis takes into account geometrical and material non-linearity, including large deflections.

In the model, the columns are built up by means of several 2-D beam elements. The integration of the longitudinal stresses and stiffness on the section is based on the fibre model; the section is supposed to be made of a certain number of parallel fibres. In fact, the same discretization as the one used for the thermal analysis is used. Each finite element of the thermal analysis, with its known material type and temperature, is considered as a fibre. The effect of thermal expansion of steel and concrete is considered in the constitutive models. More information is given in (Franssen 2005).

In this research all the mechanical properties of the steel and concrete follow the recommendations of the Eurocodes. The mechanical properties of steel are considered as reversible, which means that stiffness and strength are recovered to full initial values during cooling. The mechanical behaviour of steel follows the model of Eurocode EC3 (EN 1993-1-2 2005). In the case of varying temperature, the plastic strain is the variable describing the complete stress-strain history as illustrated in Fig. 3. The point P of the stress-strain state is recalculated after each temperature increase of decrease. For concrete, a residual thermal expansion or shrinkage is considered when the

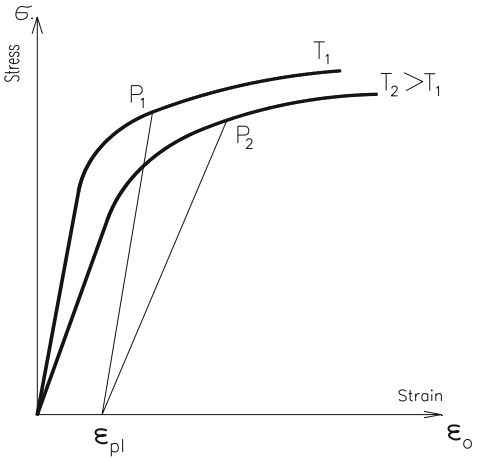


**Fig. 3.** Stress-strain state at a point with varying temperature

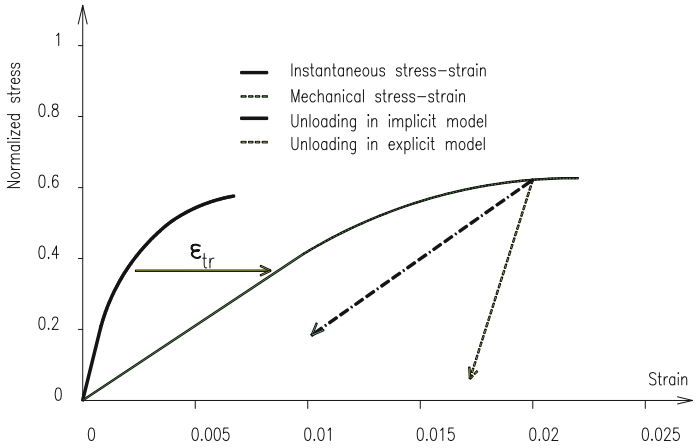


**Fig. 4.** Strain components in implicit and explicit models of concrete at high temperature

concrete is back to ambient temperature, the value of which is taken as a function of the maximum temperature according to experimental tests published in the literature (Franssen 1993). As prescribed in EC4, an additional loss of 10% of the concrete compressive strength is considered during cooling, with respect to the value at maximum reached temperature. This additional reduction during cooling is supported by many experimental studies (Li and Franssen 2011). The Explicit Transient Creep Eurocode model (explicit model) is adopted to take into account the transient creep strain irreversibility during cooling Fig. 4 (Gernay 2011).

The objective of the simulations is to assess the response of the structural member during the course of the natural fire. For a given structural member, numerical simulations are run under different natural fire exposures (see Fig. 1).

## 3 Duration of the Heating Phase (DHP) Indicator

This section describes the DHP indicator introduced by (Gernay and Franssen 2015) and adopted in this work for analyzing the behavior of composite columns under natural fire. Let us consider a structural component subjected to a certain load (demand) which is considered constant during the fire. During the fire, the temperature increase across the section of the component leads to a decrease of the mechanical properties of the constituting materials, resulting in a decrease of the load-bearing capacity of the component.

For a standardized fire, the temperature is continuously increasing in the compartment, so that the temperatures in the element are also continuously increasing and, assuming that all materials properties degrade under increasing temperatures, the load-bearing capacity is continuously decreasing. Failure occurs at the time when the capacity meets the demand, this time being defined as the Fire Resistance (R) of the component.

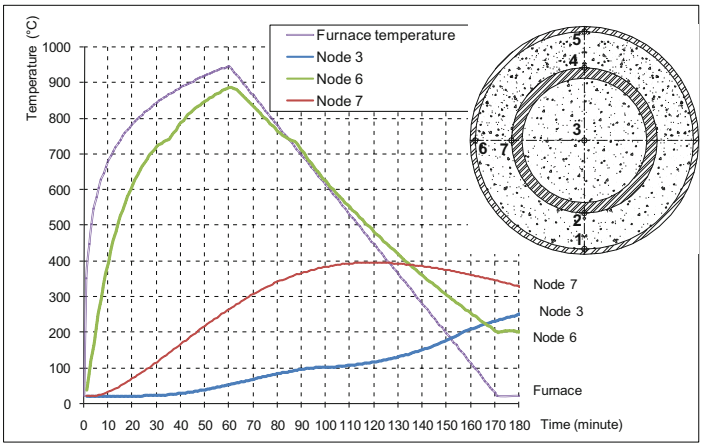


**Fig. 5.** Temperature evolution in profile 1 for the natural fire with 60 min of heating phase

For a natural fire, the temperature in the compartment is first increasing until a maximum and then decreasing back to ambient conditions. In that case, the load-bearing capacity of the component is first decreasing until reaching a minimum and then it may remain constant or recover, partially or completely, after the temperature has come back to ambient. Importantly, the time of the maximum fire temperature and the time of the minimum load-bearing capacity are generally not simultaneous, the latter arising later than the former. To illustrate this, Fig. 5 shows the temperature evolution in the section profile 1. The furnace temperature is a natural fire with 60 min of heating phase then cooling to room temperature after 170 min. The temperatures of external steel hollow section (node 6), the internal steel profile (node 7) and the concrete core (node 3) are calculated. The furnace and the external steel profile reach maximum temperature at time 60 min while the internal steel profile reaches maximum temperature after 120 min and the temperatures of concrete in center zone keep on increasing even after 180 min. The column may not fail after 60 min exposed to heating phase (if the fire resistance R is greater than 60 min) but it is possible failed after more than 60 min, during the cooling phase of the fire. Hence, the Fire Resistance R does not give enough information to characterize the performance of structures under natural fire. A new indicator is needed to complement it. This indicator must be related to a certain measure of severity of the natural fire.

By definition, the DHP represents the minimum exposure time to standard ISO fire (followed by cooling phase in accordance with the Eurocode parametric fire model as in Fig. 1) that will eventually result in the failure of the structural component (either be it in the heating phase, in the cooling phase or after termination of the fire). In terms of performance-based design, the Fire Resistance indicator is interpreted as information about the time of resistance during the heating phase of a fire, although it is obviously not a direct measure of this time since the real fire conditions will differ from the prescriptive fire conditions. The DHP is interpreted as information about the occurrence of delayed failure as a function of the instant when the fire started to decrease, whether

by self-extinction or due to the action of the fire fighters. In design or test standards only the Fire Resistance indicator is concerned, DHP is not yet introduced. DHP is always smaller than or the Fire Resistance R. It is important to notice that the DHP does not give any indication about the time of collapse (time of failure). Generally, collapse can occur several minutes or hours after the time corresponding to the DHP, and it may even occur after the end of the fire when the temperature in the compartment is back to ambient. The time of failure is noted Tfail in this study. Tfail is defined here the time column collapse when exposed to natural fire with the heating phase equal to DHP.

## 4 Parametric Studies

One of the objectives of the study is to give an insight on the parameters and conditions that affect the duration of heating phase DHP, time of failure Tfail, and the delayed time of collapse Dt (Dt = Tfail − DHP) for composite columns.

Composite columns with cross sections in Fig. 7 are analyzed. Column is divided into 10 beam- elements to take into account deformed geometry. Columns are hinged at both ends and subjected to a compression load, which is constant during the fire.

The fire resistance R, the duration of heating phase DHP, and the time of failure Tfail are calculated for columns with various cross-sections, column length, load ratio, concrete grade and fire exposure curves. Results show that DHP is always less than R. For all calculated columns, the differences (DF = R − DHP) range from 9 min to 30 min. The delayed time of collapse Dt (Dt = Tfail − DHP) is from 9 min to over 60 min in calculated columns. It is important to know the delayed time to let the fire fighters keep off the failure of the buildings.

### 4.1 Effect of Load Ratio

The parameter ‘load ratio’, defined as the ratio of axial load acting on the column to the load-carrying capacity of the column at room temperature, is of more importance than the applied load acting on the column, as the load ratio represents the extent to which the column is stressed. Thus, load ratio has a direct influence on the resulting fire resistance.

The columns were analyzed with the load ratio from 0.3 to 0.6. Results with R lower than 30 min are ignored because they are not useful in practice. Table 1 show results columns profile 4, column-height 3 m, concrete grade C30, eccentricity of axial load 1 cm. The DHP decreases with the increase in load ratio.

It can see that load ratio affects much the value of R, DHP, Tfail, DF and Dt.

DF is a measure of the propensity of the structural element to experience a delayed failure: the higher DF, the more likely the element could fail during or after the cooling phase of a natural fire. Results suggest that columns with a lower load ratio are more prone to delayed failure. The delayed times (Dt = Tfail − DHP) show the time structures could collapse after maximum temperature reaches. Table 1 shows that the lower load ratio is, the greater delayed time is. It should be noted that in columns consist of a steel profile embedded in concrete encased in a steel tube, the load resistance at a fire depends much on the strength of internal profile and depends little on

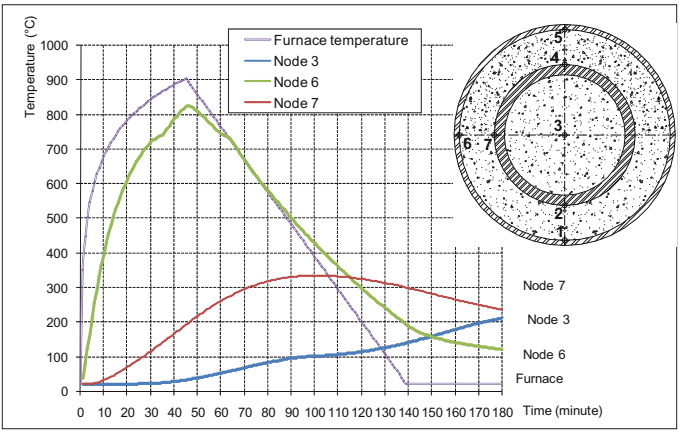


**Fig. 6.** Temperature evolution in profile 1 for natural fire with 45 min of heating phase

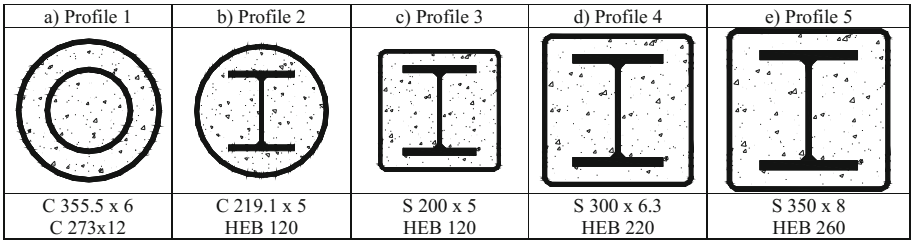


**Fig. 7.** Cross-sections of the studied columns

**Table 1.** Results of columns profile 4

| Cross-section | Load ratio | R (min) | DHP (min) | Tfail (min) | DF = R − DHP | Dt = Tfail − DHP |
|---|---|---|---|---|---|---|
| Profile 4 | 0.3 | 131 | 101 | 158 | 30 | 57 |
| Profile 4 | 0.4 | 94 | 77 | 113 | 17 | 36 |
| Profile 4 | 0.5 | 56 | 49 | 69 | 7 | 20 |
| Profile 4 | 0.6 | 37 | 32 | 41 | 5 | 9 |

the strength of external profile because the external profile loose its strength rapidly (after only 15 min to 20 min in fire). The strength of internal profile depends on its temperature. Because DHP represents the minimum exposure time to standard ISO fire (followed by cooling phase) that will eventually result in the failure of the column, column exposed to a natural fire with the heating phase equal to its DHP must fail at the time the internal steel profile reaches its maximum temperature (120 min in Fig. 5 and 100 min in Fig. 6). If not, the value of DHP would be lower. Figures 5 and 6 also show that greater DHP results in greater different time of maximum temperature in internal steel profile and maximum temperature in the furnace. It can explain the results that Dt is greater for greater DHP.

### 4.2 Effect of Slenderness of Column

The fire resistance R and duration of heating phase DHP of column profile 5 with various value of column height are shown in Table 2. Lambda is relative slenderness of the column (lambda = column height/radius of gyration of the section). DHP depends much on Lambda. As slenderness increases, the fire resistance of the column decreases owing to decreased resistance to buckling. Relationship between slenderness and DHP of columns with some types of cross-section is shown in Fig. 8. It seems that DHP could be express as a function of Lambda for various types of cross- sectional columns. Parametric studies have been doing for columns with various types of cross-section, load ratios, concrete covers, and concrete grades to find out the correlation between DHP and Lambda. Results from Tables 1 and 2 also show that the delayed time Dt is greater for greater DHP and Dt varies in large range: from 9 min to over one hour (60 min).

**Table 2.** R, DHP, Tfail and Dt with various column heights

| Lambda | R (min) | DHP (min) | Tfail (min) | Dt = Tfail − DHP |
|---|---|---|---|---|
| 9.9 | 147 | 112 | 180 | 68 |
| 14.9 | 127 | 105 | 146 | 41 |
| 19.8 | 107 | 92 | 131 | 39 |
| 24.8 | 84 | 75 | 97 | 22 |
| 29.8 | 67 | 61 | 75 | 14 |
| 34.7 | 57 | 49 | 72 | 23 |
| 39.7 | 49 | 42 | 59 | 17 |

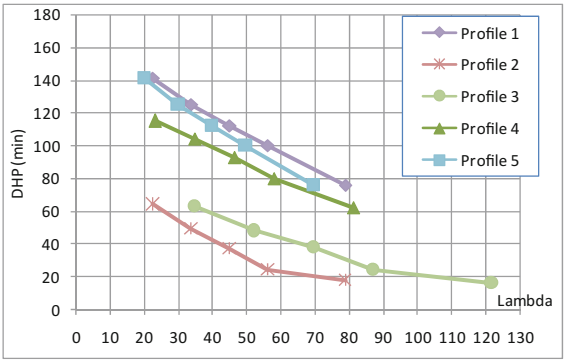


**Fig. 8.** Relationship between relative slenderness and DHP

### 4.3 Effect of Eccentricity of Load

The fire resistance R and duration of heating phase DHP of column profile 5; load ratio 0.5; column height 3 m but various value of load eccentricities are shown in

**Table 3.** The fire resistance R and duration of heating phase DHP with various load eccentricity

| Cross-section | Load ratio | Eccentricity (cm) | R (min) | DHP (min) |
|---|---|---|---|---|
| Profile 5 | 0.5 | 0 | 67 | 60 |
| Profile 5 | 0.5 | 1 | 67 | 60 |
| Profile 5 | 0.5 | 2 | 66 | 60 |
| Profile 5 | 0.5 | 3 | 66 | 60 |
| Profile 5 | 0.5 | 5 | 66 | 60 |
| Profile 5 | 0.5 | 7 | 66 | 61 |
| Profile 5 | 0.5 | 10 | 67 | 61 |
| Profile 5 | 0.5 | 15 | 66 | 60 |
| Profile 1 | 0.3 | 0 | 60 | 50 |
| Profile 1 | 0.3 | 1 | 60 | 50 |
| Profile 1 | 0.3 | 10 | 68 | 57 |
| Profile 1 | 0.3 | 15 | 71 | 60 |
| Profile 1 | 0.3 | 20 | 74 | 63 |
| Profile 1 | 0.3 | 25 | 77 | 65 |

Table 3 (load values are changed to keep load ratio unchanged). Results show that both R and DHP increase lightly with load eccentricity. In simplified method, DHP of columns under eccentric compression can be taken as DHP of columns under concentrate load, in the safe side.

### 4.4 Effect of Concrete Strength

The fire resistance R and duration of heating phase DHP of column profile 5; load ratio 0.5; column height 3 m, load eccentricity e = 1 cm but various values of concrete compression strength are shown in Table 4. Results show that concrete strength affects little on DHP (keep load ratio unchanged) but DF increase lightly with concrete compressive strength. It can be explained that when concrete contributes more (concrete strength increase), the delayed effects increase (because concrete does not recover its strength), and therefore DF increases.

**Table 4.** The fire resistance R and duration of heating phase DHP with various concrete strength

| Concrete Strength (MPa) | R (min) | DHP (min) | DF = R − DHP |
|---|---|---|---|
| 25 | 59.8 | 56 | 3.8 |
| 30 | 62.2 | 57 | 5.2 |
| 35 | 64.4 | 59 | 5.4 |
| 40 | 66.5 | 60 | 6.5 |
| 45 | 70.1 | 62 | 8.1 |
| 50 | 73.1 | 64 | 9.1 |

## 5 Conclusions

Delayed structural failures, arising during or after the cooling phase of a fire, may occur with steel-concrete composite columns. These result from different mechanisms such as the effects of thermal inertia or the additional loss of mechanical properties during cooling. This possibility of delayed failures must be correctly assessed when considering more realistic fire scenarios, notably for a better assessment of safety during fire brigades intervention.

For composite steel-concrete columns, DHP is always less than R. For all calculated columns in the research, the differences (DF = R − DHP) are from 5 min to 30 min. The higher this difference is, the more prone the column is to experience a delayed failure. The value of delay time Dt varies in the large range: from 9 min to over 60 min in calculated columns. It can be explained logically the fact that the greater DHP the greater Dt is.

Load ratio and slenderness of column affects much the value of R and DHP. The greater load ratio or greater relative slenderness the lower R and DHP is. Eccentricity of load and concrete strength has minor effects on R and DHP provided the same load ratio. More numerical studies should be done to find the correlation between DHP and Dt and main parameters such as load ratio, slenderness of column, eccentricity of load and concrete strength.

## References

Binh, C.T., Dotreppe, J.C., Franssen, J.M.: Numerical modeling of building structures in fire conditions. In: Proceedings of Construction under Exceptional Condition, Hanoi, Vietnam, pp. 41–52 (2010). http://orbi.ulg.ac.be/handle/2268/78436

EN 1991-1-2. Eurocode 1: Actions on Structures - Part 1–2: General actions – Actions on structures exposed to fire, Brussels (2002)

EN 1993-1-2. Eurocode 3 - Design of steel structures - Part 1–2: General rules - Structural fire design, Brussels (2005)

EN 1994-1-2. Eurocode 4 – Design of composite steel and concrete structures. Part 1–2: General rules – Structural fire design, Brussels (2005)

Franssen, J.M.: Thermal elongation of concrete during heating up to 700°C and cooling. Report, University of Liege, Belgium (1993). http://hdl.handle.net/2268/531

Franssen, J.M.: SAFIR. A thermal/structural program modelling structures under fire. Eng. J. AISC **42**(3), 143–158 (2005)

Gernay, T.: Effect of transient creep strain model on the behavior of concrete columns subjected to heating and cooling. Fire Technol. **48**, 313–329 (2011). doi:10.1007/s10694-011-0222-0

Gernay, T., Franssen, J.M.: A performance indicator for structures under natural fire. Eng. Struct. **100**, 94–103 (2015). doi:10.1016/j.engstruct.2015.06.005

ISO 834-1. Fire Resistance Test - Elements of building construction (1999)

Li, Y., Franssen, J.M.: Test results and model for the residual compressive strength of concrete after a fire. J. Struct. Fire Eng. **2**, 29–44 (2011). doi:10.1260/2040-2317.2.1.29

Talamona, D., Lim, L., Franssen, J.M.: Validation of a shell finite element for concrete and steel structures subjected to fire. In: Proceedings of International on Seminar on Fire and Explosion Hazards, Londonderry, University of Ulster, pp. 198–199 (2003). http://orbi.ulg.ac.be/handle/2268/15033

# On the Finite Element Modeling of the Screwed Connections of Cold-Formed Steel

Minh Toan Huynh(✉), Cao Hung Pham, and Gregory J. Hancock

The University of Sydney, Sydney, NSW, Australia
{minhtoan.huynh, caohung.pham,
gregory.hancock}@sydney.edu.au

**Abstract.** Self-drilling screws have been used extensively in cold-formed steel structures. The American Specification and Australian Standard both provide design checks for different limit states of screwed connections. However, in a connection undergoing bending, while a screw may fail, other screws may be still in the elastic state. Therefore, investigation in the load-deflection response of screw connectors before failure is required for further understanding of complex screwed connections. This paper describes a shear test using 3 screws connecting in G450 steel sheets. A 3D finite element (FE) model was developed and validated using ABAQUS software. The simulation is able to reproduce the experiment's results in term of shear strength, stiffness and ductility of the connections. The simplicity of this model allows it to be adapted into full scale connection modeling.

**Keywords:** Cold-formed steel · Screws · Screwed connection · Finite element modeling

## 1 Introduction

Cold-formed steel structural members are being used commonly in construction of steel framed housing, light-weight portal frames, roof systems and wall systems. In recent years cold-formed steel has begun to be adopted in construction of mid-rise residential and commercial buildings in the form of hybrid light steel panel and modular systems. These types of thin-wall structures give rise to a number of new connections. Cold-formed steel is often assembled by using screw fasteners because they can be drilled easily through thin sheets of steel. Compared to bolted connections, the fastening operation with screws can reduce labour time and eliminate the need for pre-drilling of holes. Screws can be used to connect cold-formed channels to supporting members and to interconnect continuous channels and steel sheets in roofs and walls. There are a large number of screws in a thin steel structure. Therefore, it is important to understand the behavior of screws connecting between cold-formed sheets and members, and then to predict their strength and stiffness.

Detailed design methods for screwed connections in cold-formed steel have been developed extensively and are included in the North American Specification for Cold-Formed Steel Structural Members NAS S100 (AISI 2012) and the Australian/New Zealand Standard for Cold-Formed Steel Structures AS/NZS 4600

© Springer Nature Singapore Pte Ltd. 2018
H. Tran-Nguyen et al. (eds.), *Proceedings of the 4th Congrès International de Géotechnique - Ouvrages -Structures*, Lecture Notes in Civil Engineering 8,
DOI 10.1007/978-981-10-6713-6_21

(Australian/New Zealand Standard 2005). AS/NZS 4600 provides design methods for screwed connections that can fail in tension, tilting and hole bearing, end distance failure of sheets and shear failure in screws. Capacity reduction factors for screwed connections range from 0.5 to 0.65. These factors, which are close to half of unity, show that there are great uncertainties in strength calculations.

Different failure modes of screwed connections are described in the European Standard – ECCS TC7 TWG 7.10: The Testing of Connections with Mechanical Fasteners in Steel Sheeting and Sections (ECCS 2009): bearing failure of connections; tilting and pull-out failure of connections; shear of fasteners; net section tension failure; and end failure of connections. Testing of screwed connections in G300 and G550 steel sheets by Rogers and Hancock (Rogers and Hancock 1999) showed that failure often occurs by a combination of different limit states, for example: bearing and tilting of screws. Furthermore, for moment connections, screws at different positions undergo different strains, hence yielding and fracture may occur in some screws while other screws are still in the elastic state. Investigation in moment connections requires a comprehensive understanding of the load-deflection response for individual screws before it reaches the ultimate limit state.

This document describes the behaviour of various types of screws connecting G450 cold-reduced steel sheets. Testing of simple screwed connections follows American and European recommendations. A finite element model was developed and validated with experiments using the ABAQUS software (Dassault Systèmes 2014). The screw model was built with solid deformable elements and contained thread's crests. Results from testing and simulation can be used to develop a numerical model for screw connectors interacting with thin steel sheets.

## 2 Screwed Connection Investigations

### 2.1 Screwed Connection in Shear Test

Screw shear tests were conducted using an MTS 810 hydraulic testing machine in the Structures Laboratory at the School of Civil Engineering, the University of Sydney. Testing was designed by following the American Standard - AISI S905: Test Methods for Mechanically Fastened Cold-formed Steel Connections (AISI 2008) and the European Standard – ECCS TC7 TWG 7.10: The Testing of Connections with Mechanical Fasteners in Steel Sheeting and Section (ECCS 2009). The G450 steel sheets tested have thickness of 2.4 mm and 3.0 mm and were cut from cold-formed steel roll. Due to the curling of rolled steel sheets, the test was modified from the standards using three screws placed parallel to the direction of the applied force (Fig. 1). Plate's length was chosen to fit 3 screws with spare length for the linear variable displacement transducers (LVDT). The resulted strength for each screw would have lower variation as the influence of the curling of the sheets and the distortion of the connections are reduced.

The fasteners used in the experiments are Buildex Hex Head Metal Tek screws. Screw sizes are 12 and 14 gauges (outer diameter of 5.5 and 6.3 mm). The size of thread crests on each screw is determined by the number of threads (crests) per inch

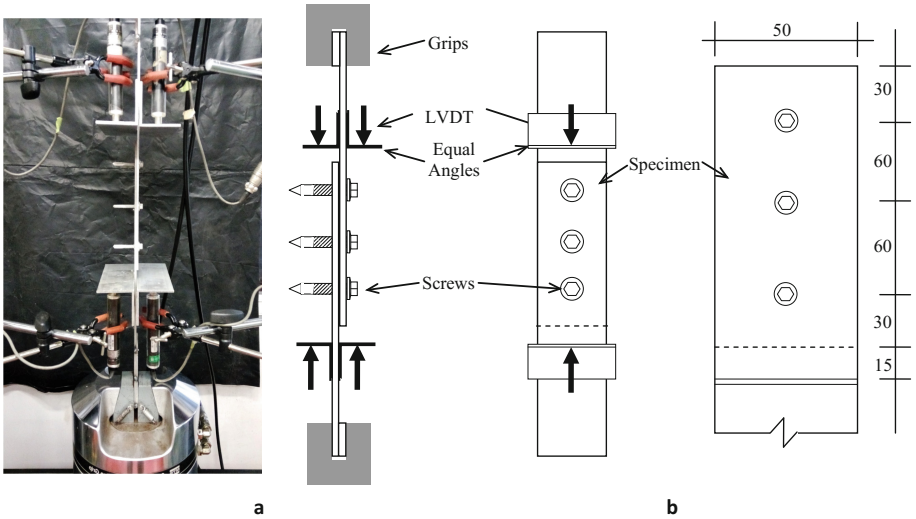


**Fig. 1.** (a) Test set-up and (b) test specimen

(TPI). Screws in the experiments have 10, 12 and 24 TPI. Screws' material is carbon steel SAE 1022 with heat treatment followed AS 3566.1 (BUILDEX 2017). Distances between screws and between screw and plate's end followed the European Standard.

Packing plates were used at the crossheads in order to apply a concentric axial load to the test specimens. However, there was still a possible moment along each specimen as the force transfer from the grip to the screws. This moment caused bending in the steel plates. Aluminum equal angles were used as support for measuring displacements with LVDT. Two equal angles were placed on each specimen to prevent distorted results caused by bending during loading.

Grips were connected to the crossheads of the MTS 810 machine. The crosshead was loaded at a rate of 0.1 mm/min using displacement-control method. The experiments were stopped when one of the three connectors failed, indicated by a sudden drop in the load. At least three tests were carried out for each type of screwed connection.

## 2.2 Explicit Solver in Finite Element Modeling

The modeling software Abaqus/CAE 6.14-1 was used to build a finite element model of the experiments. Abaqus provides two analysis tools: implicit and explicit. The implicit solver obtains unknown values by solving for true static equilibrium at a current time. The explicit solver uses known displacements, velocities and accelerations from the current time ($t$) to calculate the next state of the model (at the time $t + \Delta t$). Neither iteration nor convergence checking is required in an explicit analysis. The acceleration is assumed to be a constant during the time increment $\Delta t$, hence $\Delta t$ has to be small enough to generate correct load response over the running time.

The stable time increment in an explicit analysis is given by the minimum time that a dilatational wave moves across any element in the model (Dassault Systèmes 2014). It can be expressed as:

$$\Delta t = \frac{L_e}{c_d} = L_e \sqrt{\frac{\rho}{\lambda + 2\mu}}. \tag{1}$$

in which $L_e$ is the characteristic length of an element, $c_d$ is the dilatational wave speed and $\rho$ is the material density. The two constants $\lambda$ and $\mu$ are defined as:

$$\lambda = \frac{E\upsilon}{(1+\upsilon)(1-2\upsilon)}; \mu = \frac{E}{2(1+\upsilon)} \tag{2}$$

in which $E$ is the material's Young's modulus and $v$ is the Poisson's ratio.

It can be seen that $\Delta t$ depends on the smallest element's size in the model. Therefore verifying the mesh is an important step in building the model to minimize any geometric deviation in meshing.

The stability limit is very small in modeling steel structures. In steel, given E = 200,000 MPa, ν = 0.3 and $\rho$ = 7,850 kg/m$^3$, dilatational wave speed can exceed 6,000 m/s. $L_e$ depends on how fine the mesh is created. The model in this paper contains the screw's crests, which parts' size that has magnitude order of $10^{-1}$ mm. The consequence is the stable time increment in an Abaqus explicit job often smaller than $2 \times 10^{-8}$ s.

In order to obtain sufficiently accurate results using a reasonable computing cost, i.e. smallest solving time possible, the loading rate in the model has to be significant larger than in experiments. However, the loading rate must not be too large for the inertial dynamic effects to become significant. A simulation is considered as quasi-static or close to static when the total kinetic energy of the model is negligible compared to its total internal energy (Dassault Systèmes 2014).

For large structure modeling, using high loading rates, it is crucial to reduce the computing time. The loading rate in testing was 0.1 mm/min. In finite element modeling, different rates were used to get a suitable response with insignificant effect of kinetic energy. Figure 2 shows a model's load versus displacement responses for different loading speeds of 2,000 mm/min, 10,000 mm/min and 50,000 mm/min, corresponding to loading time of 0.12 s, 0.024 s and 0.0048 s.

In the model with 10,000 mm/min loading rate, the kinetic energy output is usually less than 1% of the internal energy. This indicates that the simulation is approaching a static state. This rate will be implemented for the other models.

### 2.3 The Finite Element Model

A simple model of a screw often includes a spring element with a given stiffness. However, real screwed connection's behaviour is more complicated than a spring. Each self-drilling screw has a teks point that can drill its own hole through up to 6 mm of steel. The thread will tap to the drilled hole and fix the screw into steel sheets. The interaction between the screw's thread and the hole, the yielding in the bearing face and

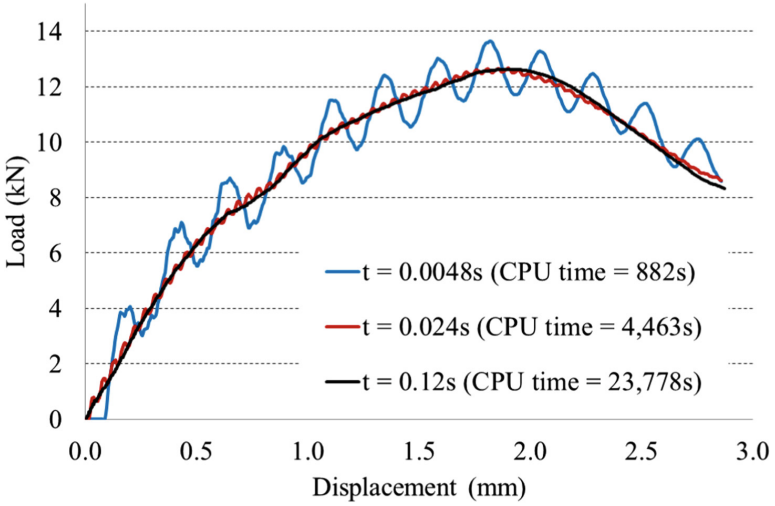


**Fig. 2.** Responses at different loading rates

curling of steel sheets make it difficult to match the response of screw connections with a spring model.

A 3D model of a screw connector is proposed and built as shown in Fig. 3. Only the threads that will be contact with steel sheets are modeled to reduce computing cost. To represent the threads tapping into the bearing hole, the threads' cross-section is model as a trapezoid with the smaller base in contact with the hole (Fig. 3b). Three dimensional eight-node solid elements with reduced integration point (C3D8R) are used for modeling screws and steel plates. The mesh is refined in screws and near the holes in specimens as fracture mainly initiated from these places. As shown in part 2.2, maximum stable time increment is proportional to the dimensions of the smallest element. Therefore, refining the mesh increases computational efficiency. Furthermore, computational cost is proportional the number of elements in a model, which escalates when elements' size reduces. Thus, the length of elements in fine-mesh area is controlled in order to yield an acceptable model solving time.

Surface to surface contact (explicit) is used for surfaces between two steel sheets, between screw threads and the inner hole, and between screw heads and the upper steel plate. Aluminium equal angles are tied to the specimen's surface. A friction coefficient is used to represent interlock between the screw thread and two steel plates. Calibration was carried out to ensure the friction is large enough to hold screws in place, but return minimal effect to the load response curve. For screwed connections of thin plates, bearing failure may cause the piling of material in front of fastener and the material can be in contact with itself. Other types of contact occur when a fracture initiates in screws or specimens, which exposes their inner material. Therefore, a general contact (explicit) definition is created for the whole model to account for any new contact that can arise during loading.

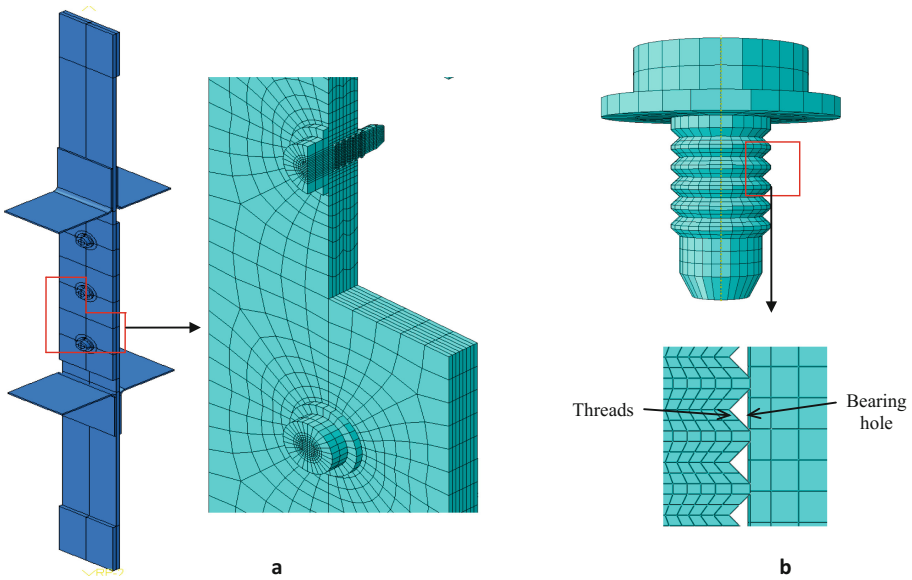


**Fig. 3.** (a) The assembly and (b) the screw

Boundary condition is defined to represent the grips from the MTS machine. The end of one specimen and the packing plate are restrained from movement in 3 directions. The other end is free to move across the load direction and restrained in other directions. There is no motion constraint in the middle part and in the screw connectors. With ample loading rate, the middle part oscillates sideways due to kinetic energy arising in the model. The effect of the oscillation is eliminated partially by taking average displacements of two aluminum equal angles. Moreover, a suitable loading rate reduces kinetic energy output and stabilizes the model.

Material properties input for G450 steel was extracted from coupon tests, with yield stress of 524 MPa and ultimate strength of 555 MPa. For the screw's material, low ductility material is used. The values of 800 MPa and 870 MPa are given for yield stress and ultimate stress. The screw material can undergo less than 1% of elongation before failure. For fracture modeling, the shear damage for ductile material is used. As observed from experiments, the fracture in screws often happens abruptly. Careful calibration was made to find the damage evolution value which can replicate the brittle failure characteristic of screws.

### 2.4 Test Results and FE Results

A data logger was used to record load and travel distance of 4 LVDT's at a rate of 5 samples/s. The load is divided by 3 to get the force carried by each screw. The displacement is the difference between the top and bottom averaged travel distances. Figure 4 shows the load response for three screw types: 12 g – 24 TPI, 14 g – 10 TPI and 14 g – 20 TPI. The graph shows the same pattern for all three types of connector.

Initially the load increases rapidly up to 4 to 6 kN, then the slope decreases until the screw reaches its ultimate strength and fails in shear. The change in slope can be explained by the plastic deformation in the bearing hole where the threads in the screw press on the hole's inner surface. This phenomenon can be seen more clearly in Fig. 5.

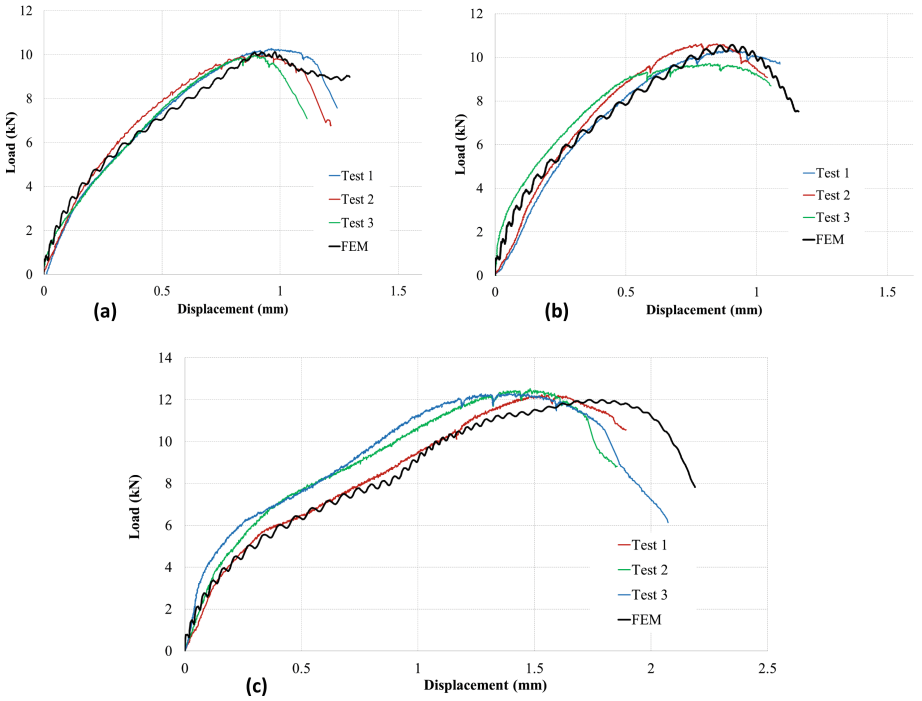


**Fig. 4.** Comparison of test results and FE modeling for 3 screw types: (a) 12 g – 24 TPI, (b) 14 g – 20 TPI and (c) 14 g – 10 TPI

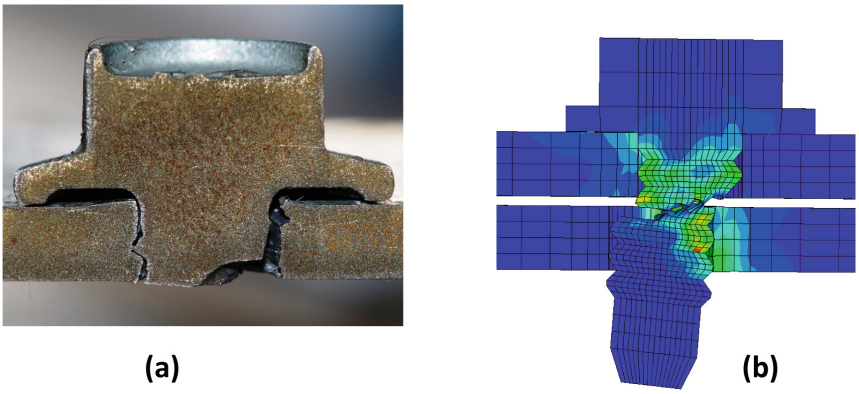


**Fig. 5.** Screw failure in (a) testing and (b) modeling

The graphs show that the connection using 14 g – 10 TPI screws has the highest ductility and bearing load. Although the outer diameter of a 14 g – 20 TPI screw is larger than of 12 g – 24 TPI screw, they both fail in similar loads. These observations depict the behaviour of a screw also depends on its inner diameter and the crest's dimension, which are not included in the screw's name. Three tests for each screw type also show the conformability in the screw's shear strength. The reason may be experiments were designed to minimize the interaction effect of the screws. For complex connections with screws positioned close together or connections under bending and shear, a reduction factor would be required in calculation of limit state design.

A FE result is also shown on each graph of Fig. 4. The model is able to reproduce the experiment's results with some variations for each type of screws. The ultimate load from FE modeling is similar to the test results. The load response is moderately consistent with the real behaviour in term of stiffness and ductility. Because of the complicated interaction between the screw thread and steel plates, the proposed model can only reflect partly what was happened in the experiments.

Figure 5 shows the screw that was cut in half to display the fracture more clearly. The FE model is able to reproduce the bearing and fracture angle between the fracture surface and the loading direction. The model does not include the effect of screw's thread tapping into steel material during the drilling process. The shape of the screw's head in the model is simplified compared with the real screw. As there was little curling in steel sheets, the contribution of bearing force between the washer and the top sheet is negligible (Lu et al. 2011).

For each screw type, screw's inner and outer diameter, size of thread crests and distance between crests were measured. These numbers are then translated to the FE model. However, the cross section of a crest in the model, which is a trapezoid (Fig. 3b), is unable to replicate the helix curve in the screw's thread, as well as the roundness at the crest's peak. Nevertheless, the advantage of this model is its simplicity. It can be adapted in building 3D model of large steel structure, while still maintains a reasonable computing cost.

Table 1 compares the ultimate shear strength of screws from testing, FE modeling and from manufacturing. The values given by Buildex company are pure shear strength of screws under laboratory conditions (BUILDEX 2017). The results from shear connection tests and modeling, however, are obtained when screws undergo bearing and tilting. Therefore, it is possible that the fracture surface of screws in the connection test and in pure shear strength test are different.

**Table 1.** Shear strength of screws

| Screws | Experiments (kN) | FEM (kN) | From manufacturer (kN) |
|---|---|---|---|
| 12 g – 24 TPI | 10.1 | 10.1 | 9.0 |
| 14 g – 20 TPI | 10.2 | 10.5 | 11.2 |
| 14 g – 10 TPI | 12.2 | 12.0 | n/a |

## 3 Conclusions

Experiments and FE analysis were carried out to study the behaviour of screws connecting cold-formed steel. The model shows good correlation with testing. The study focuses on the FE modeling methods including solver type, time increment, screw modeling, choice of element type and interactions. The model of screws contains both the washer and the thread. Careful measurement of the real screw geometry is required to create an accurate sample of the 3D model. The proposed design can be used in modeling of screws with different diameters and various numbers of threads per inch. Three screws for each test in this research are working individually with minimal interactions. Future research on complex screwed connections with interactions shall be carried out. The modeling method will be adapted for building large FE models of steel structural connections.

**Acknowledgments.** This research was carried out under the research grants "Hybrid steel-framed structural systems for mid-rise buildings" from Australian Research Council/Discovery Projects, with the support of the University of Sydney. The first author's research degree was supported by the Research Training Program (RTP) Fee Scholarship by the Australian Government. The steel sheets were provided by BlueScope Steel. The authors gratefully acknowledge for the supports.

## References

AISI: Test Methods for Mechanically Fastened Cold-formed Steel Connections, AISI S905. American Iron and Steel Institute, Washington, D.C. (2008)

AISI: North American Cold-Formed Steel Specification for the Design of Cold-Formed Steel Structural Members, AISI S100-12. American Iron and Steel Institute, Washington, D.C. (2012)

Australian/New Zealand Standard: Cold-Formed Steel Structures, AS/NZS 4600:2005. Standards Australia/Standards New Zealand, Sydney (2005)

BUILDEX. Technical Data Sheets (2017). http://www.buildex.com.au/support_data-sheets-teks_metal.html. Accessed 11 Jan 2017

Dassault Systèmes (2014). Abaqus 6.14 Online Documentation. http://129.97.46.200:2080/v6.14/. Accessed 15 Sept 2016

ECCS. The Testing of Connections with Mechanical Fasteners in Steel Sheeting and Sections, ECCS TC& TWG 7.10. Mem Martins, Portugal, European Convention for Constructional Steelwork (2009)

Lu, W., Mäkeläinen, P., Outinen, J., Ma, Z.: Design of screwed steel sheeting connection at ambient and elevated temperatures. Thin-Walled Struct. **49**(12), 1526–1533 (2011)

Rogers, C.A., Hancock, G.J.: Screwed Connection Tests of Thin G550 and G300 Sheet Steels. J. Struct. Eng. **125**(2), 128–136 (1999)

# Redistribution of Moment at Beam-Column Joints in RC Structures: Comparison Between an Experimental Study and Eurocode 2

B. Sentosa[1], Q.-B. Bui[2(✉)], J.-P. Plassiard[1], O. Plé[1], P. Perrotin[1], and H. Purnomo[3]

[1] Univ. Savoie Mont Blanc, LOCIE, CNRS, 73000 Chambéry, France
[2] Sustainable Developments in Civil Engineering Research Group, Faculty of Civil Engineering, Ton Duc Thang University, Ho Chi Minh City, Vietnam
buiquocbao@tdt.edu.vn
[3] Fakultas Teknik, Universitas Indonesia, Jakarka, Indonesia

**Abstract.** The current approaches authorized by Eurocode 2 for the design of reinforced concrete (RC) structures at the structural scale are: linear-elastic analysis, linear-elastic with limited redistribution of moments, plastic and non-linear analysis. Numerous experiments on RC beams were performed which provided interesting information for the models proposed in the standards. However, at the RC frame level where the beam-column are present, although several experiments have already been carried out in the literature, this topic is still to be investigated, due the important number of parameters: interior joint, exterior joint, stiffness ratio between beam and column, steel reinforcement type, … This paper presents firstly an experimental study on an H-form RC frame structure (two vertical columns and one horizontal beam). Several loading-unloading cycles were carried out. Displacement fields during the test were measured by the image correlation technique. Then, experimental results were compared with that of the analytical models proposed in Eurocode 2 and an advance FE code (CAST3M). The comparisons show that analytical methods presented in Eurocode 2 underestimated about 20–30% of the ultimate capacity of the structure; while the non-linear analysis with CASTEM code – when material characteristics and boundary conditions are correctly identified - could provide good results comparing to the experiments.

**Keywords:** Reinforced concrete · Beam-column frame · Experiment · Eurocode 2 · CASTEM

## 1 Introduction

Beam-column joints are commonly considered critic regions for RC frames subjected to earthquake. That is why assessing the beam-column joint capacity is an important topic, for both existing structures, especially structures constructed before the modern seismic design codes, or for buildings in post-seismic situations. In these cases, a structural evaluation is needed before a decision is taken if any reparation/retrofitting is necessary.

© Springer Nature Singapore Pte Ltd. 2018
H. Tran-Nguyen et al. (eds.), *Proceedings of the 4th Congrès International de Géotechnique - Ouvrages -Structures*, Lecture Notes in Civil Engineering 8,
DOI 10.1007/978-981-10-6713-6_22

Among the in-situ structural assessment methods, the non-destructive method using vibrational measurements (by accelerometers or velocimeters) is currently mentioned (Boutin et al. 2005, Brownjohn 2003, Bui et al. 2014a, Volant et al. 2002).

From the dynamic characteristics measured by vibrational tests (natural frequencies, mode shapes, damping ratios), several approaches were proposed in the literature to establish the relationship between the dynamic characteristics and the structure's health (Boutin et al. 2005, Chang et al. 2003, Fang et al. 2008, Maas et al. 2012). At present, the proposed approaches enables to diagnose a structure on a global scale (the whole structure), while the identification and the assessment of local damages (each element of the structure, and especially the beam-column joints) remains to be explored (Bui et al. 2014b, Maas et al. 2012).

The authors have conducted researches since several years on the topic using the vibrational measurements to identify the structural damages at the element scale, and especially for beam-column joints. An analytical method has been recently developed in the thesis of the first author of this paper (the thesis has not yet been defended and the method has not yet been published). The method consists of two main steps and the first one demand that the displacements of some specific points (corresponding to the principal mode shapes) and the actual stiffness (corresponding to the damaged structure) should be relevantly determined. So, a robust numerical or analytical model is necessary to obtain these information. The authors have chosen to use the numerical approach (FEM), by seeking a numerical model which can reproduce finely the structural behavior at the element's scale.

From the regulations' view point, the current approaches authorized by Eurocode 2 for the design of reinforced concrete (RC) structures at the structural scale are: linear-elastic analysis, linear-elastic with limited redistribution of moments, plastic and non-linear analysis. Numerous experiments on RC beams were performed which provided interesting information for the models proposed in the standards. However, at the RC frame level where the beam-column are present, although several experiments have already been carried out in the literature, the number of experiments is still modest comparing to the important number of parameters which affect the joint behaviour: interior joint, exterior joint, stiffness ratio between beam and column, steel reinforcement type, semi-rigid connections… (Bui et al. 2014b, Haselton et al. 2008, Metelli et al. 2015, Omidi and Behnamfar 2015, Sharma et al. 2011). That is why additional experimental studies in this topic is interesting for the scientific community, to improve the existing models.

In this context, the present paper has three main aims: first, presents an experimental study on an RC beam-column frame structure, which provides an additional experimental data for the further analytical models. Then, the obtained experimental results can be used to assess the relevancy of the analytical models proposed in Eurocode 2. And finally, the experimental result is used also to check the robustness of a numerical model in an advance FE code (CAST3M). If the model can provide the relevant results for the case of beam-column joints under cyclic loadings, it can be used in the second step of the method developed by the authors for the structural health evaluation by using dynamic measurements.

## 2 Experimental Study

### 2.1 Structure Studied

The structure studied is a beam-column RC structure having H-form (two columns and one beam, Fig. 1). The cross-sections of the beam and columns are (0.2 m × 0.2 m) and (0.2 m × 0.25 m), respectively. The details of the dimensions and the steel reinforcement rods are presented in Fig. 2.

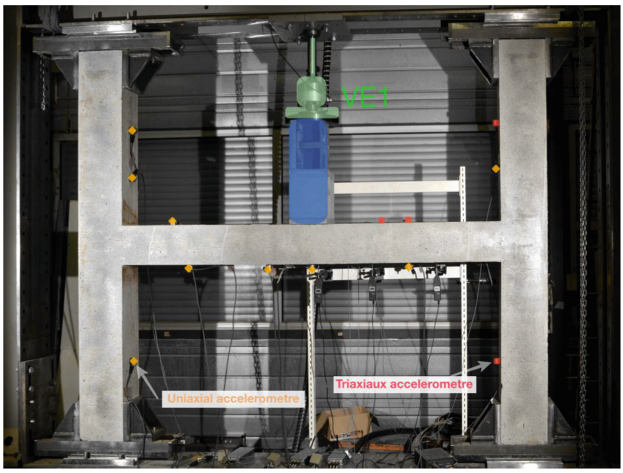


**Fig. 1.** Static loading of the H-form RC frame structure.

The RC frame structure was fixed and the ends of the columns by steel jacks (Fig. 1); then, it was loaded at the beam's mid-span by an actuator (maxi capacity of 300 kN), via a steel box placed on the beam. The actuator was controlled in displacement (0.1 mm/min). The displacements were measured at the same time by displacement sensors (under the beam, Fig. 1) and by the DIC (digital image correlation) technique (Vacher et al. 1999). The use the DIC technique, two cameras (16 MPixels) were installed and recorded the test. After a data processing, the displacement fields (on whole structure tested) can be determined. To obtain good results with DIC technique, RC beam-column structure was sprayed with black paint to have random points on its surface. Accelerometers (uniaxial and triaxial) were also installed on the structure to measure the dynamic characteristics and their relationship with the damage evolution; however, in this paper, due to the limited space, dynamic results will not be presented.

Concrete used was an industrial concrete "*béton pro 350*" of VICAT, which is similar to a C30/37 following Eurocode 2 [2]. Three cylindrical specimens (16 cm-diameter and 32 cm-height) were manufactured (Fig. 3) for uniaxial compression tests to determine the compressive strength and the Young's modulus.

The RC beam-column frame was casted at a horizontal position in a laminated-wood formwork (Fig. 4, on the left). The structure was cured in the ambient condition. At the testing moment, the structure was erected by placing a wooden beam on the column's tops (Fig. 4 at the right) and using a mechanical elevator to rise the

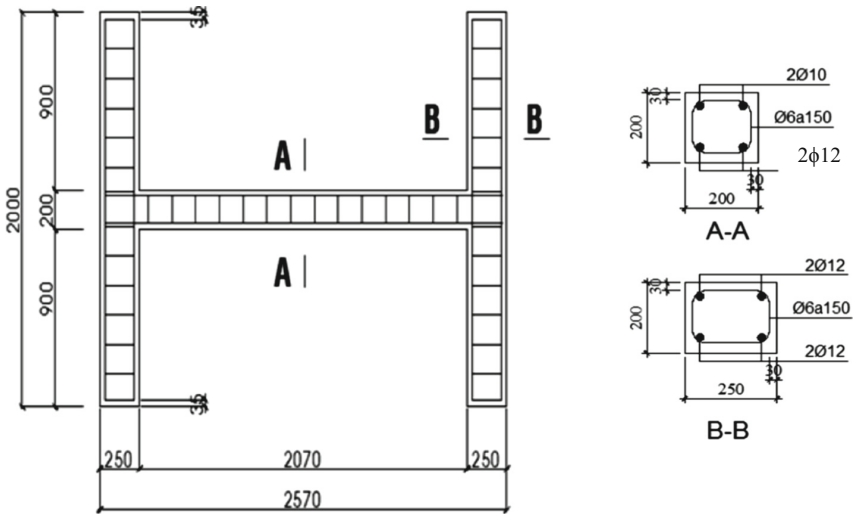


**Fig. 2.** Steel reinforcement of the studied structure.

**Fig. 3.** Cylindrical specimens during the curing (at the left) and after the paint spraying for DIC (at the right).

**Fig. 4.** Left: horizontal formwork for the concrete casting; right: preparation for the erection.

beam-column structure in vertical position. The structure was then placed on the steel loading frame (as shown in Fig. 1). The movement and placing the structure was a delicate operation which needs a particular attention and technical skills.

For the Young's modulus, the displacements were determined from the data obtained with DIC technique. Similar to the frame structure, cylindrical specimens were also painting sprayed (Fig. 3, on the right) in order to obtain better results with DIC technique. The Young's modulus was calculated for the central part of the specimen, to avoid influences of the friction between the specimen's surfaces and the press plates.

## 2.2 Experimental Results

Uniaxial compression tests on cylindrical specimens gave results of 38.55 MPa for the mean compressive strength, 33.98 GPa for the Young's modulus and 0.217% for the strain corresponding to the maximal stress. The obtained stress-strain curve will be presented in the next section.

For the test on the beam-column structure, loading and unloading cycles were performed, in order to assess the structural behavior under cyclic loadings. Figure 5 illustrates the experimental relationship between the force and the displacement at the beam's mid-span; the order of the cracks' apparition and the corresponding forces. The locations of these cracks are visualized in Fig. 6, by using the DIC technique.

Following the elastic-linear theory, the moments at the beam's mid-span and the beam's ends have the same absolute value:

$$M = P.L/8 \tag{1}$$

where $P$ is the applied force at the beam's mid-span, and $L$ is the effective length of the span).

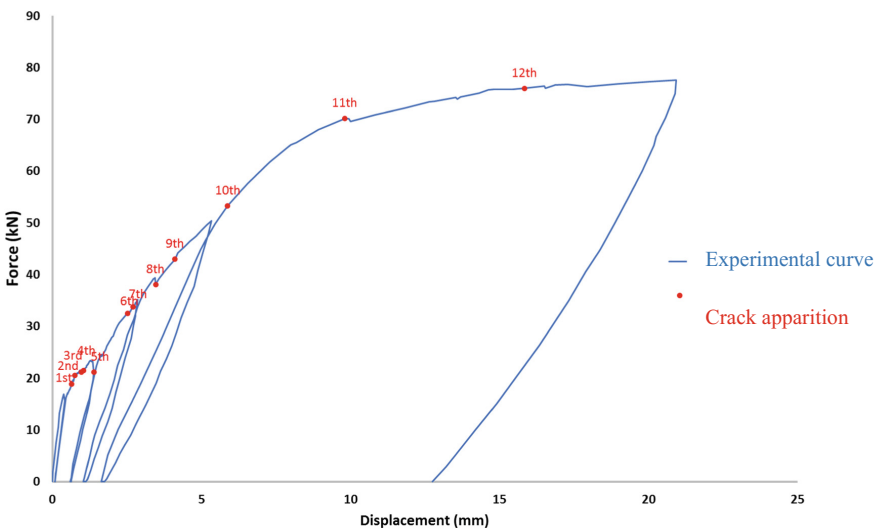


**Fig. 5.** Relationship between the force applied and the displacement at the beam's mid-span.

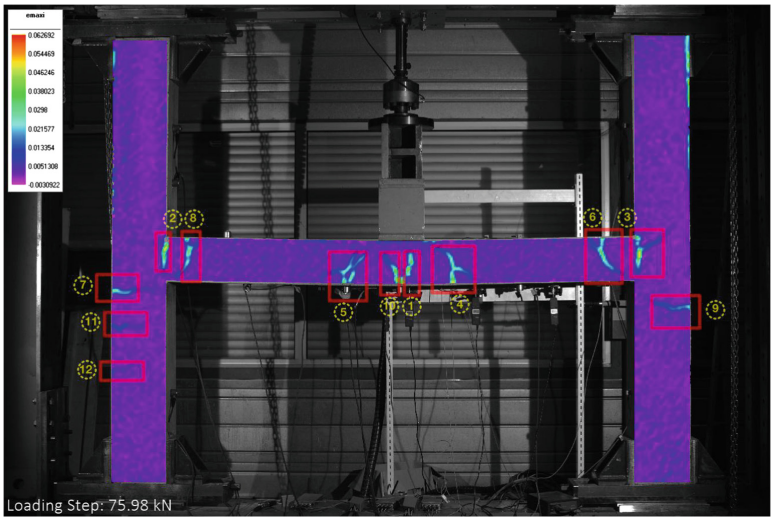


**Fig. 6.** Evolution of the cracks: order of apparition: from 1st to 12th cracks.

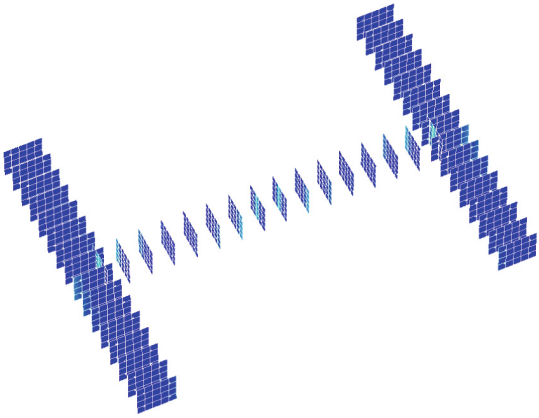

**Fig. 7.** The RC frame studied modelled by multi-fiber beam elements.

The difference is that the moment is negative at the beam's ends and positive at the beam's mid-span. So, following this remark, when the beam has bigger tensile steel reinforcements at the beam's mid-span (2 rods 12 mm-diameter, Fig. 2) than that at the beam's ends (2 rods 10 mm-diameter, Fig. 2), the resistant moment at the beam's mid-span should be greater. The experiment showed that the first crack appeared at the beam's mid-span. The second and third cracks appeared latter at the beam's ends. This showed that the moment at the beam's mid-span was probably greater than that at the beam's ends.

# 3 Analytical Results Following Eurocode 2

## 3.1 Elastic-Linear Theory

Following the elastic-linear theory, the moments at the beam's mid-span and the beam's ends can be calculated following Eq. (1). For the resistant moment, it can be calculated by the relationship authorized in Eurocode 2:

$$M_{resistant} = A_s . f_{yd} . Z \tag{2}$$

where $A_s$ is the tensile steel area; $f_{yd}$ is the steel's yield strength; and $Z$ is the lever aim between the center of the compressive part and the tensile steels' center. Eurocode 2 [2] authorizes to calculate approximately $Z = 0.81\ h$ where $h$ is the beam's cross-section height.

From the formula (2), the resistant moments for the beam mid-span and the beam ends can be calculated, and then the maximum force $P$ which can be resisted by these parts can be calculated from Eq. (1) which give the values of 65.09 and 45.47 kN respectively for the mid-span and the beam ends. This means that, the maximum force carried by the studied frame would be 45.47 kN following this theory, and the failures should be at the beam's end. This result was not the case during the experiment where the cracks appeared before at the mid-span and the mid-span had more damages than the beam's ends. Moreover, the experimental maximum force is of 77 kN which is much higher than the predicted value. It suggested that there was a moment redistribution in the frame during the test.

## 3.2 Elastic-Linear with the Moment Redistribution

To take into account the plastic hinges apparition which leads to a moment redistribution, the elastic moment at the beam ends should be multiplied by a redistribution coefficient δ (which varies from 0.7 to 1 in the case of steel S500B)

$$M_{red} = \delta . M_{elastic} \tag{3}$$

More information about δ can be found in Eurocode 2. Following this theory, the analytical maximal load applied on the studied frame should be 55.15 kN. This value is still lower than that obtained from the experiment (77 kN). This means that the calculations taken into account the moment redistribution give a better result comparing the linear-elastic theory, however, this results is still conservator (in the safety side).

# 4 Numerical Result by Using Finite Element Modelling

An advanced FE code, CAST3M, was used in the present study to assess the possibility to reproduce the experimental behavior. CAST3M is a powerful FE code which has been developed to study the nuclear structures (Combescure et al. 1982). The used model was the multifiber beam elements. The multifiber beam elements are the beams which can take into account the cross-section, so the steel reinforcements are also take

into account (Fig. 5). The concrete behavior was modelled with the model proposed by LaBorderie (1991), the steel reinforcement was modelled by the well-known Menegoto & Pinto model. The LaBorderie model was chosen because it could reproduce the plastic strains appeared during the unloading-reloading cycles.

The compressive characteristics of the concrete (compressive strength, Young's modulus, stress-strain relationship) were determined from the tests on cylindrical specimens. The tensile behavior of concrete was determined following the empirical relationships provided in Eurocode 2 (2004). The stress-strain relationship of the steel was taken following the data provided by the manufacturer (steel S500B following Eurocode 2). The characteristics of concrete and steel used for the numerical study are presented in Fig. 6 (Fig. 8).

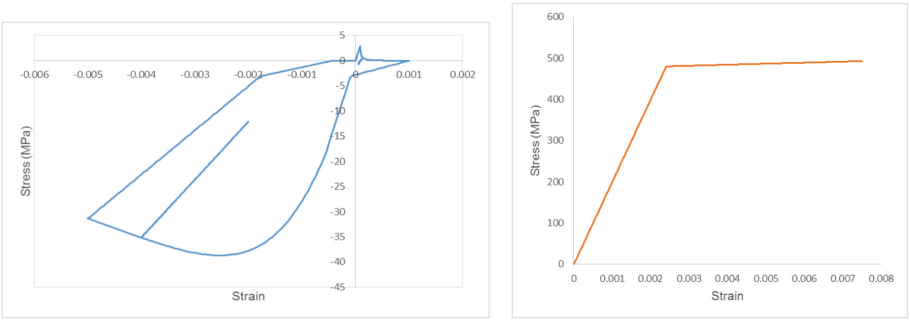


**Fig. 8.** Stress-strain relationships of concrete (left) and steel (right) used for the numerical model.

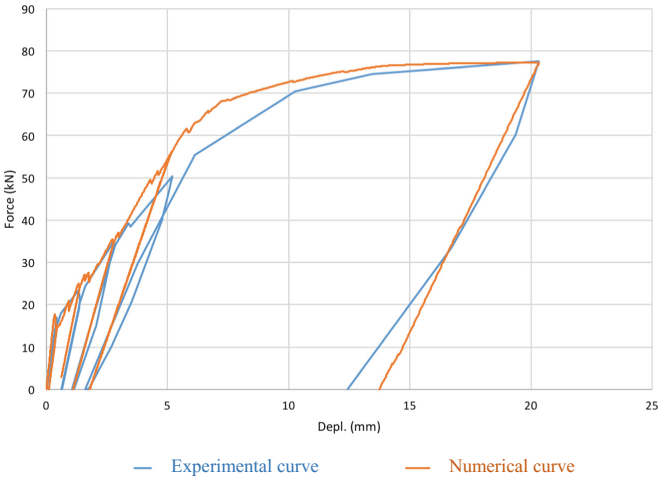


**Fig. 9.** Comparison of the results obtained by the experiment and by CASTEM.

The obtained numerical result is presented in Fig. 7, in comparison with the experimental one. The result shows that the numerical model could reproduce the global experimental behavior: maximal force, form of the curve, slopes of the unloading-reloading cycles. Just the hysteresis in the cycles was not reproduced correctly; this can be explained by the used model for concrete which does take into account the hysteresis phenomenon in the cycles (Fig. 6, on the left) (Fig. 9).

## 5 Conclusions

This paper presents first an experimental study on a RC beam-column frame structure. The experiment on a grand size specimen needed attentions in the preparation and during the test. The displacements during the test were recorded by using the DIC technique, from which the cracking evolution was observed. The results obtained in this study can be used as an additional experimental data for the further analytical models. Then, analytical models proposed in Eurocode 2 were applied and the analytical results were compared with that from the experiment. The comparison showed that the linear-elastic method was less realistic and underestimated the maximum force carried by the structure. The method taken into account the moment redistribution gave a better result but still underestimate the maximum load (which is in the safe side for the prediction). Finally, a FE model using the advance CAST3M code was developed. The result showed that the numerical model could reproduce globally the experiment, including the unloading-reloading cycles, but the hysteresis behavior was not reproduced in the cycle. That means that for the case of cyclic loading (earthquake), the model should be improved to take into account the hysteresis behavior. However, for the method developed by the author for the structural health evaluation, the measurements are realized in small deformations, so the hysteresis influences can be negligible. So, the tested model can be used for the second step of the structural health evaluation method.

## References

Boutin, C., Hans, S., Ibraim, E., Roussillon, P.: In situ experiments and seismic analysis of existing buildings. Part II: Seismic integrity threshold. Earthq. Eng. Struct. Dyn. **34**, 1531–1546 (2005)

Brownjohn, J.M.W.: Ambient vibration studies for system identification of tall building. Earthq. Eng. Struct. Dyn. **32**, 71–95 (2003)

Bui, Q.B., Hans, S., Boutin, C.: Dynamic behaviour of an asymmetric building: experimental and numerical studies. Case Studies in Nondestructive Testing and Evaluation, vol. 2, pp. 38–48, October 2014a

Bui, Q.B., Mommessin, M., Perrotin, P., Plassiard, J.P., Plé, O.: Assessing local-scale damage in reinforced concrete frame structures using dynamic measurements. Engineering Structures, pp. 22–31 (2014b)

Chang, P.C., Flatau, A., Liu, S.C.: Review paper: health monitoring of civil infrastructure. Struct. Health Monit. **2**, 257–267 (2003)

Fang, S.E., Perera, R., Roeck, G.D.: Damage identification of a reinforced concrete frame by finite element model updating using damage parameterization. J. Sound Vibr. **313**, 544–559 (2008)

Eurocode 2 Design of concrete structures - EN 1992, European Committee for Standardization (2004)

Combescure, A., Hoffmann, A., Pasquet, P.: Chapter: The CASTEM Finite Element System, in Finite Element Systems, pp 115–125 (1982)

Haselton, C.B., Liel, A.B., Lange, S.T., Deierlein, G.G.: Beam-column element model calibrated for predicting flexural response leading to global collapse of RC frame buildings, PEER report 2007/03, Pacific Earthquake Engineering Research Center (2008)

LaBorderie, Ch.: Phénomènes unilatéraux dans un matériau endommageable: modélisation et application à l'analyse de structures en béton, Ph.D. thesis (in French), Univ. Paris VI (1991)

Maas, S., Zürbes, A., Waldmann, D., Waltering, M., Bungard, V., De Roeck, G.: Damage assessment of concrete structures through dynamic testing methods. Part 1- Laboratory tests. Eng. Struct. **34**, 351–362 (2012)

Metelli, G., Messali, F., Beschi, C., Riva, P.: A model for beam–column corner joints of existing RC frame subjected to cyclic loading. Eng. Struct. **89**, 79–92 (2015)

Omidi, M., Behnamfar, F.: A numerical model for simulation of RC beam-column connections. Eng. Struct. **88**, 51–73 (2015)

Sharma, A., Eligehausen, R., Reddy, G.R.: A new model to simulate joint shear behavior of poorly detailed beam-column connections in RC structures under seismic loads. Part I: Exterior Joints Eng. Struct. **33**, 1034–1051 (2011)

Vacher, P., Dumoulin, S., Morestin, F., Mguil-Touchal, S.: Bidimensional strain measurement using digital images, Proc. Instn. Mech. Engrs., vol. 213, Part C ImechE, 811–817 (1999)

Volant, Ph., Orbovic, N., Dunand, F.: Seismic evaluation of existing nuclear facility using ambient vibration test to characterize dynamic behavior of the structure and microtremor measurements to characterize the soil: a case study. Soil Dyn. Earthq. Eng. **22**, 1159–1167 (2002)

# Shear Resistance Behaviors of a Newly Puzzle Shape of Crestbond Rib Shear Connector: An Experimental Study

Thi Hai Vinh Chu[1], Van Phuoc Nhan Le[2], Duy Kien Dao[3], Thanh Hai Nguyen[1], and Duc Vinh Bui[2(✉)]

[1] Faculty of Civil Engineering, MienTrung University of Civil Engineering, Tuy Hoa City, Phu Yen, Vietnam
{chuthihaivinh, nguyenthanhhai}@muce.edu.vn
[2] Department of Civil Engineering, Ho Chi Minh City University of Technology, District 10, Ho Chi Minh City, Vietnam
{lvpnhan, vinhbd}@hcmut.edu.vn
[3] Department of Civil Engineering, Pusan National University, Geumjeong-Gu, Busan, Korea
kiendaoduy@gmail.com

**Abstract.** A newly puzzle shape of crestbond rib shear connector is a type of ductile perfobond rib shear connector. This shear connector has some advantages, including relatively easy rebar installation and cutting, as well as the higher shear resistance strength. Thus, this study proposed a newly puzzle shape of crestbond rib with a "ʊ" shape, and its shear resistance behaviors and shear strengths were examined using push-out tests. Five main parameters were considered in the push-out specimens to evaluate the effects of shear resistance parameters such as the dimensions of the crestbond rib, transverse rebars through the crestbond dowel, concrete strength, rebar strength, and dowel action on the shear strength. The shear loading test results were used to compare the changes in the shear behaviors, failure modes, and shear strengths. It was found that the concrete strength and number of transverse rebars in the crestbond rib were significantly related to its shear resistance.

**Keywords:** Crestbond rib · Composite dowel · Push-out test · Shear connector · Shear resistance · Puzzle shape

## 1 Introduction

Shear connectors have played an important role in steel–concrete composite and mixed structures. They produce a composite action between the concrete and steel, allowing them to behave as a single unit and transfer a force from each material member. Recently, various steel–concrete composites or mixed structures have been proposed and researched to increase the span length or decrease the thickness of members. In addition, high-strength concrete has been developed and researched.

A perfobond rib shear connector [1–5] with a flat steel plate with holes for rebar is another type of connector that It resists horizontal shear and vertical uplift forces at the

© Springer Nature Singapore Pte Ltd. 2018
H. Tran-Nguyen et al. (eds.), *Proceedings of the 4th Congrès International de Géotechnique - Ouvrages -Structures*, Lecture Notes in Civil Engineering 8,
DOI 10.1007/978-981-10-6713-6_23

steelconcrete interface using a concrete end-bearing zone, concrete dowels, and transverse rebars in the rib holes. It has been studied and widely used because of its utility, easy fabrication, and high shear resistance. It was developed in Germany starting with the research by Leonhardt *et al*. [6], Oguejiofor and Hosain [7].

A crestbond rib shear connector is another type of shear connector. It is also a flat plate-type shear connector with open holes. A crestbond rib shear connector has advantages similar to those of a perfobond rib shear connector, such as a high shear strength. In this study, therefore, a newly puzzle shape of crestbond rib with a "ʊ" shape was proposed, and its shear resistance strengths and behaviors were examined in relation to shear resistance parameters such as the strength of the concrete in the concrete matrix, dimensions of the crestbond rib, and rebar in the crestbond. Therefore, six push-out test specimens were fabricated, and their shear behaviors, failure modes, and shear strengths were compared using test results.

## 2 Push-Out Test of the Newly Puzzle Shape of Crestbond Rib Shear Connector

To examine the shear strength and behaviors of a shear connector, a push-out test is generally applied. Thus, in this study, the standard push-out tests were conducted to examine and compare the shear resistance characteristics of the newly puzzle shape of crestbond rib shear connector. The test procedure and evaluation of the test results were performed according to the guideline of Eurocode 4 [8]. To compare the shear resistance strength of a typical head stud shear connector, an additional push-out test of a head stud shear connector was also conducted.

### 2.1 Push-Out-Test Specimens

In this study, push-out-test specimens were fabricated according to Eurocode 4 [8]. The composite dowels consist of different structural components interacting with each other to establish the bond between the compound materials steel and concrete, which includes the steel-dowel, the concrete-dowel and the dowel-reinforcement located within the concrete-dowel. Thus, a push-out specimen consisted of three main parts: the steel member, the newly puzzle shape of crestbond rib welded in the flange of the steel member, and concrete matrix placed at both sides of the steel member. The dimensions of all the push-out specimens were identical. The thickness of the crestbond rib was fixed at 8 mm, and the diameter of the rebars used was fixed at 12 mm. As test parameters of the crestbond rib shear connector specimens, the rib dimensions of the crestbond rib were considered, as shown in Fig. 1. In Fig. 1, category A had a crest rib open hole area of 3920 $mm^2$, and category B had a crest rib open hole area of 4490 $mm^2$. In addition, the number of rebars was changed from 0 to 2 in the test specimens, and two concrete strengths for the concrete matrix were considered, i.e., B25 (35.5 MPa) and B40 (50.0 MPa). Accordingly, the shear resistance of the newly puzzle shape of crestbond rib shear connector depended on the bearing resistance, longitudinal resistance by the concrete dowel, vertical resistance by the concrete dowel, and longitudinal resistance by the transverse rebar. The test specimens were called AS1

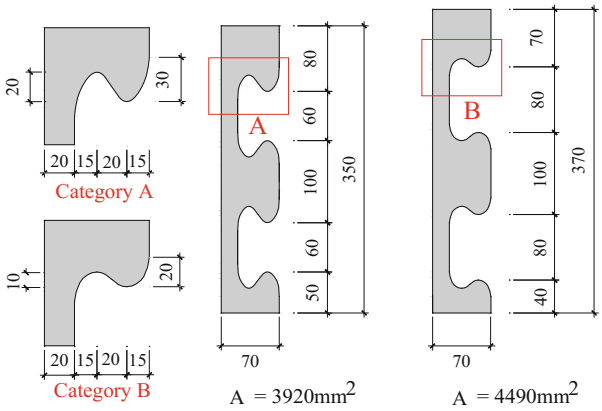


**Fig. 1.** Dimensions of the newly puzzle shape of crestbond rib shear connector

and BS1–BS5, depending on the rib dimensions, number of rebars, and concrete strength. During specimen fabrication, a gap of 20 mm was left at the end of the crestbond to exactly simulate the actual behavior of a composite beam, because a continuous crestbond rib was welded along the beam length. The width of this gap equaled the thickness of the crestbond rib. Beside that one more type of specimen was designed and denoted HS1, this type was the same size with the others, and concrete strength B25 (35.5 MPa) was also used. However, head stud shear connectors were applied in specimens HS1 to compare the shear strength of the crestbond rib with that of head stud connectors. Figure 2 shows the dimension one of test specimen. The preparation of the specimens is shown in Fig. 3. Table 1 summarizes the characteristics of the seven test specimen groups used in this study.

## 2.2 Material Properties

In this study, two concrete strengths were used for the concrete matrix: B25 and B40. For the steel crestbond rib and H beam, the CT3 grade with a yield strength $f_y$ = 250 MPa was used. A steel rebar with a 330-MPa yield strength was used.

## 2.3 Test Program

To evaluate the shear strengths and shear behaviors of the push-out specimens with the newly puzzle shape of crestbond rib, the relative slip between the concrete and steel was measured using linear variable displacement transducers (LVDTs) on both sides of the concrete matrix (LVDT-3 and LVDT-4), as shown in Fig. 4. Additionally, to identify the concrete crack propagation in the concrete slab, LVDTs (LVDT-1 and LVDT-2) were also laterally installed at the concrete surface of each concrete matrix. A load cell with a load capacity of 1000 kN was used to record the applied shear load on a push-out specimen.

An incremental loading process was performed according to Eurocode 4. In this loading process, the first loading stage consisted of 2 cycles of loading/unloading

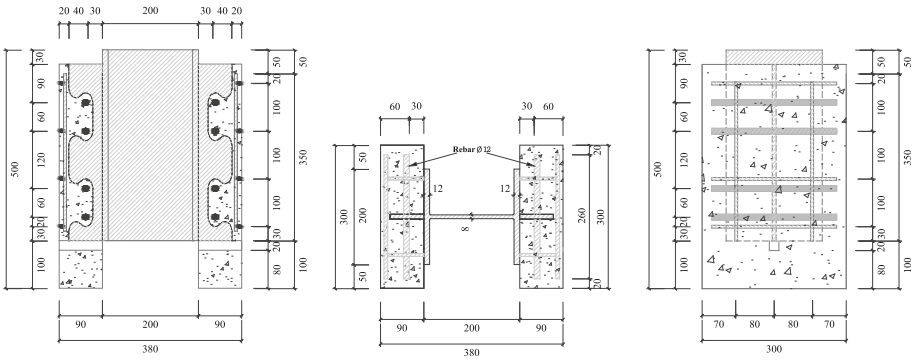


(a) crestbond rib shear connector

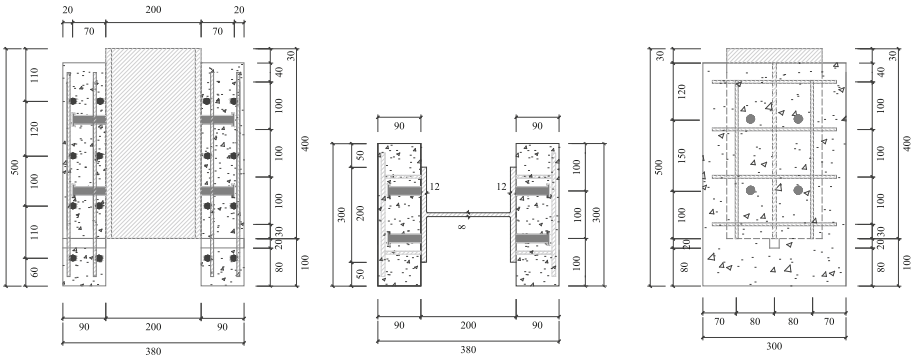

(b) Head stud connector

**Fig. 2.** Configuration and dimensions of specimen

(a) Welded crestbond rib on steel beam

(b) Test specimen

**Fig. 3.** Fabrication of test specimens

from zero to 40% of the expected failure load. The second stage included 25 cycles of loading/unloading from 10% to 40% of the expected failure load, and in the last stage, the load was gradually increased until the specimen failed.

**Table 1.** Properties of specimens

| Group | Number of specimen | Number of head stud | Section area of hole ($mm^2$) | Concrete grad | Number of rebar |
|---|---|---|---|---|---|
| AS1 | 2 | | 3920 | B25 | 2 |
| BS1 | 2 | | 4490 | B25 | 2 |
| BS2 | 2 | | 4490 | B25 | 1 |
| BS3 | 2 | | 4490 | B40 | 2 |
| BS4 | 2 | | 4490 | B40 | 1 |
| BS5 | 2 | | 4490 | B25 | – |
| HS1 | 3 | 4 | – | B25 | – |

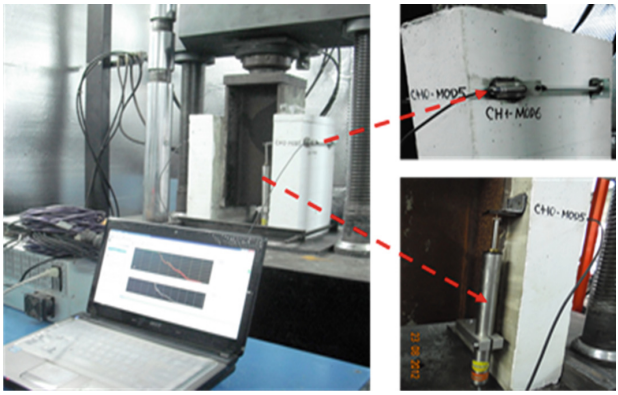

**Fig. 4.** Push-out test setup

## 3 Push-Out Test Results and Discussion

### 3.1 Push-Out Test Results and Failure Modes

Figure 5 presents the mean shear load–mean relative slip curves of the push-out test specimens. The test results are also summarized in Table 2. In Table 2, $P_{max}$ is the peak load, $P_{rk}$ is defined as the characteristic load and is equal to 90% of the peak load, $P_{rk,1}$ is the average load value per crestbond rib hole, and $\delta_u$ is the relative slip at the characteristic load. Figure 5 shows the behaviors of a typical rigid shear connector with an initially stiff shear resistance behavior before the ductile behavior begins. After the initial bearing resistance behavior of the concrete dowel, a relative slip occurred in all the specimens. The push-out specimen with the higher concrete strength (B40) and two rebars showed a higher shear-resistance strength. The number of rebars increased its shear strength as a result of the rebar resistance effect, and the shear resistance behaviors of push-out specimens with rebar showed higher shear strengths and ductile behaviors than specimens without rebar, as shown in Fig. 5(a). Push-out specimens with the B25 concrete strength also showed higher ductile behaviors for lateral cracks

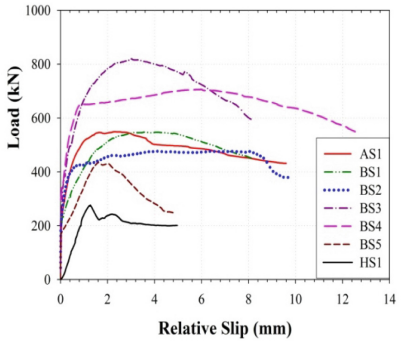


(a) Relative slip between steel beam and concrete matrix

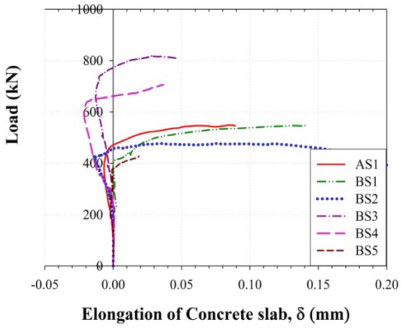


(b) Lateral elongation of concrete slab

**Fig. 5.** Summary of push-out test results

**Table 2.** Push-out test results for each group

| Group | Concrete strength (MPa) | Ultimate load (Pmax), (kN) | $P_{rk}$(kN) | Relative slip δmax (mm) | Elongation of concrete slab (mm) |
|---|---|---|---|---|---|
| AS1 | 35.5 | 549.53 | 494.6 | 8.99 | 0.19 |
| BS1 | 35.5 | 563.01 | 506.7 | 7.51 | 0.17 |
| BS2 | 35.5 | 487.2 | 438.5 | 9.34 | 0.48 |
| BS3 | 50 | 790.99 | 711.89 | 5.31 | 0.069 |
| BS4 | 50 | 693.26 | 623.94 | 6.59 | 0.020 |
| BS5 | 35.5 | 462.83 | – | 4.61 | 0.037 |
| HS1 | 60 | 205.80 | 185.22 | 1.17 | – |

than push-out specimens with the B40 concrete strength, as shown in Fig. 5(b). When comparing the shear strength of the crestbond rib with that of head stud connectors, its shear strength was 2.37–3.84 times higher than that of the head stud, although it was difficult to directly compare these shear connectors because of the application conditions and shapes.

The failure mechanism of the crestbond rib shear connector was complex, and included compression, shear, and tension. Under shear loading on a push-out test specimen, the load was first applied to the concrete dowel, which failed at the interface between the concrete dowel and crestbond, while two sides of the crestbond were in tension and cracks began in the middle of the specimen. During the test process, cracks were observed and plotted following every loading stage. Figure 6 shows the typical failure mode of the specimens after the loading tests. The crack occurrence and propagation had the same tendency for all the specimens. Cracks initiated in the middle of the concrete slab in the vertical direction, and then propagated with insignificant loading. The shear resistance strength decreased when horizontal cracks developed, and finally, cracks occurred in the front and rear faces. After reaching the ultimate shear load, cracks were initiated in the bottom of the concrete slab, and these cracks

**Fig. 6.** Crack distributions in concrete slab after push-out tests

**Fig. 7.** Deformation of shear connectors and transverse rebars in crestbond holes

propagated from the position of the crestbond rib to the bottom of the concrete slab. After the loading testing, the interiors of the push-out test specimens were also examined after removing the concrete matrix. No failure or deformation of the crestbond rib was found. For specimens with rebar, the rebars were deformed and moved from their original positions, as shown in Fig. 7.

## 3.2 Analysis of Push-Out Test Results

### 3.2.1 Effects of Dimensions of the Newly Puzzle Shape of Crestbond Rib

To compare the effects of the dimensions of the crestbond rib on its shear strength and behaviors, the shear load–relative slips are presented in Fig. 8. In this study, the crestbond specimens in categories A and B (3920 $mm^2$ and 4490 $mm^2$ cross-sectional areas for holes) showed similar shear resistance strengths and behaviors. The ductile behavior of BS1 was slightly larger than that of AS1, and the cross-sectional area of the crestbond rib also had a minor effect on the shear resistance of the crestbond rib shear connector.

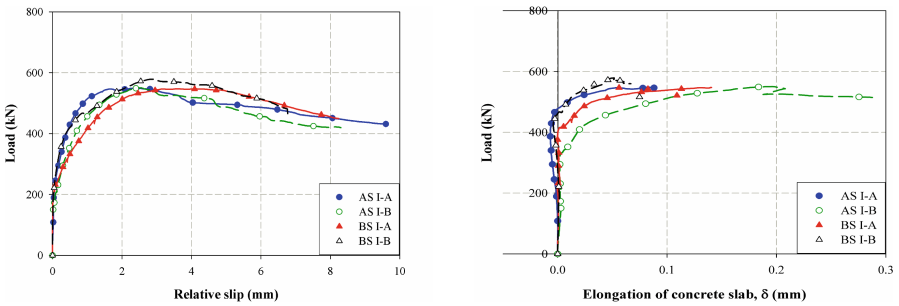


(a) Relative slip curves (b)Elongation of concrete slab

**Fig. 8.** Effects of dimensions of crestbond rib

### 3.2.2 Effect of Transverse Rebar

In order to examine the effect of the reinforcement on the shear resistance of the crestbond rib connector, push-out tests with different numbers of rebars were carried out. The number of rebars in the crestbond had an effect on its ductile behaviors. A crestbond rib connection with a single rebar produced a higher ductile behavior than a crestbond rib connection with two rebars under all the concrete strength conditions, as shown in Fig. 9.

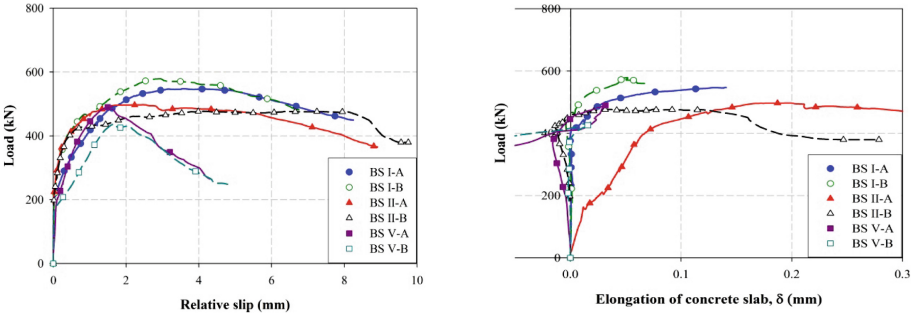


(a) Relative slip curves (b)Elongation of concrete slab

**Fig. 9.** Effects of rebar in BS1, BS2, and BS5 with 35.5-MPa concrete strength

### 3.2.3 Effect of Concrete Strength on Shear Behavior of Crestbond Rib

In order to evaluate the effect of the concrete compressive strength on the shear resistance behaviors, the results for push-out specimens BS1 and BS2, which had a concrete compressive strength of 35.5 MPa, were compared to those of push-out specimens BS3 and BS4, which had a concrete compressive strength of 50.0 MPa, as shown in Figs. 10 and 11. The ultimate shear load of specimen BS3 increased approximately 40.5% in comparison with that of specimen BS1. Nearly the same result was seen with specimens BS2 and BS4, where the ultimate load of specimen BS4

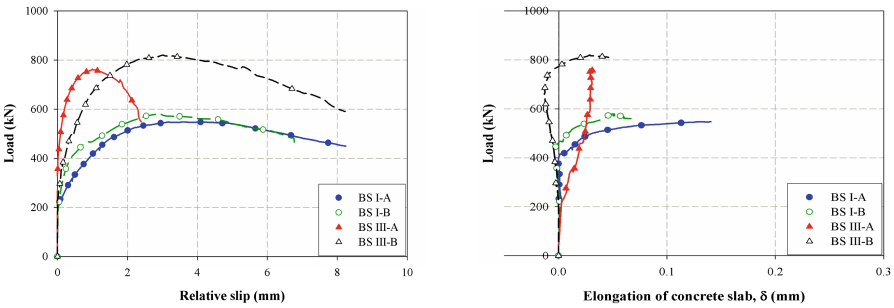


(a) Relative slip curves (b) Elongation of concrete slab

**Fig. 10.** Effects of concrete compressive strength for two rebars: BS1 (35.5 MPa) and BS3 (50.0 MPa)

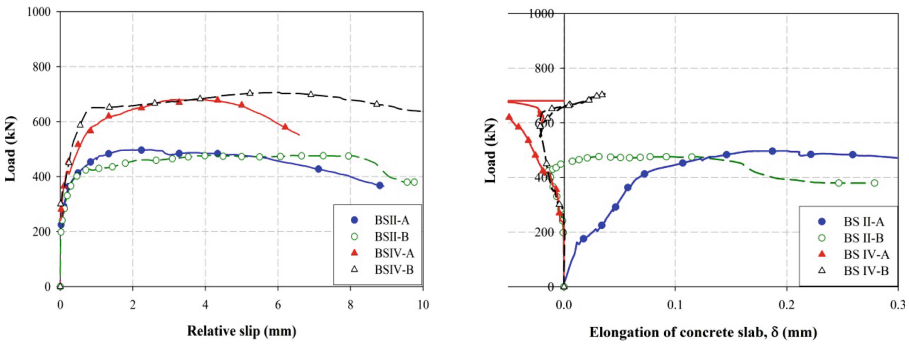


(a) Relative slip curves (b)Elongation of concrete slab

**Fig. 11.** Effects of concrete compressive strength for one rebar: BS2 (35.5 MPa) and BS4 (50.0 MPa)

increased approximately 42.3% in comparison with that of specimen BS2. This showed that the compressive strength of concrete appreciably improves the shear resistance of the connection. Therefore, it can be concluded that the concrete compressive strength significantly affects the shear resistance of the modified crestbond rib shear connection.

## 4 Conclusions

This paper presented the results of an experimental study on the newly puzzle shape of crestbond rib shear connector using push-out tests. This newly puzzle shape of crestbond rib shear connector has advantages that include relatively easy rebar installation and cutting, and a higher shear resistance strength and ductility. The test results provided the following conclusions:

(i) In these tests, the perfobond hole dimension had an insignificant effect on the connection behavior, which may be explained by the small difference in the dimensions between the hole categories. The number of reinforcements significantly affected the ultimate load and slip of the connection. The specimen without reinforcement had the smallest shear resistance and relative slip. In the case of the specimen without reinforcing bars, the relative slip was smaller than 6 mm, and this was not classified as a ductile connection. The compressive strength of the concrete had a considerable effect on the behavior of the perfobond shear connection, with an increase in the compressive strength of the concrete from 35.5 MPa to 50.0 MPa improving the ultimate load resistance by nearly 50%.

(ii) The ductility of the connector depended on the concrete strain. Thus, the concrete part enclosing the steel bars decreased when the transverse reinforcement was increased, the concrete failed more quickly, and the ductility of the connector decreased. Increasing the transverse reinforcement in the concrete slab produced significantly higher ductile behaviors, as seen in push-out test results. Thus, although the transverse rebar in a crestbond rib hole could be thought to be related to the structural characteristics, in this case the load capacity was not improved.

(iii) The occurrence and propagation of cracks followed the same rule for all the specimens. Cracks began in the middle of the concrete slab in the vertical direction, and the load capacity began to decrease when horizontal cracks developed. Cracks occurred in the front and behind faces. After reaching the ultimate load, cracks were initiated in the concrete slab bottom, and these cracks propagated from the perfobond position to the bottom of the concrete slab.

**Acknowledgments.** This study has been supported in part by HOANG VINH Technology Research and Construction Consultants (HOANG VINH TRCC) in Vietnam.

## References

1. Medberry, S., Shahrooz, B.: Perfobond shear connector for composite construction. AISC Eng. J., 1048–1056 (2002)
2. Valente, I., Cruz, P.J.S.: Experimental analysis of Perfobond shear connection between steel and lightweight concrete. J. Constr. Steel Res. **60**(3–5), 465–479 (2004)
3. Vianna, J.d.C., Costa-Neves, L.F., Vellasco, P.C.G.d.S., de Andrade, S.A.L.: Experimental assessment of Perfobond and T-Perfobond shear connectors' structural response. J. Constr. Steel Res. **65**(2), 408–421 (2009)
4. Ahn, J.H., Lee, C.G., Won, J.H.: Shear resistance of the perfobond rib shear connector depending on concrete strength and rib arrangement. J. Constr. Steel Res. **66**(10), 1295–1307 (2010)
5. Bui, D.V.: Behaviour of Steel - Concrete Composite Beams Made of Ultra High Performance Concrete. Der Wirtschaftswissenschaftlichen Fakultater Universitat Leipzig, Leipzig, 9 October 2010 (2010)

6. Leonhardt et al.: VorteilhaftesVerbundmittelfürStahlvebund–TragwerkemithoherDauerfestigkeit. Beton und Stahlbetonbau **82**(12), 325–331 (1987)
7. Oguejiofor, E.C., Hosain, M.U.: A parametric study of perfobond rib shear connectors. Can. J. Civil Eng. **21**(4), 614–625 (1994)
8. European Committee for Standardization (Hrsg.): Eurocode 4: Design of composite steel and concrete structures, September 2004. European Committee for Standardization (2004)

# Simulation of Reinforced Concrete Short Shear Walls Subjected to Seismic Loading

Khuong Le Nguyen(✉), Ba Tam Truong, and Minh Quyen Cao

University of Transport Technology, 54 Trieu Khuc, Thanh Xuan
Ha Noi, Vietnam
{khuongln, quyencm}@utt.edu.vn,
truongbatam86@gmail.com

**Abstract.** This paper addresses the strength and deformation capacity of shear wall subjected to seismic loading using experiments and analysis. Two low-rise shear walls, with the same section design and the same aspect ratio (height/length) of 0.4 have been submitted to pseudo-dynamic (PSD) tests conducted at the ELSA laboratory of the Joint Research Centre are presented. Simulation of the behavior of the shear wall retrofitted by CFRP is accurately predicted by finite element modeling. The accuracy of modeling is confirmed by comparing the simulated response with experimental one.

**Keywords:** FRP · RC shear wall · Nonlinear seismic analysis

## 1 Introduction

During an earthquake, Reinforced concrete (RC) shear walls represent one of the most widespread bracing systems for buildings. They must be carefully designed to provide not only adequate strength, but also sufficient ductility to avoid brittle failure under strong lateral loads. The behavior of a wall element is complex because it depends on its slenderness, layout plan, the importance of vertical loads, the shape of the section, character seismic excitation. In this context, current recommendations for the seismic retrofit of RC walls, provided in Eurocode 8 – Part 3 [1] and exploited by Fardis [2], aim at enhancing the strength and/or ductility through different procedures. In the last decade, composite materials such as the Carbon or Glass Fibers associated with Polymeric Matrices (CFRP and GFRP) applied to RC elements by bonding are proved to be effective for the protection and reinforcement of beams and columns. Recent research on FRP composites for strengthening RC shear walls conducted by Lim and Li [3], Antoniades *et al.* [4], Dan [5] proved their ability to restore the initial performance of the walls. Different retrofitting strategies have been considered using CFRP materials Le-Nguyen *et al.* [6], in which two lightly reinforced concrete walls have been experimentally and numerically investigate with an aspect ratio equal to 0.67 (short wall) and 2.5 (slender wall).

The behaviour of RC structures strengthened with externally bonded FRP reinforcement in the forms of thin plates or sheets is often dominated by debonding of the FRP reinforcement from concrete. Despite many researches have pointed to debonding failures in FRP-strengthened RC structures, there are still substantial uncertainties and

© Springer Nature Singapore Pte Ltd. 2018
H. Tran-Nguyen et al. (eds.), *Proceedings of the 4th Congrès International de Géotechnique - Ouvrages -Structures*, Lecture Notes in Civil Engineering 8,
DOI 10.1007/978-981-10-6713-6_24

difficulties with the finite element modelling of debonding failures due to the complex behaviour of cracked concrete. In general, there are two approaches to simulate the debonding failures in FRP-strengthened RC structures using a nonlinear FE model. The first once employ a layer of interface elements between the FRP and the concrete [7–10] in which debonding is simulated as failure of the interface elements. This approach depends on the constitutive law (i.e. the bond-slip model) specified for the interface elements. Such models are not true predictive models, although using with tests to verify/identify interfacial behaviour. Indeed, this approach shows a difficult to convergence of numerical scheme. In the second approach, the use of interface elements is avoided; instead, debonding is directly simulated by modelling the cracking and failure of concrete elements adjacent to the adhesive layer. Lu *et al.* [11] proposed a mesoscale approach with CFRP elements directly connected to the concrete elements but with very small elements, one order smaller than the thickness of the concrete layer that debonded. Lu *et al.* [12] presents an FE method of the second approach in which a non-coaxial rotating angle crack model (RACM) is employed so that debonding failures of FRP-to-concrete interfaces can be accurately predicted. The debonding behaviour in the second approach can be predicted using an appropriate constitutive model for concrete to avoid the devergennce of numerical sheme and to provide a useful tool for understanding the debonding failure process.

In this paper, the FRP strips are simply introduced as bar element and the behaviour of the interfacial FRP-concrete is taken into concrete behaviour with the regularization technique for the softening behavior of the concrete based on the classical fracture energy concept whereby the tension softening concrete model was changed by counting the presence of CFRP. This method was used by authors to estimate the interaction of steel-concrete [6, 13]. To simulate the behavior of CFRP more realistically, the effective strain in FRP laminates estimated by Eurocode is also taken in to account.

The SAFE programme (from the French acronym "Structures Armées Faiblement Elancées", i.e. lightly reinforced concrete structures) involved pseudodynamic tests on low-rise shear walls [14, 15]. The tests were conducted during the years 1997–1998 at the ELSA laboratory of the Joint Research Centre, committed by Eléctricité de France and COGEMA. The main objectives of the action research around these tests were as follows:

- Specify the margins inherent to the practice of seismic design of shear walls in the nuclear construction.
- Interesting to the dynamic effects occur when the excitation frequency is close to the natural frequency of the structure and study variation of the natural frequency with damage.
- Describe and quantify the damage phase corresponding to the appearance of the first cracks and plasticizing of the internal reinforcements.
- Test different models of RC behavior available, and different computer codes implementing.

The work presented in this paper concerns especially the first and the last point of these objectives, so the CFRP retrofitting strategies, as well as the setup of the experimental campaign are presented. Non-linear temporal analysis is then carried out

using numerical approaches for the concrete modeling with a local concrete model based on the smeared fixed crack approach and a classical regularization technique based on the fracture energy. A post-processing technique proposed by Matallah *et al.* [16] based on the fracture energy concept permits to obtain crack patterns consistent with the observed crack patterns during the tests.

## 2 Experimental Program

13 tests specimens of RC shear walls with the same ratio (height/width = 0.4) were divided to three groups:

- Group 1 (S1): T1 to T4 (dimensions 3 m × 1.2 m × 0.16 m)
- Group 2 (S2): T5 to T12 (dimensions 3 m × 1.2 m × 0.2 m)
- Group 3 (S3): T13 (dimensions 3 m × 1.2 m × 0.2 m)

The differences among the specimens were in terms of the reinforcement, the presence of an additional normal or load the theoretical mass. Nonlinear temporal analysis was subjected to T5, T6 and T8 by Ile et al. [17, 18]. A simplified model based on the structural frequency and nonlinear pushover analysis was utilized for T3, T5, T6, T8, T10, T11 and T12 by Brun *et al.* [19, 20]. In this paper, the work focus on two specimens T8 and T13 that theirs characters are identical except the CFRP retrofitting strategies was appliqued to T13. The main properties of these shear walls will be presented in the following sections.

The geometry of two specimens T8 and T13 in the SAFE program is shown in Fig. 1(a). It is composed of two stiff flanges and a web wall, with a total length $L$ of 3.00 m for an height $h$ of 1.20 m, corresponding to a very low aspect ratio $h/L$ equal to 0.4. The web thickness is equal 0.2 m and a large of 0.8 m. The wall is constructed with strong blocks up and down, with a large thickness of 1.25 m.

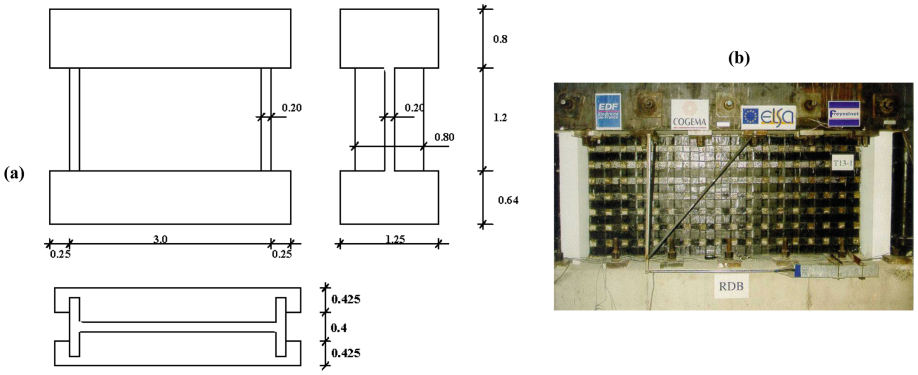


**Fig. 1.** (a) Shear wall dimensions (unit in m) and (b) specimen T13 retrofitted by CFRP

The tests T13 has a medium level of steel ratio of the reinforcement 0.4%, is identical to that of the test T8. In addition, T13 has also been externally reinforced on both sides with horizontal and vertical bands of composite materials. 17 and 8 strips CFRP of 75 mm of width were applied horizontal and vertical respectively to each face with a space of 150 mm from two strips continuity. A view of the laying of these strips is given in the Fig. 1(b).

Reinforcement bars showed yield stress and ultimate strength of 588 MPa and 665 MPa respectively. The concrete strength of each specimen was determined by averaging the values obtained using three standards 11 cm by 22 cm concrete cylinders. Tensile strength was determined by splitting tensile test. Characteristics of CFRP reinforcements are summarized in Table 1. Presented characteristics are those reported by the manufacturer.

**Table 1.** Manufacturer reported CFRP reinforcement (Freyssinet products)

| Properties | CFRP sheets (TFC©) |
|---|---|
| Tensile modulus (MPa) | 150 000 MPa |
| Ultimate strain (%) | 0.56 |
| Thickness | 0.43 mm |
| Width | 75 mm |

The loading device is illustrated in Fig. 2. The horizontal loads are applied at both sides of the upper block by the steel casing at the mid height of the wall so as to limit rotation. In addition, rotation of the upper block is prevented by two vertical actuators at the lateral borders of the block. So, the test is very close to a pure shear loading, characterised by neglected bending effects in shear walls. The lower block is clamped

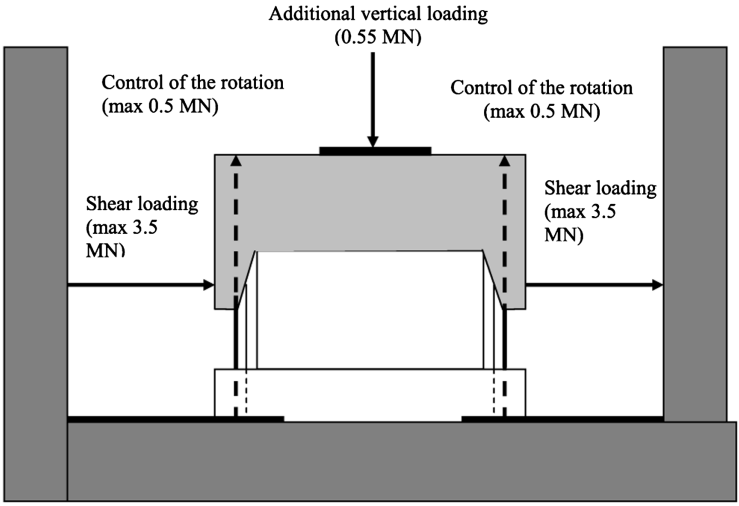


**Fig. 2.** Test setup

to the laboratory strong floor. The vertical post-tensioning force was maintained at a constant level during the test, so 250 kN for the both tests T8 and T13, corresponding to a normal stress of 0.34 MPa in each shear wall.

The horizontal displacements imposed at every time-step of the PSD test [21] are measured by optical transducers. The accelerograms assumed as input signals for the experimental sequence of the walls T8 and T13 are reported on a unique time scale obtained by adding the duration of the three tests corresponding to the three intensities (Run1, Run2 and Run3). For each test, the accelerogram was reduced to zero after about 18 s in order to reserve a time range of free vibrations to measure frequency and damping at the end of each test.

## 3 Numerical Approach by Finite Element

The classical smeared fixed crack model, labeled in the following as National Institute of Applied Sciences of French (INSA) model [22] is selected for the simulation. This model is built in the framework of the theory of plasticity under the plane stress assumption so defined by two distinctive behaviors depending whether the concrete is cracked or uncracked. In its uncracked state, the model is based on the plasticity theory with an isotropic hardening and an associated flow rule. The crack detection surface in traction is managed by a Nadai criterion. In compression, load surfaces are of the same type with different parameters in comparison to the Nadai cracking surface. The evolution of the load surface to the ultimate load surface in compression follows a positive isotropic hardening. A softening regime occurs with a negative isotropic hardening when reaching the ultimate load surface in compression.

### 3.1 Meshes and Material Properties

The panel, the top beam and the footing were modeled either by linear 2D elements with four nodes. Steels and CFRP strips were represented by uniaxial bars whose nodes are connected with the concrete nodes. The bar elements for the steel reinforcement coincide with the 2D and 3D finite ele-ments for the concrete. Initial compressive state is taken into account by applying loads of 250 kN to the top beam. The mesh size of the wall is chosen sufficiently fine, that is equal to 2.5 cm, in order to fulfill the real reinforcement configuration while adopting the perfect bond assumption (steel nodes matching with concrete nodes). The bottom beam is clamped at its base.

The parameters of the smeared fixed crack model and the coupled elastoplastic damage model for reproducing the concrete behavior are reported in Table 2.

**Table 2.** Numerical parameters of the model concrete

| | Definition | T8 | T13 |
|---|---|---|---|
| $E_0$ | Young's modulus | 28.0 GPa | 31.0 GPa |
| $f_c$ | Uniaxial compressive strength | 29.1 MPa | 41.1 MPa |
| $f_t$ | Uniaxial tensile strength | 1.74 MPa | 2.46 MPa |
| $\varepsilon_{tm}$ | Cracking strain | 2.1E−03 | 3.1E−03 |
| $\varepsilon_{rupt}$ | Fracture strain in compression | 10.E−3 | 11.1E−3 |

The steel reinforcement was modeled using linear bar elements associated with the uniaxial cyclic law proposed by Menegotto and Pinto [24]. No steel/concrete interface behavior has been taken into account. The reinforcement of shear walls are introduced into the FE model as bar elements whose nodes are the same of the concrete elements under the perfect bond assumption. In the case of the smeared fixed crack approach, the effects associated with the rebar-concrete interface such as bond-slip and dowel action, are taken into account in an approximate way by introducing some tension-stiffening into the concrete model using the fracture energy concept.

The CFRP strips were modeled by three bar elements whose total section is equal to the section of the 75 mm wide CFRP plate. The three bar nodes are directly connected to the concrete nodes under the perfect bond assumption. The assumption was that the debonding occurs in the concrete rather than in the adhesive layer. Here, conventional size elements are adopted, equal to 5 cm, assuming a perfect bond between the concrete and the CFRP strips.

### 3.2 Dynamic Response History Analysis

The dynamic responses time history are presented in Figs. 3 and 4. It can be concluded that the analytical models of both walls provided a reasonable estimate of the maximum displacement and reaction for earthquake excitations with different PGA levels. The wall T8 cracked during Run1, damaged during Run2 and ruined during Run3, whereas the wall T13 with FRP strengthening is not cracked during Run1, damaged at the end of Run2 and ruined during Run3. The resistance is reproduced as well as the ultimate displacement at the ruin of the structure. We can conclude that the T13 was not damaged under the same input acceleration in Run1 due to the strengthening system. The ductility is also improved for tha wall T13 (Fig. 4).

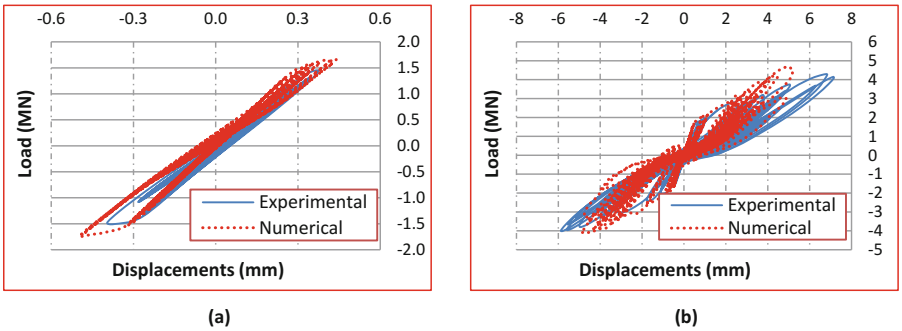


**Fig. 3.** Force – displacement relationship (a) T13 - Run 1; (b) T13 - Run 2

Crack opening can be estimated by using the method proposed by Matallah *et al.* [16]. Briefly, this post-processing method enables crack openings to be extracted for all continuum damage/plasticity models based on an energetic approach as proposed by Bažant and Oh [23]. Crack opening isovalues using this post-processing technique are

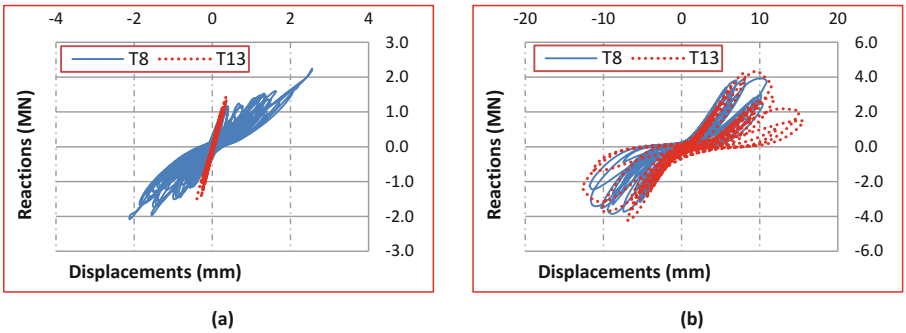


**Fig. 4.** Force/Displacement curves at the top of the walls T8 and T13 (a) Run1; (b) Run3

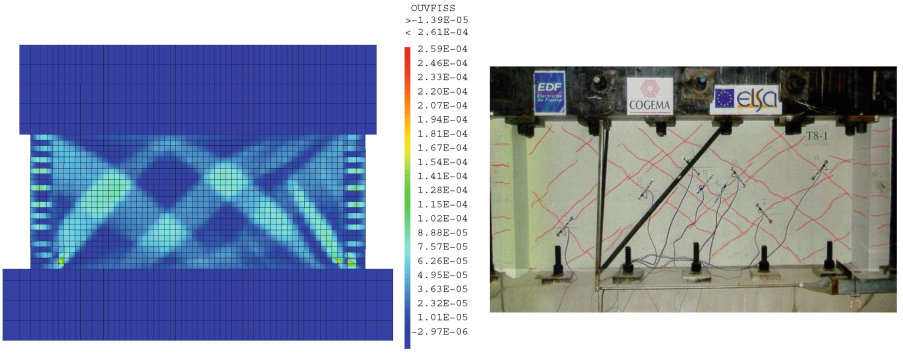


**Fig. 5.** Crack area of T8 after Run1 (Left: Numerical; Right: Experimental)

displayed and compared with the experimental cracks in Fig. 5. It can be underlined that the main cracks of the walls observed at the end of Run1 are well reproduced using the smeared fixed crack approach.

## 4 Conclusion

The programme SAFE was a first important step in investigating the behaviour of stiff and massive shear walls typical of the nuclear building. The contribution to this knowledge provided by the programme SAFE has been probably unique in Europe, while stiff shear wall are largely investigated in Japan being the basis for their nuclear design standard for the reactor buildings. The paper discusses the experimental seismic performance of two walls with the same design dimension without and strengthened by CFRP. The results show that the deformation capacity of the structure has likely been increased since the damage of the retrofit wall was significantly less than the damage of the unretrofit wall under the same seismic input Run1. Moreover, FRP retrofit allowed the wall to withstand a level of excitation, 1.4 times larger than that applied to the unretrofit wall.

The model adopts the concept of a smeared crack approach with orthogonal ficed cracks and assumes a plane stress condition was used. The ability of the concrete model to reproduce the most important characteristics of the dynamic behavior of the shear walls was evaluated by comparison with available experimental data. In numerical approach, the perfect bond between the steels and the concrete was assumed as well as between the bars representing the CFRP strips and the concrete. The model was less successful in predicting the exact the timing at the end of higher excitation (Run3) explained by energy dissipation through repeated cycles and the debonding between CFRP and concrete need a better description, but global as well as local response being reasonably close to the experimental one.

The results obtained made it possible to envisage various practical applications during the dimension step. The proposed modeling can provide important support for the various experimental and theoretical studies currently being carried out to evaluate the comparative effects of a near earthquake and a distant earthquake.

## References


1. EN 1998-3: Eurocode 8: design of structures for earthquake resistance – part 3: assessment and retrofitting of buildings, AFNOR (2005)
2. Fardis, M.N.: Seismic Design, Assessment and Retrofitting of Concrete Buildings: Based on EN-Eurocode 8. Springer (2009)
3. Li, B., Lim, C.L.: Tests on seismically damaged reinforced concrete structural walls repaired using fiber-reinforced polymers. J. Compos. Constr. **14**(5), 597–608 (2010)
4. Antoniades, K.K., Salonikios, T.N., Kappos, A.J.: Evaluation of hysteretic response and strength of repaired R/C walls strengthened with FRPs. Eng. Struct. **29**, 2158–2171 (2007)
5. Dan, D.: Experimental tests on seismically damaged composite steel concrete walls retrofitted with CFRP composites. Eng. Struct. **45**, 338–348 (2012)
6. Le Nguyen, K., Brun, M., Limam, A., Ferrier, E., Michel, L.: Pushover experiment and numerical analyses on CFRP-retrofit concrete shear walls with different aspect ratios. Compos. Struct. **113**, 403–418 (2014)
7. Wu, Z., Yuan, H., Niu, H.: Stress transfer and fracture propagation in different kinds of adhesive joints. J. Eng. Mech. **128**(5), 562–573 (2002)
8. Wong, R., Vecchio, F.: Towards modeling of reinforced concrete members with externally bonded fiber-reinforced polymer composites. ACI Struct. J. **100**(1), 47–55 (2003)
9. Lu, X.Z., Teng, J.G., Ye, L.P., Jiang, J.J.: Bond-slip models for FRP sheets/plates bonded to concrete. Eng. Struct. **27**(6), 920–937 (2005)
10. Lu, X.Z., Teng, J.G., Ye, L., Jiang, J.J.: Intermediate crack debonding in FRP-strengthened RC beams: FE analysis and strength model. J. Compos. Constr. **11**(2), 161–174 (2007)
11. Lu, X.Z., Teng, J.G., Ye, L.P., Jiang, J.J.: Meso-scale finite-element model for FRP sheets/plates externally bonded to concrete. Eng. Struct. **27**(4), 564–575 (2005)
12. Lu, X.Z., Jiang, J.J., Teng, J.G., Ye, L.P.: Finite element simulation of debonding in FRP-to-concrete bonded joints. Constr. Build. Mater. **20**(6), 412–424 (2006)
13. Ile, N., Reynouard, J.M.: Nonlinear analysis of reinforced concrete shear wall under earthquake loading. J. Earthq. Eng. **4**(2), 183–213 (2000)
14. Pegon, P.: Programme SAFE: présentation générale des essais. JRC technical note (1999)

15. Coyere, R., Dalbera, J., Chauvel, D., Molina, J., Pegon, P., Verzeletti, G.: Endommagement sismique de murs en béton armé ouverture des fissures. In: Presented at the Association française du génie parasismique, pp. 636–643. Colloque national (1999)
16. Matallah, M., La Borderie, C., Maurel, O.: A practical method to estimate crack openings in concrete structures. Int. J. Numer. Anal. Methods Geomech. **34**(15), 1615–1633 (2010)
17. Ile, N., Reynouard, J.M., Fleury, F., Chauvel, D.: Computed versus observed inelastic seismic response of low-rise R/C shear walls with boundary elements. In: Proceedings of the 12th World Conference on Earthquake Engineering, Auckland, New Zealand (2000)
18. Ile, N.: Contribution à la compréhension du fonctionnement des voiles en béton armé sous sollicitation sismique: apport de l'expérimentation et de la modélisation à la conception, Ph. D. thesis, INSA de Lyon, Lyon (2000)
19. Brun, M., Reynouard, J.M., Jezequel, L.: A simple shear wall model taking into account stiffness degradation. Eng. Struct. **25**, 1–9 (2003)
20. Brun, M., Labbe, P., Bertrand, D., Courtois, A.: Pseudo-dynamic tests on low-rise shear walls and simplified model based on the structural frequency drift. Eng. Struct. **33**, 796–812 (2011)
21. Mahin, S., Shing, P.: Pseudodynamic method for seismic testing. J. Struct. Eng. **111**(7), 1482–1503 (1985)
22. Merabet, O.: Modélisation des structures planes en béton armé sous chargement monotone et cyclique, Ph.D. thesis, INSA de Lyon, Lyon-France (1990)
23. Bažant, Z.P., Oh, B.H.: Crack band theory for fracture of concrete. Matér. Constr. **16**(3), 155–177 (1983)
24. Menegotto, M., Pinto, P.: Method of analysis for cyclically loaded reinforced concrete plane frames including changes in geometry and non-elastic behaviour of elements under combined normal force and bending. In: International Association of Bridge and Structural Engineering, Libson, Portugal, vol. 13, pp. 15–22 (1973)

# Strength Capacity of Steel Piles Filled with Concrete at Pile Top

Moeko Matoba[1(✉)], Mutsuki Sato[1], Toshiharu Hirose[2], and Yoshihiro Kimura[1]

[1] Tohoku University, Sendai, Miyagi, Japan
[2] Japanese Technical Association for Steel Pipe Piles and Sheet Piles, Tokyo, Japan

**Abstract.** In the previous papers, the steel pile ultimate strength and plastic deformation capacity for local buckling is estimated with radius thickness ratio and shear span ratio. For real structures, concrete is filled into the pile top of steel piles to fix the connection between a steel pile and a reinforced concrete footing beam in. It is considered that the local buckling strength of steel piles with concrete at the pile top is larger than that of steel piles to prevent local buckling issued from filled concrete at the pile head. On the other hand, at the pile top filled with concrete, bending stress of steel pipes is not enough transmitted to a concrete member which slips on the steel pipe. Therefore, slip stoppers are attached to the steel pile top. The stress transfer mechanism between a steel pipe with slip stoppers and a concrete member has not been clarified In this paper, cyclic load tests of steel piles filled with concrete at the pile top with different axial force ratio are performed. The local buckling behavior of steel piles at pile top is elucidated and ultimate strength, deformation capacity and hysteretic energy absorption is evaluated.

**Keywords:** Steel piles · Stiffener at pile top · Local buckling strength · Ultimate strength

## 1 Introduntion

It was reported that the steel pile's local buckling at the pile top occurred due to Hyogo-Ken-Nanbu earthquake in 1995. In the allowable stress design, the steel pile's local buckling can be prevented to apply to the restrictions on steel pile's radius thickness ratio specified in current Japanese recommendations for design of building foundation [1]. In the previous papers [2], it is confirmed that steel pile ultimate strength and plastic deformation capacity for local buckling is estimated with radius thickness ratio and shear span ratio. On the other hand, for a real structure, concrete is filled into the steel pile to fix the connection between the steel pile and a reinforced concrete footing beam. It is considered that the local buckling strength of steel tubes with concrete is larger than that of the steel tube to prevent the local buckling of the tube issued from the filled concrete. However, maximum strength and plastic deformation capacity of steel piles with filled concrete are still not clarified. At the pile top filled with concrete, the bending stress of steel tube is not enough transmitted to a

© Springer Nature Singapore Pte Ltd. 2018
H. Tran-Nguyen et al. (eds.), *Proceedings of the 4th Congrès International de Géotechnique - Ouvrages -Structures*, Lecture Notes in Civil Engineering 8,
DOI 10.1007/978-981-10-6713-6_25

concrete member which slips on a steel tube due to the pile bending moment. Therefore, slip stoppers are attached to the steel pile top. However, the stress transfer mechanism between the steel tube with slip stoppers and the filled concrete has not been clarified when piles carry axial force and bending moment. In this paper, the cyclic load tests of steel piles filled with concrete at pile top are performed to clarify the local buckling behavior at pile's top and to compare ultimate strength, plastic deformation capacity and hysteretic energy absorption for the specimens with the axial force ratio of 0.0, 0.3 and 0.6.

## 2 Outline of Experiment

Experimental equipment is shown in Fig. 1. A test specimen consists of a steel pipe with different cross-section and a concrete member at the pile top. For the steel pipe, the outside diameter and thickness of a-a' section are 488 mm and 9 mm, and those of b-b' section are 508 mm and 19 mm, respectively. Concrete is filled at the pile top up to 488 mm height same as the diameter of a-a' section. In this paper, thickness of a-a' section is thicker than that of b-b' section to clarify the local buckling behavior at the pile top filled with concrete. In addition, slip stoppers are attached on the inside of the steel pile at 122 and 244 mm height. The distance from the pile top to the loading point is 1852 mm. As described in this paper, it is assumed that the point of contrary flexure occurs at quadruple height of the pile's diameter from the pile head subjected to the

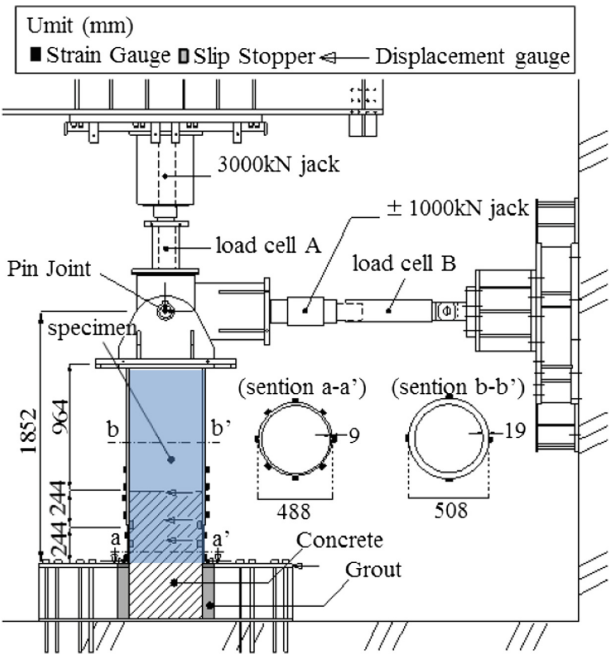


**Fig. 1.** Loading frame and specimen

horizontal force. Strain gauges and displacement gauges are placed as described in Fig. 1. The horizontal load and axial load are applied by ± 1000kN and 3000kN hydraulic jack, respectively.

The horizontal load is controlled with normalized horizontal displacement $\delta/\delta_p$ = 1, 2, 4 regardless the magnitude of axial force. Where, $\delta_p$ denotes the reference yielding displacement of the specimen as described in Fig. 2. The loading is given until 80% of ultimate strength after maximum load.

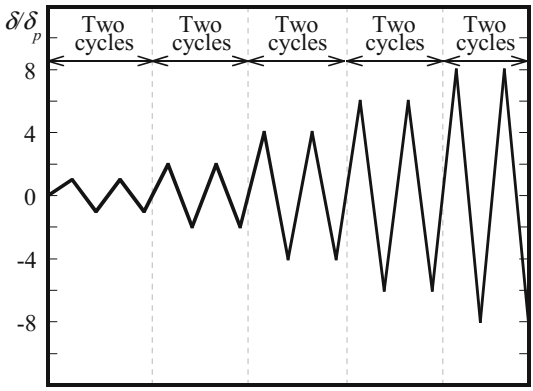


**Fig. 2.** Loading protocol of horizontal force

Table 1 presents the specimen specifications. Where, $N_y$ represents the yield strength and $N_0$ stands for the initial axial force. For the tests, there are 3 specimens with different axial ratio of 0.0, 0.3 and 0.6. Each specimen has same length and pile thickness.

**Table 1.** List of specimens

| Specimens | Specimens length $L_0$ (mm) | Pile thickness $t$ (mm) | Axial force ratio $N_0/N_y$ | Axial force $N_0$ (kN) |
|---|---|---|---|---|
| Case 1 | 1852 | 488 (section a-a') 508 (section b-b') | 0.0 | 0 |
| Case 2 | | | 0.3 | 1257 |
| Case 3 | | | 0.6 | 2514 |

Material properties are tabulated in Table 2. Here, $E_s$ denotes the steel elastic modulus, $\sigma_y$ represents the steel yield stress, $\varepsilon_y$ shows the steel yield strain, $E_c$ stands for the concrete elastic modulus, and $\sigma_B$ signifies the concrete ultimate compressive stress.

**Table 2.** Material properties

| | | | |
|---|---|---|---|
| Steel pile | $E_s$ (N/mm$^2$) | $\sigma_y$ (N/mm$^2$) | $\varepsilon_y$ (%) |
| | 2.09 × 10$^5$ | 309.4 | 0.148 |
| Concrete | $E_c$ (N/mm$^2$) | $\sigma_B$ (N/mm$^2$) | – |
| | 2.82 × 10$^4$ | 27.53 | – |

## 3 Loading Test Results

### 3.1 Hysteresis Curve and Local Buckling Behavior

Figure 3(a), (b) and (c) show the hysteresis curve of specimens with axial force ratio of 0.0, 0.3 and 0.6. Figure 3(a) portrays the result of Case 1 specimen without axial force ($N_0/N_y$ = 0.0), and Fig. 3(b) and (c) represent those of Case 2 under $N_0/N_y$ = 0.3 and Case 3 under $N_0/N_y$ = 0.3, respectively. Where, $M$ denotes the bending moment with $P$-$\delta$ effects, $M_{max}$ signifies the ultimate strength and $\theta$ stands for the deflection angle.

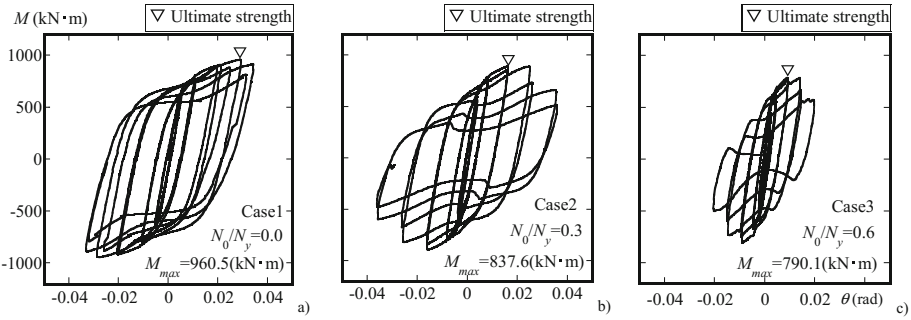


**Fig. 3.** The hysteresis curves: (a) Case 1 (b) Case 2 (c) Case 3

As shown in Fig. 3, the white triangle symbol indicates the ultimate strength. The ultimate strength of Case 1 specimen has 960.5 kNm at $\theta$ = 0.0369 rad, those of Case 2 and Case 3 reaches 837.6 kNm at $\theta$ = 0.0181 rad and 790.1kNm at $\theta$ = 0.0101 rad, respectively. The ultimate strength becomes lower as the axial force ratio of the specimen is higher. The ultimate strength of Case 2 and Case 3 specimen is approximately equal to 87.3% and 82.3% of Case 1. Additionally, the strength of the specimen with higher axial force ratio deteriorates more drastically after ultimate strength.

Photo 1(a), (b) and (c) display local buckling of the specimens around the pile top. As axial force ratio of the specimen is higher, the local buckling length becomes shorter.

**Photo 1.** Local buckling of the specimens around the pile top after cyclic loading: (a) Case 1 (b) Case 2 (c) Case 3

Photo 2 describes filled concrete around the pile top after cyclic loading test for Case 3 specimen. The surface of filled concrete between the top and bottom stoppers is scratched. As shown in Fig. 3, after the specimen reaches the ultimate strength, the strength decreased due to bond slip at the interface between the steel pile and the concrete around $\theta = 0$. It is considered that the concrete strikes the stoppers again with increase of the deflection angle, and the horizontal load increases again.

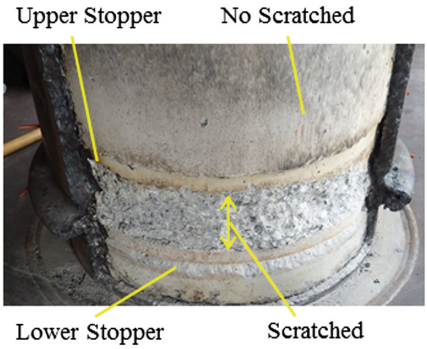


**Photo 2.** Filled concrete of Case 3 specimen after cyclic loading test

### 3.2 Transmission of Initial Axial Force

Figure 4 shows the distribution of initial axial force multiplied axial strain of the steel pile by cross-section area and the elastic modulus. Where, $x$ represents the coordinate of the pile's axial direction, which pile end is set to 0. The black triangle symbol indicates the top of filled concrete, and the white triangle symbol shows the attached slip stoppers. As described in Fig. 4(a), stain gauges are placed at the point of A-E. The cross-section at the point of E and F is corresponding to b-b' section of the steel pipe only. On the other hand, the cross-section at A-D is composed of the steel pipe and the filled concrete. The cross-section of the steel pipe at C and D is b-b' section, and that of the steel pipe at A and B is a-a' section. For Case 2 and Case 3 specimens, axial forces of 1275 kN and 2514 kN, $N_0$ are given by hydraulic jack, respectively. Axial force calculated from axial strain at E and F agree well with axial force applied by hydraulic jack. On the other hand, axial force issued from axial strain at A, B and C becomes smaller than axial force provided by hydraulic jack. It is considered that axial force is transferred from the steel pipe to the concrete by slip stoppers. It is suggested that the concrete at A for Case 2 and Case 3 approximately carries 29% and 31% of initial axial force.

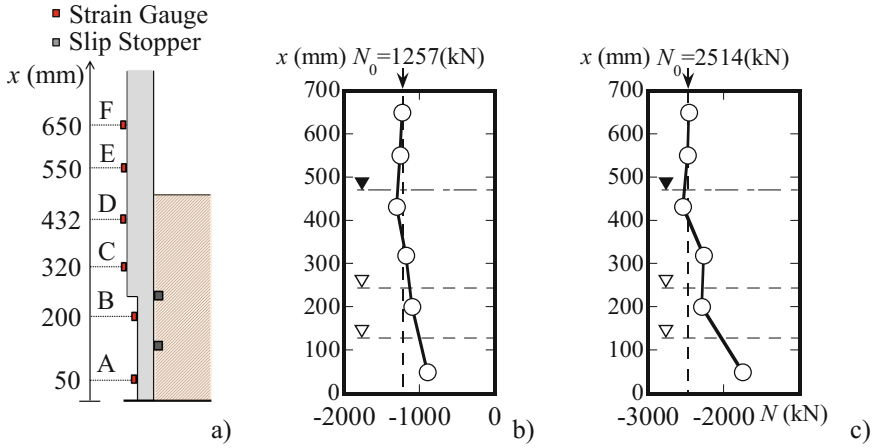


**Fig. 4.** The distribution of initial axial force: (a) strain gauges' position (b) initial axial force (Case 2) (c) initial axial force (Case 3)

## 4 Loading Test Results

### 4.1 Estimation of Initial Stiffness and Full Plastic Strength

It is considered that the initial stiffness and ultimate strength of the specimens are different from that of CFT members issued from filled concrete at the pile top only. It may be not safety to evaluate the specimen's bending stiffness as accumulated stiffness of the steel pipe and concrete. Thus, in this section, the stiffness of the specimen is revalued by the equivalent stiffness of the concrete and steel pipe stiffness. Figure 5 shows the concept of the equivalent bending stiffness of the steel pile with concrete filled at pile top. As described in Fig. 5(a), $K_{p,CFT}$, which is the slope between A and B, signifies the accumulated stiffness of the steel pipe and the concrete when the concrete member is assumed to carry the bending moment in all its section. $P_0$ denotes the horizontal load when the axial stress of the concrete under compression and bending moment becomes equal to 0 at the edge of the tensile side. In this paper, it is assumed that the concrete stiffness becomes equal to 0, and only steel pipe has stress over $P_0$. $K_{p,s}$ stands for the stiffness of the steel pipe, which is the slope between B and C. $P_{p,CFT}$ represents horizontal load calculated by ultimate strength, $M_{p,CFT}$ in [3] divided by the specimen length. $M_{p,CFT}$ denotes the accumulated stiffness of the steel pipe and the concrete. The horizontal displacement $\delta_{p,CFT}$ at $P_{p,CFT}$ is calculated from the gradient of $K_{p,s}$ from point B. On the other hand, $\delta_{p,CFT}$ of the concrete's horizontal displacement is calculated as no bending stiffness from point D to E. The slope between A and C is determined as the equivalent stiffness of the steel pile filled with concrete. Furthermore, $K_{p,concrete}$ of the slope between A and E, is defined as the equivalent stiffness of concrete. $E_cI_c$ calculated from the equivalent stiffness of concrete $K_{p,concrete}$, is the bending rigidity of concrete. The deflection angle, $\theta_{p,CFT}$ at ultimate strength of the steel pile filled with concrete is calculated using the principle of the virtual work as the following:

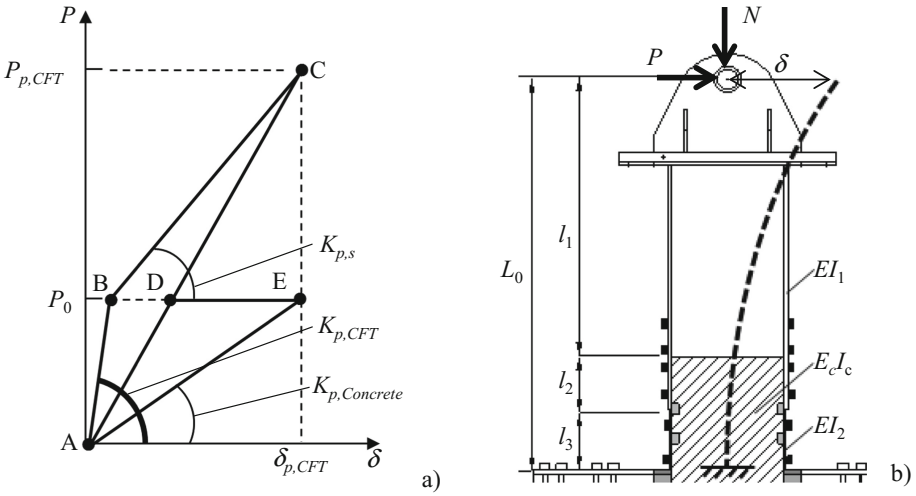


**Fig. 5.** Derivation method of the equivalent concrete stiffness: (a) definition of the stiffness (b) the bending rigidity of the specimen

$$\theta_{p,CFT} = \frac{P_{p,CFT}}{3}\left\{\frac{l_1^3}{EI_1} + \frac{(l_1+l_2)^3 - l_1^3}{EI_1 + E_cI_c} + \frac{(l_1+l_2+l_3)^3 - (l_1+l_2)^3}{EI_2 + E_cI_c}\right\}/L_0 \quad (1)$$

where, $EI_1$ denotes the bending rigidity of the steel pipe along the length of $l_1$, $l_2$, and $EI_2$ stands for the bending rigidity of steel pipe along the length of $l_3$ as shown in Fig. 5(b).

Figure 6(a), (b) and (c) show the relation between the bending moment and deflection angle of cyclic loading tests. The vertical axis represents the normalized bending moment $M/M_{p,CFT}$. The horizontal axis depicts the normalized deflection angle $\theta/\theta_{p,CFT}$. The black line show the hysteresis loop for the first cycle of cyclic load tests. The gray thin line passes through the origin and point (1.0, 1.0) of the coordinates. Although the initial stiffness of Case 1 specimen is lower than that of gray thin line, the initial stiffness of Case 2 and Case 3 are almost same as that of gray thin line and the validity of Eq. (1) is confirmed.

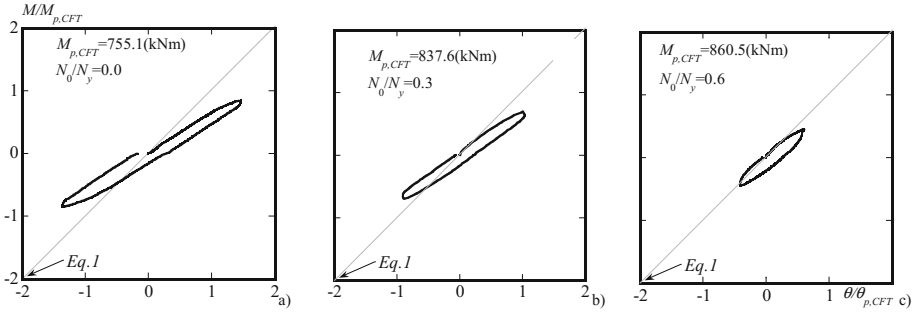


**Fig. 6.** The normalized results of the cyclic loading test: (a) Case 1 (b) Case 2 (c) Case 3

### 4.2 Comparison of Structural Capacity

Figure 7 shows the procedure to draw the skeleton curve from hysteresis curve. Figure 7(a) portrays the hysteresis curve, Fig. 7(b) describes the cumulative hysteresis curve, and Fig. 7(c) represents the skeleton curve. The hysteresis loop of a steel member can be separated into the skeleton part (drawn with bold line).

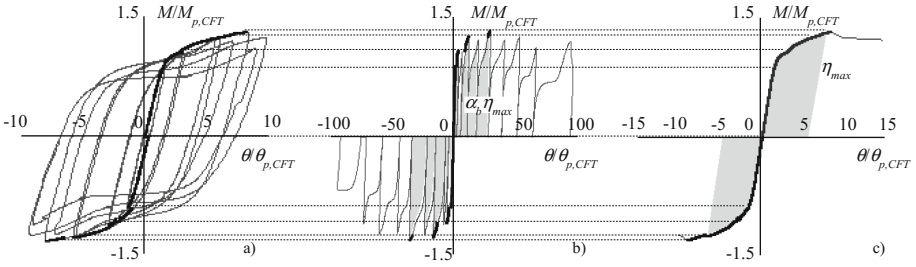


**Fig. 7.** (a) hysteresis curve, (b) accumulative hysteresis curve, (c) skeleton curve

Figure 8 describes each specimen's skeleton curve It is shown that the strength of the specimen with higher axial force ratio deteriorates more remarkably after ultimate strength.

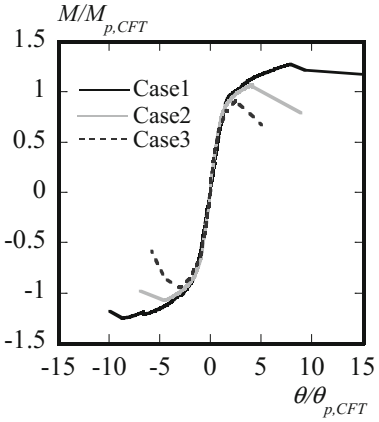


**Fig. 8.** Specimen's skeleton curve

Figure 9 shows structural capacity of the steel pile filled with concrete at pile top obtained by the cyclic load tests. Where, $M_{max}/M_{p,CFT}$ stands for ultimate strength ratio, $\mu_{max}$ signifies the plastic deformation capacity (= $\theta max/\theta p_{,CFT} - 1$), and $\eta_{max}$ denotes the cumulative plastic deformation capacity (= $1 + (M_{max}/M_{p,CFT} + 1)(\mu_{max} - 1)/2$). As axial force ratio of the specimens is higher, the full plastic moment, $M_{p,CFT}$ is larger.

Thus, ultimate strength ratio of Case 2 and Case 3 specimens becomes approximately 86% and 76% of Case 1. As specimen's axial force ratio is higher, the plastic deformation capacity, $\mu_{max}$ is also larger. The plastic deformation capacity of Case 2 and Case 3 specimens becomes about 44% and 23% of Case 1. The cumulative plastic deformation capacity, $\eta_{max}$ of Case 2 and Case 3 specimens is approximately 41% and 23% of Case 1.

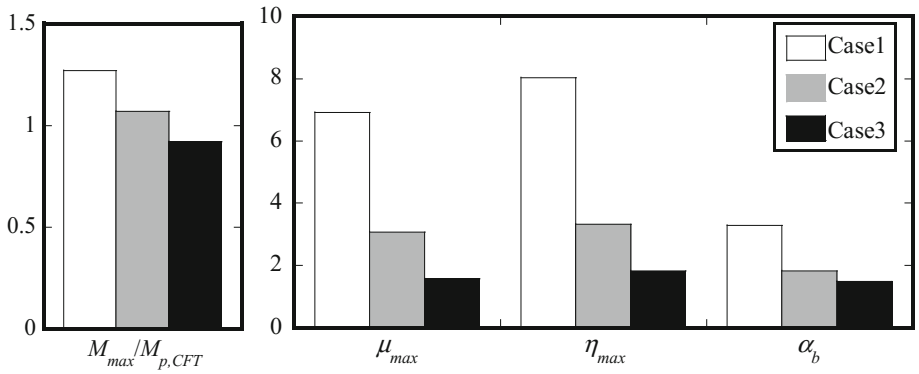


**Fig. 9.** Structural capacity of the specimens

## 5 Conclusion

In this paper, cyclic loading tests of the steel pile filled with concrete at the pile top were conducted to clarified the stress transfer mechanism between the steel pipe with slip stoppers and the filled concrete, local buckling of the pile top and its ultimate strength. The findings of this research are shown as follows:

1) The strength of the specimen with higher axial force ratio deteriorates more drastically after ultimate strength. Additionally, it is shown that the local buckling length becomes shorter.
2) Ultimate strength and the initial stiffness of the steel pile filled with concrete can be estimated with $M_{p,CFT}$ in [3] and Eq. (1)
3) For Case 2 and Case 3 specimen under axial force, ultimate strength ratio, plastic deformation capacity and cumulative plastic deformation capacity becomes approximately 86% and 76%, 44% and 23%, 41% and 23% of Case 1 without axial force, respectively.

**Acknowledgments.** This work was supported by JSPS Grant-in-Aid for Scientific Research (A) Numbers JP16H02374. The cyclic loading tests are funded by Japanese Technical Association for Steel Pipe Piles and Sheet Piles.

## References

1. Recommendations for design and building foundations, October 2001. (in Japanese)
2. Ochi, K., Kurobane, Y. Load-carrying and deformation capacities of circular tubular ctub columns. In: Proceeding of the Architectural Research Meetings in Kanto Chapter, pp. 597–598, September, 1997 (in Japanese)
3. Recommendations for design and construction of concrete filled tubular structures, January 2008 (in Japanese)

# Systematic Analysis of the Concept of Equivalent Linear Behavior in Seismic Engineering

Thuong Anh Nguyen[1(✉)], Pierre Labbé[1], Jean-François Semblat[2], and Guillaume Hervé[1]

[1] University Paris-Est, RENON (IRC-ESTP, IFSTTAR), IRC-ESTP, 28 Avenue Du Président Wilson, 94234 Cachan, France
{anguyen, plabbe, gherve}@estp-paris.eu
[2] University Paris-Est, RENON (IRC-ESTP, IFSTTAR), IFSTTAR, 6-8 Avenue Blaise Pascal, 77455 Marne-la-Vallée, France
jean-francois.semblat@ifsttar.fr

**Abstract.** In seismic engineering, taking into account the non-linear behavior of the structure into the calculation of its responses against strong ground motions, which are due to plastic and/or damage, is not easy because of the need, in terms of computation time and memory, due to many iterations required at each step in order to satisfy the equilibrium. It is common that many concepts of equivalent linear behavior have been used in order to determine the maximal response of structure without performing non-linear transient calculation. In this paper, we deal with systematic and argumentative analysis in order to establish a concept of equivalent linearization by considering the equivalence criterion through the transfer function from the time domain to the frequency domain. Its idea is to identify the frequency and damping of the equivalent linear oscillator whose theoretical transfer function of response in acceleration fits the best the experimental one of the nonlinear system. This concept will be applied to elastoplastic Sdof oscillators undergoing the filtered white noise signal Clough-Penzien. As the result, this equivalent linearization reestablishes the transferred signal through a structure with the non-linearity.

## 1 Introduction

While undergoing strong ground motions, structures may exhibit nonlinear behavior, which is characterized by hysteretic strain-stress loops during the cyclic load. It is important to note that the stiffness of the structure seems to be reduced and its damping increased versus plastic deformation (Iwan 1980; EPRI 1994; Ravikiran 2015). In cases of strong earthquakes, this leads seismic engineers to perform nonlinear transient calculation that results in the huge timing and memory consummation and raise the convergence problem.

In the geotechnical field, the concept of equivalent linearization has been introduced by (Seed and Idriss 1970), using the curves of modulus degradation and damping ratio increasing versus soil shear strain. It enables to cope the response within non-linear behavior without performing nonlinear transient analyses.

© Springer Nature Singapore Pte Ltd. 2018
H. Tran-Nguyen et al. (eds.), *Proceedings of the 4th Congrès International de Géotechnique - Ouvrages -Structures*, Lecture Notes in Civil Engineering 8,
DOI 10.1007/978-981-10-6713-6_26

In civil engineering, (Iwan 1980) had established the curve of stiffness drift ratio, so called the frequency ratio, and damping ratio increasing as functions of ductile demand increasing for a series of single degree of freedom (Sdof) consisting of a combination of linear and elastoplastic or Coulomb slip type elements (Iwan 1979). According to his concept of equivalent linearization, he used the maximum of the time history response in displacement of the mass as the equivalence's criterion. That leads to establish the equivalent linear system, the equivalent frequency and damping ratio associated to one value of ductile demand, which gives the same maximum of time history response in displacement as the nonlinear one. This concept involves some problems, which are not discussed in this article.

Then, Chopra and Goel (Chopra and Goel 1999; Chopra 2001) have defined the equivalent linear behavior of an elastoplastic oscillator by using the secant stiffness, which is linked to the slope of the straight connecting the origin and the maximal deformation of the deformation-force curve during the earthquake, and the equivalent damping ratio based on the dissipated energy within the hysteretic loop corresponding to the maximal deformation. This concept has two disadvantages, at least, at the author's point of view:

1. The equivalent stiffness is equal to the secant one but the dissipated energy is performed with the unloading stiffness equal to the elastic one. Therefore, there is an inconsistency in term of model of equivalent linearization.
2. The model bases completely on the loop of the maximum of the deformation time history but there are many loops of smaller deformation appearing before this maximum.

In this article, we will deal with the equivalent linearization through the complex transfer function. The complete procedure will be described at the next sections of this article. As the result, we establish the frequency drift ratio and damping ratio increasing as functions of ductile demand increasing. Then, the pertinence of the concept of equivalent linear behavior is demonstrated by using Andersons's criteria (Anderson 2004).

## 2 Clough and Penzien Filtered White Noise

Thanks to the simple usage, the filtered white noise is often fabricated in seismic engineering as strong ground motions. In this article, the Clough & Penzien type with a low-pass filter is used with the Kanaï-Tajimi parameters of $f_k$ = 2.5 Hz and $\xi_k$ = 50%, the Clough-Penzien parameters of $f_c$ = 0.125 Hz and $\xi_c$ = 100% and low-pass filter parameter of $f_{low}$ = 10 Hz and $\xi_{low}$ = 100%. Then, the $\alpha$-type envelope's curve is applied in order to avoid extreme values at the beginning of filtered signal. The central frequency is about 3.3 Hz and the range of frequencies is of 0–50 Hz. The signal lasts 20 s and the time steps is of 10 ms. Then, 1000 signals of the said random process are fabricated for this study.

## 3 Response of Elastoplastic Oscillator Using Beta-Newmark Scheme

The elastoplastic oscillator studied in this article consists of a combination of elastic springs ($\sigma = E^*\varepsilon$), Newtonian damper ($\sigma = C * \dot{\varepsilon}$) and Saint-Venant sliding element ($\sigma_y$). In fact, only the sdof is considered in this article so the stress $\sigma$ and strain $\varepsilon$ are converted into the force f and the displacement u. Modulus $E_1$ and $E_1$ will be replaced by $k_1$ and $k_2$, which are the stiffness of the elastic springs. Yielding stress $\sigma_y$ is translated by the yielding force $f_y$ beyond which the Saint-Venant sliding element slides without any resistance. $E_T$ is the hardening modulus so replaced by hardening stiffness $k_p$.

The dynamic equation of the motion of the mass of this elastoplastic oscillator is written as following:

$$\ddot{u} + 2\xi_0\omega_0\dot{u} + f(u)/m = -\ddot{u}_g \tag{1}$$

where:

u : Relative displacement of the mass m;

m : Mass of the elastoplastic oscillator;

$\omega_0$: Angular velocity corresponding to the elastic frequency of the oscillator $\omega_0 = 2\pi f_0$;

$\xi_0$ : Damping ratio corresponding to the angular velocity and the Newtonian viscosity $\xi_0 = \frac{C}{2m\omega_0}$;

$u_g$ : Ground motion displacement applied to the elastoplastic oscillator

By using the β-newmark ($\beta = ¼$ and $\gamma = ½$), we can solve the response of elastoplastic which raise the problem of timing and memory consummation and convergence.

## 4 Equivalent Linear Oscillator's Parameters Identification by Minimization in Frequency Domain

As mentioned at the introduction that the frequency shift and damping ratio increasing are observed by many authors (Ravikiran 2015; Labbé 2012; EPRI 1994)… as function of increasing plasticity or damage in the structure. In this paper, we execute an experimental plan in order to establish the relationship between the equivalent linear oscillator's parameters versus plasticity parameter. The damage phenomenon is not considered in this article then the ductile demand of structure is chosen as plasticity parameter. It is important to note that the ductile demand is directly and only linked to the maximal value of time history response in displacement. Nevertheless, in some seismic standards (EURO 2005), the non-linear behavior of structure is always based on the value of ductile capacity.

According to the initial parameters of the elastoplastic oscillators, some studies have showed that maximum of time history responses in displacement of elastoplastic structure depend on the relative position of initial frequency $f_0$ in respect to the central frequency of strong ground motion fc. Therefore, in this study, we examine many oscillators whose initial frequency $f_0$ goes from 0.1 * fc to 10 * fc, which correspond successively to the "very low" frequency and the high cutting frequency of filtered white noise Clough-Penzien and damping ratio $\xi_0$ is arbitrarily fixed at 5%.

In addition, we analyze also the influence of the hardening on the equivalent linearization. Therefore, an hardening measurement is defined by the ratio of hardening stiffness against the initial stiffness, so denoted $\alpha_p$. For numerical application, $\alpha_p$ takes values of 0%, 10%, 20%. By definition, the case of $\alpha_p$ equal to 0 corresponds to the elastic perfectly plastic behavior. The dependence of the ductile demand ($\mu$) on the level of signal ($\lambda$) is shown in the Fig. 1.

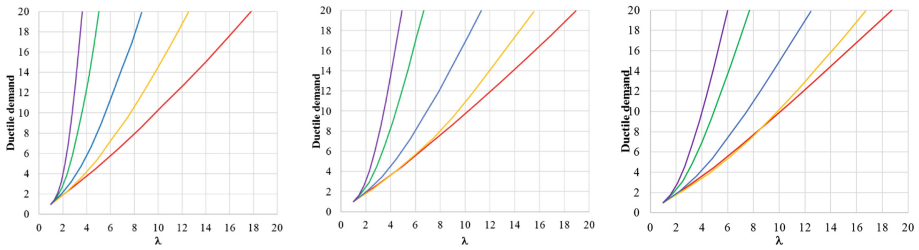


**Fig. 1.** (a): For $\alpha_p$ = 0% (b): For $\alpha_p$ = 10% (c): For $\alpha_p$ = 20%

According to the level of ground motions, for each {$f_0$ and $\xi_0$}, we determine the yielding displacement $X_{e,j}$ so that a filtered white noise signal of level 1, denoted by $g_{1,j}(t)$, leads the associated elastoplastic of {$f_0$, $\xi_0$ and $X_{e,j}$} just to its yielding point. Then, we increase the level of filtered white noise by the factor $\lambda$ ($\lambda max \geq \lambda > 1$) applied to the amplitude of the ground motion of level 1, then denoted by $g_{\lambda,j}(t) = {}^*g_{1,j}(t)$. The maximum value of $\lambda$ corresponds to the case of median value of ductile demand equal to 20. For each level of ground motion $g_{\lambda,j}(t)$, we perform nonlinear transient calculation by using the $\beta$-newmark scheme in order to determine: (1) the ductile demand and (2) the experimental transfer function. The ductile demand is equal to ratio of maximal displacement and yielding displacement and the experimental transfer function is the frequency-domain content of output and input acceleration.

The identification process of equivalent linear oscillator is described in the following figure (Fig. 2).

Where:

| | |
|---|---|
| $g_{1,j}(t)$: | Ground motion of filtered white noise Clough-Penzien type with j = 1…1000; |
| $X_{0,j}(t)$: | Time history response in displacement of elastic oscillator of {$f_0$ and $\xi_0$} undergoing the $g_{1,j}(t)$; |
| $X_{e,j} = \max\|X_{0,j}(t)\|$: | Maximal displacement of elastic oscillator of {$f_0$ and $\xi_0$} undergoing $g_{1,j}(t)$ the in m/s/s; |

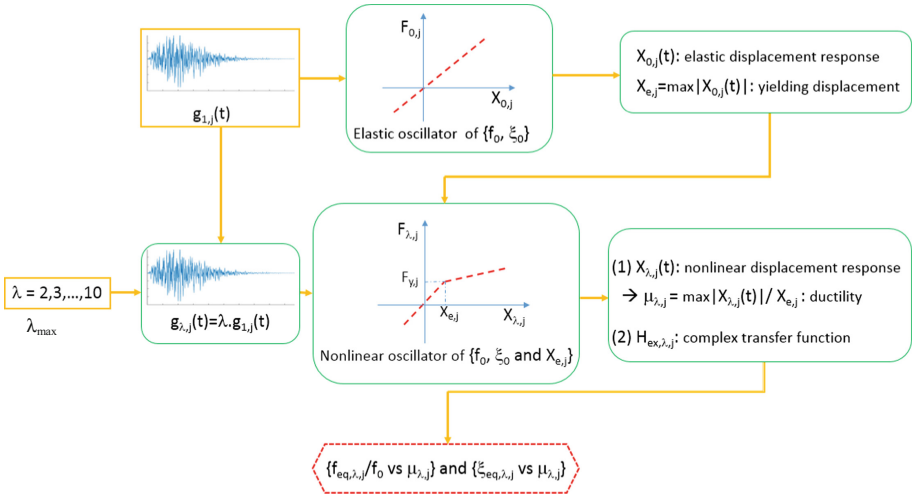


**Fig. 2.** Experimental plan

$\lambda = 2\ldots\lambda_{max}$: 10 values of amplification factor of the amplitude of ground motions. At this stage, it is certain to say that the $g_{1,j}(t)$ leads the elastoplastic oscillator of $\{f_0$ and $\xi_0\}$ and $X_{e,j} = \max|X_{0,j}(t)|$ just to the yielding point, no plastic deformation is observed. Then, $g_{\lambda,j}(t) = \lambda * g_{1,j}(t)$ makes elastoplastic oscillator to exhibit plastic deformation;

$u_{\lambda,j}(t)$: Displacement time history of elastoplastic oscillator of $\{f_0; \xi_0$ and $X_{e,j}\}$ undergoing the $g_{\lambda,j}(t) = \lambda * g_{1,j}(t)$, performed by using the β-Newmark scheme. Then, we define the ductile demand as: $\mu\lambda_{,j} = \max|u_{\lambda,j}(t)|/X_{e,j}$;

$H_{ex,\lambda,j}$: Experimental complex transfer function defined as $H_{ex,\lambda,j} = \text{fft}(a_{\lambda,j})/\text{fft}(g_{\lambda,j})$ where $a_{\lambda,j}$ is the output acceleration and fft(.) assigns the Fast Fourier Transform;

$\{f_{eq,\lambda,j}$ and $\xi_{eq,\lambda,j}\}$: Equivalent linear frequency and damping ratio defined by the procedure of equivalent linearization by minimization in the frequency domain (Fig. 3).

In fact, in the frequency domain, we determine the equivalent linear oscillator of $\{f_{eq}$ and $\xi_{eq}\}$ by minimization in the frequency domain through the complex transfer function. This procedure is completely done by using the nonlinear regression by least square solution. More precisely, for every single of $H_{ex,\lambda,j}$ with $j = 1\ldots1000$ and $\lambda = 2\ldots\lambda_{max}$, we determine the couple of $\{f_{eq,\lambda,j}$ and $\xi_{eq,\lambda,j}\}$ that minimize "the difference" between the experimental complex transfer function $H_{ex,\lambda,j}$ and theoretical one $H_{th,\lambda,j}$ of the elastic equivalent oscillator of $\{f_{eq,\lambda,j}$ and $\xi_{eq,\lambda,j}\}$. As numerically saying, the $\{f_{eq,\lambda,j}$ and $\xi_{eq,\lambda,j}\}$ are determined by minimizing this term:

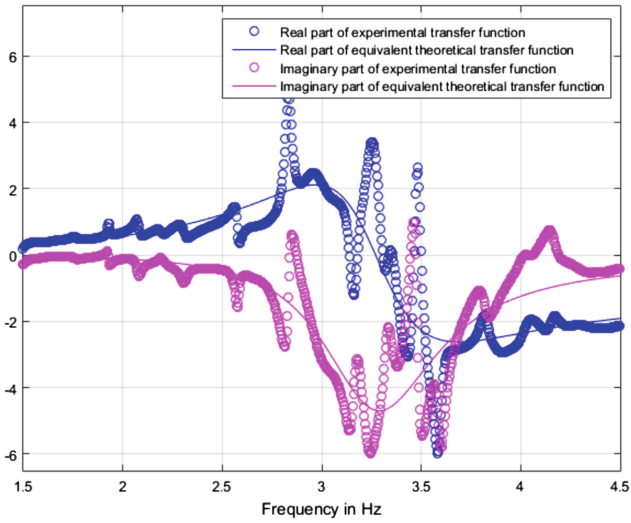


**Fig. 3.** Example of complex transfer function regression

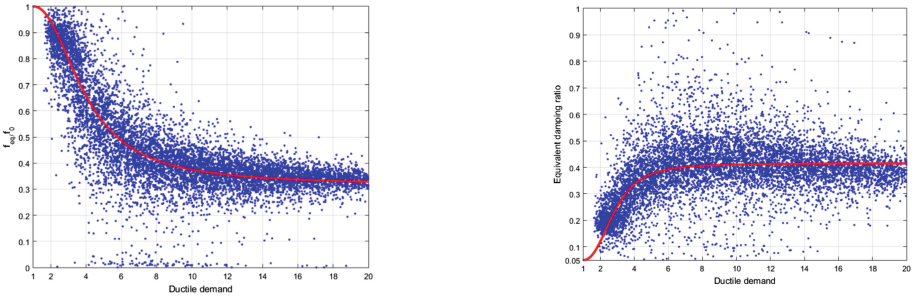


**Fig. 4.** (a): Scatter plot of $f_{eq}/f_0$ (b): Scatter plot for $\xi_{eq}$

$$J\left(f_{eq,\lambda,j};\xi_{eq,\lambda,j}\right)=\sum_{f_{\min}}^{f_{\max}}\left(\mathrm{Re}\left(H_{ex,\lambda,j}(f_i)\right)-\mathrm{Re}\left(H_{t,\{f_{eq,\lambda,j},\xi_{eq,\lambda,j}\}}(f_i)\right)\right)^2+\left(\mathrm{Im}\left(H_{ex,\lambda,j}(f_i)\right)-\mathrm{Im}\left(H_{t,\{f_{eq,\lambda,j},\xi_{eq,\lambda,j}\}}(f_i)\right)\right)^2 \tag{3}$$

where Re(.) and Im(.) assign the real and imaginary part of complex number.

For the best frequency resolution, the zeros-padding method is applied. The determination of $\{f_{eq,\lambda,j}$ and $\xi_{eq,\lambda,j}\}$ is reached by using the operator *lsqcurvefit* in matlab.

For example (**Ref**. Fig. 4), we present the result of $\{f_{eq,\lambda,j}$ and $\xi_{eq,\lambda,j}\}$ determined for $\lambda = 2$ and $j = 1$. The $X_{e,1}$ is determined by the linear analysis of the elastic

oscillator of $\{f_0 = 3.35$ Hz and $\xi_0 = 5\%\}$ and $\alpha_p = 10\%$ equal to 0.021 m. The equivalent oscillator is characterized by $\{f_{eq,2,1}$ and $\xi_{eq,2,1}\} = \{3.27$ Hz, $13.6\%\}$ and the ductile demand equal to 1.87.

By applying this procedure to each value of $\lambda = 2 \ldots \lambda_{max}$, we obtain 10 000 couples of $\{f_{eq,\lambda,j}$ and $\xi_{eq,\lambda,j}\}$ and 10 000 values of ductile demand $\mu_{\lambda,j}$. Then, we have to process the treatment of two scatter plots of $\{f_{eq,\lambda,j}$ VS $\mu_{\lambda,j}\}$ and $\{\xi_{eq,\lambda,j}$ VS $\mu_{\lambda,j}\}$ in order to get the formula of experimental curves. Here you can find an example of scatter plots of $\{f_{eq,\lambda,j}$ VS $\mu_{\lambda,j}\}$ and $\{\xi_{eq,\lambda,j}$ VS $\mu_{\lambda,j}\}$ for the oscillator of $f_0/f_c$ equal to 0.1 with 10% kinematic hardening in which the blue dots are 10 000 couples and red line is the regression using the regression.

It is important to note from these scatter plots that:

+ the ratio of equivalent frequency and initial frequency tends to the value of $\sqrt{\alpha}$. In this case, the elastoplastic is considered to be always in plastic regime.
+ the damping ratio seems to be inverse-proportional to the frequency

At this stage, we can propose experimental curves as following:

$$\begin{aligned} \frac{f_{eq}}{f_0} &= \sqrt{\alpha_p} + \frac{1 - \sqrt{\alpha_p}}{1 + \frac{(\mu-1)^d}{b}} \\ \xi_{eq} &= \xi_0 + a\left(1 - \left(\frac{f_{eq}}{f_0}\right)^c\right) \end{aligned} \tag{4}$$

The treatment of theses scatter plots consists in adjusting these parameters {b;d} for the scatter plot of $\{f_{eq,\lambda,j}$ VS $\mu_{\lambda,j}\}$ and {a,c} for the $\{\xi_{eq,\lambda,j}$ VS $\mu_{\lambda,j}\}$.

## 5 Result of Equivalent Linearization

By following the procedure described above, we apply the experimental plan for each of 5 values of $f_0$/fc ($f_0$/fc = 0.1; 0.5; 1.0; 1.5; 2.0) and 3 values of $\alpha_p$ ($\alpha_p$ = 0.0; 0.1; 0.2). The output in term of curves $\{f_{eq}$ VS $\mu\}$ and $\{\xi_{eq,}$VS $\mu\}$ is presented in Fig. 5.

## 6 Comments on the Equivalent Linearization

In respect to the central frequency of input signal, the more the initial frequency is important ($f_0$/fc important), the more the equivalent frequency is close to the initial one ($f_{eq}/f_0$ approaches to 1). That is to say, when the structure is stiff ($f_0$/fc important), excursions in plastic domain are very violent and cause the important values of ductile demand. This strong plastic excursion is not "captured" by this concept because this excursion is of very low frequencies content, which is less than the frequency discretization for the Fast Fourier Transform. This very strong excursion can be explained by the fact that during the excursion in plastic domain, the duration of excursion is smaller than the duration of changing the sign of input signal, then, no changing of sign gets done during the plastic excursion. At the contrary for oscillators of low

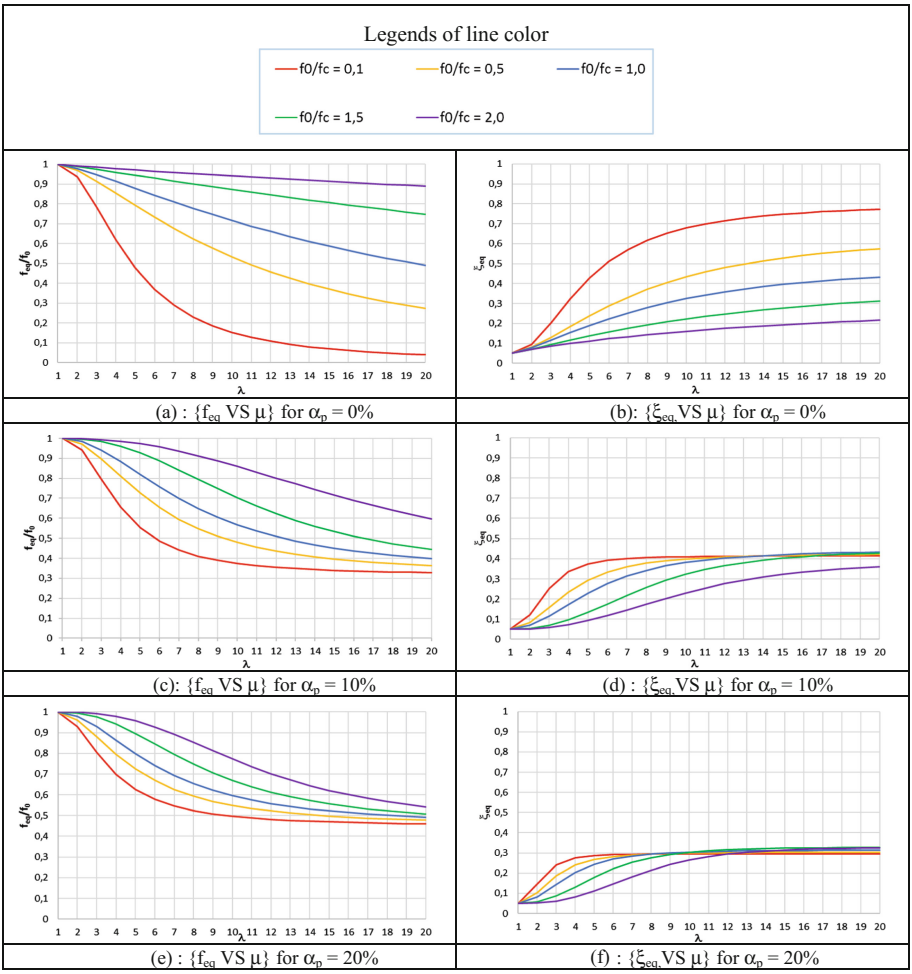


**Fig. 5.** (a): $\{f_{eq}$ VS $\mu\}$ for $\alpha_p = 0\%$ (b): $\{\xi_{eq,}$VS $\mu\}$ for $\alpha_p = 0\%$ (c): $\{f_{eq}$ VS $\mu\}$ for $\alpha_p = 10\%$ (d): $\{\xi_{eq,}$VS $\mu\}$ for $\alpha_p = 10\%$ (e): $\{f_{eq}$ VS $\mu\}$ for $\alpha_p = 20\%$ (f): $\{\xi_{eq,}$VS $\mu\}$ for $\alpha_p = 20\%$

frequencies, during the excursion, the sign changes many times so that the plastic excursion depend only on the velocity at the moment of excursion.

While $\lambda$ approaches infinity, the oscillator is logically plastic so its equivalent oscillator should take the frequency associated to the hardening. Then, the ratio of $f_{eq}/f_0$ approaches $\sqrt{\alpha_p}$. In addition, the feq reaches the asymptotic value rapidly for the oscillator of small $f_0/f_c$ and the contrary for oscillators of ig $f_0$/fc.

## 7 Pertinence of Equivalent Linear Oscillator Through Anderson's Criteria

Initially developed by Anderson (Anderson 2004) in the interest of quantitative measurement of the similarity between the artificial signal and real earthquake signal recorded in site, the ten criteria are essentially the comparison of duration, peaks and frequency content of time history signal. According to the duration, the first and second criteria evaluate successively the energy duration and Arias duration, then, the third and fourth one indicate the difference of total energy and total Arias of signal. In regard of peaks, the fifth, sixth and seventh criterion can compare the peak in accelerogram, in velocity and in displacement. These velocity and displacement are obtained by using the single and double integral of accelerogram. The last three criteria are based on the frequency content of signal, successively through the response spectrum, Fourier transform and cross-correlation. For each criteria, the similarity is noted from zero to ten (0 to 10). A score below 4 is a poor fit, a score of 4–6 is a fair fit, a score of 6 to 8 is a good fit, and a score over 8 is an excellent fit.

Using these criteria, we can evaluate quantitatively the similarity between the output acceleration of non-linear oscillator and the one of equivalent linear oscillator. In order to clarify the pertinence of equivalent linear oscillator, we show also the similarity between the output acceleration of non-linear oscillator and the linear oscillator with initial parameters $\{f_0$ and $\xi_0\}$. In this article, we can show an example for a simple case of $f_0/fc = 1.0$ for elastoplastic behavior with 10% of hardening ($\alpha_p = 10\%$) (Ref. Fig. 6).

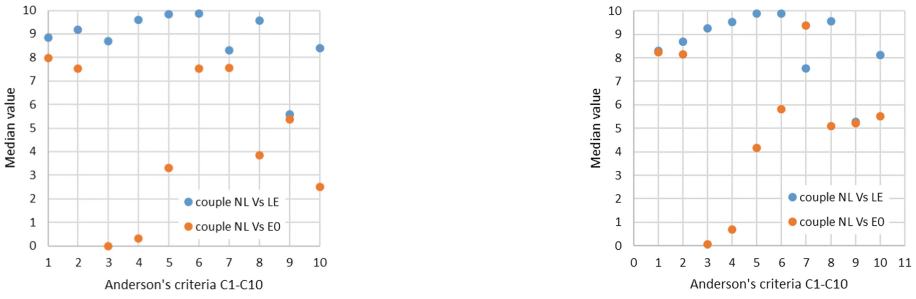


**Fig. 6.** (a): Example for $\lambda = 8$ and $\mu = 12.2$ (b): Example for $\lambda = 4$ and $\mu = 4.46$

As we established the curve of $\{f_{eq}/f_0$ VS $\mu)$ and $(\xi_{eq}$ VS $\mu)$, we can expect that the score for eighth, ninth and tenth criteria are good, and that's what we observe from the Fig. 6. The energy duration and Arias duration are quietly well the same for both couple of non-linear output acceleration VS Equivalent linear output acceleration and the one of non-linear acceleration VS linear output acceleration within initial parameters. We obtain a very good for the peak of acceleration and velocity's criteria. Nevertheless, the peak in displacement is not correlated between output acceleration of nonlinear and equivalent linear system.

## 8 Conclusions

This study deals with the equivalent linearization for elastoplastic systems through the systematic analysis of a series of oscillators using the complex transfer function as the equivalent criterion.

The frequency ratio shifts and equivalent damping for both the numeric and experimental results are not as important as the ones corresponding to secant stiffness which is widely used in practice.

The Anderson's criteria show that the output acceleration of equivalent linear oscillator conserve well the energy and Arias duration, also the total energy of output acceleration of non-linear oscillator as well as the content in frequency domain. In addition, the peak in acceleration, velocity are well similar in respect to the value of non-linear oscillator. But, the peak in displacement of equivalent linear oscillator is different in respect to the peak of displacement of non-linear oscillator because this concept of equivalent linear behavior doesn't consider the "strong" plastic excursion.

## References

Anderson, J.G.: Quantitative measure of the goodness-of-fit of synthetic seismograms. In: 13th World Conference on Earthquake Engineering Conference Proceedings, Vancouver, Canada, Paper, vol. 243 (2004)

Ravikiran, A.: Experimental and numerical studies of ratcheting in pressurized steel piping systems under seismic load, Indian (2015)

Chopra, A.K., Goel, R.K.: Capacity-demand-diagram methods based on inelastic design spectrum. Earthq. Spectra **15**(4), 637–656 (1999)

Chopra, A.K.: Dynamics of structures - theory and applications to earthquake engineering - pearson education Asia limited and Tsinghua University Press, Beijing (2001)

EPRI.: Piping and fitting dynamic reliability program EPRI- PaloAlto, CA (1994)

Standard, British. Eurocode 8: Design of structures for earthquake resistance (2005)

Iwan, W.D., Gates, N.C.: The effective period and damping of a class of hysteretic structures. Earthq. Eng. Struct. Dyn. **7**, 199–211 (1979)

Iwan, W.D.: Estimating inelastic response spectra from elastic spectra. Earthq. Eng. Struct. Dyn. **8**, 375–388 (1980)

Labbé, P.B.: Categorization of seismically-induced stresses for civil and mechanical engineering, Paris (2012)

Seed, H.B., Idriss, I.M.: Soil moduli and damping factors for dynamic response analyses. Report EERC, pp. 70–10. Earthquake Engineering Research Center (1970)

# Tensioning Process Update for Cable Stayed Bridges

Jose Antonio Lozano-Galant[1], Dong Xu[2(✉)], and Jose Turmo[3]

[1] Universidad de Castilla-la Mancha, Ciudad Real, Spain
joseantonio.lozano@uclm.es
[2] Tongji University, Shanghai, China
xu_dong@tongji.edu.cn
[3] Universitat Politècnica de Catalunya-BarcelonaTech, Barcelona, Spain
jose.turmo@upc.edu

**Abstract.** Construction of cable stayed bridges is very challenging. These structures are extremely redundant and the effect of tensioning one cable has the effect of changing the stresses of the already installed cables. In order to achieve a targeted service state at the end of the construction process careful calculations has to be done by the contractor in order to ensure it. However, deviations arise between the modelling of the tensioning process and the actual results obtained on site. In order to adjust the final stresses in the cables, a final restress of the stays is unusually required. This re-stressing operation is usually done for the whole cable, as the strand by strand stressing technique used for the first stressing operations, cannot be used anymore. This last operation is costly, time consuming and has less accuracy, compared with the strand by strand tensioning techniques. The paper will present a method to control the tensioning process on site and to modify it according to the stresses measured in the cables at each stressing stage. In this way, the chances of requiring a restressing operation are diminished.

**Keywords:** Cable stayed bridges · Construction · Temporary supports

## 1 Introduction

To design a cable-stayed bridge the definition of a target state is required. This stage is known as the Objective Service Stage (*OSS*) under some given loads known as Target Load [1]. This implies defining an appropriate set of stay forces [2, 3]. Structures under construction are more flexible than the completed bridge and are subjected to construction loads. Thus, the effects of dynamic loads, such as wind [4, 5] or earthquake [6], during construction can be even more significant than during operation. Furthermore, as cable-stayed bridges are redundant structures, tensioning one single strand affects the other elements of these structures. For these reasons, many researchers have studied the construction process of cable stayed-bridges (see [7–9]). Moreover, the development the Health Monitoring field [10] enables the structural control [6] and damage detection [11, 12] of complex structures. Cable-stayed bridges might be monitored both during construction and in service. The information obtained can be

© Springer Nature Singapore Pte Ltd. 2018
H. Tran-Nguyen et al. (eds.), *Proceedings of the 4th Congrès International de Géotechnique - Ouvrages -Structures*, Lecture Notes in Civil Engineering 8,
DOI 10.1007/978-981-10-6713-6_27

used to calibrate models linked with maintenance and structural management to assure structural safety and functionally of structures [13].

The traditional method to simulate construction process of cable-stayed bridges is to start at the *OSS* and dismantle the structure. Several authors have proposed methods based on this backward approach (see [1, 14–16]). Nevertheless, these methods cannot analyze the effects of the time-dependent phenomena, (see [17, 18]) unless a global iterative process or a backward-forward analysis is performed. To overcome all these problems, a forward simulation has been proposed (see [14, 15, 19, 20]).

Most of the simulation methods presented in the literature assume that any construction stage can be obtained by deactivating or activating group of elements, loads or boundary conditions from the following or the preceding construction stages. This hypothesis assumes that the construction process can be simulated by linear superposition of stages (see [1, 19]). Other methods avoid the use of superposition [21] and introduce the effect of time-dependent phenomena in the definition of *OSS* [22, 23].

These structures are extremely redundant and the effect of tensioning one cable has the effect of changing the stresses of the already installed cables. In order to achieve a targeted service state at the end of the construction process careful calculations has to be done by the contractor in order to ensure it. However, deviations arise between the modelling of the tensioning process and the actual results obtained on site. In order to adjust the final stresses in the cables, a final restress of the stays is unusually required. This re-stressing operation is usually done for the whole cable, as the strand by strand stressing technique used for the first stressing operations, cannot be used anymore. This last operation is costly, time consuming and has less accuracy, compared with the strand by strand tensioning techniques. This paper will present a method to control the tensioning process on site and to modify it according to the stresses measured in the cables at each stressing stage. In this way, the chances of requiring a restressing operation are diminished.

## 2 Forward Analysis

The Forward analysis presented here [19] follows the actual construction sequence at site. It is more intuitive and the modeling errors are reduced. Also, modifications of the tensioning process can be analyzed easier. This allows defining a new tensioning strategy that includes the actual state at site.

The problem of applying the forward approach is that the axial forces that have to be introduced by the jack along the construction process in order to achieve the *OSS* are unknown. Therefore, an iterative process that updates these values of the tensioning matrix is needed. In this process, characterized by the $j$ index, an initial tensioning matrix is used to model construction process of the bridge forwards. Since the axial forces in the stays are modeled by means of imposed strains, a certain strain vector during the construction process, can be obtained. This updating can be summarized in the following equations:

$$\left\{\varepsilon_{Cp}\right\}_{N\times 1}^{j+1} = \left\{\varepsilon_{Cp}\right\}_{N\times 1}^{j} + \left\{\Delta\varepsilon\right\}_{N\times 1} \tag{1}$$

$$\sum_{n=1}^{N}\left|\frac{N_{C_n}^{j,K} - N_{C_n}^{OCS}}{N_{C_n}^{j,K}}\right| \leq Tolerance \tag{2}$$

Every $Stage^{j,k,i}$ can be calculated adding the results of some *Auxiliary Models*$^{k,i}$ to the initial stage where the bridge deck is supported by the temporary supports. An equivalent way to obtain the $Stage^{j,k,i}$ consists of adding an *Auxiliary Model*$^{k,i}$ to the preceding construction stage, $Stage^{j,k-1}$. Secondly, the axial forces in the stays are modeled by means of imposed strains instead of forces as in the case of commercial programs. This way of modeling has the advantage that more information of the construction is available, e.g. stresses in the strands during construction. A local iterative process, with *i* index, is needed in order to define when the temporary supports are raised. This is summarized in the following equations.

$$Stage^{j,k,i} = Initial \quad Stage + \sum_{k=1}^{k} Auxiliary \quad Model^{k,i} \tag{3}$$

$$Stage^{j,k,i} = Stage^{j,k-1} + Auxiliary \quad Model^{k,i} \tag{4}$$

The input data includes geometry and mechanical properties of the cable-stayed bridge, Target load, *v*ector of axial forces in the stays, at *OSS*, an initial tensioning matrix and a tolerance. This last parameter is used to define the stopping criterion of the overall iterative process. Output is based on matrices of deflections, reactions and efforts during construction and tensioning matrix.

## 3 Tensioning Process Modification

The calculated and the actual tensioning process on site rarely coincide. Deviations between the actual and predicted stay forces are usually found. Usually, an additional tensioning stage is added in order to correct these deviations. This is both time-consuming and expensive. One of the main advantages of using the forward approach is that the tensioning process can be adapted to correct the measured deviations. The process can be recalculated by means of a new global iterative process. This process will start on a stage that includes the actual axial forces obtained on site. In the conference an example (Fig. 1) will be presented and the efficiency of the method will be highlighted. In this, the construction process will be modeled according to two different tensioning strategies. The first one consists of using the original process without including the measured deviations. The second tensioning strategy consists of including the measured deviations by means of updating the new unknown values of the tensioning matrix. As the deviation is detected before the last tensioning operation of all stays, the same global iterative process based on *N* stages can be applied. The analysis of this deviation case will show that when unmodified tensioning matrix is used, the initial deviations are

amplified at completion. When the tensioning matrix is updated the differences are minimized in all stays and tend to zero.

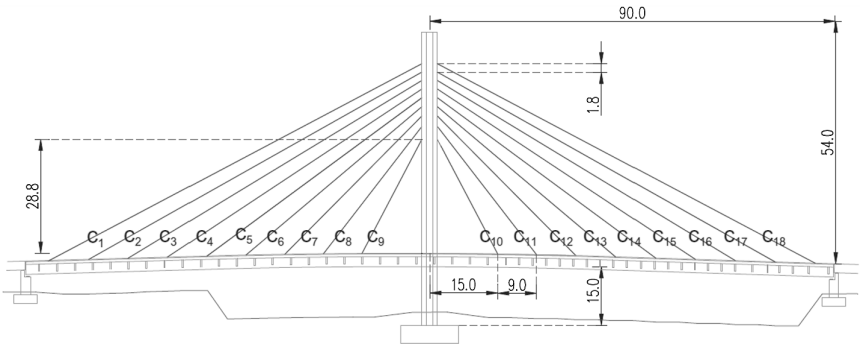


**Fig. 1.** Cable supported structure on temporary propping [1]

## 4 Conclusion

In this paper, a method is presented for the modeling of cable-stayed bridges. Unlike the traditional way of modeling the construction process that is based on the backward approach, it is based on the actual sequence of events followed at site. Deviations between the calculated axial forces and those measured on site can be efficiently corrected without the need of any additional tensioning stage on site. Therefore, it can be efficiently use for the construction control of cable-stayed bridges.

**Acknowledgements.** This work was partially funded by the Spanish Ministry of Economy and Competitiveness and the FEDER fund through the grant project (BIA2013-47290-R) directed by Jose Turmo.

## References

1. Lozano-Galant, J.A., Payá-Zaforteza, I., Xu, D., Turmo, J.: Analysis of the construction process of cable-stayed bridges built on temporary supports. Eng. Struct. **40**, 95–106 (2012)
2. Lee, T.Y., Kim, Y.H., Kang, S.W.: Optimization tensioning strategy for asymmetric cable-stayed bridge and its effects on the construction process. Struct. Multi. Optim. **35**, 623–629 (2008)
3. Hassan, M.M., Nassef, A.O., El Damatty, A.A.: Determination of optimum post-tensioning cable forces of cable-stayed bridges. Eng. Struct. **44**, 248–259 (2012)
4. Oiseth, O., Ronnquist, A., Sigbjornsson, R.: Time domain modeling of self-excited aerodynamic forces for cable-supported bridges: A comparative study. Comput. Struct. **89**, 1306–1322 (2011)
5. Korkmaz, S.: A review of active structural control: challenges for engineering informatics. Comput. Struct. **89**, 2113–2132 (2011)

6. Morgenthal, G., Sham, R., West, B.: Engineering the tower and main span construction of stonecutters bridge. J. Bridge Eng. **15**(2), 144–152 (2010)
7. Nazmy, A.S.: Three-dimensional nonlinear static analysis of cable-stayed bridges. Comput. Struct. **34**, 257–271 (1990)
8. Janjic, D., Pircher, M., Pircher, H.: Optimization of cable-tensioning in cable-stayed bridges. J. Bridge Eng. **8**, 131–137 (2003)
9. Reddy, P., Ghaboussi, J., Hawkins, M.: Simulation of construction of cable stayed bridges. J. Bridge Eng. **4**, 249–257 (1999)
10. Posenato, D., Kripakaran, P., Inaudi, D., Smith, I.F.C.: Methodologies for model-free data interpretation of civil engineering structures. Comput. Struct. **88**, l467–1482 (2010)
11. Shiradhonkar, S.R., Shrikhande, M.: Seismic damage detection in a building frame via finite element model updating. Comput. Struct. **89**, 2425–2438 (2011)
12. Danai, K., Civjan, S.A., Styckiewicz, M.M.: Direct method of damage localization for civil structures via shape comparison of dynamic response measurements. Comput. Struct. **92-93**, 297–307 (2012)
13. Castillo, E., Lozano-Galant, J.A., Nogal, M., Turmo, J.: New tool to help decision making in civil engineering. J. Civ. Eng. Manag. **21**(6), 689–697 (2015)
14. Wang, P.H., Tang, T., Zheng, H.: Analysis of cable-stayed bridges during construction by cantilever method. Comput. Struct. **82**, 329–346 (2004)
15. Han, D.J., Yan, Q.: Cable force adjustment and construction control. In: Wai-Fah, C., Lian, D. (eds.) Bridge Engineering Handbook. CRC Press, Boca Raton (2000)
16. Behin, Z., Murray, D.: A substructure-frontal technique for cantilever erection analysis of cable-stayed bridges. Comput. Struct. **42**, 145–157 (1992)
17. Erkmen, R.E., Bradford, M.A.: Time-dependent creep and shrinkage analysis of composite beams curved in-plan. Comput. Struct. **89**, 67–77 (2011)
18. de Somja, H., Ville de Goyet, V.: A new strategy for analysis of erection stages including an efficient method for creep analysis. Eng. Struct. **30**, 2871–2883 (2008)
19. Lozano-Galant, J.A., Payá-Zaforteza, I., Xu, D., Turmo, J.: Forward algorithm for the construction control of cable-stayed bridges built on temporary supports. Eng. Struct. **40**, 119–130 (2012)
20. Lozano-Galant, J.A., Ruiz-Ripoll, L., Payá-Zaforteza, I., Turmo, J.: Modification of the stress-state of cable-stayed bridge due to staggered erection of their superstructure. Baltic J. Road Bridge Eng. **9**(4), 241–250 (2014). doi:10.3846/bjrbe.2014.30
21. Lozano-Galant, J.A., Xu, D., Payá-Zaforteza, I., Turmo, J.: Direct simulation of the tensioning process of cable-stayed bridges. Comput. Struct. **121**, 64–75 (2013). doi:10.1016/j.compstruc.2013.03.010
22. Lozano-Galant, J.A., Turmo, J.: Creep and shrinkage effects in service stresses of concrete cable-stayed bridges. Comput. Concr. **13**(4), 483–499 (2014). http://dx.doi.org/10.12989/cac.2014.13.4.483
23. Lozano-Galant, J.A., Turmo, J.: An algorithm for simulation of concrete cable-stayed bridges built on temporary supports and considering time dependent effects. Eng. Struct. **79**, 341–353 (2014). http://dx.doi.org/10.1016/j.engstruct.2014.08.018

# The Roles and Effects of Friction in Cohesive Zone Modelling: A Thermodynamics-Based Formulation

Giang D. Nguyen[1(✉)] and Ha H. Bui[2]

[1] The University of Adelaide, Adelaide, SA, Australia
g.nguyen@adelaide.edu.au
[2] Monash University, Clayton, VIC, Australia
ha.bui@monash.edu

**Abstract.** Cohesive zone models have been widely used for modelling failure of interfaces in laminated composites and also for representing the behavior of the Fracture Process Zone in modelling geomaterial failure. Despite their importance and usefulness, most existing models do not adequately take into account the underlying mechanisms of dissipation at a lower scale that include both micro-cracking and friction between micro-crack surfaces. These models either rely on a single scalar damage variable to represent the deterioration process, or inadequately account for the role of friction in governing the interface behavior and failure in mixed mode conditions. In this work, we use a thermodynamics-based formulation of a damage-plasticity cohesive model for the analysis of its behavior in relation to the variation of frictional contribution to the energy dissipation budget. The advantages of the proposed formulation in directly linking frictional contribution with the mechanical responses are highlighted.

**Keywords:** Cohesive model · Damage-Plasticity · Thermodynamics · Friction

## 1 Introduction

It has been widely accepted that the behavior of a very thin zone such as an interface between plies in laminated composites, or Fracture Process Zone in concrete or rock failure can be represented by a cohesive zone model describing the traction-displacement jump across the two sides of this zone. While mathematically this zone can be conveniently considered as a zero thickness zone, physically the mechanisms of failure in this very thin zone are complex and should be appropriately accounted for in the development of cohesive model. In particular, in cement matrix composites, under pure macro mode I failure, the dominant dissipation mechanism is not the creation of surface area from micro-cracks, but friction between their faces. Deduction from experimental data by Bazant [1], confirmed by novel X-ray experiments recently by Landis et al. [2], shows that frictional loss accounts for 50–75% of the total dissipation budget. Experimental research in [3] also showed that most micro-cracks appear to have developed under mixed mode or pure shear conditions. At the macro scale, the effects of friction can be experimentally observed through the residual deformations

© Springer Nature Singapore Pte Ltd. 2018
H. Tran-Nguyen et al. (eds.), *Proceedings of the 4th Congrès International de Géotechnique - Ouvrages -Structures*, Lecture Notes in Civil Engineering 8,
DOI 10.1007/978-981-10-6713-6_28

and the long tail load-displacement curves [4, 5]. These evidences indicate that the mode I fracture energy measured by conventional methods in concrete fracture always consists of energy released due to the creation of new surface areas and that due to friction.

On the other hand, in the context of delamination in laminated composites, large permanent crack openings experimentally observed upon unloading, such as in Fan [6] on mixed-mode bending (MMB) tests and Rikards et al. [7] on double-cantilever beam (DCB) tests on composite laminates, are clear evidences of the irrecoverable deformation due to friction at the lower scales. Again, this frictional contribution to the energy dissipation budget originates from the activation, propagation of micro-cracks under pure mode I that could be followed by frictional losses between their faces.

Given clear experimental evidences on the significant contribution of friction to the macro response and failure of the interface, it is essential that this contribution should be adequately accounted for in the development of a cohesive zone model. There have been several recent works on damage and damage-plasticity cohesive zone modelling, such as Kolluri [8], Guiamatsia and Nguyen [9, 10] for the study of debonding of interface systems, Ruiz et al. [11], Moës and Belytschko [12], Elices et al. [13], Mir et al. [14], Alfaiatea and Sluys [15, 16] for concrete, Gui et al. [17] and Nguyen et al. [18] for rocks, Le et al. [19] for rock joints, Freddi and Sacco [20] and Neto et al. [21] for interface between concrete and FRP (Fiber Reinforced Polymers), and Nguyen et al. [22] for asphalt materials. However in these works, the links between frictional contribution and model responses together with frictional effects on the model responses in mixed mode loading conditions have either been neglected or not explored at length. The aim of this study is to explore the roles and effects of friction on the responses of a cohesive model formulated based on thermodynamic principles. This formulation supplies explicit links between energy dissipations due to different mechanisms and the mechanical responses, facilitating the investigation on the effects of frictions and also highlighting the importance of thermodynamic principles in constitutive modelling.

## 2 A Thermodynamics-Based Cohesive Model

### 2.1 Formulation

The formulation in this study is based on a thermodynamic framework for constitutive modelling developed by Houlsby and Puzrin [23]. Through a detailed formulation of this cohesive model, we would like to address the importance of coupling different mechanisms of dissipations in a thermodynamically consistent approach, and the benefits of such a formulation in both interpreting and investigating the mechanical behavior of the obtained model. The Helmholtz free energy takes the following form:

$$\begin{aligned}\Psi &= \frac{1}{2}(1-D)\left[K_n u_n^{e2} + K_s u_s^{e2}\right] + \frac{1}{2}DH\left(-u_n^e\right)K_n u_n^{e2} \\ &= \frac{1}{2}(1-D)\left[K_n\left(u_n - u_n^p\right)^2 + K_s\left(u_s - u_s^p\right)^2\right] + \frac{1}{2}DH\left(-u_n^e\right)K_n\left(u_n - u_n^p\right)^2 \end{aligned} \quad (1)$$

where a single damage variable $D$ is used, and $K_n$ and $K_s$ are the normal and shear elastic stiffnesses of the cohesive model. The decomposition of total displacement into elastic $\left(u_n^e\right)$ and plastic $\left(u_n^p\right)$ is used and in addition, the Heaviside function $H\left(-u_n^e\right)$ is introduced to take into account the unilateral effects upon unloading from tension to compression. The traction and damage energy, considered as generalized stresses in this thermodynamic framework, are obtained from the above free energy potential as follows:

$$t_n = \frac{\partial \Psi}{\partial u_n^e} = (1-D)K_n u_n^e + H\left(-u_n^e\right) D K_n u_n^e; \text{ and } t_s = \frac{\partial \Psi}{\partial u_s^e} = (1-D)K_s u_s^e \tag{2a, b}$$

$$\begin{aligned} \chi_D &= -\frac{\partial \Psi}{\partial D} = \tfrac{1}{2}K_n u_n^{e2} - \tfrac{1}{2}H\left(-u_n^e\right)K_n u_n^{e2} + \tfrac{1}{2}K_s u_s^{e2} \\ &= \underbrace{\tfrac{1}{2}H(t_n)\frac{t_n^2}{(1-D)^2 K_n}}_{\chi_{Dn}} + \underbrace{\tfrac{1}{2}\frac{t_s^2}{(1-D)^2 K_s}}_{\chi_{Ds}} \end{aligned} \tag{3}$$

where the damage energies corresponding to normal and shear modes are $\chi_{Dn}$ and $\chi_{Ds}$, and the fact that the normal traction has the same sign with that of the elastic normal displacement has been used.

The dissipation potential takes the following form [24]:

$$\Phi = \sqrt{\phi_D^2 + \phi_n^{p2} + \phi_s^{p2}} \tag{4}$$

where the contributions from damage and normal and shear plastic components are defined as:

$$\phi_D = \chi_D \dot{D} \Big/ \left(\frac{\chi_{Dn} R_D^n}{F_n(D)} + \frac{\chi_{Ds} R_D^s}{F_s(D)}\right); \; \phi_n^p = \frac{\sqrt{F_n(D)}\, t_n}{\sqrt{R_p^n \chi_{Dn}}} \dot{u}_n^p; \text{ and } \phi_s^p = \frac{\sqrt{F_s(D)}\, t_s}{\sqrt{R_p^s \chi_{Ds}}} \dot{u}_s^p \tag{5a, b, c}$$

In the above expression, function $F_n(D)$ and $F_s(D)$ control the softening response of the model in normal and shear modes, respectively, while the four parameters $R_D^n$, $R_D^s$, $R_p^n$ and $R_p^s$ will be later identified as the percentages of contributions from damage and frictional dissipations in normal and shear modes respectively. Further details on their roles and forms will be discussed later. Following the procedures established in Houlsby and Puzrin [23], the dissipative generalized stresses $\bar{t}_n$, $\bar{t}_s$ and $\bar{\chi}_D$ can be obtained from the proposed dissipation potential as [23, 24]:

$$\begin{aligned} \bar{t}_n &= \frac{\partial \Phi}{\partial \dot{u}_n^p} = \frac{\partial \Phi}{\partial \phi_n^p}\frac{\partial \phi_n^p}{\partial \dot{u}_n^p} = \frac{\phi_n^p}{\sqrt{\phi_D^2 + \phi_n^{p2} + \phi_s^{p2}}}\frac{\partial \phi_n^p}{\partial \dot{u}_n^p}; \text{ and } \bar{t}_s = \frac{\partial \Phi}{\partial \dot{u}_s^p} = \frac{\partial \Phi}{\partial \phi_s^p}\frac{\partial \phi_s^p}{\partial \dot{u}_s^p} \\ &= \frac{\phi_s^p}{\sqrt{\phi_D^2 + \phi_n^{p2} + \phi_s^{p2}}}\frac{\partial \phi_s^p}{\partial \dot{u}_s^p} \end{aligned} \tag{6a, b}$$

$$\bar{\chi}_D = \frac{\partial \Phi}{\partial \dot{D}} = \frac{\partial \Phi}{\partial \phi_D}\frac{\partial \phi_D}{\partial \dot{D}} = \frac{\phi_D}{\sqrt{\phi_D^2 + \phi_n^{p2} + \phi_s^{p2}}}\frac{\partial \phi_D}{\partial \dot{D}} \tag{7}$$

The Legendre transformation [23, 24] of the first order homogeneous dissipation potential (4) leads to the yield function $y^*$ in generalized stress space of the form:

$$y^* = \left(\frac{\bar{\chi}_D}{\partial \phi_D / \partial \dot{D}}\right)^2 + \left(\frac{\bar{t}_n}{\partial \phi_n^p / \partial \dot{u}_n^p}\right)^2 + \left(\frac{\bar{t}_s}{\partial \phi_s^p / \partial \dot{u}_s^p}\right)^2 - 1 \le 0 \tag{8}$$

From the above yield, the evolution rules for plastic displacements and damage can be obtained as:

$$\dot{u}_n^p = \dot{\lambda}\frac{\partial y^*}{\partial \bar{t}_n} = 2\dot{\lambda}\frac{\chi_{Dn} R_p^n}{F_n(D) t_n}; \text{ and } \dot{u}_s^p = \dot{\lambda}\frac{\partial y^*}{\partial \bar{t}_s} = 2\dot{\lambda}\frac{\chi_{Ds} R_p^s}{F_s(D) t_s} \tag{9a, b}$$

$$\dot{D} = \dot{\lambda}\frac{\partial y^*}{\partial \bar{\chi}_D} = 2\dot{\lambda}\frac{1}{\chi_D}\left(\frac{\chi_{Dn} R_D^n}{F_n(D)} + \frac{\chi_{Ds} R_D^s}{F_s(D)}\right) \tag{10}$$

in which Ziegler's orthogonality conditions [25] in the form, $\bar{t}_n = t_n$, $\bar{t}_s = t_s$ and $\bar{\chi}_D = \chi_D$, have been employed. The yield function in true stress space, which is needed for computation, is obtained by substituting Eqs. (5a, b, c) into Eq. (8) and employing the above orthogonality conditions, resulting in:

$$y = \left(\frac{\chi_D}{\chi_D \Big/ \sqrt{\frac{\chi_{Dn} R_D^n}{F_n(D)} + \frac{\chi_{Ds} R_D^s}{F_s(D)}}}\right)^2 + \left(\frac{t_n}{\frac{\sqrt{F_n(D)}\, t_n}{\sqrt{R_p^n \chi_{Dn}}}}\right)^2 + \left(\frac{t_s}{\frac{\sqrt{F_s(D)}\, t_s}{\sqrt{R_p^s \chi_{Ds}}}}\right)^2 - 1 \le 0 \tag{11}$$

The above equation leads to:

$$y = \frac{\chi_{Dn}}{F_n(D)}\left(R_D^n + R_p^n\right) + \frac{\chi_{Ds}}{F_s(D)}\left(R_D^s + R_p^s\right) - 1 \le 0 \tag{12}$$

So far, the basis of the proposed model has been completed, with four essential components: stress-displacement relationships (2a, b), evolution rules (9a, b), (10), and yield function (12). However, as mentioned earlier, there are essential details that require further interpretation to complete the formulation. They are four parameters $R_D^n$, $R_D^s$, $R_p^n$ and $R_p^s$ together with the forms of two functions $F_n(D)$ and $F_s(D)$ that govern the responses of the model. In this regard, the key features of the proposed thermodynamics-based formulation are used here to demonstrate its advantages and also benefits in coupling damage with friction (represented by plasticity) and interpreting the above parameters and functions.

### 2.2 Dissipation Properties and Parameter Identification

The total dissipation in general mixed mode loading cases can be written as:

$$\begin{aligned}\Phi &= t_n \dot{u}_n^p + t_s \dot{u}_s^p + (\chi_{Dn} + \chi_{Ds})\dot{D} = \Phi_n^p + \Phi_s^p + \Phi_n^D + \Phi_s^D = \left(\Phi_n^p + \Phi_n^D\right) + \left(\Phi_s^p + \Phi_s^D\right) \\ &= \Phi_n + \Phi_s\end{aligned} \tag{13}$$

where $\Phi_n = \Phi_n^p + \Phi_n^D$ and $\Phi_s = \Phi_s^p + \Phi_s^D$ are dissipations due to normal and shear deformation that in turn consist of plastic (frictional) and damage contributions. Using the evolution rules (9a, b–10), we can write the contributions from normal and shear behavior to the total dissipation as:

$$\Phi = \Phi_n + \Phi_s = 2\dot{\lambda}\frac{\chi_{Dn}}{F_n(D)}\left(R_p^n + R_D^n\right) + 2\dot{\lambda}\frac{\chi_{Ds}}{F_s(D)}\left(R_p^s + R_D^s\right) \tag{14}$$

We note that in general $R_D^n$, $R_D^s$, $R_p^n$ and $R_p^s$ vary with the loading conditions, reflecting the changes in the underlying mechanisms of dissipation with respect to macro stress change. This more general case, however, induces more complexities to the model and implementation and hence is not taken into account in this study. In addition, we will also show later that the simplest case of fixed ratios of contributions can be sufficient as it facilitates the interpretation and also bring physically reasonable results to the responses. For this, considering only pure normal or shear behavior, the corresponding dissipations can be obtained as:

$$\begin{aligned}\Phi_n &= t_n \dot{u}_n^p + \chi_{Dn}\dot{D} = 2\dot{\lambda}\frac{\chi_{Dn}}{F_n(D)}\left(R_p^n + R_D^n\right); \text{ and } \Phi_s = t_s \dot{u}_s^p + \chi_{Ds}\dot{D} \\ &= 2\dot{\lambda}\frac{\chi_{Ds}}{F_s(D)}\left(R_p^s + R_D^s\right)\end{aligned} \tag{15a, b}$$

Given a dissipation budget in pure normal (or shear) mode, the above equations indicate that this budget is decomposed into two parts corresponding to damage and plastic (frictional) dissipations with corresponding ratios $R_D^n$, and $R_p^n$ (or $R_D^s$ and $R_p^s$), respectively. As a consequence, $R_p^n + R_D^n = 1$, and $R_p^s + R_D^s = 1$, and these relationships are assumed in this study to hold in both pure and mixed mode loading conditions. We acknowledge that this is a strong assumption, the consequence of which is yet to be explored. However this assumption helps greatly simplify the formulation and will also be very useful in investigating the effects of friction on the model responses. It results in the yield function of the form:

$$y = \frac{\chi_{Dn}}{F_n(D)} + \frac{\chi_{Ds}}{F_s(D)} - 1 \leq 0 \tag{16}$$

Using Eq. (3), we can write the yield function in true stress space as:

$$y = \frac{1}{2}H(t_n)\frac{t_n^2}{(1-D)^2F_n(D)K_n} + \frac{1}{2}\frac{t_s^2}{(1-D)^2F_s(D)K_s} - 1 \le 0 \tag{17}$$

In addition, further details on the functions $F_n(D)$ and $F_s(D)$ should be supplied to complete the formulation. We use here the following forms:

$$F_i(D) = \frac{1}{2}\frac{f_i^2}{K_i}\left(1 + \frac{f_i^2}{2K_iG_iR_D^i - f_i^2}\right)^2 \Big/ \left[(1-D) + \frac{f_i^2}{2K_iG_iR_D^i - f_i^2}\right]^2 \tag{18}$$

where "$i$" stands for "$n$" or "$s$", and $G_i$ denotes the fracture energy in pure mode loading condition. This form guarantees that the total dissipation in pure mode loading condition is always equal to the experimentally given fracture energy $G_i$. In addition, the above form of the yield is appropriate only in tensile loadings, as the purpose of this paper is not fully on constitutive modelling, but also on the importance of energy principles in coupling different mechanisms of dissipation. The simple form of the yield function (17) that is most suitable for tensile loading ($t_n > 0$), including both pure and mixed modes, is sufficient for the investigation on frictional effects in this study. Details on how to come up with the form (18) and how to improve the model will be presented in our forthcoming papers.

## 3 Model Responses

For illustration purposes, we use the following set of properties and parameters: elastic stiffnesses $K_n = K_s = 10^5$ N/mm$^3$, yield strengths $f_n = f_s = 3.0$ N/mm$^2$, fracture energies $G_n = G_s = 0.002$ Nmm/mm$^2$, in which the normal and shear properties are intentionally kept the same to show the effects of plastic (frictional) contributions to the responses towards failure. For this, the two parameters $R_p^n$ and $R_p^s$ that control the percentages of plastic dissipations in normal and shear modes are varied to show their effects on the model responses in mixed mode loading conditions. For the used parameters, the initial yield surface and model responses in pure mode (I or II) loading condition are the same and illustrated in Fig. 1 below.

The model responses in Fig. 1b with varying frictional contributions under the same input fracture energy show different trends. While pure damage response is linear

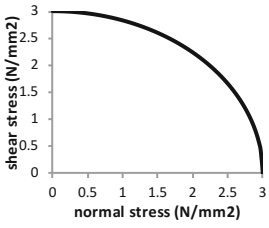


(a): initial yield surface.

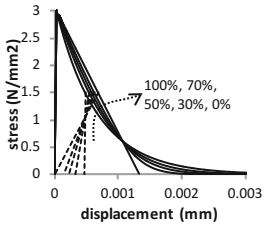


(b): effects of friction on the mechanical response.

**Fig. 1.** Initial yield surface and effects of friction on the model response.

softening, friction naturally brings nonlinearity to the model response and produces a long tail that reflects the experimental observations, besides the residual displacements at zero stress. It is noted that all these responses are produced by just varying the parameter $R_p^n$ (or $R_p^s$) that controls the frictional dissipation, while keeping the rest, including the fracture energy, unchanged.

We show in Fig. 2 the size and shape of the yield surface under different damage levels and different levels of frictional contributions in both normal and shear modes. As can be seen, given the same elastic properties, yield strengths, and fracture energies, the evolution of the yield surface is dramatically different when the frictional contributions are varied, even the same damage level is used in each case (a, b or c in Fig. 2). While the use of same level of frictional contributions from normal and shear modes result in "symmetric" yield surface (Figs. 2a, b), the differences in normal and shear frictional effects in Fig. 2c result in non-symmetric yield surfaces during the damage-induced evolution. These are just qualitative results to show how friction can significantly change the evolution of the yield surface. Further analysis needs experimental support on better estimation of frictional contributions in both pure and general mixed mode loading conditions, and also better correlation with the theoretical modelling. However the results in Figs. 1 and 2 in our opinion are strong enough to demonstrate how important to properly account for frictional effects on the mechanical responses of cohesive zone models. They also show the benefits of a thermodynamics-based formulation of a coupled damage-plasticity cohesive model.

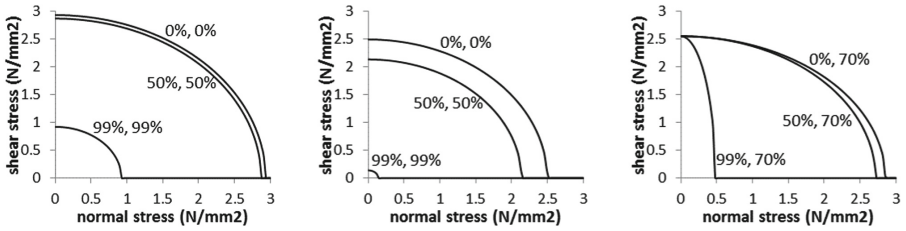


(a): $D$=0.5 (b): $D$=0.9 (c): $D$=0.7

**Fig. 2.** Effects of frictional contributions on the evolution of the yield surface (the values of $R_p^n$ and $R_p^s$ are next to the yield surface).

## 4 Conclusions

We proposed a thermodynamically consistent formulation of a coupled damage-plasticity cohesive model and used both the model formulation and its characteristics to illustrate the important roles and effects of friction. Given a pure damage model that exhibits linear softening, adding frictional effects, through plastic displacements, automatically leads to nonlinear softening responses with long tail curves and residual

displacements. The proposed thermodynamics-based formulation allows naturally integrating frictional effects by just varying two parameters controlling the frictional contributions in normal and shear modes, while maintaining the consistency of the model response with respect to the input fracture energies. We also acknowledge that the presented results are preliminary, and further experimental and theoretical works are needed to both improve the model and quantify correctly the contributions of friction to the mechanical responses.

**Acknowledgments.** The authors thank the Australian Research Council for support through projects FT140100408 (G.D. Nguyen) and DP170103793 (G.D. Nguyen & H.H. Bui).

## References

1. Bažant, Z.P.: Analysis of work-of-fracture method for measuring fracture energy of concrete. J. Eng. Mech. **122**, 138–144 (1996)
2. Landis, E.N., Nagy, E.N., Keane, D.T.: Microstructure and fracture in three dimensions. Eng. Fract. Mech. **70**, 911–925 (2003)
3. Landis, E.N., Shah, S.P.: Recovery of microcrack parameters in mortar using quantitative acoustic emission. J. Nondestruct. Eval. **12**, 219–232 (1993)
4. Reinhardt, H.W., Cornelissen, H.A.W., Hordijk, D.A.: Tensile tests and failure analysis of concrete. J. Struct. Eng. **112**, 2462–2477 (1986)
5. Perdikaris, P.C., Romeo, A.: Size effect on fracture energy of concrete and stability issues in three-point bending fracture toughness testing. ACI Mater. J. **92**, 483–496 (1995)
6. Fan, C.: Characterization and prediction of delamination in fiber-reinforced composites. Ph.D. Dissertation. University of Alberta (2008)
7. Rikards, R., Buchholz, F.G., Bledzki, A.K., Wacker, G., Korjakin, A.: Mech. Compos. Mater. **32**(5), 439–462 (1996)
8. Kolluri, M.: An in-situ experimental-numerical approach for interface delamination characterization. Ph.D. Dissertation. Eindhoven University of Technology (2011)
9. Guiamatsia, I., Nguyen, G.D.: A generic approach to constitutive modelling of composite delamination under mixed-mode loading conditions. Compos. Sci. Technol. **72**, 269–277 (2012)
10. Guiamatsia, I., Nguyen, G.D.: A thermodynamics-based cohesive model for interface debonding and friction. Int. J. Solids Struct. **51**(3–4), 647–659 (2014)
11. Ruiz, G., Pandolfi, A., Ortiz, M.: Three-dimensional cohesive modeling of dynamic mixed-mode fracture. Int. J. Numer. Meth. Eng. **52**(1–2), 97–120 (2001)
12. Moës, N., Belytschko, T.: Extended finite element method for cohesive crack growth. Eng. Fract. Mech. **69**(7), 813–833 (2002)
13. Elices, M., Guinea, G.V., Gomez, J., Planas, J.: The cohesive zone model: advantages, limitations and challenges. Eng. Fract. Mech. **69**(2), 137–163 (2002)
14. Mir, A., Nguyen, G.D., Sheikh, A.H.: A continuum model with an embedded fracture process zone modelled as a cohesive frictional interface. Appl. Mech. Mater. **846**, 360–365 (2016)
15. Alfaiatea, J., Sluys, L.J.: On the modelling of mixed-mode discrete fracture: Part I - Damage models. Eng. Fract. Mech. **182**, 157–186 (2017)
16. Alfaiatea, J., Sluys, L.J.: On the modelling of mixed-mode discrete fracture: Part II - Inclusion of dilatancy. Eng. Fract. Mech. **182**, 245–264 (2017)

17. Gui, Y.L., Bui, H.H., Kodikara, J.: An application of a cohesive crack model combining compression, tension and shear in soft rocks. Comput. Geotech. **66**, 142–157 (2015)
18. Nguyen, N.H.T., Bui, H.H., Nguyen, G.D., Kodikara, J.: A cohesive damage-plasticity model for DEM and its application for numerical investigation of soft rock fracture properties. Int. J. Plast. (2017, in press) https://doi.org/10.1016/j.ijplas.2017.07.008
19. Le, L.A., Nguyen, G.D., Bui, H.H., Sheikh, A.H., Kotousov, A., Aditya, K.: Modelling jointed rock mass as a continuum with an embedded cohesive-frictional model. Eng. Geol. **228**, 107–120 (2017)
20. Freddi, F., Sacco, E.: A damage model for a finite thickness composite interface accounting for in-plane deformation. Eng. Fract. Mech. **163**, 396–415 (2016)
21. Neto, P., Alfaiate, J., Dias-da-Costa, D., Vinagre, J.: Mixed-mode fracture and load misalignment on the assessment of FRP-concrete bond connections. Compos. Struct. **135**, 49–60 (2016)
22. Nguyen, N.H.T., Bui, H.H., Nguyen, G.D., Kodikara, J., Arooran, S., Jitsangiam, P.: A thermodynamics-based cohesive model for discrete element modelling of fracture in cemented materials. Int. J. Solids Struct. **117**, 159–176 (2017)
23. Houlsby, G.T., Puzrin, A.M.: A thermomechanical framework for constitutive models for rate-independent dissipative materials. Int. J. Plast. **16**, 1017–1047 (2000)
24. Einav, I., Houlsby, G.T., Nguyen, G.D.: Coupled damage and plasticity models derived from energy and dissipation potentials. Int. J. Solids Struct. **44**(7–8), 2487–2508 (2007)
25. Ziegler, H.: An introduction to thermomechanics, 2nd edn. North Holland, Amsterdam (1983)

# Materials For Construction (MFC)

# A Review on Immobilisation of Toxic Wastes Using Geopolymer Technique

Tran Huyen Vu[1(✉)] and Mien Van Tran[2]

[1] Mien Trung University of Civil Engineering (MUCE),
Tuy Hoa City, Phu Yen Province, Vietnam
vuhuyentran@muce.edu.vn
[2] Ho Chi Minh City University of Technology (HCMUT),
Ho Chi Minh City, Vietnam
tvmien@hcmut.edu.vn

**Abstract.** Every year, a huge amount of waste materials containing toxic substances are produced throughout the world, which causes serious damage to the environment and poses threats to human health. Among available techniques of immobilization of toxic elements in harmful by-products is geopolymerization which has been considered as an effective approach to deal with many environmental issues. Apart from being utilised as alternatives for Portland cements in construction, geopolymer materials are also used as binders in waste solidification and stabilization systems. This study focuses on the potential application of geopolymeric systems in coping with hazardous wastes regarding the immobilization mechanism and factors influencing the immobilization efficiency, which provides a better understanding of the stabilization of pollutants through geopolymerization in order to stimulate further research on addressing the hazardous waste.

**Keywords:** Geopolymerization · Immobilization · Hazardous waste · Fly ash · Slag

## 1 Introduction

The rapid industrialization gives rise to millions of tons of industrial wastes every year [1] and releases of undesirable contaminants in the environment. Heavy metal contaminants may be the most dangerous wastes because of their recalcitrance [2]. With the growing concern to environmental problems, stabilization/solidification methods have been developed across the world with the aim to immobilize contaminants bearing wastes in order to minimize environmental threat. In the immobilization of heavy metals, binders obviously have a key role and Portland cement is widely used as the cementitious material in stabilization/solidification systems [3, 4] because it has low processing costs and ability to meet stringent processing and performance requirements. However, the production of Portland cement not only consumes a huge quantity of natural resources and energy but also releases a significant amount of greenhouse gases into the atmosphere [5, 6]. Thus, stabilization/solidification methods using Portland cement could probably refer to half measures in terms of the protection of environment.

© Springer Nature Singapore Pte Ltd. 2018
H. Tran-Nguyen et al. (eds.), *Proceedings of the 4th Congrès International de Géotechnique - Ouvrages -Structures*, Lecture Notes in Civil Engineering 8,
DOI 10.1007/978-981-10-6713-6_29

Geopolymer, a kind of amorphous inorganic polymer composed of [$SiO_4$] and [$AlO_4$] tetrahedrons linked alternately by sharing all the oxygen [5], a solid and stable aluminosilicate material formed by alkali hydroxide or alkali silicate activation of a precursor [8], a new generation of cementitious materials, has been considered as a viable alternative material of Portland cement in concrete industry [7, 9–11], since the production of geopolymer materials could enable to reuse a considerable amount of by-products generated by industrial activities and the $CO_2$ emission generated by the production of cement could be reduced by 80–90%.

Davidovits [6] reported that geopolymers have the properties such as high early strength, low shrinkage, freeze-thaw resistance, sulphate resistance and corrosion resistance that make them ideal for long term containment in surface disposal facilities, while Portland cement is unsuitable for stabilization of various toxic wastes (especially those containing sodium salts of arsenate, borate, phosphate, iodate and sulphides, salts of magnesium, tin, zinc, copper, lead), and is also unsuited for solidification of end-product residues with high sulphide contents. This view was shared by Palomo and López de la Fuente [12] who suggested that excellent performances of geopolymers could be achieved in the immobilisation of certain chemical species because these materials exhibit superior properties like abundance of the very small pores, low permeability, very high alkalinity, good chemical stability, and a three-dimensional microstructure. A considerable amount of recent publications reported that the degree of heavy metal immobilization was relatively high but a few have attempted to explain how heavy metals are immobilized in geopolmeric matrices. The way how to stabilize and solidify the contaminants using geopolymers and the immobilization efficiency of some contaminants were reported one by one in a relatively detailed review [13]. In this paper, attention is focused on the mechanism and possible effects of some factors on the metal immobilization of geopolymers.

## 2 Background

### 2.1 Geopolymerization

Geopolymer can be produced from waste materials such as coal fly ash and slag, kaolinite, metakaolinite, or other natural aluminosilicate materials through a process called geopolymerizarion, or activation procedure. There are some general models for geopolymerization. Firstly, Glukhovsky [14] described that the alkali activation of materials containing silica and reactive alumina consists of a series of processes, namely destruction, coagulation, condensation and crystallization. Then many authors developed the Glukhovsky (1959) theories and proposed different models for geopolymerization. Palomo and López de la Fuente [12] claimed that the geopolymerization of raw materials might be related to a set of destruction–condensation reactions that could be divided into three stages.

Firstly, bonds such as Si-O-Si, Al-O-Al and Al-O-Si of the raw materials are broken. This process needs a stimulus, for example, the variation of the ion force of the medium when adding ions with electro-donor properties (alkaline metals), in order to redistribute the electronic density over the silicon atoms and stimulate the Si-O-Si bond

breaks. The negative electrical load of these anions is balanced by cations of alkaline metals, generating alkaline silicates. In addition, these alkaline silicates may react with divalent ions, forming Si–O–Ca–OH type complexes. The Al-O-Si bonds are influenced in the same way, and depending on the pH, complexes of the $Al(OH)_4^-$, $Al(OH)_5^{2-}$ and $Al(OH)_6^{3-}$ will be formed.

Secondly, desegregated products accumulate, generating a coagulation structure in which polycondensation processes happen.

The final stage of geopolymerization is the precipitation of products. Fernández-Jiménez et al. [15] suggested that there are three main stages in the geopolymerization of fly ash: dissolution stage (dissolution of the vitreous component of the fly ash), induction period (massive precipitation of metastable gel), silicon incorporation stage (transformation from metastable gel to Si-rich gel and increase of mechanical strength). A recent perspective of Palomo et al. [16] on activation procedures showed that three different material types (type I: materials with moderately high calcium and silicon contents such as slags, type II: materials comprising primarily aluminium and silicon such as fly ashes, type III: a combination of the preceding two) have different activation reactions and reaction products. While the main reaction product of type I activation is a C-S-H (calcium silicate hydrate) gel, that of type II is a three dimensional inorganic alkaline polymer that can be regarded as a zeolite precursor, and products of geopolymerization of type III are very complex, comprising C-A-S-H (containing sodium) and (N,C)-A-S-H (high calcium content alkaline aluminosilicate hydrated gel) gels.

## 2.2 Leaching Test

The efficiency of heavy metal immobilization is defined basically by strength and the leach resistance [17]. While the strength development is considered as an indicator of solidification, leaching test is probably the most important measure to assess the degree of heavy metal stabilization. Many leaching methods have been commonly used to acquire useful information for environmental decision-making. Yet, there is no a single leaching test that can assess the leaching behaviour of a wide variety of waste materials. Selecting an appropriate leachate test was summarized in the guide of EPA [18]. Palacios and Palomo [19] studied on three different leaching tests (ANSI/ANS 16.1, MCC1-P, and TCLP) conducted to determine the amount of lead fixed by activated fly ash systems and concluded that the different results obtained from the various leaching tests can be justified according to the nature of each individual test. Each test is found to have advantages and disadvantages regarding evaluating the results, and the major mechanism responsible for lead leaching is diffusion. According to Fernández Pereira et al. [20], with the different leaching tests, different results of immobilization efficiency are seen. The best results in geopolymers stabilized with potassium silicate were recorded with the EN 12457, whilst the TCLP test showed the best results in classic hydraulic S/S solids [20]. This is probably classic hydraulic S/S solids better resist the acid conditions of the TCLP test due to a higher acid neutralization capacity of the OPC samples. Mercury immobilisation efficiencies are consistently higher in TCLP tests than EN 12457 tests [21]. This is probably due to the fact that TCLP tests use coarser test material and that the higher final leachate pH value in EN 12457 tests possibly increases the solubility of mercury precipitates.

## 3 Mechanism for Heavy Metal Immobilization

In traditional stabilization and solidification systems, heavy metals are generally converted to low solubility precipitates such as carbonates, hydroxides, silicates, or sulfides, then there is the formation of a solid with solidification reagents [3]. In geopolymers, heavy metals might be immobilized through three general steps [22]: (1) metal ions are taken into the geopolymer network; (2) metal ions are bound into the structure for charge balancing roles; and (3) a precipitate containing heavy metals is physically encapsulated. To date, the exact mechanism of heavy metal immobilization of geopolymer materials has not been fully understood, though in principle most of the heavy metal cations are easily attracted and combined with $[AlO_4]$ tetrahedrons due to larger mass, smaller radius and higher valence [23]. Future studies on the current topic are therefore recommended.

A study on the immobilization of Cu and Pb in geopolymers derived from fly ash carried out by van Jaarsveld et al. [24] reported that these metals may be immobilized in geopolymeric matrices by physical encapsulation, chemical bonding, and adsorption. van Jaarsveld et al. [24] found that there were some differences in infrared spectra and no apparent major differences in X-ray diffraction between the geopolymer matrix containing Cu and the matrix containing Pb, while these matrices exhibited different compressive strengths and leaching behaviour. These results implied that these metals might be taken into the geopolymer network and possibly bound into the structure for charge balancing roles, and that these metals were bound into the amorphous of the product matrices. In addition to this view, physical encapsulation and chemical fixation could be predicted for the immobilization of $Hg^{2+}$ ions in the alkali-activated slag (AAS) matrix [25]. Physical encapsulation might be explained by the fact that after being cured for 28 days, the 2% Hg doped AAS matrix had approximately 75% of mesopore (<50 nm) in volume and there was the filling of amorphous metal silicate precipitates in the pore structure (detected by TG-DTG and physical test results), which prevented the HgO precipitation formed in the 2% Hg doped AAS matrix from physical leaching. However, there was no the HgO precipitation in the 0.5% Hg doped AAS matrix. Based on this result, Qian et al. [25] assumed that in the AAS matrix, chemical stabilization might be also responsible for the immobilization of Hg.

One question that needs to be asked, however, is whether the importance of physical encapsulation, chemical bonding, and adsorption are the same. van Jaarsveld et al. [24] concluded that physical micro-encapsulation is considered to be more important than chemical bonding in influencing the efficiency of immobilization, and adsorption is not considered to play a major role. This may be because the geopolymeric matrices with the smaller pore openings as well as the higher compressive strength often show the better immobilization efficiency.

The dominance of physical encapsulation was also shared in several studies [19, 26]. Findings of Phair and van Deventer [26] showed that increasing the dissolution of Al and Si from the aluminosilicate sources by raising pH of alkali silicate activation leads to a greater amount of monomeric and/or oligomeric species of both aluminate and silicate available, which is essential for insolubilising polycondensation reactions. This resulted in better reactive conditions for the immobilization of Pb, therefore, the immobilization

of Pb within geopolymer matrices was believed to be an encapsulation process of precipitates and gels, and adsorption might be negligible. Palacios and Palomo [19] also found that the lead compound formed in the fly ash matrix is a highly insoluble silicate $Pb_3SiO_5$ identified by XRD, implying that the immobilization of lead in fly ash based geopolymers is mainly by encapsulation of $Pb_3SiO_5$.

By contrast, the predominance of chemical stabilization was proved by Qian et al. [27]. Although alkali-activated slag matrix doped 2% Zn had a quite low compressive strength and coarse pore structure, over 99.99% $Zn^{2+}$ ions was fixed [27], indicating that the chemical stabilization could be responsible for the immobilization of $Zn^{2+}$ ions in the AAS matrix. As well as, these authors [27] suggested that the mechanism of Zn immobilization might involve (1) the formation of insoluble zinc silicate gel, (2) the incorporation of $Zn^{2+}$ ion into the C-S-H lattice and (3) the formation of insoluble calcium zincate precipitate.

Notwithstanding, in a recent study about the mechanism of immobilization of Pb (II), Cu(II), Cd(II) and Cr(III) in geopolymers derived from kaolin/zeolite conducted by El-Eswed et al. [28], the emphasis was placed on the adsorption process. El-Eswed et al. [28] stated that the mechanical strength and XRD properties are not influenced by incorporation of heavy metals, therefore physical encapsulation, formation of metal hydroxides or carbonates and silicates are not probably mechanisms for immobilization of metals because there is no evidence for participation of heavy metals in new reactions of geopolymerization process.

## 4 Factors Influencing Immobilization Efficiency

Conner [29] reported that the immobilization of heavy metals depends not only on the solubility of the metal precipitate, but also on the permeability of the monolith which is a function of pore structure and the amount of water present in the waste. As a consequence, all factors that can change the solubility of the metal precipitate and the permeability of geopolymeric matrix can probably have a bearing on the final immobilization efficiency of heavy metals.

### 4.1 The Characteristics of the Source Materials

Raw materials are used as the primary reagents in generating the geopolymeric binders that serve as a medium for the immobilization of metals. The increasing Al, Si species liberated from raw materials would provide better environment to form a new phase that would adequately bind and encapsulate the heavy metal into a more insoluble form. In addition, the geopolymeric matrix with the best immobilization efficiency tends to have the smaller pore openings as well as the higher compressive strength. van Jaarsveld et al. [24] stated that the source materials appear to have the greatest influence on the eventual ability of the matrix to immobilizing metals, since the source materials had an effect on structure formation on an intratetrahedral scale. The matrices produced from a six coordinated aluminum source (kaolinite) seem to be more stable under leaching conditions than those synthesised from a four coordinated aluminum source (metakaolinite), probably because the six coordinated aluminum is probably easier to

complete the process of geopolymerization than its four coordinated counterpart [24]. Palacios and Palomo [19] compared the capacity of fixation of lead in two types of fly ash activated in a highly alkaline medium. These authors [19] pointed out that the nature of the fly ash has a significant impact on the effectiveness of lead fixation in these systems. In other words, fly ash with a higher proportion of reactive silica and fine particles as well as greater specific area would result in greater containment capacity of geopolymeric matrix, and therefore make a better lead immobilisation, since lead might be mainly immobilized in geopolymeric matrix by physical encapsulation. Another investigation conducted by Phair et al. [1] on the effect of the Al sources on the Pb and Cu stabilization showed that the immobilisation of Pb is linked with the total extractable cation concentration of the Al source. It is difficult to explain this result, but it may be related to the fact that Pb precipitates are less labile, so they tend to be affected by the available amount of cations released from Al source, which can transform Pb precipitates into more stable forms, amorphous aluminosilicate phases. In contrast, the immobilisation of Cu was observed to be mainly associated with the physical characteristics of the source of Al [1]. This is possibly because precipitates of Cu may be more stable than that of Pb, so the final compressive strength of the matrix and the suspension viscosity of the Al source considerably influence the Cu immobilisation efficiency [1].

### 4.2 The PH and Type of Alkali Activator

In general, the exact pH of alkali activator is strongly affected by the type of activator and its concentration. The pH of alkali activator was considered to be a major contributing factor for the final immobilization efficiency, since increasing pH would lead to the reduction of the pore size, and therefore matrix permeability [30]. Depending on the relative proportions of silicate and hydroxide available in the alkali silicate environment, heavy metal precipitates formed in geopolymeric matrices could be either metal hydroxide and/or metal silicate species, therefore, the metal immobilization within geopolymers was considered to be strongly dependent on the pH of the alkali activator used [26]. For instance, at pH 12 the amount of silicate ions would be large enough to preferentially combine with the cations in considerable amounts, while at pH 14 there would be a tendency for cations to combine with hydroxide than at pH 12. As well as, the precipitates formed at pH 12 is more insoluble than the precipitates at pH 14, so the immobilization efficiency at pH 12 is expected to be higher than at pH 14. Notwithstanding, the matrix produced at pH 12 was found to be more porous and subsequently more permeable, and therefore reduced the efficiency of metal immobilization [26]. Thus, it could be concluded that the increase of immobilization efficiency and the increasing pH go together. In another study of Cheng et al. [31], the amount of heavy metals adsorbed on the geopolymers increased with pH of the solution. It was explained that when the concentration of $H^+$ in the solution is higher, the adsorbent tends to adsorb $H^+$, as a result, the adsorption capability of heavy metals decreases in a lower pH. A similar result was seen by Nikolić et al. [32] that increasing pH of alkali solution results in better Zn immobilization from metallurgical waste.

As for the impact of alkali activator type on the stabilization of heavy metal, Phair and van Deventer [26] reported that Cu or Pb are stabilized better in sodium silicate

solutions than potassium silicate solutions. It may be because sodium silicate is less polymerised at high pH than potassium silicate because of the larger hydration sphere of the sodium ion. In addition, the hydration spheres of sodium silicate, Cu and Pb are relatively similar, so Cu and Pb interchange with sodium silicate more easily than with potassium silicate, resulting in the better immobilization efficiency [26]. Moreover, the total porosity of the slag binders activated by waterglass was seen generally lower than that of binders activated by sodium carbonate, in which the average pore diameter for the pastes activated by waterglass was on the level 3 to 5 nm after 720 days of curing and that for the samples activated by $Na_2CO_3$ was in the range 8 to 11 nm [33]. More to the point, the characteristic pore size of geopolymers was demonstrated to be closely related to the type of the alkali cation $Na^+$ or $K^+$ used in activation [34], implying that the heavy metal stabilization is possibly bound up with the alkali choice.

### 4.3 The Characteristic of Heavy Metal and Heavy Metal Form

Atomic radius of metal has been an important factor for the metal immobilization. The immobilization of Cu in geopolymeric matrices is generally less effective compared to Pb, since the atomic radius of Cu is smaller than that of Pb, which makes diffusion, translocation and leaching of Cu much easier although the electrical charges on both Cu and Pb are the same [26]. In the slag based geopolymeric matrix, Pb shows better immobilization efficiency than Cu in the case of large dosages of heavy metals, probably because ionic radius of Pb and Cu are different, or Cu and Pb have different roles in synthesis of the slag based geopolymeric matrix [35].

The size of the hydrated ions which affects the attraction force between hydrated ion and metal, free energy of hydration (the higher level of free energy of hydration, the smaller possibility for heavy metal ions to enter the adsorbent structure), and activity of metal ions may be responsible for the adsorption of the heavy metal ions on the geopolymeric matrix [31]. Xu et al. [36] investigated the leaching behaviours of Cd, Cu, Pb and Cr in fly ash based geopolymer and stated that the leaching behaviour of heavy metals could be influenced by other heavy metals in a complex system. However, this study was unable to analyse how this influence occurred and threw up many questions in need of further investigation.

The stabilization of metals in geopolymeric matrices could be affected by the chemical properties of the metal compounds. This was proved in the case of Pb [37] and Cr [38, 39]. Three types of the Pb contaminants PbO, $PbSO_4$ and PbS common in the environment were added in the fly ash based geopolymer matrices. Pb was proved to be dispersed throughout the geopolymeric matrix in the case of PbO addition, forming leaded geopolymer via Pb-O-Al or/and Pb-O-Si, by contrast, PbS was observed to be segregated from the bulk of the binder [37]. It was concluded that when Pb compounds was supplied in the form, soluble in sodium hydroxide solution, the Pb ions would participate in the formation of geopolymer network, stimulating both chemical bonding and physical encapsulation in the immobilization process. In the case of the Pb compounds, inert to alkali, the immobilization may be mainly by the physical encapsulation in the geopolymeric matrices. As a result, the upper limit of the Pb content, which can be immobilized in the geopolymer, varies with the form of lead [37].

In nature, common oxidation states of Cr are $3^+$ and $6^+$ states. Cr(VI) is particularly toxic, soluble, and relatively mobile in the environment [40]. The matrix of alkali-activated fly ash was found to be unable to stabilize 2.6% Cr(VI) in the form of CrO3, because Cr(VI) affected the activation of fly ash due to the formation of a highly soluble compound $Na_2CrO_4.4H_2O$ (observed through XRD and FTIR) [41]. Even with a smaller dosage of Cr(IV) 0.5% as $Na_2CrO_4$ added in fly ash based geopolymers, long-term leaching tests in different media showed that more than 75% Cr extraction was observed [42]. On the contrary, Cr(III) is less toxic, less mobile, and relatively insoluble as $Cr(OH)_3$ as well as mixed hydroxide phases containing some Ca [45]. Reduction from Cr(VI) to Cr(III) was recommended as pre-treatment before immobilization of chromium wastes in several previous studies [3, 43, 44]. The most common chemical reductants for converting Cr(VI) to Cr(III) are ferrous iron Fe(II) compounds (shown in Eq. 1) and sulfur compounds.

$$FeSO_4 + Cr(SO_4)_3 \rightarrow Cr_2(SO_4)_3 + Fe_2(SO_4)_3 \quad (1)$$

In a study carried out by Zhang et al. [38], sulphur compound (Na2S.9H2O) was added to fly ash based geopolymer, and served as a reductant in order to reduce Cr(VI) as $Na_2CrO_4$, $PbCrO_4$ to Cr(III), generating precipitation in highly insoluble forms and resulting in the increasing the immobilization efficiency of Cr. In another case, a mixture of $FeCl_2.4H_2O$ and $K_2Cr_2O_7$ was used to converted Cr (VI) to Cr (III), then $Cr^{3+}$ was attracted by $[AlO_4]$ due to the electrostatic attraction and stabilized in metakaolin-based geopolymerical matrices, leading to a relatively high immobilization efficiency of Cr [39].

## 5 Conclusion

This paper provides a review on the mechanisms for the heavy metal immobilization of geopolymers as well as the possible effects of some factors on the heavy metal immobilization efficiency, so as to promote the development of the hazardous waste treatment, since a profound understanding of the mechanism for the heavy metal immobilization is extremely necessary for the management of toxic wastes. The mechanisms for the immobilization of different heavy metals in geopolymer matrices derived from fly ash, slag, and metakaolin vary significantly. In addition, kaolinite seems to be a better precursor than metakaolin in the heavy metal fixation. The porosity and pore size distribution is strongly dependent to pH and type of alkali activator, so the value of pH and the choice of alkali metal in activation solution are closely related to the heavy metal immobilization efficiency. Moreover, the final immobilization efficiency of heavy metals is under the influence of the heavy metal nature and the characteristic of heavy metal compound. Thus, the immobilization of a particular waste should be carefully tailored. Besides, this paper points out several gaps in the research of heavy metal stabilization/solidification. Firstly, the curing time and curing temperature, as well as curing methods which attract less research attention are essential to be investigated in order to lead an efficient immobilization of heavy metal and a long-term stable final product. Secondly, the heavy metal immobilization depends also on the

chemical and mineralogical composition of source materials for geopolymers. Further work needs to be done to answer the question what are characteristics of a suitable source material for geopolymers so as to obtain the efficient immobilization of heavy metals.

## References


1. Phair, J.W., van Deventer, J.S.J., Smith, J.D.: Effect of Al source and alkali activation on Pb and Cu immobilisation in fly-ash based geopolymers. Appl. Geochem. **19**, 423–434 (2004). doi:10.1016/S0883-2927(03)00151-3
2. Nwaichi, E.O., Dhankher, O.P.: Heavy metals contaminated environments and the road map with phytoremediation. J. Environ. Prot. **7**, 41–51 (2016). doi:10.4236/jep.2016.71004
3. Adaska, W.S., Tresouthick, S.W., West, P.B.: Solidification and stabilization of wastes using portland cement. Report Number: EB071.02 W, Portland Cement Association (1991)
4. Glasser, F.P.: Fundamental aspects of cement solidification and stabilisation. J. Hazard. Mater. **52**, 151–170 (1997)
5. Davidovits, J.: Geopolymers-inorganic polymeric new materials. J. Therm. Anal. **37**(8), 1633–1656 (1991)
6. Davidovits, J.: Properties of geopolymer cements. In: Proceedings of the First International Conference on Alkaline Cements and Concretes, pp. 131–49. Kiev State Technical University, Kiev, Ukraine (1994)
7. Davidovits, J.: Geopolymer chemistry and sustainable development. The Poly(sialate) terminology: a very useful and simple model for the promotion and understanding of green-chemistry. In: Davidovits, J. (ed.) Proceedings of the World Congress Geopolymer, Saint Quentin (2005)
8. Duxson, P., Fernández-Jiménez, A., Provis, J.L., et al.: Geopolymer technology: the current state of the art. J. Mater. Sci. **42**, 2917 (2007b). doi:10.1007/s10853-006-0637-z
9. Duxson, P., Provis, J.L., Lukey, G.C., van Deventer, J.S.J.: The role of inorganic polymer technology in the development of green concrete. Cem. Concr. Res. **37**(12), 1590–1597 (2007a)
10. Lloyd, N., Rangan, V.: Geopolymer concrete-sustainable cementless concrete. In: Tenth ACI International Conference on Recent Advances in Concrete Technology and Sustainability Issues, pp. 33–53, 12 October 2009
11. Neupane, K.: Fly ash and GGBFS based powder-activated geopolymer binders: a viable sustainable alternative of portland cement in concrete industry. Mech. Mater. **103**, 110–122 (2016). doi:10.1016/j.mechmat.2016.09.012
12. Palomo, A., de la Fuente, J.I.L.: Alkali-activated cementitous materials: alternative matrices for the immobilisation of hazardous wastes- part I. Stabilisation of boron. Cem. Concr. Res. **33**, 281–288 (2003)
13. Provis, J.L.: Immobilisation of toxic wastes in geopolymers. In: Provis, J.L., van Deventer, J. S.J. (eds.) Geopolymers: Structures, Processing, Properties and Industrial Applications, 1st edn. Woodhead, Cambridge (2009)
14. Glukhovsky, V.D.: Soil Silicates. Gosstroyizdat, Kiev (1959). p. 154
15. Fernández-Jiménez, A., Palomo, A., Sobrados, I., Sanz, J.: The role played by the reactive alumina content in the alkaline activation of fly ashes. Microporous Mesoporous Mater. **91**, 111–119 (2006). doi:10.1016/j.micromeso.2005.11.015
16. Palomo, A., Krivenko, P., Garcia-Lodeiro, I., et al.: A review on alkaline activation: new analytical perspectives. Mater. Constr. **64**(315), e022 (2014). doi:10.3989/mc.2014.00314

17. Malviya, R., Chaudhary, R.: Factors affecting hazardous waste solidification/stabilization: a review. J. Hazard. Mater. **B137**, 267–276 (2006). doi:10.1016/j.jhazmat.2006.01.065
18. EPA/600/R-10/170: Background information for the leaching environmental assessment framework (LEAF) test methods (2010)
19. Palacios, M., Palomo, A.: Alkali-activated fly ash matrices for lead immobilisation: a comparison of different leaching tests. Adv. Cem. Res. **16**, 137–144 (2004). doi:10.1680/adcr.16.4.137.46661
20. Fernández Pereira, C., Luna, Y., Querol, X., Antenucci, D., Vale, J.: Waste stabilization/solidification of an electric arc furnace dust using fly ash-based geopolymers. Fuel **88**, 1185–1193 (2009). doi:10.1016/j.fuel.2008.01.021
21. Donatello, S., Fernández-Jiménez, A., Palomo, A.: An assessment of Mercury immobilisation in alkali activated fly ash (AAFA) cements. J. Hazard. Mater. **213–214**, 207–215 (2012). doi:10.1016/j.jhazmat.2012.01.081
22. Zheng, L., Wang, W., Shi, Y.: The effects of alkaline dosage and Si/Al ratio on the immobilization of heavy metals in municipal solid waste incineration fly ash-based geopolymer. Chemosphere **79**, 665–671 (2010). doi:10.1016/j.chemosphere.2010.02.018
23. van Jaarsveld, J.G.J., van Deventer, J.S.J., Lorenzen, L.: The potential use of geopolymeric materials to immobilise toxic metals: part I. Theory and applications. Miner. Eng. **10**, 659–669 (1997). doi:10.1016/S0892-6875(97)00046-0
24. van Jaarsveld, J.G.J., van Deventer, J.S.J., Lorenzen, L.: Factors affecting the immobilization of metals in geopolymerized fly ash. Metall. Mater. Trans. B **29**, 283 (1998). doi:10.1007/s11663-998-0032-z
25. Qian, G., Sun, D.D., Tay, H.J.: Characterization of mercury- and zinc-doped alkali-activated slag matrix-part I. Mercury. Cem. Concr. Res. **33**, 1251–1256 (2003a). doi:10.1016/S0008-8846(03)00045-0
26. Phair, J.W., van Deventer, J.S.J.: Effect of silicate activator pH on the leaching and material characteristics of waste-based inorganic polymers. Miner. Eng. **14**(3), 289–304 (2001). doi:10.1016/S0892-6875(01)00002-4
27. Qian, G., Sun, D.D., Tay, H.J.: Characterization of mercury- and zinc-doped alkali-activated slag matrix-part II. Zinc. Cem. Concr. Res. **33**, 1251–1256 (2003b). doi:10.1016/S0008-8846(03)00045-0
28. El-Eswed, B.I., Yousef, R.I., Alshaaer, M., Hamadneh, I., Al-Gharabli, S.I., Khalili, F.: Stabilization/solidification of heavy metals in kaolin/zeolite based geopolymers. Int. J. Miner. Process. **137**, 34–42 (2015). doi:10.1016/j.minpro.2015.03.002
29. Conner, J.R.: Chemical fixation and solidification of hazardous wastes. Van Nostrand Reinhold (1990)
30. Davis, P.J., Deshpande, R., Smith, D.M., Brinker, C.J., Assink, R.A.: Pore structure evolution in silica gel during aging/drying- IV. Varying pore fluid pH. J. Non-Cryst. Solids **167**, 295–306 (1994)
31. Cheng, T.W., Lee, M.L., Ko, M.S., Ueng, T.H., Yang, S.F.: The heavy metal adsorption characteristics on metakaolin-based geopolymer. Appl. Clay Sci. **56**, 90–96 (2012). doi:10.1016/j.clay.2011.11.027
32. Nikolić, I., Đurović, D., Tadić, M., Blečić, D., Radmilović, V.: Immobilization of zinc from metallurgical waste and water solutions using geopolymerization technology. In: Proceedings of the 16th International Conference on Heavy Metals in the Environment, vol 1 (2013). doi:10.1051/e3sconf/20130141026
33. Deja, J.: Immobilization of $Cr^{6+}$, $Cd^{2+}$, $Zn^{2+}$ and $Pb^{2+}$ in alkali-activated slag binders. Cem. Concr. Res. **32**, 1971–1979 (2002). doi:10.1016/S0008-8846(02)00904-3
34. Kriven, W.M., Bell, J.L., Gordon, M.: Microstructure and nanoporosity of as-set geopolymers. Ceram. Eng. Sci. Proc. **27**(2), 491–503 (2008). doi:10.1002/9780470291313.ch47

35. Yunsheng, Z., Wei, S., Qianli, C., Lin, C.: Synthesis and heavy metal immobilization behaviors of slag based geopolymer. J. Hazard. Mater. **143**, 206–213 (2007). doi:10.1016/j.jhazmat.2006.09.033
36. Xu, J.Z., Zhou, Y.L., Chang, Q., Qu, H.Q.: Study on the factors of affecting the immobilization of heavy metals in fly ash-based geopolymers. Mater. Lett. **60**, 820–822 (2006). doi:10.1016/j.matlet.2005.10.019
37. Guo, B., Pan, D., Liu, B., Volinsky, A.A., Fincan, M., Du, J., Zhang, S.: Immobilization mechanism of Pb in fly ash-based geopolymer. Constr. Build. Mater. **134**, 123–130 (2017). doi:10.1016/j.conbuildmat.2016.12.139
38. Zhang, J., Provis, J.L., Feng, D., van Deventer, J.S.J.: The role of sulfide in the immobilization of Cr(VI) in fly ash geopolymers. Cem. Concr. Res. **38**, 681–688 (2008b). doi:10.1016/j.cemconres.2008.01.006
39. Chen, J., Wang, Y., Wang, H., Zhou, S., Wu, H., Lei, X.: Detoxification/immobilization of hexavalent chromium using metakaolin-based geopolymer coupled with ferrous chloride. J. Environ. Chem. Eng. **4**, 2084–2089 (2016). doi:10.1016/j.jece.2016.03.038
40. Katz, S.A., Salem, H.: The Biological and Environmental Chemistry of Chromium. VCH Publications, New York (1994)
41. Palomo, A., Palacios, M.: Alkali-activated cementitious materials: alternative matrices for the immobilisation of hazardous wastes -part II. Stabilisation of chromium and lead. Cem. Concr. Res. **33**, 289–295 (2003)
42. Zhang, J., Provis, J.L., Feng, D., van Deventer, J.S.J.: Geopolymers for immobilization of $Cr^{6+}$, $Cd^{2+}$, and $Pb^{2+}$. J. Hazard. Mater. **157**, 587–598 (2008a). doi:10.1016/j.jhazmat.2008.01.053
43. Eary, L.E., Ral, D.: Chromate removal from aqueous wastes by reduction with ferrous ion. Environ. Sci. Technol. **22**(8), 972–977 (1988). doi:10.1021/es00173a018
44. Lan, Y., Deng, B., Kim, C., Thornton, E.C.: Influence of soil minerals on chromium (VI) reduction by sulfide under anoxic conditions. Geochem. Trans. **8**, 4 (2007). doi:10.1186/1467-4866-1188-1184
45. Omotoso, O.E., Ivey, D.G., Mikula, R.: Quantitative X-ray diffraction analysis of chromium (III) doped tricalcium silicate pastes. Cem. Concr. Res. **26**, 1369–1379 (1996). doi:10.1016/0008-8846(96)00118-4

# Additional Carbon Dependent Electrical Resistivity Behaviors of High Performance Fiber-Reinforced Cementitious Composites

Duy-Liem Nguyen(✉), Thi-Ngoc-Han Vuong, and Tri-Thong Nguyen

Ho Chi Minh City University of Technology and Education,
Ho Chi Minh City, Vietnam
{liemnd, hanvtng}@hcmute.edu.vn,
ks.nguyentrithong@gmail.com

**Abstract.** Strain-hardening high performance fiber-reinforced cementitious composites (HPFRCCs) are classified as a smart construction material with high damage-sensing capacity in addition to high structural resistances. The damage-sensing capacity has often been evaluated by measuring the changes in the electrical resistance during test loading. Thus, the electrical resistivity behavior of HPFRCCs is a key non-structural property that should be clearly understood to develop the self damage-sensor. In this study, the electrical resistivity behaviors of HPFRCCs were experimentally investigated with various HPFRCCs as follows: plain mortar, HPFRCCs with steel fibers, HPFRCCs with steel and carbon fibers, HPFRCCs with steel and multi-walled carbon nanotubes. The electrical resistivity properties of investigated HPFRCCs were compared and discussed.

**Keywords:** High-performance fiber-reinforced cementitious composites · Electrical resistivity · Hybrid fiber · Damage-sensing · Non-structural property

## 1 Introduction

Much research has been performed to develop innovative construction materials, e.g., material with high strength, with self-strain sensing or self-damage sensing ability. Among those materials, high performance fiber reinforced cementitious composites (HPFRCCs) are expected to particularly enhance the resistance of civil infrastructure under high mechanical and environmental loads with their much higher strength, high ductility and energy absorption capacity, compared with conventional concretes, based on their unique strain hardening behavior accompanied by multiple micro-cracks [Naaman and Reinhardt (2006)]. Specially, HPFRCCs can produce by themselves the damage-sensing ability as a self-damage sensor [Nguyen et al. (2015); Song et al. (2015)].

However, the damage-sensing ability of HPFRCCs were evaluated using gauge factor computed by relative reduction in the electrical resistivity per unit strain [Wang et al. (1999)]. Note that the electrical conductivity of a material is the reciprocal of its electrical resistivity, described by Eq. (2). Therefore, the electrical resistivity behavior,

© Springer Nature Singapore Pte Ltd. 2018
H. Tran-Nguyen et al. (eds.), *Proceedings of the 4th Congrès International de Géotechnique - Ouvrages -Structures*, Lecture Notes in Civil Engineering 8,
DOI 10.1007/978-981-10-6713-6_30

or the electrical conductivity behavior, of HPFRCCs is an important property that should be clearly understood to develop the self-damage sensor.

This situation was the motivation for the experimental study reported in this paper, which focuses on the electrical resistivity behavior of various HPFRCCs under no loading in the controlled condition. The objectives of this paper are to investigate the electrical resistivity behavior of: (1) plain mortar of HPFRCCs, (2) HPFRCC using steel fibers (SF), (3) HPFRCC using steel fibers (SF) and carbon fibers (CF), and (4) HPFRCC using steel fibers and multi-walled carbon nanotubes (MWCNT).

## 2 Experimental Program

### 2.1 Materials and Preparation of Specimens

The composition and compressive strength of the mortar matrix are given in Table 1. Tables 2 and 3 show the properties of steel fibers, multi-walled carbon nanotubes, respectively. The mixer used was a Hobart-type laboratory mixer with a 20-L volume capacity. Cement, silica fume, fly ash, and sand were firstly mixed in dry state for approximately 10 min. Next, various conductive fibers and powders were added in different ways as follows:

**Table 1.** Composition and compressive strength of mortar matrix

| Cement (type 3) | Silica fume | Silica sand | Fly ash | Superplas-ticizer | Water | $f'_c$ (MPa) |
|---|---|---|---|---|---|---|
| 0.80 | 0.07 | 1.00 | 0.20 | 0.04 | 0.26 | 90 |

**Table 2.** Properties of steel and carbon fibers

| Fiber type | Carbon fiber | Steel smooth fiber |
|---|---|---|
| Product origin | Panex35 (Korea) | JKT (Korea) |
| Diameter (mm) | 0.0072 | 0.3 |
| Length (mm) | 12 | 30 |
| Aspect ratio (length/diameter) | 1667 | 100 |
| Density (g/cc) | 1.81 | 7.9 |
| Tensile strength (MPa) | 4137 | 2580 |
| Elastic modulus (GPa) | 240 | 200 |
| Electrical resistivity (kΩ-cm) | 1.2 | $2.06 \times 10^{-8}$ |

- Carbon fibers or carbon black powder was added and dry-mixed whereas steel fibers was mixed in wet state after adding water and mixed for about 5 min.
- Multi-walled carbon nanotubes was separately dispered in water using ultrasonicator then added in dry mixture, as described in Fig. 1.

In all cases, polycarbonate-based superplasticizer was gradually added and further mixed until the mortar mixture showed the suitable workability and viscosity. Finally, a

**Table 3.** Properties of multi-walled carbon nanotubes (MWCNTs)

| Parameters | Value |
|---|---|
| Product origin | Hanwha (Korea) |
| Purity (wt.%) | >90 |
| Bulk density (g/cm3) | 0.065 |
| Aspect ratio | 2000 |
| Diameter (nm) | 10–15 |
| Length (μm) | 30–40 |
| Number of wall (ea) | 10–15 |
| Ash (catalyst residue, %) | 10% |
| Surface area (m2/g) | ~1200 |

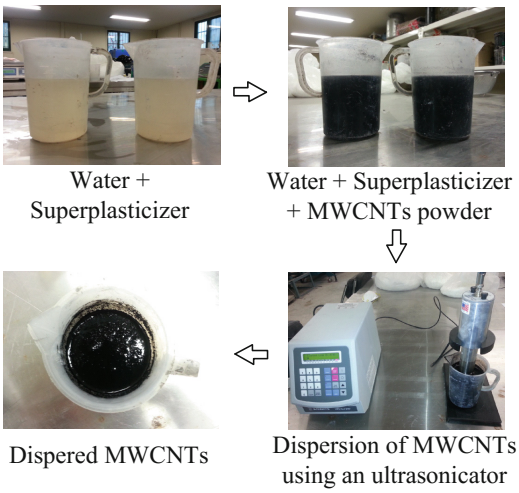


**Fig. 1.** Schematic of MWCNTs dispersion

wide scoop was used to place the mixture into molds. The specimens were then vibrated to reduce the air voids inside them. All specimens after placing were covered in plastic sheets and placed in a laboratory at room temperature for 48 h prior to demolding. After demolding, the specimens were cured in a water tank at 25 °C for 14 days. After curing, the specimens were removed from the water tank then dried at 70 °C in a drying oven for at least 12 h; this work helps minimize the influence of huminity on electrical resistivity (Fig. 2).

## 2.2 Test Set-Up and Procedure

All the specimens were tested at the age of 18 days. To measure the electrical resistivity of the specimens, a layer of silver paste was first applied onto the surfaces of the specimens to enhance the electrical conductivity between the copper tapes and specimens; subsequently, the copper tapes were attached on the silver-paste layer, as

(a) Steel smooth fiber (b) Carbon fiber (c) MWCNTs powder

**Fig. 2.** Various conductive materials added into mortar matrix

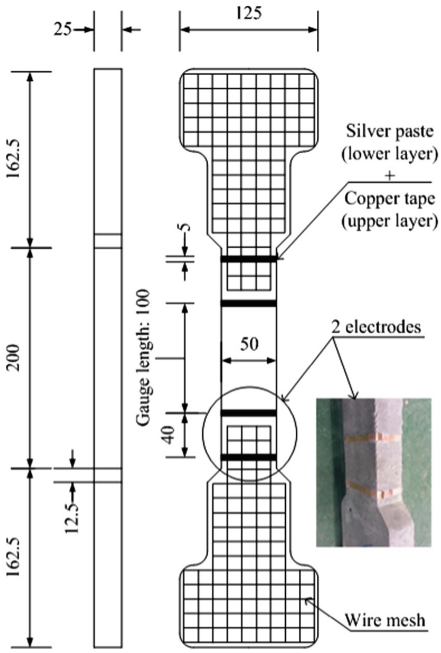


**Fig. 3.** Geometry of specimen

described in Fig. 3. Figure 4 shows the test set-up for measuring electrical resistance of specimen under controlled condition into chamber. The measured resistance of composites can be converted to electrical resistivity ($\rho$) using Eq. (1). The electrical conductivity ($\sigma$) is defined as the reciprocal of electrical resistivity and used for measuring a material ability to conduct an electric current, described by Eq. (2).

$$\rho = R \cdot \frac{A}{L} \tag{1}$$

$$\sigma = \frac{1}{\rho} \tag{2}$$

(a) Chamber for temperature & relative humidity control

(b) Measuring electrical resistance of specimen into chamber

**Fig. 4.** Test set-up for measuring electrical resistance of specimen under controlled condition

where $\rho$ and $\sigma$ are the electrical resistivity and conductivity of a material, respectively; $R$: the electrical resistance; $A$: the cross-sectional area; and $L$: the length between the two inner electrodes, which is also the gauge length of the specimen.

## 3 Electrical Resistivity Behavior of Cementitious Composites

### 3.1 Electrical Resistivity of a Two-Phase Composites

The electrical resistivity of the composite ($\rho_c$) can be estimated using Eq. (3), which was developed by Fan (1995) for determining the electrical resistivity of a two-phase composite. The equation considers the effects of the particle shape, phase distribution, and volume fraction. In this study, the investigated HPFRCCs are considered as composites comprising matrix ($m$) and conductivity ($f$) phases.

$$\frac{1}{\rho_c} = \frac{(V_m)^i}{\rho_m} + \frac{(V_f)^j}{\rho_f} + \frac{1-(V_m)^i-(V_f)^j}{\rho_m V_m + \rho_f V_f} \tag{3}$$

where $V_m$ is the volume fraction of the matrix (cement mortar); $V_f$ is the volume fraction of the conductive fibers or powders; $\rho_f$ is the electrical resistivity of the fibers; $\rho_m$ is the electrical resistivity of the matrix; and coefficients $i$ and $j$ (exponents) characterize the phase arrangement in the microstructure, which depends on the continuity of the relevant phase.

The coefficient $i$ describes the compactness of the cement mortar matrix, whereas the coefficient $j$ describes the degree of interconnection of the fibers [Wen and Chung

(2003)]. Consequently, the electrical resistance of the HPFRCCs is sensitive to changes in fiber conductivity as well as fiber volume content.

### 3.2 Electrical Polarization Phenomenon

Much research has been reported about the electrical polarization of cement pastes as well as cementitious composites [Wittmann (1973); Wen and Chung (2001a, 2001b); Cao and Chung (2004)]. Dielectric materials, including cementitious composites, generally produced the electrical polarization under an applied DC electrical field: when the polarization-induced electrical field and the applied DC electrical field are opposite in direction, the polarization increases the electrical resistivity with time [Wen and Chung (2001b); Cao and Chung (2004)].

In this study, the initial resistivity ($\rho_i$) and the stable resistivity at 20 min ($\rho_o$) would be measured and evaluated under controlled condition of 20 °C and relative humidity of 70%. Figure 5 shows the electrical resistivity versus time response of cementitious composites due to electrical polarization. As shown in Fig. 5, under electric current, the electrical resistivity quickly increases for the first 10 min due to the electrical polarization and becomes stable after 20 min.

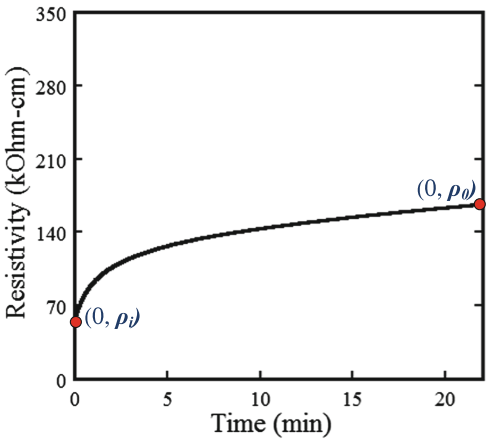


**Fig. 5.** Typical electrical polarization behavior of a cementitious composites

## 4 Result and Discussion

Figure 6 show the electrical resistivity behavior of various HPFRCCs investigated. In each figure, the curves of electrical resistivity versus time, are generally consistent although the curves in Fig. 6(a) are rather dispersed. As shown in Fig. 6, the electrical polarization is clear in case of steel fibers 1.5% by volume and in case of steel fibers 1.0% blended carbon fibers 0.5% by volume, i.e., there is much difference between $\rho_i$ and $\rho_o$ in these cases. Table 4 provides the average values of $\rho_i$ and $\rho_o$ as well as ratio between them. The plain mortar exhibits the highest electrical resistivity because it is

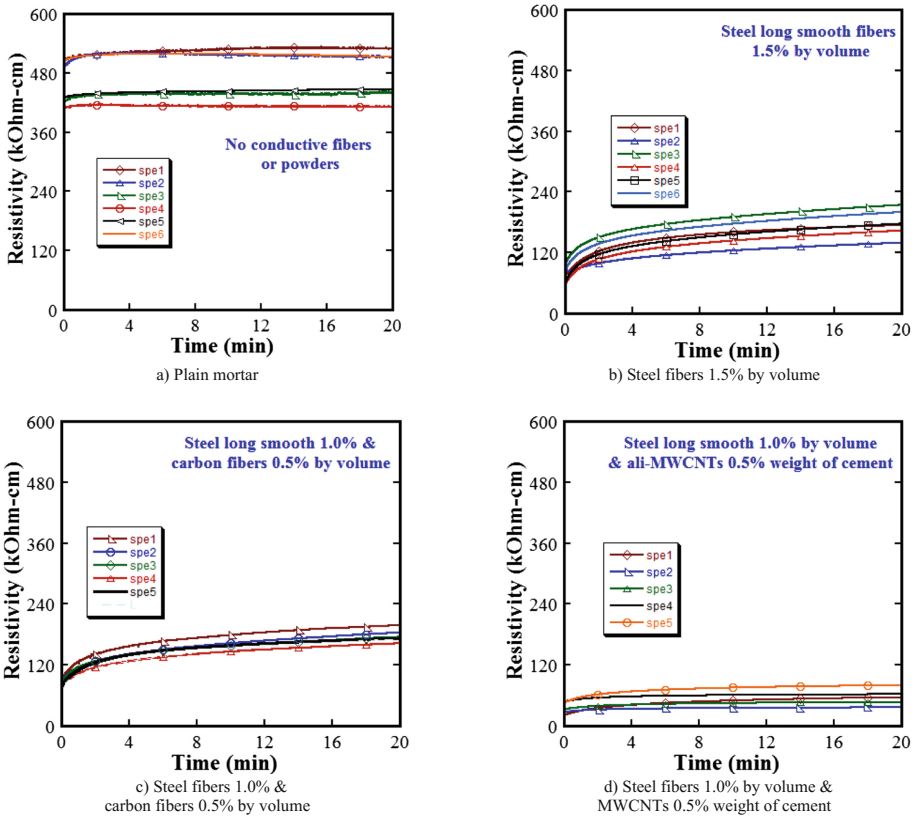


**Fig. 6.** Electrical polarization behaviors of investigated HPFRCCs

**Table 4.** Averaged electrical resistivity of investigated HPFRCCs

| HPFRCC type | $\rho_i$ (kOhm-cm) | | $\rho_o$ (kOhm-cm) | | Ratio $\rho_o/\rho_i$ |
|---|---|---|---|---|---|
| | Average value | Standard deviation | Average value | Standard deviation | |
| Plain mortar | 458.60 | 44.83 | 475.84 | 48.99 | 1.04 |
| SF 1.5% | 76.28 | 16.70 | 178.15 | 26.48 | 2.34 |
| SF 1.0% & CF 0.5% | 82.06 | 6.68 | 177.36 | 12.45 | 2.16 |
| SF 1.0% & MWCNTs 0.5% weight of cement | 39.10 | 11.73 | 65.99 | 15.57 | 1.69 |

not a conductive material. The addition of conductive fibers or powders in the matrix clearly declines its electrical resistivity, or improves its electrical resistivity in other words: the HPFRCC containing steel fibers 1.5% by volume and HPFRCC containing hybrid fibers show medium values of electrical resistivities whereas HPFRCC containing steel fibers 1.0% volume content and MWCNTs show the lowest electrical resistivity.

However, the ratios $\rho_o/\rho_i$ of HPFRCCs are different: the HPFRCC containing steel fibers 1.5% by volume produces the highest value (2.34), then the HPFRCC containing hybrid fibers 1.5% by volume (2.16), next to the HPFRCC containing steel fibers 1.0% by volume and MWCNTs (1.69), the plain mortar produces the lowest one (1.04).

The electrical resistivity of investigated HPFRCCs were normalized by that of plain matrix, as provided Table 5. According to Table 5, the HPFRCC with CNTs exhibits the most significant reduction in electrical resistivity, more than 7 times compared with plain mortar. The extreme aspect ratio and very small-sized particle of MWCNTs result the best interfacial contact with the matrix, and thus, the combination between steel fibers and MWCNTs leads to reducing the electrical resistivity of HPFRCC.

**Table 5.** Normalized electrical resistivity of investigated HPFRCCs

| Type of HPFRCC | Normalized, $\rho_i$ | Normalized, $\rho_o$ |
|---|---|---|
| Plain mortar | 1 | 1 |
| SF 1.5% | 0.17 | 0.37 |
| SF 1.0% & CF 0.5% | 0.18 | 0.37 |
| SF 1.0% & MWCNTs 0.5% weight of cement | 0.09 | 0.14 |

It is noted that the best conductivity of composites does not surely produces the best self damage-sensing capacity. The larger relative change in the electrical resistivity per unit strain exhibits under loading, the higher self damage-sensing capacity will be generated. This experimental study was only conducted under no loading, thus the self damage-sensing capacity of HPFRCCs will be evaluated in further investigation with applied load.

## 5 Conclusion

Under same controlled condition of 20 °C and relative humidity of 70%, the following observations and conclusions could be drawn from this experimental study:

(1) The electrical polarization is clear in case of steel fibers 1.5% by volume and in case of steel fibers 1.0% blended carbon fibers 0.5% by volume.
(2) The order of investigated HPFRCCs in term of the electrical resistivity is observed as follows: plain mortar > the HPFRCC containing steel fibers 1.5% by volume $\simeq$ the HPFRCC containing hybrid fibers 1.5% by volume > the HPFRCC containing steel fibers 1.0% by volume and MWCNTs.
(3) The ratios $\rho_o/\rho_i$ of HPFRCCs are ordered as follows: the HPFRCC containing steel fibers 1.5% by volume > the HPFRCC containing hybrid fibers 1.5% by volume > the HPFRCC containing steel fibers 1.0% by volume and MWCNTs > plain mortar.

**Acknowledgments.** This research was supported by Ho Chi Minh city University of Technology and Education (Vietnam). The opinions expressed in this paper are those of the authors and do not necessarily reflect the views of the sponsors.

## References

Naaman, A.E., Reinhardt, H.W.: Proposed classification of HPFRC composites based on their tensile response. Mater. Struct. **39**, 547–555 (2006)

Nguyen, D.L., Song, J., Manathamsombat, C., Kim, D.J.: Comparative electromechanical damage-sensing behavior of six strain-hardening steel-fiber-reinforced cementitious composites under direct tension. Compos.: Part B **69**, 159–168 (2015)

Song, J., Nguyen, D.L., Manathamsombat, C., Kim, D.J.: Effect of fiber volume content on electromechanical behavior of strain-hardening steel-fiber-reinforced cementitious composites. J. Compos. Mater. (2015). doi:10.1177/0021998314568169

Wang, X., Fu, X., Chung, D.D.L.: Strain sensing using carbon fiber. J. Mater. Sci. **14**(3), 790–802 (1999)

Fan, Z.Y.: A new approach to the electrical resistivity of two-phase composites. Acta Metall. Mater. **43**(1), 43–49 (1995)

Wen, S.H., Chung, D.D.L.: A comparative study of steel- and carbon-fiber cement as piezoresistive strain sensors. Adv. Cem. Res. **15**(3), 119–128 (2003)

Wittmann, F.H.: Observation of an electromechanical effect of hardened cement paste. Cem. Concr. Res. **3**, 601–605 (1973)

Wen, S.H., Chung, D.D.L.: Carbon fiber-reinforced cement as a strain-sensing coating. Cem. Concr. Res. **31**, 665–667 (2001a)

Wen, S.H., Chung, D.D.L.: Electric polarization in carbon fiber-reinforced cement. Cem. Concr. Res. **31**, 141–147 (2001b)

Cao, J., Chung, D.D.L.: Electric polarization and depolarization in cement-based materials, studied by apparent electrical resistance measurement. Cem. Concr. Res. **34**(3), 481–485 (2004)

# An Experimental Study on Earthen Materials Stabilized by Geopolymer

Q.-B. Bui[1(✉)], E. Prud'homme[2], A.-C. Grillet[3], and N. Prime[3]

[1] Sustainable Developments in Civil Engineering Research Group, Faculty of Civil Engineering, Ton Duc Thang University, Ho Chi Minh City, Vietnam
buiquocbao@tdt.edu.vn
[2] Université de Lyon, INSA Lyon, MATEIS – CNRS UMR 5510, Villeurbanne, France
[3] Université Savoie Mont Blanc, LOCIE – CNRS UMR 5271, Chambéry, France

**Abstract.** Earth is an ancient building material which has been recently the focus of scientific research due to its sustainable properties. The disadvantage of earthen material is its low strength and its sensibility to the water content. To enhance the durability and the mechanical characteristics of earthen material, hydraulic binders are currently added (cement or lime) which have high embodied energy and therefore increase the embodied energy of the stabilized earth material. This paper presents an exploratory study which uses geopolymer as a stabilizer for earthen material. Geopolymers are inorganic binders with polymeric structure obtained by alkaline activation of raw materials containing silicon and aluminum; they are obtained by dissolution/precipitation reactions at low temperature. The present study proposes to use blast furnace slag as geopolymer raw material, which was mixed with an alkaline solution activator to obtain the stabilizer for earthen material. The geopolymer effects were investigated on two types of earthen material: rammed-earth (RE, soil dynamically compacted) and soil-geopolymer-concrete (soil poured with more water content). The results show that geopolymer had more effects in soil-concrete than in rammed-earth. Indeed, RE specimens stabilized by geopolymer did not present a significant improvement of compressive strength comparing to the unstabilized RE specimens. Soil-geopolymer-concrete specimens had double compressive strength comparing to soil-cement-concrete specimens.

**Keywords:** Rammed earth · Soil concrete · Geopolymer · Compressive strength · Earth stabilization

## 1 Introduction

In-situ materials which are directly available on site are used by humanity from centuries as earth (rammed earth, adobe, cob…), stone (dry stone masonry and rubble stone masonry) and wood. The construction techniques using in-situ materials are still widely used today in developing countries, thanks to their lower construction costs in comparing to conventional constructions (such as reinforced concrete or metal

© Springer Nature Singapore Pte Ltd. 2018
H. Tran-Nguyen et al. (eds.), *Proceedings of the 4th Congrès International de Géotechnique - Ouvrages -Structures*, Lecture Notes in Civil Engineering 8,
DOI 10.1007/978-981-10-6713-6_31

structures). The reason is that conventional materials are not always available in these countries and must be imported, that significantly increases the cost. In addition, the labor cost is not expensive, so the use of in-situ materials has a positive social aspect by providing works to local workers. However, in developed countries, most of these materials were dropped consistently over the past six decades for two main reasons. First, the labor cost in these countries is high, which is not favorable for the constructions requiring important labor. Then, the current design regulations are established mainly for industrial conventional materials. There are few standards for non-industrial materials due to the lack of scientific knowledge. Nevertheless, the past few years have witnessed a renaissance of local materials in developed countries, mainly due to the urgent demands of sustainable development. Soil material gradually found its place on construction sites because it is taken and manufactured directly on site, which provides low embodied energy; walls constructed with soil material can act as a natural moisture buffering for indoor environments. From the economic view point, using the in-situ soil as construction material is also interesting for the builder because the fee to evacuate the in-situ soil before the construction is costly [1].

Several traditional techniques exist today to use soil as construction material: rammed earth, compressed earth blocks, adobes, cob. The main binder in those cases is clay. For new constructions, hydraulic binders can be added (currently cement, lime) to increase the material's mechanical properties and durability [2]. These hydraulic binders have high embodied energy and therefore increase the embodied energy of the stabilized earth material. In order to find an alternative binder, other components are tested. This paper presents an exploratory study which uses geopolymer as a stabilizer for earthen material.

The term "geopolymer" is used for products where amorphous three-dimensional inorganic structures are formed through the reaction of alumino-silicate precursor, with an alkaline solution activator [3]. The source of alumino-silicate can be natural clays, calcined clays, industrial by-products and other natural minerals. The activators are typically sodium or potassium hydroxides or silicates, but others are also possible. Using geopolymer technology for earth construction is interesting because the soils used for earthen construction has a significant amount of clay content and are a source of alumino-silicates such as kaolin and illite. Therefore the natural clay minerals within the soil can become an essential part of stabilizing mechanism, rather than simply being encapsulated by the stabilizer, as is the case of cement [4]. Compressive strength of non-calcined materials, such as kaolinite, can be increased with the addition of calcined materials including fly ash and metakaolin [5]. There are still few studies on the stabilization of earthen materials by geopolymer but the studies of Maskell et al. [4] and Cristelo et al. [6] can be cited. Maskell et al. used an alkaline activator in their investigation on the geopolymer stabilization of earthen bricks. These authors tested different compositions of geopolymer (1%, 3% and 5% of sodium hydroxyde with respectively 0%, 4%, 15% and 20% of sodium hydroxyde) and investigated also the effect of curing temperature (at 20° and 105 °C) on the compressive strength. However, the specimens tested were small specimens (1.8-cm-diameter and 3.6-cm-height), so the correlation with the workability at the real scale should still be investigated. Cristelo et al. [6] studied the effectiveness of alkaline activation of low-calcium fly ash on rammed-earth material. Different liquid/solid ratios, alkali concentrations and $Na_2O$/ash ratios were tested. Effect of calcium hydroxide, sodium chloride and concrete

superplasticizer was also investigated. The specimens were cured at 60 °C. Results showed that there was an optimum value for the activator/solids ratio and the alkali concentration, and that a decrease in the $Na_2O$/ash ratio resulted in a strength increase. No improvement was observed with the sodium chloride or the superplasticizer, while the calcium produced only an increase of early age strength.

The present study proposes to use blast furnace slag as a raw material, to be mixed with an alkaline solution activator to obtain a binder for earthen material. The furnace slag is an industrial waste and its recycling reduces the binder's environment impact. Due to its high content of calcium, silicon and aluminum, blast furnace slag presents good ability for alkaline activation and geopolymerization, which is reflected by obtaining very high mechanical performances on alkali activated blast furnace slag [7]. The geopolymer effects were investigated on two types of earthen material: rammed-earth and soil-concrete.

Rammed-earth (RE) is chosen here because this technique is largely liked in modern "green" buildings. RE is a monolithic wall which is built from several earthen layers. For each layer, the soil is poured about 15 cm thick into a formwork and then rammed by a rammer (manual or pneumatic). The soil is compacted at its optimum water content, which provides the highest dry density for the given compaction energy [8]. The usual manufacturing water content for rammed earth is about 10–13%, in function of the material composition and the compaction energy. In developed countries, rammed earth is preferred to other earthen construction techniques (adobes, compressive earth blocks …) thanks to its esthetic and its construction rapidity, comparing to traditional earthen constructions. The soil-concrete technique is also tested here because it is recently used in building construction, due to its rapidity comparing to other traditional earth construction (including rammed earth) because the wall is casted once, not in several layers. In order to be "poured" as a conventional concrete, more water should be added to increase the workability but this influences also on the mechanical properties of the concrete obtained.

## 2 Specimen Manufacturing

### 2.1 Soil Used

The soil used in this study was taken from a site of rammed earth construction. Table 1 presents the composition of the soil which was obtained by sieving (for elements >80 μm) and sedimentometric tests (for elements <80 μm). The methylene blue tests were carried out following French Standard to obtain methylene blue values. The clay activity index ACB was calculated from the methylene blue values. That index enables to identify the soil's mineralogical composition (Table 2) following an abacus given by Lautrine [9].

**Table 1.** Global composition of the soil used in this study (in weight)

| | Clay | Silt | Sand | Gravel |
|---|---|---|---|---|
| Soil | 19% | 65% | 16% | 0% |

**Table 2.** Clay's mineralogical composition of the soil used (in weight)

| | Kaolinite | Illite | Montmorillonite |
|---|---|---|---|
| Soil | 0% | 65% | 35% |

## 2.2 Formulation of the Geopolymer and the Materials Used

The geopolymer part in this study is composed of sodium silicate solution (noted SiNa, supplied by FisherScientific) with the following formula: $Na_2SiO_3.nH_2O$, a molar ratio $SiO_2/Na_2O$ of 2.2, a density of 1.5 $g.cm^{-3}$, and contains 55% of water. The sodium hydroxide pellets (supplied by FisherScientific) are noted NaOH and is 99% pure. The blast slag furnace (noted BFS, density d = 2.9 $g.cm^{-3}$, $D_{50}$ = 12.65 µm) is supplied by ECOCEM France. Its oxide composition is given Table 3.

**Table 3.** Oxide composition of BFS (weight %).

| Oxide | CaO | $SiO_2$ | $Al_2O_3$ | MgO | $SO_3$ | $Fe_2O_3$ | $TiO_2$ | $Mn_2O_3$ | $K_2O$ | $Na_2O$ |
|---|---|---|---|---|---|---|---|---|---|---|
| BFS | 41, 2 | 36.0 | 10, 3 | 7, 5 | 2, 9 | 0, 8 | 0, 5 | 0, 4 | 0, 3 | 0, 1 |

The effect of curing temperature was not investigated because the scope of this study is for an in-situ application (rammed-earth or concrete). A preliminary study on small specimens (3-cm-diameter and 6-cm-height) had been carried out to search a formula which was used for tests on standard specimens of civil engineering. Finally, the ratio of blast furnace slag: sodium silicate: sodium hydroxide was chosen based on the work of Prud'homme et al. [7]. The amount of furnace slag was chosen at 10% of the total mixture (with soil and water).

*Rammed Earth Specimens:* A primary study was performed that showed that the optimum water content - for the unstabilized soil and the used compaction energy - was by 11.8%, which gave the highest dry density (1.85). The representativeness of the compaction energy and the manufacturing optimum water content for RE specimens was discussed in Bui et al. [8]. For this exploratory study, RE specimens stabilized by geopolymer were also manufactured at this water content of unsatiblized RE. The water for the preparation of the activator (sodium silicate + sodium hydroxide) was 1.7% and other 10% (including 2% water content already present in the soil) was added directly to the soil. The detail of RE composition is presented in Table 4.

**Table 4.** Composition of RE specimens

| Soil | Water (mixed with soil) | Geopolymer |
|---|---|---|
| 75% | 10% | 10.4% |

Before the adding of alkaline activator (under the form of a liquid), the soil and the furnace slag (form of powder) should be mixed to obtain a homogeneous mixture. Two processes for the mixture of the soil and the slag were tried. First, the soil and the slag were mixed at natural state (quasi-dry). But this process causes too many dusts during

the mixing. That was why the second process was adopted: the soil was humidified beforehand until 10% of water content and then the slag was added and mixed. This enabled to avoid the dust during the mixing and the slag was better mixed with the soil and the water. Then, the alkaline activator solution (sodium silicate + sodium hydroxide + 1.8% water) was added and mixed. Two types of mold were used to manufacture geopolymer stabilized RE specimens: first, cubic molds, 15 × 15 × 15 $cm^3$: each specimen has 3 earthen layers (Fig. 1, at the left); these specimens will be tested in two directions: perpendicular and parallel to earthen layers; Second, cylindrical molds, 16 cm- diameter × 32 cm-height: each specimen has 6 earthen layers (Fig. 1, at the right); these specimens were only tested in the direction perpendicular to the layers. In parallel, cylindrical unstabilised RE specimens were also manufactured as reference for the comparison and so only tested in compression perpendicular to the earthen layers.

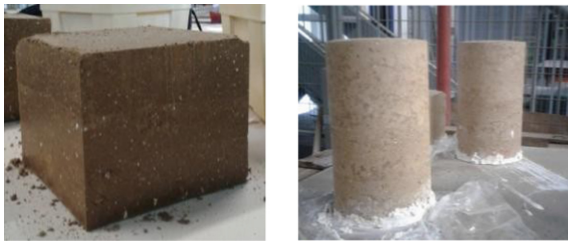

**Fig. 1.** Geopolymer stabilized RE specimens.

After demolding, several slag grains were still visible on the specimens, this shows that the slag was not really well mixed with soil and alkaline activator.

*Soil-Concrete Specimens:* For soil-geopolymer-concrete specimens, only the water amount was changed. The mixture was mixed in a concrete mixer and water was added until an acceptable workability of a plastic concrete was obtained (corresponding to a slump of about 6 cm). The total water content was 18%. With this water content, it was observed that the slag was better mixed with soil and alkaline activator than in the case of geopolymer RE specimens. The composition soil-geopolymer-concrete is presented in Table 5.

**Table 5.** Composition of the soil-geopolymer-concrete specimens

| Soil | Water (mixed with soil) | Geopolymer |
|---|---|---|
| 71% | 16% | 13% |

The concrete casting was performed with cylindrical molds of 16 cm-diameter and 32 cm-height, using a current concrete vibrator. However, after demolding, several air bulks were still observed on the specimens (Fig. 2).

**Fig. 2.** Soil-geopolymer-concrete specimens

For the comparison, soil-cement-concrete specimens were also casted. A cement quantity of 8% (in weight) and 18% of water content were used. The cement amount was chosen at 8% because beyond this value, the material's embodied energy will be high and the soil-concrete will not be interesting.

## 3 Uniaxial Compression Tests

### 3.1 Tests on Rammed Earth Specimens

*Compression Tests in the Perpendicular Direction to Earthen Layers:* Before the compression tests, specimens were surfaced by a lime mortar to have two plane and horizontal faces (Fig. 3). The specimens were tested in force-piloted and were loaded at a rate of 0.4 kN/s.

**Fig. 3.** Compression in the direction perpendicular to earthen layers

After the tests, the specimens' moisture contents were measured and their dry densities were also determined. The dry density values were of $1.78 \pm 0.01$ and $1.85 \pm 0.02$ respectively for prismatic and cylindrical specimens. This result is not surprising because it has already been observed that the prismatic specimens had dry densities less than that of the cylindrical specimens. Indeed, the dynamic compaction in the corners of prismatic specimens is not easy and the results obtained on prismatic specimens are usually lower than that of cylindrical specimens [10].

*Compression Tests in the Parallel Direction to Earthen Layers:* Cubic specimens were also tested in the direction parallel to earthen layers (Fig. 4). No surfacing was needed because the upper and lower faces were plane and horizontal. The failure of specimens tested in direction parallel to earthen layers was similar to that of specimens tested in direction perpendicular to layers (Fig. 4 at the left), which showed a satisfying cohesion between earthen layers.

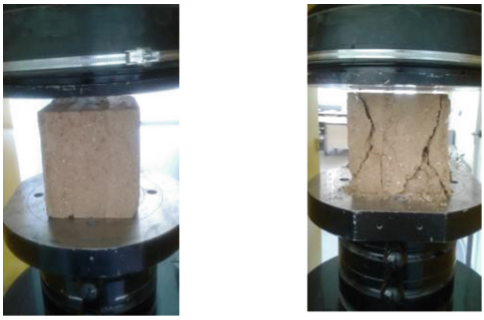

**Fig. 4.** Compression in the direction parallel to earthen layers, before and after the test.

### 3.2 Tests on Soil–Concrete Specimens

Because there are not layers in soil-concrete material, cylindrical specimens were tested only in one direction. Specimens were also surfaced and tested at a rate of 0.4 kN/s. This rate is lower than that applied for ordinary concrete specimens, in order that each test takes a couple of minutes, similar to in the case of ordinary concrete specimens.

### 3.3 Results and Discussions

A summary of the results is presented in Table 6. It is important to note that due to a small slenderness ratio of cubic specimens (height/width = 1), the frictions during the compression test, between the specimen and the upper and lower steel plateaus of the press, play a non-negligible role and the results obtained are overestimated. That is why it is well-known that results obtained on cubic specimens should be multiplied by a correction factor. Following Eurocode 2 for concrete, this correction factor depends to the concrete class (strength) but is about 0.85–0.87 for mean compressive strength of low strength concrete. In absence of specific recommendations for earthen specimens, a correction factor of 0.9 was adopted here for geopolymer RE cubic specimens. The corrected results are illustrated in Fig. 6.

As mentioned above, the dry density of prismatic specimens were less than that of the cylinders and one-scale RE walls [8], so the compressive strengths obtained on prismatic specimens are lower and not representative for RE walls. The tests on prismatic specimens are presented here just in order to assess the anisotropy of the geopolymer RE specimens. The results shows that the results obtained in perpendicular and parallel to earthen layers were similar (difference less than 8%). This confirms the results obtained in a previous study on unstabilized RE [11].

**Table 6.** Summary of the results obtained on different specimens.

| Specimens | Dry density | Moisture content (%) | Test direction | fc (MPa) | Age |
|---|---|---|---|---|---|
| Geopolymer RE Cube | 1.78 | 5 | Parallel to layers | 1.2 | 2 weeks |
| | | 3 | | 1.8 | 4 weeks |
| | | 5 | Perpendicular to layers | 1.3 | 2 weeks |
| | | 3 | | 1.9 | 4 weeks |
| Geopolymer RE Cylinder | 1.85 | 5 | Perpendicular to layers | 1.6 | 2 weeks |
| | | 3 | | 2.4 | 4 weeks |
| Unstabilsed RE | 1.85 | 3 | Perpendicular to layers | 1.8 | 4 weeks |
| Soil-geopolymer-concrete | 1.64 | 12 | NA | 0.9 | 2 weeks |
| | | 6 | | 1.2 | 4 weeks |
| Soil-cement concrete | 1.78 | 4 | NA | 0.6 | 4 weeks |

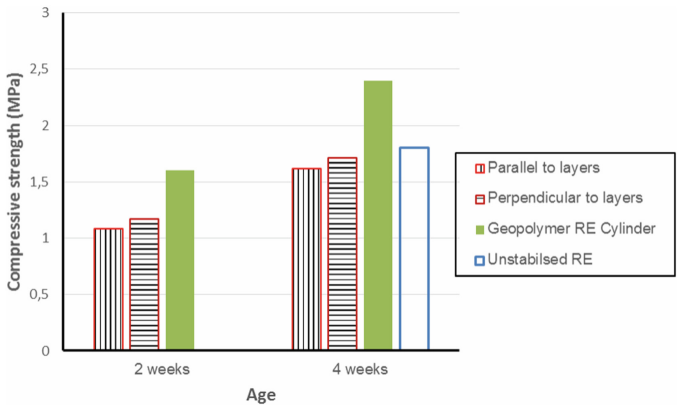


**Fig. 5.** Compression strengths of geopolymer RE specimens after 2 and 4 weeks. Note: a correction factor was used for cubic specimens.

Figure 5 shows that there is an improvement (50%) of the strength of geopolymer RE from 2 weeks to 4 weeks. Then, compared to cylindrical unstabilised RE specimens, the strength of cylindrical geopolymer RE specimens increased by 33%.

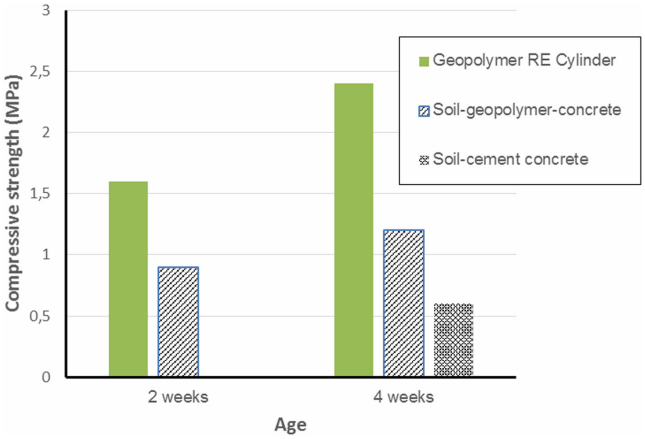


**Fig. 6.** Compression strengths of geopolymer RE, soil-geopolymer-concrete and soil-cement concrete specimens.

Figure 6 presents a comparison of compression strengths obtained on different cylindrical specimens: geopolymer RE, soil- geopolymer-concrete and soil-cement concrete. The result of soil-cement concrete (8% cement) was very low, probably due to the high quantity of water used. Indeed, with a soil containing 19% clay, a high amount water (18%) was necessary to obtain an acceptable workability. In a previous study [1], with a soil having a lower clay content, the water content necessary was lower and the compressive strength obtained was better.

For the soil-geopolymer-concrete specimens, an evolution of the strength in function of time was also noted. At 4 weeks, soil- geopolymer-concrete specimens had compressive strength twice of soil-cement concrete specimens. However, these results are still low comparing to geopolymer RE specimen and for construction materials in general. The high amount of water used was probably the reason of these results.

## 4 Conclusions and Outlook

This paper presents an exploratory investigation on the use of alkaline activator to stabilize two types of earthen material: rammed earth and soil-concrete. The results showed that geopolymer stabilization improved 33% of compressive strength of RE specimens, comparing to unstabilised RE. However, the obtained results (2.4 MPa at 4 weeks) was not as high as expected to be a material for bearing walls in the viewpoint of modern regulations. It was also observed that the slag was not well mixed with soil and alkaline activator, so if a better mixing method is found, better compressive strengths can be expected.

When more water was added (the case of soil-geopolymer-concrete), the effect of geopolymer was more positive than cement in soil-cement-concrete specimens (at 8% of cement in weight). However, due to an important amount of water, the compressive strength of the specimens was not as high as expected (1.2 MPa at 4 weeks).

The soil used in this study does not contain kaolinite. It will be interesting to study other soils which contain different quantities and types of clay.

Due to the sustainable and economic reasons, only a low amount of sodium silicate (2.5%) was used in this study. Other compositions of geopolymer will be searched to improve the compressive strength.

**Acknowledgments.** The authors wish to thank Dang-Mao Nguyen, Ranime El-Nabouch from LOCIE - University Savoie Mont Blanc and Van-Huong Tran from ENTPE-Filiaterre for their help during the specimen castings.

## References

1. Bui, Q.B., Morel, J.C., Tran, V.H., Hans, S., Oggero, M.: How to use in-situ soils as building materials. Proc. Eng. **145**, 1119–1126 (2016)
2. Bui, Q.B., Morel, J.C., Reddy, B.V.V., Ghayad, W.: Durability of rammed earth walls exposed for 20 years to natural weathering. Build. Environ. **44**, 912–919 (2009b)
3. Davidovits, J.: Chemistry and Applications. Institut Géopolymère, USA (2008)
4. Maskell, D., Heath, A., Walker, P.J.: Geopolymer stabilization of unfired earth masonry units. In: Key Engineering Materials, vol. 600, pp. 175–185 (2014)
5. Xu, H., Deventer, J.S.J.V.: Geopolymerisation of multiple minerals. Miner. Eng. **15**(12), 1131–1139 (2002)
6. Cristelo, N., Glendinning, S., Miranda, T., Oliveira, D., Silva, R.: Soil stabilisation using alkaline activation of fly ash for self compacting rammed earth construction. Constr. Build. Mater. **36**, 727–735 (2012)
7. Prud'homme, E., Ambroise, J., Michel, M.: Impact of alkaline solution and curing temperature on microstructure and mechanical properties of alkali-activated blast furnace slag. Ceram. Eng. Sci. Proc. **36**(8), 61–75 (2015)
8. Bui, Q.B., Morel, J.C., Hans, S., Meunier, N.: Compression behaviour of nonindustrial materials in civil engineering by three scale experiments: the case of rammed earth. Mater. Struct. **42**, 1101–1116 (2009a)
9. Lautrin, D.: Utilisation pratique des paramètres dérivés de l'essai au bleu de méthylène dans les projets de génie civil. Bull. des Liaison des Lab. des Ponts et Chaussées **160**, 29–41 (1989)
10. Bui, Q.B., El-Nabouch, R., Perrotin, P., Plé, O.: Assessing a nondestructive method to determine the young's modulus of rammed earth material. In: 6th BIOT Conference on Poromechanics, Paris, 13–17 July 2017
11. Bui, Q.B., Morel, J.C.: Assessing the anisotropy of rammed earth. Constr. Build. Mater. **23**, 3005–3011 (2009c)

# Analysis Behavior of Reinforcement in a Reinforced Concrete Beam Using Steel Slag Replacing Crushed-Stone Aggregate

Anh-Thang Le(✉), Trong-Quang Hoang, and Tat-Thanh Nguyen

Civil Engineering, Ho Chi Minh City University of Technology and Education, Ho Chi Minh, Vietnam
thangla@hcmute.edu.vn, hoanghuykt@yahoo.com.vn, ksnguyentatthanh92@gmail.com

**Abstract.** Quarrying cause pollution and environmental destruction, natural resources dwindling, while sand mining could cause the river erosion, change in flow, and ecological imbalance. Besides, steel slag is scrap produced along with the development of the iron industry. This waste without proper treatment will affect the environment. The utilization of steel slag as raw material replaced crushed rock in concrete production is a study topic in order to reduce environmental pollution caused by steel slag. The behaviors of reinforcement in a reinforced concrete beam using steel slag replacing crushed-stone aggregate, which is called as SRCB, are explored in the article. It is presented in comparison with reinforcement in crushed-stone aggregate concretes (RCB).

**Keywords:** Steel slag · Steel slag replacing crushed-stone aggregate · Reinforced concrete beam · The behaviors of reinforcement

## 1 Introduction

According to steel producing technology, every tons of steel produces about 110–150 kilograms of steel slag. Steel slag has good mechanical properties due to its special crystal structure, which is better than natural stone. Steel slag has specific mechanical properties such as heavier than natural aggregates, high friction and high durability. However, it is considered as industrial waste that causes environmental pollution. In the USA, Europe and Japan, steel slag has been widely used in construction. They are utilized in civil, industrial, and transportation. Normally, steel slag is used to replace the natural materials in asphalt or cement concrete.

Vietnam is a nation where demand for infrastructure construction is still huge. To serve this demand, exploitation of natural resources (sand and natural stone) occurs massively that leads to serious problems such as pollution, environmental degradation, increasingly exhausted natural resources. Besides, the development of steel factories in Vietnam produces huge volume of steel slag. If steel slag do not treated properly, it will affect heavily the environment. Therefore the utilization of steel slag as raw material replaced crushed stone in concrete is a recently study topic of several research groups in the country.

© Springer Nature Singapore Pte Ltd. 2018
H. Tran-Nguyen et al. (eds.), *Proceedings of the 4th Congrès International de Géotechnique - Ouvrages -Structures*, Lecture Notes in Civil Engineering 8,
DOI 10.1007/978-981-10-6713-6_32

With an effort utilized steel slag replacing natural rock, concrete beams of steel slag and conventional crushed stone have been done in the laboratory of the UTE (Ho-Chi-Minh City University of Technical and Education). They are tested by three-point flexural experiment and simulated in ABAQUS environment.

This article explores the tensile stress values in reinforcement bars of test beams in which crushed-stone aggregates are replaced by steel slag. Besides, they are compared with tensile stresses in reinforcement bars of reinforced concrete test beams using crushed-stone aggregates, conventional concrete beams.

## 2 Material

### 2.1 Unbound Materials

Crushed stone are from the Hoa-An mine, Dong-Nai province. They are cleaned, dried and sieved. The average aggregate size is 10 × 20 mm. The quality and strength of stone meet the national standard, TCVN 1771-1986 [1]. Steel slag is taken from a steel factory in Phu-My-1, an industrial Park located in Tan-Thanh District, Ba-Ria Province. Steel slag was determined basic properties such as composition, specific gravity, volume, compressive strength and the ability of released heavy metals into the environment. Based on experiment results, there is a conclusion that the steel slag properties are similar to the steel slag utilized in concrete in the world. River sand is taken from Dong-Nai River. It is washed, dried, screened. The particle size module is controlled following TCVN 6227-1996 [2]. The cleanliness of sand meets TCVN 1770-1986 [3].

### 2.2 Concrete Mixture

The concrete mixtures proportions are summarized in the Table 1. There are three concrete mixtures of crushed-stone and two of steel slag. They are named as CPD1, CPD2, CPD3, CPX1, and CPX2. CPD is abbreviation of crushed-stone aggregate. CPX is abbreviation of steel slag aggregate. The CPX1 has the similar mix proportions to CPD1, while The CPX2 has the similar mix proportions to CPD2 and CPD3. Two beam specimens of 3300 × 300 × 200 and six cubic specimens of 150 × 150 × 150 are created for each concrete mixture proportions. The total length of the beams is 3300 mm and the cross section is 300 × 200 mm.

**Table 1.** Mix proportions in a cubic meter of concrete

| | Cement (kg) | Sand (kg) | Steel slag/Crushed-stone (kg) | Water (l) | Water/ Cement | Additives (ml) | Rn (MPa) | Notes |
|---|---|---|---|---|---|---|---|---|
| CPD1 | 411.7 | 687.1 | 1173.3 | 190 | 0.46 | 4.1 | 29.3 | Crushed-stone |
| CPD2 | 375.0 | 591.5 | 1364.4 | 180 | 0.45 | 3.0 | 28.6 | Crushed-stone |
| CPD3 | 375.0 | 591.5 | 1364.4 | 180 | 0.45 | 3.0 | 25.7 | Crushed-stone |
| CPX1 | 411.7 | 687.1 | 1431.3 | 190 | 0.46 | 4.1 | 40.7 | Steel slag |
| CPX2 | 360.0 | 591.5 | 1664.4 | 162 | 0.45 | 2.9 | 37.5 | Steel slag |

## 3 Experiment Results

Average compressive strengths of cubic specimens after 28 days age (Rn) are presented in Table 1. The experiment results show that the concrete specimens of steel slag have the higher compressive strength than conventional concrete with the same proportions of material.

Three-point flexure tests of the reinforced concrete beams have been done in the laboratory of the UTE. The reinforced concrete beams in which have steel slag is hereafter named as SRCB. The reinforced concrete beam in which has conventional crushed stone is hereafter named as RCB.

SRCB and RCB is conducted three-point flexure test as shown in Fig. 1. The bending load speed is 0.05 KN/s. In the process of the experiment, the LVDTs (Linear Variable Differential Transformers) are installed at locations of 1/4 and 1/2 of beam length for measuring displacement. Steel bars layout in the beams is shown in Fig. 1. Five longitudinal reinforcement steel of 14 mm dia. are arranged at the bottom of beam, and two hanger steel bars of 12 mm dia. are arranged at the top layer of beam. Stirrup bars of 6 mm dia. are arranged at 150 mm center-to-center. Protective layer is 25 mm. Steel has the Young's modulus of 200 GPa, and tensile yield strength of 365 MPa. Longitudinal reinforcement steel bars are placed following TCVN 5574-2012 for standing a bending load of 60 kN [4]. As a result, SRCBs are broken at bending force of 113 kN and RCBs are broken at bending force of 80 kN.

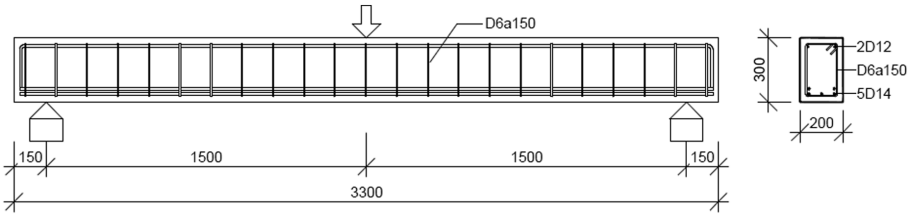


**Fig. 1.** Elevation layout of reinforcement in beam and cross-section.

Alizadeh et al. [5] report that slag aggregate concretes shows significantly higher compressive strength than natural aggregate concretes. Besides, they also report that slag aggregate concretes has the higher values of tensile strength, flexural strength and modulus of elasticity, compared to natural aggregate concretes. So, experiment results are good agreement with Alizadeh's reported results.

## 4 Computational Models

Simulation models of beam are created on ABAQUS environment [8]. They are validated for further exploration. Element sizes are selected so that they do not affect to analysis results. The meshing size of 80 mm is proposed for the model.

### 4.1 Models of Steel and Concrete Material

Elasto-plastic law model and a model proposed by Hsu – Hsu [6] are selected as model of steel and concrete, respectively. In the elasto-plastic law model, stress-strain relationship is defined by the *Young's* modulus and tensile yield strength $f_y$ as shown in Fig. 2b. In the model of Hsu – Hsu, stress-strain curve is derived based on experimentally verifying process. The model describes the stress-strain relationship under uni-axial compression using the maximum compressive strength ($\sigma_{cu}$). Figure 2 defines the ultimate compressive stress ($\sigma_{cu}$), and strain ($\varepsilon_0$) at $\sigma_{cu}$.The ultimate compressive stress is determined based on experiment results, $\sigma_{cu} = f_c^{'}$.

Figure 2 presents that a linear stress-strain relationship which obey Hooke's law is assumed up to 50% of the ultimate compressive strength ($\sigma_{cu}$). Then, the stress-strain curve between the yield point (0.5 $\sigma_{cu}$) of descending portion and the end point (0.3 $\sigma_{cu}$) of ascending portion is formulated by Eq. (1). The strain corresponds to the stress at 0.3 $\sigma_{cu}$ in the descending portion is called as $\varepsilon_d$.

$$\sigma_c = \left(\frac{\beta(\varepsilon_c/\varepsilon_0)}{\beta - 1 + (\varepsilon_c/\varepsilon_0)}\right) \tag{1}$$

Where $\varepsilon_c$ is compressive stress, the parameter $\beta$ and the strain at peak stress $\varepsilon_0$ is given by Eq. (2), and Eq. (3). Values of $\sigma_c$, $\sigma_{cu}$, $E_c$ are in ksi.

$$\beta = \frac{1}{1 - (\sigma_{cu}/\varepsilon_0 E_0)} \tag{2}$$

$$\varepsilon_0 = 1.291 \times 10^{-5}\sigma_{cu} + 2.114 \times 10^{-3} \tag{3}$$

The stress-strain numerical model for concrete under tension is also described in the Fig. 2. It is based on the maximum tensile strength ($\sigma_{cr}$) and strain corresponding to the maximum tensile strength ($\varepsilon_{cr}$). The maximum tensile strength is estimated based on compression strength of prismatic shape specimens ($f_c^{'}$) as clause 9.5.2.3 of ACI 318. Maximum tensile strength is estimated following Hooke's law.

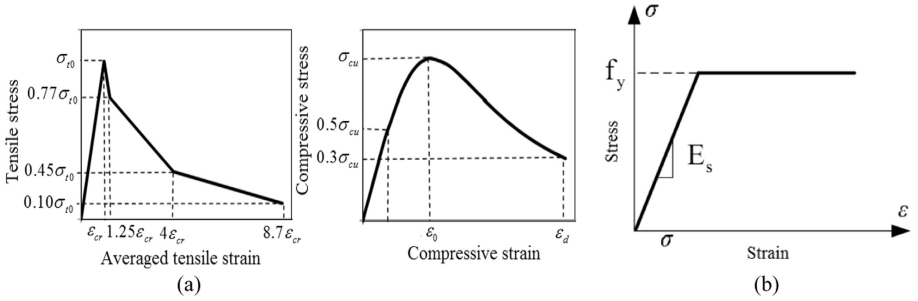


**Fig. 2.** Material models: (a) Stress-strain curve for concrete under tension and compression, (b) Elasto-plastic constitutive law of reinforcement.

For steel slag concrete, modulus $E_0$ is given by Eq. (4) [7].

$$E_o = 0,040231\gamma^{1.5}\sqrt{f_c'} + 7291,65 \text{ (MPa)} \quad (4)$$

Where, $\gamma$ is the density of concrete in kg/m$^3$, and $f_c'$ is compression strength in MPa.

### 4.2 Models Validation

Figure 3 shows the comparison results between experiment and simulation. The curves in Fig. 3 show relationship of loading and deflection of beam at mid-span. There is a gap between curve obtained from experiment and that of simulation. The largest gap is approximately 5%. It may be caused by the assumption of fully bonding between reinforcement steel and concrete. The small gap value indicates that beam models are verified and they could be employed for reinforcement steel exploration.

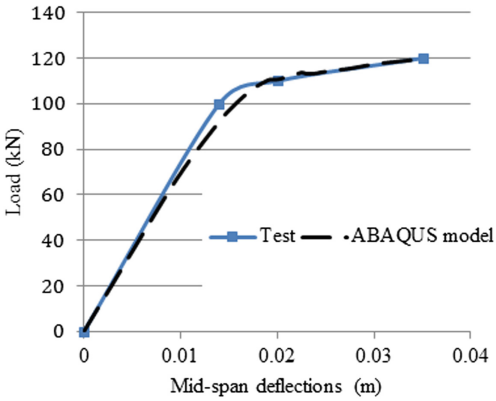


**Fig. 3.** Mid–span deflection versus bending load.

## 5 Exploration of Stress in Steel Bars

Stresses in reinforcement steels are determined based on simulation models. As tensile stress in steel bars is always increased following bending load, stresses are explored from initial to the load causing beam broken. Stresses in reinforcement steels of RCBs and SRCBs are presented in a diagram for comparison.

### 5.1 Stress in Reinforcement Steel Bars

It could be seen from the curve of SRCB in Fig. 4 that stress of reinforcement steel is in elasticity zone with the bending load less than 86 kN. It is about 0.36 kN/cm$^2$ at a load of 86 kN. After the level of 86 kN, stress in reinforcement bar increases a little although bending load keeps increasing. Reinforcement steels work in plastic zone (the yield

plateau). After the yield plateau, stress again increases with bending load increasing until the beam completely failure.

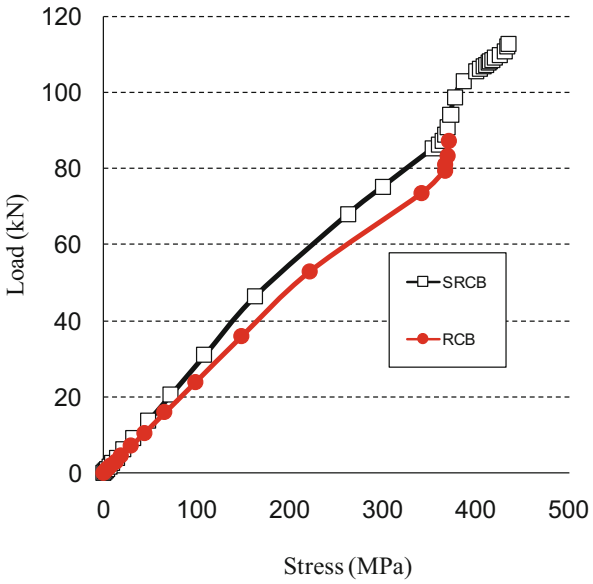


**Fig. 4.** Longitudinal reinforcement steel stresses in SRCB and RCB.

In case of RCB, the relationship of bending load and stress in reinforcement steel is a linear line as the bending load less than 78 kN. Stress is about 0.37 kN/cm$^2$ at a load of 78 kN. Then, stress in reinforcement bar increases a little until the beam is completely failure. Beam is broken at the load 78 kN, which is higher than the design load of 60 kN. Beam is broken as the stress in longitudinal reinforcement steel is in the yield plateau.

Figure 4 shows that stress in longitudinal reinforcement steel of RCB, conventional concrete, is higher than that of steel slag concrete with the same level of bending load.

Table 2 summaries the percent difference of stress in longitudinal reinforcement steel bars corresponding to bending load. Table 2 shows that stress in reinforcement steel of SRCB is higher than stress in the reinforcement steel of RCB about 12.5%.

**Table 2.** Percent difference of stress in longitudinal reinforcement steel bars

| Load (kN) | 20 | 40 | 60 | 80 |
|---|---|---|---|---|
| Reinforced stress in SRCB (kN/cm$^2$) | 700 | 1350 | 2230 | 3250 |
| Reinforced stress in RCB (kN/cm$^2$) | 800 | 1600 | 2650 | 3660 |
| Percent difference of stress (%) | 12.5 | 15.6 | 15.8 | 11.2 |

Figure 5 shows the relationship of bending loads and stresses in stirrup bars of a SRCB. Stresses in stirrup bars located at mid-spans of beam increases quickly after tensile stresses in the longitudinal reinforcement bars reach the yield plateau, while stresses in stirrup bars in ends of beam are still increase linearly. This behavior may reasonable since this is three-point flexural test. The maximum tensile stress in stirrup bars is about 56% of those in the longitudinal reinforcement steel bars as the beam broken. Based on analysis results, the steel grade used for the stirrup bars in a SRCB could be selected lower than the steel grade of longitudinal reinforcement steel bars.

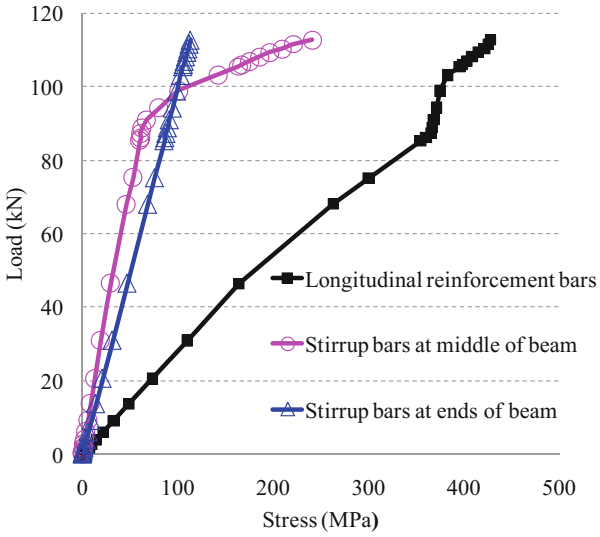


**Fig. 5.** Relationship of bending load and stresses in stirrup bars.

## 5.2 Crack Width

The cracks in the beam are quite important since they affect the strength of beam and causes corrosion of the reinforcement. The crack widths developing in a bending beam are usually related to stress in longitudinal reinforcement steel bars, so crack widths under bending load are explored in the section. Crack width is calculated according to stress in longitudinal reinforcement steel bars as showed in Eq. 5. The equation is utilized as crack widths are smaller than 0.3 mm.

Analysis results are presented in Fig. 6a. With crack widths over 0.3 mm, they are estimated directly based on beam's image taking during experiment. Measured crack widths are presented in Fig. 6b. The crack width of SRCB will be surveyed and compared to the cracks of RCB in Fig. 6.

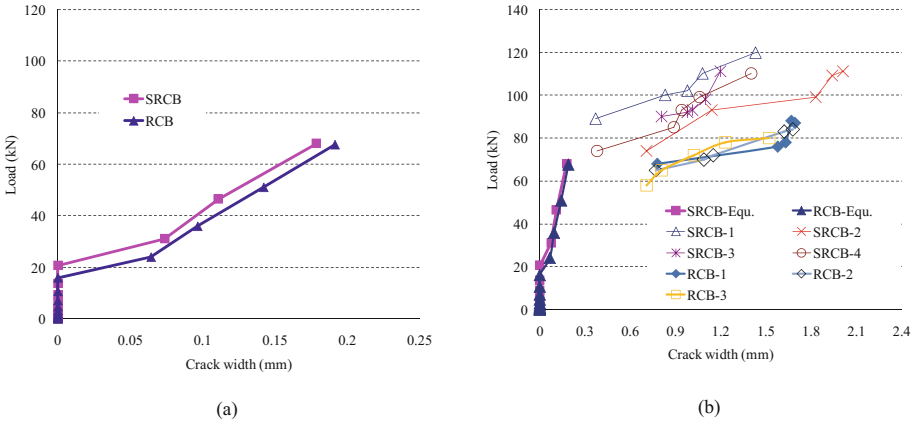


**Fig. 6.** Relationship of bending load and crack widths: (a) crack width under 0.3 mm, (b) crack width over 0.3 mm.

$$w = 1,3 \times 10^{-6} f_s \sqrt[3]{d_c A} \tag{5}$$

Where, $d_c$ is protective layer thickness estimated up to centre point of tensile steel group; A is area of concrete that cover a steel bar in beam; and $f_s$ is stress in longitudinal reinforcement steel bar.

Figure 6 shows crack does not appear as the bending load is still small. Crack appears as the tensile stress in the concrete is higher than tensile strength of concrete. In Fig. 6, cracks develop as load increasing over 18kN with RCB and over 20kN with SRCB. It indicates that tensile strength of SRCB under bending load is little bit higher than that of RCB. However, there are not much difference in crack widths between SRCB and RCB. As crack widths developing under 0.3 mm, crack widths of SRCB is smaller than that of RCB. And crack widths of SRCB and RCB are equivalent each other as crack widths developing over 0.3 mm as shown in Fig. 6b.

## 6 Conclusions and Remarks

In the paper, behavior of stress in reinforcement steel is explored for concrete beams with and without steel slag. According to the analysis results, the followings are concluded:

- Results of the experiments indicate that slag aggregate concretes achieved higher values of compressive strength, flexural strength compared to natural aggregate concretes.
- Stress in longitudinal reinforcement steel of conventional concrete is higher than that of steel slag concrete with the same level of bending load. The percent difference of tensile stresses is about 12.5%.

- In the concrete beam of steel slag, the maximum stress of stirrup bars is about 56% of those in the longitudinal reinforcement steel bars as the beam broken.
- Crack widths of slag aggregate concretes are similar to those of conventional concretes. Although crack in the conventional concrete beams may be initiated earlier than crack in the slag aggregate concrete beams.

Recycling steel slag as aggregate in concrete not only improves mechanical properties of concrete as noticed in previous researches, but also helps reinforcement steel bars working efficiently. Since the number of experiment examples is small, further experiments would be necessary.

**Acknowledgement.** This research was partially supported by HCMUTE. We thank our colleagues from Faculty of Civil Engineering who provided insight and expertise that greatly assisted the research.

## References

1. TCVN 1771-1987: Fine and coarse aggregates, grovels – technical requirements. Vietnamese standard, Vietnam (1987)
2. TCVN 6227-1996: ISO standard sand for determination of cement strength. Vietnamese standard, Viet Nam (1996)
3. TCVN 1770-1986: Sand for construction - technical requirements. Vietnamese standard, Vietnam (1986)
4. TCVN 5574-2012: Concrete and reinforced concrete structures – design standard. Vietnamese standard, Vietnam (2012)
5. Alizadeh, R., Chini, M., Ghods, P.: Utilization of EAFS as aggregate in concrete – Environmental issue. In: Sixth CANMET/ACI International Conference on Recent Trends In Advanced Concrete Technology, Bucharest, Romania, pp. 451–464 (2003)
6. Hsu, L.S., Hsu, C.-T.T.: Complete stress-strain behavior of high-strength concrete under compression. Mag. Concr. Res. **46**, 301–312 (1994)
7. Hang Nguyen, T.T.: The bending behavior of steel slag concrete beams. Magazine of Constructor, Vietnam (2015)
8. Abaqus Theory Manual Version 6.13. ABAQUS Inc (2013)

# Application of Empirical Models to Optimizing Concrete Pumpabiltity

Tien-Tung Ngo[1(✉)], Chanh-Trung Mai[2], El-Hadj Kadri[1], and Abdelhak Kaci[1]

[1] Laboratory L2MGC (4114), University of Cergy Pontoise, F9500 Cergy Pontoise, France
{tien-tung.ngo, el-hadj.kadri, abdelhak.kaci}@u-cergy.fr
[2] The University of Da Nang, University of Science and Technology, 54 Nguyen Luong Bang, Da Nang, Vietnam
mctrung@dut.udn.vn

**Abstract.** Pumbability of freshly-mixed concrete is a great challenge in the construction field; this attracts a growing number of researchers willing to study. This study pays attention on the use of empirical models that are established from the experimental data to evaluate the concrete pumpability. The purpose of the study is to reduce the amount of cost and time involved in the project construction. The models permit to directly estimate interface parameters (i.e., the viscous constant ($\eta$) and the interface yield stress ($\tau_{0t}$)) from the concrete formulation. These parameters directly affect the interface friction ($\tau$) between the concrete and the wall of the pumping pipe, and thus the concrete-mix mobility (i.e., the pumping flow rate) can be improved by reducing the interface friction. The calculated interface parameters are then validated with measurement parameters using a tribometer. In this study, a parametric approach is also employed by varying formulation parameters such as water/cement ratio, cement paste volume, and aggregates/sand ratio of the concrete-mix. The obtained results demonstrates that the empirical model is reliable with a high precision. They permit to validate a theoretical approach to estimate and to optimize the pumping parameters and the concrete pumpability.

**Keywords:** Empirical models · Pumping parameter · Interface friction · Viscous constant · Interface yield stress · Concrete pumpabiltity

## 1 Introduction

Previous studies in the field of concrete pumping concluded that at the beginning of the pumping processes, where the pumping flow is low, concrete flows occur as a plug in the pumping pipe (e.g., Le 2014; Ngo et al. 2011; Morinaga 1973; Best and Lane 1980; Chapdelaine 2007; Kaplan 2000). In this case, the concrete moves by sliding thanks to a concrete boundary layer formed at the interface. From a theoretical point of view, pumping of concrete would not be possible without the formation of this layer (Morinaga 1973). When the pumping speed increases and the interface shear stress ($\tau$)

© Springer Nature Singapore Pte Ltd. 2018
H. Tran-Nguyen et al. (eds.), *Proceedings of the 4th Congrès International de Géotechnique - Ouvrages -Structures*, Lecture Notes in Civil Engineering 8,
DOI 10.1007/978-981-10-6713-6_33

is higher than the concrete yield stress ($\tau_0$), the concrete zone near the wall starts to be sheared. In this case, the concrete moves by sliding and shearing in the pipe.

The relationship between the interface parameters and the interface shear stress that determines the pumping pressure has been presented by Kaplan 2000, as given by the following equation:

$$\tau = \tau_{ot} + \eta v \tag{1}$$

where $\tau$ is the interface shear stress (Pa), $\eta$ is the viscous constant (Pa.s/m), and $\tau_{0t}$ is the interface yield stress (Pa).

In order to measure these parameters, it is necessary to use a tribometer, as mentioned in (Morinaga 1973), Best and Lane (1980), (Chapdelaine 2007); Kaplan (2000), and (Ngo et al. 2009). Equation (1) shows an important role of the interface parameters on the pumping pressure. It shows that the viscous constant ($\eta = \partial\tau/\partial v$) determines the evolution of the interface shear stress with the pumping speed when the pumping regime is established, and the interface yield stress ($\tau_{0t}$) determines the initial pumping pressure which is necessary to initiate the concrete flow as discussed by Ngo et al. 2011.

This study estimates the interface parameters of ordinary concrete whose the rheological behavior can be described as Binghamian fluids (see among: Chapdelaine 2007; Kaplan 2000; Tattersall 1983; De Larrard et al. 1996; Ngo et al. 2010a; Feys et al. 2007; De Larrard and Belloc 1999; Ngo et al. 2010b). Based on a tribometer developed by Ngo et al. 2009, an experimental program has been carried out in which principal formulation parameters, e.g., water/cement, cement paste volume, aggregates/sand of the concrete-mix, have been varied. Empirical models used to calculate the interface parameters from the concrete formulation are proposed and validated using the experimental database.

## 2 Building of Experimental Database

### 2.1 Tribometrical Measurement

In this study, a tribometer developed by Ngo et al. 2009 is used to achieve the measurements. The apparatus is composed of three principal parts: (i) an agitator with electronic speed regulation and torque recording; (ii) a smooth steel cylinder of 10 cm height and 10.7 cm diameter; and (iii) a container of 20 cm height and 30 cm diameter (see Fig. 1(a)). The tribological test procedure is composed of 5 steps: (1) Fill the first concrete layer up to half of the container and pierce through this layer 25 times; (2) Locate the cylinder at the centre of the container and let it stand on the concrete surface by its own weight, the cylinder is then fixed to the agitator axis; (3) Measure the friction torque corresponding to different imposed velocities, as seen in Fig. 1(b); (4) Once step 3 is finished, fill the second layer on top of the first layer to the top of the container and pierce through this layer 25 times; (5) Repeat step 3 and record the new results.

(a)

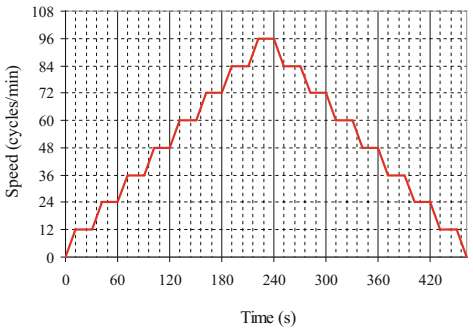


(b)

**Fig. 1.** The used tribometer and the imposed steed profile (Ngo et al. 2009)

The interface friction torque is obtained by subtracting results of step 3 from those from step 5. For each imposed speed level, the average interface friction on the cylinder circumferential area during the constant rotation speeds is obtained. The obtained interface friction torque is recorded for the decreasing speeds direction to identify the pumping parameters. The test results can be approximated by an empirical linear function as follows:

$$T = T_0 + k.V \tag{2}$$

where $T$ (N.m) is the applied torque to the revolving cylinder, $T_0$ (N.m) is the initial torque, $k$ (N.m.s) is the linear coefficient, and $V$ (cycles/s) is the cylinder rotating speed.

Using the the values of $T_0$ and $V$ (fundamental units) obtained from Eq. (2), in taking into account the cylinder shape and its dimensions, the interface parameters ($\tau_{0t}$ and $\eta$) can be calculated by Eq. (3):

$$\tau_{0t} = \frac{T_0}{2\pi R^2 h} \text{ and } \eta = \frac{k}{(2\pi)^3 R^3 h} \tag{3}$$

## 2.2 Experimental Program

All studied ordinary concretes in this work are produced with the cement CEM I 52.5 which is based on clinker without additions. A granular skeleton is formed by regular concrete sand with grain-size distributions of 0/4 mm and different crushed aggregates of grain-size distributions 10/20. All coarse aggregate and sand materials have specific gravities of 2.5. A super-plasticizers of the nature "polycarboxylate modified" is tested. For every studied series in this program, in order to highlight effect of each composition parameter on the pumping parameters, only one formulation parameter is varied while keeping other parameters constant. Table 1 collects the composition of tested concrete mixtures. The studied parameters are cement paste volume (series 1), water/cement (W/C) ratio (series 2), and aggregates/sand (A/S) ratio (series 3).

## 3 Analysis of Experimental Results

The results of the program are summarized in Fig. 2. Concerning the effect of the cement paste volume, Fig. 2(a) proves that the increase of the cement paste volume reduces the interface parameters; this promotes the concrete pumpability. The linear decrease of the viscous constant and of the interface yield stress can be explained by the augmentation of the inter distance between aggregate grains when the cement paste volume is more important. A higher inter distance favours the creation of the boundary layer at the interface concrete-wall of the pumping pipe, as discussed by Ngo et al. 2010a, 2012. In literature, this inter distance between aggregate gains ($E_{max}$) has been

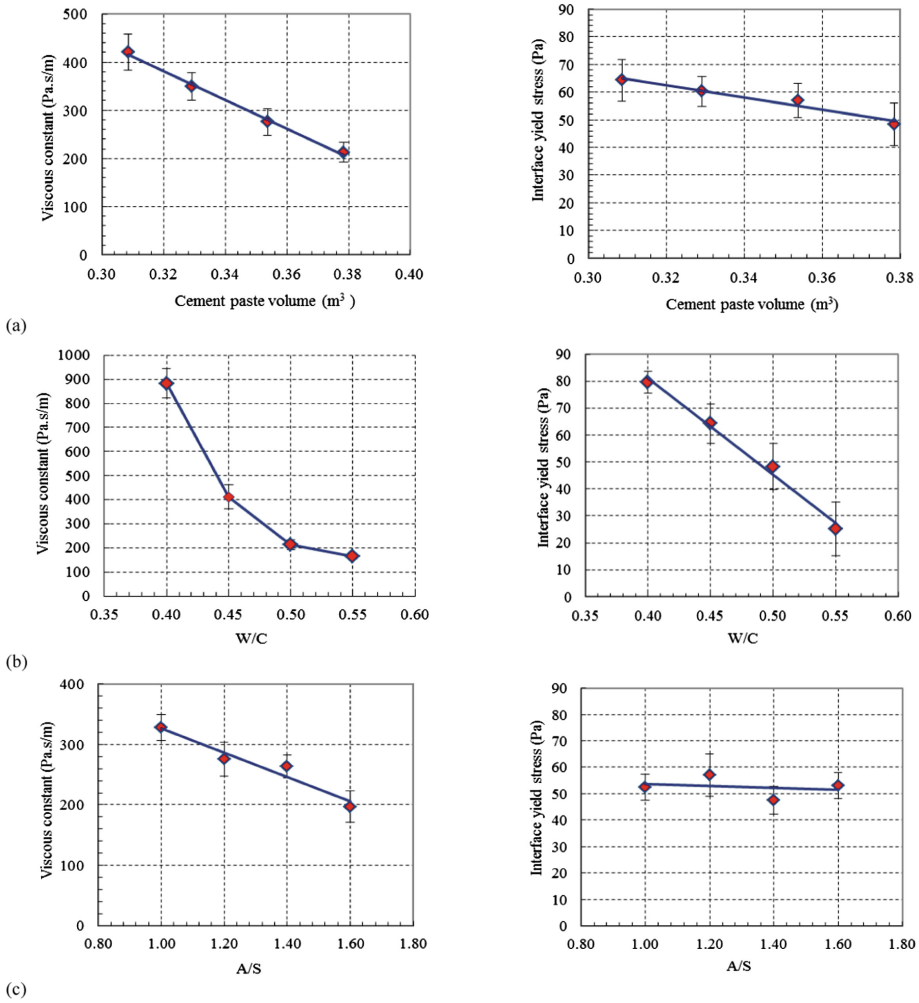


**Fig. 2.** Results of the experimental program: (a) Influence of the cement paste volume; (b) Influence of water/cement ratio; (c) Influence of aggregates/sand ratio.

described by a model (see De Larrard and Belloc 1999). The model also shows that this inter distance depends not only on the maximal size of the aggregates gains but also on the compactness of the granular mixture which vary with the aggregate size range and the A/S ratio in concretes.

It is also known that the W/C ratio plays an important role in concrete plastic viscosity that influences the formation of the boundary layer at the interface and thus the interface friction. Figure 2(b) shows that the interface parameters decrease with the increase of the W/C ratio, keeping the same cement paste volume and A/S ratio. In fact, when the W/C ratio increases, the cement paste of concrete is diluted and thus its plastic viscosity decreases. It promotes the formation of a boundary layer which is less viscous and thicker. Knowing that this layer is formed by cement, water and sand fines particles come from concrete during the test, as discussed by Ngo et al. 2010a. Consequently, a less viscous and thicker boundary layer reduces the interface friction and thus the interface parameters.

Concerning the A/S ratio, the increase of this ratio, keeping the same W/C ratio and the same cement paste volume, reduces the quantity of sand in concrete as shown in Table 1 (series 3). Therefore, the boundary layer is formed with less fine particles which is proceed from the sand of concrete. It diminishes the viscous constant when the A/S ratio increases (see Fig. 2(c)). Nevertheless, the interface yield stress is not so sensitive with the variation of the A/S ratio. That is probably due to the concrete slump which does not change when the A/S varies. More explanation for this phenomenon is provided in the conclusion of this article.

The analyses of the experimental results and of the parameters sensitivity, two empirical models have been proposed following:

(i) The viscous constant (η) model proposed is given by Eq. (4):

$$\eta = \frac{10^{(3{,}7\frac{\phi}{\phi^*}+0{,}37)}}{e_{boundary\quad layer}} \tag{4}$$

**Table 1.** Composition of tested concrete mixtures and results.

| Concretes | W/C | A/S | $V_{paste}$ ($m^3$) | Cement (kg) | Water (kg) | Agregates (kg) | Sand (kg) | Slump (cm) | $\eta_{exp.}$ (Pa. s/m) | $\tau_{0t\ exp.}$ (Pa) | $\eta_{model}$ (Pa. s/m) | $\tau_{0t\ model}$ (Pa) |
|---|---|---|---|---|---|---|---|---|---|---|---|---|
| B11 | 0.5 | 1.2 | 0.378 | 460 | 230 | 848 | 706 | 21 | 212.3 | 48.3 | 229.2 | 43.9 |
| B12 | | | 0.354 | 430 | 215 | 881 | 734 | 19 | 275.6 | 57.1 | 276.5 | 50.2 |
| B13 | | | 0.329 | 400 | 200 | 915 | 763 | 15 | 349.1 | 60.3 | 385.6 | 62.9 |
| B14 | | | 0.308 | 375 | 188 | 943 | 786 | 13 | 420.4 | 64.3 | 481.6 | 69.3 |
| B21 | 0.55 | 1.2 | 0.378 | 434 | 239 | 848 | 706 | 23 | 163.6 | 25.2 | 168.1 | 37.5 |
| B22 | 0.5 | | | 460 | 230 | | | 21 | 212.3 | 48.3 | 229.2 | 43.9 |
| B23 | 0.45 | | | 490 | 220 | | | 18 | 411.0 | 64.2 | 376.3 | 53.4 |
| B24 | 0.4 | | | 524 | 210 | | | 11 | 882.8 | 79.5 | 917.0 | 75.6 |
| B31 | 0.5 | 1 | 0.354 | 430 | 215 | 808 | 808 | 19 | 328.1 | 52.4 | 283.9 | 50.2 |
| B32 | | 1.2 | | | | 881 | 734 | 19 | 275.6 | 57.1 | 276.5 | 50.2 |
| B33 | | 1.4 | | | | 943 | 673 | 19 | 263.5 | 47.5 | 271.9 | 50.2 |
| B34 | | 1.6 | | | | 994 | 621 | 19 | 197.2 | 53.2 | 269.0 | 50.2 |

where

$$e_{\text{boundarylayer}} = \begin{cases} K.(1,18E_{\max} + 4,87) & \text{if} \quad 1,3 \text{ mm} \leq E_{\max} \leq 3,5 \text{ mm} \\ 9 \text{ mm} & \text{if} \quad E_{\max} > 3,5 \text{ mm} \end{cases} \tag{5}$$

$$K = \begin{cases} 1 & \text{if} \quad \text{slump} \geq 21 \text{ cm} \\ 0.048Sl & \text{if} \quad \text{slump} < 21 \text{ cm} \end{cases} \tag{6}$$

$$E_{\max} = D\left(\sqrt[3]{g^*/g} - 1\right) \tag{7}$$

where Φ, Φ* is the solid concentration and the maximum compactness of granular mixture, respectively; g, g* is the volumetric proportions and the maximum compactness of the granular mixture, respectively; and D is the maximum diameter of the aggregates (mm).

(ii) The interface yield stress model proposed is given by Eq. (8):

$$\tau_{0t} = 0.044\tau_{0t} + 6 - 14\frac{Sp}{Sp*} \tag{8}$$

where

$$\tau_0 = (300 - Sl)\frac{\rho_{sg}}{0.347} + 214 \tag{9}$$

where $\tau_0$ is the concrete yield stress (Pa); $S_p$ and $S_p$* are respectively the dosage and the saturation dosage of superplasticizer (%); ρ is the density of concrete; $\rho_{sg}$ is the specific gravity ($\rho_{sg} = \rho/\rho_{ref}$), and $\rho_{ref}$ is the density of water ($\rho_{ref}$ = 1000 kg/m$^3$ at 4 °C).

Table 1 and Fig. 3 represent the comparison between the interface parameters calculated by the model and that measured with the tribometer. The result shows that the two proposed models can predict well the interface yield stress and its evolution tendency when the concrete composition parameters vary. The calculated error of the viscos constant model is ±11% and that of the interface yield stress model is ±13%.

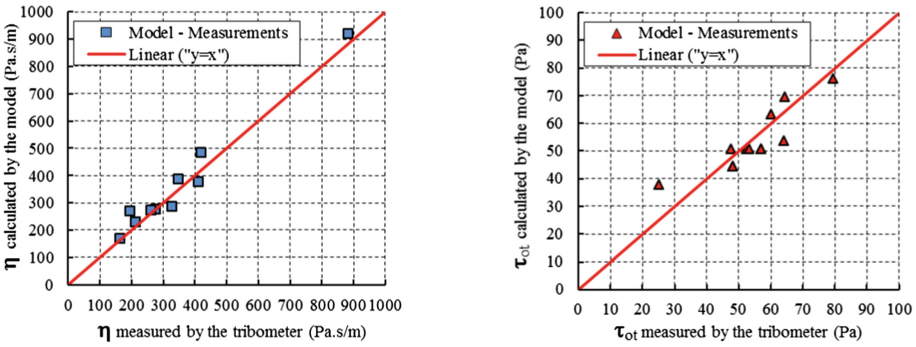


**Fig. 3.** Comparison of the interface parameters calculated by the proposed models (η model and $\tau_{0t}$ model) and measurements.

## 4 Conclusions

The important role of the interface parameters ($\tau_{0t}$ and $\eta$) on the pumping pressure has been presented in this study. Above mentioned tribometer developed by Ngo et al. 2009 has been used in order to investigate the variation of the interface yield stress ($\tau_{0t}$) according to the concrete composition parameters. According to the study results, it can be concluded that:

(i) The increase of the cement paste volume reduces the interface friction. It is confirmed by the decrease linearly of the viscous constant and of the interface yield stress.
(ii) When the W/C ratio increases, the viscous constant and the interface yield stress decrease following two different tendencies. The interface yield stress decreases linearly with the rise of the W/C ratio. However, the viscous contant reduces significantly following a non-linear function when the W/C ratio increases.
(iii) The increase of the A/S ratio results in a linear reduction of the viscous constant. Whereas, the interface yield stress is not so sensitive with the variation of the A/S ratio because there is a relation between this parameter and the concrete yield stress, which does not vary when the slump of the tested concrete is constant (see the proposed interface yield stress model).

Based on the experimental results, two empirical models have been proposed to directly calculate the pumping parameters from the composition parameters and the concrete slump with a good precision.

## References

Le, H.-D.: Etude de l'effet de la couche limite sur les profils de vitesse du béton pompé. Ph.D. University of Cergy Pontoise, France (2014)

Ngo, T.-T., Kadri, E.-H., Cussigh, F., Bennacer, R.: Measurement and modeling of fresh concrete viscous constant to predict pumping pressures. Can. J. Civ. Eng. **38**(8), 944–956 (2011)

Morinaga, S.: Pumpability of concrete and pumping pressure in pipelines. In: Paper Presented at the Proceedings of Rilem Seminar, Leeds (1973)

Best, J., Lane, R.: Testing for optimum pumpability of concrete. Concr. Int. **2**(10), 9–17 (1980)

Chapdelaine, F.: Étude fondamentale et pratique sur le pompage du béton. Ph.D. Faculty of the Higher Studies of Laval University, Canada (2007)

Kaplan, D.: Pompage des bétons, Etudes et recherches des laboratoires des Ponts et Chaussées. Rapp. LCPC, Paris, France (2000)

Ngo, T.-T., et al.: Influence de la composition des bétons sur les paramètres de pompage et validation d'un modèle de prévision de la constante visqueuse. Ph.D. University of Cergy Pontoise, France (2009)

Tattersall, G.H., Banfill, P.: The Rheology of Fresh Concrete, vol. 759. Pitman, London (1983)

De Larrard, F., Sedran, T., Hu, C., Szitkar, J., Joly, M., Derkx, F.: Evolution of the workability of superplasticised concretes: assessment with the BTRHEOM rheometer. In: Paper Presented at the RILEM Proceedings (1996)

Ngo, T., Kadri, E., Bennacer, R., Cussigh, F.: Use of tribometer to estimate interface friction and concrete boundary layer composition during the fluid concrete pumping. Constr. Build. Mater. **24**(7), 1253–1261 (2010a)

Feys, D., Verhoeven, R., De Schutter, G.: Evaluation of time independent rheological models applicable to fresh self-compacting concrete. Appl. Rheol. **17**(5), 56244–57190 (2007)

De Larrard, F., Belloc, A.: L'influence du granulat sur la résistance à la compression des bétons. Bull. Lab. Ponts Chaussées (219) (1999)

Ngo, T.-T., Kadri, E.-H., Cussigh, F., Bennacer, R., Duval, R.: Practical tribometer to estimate pumpability of fresh concrete. J. Asian Archit. Build. Eng. **9**(1), 229–236 (2010b)

Ngo, T.-T., Kadri, E.-H., Cussigh, F., Bennacer, R.: Relationships between concrete composition and boundary layer composition to optimise concrete pumpability. Eur. J. Environ. Civ. Eng. **16**(2), 157–177 (2012)

# Behavior of Concrete-Filled Hybrid Large Rupture Strain FRP Tubes Under Cyclic Axial Compression

Monika Nain[1], Mohanad M. Abdulazeez[1], and Mohamed A. ElGawady[2(✉)]

[1] Graduate Research Assistance, Department. of Civil, Architectural, and Environmental Engineering, Missouri University of Science and Technology, Rolla, MO 65409, USA
{mnb94, mma548}@mst.edu

[2] Benavides Associate Professor, Department. of Civil, Architectural, and Environmental Engineering, Missouri University of Science and Technology, Rolla, MO 65409, USA
elgawadym@mst.edu

**Abstract.** This paper experimentally investigates the behavior of concrete filled fiber reinforced polymer (FRP) cylinders under cyclic axial compression. The FRP used in this study were either Glass FRP or hybrid Large Rupture Strain (LRS-FRP) and conventional Glass FRP (GFRP). LRS-FRP are manufactured out of polyethylene naphthalate (PEN) and polyethylene terephthalate (PET) obtained from recycled plastics. Hence, they are much cheaper and environment-friendly than conventional GFRP or carbon FRP (CFRP). LRS-FRP has high tensile rupture strain (usually greater than 5%) compared to 1-2% for GFRP and CFRP. This study presents the results of a total of 5 specimens having different confinement ratios to investigate the behavior of concrete filled LRS-FRP or hybrid LRS-FRP and GFRP tubes in terms of ductility, ultimate strain, and strength improvement. The results showed that using LRS-FRP significantly improved the ductility of the confined concrete. However, the improvement in strength was limited. The hybrid confinement improves both the ductility and strength.

**Keywords:** Confinement · Concrete filled fiber reinforced polymer tube (CFFT) · Large rupture strain FRP · Cyclic loading

## 1 Introduction

Fiber Reinforced Polymer (FRP) composites have been found to be a very promising material in structural engineering because of their high strength, ductility, ease of installation and relatively low maintenance cost. The advantages also include its lightweight nature, corrosion resistance and excellent seismic resistance. Both the strength and the ductility of concrete can significantly increase by the lateral confinement form of FRP tubes, which applies tension on the FRP tube in the hoop direction.

© Springer Nature Singapore Pte Ltd. 2018
H. Tran-Nguyen et al. (eds.), *Proceedings of the 4th Congrès International de Géotechnique - Ouvrages -Structures*, Lecture Notes in Civil Engineering 8,
DOI 10.1007/978-981-10-6713-6_34

In the past few decades, rapid growth has been observed in the application of FRP-confining jackets for the strengthening/retrofit of reinforced concrete columns. Carbon FRP, Glass FRP and Aramid FRP are the most common commercially-used FRP composites (Youssf et al. 2014, Abdelkarim and ElGawady 2015a, Youssf et al. 2015, Moustafa and ElGawady 2016, Abdelkarim and ElGawady 2016) In recent years, a new type of FRP composite has emerged as an alternative to conventional FRPs (Dai et al. 2011; Anggawidjaja et al. 2006). This new type of FRP composite consists of polyethylene naphthalate (PEN) and polyethylene terephthalate (PET) fibers. They are much cheaper and more environmentally-friendly than the conventional FRP composites. PET and PEN FRP show bilinear stress-strain relationships between elastic and tangent moduli with large rupture strains that are greater than 6%. Hence, the new FRP composites are called large rupture strain FRPs (LRS-FRPs).

For the safe and reliable design of structural members, it is important to properly understand and model the stress-strain behavior of LRS-FRPs' confined concrete. Extensive study has been done in this field but it focuses exclusively on the monotonic behavior (Anggawidjaja et al. 2006, Dai et al. 2014). Studies that feature concrete-filled FRP tubes with PET and PEN that have large rupture strains could efficiently improve the ductility, irrespective of having low stiffness. In its ultimate state, the large strain allows the fiber composite to contribute enough shear force while avoiding fiber rupture (Anggawidjaja et al. 2006, Dai et al. 2014). It has also been observed that the LRS-FRP confined concrete's response increases almost linearly with an increase in the number of layers of FRP (Moon et al. 2012).

A large number of research projects have presented studies comparing the behavior of CFFTs with conventional FRPs (carbon, glass and aramid) and LRS-FRPs (PET & PEN), but very few researchers have thought of combining both of the FRPs materials in addition to studying the different combinations of both of the FRPs under monotonic axial compressive loading (Abdelkarim and ElGawady 2015b). The presented study introduces an experimental investigation into the behavior of concrete-filled hybrid LRS-FRP and GFRP tubes under cyclic axial compressive loading. This study is to explain the seismic behavior of such FRPs in terms of ductility and strength improvement.

## 2 Experimental Works and Instrumentations

A total of 5 specimens of different confinement ratios were made manually, via the wet layup method of developing of FRPs around the Sonotube, and concrete was poured in one batch of the FRP tubes. The variable in this test was the confinement ratio, or the number of layers. All of the cylinders had a cross section of 156 × 305 mm. The cylinders were tested after 28 days under cyclic axial compression (Table 1).

Five CFFT were fabricated manually through the wet layup process around the Sonotube, using epoxy to create a 30% overlap of the FRP layer. Three different types of FRPs, (Glass, PET and PEN) were used in different combinations. The properties of PET and PEN were determined from the coupon test, and the glass properties were

**Table 1.** Parametric study

| Cylinder Label | Parameter | Diameter (mm) | Height (mm) | FRP-layers | LRSFRP-thickness (mm) | Glass FRP thickness (mm) | f'c (MPa) | Confinement ratio |
|---|---|---|---|---|---|---|---|---|
| CG | Glass | 156 | 305 | 3 Layer (GLASS) | – | 3.81 | 48.2 | 0.58 |
| CH 1 | PET-Glass (in/out) | 156 | 305 | 2PET-1GLASS | 6.6 | 1.27 | 48.2 | 0.49 |
| CH 2 | PEN-Glass (in/out) | 156 | 305 | 2PEN-1GLASS | 6.1 | 1.27 | 48.2 | 0.57 |
| CH 3 | PET-Glass (out/in) | 156 | 305 | 1GLASS-2PET | 6.6 | 1.27 | 48.2 | 0.53 |
| CH 4 | PEN-Glass (out/in) | 156 | 305 | 1GLASS-2PEN | 6.1 | 1.27 | 48.2 | 0.57 |

**Table 2.** Properties of FRP types

| Properties | Glass | PET | PEN |
|---|---|---|---|
| Thickness (mm) | 1.27 | 3.3 | 3.0 |
| E2 (GPa) | 26.1 | 2.2 | 3.9 |
| Ultimate strain (%) | 2.2 | 7.6 | 5.9 |

provided by the manufacturer (TYFO® SHE-51) and used for investigation. Coupons of PET and PEN FRP composites were prepared and tested according to ASTM D3039 (Table 2).

All FRP cylinders were poured in one batch and compressive strength of concrete cylinders after 28 days was 55 MPa. The concrete mix design is shown in Table 3.

**Table 3.** Concrete mix

| w/c | Cement ($kg/m^3$) | Water ($kg/m^3$) | Fine aggregate ($kg/m^3$) | Coarse aggregate ($kg/m^3$) |
|---|---|---|---|---|
| 0.5 | 451 | 226 | 512 | 512 |

The hoop and axial strains of the cylinders were measured by installing strain gauges halfway (152 mm) up the cylinder. Both strain gauges were fixed at 8 positions at regular intervals. The respective position of the strain gauges is shown in Fig. 1(a).

Four pushpots, spaced equally, were installed in the middle third of the specimen for a local analysis of displacement, and two LVDTs were installed 180° apart at the top of the specimen to measure the global vertical displacement. The instrumentation layout is illustrated in Fig. 1(b).

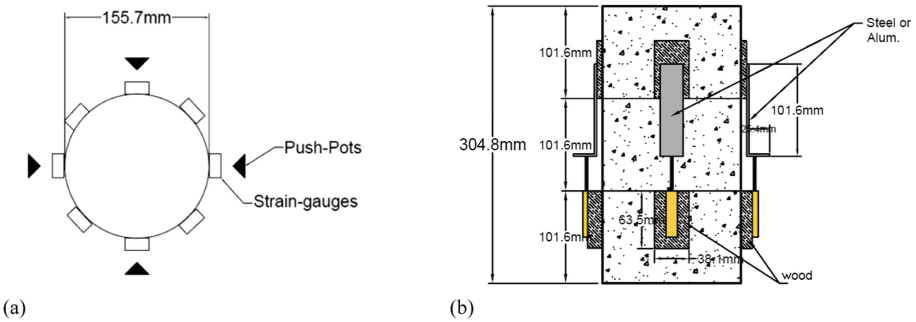


**Fig. 1.** (a) Positions of strain gauges, (b) Instrumentation layout

## 3 Test Loading Protocol

The cylinders were tested using MTS 2500 with a capacity of 2,225 kN. The displacement control was tested with a constant loading rate of 0.5 mm/min, and the cylinders were subjected to cyclic axial compression loading. The cylinders were loaded until the final rupture of the FRP, and the data from the strain gauges, pushpots and LVDTs were recorded by the data logger. The MTS 2500 was preloaded to 44.5 kN at the start of the test.

The four concrete-filled hybrid Large Rupture Strain FRP Tube specimens were tested under compression loading on a cyclic scheme as shown in Fig. 2. Each loading step was repeated for three cycles (Carter et al. 2014).

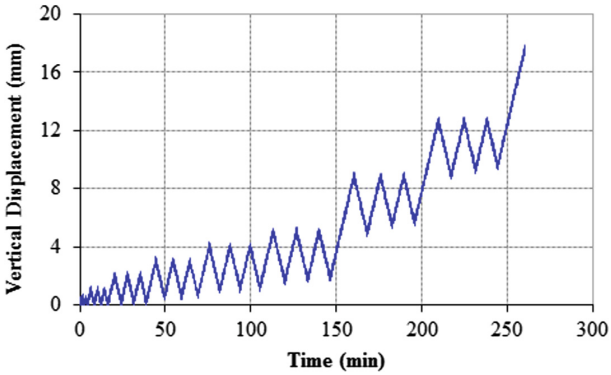


**Fig. 2.** Cyclic compression loading regime

## 4 Results and Discussions

The behavior of concrete-filled hybrid LRS-FRP and GFRP tubes under cyclic axial compressive loading was investigated. As compared to conventional FRP, the new hybrid FRP composites have a large rupture strain of 4-6%. The compressive strength

of the FRP cylinder was increased significantly, around three times, in relation to an unconfined concrete cylinder. The reason for this was the lateral confinement provided by the FRP tubes, which applies tension on the FRP tube in the hoop direction and prevents concrete failure. With the increase in strength, the hybrid system also improves the ductility and energy dissipation of the CFFTs to a large extent. This new hybrid system can be used to improve the seismic performance.

The Hybrid FRP system was investigated with different fiber sequences by placing GFRP at the inner surface (in) and PET FRP at the outer (out) surface and vice versa. The same installing sequence was repeated for GFRP and PEN FRP tubes. The concrete-filled hybrid LRS-FRP and GFRP tubes' test results are shown in Figs. 3, 4, 5, and 6.

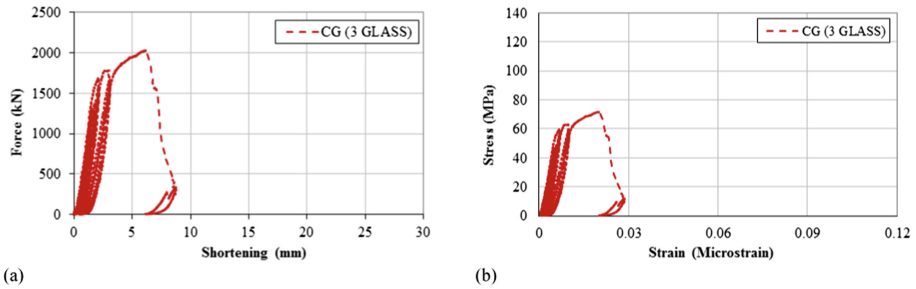


**Fig. 3.** CFFT sample CG (3GFRP) (a) Load - axial shortening curve; (b) Stress via strain curves

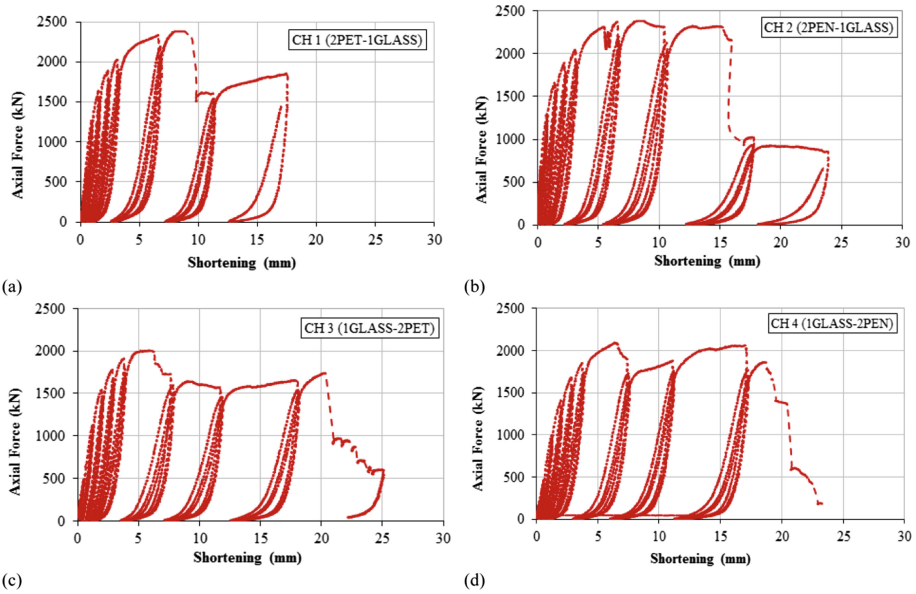


**Fig. 4.** Load - axial shortening curves of CFFT samples (a) CH1 (2 PET-1GFRP (in/out)); (b) CH 2 (2PEN-1GFRP (in/out)); (c) CH 3 (1GFRP-2PET (out/in)); (d) CH 4 (1GFRP-2PEN (out/in))

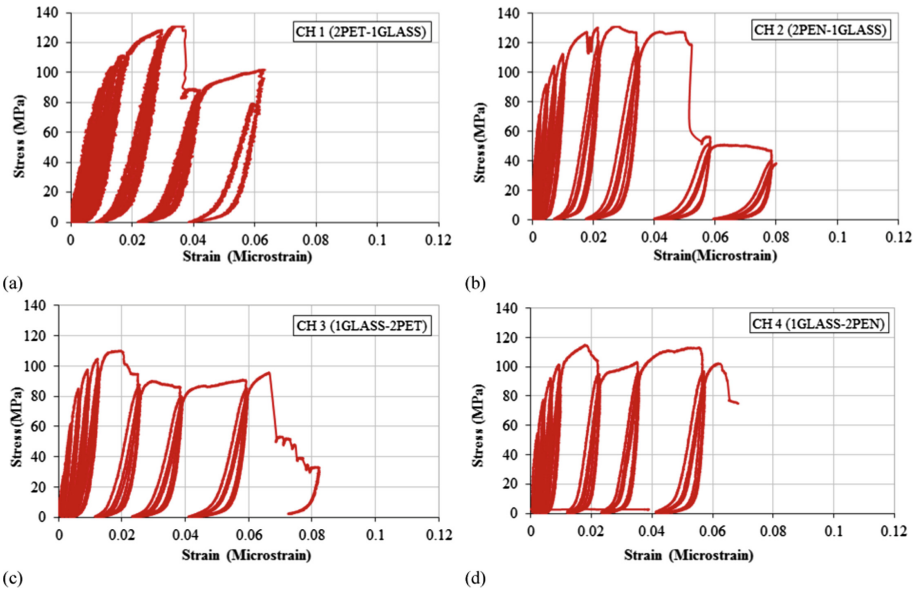


**Fig. 5.** Stress via strain curves (a) CH1 (2 PET-1GFRP (in/out)); (b) CH 2 (2PEN-1GFRP (in/out)); (c) CH 3 (1GFRP-2PET (out/in)); (d) CH 4 (1GFRP-2PEN (out/in))

Placing LRS FRP inside and GFRP outside improved the performance of such CFFTs in terms of strength and ductility. The reason for this was the difference between the rupture strain values. Since LRS FRP was placed inside, the outer GFRP was controlled by LRS FRP, which caused the rupture to take place at a higher hoop strain. However, when the GFRP was placed inside, it ruptured before the LRS FRP because of the lower rupture strain. Hence, LRS FRP is controlled by GFRP, which is ruptured at a lower strain (Figs. 5 (c and d) and 6 (d and e)).

Failure was caused by the rupture of FRP in the overlapping area. The reason could have been an improper bond or insufficient overlapping length. However, the rupture of the conventional FRP was very loud and sudden because of the linear elastic tensile stress-strain behavior of FRP. Failure in CFFTs with PET and PEN FRP jackets was also found in the hoop tensile of the FRP jacket, but it only made a very limited noise. In the case of LRS-FRPs, the rupture was found locally in the middle of the FRPs instead of over a large area as is the case of conventional FRPs. This explains the noise difference between LRS-FRP and conventional FRP (Figs. 6 (b and c)).

In the case of hybrid FRP systems, when LRS FRP was inside and GFRP was outside, the failure was due to FRP rupture. However, when LRS FRP was outside and GFRP was inside, failure was initiated from overlapping layer slippage (Figs. 6(d and e)).

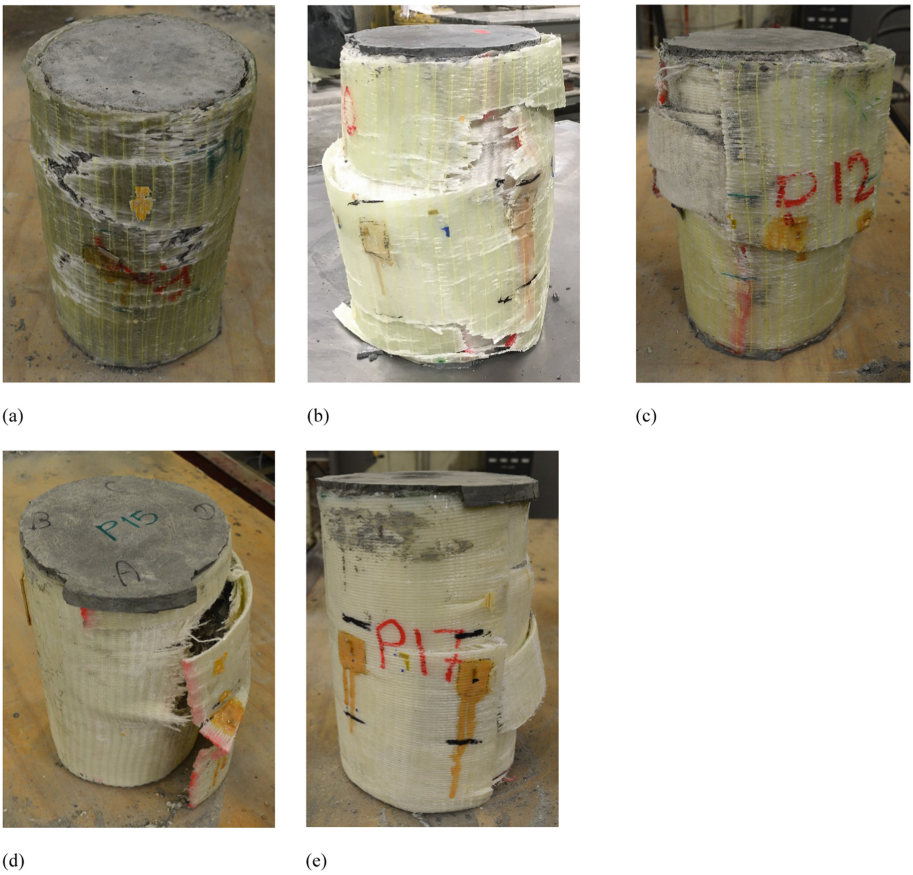


(a) (b) (c)

(d) (e)

**Fig. 6.** Failure mode of concrete filled tubes (a) 3GFRP; (b) CH1 (2 PET-1GFRP (in/out)); (c) CH 2 (2PEN-1GFRP (in/out)); (d) CH 3 (1GFRP-2PET (out/in)); (e) CH 4 (1GFRP-2PEN (out/in))

## 5 Conclusion

In this paper, an experimental study was investigated to explain the cyclic compressive behavior of concrete confined in a new hybrid FRP system. Placing LRS FRP inside and GFRP outside is effective in terms of strength, and the ultimate axial strain is also increased. This new hybrid system will be more effective and economical than using only conventional FRP. Out of PET and PEN FRP, PET FRP performs better in terms of axial strain because of its higher modulus of elasticity. Failure occurred due to slippage in the overlapping zone. To prevent slippage, research on the overlapping zone length and on the epoxy resin used for bonding is required.

In conclusion, the new hybrid LRS FRP and GFRP is a promising system for durability and strength; however, more research is required to study other characteristics such as fire resistance and energy dissipation. Behavior with different numbers of layers of FRPs can also be investigated.

## References

Youssf, O., ElGawady, M.A., Millsa, J.E., Ma, X.: Finite element modelling and dilation of FRP-confined concrete columns. Eng. Struct. **79**(15), 70–85 (2014)

Abdelkarim, O., ElGawady, M.A.: Analytical and finite-element modeling of FRP-concrete-steel double-skin tubular columns. J. Bridge Eng. 20(8), B4014005, ASCE (2015a)

Youssf, O., ElGawady, M.A., Mills, J.: Displacement and plastic hinge length of for FRP-confined circular reinforced concrete columns. Eng. Struct. **101**(456), 476 (2015)

Moustafa, A., ElGawady, M.A.: Strain rate effect on properties of rubberized concrete confined with glass fiber– reinforced polymers. J. Compos. Construct. 20(5), 04016014-1:13, ASCE (2016)

Abdelkarim, O., ElGawady, M.A.: Performance of hollow-core FRP-concrete-steel bridge columns subjected to vehicle collision. Eng. Struct. **123**, 517–531 (2016)

Dai, J.-G., Bai, Y.-L., Teng, J.: Behavior and modeling of concrete confined with FRP composites of large deformability. J. Compos. Constr. **15**, 963–973 (2011)

Anggawidjaja, D., Ueda, T., Dai, J., Nakai, H.: Deformation capacity of RC piers wrapped by new fiber-reinforced polymer with large fracture strain. Cem. Concr. Compos. **28**, 914–927 (2006)

Dai, J G., Bai, Y.L.: Large rupture strain (LRS) fibre reinforced polymer (FRP) composites for seismic retrofit of reinforced concrete (RC) piers. Adv. Compos. Bridge Constr. Repair 117–139, Woodhead, Cambridge, U.K. (2014)

Moon, J., Lehman, D.E., Roeder, C.W., Lee, H.-E.: Strength of circular concrete-filled tubes with and without internal reinforcement under combined loading. J. Struct. Eng. 139 (2012). doi:10.1061/(ASCE)ST.1943–541X.0000788

Abdelkarim, O., ElGawady, M A.: Concrete-filled-large deformable FRP Tubular columns under axial compressive loading. Fibers 3, 432–449 (2015b). doi:10.3390/fib3040432

Carter, J.D., Abdelkarim, O.I., ElGawady, M.A., Khayat, K.H.: FRP confinement of high strength self-consolidating concrete. In: 10th US National Conference on Earthquake Engineering, Alaska, USA. 2014

# Chemical Shrinkage Characteristics of Binder Pastes in Ultra High Performance Concrete Made from Different Types of Cement

Quoc Si Bach(✉)

Department of Civil Engineering, Danang College of Technology, University of Danang, 48 Cao Thang Street, Danang City, Vietnam
bachquocsi@gmail.com

**Abstract.** The using of silica fume replaces a part of cement in concrete production leading to the cement hydration mechanism in binder paste has changed. The hydration of cement and the accompanying phenomena such as heat generation, chemical shrinkage development are the results of interrelated chemical processes. Therefore, the chemical composition in pure cement directly affect to a specific concrete mixture.

The Reactive Powder Concrete (RPC) is Ultra-High Performance Concrete (UHPC). It is composed of the small aggregates and the ultrafine such as the silica fume (SF) for reaching a high compact. The high compact and the using less water in concrete can lead up to the high durability as well as ultra-high strength in the material concrete. The high durability and ultra-high strength of concrete with the using of silica fume for concrete production contributes to reduce environmental pollution.

In this paper, the characteristics of the development of chemical shrinkage from 2 days to 7 days in RPCs are analyzed. These RPCs are made from three different types of cement with different content of of mineral components in its. The analysis focuses on the characteristics of the hydration pore (as well as the chemical shrinkage) formation in concrete by time when the content of minerals composition in the cement changes.

The hydration pore model is calculated basing on the simulation program for microstructure development of cement-SF paste in the process of cement hydration. The program of the hydration is verified via measuring heat flux emitted from hydration process by isothermal calorimetry for all concrete samples containing different types of cement. As parallel, the development of the hydration pore (as well as the chemical shrinkage) is determined by experiment on measuring by gravimetry for these RPCs.

**Keywords:** Modeling · Cement paste · Concrete · UHPC · Chemical shrinkage · Hydration · Silica fume

## 1 Introduction

Chemical shrinkage is defined as the volume reduction associated with the reaction between cement and water in hydrating cement paste. For this phenomenon, the volume of the hydrate produced by the reaction between unhydrated cement and water is

© Springer Nature Singapore Pte Ltd. 2018
H. Tran-Nguyen et al. (eds.), *Proceedings of the 4th Congrès International de Géotechnique - Ouvrages -Structures*, Lecture Notes in Civil Engineering 8,
DOI 10.1007/978-981-10-6713-6_35

smaller than the total volume of the cement and water. The volume change of concrete is considered as the main mechanism leading to cracking in concrete and this make reducing the performance of the concrete. The effect of shrinkage on the performance of concrete in the early age is more meaningful when the hydration of cement is developing rapidly.

The hydration of cement is the chemical reaction of mineral components of cement with water. Therefore, the mineral constituents characteristics in cement regulate the chemical shrinkage characteristics in concrete. On the other hand, the characteristics of the cement hydration process are changed when the cement paste containing the types of mineral additive such fly ash, ground-granulated slag, and silica fume (SF). This due to these active puzzolans react with the hydration products of cement. The addition in the concrete by the active puzolans aims to improve the performance of concrete as well as contributing to reduce environmental pollution.

In this study, the chemical shrinkage characteristics of binder pastes in Ultra High Performance Concrete (UHPC) made from different types of cement were evaluated and analyzed. The evaluation and analysis based on the experimental results and the model results on the chemical shrinkage. Chemical shrinkage experiments were conducted on three UHPC samples which were made from of three different types of cement. Chemical shrinkage model is established on the hydration pore model which is built on the simulation of microstructure development in cement-SF binder paste. This simulation is calculated by the program of the hydration cement blended with SF and it is verified via mesuring emitted heat by isothermal calorimetry.

## 2 Materials and Methods

### 2.1 Materials

For producing the Reactive Powder Concrete (RPC), the materials used in this study are SF; the Quartz crushed (QB) with a maximum nominal size of 0.41 mm; the fine sand (SB); the Superplasticiser; and the ordinary Portland cement (OPC). Three clinkers were chosen from three types of OPC: Type I, Type II/V and Type IV (according to the ASTM classification) and their chemical compositions, physical properties, Bogue's composition are given in the Table 1. The characteristics of the concrete mixtures for studying are given in the Table 2. In the Table 2, these concrete mixtures used to make concrete samples. The samples are names as B1 to B3. All of these samples were tested on chemical shrinkage and on cumulative heat development at a temperature of 20 °C.

### 2.2 Measuring the Cumulative Heat Development by Isothermal Calorimetry

The heat of hydration was measured by the thermometric-isothermal calorimeter (TAM-Air). The Fig. 1 shows the schematic of measuring on the heat release from binder paste during the reaction process, this value is calculated by formula in Eq. (1). The hydration reactions of Portland cement is an exothermic process, and the total

**Table 1.** Chemical composition and physical properties of cementitious materials

| Chemical composition ratio by weight, (%) | | | | Mineral composition ratio by weight : $r(t_0)_{i/C}^{mass}$, (%) | | | |
|---|---|---|---|---|---|---|---|
| Item | OPC type I | OPC type II/V | OPC type IV | Item | OPC type I | OPC type II/V | OPC type IV |
| $SiO_2$ | 21.86 | 21.00 | 25.13 | $C_3S$ (Tricalcium silicate) | 62.501 | 60.08 | 44.23 |
| $Al_2O_3$ | 5.31 | 4.10 | 2.51 | $C_2S$ (Dicalcium silicate) | 15.522 | 14.87 | 38.67 |
| $Fe_2O_3$ | 3.43 | 3.70 | 3.48 | $C_3A$ (Tricalcium aluminate) | 8.268 | 4.60 | 0.76 |
| CaO | 66.34 | 63.50 | 63.03 | $C_4AF$ (Tetracalcium aluminoferrite) | 10.437 | 11.25 | 10.59 |
| MgO | 0.96 | 2.3 | 1.66 | $C\check{S}H_2$ (gypsum) | 1.3 | 1.3 | 1.3 |
| Cl | 0.02 | – | 0.01 | *Physical properties* | | | |
| $SO_3$ | 0.30 | 2.10 | 2.05 | Item | OPC type I | OPC type II/V | OPC type IV |
| $K_2O$ | 0.28 | 0.67 | 0.64 | Density: $\rho^C$, (g/cm$^3$) | 3.18 | 3.20 | 3.15 |
| $Na_2O$ | 0.10 | 0.09 | 0.04 | Blaine fineness: $\Phi^C$, (m$^2$/kg) | 372 | 382 | 347 |
| LOI | 0.09 | 2.01 | 1.25 | | | | |

**Table 2.** Mix proportions of concrete containing different amounts of silica fume

| Unit | Mass to cement ratio, [−] | | | Mass of 1 m$^3$, [kg/m$^3$] | | |
|---|---|---|---|---|---|---|
| Mix no. | B1 (Type I) | B2 (Type II/V) | B3 (Type IV) | B1 (Type I) | B2 (Type II/V) | B3 (Type IV) |
| Cement | 1.00 | 1.00 | 1.00 | 1030.68 | 1032.77 | 1027.51 |
| Sand | 1.1 | 1.1 | 1.1 | 1133.75 | 1136.05 | 1130.26 |
| Silica fume | 0.10 | 0.10 | 0.10 | 192.40 | 103.27 | 102.75 |
| Crushed quartz | 0.05 | 0.05 | 0.05 | 51.53 | 51.63 | 51.37 |
| Superplasticiser | 0.018 | 0.018 | 0.018 | 18.55 | 18.59 | 18.49 |
| Water | 0.16 | 0.16 | 0.16 | 164.91 | 165.24 | 164.40 |

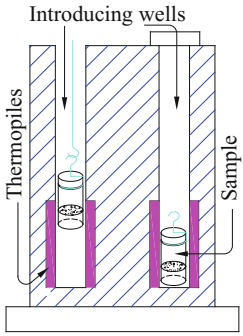


**Fig. 1.** Schematic of measuring on cumulative heat development during the reaction process of blended cement paste by the Thermometric-Isothermal calorimeter (TAM-Air)

amount of heat generated during the hydration reaction is used to measure the reaction degree of binder paste in Eq. (2). In Eq. (2), the $Q_{\mathrm{L}}^{com}$ is the total heat of reaction of the binder at complete reaction and calculated according to the Eq. (3). The ingredients in the Eqs. (1), (2) and (3) are defined as follows: $q(t)^{\mathrm{Test}}$ is rate of heat development at the instant (t); $P_C$ is the percentage by mass of cement in dry binder (cement-SF); $P_{SF}$ is the percentage by mass of silica fume in dry binder; $r(t_0)_{\mathrm{i/C}}^{mass}$ is the mineral composition ratio by weight of each phase "i" in cement; the $r(t_0)_{\mathrm{S/SF}}^{\mathrm{mass}}$ is the silicon dioxide composition ratio by weight in silica fume; $Q_i^{\mathrm{com}}$ is the maximum heat liberated when a mass unit of the phase "i" has hydrated completely; $Q_S^{\mathrm{com}}$ is the maximum heat liberated when a mass unit of the silica fume completely solubilized by pozzolanic reaction; the phase "i" is the clinker phase (i = $C_3S$, $C_2S$, $C_3A$, $C_4AF$) and the phase "S" is the silica dioxide (S = $SiO_2$ of silica fume). The values of $Q_i^{\mathrm{com}}$ and $Q_S^{\mathrm{com}}$ are referenced in (Lea et al. 1998; Taylor 1997; Maekawa et al. 2009).

$$Q(t)^{\mathrm{Test}} = \int_0^t q(t)^{\mathrm{Test}}.dt \tag{1}$$

$$\xi(t)_{binder}^{\mathrm{Test}} = \frac{Q(t)^{\mathrm{Test}}}{Q_{\mathrm{L}}^{com}} \tag{2}$$

$$Q_L^{com} = P_C \cdot \sum r(t_0)_{\mathrm{i/C}}^{mass} \cdot Q_{\mathrm{i}}^{com} + P_{SF} \cdot \sum r(t_0)_{\mathrm{S/SF}}^{mass} \cdot Q_S^{com} \tag{3}$$

### 2.3 Measuring the Chemical Shrinkage by the Weight Method

The Fig. 2 show the schematic of measuring the hydration pore in the binder paste during the reaction process. From the measurement results of hydrolysis pore, the chemical shrinkage can be calculated as the following Eq. (4).

$$S(t)_{Chemical_shrinkage}^{\mathrm{Test}} = \frac{V(t)_{Hy_pore}^{\mathrm{Test}}}{\left[M(t_0)^C + M(t_0)^{SF}\right]} \tag{4}$$

where: $S(t)_{Chemical_shrinkage}^{\mathrm{Test}}$ is the chemical shrinkage value at the instant (t) by experiment; $V(t)_{Hy_pore}^{\mathrm{Test}}$ is the volume of the hydration pore (chemical shrinkage pore) by measuring; the $M(t_0)^C$ is the initial mass of the cement in the sample; the $M(t_0)^{SF}$ is the initial mass of the silica fume in the sample.

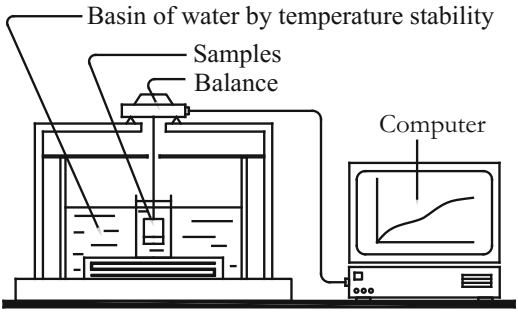


**Fig. 2.** Schematic of measuring on chemical shrinkage by the weight method

## 3 Hydration Kinetic Model for Portland Cement Containing the Silica Fume

### 3.1 Mechanism of the Hydration of Cement Containing the Silica Fume

$$C_3S + 5,3\,H \rightarrow C_{1,7}SH_4 + 1,3\,CH \quad \text{(A)}$$

$$C_2S + 4,3\,H \rightarrow C_{1,7}SH_4 + 0,3\,CH \quad \text{(B)}$$

$$C_3A + 3C\overline{S}H_2 + 26H \rightarrow C_6A\overline{S_3}H_{32} \quad \text{(C)}$$

$$C_3A + 0.5C_6A\overline{S_3}H_{32} + 2\text{H} \rightarrow 1.5\text{C}_4\text{A}\overline{\text{S}}\text{H}_{12} \quad \text{(D)}$$

$$C_3A + CH + 12\text{H} \rightarrow \text{C}_4\text{AH}_{13} \quad \text{(E)}$$

$$C_4AF + 2CH + 10H \rightarrow C_3AH_6 + C_3FH_6 \quad \text{(F)}$$

$$S + 1,7\,CH + 2,3H \rightarrow C_{1,7}SH_4 \quad \text{(G)}$$

The four main components of cement minerals include: $C_3S$, $C_2S$, $C_3A$, $C_4AF$. These mineral composition are hydrated when interacted with water. These chemical reactions are shown by simple chemical equations as describes for each compound with coexisting $C\overline{S}H_2$ (gypsum) in cement at ordinary temperature following from (A) to (F). For a pozzolanic reaction, the chemical reaction between $S$ (silica fume) and $CH$ (Portlandite) is described through the equation (G). These chemical reactions are occurring in a certain order is described as shown in Fig. 3. The descriptions of the cement hydration in the binder systems Cement – SF according to the equations of chemical reaction from (A) to (G) are referenced in (Lea et al. 1998) and (Taylor 1997).

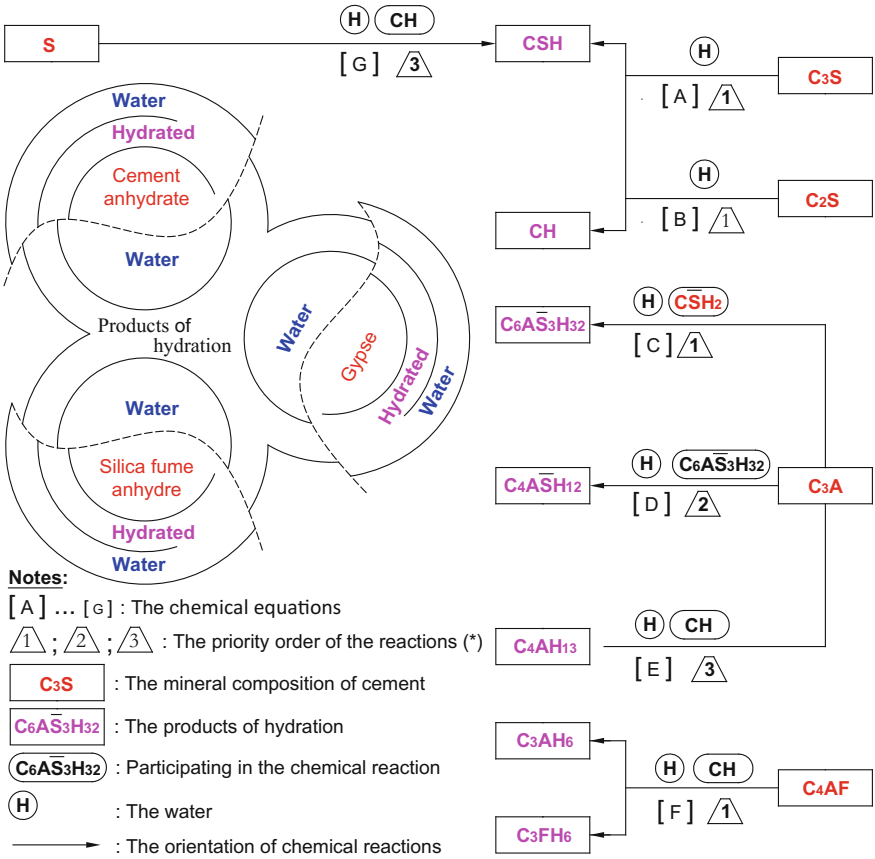


**Fig. 3.** The chemical reaction mechanism in a binder systems Cement - Silica Fume

### 3.2 Model of the Evolution of Phases in Binder Paste of UHPC

The evolution of the volume of the phases in the binder paste (cement and SF) during the reaction process are calculated as follows from Eq. (5) to Eq. (13). In these formulas, the model approach determinating the evolution volume of each phase in the binder paste (unhydrated cement and hydrates) are calculated basing on the evolution of the hydration degree of each mineral phase in cement.

$$V(t)_{\mathrm{Hy_i},S} = \xi(t)_{\mathrm{i},S} \cdot V(t_0)_{\mathrm{i},S} \tag{5}$$

$$V(t)_{\mathrm{Unhy_i},S} = \left[1 - \xi(t)_{\mathrm{i},S}\right] \cdot V(t_0)_{\mathrm{i},S} \tag{6}$$

$$V(t)^{\overset{e}{\leftrightarrows}}_{\text{Pro_hy_j}} = r^{\overset{e}{\leftrightarrows}}_{\text{i,S/j_stoichiometry}} \cdot \left(M^{\text{molar}}_{\text{i,S}} / M^{\text{molar}}_{j}\right) \cdot \left(\rho_{\text{i,S}} / \rho_{j}\right) \cdot V(t_0)_{\text{i,S}} \cdot \xi(t)_i \tag{7}$$

$$V(t)_{Hy} = \sum V(t)_{\text{Hy_i,S}} \tag{8}$$

$$V(t)_{Un_hy} = V(t_0)_{Dry_binder} - V(t)_{Hy} \tag{9}$$

$$V(t)_{\text{Pro_hy}} = \sum V(t)^{\overset{e}{\leftrightarrows}}_{\text{Pro_hy_j}} \tag{10}$$

$$V_{\text{E_gel}} = V_{\text{Pore_gel}} = 0.28.V_{CSH} \tag{11}$$

$$V_{\text{E_cap}} = V_{\text{Pore_cap}} = V(t_0)^{E} - V(t)_{\text{E_gel}} - V(t)_{\text{E_non_evaporable}} \tag{12}$$

$$V(t)^{Model}_{Hy_pore} = V(t_0)_{Binder} - V(t)_{Unhy} - V(t)_{\text{Pro_hy}} - V(t)_{Pore_cap} - V_{\text{Pore_gel}} \tag{13}$$

where: $\xi(t)_{\text{i,S}}$ are the hydration degree of the phase i and of the phase S ($SiO_2$ of silica fume) at time t and they are are referenced in (Bach 2014); $V(t)_{\text{Hy_i,S}}$ is the volume of hydrated of phase i (or S) of clinker at time t; $V(t)_{\text{Unhy_i,S}}$ is the volume of un-hydrated of phase "i" (or S) of clinker at time t; $V(t)^{\overset{e}{\leftrightarrows}}_{\text{Pro_hy_j}}$ is the volume of hydration products of phase j at t by the equation of chemical reaction e (e = [A], [B], [C], [D], [E], [F], [G]); $V(t)_{Hy}$ is the total volume of four major phases hydrated of dry-binder at t; $V(t)_{Un_hy}$ is the total volume of un-hydrated dry-binder at time t; $V(t)_{\text{Pro_hy}}$ is the total volume of the solid products of hydration in binder paste at time t; $V(t_0)_{\text{i,S}}$ is the initial volume of minerals constituent "i" (or S) of clinker; $r^{\overset{e}{\leftrightarrows}}_{\text{i,S/j_stoichiometry}}$ is the stoichiometry ratio between phase "j" and phase "i" in the reaction at the equation "e" (j is the phases of products of hydration: CSH, CH, …); $M^{\text{molar}}_{\text{i,S,j}}$ is the molar weight of each phase "i", "S" and "j"; $\rho_{\text{i,S,j}}$ is the density of each phase "i", "S" and "j"; $V(t_0)_{Dry_binder}$ is the initial dry-binder volume; $V_{\text{E_gel}}$ is the volume of gel water; $V_{\text{Pore_gel}}$ is the volume of gel pore; $V_{\text{E_cap}}$ is the volume of capillary water; $V(t)_{\text{E_non_evaporable}}$ is the volume of non-evaporable water; $V_{\text{Pore_cap}}$ is the volume of capillary pores; $V(t)^{Model}_{Hy_pore}$ is the volume of hydration pore at time t of binder by computational model.

### 3.3 Model of the Chemical Shrinkage

The predictive model for chemical shrinkage is calculated based on the computational model for the development of the volume of hydration pore. Therefore, the

computational formula for chemical shrinkage of the binder is calculated by the following formula:

$$S(t)^{Model}_{Chemical_shrinkage} = \frac{V(t)^{Model}_{Hy_pore}}{\left[M(t_0)^{C} + M(t_0)^{SF}\right]} \tag{14}$$

### 3.4 Model of the Heat Liberated and the Rate of Heat Evolution

When the blended cement is mixed with water, the chemical reactions occur with the exothermic. The predictive model of the heat liberated at time t for binder system during the reaction process are calculated following from Eqs. (15) to (19). And the rate of heat evolution at time t for binder system is determined according as the Eq. (20).

$$Q(t)_L = \ Q(t)_C \ + \ Q(t)_S \tag{15}$$

$$Q(t)_C = \ P_C \cdot \left[\sum_i r(t_0)^{mass}_{i/C} \cdot Q(t)_i\right] \tag{16}$$

$$Q(t)_S = \ P_{SF} \cdot \left[r(t_0)^{mass}_{S/SF} \cdot Q(t)_S\right] \tag{17}$$

$$Q(t)_i = \xi(t)_i \cdot Q_i^{com} \tag{18}$$

$$Q(t)_S = \ \xi(t)_S \cdot Q_S^{com} \tag{19}$$

$$\frac{dQ(t)_L}{dt} = \ P_C \cdot \left[\sum_i r(t_0)^{mass}_{i/C} \cdot Q_i^{com} \cdot \frac{d\xi(t)_i}{dt}\right] \ + P_{SF} \cdot \left[r(t_0)^{mass}_{S/SF} \cdot Q_S^{com} \cdot \frac{d\xi(t)_S}{dt}\right] \tag{20}$$

where: $Q(t)_L$ is the heat liberated at time t of dry-binder; $Q(t)_C$ is the heat liberated at time t of cement; $Q(t)_S$ is the heat liberated at time t of the silica fume. The $Q(t)_i$ is the heat liberated at time t of the each minerals constituent "i" in cement; the $Q(t)_S$ is the heat liberated at time t of the S in silica fume during the reaction process.

## 4 Results and Discussion

From the results of the heat liberated model and the rate of heat evolution model as described in Sect. 3.4, we perform comparison to the experimental results as described in Sect. 2.2, a typical result is shown in Fig. 4 for sample No. B1 which was made from OPC of Type I. A similar way for the chemical shrinkage, taking a comparison between the chemical shrinkage measuring results according to Eq. (4) and the chemical shrinkage calculation results according to Eq. (14), these comparisons are performed on all UHPC samples from No. B1 to No. B3 and we can see the typical in Fig. 5 for UHPC sample No. B1.

From the Fig. 4, we can comment that the experimental results and modeling results are closely together, this allows us to believe in the hydration kinetic model for Portland cement containig the silica fume as mentioned above. We can recognize that, in the formula (4) for calculating chemical shrinkage by experimental and in the formula (14) for calculating chemical shrinkage by modeling there are the grandeurs of hydration pore. In the Fig. 5, the concur of the results of measuring and calculating shows us the correctness of model chemical shrinkage. This means that the results modeled of hydration pore are very closely with the experimental results. In other words, the model of the evolution of the phases in UHPC according to Equations from (5) to (13) is very reliable. In addition, we can see the model of the evolution of the phases in UHPC according to Equations from (5) to (13) is shown in Fig. 6 for the typical UHPC No. B1.

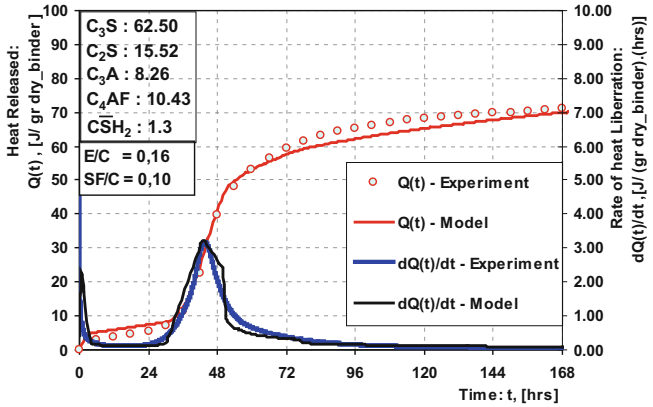


**Fig. 4.** Comparison between the measuring results and the calculation results on the heat liberated and the rate of heat evolution for B1.

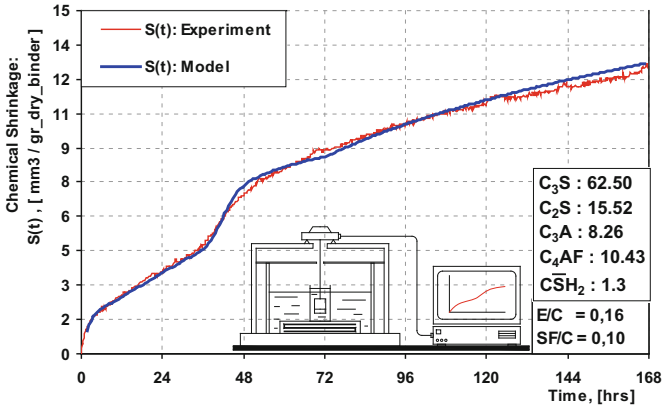


**Fig. 5.** Comparison between the chemical shrinkage measuring results and the chemical shrinkage calculation results for B1.

The experimental chemical shrinkages of the binder pastes on UHPCs (B1, B2, B3) made from different types of cement were shown in Fig. 7. In this Figure, the chemical shrinkage of the cement Type IV (B3) is lower than the cement Type II/V (B2) and the chemical shrinkage of the cement Type II/V (B2) is lower than the cement Type I (B1) in all time. And we also easily recognize that the reduction of the chemical shrinkage on the UHPCs goes along with the decrease of mineral composition content of C3A and C4AF in cement. The relationship between the (C3A + C4AF) content and chemical shrinkage of the binder pastes made with different types of cements studied is shown in Fig. 8 from 12 h to 168 h.

In this Figure, it illustrates that the chemical shrinkage is influenced clearly by the C3A + C4AF content and these relationships are strong for the age from 36 h to 168 h. As we pay attention to Fig. 4, the rate of heat evolution and the heat liberated during the hydration process of cement reache high values starting after 36 h. This due to the rapidly increased hydration degree of C3A and C4AF. The rise of hydration degree of C3A and C4AF lead to a rapid increase the chemical shrinkage in binder pastes. On the

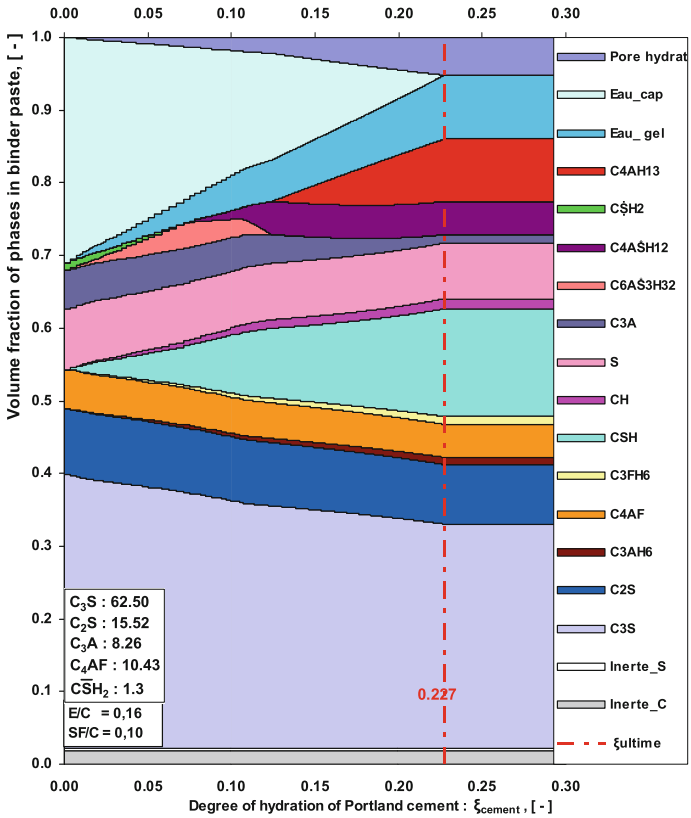


**Fig. 6.** The evolution of the volume fractions of the different component phases of a binder paste as function of the hydration degree of pure cement.

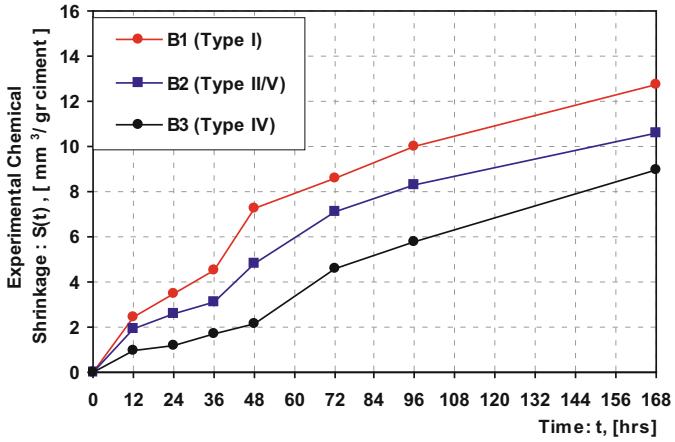


**Fig. 7.** Experimental chemical shrinkages on UHPCs made from different types of cement as function of time.

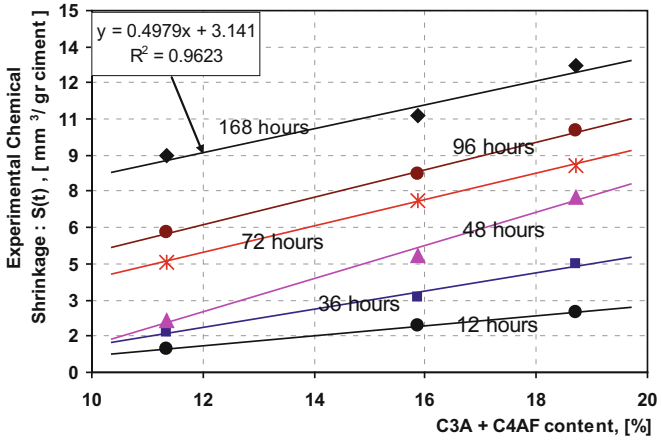


**Fig. 8.** Relationship between C3A + C4AF content and experimental chemical shrinkage.

other hand, the hydration a unit of mass of C3A and C4AF always lead to a volume of the chemical shrinkage which have a volume greater than when hydrating a unit of mass of C3S or and a unit of mass of C2S. This can be realized when we pay attention to the chemical reaction equations from (A) to (F) and the equations from (5) to (13) for computing microstructure development in binder pastes.

## 5 Conclusions

In this study, the chemical shrinkage characteristics of binder pastes in UHPC made from different types of cement have been investigated. The specific conclusions which can be drawn from the results of this study are as follows:

(i) A kinetic model for hydration of cement paste contains the silica fume is established and verified via measuring isothermal calorimetry.
(ii) The hydration pore in UHPC is calculated by the assistant a microstructure development model and compared with the experimental results. Each mineral component existing in UHPC consided in the microstructure development model.
(iii) The chemical shrinkage model of UHPC is calculated basing on the hydration pore model and the curves for predicting the chemical shrinkage agree well with the experimental results.
(iv) In the binder pastes in UHPC, the C3A composition and the C4AF composition in binder pastes play an important role in chemical shrinkage plays of binder pastes. Using the high content of C3A and C4AF in cement to produce UHPC will lead to the high chemical shrinkage.

## References

Arkamitra, K., Indrajit, R., Avinash, U., Julio, F.D.: Composite modeling to predict shrinkage of concretes containing supplementary cementitious materials from paste volumes. Constr. Build. Mater. **43**, 139–155 (2013). doi:10.1016/j.conbuildmat.2013.01.002

Bentz, D.P.: Modeling the influence of limestone filler on cement hydration using CEMHYD3D. Cem. Concr. Compos. **28**(2), 124–129 (2005). doi:10.1016/j.cemconcomp.2005.10.006

Brouwers, H.J.H.: Chemical reactions in hydrated ordinary portland cement based on the work by powers and brownyard. In: Proceedings 15th, International Conference on Building Materials, Weimar, pp. 553–566 (2003). purl.utwente.nl/publications/45404

Copeland, L.E., Kantro, D.L., Verbeck, G.: Chemistry of hydration of Portland cement. Tech Rep Bull 153, Res Lab of Portland Cement Association: Washington, USA (1960). doi:10.1.1.461.6808

Feldman, R.F., Huang, C.Y.: Properties of portland cement-silica fume pastes I. Porosity and surface properties. Cem. Concr. Res. **15**, 765–774 (1985a). doi:10.1016/0008-8846(85)90141-3

Feldman, R.F., Huang, C.Y.: Properties of portland cement - silica fume pastes II - mechanical properties. Cem. Concr. Res. **15**, 943–952 (1985b). doi:10.1016/0008-8846(85)90083-3

Fujii, K., Kondo, W.: Kinetics of the hydration of tricalcium silicate. J. Am. Ceram. Soc. **11**, 492–497 (1974)

Hamlin, M.J.: A Model for the microstructure of calcium silicate hydrate in cement paste. Cem. Concr. Res. **30**, 101–116 (2000). doi:10.1016/S0008-8846(99)00209-4

Kishi, T., Maekawa, K.: Multi-component model for hydration heating of blended cement with blast furnace slag and fly ash. Proc. JSCE **30**, 125–139 (1997)

Tazawa, E., Miyazawa, S., Kasai, T.: Chemical shrinkage and autogenous shrinkage of hydrating cement paste. Cem. Concr. Res. **25**, 228–292 (1995). doi:10.1016/0008-8846(95)00011-9

Lea, F.M., et al.: Lea's Chemistry of Cement and Concrete. Elsevier Butterworth-Heinmann, New York (1998)
Maekawa, K., Ishida, T., Kishi, T.: Multi-scale Modeling of Structural Concrete. Taylor & Francis, London (2009)
Taylor, H.F.W.: Cement Chemistry. Thomas Telford, London (1997)
Bach, Q.S.: Développement, caractérisation et modélisation des Bétons de Poudres Réactives à impact environnemental réduit. Thèse de Doctorat, Université de Nantes, France (2014)

# Chloride Binding Ability and Anti-corrosion Properties of Supersulfated Cement in Seawater/Sand Mixing Concrete

Khanh Son Nguyen[1(✉)], Anh Toan Nguyen-Phung[1], Hong Thai Le[1], Thanh Tri Ho[1], Tri Huynh Nguyen-Ngoc[1], Soon Poh Yap[2], Nobuhiro Chijiwa[3], and Nobuaki Otsuki[3]

[1] Department of Materials Engineering, BACH KHOA University – VNU HCM (Former Ho Chi Minh City University of Technology), Ho Chi Minh City, Vietnam
ksnguyen@hcmut.edu.vn

[2] Department of Civil Engineering, Faculty of Engineering, University of Malaya, Kuala Lumpur, Malaysia

[3] Department of International Development of Engineering, Tokyo Institute of Technology, Tokyo, Japan

**Abstract.** In this study, we aim to shift attention to ability of chloride binding of supersulfated cement and its use for formulating sea water/sand mixing concrete. To formulate SSC cement, slag as main component is activated by high alkaline of C-H and the following reaction with $SO_4^{2-}$. Material analysis (XRD, SEM/EDX) showed that effectively low-Ca-ettringite products were formed abundantly at early age and others chloride binding products such as Friedel's salt, hydrotalcite in their turn were resulted at later age in high $Cl^-$ solution. Notable high ratios of bound $Cl^-$ on total $Cl^-$ indicate eventually capacity of hydrated cement matrix in neutralizing chloride content in seawater. As an addition, very low $Cl^-$ permeability of mortar specimen could be taken into account. By monitoring the corrosive state of embedded steel bar $\phi$8 mm (inside mortar prism 40 × 40 × 160 mm, with seawater exposure condition), we observe no major deterioration due to such natural anti-corrosion phenomenon.

**Keywords:** Supersulfated cement · SSC · Chloride binding · Seawater mixing concrete · Concrete durability

## 1 Introduction

In practice, aggressive solution in surrounding environment might affect to durable character of reinforced concrete elements. Hence, the impact of seawater conditions is one of the most important research topics among the community of civil engineer all over the world. First investigation on sea water/sand mixing concrete began in some country where they had the same situation lack resource of river sand or with fresh-water shortage such as construction in remote island. For example, in Japan, the technical committee of JCI (in September 2015) already concluded on the use of sea water in concrete in their country as follow: (i) in the case of plain concrete, seawater

© Springer Nature Singapore Pte Ltd. 2018
H. Tran-Nguyen et al. (eds.), *Proceedings of the 4th Congrès International de Géotechnique - Ouvrages -Structures*, Lecture Notes in Civil Engineering 8,
DOI 10.1007/978-981-10-6713-6_36

can be used almost 100%; (ii) in the case of reinforced concrete, there is a good possibility to used seawater with appropriate mineral admixtures; (iii) with stainless steel, even in reinforced concrete, seawater can be used almost 100%; (iv) in some cases, the performance of concrete may be better with the use of seawater. Furthermore, the committee hoped that those conclusions will contribute to the use seawater as one of the ways to save freshwater resources in Japan and more particularly in countries with freshwater shortages in the near future (Japan Concrete Institute 2015).

In Vietnam, there exists a priority to expansion of marine economy from the central government. Ultimate objective is taking advantage of natural geography of our country with 3000 km of seacoast and hundred far islands. Such evidence coupled with the global context of climate change and raising sea level in Mekong delta pose extensively the problem of concrete durability in infrastructural development. To formulate special cement type that refers to practical usage in sea water environment attract much attention from local material engineer. As mentioned in the literature, supersulfated cement (SSC) is fundamentally different from ordinary Portland cement (PC) in term of production and usage. The production of SSC consists of intergrinding a mixture of 80 to 85 percent of granulated blast-furnace slag (GBFS) with 10 to 15 percent of calcium sulfate (in the form of dead-burnt gypsum or anhydrite) and up to 5 percent of PC clinker (Hewlett 2003). Remarkable performance of SSC includes its high resistance to sulfates solution, peaty acids or oils in sea water, ground water and others contaminated soil (Neville 2011). That is also the reason why they used SSC in concreting structural elements of municipal sewage system and port harbor. Moreover, considering its low $CO_2$ impact, supersulfated cement contains in general more than 70% blast furnace slag instead of sintering clinker, is a very good candidate for sustainable production (Stark et al. 1999). Most of research issues about supersulfated cement aim to optimize formulation of SSC to appropriate application in civil engineering (Phelipot-Mardelé et al. 2015).

In the following paragraphs, we conduct studies on the durable behavior of mortar samples that were formulated from SSC as binder, fine aggregate of seawater sand and were cured in sea water environment. Considering the previous results (Nguyen et al. 2016), we supposed to use proportional mixture of SSC as follow: 82.5%wt GBF Slag, 15.5%wt anhydrite, 1%wt PC clinker and 1%wt hydrated lime. We combine the investigation of composition of hardened cement product (small scale) and of the performance of anti-corrosion of mortar samples. Ability of chloride binding of SSC in seawater condition will be particularly discussed on, in order to expanse the laboratory proven study to the sea water/sand mixing concrete manufacturation in the context of infrastructural development in coastal area and island in Vietnam.

## 2 Formulating SSC and Methodology

### 2.1 Raw Materials and Formulation of SSC

Starting material for mix design includes GBF Slag, synthesized anhydrite, Portland cement clinker and hydrated lime. With regards to the hydration mechanism of SSC, the reaction between slag and calcium sulfate is followed by primary dissolution of slag

in alkali solution (Matschei et al. 2005). The following Table 1 tabulated some intrinsic properties of raw materials that we used in this study.

**Table 1.** Main physical, chemical, and mineralogical characteristics of 4 starting materials

| | GBF Slag | Anhydrite | PC clinker | Hydrated lime |
|---|---|---|---|---|
| *Physical properties* | | | | |
| Mean diameter, µm | 30 | 100 | 32 | 6.5 |
| Blaine surface area, $cm^2/g$ | 4270 | 2950 | 3740 | - |
| % retained on 45 µm sieve, % wt | 3.4 | 50.5 | 2.32 | 1.5 |
| Specific gravity, $g/cm^3$ | 2.91 | 2.32 | 3.17 | 2.62 |
| *Chemical composition (%wt)* | | | | |
| $SiO_2$ | 33.65 | 2.00 | 22.27 | 0.13 |
| $Al_2O_3$ | 15.60 | 1.00 | 4.11 | - |
| CaO | 42.14 | 49.68 | 61.87 | 71.7 |
| $SO_3$ | 0.16 | 46.27 | 1.18 | - |
| MgO | 6.40 | 0.16 | 2.21 | 0.99 |
| $Fe_2O_3$ | 0.84 | 0.33 | 4.51 | 0.10 |
| Others | 0.17 | 0.78 | 0.17 | - |
| Loss on ignition | 0.56 | 0 | 0.71 | 26.9 |
| *Others characteristics* | | | | |
| Insoluble residues | 0.49 | - | 0.48 | - |
| Main mineral phases | Amorphous | $CaSO_4$ | 45.2%wt $C_3S$; 29.7%wt $C_2S$; 3.2%wt $C_3A$; 13.7%wt $C_4AF$ | 72%wt Ca $(OH)_2$; 28%wt $CaCO_3$ |
| Strength activity index 28days, % | 110 | - | - | - |

Slag gravel was ground into fine powder in industrial ball mill. Powder fineness are characterized by Blaine 4270 $cm^2/g$ and 2.5%wt retained on 45 µm sieve. An important content of aluminum oxide 15.6%wt was recorded in the compositional analysis of slag. Calculated results of both basicity %wt CaO/%wt $SiO_2 > 1$, and chemical indice (%wt $CaO^+$ %wt $MgO^+$ %wt $Al_2O_3$)/%wt $SiO_2 \gg 1$ led us to classify this slag in the range of high quality product (Matschei et al. 2005). Portlandite in both hydrated lime and hydrated product of PC provides alkali solution for slag dissolution. As mentionned, the proportional mixture was set at 82.5%wt of GBFS, 15.5%wt of anhydrite, 1%wt of PC clinker and 1%wt hydrate lime. Powder mixture was prepared in V-type mixer (10 min) and kept closing in nylon bag in order to prevent natural

carbonation. In the previous study, we conducted test on prepared cement for product specification of supersulfated cement. As given in the Table 2, most of physio-mechanical properties of prepared cement fully met the requirement of BS EN 15743 for grade 42.5 L. We highlight remarkable high value of mechanical resistance of cement mortar and very low heat released during the hardening period. Such evidence opens the possibility to use formulated cement under aggressive environment.

**Table 2.** Specific characters of prepared cement SSC, conform to the requirement of BS EN 15743

| | Formulated SSC | Standard (grade 42.5L) |
|---|---|---|
| *Physio-mechanical characters* | | |
| Compressive strength, MPa | - | - |
| - 2 days | 32-39 | $\geq$ 16 |
| - 7 days | 47-52 | $\geq$ 42.5 and $\leq$ 62.5 |
| - 28 days | 110 | $\geq$ 60 |
| Setting time, mins Heat of hydration at 7 days, J/g | 182 | $\leq$ 220 |
| *Others characters* | | |
| Insoluble residues (%wt) | 0.45 | $\leq$ 5 |
| Loss on ignition (%wt) | 1.64 | $\leq$ 5 |
| $SO_3$ (%wt) | 7.13 | $\geq$ 5 and $\leq$ 12 |
| Cl (%wt) | - | $\leq$ 0.1 |

## 2.2 Methodology

We carried out experimental studies on cement paste scale with specific technique of material analysis and on mortar specimens scale with measurement of eventual degradation and corrision behavior of embeded steel bar in sea water exposure condition. Specimens of cement paste were prepared from mixture of SSC and both simulated sea water (NaCl 3.0%wt and NaCl 3.0%wt + $Na_2SO_4$ 2.0%wt) and natural sea water (NaCl 2.8%wt). It is noted that high content of fine slag could affect the consistency of paste mixture. Therefore we need adopt deep mixing approach (5 min) in planetary mixer in order to liberate blocked water of the solid part. Set cement paste was then characterized by XRD, SEM/EDX analysis for respectively qualitative and quantitative examination. We had recourse to the technique of potential difference (electrical probe DY 2510B, ASTM C1218/ASTM C1152) to estimate the proportion of free chloride and total chloride content (Fig. 1-centre). Mortar sample with embedded steel bar were casted in prismatic mold 40 $\times$ 40 $\times$ 160 mm. With caution, a $\phi$8 steel bar was placed horizontally in the middle of 40 $\times$ 40 mm section (Fig. 1-left). Bars sample then placed curing in tap water and sea water tank in two modes. The first consisted of putting 160 mm in height of bars sample in water (totally submerged) and the second consisted of putting a half of 160 mm in height of bars sample in water and another half of bars sample in moisture air (partially submerged). During the curing period in tap water, natural sea water environments, we monitored

corrosive state of steel bar. Cylindrical samples $\phi 100 \times 200$ mm were also prepared in the same manner for the test of chloride penetration resistance after 28, 60 and 120 days of curing time (Fig. 1-right). To formulate cement mortar, seawater dredged sand Vung Tau was used as fine aggregate. Its grading curve was adapted conform to standard sand's curve and fineness modulus M was fixed as 2.3. We also highlighted the chloride content 0.11 that is superior to the threshold limit of national standard TCVN 342 – 1986. That means such seawater dredged sand is not regulated as concreting materials in normal condition with Portland cement.

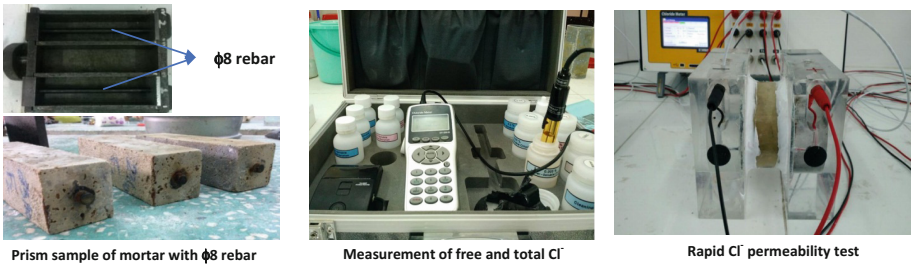


**Fig. 1.** Different experiments on SSC cement mortar sample and cement paste.

## 3 Results and Discussion

### 3.1 Materials Analysis of Hydrated Product

In the Fig. 1, XRD spectrum (diffractometer D8 ADVANCE, $2\theta = 5–80^0$, CuK$\alpha$ radiation) shows mineralogical composition of hydrated cement after 7 and 28 days of curing time. They appeared major peaks that correspond to the main phases such as ettringite (E), C-S-H (Cs), calcite (C), hydrotalcite (Ht), Friedel's salt (F), gypsum (G) and anhydrite (A). It is also noted that amorphous phase as the base of spectrum might refer to unreacted slag or poor crystallized phase. Among them, ettringite seems to be the most abundant phase mineral of hydration reaction after 7 days. On the contrary with the instability over time of early ettringite phase in Portland cement, such ettringite phase remaind the stability at the age of 60 days. Effectively, some authors qualified it as low-Ca-ettringite products (Gruskovnjak et al. 2008). With regard to the impact of different curing environment, it must be taken into account the role of rich sulfate ion in solution. Last factor might strengthen the formation of ettringite. In the long term, Friedel's salt was recognized arbitrary with minor peaks at $2\theta = 11.6°$. The evidence of Friedel's salt and hydrotalcite phase might contribute to explain the ultimate durable property of cement mortar. In addition, a part of hydration product is carbonated, forming bright calcite on the surface.

Figure 3 illustrates SEM cliches (magnification $\times$ 20,000) of set cement paste at the age of 60 days of curing time. To better understand the illustration of SEM, we realized a quantitative analysis EDX for determining the element composition (Fig. 4). In general, we highlight compact microstructure with various position of crystallized

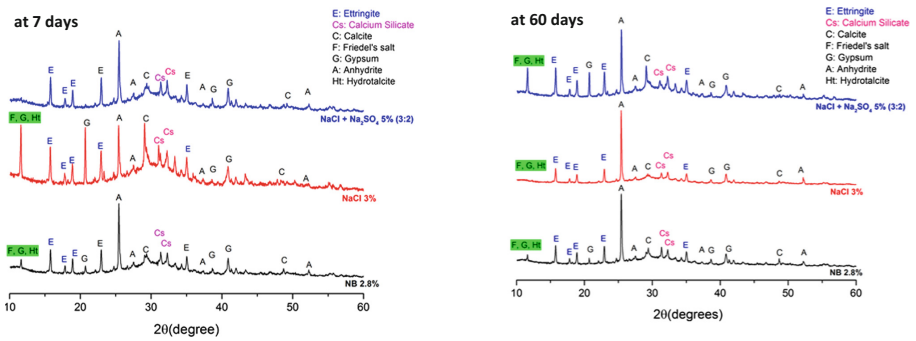


**Fig. 2.** X-ray diffraction spectrum of set cement paste SSC, CuKα: (left) at the age of 7 days (right) at the age of 60 days.

mineral. No major cracks due to dry shrinkage were exposed in three cliches. Recognized rod-shaped crystal could be attributed to ettringite mineral and/or calcium silicate hydrate phases. EDX result in the Fig. 4-c seems confirm the such identification, including the presence of Ca Si Al S as main elements and high ratio of Ca:Si. Among three cliches, high sulfate ion in case of NaCl/$Na_2SO_4$ solution mixing cement permet generating abundant of ettringite phase (Fig. 3-(3)). Small plate-shaped particles (bright color) could be considered as the remaining slag powder after hydration reaction. Elemental composition analysis in the Fig. 4-a approved last result with an exclusively high percentage of S.

As mentioned in XRD analysis, Friedel's salt was formed at later age in aggressive environment. It seems to be associated formed mineral with white flake's position B (Fig. 3-(2)). With regards to the chemical formula of Friedel's salt and ettringite, we can see the same group of AFt mineral, but there exist high percentage of Cl in case of Friedel's salt. That is also the same way when we compared obtained result in the EDX analysis of Fridel's salt in the Fig. 4-b and ettringite in the Fig. 4-c. Considering the impact of different seawater mixing, it seems high sulfate content in simulated solution affected to the forming Friedel's salt, although such sulfate ion already gave favor in forming the above ettringite phase.

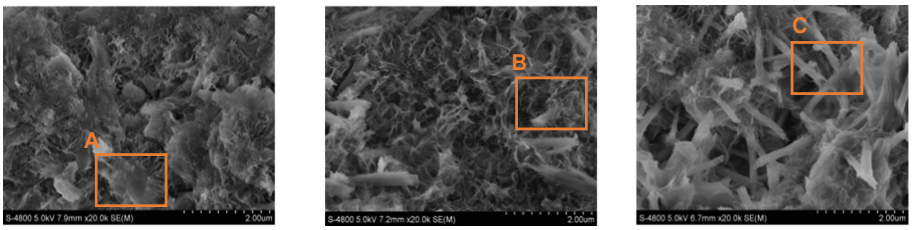


**Fig. 3.** SEM cliché of set cement paste at the age of 60 days.

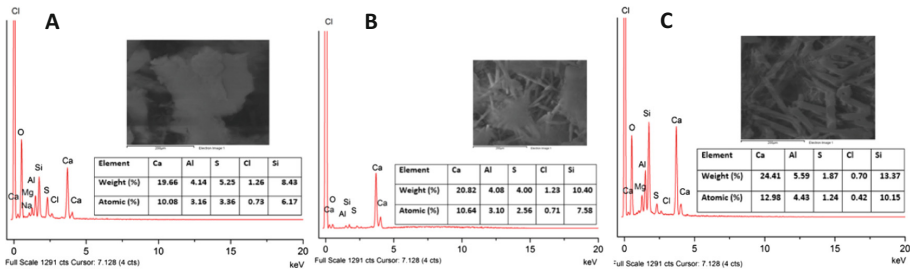


**Fig. 4.** Results of element composition by EDX technique.

### 3.2 Free $Cl^-$ and Bound $Cl^-$ Content

Table 3 lists the measured values of chloride content in three sample series of cement paste. According to the instruction of standard ASTM C1218/ASTM C1152, total chloride content compose of free chloride content with an addition of bound chloride ion of hydrated product.

**Table 3.** Measured values of $Cl^-$ content and calculated ratio of bound $Cl^-$/total $Cl^-$

| | | Sample series of cement paste | | |
|---|---|---|---|---|
| | | (1) With sea water mixing | (2) With NaCl 3%wt mixing | (3) with NaCl 3% wt + Na2SO4 2%wt mixing |
| at 28 days | Free $Cl^-$ | 0.0225 | 0.0119 | 0.0109 |
| | Total $Cl^-$ | 0.1464 | 0.0892 | 0.0736 |
| | Ratio of bound $Cl^-$/total $Cl^-$ | 0.85 | 0.87 | 0.85 |
| at 60 days | Free $Cl^-$ | 0.0135 | 0.0124 | 0.0098 |
| | Total $Cl^-$ | 0.0544 | 0.0441 | 0.0408 |
| | Ratio of bound $Cl^-$/total $Cl^-$ | 0.75 | 0.72 | 0.76 |

First, we could point out a notable difference between measured values at 28 and 60 days. In particular, there existe a downward trend in the global result of total chloride at long term. Such evidence could be considered as an advantage for durability property. As defined in almost nation and international standard, to cross the threshold of chloride content signalizes the phenomenon of steel corrosion. Second, we estimated ratio of bound $Cl^-$ on total $Cl^-$ content. They reveal very important results of bound chloride were recorded in all samples. Bound $Cl^-$ is obviously associated with the natural anti-corrosion of cement matrix. Fixed chloride ion eventually decrease reaction of ion exchange with iron. Similar effet was reported in the study of Otsuki et al. (2012) while the author used slag cement with 65%wt GBFS. More mortar samples expose to seawater condition in which high content of chloride present, more significant effect of

chloride binding was recognized. It seems that there is a linkage between the result of bound $Cl^-$ and the sulfate component of different water solution mixing. High sulfate ion affected on the formation of Friedel's salt phase and such mineral phase determine the chemically bound chloride content. A downward trend is also noted for ability of chloride binding at later age. But more results of analytical analysis and measurement need to be considered for a conclusion of global performance.

### 3.3 $Cl^-$ Permeability Test and Corrosive State of ϕ8 Embedded Steel Bar

It is clear that nitial chloride ion of seawater or seawater sand mixing component determine the resulted chloride content in cement paste. The phenomenon of chloride ingress must be taken into account in order to interperet the possible interaction with curing environment. Natural seawater was used as curing solution. As given in the Fig. 5, we obtained the results of electrical charge in Coulomb of two sample series (1) slice 5 cm thickness of cement mortar with seawater sand and freshwater mixing; (2) slice 5 cm thickness of cement mortar with seawater sand and seawater mixing. Following the instructions in standard, most of charge value was stable with a maximal peak after 360 min of measurement. Results in case of freshwater mixing mortar was respectively 472C for 28 age days specimen, 854C for 60 age days specimen and 976C for 120 age days specimen. The three last values are inferior to boundary limit of the level very low $Cl^-$ penetration in accordance with national standard TCVN 9337:2012. That means mortar sample presented good performance of $Cl^-$ impermeability from seawater environment. In the same way, obtained results of charge in case of seawater mixing mortar met the boundary limit of the level of very low $Cl^-$ penetration. Even more considerable, those results values are not various (around 530C) over different periods of curing time 28, 60 and 120 days. In general, the solid microstructure with a tightness of hydrated cement product permits to explain the low permeability. Such evidence allows us improving the phenomenon of anti-corrosion of embedded steel bar from exposure condition. As we mentioned, both seawater and sea sand were used in the formulating cement mortar. To combine the last remark with the above result of chloride binding of SSC cement matrix, we seem to diminish the impact of high chloride content in seawater for concreting material.

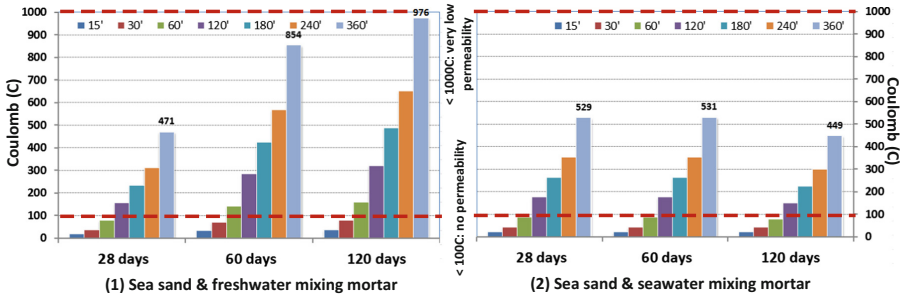


**Fig. 5.** Results of chloride ingress across 5 cm thickness of cement mortar after curing in seawater environement 28, 60 and 120 days.

In the following Fig. 6, we examined the corrosive condition of ϕ8 rebar after 28 and 60 days. It is noted that prismatic mortar was placed in vertical curing in seawater tank by two modes: (i) partially submerged and (ii) totally submerged in water. The corrosion issue of reinforced steel bar in the context of sea water exposure correspond to the content of free chloride in cement matrix (locally exist and ion penetration) (Ferreira et al. 2004). Such undesired chloride contact directly around rebar embedded in concrete and progressively reduce the working section of reinforced elements. As we could observe, the corrosion rate of rebar is related to different position and curing method. They appear clear rust on the two extremities of rebar that contact directly to aggressive solution. Others part covered by 20 mm mortar and stay be well protected from attack with no major deterioration. That means accordance with the result of chloride ingress (very low) and free chloride content. With regards to tap water and seawater mixing in the stage of mortar sampling, we obtained the similar characters in those broken sample. It should monitor mortar sample for longer period of curing time in order to have more serious conclusion. More attention should be paid to the sample that cured by 2nd mode in seawater (Fig. 6-below). We must highlight an accelerating corrosion rate compared to mortar samples that were cured by 1st mode (Fig. 6-above). It seems that high moisture condition and high oxygen concentration constitute a real impact in this curing mode.

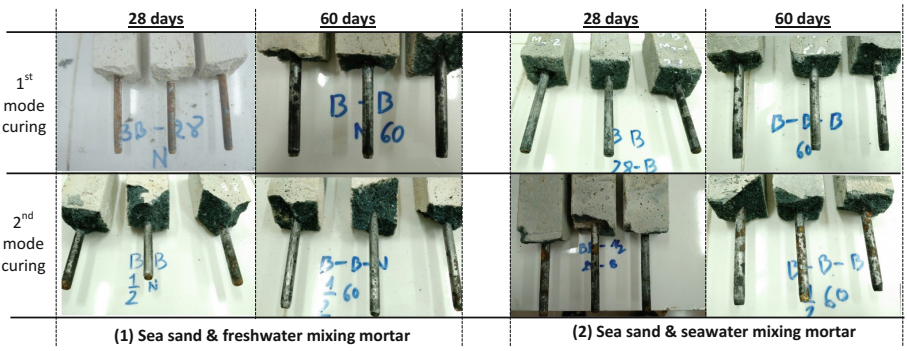


**Fig. 6.** Corrosive state of ϕ8 rebar embedded in cement mortar samples that were cured in seawater environment.

## 4 Conclusions

This paper has investigated on the possibility using supersulfated cement in seawater mixing concrete or durable concrete under severe condition. We formulated SSC from mixture of 82.5 wt% of GBFS, 15.5 wt% of anhydrite, 1 wt% of PC clinker and 1 wt% hydrate lime. Results of almost test on product specification met the requirement of BS EN 15743-2010 for supersulfated cement, grade 42.5L. In term of compositional analysis of hydrated product of cement, they revealed the proof of an abundant and stable ettringite phase that constitue ultime mechanical resistance of specimens. In addition, Friedel's salt and hydroalcite were also presented at later age in hardened cement paste

mixing with natural and simulated seawater. In term of a quantitative analysis on the chloride content, we can see notable high ratio of bound $Cl^-$ on total $Cl^-$ in almost three sample series of SSC cement paste. That means a benefit of natural anti-corrosion in seawater condition due to the effect of fixed chloride in hydrated cement matrix. In term of durability in aggressive enviroment, given that the use of seawater sand Vung Tau as fine aggregate in cement mortar, but we found good performance of $Cl^-$ impermeability for hardened mortar sample. To combine the last evidence and ability of chloride binding in SSC cement matrix, the impact of high chloride content in seawater mixing component of concrete could be eventually diminished. The last finding refers to positif aspect while we monitored the corrosion issue of $\phi 8$ rebar embedded in cement mortar samples. In spite of a prelimiary result after 60 days, but in general no major deteoriation was highlighted in case of mortar sample with natural seawater exposure. Further experiments at larger scale of concrete are in progress for the ultimate objectif of producing sea water/sand mixing concrete structure.

**Acknowledgments.** Corresponding author would like to thank for material support from Saigon cement industry (SDC corp.) and JICA-AUN/SEED-net for financial support (research project HCMUT-CRC1601).

## References

Japan Concrete Institute: Report of Technical Committee on the Use of Sea Water in Concrete JCI-TC-121 Chair by Prof. Nobuaki Otsuki, September 2015. Japan Concrete Institute (2015). ISBN 978-4-86384-067-6-C3050

Hewlett, P.: Lea's Chemistry of Cement and Concrete. Butterworth-Heinemann, Oxford (2003)

Neville, A.M.: Properties of Concrete. Pitman Publishing, London (2011)

Stark, J., et al.: Investigations with supersulfated cement. In: Dhir, R.K., Dyer, T.D. (eds.) Modern Concrete Materials: Binders, Additions and Admixtures: Proceedings of the International Conference Held at the University of Dundee, Scotland, UK, 8–10 September 1999, p. 349, Thomas Telford (1999)

Phelipot-Mardelé, A., et al.: Super sulfated cement: formulation and uses. In: Proceedings of the Fifth International Conference on Construction Materials: Performance, Innovations and Structural Implications, 19–21 August 2015, Canada (2015)

Nguyen, K.S., et al.: Using super-sulfated cement for concrete durability in marine environment. In: Proceeding of the 7th International Conference of Asian Concrete Federation - ACF2016, Vietnam, 30 October – 3 November 2016 (2016)

Matschei, T., Bellmann, F., Stark, J.: Hydration behaviour of sulphate-activated slag cements. Adv. Cem. Res. **17**(4), 167–178 (2005). doi:10.1680/adcr.2005.17.4.167

Gruskovnjak, A., Lothenbach, B., Winnefeld, F., et al.: Hydration mechanisms of super sulphated slag cement. Cem. Concr. Res. **38**(7), 983–992 (2008). https://doi.org/10.1016/j.cemconres.2008.03.004

Otsuki, N., Saito, T., Tadokoro, Y.: Possibility of sea water as mixing water in concrete. J. Civ. Eng. Archit. **6**(10), 1273 (2012). ISSN 1934-7359

Ferreira, R.M., Liu, G., Nilsson, L., Gjørv, O.E.: Blast-furnace slag cements for concrete durability in marine environment. In: Oh, B.H., et al. (eds.) Proceedings of The 4th International Conference on Concrete under Severe Conditions of Environment and Loading (CONSEC 2004), 27–30 June 2004, Korea (2004)

# Correlation Between Resilient Modulus and Permanent Deformation During a Large Scale Model Experiment of Unbound Base Course

Makhaly Ba(✉)

Department of Geotechnical Engineering, University of Thies, Thies, Senegal
makhaly.ba@univ-thies.sn

**Abstract.** Unbound base course performance is highly dependent to resilient modulus and permanent deformation of unbound layers. Plastic strains are affected by the number of traffic loading. A Large Scale Model Experiment (LSME) test was conducted on unbound granular materials for 10,000 load repetitions and different thicknesses to determine the relationship between resilient modulus and plastic deformations. The results show that this relation is linear and can be explained by a progressive accumulation of the plastic deformations, reducing the voids and increasing the rigidity of the material. This proves that, in situ, the modulus varies with the repetition of traffic and this behavior is important for predicting the modulus for pavement rehabilitation. The moduli do not show large variations with the number of load cycles but increase with the thickness of the base layer. Plastic deformation decreases with increasing modulus of the material and the modulus itself increases with the thickness of the layer. Between 20 cm and 30 cm, permanent deformation decreases slightly, but the modulus after 10,000 cycles increases about 35%. To predict the plastic strain of unbound layers under repetitive loading, regression models are proposed.

**Keywords:** Correlation · Resilient modulus · Permanent deformation · Large Scale Model Experiment · Unbound base course

## 1 Introduction

Unbound pavement system consists of three or more layers including granular base or subbase course, subjected to continuous repeated loading due to traffic. Under each application of loading, resilient and plastic strains occur. Characterization of the resilient response and the permanent deformation of granular materials is a key element for designing pavement structures (Yang et al. 2008). The resilient modulus is the mechanical property used to describe stress-stain relationship and permanent deformation the parameter used to predict rutting of granular material subjected to cyclic loading. Rutting is one of the major modes of load-associated distresses for flexible pavement, resulting from the accumulated permanent deformation in the different unbound layers under repeated traffic loading (Ba et al. 2015). However, few studies have been devoted to the evolution of the resilient modulus with the number of load cycles, and permanent deformation. Yang et al. (2008) perform up to 100,000 loading

© Springer Nature Singapore Pte Ltd. 2018
H. Tran-Nguyen et al. (eds.), *Proceedings of the 4th Congrès International de Géotechnique - Ouvrages -Structures*, Lecture Notes in Civil Engineering 8,
DOI 10.1007/978-981-10-6713-6_37

cycles on lateritic gravels and find a power correlation between the resilient modulus and the permanent deformation. The objective of this research is to propose models that allow to evaluate the permanent deformation of a base layer of a roadway in service using the in situ resilient modulus and the traffic expressed by the number of load repetions (N). An apparatus for simulating cyclic loading on a pavement structure established in the laboratory was developed by the Department of Civil and Environmental Engineering (University of Wisconsin - Madison, USA) to assess the performance of different materials to be used as a base layer of pavement.

## 2 Material and Method

### 2.1 Materials

The base-course aggregates were collected from varying geographical locations within Senegal. Four (04) base-course materials including Bakel Black Quartzite (GNB), Bakel Red Quartzite (GRB), Diack Basalt (BAS) and Bandia Limestone (BAN) were characterized in this study (Ba et al. 2011, Ba et al. 2012). Compaction characteristics, some physical and mechanical properties are presented in Table 1.

**Table 1.** Compaction and physical properties of the aggregates (Ba et al. 2011, Ba et al. 2012)

| Materials | $\gamma_{dmax}$ (kN/m$^3$) | $w_{opt}$ (%) | $G_s$ | MDE (%) | USCS | Fines (%) |
|---|---|---|---|---|---|---|
| Bakel Red Quartzite | 21.00 | 5.5 | 2.65 | 3.1 | GW | 7.7 |
| Bakel Black Quartzite | 21.09 | 4.5 | 2.65 | 4.2 | GW | 9.4 |
| Diack Basalt | 23.74 | 4.2 | 2.95 | 5.6 | GP | 7.1 |
| Bandia Limestone | 20.25 | 7.6 | 2.56 | 40 | GP | 7.4 |

### 2.2 Laboratory Resilient Modulus and Permanent Deformation Tests

Cyclic loading triaxial tests were performed using a MTS closed-loop servo-electro-hydraulic testing system (Fig. 1), which is capable of applying repeated loads in haversine waveform with a wide range of load duration. The axial deformations (elastic and plastic) were measured by Linear Variable Differential Transducers (LVDTs) mounted inside the triaxial cell. The specimens were submitted to cyclic loading triaxial tests according to the NCHRP 1–28 A (NCHRP 2004) test protocol, which was used to establish the 30 loading sequences. The loading involves conditioning, which attempts to establish steady-state or resilient behavior, through the application of 1000 cycles of 207-kPa deviator stress at 103.5-kPa confining pressure. The cycles are then repeated 100 times for 30 loading sequences with different combinations of deviator stress and confining pressure. The Mr is calculated as the mean of the last five cycles of each sequence from the recoverable axial strain and cyclic axial stress. It is an elastic modulus defined as ratio between the applied deviatoric stress, $\sigma_d$ (= $\sigma_1 - \sigma_3$) and the recoverable strain, $\varepsilon_r$ (Eq. 1).

$$M_r = \frac{\sigma_d}{\varepsilon_r} \tag{1}$$

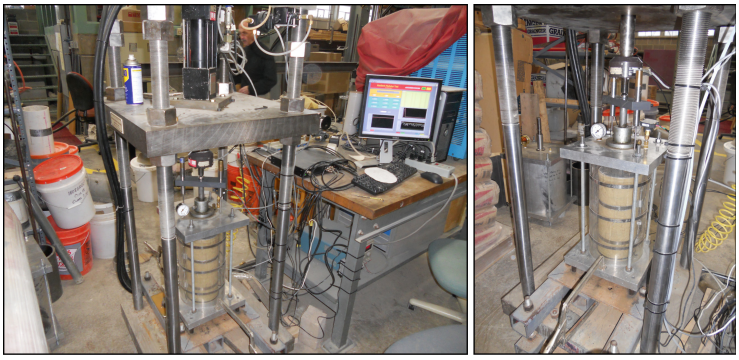

**Fig. 1.** Photo of the repeated loading machine illustrating the resilient modulus test (from the UW-Madison, USA)

The procedure developed to study the permanent deformations behaviour is to estimate the stress level usually found in the base layer ($\sigma_3$ = 35 kPa; $\sigma_d$ = 103 kPa) and apply it to the sample with 100,000 load cycles to study the evolution of permanent deformation (Ba et al. 2015).

### 2.3 Large Scale Model Experiment (LSME)

The Large-Scale Model Experiment (LSME) configuration consists of a pavement profile in a 3 × 3 × 3 m test pit (Fig. 2). The pavement profile consists of 2.5 m of uniform sand, simulating a deep subgrade, and a base course layer. A loading frame (100 kN actuator with 165 mm stroke) and a steel loading plate (125 mm radius and 25 mm thickness) were used to apply cyclic loading to the surface of the pavement. The simulated pavement was subjected to traffic wheel loads corresponding to 4-axle trucks (70 kN per axle and 35 kN per wheel set) with a tire pressure of 700 kPa, which results in a contact area of 0.05 $m^2$ under 35 kN load. Elastic and plastic deformations of base course materials were measured. The LSME allows determination of the resilient modulus and plastic strain of the base course materials under cyclic loading

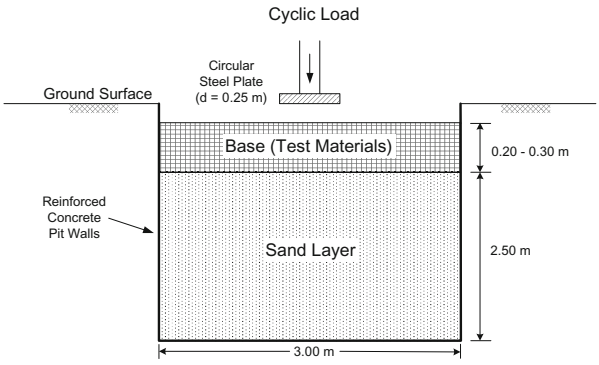


**Fig. 2.** Large-scale model experiment used for prototype pavement testing (Tanyu et al. 2003)

similar to the field conditions. During the test, there is no surface layer on the base course. In the absence of surface layer, the stress applied at the surface of the base course was estimated by conducting nonlinear finite-element simulations of a pavement profile similar to the one in the LSME but with a 0.125 m thick HMA layer using the MichPave program (Harichandran et al. 1989).

## 3 Results and Analyses

### 3.1 Laboratory Resilient Modulus vs Permanent Deformation Relationship

Figure 3 shows the relationship between plastic strain and resilient modulus for Bakel black quartzite, Diack basalt and Badia limestone, respectively. Experimental results show that the resilient modulus increases as the number of cycles increases. At the same time, the permanent deformations also increase with the number of cycles. So, there is a simultaneous evolution of the resilient modulus and the permanent

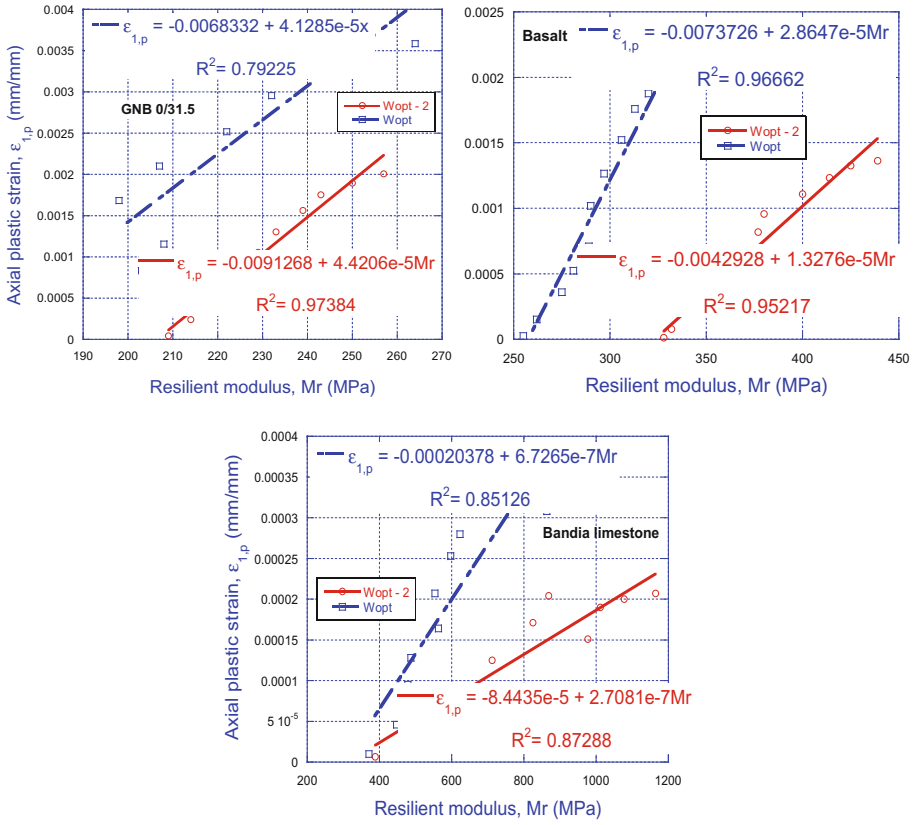


**Fig. 3.** Linear relationship between the resilient modulus and the permanent deformations (GNB 0/31.5 basalt, Bandia limestone).

deformation as a function of the number of cycles. This is due to a continuous change in the structure of the soil by progressive reduction of the voids, resulting in an accumulation of permanent deformations and thus a hardening of the material. The Bandia limestone shows an alternation of increase and decrease of the resilient modulus as a function of the number of cycles. This instability was even observed during the resilient modulus test due to the transformation of this material during the test. The aggregates of Bandia limestone "break" during loading, thus changing the state of the material, which results in an instability of the values of the measured moduli. Results show also a linear relationship between the resilient modulus and the permanent deformations as expressed in Fig. 3. Correlation equations are deduced to express the permanent deformation as a function of the resilient modulus, for each unbound aggregate.

### 3.2 Resilient Modulus vs Permanent Deformation During the LSME

Figure 4 shows the relationship between axial permanent deformation and the resilient modulus during the large scale model experiment, for different materials tested in the LSME at their optimum water content and 98% of the modified Proctor density. As

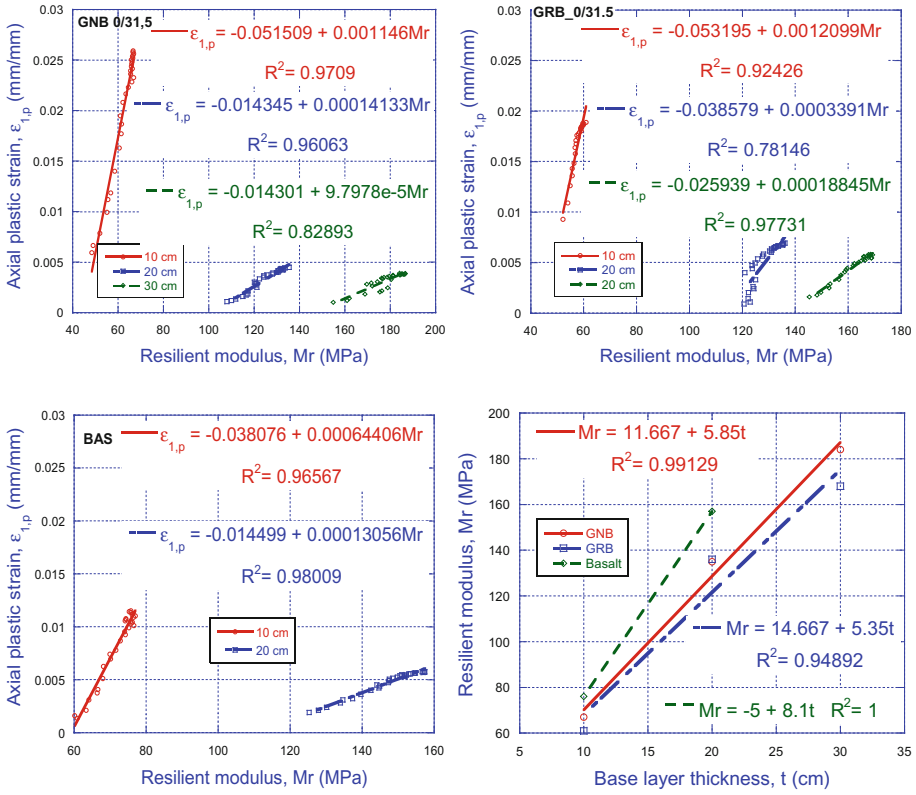


**Fig. 4.** Linear relation between resilient modulus and axial permanent deformation or thickness of the base layer determined from the LSME

shown previously, this relationship is linear and is explained by a gradual accumulation of plastic deformations, which reduces the voids and increases the stiffness of the material. This proves that, in situ, the modulus varies with the repetition of traffic and this behavior is important for predicting the modulus for pavement rehabilitation. The plastic deformations decrease with the increase in the modulus of the material and that the modulus itself increases with the thickness of the layer. Between 20 cm and 30 cm, permanent deformation decreases slightly, but the modulus after 10,000 cycles increases by about 35%.

Figures 5 and 6 show the evolution of the resilient modulus and the permanent deformation as a function of the number of loading cycles based on the total elastic deflections measured during the LSME and the thicknesses of the various base layers tested. These figures show that, whatever the case, the modulus follows the same behavior as the permanent deformations and increases rapidly during the first loading cycles and then tends to stabilize when the number of cycles becomes very high.

Permanent deformations decrease as the thickness of the base layer increases. At a thickness of 10 cm, the Bakel gravels and Diack basalt show higher plastic deformations, around 2% and 1%, respectively, and do not tend to stabilize. This type of

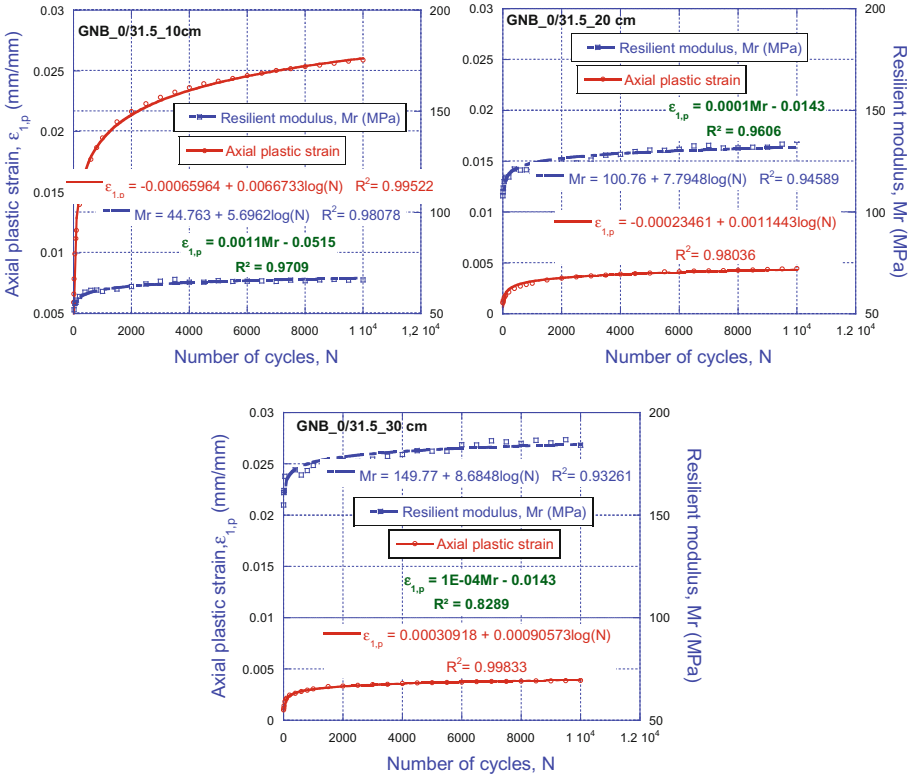


**Fig. 5.** Relation between resilient modulus and permanent deformation measured with the LSME at different base layer thicknesses (GNB)

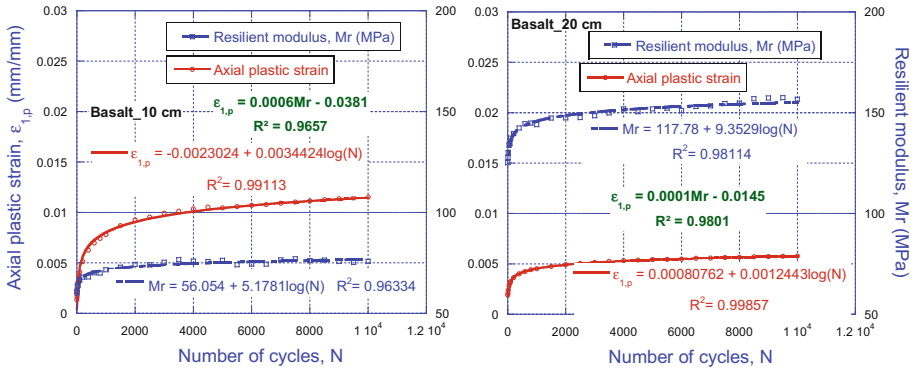


**Fig. 6.** Relation between resilient modulus and permanent deformation measured with the LSME at different base layer thicknesses (basalt)

behavior leads very quickly to the ruin of the structure, due to very high rut depths. At 20 cm, the plastic deformation decreases considerably and stabilizes after approximately 2,000 cycles between 0.6% and 0.5% of the thickness of the layer.

The moduli, on the other hand, do not show large variations with the number of load cycles. Indeed, after 2,000 cycles, the modulus varies only slightly with the number of cycles. Nevertheless, it increases with the thickness of the base layer.

Comparison between materials shows that the basalt has higher moduli and lower permanent deformations compared to those of Bakel quartzite. However, the values of the permanent deformations reached in situ and measured at LSME show very acceptable levels of plastic deformations for thicknesses ranging from 20 to 30 cm.

## 4 Conclusion

The results from this study show that there is a simultaneous evolution of the resilient modulus and the permanent deformation as a function of the number of cycles. The modulus follows the same behavior as the permanent deformations and increases rapidly during the first loading cycles and then tends to stabilize when the number of cycles becomes very high. The relationship between resilient modulus and plastic strain is linear and is explained by a gradual accumulation of plastic deformations, which reduces the voids and increases the stiffness of the material. The plastic deformations decrease with the increase in the modulus of the material and that the modulus itself increases with the thickness of the layer. Between 20 cm and 30 cm, permanent deformation decreases slightly, but the modulus after 10,000 cycles increases by about 35%. The moduli, on the other hand, do not show large variations with the number of load cycles. Indeed, after 2,000 cycles, the modulus varies slightly with the number of cycles. Nevertheless, it increases with the thickness of the base layer.

**Acknowledgments.** Support for this study was provided by the "Entreprise Mapathé Ndiouck SA" (Senegal). The Geological Engineering (GLE) group of the University of Wisconsin-Madison (USA) is also acknowledged for the valuable input in this research study.

## References

Ba, M., Fall, M., Samb, F., Sarr, D., Ndiaye, M.: Resilient modulus of unbound aggregate base courses from Senegal (West Africa). Open J. Civ. Eng. **1**(1), 1–6 (2011). doi:10.4236/ojce.2011.11001

Ba, M., Fall, M., Sall, O.A., Samb, F.: Effect of compaction moisture content on the resilient modulus of unbound aggregates from Senegal (West Africa). Geomaterials **1**(2), 19–23 (2012). doi:10.4236/gm.2012.21003

Ba, M., Tinjum, J.M., Fall, M.: Prediction of permanent deformation model parameters of unbound base course aggregates under repeated loading. Road Mater. Pavement Des. **16**(4), 854–869 (2015). doi:10.1080/14680629.2015.1063534

Harichandran, R.S., Baladi, G.Y., Yeh, M.: Development of a computer program for design of pavement systems consisting of bound and unbound materials. Department of Civil and Environmental Engineering, Michigan State University, Lansing, Michigan (1989)

NCHRP: Guide for mechanistic-empirical design of pavement structures. national cooperative highway research program. ARA, Inc., ERES Consultants Division, Champaign, IL (2004)

Tanyu, B., Kim, W.H., Edil, T.B., Benson, C.H.: Comparison of laboratory resilient modulus with back-calculated elastic moduli from large-scale model experiments and FWD tests on granular materials. In: Durham, G.N., Marr, A.W., De Groff, W.L., (eds.) Resilient Modulus Testing for Pavement Components, ASTM STP 1437, Paper ID 10911, ASTM International, West Conshohocken, PA (2003)

Yang, S.R., Huang, W.H., Liao, C.C.: Correlation between resilient modulus and plastic deformation for cohesive subgrade soil under repeated loading. Transp. Res. Rec. J. Transp. Res. Board, no. 2053, pp. 72–79 (2008). Transportation Research Board of the National Academies, Washington, D.C. doi:10.3141/2053-09

# Correlations Between DCP Penetration Index and Properties of Pavement Layer Materials

Suppakorn Wachiraporn[1], Auckpath Sawangsuriya[2(✉)], and Wilailak Sramoon[1]

[1] Faculty of Engineering, Mahanakorn University of Technology, Bangkok, Thailand
wachiraporn08@gmail.com, wilailakk@gmail.com
[2] Department of Highways, Bureau of Road Research and Development, Bangkok, Thailand
sawangsuriya@gmail.com

**Abstract.** This paper presents correlations between penetration index measured from dynamic cone penetrometer (DCP) and properties of pavement layer materials. A series of DCP tests were conducted both in the laboratory and in the field. The DCP data were analyzed and interpreted to generate a representative value of penetration per blow or DCP penetration index (DPI) for the material being tested at a given test condition. Basic properties of pavement layer materials e.g. crushed rock base, soil-aggregate subbase, sand embankment, natural subgrade etc. were tested and reported herein. By achieving appropriate moisture content and compaction quality, the empirical relationships between DPIs and properties of pavement layer materials from different test conditions indicated reasonable trends and thus confirmed its potential adoption for routine pavement layer evaluation in Thailand.

**Keywords:** DCP · Strength · Penetration · Pavement · Material

## 1 Introduction

Mechanical property-based in situ tests for pavement layer evaluation such as Light Weight Deflectometer (LWD), Portable Falling Weight Deflectometer (PFWD), Soil Stiffness Gauge (SSG), Briaud Compaction Device (BCD), Dynamic Cone Penetrometer (DCP), Clegg Impact Tester are widely adopted in the transportation geotechnics and pavement engineering communities. They provide in-place mechanical properties (i.e., stiffness and strength) assessment of pavement materials and gain popularity over years as alternative portable tools for pavement layer evaluation.

A DCP is widely known for its simple, rugged, convenient and economical tool that provides an instantaneous in-place strength index of compacted materials. In this study, the DCP was employed to assess the penetration index of various pavement materials used in road construction in Thailand. A series of DCP tests were conducted both in the laboratory and in the field. The DCP data were analyzed and interpreted to generate a representative value of penetration per blow or DCP penetration index (DPI) for the material being tested at a given test condition. Basic properties of pavement layer

© Springer Nature Singapore Pte Ltd. 2018
H. Tran-Nguyen et al. (eds.), *Proceedings of the 4th Congrès International de Géotechnique - Ouvrages -Structures*, Lecture Notes in Civil Engineering 8,
DOI 10.1007/978-981-10-6713-6_38

materials e.g. crushed rock base, soil-aggregate subbase, sand embankment, natural subgrade etc. were tested and reported herein. Under the proper compaction quality, the correlations between DPIs and properties of pavement layer materials were investigated for possible adoption of DCP for routine pavement layer evaluation in Thailand.

## 2 Dynamic Cone Penetrometer

Dynamic Cone Penetrometer (DCP) is a simple, rugged, convenient, and economical tool that can provide a rapid in situ index of strength of undisturbed soil and compacted materials under existing field conditions. The DCP assesses the material resistance to penetration (i.e., penetration rate) while the cone of the device is being driven into the pavement structure. The typical DCP consists of an 8-kg hammer that vertically drops over a height of 575 mm and drives a 60-degree 20-mm base diameter cone tip vertically into the pavement structure. The steel rod to which the cone is attached has a smaller diameter than the cone (16 mm) to reduce skin friction. The number of blows during operation is recorded with depth of penetration.

Since DCP testing is basically a measure of penetration resistance (i.e., a slope of the relationship between number of blows and depth of penetration at a given linear depth segment) expressed as DCP penetration index (DPI) in millimetres per blow, the analysis of the DCP data must be interpreted to generate a representative value of penetration per blow for the material being tested. This representative value can be obtained by averaging the DPI across the entire penetration depth at each test location. Two methods of calculating the representative DPI value for a given penetration depth of interest are: (i) arithmetic average and (ii) weighted average [1]. Since the weighted average method yielded narrower standard deviation for the representative DPI value and provided better correlations to other field tests than the arithmetic average method based on field data available [1]. Thus, the weighted average method was employed to calculate the representative DPI value in this study. The weighted average technique can be obtained as follows [1]:

$$DPI = \frac{1}{H}\sum_{i}^{N}\left[(DPI)_i \cdot (z)_i\right] \tag{1}$$

where z is the penetration distance per blow set and H is the maximum penetration depth of interest., which can be used to estimate in situ CBR and shear strength characteristics in shallow pavement according to ASTM D6951 [2].

## 3 DCP Penetration Index and Material Properties

In this study, the maximum penetration depth of 150 mm was selected to calculate the representative DPI value (i.e., $DPI_{150mm}$) based on the weighted average technique aforementioned. This maximum penetration depth was considered in order to take into account the laboratory test geometry and lift thickness during field compaction process. A series of DCP measurements were collected and reported from different test

conditions, i.e., a laboratory test mold, a laboratory test box, and a field trial. Details for each test are described below.

### 3.1 Laboratory Test Mold

A cylindrical mold having a diameter of 150 mm and 300 mm high typically used for a concrete specimen preparation was used in this study (Fig. 1a). Disturbed subgrade, soil-aggregate subbase, and crushed rock base samples were collected from nine sources in Thailand and were compacted in the mold in accordance with the ASTM procedures. Their basic properties and compaction characteristics are summarized in Table 1. The compaction energy was adjusted to achieve the standard Proctor compaction energy according to ASTM D698 [3] for the subgrade samples and the modified Proctor compaction energy according to ASTM D1557 [4] for the soil-aggregate subbase and crushed rock base samples. The laboratory CBR test was conducted in accordance with the ASTM D1883 [5]. A single DCP measurement was made at the center of the mold. Only the $DPI_{150\ mm}$ values determined from those samples compacted near the optimum moisture content were considered and reported in Table 1.

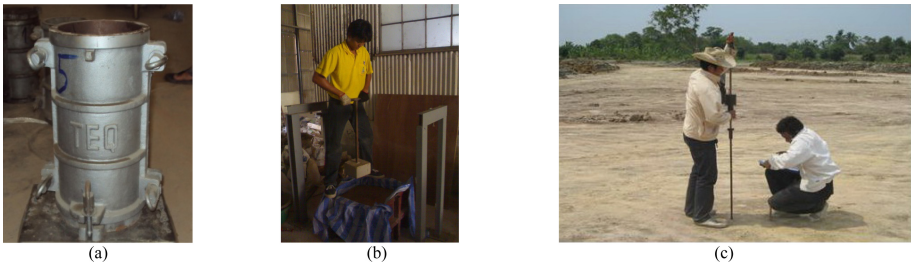

(a) (b) (c)

**Fig. 1.** DCP measurements at different test conditions: (a) laboratory test mold, (b) laboratory test box, and (c) field trial.

### 3.2 Laboratory Test Box

A laboratory test box having the dimension of $0.60 \times 0.60 \times 0.25\ m^3$ was built in this study (Fig. 1b). Disturbed subgrade, soil-aggregate subbase, and crushed rock base samples were collected from a road construction site in Thailand. Their basic properties and compaction characteristics are summarized in Table 1. The sample was compacted in layers for a total of five layers (e.g. 50 mm thick per layer) using a 14-kg concrete block connected to a steel rod. The impact compaction procedure was manually and uniformly applied at 50, 100, 300, and 550 blows per layer with a drop height over 250 mm. The laboratory CBR test was conducted in accordance with the ASTM D1883 [5]. Four DCP measurements were made along the diagonal lines of the test box. Only the $DPI_{150\ mm}$ values determined from those samples compacted at the highest compaction energy (e.g. 550 blows per layer) and near the optimum moisture content were averaged and reported in Table 1.

**Table 1.** Summary of material properties and DPIs

| Test condition | Pavement layer material | % Gravel | % Sand | % Fine | LL | PI | Optimum moisture content (%) | Max dry density ($t/m^3$) | Lab CBR (%) | $DPI_{150\ mm}$ (mm/blow) |
|---|---|---|---|---|---|---|---|---|---|---|
| Test mold | Subgrade 1 | 50.5 | 49.6 | 1.3 | 26.7 | 14.5 | 6.7 | 2.0 | 14 | 5.8 |
| Test mold | Subgrade 2 | 13.2 | 86.8 | 20.4 | 24.4 | 11.3 | 8.6 | 2.1 | 13 | 16.2 |
| Test mold | Subbase 1 | 54.5 | 45.5 | 1.5 | 31.0 | 12.4 | 7.3 | 2.1 | 32 | 5.0 |
| Test mold | Subbase 2 | 45.9 | 54.1 | 22.8 | 18.6 | 13.1 | 5.0 | 2.2 | 33 | 4.6 |
| Test mold | Subbase 3 | 50.3 | 49.7 | 2.5 | 16.9 | 5.3 | 6.5 | 2.2 | 26 | 5.3 |
| Test mold | Crushed rock base 1 | 54.5 | 45.5 | 1.6 | 17.0 | 6.7 | 6.4 | 2.3 | 69 | 12.0 |
| Test mold | Crushed rock base 2 | 40.9 | 59.1 | 2.6 | 17.5 | 5.9 | 6.2 | 2.3 | 42 | 8.8 |
| Test mold | Crushed rock base 3 | 64.2 | 35.8 | 0.1 | 23.0 | 9.1 | 7.0 | 2.3 | 51 | 4.0 |
| Test mold | Crushed rock base 4 | 64.6 | 35.4 | 0.1 | 18.0 | 6.4 | 6.5 | 2.3 | 78 | 5.4 |
| Test box | Subgrade | 14.8 | 85.2 | 41.3 | 41.0 | 14 | 13.2 | 1.9 | 21 | 14.5 |
| Test box | Soil-aggregate subbase | 72.8 | 27.2 | 9.0 | 27.0 | 19.3 | 8.5 | 2.1 | 35 | 11.6 |
| Test box | Crushed rock base | 47.6 | 52.4 | 9.8 | 19.0 | 9.0 | 6.8 | 2.4 | 68 | 9.8 |
| Field trial | Subgrade 1 | 27.8 | 72.2 | 6.7 | 44.6 | 34.8 | 14.5 | 1.8 | 3 | 13.4 |
| Field trial | Subgrade 2 | 14.8 | 85.2 | 41.3 | 41.0 | 14.0 | 13.2 | 1.9 | 18 | 9.8 |
| Field trial | Sand embankment | 2.5 | 98.5 | 24.1 | NP | NP | 9.5 | 1.9 | 26 | 17.8 |
| Field trial | Soil-aggregate subbase 1 | 59.9 | 40.1 | 8.1 | 23.4 | 7.6 | 6.5 | 2.3 | 27 | 6.1 |
| Field trial | Soil-aggregate subbase 2 | 72.6 | 27.5 | 9.0 | 27.0 | 19.0 | 8.5 | 2.1 | 42 | 7.1 |
| Field trial | Fine-grained aggregate subbase | 36.2 | 63.8 | 12.4 | NP | NP | 5.4 | 2.2 | 58 | 8.1 |
| Field trial | Crushed rock base 1 | 53.0 | 47.0 | 10.0 | NP | NP | 5.7 | 2.3 | 83 | 4.1 |
| Field trial | Crushed rock base 2 | 57.9 | 42.1 | 6.9 | NP | NP | 6.0 | 2.3 | 105 | 1.5 |
| Field trial | Crushed rock base 3 | 47.6 | 52.4 | 9.8 | 19.0 | 9.0 | 6.8 | 2.4 | 68 | 7.5 |

### 3.3 Field Trial

A number of field trial strips as part of road construction projects in Thailand were selected in this study (Fig. 1c). Each field trial had a typical distance of approximately 100–200 m. After the compaction procedure, the DCP measurements were made at every 10 m depending on the total length of field trial strip. The DCP tests were performed on natural subgrade, sand embankment, fine-grained aggregate subbase, soil-aggregate subbase, and crushed rock base. The basic properties and compaction characteristics of these materials are summarized in Table 1. The laboratory CBR test was conducted in accordance with the ASTM D1883 [5]. A single DCP measurement per test location was made along the strip. Only those $DPI_{150\ mm}$ values determined from the pavement layers achieving the compaction quality control requirement were averaged and reported in Table 1.

## 4 DPI-Material Properties Correlations

A number of relationships between representative $DPI_{150\ mm}$ values and properties of pavement layer materials were investigated for different test conditions aforementioned. The $DPI_{150\ mm}$ values (mm/blow) determined from the laboratory samples compacted near the optimum moisture content and proper compaction as well as those from the pavement layers achieving the compaction quality control requirement were correlated with various material properties including percent gravel (%), percent sand (%),

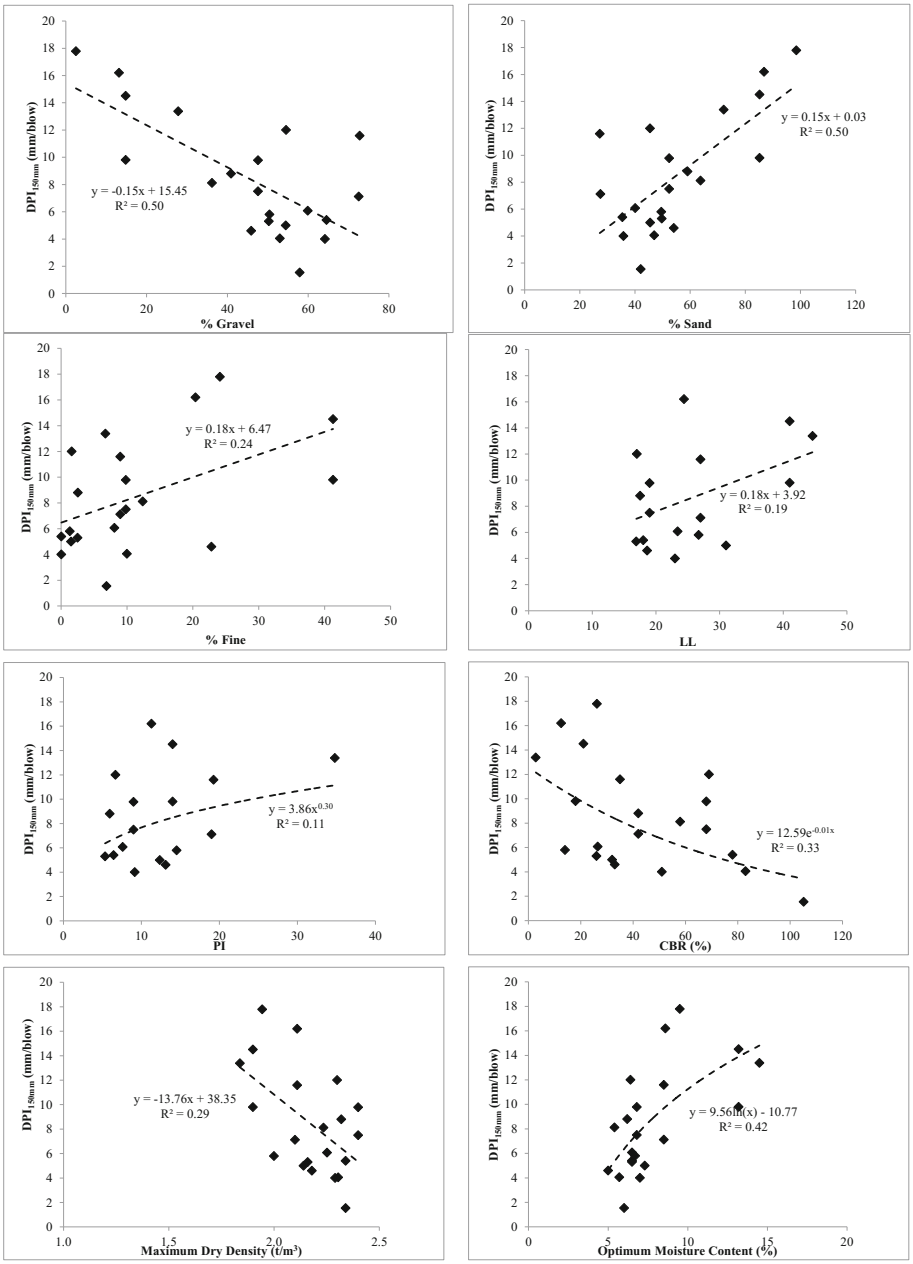


**Fig. 2.** DPI-material properties correlations.

percent fines (%), liquid limit (LL), plasticity index (PI), CBR (%), maximum dry density (t/m$^3$), and optimum moisture content (%) as shown in Fig. 2. In general, the $DPI_{150\ mm}$ values tended to give reasonable correlations with material properties. The

findings were also consistent with Sawangsuriya [6]. The highest $R^2$ of 0.50 was observed between the $DPI_{150\ mm}$ values and percent gravel and sand, while the lowest $R^2$ of 0.11 was observed between the $DPI_{150\ mm}$ values and plasticity index. Regardless of different test conditions, this study clearly indicated that the $DPI_{150\ mm}$ value could be effectively used for quality index quantification in terms of the index, physical, and engineering properties of a given pavement layer material with proper compaction and near the optimum moisture content. However, cautions shall be exercised when adopting the DCP for field compaction acceptance as there are several factors e.g. soil type, soil structure, dry density, moisture content, matric suction etc. [7] that can affect the DPI values.

## 5 Conclusions

This paper presents correlations between penetration index measured from dynamic cone penetrometer (DCP) and properties of pavement layer materials. A convenient DCP was employed to assess the penetration index of various pavement materials e.g. crushed rock base, soil-aggregate subbase, sand embankment, natural subgrade etc. used in road construction in Thailand. A series of DCP tests were conducted in the laboratory test mold, the laboratory test box, and the field trials. Based on the weighted average technique, the DCP data were analyzed and interpreted to generate the representative DCP penetration index (DPI) for the maximum penetration depth of 150 mm (i.e., $DPI_{150\ mm}$). Basic properties of pavement layer materials including percent gravel (%), percent sand (%), percent fines (%), liquid limit (LL), plasticity index (PI), CBR (%), maximum dry density ($t/m^3$), and optimum moisture content (%) were tested and reported herein. By achieving appropriate moisture content and compaction quality, the empirical relationships between DPIs and properties of pavement layer materials from different test conditions indicated reasonable trends and thus confirmed its potential adoption for routine pavement layer evaluation in Thailand. Since the DPIs are affected by several factors including soil type, soil structure, dry density, moisture content, matric suction etc. [7]. In addition, the effect of horizontal confinement on the DPI is also significant [8] and shall be considered during the field application. Therefore, field verifications are required to verify these correlations prior to the future adoption in practice. In order to use the DCP as a quality control tool for field compaction acceptance of pavement layer materials, one of the approaches is to establish a calibration equation between DPI and the level of compaction achieved at the optimum moisture content for a given soil type.

## References

1. Sawangsuriya, A., Edil, T.B.: Evaluating stiffness and strength of pavement materials. Proc. Inst. Civ. Eng.-Geotech. Eng. **158**(4), 217–230 (2005)
2. ASTM D6951: Standard test method for use of the dynamic cone penetrometer in shallow pavement applications, ASTM International, West Conshohocken, PA (2015)

3. ASTM D698: Standard test methods for laboratory compaction characteristics of soil using standard effort (12,400 ft-lbf/ft3) (600 kN-m/m3)), ASTM International, West Conshohocken, PA (2012)
4. ASTM D1557: Standard test methods for laboratory compaction characteristics of soil using modified effort (56,000 ft-lbf/ft3) (2,700 kN-m/m3), ASTM International, West Conshohocken, PA (2012)
5. ASTM D1883: Standard test methods for California bearing ratio (CBR) of laboratory-compacted soils, ASTM International, West Conshohocken, PA (2016)
6. Sawangsuriya, A.: Performance-based in situ tests for compaction quality control of pavement layers. In: International Conference on Maintenance and Rehabilitation of Constructed Infrastructure Facilities (MAIREINFRA), Seoul (2017, in press)
7. Edil, T.B., Sawangsuriya, A.: Investigation of the DCP and SSG as alternative methods to determine subgrade stability, Report No. 0092-01-05, Wisconsin Department of Transportation, WI (2005)
8. Ampadu, S.I.K., Ackah, P., Nimo, F.O., Boadu, F.: A laboratory study of horizontal confinement effect on the dynamic cone penetration index of a lateritic soil in the laboratory. Transp. Geotech. **10**, 47–60 (2017)

# Crumb Rubber as a Sustainable Aggregate in Chip Seal Pavement

Ahmed A. Gheni and Mohamed A. ElGawady(✉)

Missouri University of Science and Technology, Rolla, USA
{aagmr6, elgawadym}@mst.edu

**Abstract.** The U.S. companies need to mine billions of tons of raw natural aggregates each year. In the same time, billions of scrap tires are going to landfills every year which makes the replacement of using natural aggregate with recycled and sustainable one is more beneficial to both industry and environment. This paper presents an extensive study on the performance of the chip seal pavement surfaces in terms of aggregate retention and performance. This study introduces a new eco-friendly chip seal by implementing the crumb rubber made of recycled tires as aggregates for such surface dressing. Twenty four specimens of chip seal were prepared and tested under three tests investigating the aggregate retention. The tests included the standard Vialit test, modified Vialit test, and sand patch test. Two types of emulsions, two types of binders, and three types of aggregates including the crumb rubber were examined in the tested specimens. This study revealed that the crumb rubbers from recycled tires would be used in the chip seal as aggregates but it is preferable to be used in conjunction with the conventional aggregates. The crumb rubber showed a remarkable performance in aggregate retention. This performance was mainly because of the low weight of the crumb rubber and its rough surface, which increased holding the crumb rubber into the asphalt emulsion or binder. In addition, crumb rubber as a partial or total replacement for the mineral aggregate was successfully implemented in the field using the traditional procedure and equipment.

**Keywords:** Chip seal · Road sealing · Crumb rubber · Aggregate retention · Eco-friendly

## 1 Introduction

Depletion of natural resources forces the construction industry to explore using recycled material as replacements of or additives to virgin construction materials. In the same time, the world is facing a serious problem dealing with scrap tires. As shown in Fig. 1, approximately more than four million tons of scrap tires were dumped in the U. S. during 2015 alone taking up valuable space in the landfill and wasting valuable resources in the form of the rubber material, textile and metal cord (RMA 2016). Researchers have shown that crumb rubber obtained from scrap tires can be used to replace mineral aggregate leading to more environment-friendly construction industry (Rangaraju and Gadkar 2012; Shuler 2011; Amirkhanian 2001; Papagiannakis and Lougheed 1995; Youssf et al. 2015; Gheni et al. 2017). Recycled crumb rubber has

© Springer Nature Singapore Pte Ltd. 2018
H. Tran-Nguyen et al. (eds.), *Proceedings of the 4th Congrès International de Géotechnique - Ouvrages -Structures*, Lecture Notes in Civil Engineering 8,
DOI 10.1007/978-981-10-6713-6_39

been widely used in concrete to improve durability, seismic behavior, and sustainability (Gou and Liu 2014; Siddique and Naik 2004; Youssf et al. 2016; Batayneh et al. 2008; Pacheco-Torgal et al. 2014; Sukontasukkul 2009). Rubber also altered the physical properties of concrete. Rubberized concrete has a higher sound absorption, a higher noise reduction coefficient, and lower heat transfer properties than those of conventional concrete. As a result, rubberized concrete has a greater ability to retain stored heat energy (Turgut and Yesilata 2008; Hall et al. 2012).

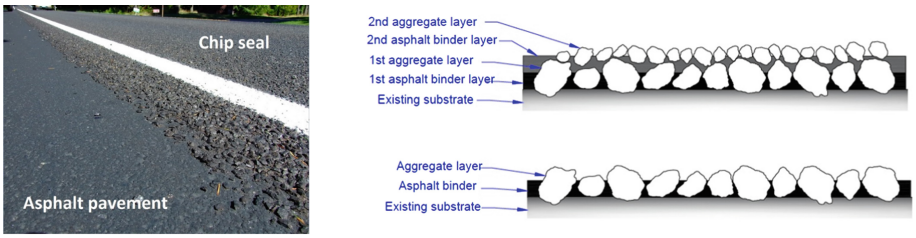


**Fig. 1.** Chip seal pavement, (a) chip seal vs asphalt pavement and, (b) types of chip seal

On the same level, transportation infrastructure is a major contributor to global greenhouse gas emissions with 23% of global carbon dioxide ($CO_2$) emissions, which makes it the second largest contributor, only behind electricity generation (Ang and Marchal 2013). As a result, using recycled material in the construction of the transportation infrastructure will help to cut the ($CO_2$) emissions significantly. One application is using scrap tire material in the roadway construction. Previous studies used crumb rubber as asphalt binder modifier, which improves the general performance of the binders in terms of temperature susceptibility, viscosity, and stiffness (Lee et al. 2008; Presti 2013).

Chip seal is a type of pavement coating treatment that consists of a single application of asphalt directly on the existing pavement or substrate, followed by the application of aggregate chips that are rolled with a pneumatic roller. In this process, the aggregate chip layer is one stone thick (Fig. 1a). Chip seal types include single (conventional), double (Fig. 1b). According to the best knowledge of the researcher, there has been no research on using crumb rubber into chip seal. This research aims at investigating the potential use of crumb rubber as an aggregate in chip seal which, if successful, will significantly increase the sustainability of chip seal.

## 2 Experimental Program

### 2.1 Material Characterization and Properties

Two types of asphalt cement, namely PG 64-28 and PG 70-28, and two types of emulsions, namely CRS-2P and CHFRS-2P, were used during this study. Both emulsion 1 and emulsion 2 are Cationic, which is defined as the migration of asphalt

particles under an electric field towards the cathode (negative electrode). Emulsion 1 is a rapid-setting and high-viscous type, while emulsion 2 is a high-float, rapid-setting, high-viscous type. The main difference between the two asphalt cement types is the softening temperature. The main difference between asphalt cement and emulsion is the water content and other admixtures such as emulsifiers that keep the emulsions flowable and workable at a low temperature of 35 °C compared to 165 °C for asphalt cement. The water breakout of the emulsions was examined for weight loss during exposure time at a varied temperature from 35 to 65 °C, as shown in Fig. 2. The figure shows that approximately 81% of the water breakout occurred after 6 h for the both types of emulsions, while there was almost no evaporation after 24 h of exposure.

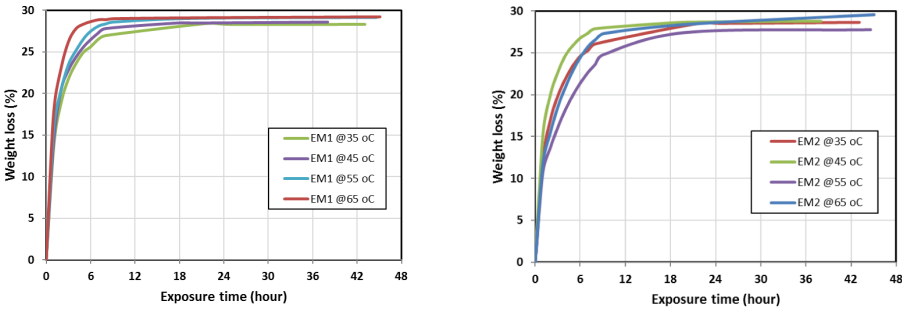


**Fig. 2.** Emulsion weight loss due to water breakout, (a) emulsion 1, (b) emulsion 2

Two types of mineral aggregates, namely creek gravel, and trap rock were used during this study (Fig. 3a and b). Hereinafter these two types will be referred as aggregate 1, and aggregate 2, respectively. A third synthetic aggregate, crumb rubber, obtained from recycled tires was used during this study (Fig. 3c). Two grades for each aggregate type were used during this study with a contribution of 50% of each grade. The first grade was aggregate passing the 9.5 mm (0.37 in.) sieve and retained on the 6.3 mm (0.25 in.) sieve. The second grade was aggregate passing the 6.3 mm (0.25 in.) sieve and retained on the 4.75 mm (0.19 in.) sieve. Table 1 present the properties of the three types of aggregates, respectively. As shown in Table 1, the rubber had much higher Micro-Deval and Los Angeles abrasion resistance compared to the other two types of mineral aggregates.

**Fig. 3.** Aggregates used throughout this study (a) creek gravel, (b) trap rock, and (c) crumb rubber

**Table 1.** Aggregates properties

| Type of aggregate | | Rubber | Aggregate 1 (creek aggregate) | Aggregate 2 (crushed trap rock) |
|---|---|---|---|---|
| Bulk specific gravity | | 0.87 | 2.35 | 2.62 |
| Absorption, % | | 0.1% | 4.7% | 0.8% |
| Coefficient of uniformity | | 1.9 | 1.9 | 1.3 |
| Fractured faces | Percent of non-fractured faces | 0.0% | 4.6% | 0.0% |
| | Percent of faces with one or more faces | 100.0% | 95.4% | 100.0% |
| | Percent of faces with two or more faces | 88.7% | 93.1% | 100.0% |
| Loose dry unit weight, kg/m$^3$ | | 423 | 1,180 | 1,249 |
| Voids in loose aggregates, % | | 15.4 | 49.8 | 52.8 |
| Los Angeles loss by abrasion and impact, % | | 0.3% | 18.7% | 8.2% |
| Micro-Deval weight loss, % | | 0.0% | 6.0% | 2.1% |
| Materials passing No. 200 sieve, % | | 0.20% | 0.50% | 0.52% |
| Median particle size, mm | | 6.5 | 6.2 | 6.1 |
| Flakiness index, % | | 31.3% | 37.6% | 42.0% |

## 2.2 Standard and Modified Vialit Tests

A standard Vialit test was conducted on 12 chip seal specimens according to the British Standard 12272–3 (EN 2003) to investigate the aggregate retention, as listed in Table 2.

The procedure of the Vialit test started by applying the emulsion at 60 °C (140 °F) or asphalt cement at 165 °C (329 °F) to standard square steel pan with dimensions of 200 mm (7.8 in.) × 200 mm (7.8 in.). Thereafter, 100 aggregates with a uniform size of approximately 9.5 mm (0.375 in.) were applied in a uniform grid of 10 × 10. Then, the specimens were cured in the oven at 60 °C (140 °F) for 48 h (Fig. 4).

The pan was then removed from the oven and allowed to cool for 30 min at 25 ± 5 °C (77 ± 41 °F). Each specimen was placed after that in a freezer with a temperature below 0 °C for 30 min and was tested within 10 s after being removed from the freezer. Each steel pan was turned upside down and fixed in the test setup at four points as shown in Fig. 4. Then, a standard stainless steel ball was dropped three times from a height of 500 mm on the steel pan as shown in Fig. 4c. The fallen aggregates were counted and recorded after each impact of the ball on the steel pan. The retention percentage after each impact was then calculated. The standard Vialit test, which requires three drops of the stainless-steel ball on a test specimen, was adequate to distinguish the performance of the specimens made out of asphalt cement. However, it was not enough to distinguish the performance of the different specimens made out of emulsions. Therefore, a modified Vialit test was conducted by increasing the number of ball drops to 30 and 40 as listed in Table 2.

**Table 2.** Specimens variables of the standard and modified Vialit tests

| Groups | Specimen label | Type of test | No. of drops | Emulsion/ asphalt cement type | Aggregate type | Percentage of retained aggregates |
|---|---|---|---|---|---|---|
| Group A | CS-1 | Standard Vialit test | 3 | Emulsion 1 | Rubber | 100.0% |
| | CS-2 | | | | Aggregate 1 | 100.0% |
| | CS-3 | | | | Aggregate 2 | 100.0% |
| | CS-4 | | | Emulsion 2 | Rubber | 100.0% |
| | CS-5 | | | | Aggregate 1 | 100.0% |
| | CS-6 | | | | Aggregate 2 | 100.0% |
| | CS-7 | | | Asphalt cement 1 | Rubber | 100.0% |
| | CS-8 | | | | Aggregate 1 | 60.0% |
| | CS-9 | | | | Aggregate 2 | 41.0% |
| | CS-10 | | | Asphalt cement 2 | Rubber | 100.0% |
| | CS-11 | | | | Aggregate 1 | 71.0% |
| | CS-12 | | | | Aggregate 2 | 52.0% |
| Group B | CS-13 | Modified Vialit test | 30 | Emulsion 1 | Rubber | 100.0% |
| | CS-14 | | | | Aggregate 1 | 88.0% |
| | CS-15 | | | | Aggregate 2 | 75.0% |
| | CS-16 | | | Emulsion 2 | Rubber | 100.0% |
| | CS-17 | | | | Aggregate 1 | 96.0% |
| | CS-18 | | | | Aggregate 2 | 89.0% |
| Group C | CS-19 | | 40 | Emulsion 1 | Rubber | 100.0% |
| | CS-20 | | | | Aggregate 1 | 80.0% |
| | CS-21 | | | | Aggregate 2 | 68.0% |
| | CS-22 | | | Emulsion 2 | Rubber | 100.0% |
| | CS-23 | | | | Aggregate 1 | 92.0% |
| | CS-24 | | | | Aggregate 2 | 75.0% |

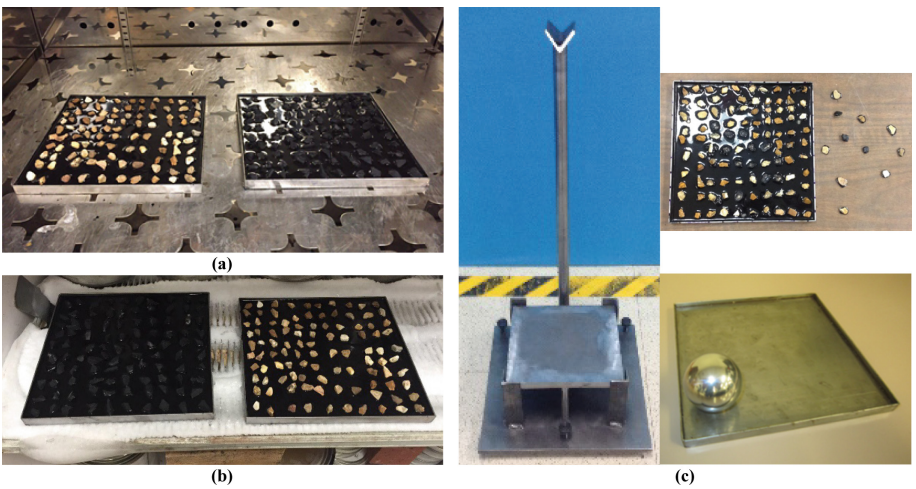


**Fig. 4.** Vialit drop test (a) specimens curing for 48 h at 60 °C, (b) specimens freezing for 30 min at −22 °C, and (c) test setup

### 2.3 Field Implementation

The main object of this stage was to ensure the feasibility of constructing rubberize chip seal using the same set of equipment, tools, and procedures that are used today by an average contractor to apply a conventional chip seal. Two chip seal sections with two different crumb rubber replacement ratios namely 50% and 100% were examined. Each section was about 350 feet long. Without any modification, the traditional chip seal procedure was used to apply the new rubberized chip seal (Fig. 5). An ambient processed crumb rubber was used with a size of 2.3–6 mm. This was similar in size to the creek gravel aggregate used in the blend. Emulsion type CRS2P with a temperature of 130 °F was used while the air temperature was 78 °F. During the compaction, it was noticed that rubber particles were adherent to the tiers of the rubber tires compactors (Fig. 5). The reason behind this was the flexibility of the rubber particles that allowed the rubber tires to penetrate and squeeze the crumb rubber layer and reach to the emulsion. As a result, the rubber tires compactors were replaced by steel roller compactor which did the compaction appropriately.

**Fig. 5.** Field implementation of new rubberized chip seal with 100% crumb rubber replacement ratio

## 3 Results and Discussions

### 3.1 Standard and Modified Vialit Tests Results

The number of retained aggregates out of 100 aggregates in the binder was recorded for each specimen. Table 2 summarizes the results of the standard Vialit test. The performance of the three types of aggregates in conjunction with each type of asphalt cement for the standard Vialit test is shown in Fig. 6.

Aggregate 1 and 2 had better performance with the two emulsions than with the two asphalt cement during the standard test (Fig. 6a). The retention rate was 100% for both emulsions while it ranged from 40% to 60% and 50% to 70% for binder 1 and binder 2, respectively. This behavior occurred because the asphalt cement shrank after the curing time more than the emulsions, causing some tension on the bond with the aggregate, and the asphalt cement became glassy and fragile after freezing the specimens at −25 °C per the test requirements.

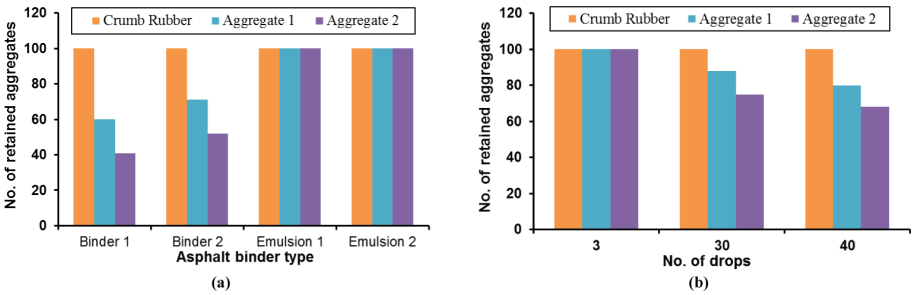


**Fig. 6.** Vialit test results (a) number of retained aggregates in Vialit test and, (b) number of retained aggregates versus no. of drops for specimens constructed out of emulsion 1

The crumb rubber showed a superior performance of 100% retained aggregates for the two asphalt cement and two emulsions due to the compatibility between the rubber and the asphalt cement/emulsion as both the rubber and asphalt cement/emulsions are made with hydrocarbon organic base. This compatibility gave high cohesion strength between the crumb rubber's outer surface and the asphalt cement.

### 3.2 Sand Patch Field Test

The standard sand patch method was used to determine the MTD of the chip seal coating with the two different crumb rubber replacement ratios. Two volumes of sand namely 125 ml and 60 ml, passing a No. 60 sieve and retained on a No. 80 sieve were prepared in containers. Then, it was spread uniformly on the surface of each of the investigated spots using an ice hockey puck with its bottom surface be covered with a hard rubber material as shown in Fig. 7.

**Fig. 7.** On-site sand patch test

The diameter of the spreading sand on each investigated spot was measured at least four times in different orientations (Fig. 7).

The average diameter, D, was determined and implemented in Eq. 1 to determine the macrotexture depth (MTD) which is an indication of the aggregate embedment depth.

$$MTD = \frac{4V}{\pi D^2} \tag{1}$$

where V is the sand volume.

The results of the sand patch for the field implementation were compared to lab specimens with different aggregate particle size same trend was noticed for both lab and field specimens as shown in Fig. 8. As shown in the figure the MTD significantly increased with increasing the rubber content.

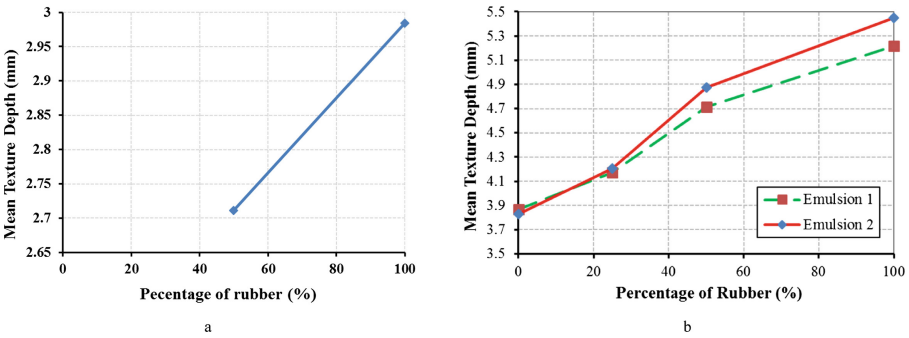


**Fig. 8.** Percentage of crumb rubber versus the macrotexture depth from sand patch test. (a) Field implementation specimens with aggregate size equal to 6 mm. and (b) Lab specimens with aggregate size equal to 10 mm.

## 4 Findings, Conclusions, and Recommendations

This study revealed that the crumb rubber from recycled tires could be used in the chip seal as aggregates. The crumb rubber showed remarkable performance in aggregate retention because of its low weight and rough surface, which increased the adhesions of the crumb rubber to the asphalt emulsion or asphalt cement. In addition, using crumb rubber improved macrotexture of chip seal. This study revealed the following particular findings and conclusions:

- Chip seal constructed with emulsions and mineral aggregates or 100% crumb rubber aggregate passed the standard Vialit test with no aggregate loss. However, increasing the number of drops to 40 showed that the crumb rubber aggregate outperformed the mineral aggregates with 100% retention versus 65% to 90% for the mineral aggregates. and 40% to 50% for the mineral aggregates in the case of asphalt cement.
- The retention of crumb rubber aggregate with cement asphalt measured using Vilait test outperformed that of the mineral aggregate. Crumb rubber aggregate showed 100% aggregate retention versus 40% to 50% in the case of mineral aggregate based on the cement asphalt type.

- Using crumb rubber as a partial or total replacement for the mineral aggregate was successfully implemented in the field using the traditional procedure and equipment. However, it was required to use steel roller compactor instead of rubber tires compactor to compact the chip seal.
- Sand patch and section image processing showed that replacing mineral aggregates with crumb rubber can improve the macrotexture of chip seal. An increase of 25% and 33% in mean texture depth (MTD) was observed when 100% of the trap rock and creek gravel were replaced with crumb rubber, respectively.

**Acknowledgments.** This research was conducted at the Missouri University of Science and Technology and supported by the Missouri Department of Natural Resources. However, any opinions, findings, conclusions, and recommendations presented in this paper are those of the authors and do not necessarily reflect the views of the sponsors.

## References

Amirkhanian, S.N.: Utilization of crumb rubber in asphaltic concrete mixtures–South Carolina's experience. See Ref **3**, 163–174 (2001)

Ang, G., Marchal, V.: Mobilising private investment in sustainable transport: the case of land-based passenger transport infrastructure. OECD Environ. Work. Pap. (56), 0_1 (2013)

Batayneh, M.K., Marie, I., Asi, I.: Promoting the use of crumb rubber concrete in developing countries. Waste Manag **28**(11), 2171–2176 (2008)

Gheni, A.A., ElGawady, M.A., Myers, J.J.: Mechanical characterization of concrete masonry units manufactured with crumb rubber aggregate. ACI Mater. J. **114**(01), 65–76 (2017)

Gou, M., Liu, X.: Effect of rubber particle modification on properties of rubberized concrete. J. Wuhan Univ. Technol.-Mater. Sci. Ed. **29**(4), 763–768 (2014)

Hall, M.R., Najim, K.B., Hopfe, C.J.: Transient thermal behaviour of crumb rubber-modified concrete and implications for thermal response and energy efficiency in buildings. Appl. Therm. Eng. **33**, 77–85 (2012)

Lee, S.-J., Akisetty, C.K., Amirkhanian, S.N.: The effect of crumb rubber modifier (CRM) on the performance properties of rubberized binders in HMA pavements. Constr. Build. Mater. **22** (7), 1368–1376 (2008)

Pacheco-Torgal, F., Lourenço, P.B., Labrincha, J., Kumar, S.: Eco-efficient Masonry Bricks and Blocks: Design, Properties and Durability. Woodhead Publishing, Sawston (2014)

Papagiannakis, A., Lougheed, T.: Review of crumb-rubber modified asphalt concrete technology (1995)

Presti, D.L.: Recycled tyre rubber modified bitumens for road asphalt mixtures: a literature review. Constr. Build. Mater. **49**, 863–881 (2013)

Rangaraju, P., Gadkar, S.: Durability evaluation of crumb rubber addition rate on Portland cement concrete. Department of Civil Engineering, Clemson University, Clemson, pp. 1–126 (2012)

RMA: Scrap tire markets in the United States (2016)

Shuler, S.: Use of waste tires, crumb rubber, on colorado highways. Colorado Department of Transportation, DTD Applied Research and Innovation Branch (2011)

Siddique, R., Naik, T.R.: Properties of concrete containing scrap-tire rubber–an overview. Waste Manag **24**(6), 563–569 (2004)

Sukontasukkul, P.: Use of crumb rubber to improve thermal and sound properties of pre-cast concrete panel. Constr. Build. Mater. **23**(2), 1084–1092 (2009)

Turgut, P., Yesilata, B.: Physico-mechanical and thermal performances of newly developed rubber-added bricks. Energy Build. **40**(5), 679–688 (2008)

Youssf, O., ElGawady, M.A., Mills, J.E.: Experimental investigation of crumb rubber concrete columns under seismic loading. In: Structures. Elsevier, pp 13–27 (2015)

Youssf, O., ElGawady, M.A., Mills, J.E.: Static cyclic behaviour of FRP-confined crumb rubber concrete columns. Eng. Struct. **113**, 371–387 (2016)

# Development of Geopolymer-Based Materials from Coal Bottom Ash and Rice Husk Ash with Sodium Silicate Solutions

Hoc Thang Nguyen[1(✉)], Trung Kien Pham[2], and Michael A.B. Promentilla[3]

[1] Faculty of Chemical Technology, Ho Chi Minh City University of Food Industry, Ho Chi Minh City, Vietnam
thangnh@cntp.edu.vn

[2] Faculty of Material Engineering, Ho Chi Minh City University of Technology, Ho Chi Minh City, Vietnam
phamtrungkien@hcmut.edu.vn

[3] Department of Chemical Engineering, De La Salle University, Manila, Philippines
michael.promentilla@dlsu.edu.ph

**Abstract.** The coal bottom ash is a solid waste generated from coal-fired thermal power plants that contains high alumino-silicates resources. Rice husk ash was burned from rice husk which has over 80% silica in its chemical composition. The alumino silicates resources in these materials have high reactivity in various conditions such as that of alkaline reactions and thermal reactions. Therefore, both coal bottom ash (CBA) and rice husk ash (RHA) are promising raw materials for synthesizing alkali activated materials through geopolymerization. This study focuses on utilization of CBA and RHA to produce geopolymer – based materials using sodium silicate solution as an alkali activator. This is one of the potential solutions that would not only manage the coal bottom ash but also an avenue to utilize the waste to produce green materials. The production of geopolymer-based materials results to lower energy consumption, minimal $CO_2$ emissions and lower production cost as it valorizes industrial waste. The CBA and RHA were mixed with sodium silicate solution to obtain the geopolymeric pastes. The pastes were molded in 5-cm cube molds according to ASTM C109/C109 M 99, and then cured at room temperature for 28 days. The 28-day geopolymer specimens were tested for engineering properties such as compressive strength (MPa), volumetric weight ($kg/m^3$), water absorption ($kg/m^3$) and thermal conductivity (W/m.K). Microstructure of the best geopolymer sample was characterized by using X-ray diffraction (XRD), Fourier transform infrared spectroscopy (FTIR), and scanning electron microscope (SEM).

## 1 Introduction

Geopolymer, as coined by (Davidovits, 2011), is an inorganic polymer composite which could be a potential sustainable construction material because of its lower energy and carbon footprint as compared to Portland cement-based materials (Li et al., 2004). Such

© Springer Nature Singapore Pte Ltd. 2018
H. Tran-Nguyen et al. (eds.), *Proceedings of the 4th Congrès International de Géotechnique - Ouvrages -Structures*, Lecture Notes in Civil Engineering 8,
DOI 10.1007/978-981-10-6713-6_40

material uses industrial waste such as coal ash as raw material which reduces its cost of production. Geopolymerization has become a promising technology as it offers attractive possibilities for commercial applications such as fast hardening, high and early compressive strength, optimal acid resistance, long term durability, high fire and erosion resistances (Davidovits, 2011). Geopolymer matrices can also stabilize metallic and radioactive wastes or industrial wastewater (Promentilla et al., 2016; Nguyen et al., 2017).

Rice husk ash (RHA) is a high–silica material produced from burning rice husk. Rice husk takes up about 20% weight of rice and its compositions include 15–20% $SiO_2$, the others are cellulose and lignin (Chandra, 1997; Siddique and Khan, 2011; Babcock & Wilcox Company, 1978). After the burning process, total weight of obtained RHA is about 20% weight of rice husk. This characteristic mainly depends on burning conditions such as temperature, holding time, among others. In 2011, rice production were over 700 million metric tons globally, wherein more than 90% came from Asian countries such as China, India, Indonesia, Bangladesh, Vietnam, Burma, Thailand, and the Philippine. Hence, the total estimated RHA reserves are over 28 million metric tons every year (Siddique and Khan, 2011).

Coal bottom ash (CBA) is the coarse, granular, incombustible by-products that are collected from the bottom of furnaces that burn coal for the generation of steam, the production of electric power, or both. The majority of these coal by-products are produced at coal-fired electric utility generating stations, although considerable bottom ash is also produced from many smaller industrial or institutional coal-fired boilers and from coal-burning independent power production facilities. The type of by-product (i.e., bottom ash) produced depends on the type of furnace used to burn the coal. The most common type of coal-burning furnace in the electric utility industry is the dry, bottom pulverized coal boiler. When pulverized coal is burned in a dry, bottom boiler, about 80% of the unburned material or ash is entrained in the flue gas and is captured and recovered as fly ash. The remaining 20% of the ash is dry bottom ash, a dark gray, granular, porous, predominantly sand size minus 12.7 mm material that is collected in a water-filled hopper at the bottom of the furnace (Hecht and Duvall, 1975). When a sufficient amount of bottom ash drops into the hopper, it is removed by means of high-pressure water jets and conveyed by sluiceways either to a disposal pond or to a decant basin for dewatering, crushing, and stockpiling for disposal or use (Hecht and Duvall, 1975).

## 2 Materials and Methods

In this research, both CBA and RHA from Vietnam were used to produce geopolymer-based materials. They are the raw materials in geopolymerization reactions to create the mechanical strength for the products. CBA was dried (Venticell drier) for 24 h, ground (Ball Miller) in 30 min, and sieved through 90 μm- mesh (Retsch AS-200 Seive Shaker). The coal bottom ash contains high alumina in amorphous or semi-crystalline structure which serves as one of the reactants in the geopolymerization process. On the other hand, rice husks from Mekong delta, South of Viet Nam were burned at 700 °C for 1 h at Laboratory of Ceramic Materials to obtain rice husk ash, and then also ground in 30 min and passed through 90 μm-mesh. Note that the rice

husk ash (RHA) contains high amorphous silica which also serves as one of the reactants in geopolymerization. Both CBA and RHA were characterized for physico-chemical and microstructural properties before carrying out the mixing to form the geopolymer mortar.

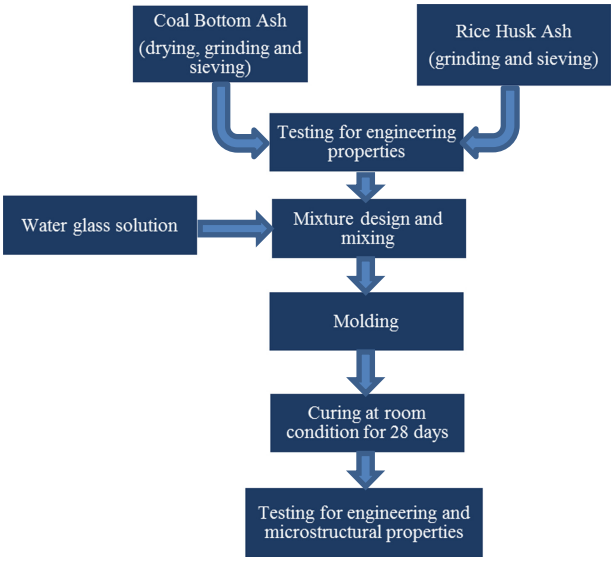


**Fig. 1.** Flowchart of the experiment

Both coal bottom ash and rice husk ash were mixed for 20 min with water glass solution (Lab cement mixer) and water was added to get a pH value around 12. Geopolymer mixtures were molded in 50 × 50 × 50 mm cube-cement mold and cured at room temperature (28 °C, 80% humidity) (Fig. 2). The 28-day geopolymer specimens were tested for compressive strength, volumetric weight, and water absorption. Then, the geopolymer specimens with the highest value of compressive strength and lowest value of water absorption were characterized using XRD, SEM, and FTIR. Figure 1 describes the flow of the experiment.

**Fig. 2.** Geopolymer specimens from coal bottom ash and rice husk ash.

**Table 1.** Mix design of the ash geopolymer using WGS

| Sample | Percentage of solid powders (%, in weight) | | Ratio of WGS (%, in weight) |
|---|---|---|---|
| | CBA | RHA | |
| A | 50 | 50 | 0 |
| B | 45 | 45 | 10 |
| C | 40 | 40 | 20 |
| D | 35 | 35 | 30 |
| E | 30 | 30 | 40 |

For mixture proportion, there were two phases used to form geopolymer paste. The solid phase was the powders of CBA and RHA with weight ratio of one is to one (CBA: RHA = 1:1). The liquid phase is composed of water glass solution (WGS) and water. For the alkali activator, sodium silicate (72% $SiO_2$, 28% $Na_2O$) with silica modulus of 2.5 was used from Bien Hoa chemical factory (Bien Hoa City, Dong Nai province, Vietnam). This chemical was added with water to obtain the solution with 55% $H_2O$ and 45% solid phase. The concentration of WGS was changed from 0 to 40% (by weight). The water was just added to obtain geopolymeric paste with suitable viscosity for molding process. The label of the 5 specimens and the proportion of the raw materials are shown in Table 1.

## 3 Results and Discussions

### 3.1 Engineering Properties of the Raw Materials

The CBA has a bulk density at 2560 kg/m$^3$ and a mean particle size of around 32.11 μm based from the laser diffraction method. On the other hand, RHA is seen as lightweight material with a bulk density of 1.05 kg/m$^3$ and its mean particle size is 10.20 μm based from laser diffraction method.

Table 2 summarizes the chemical composition of these alumino-silicate raw materials. As indicated in the XRD pattern of these materials (see Fig. 4), the raw materials contain both amorphous alumina and silica suitable for geopolymerization reaction at high alkali condition. This also suggests the presence of crystal structures in the CBA and RHA. Results also show that CBA and RHA have L.O.I values at 8.61%

**Table 2.** Chemical composition of the raw materials using XRF

| Materials | Oxides (%) | | | | | | | | | |
|---|---|---|---|---|---|---|---|---|---|---|
| | $Al_2O_3$ | $SiO_2$ | $Fe_2O_3$ | $SO_3$ | $K_2O$ | MgO | CaO | $TiO_2$ | $Na_2O$ | LOI |
| CBA | 20.85 | 52.63 | 9.08 | 0.75 | 4.75 | 0.90 | 0.82 | 1.39 | 0.22 | 8.61 |
| RHA | 0.37 | 83.20 | 1.70 | 0.61 | 6.60 | 0.62 | 1.50 | – | – | 4.60 |
| Sodium silicate | – | 72.00 | – | – | – | – | – | – | 28.00 | – |

LOI: Loss on ignition

and 4.60%, respectively. The RHA composition meet the requirements of ASTM C618 with 4.61% L.O.I (< 6%) and 83.20% $SiO_2$ (> 70%).

### 3.2 Engineering Properties of the Geopolymer-Based Materials

Table 3 summarizes the results of the engineering properties of geopolymer at different mix proportions of raw materials with varying concentration of sodium silicate solution ranging from 0% to 40% (in weight). In this study, the geopolymer-based materials have volumetric weight from 1472 kg/m$^3$ to 1506 kg/m$^3$ that belong to lightweight materials as classified in ASTM C55 and C90, the values of thermal conductivity are in the range of 0.475 W/m.K to 0.481 W/m.K. The 28-day compressive strength of the specimens is in the range of 2.45 to 17.41 MPa. This geopolymer product will be used as an alternative to lightweight concrete brick. Note that a 28-day compressive strength of 11.7 MPa and more is desirable for concrete brick according to ASTM C55 and C90-99a standards. The specimens with over 11.7 MPa of compressive strength included C (20% WGS), D (30% WGS), E (40% WGS). The results showed that the highest value of compressive strength obtained is 17.41 MPa for geopolymer sample D mixed with 30% WGS as shown in Fig. 3. The compressive strength of such sodium silicate activated geopolymer-based materials is attributed to the formation of alumino-silicate networks in geopolymer structures. The geopolymer D specimen with 35% CBA, 35% RHA and 30% WGS has the lowest water absorption values at 189.94 kg/m$^3$ whereas geopolymer A has the highest water absorption value (314.10 kg/m$^3$) as shown in Fig. 3. The water absorption of most of the geopolymer samples such as B, C, D, and E are lower than 288 kg/m$^3$ which is the prescribed limit according to ASTM C55 or C90 requirements for lightweight concrete brick material.

**Table 3.** Engineering properties of geopolymer-based materials

| Samples | Compressive strength (MPa) | Water absorption (kg/m$^3$) | Volumetric weight (kg/m$^3$) | Thermal conductivity (W/m.K) |
|---|---|---|---|---|
| A | 2.45 | 314.10 | 1494.40 | 0.476 |
| B | 6.23 | 267.61 | 1472.34 | 0.477 |
| C | 14.10 | 214.79 | 1506.47 | 0.479 |
| D | 17.41 | 189.94 | 1485.30 | 0.481 |
| E | 12.35 | 246.12 | 1483.56 | 0.475 |

Figure 3 shows relationships among engineering properties (compressive strength and water absorption) with the concentration of water glass solution in geopolymer based materials from CBA and RHA. Note that the geopolymer D specimen is the best sample and was chosen for microstructure analysis using XRD, SEM, and FTIR.

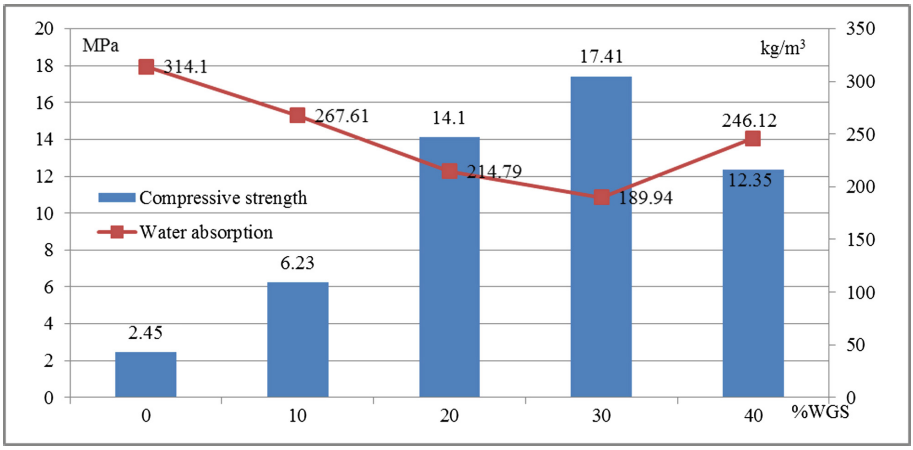


**Fig. 3.** Relationships among engineering properties (compressive strength and water absorption) to concentration of water glass solution in geopolymer based materials from CBA and RHA

### 3.3 Microstructural Properties of the Geopolymer-Based Materials

Figure 4 showed crystalline structures among geopolymer sample D and raw materials (CBA and RHA) based on the XRD patterns. The highest peak at 26.67° of 2-Theta is of quartz ($SiO_2$) which came from coal bottom ash, the very low peaks are of cristobalite ($SiO_2$) and hematite ($Fe_2O_3$) from RHA and CBA, respectively. There was no new peak observed but all of the peaks in the XRD patterns of the geopolymer can also

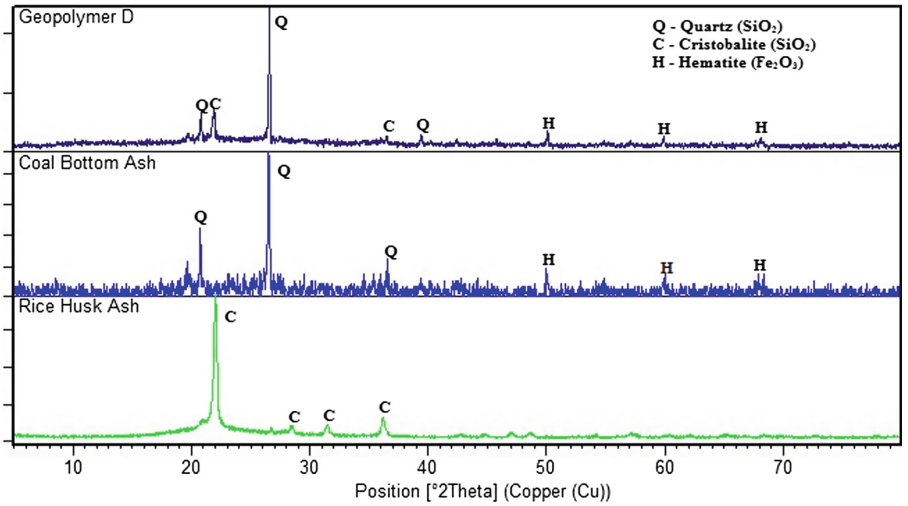


**Fig. 4.** XRD patterns of the geopolymer specimen D and raw materials (coal bottom ash and rice husk ash).

be observed from the raw materials. Thus, this suggests that the new phases formed in the geopolymerization process are amorphous in structure as indicated by the broad hump in the XRD patterns. Besides, there was also no existence of the peaks for sodium silicate crystal. Moreover, there is no evidence of any zeolite crystal-like formation in the geopolymer materials since this study only consider curing at room temperature. Note that zeolite-like structure would most likely form at higher temperature condition, for example, over 50°C in hydrothermal condition (Cundy and Cox, 2005; Santra and Luke, 2006).

Figure 5C shows the geopolymer microstructure with main structures such as the solid matrix contains powder. Note the appearance of a new phase with many long and thin rods as this morphology did not appear in any SEM of the raw materials (for RHA and CBA see Fig. 5A and B). In combination with the XRD patterns, it is clear that the new structures are in amorphous phase because there has been no characteristic peak detected for the new phase. They were formed from the dissolution of alumino-silicate resources and reacted at high alkali condition producing geopolymer networks after 28-day curing. These rods are similar to ettringite structure in cement-based materials (Tosun and Baradan, 2010; Binici et al., 2012) which could be the reason in the increased compressive strength of geopolymer binder. In addition, the SEM images in Fig. 5 showed no evidence of any specific seed of zeolite crystals that was reported in Cundy and Cox (2005). Thus, from the XRD pattern (Fig. 4) and SEM results, it confirms the absence of zeolite structures in the sodium silicate activated geopolymer-based materials produced in this research.

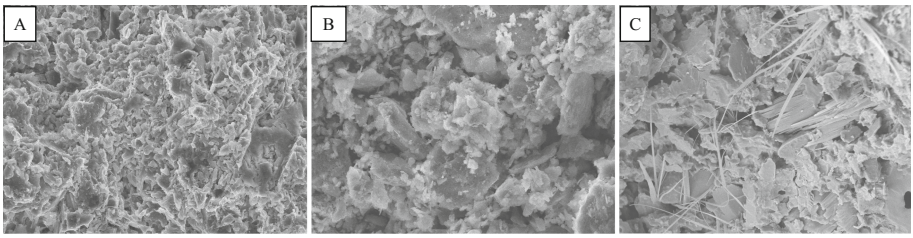


**Fig. 5.** SEM of RHA (A), CBA (B), and geopolymer D (C).

Another important analysis to provide evidence on the formation of alumino-silicate networks in geopolymer would come from FTIR analysis of the specimen. The IR spectra are divided in two ranges: 400–1400 $cm^{-1}$ which is related to the vibrational modes of –T–O–T– and –T–O–Na units (T refers to tetrahedral such as that of Si or Al) and 1400–4000 $cm^{-1}$ which is related to the vibrational modes of –OH and H–O–H (Jaarsveld and Deventer, 1999; Provis and Deventer, 2014) (Fig. 6).

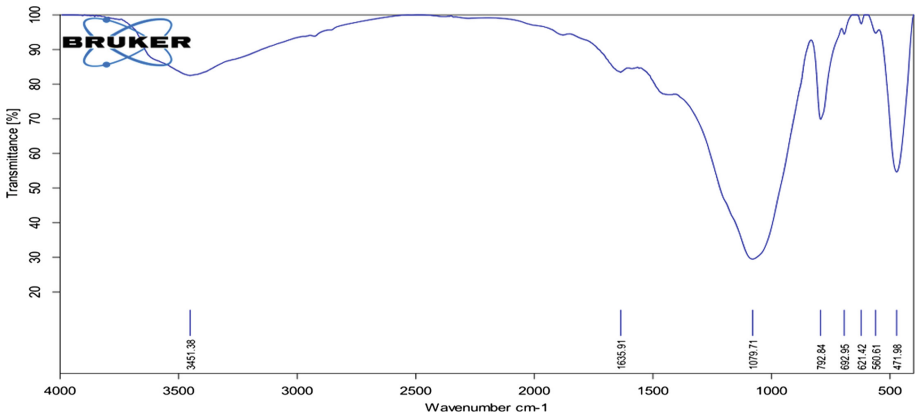


**Fig. 6.** FTIR of geopolymer based material (geopolymer D) from coal bottom ash and rice husk ash.

## 4 Conclusions

This study has evaluated a novel geopolymer binder system from a ternary blend of coal bottom ash (CBA) waste, rice hull ash (RHA) and water glass solution (WGS). Raw materials (CBA and RHA) were characterized to obtain the physical, chemical properties, and mineral compositions. High silica in RHA (83.2% $SiO_2$) and CBA (53.6% $SiO_2$), high alumina in CBA (20.8% $Al_2O_3$) in the raw materials were determined from the XRF analysis. Thus, the mixture of these raw materials provides the alumino-silicate resource for the geopolymerization process to occur. Mechanical properties of the sodium silicate activated geopolymer were evaluated and these engineering properties satisfied the requirements of ASTM C55 and C90 for a lightweight concrete brick. The microstructure properties of sodium silicate activated geopolymer were characterized for geopolymer D with 35% RHA, 35% CBA and 30% WGS. The formation and presence of amorphous alumino-silicate polymeric networks in the geopolymer-based material was inferred from the complementary results of XRD, SEM, and FTIR. Long-thin and short-thick rods associated with this inorganic polymer were observed from the micrograph.

**Acknowledgments.** The research group would like to thank and appreciation to the Japan International Cooperation Agency (JICA) for the financial support of our study. And also we would like to thank to the Department of Chemical Engineering in De La Salle University (DLSU) and Viet Nam – German Technology Center in Ho Chi Minh City University of Food Industry (HUFI) as well as Department of International Development Engineering, Tokyo Institute of Technology (TIT).

## References

Babcock and Wilcox Company: Steam: Its Generation and Use. Babcock and Wilcox, New York NY (1978)

Binici, H., Kapur, S., Arocena, J., Kaplan, H.: The sulphate resistance of cements containing red brick dust and ground basaltic pumice with sub-microscopic evidence of intra-pore gypsum and ettringite as strengtheners. Cement Concr. Compos. **34**, 279–287 (2012)

Chandra, S.: Waste Materials Used in Concrete Manufacturing. Noyes Publications, USA (1997)

Cundy, C.S., Cox, P.A.: The hydrothermal synthesis of zeolites: precursors, intermediates and reaction mechanism. Microporous Mesoporous Mater. **82**, 1–78 (2005)

Davidovits, J.: Geopolymer Chemistry and Application, 3rd edn. Institute Géopolymère, France (2011)

Hecht, N.L., Duvall, D.S.: Characterization and Utilization of Municipal and Utility Sludges and Ashes: Volume III – Utility Coal Ash. National Environmental Research Center/U.S. Environmental Protection Agency, Cincinnati (1975)

Jaarsveld, J.G.S.V., Deventer, J.S.J.V.: The effect of metal contaminants on the formation and properties of waste-based geopolymers. Cem. Concr. Res. **29**, 1189–1200 (1999)

Li, Z., Ding, Z., Zhang, Y.: Development of sustainable cementitious materials. In: Proceedings of the International Workshop on Sustainable Development and Concrete Technology, 20–21 May 2004, Beijing, China, pp. 55–76 (2004)

Nguyen, H.T., Pham, T.K., Abdullah, M.M.: Lightweight heat resistant geopolymer-based materials synthesized from red mud and rice husk ash using sodium silicate solution as alkaline activator. In: MATEC Web of Conferences, vol. 97, no. 01119, pp. 1–6 (2017)

Promentilla, M.A.B., Nguyen, H.T., Pham, T.K., Hinode, H., Bacani, F.T., Gallardo, S.M.: Optimizing ternary-blended geopolymers with multi-response surface analysis. Waste Biomass valorization **7**, 929–939 (2016)

Provis, J.L., van Deventer, J.S.J.: Alkali Activated Materials: State of the art report. RILEM-TC244 AAM. Dordrecht, Heidelberg (2014)

Santra, A.K., Luke, K.: Zeolite compositions having enhanced compressive strength. US 7,048,053 B2 (2006)

Siddique, R., Khan, M.I.: Supplementary Cementing Materials. Engineering Materials, Springer-Verlag, Berlin Heidelberg. (2011). doi:10.1007/978-3-642-17866-5_5

Tosun, K., Baradan, B.: Effect of ettringite morphology on DEF-related expansion. Cement Concr. Compos. **32**(4), 271–280 (2010)

# Development of New Type of Screwed Pile with Large Bearing Capacity and Ecological Driving Method "Tsubasa Pile™"

Marina Kawai[1(✉)], Kazuomi Ichikawa[2], and Kenji Kono[1]

[1] JFE Steel Corporation Civil Engineering Sec Construction Materials and Business Development Department, Tokyo, Japan
{ma-kawai, k-kono}@jfe-steel.co.jp
[2] JFE Steel Research Laboratory Civil Engineering Research Department, Tokyo, Japan
k-ichikawa@jfe-steel.co.jp

**Abstract.** "Tsubasa Pile™" developed by JFE Steel is a Rotary penetration steel pipe pile with toe wing, Toe wing is formed by installing two semicircular steel plates in a crosswise position to each other at the end of the steel pipe pile. "Tsubasa Pile™" has been increasingly used in various fields by taking advantage of large bearing capacities and environmentally-friendliness such as driving without removing any soil, low noise and non-use of cement milk. In addition, JFE Steel is developing new technologies including the use of batter piles.

**Keywords:** "Tsubasa Pile™" · Open-end type · Closed-end type · Environmentally friendly · Easy to withdraw · Batter piles

## 1 Introduction

In the evolution of foundation piles, various construction methods have been developed and used at actual construction sites. However, in the relationship between pile construction and the environment, focus of attention has been on problems such as noise and vibration during construction, treatment of surplus soil, groundwater pollution, etc. JFE Steel developed "Tsubasa Pile™", which is a steel pipe pile with a toe wing mounted on the leading toe, because of this features "Tsubasa Pile™" not only provides large bearing capacity (vertical bearing capacity, uplift resistance), but also has the important merit of being an ecological product, this innovative line of steel pipe piles has been adopted in diverse fields, including building foundations, highway bridge foundations, railway bridge foundations, and others, and is continuing to extend its sales record. This report describes the features of "Tsubasa Pile™".

© Springer Nature Singapore Pte Ltd. 2018
H. Tran-Nguyen et al. (eds.), *Proceedings of the 4th Congrès International de Géotechnique - Ouvrages -Structures*, Lecture Notes in Civil Engineering 8,
DOI 10.1007/978-981-10-6713-6_41

## 2 Features of "Tsubasa Pile™"

### 2.1 General Items

#### 2.1.1 Structure

"Tsubasa Pile™" is a steel pipe pile with a toe wing mounted on the leading toe of the steel pipe. The wing-shaped part comprises two intersecting semicircular flat steel plates having a diameter 1.5 to 3.0 times the diameter of the steel pipe. Two types of tip shapes are available, one in which the hole (1/2 the diameter of the pipe) in the center of the wing is open and the steel plates intersect at the outer surface of the pipe, and the other in which the tip is completely closed and the plates intersect at the center of the pipe. These two types have been commercialized under the trade names "Tsubasa Pile™" (Open end) (Fig. 1) and "Tsubasa Pile™" (Closed end) (Fig. 2).

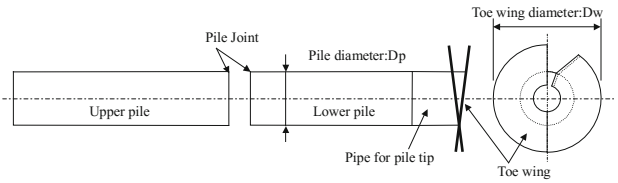


**Fig. 1.** Composition of "Tsubasa Pile™" (Open end)

Enlarged head type (Photo 1), in which the diameter of the steel pipe at the pile head is increased than that at the pile end part (maximum of 1.6 times larger is possible) and is joined by welding by way of a steel disk. This type can be used in soft soil, etc. where large horizontal resistance is necessary.

The specifications of these products have been standardized for each pile diameter and toe wing enlargement ratio based on experiments and finite element method (FEM) analysis, and can be selected corresponding to the conditions at the site.

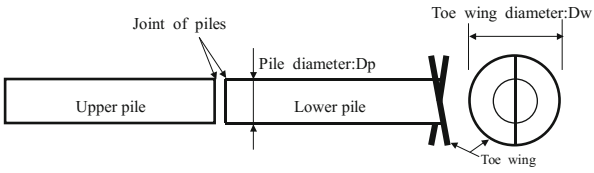


**Fig. 2.** Composition of "Tsubasa Pile™" (Closed end)

**Photo 1.** Enlarged pile head (Dp: 800 mm + 1200 mm)

### 2.1.2 Construction Machinery

Placement of "Tsubasa Pile™" does not require special construction machinery, but rather, can be performed with construction machinery in general use. The machinery used differs, depending on the pile diameter and soil conditions, but is roughly classified as shown in Fig. 3. Views of the respective construction machinery are shown in Photo 2. As the general practice, with small diameter piles, the Three-point pile driver is rotated, and with large diameter piles, the Rotary all casing boring machine is rotated.

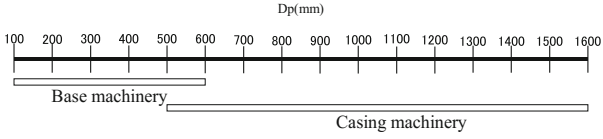


**Fig. 3.** Machinery type according to $D_p$

Three-point pile driver

Rotary all casing boring machine

**Photo 2.** Construction machinery

## 2.2 Range of Application

"Tsubasa Pile™" has received performance evaluations by General Building Research Corporation of Japan in the building construction field, by the Public Works Research Center in the highway field, and by the Railway Technical Research Institute in the railway field [1–5]. The range of application in these respective fields is shown in Table 1. Although the values differ in each field, this is because the timing and standards when "Tsubasa Pile™" was evaluated were different, and does not mean that this pile cannot be used in other fields of application.

**Table 1.** Scope of application

| Type | Field | Diameter | | Max. depth | Upper row: Pile diameter (mm)<br>Lower row: Magnification of toe wing | | |
|---|---|---|---|---|---|---|---|
| | | Min. | Max. | | | | |
| | | mm | mm | m | | | |
| Open end | Building | 114.3 | 1200 | 87 | 114.3–609.6 | 700–1200 | |
| | | | | | 1.5–3.0 | 1.5–2.0 | |
| | Road bridge | 318.5 | 1600 | 77 | 318.5–1200 | 1300–1600 | |
| | | | | | 1.5–2.0 | 1.5 | |
| | Railway bridge | 400 | 1600 | – | 400–1600 | | |
| | | | | | 1.5 | | |
| Closed end | Building | 114.3 | 1200 | 60 | 114.3–267.4 | 318.5–508.0 | 600–1200 |
| | | | | | 2.0–3.0 | 2.0–2.5 | 1.5–2.0 |
| | Road bridge | 318.5 | 1200 | 60 | 318.5–1200 | | |
| | | | | | 1.5–2.0 | | |
| | Railway bridge | 400 | 800 | – | 400–800 | | |
| | | | | | 2.0 | | |

### 2.3 Differences Between Open End Type and Closed End Type

"Tsubasa Pile™" is available in two types, the open end type and the closed end type, and can be applied taking advantage of their respective features. Outlines of the two types are presented below.

#### 2.3.1 Open End Type

Practical application of the open end type began in 2007 with the aim of improving workability.

Because soil can enter the pipe during pile construction, open end type features excellent workability in large-diameter piles ($\varphi$700 mm and larger) and is particularly suitable for ground with a hard intermediate layer.

#### 2.3.2 Closed End Type

The closed end type was first use in practical applications in 1999 and now has an extremely large record of use. With a simple, high rigidity structure, it can be manufactured at low cost. The closed end type is mainly used in small- and medium-diameter piles ($\varphi$609.6 mm and smaller).

## 3 Ecological Construction Features

### 3.1 Environmental Impacts

#### 3.1.1 No Soil Removal During Construction

When turning driving force (torque) is applied to "Tsubasa Pile™" at the ground surface, the pile penetrates the ground because the toe wing exerts a propulsion effect like that of a wood screw. In this process, soil corresponding to the volume of the pile is moved by the following (1) and (2). As a result, absolutely no soil is excavated aboveground from pile construction through the completion of construction (Photo 3).

**Photo 3.** Situation after construction

(1) Accompanying rotation of the toe wing, the soil below the wing is moved to above the wing, and inside the pile pipe, in the case of the open end type.
(2) Soil that has been moved to above the wing is compacted laterally by the pipe. The process of the above-mentioned soil movement during construction is shown schematically in Fig. 4.

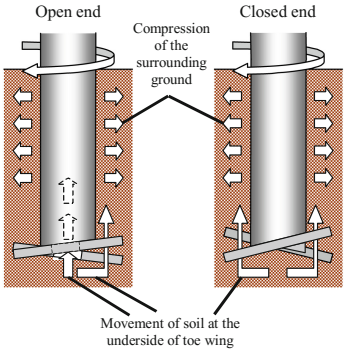


**Fig. 4.** Movement of soil during construction

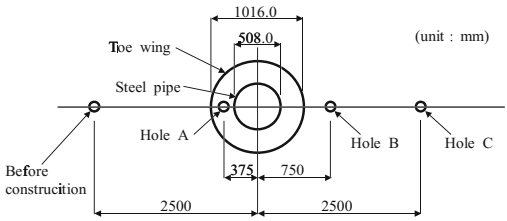


**Fig. 5.** Investigation points

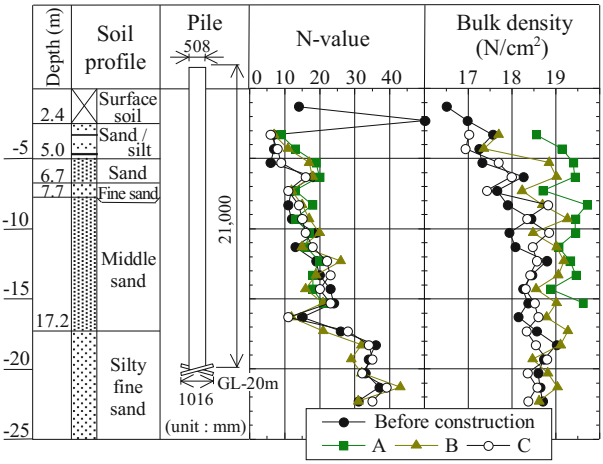


**Fig. 6.** Soil investigation result

An example comparing the measured ground density and *N*-value around the pile before and after construction is shown in Figs. 5 and 6. From the fact that density and the *N*-value increased at points near the pile (A, B) after construction, it can be

understood that the ground around the pile undergoes compaction accompanied by the pile construction.

As merits of no earth removal construction, not only is the cost of treating surplus soil zero, there is no effect on vehicular traffic in the area because dump trucks are not necessary for disposal of the soil, and construction is also possible at former factory sites, etc., where the ground may be affected by soil pollution.

### 3.1.2 No Use of Cement Milk

In order to realize a large toe bearing capacity, the general practice with conventional piles requires construction of foot protection bulb in the support layer, and in the case of cast-in-place piles, the full length of the pile is constructed of concrete. In either case, pollution of the groundwater by cement milk is unavoidable.

However, with "Tsubasa Pile™", absolutely no cement milk is required because the toe bearing capacity is supplied by the rigidity of the toe wing itself. Therefore, piles can be constructed without polluting the groundwater, and construction is possible in areas that use well water and areas where river bed water or confined (artesian) water exists.

### 3.1.3 Low Noise/Low Vibration

Because "Tsubasa Pile™" is constructed by screwing a steel pipe into the ground, low noise/low vibration construction is possible, without generating the loud impact noise associated with conventional pile-driving. Figure 7 shows the results of measurements of noise and vibration (4 sites) during actual pile construction. In all cases, it can be

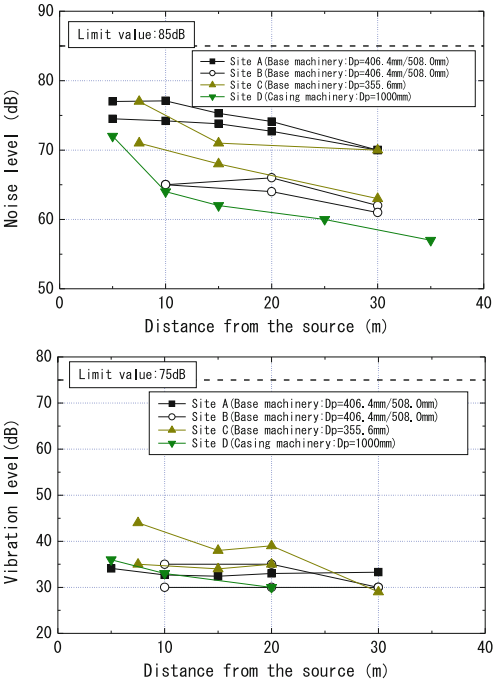


**Fig. 7.** Measurement of noise and vibration

understood that the values are substantially lower than the limit values (noise: 85 dB, vibration: 75 dB).

### 3.2 Development to New Applications

With the closed end type, added value can be given to ordinary support piles by utilizing the space inside the pipe after construction is completed. The following is actual example of value-added applications.

#### 3.2.1 Treatment of Surplus Soil of Construction

At construction sites, generation of surplus soil from various processes other than pile construction is possible. If this surplus soil is placed inside "Tsubasa Pile™" after pile construction, disposal is possible without discharging the surplus soil off-site. This can significantly reduce soil transportation and treatment costs.

## 4 Bearing Capacity Performance of "Tsbasa Pile™"

An extremely large toe bearing capacity can be expected with "Tsubasa Pile™" because bearing capacity is supplied by the surface area of the toe wing, which has a diameter 1.5 to 3.0 times that of the pile pipe. Bearing capacity performance comprises two types, namely, vertical bearing capacity (compressive load) and uplift resistance (tensile load). These two types of bearing capacity are confirmed by large-scale load tests, respectively. However, because the standards differ depending on the field of application, the equations used in evaluations also differ. Since the highway field (open end type, closed end type) and the railway field (open end type) use similar construction methods, a unified bearing capacity equation has been proposed as "screwed steel pipe pile" [6, 7].

### 4.1 Vertical Bearing Capacity (Compressive Load)

A combined total of 36 static axial compressive load tests was performed with open end type and closed end type "Tsubasa Pile™" and a design vertical bearing capacity equation was established based on the test results. The conditions of the compressive load tests are shown in Fig. 8.

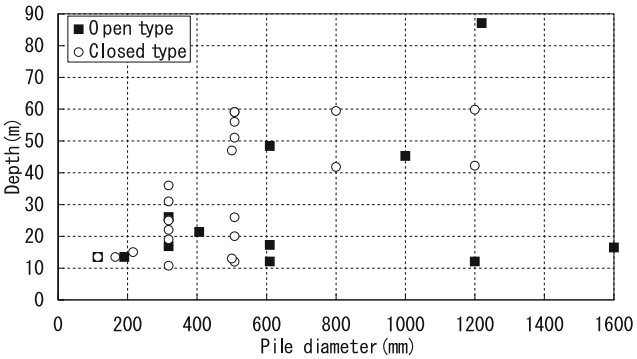


**Fig. 8.** List of compressive load tests

Outlines of the design equations in each field are presented in Sects. 4.1.1 and 4.1.3. The common symbols are given below:

$R_u$: Ultimate vertical bearing capacity of pile head (kN)
$D_p$: Diameter of pile (m)
$D$: Diameter of enlarged pile head part (m)
$D_w$: Diameter of toe wing (m)
$D_{wi}$: Inner diameter of toe wing (m), $D_{wi} = 0.5\ D_p$
$L_s$: Total length in contact with sandy ground (m)
However, excludes the section $1D_w$ from the pile toe.
$L_c$: Total length in contact with clay ground (m)
However, excludes the section $1D_w$ from the pile toe.
$L_i$: $i$th layer thickness considering surface frictional force (m)
$\Psi$: Circumference of pile (m)
$\Psi = \pi \cdot D_p$ (General part of conventional type/enlarged pile head type piles)
$\Psi = \pi \cdot D$ (Enlarged pile head part of enlarge pile head type pile).

### 4.1.1 Building Construction Field

Vertical bearing capacity is evaluated by using the following equation as a standard.

$$R_u = \alpha \cdot \bar{N} \cdot A_p + (\beta \cdot \bar{N}_s \cdot L_s + \gamma \cdot \bar{q}_u \cdot L_c)\Psi \quad (1)$$

$\alpha$: Bearing capacity coefficient of pile toe (common to sand and gravel)
Open end type ($\alpha$ = 150), Closed end type ($\alpha$ = 132)
$\beta$: Surface friction coefficient of pile in sandy ground
Open end type and Closed end type ($\beta$ = 2.0)
$\gamma$: Surface friction coefficient of pile in clay ground
Open end type and Closed end type ($\gamma$ = 0.5)
$\bar{N}$: Mean value of number of blows in standard penetration test of ground in range of $1D_w$ below and $1D_w$ above pile toe (times)
Open end type: $12 \le \bar{N} \le 60$
Closed end type: $13 \le \bar{N} \le 60$
$A_p$: Effective cross-sectional area of toe of foundation pile
Open end type:
$A_p = (1.40 - 0.25 \times D_w/D_p) \times \pi/4 \times (D_w^2 - D_{wi}^2)$
Closed end type:
$A_p = \pi/4 D_w^2$
$\bar{N}_s$: Mean number of blows in standard penetration test for sandy soil (times)
Open end type: $2 \le \bar{N}_s \le 30$
Closed end type: $4 \le \bar{N}_s \le 30$
$\bar{q}_u$: Mean value of uniaxial compressive strength of clay ground (kN/m$^2$)
Open end type: $23 \le \bar{q}_u \le 200$
Closed end type: $43 \le \bar{q}_u \le 200$.

### 4.1.2 Highway Field

Vertical bearing capacity is evaluated using the following equation as a standard. This is the equation for the screwed steel pipe pile and is the same for both the open end type and the closed end type.

$$R_u = q_d \cdot A_w + \Psi \cdot \Sigma(L_i \cdot f_i) \tag{2}$$

$q_d$: Ultimate bearing capacity of pile toe (kN/$m_2$)
By type of ground:
Sandy: 120 $N$ for 1.5 × wing, 100 $N$ for 2.0 × wing,
Gravel: 130 $N$ for 1.5 × wing, 115 $N$ for 2.0 × wing,

$N$: $N$-Value of ground at pile toe ($N \leq 50$)

$A_w$: Projected area of wing ($m^2$) $A_w = \pi/4D_w^2$

$f_i$: Maximum surface frictional force of $i$th layer, considering surface frictional force (kN/$m^2$)
Sandy soil: 3 $N$ ($\leq 150$)
Clay soil: c or 10 N ($\leq 100$)
$c$: Viscosity (kN/$m^2$)
$N$: $N$-Value of ground at pile surface.

### 4.1.3 Railway Field

Vertical bearing capacity is evaluated using the following equation as a standard. For the open end type, this is the equation for the screwed steel pipe pile.

$$R_u = q_{tk} \cdot A_t + \Psi \cdot \Sigma r_{fk} \cdot L_i \tag{3}$$

$q_{tk}$: Standard bearing capacity of pile toe (kN/$m^2$)
Open end type:
150 $N$ ($\leq 10\,000$) (Common for sand and gravel)

$N$: Minimum $N$-value of the section $1D_p$ above and $3D_p$ below pile toe
Closed end type:
Sand: 75 $N$ ($\leq 6\,000$),
Gravel: 75 $N$ ($\leq 7\,500$)
$N$: $N$-Value in vicinity of pile toe

$A_t$: Area of pile toe ($m^2$)
Open end type: $A_t = \pi/4 \times (D_w^2 - D_{wi}^2)$
Closed end type: $A_t = \pi/4D_w^2$

$r_{fk}$: Standard surface bearing capacity (kN/$m^2$)
Open end type:
Sandy soil: 2.5 $N$ ($\leq 100$),
Clay soil: 5 $N$ ($\leq 100$) or 0.3$c$ ($\leq 100$)
Closed end type:
Sandy soil: 2 $N$ ($\leq 100$),
Clay soil: 4 $N$ ($\leq 100$)

$N$: $N$-Value of ground at pile surface, $c$: Viscosity (kN/$m^2$).

### 4.2 Uplift Resistance (Tensile Load)

A combined total of 10 tensile load tests was performed with the open end type and closed end type of "Tsubasa Pile™." A design uplift resistance equation was established based on the results of these tests. The conditions of the tensile load tests are shown in Fig. 9.

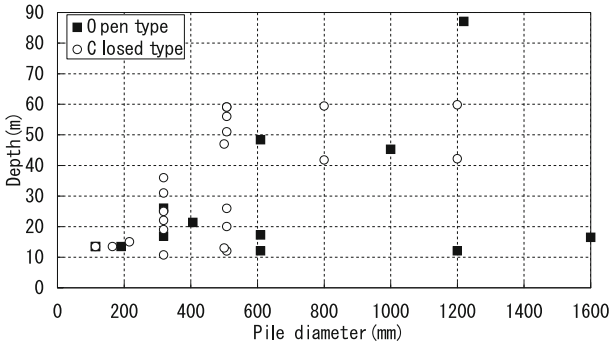


**Fig. 9.** List of compressive load tests

Outlines of the design equations in the respective fields are presented in Sects. 4.2.1 and 4.2.2. The common symbols are as follows:

$R_t$: Ultimate uplift resistance of pile head (kN)
$D_p$: Diameter of pile (m)
$D$: Diameter of enlarged pile head part (m)
$D_w$: Diameter of toe wing (m)
$L_s$: Total length in contact with sandy ground (m)
However, excludes the section $2D_w$ from the pile toe.
$L_c$: Total length in contact with clay ground (m)
However, excludes the section $2D_w$ from the pile toe.
$\Psi$: Circumference of pile (m)
$\Psi = \pi \cdot D_p$ (General part of conventional type/Enlarged pile head type piles)
$\Psi = \pi \cdot D$ (Enlarged pile head part of enlarge pile head type pile)
$\gamma_i$: Effective unit weight of soil of $i$th layer from ground surface higher than support layer (kN/m$^3$)
$L_i$: Thickness of $i$th layer from ground surface higher than support layer (m)
$\gamma$: Effective unit weight of soil of support layer (kN/m$^3$)
$H$: Penetration depth to height that the local shear fracture region extends above the wing (m)
Assuming $H \leq 2.5D_w$ (Highway field)
Assuming $H \leq 1D_w$ (Railway field)
$\beta$: Uplift coefficient. Expresses the coefficient of resistance of the shear fracture plane; A value corresponding to the internal friction angle of the support layer is applied (Table 2).
$\varphi$: Internal friction angle of support layer (°).

**Table 2.** Uplift coefficient, $\beta$

| Internal friction angle of support layer, $\phi$ | Uplift coefficient $\beta$ |
|---|---|
| 35° | 2.16 |
| 36° | 2.40 |
| 37° | 2.65 |
| 38° | 2.89 |
| 39° | 3.14 |
| 40° | 3.38 |
| 41° | 3.77 |
| 42° | 4.16 |
| 43° | 4.55 |
| 44° | 4.93 |
| 45° | 5.30 |

### 4.2.1 Building Construction Field

Uplift resistance is evaluated using the following equation as a standard. This equation is the same for the open end type and the closed end type.

$$R_t = \kappa \cdot \bar{N}_t \cdot A_{tp} + (\lambda \cdot \bar{N}_s \cdot L_s + \mu \cdot \bar{q}_u \cdot L_c) \cdot \Psi \tag{4}$$

$\kappa$: Bearing capacity coefficient of pile toe (common to sand and gravel)
$\kappa = 63$ ($0.114\ 3 \leq D_p \leq 0.609\ 6$)
$\kappa = 44$ ($0.7 \leq D_p \leq 1.2$)

$\lambda$: Surface frictional force coefficient of pile in sandy ground
$\lambda = 0.05$ ($0.114\ 3 \leq D_p \leq 0.609\ 6$)
$\lambda = 0.03$ ($0.7 \leq D_p \leq 1.2$)

$\mu$: Surface frictional force coefficient of pile in clay ground
$\mu = 1.02$ ($0.114\ 3 \leq D_p \leq 0.609\ 6$)
$\mu = 0.71$ ($0.7 \leq D_p \leq 1.2$)

$\bar{N}_t$: Mean value of the number of blows in standard penetration test of ground in range of $2D_w$ above pile toe (times)
$12 \leq \bar{N}_t \leq 60$

$A_{tp}$: Area of protruding toe wing ($m^2$)
$A_{tp} = \pi/4 \times (D_w^2 - D_{wi}^2)$

$N_s$: Mean value of the number of blows in standard penetration test of sandy ground (times)
$6 \leq \bar{N}_s \leq 30$

$q_u$: Mean value of uniaxial compressive strength of clay ground ($kN/m^2$)
$50 \leq q_u \leq 200$.

### 4.2.2 Highway Field

Uplift resistance is evaluated using the following equation as a standard. This equation is the same for the open end type and the closed end type.

$$R_t = \pi \cdot D_w \cdot \left(\Sigma_{\gamma i} \cdot L_i + \gamma \cdot H/2\right) \cdot H \cdot \beta \cdot tan\,\varphi + \Psi \cdot \Sigma(L_i \cdot f_i) \quad (5)$$

It should be noted that the first term in Eq. (5) is the anchor effect of the pile toe. The mechanism of the anchor effect (uplift resistance) attributable to the toe wing is considered to be as shown in Fig. 10. The second term is the same at that for vertical bearing capacity.

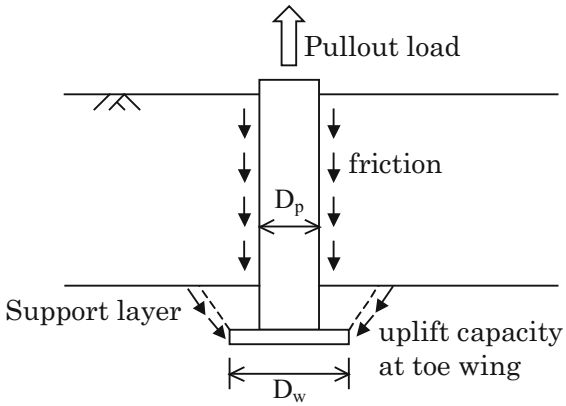


**Fig. 10.** Anchor effect of toe wing

### 4.3 Application to Batter Piles

Batter pile construction is comparatively easy because "Tsubasa Pile™" penetrates the ground by a screwing action. Since horizontal displacement can be suppressed by using batter piles, substantial cost reductions, such as reduction of the number of piles, etc., can be expected, depending on the load conditions.

This section describes the outline of a construction test which was carried out using a crawler type pile driver, which is a general type of construction machinery. Piles up to

**Table 3.** Specification of test

| Type | Inclination angle (degree) | Diameter (mm) | Magnification of toe wing | Depth (m) | Support layer |
|---|---|---|---|---|---|
| Open end | 15 | 600 | 2.0 | 21.51 | Gravel |

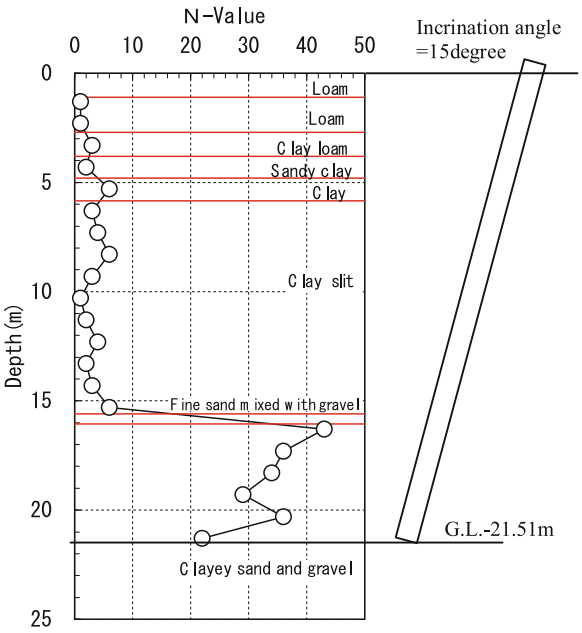


**Fig. 11.** Soil profile and pile shape

**Photo 4.** Construction test of batter pile

approximately $\varphi$600 mm were constructed. The test conditions are shown in Table 3, the soil profile and pile shape are shown in Fig. 11, and views of the construction test are shown in Photo 4.

In this test, the control target value of the inclination angle was set at 15 ± 0.5°, and piles were placed while measuring the angle periodically. The results of measurements are shown in Table 4. A nearly constant angle was maintained during construction, confirming the applicability of "Tsubasa Pile™" to batter piles. Similar construction is also possible with whole circumference rotary machines, and "Tsubasa Pile™" already has a record of application in actual construction by this method.

**Table 4.** Measurement of inclination angle

| Depth (m) | Inclination angle (degree) | |
|---|---|---|
| | Direction of slope | Direction of perpendicular to slope |
| 0.0 | 15.0 | 0.4 |
| 7.25 | 15.0 | - |
| 9.87 | 15.0 | 0.2 |
| 9.87 | 15.0 | 0.5 |
| 15.00 | 15.0 | 0.2 |
| 21.51 | 15.2 | 0.0 |

## 5 Conclusion

This report described the features of "Tsubasa Pile™", centering on environmental aspects and bearing capacity. Although "Tsubasa Pile™" has a construction record which already exceeds 500 projects, the authors will continue to work to increase these results in the future.

## References

1. Minister of Land, Infrastructure and Transport authorization TACP-0413, "Tsubasa Pile™ (Open end)"
2. Minister of Land, Infrastructure and Transport authorization TACP-0395, "Tsubasa Pile™ (Closed end)"
3. Public Works Research Center. Construction Technology Review and Certification "Tsubasa Pile™ (Open end)". No. 1013 (2011)
4. Public Works Research Center. Construction Technology Review and Certification "Tsubasa Pile™ (Closed end)". No. 0104 (2011)
5. Railway Technical Research Institute. Evaluation of bearing capacity of "Tsubasa Pile™" (2008)
6. Japan Road Association. Specification for Highway Bridges (2012)
7. Railway Technical Research Institute. Design Standards of Railway Structures and Commentary (2012)

# Durability of Polyester-Based GFRP Subjected to Hybrid Environmental and Mechanical Loads

Song Wang and Mohamed ElGawady(✉)

Civil, Architectural and Environmental Engineering Department,
Missouri University of Science and Technology, Rolla, MO 65401, USA
{sw2k6, elgawadym}@mst.edu

**Abstract.** Fiber reinforced polymer (FRP), as a new alternative construction material compared to conventional materials like concrete and steel, has been introduced into civil infrastructure area for centuries and gained increasing interests by many researchers and contractors. FRP exbits several property advantages, such as high strength-to-mass ratio, ease of handling, and relatively high resistance to corrosion. However, one problem that hinders this material from wider acception in civil infrastructure application is the durability of FRP subjected to harsh complicated environmental conditions has not been fully investigated yet. This paper is aim to study the performance of the polyester-based glass fiber reinforced polymer (GFRP) subjected to combined cement alkaline solution, freeze-thaw cycles, wet-dry cycles, heating-cooling cycles, and sustained mechnical load. Concrete was poured into GFRP tube to make concrete-filled FRP tube (CFFT) cylinders, and the cylinders were put into environmental chamber with sustained axial load on. The concrete core of the CFFT cylinders was removed after 72-day's conditioning, and the outer GFRP tube was cut into ring specimens to conduct hoop tensile tests. Test results indicated that the conditioned GFRP was slightly degraded in strength, but had significant decrease in strain. Sustained load had negligible effect on the strength of GFRP specimens, but did further deteriorate the strain of loaded specimens compared to unloaded specimens.

**Keywords:** GFRP · CFFT · Freeze-thaw · Wet-dry · Heating-cooling · Sustained load · Split-disk tensile test

## 1 Introduction

During the past few decades, fiber-reinforced polymer (FRP) composite has found increasing application in civil engineering market due to its high strength-to-mass ratio, ease of fabrication, and relatively good corrosion resistance (Hollaway 2010). Concrete-filled FRP tube (CFFT) columns, as alternatives to conventional reinforced concrete bridge columns, have gained increasing popularity from bridge engineers. Since a bridge column is often subjected to various severe weather conditions including freeze/thaw, wet/dry and heating/cooling cycles during its service life (Micelli and Myers 2008), the rigorous durability evaluation of the FRP to such complicated

© Springer Nature Singapore Pte Ltd. 2018
H. Tran-Nguyen et al. (eds.), *Proceedings of the 4th Congrès International de Géotechnique - Ouvrages -Structures*, Lecture Notes in Civil Engineering 8,
DOI 10.1007/978-981-10-6713-6_42

conditions should be properly addressed before its wider application. The durability of the FRP composite depends on the durability of its three components: fiber, resin, and fiber/matrix interphase, and these will be introduced in below.

Glass fibers are most often used as the fiber component in FRP composite, namely glass fiber reinforced polymer (GFRP), due to their high performance-to-cost ratio. Bare glass fibers are readily attacked by high pH environment through hydroxylation and hydrolysis mechanisms (Karbhari et al. 2002a, 2003; Robert and Benmokrane 2013; Robert and Fam 2012). Glass fibers are also susceptible to water, strong acid and chloride ions (Chen et al. 2007; Zaman et al. 2013).

Polyester is one of the primary resins used to fabricate FRP composite. Hydroxyl ions can break the ester group, which is the weakest bond in polyester resin, causing molecule weight loss and properties degradation of the resin. This hydrolysis reaction is greatly accelerated at the presence of acid or alkali (Chen et al. 2007). Moisture absorbed by the resins, on the other hand, could plasticize the resin, leading to the reduced modulus and glass transition temperature ($T_g$) (Bank and Gentry 1995; Robert and Benmokrane 2013). Damages due to hydrolysis are permanent while plasticization effect is considered reversible if the resin is dried (Ferguson and Qu 2006; Hamim and Singh 2014; McBagonluri et al. 2000). Properties of the resin can also be influenced by temperature changes. Residual stresses can be induced in matrix phase upon ambient temperature changing due to the large differences in coefficients of thermal expansion (CTEs) and stiffness between fibers and resin. The residual stresses can cause micro-cracks in the resin, through which additional moisture can penetrate and further impair the FRP (Assafi and Mosallam 2004; Chin et al. 1999; and Dutta 1988). The modulus of resin will be reduced if exposed to high temperature environment while sub-zero condition can stiffen but also embrittle the resin (ACI 440R 2007; Dutta and Hui 1996).

The fiber/matrix interphase is an inhomogeneous anisotropic layer with a thickness of about one micrometer (Chen et al. 2007). Both moisture and temperature changes can bring concentrated stress and strain along the fiber/matrix interface because of the differences in volume expansion between the fiber and matrix components upon moisture and temperature changing. The concentrated stress and strain can break the interphase bond and disintegrate the FRP (Ray 2006; Zaman et al. 2013).

Although many researchers have investigated the single environmental effect on FRP specimens (El-Hacha et al. 2010; Karbhari et al. 2000, 2002b; Kshirsagar et al. 2000; Silva et al. 2014; Toutanji and El-Korchi 1999), the effect of combined freeze/thaw, wet/dry and heating/cooling cycles on FRP while under sustained load has rarely been studied before. These conditions represent the environmental and mechanical loads that a bridge column will sustain throughout its service life. This paper presents the study on durability evaluation of polyester-based GFRP subjected to the hybrid freeze/thaw, wet/dry, and heating/cooling cycles while the sustained load was applied simultaneously. CFFT cylinders using isophthalic polyester-based GFRP tube were cast, moved to the environmental chamber and applied sustained axial load. Split-disk tensile tests were conducted on GFRP rings cut from the tubes, for both pre and post-conditioned samples.

## 2 Experimental Work

### 2.1 Materials

Strands of continuous glass filaments were impregnated with isophthalic polyester thermosetting resin through a filament winding process to manufacture the GFRP tubes used in this experiment (Table 1). The winding angles of fibers were $\pm 53^{\circ}$. Tubes were cut into coupons and rings to test longitudinal and hoop tensile strength according to ASTM D3039 and ASTM D2290, respectively.

**Table 1.** Dimensions and mechanical properties of the GFRP tube

| Parameter | OD* (mm) | t* (mm) | $f_L^*$ (MPa) | $E_L^*$ (MPa) | $\varepsilon_L^*$ (%) | $f_H^*$ (MPa) | $E_H^*$ (MPa) | $\varepsilon_H^*$ (%) |
|---|---|---|---|---|---|---|---|---|
| Test data | 167.6 | 3.2 | 58.1 | 10501 | 0.71 | 151.7 | 13348 | 1.73 |

*OD = outer diameter; t = wall thickness; $f_L$ and $f_H$ = ultimate tensile strength in longitudinal and hoop directions, respectively; $E_L$ and $E_H$ = elastic modulus in longitudinal and hoop directions, respectively; $\varepsilon_L$ and $\varepsilon_H$ = failure strain in longitudinal and hoop directions, respectively.

All of the CFFT cylinders were cast with self-consolidating concrete (SCC) with mix design shown in Table 2. At least three 102 mm * 204 mm plain concrete cylinders were tested according to ASTM C39 at the 28$^{th}$ day, and the average 28$^{th}$ day compressive strength was 46.5 MPa.

**Table 2.** SCC mix proportions

| w/cm | Cement (kg/m$^3$) | Fly Ash (kg/m$^3$) | Water (kg/m$^3$) | Fine aggregate (kg/m$^3$) | Coarse aggregate (kg/m$^3$) | HRWRA* (kg/m$^3$) | VEA* (kg/m$^3$) |
|---|---|---|---|---|---|---|---|
| 0.38 | 350 | 175 | 199 | 837 | 837 | 2.1 | 0.7 |

*HRWRA: high range water reducer admixture; VEA: viscosity enhancing admixture.

### 2.2 Specimen Preparation

There were three different sets of CFFT cylinders (Fig. 1a) in this experiment: unconditioned unloaded (control), conditioned unloaded, and conditioned loaded. Each group was nominated as UC, FT, and FT+S for short in the following sections. Each group had four CFFT specimens: three 305 mm height and one 229 mm height. This paper only focuses on the 229 mm height CFFT cylinders while the 305 mm height cylinders were for the author's other research purpose. For the conditioned loaded specimens, four cylinders in series were compressed between two steel plates with post-tensioned Dywidag bars. The sustained load was applied by a hydraulic jack and a load cell was used to monitor the load during the loading process. The target sustained stress was 6.9 MPa which is approximately 10% of the CFFT's ultimate compressive strength. Strain gauges were applied on each Dywidag bar to monitor if there was any load relaxation, and the setup was reloaded if necessary. All of the FT and FT+S specimens were moved into an environmental chamber for conditioning (Fig. 1b).

(a) (b)

**Fig. 1.** Specimen preparation: (a) CFFT cylinders; (b) test setup in the environmental chamber

### 2.3 Environmental Exposure Regime

The environmental exposure regime starts with one set of freeze/thaw cycles (−20°C to 10°C) followed by three sets of heating/cooling cycles (20°C to 50°C) and three sets of wet/dry cycles (60% RH to 95% RH) alternately. Micelli and Nanni (2004) first proposed this regime to simulate weather cycles in the midwest based on 20-year period. There were 50 cycles for each set of condition with a total of 350 cycles in 72 days for the whole regime (Fig. 2).

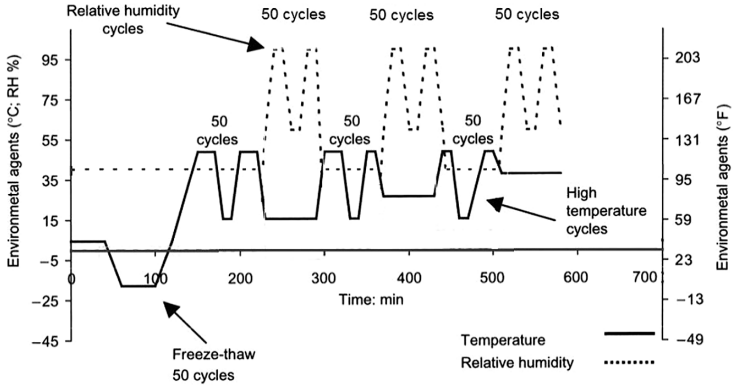


**Fig. 2.** Exposure regime used in the environmental chamber

### 2.4 Instrumentation and Setup Split-Disk Tensile Test

All of the CFFT cylinders were kept in the lab for at least one week after being removed from the environmental chamber at the end of the conditioning. The concrete core of the 229 mm high cylinder was carefully chiseled out using an air chisel gun in

order to separate the GFRP tube out. The tube was then cut into 25 mm wide rings prepared for the split-disk tensile test. The split-disk tensile test was conducted on the MTS 880 machine (Fig. 3).

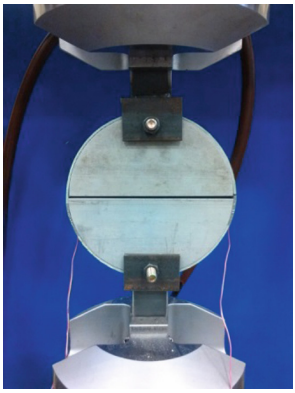

**Fig. 3.** Test setup for split-disk tensile test

Two semicircle steel plates were placed inside the GFRP ring while the loading head pulled apart the steel plates through extension arms. The loading rate was 0.25 mm/min. A strain gauge was applied on each side of the ring at middle height in order to capture the hoop strain history.

## 3 Test Results and Discussion

The fracture face of the GFRP rings basically happened at the middle height where the strain gauges were applied (Fig. 4a). The fracture face followed the direction of the fiber winding angles. The failure was mainly caused by fiber fracture and delamination between FRP layers. The stress-strain curves of the GFRP ring under tension were basically consisted of two parts (Fig. 4b). The first part started from the zero strain to the maximum negative strain, where the GFRP ring at the middle height bended inward initially due to the small gap between the two semicircle steel plates. The negative strain stopped increasing until the GFRP ring at the middle height was stretched from curved shape to flat shape. After that, the flat part was kept stretching until the specimen failed and the strain went from the maximum negative to the maximum positive, which was the second part. Although the ASTM standard for this test does not define how to calculate the stiffness of the ring, the similar trends and slopes between each curve in Fig. 4b can tell the stiffness of the GFRP tube didn't change after the environmental conditioning. It is expected because the stiffness of the GFRP tube was affected by plasticization effect due to moisture absorption. The plasticization effect occurred on the GFRP tube during wet/dry cycles was recovered after the specimen was dried under the lab condition, and so did the stiffness.

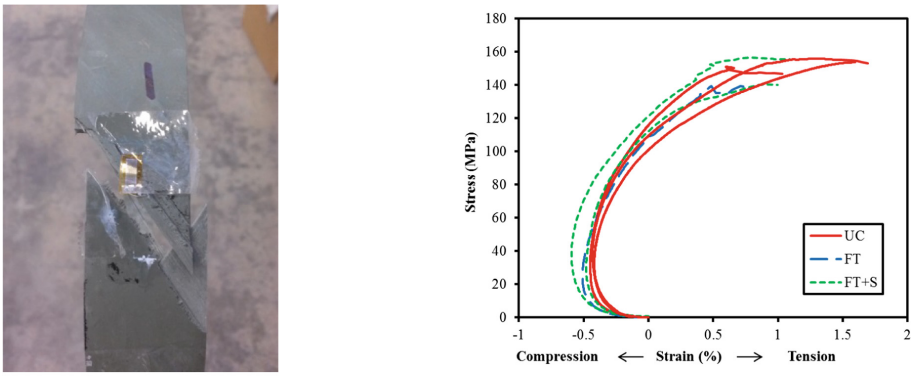


(a) (b)

**Fig. 4.** (a) Fracture face of the GFRP ring; (b) stress-strain history of representative rings

The environmental conditioning caused negligible degradation on both strain and strength of the conditioned unloaded GFRP tubes. The conditioned loaded GFRP tubes also demonstrated insignificant reduction on the maximum strength, but the maximum strain was decreased significantly due to the combined environmental and mechanical loads (Fig. 5). The FT specimens were decreased by 3% and 5% on maximum strength and maximum strain, respectively, while the FT+S specimens showed 3% and 15% reduction on maximum strength and maximum strain, respectively (Table 3).

The negligible reduction on the GFRP strength for the conditioned specimens reflected that hydrolysis effect didn't happen on the GFRP tube during wet/dry cycles. The hydrolysis reaction between ester group in polyester and water were so slow and can only be accelerated at the presence of acid or alkali (Dutta and Hui 1996). Any reduction on the strain of the GFRP tube was probably because of the residual stress

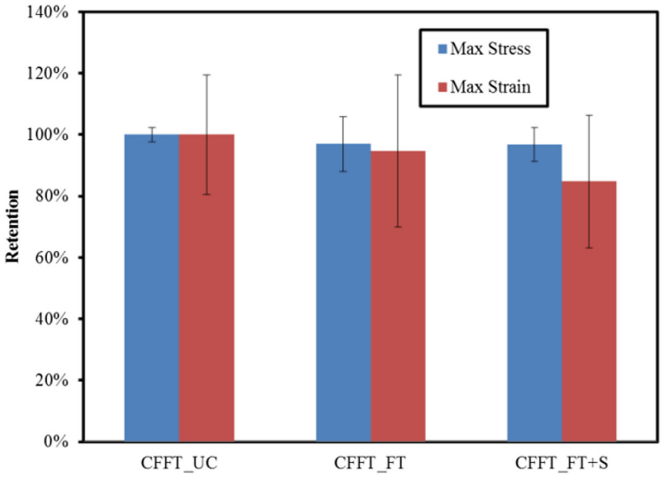


**Fig. 5.** Average values of tensile properties of GFRP rings with ± one standard deviation

**Table 3.** Mechanical properties for GFRP rings under tention

| Specimen | | Maximum stress (MPa) | Maximum strain (%) |
|---|---|---|---|
| CFFT_UC | Average | **153.4** | **2.24** |
| | Standard deviation | 0.51 | 0.44 |
| | COV | 2% | 20% |
| | Retention | **100%** | **100%** |
| CFFT_FT | Average | **148.8** | **2.12** |
| | Standard deviation | 1.93 | 0.52 |
| | COV | 9% | 25% |
| | Retention | **97%** | **95%** |
| CFFT_FT+S | Average | **148.4** | **1.90** |
| | Standard deviation | 1.18 | 0.41 |
| | COV | 5% | 22% |
| | Retention | **97%** | **85%** |

which caused microcracking in the matrix and/or fiber/matrix interphase debonding. The small reduction on the strain for the conditioned unloaded GFRP tubes revealed that the temperature and moisture changes during the current environmental exposure were not severe enough to induce much residual stresses. However, the sustained load on the CFFT cylinders, which was transferred to radial pressure on the GFRP tube applied by the expanded concrete core, resulted in significant increases of the hoop stress in the GFRP tube in addition to the residual stress. Such stress state disintegrated the matrix and fiber/matrix interphase, eventually led to reduced strain of the GFRP.

## 4 Conclusion

Experimental work has been done to investigate the combined freezing-thawing, heating/cooling, and wet/dry cycles on performance of GFRP tube while under sustained loading. Several conclusions can be drawn and shown as below:

1. The environmental exposure didn't cause significant degradation on strength and strain of the conditioned unloaded GFRP tubes. The conditioned loaded GFRP tube also showed negligible decrease in strength, but showed pronounced reduction in strain due to combined environmental and mechanical loads.
2. The sustained load can further deteriorate the durability of the GFRP by inducing additional microcracks in resin phase and/or fiber/matrix interphase.

## References

American Concrete Institute: Report on Fiber-Reinforced Polymer (FRP) Reinforcement for Concrete Structures. ACI 440R-2007, Farmington Hills, MI (2007)

Assafi, S., Mosallam, A.: Impact of aqueous environments on performance of pultruded composites. HBRC International Conference, Cairo, Egypt (2004)

Bank, L.C., Gentry, T.R.: Accelerated test methods to determine the long-term behavior of FRP composite structures: environmental effects. J. Reinf. Plast. Compost. **14** (1995)

Chen, Y., Davalos, J.F., Ray, I., Kim, H.Y.: Accelerated aging tests for evaluation of durability performance of FRP reinforcing bars reinforcing bars for concrete structures. Compos. Struct. **78**(1), 101–111 (2007)

Chin, J.W., Nguyen, T., Aouadi, K.: Sorption and diffusion of water, salt water, and concrete pore solution in composite matrices. J. Appl. Polym. Sci. **71**, 483–492 (1999)

Dutta, P.K.: Structural fiber composite materials for cold regions. J. Cold Reg. Eng. **2**(3) (1988)

Dutta, P.K., Hui, D.: Low-temperature and freeze-thaw durability of thick composites. Compos. Part B: Eng. **27**(3–4), 371–379 (1996)

El-Hacha, R., Green, M., Wight, G.: Effect of severe environmental exposures on CFRP wrapped concrete columns. J. Compos. Constr. **14**(1), 83–93 (2010)

Ferguson, T.P., Qu, J.: Elastic modulus variation due to moisture absorption and permanent changes upon redrying in an epoxy based underfill. IEEE Trans. Compon. Packag. Technol. **29**(1), 105–111 (2006)

Hamim, S.U., Singh, R.P.: Effect of hygrothermal aging on the mechanical properties of fluorinated and nonfluorinated clay-epoxy nanocomposites. Int. Sch. Res. Not. **2014**, 13 p. (2014). Article ID 489453

Hollaway, L.C.: A review of the present and future utilisation of FRP composites in the civil infrastructure with reference to their important in-service properties. Constr. Build. Mater. **24** (12), 2419–2445 (2010)

Karbhari, V.M., Rivera, J., Dutta, P.K.: Effect of short-term freeze-thaw cycling on composite confined concrete. J. Compos. Constr. **4**(4), 191–197 (2000)

Karbhari, V.M., Murphy, K., Zhang, S.: Effect of concrete based alkali solutions on short-term durability of e-glass/vinylester composites. J. Compos. Mater. **36**(17), 2101–2121 (2002a)

Karbhari, V.M., Rivera, J., Zhang, J.: Low-temperature hygrothermal degradation of ambient cured E-glass/vinylester composites. J. Appl. Polym. Sci. **86**(9), 2255–2260 (2002b)

Karbhari, V.M., Chin, J.W., Hunston, D., Benmokrane, B., Juska, T., Morgan, R., Lesko, J.J., Sorathia, U., Reynaud, D.: Durability gap analysis for fiber-reinforced polymer composites in civil infrastructure. J. Compos. Constr. **7**(3), 238–247 (2003)

Kshirsagar, S., Lopez-Anido, R.A., Gupta, R.K.: Environmental aging of fiber-reinforced polymer-wrapped concrete cylinders. ACI Mater. J. **97**(6), 703–712 (2000)

McBagonluri, F., Garcia, K., Hayes, M., Verghese, K.N.E., Lesko, J.J.: Characterization of fatigue and combined environment on durability performance of glass/vinyl ester composite for infrastructure applications. Int. J. Fatigue **22**(1), 53–64 (2000)

Micelli, F., Myers, J.J.: Durability of FRP-confined concrete. Proc. ICE-Constr. Mater. **161**(4), 173–185 (2008)

Micelli, F., Nanni, A.: Durability of FRP rods for concrete structures. Constr. Build. Mater. **18**, 491–503 (2004)

Ray, B.C.: Temperature effect during humid ageing on interfaces of glass and carbon fibers reinforced epoxy composites. J. Colloid Interface Sci. **298**(1), 111–117 (2006)

Robert, M., Fam, A.: Long-term performance of GFRP tubes filled with concrete and subjected to salt. J. Compos. Constr. **16**(2), 217–224 (2012)

Robert, M., Benmokrane, B.: Combined effects of saline solution and moist concrete on long-term durability of GFRP reinforcing bars. Constr. and Build. Mater. **38**, 274–284 (2013)

Silva, M.A.G., Cidade, M.T., Biscaia, H., Marreiros, R.: Composites and FRP-strengthened beams subjected to dry/wet and salt fog cycles. J. Mater. Civ. Eng. **26**(12) (2014)

Toutanji, H.A., El-Korchi, T.: Tensile durability of cement-based FRP composite wrapped specimens. J. Compos. Constr. **3**(1) (1999)

Zaman, A., Gutub, S.A., Wafa, M.A.: A review on FRP composites applications and durability concerns in the construction sector. J. Reinf. Plast. Compos. **32**(24), 1966–1988 (2013)

# Effect of Manufacturing Process on Material Properties at the Corners of G450 Cold-Formed Steel Channel Sections

Huu Nam Trinh, Gwénaëlle Proust(✉), and Cao Hung Pham(✉)

School of Civil Engineering, The University of Sydney,
Camperdown, NSW 2006, Australia
{huunam.trinh, gwenaelle.proust,
caohung.pham}@sydney.edu.au

**Abstract.** The use of cold-formed steel structures in the construction industry has become widely popular over the past decade. This has led to the necessary understanding of the effects of cold-working process on cold-formed steel members. The manufacturing process of cold-formed steels starts with cold-rolling the hot-rolled steel sheet under a series of rollers until a thickness is achieved. The process is followed by cold-bending to create cold-formed sections with desired shapes at ambient temperature. The plastic deformation associated with the rolling and bending processes results in strain hardening of the material and this in turn affects the properties. This paper presents both microstructural and micromechanical investigations on the blank and bent areas of 3.0 mm thick C-shaped cold-formed sections. Vickers hardness tests show a hardness increase at the bent areas. The observation of the bent region using scanning electron microscopy (SEM) reveals changes in the grain structures. Additionally, electron backscatter diffraction (EBSD) measurements have been conducted for an in-depth characterization. Understanding the changes in the microstructure of the material will provide insight on the mechanical behavior of these members.

**Keywords:** Cold-formed steel · Cold-working · Roll-forming · Microstructure · Microhardness · Corner properties · EBSD

## 1 Introduction

High strength cold-formed steel members are manufactured from cold-reduced steel sheets and have become widely popular over the past decade due to the high strength to weight ratio and easy installation. At first, cold-formed steel members had been used mainly in warehouses and industrial buildings as secondary structural members such as purlins, roofing and wall cladding [1]. In recent years, the application of cold-formed steel members has extended to steel framing systems for mid-rise structures in retail, school and office buildings.

Cold-formed steel members are manufactured from sheet steels which have undergone a thickness reduction process at ambient temperature. This involves cold rolling steel sheets under a series of rollers until a particular thickness is achieved.

© Springer Nature Singapore Pte Ltd. 2018
H. Tran-Nguyen et al. (eds.), *Proceedings of the 4th Congrès International de Géotechnique - Ouvrages -Structures*, Lecture Notes in Civil Engineering 8,
DOI 10.1007/978-981-10-6713-6_43

Afterwards, the steel sheets go through a bending process, in which a long strip of steel is continuously and gradually formed into a profile with a desired cross-section by passing a series of rotating mills arranged in tandem.

Throughout the cold-work forming process there is a significant increase in the yield strength of the steel. As the steel sheets have undergone plastic deformation during the cold working, they do not exhibit a yield point with a yield plateau as can be found in the hot-rolled steel [2]. The yield strength is now closer to the ultimate tensile strength with significantly less ductility. The outer surface of the steel sheet is in tension and the inner surface is in compression due to the bending process. Thus, this leads to microstructural changes that induce changes in association with the micromechanical properties of the steel members.

The high strength cold-formed channel sections using G450 sheet steels to AS1397 [3] have been used for the investigation. The steel in the ferrite phase with a body centered cubic (BCC) unit cell.

To the best of the authors' knowledge, no studies have been conducted on the microstructural and micromechanical properties at the corners of G450 steel. In this paper, the research has been conducted to achieve a deeper understanding of the relationship between microstructure, micromechanical properties and the deformation during cold work forming processes.

## 2 Experimental Procedures

Specimens used in this investigation were taken from a corner part of the G450 high strength cold-formed steel channel sections. The chemical composition of steel base is presented in Table 1.

**Table 1.** Typical chemical composition of steel base of G450 (wt.%).

| | C | Mn | Al | P | S | Si | Fe |
|---|---|---|---|---|---|---|---|
| G450 | 0.035–0.07 | 0.2–0.3* | 0.02–0.07 | 0.00–0.02 | 0.00–0.02 | 0.00–0.02 | Balanced |

*Energy dispersive X-ray spectroscopy (EDS) measurements carried out in this study indicated that the amount of Mn is higher at 1% contradictory to the manufacturer data sheet.

At first, the mentioned corner part was cut into smaller pieces using a wire cutting machine, Fanuc Robocut α-C400iA. A marking code system was used to localize the different specimens (Fig. 1).

Specimens No. 1X2 and No. 3X4 are in the blank area of a C-shaped section. Meanwhile, specimens No. 5X6 include the bent area. In order to examine the difference between the inner edge and the outer edge of the bent part, the respective test data of these two areas were measured accordingly (Fig. 2).

For all the experimental techniques used in this study, the sample preparation includes mounting specimens in epoxy blocks (using Clarofast powder by Struers), grinding them using SiC papers through several grades #120, #220, #1200 and #4000, and rinsing them in tap water.

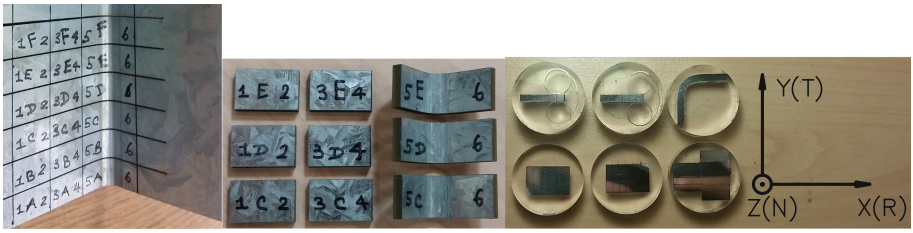


**Fig. 1.** Sample preparation (a) L-shaped steel bar cut out from a C-shaped cold-formed steel section; (b) Specimens after being cut using a wire cutting machine; (c) Specimens after being mounted in epoxy blocks (the reference frame indicate the orientation of each specimen relative to the original sheet, the z-direction representing the direction normal to the rolling plane).

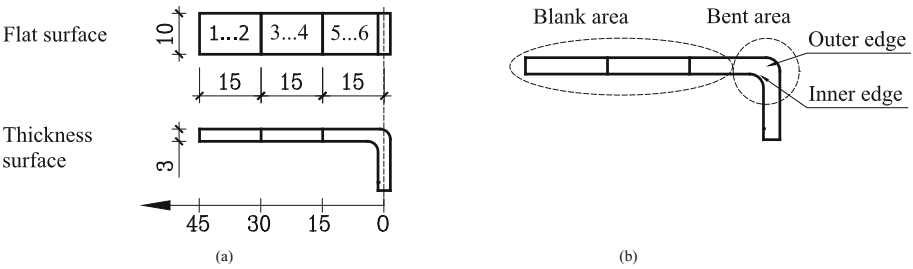


**Fig. 2.** Sample details including (a) Sample dimensions (in mm) with the indication of the origin of the x-axis for Fig. 3; (b) Investigated areas.

For Vickers hardness test, after the last grinding step, specimens were marked with pen in order to investigate the hardness at locations having the same distance to the bend. Hardness tests were conducted using Vickers hardness tester LV700AT with 1 kg load and 10 s dwell time. As the grains of cold-formed steel elongate in the rolling direction, the material properties in different directions may not be the same. Thus, hardness was measured on both flat and thickness surfaces (Fig. 1c).

For microstructure inspection using scanning electron microscopy (SEM), the specimens were etched with a 2% Nital solution for 3 s. Images were taken using a Zeiss Sigma HD field emission gun SEM.

For electron backscatter diffraction (EBSD), the specimens were polished with diamond paste of 3 µm and then 1 µm size. Next, the samples were polished with colloidal silica and rinsed with ethanol and tap water. To fix the specimens inside the SEM chamber, they were stuck on SEM/EBSD stub using carbon tabs. Silver paint was also used to avoid charging during the scanning process. The equipment used for EBSD imaging was a Zeiss Ultra field emission gun SEM equipped with Oxford Instruments AZtec integrated EDS and EBSD system, with X-Max 20 $mm^2$ silicon drift EDS detector and Nordlys-nano EBSD detector.

The EBSD data were post processed using HKL Channel 5 software. Powerful tools such as grain boundary map (with tolerance angle higher than 2°) and local

misorientation map were used to characterize the material. Ferrite (alpha iron) with a BCC crystalline structure has been indexed as the main phase of the material.

## 3 Experimental Results

### 3.1 Vickers Hardness Test

Vickers hardness tests were conducted to measure the hardness of both flat and thickness surfaces. Figure 3 depicts the hardness at different locations on three different surfaces (thickness, inner flat and outer flat). The used coordinate is shown in Fig. 2a.

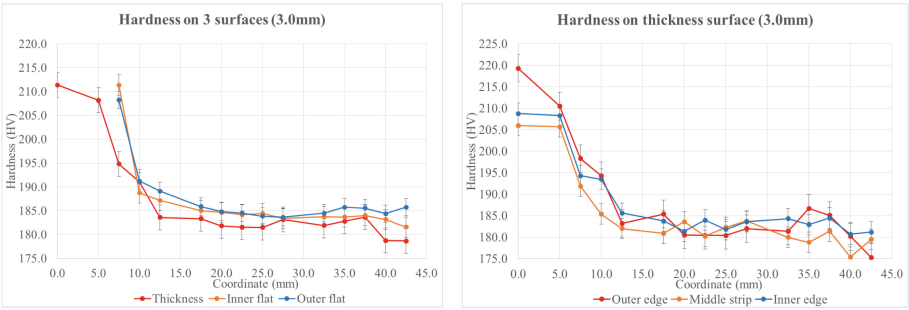


**Fig. 3.** (a) Hardness test results measured on three different surfaces: thickness, inner flat and outer flat; (b) Hardness test results measured on thickness surface: outer edge, middle strip and inner edge.

Generally speaking, it is clearly seen that the hardness values corresponding to the bent area are approximately 15% higher than those of the blank area.

In the case of the flat surface, there was roughly no difference between hardness values of the inner and the outer surfaces. However, the values collected from the thickness surfaces show that the inner edge and outer edge are slightly harder than the middle area as it gets closer to the bend, particularly, starting from the distance of 17.5 mm from the bend (see Fig. 3b).

### 3.2 Scanning Electron Microscopy (SEM)

SEM produces high-magnification-level-image of the steel's microstructure. With the aid of 2% Nital etchant, the grain shapes of the specimens were captured as shown in Fig. 4.

The images in Figs. 4a, c and e correspond to the microstructure at the blank and bent areas on the thickness surfaces; those in Figs. 4b, d and f present the studied areas on the flat surfaces. Note that all the specimens were investigated as per the sample coordinate system presented in Fig. 1c.

Figures 4a, c and e clearly reveal the difference in the grain shape on the thickness surface of the G450 steel after the forming process. Under the effect of cold bending to

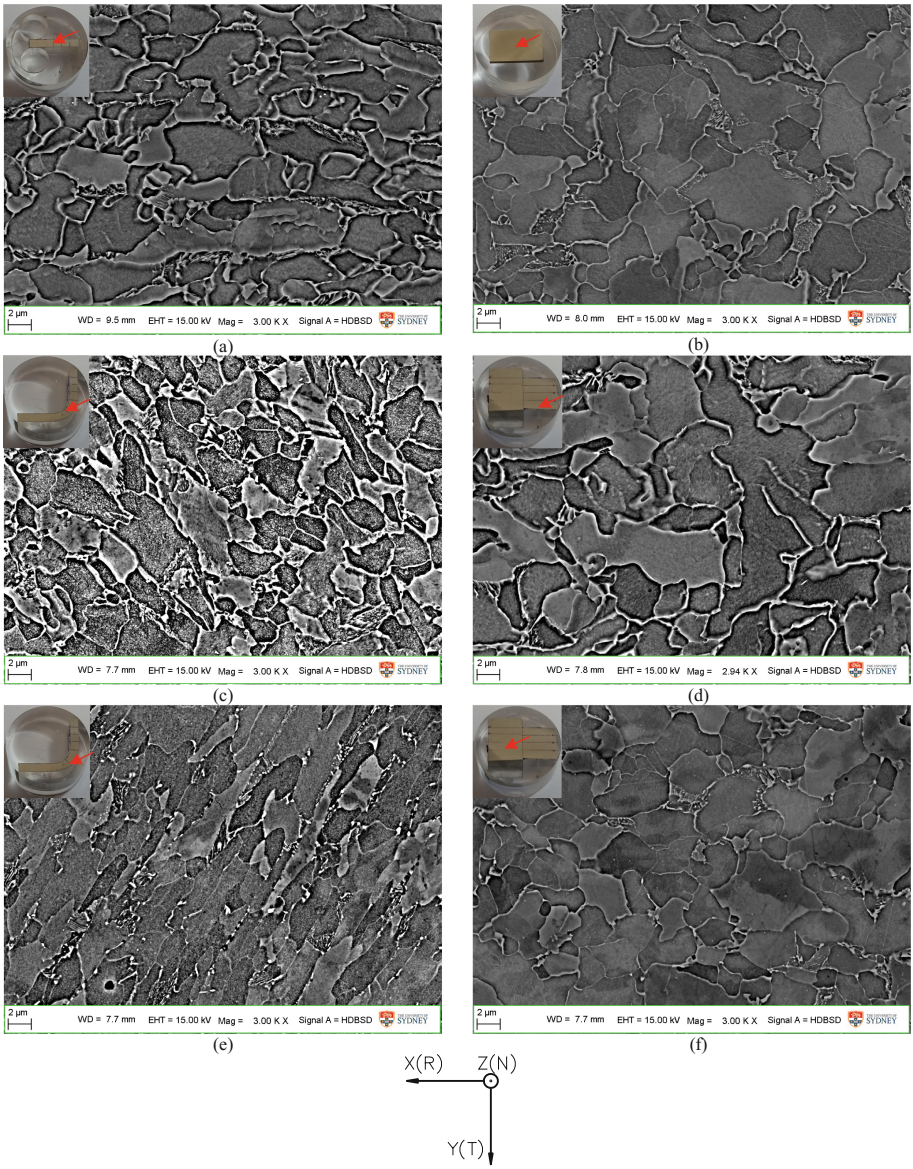


**Fig. 4.** SEM images at (a) Thickness surface of blank area; (b) Flat surface of blank area; (c) Thickness surface of the bent inner edge; (d) Inner flat surface 5 mm from the bend; (e) Thickness surface of the bent outer edge; (f) Outer flat surface 5 mm from the bend.

create the corner section, at the bent area, the outer and the inner edges were subjected to tension and compression respectively. As a result, compared to the grain structure of the blank area in Fig. 4a, it is apparently seen that the grains are stretched along the

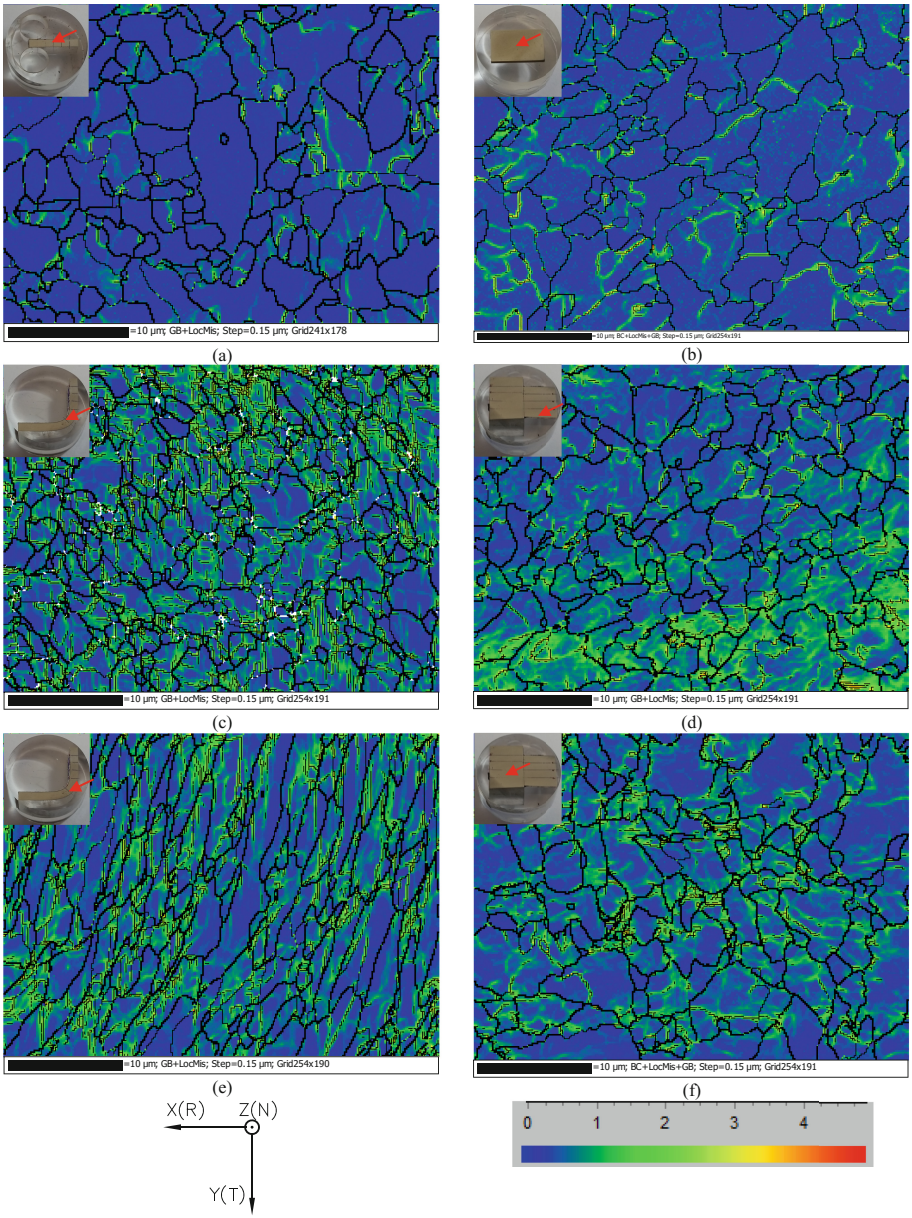


**Fig. 5.** Local misorientation maps at (a) Thickness surface of blank area; (b) Flat surface of blank area; (c) Thickness surface of the bent inner edge; (d) Inner flat surface 5 mm from the bend; (e) Thickness surface of the bent outer edge; (f) Outer flat surface 5 mm from the bend.

bend at the outer edge (Fig. 4e). Meanwhile, at the inner edge, due to the compressive stress, the elongation direction of the grains is roughly perpendicular to that of the outer-edge-grain.

On the flat surface, the change in the grain size and shape when moving from the blank to the bent area is not as apparent (Figs. 4b, d and f).

### 3.3 Electron Backscatter Diffraction (EBSD)

EBSD, which is a technique based on the Kikuchi diffraction pattern created by the interaction of electron of the beam with the atom planes at the surface of the specimen, is a powerful tool for phase identification, grain boundary study and strain distribution investigation at the sample's surface [4]. As per the acquired result, ferrite was indexed as the main phase with an indexing success rate higher than 98%.

Figure 5 includes the local misorientation maps, which have been created using HKL Chanel 5 software, of the studied areas as mentioned in Fig. 4. These maps show a representation of the dislocation density and residual strain distribution in the sample [5–7]. The maps were created by calculating crystallographic misorientations using up to three neighbors of a point without considering misorientation higher than 5° (Filter size: 3 × 3 and subgrain angle: 5°). The results were colored in a rainbow scale, in which the blue color represents minimum local misorientation (0°) within the grain and the red color represents the maximum value of 5° misorientation.

Moving towards the bend, it is clearly seen from Fig. 5 that more regions in the map are colored in green, which means there is an increase in the local crystalline misorientation at these particular locations. Figure 5d, which is the local crystalline misorientation map of the inner flat surface located 5 mm from the bend, reveals that the effect of cold bending process may take place approximately from this point onwards. The grain size and aspect ratio were also calculated using HKL Chanel 5 (Table 2).

**Table 2.** Grain size shape at the locations in Fig. 5.

| Figure 5 | a | b | c | d | e | f |
|---|---|---|---|---|---|---|
| Aver. grain size (μm) | 3.05 | 2.39 | 2.19 | 2.87 | 2.82 | 3.08 |
| Aspect ratio | 2.06 | 1.87 | 2.13 | 2.12 | 3.99 | 2.01 |

## 4 Discussion

As the steel sheet coil has undergone cold reduction and cold bending process, the surface layers have experienced severe deformation due to the shear stress and this leads to the increase in the hardness of cold-formed steel. In addition, the local misorientation maps acquired by EBSD analysis indicate the distribution of plastic strain within the grains. This helps prove the positive correlation among deformation, residual strain and higher strength (indicted here with a higher hardness value).

The hardness values start increasing significantly from the distance of 17.5 mm from the bend (as per Fig. 3a) suggesting that this is the effect range of the cold bending. This statement is supported by the misorientation maps at the flat surface in blank area and 5 mm from the bend (Figs. 5b and d): more and more grains are colored in green as it gets closer to the bend showing an increase in residual strain.

SEM images indicate the difference in the grain deformation level at the inner edge and the outer edge of thickness surface: grain shapes at the outer edge tend to be thinner and longer. The grain shape information (Table 2) obtained from grain boundary map in Fig. 5 clearly shows the grain elongation at the thickness outer edge (Fig. 5e) with the aspect ratio of 3.99, which is nearly twice the values at other locations. Figure 3b also proves that from the distance of 17.5 mm from the bend, the hardness values measured at the outer edge is slightly higher (about 1.5%). The grain shapes difference at various locations of the thickness and along the sheet length also demonstrates the effect of cold forming on the microstructure of the material, which will then have effects on local mechanical properties. It is interesting to note that at the inner edge, grains elongate in the direction approximately perpendicular to that of the outer-edge-grains and the average grain size at the inner surface and edge is larger than that at the outer ones.

## 5 Conclusion

The microstructural and micromechanical investigations on the blank and bent areas of 3.0 mm thick C-shaped cold-formed sections G450 have proven that plastic deformation caused by cold forming has strong consequence as regards microstructure and properties changes on the steel. Hardness values, observation of SEM images and data from the EBSD analysis indicate the positive correlation among deformation, hardness and plastic strain within the constituent grains. The results also suggest further research on quantifying residual stresses and strain at the bent area using X-ray diffraction method to clearly understand the effects of cold work on the microscopic and macroscopic behavior of cold-formed steel G450.

**Acknowledgment.** The authors acknowledge the facilities and assistance of the Australian Microscopy & Microanalysis Research Facility at the Australian Centre for Microscopy & Microanalysis at the University of Sydney.

## References

1. Nowak, M., Shoemaker, W.L.: Trends in Cold-Formed Steel. Insights (2012). http://www.structuremag.org/wp-content/uploads/D-InSights-Nowak-Mar121.pdf
2. Hancock, G.J.: Cold-Formed Steel Structures (2007)
3. Australian standard AS 1397: Continuous hot-dip metallic coated steel sheet and strip - coatings of zinc and zinc alloyed with aluminum and magnesium (2011)
4. Randle, V.: Electron backscatter diffraction: strategies for reliable data acquisition and processing (2009)
5. Li, H., Hsu, E., Szpunar, J., Utsunomiya, H., Sakai, T.: Deformation mechanism and texture and microstructure evolution during high speed rolling of AZ31B Mg sheets. J. Mater. Sci. **43** (22), 7148–7156 (2008)
6. Wright, S.I., Nowell, M.M., Field, D.P.: A review of strain analysis using electron backscatter diffraction. Microsc. Microanal. **17**(3), 316–329 (2011). doi:10.1017/S1431927611000055
7. Ruiz-Andres, M., Conde, A., de Damborenea, J., Garcia, I.: Microstructural and micromechanical effects of cold roll forming on high strength dual phase steels (2015)

# Effect of Pre-compressive Stress on Chloride Permeability of Concrete Used Anti-permeable Admixture

The Truyen Tran[1(✉)], Xuan Tung Nguyen[2], and Xuan Ba Ho[2]

[1] University of Transport and Communications (UTC), Ha Noi, Vietnam
tranthetruyen@utc.edu.vn
[2] University of Transport and Communications (UTC2) – Campus at HCM City, Ho Chi Minh City, Vietnam
{nxtung, hxba}@utc2.edu.vn

**Abstract.** This article presents experimental study to analyse the effect of pre-compressive loading on the chloride permeability of concrete used in anti-permeable admixture; the admixture was mixed in concrete with compression resistance of 30 MPa for casting specimens. Specimens was pre-compressive loaded at different stress levels including values in elastic phase and in diffused damage phase. After reloading, specimens were treated and put into measurement cell for chloride permeability evaluation. The results show significant effect of pre-compressive stress on chloride permeability of concrete, especially when damage appeared. effect of anti-permeable admixture on concrete permeability was also clarified.

**Keywords:** Permeability · Concrete · Chloride · Admixture · Load · Test · Crack · Damage

## 1 Introduction

Effects of compressive stress on chloride permeability, water permeability, and gas permeability of concrete have been studied by many authors in the literature [6–8], [11, 12]. The results show significant influence of mechanical load on the permeability values, especially when damage state appeared in concrete; a strong increase of permeability was proved after a threshold from which micro-cracks began to initiate and propagate, i.e., the beginning of diffused damage state in concrete.

Chloride ingress is recognized as the major cause of corrosion phenomenon in reinforced concrete structures. Many studies have been carried out in the literature to evaluate the effect of chloride ion on the durability of civil engineering structures, especially for reinforced concrete structures in marine condition [9], [13]. To improve the impermeability of concrete, using anti-permeable admixture is a solution that many entrepreneurs frequently apply in reality to protect concrete structures from chloride attack and carbonation phenomenon. The advantage of anti-permeable admixture has been proved for non-loading concretes. However, concrete is always stressed in reality;

© Springer Nature Singapore Pte Ltd. 2018
H. Tran-Nguyen et al. (eds.), *Proceedings of the 4th Congrès International de Géotechnique - Ouvrages -Structures*, Lecture Notes in Civil Engineering 8,
DOI 10.1007/978-981-10-6713-6_44

a problem proposed for the impermeable capacity of concrete using anti-permeable admixture when this concrete is loaded must be clarified the effect of load on chloride ingress into this concrete.

An experimental program was carried out in this study to determine chloride permeability of a typical concrete using anti-permeable admixture. The considered concrete with compression resistance of 30 MPa is normally used for casting bridge substructures or bridge slab where concrete may contact with water containing chloride. The results will clarify this admixture on the chloride diffusion coefficient of concrete by comparison with the reference case (without admixture).

## 2 Experimental Program

Experiment works were set up according to the ACI 211.1; concrete aggregates were tested and checked according to ASTM C33, ASTM C127, ASTM C29; rapid chloride permeability test in concrete according to the ASTM C1202 (or TCVN 9337) [1–4], [10]. The experiments were performed at the Laboratory of University of Transport and Communications.

Chloride permeability tested on loading is normally complicated. It is necessary to use simpler experimental process that measured data which still has value; one of those methods measures the chloride permeability of concrete after unloading [7], [12]. In this study, chloride permeability of the concrete was measured after unloading of concrete specimens from pre-compressive load to the expected stress: $0.2\sigma_{max}$; $0.4\sigma_{max}$; $0.6\sigma_{max}$; $0.8\sigma_{max}$ và $0.9\sigma_{max}$ ($\sigma_{max}$ – peak stress).

### 2.1 Test Specimens

Test specimens were divided into two sets: the reference set without anti-permeable admixture, and the second set used admixture KIM; anti-permeable admixture KIM was mixed in concrete with a ratio of 2% of used cement. Each set includes of 3 cylindrical specimens with 150 mm diameter, 300 mm height and 12 cylindrical specimens with 100 mm diameter, 200 mm height. Test specimens were maintained in the laboratory within 24 h after concreting. After that, specimens were removed from molds and cured in water during 28 days. The three cylindrical specimens with d = 150 mm, h = 300 mm were used to determined average compressive resistance of concrete according to ASTM C39 [5]; the remain specimens were pre-compressive loaded at different stress levels in concrete including values of $0.2\sigma_{max}$; $0.4\sigma_{max}$; $0.6\sigma_{max}$; $0.8\sigma_{max}$, and $0.9\sigma_{max}$ ($\sigma_{max}$ – peak stress). After reloading, specimens were cut with 100 mm diameter and 50 mm thick (Fig. 1).

### 2.2 Chloride Permeability Test Procedure

Surrounding surface of chloride ingress test specimens were clean, and coated by impermeable paint (Fig. 1). After that, these specimens were put into the Vacuum Saturation Apparatus (VSA) (Fig. 2).

**Fig. 1.** Test specimens for chloride ingress tests were treated from cylindrical specimens 100 × 200 mm

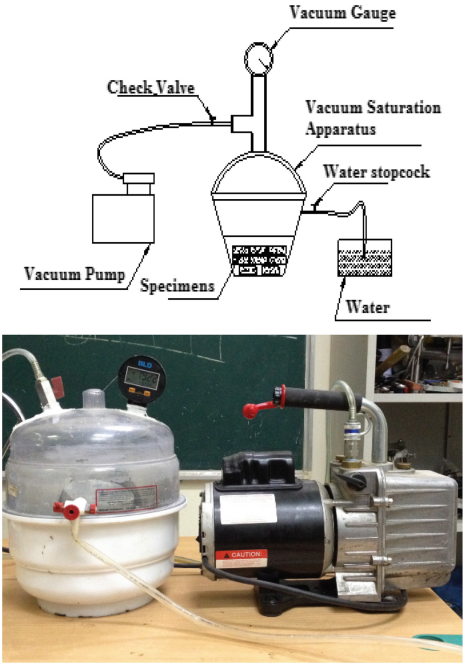


**Fig. 2.** Vacuum saturation apparatus

Pour the potable water into the VSA. Close water stopcock. Start the vacuum pump and maintain the pressure not less than 1 mm Hg during 24 h. When the vacuum pump is still running, open the water stopcock and drain sufficient water into container to cover specimens. Close the water stopcock and allow vacuum pump to run for three hours additionally. After that, turn off the vacuum pump and remove specimens from VSA and soak specimens in water during18 h.

Remove specimens from water, blot off excess water, and then put specimens into measurement cell (Fig. 3).

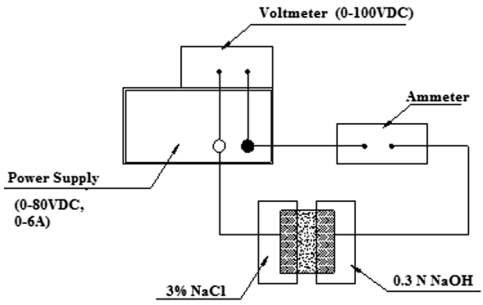


**Fig. 3.** Electrical block diagram

The left side of the cell with 3% NaCl solution was connected to the negative terminal of the power supply and the right side of the cell with 0.3 N NaOH solution was connected to the positive terminal of the power supply. Turn power supply on, set to 60 V, and record parameters including the intensity of electric current, temperature in the cell of NaCl in 6 h. This process is automatically realized with data logger and computer connected Fig. 4.

**Fig. 4.** Result of testing

## 3 Results and Discussion

With reference set (concrete without KIM), chloride permeability measurement results are shown in Fig. 5. When the pre-compressive stress on concrete: $\sigma/\sigma_{max} = 0.2-0.8$, the chloride permeability increase slowly; After the threshold $\sigma/\sigma_{max} \approx 0.8$ the chloride permeability increase quickly; that can be explained by the appearing of micro cracks in concrete due to the effect of pre-compressive stress.

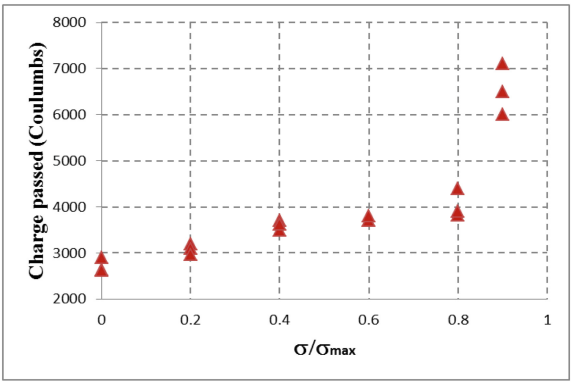


**Fig. 5.** Charge passed (Coulombs) (concrete without KIM)

With specimens used in anti-permeable admixture KIM; the chloride permeability variation with pre-compressive stress is shown in Fig. 6. When the pre-compressive stress $\sigma \leq 0.6\sigma_{max}$, the chloride permeability increases very slowly; after that, the chloride permeability increases faster, and increases significantly when $\sigma/\sigma_{max} > 0.8$.

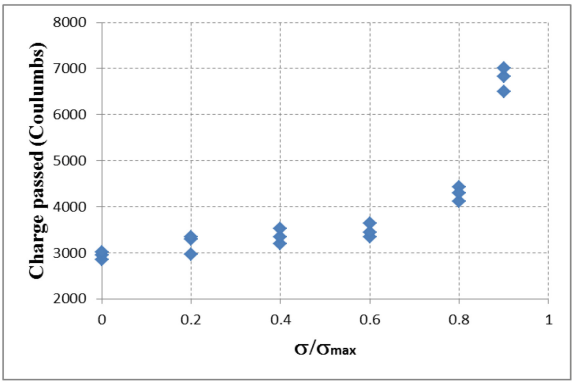


**Fig. 6.** Charge passed (Coulombs) (concrete with KIM)

Experimental results show that chloride permeability is sensitive to pre-compressive stress in the concrete with the relative value approximately equal to 0.6 to 0.8 depending on the case used KIM or not. Concretes used admixture KIM have better impermeability when concrete remains intact, i.e., no micro-cracks appeared after loading. However, when cracks appears, the permeability of reference concrete is less sensitive.

## 4 Conclusion

Chloride permeability tests of two concretes with and without anti-permeable admixture considering the residual effect of pre-compressive stress shows the role of anti-permeable admixture for improving the impermeability of concrete. However, when concrete is damaged due to mechanical loads, the advantage of admixture was not proved. It is necessary to consider the concrete permeability inducing the corrosion of reinforced concrete structures even when anti-permeable admixture was mixed in concrete during construction process.

## References

1. ASTM C1202-12: Standard Test Method for Electrical Indication of Concrete's Ability to Resist Chloride Ion Penetration. ASTM International, West Conshohocken, PA, 2012 (2012)
2. ASTM C127-15: Standard Test Method for Relative Density (Specific Gravity) and Absorption of Coarse Aggregate. ASTM International, West Conshohocken, PA, 2015 (2015)
3. ASTM C29/C29M-17: Standard Test Method for Bulk Density ("Unit Weight") and Voids in Aggregate. ASTM International, West Conshohocken, PA, 2017 (2017)
4. ASTM C33/C33M-16e1: Standard Specification for Concrete Aggregates. ASTM International, West Conshohocken, PA, 2016 (2016)
5. ASTM C39/C39M-16b: Standard Test Method for Compressive Strength of Cylindrical Concrete Specimens. ASTM International, West Conshohocken, PA, 2016 (2016)
6. Banthia, N., Birpava, A., Mindess, S.: Permeability of concrete under stress. Cem. Concr. Res. **35**, 1651–1655 (2005)
7. Choinska, M., Khelidj, A., Chatzigeorgiou, A., Pijaudier Cabot, G.: Effects and interaction of temperature and stress-level related damage on permeability of concrete. Cem. Concr. Res. **37**, 79–88 (2007)
8. Picandet, V., Khelidj, A., Bastian, G.: Effect of axial compressive damage on gas permeability of ordinary and high-performance concrete. Cem. Concr. Res. **31**, 1525–1532 (2001)
9. Tang, S.W., Yao, Y., Andrade, C., Li, Z.J.: Recent durability studies on concrete structure. Cem. Concr. Res. 78 (2015)
10. TCVN 9337: 2012 Heavy concrete - Method for electrical indication of concrete's ability to resist chloride ion penetration. Ministry of Construction, Vietnam, 2012 (2012)
11. Tegguer, A.D., Bonnet, S., Khelidj, A., Baroghel, B.V.: Effect of uniaxial compressive loading on gas permeability and chloride diffusion coefficient of concrete and their relationship. Cem. Concr. Res. 131–139 (2013)
12. Tran, T.T., Charlier, R.: A method for evaluating the gas permeability of damaged concrete. Sci. J. Transp. Especial (3), 151-160, International Journals, MADI-SWJTU-UTC (2011)
13. Xianming, S., Ning, X., Keith, F., Jing, G.: Durability of steel reinforced concrete in chloride environments: an overview. Constr. Build. Mater. **30**, 125–138 (2012)

# Effect of Thermal-Humid Media on Durability of CFRP-Wrapped Reinforced Concrete Columns

Van Mien Tran(✉) and Dong Viet Phuong Tran

Department of Construction Materials,
Ho Chi Minh City University of Technology, Ho Chi Minh City, Vietnam
tvmien@hcmut.edu.vn, tvpdong@gmail.com

**Abstract.** The objective of this study was to evaluate the effect of artificial aggressive conditions on durability of reinforced concrete (RC) columns wrapped with CFRP. Three groups of RC columns (150 × 300 mm) were casted and cured in same condition. They were, subsequently, exposed to three accelerated corrosion conditions, wrapped with one CFRP sheet, and then subjected to further post-repair corrosion. Artificial aggressive conditions were created by using mixed chloride and sulfate solutions, environmental cycling and temperature - humidity chamber. Initially, CFRP sheet worked as a protection barrier. It prevented aggressive agents ($Cl^-$ and $SO_4^-$) from penetrating into concrete layer and declined possibility of corrosion of reinforcing steel. Nevertheless, anti-corrosion performance of CFRP sheet decreased sharply under the impact of high thermal condition. Eventually, the results revealed the anti-corrosion performance of CFRP-wrapped RC columns depend on the remaining content of harmful factors in concrete layer before being wrapped.

**Keywords:** CFRP · Durability · Anti-corrosion · Artificial conditions

## 1 Introduction

Corrosion of reinforcing steel in concrete is the main cause lead to the reduction of construction's lifespan. Currently, methods which have been applied to protect reinforced concrete (RC) structures from corrosion, such as sacrificial anode, coating, and cathode protection are not as effective as expected. Recent years, many studies have been proceeded to evaluate the performance of fiber reinforced polymer (FRP) in order to improve the anti-corrosive ability of RC structures.

Initially, there are some opposite comments on repairing corroded structures using non-structural materials. Using wood and glass fiber as protection jackets against future corrosion might lead to the acceleration of corrosion (Sohanghpurwala and Scannell 1994). "Capillary action allowed water from submerged section of the pile to rise up the pile". Despite chloride from outside source could not enter the pile because of the jackets, corrosion of reinforcing steel was still occurring. No need to remove all of chloride content contaminated concrete because FRP materials would stop any further corrosion (Leeming and Peshkam 1995). "Unless the corrosion problem has been

© Springer Nature Singapore Pte Ltd. 2018
H. Tran-Nguyen et al. (eds.), *Proceedings of the 4th Congrès International de Géotechnique - Ouvrages -Structures*, Lecture Notes in Civil Engineering 8,
DOI 10.1007/978-981-10-6713-6_45

properly determined and addressed, encapsulation will most likely accelerate the corrosion process in the existing structure" (Emmons et al. 1998). However, recent experimental results revealed the advantages of this method on preventing corrosion process and partially restoring load capacity of wrapped structures. FRP layer wrapping around structure was not only one that delayed corrosion rate of reinforcing steel but also one that improved loading capacity of structure (Lee et al. 2000). After wrapping, carbon fiber reinforced polymer (CFRP) layer was improved strength and ductility of corroded structure. Loading capacity of repaired column increased by 28% and corrosion rate decreased by 50%. Corrosion rate of repaired reinforced concrete beams decreased on average 2.4 times after being wrapped with FRP layer (Masoud and Soudki 2006). Half-cell potential value and mass loss showed a gradual decrease of corrosion rate of steel in concrete. FRP layers limited the diffusion of oxygen and moisture into concrete layer. However, half-cell potential value of reinforcing steel in the vicinity of salted concrete zone was between 50% and 90% possibility of corrosion. The effect of combined environment cycles on CFRP-wrapped specimens was less than that on glass fiber reinforced polymer (GFRP) wrapped specimens (Belarbi and Bae 2007). Effect of saline solution on GFRP-wrapped specimens was higher by comparison with CFRP-wrapped specimens. However, results demonstrated that corrosion process of steel in wrapped specimens continued after corrosion source was removed. (Soudki et al. 2007) studied the behavior of CFRP-wrapped RC beam in corrosive environment. Results pointed out the benefits of repair corroded RC beams using CFRP, including: 1. The performance of wrapped beams was significantly enhanced; 2. Corrosion rate increased as the number of wet-dry cycle increased; 3. The critical chloride content reached the reinforcing steel at 200 wet-dry cycles; 4. CFRP layer and the resin reduced diffusion rate of chloride ionic and partially decreased the corrosion rate. Another study was conducted to evaluate the effect of number of CFRP layers and method of application on the effectiveness of repairing corroded structures (Kwangsuk et al. 2010). Based on mass loss, 2-layer wrapped columns showed the best performance. Besides, full repair and epoxy injection showed good performance on repaired columns subjected to further post-repair corrosion. Two experimental parameters, CFRP thickness and corrosion level, were used to evaluate the rehabilitation of corrosion-damaged beams with CFRP (Xie and Hu 2012). The results revealed these repair methods improve loading capacity and flexural stiffness for corrosion-damaged beams. However, "bonded CFRP could not work for the damaged beams which had more than 50% mass loss of tensile steel".

Based on the previous studies' results, the main objective of this study is to evaluate the effect of thermal-humid media on durability of CFRP-wrapped RC columns. Specific objectives of study reported herein including:

(i) Evaluating the effect of thermal media on anti-corrosive durability of CFRP-wrapped RC columns.
(ii) Evaluating the effect of humid media on anti-corrosive durability of CFRP-wrapped RC columns.

## 2 Experimental Strategy

Table 1 showed the proportion of concrete mixture which was used to cast specimens of this study. Mixing water was added 3% sodium chloride - NaCl by weight of cement. Reinforced concrete specimens were casted and cured in standard conditions in 28 days. Dimension of specimens was 150 mm in diameter and 300 mm in height with a steel bar being embedded in their center, 10 mm in diameter (Fig. 1 and Table 2).

**Table 1.** The proportion of concrete mixture

| | |
|---|---|
| Water (l/m$^3$) | 157.3 |
| Cement (kg/m$^3$) | 338.2 |
| Coarse aggregate (kg/m$^3$) | 1022.3 |
| Sand (kg/m$^3$) | 770.7 |
| Superplasticizer (ml/m$^3$) | 3300 |
| NaCl (kg/m$^3$) | 10.15 |

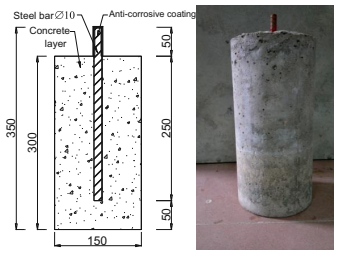


**Fig. 1.** Reinforced concrete specimen.

**Table 2.** Three artificial corrosive conditions

| Artificial environment | Condition | |
|---|---|---|
| | Humidity % RH | Temperature $^o$C |
| Temperature cycle | 0 | 70±2 |
| | 100 | 27 |
| Thermal-humid cycle | 70 | 50–60 |
| | 88–90 | 28 |
| Wet-dry cycle | 70 | 30±2 |
| | 100 | 27 |

Firstly, all specimens were determined experimental parameters before being exposed to artificial aggressive environments, including: chloride content, resistivity, and half-cell potential. They were, then, divided into 3 groups and exposed to 3

artificial conditions respectively in 150 days. Along with the effect of artificial conditions, all groups also were exposed to mixed solution, sodium chloride - NaCl 5% and magnesium sulfate - $MgSO_4$ 5%. In the first artificial environment, thermal-humid cycle, specimens were subjected to temperature [50–60 °C] and humidity [70–80% RH] in 12 h, after which they were submerged partially in corrosive solution, humidity was in the 60–80% RH range. In the second artificial environment, wet-dry cycle, after being immersed in corrosive solution in 12 h, specimens were dried naturally in the remaining 12 h. In the third artificial environment, temperature cycle, specimens were subjected to temperature 70 °C ± 2 in 12 h were subsequently immersed in corrosive solution in the remaining 12 h.

After thirty exposure days, specimens were wrapped with one CFRP layer around concrete surface (Fig. 2) and then they were placed in laboratory condition in 1 week before being subjected to further corrosion.

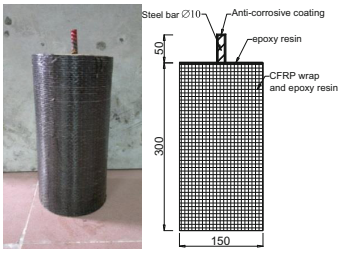


**Fig. 2.** CFRP-wrapped RC specimen.

Experimental parameters of each group were determined after every thirty exposure days. In this study, thermal-humid tank and drying oven were used to controlled temperature and humidity for the first and third artificial environments. Resistivity and half-cell potential were determined by PROCEQ equipment.

## 3 Results and Discussion

There are two abbreviations located in all figures, including: N.C and C. N.C – Non-CFRP referred to the initial period before wrapping. C – CFRP referred to the later period after wrapping.

### 3.1 Resistivity

Wenner four-probe method was used to determine the resistivity value of the concrete layer (Fig. 3) after every thirty exposure days. Based on the suggestion of Langford and Broomfield (Table 3), evaluating corrosion rate of reinforcing steel in concrete by resistivity value.

**Fig. 3.** Determining resistivity.

**Table 3.** Relation between resistivity and corrosion rate (Broomfield 1997)

| Resistivity (kΩ.cm) | Corrosion rate |
|---|---|
| >20 | Very low |
| 10–20 | Low |
| 5–10 | High |
| <5 | Very high |

Figures 4 and 5 showed the variation of resistivity of concrete layer in various temperature and humidity. As can be seen from the line graphs, there was a slight difference between each group's resistivity in the first 30 days when the increasing of temperature and humidity. Resistivity increased by 8.7% and 5.6% respectively as temperature and humidity increased. After being wrapped with CFRP layer, resistivity of each group experienced a gradual decrease with time. The decrease of resistivity depends on ambient temperature and humidity. After 150 exposure days, resistivity of concrete layer decreased by 22.6% when increasing temperature. In contrast, resistivity of concrete layer increased by 45.8% after 150 exposure days when increasing humidity.

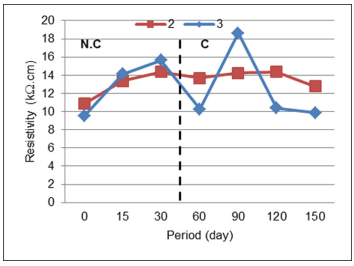


**Fig. 4.** Resistivity of concrete layer when increasing temperature.

Based on the resistivity value on the 150th day, corrosion rate of reinforcing steel increased from low corrosion region to high corrosion region when increasing temperature. On the other aspect, corrosion rate of reinforcing steel remained constant in low corrosion region when increasing humidity after 150 exposure days.

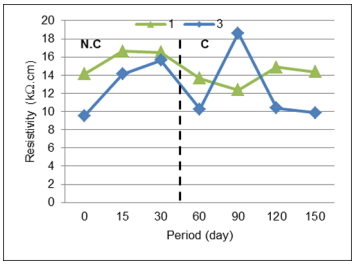


**Fig. 5.** Resistivity of concrete layer when increasing humidity.

### 3.2 Chloride Content

Distribution of chloride content in the concrete layer was determined based on ASTM C 1152 (ASTM 1997). Critical chloride content which was attributed on corrosion of reinforcing steel in concrete depends on the type of structure and their working environment. Table 4 showed critical chloride content of structure based on some standards such as BS, ACI. Figures 6, 7, 8, 9, 10 and 11 showed the change of chloride content in concrete layer by weight of concrete in 150 exposure days.

**Table 4.** Maximum total chloride content (% wt of cement) (Otieno et al. 2010).

| Type of structure | BS 8110 | ACI 201 | ACI 357 | ACI 222 |
|---|---|---|---|---|
| Prestressed concrete | 0.1 | - | 0.06 | 0.08 |
| RC exposed to chloride | 0.2 | 0.1 | 0.1 | 0.2 |
| RC that will be protected from moisture | 0.4 | - | - | - |
| Other RC | - | 0.15 | - | - |

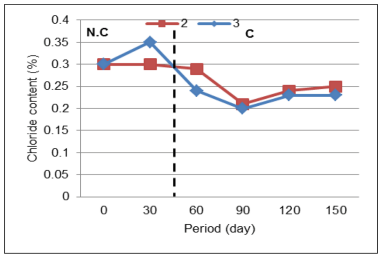


**Fig. 6.** Chloride content in depth of 0–25 mm when increasing temperature.

Chloride content was distributed unequally in the concrete layer with depth and exposure time in each artificial environment. Temperature and humidity factor showed a great impact on chloride content in concrete layer of each group. On the 150th day, the increase of temperature led a decrease by 8% in depth of 0–25 mm and an increase by 12.5% and 27.7% in depth of 25–50 mm and 50–70 mm respectively. On the 150th day, the increase of humidity led an increase by 13% in depth of 0–25 mm and a decrease by 3.7% and 8.3% in depth of 25–50 mm and 50–70 mm respectively.

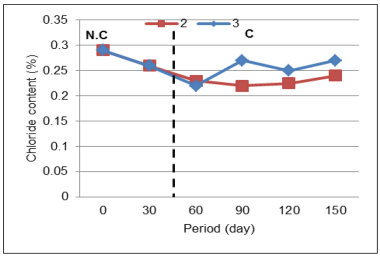


**Fig. 7.** Chloride content in depth of 25–50 mm when increasing temperature.

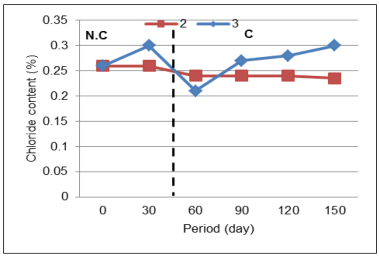


**Fig. 8.** Chloride content in depth of 50–70 mm when increasing temperature.

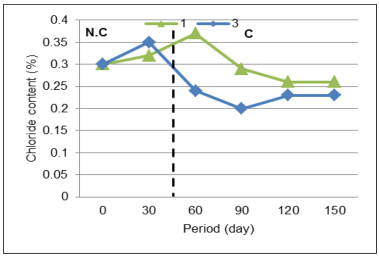


**Fig. 9.** Chloride content in depth of 0–25 mm when increasing humidity.

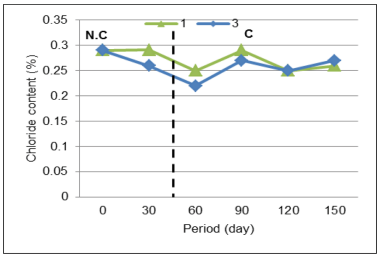


**Fig. 10.** Chloride content in depth of 25–50 mm when increasing humidity.

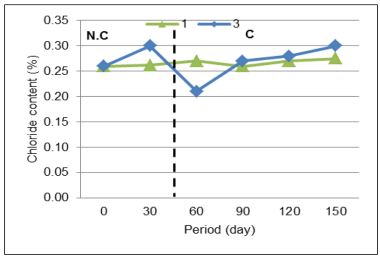


**Fig. 11.** Chloride content in depth of 50–70 mm when increasing humidity.

These above parameters, resistivity and chloride content, which showed the benefit of CFRP layer on reducing of penetration of chloride and improving durability of RC structures. Anti-corrosion performance of CFRP layer, however, depends on corrosive factors in environment, especially temperature. Temperature decreased the quality of CFRP layer sharply, thus corrosive factors penetrated into concrete layer and reached the vicinity of reinforcing steel. Under the influence of high temperature, resistivity of concrete layer went down when chloride content in concrete layer went up, especially in the vicinity of reinforcing steel. Meanwhile, quality of CFRP layer remained constant under the concomitant influence of temperature and humidity. Resistivity and chloride content of specimens which were exposed to high temperature and humidity fluctuated slowly.

### 3.3 Half-Cell Potential

Half-cell potential (HCP) of specimens was determined after every 30 exposure days according to ASTM C 876. Table 5 showed the relation between HCP and possibility of corrosion of steel in concrete. Equipment which was used to determine HCP was showed in Fig. 1 with Copper/Copper sulfate electrode - $Cu/CuSO_4$ being used as a reference electrode (Fig. 12).

**Table 5.** Relation between HCP and possibility of corrosion (ASTM 1991).

| Half-cell potential (mV) | Possibility of corrosion |
|---|---|
| >−200 | Low (less than 10%) |
| −200 ~ −350 | Moderate (about 50%) |
| <−350 | High (more than 90%) |

Figures 13 and 14 showed the variation of HCP with increasing temperature and humidity in 150 exposure days. Before being wrapped with CFRP layer, HCP value of specimens increased with exposure time in each artificial environment. On the 30th day, HCP value pointed out that the possibility of corrosion of reinforcing steel located in high corrosion region (possibility of corrosion more than 90%). After being wrapped with CFRP layer, the variation of HCP value was divided into 2 stages.

**Fig. 12.** Determining half-cell potential.

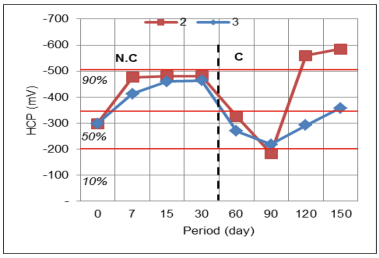


**Fig. 13.** HCP value of reinforcing steel when increasing temperature.

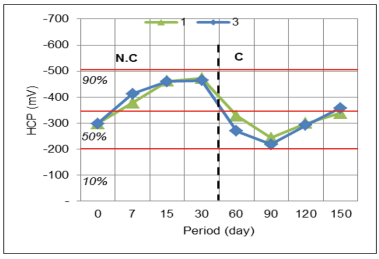


**Fig. 14.** HCP value of reinforcing steel when increasing humidity.

HCP value went down sharply in first 60 days after being wrapped and then went up in the last 60 days. In the first stage, HCP value showed the possibility of corrosion of reinforcing steel decreased and the speed of decrease was inversely proportional to the increase of temperature or humidity. HCP value was higher about 19.1% and 11.6% respectively when increasing temperature and humidity. The possibility of corrosion of reinforcing steel of the second group decreased from high corrosion region to low corrosion region on the 60th day after being wrapped with CFRP layer. In the later stage, HCP value was lower approximately 38.8% and 5.6% respectively when increasing temperature and humidity.

The dramatic reduction of possibility of corrosion was attributed to the presence of CFRP layer. CFRP layer acted as a protection barrier for RC structures from water, oxy, chloride, which induced corrosion of reinforcing steel in concrete. Nevertheless, the quality of concrete layer and method of application before wrapping directly impacted on the effectiveness of this method. In this study, method of application (type of carbon fiber, type of resin, number of layers, static period before and after wrapping) was the same for three groups. Before being wrapped, however, quality of concrete layer of three groups along with moisture content and chloride content in concrete layer of three groups was different due to various artificial conditions. Simultaneously, the rate of degradation of CFRP was different due to the range of temperature and humidity. The deterioration of both CFRP layer and of the concrete layer allowed the harmful ions penetrated continuously into concrete layer that caused the increase of possibility of corrosion in the later stage.

## 4 Conclusions

Initially, CFRP layer showed a good advantage on protecting RC structures with the role as a low-permeability barrier. However, quality of CFRP layer decreased significantly under the effect of thermal-humid media in corrosive environments. Experimental results also pointed out the great impact of chloride content and moisture content which were available in concrete layer before being wrapped on durability of CFRP-wrapped RC structures.

## References

ASTM: Standard Test Method for Half Cell Potential of Uncoated Reinforcing Steel in Concrete. C 876 (1991)

ASTM: Standard Test Method for Acid Soluble Chloride in Mortar and Concrete. C 1152 (1997)

Belarbi, A., Bae, S.W.: An experimental study on the effect of environmental exposures and corrosion on RC columns with FRP composite jackets. Compos. B Eng. **38**, 674–684 (2007)

Broomfield, J.P.: Corrosion of Steel in Concrete. E & FN Spon, London (1997)

Emmons, P.H., Alexander, M.V., Jay, T.: Strengthening concrete structures Part II. Concr. Int. **20**, 56–60 (1998)

Kwangsuk, M., Gray Mullin, M., Rajan Sen, F., Winters, D.: Effective repair for corrosion control using FRP wraps. J. Compos. Constr. **14**, 388–396 (2010)

Lee, C., et al.: Accelerated corrosion and repair of reinforced concrete columns using carbon fiber reinforced polymer sheets. Can. J. Civ. Eng. **27**, 941–948 (2000)

Leeming, M.B., Peshkam, V.: Robust solution to strengthening bridges. In: Proceeding of Fifth International Conference, Structural Faults and Repairs, Edinburgh (1995)

Masoud, S., Soudki, K.: Evaluation of corrosion activity in FRP repair RC beams. Cem. Concr. Compos. **28**, 969–977 (2006)

Otieno, M., Alexander, M., Deushausen, H.: Transport mechanism in concrete, Cape Town, South Africa (2010)

Sohanghpurwala, A., Scannell, W.T.: Repair and protection of concrete exposed to seawater (1994)

Soudki, K., El-Salakawy, E., Craig, B.: Behavior of CFRP strengthened reinforced concrete beams in corrosive environment. J. Compos. Constr. **11**, 291–298 (2007)

Xie, J., Hu, R.: Experimental study on rehabilitation of corrosion damaged reinforced concrete beams with carbon fiber reinforced polymers. Constr. Build. Mater. **38**, 708–716 (2012)

# Effective Design of Flexible Pavement on Treated Expansive Soil

Raju Sarkar[1,2(✉)], Ankur Mudgal[2], Ritesh Kurar[2], and Varun Gupta[2]

[1] College of Science and Technology, Royal University of Bhutan, Phuentsholing, Bhutan
rajusarkar.cst@rub.edu.bt
[2] Delhi Technological University, Delhi, India
ankur.mud@gmail.com, riteshkurar95@gmail.com, vrngupta007@gmail.com

**Abstract.** Expansive soil poses plenteous problems to the structures placed over it, such as, road pavements, buildings and canals, etc., mainly because of high swell index induced by its high-water retention capacity. Flexible pavements with expansive soil as a subgrade material are characterized with meager performance mainly due to cracking and differential settlement. The current study engages with the cost effectiveness of treated expansive soil as subgrade material. Lime and stone dust have been blended with soil at varied percentages to enhance the suitability of this mix as subgrade material. To catch on the extent of influence of stabilizing mixture, Modified Proctor and California Bearing Ratio tests have been performed on treated soil. The thickness of various layers of pavement has then been evaluated in conformity with IRC: 37 [1] and then cost analysis has been made for pavements with both untreated and treated subgrade course. It has been discerned that when expansive soil is stabilized with lime-stone dust mix (5–12% by weight of mix), the drop in the cost of flexible pavement is found to be maximum, i.e., 6.55% of cost reduction can be achieved if the pavement subgrade section is made up of treated soil instead of untreated one.

**Keywords:** Expansive soil · Lime · Stone dust · Cost analysis · SEM · XRD · Subgrade

## 1 Introduction

Infrastructural development is chiefly influenced by the transportation system of a country. Over the few bygone years, the perpetual demand on India's roadways and the requirement for laying down a safe, efficient and cost effective road transport system under limited budget funds has become a prerequisite for providing low-cost road constructions in India. Issues associated with pavement construction become even more demanding in an economically strained country like India, particularly in regions where the subgrade consists of expansive soils. The characteristics of a subgrade shape the sensitivity of pavement structural response, which in-turn supports the pavement structures. In India, expansive soils cover about 650000 $km^2$ area which is a shade more than 20% of country's total land area and extends throughout the states of Andhra Pradesh, Maharashtra, Telangana, Madhya Pradesh, some regions of Karnataka,

© Springer Nature Singapore Pte Ltd. 2018
H. Tran-Nguyen et al. (eds.), *Proceedings of the 4th Congrès International de Géotechnique - Ouvrages -Structures*, Lecture Notes in Civil Engineering 8,
DOI 10.1007/978-981-10-6713-6_46

Rajasthan, and interiors of Gujarat [2]. Due to varied moisture content in different seasons, this untreated subgrade often undergoes substantial volumetric changes which results in heaving during rainy seasons and shrinkage during dry seasons. Reason behind this atypical behavior of expansive soil is due to the presence of clay minerals, chiefly, montmorillonite. Hence, to phase out these problems it is highly imperative to provide an economical solution for road networks on such soils.

Huge measure of research has been administered on expansive soil to regulate its expansive behavior with various admixtures. Such as, lime addition provides an abundance of Calcium ions and Magnesium ions to expansive soil. These ions tend to replace other common cations such as Sodium and Potassium ions, in a process known as cation exchange. Calcium ions replace Sodium and Potassium ions which significantly lowers the plasticity index of the clay. A reduction in plasticity is usually accompanied by reduced potential for swelling. Thus, addition of lime increases the soil pH and cation exchange capacity. Moreover, the annual generation of stone dust is round about 200 million tons in India. Minimal measures of researches are available instigating the blend of stone dust with lime for treating expansive soils. Thus, this paper aims to provide reliable means of incorporating stone dust into lime into operable layers of pavement construction. The aim is conclusively achieved by the production of design charts to steer users to the appropriate material and thickness of pavement layer and by providing a descriptive cost comparison.

## 2 Material Used

### 2.1 Expansive Soil

For the present study, expansive soil sample has been amassed from Gwalior-Jhansi road, by Tekanpur BSF area (NH-75), Gwalior, Madhya Pradesh, India. The top layer of the soil has been withdrawn with the help of a shovel up to a depth of 0.5 m before gathering the soil sample. The geotechnical properties of expansive soil sample used in this study are given in Table 1.

**Table 1.** Physical properties of the soil

| Properties | Value |
|---|---|
| Specific gravity | 2.62 |
| Percentage passing IS Sieve 75 micron (%) | 58.0 |
| Liquid limit (%) | 56.0 |
| Plastic limit (%) | 31.7 |
| Plasticity index (%) | 26.3 |
| Differential free swell (%) | 43.0 |
| Unified soil classification system (USCS) | CH |
| Maximum dry density (gm/cc) | 1.63 |
| CBR (soaked) (%) | 1.90 |

## 2.2 Lime

Lime has been collected from a retail store of Azadpur, Delhi, India. The chemical composition is shown in Table 2.

**Table 2.** Chemical composition of lime [3]

| Properties | Value (%) |
|---|---|
| Minimum array (Acidimetric) | 95.0 |
| Maximum limits of impurities | |
| Chloride (Cl) | 0.10 |
| Sulphate ($SO_4$) | 0.50 |
| Iron (Fe) | 0.10 |
| Lead (Pb) | 0.02 |
| Loss on ignition | 10.0 |

**Table 3.** Cost analysis of subgrade course [7].

| Taking output: 100 $m^3$ | | | | | | |
|---|---|---|---|---|---|---|
| | SI. no. | Item | Unit | Quantity | Rate (Rs.) | Amount (Rs.) |
| (a) Labour component | 1 | Mate | Day | 0.04 | 360.49 | 14.42 |
| | 2 | Labour (unskilled) | Day | 1.50 | 238.07 | 357.11 |
| | Total | | | | | 371.53 |
| | Total per $m^3$ | | | | | 3.72 |
| (b) Machinery | 1 | Grader | Hr | 2.00 | 1,800.00 | 3,600.00 |
| | 2 | Dozer | Hr | 0.50 | 1,200.00 | 600.00 |
| | 3 | Water tanker | Hr | 5.00 | 350.00 | 1,750.000 |
| | 4 | Vibratory compactor | Hr | 1.25 | 760.00 | 950.00 |
| | 5 | Dumper | Hr | 1.25 | 1,400.00 | 1,750.00 |
| | 6 | Excavator | Hr | 1.00 | 1,700.00 | 1,700.00 |
| | 7 | soil spreading unit | Hr | 0.36 | 2,250.00 | 810.00 |
| | Total | | | | | 1,160.00 |
| | Total per $m^3$ | | | | | 111.60 |
| | Contractor's profit and overhead charges@12.5% | | | | | 13.95 |
| | Grand total | | | | | 125.55 |

## 2.3 Stone Dust

Remarkable quantities of stone dust have been acquired from stone crusher plant of Aman Vihar Industrial Area, Delhi, India.

# 3 Sampling and Tests

## 3.1 Aim

The aim of this study is to determine ways of using the optimized merger of expansive soil, lime and stone dust as a subgrade material in pavement construction that deliver capable structural performance, and is cost effective. To accomplish this general aim, an experimental study was carried out to understand the behavior of expansive soil mixed with admixtures, namely lime and stone dust. The intendment of blending these additives with expansive soil is to enhance the strength, durability, volumetric stability (shrinkage and swelling), and erodibility of the mix for their intended use in the pavement construction.

## 3.2 Optimum Design Mix

Bulk quantities of expansive soil in wet state have been attained from the sites of Gwalior-Jhansi National Highway-75. The samples have been personally collected; moreover, the samples have been procured promptly at onset of the study and stored properly. The collected soil samples have then been characterized by determining the physical and geotechnical properties in the geotechnical laboratory of Delhi Technological University, Delhi, India.

**Table 4.** Cost analysis of admixtures used for treatment of expansive soil [7].

| Taking Output:300 $m^3$ | | | | | | |
|---|---|---|---|---|---|---|
| | SI. no. | Item | Unit | Quantity | Rate (Rs.) | Amount (Rs.) |
| (a) Labour component | 1 | Mate | Day | 0.48 | 360.49 | 173.04 |
| | 2 | Labour (skilled) | Day | 2.00 | 292.45 | 584.90 |
| | 3 | Labour (unskilled) | Day | 10.00 | 238.07 | 2,380.70 |
| | Total | | | | | 3,138.64 |
| | Total per $m^3$ | | | | | 10.46 |
| (b) Machinery | 1 | Grader | Hr | 6.00 | 1,800.00 | 10,800.00 |
| | 2 | Water tanker | Hr | 5.00 | 350.00 | 1,750.00 |
| | 3 | Vibratory compactor | Hr | 10.00 | 760.00 | 7,600.00 |
| | 4 | Tractor with rotavator | Hr | 10.00 | 360.00 | 3,600.00 |
| | Total | | | | | 23,750.00 |
| | Total per $m^3$ | | | | | 79.17 |
| (c) Material cost | 1 | Lime (5% by weight of mix) | T | 50.25 | 6,000.00 | 3,01,500 |
| | 2 | Stone Dust (12% by weight of mix) | T | 65.88 | 200.00 | 13,176 |
| | Total | | | | | 3,14,676 |
| | Total per $m^3$ | | | | | 1,048.92 |
| | Contractor's profit and overhead charges@12.5% | | | | | 131.11 |
| | Preparation cost for subgrade course per $m^3$ | | | | | 125.55 |
| | Grand total | | | | | 1,305.58 |

Firstly, modified Proctor compaction tests have been carried out on untreated soil sample and on treated samples of expansive soil by the addition of varied percentages of lime by weight of soil (2, 4, 6 and 8%) within practical limits. The optimum percentage of the lime (=6%) as an admixture is based upon maximum dry density as calculated from these tests. Then, stone dust has been blended at varied percentage by weight of soil (5, 10, 15, 20 and 25%) in the optimized lime (=6% by weight)-expansive soil mix. Thus, we attain the effective design mixture of expansive soil-lime-stone dust (83-5-12% by weight of mix), also based on maximum dry density as attained from modified Proctor tests. The details of the experimental program are summarized in Table 4. The tests were performed conforming to Indian standard specifications listed in Table 5.

**Table 5.** Construction costs of different layers including subgrade layer made of untreated expansive soil

| SI. no. | Pavement component | Top width (m) | Bottom width (m) | Height (m) | Volume ($m^3$) | Rate per $m^3$ (Rs.) | Cost (Rs.) | Total Cost (Rs.) (1 + 2 + 3 + 4 + 5 + 6) |
|---|---|---|---|---|---|---|---|---|
| 1 | Bituminous course | 3.75 | 3.95 | 0.050 | 192.5 | 6402.75 | 12,32,529 | 1,10,75,925.00 |
| 2 | DBM course | 3.95 | 4.73 | 0.195 | 846.3 | 5429.45 | 45,94,944 | |
| 3 | WBM course | 4.73 | 5.73 | 0.250 | 1307.5 | 1371.14 | 17,92,766 | |
| 4 | Sub-base course | 5.73 | 7.57 | 0.460 | 3059.0 | 953.81 | 29,17,705 | |
| 5 | Subgrade | 7.57 | 9.57 | 0.500 | 4285.0 | 125.55 | 5,37,981 | |

### 3.3 Compaction Test

The tests has been performed as per Indian Standard [IS 2720 Part 8]. Maximum dry density (MDD) and optimum moisture content (OMC) has been calculated for each test sample (Table 6).

**Table 6.** Construction costs of different layers including subgrade layer made of expansive soil treated with blend of lime (6% by weight of soil) and (15% by weight of soil) stone dust.

| SI. no. | Pavement component | Top width (m) | Bottom width (m) | Height (m) | Volume ($m^3$) | Rate per $m^3$ (Rs.) | Cost (Rs.) | Total cost (Rs.) (1 + 2 + 3 + 4 + 5 + 6) |
|---|---|---|---|---|---|---|---|---|
| 1 | Bituminous course | 3.75 | 3.95 | 0.050 | 192.5 | 6,402.75 | 12,32,529 | 1,03,49,821.60 |
| 2 | DBM course | 3.95 | 4.27 | 0.080 | 328.80 | 5,429.45 | 17,85,203.16 | |
| 3 | WBM course | 4.27 | 5.27 | 0.250 | 1,192.5 | 1,371.14 | 16,35,084.45 | |
| 4 | Sub-base course | 5.27 | 6.07 | 0.200 | 1,134 | 953.81 | 10,81,620.54 | |
| 5 | Subgrade | 6.07 | 8.07 | 0.500 | 3,535 | 1,305.625 | 46,15,384.40 | |

### 3.4 California Bearing Ratio Test

Soaked CBR tests has been conducted on untreated expansive soil and soil mixed with admixtures as per Indian Standards. Sample has been prepared by compacting in five layers in a cylindrical mould. Then, the compacted sample along with mould has been kept under water for 72 h. After which, the CBR test has been performed under a constant strain rate of 1.25 mm/min.

### 3.5 Morphology

The morphologies of treated and untreated expansive soil have been analyzed by Scanning Electron Microscopic (SEM) Hitachi S 3700. Samples have been taken after 28 days of curing. Referring Fig. 1(a)–(e), it can be clearly seen from the micrograph

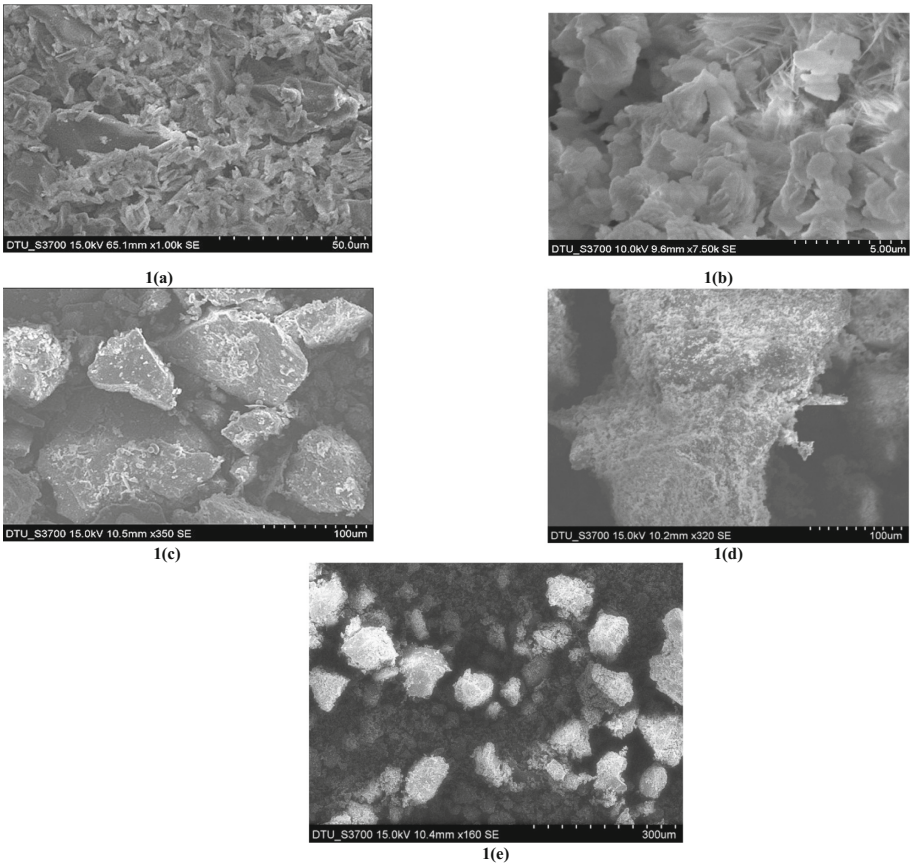


**Fig. 1.** Scanning electron micrographs of (a) expansive soil (b) lime (c) stone dust (d) expansive soil + 6% lime (by weight of soil) (e) expansive soil + 6% lime (by weight of soil) + 15% stone dust (by weight of soil) [4]

that expansive soil, lime and stone dust have undergone a pozzolanic reaction, where, stone dust and lime particles have accumulated over the expansive soil forming various cementitious compounds.

## 4 Results and Discussions

### 4.1 Compaction Behavior

Figure 2 shows the variation of MDD with percentage of lime. It has been observed that MDD value increases from the initial 1.63 gm/cc to the maximum of 1.68gm/cc when 6% of lime by weight of soil is added and it decreases thereafter. Lime makes the soil more workable and increases its strength and stiffness up to a certain value by coagulating or flocculating its particles.

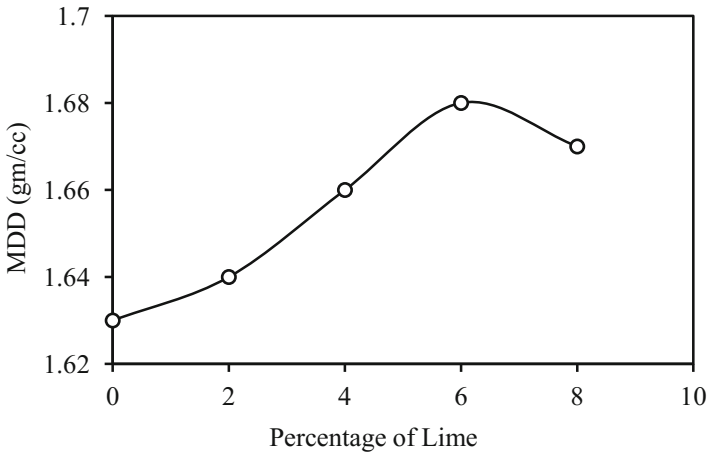


**Fig. 2.** Variation of MDD with percentage of lime [4]

Figure 3 depicts the variation of MDD with percentage of Stone Dust in soil-lime (=6% by weight) mix. It has been observed that MDD of lime stabilized soil increases upon addition of stone dust up to 15% by weight of soil. Upon further addition of stone dust, the value of MDD decreases. This may be due significant amount of heavy particles of stone dust blended in the soil-lime mix. Beyond addition of 15% of stone dust in lime stabilized expansive soil, the strength of the mix decreases due to segregation of particles induced by excessive stone dust content.

### 4.2 CBR Tests

Figure 4 shows the variation of CBR with percentage of lime. The CBR value of untreated expansive soil is 1.90%. It has been duly noted that the trend of variation of MDD with percentage of lime (Fig. 1) conforms the trend of variation of CBR with percentage of lime.

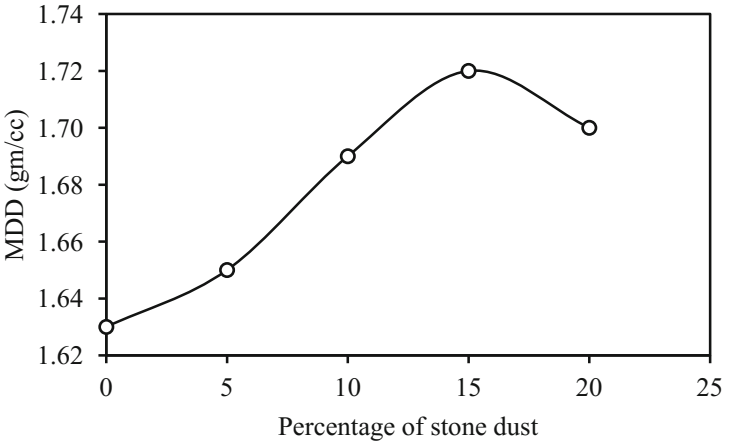


**Fig. 3.** Variation of MDD with percentage of stone dust in soil-lime (=6% by weight of soil) mix [4]

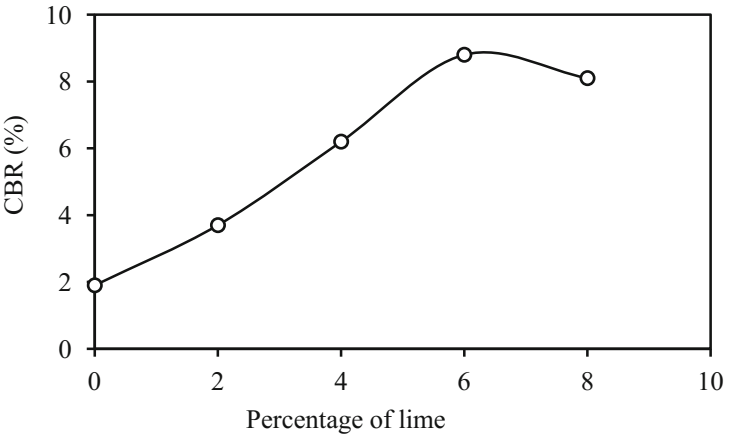


**Fig. 4.** Variation of CBR with percentage of lime [4]

Figure 5 depicts the variation of CBR with percentage of Stone Dust in soil-lime (=6%) mix. It is observed that the soaked CBR value attains its highest value when 15% of stone dust by weight has been added in lime stabilized soil. The increase of CBR value up to 15% addition of stone dust is due to the fact that silica existing in the finer particles of soil gets used up to this value and upon further addition of stone dust in the soil-lime mix, the essence becomes counterproductive thereafter.

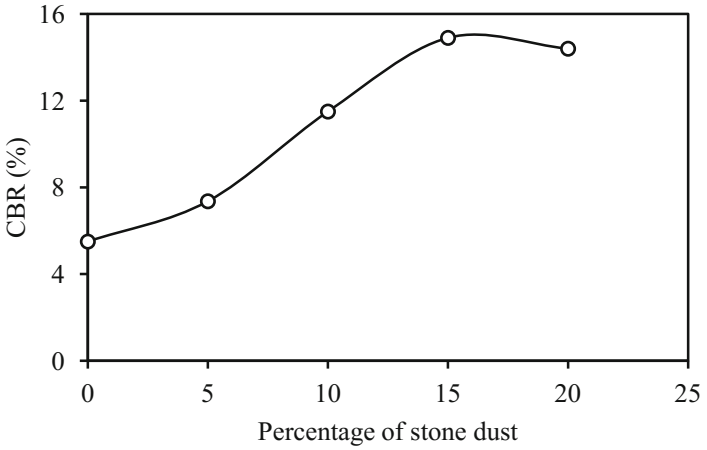


**Fig. 5.** Variation of CBR with percentage of stone dust in soil-lime (=6% by weight) mix [4]

### 4.3 Mineralogical Characterization

Due to pozzolanic reaction between soil and admixtures, mineralogical characteristics of soil is modified. Hence, the mineralogical analysis of the treated soil has become imperative. Therefore, XRD-analysis has been performed on the treated soils with the help of X-Ray diffractometer, Hitachi, which employ a Cu-Kα radiation (step of 0.05° 2θ and range of 0°–70° 2θ). Sulphate present in the soil reacts with calcium (from lime) and alumina (from stone dust and clay) results in the formation of a mineral ettringite. This ettringite mineral improves the soil strength and reduce the swelling tendency of the soil. The description of the sequence given by Hunter [5] is as below (Eq. 1):

$$6Ca + 2Al(OH)_4^- + (OH)^- + 3(SO_4)^{2-} + 26H_2O \rightarrow Ca_6\left[\left(Al(OH)_6\right)\right]_2(SO_4)_3 26H_2O \quad (1)$$

### 4.4 Analysis of Cost of Pavement Section

In the present study, the pavement is designed for a single subgrade soil. The various layers which are taken into consideration as follows:

- Subgrade (SG)
- Subbase (SB)
- Water Bound Macadam (WBM)
- Dense Bituminous Macadam (DBM)
- Bituminous Concrete (BC)

The design data was assumed as per as per IRC:37 [1] and it is as below:

Initial traffic in the year of completion of construction = 100 msa
Design Life = 10 years
Design for a 1 km long pavement

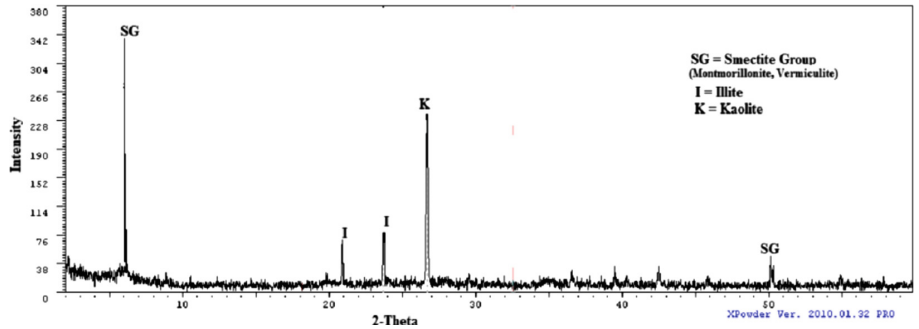


6(a)

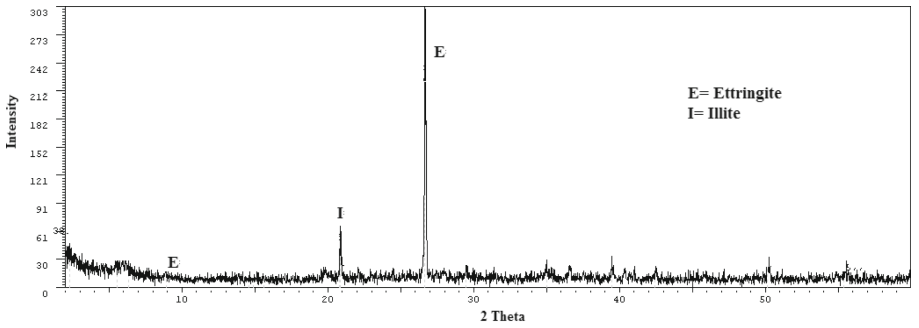


6(b)

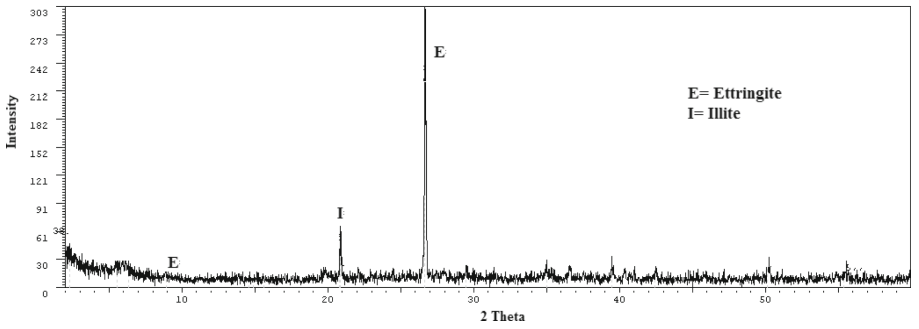


6(c)

**Fig. 6.** X-ray diffraction patterns of (a) expansive soil (b) stone dust (c) expansive soil + 6% lime (by weight of soil) + 15% stone dust (by weight of soil) [4]

Figure 7 shows the pavement section as per IRC: 37 [1] for subgrade which has been made up of untreated expansive soil (CBR = 1.9%). Similarly, Fig. 8 shows the pavement section as per IRC: 37 [1] for subgrade which has been made up of treated expansive soil (CBR = 7.8%).

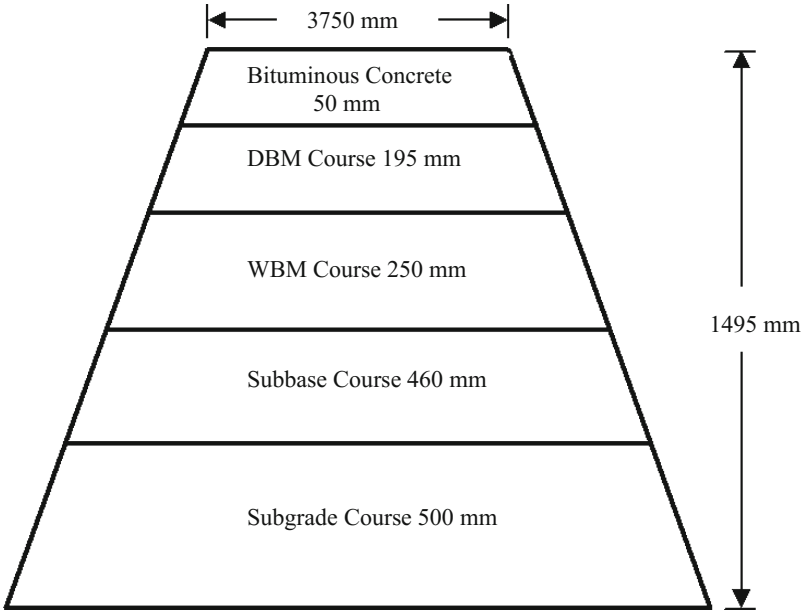


**Fig. 7.** Pavement section showing thickness of various layers for untreated expansive soil [6]

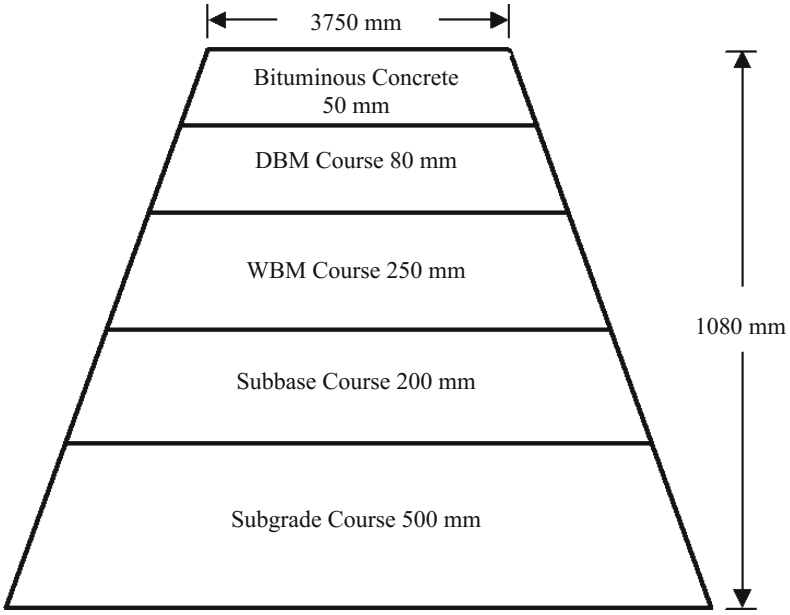


**Fig. 8.** Pavement section showing thickness of various layers for treated expansive soil [6]

## 5 Conclusions

The following conclusions have been obtained from test results and cost analysis.

- It has been discerned that the Maximum dry density (=1.72 gm/cc) and CBR value (=14.9%) of the treated expansive soil is maximum when lime is added by 6% of weight of soil and stone dust is added by 15% of weight of soil. The gain in strength is due the pozzolanic reactions of lime with the amorphous silica and alumina present in soil and stone dust.
- SEM Pictures of treated sample clearly depicts coarser bonded particles of expansive soil, lime and stone dust.
- X-Ray diffraction of samples shows the presence of montmorillonite, vermiculite (minerals of smectite group), in expansive soil, whewellite and quartz in stone dust, also dolomite and calcite in lime.
- Accordingly, we conclude that the optimum design mix for a subgrade made up of expansive soil when treated with blend of lime and stone dust is 83:5:12 by weight of mix respectively.
- 6.55% drop in cost has been attained in pavement section having treated expansive soil subgrade course (with aforementioned design mix) when compared with pavement having untreated expansive soil subgrade course.

## References

1. IRC 37: Guidelines for the Design of Flexible Pavements (Third Revision). Indian Road Congress, New Delhi (2012)
2. Choudhary, A.K., Gill, K.S.: Improvement in CBR values of expansive soil subgrade using Geosynthetics. In: 50th Proceedings of Indian Geotechnical Conference, Kochi, India (2011)
3. Sarkar, R., Abbas, S.M., Shahu, J.T.: A comparative study of geotechnical behavior of lime stabilized pond ashes from Delhi region. Int. J. Geomate Jpn. **03**(01), 273–279 (2012)
4. Mudgal, A., Sarkar, R., Sahu, A.K.: Effect of lime and stone dust in the geotechnical properties of black cotton soil. Int. J. Geomate Jpn. **7**(2), 1033–1039 (2014)
5. Hunter, D.: Lime induced heave in sulphate bearing clay soils. ASCE J. Geotech. Eng. **1**(14), 150–167 (1988)
6. Sarkar, R., Daalia, A., Narang, K., Garg, S., Agarwal, P., Mudgal, A.: Cost effectiveness of flexible pavement on stabilized expansive soil. Int. J. Geomate Jpn. **10**(1), 1595–1599 (2016)
7. Sarkar, R.: Geotechnical characteristics and utilization of pond ash available in NCR Delhi. Ph.D. thesis, Department of Civil Engineering, JMI-Delhi (2012)

# Experimental Approach to Identify the Thermomechanical Behaviour of a Textile Reinforced Concrete (TRC) Subjected to High Temperature and Mechanical Loading

Tala Tlaiji[1], Xuan Hong Vu[1(✉)], Emmanuel Ferrier[1], and Amir Si Larbi[2]

[1] Laboratoire Des Matériaux Composites Pour La Construction LMC2, Université Lyon 1, 82 Bd Niels Bohr, 69622 Villeurbanne, France
Tala.Tlaiji@etu.univ-lyonl.fr, {Xuan-Hong.Vu, emmanuel.ferrier}@univ-lyonl.fr

[2] Laboratoire de Tribologie et Dynamique Des Systèmes (LTDS), Université de Lyon, ENISE, 58 Rue Jean Parot, 42000 St-Etienne, France
amir.si-larbi@enise.fr

**Abstract.** Textile reinforced concrete (TRC), a new generation of cementitious material, is used for different applications in civil engineering. The aim of this paper is to propose a methodology to identify the thermo-mechanical behaviour of the TRC material. The studied TRC composite is made with a cementitious matrix and grid alkali-resistant glass textile. In this study, TRC specimens are subjected to two types of thermomechanical test designated by the loading path 1 and the loading path 2. The results of the thermo-mechanical tests are discussed. This study presents also an experimental methodology, using the digital image correlation (DIC) technique, which permits to identify the specific cracking mode, the crack width and the distance between the cracks of the preheated-cooled TRC specimens as a function of the uniaxial monotonic axial stress. The experimental study is then followed by an analytical model that aims to calibrate existing analytical models (Gibson and Bisby models) for the prediction of the evolution of properties (ultimate stress and post-cracked stiffness) of the TRC material as a function of the temperature.

**Keywords:** Textile reinforced concrete (TRC) · Thermomechanical test · High temperature · Digital image correlation (DIC) technique

## 1 Introduction

Textile reinforced concrete (TRC) consists of fibre reinforcements, e.g., glass or carbon fibres, which ensure the mechanical strength, and a protective cementitious matrix, which ensures the retransmission of loads towards the reinforcement. TRC combines the favourable material properties of these two components. This composite material has been shown to have potential to be used to design slender, lightweight, modular and freeform structures. This material eliminates the risk of corrosion and provides

© Springer Nature Singapore Pte Ltd. 2018
H. Tran-Nguyen et al. (eds.), *Proceedings of the 4th Congrès International de Géotechnique - Ouvrages -Structures*, Lecture Notes in Civil Engineering 8,
DOI 10.1007/978-981-10-6713-6_47

high strength in compression and in tension [Brameshuber 2006, Rambo et al. 2015]. It has also been shown to be a suitable solution for strengthening and repairing structural elements [Contamine et al 2011, Colombo et al 2015]. Another important desirable function of TRC is the ability to make textiles fireproof. When structures are subjected to fire, they are simultaneously submitted to very high temperatures (potentially up to 1200 °C) and mechanical loadings. Several studies have focused on the tensile or bending behaviour of textile-reinforced concretes at ambient temperature [Hegger and Voss 2005, Raupach et al 2006]. Some authors [Blom et al 2014, Ji et al 2013] have studied the high-temperature behaviour, at up to 500 °C, of steel-reinforced concrete beams externally reinforced with textile-reinforced mortar (TRM) or fibre-reinforced cementitious matrix (FRCM). The performance of textile-reinforced mortar (TRM) jacketing in the shear strengthening of reinforced concrete members subjected to ambient and elevated temperatures (up to 250 °C) has also been investigated [Chowdhury et al 2012]. Until now, studies on the behaviour of textile-reinforced concrete under fire loadings [Palmieri et al., Naser et al 2012] are still rare. There have been a few studies conducted on the residual behaviour of TRC after exposure to a thermal heating process (up to a desired temperature) and to a non-controlled cooling process [Lopez et al 2013, Bisby 2016]. Few studies have been conducted investigating the thermomechanical behaviour of TRC. This study presents an experimental methodology which permits to identify the non-linear behaviour law in tension, the ultimate resistance and specific cracking mode. Finally, analytical models to predict the evolution of TRC properties (ultimate stress, post-cracked stiffness) as a function of the temperature are presented.

## 2 Experimental Work

### 2.1 Experimental Device

A 20 kN-1200 °C thermomechanical machine was used for the tensile tests (Fig. 1a). The temperature in the furnace (Fig. 1b) can reach 1200 °C. It was applied by a high-temperature resistance in the furnace and controlled by integrated thermocouple. The furnace was heated with heating rate corresponding for each target temperature. This machine is presented in detail in [Tlaiji et al 2016].

### 2.2 Testing Procedure

#### 2.2.1 Thermomechanical Test (Path 1)

In thermomechanical tests, the specimens were heated to a specified temperature then loaded until failure while the same temperature was maintained. All samples are subjected with a heating increase rate in the furnace (ranging from 2, 5 °C/min to 20 °C/min) corresponding to each temperature level (ranging from 75 °C to 600 °C). When the temperature reached the target value, it is then kept constant for one hour. The tensile force applied on the specimen is monotonically increased until the maximum force that the specimen can resist. The increase in the axial force was controlled and

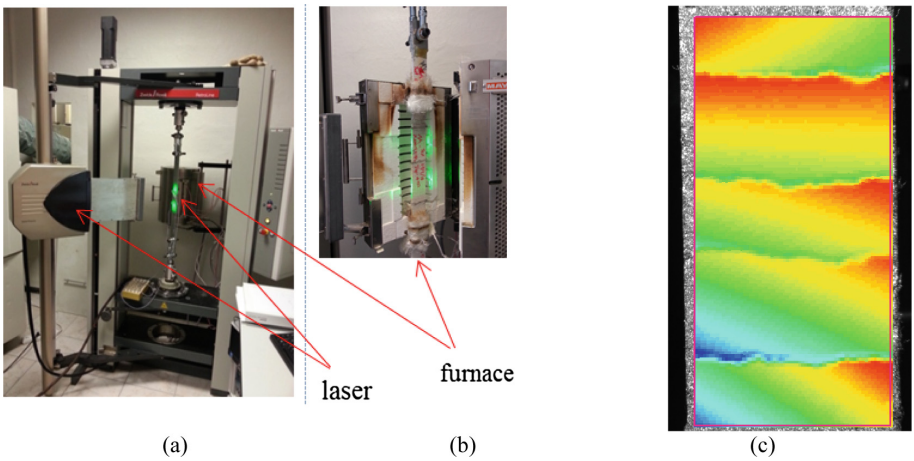


**Fig. 1.** (a) The machine Zwick 20 kN-furnace; (b) Furnace and specimen installed for a thermomechanical tensile test; (c) Digital image correlation (DIC) technique: example of a displacement field.

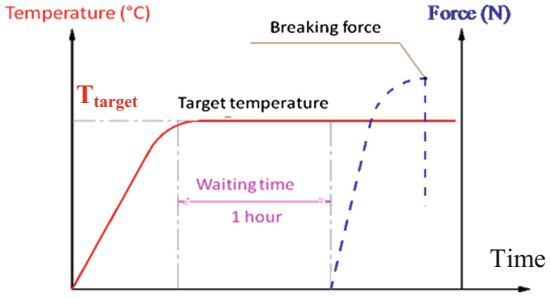


**Fig. 2.** Thermomechanical path

piloted by transverse displacement with a displacement rate of 3000 µm/min. This mechanical load was combined with the measurement of the axial strain of the specimen using a laser sensor. Figure 2 presents this test in terms of the evolution of the temperature and of the force as a function of time.

### 2.2.2 Transient-State Test (Path 2)

In the transient-state tests, showed in Fig. 3, the specimens were initially gripped at both ends and then subjected to a tensile force with a maximum load equal to a selected percentage of the maximum strength of TRC obtained at 25 °C (30% and 50%). After that, the temperature rises to the maximum level that the TRC can resist.

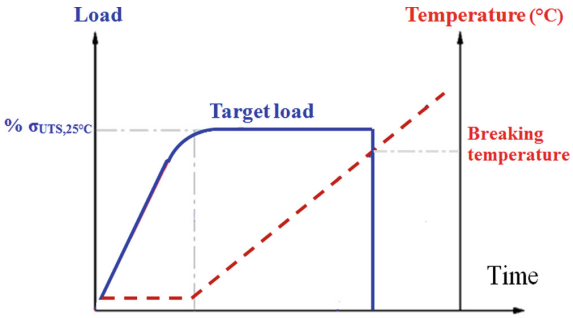


**Fig. 3.** Transient-state path

## 2.3 Specimens

### 2.3.1 Materials Used

The main composition of the TRC material tested in this study consists of a cementitious matrix and three layers of grid alkali-resistant (AR) glass textile. The compressive strength and the tensile strength of this matrix are respectively 23 MPa and 4.5 MPa. The textile type (grid AR-glass) used in this study has the same thread in two directions of the grid. This grid is large and the opening between the meshes axis is 8 mm × 8 mm which allows the passage of small aggregates.

### 2.3.2 Specimen Preparation

The cementitious matrix and the reinforcement textiles are cast in a mold to obtain a plate of TRC having the dimension 800 mm × 500mm × 5 mm (length × width × thickness). After 7 days, the rectangular plates were cut, resulting in specimens of 700 mm 45 mm × 5 mm (length × width × thickness). To prepare the specimen for the test, four aluminium plates are glued to the ends of each specimen using an epoxy adhesive (Eponal 380) to ensure transfer efficiency of the mechanical load. At least 3 days after the bonding, the TRC sample was drilled at each end to be compatible with the used loading heads. The specimen preparation is presented in detail in [Tlaiji et al 2016].

## 2.4 Digital Image Correlation (DIC) Technique

Before the measurement with the digital image correlation (DIC) technique, a speckled pattern of black and white paint was sprayed onto the surface of the sample to improve resolution of displacement. A reference image is taken before applying load and then a set of images are taken at sampling rate of 0.5 s till the end of the test. The displacement of the points in the measured zone during the increase of the load can be observed from the images. As a result, the speckles at the surface of the sample displace from their initial location. By correlating the information from the two images, using the ICASOFT software, the movement of different points from the initial image to the final image was identified. The results are treated on the basis of image representing the

displacement values obtained after analysis of the images by the ICASOFT software; these represent the displacement field of the specimen (c). The measurement of the displacement along the axis at the different loads makes it possible to plot the graph representing the displacement (in mm) as a function of the position on the longitudinal axis (in mm) at each loading level. Finally, using the results obtained by the software, the distance between the cracks was identified and their opening as a function of the loading was also determined. In this study, the 3G.AR composite samples were heated to several desired temperature levels (25 °C, 75 °C, 150 °C, 300 °C, 400 °C and 600 °C) and then cooled before the measurement of the displacement, using the Digital Image Correlation (DIC) technique.

## 3 Test Results

### 3.1 Results of the 3G.AR Composite in the Thermomechanical Path (TM)

Figure 4 shows the results of tests on the 3G.AR composite in the thermomechanical path. This figure represents the axial stress as a function of the thermomechanical axial strain and of the temperatures varying from 25 °C to 600 °C. In Fig. 4, there is one average stress-strain curve for each temperature. This figure shows the result of the 3G.AR specimens that were exposed to different temperatures (25 °C, 75 °C, 150 °C, 300 °C, 400 °C and 600 °C) during 1 h and were then submitted to uniaxial monotonic tensile loading. The curves at temperatures varying from 25 °C to 150 °C show three distinguishable phases in the behaviour of the 3G.AR composite. However, at 300 °C and 400 °C, two phases are observed. Additionally, at 600 °C, the curve is quasi-linear, and only one phase is shown.

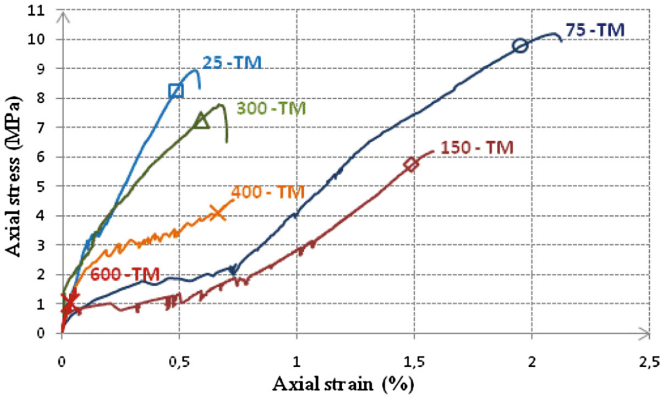


**Fig. 4.** Thermomechanical behaviour of the 3G.AR composite in different target temperature levels

### 3.2 Thermomechanical Properties of the 3G.AR Composite

The interaction between the matrix and the reinforcement leads to multilinear behaviour. In general, at ambient temperature, the curve characterizing the behaviour of a TRC is formed from three phases: the first phase corresponds to the semi-elastic response of the material, the second phase corresponds to the progressive damage of the matrix from the occurrence and development of cracking, which is responsible for the reduction in the stiffness of the composite, and the third phase, which is quasi-linear, corresponds to the mechanical behaviour of the fibres alone. To refine the analysis of the influence of the temperature on the thermomechanical behaviour, in this study, a notation is used for the three curves representing three examples for each multilinear curve (Fig. 5). In Fig. 5, idealized stress/strain curves of the behaviour of the 3G.AR composite are shown. The used notation is detailed below: $\boldsymbol{\sigma_{UTS}}$: ultimate stress level of the composite corresponding to point UTS; $\mathbf{E_{c3}}$: stiffness of the third phase (or stiffness of the post-cracked composite). After using these notations, the evolution of some parameters, such as $\boldsymbol{\sigma_{UTS}}$, $\mathbf{E_{c3}}$ of the 3G.AR composite in thermomechanical loading path according as a function of the temperature was identified and is presented in the following sections.

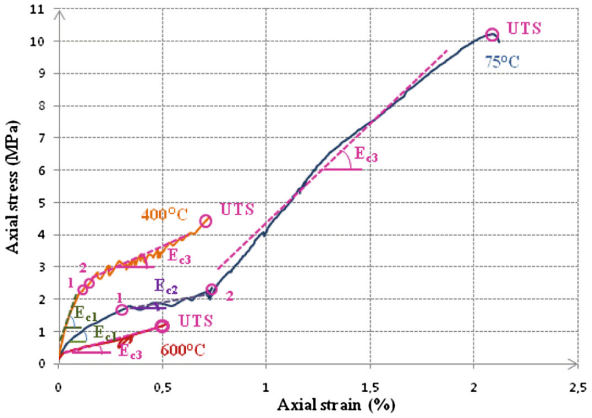


**Fig. 5.** Idealized stress/strain curves of the behaviour of the 3G.AR composite

#### 3.2.1 Evolution of the Ultimate Tensile Stress as a Function of the Temperature

Figure 6 represents the results of the thermomechanical (TM) tests and for each temperature (25 °C, 75 °C, 150 °C, 300 °C, 400 °C and 600 °C) in terms of the average ultimate tensile strength as a function of the temperature. The average ultimate tensile

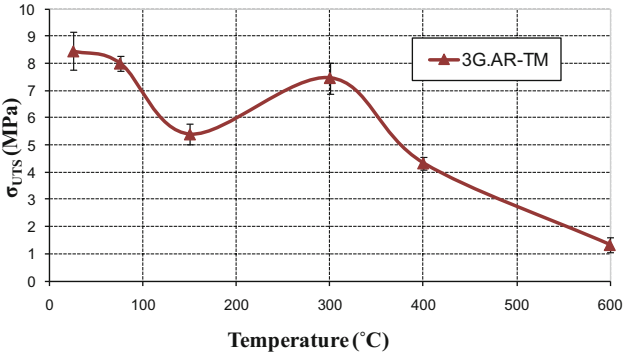


**Fig. 6.** Average ultimate tensile strength as a function of the temperature

strength of this composite is slightly reduced when this one is subjected to temperatures below 150 °C during the thermomechanical tests. However, after 150 °C, the material takes up part of its initial strength (at 25 °C) before decreasing again from 300 °C to 600 °C.

### 3.2.2 Evolution of the Stiffness $E_{c3}$ as a Function of the Temperature

The evolution of the post-cracked composite stiffness ($\mathbf{E_{c3}}$) in the third phase of the behaviour of 3G.AR composite $\mathbf{E_{c3}}$ as a function of the temperature ranging from 25 °C to 600 °C is shown in Fig. 7. From 25 °C to 75 °C, a post-cracked composite stiffness drop is observed. Then this stiffness increases from 75 °C to 300 °C before decreasing again after 300 °C.

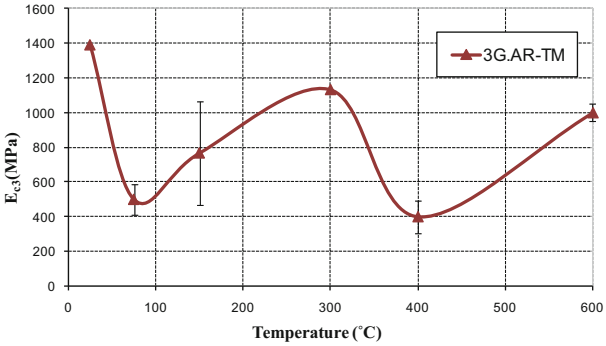


**Fig. 7.** Evolution of the stiffness $E_{c3}$ as a function of temperature

### 3.3 Results of the 3G.AR Composite in the Transient-State Path

The failure temperature for each percentage of maximal strength obtained on 25 °C (30% $\sigma_{UTS,\ 25\ °C}$ and 50% $\sigma_{UTS,\ 25\ °C}$) was reached when the tensile load could no longer be sustained. Figure 8 shows the temperature to cause failure of the specimens for 30% $\sigma_{UTS,\ 25\ °C}$ and 50% $\sigma_{UTS,\ 25\ °C}$ tensile load. In this figure, the horizontal axis represents the failure temperature of the specimen, and the vertical axis represents the ultimate load. The failure temperatures of the test specimens are given in the Table 1. It should be noted, according to the results shown in the Table 1, that there was a brutal drop (of 72%) of failure temperatures when the stress was increased from 30% $\sigma_{UTS,\ 25\ °C}$ to 50% $\sigma_{UTS,\ 25\ °C}$.

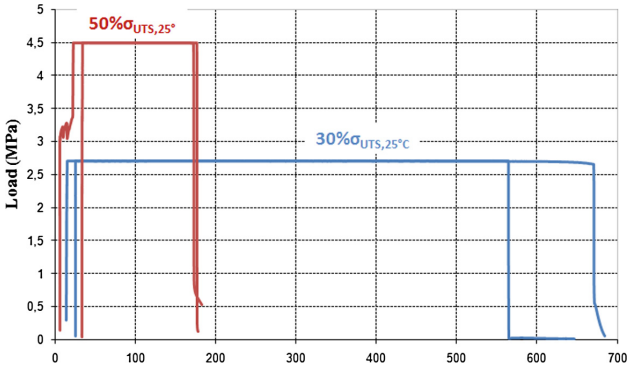


**Fig. 8.** Failure temperature for 30% $\sigma_{UTS,\ 25\ °C}$ and 50% $\sigma_{UTS,\ 25\ °C}$ tensile load

**Table 1.** Failure temperatures of the test specimens

| | Load (MPa) | Failure temperature (°C) |
|---|---|---|
| 30% $\sigma_{UTS,\ 25\ °C}$ (Test number 1) | 2.7 | 660 |
| 30% $\sigma_{UTS,\ 25\ °C}$ (Test number 2) | 2.7 | 570 |
| 50% $\sigma_{UTS,\ 25\ °C}$ (Test number 1) | 4.5 | 168 |
| 50% $\sigma_{UTS,\ 25\ °C}$ (Test number 2) | 4.5 | 173 |

### 3.4 Results Obtained by the Digital Image Correlation (DIC) Technique

Figure 9 below shows the maximum crack width of the preheated-cooled 3G.AR composite specimens as a function of the axial stress for the different temperature levels (25 °C, 75 °C, 150 °C, 300 °C, 400 °C and 600 °C). The crack width of the preheated-cooled 3G.AR composite specimens is small (inferior to 0.42 mm) for all

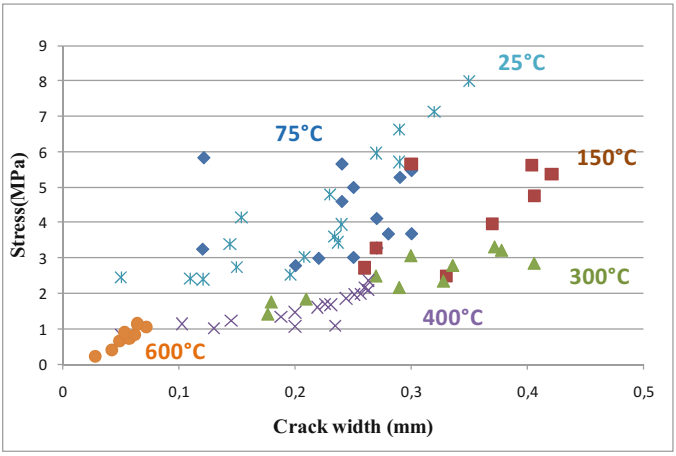


**Fig. 9.** Maximum crack width of the preheated-cooled 3G.AR specimens as a function of the axial stress at each temperature level

**Table 2.** Maximum crack width and spacing between cracks

| Preheated-cooled specimen | 3G.AR | | | | | |
|---|---|---|---|---|---|---|
| Preheated temperature (°C) | 25 | 75 | 150 | 300 | 400 | 600 |
| Maximum crack width (mm) | 0.35 | 0.3 | 0.42 | 0.41 | 0.27 | 0.07 |
| Corresponding stress (MPa) | 8 | 5.5 | 5.5 | 3 | 2.5 | 1.2 |
| Spacing between cracks (mm) | 14 | 16 | 16 | 13 | 15 | 15 |

temperature levels. The first crack appears on a different loading level for each temperature. The maximum crack width before specimen failure reaches 0.42 mm for the preheated temperature level of 150 °C. Table 2 below shows the maximum crack width of the preheated-cooled 3G.AR composite specimen with its corresponding stress and the average distance between cracks at the ultimate load for each preheated temperature level varying form 25 °C to 600 °C.

## 4 Prediction Models

In parallel with experimental studies carried out, several semi-empirical analytical models (Bisby and Gibson model 2015) have been developed to simulate the behavior of fiber-reinforced polymer (FRP) composite materials at high temperature. However, we do not find in the literature models that concern TRC composite materials. The objective of this section is to identify and calibrate these models (Bisby and Gibson) with the obtained experimental results of the 3G.AR composite in order to describe the evolution of the thermomechanical properties of the TRC composite materials.

### 4.1 Gibson Model

Gibson [Firmo et al 2015] proposed a general model which takes the form of a hyperbolic tangent function and which describes the reduction of the mechanical properties of the FRP composite as a function of temperature:

$$P(T) = R^n\left[\frac{P_u + P_r}{2} - \frac{P_u - P_r}{2}\tanh\{K_m(T - T_g)\}\right]$$

$P(T)$: Mechanical property at temperature T; $P_u$: Mechanical property at room temperature; $P_r$: Mechanical property after the glass transition; $K_m, T_g$: Parameters obtained by fitting the experimental data; $R$: Residual resin content (0 < R < 1); $n$: depends on the stress state (n = 1 → resin, n = 0 → fiber). By calibrating this model with the experimental data of 3G.AR (ultimate stress as function of temperature), we propose for this model the following parameters represented in Table 3.

**Table 3.** Corresponding parameters for Gibson model;

| Mechanical property | Strength $\sigma_{UTS}$ (MPa) | Stiffness $E_{c3}$ (MPa) |
|---|---|---|
| $P_u$ | 8.45 | 1400 |
| $P_r$ | 2.5 | 400 |
| $T_g$ | 500 | 400 |
| $R$ | 1 | 1 |
| $n$ | 0 | 0 |
| $K_m$ | Depends on temperature (T) | Depends on temperature (T) |

### 4.2 Bisby Model

Bisby [Firmo et al 2015] proposed the following semi-empirical model: $\frac{P(T)}{P_u} = \frac{(1-a)}{2}\tanh[-b(T-c)] + \frac{(1+a)}{2}$where $P(T)$: Mechanical property at temperature T; $P_u$: Mechanical property at room temperature; a, b and c are empirical parameters based on experimental results. For 3G.AR a, b and c were taken as follow in Table 4. Finally, the two models described above were successfully used to describe the degradation in the tensile properties of the 3G.AR composite and presented in the figures below (Figs. 10 and 11).

**Table 4.** Corresponding parameters for Bisby model

| Mechanical property | Strength $\sigma_{UTS}$ (MPa) | Stiffness $E_{c3}$ (MPa) |
|---|---|---|
| a | 0.15 | 0.15 |
| b | 0.0081 | 0.005 |
| c | Depends on temperature (T) | Depends on temperature (T) |

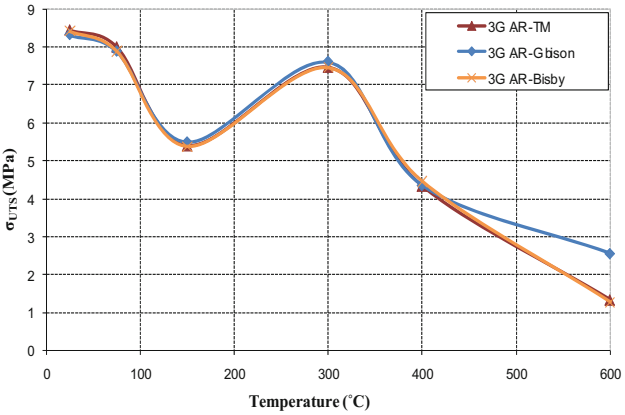


**Fig. 10.** Bisby and Gibson model for the prediction of the $\sigma_{UTS}$ of the 3G.AR composite

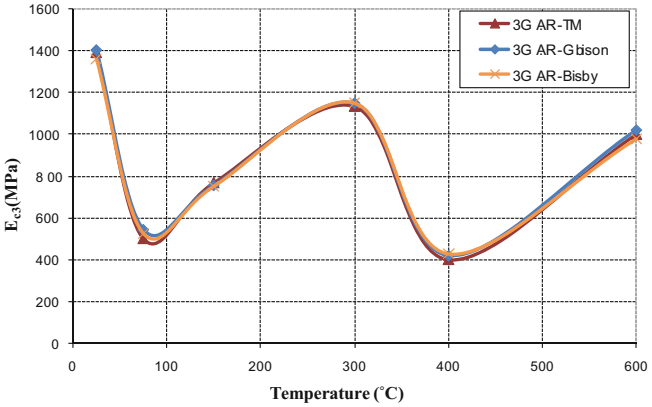


**Fig. 11.** Bisby and Gibson model for the prediction of the $E_{c3}$ of the 3G.AR composite

## 5 Conclusion

This study concerns the experimental study of the thermomechanical behaviour and the transient-state behavior of the textile reinforced concrete (TRC) subjected to high temperature levels varying from 25 °C to 600 °C. The TRC is made with a cementitious matrix and three layers of alkali-resistant grid glass textile. The results of this work show that during a rise in target temperature level, the behaviour of the studied TRC (called 3G.AR) changes. The stress-strain behaviour of glass textile reinforced cementitious composites in tension is highly non-linear. This study was also focusing on the propagation of the cracks. An investigation of the crack width and the distance between the cracks is done by using the Digital Image Correlation technique. Finally,

this experimental study is followed by an analytical model that aims to calibrate existing analytical models for the prediction of the evolution of properties of the TRC as a function of the temperature.

**Acknowledgements.** This research was performed with the financial subvention of the European Regional Development Fund of the European Union and of the Rhône-Alpes-Auvergne region, France for the lot 5 "Characterization of composite materials" of the PRORETEX II research project. This project is the collaborative research project between four industrial partners (SULITEC - project leader; FOTIA; ER2I; CIMEO) and two academic partners (UCBL/LMC2; ENISE/LTDS). We also would like to thank Mr. HAMELIN Patrice for his scientific support as well as the team of technicians (Mr. Emmanuel JANIN, Mr. Nobert COTTET) from the Civil Engineering Department at IUT Lyon 1 and LMC2, University Lyon 1 for their technical support.

## References

Brameshuber, W.: Textile reinforced concrete. State-of-the-Art Report (n°36) of RILEM Tech. Committee, TC 201-TRC.T (2006)

Rambo, D.A.S., De Andrade Silva, F., Filho, R.D.T., Da Fonseca Martins Gomes, O.: Effect of elevated temperatures on the mechanical behavior of basalt textile reinforced refractory concrete. Mater. Des. **65**, 24–33 (2015)

Contamine, R., Si Larbi, A., Hamelin, P.: Contribution to direct tensile testing of textile reinforced concrete (TRC) composites. Constr. Build. Mater. **24**, 1928–1936 (2011)

Colombo, I.G., Colombo, M., Di Prisco, M.: Bending behaviour of textile reinforced concrete sandwich beams. Constr. Build. Mater. **95**(2015), 675–685 (2015)

Hegger, J., Voss, S.: Textile reinforced concrete – bearing behaviour, design, application. In: 3rd International Conference Composites in construction, Lyon, France (2005)

Raupach, M., Orlowsky, J., Büttner, T., Dilthey, U., Schleser, M.: Epoxy impregnated textiles in concrete – load bearing capacity and durability. In: 1st International RILEM Conference on Textile Reinforced Concrete (ICTRC) pp. 77–88 (2006)

Blom, J., El Kadi, M., Wastiels, J., Aggelis, D.G.: Bending fracture of textile reinforced cement laminates monitored by acoustic emission: influence of aspect ratio. Constr. Build. Mater. **70**, 370–378 (2014)

Ji, G., Li, G., Alaywan, W.: A new fire resistant FRP for externally bonded concrete repair. Constr. Build. Mater. **42**, 87–96 (2013)

Chowdhury, E., Bisby, L., Green, M., Bénichou, N., Kodur, V.: Heat transfer and structural response modelling of FRP confined rectangular concrete columns in fire. Constr. Build. Mater. **32**, 77–89 (2012)

Palmieri, A., Matthys, S., Taerwe, L.: Fire endurance and residual strength of insulated concrete beams strengthened with near-surface mounted reinforcement. J. Compos. Construct. 454–462 (2013)

Naser, M., Abu-Lebdeh, G., Hawileh, R.: Analysis of RC T-beams strengthened with CFRP plates under fire loading using ANN. Constr. Build. Mater. **37**, 301–309 (2012)

Lopez, C., Firmo, J.P., Correia, J.R., Tiago, C.: Fire protection systems for reinforced concrete slabs strengthened with CFRP laminates. Constr. Build. Mater. **47**, 324–333 (2013)

Bisby, L.: Fire resistance of textile fiber composites used in civil engineering. Text. Fibre Compos. Civ. Eng. 169–185 (2016)

Tlaiji, T., Vu, X.H., Si Larbi, A., Ferrier, E.: Experimental and comparative study of the thermomechanical behavior and the residual one of the textile reinforced concrete (TRC) subjected to high temperature loading. AUGC2016 conference Proceeding, Liège, Belgium (2016)

Firmo, J.P., Correia, J.R., Bisby, L.A.: Fire behaviour of FRP-strengthened reinforced concrete structural elements: a state-of-the-art review. Compos. Part B Eng. **80**, 198–216 (2015)

# Experimental Study on the Thermo-Mechanical Behavior of Hand-Made Carbon Fiber Reinforced Polymer (H-CFRP) Simultaneously Subjected to Elevated Temperature and Mechanical Loading

Phi Long Nguyen[1,2], Xuan Hong Vu[1(✉)], and Emmanuel Ferrier[1]

[1] Laboratory of Composite Materials for Construction (LMC2), Université Lyon 1, Université de Lyon, 82 bd Niels Bohr, 69622 Villeurbanne, France
Xuan-Hong.Vu@univ-lyonl.fr

[2] Faculty of Construction Engineering, Ho Chi Minh City University of Transport, Campus 1: Number 2, D3 Street, Ward 25, Binh Thanh District, Ho Chi Minh City, Vietnam

**Abstract.** Among two common forms of CFRP used in strengthening/repairing construction structures (pultruded and hand-made), hand-made CFRP is popularly used with column and other structures where the strengthening surfaces are complicated. Normally, the hand-made CFRP (H-CFRP) includes woven carbon fibers, prefabricated in the factory and the polymer matrix which is added during the installation process. When a fire happens, structures and reinforced material are simultaneously exposed to high temperatures (up to 1200 °C) and mechanical loadings, which are complicated and difficult to be experimentally simulated. As far as the authors concern, the studies of CFRP and structure reinforced with CFRP in fire are rare due to expensive cost of experiments and insufficient theoretical calculations. For these reasons, this study aims to investigate the thermo-mechanical behavior of H-CFRP via two different elevated-temperature and mechanical load regimes. The first regime studies the ultimate-strength evolution as the exposed temperature increases while the second studies the variation of rupture temperature when applied load changes. The results from the first regime show that the ultimate strength and the Young modulus of H-CFRP generally reduce 50% and 25% when the applied temperature level increases from 20 °C to 400 °C. The second series show that the rupture temperature of H-CFRP steadily reduces from about 640 °C to about 467 °C as its mechanical stress ratio increases from 0.1 to 0.5 (of its ultimate strength at 20 °C). Remarkably when the mechanical stress ratio of H-CFRP increases to 0.75, the rupture temperature dramatically drops to about 50 °C. The rupture modes and correlation between two regimes will also be discussed.

**Keywords:** Handmade carbon fiber reinforced polymer (H-CFRP) · Elevated temperature · Thermo-mechanical behavior · Mechanical loading

© Springer Nature Singapore Pte Ltd. 2018
H. Tran-Nguyen et al. (eds.), *Proceedings of the 4th Congrès International de Géotechnique - Ouvrages -Structures*, Lecture Notes in Civil Engineering 8,
DOI 10.1007/978-981-10-6713-6_48

## 1 Introduction

In recent decades, there is an increase in the use of carbon fiber reinforced polymer (CFRP) in civil engineering for both reinforcing and retrofitting structures. CFRP, with the light weight, high strength character as well as good properties in corrosion resistance and fatigue, is normally used to reinforce the tensile working region to enhance the strength, stiffness and ductility of concrete structures (column, beam and slab). Since the first application in the civil engineering, the ability of CFRP to work in fire condition is always an important concern. Considerable researches have concentrated on the mechanical performance and properties of CFRP at elevated temperature. The general result indicates that CFRP experiences degradation in its tensile properties at elevated temperature. Basically, the evolution of tensile performance of CFRP has been studied following two procedures: in the first procedure, specimens were heated up to an predefined temperature, then mechanically tested until rupture following direct tensile test program (thermo-mechanical procedure); in the second procedure, after being heated up to predefined temperature and then cooled to ambient temperature, specimens were tested following direct tensile test program (residual procedure); Wang et al. performed a series of tensile test on CFRP rod at temperature ranging from 20 °C to 600 °C following thermo-mechanical procedure (Wang et al. 2007). The results showed that the tensile strength of CFRP reduced approximately 50% as the temperature increased up to 240 °C and this strength reduced almost 90% at 600 °C. Wang et al. measured the tensile strength of the pultruded CFRP strip following thermo-mechanical procedure at temperature ranging from 22 °C to 706 °C (Wang et al. 2011). The results displayed a reduction in tensile strength of pultruded CFRP strip approximately 50% at 350 °C and more than 80% at 600 °C. Foster et al. observed the evolution of residual tensile properties of carbon-epoxy system from 20 °C to 400 °C (Foster and Bisby 2005). The results showed that residual strength of this material decreased about 20% at 300 °C and about 80% at 400 °C whereas the tensile modulus varied less than 10% up to 400 °C. Yu and Kodur studied the influence of temperature between 20 °C to 600 °C on the degradation of tensile properties of CFRP pultruded products (strips and rods) following thermo-mechanical procedure (Yu and Kodur 2014). As these results, the tensile strength reduced about 50% (strips) and 40% (rods) at 300 °C and roughly 90% (both strips and rods) at 600 °C. On the other hand, the tensile modulus decreased about 30% (both strips and rods) of its value at 400 °C and respectively 67% and 47% at 500 °C for strips and rods. Cao et al. tested the thermo-mechanical tensile strength of CFRP sheets with two loading-control methods (by load increment and displacement increment) at the temperature between 16 °C and 200 °C (Shenghu Cao et al. 2009). The results indicated that tensile strengths of CFRP sheets significantly reduced with increasing temperature. From 16 °C to 55 °C, the tensile strength reduced approximately 30% and varied around this value up to 200 °C. When subjected to the thermal load, most thermosetting resins and amorphous polymers show one major transition. This transition occurs in a narrow range of about several tens of degrees called glass transition temperature (Tg). With commercial products used in civil infrastructure applications, Tg varied between 50 °C and 90 °C (Foster and Bisby 2008). When the material temperature reaches the transition

temperature of the polymer matrix, the matrix becomes soften and the material's mechanical properties (Young's modulus, tensile strength) are significantly reduced. Therefore, the contribution of the matrix to the composite tensile strength gradually becomes negligible. This contribution reduces to zero after total decomposition of the matrix, characterized by a decomposition temperature Td (250–500 °C) (Mouritz and Gibson 2006; Correia et al. 2010). The matrix decomposition process usually releases heat, smoke, soot and toxic/combustible volatiles (Mouritz and Gibson 2006). This possibly hastens the matrix decomposition itself, influences the mechanical properties of fiber and also hinders the deformation measurement. Among studies considering performance of CFRP at elevated temperature, there are few experimental studies which can provide data regarding the "stress-strain" relationship, due to technical or experimental difficulty in measuring the deformation at high temperature. Wang's experiments were conducted by pulling on cylindrical specimens of CFRP in the range of a temperature of 20 ÷ 600 °C (Wang et al. 2007). However, according to the authors, the displacement sensor system had failed to record data for tests at very high temperatures (more than 400 °C) due to the oxidation of the polymer matrix. Wang observed the stress-strain relation on laminate type specimens of CFRP using the results which were not based on the displacement between two points on the tested region but on the clamp-displacement of the traction machine (Wang et al. 2011). Foster et al. observed stress-strain curves of a preheated then cooled laminate CFRP using an strain gauges to measure the deformation of the tested pieces (Foster and Bisby 2005). However, the authors also reported that the strain gauges were detached before the rupture of most specimens. Yu and Kodur (Yu and Kodur 2014) used LVDT to measure the movement of two clamping brackets of the tensile direct machine to estimate the elongation of CFRP specimens. According to Cao et al. (Shenghu Cao et al. 2009), it was difficult to use strain gauges o measure deformation at high temperature.

This paper presents the experimental investigation of the tensile response of Hand-made Carbon Fiber Reinforced Polymer (H-CFRP) simultaneously exposed to a thermal and mechanical load by an innovative thermo-mechanical machine TM20kN-1200C of the Laboratory LMC2 (Lyon, France). In the following, the experimental work with testing devices, specimens, and test procedure are detailed. The paper then describes and discusses the results of tests carried out on the studied material. The presentation of the main conclusion ends this paper.

## 2 Experimental Work

### 2.1 Experimental Devices

In this research, a thermo-mechanical testing system (Fig. 1) is used to study the thermo-mechanical behavior of H-CFRP material. The system including two main parts: the thermo-mechanical machine (called TM20kN-1200C ) and laser extensometer. During the test, the TM20kN-1200C controls the force and temperature applied on the sample following a determined procedure during while the laser extensometer measures the tensile strain of CFRP sample. The TM20kN-1200C

includes a mechanical part (Fig. 1a) and a furnace (Fig. 1b). The mechanical part can perform direct tensile loading onto the testing specimen with loading capacity up to 20 kN with programmable loading speed. The furnace is a cylinder oven which external dimensions are 40 cm in height and 30 cm in diameter and the heating-chamber dimensions are 28 cm in height and 10 cm in diameter. This furnace can generate high temperature up to 1200 °C with the maximum heating rate of 30 °C/min. The temperature level and the heating rate are set so that the testing system can auto-control the test with different target temperature levels and heating rates depending on the test. The furnace is insulated to guarantee the temperature of the closed system inside the furnace is as established by testing program. There is a rectangular opening on the side of the furnace allowing two laser rays from the laser extensometer to measure the elongation of specimen. This opening can be closed in case the laser extensometer is unused. When a fire happens, structures are subjected to the heat and mechanical loads at the same time. In order to intensively observe the fire responses of structure, it is very important to measure mechanical load, temperature, deformation as they indicate the working status of structures. For measuring loading level, a force sensor is placed outside the furnace to measure as well as control the applied force. Six thermo-couples are placed inside the furnace including three on the wall of heating chamber and three on sample surface to follow real-time temperature and control the furnace during the test. However, it is difficult to identify the deformation of specimen in elevated temperature condition due to the influence of high temperature to the measurement devices. In this study, a laser extensometer (Fig. 1c) is used to measure the deformation of testing sample. The laser extensometer consists of two measuring heads with digital cameras and laser light sources mounted on motorized slides. This method is non-contacted, thus reduces the errors caused by the temperature to the testing device. The laser extensometer is used to measure the longitudinal strain of the specimen at elevated temperature via two laser bobbins passing through a rectangular guiding tube and projecting on the surface of the specimen to evaluate the strain. The guiding tube helps minimizing the influence of the environment such as air current to the measurement algorithm. There is a transparent glass wall which separates the heating chamber and the space inside the guiding tube to reduce the mutual thermal-violation between the furnace and laser extensometer. The development and validation of the laser extensometer measurement have been mentioned in previous works (Nguyen et al. 2016). The mechanical part is able to apply an axial tensile force into the testing specimen during while heating chamber of the furnace can increase the temperature surrounding specimen at different rate (maximum heating rate of the furnace is 30 °C/min). This system is automatic and servo-controllable and can simultaneously generate the mechanical and thermal loadings.

### 2.2 Specimens

In this research, the studied handmade CFRP is made from unidirectional woven carbon fibers added with polymer matrix. The woven carbon fiber weights 310 g/m$^2$ and has the thickness of 0.32 mm. The tensile strength of carbon fiber is 4902 MPa and its tensile modulus is 230 GPa (supplier's data). The elongation failure of carbon fiber

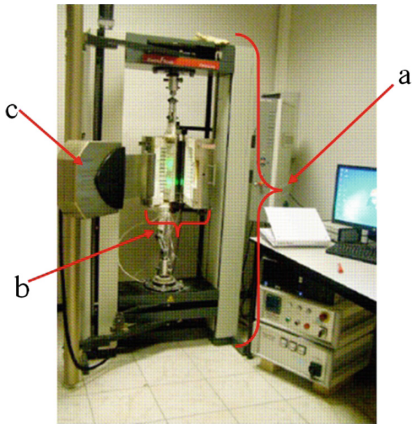


**Fig. 1.** Thermo-mechanical testing system; (a) mechanical machine; (b) furnace; (c) laser extensometer

is 2.1% (supplier's data). The minimum bond strength and shear strength of the polymer matrix are 14 MPa and 12 MPa respectively. The elastic modulus of polymer is 2 GPa and its glass transition temperature is 40 °C (supplier's data). The studied textile carbon fiber (Fig. 2) is first divided into testing size (includes 4 fiber tows) and aligned in flat surface. The polymer matrix is prepared by mixing two components of epoxy as the advised ratio and then swept on the textile. A waiting duration is needed to allow the polymer matrix harden to achieve its mechanical characteristics and well-bonded with the carbon fiber. In tensile test, the sample is normally placed in middle and their two ends are gripped by two clamps of the machine. Basically, the tensile axial force transmitted to the sample by the friction of the contacted regions between the clamps and the sample. However, the tensile strength of the tested material is much greater the friction force. Therefore, in order to effectively transmit the tensile force from the mechanic parts to the composite material, two aluminum plates are attached in each end by epoxy resin (EPONAL 380). The shear resistance and tensile resistance of the used epoxy are 15 MPa and 29.5 MPa respectively. Figure 3 shows the details of the tested specimen.

**Fig. 2.** Textile carbon fiber

### 2.3 Test Procedures

In this research, the H-CFRP will be tested following two thermo-mechanical regimes: the one carried out at constant temperature (TM1) and the one carried out at constant

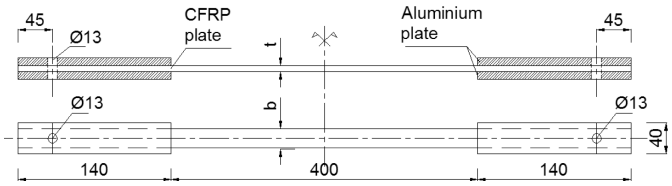


**Fig. 3.** Detail of sample

load (TM2). The first regime is to identify the mechanical behavior of material during exposing to elevated temperature while the second is to identify the rupture temperature corresponding to mechanical load that imposing on the material. In the first regime (or TM1, Fig. 4), the temperature surrounding sample will be homogeneously increased up to desired level (target temperature, $T_t$) in the first phase. The temperature level is then maintained for a determined duration called waiting time ($T_w$, Fig. 4). When $T_t$ is higher than combustion temperature of the polymer matrix, the test experiences the leaking smoke that feasibly influences visual field of laser extensometer. This combustion process occurs in approximately 30 min depending on the type of polymer matrix and the level of $T_t$. Therefore, in this study, in order to let the polymer matrix to be completely oxidized, the $T_w$ is chosen at 1 h. In the third phase, the mechanical tensile load will act on the material and monotonically increase until rupture of the specimen. This rupture force is identified as the ultimate force that acts on the sample at the target temperature level and then used to calculate ultimate thermo-mechanical stress of H-CFRP ($\sigma_{U.\ TM}$). In the second regime (or TM2, Fig. 5), the specimen is first loaded with a force called working force ($F_w$) in the first phase. In the second phase, while the $F_w$ is maintained, the temperature surrounding the specimen increases with the ramp rate at 30 °C/min from ambient temperature until rupture of the specimen. The temperature, at which specimen is broken, is identified as rupture temperature ($T_r$) corresponding to the load level $F_c$. The details of tests undertaken following two regimes in this study are presented in Tables 1 and 2.

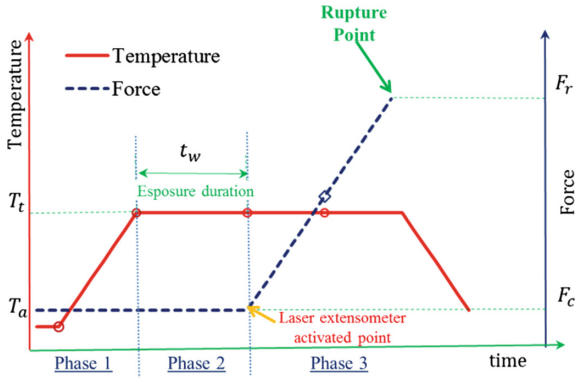


**Fig. 4.** Thermo-mechanical regime 1 (TM1) test (In which: Ta: ambient temperature; Tt: target temperature; Fr: rupture force; tw: waiting time; Fc: control force)

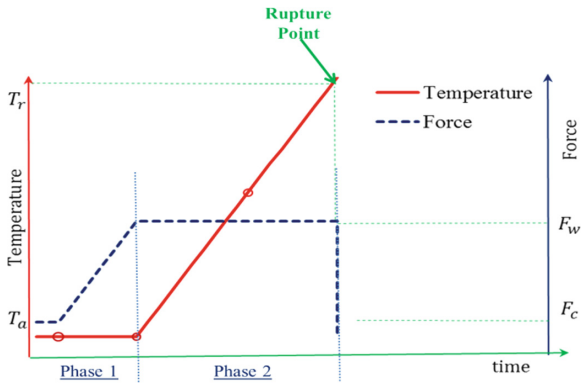


**Fig. 5.** Thermo-mechanical regime (TM2) test (In which: Ta: ambient temperature; Tr: rupture temperature; Fc: control force; Fw: working force)

**Table 1.** Summary of TM1 test

| Sample | Test procedure | Temp. (°C) | Waiting time (mins) | Number of test |
|---|---|---|---|---|
| C.20.01-03 | – | 20 | – | 3 |
| C.T1.200.01-03 | TM1 | 200 | 60 | 3 |
| C.T1.400.01-03 | TM1 | 400 | 60 | 3 |
| C.T1.600.01-03 | TM1 | 600 | 60 | 3 |

**Table 2.** Summary of TM2 test

| Sample | Test procedure | Load ratio | Number of test |
|---|---|---|---|
| C.T2.10.01-03 | TM2 | 0.10 | 3 |
| C.T2.25.01-03 | TM2 | 0.25 | 3 |
| C.T2.50.01-02 | TM2 | 0.50 | 2 |
| C.T2.75.01-03 | TM2 | 0.75 | 3 |

## 3 Results

Tables 3 and 4 display the ultimate strength of H-CFRP corresponding to exposure temperature (obtained from TM1 tests) and rupture temperature of H-CFRP corresponding to imposed load (obtained from the TM2 tests). For the TM1 regime (Table 3), the ultimate strength of H-CFRP at 20 °C ranges from 817–1001 MPa while the Young modulus ranges from 58.2–67.9 GPa. At 200 °C, these values are about 525–660 MPa with ultimate strength and 53–77 GPa with Young modulus. The ultimate strength reduce about 35% while Young modulus increase about 5% in average. At 400 °C, in average, the ultimate strength is about 449–473 MPa (less than 50%) while the Young modulus remains about 63–69 GPa. At 600 °C the ultimate strength remains less than 20% of that at 20 °C (about 135–177 MPa), while Young modulus remains approximately 70% of that at 20 °C (about 34–51 GPa). For regime TM2

**Table 3.** Principal results of TM1 tests

| Sample | Temperature (°C) | Ultimate stress (MPa) | Young modulus (GPa) |
|---|---|---|---|
| C.20.01 | 20 | 922.8 | 58.2 |
| C.20.02 | 20 | 816.5 | 60.6 |
| C.20.03 | 20 | 1001.3 | 67.9 |
| C.T1.200.01 | 200 | 606.0 | 77.3 |
| C.T1.200.02 | 200 | 525.1 | 67.4 |
| C.T1.200.03 | 200 | 660.9 | 52.5 |
| C.T1.400.01 | 400 | 448.4 | 68.8 |
| C.T1.400.02 | 400 | 448.8 | 63.3 |
| C.T1.400.03 | 400 | 473.3 | 68.3 |
| C.T1.600.01 | 600 | 134.9 | 34.2 |
| C.T1.600.02 | 600 | 176.9 | 51.1 |
| C.T1.600.03 | 600 | 107.8 | 0 |

**Table 4.** Principal results of TM2 tests

| Sample | Stress ratio | Rupture temperature (°C) |
|---|---|---|
| C.T2.10.01 | 0.10 | 630.1 |
| C.T2.10.02 | 0.10 | 629.3 |
| C.T2.10.03 | 0.10 | 649.9 |
| C.T2.25.01 | 0.25 | 578.4 |
| C.T2.25.02 | 0.25 | 598.4 |
| C.T2.25.03 | 0.25 | 612.5 |
| C.T2.50.01 | 0.50 | 539.6 |
| C.T2.50.02 | 0.50 | 393.0 |
| C.T2.75.01 | 0.75 | 46.0 |
| C.T2.75.02 | 0.75 | 45.4 |
| C.T2.75.03 | 0.75 | 63.8 |

(Table 4), the rupture temperature is about 629–650 °C at the imposed stress ratio 0.1. The rupture temperature slightly reduces to roughly 578–612 °C when the stress ratio rises to 0.25. When this stress ratio increases to 0.50, the rupture temperature decreases to approximately 393–539 °C. At the stress ratio 0.75, the rupture temperature drops to 45–64 °C.

Figure 6 shows the typical correlation between stress and strain at different temperatures of the studied H-CFRP obtained from the TM1 regime. Overall, the stress-strain curves exhibit the linear trend at most of the temperature levels. The collected curves are used to identify the Young modulus of H- CFRP at different temperatures (presented in Table 3).

Tables 5 and 6 show the failure modes of H-CFRP obtained from both tested regimes. For the TM1 regime (Table 5), the failure modes of H-CFRP depended on the exposure temperature level. At 20 °C, the H-CFRP is ruptured at random position in

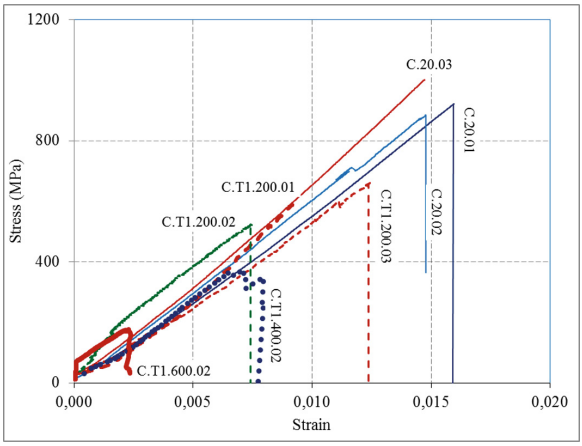


**Fig. 6.** Typical thermo-mechanical stress-strain relation at different temperature levels (TM1 regime)

**Table 5.** Typical failures at different temperatures (TM1 regime).

| Temp. (°C) | Samples | Failure image | Rupture mode |
|---|---|---|---|
| 20 | C.T1.20.02 | | A |
| | C.T1.20.03 | | A |
| 200 | C.T1.200.01 | | B |
| | C.T1.200.02 | | B |
| 400 | C.T1.400.02 | | C |
| | C.T1.400.03 | | C |
| 600 | C.T1.600.01 | | D |
| | C.T1.600.02 | | D |

the middle of specimen (failure mode A). In this type of failure, both carbon fiber and polymer matrix are brittlely broken. At 200 °C, the specimen failure happens in the middle of specimens and is mainly contributed by the failure of carbon fibers. At this temperature, the polymer matrix has been melted and unable to contribute to tensile capacity but horizontally hold the carbon fibers together (failure mode B). At 400 °C, the specimen failure shows that the polymer matrix starts decomposing and only the carbon fiber contributes to the tensile performance of H-CFRP. At this temperature, the polymer matrix seems not able to hold the carbon fiber well anymore (failure mode C). At 600 °C, the polymer matrix is completely burnt and the carbon fiber is partly

**Table 6.** Typical failure at different mechanical stress ratios of TM2

| Load ratio | Samples | Failure image | Rupture mode |
|---|---|---|---|
| 0.10 | C.T2.10.02 | | D |
| | C.T2.10.03 | | D |
| 0.25 | C.T2.25.01 | | D |
| | C.T2.25.03 | | D |
| 0.50 | C.T2.50.01 | 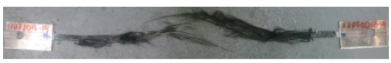 | D |
| 0.75 | C.T2.75.01 | | A |
| | C.T2.75.03 | | A |

oxidized. The H-CFRP is broken when loading stress exceeds the resistance of carbon fiber (failure mode D). This shows the similarity to what have been observed with pultruded CFRP by K. Wang (Wang et al. 2011). For the TM2 regime (Table 6), when the imposed-stress ratio ranges from 0.1, 0.25 to 0.5, the failure of H-CFRP conforms to mode D as described in the TM1 regime. This reasonably is in accordance to the rupture temperature of H-CFRP at about 400–650 °C (Table 4). When the H-CFRP is load at 75% of its ultimate strength at 20 °C, the specimen failures follow the mode A as described in the TM1 regime, reasonably agrees with the rupture temperature between 45–64 °C.

## 4 Discussion

For both regimes (TM1 and TM2), the results show that the exposure temperature and the imposed load have a significant influence on the performance of H-CFRP. As can be seen in the TM1 regime (Fig. 7), when exposure temperature increases, the thermo-mechanical ultimate strength and Young modulus of H-CFRP reduce differently. From 20 °C to 200 °C, the ultimate strength reduces approximately 35% while the Young modulus increases about 5%. With temperature ranging between 200–400 °C, the remaining ultimate strength reduces from 65% to less than 50% although the Young modulus slightly varies (further increases less than 2%). At the temperature level at 600 °C, the ultimate strength remains less than 20% of that at 20 °C whereas the Young modulus remains approximately 70%. The results of this regime confirm the overall evolution investigated by previous researches (Wang et al. 2007, 2011), (Yu and Kodur 2014), (Shenghu Cao et al. 2009). The variation of ultimate strength of H-CFRP is much greater than the variation of Young modulus with the same increment of temperature.

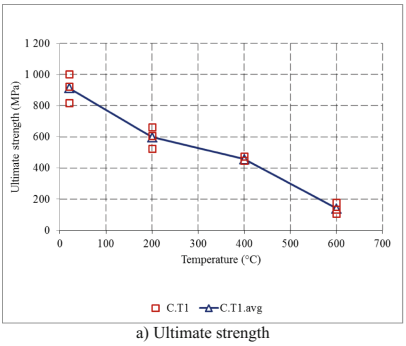


a) Ultimate strength

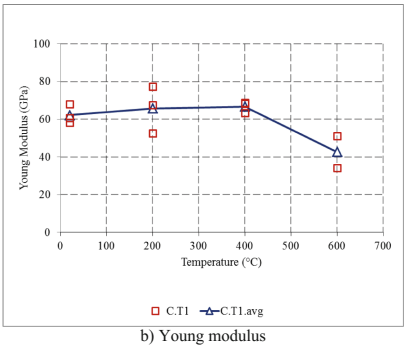


b) Young modulus

**Fig. 7.** Evolution of thermo-mechanical properties as the temperature increases (TM1 regime)

As the TM2 regime (Fig. 8), the rupture temperature decreases as the imposed stress ratio increases. When the stress ratio increases from 0.1 to 0.5, the rupture temperature steadily reduces from about 640 °C to about 466 °C in average. When the stress ratio increases to 0.75, the rupture temperature dramatically drops to about 52 °C. Figure 9 shows the correlation between the evolution of thermo-mechanical ultimate strength as temperature increases and the evolution of rupture temperature as the imposed stress ratio increases. The results are displayed with the upper and lower boundary for each objective in each testing regime. The value of $\sigma_i$ (vertical axis) in the graph is identified depending on the test regime. For the TM1 regime, $\sigma_i$ is the ultimate strength of H-CFRP at exposure temperature level while for the TM2 regime, $\sigma_i$ is the imposed stress acting on the H-CFRP specimen during test. As in the figure, the lower and upper boundary (C.T1) obtained from the TM1 regime limits the failure region of the ultimate strength of H-CFRP in the TM1 regime; the lower and upper boundary (C.T2) obtained from the TM2 regime limits the failure region for rupture temperature of H-CFRP in the TM2 regime. There is an overlapping between two failure regions obtained from two different regimes. This indicates that the ultimate strength and rupture temperature of H-CFRP have mutual influence.

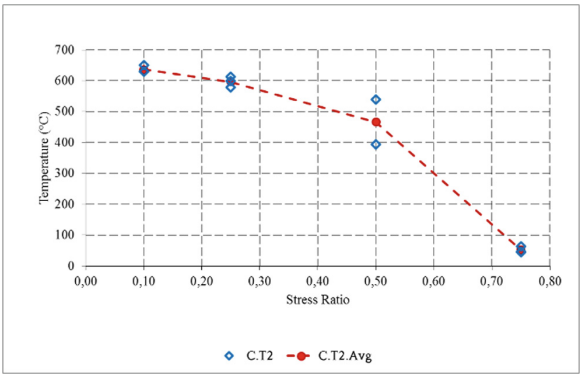


**Fig. 8.** Evolution of rupture temperature as the stress ratio increases (TM2 regime)

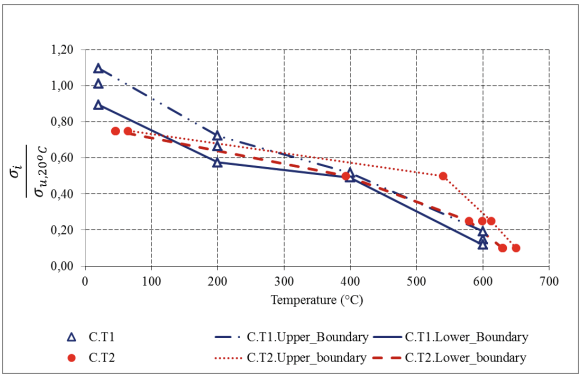


**Fig. 9.** Correlation of two thermo-mechanical testing regimes; results obtained by the TM1 regime (C.T1) and the TM2 one (C.T2)

## 5 Conclusion

The aim of this work is to investigate the performance of H-CFRP at two different thermo-mechanical testing regimes and identify the correlation between them. As the TM1 regime, the evolution of the ultimate tensile stress and of the Young modulus of the H-CFRP material as a function of the temperature level has been experimentally identified. When H-CFRP is exposed to elevated temperature, its ultimate strength and Young modulus reduce. The rate of reduction depends on the level of exposure temperature: the ultimate strength reduces 50% at 400 °C and the Young modulus reduces 30% at 600 °C. Similarly, as in the TM2 regime, when H-CFRP exposes to increasingly temperature, the rupture temperature depends on the level of imposed load. The rupture temperature decreases as the level of imposed load increases. For the stress ratio which is greater than 0.5, the rupture temperature dramatically drops. The results from both regimes also show that the imposed load and level of exposure temperature have mutual influence. The increase of one factor may reduce the capacity of the other. In addition, the failure mode of H-CFRP material varies depending on the temperature level that the material is exposed and the regime that the test is taken. When the temperature level increases, the polymer matrix is melted and then burnt with the increase in the ratio of burning part. Therefore, the original unidirectional woven carbon fibres lose their skeleton and the failure mode transforms brittle fibre material into more soften one.

**Acknowledgements.** This research has been performed with the financial support of the LMC2 (thanks to its industrial projects) for the experimental works. This research has also been realized with the financial support of a doctoral scholarship from the Ministry of Education and Training of Vietnam. We would like to thank the team of technicians (Mr. Emmanuel JANIN and Mr. Nobert COTTET) from the Civil Engineering department of the IUT Lyon 1 and the LMC2, University Lyon 1 for their technical support.

## References

Mouritz, A.P., Gibson, A.G.: Fire Properties of Polymer Composite Materials Solid Mechanics and Its Applications. Springer, Netherlands, Dordrecht (2006)

Correia, J.R., Branco, F.A., Ferreira, J.G., Bai, Y., Keller, T.: Fire protection systems for building floors made of pultruded GFRP profiles: part 1: experimental investigations. Compos. Part B Eng. **41**, 617–629 (2010). doi:10.1016/j.compositesb.2010.09.018

Foster, S.K., Bisby, L.A.: Fire survivability of externally bonded FRP strengthening systems. J. Compos. Constr. **12**, 553–561 (2008)

Foster, S.K., Bisby, L.A.: High temperature residual properties of externally bonded FRP systems. In: Proceedings of the 7th International Symposium on Fiber Reinforced Polymer Reinforcement for Reinforced Concrete Structures (FRPRCS-7), SP-230-70, pp. 1235–1252 (2005)

Nguyen, T.H., Vu, X.H., Si Larbi, A., Ferrier, E.: Experimental study of the effect of simultaneous mechanical and high-temperature loadings on the behaviour of textile-reinforced concrete (TRC). Constr. Build. Mater. **125**, 253–270 (2016). doi:10.1016/j.conbuildmat.2016.08.026

Cao, S., Wu, Z., Wang, X.: Tensile properties of CFRP and hybrid FRP composites at elevated temperatures. J. Compos. Mater. **43**, 315–330 (2009). doi:10.1177/0021998308099224

Wang, K., Young, B., Smith, S.T.: Mechanical properties of pultruded carbon fibre-reinforced polymer (CFRP) plates at elevated temperatures. Eng. Struct. **33**, 2154–2161 (2011). doi:10.1016/j.engstruct.2011.03.006

Wang, Y.C., Wong, P.M.H., Kodur, V.: An experimental study of the mechanical properties of fibre reinforced polymer (FRP) and steel reinforcing bars at elevated temperatures. Compos. Struct. **80**, 131–140 (2007). doi:10.1016/j.compstruct.2006.04.069

Yu, B., Kodur, V.: Effect of temperature on strength and stiffness properties of near-surface mounted FRP reinforcement. Compos. Part B Eng. **58**, 510–517 (2014). doi:10.1016/j.compositesb.2013.10.055

# Fresh Properties and Early Compressive Strength of Alkali-Activated High Calcium Fly Ash Paste

Eslam Gomaa, Simon Sargon, Cedric Kashosi, and Mohamed ElGawady(✉)

Missouri University of Science and Technology, Rolla, MO, USA
{eyg9qc, ssk36, cckgbc, elgawadym}@mst.edu

**Abstract.** This paper reports the influence of high calcium content in alkali-activated fly ash (AAFA) paste mixtures on the compressive strength, setting time, and workability. Class C fly ash was used to prepare alkali-activated paste mixtures. Four different sodium silicate to sodium hydroxide ratios of 2.5, 1.5, 1.0, and 0.5 were used as alkaline activators with a constant sodium hydroxide concentration of 10 M. Two curing regimes were also applied, oven curing at (70 °C) for 24 h, and ambient temperature at (23 ± 2 °C). The delay time between mixing and starting curing the specimens in the oven regime is 2 h. The compressive strength of the specimens was tested at 7 days for both curing regimes. The results showed that the fresh AAFA pastes had shorter setting time and lower workability with increasing the ratio of alkaline activators to fly ash ratio. However, the compressive strength of hardened AAFA was increased when the ratio of alkaline activators to fly ash ratio increased. A water to fly ash ratio of 0.3 with alkaline activators to fly ash ratio of 0.25, which displayed a balance between the fresh and hardened AAFA properties. The optimum sodium silicate to sodium hydroxide ratios were 1.0 for ambient curing and 1.5 for oven curing. The compressive strength of AAFA has reached up to 8 ksi after 7 days for ambient curing and 10 ksi for oven curing with initial setting time of approximately 180 min.

**Keywords:** Alkali activated fly ash · High calcium fly ash · Compressive strength · Setting time · Workability

## 1 Introduction

There is a current momentum around the world to increase concrete sustainability through using recycled materials in concrete manufacturing. For example, recycled tires were used to replace natural aggregates in concrete (Gheni et al. 2017; Youssf et al. 2016; Moustafa and ElGawady 2016, 2015; Youssf et al. 2015).The current manufacture process of Portland cement consumes a lot of energy and released $CO_2$ emissions into the atmosphere. Hence, there is an urgent need to partially or completely replace Portland cement as a binder with an alternative material that has less harmful effects on environment and display superior performance. One of the currently used Portland cement replacement materials is fly ash. Alkali activated fly ash (AAFA) is a

© Springer Nature Singapore Pte Ltd. 2018
H. Tran-Nguyen et al. (eds.), *Proceedings of the 4th Congrès International de Géotechnique - Ouvrages -Structures*, Lecture Notes in Civil Engineering 8,
DOI 10.1007/978-981-10-6713-6_49

different type of concrete where the Portland cement has completely replaced with pozzolanic materials such like fly ash. When pozzolanic material is activated with alkali material such as sodium hydroxide and/or sodium silicate polymer chains are formed creating alkali activated cement. These materials provide behavior comparable to Portland cement in terms of compressive strength (Rangan 2005), fire resistance, low thermal conductivity, and chemical attack resistance (Davidovits and Davidovics 2008). As per ASTM C618-15 (Standard Specification for Coal Fly Ash and Raw or Calcined Natural Pozzolan for Use in Concrete 2015), fly ash is classified as either Class-F or Class-C. The main difference in the chemical composition between these classes is the pozzolanic compounds (silica oxide, alumina oxide, and iron oxide). Class F fly ash contain at least 70% pozzolanic compounds, while Class C fly ashes have between 50% and 70% of the pozzolanic compounds. Fly ash class-F is produced by burning bituminous or anthracite coals (Palomo et al. 1999; Swanepoel and Strydom 2002) while fly ash class-C is produced from burning lignite or sub-bituminous coals (Guo et al. 2010a). Mainly, fly ash class C had higher calcium content than class F. This calcium content makes the AAFA concrete has the potential to be curried in ambient temperature like the conventional concrete that would increase its applications in the concrete industry. In this study, the effect of water to fly ash ratio, alkali activators to fly ash ratio, sodium silicate to sodium hydroxide ratio, in addition curing regime were studied.

## 2 Experimental Details

### 2.1 Material

A high calcium fly ash from Thomas Hill power plant in the State of Missouri, U.S. was used in this study. Table 1 shows the chemical composition of the fly ash determined using the X-ray Fluorescence analysis following the procedure described in ASTM D4326-13 (Standard Test Method for Major and Minor Elements in Coal and Coke Ash By X-Ray Fluorescence 2013). As shown in the table, sum of the $SiO_2$ + $Al_2O_3$ + $Fe_2O_3$ is 61.51 which is less than 70% and larger than 50%. Hence this fly ash can satisfy the requirements of a class C fly ash per ASTM C618-15 (Standard Specification for Coal Fly Ash and Raw or Calcined Natural Pozzolan for Use in Concrete 2015). The specific gravity of the fly ash is 2.60 which was determined per ASTM C188-16 (Standard Test Method for Density of Hydraulic Cement 2016). Two different alkali activators were used in this study: Sodium silicate ($Na_2SiO_3$) solution type D obtained from PQ Corporation and sodium hydroxide (NaOH) in solid pellets form obtained from Bulk Apothecary Company. The amount of solids sodium silicate in the solution were 44.1% (w/w) with 14.7% $Na_2O$ and 29.4% $SiO_2$ while water content was 55.9% (w/w). The sodium hydroxide was prepared by mixing the solid pellets with distilled water at least 24 h prior to the paste-mixing day to let the solution cool down to the room temperature. The molarity of the sodium hydroxide remained constant at 10 M.

**Table 1.** Chemical composition of fly ashes (XRF)

| Compsition | SiO2 | Al2O3 | Fe2O3 | CaO | MgO | Na2O | K2O | TiO2 | LOI[a] | MC[b] |
|---|---|---|---|---|---|---|---|---|---|---|
| % By weight | 38.25 | 16.69 | 6.57 | 23.15 | 9.92 | 4.01 | 0.03 | 1.39 | 1.09 | 0.08 |

[a] LOI: Loss on ignition
[b] MC: Moisture contnet

## 2.2 Mix Proportion

Several samples were prepared to examine the influential variables on the setting time and workability and compressive strength of AAFA paste. The variables include water to fly ash ratio, alkali activators to fly ash ratio, sodium silicate to sodium hydroxide ratio, and the curing regime.

The water to fly ash ratio ranged from 0.25 to 0.45. The water content included both the water in the mixed alkali activators and the extra water added to each mixture. The amount of extra added water was adjusted for different samples to obtain the desired water content depending on the amount of water in the alkali activators. The alkali activators to fly ash ratio varied from 0.25 to 0.40. The sodium silicate to sodium hydroxide ratio ranged from 0.5 to 2.5. Table 2 shows the details of the mixture ratios.

**Table 2.** Sample tables with values

| Mix | Water to fly ash ratio | Alkali activators to fly ash ratio | Sodium silicate to sodium ratio |
|---|---|---|---|
| W0.325-A0.3-S1.0 | 0.325 | 0.3 | 1.0 |
| W0.35-A0.3-S1.0 | 0.35 | 0.3 | 1.0 |
| W0.375-A0.3-S1.0 | 0.375 | 0.3 | 1.0 |
| W0.25-A0.25-S1.0 | 0.25 | 0.25 | 1.0 |
| W0.275-A0.25-S1.0 | 0.275 | 0.25 | 1.0 |
| W0.3-A0.25-S1.0 | 0.3 | 0.25 | 1.0 |
| W0.4-A0.3-S1.0 | 0.4 | 0.3 | 1.0 |
| W0.4-A0.35-S1.0 | 0.4 | 0.35 | 1.0 |
| W0.4-A0.4-S1.0 | 0.4 | 0.4 | 1.0 |
| W0.4-A0.35-S0.5 | 0.4 | 0.35 | 0.5 |
| W0.4-A0.35-S1.5 | 0.4 | 0.35 | 1.5 |
| W0.4-A0.35-S2.5 | 0.4 | 0.35 | 2.5 |
| W0.3-A0.25-S0.5 | 0.3 | 0.25 | 0.5 |
| W0.3-A0.25-S1.5 | 0.3 | 0.25 | 1.5 |

## 2.3 Mixing and Curing Conditions

The mixing procedure of the paste consists of the following four steps. (1) The fly ash was mixed for 30 s to homogenously spread the particles with low mixing speed of 136 rpm. (2) The water was added while mixing at the same mixing speed for one min which helped in wetting all fly ash particles and preventing the agglomeration of the

paste ingredients. (3) The sodium silicate and sodium hydroxide were mixed together before adding them to the mix with the same mixing speed for another one min. (4) The mixture continued for another four min while the mixing speed was increased to 281 rpm which was found to increase the paste slump flow. During the mixing process, after adding the water and the chemicals, the mixing was stopped to scrap the parts of the paste that attached to the wall of the pan for 40 s. The mixing was done at the room temperature, i.e. 23 ± 2 °C.

The fresh AAFA paste was casted into 2 × 2 × 2 in. cube molds as per the ASTM C109-16a (Standard Test Method for Compressive Strength of Hydraulic Cement Mortars (Using 2-in. or [50-mm] Cube Specimens) 2016). After casting the molds, two different curing regimes were applied on the AAFA paste. (1) Oven curing at 70 °C (158 °F) for 24 h. The molds have been encased in plastic oven bags to prevent moisture loss during the curing period inside the oven. (2) Ambient curing at 23 ± 2 °C (73 ± 3 °F). All the cubes have been demolded after 24 h then left in the room temperature until the testing day.

### 2.4 Setting Time, Workability, and Compressive Strength Tests

The initial and final setting times of the AAFA pastes were measured using Vicat Needle per the ASTM C191-13 (Standard Test Methods for Time of Setting of Hydraulic Cement by Vicat Needle 2013). The workability (flow) of the pastes were tested per the ASTM C1437-15 (Standard Test Method for Flow of Hydraulic Cement Mortar 2015). The compressive strengths of the AAFA pastes were determined at the age of 7 days following the ASTM C109-16a (Standard Test Method for Compressive Strength of Hydraulic Cement Mortars (Using 2-in. or [50-mm] Cube Specimens) 2016) procedure for both curing regimes. The reported results are the mean of three cubes. Data that deviated from the mean by more than 10% were excluded, although this took place rarely.

## 3 Results and Disscssion

### 3.1 Setting Time and Workability

The results of initial and final setting times and workability of AAFA pastes are shown in Figs. 1 through 5. The results showed that the initial and final setting times, and workability depended on the water to fly ash ratio, alkali activators to fly ash ratio, and sodium silicate to sodium hydroxide ratio. As shown in Figs. 1 and 2, for alkali activators to fly ratio of 0.30 and 0.25, and sodium silicate to sodium hydroxide ratio of 1.0, the setting time and the workability increased with increasing the ratio of water to fly ash ratio. However, the increase in the setting time is not preferable in the field to allow starting the finishing of the AAFA concrete as soon as possible after casting to save the labor cost. The maximum acceptable initial setting time of the Portland cement measured by Vicat Needle test is 375 min. (Standard Specification for Portland Cement 2017). Therefore, for alkali activators to fly ash ratios ranging from 0.25 to 0.35, the water to fly ash ratio should range from 0.30 to 0.40 respectively. As shown in Fig. 3,

for water to fly ash ratio of 0.40 and sodium silicate to sodium hydroxide ratio of 1.0, the setting time and workability decreased with increasing the ratio of alkali activators to fly ash ratio. For given water and alkali activators to fly ash ratios, the workability decreased with increasing the sodium silicate to sodium hydroxide ratio from 0.5 to 1.0, 1.5, and 2.5. The sodium silicate solution has high viscosity which result in poor workability of AAFA pastes (Provis and Bernal 2014; Vail 1952). The longest setting time was at sodium silicate to sodium hydroxide ratio of 1.0. Increasing the sodium silicate content in the mixture will increase the soluble silica ($SiO_2$) and alkali ($Na_2O$) content in the mixture. The $SiO_2/Al_2O_3$ molar ratio of the fly ash is 3.89. Therefore, increasing the silica by adding more sodium silicate increases this ratio which decreases the setting time where the $Ca^{+2}$ ions are highly consumed in presence extra silica in the system resulting in shorter setting time (Chindaprasirt et al. 2012). The geopolymerization process was enhanced with increasing the silica and alkali in the paste and it took less time to complete the dissolution reaction, resulting in decreasing the setting time (Siyal et al. 2016). Increasing the amount of sodium hydroxide in the mixture, increases hydroxide ion concentration in the paste (Somna et al. 2011) which

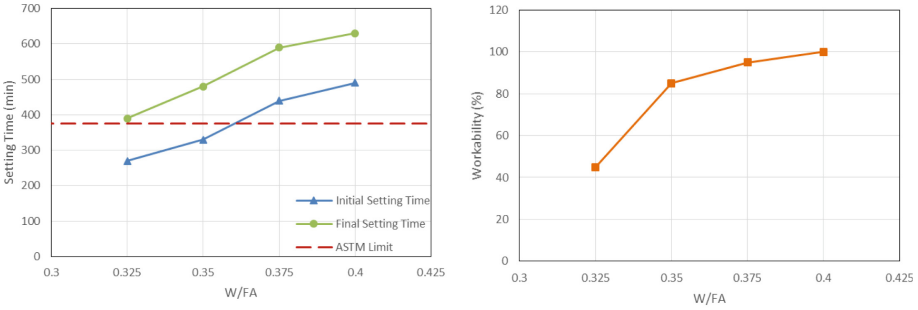


(a) (b)

**Fig. 1.** Effect of water to fly ash (W/FA) ratio on (a) setting times and (b) workability for alkali activator to fly ash ratio of 0.30 and sodium silicate to sodium hydroxide ratio of 1.0.

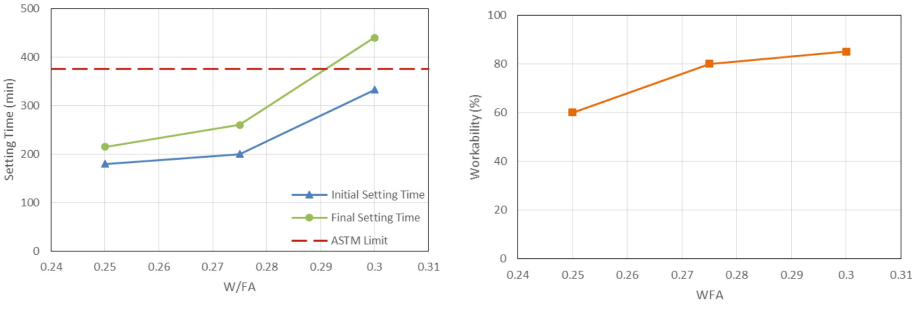


(a) (b)

**Fig. 2.** Effect of water to fly ash (W/FA) ratio on (a) setting times and (b) workability for alkali activators to fly ash ratio of 0.25 and sodium silicate to sodium hydroxide ratio of 1.0.

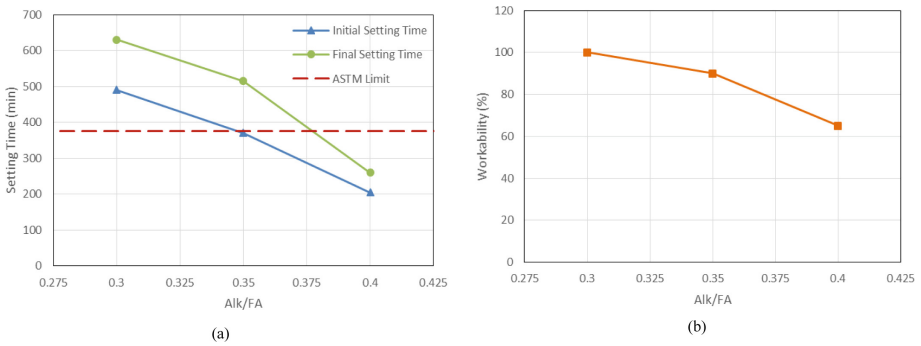


**Fig. 3.** Effect of alkali activators to fly ash (Alk/FA) ratio on (a) initial and final setting times (b) and workability for water to fly ash ratio of 0.40 and sodium silicate to sodium hydroxide ratio of 1.0.

accelerates dissolution of fly ash and resulted in reduction in the setting time. So, the sodium silicate to sodium hydroxide ratio of 1.0 showed a balance between the required hydroxide ions, alkali, and silica which required for geopolymerization process and the required silica content which is necessary for hydration reaction (Fig. 4).

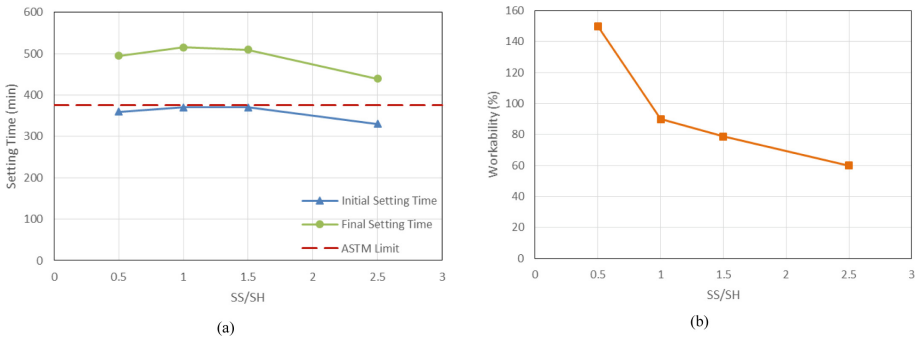


**Fig. 4.** Effect of sodium silicate to sodium hydroxide (SS/SH) ratio on (a) setting times and (b) workability for constant water to fly ash ratio of 0.4 and alkali activators to fly ash ratio of 0.35.

### 3.2 Compressive Strength

The compressive strength of the AAFA pastes synthesized at different water to fly ash, alkali activators to fly ash, and sodium silicate ratios are shown in Figs. 6 through 10. As shown in the figures, the oven-curing regime showed higher compressive strengths compared to those of the similar specimens cured at ambient temperature because to obtain a higher AAFA paste strength, the required curing temperature is 40−75 °C (Bakharev 2006). Ambient cured specimens gained their strength without elevated heating mainly because presence of high calcium content which has the ability to

harden at ambient temperature (Temuujin et al. 2009). The calcium can react with the silica and alumina, in addition to the water and formed calcium silicate hydrate (CSH) (Yip et al. 2005; Guo et al. 2010a) which increased the mechanical strength at early ages comparing with low calcium fly ash.

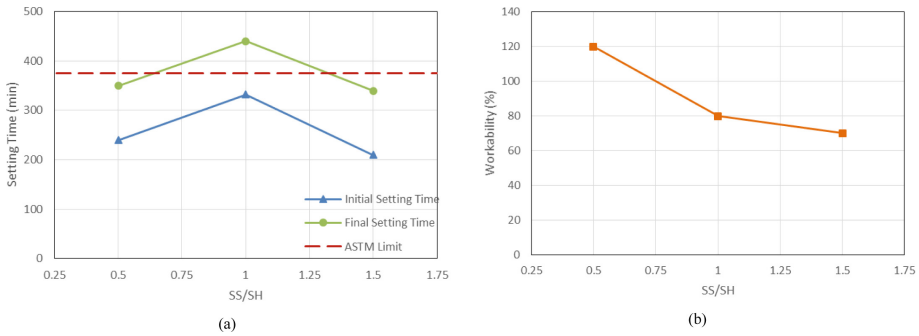


**Fig. 5.** Effect of sodium silicate to sodium hydroxide (SS/SH) ratio on (a) setting times and (b) workability for water to fly ash ratio of 0.3 and alkali activators to fly ash ratio of 0.25.

The AAFA showed trend similar to that of conventional Portland cement concrete, the compressive strength decreased with increasing the paste water content while keeping the alkali activators to fly ash ratio and sodium silicate to sodium hydroxide ratio constants (Figs. 6 and 7).

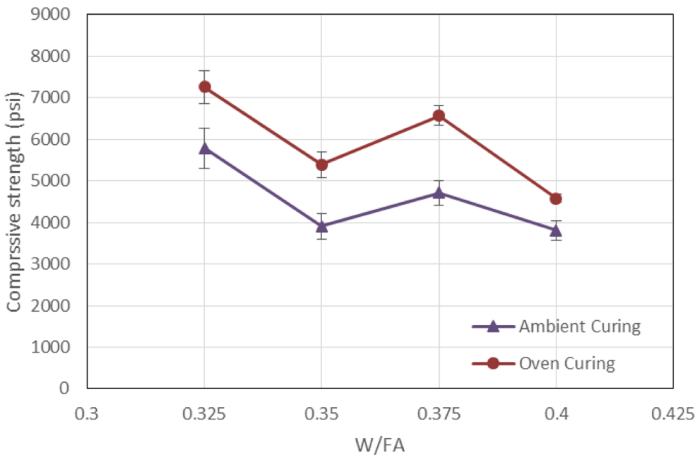


**Fig. 6.** Effect of water to fly ash (W/FA) ratio on compressive strength with constant alkali activators to fly ash ratio of 0.3 and sodium silicate to sodium hydroxide ratio of 1.0.

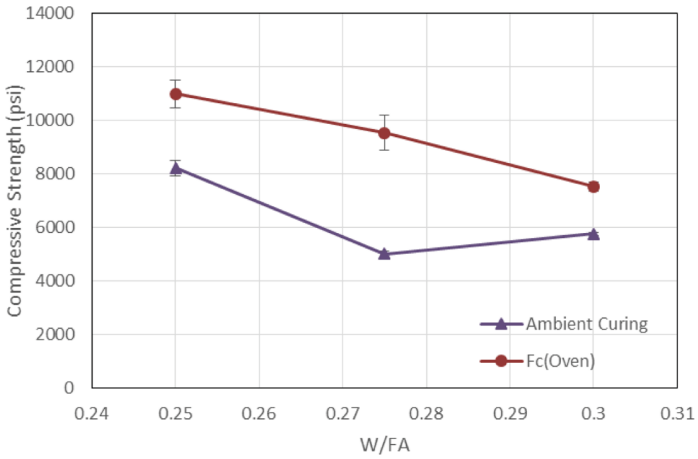


**Fig. 7.** Effect of water to fly ash (W/FA) ratio on compressive strength with constant alkali activators to fly ash ratio of 0.25 and sodium silicate to sodium hydroxide ratio of 1.0.

Increasing the alkali activator, i.e., sodium silicate and sodium hydroxide resulted in higher compressive strength. Increasing the activator increase the $Na_2O$ concentration which increase the solubility of the silica and alumina (Guo et al. 2010b) in case of constant water to fly ash ratio as shown in Fig. 8.

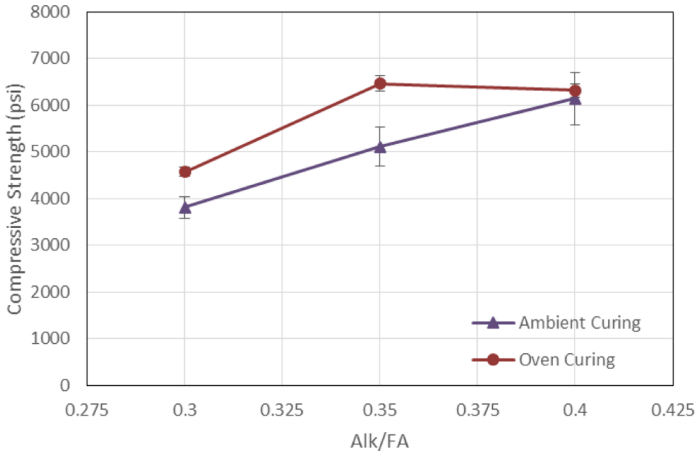


**Fig. 8.** Effect of alkali activators to fly ash (Alk/FA) ratio on compressive strength with constant water to fly ash ratio of 0.40 and sodium silicate to sodium hydroxide ratio of 1.0.

The specimens that had low sodium silicate to sodium hydroxide ratio of 0.5 exhibited lower compressive strength than those of specimens that had ratios of 1.0 and 1.5 (Figs. 9 and 10). Decreasing the sodium silicate to sodium hydroxide ratio increases the free hydroxide ions in the paste which accelerate the dissolution of the fly

ash and precipitate the aluminosilicate gel at very early stages, thus resulting in lower strength AAFA paste (Somna et al. 2011; Part et al. 2015). Increasing the sodium silicate to sodium hydroxide ratio of 2.5 caused a reduction in the compressive strength due to increasing the silica content in the paste which hindered the water evaporation and structure formation (Chindaprasirt et al. 2012; Morsy et al. 2014). Ambient-cured specimens that had sodium silicate to sodium hydroxide ratio of 1.0 and 1.5 showed higher compressive strength. Specimens that had sodium silicate to sodium hydroxide ratio of 1.5 showed higher compressive strength than specimens having sodium silicate to sodium hydroxide ratio of 1.0 in case of oven-curing regime. Increasing the ratio of

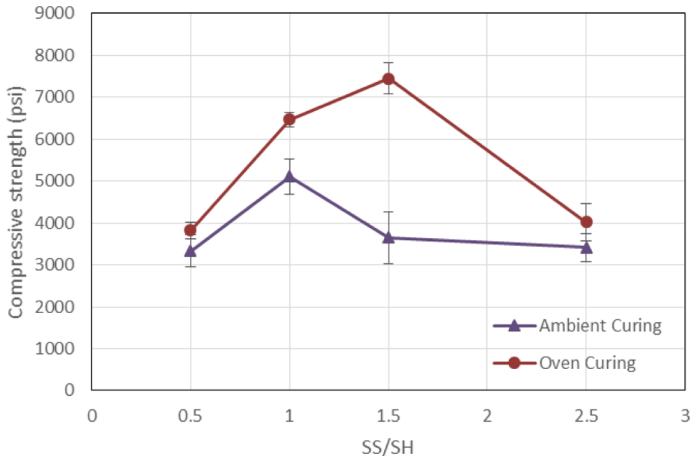


**Fig. 9.** Effect of sodium silicate to sodium hydroxide (SS/SH) ratio on compressive strength with constant water to fly ash ratio of 0.4 and alkali activators to fly ash ratio of 0.35.

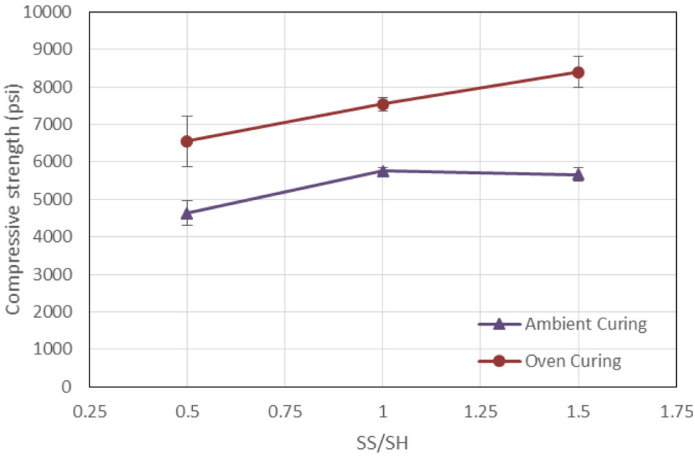


**Fig. 10.** Effect of sodium silicate to sodium hydroxide (SS/SH) ratio on compressive strength with constant water to fly ash ratio of 0.3 and alkali activators to fly ash ratio of 0.25.

sodium silicate to sodium hydroxide from 1 to 1.5 increase the amount of silica in the specimens which is necessary for the geopolymerization process which require an elevated temperature to obtain high strength.

## 4 Conclusion

This paper presents the effect of water to fly ash, alkali activators to fly ash ratio, and sodium silicate to sodium hydroxide ratio on the fresh and hardened properties of alkali activated high calcium fly ash pastes. High setting times and workability were obtained with increasing the water to fly ah ratio with keeping both alkali activators to fly ash and sodium silicate to sodium hydroxide ratios constant, however the compressive strength decreased in the case of both curing regimes. Short setting time and low workability occurred in the case of increasing the alkali activators to fly ash ratio with keeping both water to fly ash and sodium silicate to sodium hydroxide ratios constant, while the compressive strength increased. Increasing the ratio of sodium silicate to sodium hydroxide from 0.5 to 2.5, the workability started to reduce gradually. The setting time increased with increasing the sodium hydroxide to sodium silicate ratio from 0.5 to 1.0. Thereafter, it decreased with increasing the ratio from 1.0 to 2.5. It was shown also that the highest compressive strength were gained at ratio of 1.0 for the ambient curing regime and 1.5 for oven curing regime.

**Acknowledgments.** This research was supported by the Missouri Department of Transportation (MoDOT) and Ameren Corporation. In kind contribution of the fly ash from Headwaters Resources is appreciated. However, any opinions, findings, conclusions, and recommendations presented in this paper are those of the authors and do not necessarily reflect the views of the sponsors.

## References

Bakharev, T.: Thermal behaviour of geopolymers prepared using class F fly ash and elevated temperature curing. Cem. Concr. Res. **36**(6), 1134–1147 (2006). doi:10.1016/j.cemconres.2006.03.022

Chindaprasirt, P., De Silva, P., Sagoe-Crentsil, K., Hanjitsuwan, S.: Effect of SiO2 and Al2O3 on the setting and hardening of high calcium fly ash-based geopolymer systems. J. Mater. Sci. **47** (12), 4876–4883 (2012). doi:10.1007/s10853-012-6353-y

Davidovits, J., Davidovics, M.: Geopolymer: room-temperature ceramic matrix for composites. In: Proceedings of the 12th Annual Conference on Composites and Advanced Ceramic Materials, Ceramic Engineering and Science Proceedings. Wiley, pp. 835-841 (2008). doi:10.1002/9780470310496.ch34

Gheni, A.A., ElGawady, M.A., Myers, J.J.: Mechanical characterization of concrete masonry units manufactured with crumb rubber aggregate. Mater. J. **114**, 01 (2017). doi:10.14359/51689482

Guo, X., Shi, H., Chen, L., Dick, W.A.: Alkali-activated complex binders from class C fly ash and Ca-containing admixtures. J. Hazard. Mater. **173**(1–3), 480–486 (2010a). doi:10.1016/j.jhazmat.2009.08.110

Guo, X., Shi, H., Dick, W.A.: Compressive strength and microstructural characteristics of class C fly ash geopolymer. Cem. Concr. Compos. **32**(2), 142–147 (2010b). doi:10.1016/j.cemconcomp.2009.11.003

Hardjito, D., Rangan, B.V.: Development and properties of low-calcium fly ash-based geopolymer concrete. Research Report GC 1, Curtin University of Technology, Perth, Australia (2005)

Morsy, M.S., Alsayed, S.H., Al-Salloum, Y., Almusallam, T.: Effect of sodium silicate to sodium hydroxide ratios on strength and microstructure of fly ash geopolymer binder. Arab. J. Sci. Eng. **39**(6), 4333–4339 (2014). doi:10.1007/s13369-014-1093-8

Moustafa, A., ElGawady, M.A.: Mechanical properties of high strength concrete with scrap tire rubber. Constr. Build. Mater. **93**, 249–256 (2015). doi:10.1016/j.conbuildmat.2015.05.115

Moustafa, A., ElGawady, M.A.: Strain rate effect on properties of rubberized concrete confined with glass fiber-reinforced polymers. J.Compos. Constr. 20(5) (2016). doi:10.1061/(ASCE)CC.1943-5614.0000658

Palomo, A., Grutzeck, M.W., Blanco, M.T.: Alkali-activated fly ashes: a cement for the future. Cem. Concr. Res. **29**(8), 1323–1329 (1999). doi:10.1016/S0008-8846(98)00243-9

Part, W.K., Ramli, M., Cheah, C.B.: An overview on the influence of various factors on the properties of geopolymer concrete derived from industrial by-products. Constr. Build. Mater. **77**, 370–395 (2015). doi:10.1016/j.conbuildmat.2014.12.065

Provis, J.L., Bernal, S.A.: Geopolymers and related alkali-activated materials. Ann. Rev. Mater. Res. **44**, 299–327 (2014). doi:10.1146/annurev-matsci-070813-113515

Siyal, A.A., Azizli, K.A., Man, Z., Ullah, H.: Effects of parameters on the setting time of fly ash based geopolymers using Taguchi method. Procedia Eng. **148**, 302–307 (2016). doi:10.1016/j.proeng.2016.06.624

Somna, K., Jaturapitakkul, C., Kajitvichyanukul, P., Chindaprasirt, P.: NaOH-activated ground fly ash geopolymer cured at ambient temperature. Fuel **90**(6), 2118–2124 (2011). doi:10.1016/j.fuel.2011.01.018

Standard Specification for Coal Fly Ash and Raw or Calcined Natural Pozzolan for Use in Concrete. ASTM International (2015)

Standard Specification for Portland Cement. ASTM International (2017)

Standard Test Method for Compressive Strength of Hydraulic Cement Mortars (Using 2-in. or [50-mm] Cube Specimens). ASTM International (2016)

Standard Test Method for Density of Hydraulic Cement. ASTM International (2016)

Standard Test Method for Flow of Hydraulic Cement Mortar. ASTM International (2015)

Standard Test Method for Major and Minor Elements in Coal and Coke Ash By X-Ray Fluorescence. ASTM International (2013)

Standard Test Methods for Time of Setting of Hydraulic Cement by Vicat Needle. ASTM International (2013)

Swanepoel, J.C., Strydom, C.A.: Utilisation of fly ash in a geopolymeric material. Appl. Geochem. **17**(8), 1143–1148 (2002). doi:10.1016/S0883-2927(02)00005-7

Temuujin, J., van Riessen, A., Williams, R.: Influence of calcium compounds on the mechanical properties of fly ash geopolymer pastes. J. Hazard. Mater. **167**(1–3), 82–88 (2009). doi:10.1016/j.jhazmat.2008.12.121

Vail, J.G.: Soluble Silicates - Their Properties and Uses. Reinhold, New York (1952)

Yip, C.K., Lukey, G.C., van Deventer, J.S.J.: The coexistence of geopolymeric gel and calcium silicate hydrate at the early stage of alkaline activation. Cem. Concr. Res. **35**(9), 1688–1697 (2005). doi:10.1016/j.cemconres.2004.10.042

Youssf, O., ElGawady, M.A., Mills, J.E.: Experimental investigation of crumb rubber concrete columns under seismic loading. Structures **3**, 13–27 (2015). doi:10.1016/j.istruc.2015.02.005

Youssf, O., ElGawady, M.A., Mills, J.E.: Static cyclic behaviour of FRP-confined crumb rubber concrete columns. Eng. Struct. **113**, 371–387 (2016). doi:10.1016/j.engstruct.2016.01.033

# Hygric and Thermal Insulation Properties of Building Materials Based on Bamboo Fibers

Dang Mao Nguyen[1(✉)], Anne-Cécile Grillet[1], Thi My Hanh Diep[2], Thi Vi Vi Do[3], Chi Nhan Ha Thuc[3], and Monika Woloszyn[1]

[1] LOCIE, UMR Université de Savoie Mont Blanc - CNRS, 73000 Chambéry, France
{mao.nguyen-dang, anne-cecile.grillet, Monika.Woloszyn}@univ-savoie.fr
[2] Research Center Scientific for Conservation of Natural Resources, University of Sciences, Vietnam National University Ho Chi Minh City (VNU), Ho Chi Minh City, Vietnam
mhg286@gmail.com
[3] Faculty of Material Science, University of Science, Vietnam National University Ho Chi Minh City (VNU), Ho Chi Minh City, Vietnam
dtvvi@hcmuns.edu.vn, htcnhan@hcmus.edu.vn

**Abstract.** This study focuses on manufacturing bio-insulation fiberboards from bamboo fibers and bone glue, modified with sodium lignosulfonate. The microstructure of these boards is investigated by mercury intrusion porosimetry. The porosity and average pore size of boards are decreased; however, the specific pore surface is increased with the presence of bio-glues in boards. The hygric properties are examined through kinetics of water vapor sorption at equilibrium states. The thermal conductivity and bending properties are also studied. The thermal conductivity is dependent on relative humidity levels and moisture content of the fiberboards. The bending property is increased with 30% (w/w) of mixture glue between bone and sodium lignosulfonate in boards.

**Keywords:** Thermal conductivity · Bamboo fiberboards · Kinetics of vapor sorption · Microstructure · Bio-insulation material

## 1 Introduction

In a context of reducing energy consumption for future buildings, this research deals with bio-insulation materials incorporating between bamboo fibers and biological protein/lignin binders. The materials are applied inside buildings in order to control humidity when environmental condition changes. Especially, they can improve the moisture buffering capacity due to their porous structure and high moisture absorbing capacity inducing by protein and protein/sodium lignosulfonate mixture glues. The protein based bone glue and mixture between bone and sodium lignosulfonate compound are currently interested in as effective binders for wood-based products industry.

© Springer Nature Singapore Pte Ltd. 2018
H. Tran-Nguyen et al. (eds.), *Proceedings of the 4th Congrès International de Géotechnique - Ouvrages -Structures*, Lecture Notes in Civil Engineering 8,
DOI 10.1007/978-981-10-6713-6_50

On the other hand, in the past, the most popular board materials such as fiberboard, particleboard, medium-density fiberboard (MDF) and high-density fiberboard (HDF) used phenol–formaldehyde (PF), urea–formaldehyde (UF), urea–melamine–formaldehyde (UMF) as effective glues for providing excellent mechanical properties and high-water resistances under various conditions. However, these products release formaldehyde into the air causing a great problem for the environment and for humans. Indeed, exposure to air born formaldehyde can result in health effects such as skin irritation, watery eyes, coughing and nausea. Furthermore, prolonged exposure to formaldehyde can cause certain types of cancer such as nasopharyngeal cancer (Hauptmann et al. 2004; Michael et al. 2009). Consequently, there is a strong need for the development of environment-friendly fiberboards. For example, research works are conducted on fiberboards based on natural fibers, agricultural waste combined with bio-adhesives such as vegetable oil, chitin, lignin and protein because they are renewable, biodegradable and highly hygroscopic products with low environmental impact. In order to produce new glues, the modification of different proteins has been investigated by researchers. Lignin is often used to modify various proteins including proteins based on wheat gluten (Duval et al. 2013; Kaewtatip et al. 2010; Khosravi et al. 2011; Kunanopparat et al. 2009; Kunanopparat et al. 2012), soybean (Huang and Chen 2003; Zhigang et al. 2013) and protein from maize (Cong et al. 2013). Lignin has a good compatibility with mixtures of proteins leading to an increase in mechanical properties and water resistance. In fact, the lignin has effective interactions with many kinds of proteins and natural fibers via hydrogen or covalent bonds.

The natural fibers based building insulation materials are well known of porous structure, the microstructure and hygrothermal performance link to their porous structure. The porous structure of materials was investigated through many techniques; the most widely used methods are focused on nitrogen sorption isotherms, mercury intrusion porosimetry (MIP) and scanning electron microscopy (SEM). In particular, porous structure and water vapor sorption of hemp-based materials were examined via MIP technique and water vapor sorption with BJH mode (Collet et al. 2008). Moreover, the total pore surface area, porosity and micropores structure of waste wood based cement-bonded particleboards were studied by MIP method and the pores size distribution was classified into three zones of pores (capillary, mesopores and air) (Wang et al. 2017). The same MIP tested method and classifications were also applied for microstructure characterization of waste wood based noise and thermal insulating cement-bonded particleboards (Wang et al. 2016).

Moreover, the hygrothermal properties of insulation materials are evaluated by their thermal conductivity (k-value). Energy used for space heating and cooling can be decreased by using low-thermal-conductivity materials. The k-value of insulation materials depends on the material's density, porosity, moisture content and temperature. In general, a higher temperature leads to higher k-values at higher material density (Bo-Ming et al. 2008; Budaiwi and Abdou 2013; Budaiwi et al. 2002). The thermal conductivity is also linked to the moisture content inside the material, higher k-values are obtained when the moisture content raises (Budaiwi and Abdou 2013; Kondo et al. 2010). Consequently, the variations of k-value with moisture content of insulation materials must be investigated in order to evaluate their influence on building's energy performance.

This study investigates the manufacturing of novel bio-insulation materials based on bamboo fibers and bone glue, pure or modified by sodium lignosulfonate. The hygrothermal behavior of these materials is investigated by experiments under controlled conditions. In particular, the hygrothermal performance is evaluated through thermal conductivity and isothermal vapor sorption at equilibrium state. Moreover, mechanical properties are assessed through bending measurement.

## 2 Materials and Experiment

### 2.1 Materials

Bone glue is a protein-based adhesive made from collagen of bones. It has a granular form and is soluble in water. It was supplied by Briançon Inc., France.

Sodium lignosulfonate is used in the food industry as a de-foaming agent for paper production and in adhesives for items that come in contact with food. It was purchased from Carl Roth GmbH$^+$ Co. KG Inc., Karlsruhe, Germany. It is in powder form and its miscibility with water at 20 °C is 600 g/l. Its melting point is higher than 130 °C and it has a bulk density at 20 °C of 500 kg/m$^3$.

Bamboo fibers (bambusa stenostachya) were collected at scientific research center for conservation of natural resources, Vietnam. The fibers were extracted from bamboo trees by roller mill technique (RMT) (Deshpand et al. 2000). Then, the fibers were more finely separated by using a specific machine at high speed (29,000 rpm) for one min.

### 2.2 Preparation of Bamboo Fiberboards

The fiberboards were prepared by pressed method on a hydraulic press. The glues solutions were prepared by swelling 30 g of glues in 200 g of water until completely dissolved. The bamboo fibers and glue solutions were manual mixed and kept in oven at 100 °C for 24 h in order to remove water. Once dried, the mixture was poured into an aluminum mold which has been covered by an adhesive anti-stick coated. The press conditions set up at 150 kgf/cm$^2$, 160 °C and 15 min. The fiberboards were removed

**Table 1.** Bamboo fiberboards components

| Components | | | |
|---|---|---|---|
| Samples | Bamboo fibers %(w/w)* | Bone glue %(w/w) | Sodium lignosulfonate %(w/w) |
| F100 | 100 | 0 | 0 |
| FB9010 | 90 | 10 | 0 |
| FB7030 | 70 | 30 | 0 |
| FBS70273 | 70 | 27 | 3 |
| FBS70219 | 70 | 21 | 9 |
| FS7030 | 70 | 0 | 30 |

*w/w: weight ratio

from the mold after cooling to room temperature at least 24 h to avoid warping phenomena. The composition of materials is listed in Table 1. The specimens of each material are prepared for further characteristics tests.

### 2.3 Density Fiberboards Measurement

The density of fiberboards was determined according to EN 323 standard. The specimens were cut and pre-conditioned at 57%RH and 25 °C before being tested. At least five specimens of each material were tested. The density value (kg/m$^3$) was calculated with the formula below:

$$\rho = W/(a \times b \times c)$$

where: a, b, c (m) and W (kg) is the length, width, thickness and weight of specimen respectively.

### 2.4 Hygrothermal Characterization Tests

#### 2.4.1 Test Facility

In this study, all hygrothermal properties of insulation materials were measured using closed climatic chamber (called "RH-Box") (Fig. 1) which is made by two chambers connected by an airlock. Temperature and relative humidity in the RH-Box are controlled by heat exchangers and saturated salt solutions. Two fans inside the RH-Box homogenize the atmosphere when the humidity level is changed, but they are stopped when the experiments are in progress. The mass change of specimens during testing can be measured directly in the chamber through a holder that is connected with a microbalance located on the top of the chamber. The temperature and the relative humidity inside the RH-box are recorded with hygrothermal sensors.

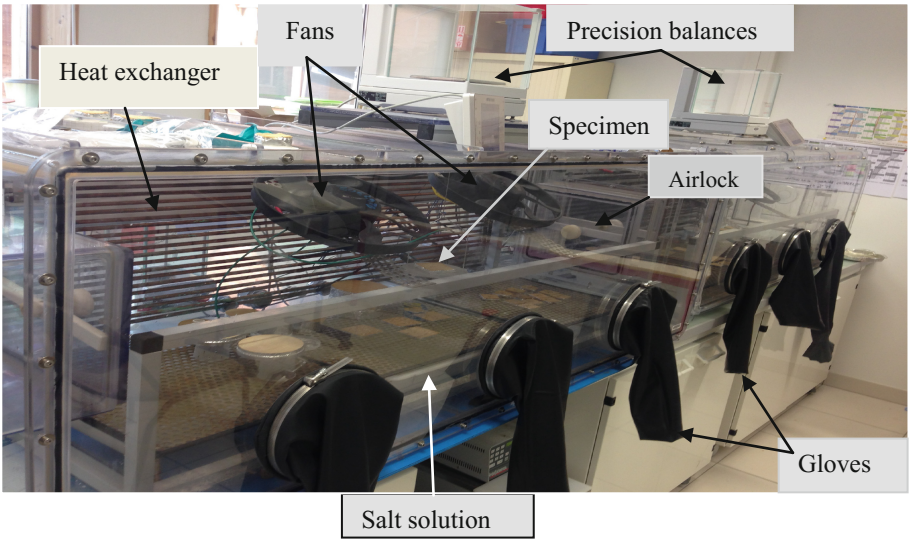


**Fig. 1.** Climatic chamber (RH-Box)

### 2.4.2 Water Vapor Sorption Kinetics Until Equilibrium

The kinetic of water vapor sorption isotherm of the fiberboards were examined at three successive relative humidity steps: 33% with $MgCl_2$ solution, 75% with NaCl solution and 33% again. In addition, before being tested, all the specimens were pre-conditioned at 9% RH with a KOH solution at 25 °C. During the period test, the specimen weight evolution is recorded by a precision balance (±0.2 mg), connected to an automatic recording system until reaching at equilibrium state. The temperature during this experiment was kept constant at 25 °C. The water vapor sorption kinetics at equilibrium curves of the specimens were obtained by plotting weight gain/loss percentages function of time.

## 2.5 Porous Structure of Materials

In this study, porosity degree, average pores diameter, specific surface area and pore size distribution of fiberboards were determined by mercury intrusion porosimetry. In general, the MIP method is based on the non-wetting liquid will only intrude capillaries under pressure, the mercury is slowly intruded into the pores of the materials (ISO15901-1). Before being tested, the samples are air-dried for 24 h; the dried specimens are cut into small pieces and placed in glass vessels. The pores structure parameters are performed by a mercury porosimetry technique (Micromeritics AutoPore IV 9520) under a pressure up to 400 MPa. The MIP method can detect the pores with the radius ranging from 7 nm up to 400 μm. The pore size distribution is identified from the volume of mercury intruded at each pressure increment, while the total porosity is based on the total intruded volume. The equivalent pore radii $(r)$ is calculated based on the known intrusion pressure of mercury ($p_{Hg}$):

$$r = -\frac{2\gamma_{Hg}.\cos\theta_{Hg}}{p_{Hg}}$$

where: the surface tension of mercury $\left(\gamma_{Hg}\right)$ is assumed as 0.48 N/m and the contact angle of mercury on the hardened mortar surface $\left(\theta_{Hg}\right)$.

## 2.6 Thermal Conductivity Measurement

The thermal conductivity of fiberboards was measured at 25 °C according to the EN 12664 standard with a TCi-Therm device using the modified transient plane source (MPTS) technique. The test specimens were cut into squares measuring 50 ± 1 mm and pre-conditioned at 57% RH and 25 °C until reaching a constant mass before being tested. Thermal conductivity was then measured inside the RH-Box at different relative humidity levels. This enables to measure the variation of thermal conductivity according to the variation of the moisture content of the specimens. The relationship between the thermal conductivity and the density, the relative humidity and the moisture content was investigated.

### 2.7 Mechanical Properties

The bending properties including the bending strength and elastic modulus were evaluated according to the EN 310 standard. The test specimens were cut to 150 mm × 25 mm × 6 mm. Before being tested, all the specimens were preconditioned at 57% RH and 25 °C until reaching a constant mass. The average values of the elastic modulus and bending strength at break were calculated based on at least five measurements.

## 3 Results and Discussion

### 3.1 Characteristics of Bamboo Fibers

The various components and distribution of the length and diameter of bamboo fibers in this study are shown in Fig. 2. The results indicate that the length distribution ranges from 0 to 7.0 cm and is mainly concentrated at approximately 1.0–2.0 cm, whereas the diameter ranges from 0.16 to 0.52 mm and is mainly concentrated between 0.24 and 0.40 mm. It can be observed that the bamboo fibers have a narrow distribution of diameter and length. Indeed, the preparation of bamboo fibers using rollers is a suitable method to extract a large amount of fibers of quite homogeneous length and small diameter. In addition, this kind of bamboo contains the same amount of components as other different bamboo fibers, but they differ from the components of other natural fibers (Hill et al. 2009).

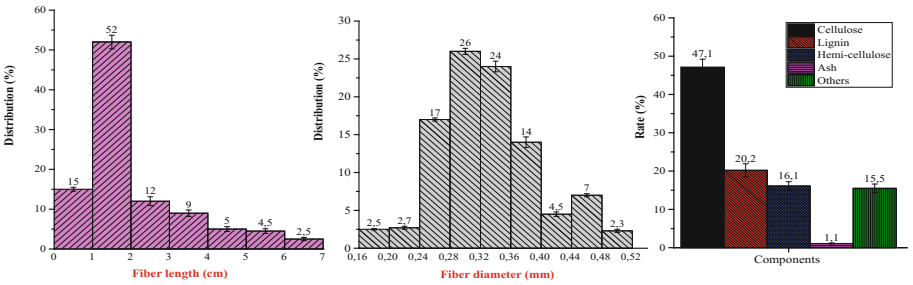


**Fig. 2.** Length, diameter distribution and components of bamboo fibers (Nguyen et al. 2017).

### 3.2 Mercury Intrusion Porosimeter (MIP)

Microstructure of the three highlighted fiberboards was examined by mercury intrusion porosimeter method. Their porosity, average pore diameter, pore volume and pore size distribution were illustrated in Fig. 3 and Table 2. The MIP result shows a higher porosity at 76% for the fiberboard without glue (F100), 64% porosity for FB7030, which used 30% bone glue and 49% porosity for FBS70219 using 30% mixture glue between bone and sodium lignosulfonate. In addition, the pore size distribution of three fiberboards is largely ranged from 0.005 to 100 μm and it was classified to three

categories: capillary pores (0.005–0.1 μm), mesopores (0.1–10 μm) and air pores (>10 μm) as previous literature (Penttala 1989; Wang et al. 2017). This result could be contributed by the level of compaction, the effective adhesion of glues which verified through mechanical properties of these boards as Fig. 8 (Wang et al. 2016). In particular, the effective of binders influenced on the average pores diameter of fiberboards, which represents 82 nm for FBS70219 and 219 nm for FB7030 while the F100 exhibited the largest average pores diameter of 1,135 nm, which consist of more voids between the fibers, leading to more incremental pore volume and porosity (Choi et al. 2009; Westermarck et al. 1998). Conversely, the F100 has a lowest total pore area at 7.4 ($m^2/g$) in comparison to FB7030 (23.5 $m^2/g$) and FBS70219 (27.7 $m^2/g$) respectively. The results can be explained by the large pores and densely distributed pores can result in a much smaller total surface area in the same volume. Indeed, the small pores have a significant influence on the total surface area and interface of fiberboards (Choi et al. 2009). Additionally, the higher specific pore surface leads to higher hygroscopic capacity of boards.

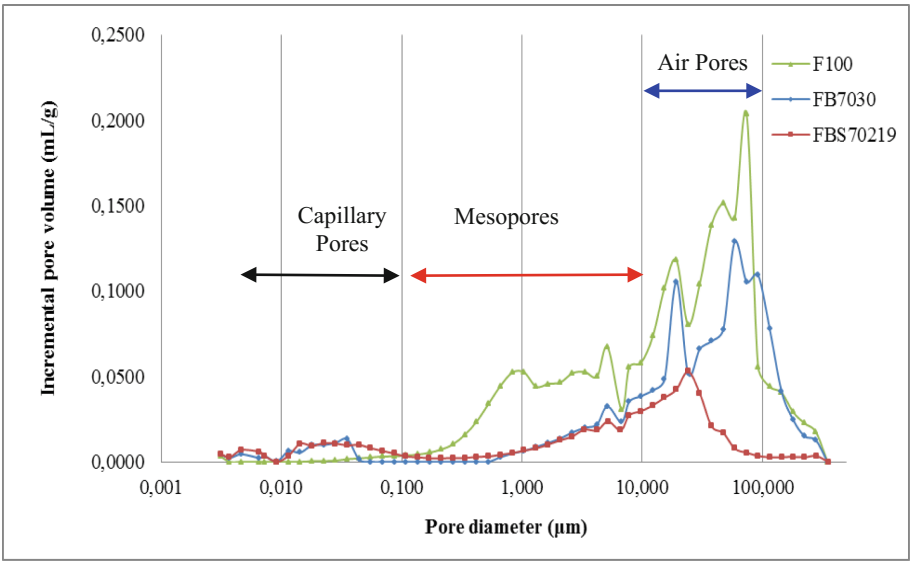


**Fig. 3.** Microstructure properties of three highlighted boards: pore volume function with pore diameter distribution

**Table 2.** The porous structure parameters of bamboo boards obtained by MIP

| Material | Porosity (%) | Average pore diameter (nm) | Specific total pore area ($m^2/g$) |
|---|---|---|---|
| F100 | 76.1 | 1,135 | 7.4 |
| FB7030 | 64.6 | 219 | 23.5 |
| FBS70219 | 49.7 | 82 | 27.7 |

### 3.3 Kinetics of Water Vapor Sorption

The vapor sorption kinetics of the bamboo fiberboards were examined under temperature and relative humidity protocol described in scheme Fig. 4a. The amount of moisture absorbed, and residual moisture as well as moisture sorption behavior of the fiberboards at three equilibriums at 33-75-33% RH are observed in Fig. 4b.

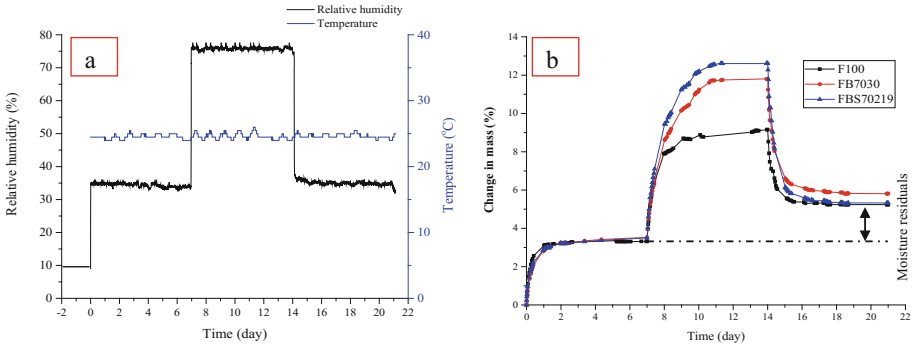


**Fig. 4.** Kinetics of water vapor sorption at equilibrium state: (a) humidity and temperature protocol (9-33-75-33% RH) at 25 °C, (b) kinetics curves and moisture sorption capacity

The first equilibrium was reached at 33%RH after pre-conditioning at 9%RH. The three fiberboards absorbed the same amount of moisture (about 3.5%) after less than two days with a similar shape of absorption curves. During the equilibrium at 33%RH, that the water molecules are absorbed as monolayer on the pores surfaces (Latif et al. 2014). This phenomenon leads to the same amount of moisture uptake capacity of three boards.

The second equilibrium was reached at 75%RH. The F100 exhibited an amount of moisture uptake about 9.5% after reaching equilibrium, which is lower than for FB7030 and FBS70219 with around 11.8% and 12.6% respectively. The board F100 reaches the second equilibrium after 3 days while FB7030 and FBS70219 required 4 days. The time required to reach equilibrium of these fiberboards associated to their moisture absorption capacity (Ge et al. 2014). At equilibrium (75%RH), the FBS70219 has a higher moisture uptake value (12.6%) compared to the FB7030 (11.8%) and F100 (9.5%). The different amount of equilibrium moisture absorption is due to the higher moisture absorption capacity of sodium lignosulfonate and protein based on bone glues compared to bamboo fibers.

Additionally, during the equilibrium, between 33% and 75% RH, the water molecules are absorbed as multilayers and condensation can occur in pores and capillaries (Latif et al. 2014). Thus the higher amount of moisture absorbed by the boards FBS70219 and FB7030 is also due to their pore volume in capillary zone (Fig. 3), as well as their average pore diameter compares to F100.

During the RH decrease to the last equilibrium at 33%, the moisture desorption of the fiberboards appeared rapidly and equilibrium is reached after only one day exposure to 33%RH. However, the amount of moisture uptake in absorption process (from 33% to 75%RH) is not totally discharged in desorption process and doesn't return to the level reached during the first exposure at 33%RH. Consequently, a significant amount of residual moisture remains in the three fiberboards. The Fig. 4b exhibits an amount of residual moisture about 2.3% for FB7030, 1.9% for F100 and 1.8% for FBS70219 compared to the first equilibrium at 33%RH. The residual moisture phenomenon of fiberboards was explained via the capillary condensation hysteresis and the moisture trapped inside large pores with small necks (ink-bottle effect) (Collet et al. 2008).

## 3.4 Thermal Conductivity of the Fiberboards

### 3.4.1 Influence of Density

Figure 5 shows the thermal conductivity as function of the density at 57%RH and 25 °C. The result indicates that the FBS70219 board has a highest density about 538 ± 12 kg/m$^3$, associating with the highest thermal conductivity of approximately 0.088 W m$^{-1}$K$^{-1}$. The two FS7030 and FB9010 boards with a low-range density, about 311 ± 22 and 320 ± 24 kg/m$^3$ respectively, correspond to low thermal conductivity values around 0.055 and 0.057 W m$^{-1}$K$^{-1}$. The three other boards (F100, FB7030 and FB70273) have intermediate densities (431 ± 15, 382 ± 18 and 442 ± 18 kg/m$^3$ respectively) with a similar range of thermal conductivity values: 0.077, 0.082 and 0.081 W m$^{-1}$K$^{-1}$ respectively. The different thermal conductivity is due to the different density of bamboo fiberboards. The influence of bone, sodium lignosulfonate and

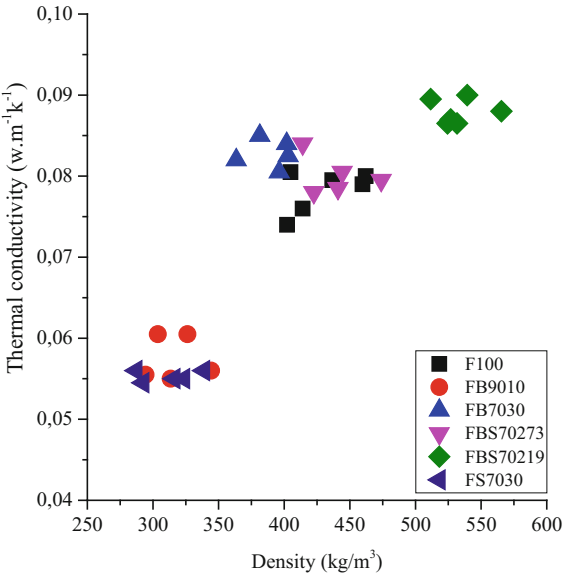


**Fig. 5.** Thermal conductivity versus density of fiberboards at 57%RH, 25 °C (Nguyen et al. 2017)

fibers/glue ratio induced the different compaction levels of the boards (Ratiarisoa et al. 2016). Low-density boards with the lack of glues contain more voids and thus more air. Thermal conductivity of air being lower than that of solid materials, the presence of voids in the boards results in a lower thermal conductivity for the low-density boards (Abdou and Budaiwi 2013; Sjöström and Blomqvist 2014; Suleiman et al. 1999).

Compared to other published literature, the thermal conductivity of bamboo fiberboards is lower than that of corn cob board (Verdier and Granulats 2012), cotton stalk fiberboard (Zhou et al. 2010), durian peel/coconut coir board (Khedari and Teekasap 2004) and wood (pine) board (Xu et al. 2004). It can be observed that the thermal conductivity of bamboo fiberboards is in the low range for such insulating building materials.

### 3.4.2 Influence of Moisture

Figure 6 shows the influence of relative humidity levels on thermal conductivity at 25 °C. Thermal conductivity was measured when the specimens reached equilibrium state at 33% and 75%RH. It can be observed that at a relative humidity level of 75%, the thermal conductivity of these boards was increased and it was decreased when specimens were exposed to a lower relative humidity (33%RH). The increase of thermal conductivity at 75%RH is due to the rise of moisture amount in the specimens. The reverse behavior (decrease) was observed when the specimens were moved from 75%RH to 33%RH because the moisture evaporated leading to more voids in the fiberboards (Abdou and Budaiwi 2013; Shiva et al. 2014; Sjöström and Blomqvist 2014; Suleiman et al. 1999). Additionally, the thermal conductivity variations according to relative humidity levels (33% and 75%RH) are indicated in Table 3.

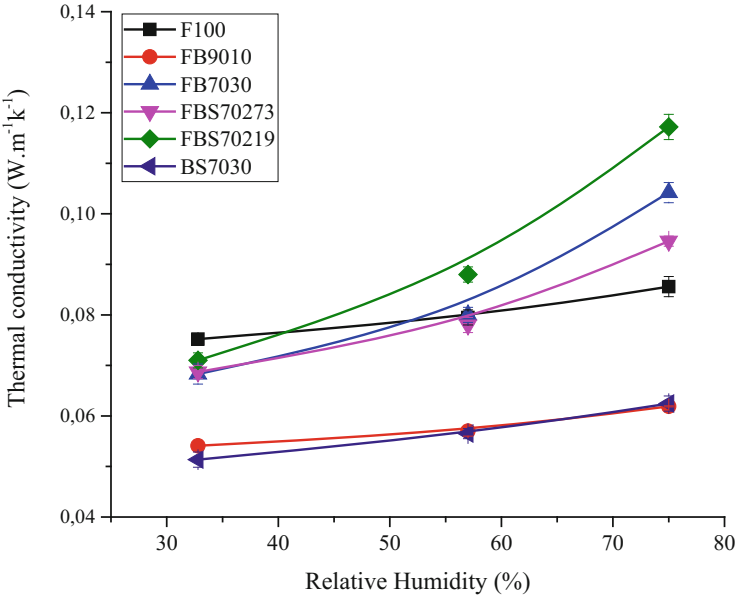


**Fig. 6.** Variation of thermal conductivity with relative humidity at 33% and 75%RH at 25 °C

**Table 3.** Variation of the thermal conductivity (Δk-value) with moisture uptake/release (ΔMC) of fiberboards at 33 and 75% relative humidity (Nguyen et al. 2017).

| Samples | Density ($kg/m^3$) | ΔMC uptake at 75%RH (%) | ΔMC release at 33%RH (%) | (Δk-value) increase at 75%RH (%) | (Δk-value) decrease at 33%RH (%) |
|---|---|---|---|---|---|
| F100 | 431 ± 25 | 3.2 ± 0.4 | 0.4 ± 0.1 | 11.6 ± 2.4 | 3.5 ± 1.0 |
| FB9010 | 320 ± 24 | 4.6 ± 0.6 | 1.4 ± 0.3 | 7.5 ± 1.5 | 8.9 ± 1.2 |
| FB7030 | 382 ± 18 | 7.0 ± 0.7 | 2.9 ± 0.6 | 26.8 ± 3.2 | 16.7 ± 1.6 |
| FBS70273 | 442 ± 28 | 7.7 ± 0.6 | 2.8 ± 0.2 | 16.8 ± 3.0 | 15.2 ± 1.4 |
| FBS70219 | 538 ± 27 | 9.0 ± 0.8 | 2.7 ± 0.3 | 34.2 ± 3.4 | 19.2 ± 1.8 |
| FS7030 | 311 ± 22 | 5.8 ± 1.1 | 3.6 ± 0.7 | 12.8 ± 2.2 | 7.1 ± 1.6 |

Additionally, a linear regression was observed for relationship between thermal conductivity and relative humidity for each sample (Fig. 6). However, the slopes are different due to the different materials' vapor sorption capacity (Table 3). In fact, the thermal conductivity evolves linearly until the value corresponding to the equilibrium moisture level. It can be thought that the moisture penetrates quickly all the sample volume from the beginning of the moisture exposition instead of accumulating in the surface region before migrating to the inner layers. This result match with some materials in previous literature such as: wood fiber, oriented strand board, and narrow-ring wood (Abdou and Budaiwi 2013; Vololonirin et al. 2014).

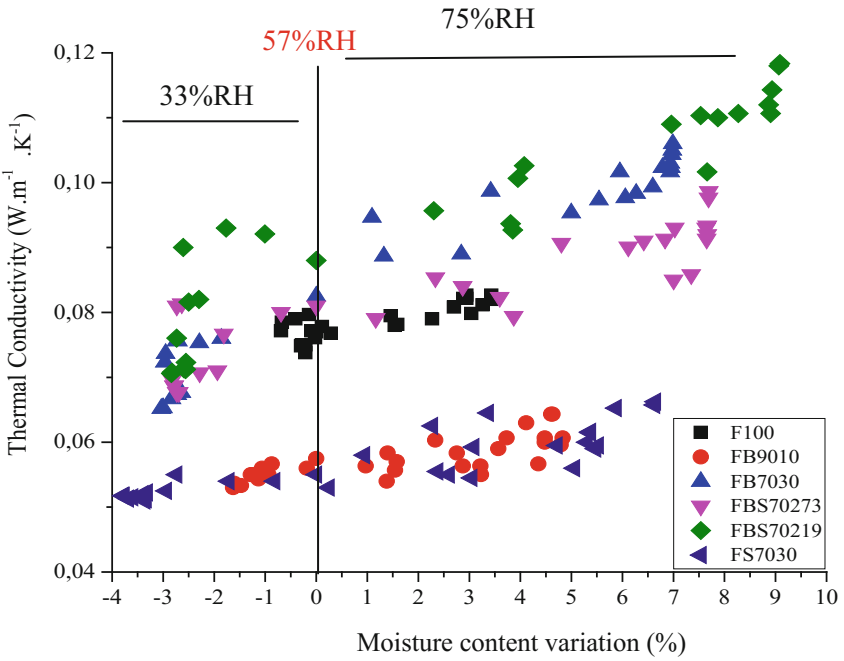


**Fig. 7.** Evolution of thermal conductivity with moisture content variations for the fiberboards at 25 °C between 33% and 75%RH

Moreover, the thermal conductivity was measured all along the moisture uptake from 33% RH to 75% RH. The variation moisture content (ΔMC) was calculated from weight increment or decrement and weight at pre-conditioned at 57%RH. The relationship between thermal conductivity and moisture content variations of all fiberboards is shown in Fig. 7.

### 3.5 Bending Properties

The elastic modulus and bending strength of all bamboo fiberboards are shown in Fig. 8. The elastic modulus and the bending strength reach 3131 MPa and 7.3 MPa for 30% (w/w) bone glue (FB7030) compared to the board without glue (F100) (elastic modulus of 1310 MPa and bending strength of 2.7 MPa). In fact, bone glue acts as an internal binder and ensures the cohesion inside the fiberboards (Evon et al. 2010). However, 10% (w/w) bone glue is not sufficient to ensure a good adhesion between the fibers, whereas 30% (w/w) bone glue provides better adhesion at the interfaces between the bone glue and bamboo fibers.

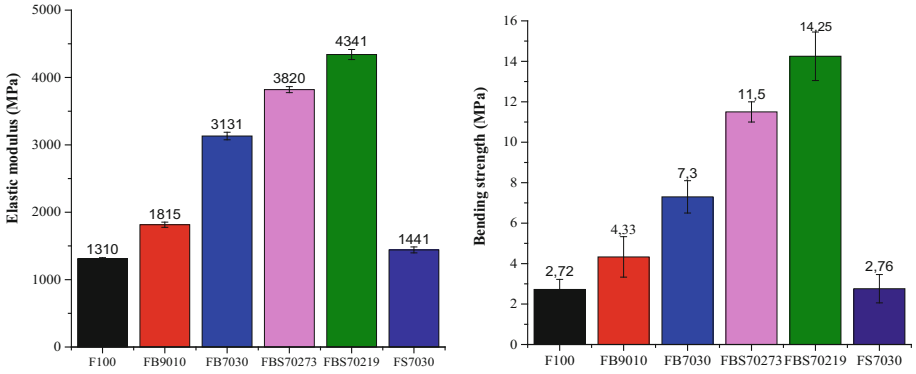


**Fig. 8.** Bending properties of fiberboards at 57% RH and 25 °C (Nguyen et al. 2017)

On the other hand, the bending properties of the fiberboards are strongly affected by the addition of sodium lignosulfonate. Adding sodium lignosulfonate to bone glue improves the elastic modulus and bending strength of fiberboards. The FBS70219 boards with 9% (w/w) of sodium lignosulfonate presented an increase of elastic modulus of approximately 4341 MPa and a bending strength about 14.3 MPa. This result can be explained that the sodium lignosulfonate is stiffer than protein, high molecular weight and the large quantity of aromatic rings of sodium lignosulfonate provide a stiffer material and improve its mechanical properties (Baumberger et al. 1998). A cross-linked network is formed between protein molecules of bone glue and sodium lignosulfonate leading to strong interactions in the boards as covalent bonds and also hydrogen and hydrophobic interactions (Frihart and Birkeland 2014; Huang and Chen 2003).

## 4 Conclusion

Six different types of bio-insulation materials have been manufactured from bamboo fibers and different bio-glues by thermo-pressing. The optimum fiberboard mechanical properties are obtained with a ratio of 70% (w/w) bamboo fibers and 30% (w/w) mixture glue of bone and sodium lignosulfonate (FBS70219, E = 4341 MPa and $\sigma_r$ = 14 MPa). The thermal conductivity of fiberboards from bamboo fibers and different glue ratios is fairly low, varying between 0.057 and 0.088 W $m^{-1}K^{-1}$ at 25 °C and 57%RH. Variation of thermal conductivity k with relative humidity and moisture content plays an important role in evaluating the hygrothermal performance of materials. As expected, k increases with moisture content variations of the samples. For all the fiberboards with 30% of glue this increase is proportionally nearly the same. It can be concluded that the bamboo fiberboards and more specially the FBS70219 panel are promising materials to participate in buildings' moisture control and is saving energy.

**Acknowledgements.** The authors would like to thank the Eiffel Excellence Scholarship Programme, Région Rhône-Alpes and Agence Nationale de la Recherche (ANR) for financial support. This work was also supported by a grant from Vietnam National University Ho Chi Minh City (VNU-HCM) project number HS2014-48-01. We thank all the participants for their enthusiasm, discussions and cooperation in this study.

## References

Abdou, A., Budaiwi, I.: The variation of thermal conductivity of fibrous insulation materials under different levels of moisture content. Constr. Build. Mater. **43**, 533–544 (2013)

Baumberger, S., Lapierre, C., Monties, B.: Utilization of pine kraft lignin in starch composites: impact of structural heterogeneity. J. Agric. Food Chem. **46**, 2234–2240 (1998)

Bo-Ming, Z., Zhao, S., He, H.: Experimental and theoretical studies of hightemperature thermal properties of fibrous insulation. J. Quant. Spectrosc. Radiat. Transf. **109**, 1309–1324 (2008)

Budaiwi, I., Abdou, A.: The impact of thermal conductivity change of moist fibrous insulation on energy performance of buildings under hot-humid conditions. Energy Build. **60**, 388–399 (2013)

Budaiwi, I., Abdou, A., Homoud, M.A.: Variation of thermal conductivity of insulation materials under different operating temperatures: impact on envelope-induced cooling load. J. Archit. Eng. **8**, 125–132 (2002)

Choi, H.Y., Han, S.O., Lee, J.S.: The effects of surface and pore characteristics of natural fiber on interfacial adhesion of henequen fiber/PP biocomposites. Compos. Interfaces **16**, 359–376 (2009)

Collet, F., Bart, M., Serres, L., Miriel, J.: Porous structure and water vapour sorption of hemp-based materials. Constr. Build. Mater. **22**, 1271–1280 (2008)

Cong, F., Diehl, B.G., Hill, J.L., Brown, N.R., Tien, M.: Covalent bond formation between amino acids and lignin: cross -coupling between proteins and lignin. Phytochemistry **96**, 449–456 (2013)

Deshpand, A.P., Bhaskar, R.M., Lakshmana, R.C.: Extraction of bamboo fibers and their use as reinforcement in polymeric composites. J. Appl. Polym. Sci. **76**, 83–92 (2000)

Duval, A., Molina-Boisseau, S., Chirat, C.: Comparison of kraft lignin and lignosulfonates addition to wheatgluten-based materials: Mechanical and thermal properties. Ind. Crops Prod. **49**, 66–74 (2013)

Evon, P., Vandenbossche, V., Pontalier, P.Y., Rigal, L.: Thermo-mechanical behaviour of the raffinate resulting from the aqueous extraction of sunflower whole plant in twin-screw extruder: manufacturing of biodegradable agromaterials by thermo-pressing. Adv. Mater. Res. **112**, 67–72 (2010)

Frihart, C.R., Birkeland, M.J.: Soya Properties and Soy Wood Adhesives. American Chemical Society, Washington, D.C. (2014)

Ge, H., Yang, X., Fazio, P., Rao, J.: Influence of moisture load profiles on moisture buffering potential and moisture residuals of three groups of hygroscopic materials. Build. Environ. **81**, 162–171 (2014)

Hauptmann, M., Lubin, J.H., Stewart, P.A., Hayes, R.B., Blair, A.: Mortality from solid cancers among workers in formaldehyde industries. Am. J. Epidemiol. **159**, 1117–1130 (2004)

Hill, C.A.S., Norton, A., Newman, G.: The water vapor sorption behavior of natural fibers. J. Appl. Polym. Sci. **112**, 1524–1537 (2009)

Huang, J., Chen, L.Z.P.: Effects of lignin as a filler on properties of soy protein plastics. II. Alkaline lignin. J. Appl. Polym. Sci. **88**, 3291–3297 (2003)

ISO15901-1: Evaluation of pore size distribution and porosimetry of solid materials by mercury porosimetry and gas adsorption – part 1: mercury porosimetry

Kaewtatip, K., Menut, P., Auvergne, R.: Interactions of kraft lignin and wheat gluten during biomaterial processing: evidence for the role of phenolic groups. J. Agric. Food Chem. **58**, 4185–4192 (2010)

Khedari, J., Teekasap, S.: New low-cost insulation particleboards from mixture of durian peel and coconut coir. Build. Environ. **39**, 59–65 (2004)

Khosravi, S., Nordqvist, P., Khabbaz, F., Johansson, M.: Protein-based adhesives for particleboards—effect of application process. Ind. Crops Prod. **34**, 1509–1515 (2011)

Kondo, Y., Hvamac, A., Nagasa, W.L.Y., Fujimoto, T., Kikuchi, Y., Tasaka, T.: Experiments on influence of moisture on thermal performance change of insulations: Long term thermal performance of building insulation materials Part 2. J. Environ. Eng. **75**, 261–269 (2010)

Kunanopparat, T., Menut, P., Morel, M.H.N., Guilbert, S.: Modification of the wheat gluten network by kraft lignin addition. J. Agric. Food Chem. **57**, 8526–8533 (2009)

Kunanopparat, T., Menut, P.P., Morel, M.H., Guilbert, S.: Improving wheat gluten materials properties by kraft lignin addition. J. Appl. Polym. Sci. **125**, 1391–1399 (2012)

Latif, E., Tucker, S., Ciupala, M.A., Wijeyesekera, D.C., Newport, D.: Hygric properties of hemp bio-insulations with differing compositions. Constr. Build. Mater. **66**, 702–711 (2014)

Michael, H., Patricia, A.S., Jay, H.L.: Mortality from lymphohematopoietic malignancies and brain cancer among embalmers exposed to formaldehyde. J. Natl Cancer Inst. **101**, 1696–1708 (2009)

Nguyen, D.M., Grillet, A.C., Diep, T.M.H., Ha-Thuc, C.N., Woloszyn, M.: Hygrothermal properties of bio-insulation building materials based on bamboo fibers and bio-glues. Constr. Build. Mater. **155**, 852–866 (2017)

Penttala, V.: Effects of microporosity on the compression strength and freezing durability of high-strength concretes. Mag. Concr. Res. **41**, 171–181 (1989)

Ratiarisoa, R.V., Magniont, C., Ginestet, S., Oms, C., Escadeillas, G.: Assessment of distilled lavender stalks as bioaggregate for building materials: hygrothermal properties, mechanical performance and chemical interactions with mineral pozzolanic binder. Constr. Build. Mater. **124**, 801–815 (2016)

Shiva, K.M., Durga, P.B., Basavaraj, M.: Effect of moisture content and temperature on thermal conductivity of Psidium Guajava L. by line heat source method (transient analysis). Int. J. Heat Mass Transf. **78**, 354–359 (2014)

Sjöström, J., Blomqvist, P.: Direct measurements of thermal properties of wood pellets: elevated temperatures, fine fractions and moisture content. Fuel **134**, 460–466 (2014)

Suleiman, B.M., Larfeldt, J., Leckner, B., Gustavsson, M.: Thermal conductivity and diffusivity of wood. Wood Sci. Technol. **33**, 465–473 (1999)

Verdier, T., Granulats, V.D.: Végétaux Dans Un Matériau De Construction À Matrice Minérale. Université Paul Sabatier, Toulouse (2012)

Vololonirin, O., Coutand, M., Perrin, B.: Characterization of hygrothermal properties of wood-based products – impact of moisture content and temperature. Constr. Build. Mater. **63**, 223–233 (2014)

Wang, L., Chen, S.S., Tsang, D.C.W., Poon, C.S., Dai, J.G.: CO2 curing and fibre reinforcement for green recycling of contaminated wood into high-performance cement-bonded particleboards. J. CO2 Util. **18**, 107–116 (2017)

Wang, L., Chen, S.S., Tsang, D.C.W., Poon, C.S., Shih, K.: Value-added recycling of construction waste wood into noise and thermal insulating cement-bonded particleboards. Constr. Build. Mater. **125**, 316–325 (2016)

Westermarck, S., Juppo, A.M., Koiranen, K., Yliruusi, J.: Mercury porosimetry of pharmaceutical powders and granules. J. Porous Mater. **5**, 77–86 (1998)

Xu, J.Y., Sugawara, R., Widyorini, R., Han, G., Kawai, S.: Manufacture and properties of low-density binderless particleboard from kenaf core. J. Wood Sci. **50**, 62–67 (2004)

Zhigang, X., Yonghui, L., Xiaorong, W., Guangyan, Q., Ningbo, L., Zhang, K., Donghai, W.D., Xiuzhi, S.S.: Utilization of sorghum lignin to improve adhesion strength of soy protein adhesives on wood veneer. Ind. Crops Prod. **50**, 501–509 (2013)

Zhou, X.Y., Zheng, F., Li, H.G., Lu, C.L.: An environment-friendly thermal insulation material from cotton stalk fibers. Energy Build. **42**, 1070–1074 (2010)

# Investigation on the Blended Cement Mixture of Sintered Clinker of Calcium Sulfoaluminate Cement and Granulated Blast Furnace Slag

Khanh Son Nguyen(✉), Tuan Nghia Le, Anh Quyen Nguyen-Thi, Anh Toan Nguyen-Phung, Tri Huynh Nguyen-Ngoc, and Quang Minh Do

BACH KHOA University – VNU HCM (Former Ho Chi Minh City University of Technology), Ho Chi Minh City, Vietnam
ksnguyen@hcmut.edu.vn

**Abstract.** In this paper, we present studies in laboratory where we used bauxite Tan Rai and synthetic gypsum DAP Dinh Vu to fabricate cement clinker of calcium sulfoaluminate. Results of compositional analysis by XRD revealed major phases of ye'elimite $4CaO.3Al_2O_3.SO_3$ ($C_4A_3\check{S}$), belite $2CaO.SiO_2$ ($C_2S$), anhydrite $CaO.SO_3$ ($C\check{S}$) in the sintered product. With the aim of combining two hydration mechanisms of CSA cement (rapid) and slag cement (slow), we then formulated blended cement from mixture of 15.58%wt CSA clinker and 73.36% wt fine ground granulated blast furnace slag and 11.06%wt synthetic gypsum. Specification tests of prepared cement were conducted conforming to the requirement of standard BS EN 15743 for supersulfated cement. In term of strength development, we noted quite high strength gain after 7 days in both tap water and sea water mixing cement. The global compressive strength of cement mortar met the grade 40 MPa of standard. Considering its practical application, we discuss on the perspective using this special cement for concrete under severe condition after taking into account further study on durability.

**Keywords:** Calcium sulfoaluminate cement · Supersulfated cement · GBFS · Low CO2 cement · Durability

## 1 Introduction

In general, to sinter Portland clinker cement at 1450 °C, we need feed huge amount fossil fuel in rotary kiln and decarbonation process of major raw material of calcite in calciner provoke environmental impact. Calcium sulfoaluminate (CSA) and CSA-based cements are now considered as a good alternative to Portland cement for sustainability (Edwards 2011). To sinter CSA clinker cement, less energy are required to heat up temperature 1250 °C and $CO_2$ emmision is lower due to partly replacement of calcite by gypsum in raw mixing (Gartner and Barcelo 2012). Different types of CSA cement product are formulated by intergrinding CSA clinker, gypsum and others hydraulic component such as Portland cement clinker. Regarding to the material specification, high strength development at early age, reducing shrinkage and durability in aggressive condition are ussually reported with commercial CSA cement mortar/concrete (Hewlett

© Springer Nature Singapore Pte Ltd. 2018
H. Tran-Nguyen et al. (eds.), *Proceedings of the 4th Congrès International de Géotechnique - Ouvrages -Structures*, Lecture Notes in Civil Engineering 8,
DOI 10.1007/978-981-10-6713-6_51

2003). Such evidence is primary different comparing to the case of ordinary Portland cement which is well-known by its later strength development and major deterioration during exposure to severe conditions. Almost in CSA cement, mineral compostion of ye'elimite ($C_4A_3\check{S}$) takes in charge early age strength evolution and belite ($C_2S$) mineral serves for later age resistance of cement mortar (Hargis et al. 2013). High cost of raw material and hardly-controlled sintering temperature might contribute to explain the limit production of CSA cement (Gartner and Barcelo 2012, Walenta 2011). Many research issues and technology developer supposed different approach to overcome those inconveniences. Belite CSA, alite CSA or CSA Portland cement are primarily based on the principle of less modified clinkerization technology of Portland cement in conventional rotary kiln system. Others research reported a great variety of industrial solid-wastes such as fly ash (Sahu and Majling 1994), red mud (Ukrainczyk et al. 2013), marble sludge (El-Alfi and Gado 2016), desulfurized gypsum (Zhang et al. 2012), iron/steel slag… (Adolfsson et al. 2007) that could be used in raw materials mixture.

In the following paragraphs, we will conduct experimental studies on the combination of CSA and slag cement. The first step consisted of using local materials such as limestone, clay, bauxite and phosphogypsum to synthesize clinker CSA cement. The next step is dedicated to investigate on material characterization of formulated mixture of CSA cement and a high proportion (>75 wt%) of granulated blast furnace slag composition. In term of strength development, the use of CSA cement could be seen in one hand, as a setting regulator at early age for slag cement (Michel et al. 2012). And on the others hand, the use of slag allows us discussing on the long term behavior in case of seawater mixing concrete. Our motive to use industrial waste such as phosphogypsum, slag and a marketable product with high value added. Manufacturing CSA cement from natural bauxite acquires an increasing demand in both industrial and environmental sector. In the current context of sea water rise, to develop infrastructure for Mekong Delta area (where due to global climate change, research report predicted that around 39% of region will be inundated with water or salinity intrusion in 2100) demand durable materials solution than ordinary Portland cement. The feasibility of this laboratory investigation permit us to extend our study at larger scale in cement industry.

## 2 Materials and Experiments

Limestone, clay, bauxite and gypsum are conventionally used to produce CSA cement clinker. But, there is a fact that no stoichiometry formula of raw materials pre-mix is reported in literature (Odler 2003).

Limestone and clay Ta Thiet (Binh Phuoc province) are two natural resources. They are currently used as raw materials for manufacturing Portland cement clinker at Binh Phuoc Factory - Vicem Ha Tien. Phosphogypsum residue is a by-product of the fertilizer production from Vinachem - DAP Dinh Vu plant. From this waste material, synthetic gypsum that we used in this study is fabricated via a purification process. Such synthetic product is already commercialized as setting regulator for intergrinding with Portland cement clinker. Bauxite Tan Rai (Lam Dong province) is the main resource of $Al_2O_3$ in this experiment campaign. This is also one of the most important

natural mineral in Vietnam's central highland. As given in the Table 1, results of XRF analysis revealed the main chemical composition of four mentioned materials. We highlight quite high content of $Fe_2O_3$ 17.68 wt% in bauxite Tan Rai. That could be reason for reddish color of such natural bauxite. Synthetic gypsum shows very high content of $SO_3$ and low insoluble residue content. It means high quality product of chemical treatment. But, the calculated ratio of $CaO/SO_3$ = 1.31 is not corresponding to stoichiometric value 0.7 of natural gypsum. We can explain by the presence of others impurities such as calcite and silicates materials. Last statement could be confirmed with lower result of loss on ingition test 19.08 wt% than those of natural gypsum 20.93 wt%.

**Table 1.** Chemical composition of raw materials

| | $SiO_2$ | $Al_2O_3$ | $Fe_2O_3$ | CaO | MgO | $SO_3$ | $K_2O$ | $TiO_2$ | MnO | $P_2O_5$ | L.O.I. |
|---|---|---|---|---|---|---|---|---|---|---|---|
| Limestone | 1.81 | 0.55 | 0.28 | 50.35 | 1.76 | 0.22 | 0.16 | 0.04 | 0.00 | 0.02 | 44.81 |
| Clay | 61.08 | 14.85 | 8.01 | 0.77 | 1.36 | 0.03 | 2.07 | 0.61 | 0.08 | 0.22 | 10.92 |
| Bauxite | 2.09 | 49.74 | 17.68 | 0.00 | 0.26 | 0.00 | 0.05 | 0.00 | 0.00 | 0.00 | 30.18 |
| Synthetic gypsum | 5.26 | 0.54 | 0.28 | 41.26 | 0.40 | 32.15 | 0.14 | 0.19 | 0.15 | 0.56 | 19.08 |
| GBF slag | 33.81 | 15.67 | 0.84 | 42.34 | 6.43 | 0.16 | – | 0.10 | – | 0.07 | 0.56 |

We can find a strong correlation between maximizing ye'elimite phase in sintered CSA clinker and high strength gain at early age of cement mortar. Based on result of preliminary study, three proportional mixtures of raw materials are given in the Table 2. The Bogue method of Portland cement chemistry (Hewlett 2003) was adopted in order to estimate the expected phases of clinker.

$$\%wt\ C_4A_3\check{S} = 1.995(\%wt\ Al_2O_3) - 1.273(\%wt\ Fe_2O_3)$$
$$\%wt\ C_2S = 2.867(\%wt\ SiO_2)$$
$$\%wt\ C\check{S} = 1.700(\%wt\ SO_3) - 0.445(\%wt\ Al_2O_3) + 0.284(\%wt\ Fe_2O_3)$$
$$\%wt\ C_4AF = 3.043(\%wt\ Fe_2O_3)$$
$$\%wt\ C = 1.00(\%wt\ CaO) - 1.867(\%wt\ SiO_2) - 1.054(\%wt\ Fe_2O_3) - 0.550(\%wt\ Al_2O_3) - 0.700(\%wt\ SO_3)$$

Obtained results showed that Mix1 contains relatively 23.7%wt $C_4A_3\check{S}$, 36.7%wt $C_2S$, 18.0%wt $C\check{S}$, 0.5%wt C and 18.5%wt $C_4AF$; Mix2 contains relatively 24.8%wt $C_4A_3\check{S}$, 29.8%wt $C_2S$, 22.2%wt $C\check{S}$, 2.0%wt C and 18.8%wt $C_4AF$; Mix3 contains relatively 26.3%wt $C_4A_3\check{S}$, 25.2%wt $C_2S$, 24.0%wt $C\check{S}$, 2.7%wt C and 19.6%wt $C_4AF$.

**Table 2.** Proportional mixture of raw materials in three mix design

| | Limestone (%wt) | Bauxite (%wt) | Clay (%wt) | Synthetic gypsum (%wt) | Total (%wt) |
|---|---|---|---|---|---|
| Mix1 | 43 | 18 | 10 | 29 | 100 |
| Mix2 | 38 | 20 | 7 | 35 | 100 |
| Mix3 | 35 | 22 | 5 | 38 | 100 |

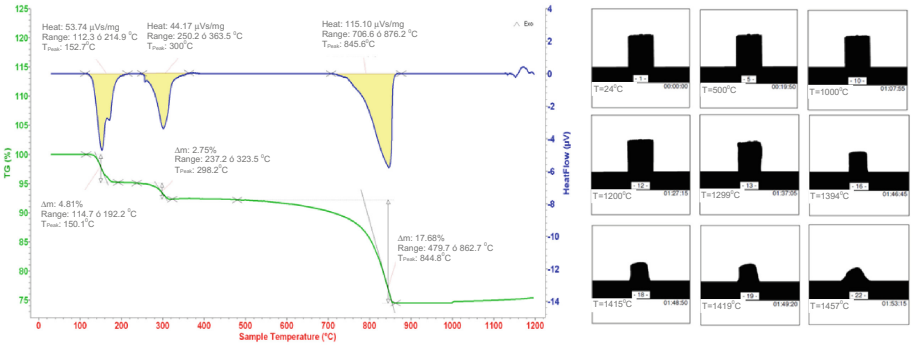


**Fig. 1.** Result of DSC/TG analysis of Mix1 (left) and observation of sample profile via heating microscope (right)

Three major phases of ye'elimite, belite and anhydrite are mostly expected. More we use bauxite in the mixture design, more we expect to obtain ye'elimite phase in the clinker production. Meanwhile, more we use clay in the mixture design, more we expect to obtain belite phase in the final clinker. We remind that portlandite as hydrated product of belite is theorically a main activator of slag reaction in slag cement combination (Taczuk et al. 1992). From this point of view, there must be a compromise between high strength gain and slag activation process, we supposed to use the mix design Mix1 for the sintering process.

Figure 1 shows both result of thermogravimetry TG (Setaram LABSYS Evo TG-DSC 1600 °C, heating rate 10 K/min) and heating microscope (Hesse Instruments EM-201 1750 °C) analysis of raw mixture Mix1. A total mass loss 25.06%wt was recorded for temperature range 30 °C - 1000 °C. The most important mass loss was 17.68%wt between 480–882 °C that attributed to the decarbonation reaction of calcite, dolomite. Below 400 °C, two others mass loss around 4.81%wt and 2.75%wt associated with two endothermic peaks on DSC curve that correspond to free water evaporation, coupling reaction of dehydration of gypsum and dehydration of chemically bound water in clay, gibbsite. Above 1200 °C, they existed a small fluctuation of mass gain on the TG curve due to volumetric deformation and/or new phase formation at high temperature. Regarding to the result of heating microscope measurement, we noted no change in sample profile at temperature point 1200 °C. A light transformation of sample profile at temperature point 1299 °C mean the appearance of solid-liquid phase change. Final transformation from cylinder to quasi-hemisphere profile of testing sample was only determinated with thermal loading of above 1457 °C. Combined results of material analysis help us fix a firing conditions in case of laboratory furnace. They are composed of sintering temperature point at 1250 °C for a period of 2 h and following regime of natural cooling to room temperature.

Figure 2 schematizes the experience with two consecutives stages: clinkerization process and formulation of slag-CSA cement. Raw slag gravel (produced by JFE corp.-Japan) was ground into slag powder with fineness control (Blaine 4270 $cm^2/g$ and 2.5%wt retained on 45 µm sieve). As given in the Table 1, the main oxides composition

of slag include 15.67%wt of $Al_2O_3$, 33.81%wt $SiO_2$ and 42.34%wt CaO. Calculated values of both basicity %wt CaO/%wt $SiO_2 > 1$, and chemical indice (%wt CaO + %wt MgO + %wt $Al_2O_3$)/%wt $SiO_2 \gg 1$ led us to classify this slag in the range of high quality product with high alumine content. The strength activity index 28 days was registered as around 110%. In general, fine slag powder met the requirement of BS EN 15743 of slag component in supersulfated cement fabrication. With regard to the recommendation in the BS EN 15743 for supersulfated cement, our formulating slag-CSA cement consist of 15.58%wt CSA, 73.36%wt GBF slag and 11.06%wt synthetic gypsum. The reason of high content of slag used in the formulation could be explained by the expecting material for practical usage under severe condition. Different tests were realized to investigate physio-mechanical properties of the formulated cement mortar. At early age, we conducted tests on water demand, setting time, soundness and hydration heat of cement paste (Calorimeter Matest E061N). At later age, we conducted tests on strength development over curing time of mortar samples (mixing with tap and sea water) and SEM and XRD analysis of final set paste.

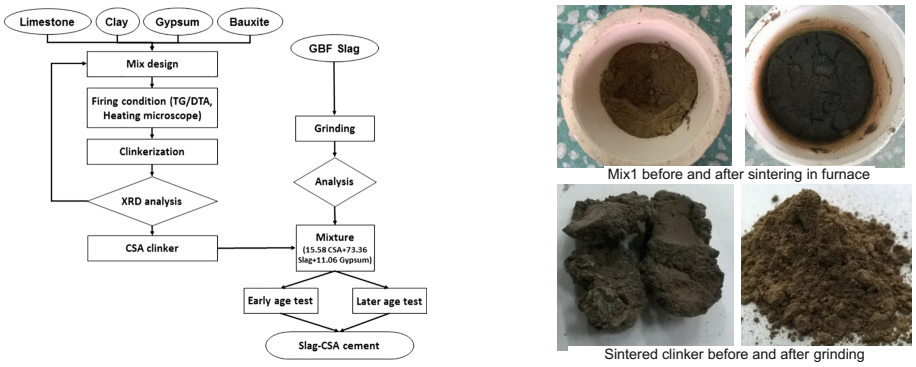


**Fig. 2.** Schema of experimental study (left) and illustration of mixture and sintered product of CSA cement (right).

## 3 Results

### 3.1 Characterization of Sintered Clinker

Figure 2-right shows the evidence of gray brown color product of sintered clinker. It seems obviously that prepared clinker is more friable and softer than the case of Portland cement clinker. We noted that conventional Portland cement clinker is commonly fabricated by liquid phase sintering in rotary kiln. The fact is that was not the same process of clinkerization of our obtained clinker. Moreover, softer means easier to grind that could be considered as an advantage of this type of cement. We analyzed the mineralogy composition by using XRD diffractometer D8 ADVANCE, $2\theta = 10°–80°$, CuK$\alpha$ radiation. As given in the XRD spectrum (Fig. 3), major peaks at $2\theta = 23.66°$; 33.74°; 41.63° (N°1) refer to the ye'elimite phase. The β-belite phase

appeared with peaks N°2 at 2θ = 32.48°; 33.05°; 29.36°; 33.53°. Peaks N°3 correspond to the phase of ternesite. Such ternesite is an intermediate that was formed at lower temperature than the more stable phase of ye'elimite (Winnefeld and Lothenbach 2010). We also noted the presence the trace of anhydrite (peaks N°4 at 2θ = 25.85°; 31.35°; 41.20°). That could be explained by the uncompleted reaction during clinkerization under high temperature condition. Others minor phase such as C4AF, unreacted composition and/or glassy product constitued amorphorous base of spectrum. Considering the percentage of phase quantification by X'pert Highscore Plus (Schmidt and Pöllmann 2000), we highlight quite high percentage of anhydrite and ternesite phases in the final clinker product. We compare side-by-side such estimation with above calculated results by Bogue method. Both results of ye'elimite phase determinate by two methods are equivalent, but less belite phase percentage is taken into account in the sintering product according to materials analysis. $C_4AF$ phase could not be estimated due to its amorphous state.

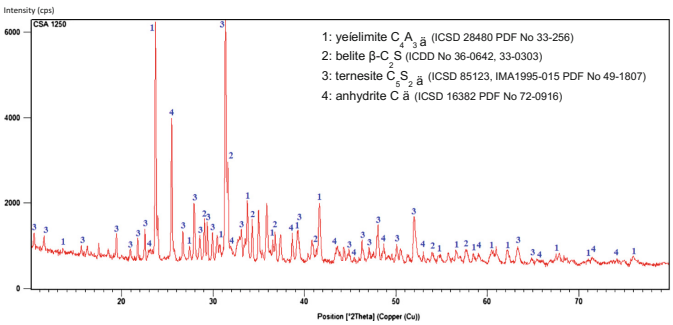


| Mineral phase¤ | %wt¤ |
|---|---|
| C4A3Š¤ | 25.23¤ |
| C2S¤ | 21.64¤ |
| CŠ¤ | 22.27¤ |
| C5S2Š¤ | 23.04¤ |
| Total¤ | 92.19¤ |

**Fig. 3.** Result of XRD spectrum of sintered clinker, CuKα (left) and calculated amount of the main phases by X'pert Highscore Plus (right).

### 3.2 Characterization of Formulated Cement CSA-Slag (15.58%wt CSA, 73.36%wt GBF Slag and 11.06%wt Synthetic Gypsum)

- Heat of Hydration Reaction

Regarding in literature, the first step of hydration reaction of calcium sulfoaluminate cement is described by two following reactions (Odler and Zhang 1996):

$$3CaO.3Al_2O_3.CaSO_4 + 2CaSO_4.2H_2O + 34H_2O \rightarrow 3CaO.Al_2O_3.3CaSO_4.32H_2O + 4Al(OH)_3$$
$$3CaO.3Al_2O_3.CaSO_4 + 18H_2O \rightarrow 3CaO.Al_2O_3.CaSO_4.12H_2O + 4Al(OH)_3$$

Those reactions of ye'elimite take place rapidly and associated with exothermic phenomenon. Obtained results of hydration heat of formulated cement paste at 7 and 28 days are respectively 271.4 and 701.7 kJ/kg. As given in the ASTM C186, those results correspond to the difference of heat releasing between unreacted cement (initial mixture) and partially reacted cement at 7 and 28 days. They show the evidence of

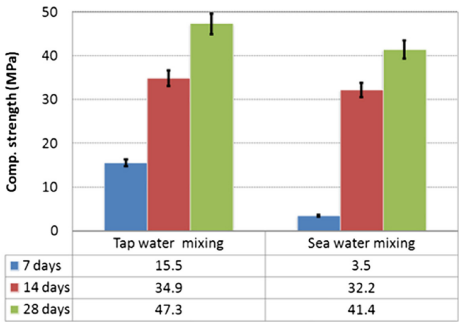


**Fig. 4.** Formulated cement of slag-CSA and preparation of mortar sample according to TCVN 2682-2009 (left) and result of strength development (right).

exothermic reaction of formulated cement at later age. That is not the same circumstance in case of ordinary Portland cement with respectively values of hydration heat 411.3 kJ/kg at 7 days and 551.2 kJ/kg at 28 days. It is noted that hydration reaction of slag is low heat, so the contribution of hydration heat is mainly controlled by 15.58%wt of CSA cement clinker. In pratice, such phenomenon of heat releasing could be constated after casting cement mortar in mold. To compare with the requirement of ASTM C115M-11 for low heat cement, both measured values at 7 days and 28 days was superior to the limit values ($\leq$250 kJ/kg at 7 days and $\leq$290 kJ/kg at 28 days). Formulated cement slag-CSA did not meet the requirement of standard. That is an important result while combining two mechanisms of hydration reaction in cement.

- Strength development

Mortar casting was in prismatic mold 40 × 40 × 160 mm (Fig. 4-left). As we mentionned in the introduction section, tap water and sea water were used as mixing component and curing environment. Figure 4-right shows the strength evolution of two series of mortar samples over curing period 7-14-28 days. It is noted that formulated product seems obviously late set cement and 3 age days strength was difficult to measure. Such result is logically consisting with the previous study on the hydraulic reactivity. For the global trend of mechanical resistance, two series of sample show the evidence of normal strength development at later age. Higher compressive strength of mortar sample was revealed in case of tap water mixing cement mortar, but both samples could met the requirement of grade 40 MPa at 28 days. We might attribue high strength gain after 7 days due to the large difference of strength values between 7 and 14 days, especially in case of sea water mixing sample. Low resistance 3.5 MPa at 7 days of sea water mixing mortar could be explained by the fact of high sulfate content in sea water solution. Sulfate ions in sea water are reported in litterature to affect the reaction of slag at the early age.

- Analysis of hydrated product

Results of compositional analysis of hardenning cement paste are given by the XRD spectrum in the Fig. 5-left. Major peaks ($N^0 1$) at $2\theta = 9.14^0$; $15.87^0$; $23.05^0$ correspond

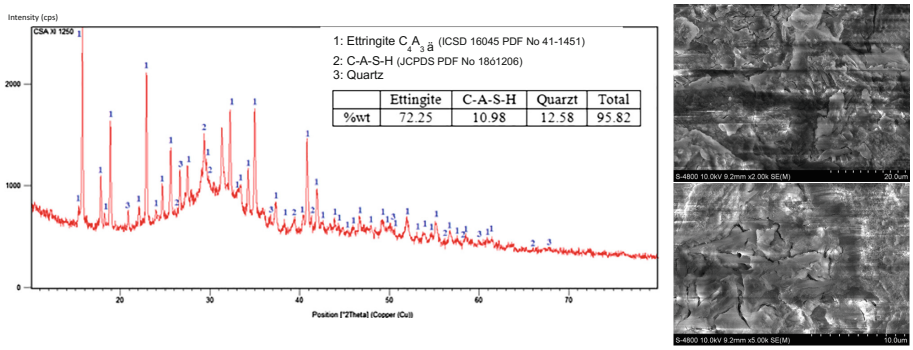


**Fig. 5.** XRD spectrum of hydrated cement slag-CSA, CuKα (left) and SEM clichés of set paste after 28 days (right).

to the main phase of ettringite ($3CaO.Al_2O_3.3CaSO_4.32H_2O$). Others minor peaks were attribued to hydrated product of C-A-S-H and quartz phase. There is also amorphous phase of unreacted component and/or gels of poor crystallized product (Kasselouri et al. 1995). Calculated amount of the main phases by X'pert Highscore Plus also showed the abundant ettringite product 72.25%wt in the setting paste of formulated cement. As we known, ettringite are main product of ye'elimite and slag reaction. Such ettringite contribute logically to global resistance of cement mortar. No trace of portlandite was regconized in the XRD spectrum, that means its served completely as alkalie activator of GBF slag. Regarding to the microstructure of cement paste, two SEM cliches with magnification ×2000 (up) and ×5000 (down) illustrate a compact structutre. We observed also some position of micro cracks and unreacted slag particle < 1 μm. Rod-shape crystals that commonly refer to ettringite mineral were also distributed separately in the microstructural image.

## 4 Conclusions

For concluding, we investigated on the preparation of calcium sulfoaluminate cement clinker from five local materials in laboratory. Mixture proportion composed of 43 wt% limestone Ta Thiet, 10 wt% clay Ta Thiet, 29 wt% synthetic gypsum and 18 wt% bauxite Tan Rai. Firing condition for clinkerization process was set as follow: sintering temperature 1250 °C during 2 h and normal cooling phase in electric furnace. XRD analysis of clinker product revealed mostly main phases of ye'elimite, belite, anhydrite and one part of ternesite as intermediate phase. Formulated cement of slag-CSA was fabricated from mixture of 15.58%wt CSA, 73.36%wt GBF slag and 11.06%wt synthetic gypsum. In term of mechanical resistance, both tap water mixing and sea water mixing mortar samples met the requirement of grade 40 MPa after 28 age days. Futhermore, others character of prepared slag-CSA cement included high hydration heat 701.7 kJ/kg at later age, abundant ettringite phase as hydrated product and compact microstructure. Further studies on durability of sea water mixing cement concrete could be envisageable for final conclusion on sustainable aspect of GBF slag – CSA system.

**Acknowledgments.** The author would like to thank for materials support from Binh Phuoc Factory - Vicem Ha Tien and Vinachem - DAP Dinh Vu and for financial support from Ho Chi Minh city University of Technology, VNU-HCM.

## References

Edwards, P.: Future Cement - Looking beyond OPC in Cement Industry News, Events and Research from Global Cement Magazine (2011). http://www.globalcement.com/magazine/articles/315-future-cement-looking-beyond-opc. Accessed 15 Oct 2013

Gartner, E., Barcelo, L.: The "sustainability" of cement and concrete. In: Paper presented at LNEC meeting in Lisbon, Portugal on June 18, 2012 (2012). http://jornadas2012.lnec.pt/site_2_Cidades_e_Desenvolvimento/APRESENTACOES_POSTERS/C2_GARTNER_a.pdf. Accessed 10 Oct 2013

Hewlett, P.: Lea's Chemistry of Cement and Concrete. Butterworth-Heinemann, Oxford (2003)

Hargis, C.W., Kirchheim, A.P., Monteiro, P.J., Gartner, E.M.: Early age hydration of calcium sulfoaluminate (synthetic ye'elimite) in the presence of gypsum and varying amounts of calcium hydroxide. Cem. Concr. Res. **48**, 105–115 (2013). doi:10.1016/j.cemconres.2013.03.001

Walenta, G.: CCS, CCT & Aether: innovative approaches to reducing $CO_2$ emissions in cement production. In: Paper presented at CemTech Conference, Warsaw on 25–28 September 2011 (2011). http://www.aether-cement.eu/fileadmin/user/pdf/2011.09.25_CemTech_Warsaw_Final.pdf. Accessed 20 Oct 2013

Sahu, S., Majling, J.: Preparation of sulphoaluminate belite cement from fly ash. Cem. Concr. Res. **24**(6), 1065–1072 (1994). doi:10.1016/0008-8846(94)90030-2

Ukrainczyk, N., Frankoviæ Mihelj, N., Šipušić, J.: Calcium sulfoaluminate eco-cement from industrial waste. Chem. Biochem. Eng. Q. vol. 27(1), pp. 83–93 (2013). http://hrcak.srce.hr/99441, Accessed 15 Sept 2013

El-Alfi, E.A., Gado, R.A.: Preparation of calcium sulfoaluminate-belite cement from marble sludge waste. Constr. Build. Mater. **113**, 764–772 (2016). doi:10.1016/j.conbuildmat.2016.03.103

Zhang, X., Zhao, M., Zhang, Y.: Preparation and properties of self-pulverizing calcium sulfoaluminate cement. Constr. Build. Mater. **34**, 107–113 (2012). doi:10.1016/j.conbuildmat.2012.02.006

Adolfsson, D., Menad, N., Viggh, E., Björkman, B.: Steelmaking slags as raw material for sulphoaluminate belite cement. Adv. Cem. Res. **19**(4), 147–156 (2007). doi:10.1680/adcr.2007.19.4.147

Michel, M., Georgin, J.F., Ambroise, J.: Improving the mechanical performance of high-grade slag cement by the addition of Portland cement and sulfoaluminate cement. Constr. Build. Mater. **37**, 291–300 (2012). doi:10.1016/j.conbuildmat.2012.04.041

Odler, I.: Special Inorganic Cements. CRC Press, Boca Raton (2003)

Taczuk, L., Bayoux, J.P., Sorrentino, F., Capmas, A.: Understanding of the hydration mechanisms of C4A3S–Portland clinker–CaSO4 mixes. In: Proceedings of International Congress on the Chemistry of Cements, New Delhi, India on 23–28 November 1992, Vol. IV, 278–284 (1992)

Winnefeld, F., Lothenbach, B.: Hydration of calcium sulfoaluminate cements—experimental findings and thermodynamic modelling. Cem. Concr. Res. **40**(8), 1239–1247 (2010). doi:10.1016/j.cemconres.2009.08.014

Schmidt, R., Pöllmann, H.: Quantification of calcium sulpho-aluminate cement by rietveld analysis. In: Materials Science Forum, vol. 321, pp. 1022–1027. Trans Tech Publications (2000). doi:10.4028/www.scientific.net/MSF.321-324.1022

Odler, I., Zhang, H.: Investigations on high SO3 portland clinkers and cements I. Clinker synthesis and cement preparation. Cem. Concr. Res. **26**(9), 1307–1313 (1996). doi:10.1016/0008-8846(96)00128-7

Kasselouri, V., Tsakiridis, P., Malami, C., Georgali, B., Alexandridou, C.: A study on the hydration products of a non-expansive sulfoaluminate cement. Cem. Concr. Res. **25**(8), 1726–1736 (1995). doi:10.1016/0008-8846(95)00168-9

# Numerical Tool for the Evaluation of the Hygrothermal Performance of a Hemp-Lime Concrete

S. Moissette[1], M. Bart[1], Y. Aït Oumeziane[2], C. Lanos[1(✉)], F. Collet[1], and S. Prétot[1]

[1] LGCGM, Laboratoire de Génie Civil et de Génie Mécanique UR1, Rennes, France
Christophe.lanos@univ-rennesl.fr
[2] Institut FEMTO-ST UFC, Belfort-Montbeliard, France

**Abstract.** Hemp concrete is a non-loadbearing material used as filling material to form the building envelope. Hemp concrete is an hygroscopic bio-material characterized by a strong hysteretic hydric behavior and interesting thermal conductivity. A numerical tool able to model the hysteretic behavior of the hemp concrete sorption process is presented. The implementation of a suited hysteresis model in a heat and moisture transfer model allow evaluating and discussing the influence of this phenomenon in the transient hygrothermal response of hemp concrete to hydric loadings. The governing system of strongly coupled unsteady differential equations is implemented in Matlab with a finite differences method. Numerical transient hygrothermal responses of hemp concrete submitted to cyclic hydric isothermal loadings are then produced and compared with experimental results.

**Keywords:** Hemp concrete · Hysteretic hydric behavior · Heat transfer · Moisture transfer

## 1 Introduction

Hemp concrete, a mixture of hemp shiv and lime, participates in a process of sustainable development in the housing field by reducing environmental impact and improving hygrothermal comfort. This kind of hygroscopic bio-material is characterized by a strong hysteretic hydric behavior, intermediate thermal performances but poor mechanical strengths (Amziane and Arnaud 2013). Such material is then used as filling material to form multi-layer wall composed with a hemp concrete as core material protected by renders and plasters. As for many hygroscopic materials, vegetal or mineral, a significant hysteresis occurs in hemp concrete sorption process. The hysteresis phenomenon is attributed mainly to the pore morphology ("ink bottle effect"), the effects of spatial arrangement of pores and variation in liquid-solid contact angle. In adsorption phase, an increase of relative humidity involves an increase of moisture content. In desorption phase, less moisture is released from the material than moisture up taken in adsorption. As a consequence, the equilibrium moisture content depends

© Springer Nature Singapore Pte Ltd. 2018
H. Tran-Nguyen et al. (eds.), *Proceedings of the 4th Congrès International de Géotechnique - Ouvrages -Structures*, Lecture Notes in Civil Engineering 8,
DOI 10.1007/978-981-10-6713-6_52

not only on the relative humidity but also on the hydric history. The differences in moisture content at the same relative humidity for hemp concrete during adsorption and desorption cycles affect moisture and heat transfers in such hygroscopic building materials. In this paper, the development of a numerical tool able to simulate the thermal and moisture study on hysteretic behavior of the hemp concrete sorption process is presented. Two types of use of the developed tool are detailed. Numerical transient hygrothermal responses of hemp concrete submitted to cyclic hydric isothermal loadings are produced and compared with experimental results, highlighting the large influence of the initial moisture content. The numerical analysis of the hygrothermal behavior of a wall exposed to mastered hygrothermal conditions is performed and compared to experimental results collected on a hemp concrete wall placed between two climatic rooms. The influence and the interest of model with hysteresis can then be discussed analyzing energy balance.

## 2 Heat and Moisture Transfer Model and Hysteresis Model

### 2.1 Heat and Moisture Transfer

The developed numerical tool correspond to the 1D hygrothermal transfer through a multilayer wall. According to Künzel formalism, the driving flow potentials are temperature T and relative humidity φ. According to Künzel formalism (Künzel 1995), the driving potentials of the 1D hygrothermal model can be expressed in terms with two flow potentials temperature T and relative humidity φ. The governing system of equations of moisture and heat transfer is given in Eqs. (1) and (2).

$$\xi_\varphi \frac{\partial \varphi}{\partial t} = \nabla\left[\delta_p \nabla(\varphi p_{sat})\right] + \nabla[D_l \nabla(\varphi)] \tag{1}$$

$$\begin{aligned} &\rho_0 c^* \frac{\partial T}{\partial t} + \left[c_l\left(T - T_{ref}\right)\xi_\varphi\right] \\ &= \nabla\left[\lambda \nabla T + \left(l_v + c_v\left(T - T_{ref}\right)\right)\left[\delta_p \nabla(\varphi p_{sat})\right]\right] \\ &+ \nabla\left[c_l\left(T - T_{ref}\right) D_l \nabla(\varphi)\right] \end{aligned} \tag{2}$$

In these equations, $\xi\varphi$ [kg.m$^{-3}$] is the hydric capacity $\xi\varphi = \rho_0.du/d\varphi$ with u [kg/kg] the moisture content and $\rho_0$ [kg.m$^{-3}$] the density of the dry material. $\delta p$ [kg.m$^{-1}$.s$^{-1}$.Pa$^{-1}$] is the vapour permeability, $p_{sat}$ [Pa] the saturated vapour pressure, $D_l$ [kg.m$^{-1}$.s$^{-1}$] the liquid conduction coefficient, $T_{ref}$ [K] the reference temperature (equal to 296.15 K), $c_v$ [J.kg$^{-1}$.K$^{-1}$] and $c_l$ [J.kg$^{-1}$.K$^{-1}$] the specific heat capacity of respectively vapor and liquid water, c* [J.kg$^{-1}$.K$^{-1}$] the equivalent specific heat capacity of the moist material, $\lambda$ [W.m$^{-1}$.K$^{-1}$] the thermal conductivity of the moist material and $l_v$ the latent heat of evaporation ($2.45.10^6$ J.kg$^{-1}$ at the reference temperature of 296.15 K). Neumann boundary conditions are implemented. Heat transfer coefficients are fixed or calculated by a set of usual correlations under the hypothesis of an isothermal rough plate submitted to natural convection (Incropera et al. 2007). The surface of hemp concrete is rough increasing surface exchange. For hemp concrete, a

roughness coefficient of 2 gives a good estimation of the surface exchange (Aït Oumeziane 2013). Mass transfer coefficients are deduced from the Lewis relation (Lewis 1922). The governing system of strongly coupled unsteady differential equations is implemented in Matlab with a finite differences method. The model was benchmarked against the international benchmark HAMSTAD WP2 (Hagentoft et al. 2004). The exercises of this benchmark are suited to assess the performance and accuracy of hygrothermal models in one dimensional configuration for multi-layered wall submitted to relative humidity, temperature or total pressure gradients. The model was validated against all the test cases of the benchmark in Aït Oumeziane et al. (2011).

### 2.2 Hysteresis Model

At a given relative humidity φ, hysteresis results in more or less differences between the equilibrium moisture content u obtained during adsorption or desorption. Three main groups of hysteresis models can be found in literature. Phenomenological hysteresis models based on the ink bottle concept were developed by Mualem (1974). This group of models has been improved by successive studies giving more accurate results by considering the phenomenon of blockage against air (and water) entry (Mualem 1984, 2009). A second approach proposed by Scott et al. (1983) describes the scanning curves with the same shape parameters as those for the main adsorption and desorption curves. Empirical models like Pedersen's model use the weighted values of the hydric capacity to model scanning curves (Pedersen 1990). Comparisons between experimental results show that among the investigated models, Huang's hysteresis model (Huang et al. 2005) is the most suitable to represent the hydric behavior of hemp concrete (Aït Oumeziane 2013) (Aït Oumeziane et al. 2014). This hysteresis model is based on the knowledge of the main adsorption and desorption curves respectively built from the dry to the saturated state and from the saturated to the dry state. Equations (3) and (4) respectively describe the adsorption and desorption scanning curves after a series of alternating processes of desorption and adsorption:

$$u(\varphi, i) = u_r(i) + (u_s(i) - u_r(i)) \frac{u_{ads}(\varphi)}{u_{sat}} \tag{3}$$

$$u(\varphi, i) = u_r(i) + (u_s(i) - u_r(i)) \frac{u_{des}(\varphi)}{u_{sat}} \tag{4}$$

where $u_r(i)$ and $u_s(i)$ are respectively the residual and saturated moisture contents of the scanning curve indexed i. The main adsorption and desorption curves give residual and saturated moisture content values at order 0: $u_r(0) = 0$ and $u_s(0) = u_{sat}$. The calculation of these parameters is based on the perfect closure of the scanning curve at reversal points. Scanning curve indexed i includes the last reversal point ($\varphi_i$, $u_i$) and the penultimate reversal point ($\varphi_{i-1}$, $u_{i-1}$). Calculating $u_r(i)$ and $u_s(i)$ finally leads to solve a linear system of two equations. In a theoretical framework, main adsorption and desorption curves are physical bounds of sorption process in a range between 0% and 100% RH. In this paper, Van Genuchten (VG)'s is used to model these curves (Van Genuchten 1980). Other equation can be preferred.

$$u(\varphi, i) = u_r(i) + (u_s(i) - u_r(i)) \frac{u_{des}(\varphi)}{u_{sat}} \quad u_j(\varphi) = u_{sat} \left[ \left( 1 + \left| \alpha_j \frac{RT}{M_l g} \ln(\varphi) \right|^{\eta_j} \right)^{-\left(1 - \frac{1}{\eta_j}\right)} \right] \tag{5}$$

where $u_{sat}$ [kg/kg] is the saturated moisture content (calculated using the value of the open porosity), R [8.314 J.mol$^{-1}$.K$^{-1}$] the ideal gas constant, Ml [0.018 kg.mol$^{-1}$] the molar water mass, g [9.81 m$^2$.s$^{-1}$] the gravity acceleration and T [296.15 K] the reference temperature. As it is often the case for porous materials, the model parameters $\alpha$ and $\eta$ are derived to fit the experimental data. Index j indicates which sorption process is considered, adsorption or desorption. Usually, the dry state is experimentally achieved drying samples under vacuum in silica gel. Even if silicate gel monitors ambient air at 2–3% RH, the corresponding moisture content at this value is equivalent to one at 0%. To model the main adsorption curve, the parameters $\alpha_{ads}$ and $\eta_{ads}$ are derived to fit the experimental adsorption.

### 2.3 Numerical Tool

The developed numerical tool included database for materials or possibility to enter new material data. Required data include evolution of thermal conductivity and heat capacity with water content, principal sorption curves, moisture permeability and liquid diffusion (Fig. 1). 1D simulation is realized introducing hydrothermal conditions and thermal exchange parameter on the two face of a mesh. The computing time step duration must be adjusted by the user to ensure de accuracy of the results. The outputs of the numerical tool consist in the evaluation of the moisture content distribution inside the studied sample versus time. The Fig. 2 presents some results obtained exposing a sample of hemp concrete to cyclic hygric evolution of the external environment to simulate the case of Moisture Buffer Value test (MBV test) in accordance with the Nordtest protocol (Rode 2005). The experimental set up is described in details in (Collet et al. 2013).

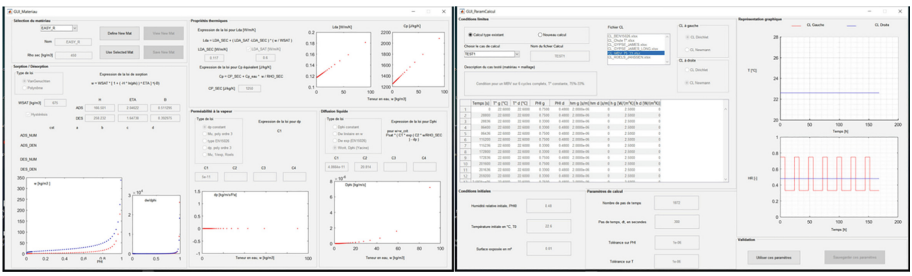

**Fig. 1.** Screenshot of the numerical tool interface for material selection in the database. Screenshot of the interface for boundary conditions entry.

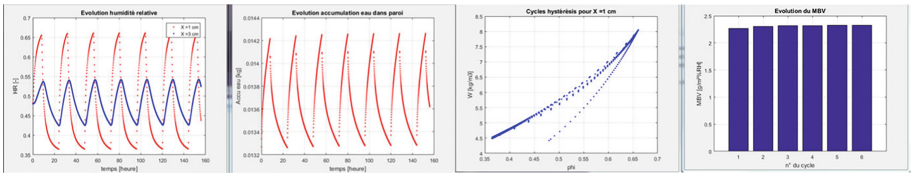


**Fig. 2.** Example of outputs of the numerical tool: evolution of relative humidity inside the studied sample (for different positions), cumulate moisture content, evolution of the intermediate sorption curves, evolution of Moisture Buffer Value (MBV).

## 3 Adjustment of Hysteresis Phenomenon

The material database of the numerical tool was initiated with experimental results obtained with various types of hemp concretes. As example, hysteresis on sorption curves is presented for two hemp concretes (HC1 and HC2). Both hemp concrete have the same mix design with a weight ratio of hemp shiv and lime-based binder of about 2/3. HC1 and HC2 differ in bulk density because of the heterogeneity of compaction: $\rho HC1 = 450\ kg.m^{-3}$ and $\rho HC2 = 396\ kg.m^{-3}$. All details regarding the measurement of physical and hygrothermal characteristics are in (Chamoin 2013) and (Collet and Prétot 2014). Main adsorption and desorption curves of HC1 were investigated and Fig. 3 shows experimental measurements and hysteresis model adjustment. Portions of intermediate scanning curves are produced using experimental tests carried out to identify HC2 hemp concrete hysteresis behavior in current relative humidity range. The glass jar method was used to determine the sorption isotherm up to 81% RH and two sorption cycles in compliance with the EN ISO 12571 procedure. All samples were first dried under vacuum in silica gel at 23 °C to constant mass. After conditioning, samples were placed in glass jars above a saturated salt solution at 23 °C. The measurements were performed at four relative humidity levels: 23, 43, 53 and 81%. Then the samples were divided into two batches of 6 samples each. Six samples were taken stepwise from dry state to 23 and 53% RH to determine main adsorption isotherm data points. These samples were then taken stepwise from 53 to 23% RH and back to 53% RH to determine intermediate scanning curve data points (primary desorption and secondary adsorption). The other six samples were taken stepwise from dry state to 81% RH to determine main adsorption isotherm data point. These samples were then taken stepwise from 81 to 43 and 23% RH and back to 43 and 81% RH to determine intermediate scanning curve data points (primary desorption and secondary adsorption). The experimental results are presented in Fig. 3. HC2 has higher moisture content than HC1. This is due to the lower compaction of HC2. The compaction affects the pore structure of the material (HC2 has a higher open porosity than HC1) and modifies moisture storage. As expected, the slopes of the intermediate scanning curves are lower than the slope of the main adsorption curve. The hydric capacity of hemp concrete is significantly reduced during sorption cycles. These results confirm that hysteresis plays a significant role in the storage and release of moisture. The primary desorption curve is very close to the secondary adsorption curve. This suggests that the hydric capacity is mainly modified when a shift in adsorption/desorption occurs on the main curve. It

could be due to the low level of the higher relative humidity (81%). A cycle sorption at a relative humidity near asymptotic hydric behavior (for example 95% RH) would probably lead to significant differences. Reach the saturated state is quite impossible with hemp concrete then desorption curve is unaccessible. Generally, only experimental data of moisture contents between 0 and 97% RH are known. As the main adsorption curve is almost asymptotic at 100% RH, the corresponding moisture content at this value is significantly different from the moisture content at 97% RH. The experimental desorption curve 97–0% RH is usually considered as a main curve but it corresponds in practice to a primary desorption scanning curve. According to this assertion, an alternative approach is proposed (Aït Oumeziane et al. 2014): the parameters ($\alpha_{des}$, $\eta_{des}$) of the main desorption curve are calculated by fitting the experimental primary desorption curve 97–0% RH. This primary scanning curve (indexed 1) is given by Eq. 4. The last reversal point is ($\varphi_1$ = 97%, u1 = $u_{ads}$ (97%)). The penultimate reversal point is ($\varphi_0$ = 0%, $u_0$ = $u_{ads}$(0%)). The least squares method is used to fit the models to the experimental desorption curve of 97–0% RH. Once main adsorption and desorption curves are fitted to experimental data, any scanning curve can then be modelled using hysteresis models. Using this approach, the main adsorption and desorption curves were fitted to experimental data. The obtained parameters are listed in Table 1, and Fig. 3 provides the experimental data and the fitted main adsorption and desorption curves. In order to estimate the impact of hysteresis in a current relative humidity range, the primary desorption curve 81–23% RH for HC1 is also built in Fig. 3. Compared with the hydric capacity derived from the main adsorption curve, Huang's model decrease the hydric capacity by about 18%. For HC2 the experimental desorption curve (97–0%) was unknown. Then the parameters $\alpha_{des}$ and $\eta_{des}$ were fitted taking the experimental primary desorption curve 81−43−23% RH. These parameters are provided in Table 1. Figure 3 gives the experimental data, the fitted main adsorption and primary desorption 81−43−23% curves and the predicted primary desorption 53–23% RH and secondary adsorption 23−43−81% RH and 23−53% RH curves. All predicted (desorption as well as adsorption) scanning curves are in good agreement with the experimental data.

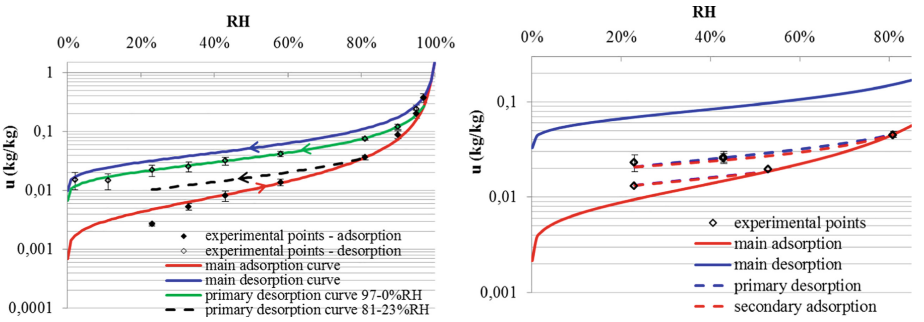


**Fig. 3.** HC1 and HC2 experimental and numerical (built with Huang's model) adsorption and desorption curves.

**Table 1.** Parameters of VG's model for HC1 and HC2

| Hemp concrete | Parameter | Values |
|---|---|---|
| HC1 | $u_{sat}$ | 1.5 kg/kg |
| | $\alpha_{ads}$ | 0.0119 |
| | $\eta_{ads}$ | 2.0462 |
| | $\alpha_{des}$ | 0.0185 |
| | $\eta_{des}$ | 1.6474 |
| HC2 | $u_{sat}$ | 1.805 kg/kg |
| | $\alpha_{ads}$ | 0.0319 |
| | $\eta_{ads}$ | 1.8096 |
| | $\alpha_{des}$ | 0.0151 |
| | $\eta_{des}$ | 1.4058 |

# 4 Comparison Between Numerical and Experimental Results

## 4.1 Simulation of MBV Test

The performance of the hysteresis model under transient conditions is analyzed using the MBV test. HC1 hemp concrete specimens are placed in a climatic chamber at 23 °C. Initially in equilibrium state at 50% RH, specimens sealed on all but one surface with aluminum tape are then submitted to daily cyclic hygric variations: 8 h at 75% RH and 16 h at 33% RH. The samples are weighted and the cycles are repeated until the weight variations become constant. Heat and mass transfer through sample is considered as one dimensional. Figure 4 provides experimental data and predicted evolution of the moisture mass during the hydric loading cycles for four numerical setups: model without hysteresis and hysteresis model using three assumed values of the initial moisture contents $u_{i,low}$, $u_{i,inter}$ and $u_{i,high}$. To underline the effects of hysteresis, numerical results without hysteresis were performed by using the main adsorption curve to model the evolution of the moisture content. During the test, the moisture mass globally decreases. Numerical predictions of hysteresis model using initial moisture contents $u_{i,low}$ and $u_{i,high}$ depict large deviations with experimental data. These curves at least give physical boundaries of the evolution of the moisture content, and as a consequence, the experimental results remain between both. Hysteresis model using initial moisture content $u_{i,inter}$ predicts numerical results in very good agreement with the experimental ones. Discrepancies between models without hysteresis and with hysteresis ($u_{i,inter}$) are negligible for the first cycles but become more significant for the last ones. In conclusion, hysteresis model with relevant initial moisture content assesses with more accuracy the moisture content of hemp concrete under transient conditions. The hysteresis model using $u_{i,inter}$ reduces the hydric capacity by 20% (compared to the model without hysteresis), which explain the better agreement with the experimental data.

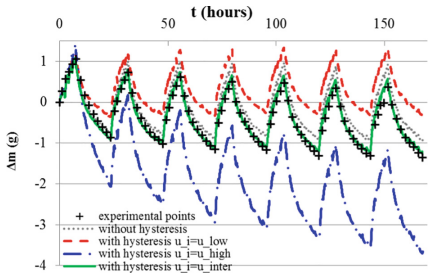


**Fig. 4.** HC1 experimental and numerical specimen masse changes during MBV tests.

### 4.2 Heat and Moisture Transfer in a Hemp Concrete Wall

An experimental study was performed to investigate at full scale the response of a hemp concrete wall submitted to transient hygrothermal conditions. The experimental setup of the wall is described in details in (Prétot and Collet 2012). A mixed wall built with 31 blocks of precasted hemp concrete and timber framework stands as the wall separation between two climatic rooms. The dimensions of the wall are 2.4 m × 2.1 m × 0.3 m. This wall is representative of a French typical house built with hemp concrete blocks. Climatic room 1 is able to set ambient air temperature between 18 °C and 27 °C and relative humidity between 30% and 60%, climatic room 2 temperature between −5 °C and 35 °C and relative humidity between 30% and 90%. Temperature and relative humidity sensors have been put inside the wall (at 4 different depths), at wall surfaces and in both surroundings to collect temperature and relative humidity variations. Before the beginning of the test, the wall is stabilized at 40% RH and 23 °C by keeping constant relative humidity and temperature in rooms 1 and 2. The mean values collected at the beginning of the test in the wall (time t = 0) are 41% RH and 23 °C. During the test, temperature is set to 23 °C in both rooms. Relative humidity in room 1 is set to 40% and relative humidity in room 2 varies between 30% and 80% imposing to the wall adsorption phase and desorption phase.

For numerical simulations, hemp concrete properties are identified (Aït Oumeziane 2013). Numerical initial conditions are fixed at 41% for relative humidity and at 23 °C for temperature. Unfortunately, the moisture history of the material is not known and the knowledge of moisture content is experimentally non accessible. Before the construction of the wall, hemp concrete blocks were stored and submitted to indoor hydric and thermal variations. Then the wall was submitted to continuous thermal and hydric variations during the successive tests before the selected test sequence. Due to the hysteretic behavior of hemp concrete, the initial moisture content at the beginning of the test sequence remains unknown. To discuss the influence of the initial moisture content, two cases are considered: low initial moisture content taken on the main adsorption curve at 41% RH and high initial moisture content taken on the main desorption curve at 41% RH. For low initial moisture content, two numerical runs are performed: in the first one the evolution of the moisture content is described by the main adsorption curve (without hysteresis) and in the second one by Huang's hysteresis model ($u_{i,low}$). For high initial moisture content ($u_{i,high}$), one numerical run is performed with the moisture

content described by the Huang hysteresis model. Moreover, a third hydric scenario is selected. It aims to simulate a possible moisture history known by the wall before the test sequence. In this scenario, both room 1 and room 2 temperatures are set to 23 °C. Relative humidity in room 1 is set to 41% whereas relative humidity in room 2 is set to 75% during 10 days then stabilized after a final stage at 41% RH during 30 days. At the beginning of the test sequence (time t = 0), the hydric pre-loading result in an initial moisture content gradient induced through the wall. Experimental and numerical results for relative humidity and temperature are presented at two depths from the room 1 side: at 22.5 cm (Fig. 5a) and at 7.5 cm (Fig. 5b). The effect of hysteresis on temperature distributions confirms the influence of moisture transfer on heat transfer. For low initial moisture content, temperature distributions with and without hysteresis are the same in adsorption phase. In desorption phase, figure shows that temperature is higher with hysteresis than without. In the studied test sequence, adsorption/desorption and evapo-condensation phenomena mainly govern the temperature variations during the successive sorption processes. Simulation of the hydric history improves the numerical results. If no significant differences are observed at 22.5 cm, the implementation of a hydric scenario provides simulated results in better agreement with experimental ones in areas close to the room 1 at 7.5 cm both for temperature and relative humidity evolutions. In comparison with the results of the previous simulations, the reduction of the hydric capacity and the higher moisture content level in the wall is not limited to the desorption stage but also occur during adsorption stage.

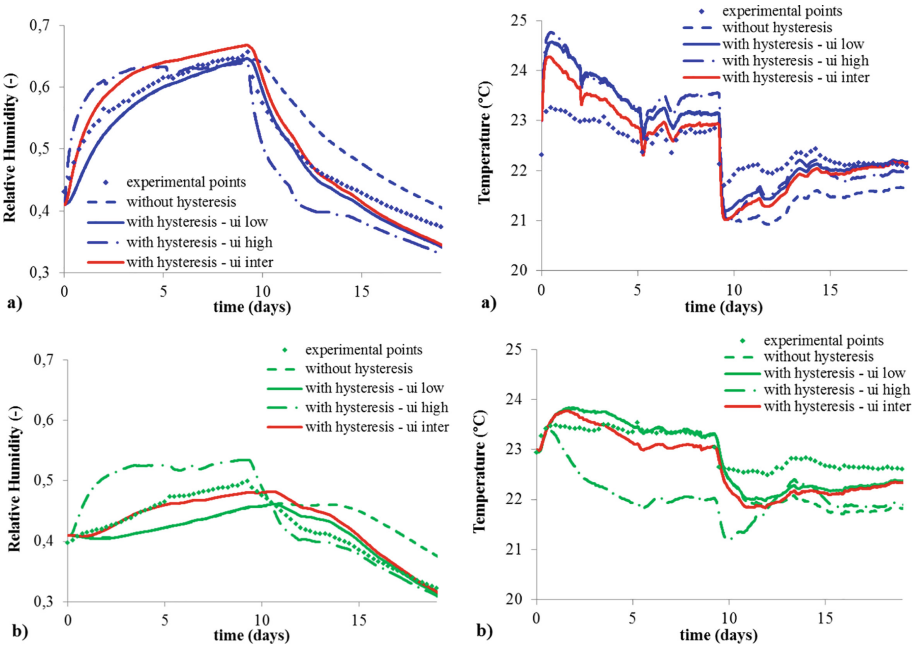


**Fig. 5.** Experimental and numerical relative humidity evolutions at depth 22.5 cm (a) and 7.5 cm (b) from the room 1 side.

## 5 Conclusions

This paper provides some examples of effect of the hysteresis sorption behavior of hemp concrete. This phenomenon affects the relative humidity and temperature distributions through the wall. The comparison of the experimental and numerical results highlights the relevance to consider hysteresis and shows the importance to identify the effective initial moisture content of the wall. By comparing experimental and numerical hygrothermal responses with and without hysteresis modeling, this study confirms that the simple use of the main adsorption curve is insufficient to describe the effective evolution of the moisture content. Considering hysteresis phenomenon with a model suited to the hemp concrete hydric behavior has significantly improved the numerical results. Furthermore, more accurate estimation of moisture storage improves both temperature and relative humidity in the wall. The better evaluation of the relative humidity distribution allows a better representation of vapor pressure gradients, driving force of heat transport by evaporation and condensation. Simulated temperature distributions are also in better agreement with experimental ones. The moisture content through the wall is also affected by the moisture history of the material. In this paper, simulating a relevant hydric history of the material gives relevant results on the full depth of the wall. Identifying the moisture content distribution through the wall seems thus necessary to predict the hygrothermal response of a wall submitted to climatic variations. Within this framework, numerical simulations are valuable tools. Finally, the hygrothermal modelling, taking into account the hysteretic behavior of hemp concrete, would allow accurate energy balance of the wall. It would highlight the effect of hydric behavior on this balance.

## References

Aït Oumeziane, Y.: Evaluation des performances hygrothermiques d'une paroi par simulation numérique: application aux parois en béton de chanvre [In French]. Ph.D thesis. INSA Rennes, France (2013)

Chamoin, J.: Optimisation des propriétés (physiques, hydriques et mécaniques) de bétons de chanvre par la maîtrise de la formulation [In French]. Ph.D. thesis. INSA Rennes, France (2013)

Künzel, H.M.: Simultaneous Heat and Moisture Transport in Building Components. Ph.D thesis. Fraunhofer IRB Verlag, Stuttgart, Germany (1995)

Lewis, W.K.: The evaporation of liquid into a gas. Trans. Am. Soc. Mech. Eng. **1849**, 325–340 (1922)

Mualem, Y.: A conceptual model of hysteresis. Water Resour. Res. **10**(3), 514–520 (1974)

Mualem, Y.: A modified dependent-domain theory of hysteresis. Soil Sci. **137**, 283–291 (1984)

Mualem, Y.: General scaling rules of the hysteretic water retention function based on Mualem's domain theory. Eur. J. Soil Sci. **60**, 652–661 (2009)

Pedersen, C.R.: Transient calculation on moisture migration using a simplified description of hysteresis in sorption isotherms. In: Proceedings of 2nd Nordic Symposium on Building Physics, Trondheim, Norway (1990)

Rode, C.: Moisture buffering of building materials. (2005) Report BYG DTU R-126, ISSN 1601–2917, ISBN 87–7877-195

Van Genuchten, M.T.: A closed-form equation for predicting the hydraulic conductivity of unsaturated soils. Soil Sci. Soc. Am. J. **44**, 892–898 (1980)

Amziane, S., Arnaud, L.: Bio-aggregate-based Building Materials, Applications to Hemp Concrete, ISTE Ltd Wiley, Inc.(2013)

Collet, F., Prétot, S.: Thermal conductivity of hemp concretes: variation with formulation, density and water content. Constr. Build. Mater. **65**, 612–619 (2014)

Prétot, S., Collet, F.: Experimental study of hygrothermal behavior of a hemp concrete wall (without and with coating). In: 2nd International Conference on Building Energy and Environment, Boulder, United States (2012)

Aït Oumeziane, Y., Bart, M., Moissette, S., Lanos, C., Prétot, S., Collet, F.: Hygrothermal behaviour of a hemp concrete wall: influence of sorption isotherm modelling. In: Proceedings of 9th Nordic Symposium on Building Physics, Tampere, Finland (2011)

Aït Oumeziane, Y., Bart, M., Moissette, S., Lanos, C.: Hysteretic behaviour and moisture buffering in hemp concrete. Transp. In Porous Media **103**, 515–533 (2014)

Collet, F., Chamoin, J., Prétot, S., Lanos, C.: Comparison of the hygric behaviour of three hemp concretes. Energy Build. **62**, 294–303 (2013)

Hagentoft, C.E., Kalagasidis, A.S., Adl-Zarrabi, B., Roels, S., Carmeliet, J., Hens, H., Grunewald, J., Kunk, M., Becker, R., Shamir, D., Adan, O., Brocken, H., Kumaran, K., Djebbar, R.: Assessment method for numerical prediction models for combined heat, air and moisture transfer in building components: benchmarks for one-dimensional cases. J. Therm Envelope Build Sci. **27**(4), 327–352 (2004)

Huang, H.C., Tan, Y.C., Liu, C.W., Chen, C.H.: A novel hysteresis model in unsaturated soil. Hydrol. Process. **19**(8), 1653–1665 (2005)

Incropera, F.P., Dewitt, D.P., Bergman, T.L., Lavine, A.S.: Fundamentals of Heat and Mass Transfer, 7th edn (2007)

Scott, P.S., Farquhar, G.J., Kouwen, N.: Hysteretic effects on net infiltration. Adv. Infiltration **83** (11), 163–170 (1983)

# Seismic Performance of Hollow-Core Composite Columns Under Cyclic Loading

Mohanad M. Abdulazeez and Mohamed A. ElGawady(✉)

Department of Civil, Architectural, and Environmental Engineering, Missouri University of Science and Technology, Rolla, MO 65409, USA
{mma548, elgawadym}@mst.edu

**Abstract.** This paper experimentally investigates the seismic behavior of a large-scale, hollow-core, fiber-reinforced, polymer-concrete-steel HC-FCS column under cyclic loading. The typical precast HC-FCS member consists of a concrete wall sandwiched between an outer fiber-reinforced polymer (FRP) tube and an inner steel tube. The FRP tube provides continuous confinement for the concrete wall, along the height of the column. The column is inserted into the footing and temporarily supported; then, the footing is cast in place around the column. The seismic performance of the precast HC-FCS columns was assessed and compared with previous experimental work. The compared column had the same geometric properties; but the steel tube was 25% thicker than the column that was tested in this study. This paper revealed that these HC-FCS column assemblies were deemed satisfactory by developing the whole performance of such columns and using that performance to provide excellent ductility with inelastic deformation capacity by alleviating the damage at high lateral drifts.

**Keywords:** Seismic performance · Composite columns · Hollow core · Fiber reinforced polymer · Cyclic loading · Energy dissipation

## 1 Introduction

The Federal National Bridge Inventory (FHWA 2013) classifies 63,522 bridges as "structurally deficient", 84,348 bridges as 'functionally obsolete" and many others as needing to be repaired, rehabilitated or replaced. Therefore, there is an urgent need for a rapid construction method to address this challenge.

Accelerating bridge construction (ABC) will reduce traffic disruptions and life-cycle costs as well as improve construction quality and safety, resulting in more sustainable development (Dawood et al. 2014). The use of precast concrete bridge elements is one strategy that can reduce on-site construction time, field labor requirements and traffic impacts. Precasting also improves the safety and quality of construction.

Recently, there has been a large and rapidly-growing interest in using fiber-reinforced polymer (FRP) tubes in construction as a replacement for the outer steel tube of the DSTCs column (Teng and Lam 2004; Teng et al. 2007). The proposed column is introduced as a hollow core FRP-Concrete-Steel (HC-FCS) column. The column consists of an inner steel tube and an outer FRP tube, with a concrete shell placed in between the two tubes (Fig. 1(a)). FRP fibers are oriented in the hoop direction to

© Springer Nature Singapore Pte Ltd. 2018
H. Tran-Nguyen et al. (eds.), *Proceedings of the 4th Congrès International de Géotechnique - Ouvrages -Structures*, Lecture Notes in Civil Engineering 8,
DOI 10.1007/978-981-10-6713-6_53

increase the concrete confinement and provide more shear resistance (Zhang et al. 2012). HC-FCS composite columns as a precast element have several advantages over conventional reinforced concrete or structural steel that can be delivered from the combination of all three-component materials. The concrete infill is confined by both FRP and steel tubes, which results in a triaxial state of compression that increases the strength and strain capacity of the concrete infill and enhances the seismic performance of such columns (Abdelkarim and ElGawady 2014; Abdelkarim and ElGawady 2015; Abdelkarim and ElGawady 2016; Abdulazeez et al. 2017).

The main objective of this study is to investigate the performance of HC-FCS columns under axial and static dynamic loads in the hope of achieving a robust column under inelastic cyclic deformations that is of high-quality and easy to construct.

## 2 Experimental Program

In this study, a 0.4-scale HC-FCS column, F4-24-E3(1.5)4, with an embedment steel tube length of 635 mm corresponding to 1.6 $D_i$ ($D_i$ is the inner diameter of the steel tube) was tested under a constant axial load and a lateral cyclic load. The F4-24-E3(1.5)4 column had a circular cross-section with an outer diameter of 610 mm and a clear height of 2,032 mm. The lateral load was applied at a height of 2,413 mm with a shear span-to-depth ratio of approximately 4.0. The column consisted of an outer filament-wound GFRP tube with a constant thickness of 9.5 mm, along the height of the column. The inner steel tube had an outer diameter of 406 mm and a thickness of 4.8 mm. A concrete wall with a thickness of 102 mm was sandwiched between the steel and FRP tubes (Fig. 1(a)).

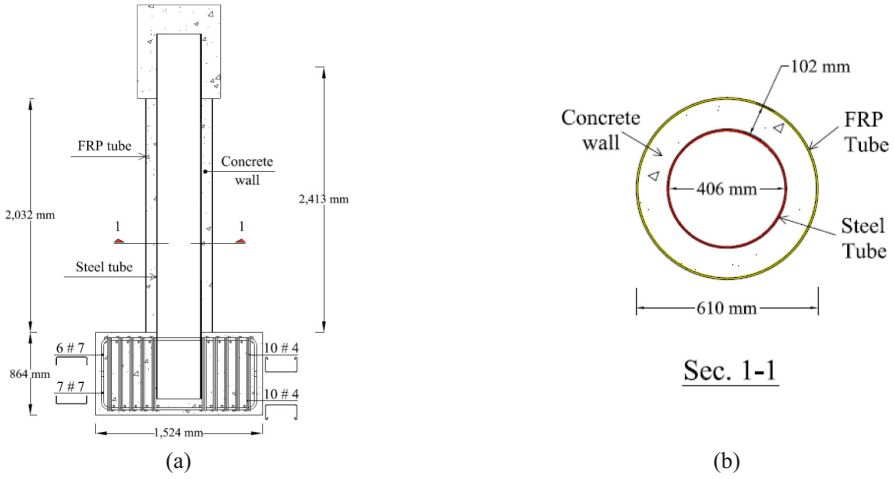


**Fig. 1.** Construction layout of the column (a) elevation, (b) column cross-section

The columns' label used in the current experimental work consists of four segments. The first segment is a letter F referring to the flexural testing followed by the column's height-to-outer diameter ratio ($H/D_o$). The second segment refers to the column's outer diameter ($D_o$) in inches. The third segment refers to the GFRP matrix using E for epoxy base matrices; this is followed by a GFRP thickness of 1/8 in. (3.2 mm), steel thickness of 1/8 in. (3.2 mm) and concrete wall thickness of one inch (25.4 mm).

The concrete footing that was used in this study was 1,524 mm long × 1,220 mm wide × 864 mm deep with bottom reinforcements of 7-#7, top reinforcements of 6-#7 and a shear reinforcement of #4 @ 64 mm (Fig. 1). The steel cage of the footing was installed into the formwork. The construction steps are: (1) preparing and installing the reinforcement cages of the footings, (2) installing the steel tube inside the footing cage with an embedded length of 635 mm, (3) pouring the concrete of the footing (Fig. 2(a)), (4) installing the GFRP tube and pouring the concrete of the column (Fig. 2(b)) and (5) installing the reinforcement cage of the column head and concrete pouring to finally get the HC-FCS column (Fig. 2(c)). The mechanical properties of the steel tube and rebar are summarized in Table 1. The rebar properties are based on the manufacturer's data sheet, while the steel tube properties were determined through tensile steel-coupon testing according to ASTM A 1067 (2012). The concrete mix design is shown in Table 2. Pea gravel with a maximum aggregate size of 9.5 mm was used for the concrete mixtures. Table 3 summarizes the unconfined concrete strength for the footings and columns. The material properties of the glass FRP tubes are presented in Table 4.

**Fig. 2.** Constructing procedure (a) footing casting aroung the inner steel tube; (b) placing the FRP tube and pouring the concret wall; (c) the HC-FCS column

**Table 1.** Steel properties of the rebars and steel tube

| | Elastic modulus (E, GPa) | Yield stress ($f_y$, MPa) | Ultimate stress ($f_u$, MPa) | Ultimate strain ($\varepsilon_u$, mm/mm) |
|---|---|---|---|---|
| Steel rebar | 200 | 413.7 | 620.5 | 0.08 |
| Steel tube | 200 | 399 | 441 | 0.22 |

**Table 2.** Concrete mixture proportions

| w/c | Cement ($kg/m^3$) | Fly ash ($kg/m^3$) | Water ($kg/m^3$) | Fine aggregate ($kg/m^3$) | Coarse aggregate ($kg/m^3$) |
|---|---|---|---|---|---|
| 0.5 | 350 | 101 | 225 | 848 | 848 |

**Table 3.** Summary of the unconfined concrete strength of the columns and the footings

| | F4-24-E3(1.5)4 | | F4-24-P324 | |
|---|---|---|---|---|
| | Column | Footing | Column | Footing |
| $f'c$ at 28 days (MPa) | 35 | 55 | 32.6 | 36.6 |
| $f'c$ day of test (MPa) | 46.5 | 56.7 | 36 | 39 |

**Table 4.** FRP tubes properties

| Elastic modulus (GPa) | Hoop elastic modulus (GPa) | Axial ultimate stress (MPa) | Hoop rupture stress (MPa) |
|---|---|---|---|
| 4.7 | 21 | 83.8 | 276.8 |

## 2.1 Experimental Set-up and Instrumentations

Sixteen Linear-Variable-Displacement-Transducers (LVDTs) and String Potentiometers (SPs) were assigned for measuring displacement along the tested column F4-24-E3 (1.5)4. A layout of the LVDTs and SPs is shown in (Fig. 3(a)). Four LVDTs were mounted on each of the north and south faces for the vertical displacement measurements at the potential plastic hinge region. Two more LVDTs were attached for measuring the uplift and sliding of the footing during the test. The effect of the footing

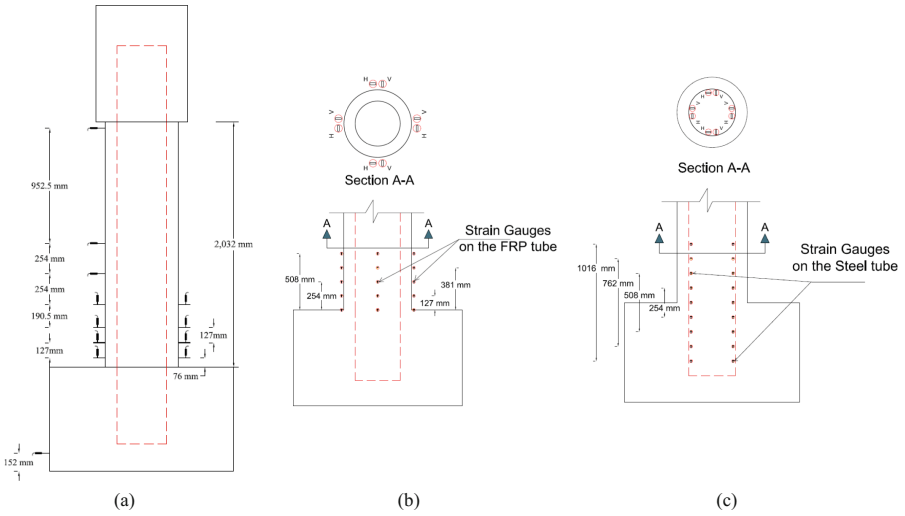


(a) (b) (c)

**Fig. 3.** Straing gauges layout: (a) LVDT's and SP's installing; (b) mounted on GFRP tube; and (c) mounted on steel tube

uplift and sliding were considered before calculating the lateral displacement and curvature of the column.

Forty strain gauges were installed on the FRP tube at five levels with 127 mm of space between them. Four horizontal and four vertical strain gauges were installed at each level as shown in (Fig. 3(b)). Seventy-two strain gauges were installed inside the steel tube at seven levels with a spacing of 127 mm (Fig. 3(c)). Four horizontal and four vertical strain gauges were installed at each level here as well. A high-definition webcam was hung vertically inside the steel tube at 635 mm from the top of the footing level.

## 2.2 Loading Protocol and Test Setup

The constant axial load, P, of 489.3 kN corresponds to 5% of the axial load capacity of the equivalent RC-column, $P_o$, and has the same diameter. A 1% longitudinal reinforcement ratio was applied to the column using six external prestressing strands (Fig. 4(a)). The $P_o$ was calculated using Eq. 1 (AASHTO-LRFD 2012):

$$P_o = A_s F_y + 0.85(A_c - A_s) f'c \tag{1}$$

Where $A_s$ = the cross-sectional area of the longitudinal steel reinforcements, $A_c$ = the cross sectional area of the concrete column, $F_y$ = the yield stress of the longitudinal steel reinforcements, and $f'c$ = the cylindrical concrete's unconfined compressive stress. The prestressing strands were supported by a rigid steel beam atop the column and the column's footing. The prestressing force was applied using two servo-controlled jacks to keep the prestressing force constant during the test.

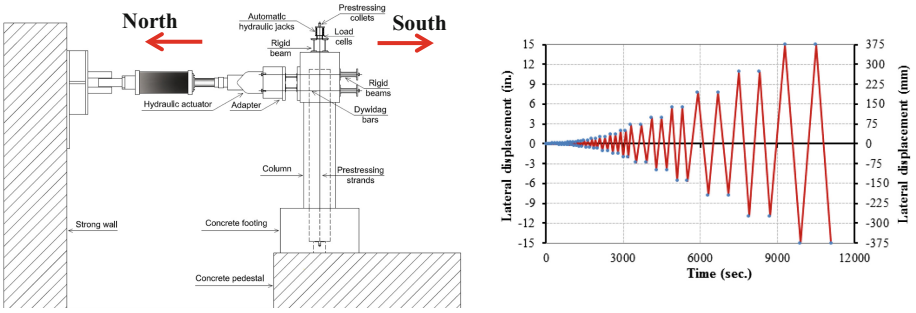


**Fig. 4.** (a) Layout of the test setup; (b) lateral displacement loading regime

After applying the axial load, the cyclic lateral load was applied in a displacement control using two hydraulic actuators connected to the column loading stub. The loading regime is based on the recommendations of FEMA in 2007 where the displacement amplitude $a_{i+1}$ of the step i + 1 is 1.4 times the displacement amplitude of the proceeding step (ai). Two cycles were executed for each displacement amplitude.

Figure 4(b) illustrates the loading regime of the cyclic lateral displacement. Each loading cycle was applied in 100 s., corresponding to a loading rate which ranged from 0.254 mm/s to 1.27 mm/s.

## 3 Results and Discussions

The moment-lateral drift plot is shown in (Fig. 5(a)). The lateral drift ($\delta$) was calculated by dividing the lateral displacement, which was measured from the actuators' displacement transducers by the shear span of 2,413 mm. The moment (M) at the base of the column was obtained by multiplying the force measured by the actuators' loading cells by the column's height of 2,413 mm. Figure 5(a) and Table 5 illustrate the comparison between the cyclic response of the two columns F4-24-E324 and F4-24-E3(1.5)4. As shown in the figure and the table, column F4-24-E3(1.5)4 displayed 7% less flexural strength at 680 kN.m and 35% less maximum lateral drift at 8.4% compared to column F4-24-E324. Gradual stiffness degradation occurred beyond that until the end of the test. The stiffness degradation occurred because of the concrete damage inside the tube. The buckling of the steel tube led to the initiation of ductile tearing at 8.0% of the column-footing interface area and, thereby, the end of the test.

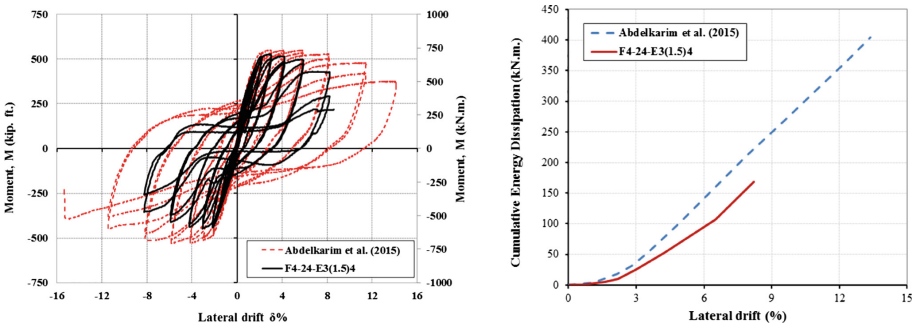


(a) (b)

**Fig. 5.** Moment vs. lateral drift for columns F4-24-E3(1.5)4 and F4-24-E324 (Abdelkarim et al. 2015a, b), (b) Cumulative energy dissipation vs. lateral drift for columns F4-24 E3(1.5)4 and F4-24-E324 (Abdelkarim et al. 2015a, b)

**Table 5.** Result Summary of the two tested columns

| Tested column | Moment capacity (kN.m) | Lateral drift at max. moment (%) | Lateral drift at failure (%) | Mode of failure |
|---|---|---|---|---|
| F4-24-E3(1.5)4 | 680.0 | 2.7 | 8.4 | Steel tube local buckling, concrete crushing, and steel tube ductile tearing |
| F4-24-E324 (Abdelkarim et al. 2015a, b) | 732.0 | 2.8 | 13.0 | Steel tube local buckling, concrete crushing, and FRP tube rupture |

For the investigated columns, the energy dissipation at each lateral drift was determined by the area enclosed in the hysteretic loop of the first cycle at this drift level. Dissipating higher hysteretic energy reduces the seismic demand on a structure. Figure 5(b) illustrates the relationship between the cumulative energy dissipation and the lateral drift for columns F4-24-E3(1.5)4 and F4-24-E324 that have been tested by Abdelkarim et al. (2015a, b). As shown in the figure, both columns dissipated the same level of energy until a drift of approximately 2.5% was reached. Beyond that, column F4-24-E3(1.5)4 dissipated a much smaller amount of energy due to the severe local buckling followed by the ductile tearing of the steel tube. At a drift of 8.4% when column F4-24-E3(1.5)4 failed, column F4-24-E324 dissipated 240% more energy.

## 4 Conclusions

This paper presents the experimental results of a hollow-core, fiber-reinforced, polymer-concrete steel (HC-FCS) precast column. The HC-FCS column consists of a concrete hollow cylinder sandwiched between an outer fiber-reinforced polymer (FRP) tube and an inner steel tube. The column had an outer diameter of 610 mm, an inner steel tube diameter of 406 mm and a height-to-diameter ratio of 4.0. The steel tube was embedded into reinforced concrete footing with an embedded length of 1.6 times the steel tube's diameter, while the FRP tube acted as a formwork, provided a continuous confinement for the concrete wall and was curtailed at the top surface of the footing. The column was subjected to constant a axial load and lateral cyclic load during this study and compared to the HC-FCS column that was tested by Abdelkarim et al. (2015a, b) under the same loading regime. The HC-FCS F4-24-E3(1.5)4 column failed at a drift of 8.4% due to the concrete wall crashing and the steel tube buckling, followed by ductile tearing at the column-footing interface level.

**Acknowledgement.** Missouri University of Science and Technology conducted this research with funding provided by Missouri Department of Transportation (MoDOT) and Mid-American Transportation Center (MATC). The contribution from ATLAS Tube is greatly appreciated. The discounts on FRP tubes from Grace Composites and FRP Bridge Drain Pipe are also appreciated.

## References

Abdelkarim, O.I., ElGawady, M.A.: Analytical and finite-element modeling of FRP-concrete-steel double-skin tubular columns. J. Bridge Eng. (2014)

Abdelkarim, O.I., ElGawady, M.A.: Concrete-filled-large deformable FRP tubular columns under axial compressive loading. Fibers **3**(4), 432–449 (2015)

Abdelkarim, O.I., ElGawady, M.A.: Behavior of hollow FRP–concrete–steel columns under static cyclic axial compressive loading. Eng. Struct. **123**, 77–88 (2016)

Abdelkarim, O.I., Gheni, A., Anumolu, S., ElGawady, M.A.: Seismic behavior of hollow-core FRP-concrete-steel bridge columns. In: Proceedings of Structures Congress 2015, pp. 585–596 (2015a)

Abdelkarim, O.I., Gheni, A., Anumolu, S., Wang, S., ElGawady, M.: Hollow-Core FRP-Concrete-Steel Bridge Columns Under Extreme Loading (2015b)

Abdulazeez, M.M., Abdelkarim, O.I., Gheni, A., ElGawady, M.A., Sanders, G.: Effects of Footing Connections of Precast Hollow-Core Composite Columns (2017)

Dawood, H., Elgawady, M., Hewes, J.: Factors affecting the seismic behavior of segmental precast bridge columns. Front. Struct. Civ. Eng. **8**(4), 388–398 (2014)

Teng, J., Lam, L.: Behavior and modeling of fiber reinforced polymer-confined concrete. J. Struct. Eng. **130**(11), 1713–1723 (2004)

Teng, J., Yu, T., Wong, Y., Dong, S.: Hybrid FRP–concrete–steel tubular columns: concept and behavior. Constr. Build. Mater. **21**(4), 846–854 (2007)

Zhang, B., Teng, J., Yu, T.: Behaviour of hybrid double-skin tubular columns subjected to combined axial compression and cyclic lateral loading (2012)

ASTM A1067/A1067M-12a: Standard specification for test coupons for steel castings. In: ASTM International, West Conshohocken, PA (2012). www.astm.org

AASHTO: AASHTO-LRFD Bridge Design Specifications – Customary US Units, 6th edn., Washington, D.C. (2012)

Federal Emergency Management Agency: Interim Testing Protocols for Determining the Seismic Performance Characteristics of Structural and Nonstructural Components. FEMA Report 461, Washington (2007)

# Semi-flexible Material: The Sustainable Alternative for the Use of Conventional Road Materials in Heavy-Duty Pavement

T. Nhan Tran[1(✉)], H.T. Tai Nguyen[1,2], K. Son Nguyen[3], and N.T. Huynh Nguyen[3]

[1] R&D Department, BMT Construction and Investment J.S.C., Ho Chi Minh City, Vietnam
nhantt@bmt-rnd.vn
[2] Department of Architecture and Civil Engineering, Thu Dau Mot University, Thu Dau Mot, Binh Duong Province, Vietnam
[3] Department of Materials Technology, Bach Khoa University, Ho Chi Minh City, Vietnam

**Abstract.** Semi-flexible material is a composite pavement surfacing that uses both asphalt concrete (AC) with a unique structure and Portland cement concrete (PCC) in the same layers. The AC introduced in this kind of pavement is initially designed with the air-void content in the range of 25–35%, while the grout of Portland cement is the mixture of Portland cement, silica fume, silica sand, water and a suitable amount of plasticity additive. The process of producing and pouring cement grout into AC layers is conducted when AC layers are totally cool down, which is estimated at least 24 h after finishing the last rolling. Semi-flexible material is believed to have a better rutting resistance compared to that of the conventional AC, this is resulted from the appearance of cement grout. Furthermore, joints are not required in this kind of pavement. As the results, the significant advantages of the material are the combinations of those of AC and PCC. In this paper, the authors intend to access the rutting and indirect tensile strength of this material. The applications of semi-flexible material in the pavements of airport, airfield, port, warehouse and other high traffic areas are feasible.

**Keywords:** Semi-flexible material · Grouted macadam · Cement grout · Asphalt concrete · Rutting resistance · Fatigue resistance

## 1 Introduction

Surface course is the upper layer of pavement structure playing a crucial role in carrying directly vehicles load and reducing load pressure on the sub-layers by spreading it over a large area. In addition, it must meet the strict requirements during its service life, for example: skid resistance, noise reduction, and high smoothness. Especially, the new constructed surface course ought to highly prevent water from penetrating into base courses or subgrade course, leading to the failure of pavement structure as a whole.

© Springer Nature Singapore Pte Ltd. 2018
H. Tran-Nguyen et al. (eds.), *Proceedings of the 4th Congrès International de Géotechnique - Ouvrages -Structures*, Lecture Notes in Civil Engineering 8,
DOI 10.1007/978-981-10-6713-6_54

In over the world, there have been many studies about materials which can provide surface course with characteristics mentioned previously. These materials are separated according to the used binders: organic binder (flexible material) and inorganic binders (rigid material). In their service life, however, there are a handful of drawbacks that should be properly researched and improved. Table 1 below shows some advantages and disadvantages of conventional road material using for surface course.

**Table 1.** The characteristics of popular road materials (Setyawan 2003)

| Road materials | Advantages | Disadvantages |
|---|---|---|
| AC (Flexible material) | High smoothness, and joint-less | Limited service life, worse load capacity |
| PCC (rigid-material) | High strength, good load capacity | Intense construction time, joint, cracking |
| Semi-rigid | High load capacity and smoothness | Cracking in PCC, reflection cracking, rutting in asphalt layer |

Semi-flexible material was first studied and coined in France in 1950s (Van de Ven and Molenaar 2004) with the main function of resisting the risk of oil spillage. The material was named commercially "Salviacim". After gaining some significant results, the material was subsequently widely used in The United Kingdom, South Africa, Japan and Australia, … as a complemented solution alongside with two conventional road materials—namely: AC and PCC. This is because this material provides surface course with a high smoothness, an improved load capacity compared to AC, without joints, and shortened curing time. It has the skeleton of asphalt concrete with the air-void content ranging from 25 to 35%, filled with highly flowable cement-based grout. At this air-void percentage range, grout is able to easily penetrate into AC's structure. If more than 35% of air-void content is applied, the more unstable after finishing paving of AC structure tends to become, and the final pavement is likely to be similar to PCC (Oliveira 2006). On the other hand, construction process is relatively sophisticated, and this material is most suited to low velocity areas. Further research, therefore, should take these into consideration and address these weak points or at least fully understand these problems to resist unexpected dilemmas in later constructions.

According to visual assessment of Anderton from 1987 to 2000, the semi-flexible material layer constructed in military areas with the depth of 5 cm, was loaded with heavy vehicles including tanks. He made valuable conclusions about its good rut resistance ability. However, he also observed that there was reflection cracking phenomenon in the areas with the lower layer was constructed with PCC (Anderton 2000).

In the thesis of doctor of philosophy, Oliveira emphasized the importance of load bearing capacity of underlying layers. He made a conclusion that the characteristics of surface layer during its service life significantly depend on the behaviors of lower layers (Oliveira 2006).

Semi-flexible was researched and implemented for its high rut resistance and smoothness. In recent years, there has been a trial project using semi-flexible material in Viet Nam, for example: Trung Luong–My Thuan express way (close to Binh Thuan

intersection). There has not been, however, any study demonstrating the rut resistance of this kind of material in the conditions of Viet Nam. In this research, the authors would like to provide two of fundamental characteristics of semi-flexible material—namely: Indirect tensile strength, and rut resistance.

## 2 Materials

### 2.1 Aggregate

Aggregate used in this study was obtained from the quarry of Tan Dong Hiep – Vietnam. Some of fundamental characteristics of the aggregate are showed in Table 2 below. The coarse aggregate was initially subjected to vertical shaft impact factor, which made the aggregate more angular. The more angular the coarse particles are, the more stable the interconnection between coarse particles is.

**Table 2.** Physical characteristics of the aggregate used in this research

| Properties | Standards | Results | Specification limits |
|---|---|---|---|
| Los Angeles abrasion (%) | ASTM C131 2003 | 17.20 | Max 30 |
| Flat and elongated particle (%) | ASTM D4791 2011 | $\leq 6$ | Max 10 |
| Compressive strength (MPa) | ASTM C170 1999 | 130 | Max 100 |
| Water absorption (%) | ASTM C127 2001 | 0.27 | Max 2 |
| Specific gravity of coarse aggregate (g/cm$^3$) | ASTM C127 2001 | 2.685 | – |
| Specific gravity of fine aggregate (g/cm$^3$) | ASTM C128 2009 | 2.696 | – |
| Specific gravity of filler (g/cm$^3$) | ASTM D854 2014 | 2.718 | – |

The gradation of the mixture contained a high proportion of coarse aggregate, which was larger than 60% by weight of aggregate. The aim of this was that the authors desired to design AC structure with the air void content of 25–35%. At the target air void content, the later AC layer will stay in stable condition for next stages, and grout easily flow into the skeleton of AC.

### 2.2 Binder

The binder implemented in this study was one type of neat bitumen graded 60/70. The proportion of bitumen was 3.0% by weight of the mixture, which was considered the optimal bitumen content for the studied gradation and aggregate. At the optimal content, binder covers successfully surface of aggregate, and strengthen the interconnections between coarse particles. Furthermore, a small content of cellulose fiber was used as a stabilizing additive to prevent bitumen at high temperature from draining off the mixture. Fiber chosen in this study was Topcel (CFF) with the content of 0.3% by weight of mixture to resist bitumen from the drainage phenomenon. The authors conducted the binder drainage test according to EN 12697-18 2007, the drain-down did

not appear in both mixtures containing and not containing fibers, this is due to the fact that the bitumen content is relatively low. But in the compacting process, in without-fiber mixture, there was an amount of binder draining off from the AC mixture which could reduce the continuity of the air void inside asphalt concrete structure, and the phenomenon could be determined visually on the surface of specimens, while AC with 0.3% cellulose fiber well performed in compaction process. This could be explained that the appearance of cellulose fiber absorbed an amount of binder at the high temperature and reduced effect of bitumen leaking caused by loading. Therefore, the asphalt mixture tended to be more stable. Some of characteristics of binder are given in Table 3 below.

**Table 3.** Characteristics of bitumen used in this study

| Properties | Standards | Results | Specification limits |
|---|---|---|---|
| Softening point (°C) (Ring and ball method) | ASTM D36 2000 | 48.7 | Min 46.0 |
| Penetration at 25 °C (/10 mm) | ASTM D5 2006 | 64.5 | 60.0–70.0 |
| Ductility at 25 °C (cm) | ASTM D113 2007 | >140(*) | Min 100 |
| Specific gravity at 25 °C | ASTM D70 2003 | 1.04 | 1.00–1.05 |

(*) The maximum dimension of the machine ruler is 140 cm

## 2.3 Grout Mixture

Grout is the mixture of Portland cement, silica fume, fly ash, fine sand, water and super plasticizer additive. While PC cement, silica fume and fine sand contribute to the strength of semi-flexible material, water and super plasticizer play a crucial part in creating a mixture that could easily penetrate into AC air void. The final grout had to meet the requirements of a grout mixture flowing quickly, and preventing itself from segregation. The grout has almost 45 to 60 min to fully penetrate into the AC layer before the workability of this fluid becomes too low. In addition, the overall strength of mixture ought to be guaranteed. The authors, therefore, evaluate and chose the optimal proportions of grout based on IDTS, rut resistance, and their ability to fill completely the whole depth. The IDTS at 25 °C of this grout after being cured 7 days in the cabinet at 27 °C and humidity of 95% is 1.1 MPa. The proportion of grout mixture is illustrated in Table 4.

**Table 4.** The proportion of grout mixture studied in this research

| Materials | Studied content (%) | Dosage (%) (by weight of mixture) |
|---|---|---|
| Portland cement (PC40) | 30–40 | 37 |
| Sand | 10–20 | 16 |
| Silica fume | 10–20 | 11 |
| Fly ash | 0–10 | 4 |
| Water | 20–30 | 28 |
| Super plasticizer | 2–4 | 4 |

# 3 Methods

## 3.1 Gradation Curve Design

As mentioned previously, whether or not the final air void content ranging from 25 to 35%, is mainly attributable to the percentages of mixed components. At this range of air-void content, the cement-base grout easily penetrates into AC layer and that the whole thickness of the layer is complete filled. The problem, therefore, is about how to design not only the suitable constituents of cementitious grout but also an AC skeleton which enable the designed grout to flow fully to the whole depth of the layer. The gradation curve of aggregate and proportion of AC in this study is shown in Table 5 below.

**Table 5.** The proportion of AC mixture

| Materials | References | Dosage (%) |
|---|---|---|
| Aggregate passing (Sieve size) | Anderton limit (%) | (by aggregate) |
| 19 | 100–100 | 100 |
| 12.5 | 54–76 | 71.7 |
| 9.5 | 38–60 | 59.7 |
| 4.75 | 10–26 | 14.2 |
| 2.36 | 8–16 | 8.9 |
| 0.6 | 4–10 | 4.8 |
| 0.075 | 1–3 | 1.1 |
| Bitumen (grade 60–70) (by total weight of mixture) | – | 3.0 |
| Cellulose fiber (by total weight of mixture) | – | 0.3 |
| Air-void content (by mass of compacted specimens) | 25–35 | 28.5–30 |

## 3.2 Laboratory Testing Methods

The fabrication and testing of this kind of material were divided into three main steps, these were:

**The First Step:** Aggregate was heated up and kept in the oven at 150 °C until the temperature of the mixture from bottom to the top of container rose up to 150 °C. The aggregate was later mixed with 0.3% of cellulose fibre. The additive was then torn apart and diffused in the mixture. After almost a minute, bitumen was poured into the initial mixture as the binder. Total time set for the mixing process was 2 min. The final AC mixture was subsequently stored in the oven at 130 °C until asphalt mixture obtained this temperature as a whole. Then, samples were fabricated in two forms, cylindrical samples and slabs according to the aims of test methods. In term of evaluating the indirect tensile strength, samples of 101.6 mm in diameter and 63.5 mm in high were used, while slabs of 320 × 260 × 60 $mm^3$ were fabricated to assess its rut resistance ability. The samples were kept at room temperature for 24 h before being moved to next stage.

**The Second Step:** Grout was only prepared when the samples totally cooled down. Both cylindrical samples and slabs had to be covered at sides and bottom with paper and plastic as the mold for grout pouring. The process of mixing grout and pouring it into skeleton of open graded AC lasted roughly 3 min for every sample (2 min for grout mixing, and a minute for pouring). The requirement was strictly controlled because of the water evaporation and the segregation of grout components. A grout mix was spread on the surface of the existing porous asphalt concrete with the aid of a rubber scraper. The authors used a steel rod to tap slightly the surface of AC, which functions as a slight steel roller activated the vibration mode. The process take place until bubbles did not appear and that the workability of grout was too low or grout was fully fill the whole depth of AC layer. The specimens were then cured in the cabinet at 27 °C and the humidity of 95% for two periods of time: 7 days, 14 days.

**The Third Step:** The cylindrical samples were placed in a room at the temperature of 25 °C for 4 h. Then they were subjected to the indirect tensile strength test (ASTM D6931 2012). The values of IDTS were calculated by the Eq. (1) as below:

$$IDTS = \frac{2P}{\pi Dh} \tag{1}$$

where P is maximum load that spits sample into two parts, D is diameter of cylindrical sample and h is high of sample.

The slabs were used to evaluate the rut resistance of semi-flexible material by means of Hamburg Wheel Tracking test device (EN 12697-22 2007). The parameters chosen to conduct this test were: (i) the temperature of testing was 70 °C; (ii) dry environment; (iii) rubber wheel, and; (iv) number of crossing was 40,000. The test took roughly 16 h to finish, and the rut depth was instantly recorded and plotted in a chart showing the relationship between rut depth and number of cycles at that point.

## 4 Results and Discusses

This study shows initial results of semi-flexible material, which are indirect tensile strength and rut resistance.

The indirect tensile strength of semi-flexible material with the specific condition of material in this research was 1.15 (MPa) at 25 °C after seven days of curing. This result is relatively similar to that of conventional AC.

The rut resistance of semi-flexible material, in the other side, was extremely higher than that of polymer modified asphalt concrete (PMAC). Figure 1 below shows the final rut depth and the relationship between rut depth and number of cycles at that point. The rut slope in final 10,000 crossings of semi-flexible material was $4 \times 10^{-3}$ mm/1,000 cycles, which is almost four times smaller ($14 \times 10^{-3}$) of PMAC. While PMAC is considered the optimal solution for surface courses due to their ability to resist permanent deformation, which is attributable to their polymer modified bitumen, semi-flexible material reduces greater than 2.5 times. Therefore, this is obviously a promising alternative.

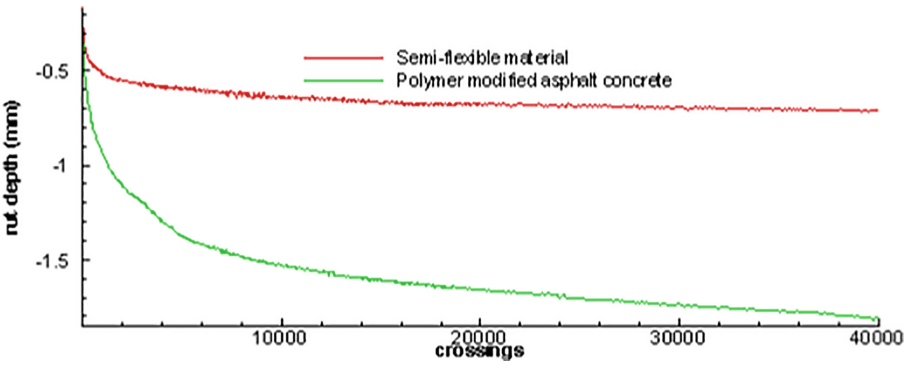


**Fig. 1.** Rut depth of semi-flexible material and PMAC.

While the result of rut depth was remarkable, there was a concern about cracking phenomenon due to the brittle nature of the grout. In fact, as can be seen in Fig. 2, the cracks appeared almost on the surface of wheel tracked part and the vicinity of this area where the material undergoes high stresses due to the wheel action.

**Fig. 2.** Crack phenomenon apprears on the tracked part.

## 5 Conclusions

The study provides practices in laboratory on fabricating samples, pouring grout into skeleton of AC. Although the number of test is limited, two main characteristics of semi-flexible material are demonstrated – namely high rut resistance and sensibility to cracking. That would be a promising solution for the problem of rutting on the high-traffic areas in Vietnam, but at the condition that cracking is well controlled. The study lacks evaluations in crack resistance of this material, especially fatigue crack. In further research, the authors would like to address this limitation and to improve grout in order to enhance both rut resistance and crack resistance.

## References

Anderton, G.L.: Engineering Properties of Resin Modified Pavement (RMP) for Mechanistic Design. ERDC/GL TR-00-2. U.S. Army Corps of Engineers, Vicksburg (2000)

ASTM Standard. ASTM C131: Resistance to Degradation of Small-Size Coarse Aggregate by Abrasion and Impact in the Los Angeles Machine. The American Society of the International Association for Testing and Materials (2003)

ASTM Standard. ASTM D4791: Standard Test Method for Flat Particles, Elongated Particles, or Flat and Elongated Particles in Coarse Aggregate. The American Society of the International Association for Testing and Materials (2011)

ASTM Standard. ASTM C170: Standard Test Method for Compressive Strength of Dimension Stone. The American Society of the International Association for Testing and Materials (1999)

ASTM Standard. ASTM C127: Standard Test Method for Specific Gravity and Absorption of Coarse Aggregate. The American Society of the International Association for Testing and Materials (2001)

ASTM Standard. ASTM C128: Standard Test Method for Density, Relative Density (Specific Gravity), and Absorption. The American Society of the International Association for Testing and Materials (2009)

ASTM Standard. ASTM D854: Standard Test Methods for Specific Gravity of Soil Solids by Water Pycnometer 1. The American Society of the International Association for Testing and Materials (2014)

ASTM Standard. ASTM D36: Standard Test Method for Softening Point of Bitumen (Ring-and-Ball Apparatus). The American Society of the International Association for Testing and Materials (2000)

ASTM Standard. ASTM D5: Standard Test Method for Penetration of Bituminous Materials. The American Society of the International Association for Testing and Materials (2006)

ASTM Standard. ASTM D113: Standard Test Method for Ductility of Bituminous Materials. The American Society of the International Association for Testing and Materials (2007)

ASTM Standard. ASTM D70: Standard Test Method for Specific Gravity and Density of Semi-Solid Bituminous Materials. The American Society of the International Association for Testing and Materials (2003)

ASTM Standard. ASTM D6931: Standard Test Method for Indirect Tensile (IDT) Strength of Bituminous Mixtures. The American Society of the International Association for Testing and Materials (2012)

EN Standard. EN 12697: Bituminous mixture-test method for hot-mix asphalt- Part 18: Binder drainage. European Standard (2007)

EN Standard. EN 12697: Bituminous mixture-test method for hot-mix asphalt- Part 22: Wheel tracking. European Standard (2007)

Oliveira, J.R.M.: Grouted macadam: mechanical characterization for pavement design. Ph.D. thesis, University of Nottingham, Nottingham, UK (2006)

Setyawan, A.: Development of semi-flexible heavy-duty pavements. Ph.D. thesis, University of Leeds, Leeds (2003)

Van de Ven, M.F.C., Molenaar, A.A.A.: Mechanical characterization of combi-layer. J. Assoc. Asphalt Paving Technol. **73**, 1–22 (2004)

# Shear Behavior of High Performance Concrete Beams Using Digital Image Correlation Technique

Touhami Tahenni[1(✉)], Mohamed Chemrouk[2], and Thibaut Lecompte[3]

[1] University Djilali Bounaama, Khemis Miliana, Algeria
t.tahenni@univ-dbkm.dz
[2] University of Sciences and Technology Houari Boumediene, Algiers, Algeria
mchemrouk@yahoo.fr
[3] University of Bretagne-Sud, Lorient, France
thibaut.lecompte@univ-ubs.fr

**Abstract.** Four-points bending tests were carried out on high performances concrete beams without stirrups and with stirrups, designed to consider shear behavior, and using digital image correlation technique (DIC). In the experimental device, the shear zone between the support and the loading point was digitized by high resolution camera. The numerical analysis of the recorded images is performed by Gom-Aramis software to obtain the deformation of concrete and to monitor the crack evolution in terms of width, spacing and length. The different models to determine the capacity of shear strength of reinforced concrete beams, used by the principal universal design codes such as the American ACI 318, the British Standard 8110, the European Eurocode 2 and the New Zealand NZS 3101, were extrapolated to high performance concrete to evaluate the applicability of these regulations originally developed for the ordinary concrete to the high performance concrete. The experimental results show that all the code models underestimate the shear contribution of high performance concrete and at the same time greatly overestimate the transverse reinforcement contribution. Among the four models, Eurocode 2 yields the best predictions of the ultimate shear strength of high performance concrete.

**Keywords:** Reinforced concrete · High performance concrete · Shear strength · Diagonal cracking · Ductility

## 1 Introduction

The shear behavior of high performance concrete (HPC) remains insufficiently explained comparatively to the abundant literature on ordinary concrete (OC). In the absence of consequent experimental results, the empirical design methods to determine the ultimate shear strength of reinforced concrete beams, developed for OC are extrapolated to HPC, and therefore needs more calibration. As a precautionary measure and especially because of insufficient understanding of the phenomenon of the shear

© Springer Nature Singapore Pte Ltd. 2018
H. Tran-Nguyen et al. (eds.), *Proceedings of the 4th Congrès International de Géotechnique - Ouvrages -Structures*, Lecture Notes in Civil Engineering 8,
DOI 10.1007/978-981-10-6713-6_55

behavior of reinforced concrete, the design calculations are always based on the maximum shear stress considered conservatively as distributed uniformly throughout the section of reinforced concrete beam. The internal parameters of the concrete contribution to the shear strength are not clearly identified according to their contribution. As a consequence of this lack of understanding, the universal design codes of reinforced concrete elements have completely divergent approaches to determine this solicitation by comparison with their convergent approaches to determine the solicitation of bending. This reflects a better understanding of the bending principle compared to that of shear. The present work would lead to recommendations with a view to improve the behavior of high performance reinforced concrete beams towards shear, and thus ameliorate the performances of the built environment to meet the requirements of a sustainable development. In particular, the risk of excessively wide cracking that might lead to durability problems at the longer term or even to premature collapses would be greatly reduced. It has been reported in the literature (Pendyala 2000, Johnson 1989, Cladera 2005) that high performance concrete is not highly resistant towards shear, because the cracks are relatively smooth and trans-granular, with no interlocking between the aggregates particles, indicating that the contribution of aggregates to the shear strength of the material is slightly reduced. In the absence of sufficient aggregate interlocking, the cracking of high performance concrete appears in the form of a straight fracture and widens up.

## 2 Experimental Program

### 2.1 Materials

There is no single branded procedure available for mix proportion for HPC, therefore careful selection of the materials is also effective in production of HPC (Khuntia 2001). The materials used in the concrete mixes were ordinary Portland cement, river rounded sand (0/4 mm), crushed gravel (4/15 mm), blast furnace slag, limestone fillers, potable tap water and high range water reducing admixture. Table 1 shows the mixture proportion for concrete.

**Table 1.** Mixture proportion for concrete (kg/m$^3$)

| Concrete | Cement | Slag (10%)* | Limestone filler (23%)* | Gravel | Sand | Water | Admixture (2.5%)* | W/C | Slump test (cm) |
|---|---|---|---|---|---|---|---|---|---|
| HPC | 382.5 | 38.25 | 88.0 | 1029 | 700 | 148.8 | 9.56 | 0.38 | 15 |

* By weight of cement

High yield deformed bars were used as reinforcement of beams, in diameters of 10 mm in the tension zone, 8 mm in the compression zone and 6 mm for the transverse stirrups with a constant spacing of 100 mm. The steel was characterized in a direct

tension machine to determine the Young's modulus and the elastic limit. An average Young's modulus of 204 GPa and an elastic limit of 500 MPa were obtained for the used reinforcement steel.

### 2.2 Test on Concrete Cylinder

The compressive strengths ($f_c$) and the tensile strength ($f_t$) of HPC (Table 2) used in making the beam specimens without stirrups and with stirrups were measured through the crushing and splitting tests of cylindrical concrete specimens of 80 × 160 mm dimensions, using a press with capacity of 500 kN. Measurements of the longitudinal compressive strains were carried out with the help of an extensometer and enabled the modulus of elasticity ($E_c$) to be worked out for the concrete.

**Table 2.** Average mechanical properties of concrete

| Concrete | $f_c$ (MPa) | $E_c$ (GPa) | $f_t$ (MPa) |
|---|---|---|---|
| HPC | 65.0 (± 3) | 42.6 (± 5) | 5.9 (± 1) |

### 2.3 Test on Reinforced Concrete Beams

A total of eight reinforced high performance concrete beams divided into two series were cast:

- One series of beams containing transverse reinforcement in the form of stirrups, noted HPC-S1.
- One series of beams without transverse reinforcement, noted HPC-S0.

Every series of beams consisted of four beam specimens to assess the repeatability and work on average values. All the beams had a constant rectangular cross section of 100 × 150 mm and a span length of 900 mm. The longitudinal tension reinforcement consisted of two high yield bars of 10 mm diameter placed with a clear concrete cover of 10 mm in the tension zone, giving an effective depth of 135 mm. This gives a tension steel ratio of 1.16%. The beams were tested in bending under two concentrated loads as shown in Fig. 1. The static scheme of the loading pattern results in a constant shear span of 300 mm, giving a constant shear-span/effective depth ratio of 2.2. The beam specimens were tested under monotonic static loading using a 250 kN servo-controlled hydraulic jack. One LVDT was attached to the bottom surface of the test beams at mid-span to measure the deflection. A high resolution video camera was used to detect the development of cracks, monitor the evolution of the diagonal cracks as the load was gradually increased and measure their widths. The system follows the movements of some reference points indicated beforehand in each beam as the load increases. The numerical analysis of the recorded images is performed by Gom-Aramis software to obtain the deformation of concrete and to monitor the crack evolution in terms of width, spacing and length.

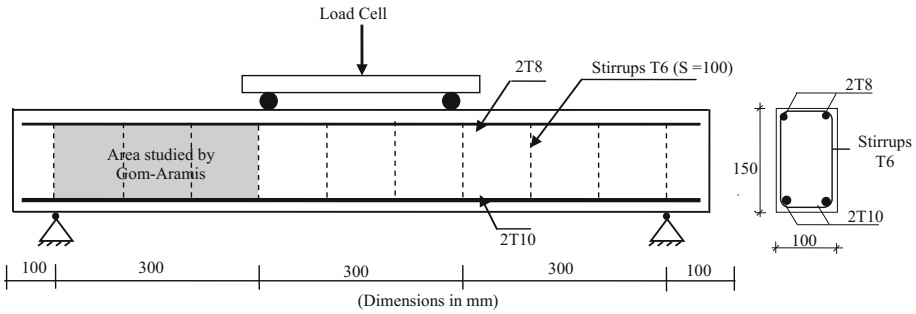


**Fig. 1.** Reinforcement of the beam and the flexural devise

## 3 Results and Discussions

### 3.1 Cracking and Modes of Failure of the Beams

On loading the HPC beams, vertical flexural cracks are the first to develop vertically in the tension zone at the maximum moment region. Before the occurrence of the inclined cracks, the effect of transverse reinforcement cans be considered negligible. With the increase of loading, from 60% to 70% of ultimate load, the diagonal cracks formed from a flexural crack within the shear zone in the direction of the support and the loading point. In some cases, the diagonal cracks formed independently of flexural cracks. The presence of the transverse reinforcements limits the development of diagonal crack with, and therefore prevents the shear failure of the beam. The diagonal crack would penetrate into the compression zone at the loading point and cause the crushing of concrete as shown in Fig. 2(a). This mode of failure is designated by shear-compression. The beams with transverse reinforcement showed no crack along the longitudinal reinforcements and have developed many diagonal cracks. In the series of the beams without transverse reinforcement, the mode of failure is characterized by the appearance of one diagonal crack within the shear zone, which forms in the direction of the support and the loading point independently of the flexural crack and by detachment of the concrete located below the longitudinal tension reinforcement. When this crack becomes sufficiently open, the failure was also by diagonal crack as shown in Fig. 2(b). This mode of failure is designated by shear. The diagonal cracks are inclined of about 45° with the longitudinal axis of the beam. The trajectory of the diagonal cracks seems to be straight and trans-granular with smooth crack faces. The Fig. 3 shows the modes of failure for all tested beams.

Table 3 below gives the experimental results of the first crack loads ($P_{cr}$), the diagonal cracking loads ($P_d$) and the ultimate loads ($P_u$) for all tested beams. The beams for which no values of the first crack loads and the diagonal cracking loads are given, have not been analyzed by Gom-Aramis software for absence of recording by the digital camera during the test. The presence of the transverse reinforcements retards the occurrence of the diagonal cracking and improves the resistance reserve of the beams beyond the diagonal cracking. An increase in the ultimate load varies of around 50% has been recorded for the beams with stirrups by comparison to those without stirrups.

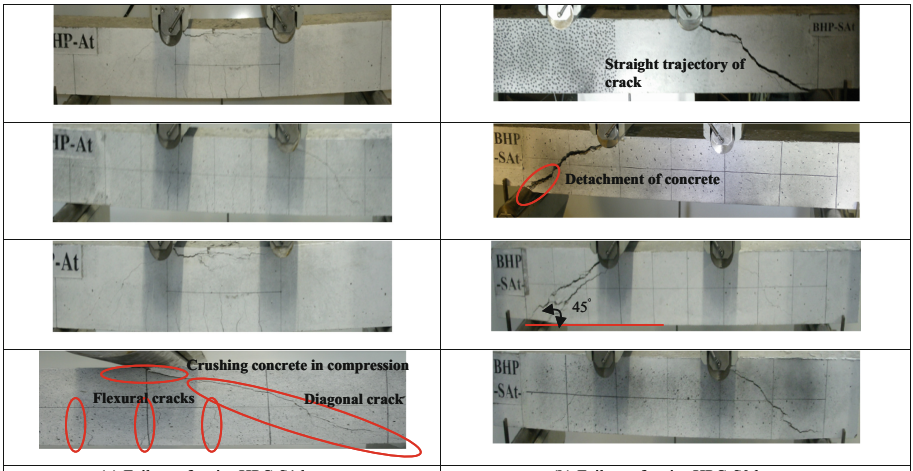


**(a)** Failure of series HPC-S1 beams (with stirrups)

**(b)** Failure of series HPC-S0 beams (without stirrups)

**Fig. 2.** Modes of failure of the test beams

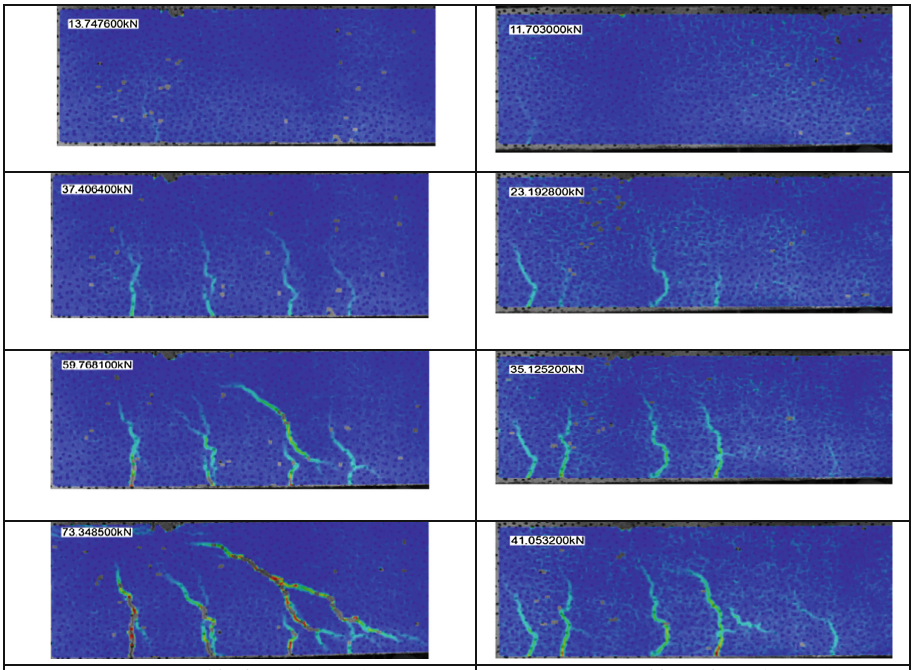


**(a)** Beams with stirrups (HPC-S1)

**(b)** Beams without stirrups (HPC-S0)

**Fig. 3.** A sequence of crack development within the shear zone of the beams, (Photos obtained by digitizing video Gom-Aramis)

**Table 3.** Diagonal cracking loads and ultimate loads of the tested beams

| Identification of beams | $f_c$ (MPa) | a/d | ρ (%) | $\rho_w$ (%) | $P_f$ (KN) | $P_d$ (KN) | $P_u$ (KN) | $P_d/P_u$ | Mode of failure |
|---|---|---|---|---|---|---|---|---|---|
| HPC-S0 | 64.8 | 2.2 | 1.16 | 0.00 | 16.93 | 49.77 | 58.59 | 0.85 | Shear |
| HPC-S1 | 64.8 | 2.2 | 1.16 | 0.56 | 17.56 | 63.70 | 85.14 | 0.79 | Flexion Shear-Compression |

a/d = shear span/effective depth ρ = longitudinal reinforcement ratio $\rho_w$ = transverse reinforcement ratio

Comparable results have been reported in the literature (Hamrat 2010a, Hamrat 2010b, Tahenni 2016a) on beams made of different strength of concrete ranging from 20 and 68 MPa. This shows that the effect of the transverse reinforcement is practically the same in any type of concrete.

A typical monitoring of a diagonal crack with the digital image correlation is shown in Fig. 3.

### 3.2 Load-Deflection Characteristics

The load-deflection curves of the test beams are shown in Fig. 4. It can be seen that the behavior of the beams with stirrups (HPC-S1) presents three main stages: a linear behavior, where the deflection is proportional to the load; this is the elastic stage up to the occurrence of the first crack. A second stage of linearity where the slope of the curve is slightly reduced under the influence of the first flexural crack. The deflection increases with the load but at a relatively higher rate. After full cracking and development of the cracks, beams without stirrups (HPC-S0) lose their rigidity and fail without undergoing further sufficient deflection compared to those containing stirrups

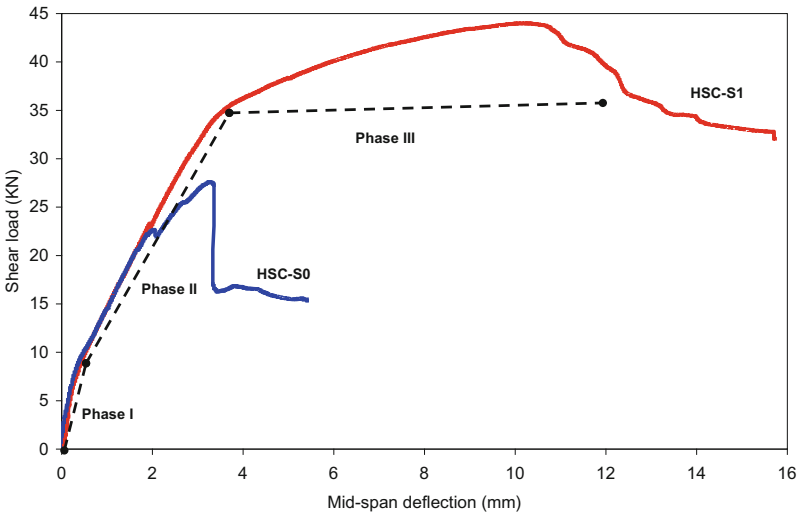


**Fig. 4.** Shear load versus deflection for the tested beams

(HPC-S1). A third stage where the non-linear deflection becomes more important until failure in relation to the load which remains almost constant; this corresponds to the plastic flow or plastic behavior of the concrete beam inducing important plastic deformations before failure. This behavior reflects a typical ductile behavior.

### 3.3 Comparison Between Test Results and Theoretical Predictions of the Shear Strength

In a reinforced concrete beam, it is generally accepted that the total ultimate shear force $V_u$ is resisted by the shear contributions across the compression zone $V_{cy}$, across the aggregate interlocking $V_{ay}$, and across the dowel action effect of the longitudinal steel $V_d$ and by the contribution of the transverse reinforcement $V_s$. This can be written as:

$$V_u = V_{cy} + V_{ay} + V_d + V_s \tag{1}$$

($V_{cy}$ + $V_{ay}$ + $V_d$) expresses the shear resistance of concrete $V_c$.

In HPC, however, it has been reported that the aggregate interlocking contribution to the shear resistance is considerably reduced (Hamrat et al. 2010a, Hamrat 2010b, Tahenni 2016a, Tahenni 2016b, Mphonde 1988). This is thought to be due to the nature of diagonal cracking, straight and trans-granular with smooth crack faces. On the contrary, the compression zone and the dowel action effect contributions to the shear resistance of HPC are both improved owing to the higher compressive strength of the material and the relatively better bond between the longitudinal reinforcement and concrete. It should be reported however, that these three shear components and their interaction are still not yet clearly defined and no analytical method unifying these three shear resistance parameters in a rational manner exists up to now. This explains the use of different empirical formulas in design throughout the world and justifies the on-going research on the topic. The main methods to determine the ultimate shear strength of reinforced concrete beams as given in the different universal design codes that have gained wider acceptance throughout the world, namely the American ACI 318 (2002), the British Standard 8110 (1997), the European Eurocode 2 (2004) and the New Zealand NZS 3101 (2006), are shown from Eqs. (2) to (5).

$$\text{ACI}\,318{-}02: \; V_u = \frac{1}{7}\left(\sqrt{f_c} + 120\rho\frac{d}{a}\right) b_w d + \frac{A_v f_{sv} d}{s} \tag{2}$$

$$\text{BS}\,8110{-}97: \; V_u = \frac{0.79}{\gamma_m}(100\rho)^{\frac{1}{3}}\left(\frac{400}{d}\right)^{\frac{1}{4}}\left(\frac{f_{cu}}{25}\right)^{\frac{1}{3}} \mathrm{b_w} d + 0.87\frac{\mathrm{A_v} f_{sv} d}{s} \quad \text{for a/d} \geq 2 \tag{3}$$

$$\text{Eurocode}\,2{-}04: \; \mathrm{V_u} = 0.18\left[\mathrm{k.(100.\rho\,.f_c)^{\frac{1}{3}}}\right] \mathrm{b_w d} + \frac{\mathrm{A_v f_{sv} z(\cot\theta + \cot\alpha)}}{\mathrm{s}} \sin\alpha \tag{4}$$

$$\text{NZS}\,3101{-}06: \; V_u = (0.07 + 10\rho)\sqrt{f_c} b_w d + \frac{A_v f_{sv} d}{s} \tag{5}$$

where, $f_c$ = cylinder compressive strength, d = effective depth of beam, a = shear span, $b_w$ = width of beam, $A_v$ = section of stirrup, $f_{sv}$ = yield strength of stirrups, s = stirrups spacing, $\rho = A_s/b_w d$, $f_{cu}$ = cube compressive strength, $\gamma_m$ = material partial safety factor for shear, taken as 1.25, $\alpha$ = inclination of stirrups ($\alpha = 90°$), $\theta$ = angle between inclined concrete struts and the main tension chord ($\theta = 45°$),

$$k = 1 + (200/d)^{1/2},\ d\,(\text{mm}), z = \text{lever arm} = 0.9d.$$

The ultimate shear strength of HPC beams is made up of a concrete contribution $V_c$ and a transverse steel contribution $V_s$. The beams of series HPC-S0 are not reinforced transversally and hence the ultimate shear strength of these beams is governed by that of concrete $V_c$. Figure 5 illustrates the values of the ultimate shear strength of series HPC-S0 beams. The ultimate shear strength of these beams is also predicted by the considered universal codes. The results show that all the code models underestimate the shear contribution of HPC. Among the four models, Eurocode 2 yields the best predictions, though still underestimating by around 25% the shear capacity of this highly performing concrete material. By comparison, the American ACI is the most conservative in predicting the ultimate shear capacity of HPC with a prediction of around 45% below the test values. This calls for a sustained effort to refine these models to faithfully reflect the HPC contribution to the shear resistance.

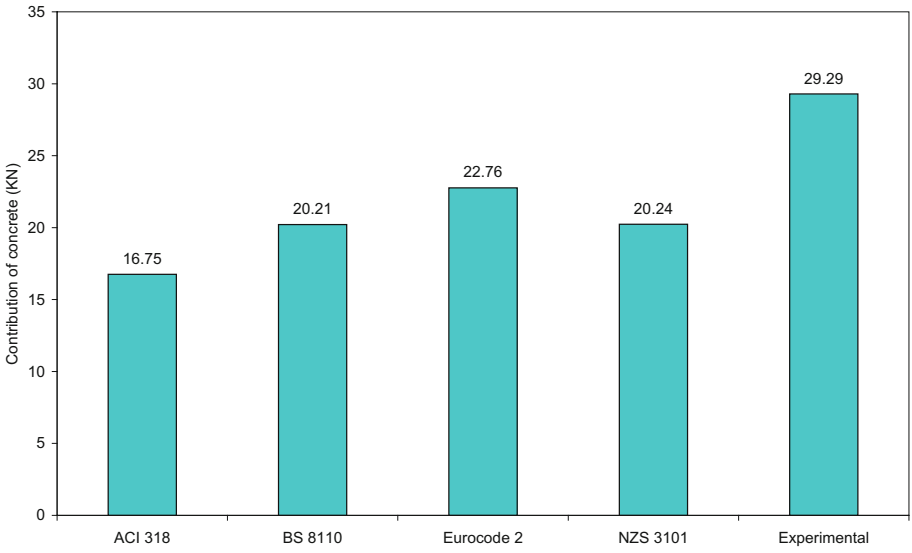


**Fig. 5.** Contribution of concrete to the shear strength, (Average ultimate shear strength of HPC-S0 beams)

The contribution of transverse reinforcement ($V_s$) to the shear strength of series HSC-S1 beams is also shown in Fig. 6 ($V_{s\text{-Test}} = V_{u\text{-HPC-S1}} - V_{u\text{-HPC-S0}}$). On average, the concrete contribution $V_c$ to the shear strength represents 70% of the total shear

capacity and the steel contribution $V_s$ 30%. Hence, the presence of the transverse reinforcement has improved the ultimate shear strength of HPC beams by around 30%. For comparison purposes, the contribution of the transverse reinforcement to the shear strength of HPC-S1 beams is predicted by the four considered code models. This transverse steel contribution to the shear strength is based on the Richter-Morsh analogy for the four considered universal codes and hence gives comparable values of $V_s$. It can be clearly seen that the code models greatly overestimate the transverse reinforcement contribution to the shear strength of HPC beams; the average overestimation is around 45% for the four code models considered. This is due to the fact that the transverse reinforcement contribution to the shear strength adopted in the four code models is based on the yielding of this reinforcement, as expressed by the code's formulas given above. In the presence of transverse reinforcement, failure by crushing of concrete in the inclined strut or at the compression zone immediately at the top of a diagonal crack is not considered by the Richter-Morsh truss analogy and hence not considered by these models. The transverse reinforcement contribution to the shear strength would be greatly overestimated when based on the yielding hypothesis of this transverse reinforcing steel; the present tests have shown that at failure, the transverse stirrups have not yet yielded. On adding up the concrete contribution and the steel contribution to the shear resistance of HPC beams, Eurocode 2 seems to give the best predictions for the ultimate shear strength of the four code models, though still unrealistic since underestimating the concrete contribution $V_c$ of HPC and greatly overestimating the transverse reinforcement contribution $V_s$. The four universal design codes require more refinement to reflect the real contributions of both concrete and transverse reinforcement to the shear strength of HPC material.

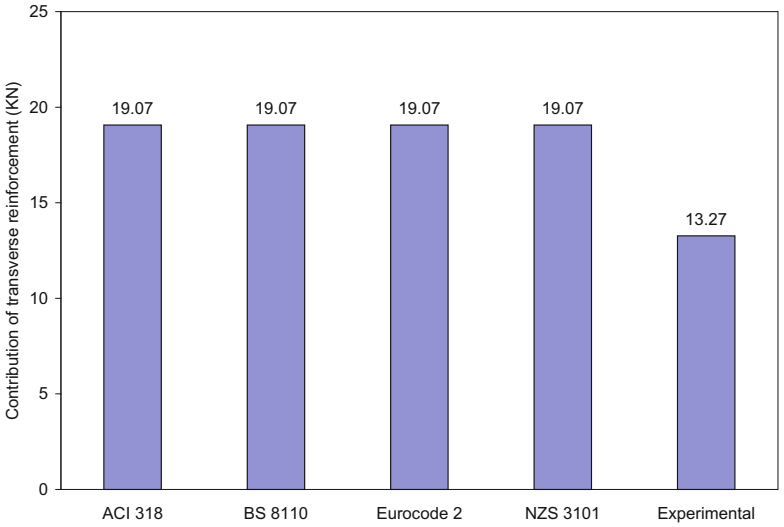


**Fig. 6.** Contribution of transverse reinforcement to the shear strength of HPC-S1 beams

## 4 Conclusions

From the present experimental work on the shear strength of high performance reinforced concrete beams, the following conclusions can be made:

- The mode of failure of HPC was sudden, expressing the brittleness of the concrete material.
- The HPC beams without transverse reinforcements exhibit a relatively fragile behavior.
- The presence of the transverse reinforcement improves the ductility of HPC beams. Such ductile structural behavior is particularly needed in seismically active regions to avoid any eventual brittle and catastrophic failure such as those which have occurred in many earthquake active parts of the world.
- The transverse reinforcements restrain efficiently the diagonal cracks and take up residual stresses beyond the cracking. In this sense, their formation is delayed and their width is very much contained and did not reach the serviceability limit of cracking which is equal to 0.3 mm, even at failure.
- The shear strength is increased with the addition of transverse steel, the increase varied of around 50% on average.
- The major universal codes underestimate the concrete contribution and overestimate the transverse steel contribution to the shear strength of HPC beams. These design codes need more refinement to reflect the improved shear capacity of HPC and to simulate effectively the shear contribution of the transverse reinforcement.

**Acknowledgments.** The work presented in this paper was sponsored by the Ministry of Higher Education and Scientific Research of Algeria within the framework of an international scientific research convention between the University of Sciences and Technology Houari Boumediene (USTHB), Algiers, Algeria and the University of Bretagne Sud (UBS), Lorient, France. The tests were carried out at Laboratory of Engineering of the Materials of Bretagne (LIMATB-Lorient). Also, Prof. Mohamed Chemrouk at USTHB and Dr. Thibaut Lecompte at UBS, are gratefully thanked for their willing discussion and active participation in the project.

## References

ACI Committee 318 Building Code Requirements for Structural Concrete (ACI 318-02) and Commentary (ACI 318R-02), Farmington Hills (2002)

BS 8110 Part1 Structural Use of Concrete, Code of Practice for Design and Construction, British Standards, Institution, London (1997)

Cladera, A., Mari, A.: Experimental study on high-strength concrete beams failing in shear. Eng. Struct. J. **27**, 1519–1527 (2005)

Eurocode 2 Part 1-1 Design of Concrete Structures, General Rules and Rules for Buildings, EN1992-1-1, R (2004)

Hamrat, M., Boulekbache, B., Chemrouk, M., Amziane, S.: Shear Behavior of RC Beams Without Stirrups Made of Normal Strength and High Strength Concretes. Adv. Struct. Eng. **13**(1), 29–41 (2010a)

Hamrat, M.: Structural behavior of high performances concrete (bending and shear). Doctoral thesis, University of Science and Technology Houari Boumediene, Algiers, Algeria (2010b)

Johnson, M.K., Ramirez, J.A.: Minimum shear reinforcement in beams with higher strength concrete. ACI Struct. J. **86**(4), 376–382 (1989)

Khuntia, M., Stojadinovic, B.: Shear strength of reinforced concrete beams without transverses reinforcement. ACI Struct. J. **98**(5), 648–656 (2001)

Mphonde, A.G.: Aggregate interlock in high strength reinforced concrete beams. In: Proceeding of the Institution of Civil Engineers, vol. 85 no. 3, pp. 397–413. Structural Engineering Group (1988)

National Standards of New Zealand NZS 3101-Part 1 Concrete Structures Standard; Standards New Zealand, Wellington, New Zealand (2006)

Pendyala, R.S., Mendis, P.: Experimental study on shear strength of high strength concrete beams. ACI Struct. J. **97**(4), 564–571 (2000)

Tahenni, T.: Study of the shear capacity of steel fibers reinforced concrete beams with a particular reference to high performance concrete beams. Doctoral thesis, University of Science and Technology Houari Boumediene, Algiers, Algeria (2016a)

Tahenni, T., Chemrouk, M., Lecompte, T.: Effect of steel fibers on the shear behavior of high strength concrete beams. Constr. Build. Mater. **105**, 14–28 (2016b)

# Study on Effect of Cornsilk Fiber in Cemented Soil Stabilization

Khiem Quang Tran, Tomoaki Satomi, and Hiroshi Takahashi(✉)

Graduate School of Environmental Studies, Tohoku University, Sendai, Japan
hiroshi.takahashi.b3@tohoku.ac.jp

**Abstract.** Fiber-cement stabilized soil is one of many methods for strengthening soil. However, the kind of fiber material used in this method plays an important role. So far, many researchers have studied on many kinds of fiber to stabilize soil such as rice straw, rice husk, pineapple leaf, banana leaf, etc. These fiber materials are abundant, cheap and easy to obtain from the agricultural field because most of them are discarded. Furthermore, the traditional way to dispose of agriculture waste is burning causing some environmental pollution problems. Therefore, the utilization and direct use of waste materials are of much benefit to environment and economy. Nowadays, corn is the third most cultivated crop in the world, so the by-product from corn such as cornsilk is redundant and easy to collect from the field. Hence, the present work aims to study the effect of new waste fiber material as raw cornsilk fiber in strengthening soil. This study uses the unconfined compressive test to evaluate the strength and strain of cemented soil and fiber-cemented soil. Soil used in this study is artificial soil, which is made of clay and silt with the ratio of 2:3, respectively. Cemented soil admixtures are made with cement contents of 30, 35, 40 kg/m$^3$. The effect of fiber content is studied in this study by changing the fiber content added to cemented soil admixtures at different levels of 5, 10, 15, 20, 25, 30 kg/m$^3$. The results of this study show that it is possible to utilize of cornsilk as fiber material in cemented soil stabilization.

**Keywords:** Soil stabilization · Fiber-cement stabilized soil · Fiber reinforced soil · Cornsilk fiber

## 1 Introduction

Nowadays, more and more constructions are built on soft soil because of lacking good land resources. In addition, weak or soft soil considered as a by-product is produced from many implementing underground construction works, dredging canal, and natural disasters. In Viet Nam, heavy rainfall usually occurs causing landslide frequently. When landslides occur, a large amount of soft soil or sludge is generated and this is an obstacle for prompt recovery. Moreover, the use of new materials such as mountain soils from other sites to restore those destroyed slopes is not good for economic and environmental aspect. For this reason, the recycling of soft soil at landslide places or construction works should be concerned.

© Springer Nature Singapore Pte Ltd. 2018
H. Tran-Nguyen et al. (eds.), *Proceedings of the 4th Congrès International de Géotechnique - Ouvrages -Structures*, Lecture Notes in Civil Engineering 8,
DOI 10.1007/978-981-10-6713-6_56

During past decades, many researchers have been studied on soil stabilization by various stabilizers such as fiber, cement, lime, rice husk ash, etc. (Negi et al. 2013; Shrivastava et al. 2014; Soundara and Senthil Kumar 2015). There are many reinforcement methods to stabilize soft soil. These methods have been considering the effect of chemical additives, compaction control, moisture control, etc. In Japan, a large amount of sludge was produced from huge tsunami disaster, which was generated by a big earthquake with the magnitude of 9.0 in 2011. A method named fiber-cement stabilized soil method was applied to recycle tsunami sludge. Satomi et al. (2014) used paper debris in strengthening sludge. However, the cost of paper debris material is increasing, so it is not economical when using paper debris to modify sludge. Hence, finding a local and cheap material is necessary to apply in fiber-cement stabilized soil method.

Cornsilk fiber is considered as a by-product from corn product and its yield every year is redundant because corn is the third most cultivated crop in the world. In Viet Nam, the price of cornsilk fiber is cheap and low recycling rate. In addition, cornsilk easily obtains from the cultivated field. If the cornsilk fiber is used as new material replacing for paper debris in fiber-cement stabilized soil method, it will bring in many benefits of economy and environment. However, the workability of cornsilk fiber in this method has been never studied yet, this paper researches on the effect of cornsilk fiber on soil stabilization by using fiber-cement stabilized soil method.

In summary, the objectives of this study are to investigate the performance of cornsilk fiber and cement in soil stabilization to apply for bank materials based on the concept of a new recycling system for high water content mud by using unconfined compression test.

## 2 Materials

Artificial sludge was used in this study because it was impossible to obtain the real sludge in Mekong Delta River, Viet Nam for the experiments carried out in Japan. Soil consisted of Kasaoka clay and silt with the ratio of 40:60 in dry mass, respectively. The artificial sludge was made by adding water of 50% by soil weight. Chemical and physical properties of soil are shown in Tables 1 and 2. Grain particle size of soil for making sludge is also shown in Fig. 1.

**Table 1.** Chemical properties of Kasaoka clay and silt

| Compound | Kasaoka clay (%) | Silt (%) |
|---|---|---|
| $SiO_2$ | 77.85 | 69.07 |
| $Al_2O_3$ | 12.88 | 20.22 |
| $Fe_2O_3$ | 2.08 | 5.46 |
| CaO | 1.88 | 0.91 |
| MgO | 0.28 | 0.807 |
| MnO | 0.072 | 0.027 |
| $Na_2O$ | 1.97 | 1.477 |
| $K_2O$ | 2.417 | 2.75 |

**Table 2.** Physical properties of imitation soil

| Properties | Values |
|---|---|
| Specific gravity | 2.47 |
| *Grain size* | |
| Gravel (%) | 0 |
| Sand (%) | 8.1 |
| Silt (%) | 83.5 |
| Clay (%) | 8.5 |
| *Atterberg limits* | |
| Liquid limit (%) | 46.1 |
| Plastic limit (%) | 29.4 |
| Plasticity index (%) | 16.7 |
| *Compaction parameters* | |
| Optimum moisture content (%) | 30.8 |
| Maximum dry unit weight (kN/m$^3$) | 12.85 |
| Unconfined compressive strength (kN/m$^2$) | 72.98 |
| *Soil classification* | |
| USCS | OL |
| AASHTO | A-7-6 |

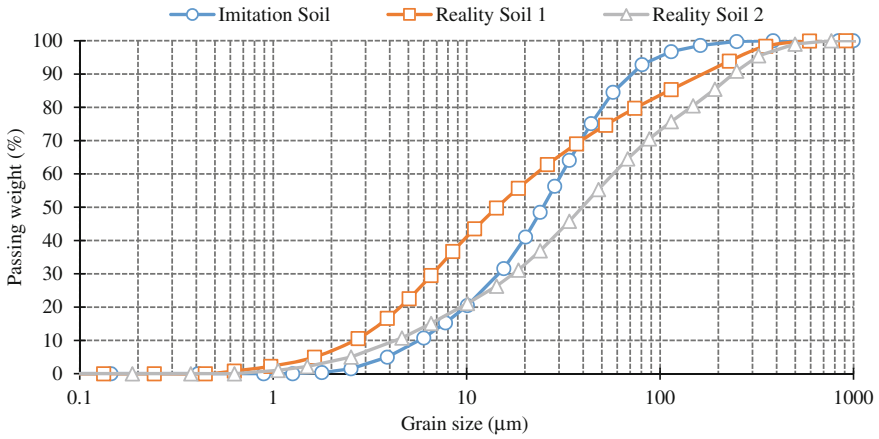


**Fig. 1.** Grain size distribution curve

Cornsilk fiber used in this study was provided by Thanh Binh Company, Viet Nam. It was washed with water to make it clean and then drying it in the drying oven at 40 °C. The average of fiber length and fiber diameter are 5.8 and 0.03 cm, respectively.

## 3 Experimental Procedure

According to the new recycling system of high water content mud (Mori et al. 2003); this study is based on this procedure to investigate the workability of cornsilk fiber. At first, the artificial sludge was made by mixing clay Kasaoka, silt, and water. After that, the cornsilk fiber was added to the sludge and mixed to get a uniform mixture. Finally, cement was added and mixed until getting a uniform mixture. The mixtures were cured for 3 days at 20 °C. This procedure is shown in Fig. 2.

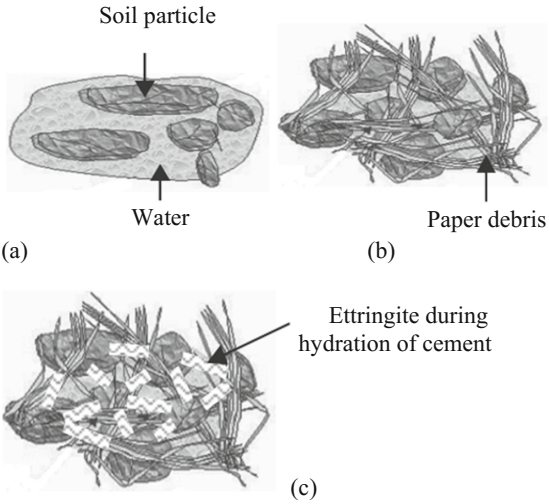


**Fig. 2.** Principles of fiber-cement stabilized soil method (Mori et al. 2003)

Modified soil was compacted following Japanese criteria. Experimental equipment to make specimens for unconfined compression test are mold and rammer. Mold is 10 cm in height and 5 cm in diameter. The weight and falling height of rammer are 1.5 kg and 20 cm, respectively. There are four layers to compact with the falling rammer times of 5, 10, 10, and 20, respectively. After compaction process, the specimens were covered with plastic film and put in the curing oven at 20 degree Celsius for 7 days. The unconfined compressive strength test according to ASTM D1633 was carried out to investigate failure strength and strain of specimens. A representative relationship curve between compressive stress and strain is shown in Fig. 3.

In this study, the water content of sludge was kept constant at 50% by weight of dry soil. The additive amount of fiber and cement are shown in Table 3.

In this present work, the target values of the failure strength and the failure strain were determined based on the previous studies (Mori et al. 2003; Satomi et al. 2014) as follows:

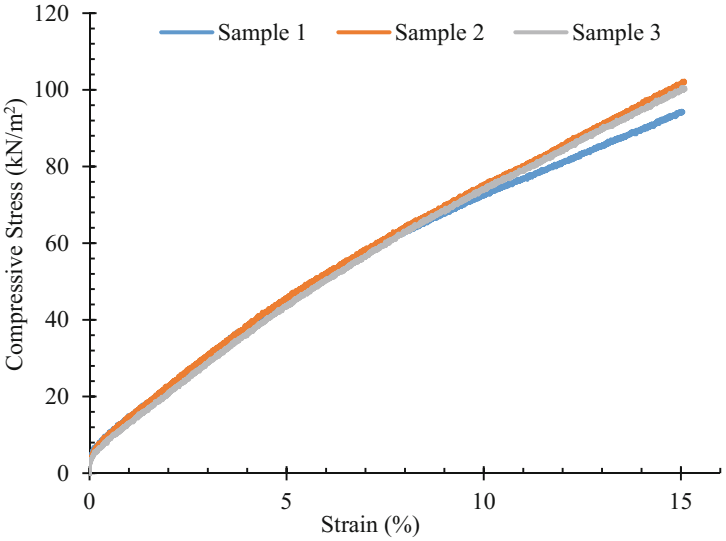


**Fig. 3.** The relationship between compressive stress and strain of W50C30CS30

**Table 3.** Additive amount of cement and fiber

| Number series | Water content (W) (%) | The additive amount of cement (C) (kg/m$^3$) | The additive amount of fiber (CS) (kg/m$^3$) |
|---|---|---|---|
| 1 | 50 | 30 | 0 |
| 2 | | | 5 |
| 3 | | | 10 |
| 4 | | | 15 |
| 5 | | | 20 |
| 6 | | | 25 |
| 7 | | | 30 |
| 8 | | 35 | 0 |
| 9 | | | 5 |
| 10 | | | 10 |
| 11 | | | 15 |
| 12 | | | 20 |
| 13 | | | 25 |
| 14 | | | 30 |
| 15 | | 40 | 0 |
| 16 | | | 5 |
| 17 | | | 10 |
| 18 | | | 15 |
| 19 | | | 20 |
| 20 | | | 25 |
| 21 | | | 30 |

- Failure strength: larger than 123 kN/m$^2$.
- Failure strain: larger than 5%. In addition, following ASTM D2166, the failure strain should not exceed 15%, so the maximum failure strain in this paper is 15%.

## 4 Results and Discussion

The results of cement stabilized sludge and fiber-cement stabilized sludge from unconfined compression test are shown in Figs. 4, 5, and 6.

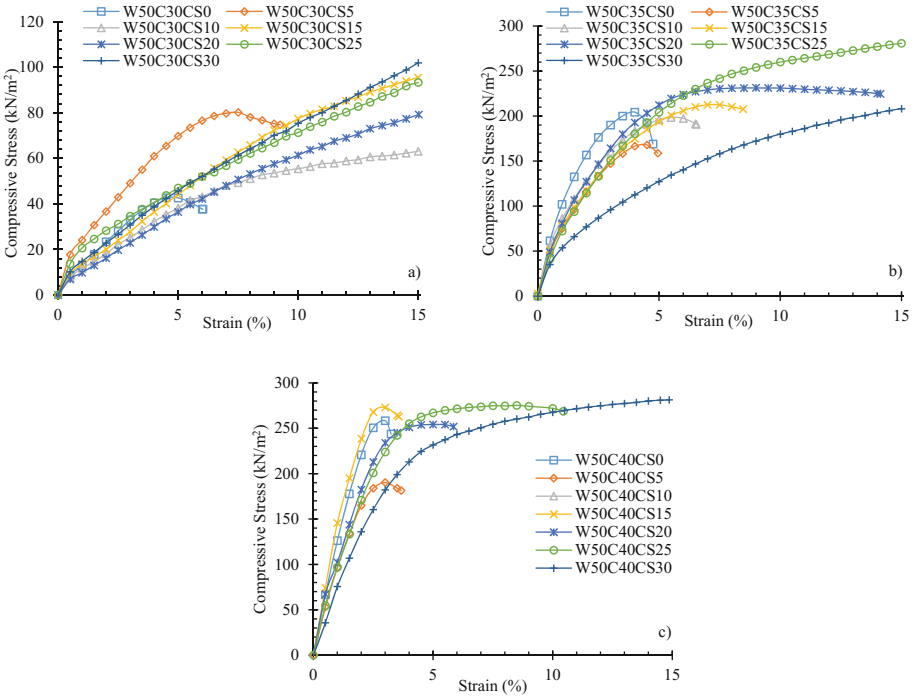


**Fig. 4.** The stress-strain curves with variations of fiber and cement content

From the results in Fig. 4. The tendency of stress-strain curves after obtaining peak stress between cemented soil and fiber-cemented soil was different. The curve slope after peak stress achieved without fiber inclusion was steeper than that with fiber inclusion. Besides, that slope also decreased with increasing fiber content. Especially, the compressive stress still increased after obtaining a strain of 15% when using much fiber and less cement in compounds such as W50C30CS25, W50C30CS30, etc. Therefore, it could be seen that the behavior of fiber cement stabilized soil was ductile and the fiber addition increased the both of compressive stress and strain in general.

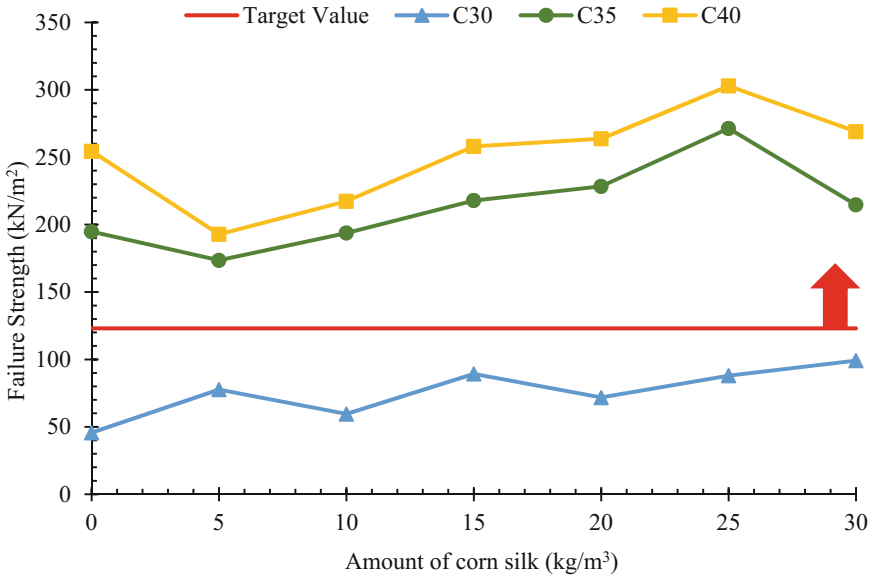


**Fig. 5.** Relationship between failure strength and additive amount of corn silk with different additive amount of cement

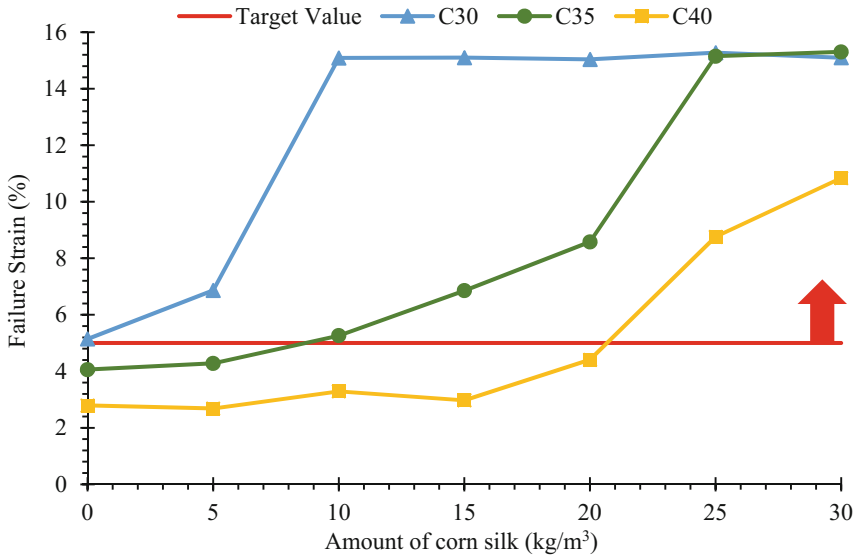


**Fig. 6.** Relationship between failure strain and additive amount of corn silk with different additive amount of cement

The failure strength and strain were determined from the peak point of the stress-strain curve. The value of these parameters was shown in Figs. 5 and 6. The failure strength increased with increasing the additive amount of cement. On the other hand, the failure strain decreased with increasing the additive amount of cement. Meanwhile, the effect of fiber content on modified soil was quite different. Almost the failure strain increased with increasing fiber content in general. Nevertheless, there were two tendencies of failure strength when adding fiber. The first tendency for cement of 30 kg/m$^3$ was both failure strength and strain increasing with increasing fiber content in general. The other one was for cement of 35 and 40 kg/m$^3$. In the second tendency, there were three developing failure strength stages when increasing fiber content. The first was failure strength decreasing with increasing fiber content. It was attributed that the workability between cement and fiber was not good because the additive amount of fiber was too small. When the fiber content continued increasing, the failure strength increased. The increasing failure strength in this stage may be due to proper fiber and cement content causing better workability of the mixture (10, 15, 20, 25 kg/m$^3$). The failure strength increased in the last stage of developing failure strength process with increasing fiber content. Its trend may happen because of lacking water for hydration reaction of cement due to fiber absorbing too much water in the mixture.

Comparing with the target values mentioned above, it is necessary to determine the smallest amount of fiber and cement content to satisfy the target value correlating with 50% water content in the mixture. As for cement of 30 kg/m$^3$, although the failure strain could satisfy the target value, the failure strength was not able to satisfy with increasing fiber content from 0 to 30 kg/m$^3$. At cement of 35, 40 kg/m$^3$, the optimum fiber contents determined from interpolate linearly method to satisfy the target values were 9 and 21 kg/m$^3$, respectively. It was clear to conclude that the optimum fiber and cement content for the water content of 50% were 9 and 35 kg/m$^3$.

The behavior of cement stabilized soil has been studied in previous works by many investigators such as Abdulla and Kiousis (1997), Consoli et al. (1998), etc. The authors concluded that the cemented soil behavior is brittle. Consoli et al. (1998) also indicated the fiber inclusion changing the cemented soil behavior from brittle to ductile and it is the main advantage of fiber reinforcement. According to the results in the present work and previous studies, the behavior of cement stabilized soil reinforced by cornsilk fiber and other fiber kinds was quite similar. Nevertheless, since cornsilk fiber is natural and waste material, it is available and sustainable material. Furthermore, the number of research works studied on natural fiber is limited (Khelifi et al. 2016). Hence, that is the reason why this present work has been carried out to evaluate the effect of cornsilk fiber on the cement stabilized soil.

## 5 Conclusions

This study aimed to stabilize soft soil by using fiber-cement stabilized soil method in investigating the effect of new natural fiber such as cornsilk on soil stabilization. Furthermore, this study was also considered the workability of modified soil as ground material for landslide area restoration by using cornsilk fiber and cement. According to

experimental results in this study, it can be concluded that it was possible to use cornsilk fiber as a stabilizer for soil stabilization by using fiber-cement stabilized method.

## References

Abdulla, A.A., Kiousis, P.D.: Behavior of cemented sands: I testing. Int. J. Numer. Anal. Methods Geomech. **21**, 533–547 (1997). doi:10.1002/(sici)1096-9853(199708)21:8<533::aid-nag889>3.0.co;2-0

Soundara, B., Senthil Kumar, K.P.: Effect of fibers on properties of clay. Int. J. Eng. Appl. Sci. (IJEAS) **2**, 123–128 (2015)

Consoli, N.C., et al.: Influence of fiber and cement addition on behavior of sandy soil. J. Geotech. Geoenviron. Eng. **124**(12), 1211–1214 (1998). doi:10.1061/(ASCE)1090-0241(1998)124:12(1211)

Mori, M., et al.: A proposal of new recycling system of high water content mud by using paper debris and polymer and strength property of recycled soil. J. MMIJ **119**, 155–160 (2003). doi:10.2473/shigentosozai.119.155

Negi, A.S., et al.: Soil stabilization using lime. Int. J. Innov. Res. Sci. Eng. Technol. **2**, 448–453 (2013)

Shrivastava, D., et al.: Effect of lime and rice husk ash on engineering properties of black cotton soil. Int. J. Eng. Res. Sci. Technol. **3**, 292–296 (2014)

Satomi, T., et al.: Evaluation of failure strength property and permeability of fiber-cement-stabilized soil made of Tsunami sludge. J. JSEM **14**, 303–308 (2014)

Khelifi, H., et al.: Mechanical enhancement of cement-stabilized soil by flax fibre reinforcement and extrusion processing. Mater. Struct. **49**, 1143–1156 (2016). doi:10.1617/s11527-015-0564-z

# Study on Strength of Modified Sludge Produced By Fiber-Cement Stabilized Soil Method Using Several Kinds of Fiber Materials

Thanh Nga Duong, Tomoaki Satomi, and Hiroshi Takahashi(✉)

Graduate School of Environmental Studies, Tohoku University, Sendai, Japan
hiroshi.takahashi.b3@tohoku.ac.jp

**Abstract.** In the South of Viet Nam, every year, a large amount of excavated sludge from construction sites has been disposed directly in the final disposal, but the recycling rate of sludge is low. Therefore, in this study, fiber-cement stabilized soil method was applied to recycle sludge in Viet Nam. Moreover, paper, rice straw, rice husk, and cornsilk were used as fiber materials in this method because they are waste materials and easily obtained in Viet Nam. Four kinds of fiber and cement were used to improve sludge and unconfined compression tests were carried out to collect failure strength and strain data. The experiments were performed under 28 mixing conditions. The water, fiber, and cement content were changed to find out which fiber material is the most suitable to modify sludge in Viet Nam. The results showed that rice straw gave the best results to modify sludge by using fiber-cement stabilized method.

**Keywords:** Fiber material · Fiber-cement stabilized soil method · Failure strength · Modified sludge

## 1 Introduction

The sludge produced from construction sites in The South, Viet Nam is very huge. As the recycling rate of the sludge is low, most of the construction sludge has been disposed directly in the final disposal sites (Viet et al. 2013). This is not economical and seriously impacts on the environment. It is necessary to recycle construction sludge to solve these problems. Soil stabilization by cement addition has been studied to improve the soil by several previous researchers (Clough et al. 1981; Basha et al. 2004; Consoli et al. 2007). The cement addition increases soil strength, but stiffness and brittleness properties of soil also significantly increase. Thus, we have already developed a new recycling system for the sludge named "Fiber-cement stabilized soil method" (Mori et al. 2003). In this method, paper debris and cement are mixed with the sludge. The modified sludge produced by this method has several features such as high failure strength, high failure strain, and high durability for drying and wetting. Figure 1 shown the concept of fiber-cement stabilized soil method (Mori et al. 2003). In the original construction sludge, because of high water content, soil particles freely move in the water. After adding paper debris, water in the construction sludge is absorbed into debris paper. Therefore, the superficial water content of sludge decreases. Finally, in order to obtain the necessary strength, cement is added to produce modified soil.

© Springer Nature Singapore Pte Ltd. 2018
H. Tran-Nguyen et al. (eds.), *Proceedings of the 4th Congrès International de Géotechnique - Ouvrages -Structures*, Lecture Notes in Civil Engineering 8,
DOI 10.1007/978-981-10-6713-6_57

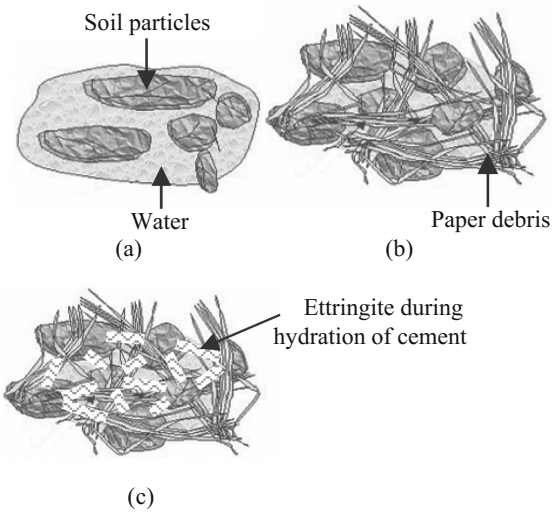


**Fig. 1.** The concept of fiber-cement stabilized soil method (a) high water content sludge (b) addition of paper debris (c) addition of cement

This method has already been used widely in Japan (Takahashi et al. 2011). However, it is hard to obtain a large amount of paper debris, so the local fiber materials should be used in order to apply this method for the sludge in Viet Nam. Besides, Viet Nam is an agricultural country, the size of the crop is very huge. Thus, the yield of the by-product is very high, for example, rice straw, rice husk, cornsilk, etc. Most of the by-products from agriculture are used for feeding livestock, combusting, planting mushroom, the recycling rate is low. It is necessary to consider by-product from agriculture as the fiber materials for fiber-cement stabilized soil method. This utilization solves a lot of environmental problems. When fiber-cement stabilized soil method is applied for the sludge in Viet Nam, it is not still clear that which material is the best to modify the high water content sludge. Therefore, rice straw, rice husk, and cornsilk were considered as the fiber materials. Furthermore, paper debris was also used for comparison. The current work aimed to study the strength of modified sludge by applying fiber-cement stabilized soil method using four kinds of fiber material, such as rice straw, rice husk, cornsilk, and paper debris.

## 2 Materials and Experimental Procedures

In order to carry out the systematic experiments under constant conditions, this study used artificial sludge which imitated real sludge of The Southern, Viet Nam. The main component of imitation sludge is Kasaoka clay and silt with the ratio of 40:60 in dry mass, respectively. The grain fine distribution, properties of imitation soil, and compound of Kasaoka clay and silt are shown in Fig. 2, Tables 1 and 2.

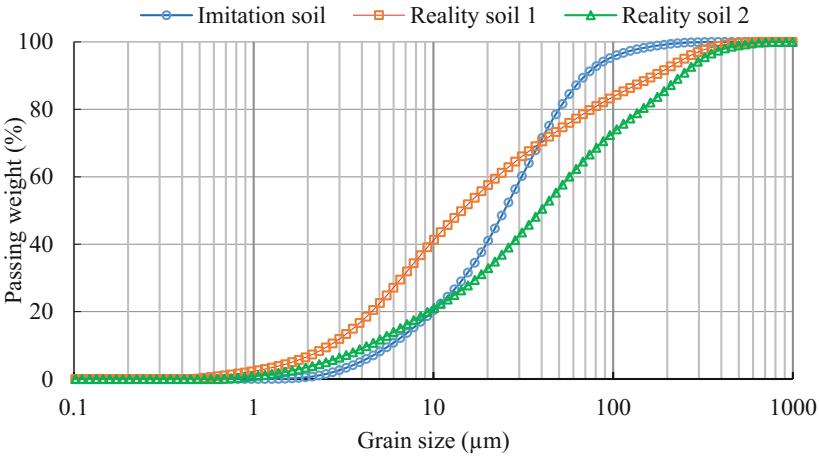


**Fig. 2.** Grain size distribution curve

**Table 1.** Imitation soils properties

| Properties | Value |
|---|---|
| Specific gravity | 2.47 |
| Gravel (%) | 0 |
| Sand (%) | 8.0 |
| Silt (%) | 83.5 |
| Clay (%) | 8.5 |
| Liquid limit (%) | 46.1 |
| Plastic limit (%) | 29.4 |
| Plasticity index (%) | 16.7 |
| Optimum moisture content (%) | 30.8 |
| Maximum dry unit weight (kN/m$^3$) | 13.07 |
| Unconfined compressive strength (kN/m$^2$) | 72.98 |
| USCS | OL |
| AASHTO | A-7-6 |

**Table 2.** Chemical properties of imitation soil

| Compound | Kasaoka clay (%) | Silt (%) |
|---|---|---|
| $SiO_2$ | 77.85 | 69.07 |
| $Al_2O_3$ | 12.88 | 20.22 |
| $K_2O$ | 2.417 | 2.75 |
| $Fe_2O_3$ | 2.08 | 5.46 |
| $Na_2O$ | 1.97 | 1.477 |
| CaO | 1.88 | 0.91 |
| MgO | 0.28 | 0.807 |
| MnO | 0.072 | 0.027 |

GEOSET 200 cement manufactured by Taiheiyo Cement Corporation, Japan is used for the experiments. Paper debris, rice straw, and rice husk are obtained from Miyagi prefecture, Japan. Cornsilk is from Ho Chi Minh City, Viet Nam. Raw rice straw segments of 30 mm were soaked in water for more than 3 h. The blender was used to mill the mixture of the rice straw segments and water. Finally, crushed rice straw was dried under 40 ± 3 °C to constant weight. The maximum length of dry rice straw fiber was 30 mm. Raw cornsilk included corn leaves and dust were cleaned in the water. Wet cornsilk was dried under 40 ± 3 °C to constant weight. The range of cornsilk length was from 10 to 80 mm.

To determine the strength characteristic of modified soil added four kinds of fiber materials and cement, unconfined compression tests are conducted according to ASTM D2166 on cylindrical specimens in 50 mm of diameter, and 100 mm of height. The capacity of used unconfined compression testing machine is 2 kN. The specimens are loaded at an axial deformation rate of 1 mm/min. The strain and stress data are continuously recorded until the stress value decreases or the strain value reach 15%. The procedure for making cylindrical specimens is shown as follows

i. Adding the water content with the mixture of Kasaoka clay and silt to create imitation sludge. In this study, water content ratio is 60, 70, and 80% by weight of dry soil. The mixing ratio of Kasaoka clay and silt is 40:60.
ii. The fiber material is added to the artificial soil and agitated until mixture is homogenous.
iii. Addition and agitation of cement.
iv. For the initial cure, the mixture is put into the tight chamber and kept at 20 ± 3 °C for three days.
v. After three days, the specimens are made by compaction using general size mold of 50 mm in diameter, and 100 mm in height.
vi. The specimens are cured at 20 ± 3 °C for seven days.

The unconfined compression test is carried out after curing seven days to obtain failure strength and failure strain value of the specimens. The additive amount of cement and fiber materials are shown in Table 3.

**Table 3.** Additive amount of cement and fiber material

| Water content (%) | Cement (kg/m$^3$) | Fiber material (kg/m$^{3)}$ |
|---|---|---|
| 60 | 40 | 30 |
| | | 40 |
| | | 50 |
| 60 | 40 | 30 |
| | 50 | |
| | 60 | |
| 60 | 50 | 30 |
| 70 | | |
| 80 | | |

## 3 Experimental Results

Experimental results are shown from Figs. 3, 4, 5, 6, 7, 8, and 9. In these figures, W, C, and F indicate the water content of sludge, additive amount of cement and additive amount of fiber, respectively. For example, W60C40F30 means that water content, the additive amount of cement, and the additive amount of fiber is 60%, 40 kg/m$^3$, and 30 kg/m$^3$, respectively.

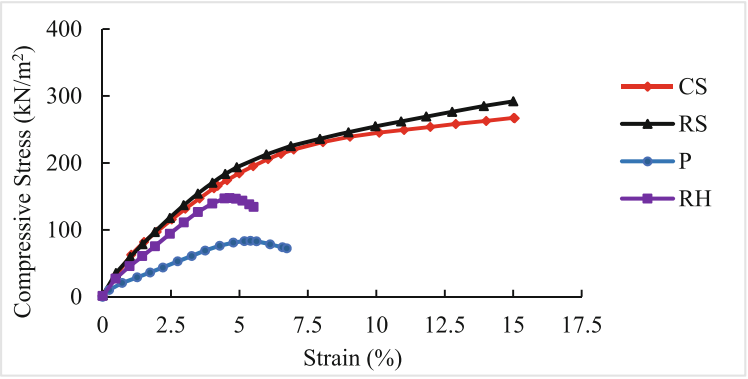


**Fig. 3.** Stress-strain curves of modified sludge including four fiber materials

Figure 3 showed typical stress-strain curves of modified sludge including cornsilk (CS), rice straw (RS), rice husk (RH), and paper debris (P) obtained from unconfined compression tests. Failure strength and failure strain were the value determined from the peak stress point of the stress-strain curve. It can clearly be seen that cement-soil including paper debris and rice husk reached failure strength at an axial displacement between 4 and 6%. However, the stress value of cement-soil reinforced by cornsilk and rice straw was recorded until strain value of 15%. It may happen because the length of paper debris and rice husk is shorter than that of cornsilk and rice straw.

From Fig. 4, it can be seen that the failure strength of rice husk and paper debris increased with the increase of the additive fiber amount. However, failure strength value of rice straw and cornsilk increased, then decreased at fiber content of 50 kg/m$^3$. This phenomenon may happen because the water in the mixture absorbed by rice straw and cornsilk is more than that of paper debris and rice husk materials. Hence, there was not enough water for hydration reaction of cement. Figures 6 and 8 showed that failure strength increased with the increase of the additive cement amount and with the decrease of the water content. This result was in agreement with finding reported by Consoli et al. 1998; Estabragh et al. 2012. Figures 4, 6 and 8 showed that the failure strength of specimens under the same mixing conditions in descending order was rice straw, cornsilk, paper debris, and rice husk. However, the order of cornsilk and paper debris changed at the additive cement amount of 60 kg/m$^3$ (Fig. 6).

As for failure strain, Fig. 5 showed that failure strain changed slightly according to fiber amount. Furthermore, the more cement amount was added, the more failure strain

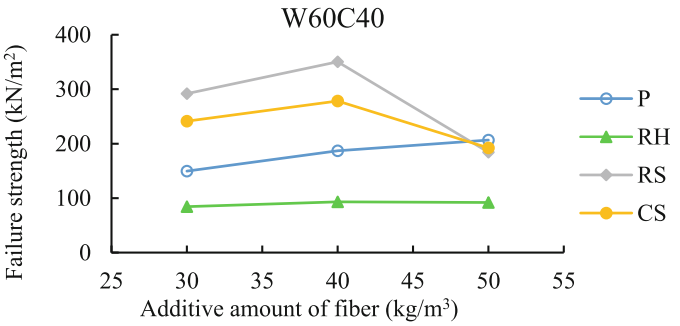


**Fig. 4.** The relationship between additive amount of fiber and failure strength

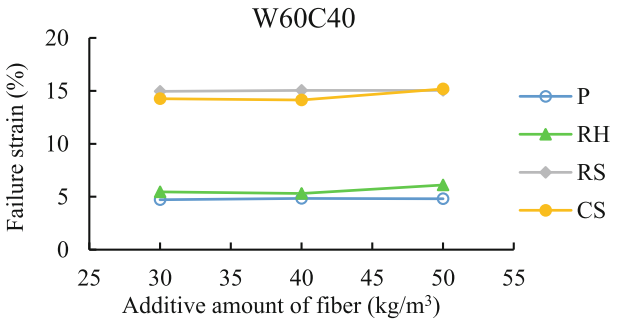


**Fig. 5.** The relationship between additive amount of fiber and failure strain

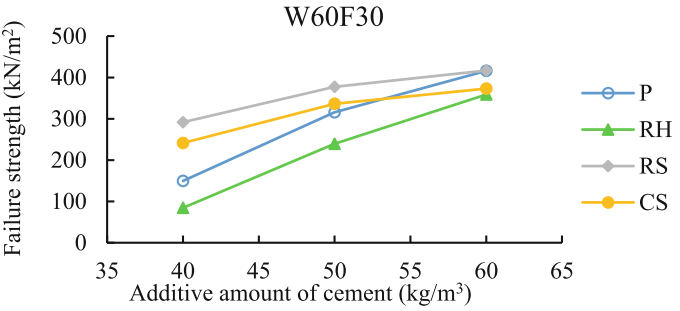


**Fig. 6.** The relationship between additive amount of cement and failure strength

reduced. This phenomenon was different when changing water content of sludge showed in Fig. 9, that is, the failure strain increased with the increase of water content. Figures 5, 7, and 9 indicated that fiber materials divided into two groups. The first group included cornsilk and rice straw had high failure strain. The other group was paper debris and rice husk which had low failure strain. As mentioned above, this may

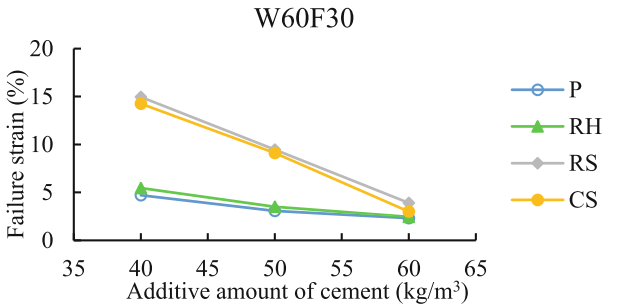


**Fig. 7.** The relationship between additive amount of cement and failure strain

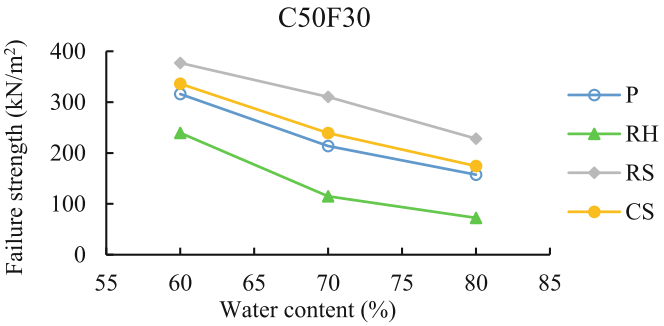


**Fig. 8.** The relationship between water content and failure strength

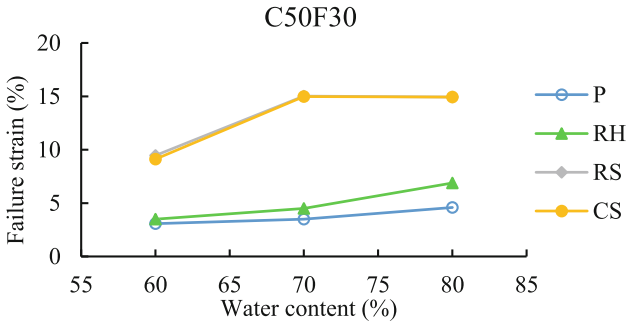


**Fig. 9.** The relationship between water content and failure strain

happen due to the impact of the fiber length. The failure strain of the specimens under the same mixing conditions in descending order was rice straw, cornsilk, rice husk, and paper debris.

## 4 Conclusions

This study carried out 28 experiments under seven mixing conditions. The unconfined compression tests were carried out to estimate the strength of modified sludge produced by fiber-cement stabilized soil method using four kinds of fiber material. The experiments with four kinds of fiber material were conducted under the same mixing conditions. The results indicated that the descending failure strength order of modified soil reinforced by different kinds of fiber material was rice straw, cornsilk, paper debris, and rice husk. Meanwhile, the descending failure strain order was rice straw, cornsilk, rice husk, and paper debris. The failure strength value increased and failure strain value decreased with the increase of additive cement amount. On the other hand, the failure strength value decreased and failure strain value increased with the increase of water content.

## References

Takahashi, H., Mori, M.: A new recycling system for high water content mud and strength characteristics of modified soils produced by this system. In: Proceeding of the 1st Vietnam/Japan Joint Symposium on Saigon River Bank Erosion, Shiga, Japan, pp. 79–88 (2011)

Clough, G.W., Sitar, N., Bachus, R.C., Rad, N.S.: Cemented sands under static loading. J. Geotech. Eng. Div. **107**(6), 799–817 (1981)

Consoli, N.C., Prietto, Pedro D.M., Ulbrich, L.A.: Influence of fiber and cement addition on behavior of sandy soil. J. Geotech. Geoenviron. Eng. **124**(12), 1211–1214 (1998)

Mori, M., Takahashi, H., Ousaka, A., Horii, K., Kataoka, I., Ishi, T., Kotani, K.: A proposal of new recycling system of hight-water content mud by using paper debris and polymer and strength property of recycled soils. J. Min. Mater. Process.Inst. Jpn. **119**(4–5), 155–160 (2003)

Basha, E.A., Hashim, R., Mahmud, H.B., Muntohar, A.S.: Stabilization of residual soil with rice husk ash and cement. Constr. Build. Mater. **19**(2005), 488–543 (2004)

Consoli, N.C., Foppa, D., Festugato, L., Heineck, K.S.: Key parameters for strength control of artificially cemented soils. J. Geotech. Geoenviron. Eng. **133**(2), 197–205 (2007)

Estabragh, A.R., Namdar, P., Javadi, A.A.: Behavior of cement-stabilized clay reinforced with nylon fiber. Geosynth. Int. **19**(1), 85–92 (2012)

Viet, N.T., Dieu, T.T.M., Loan, N.T.P.: Current status of sludge collection, transportation and treatment in Ho Chi Minh City. J. Environ. Prot. 1329–1335 (2013). doi:10.4236/jep.2013.412154

# Synergic Effects of Activation Routes of Ground Granulated Blast-Furnace Slag (GGBS) Used in the Precast Industry

Martin Cyr[1(✉)] and Ludovic Andre[1,2]

[1] LMDC, Université de Toulouse, INSA, UPS, Toulouse, France
{martin.cyr, ludovic.andre}@insa-toulouse.fr
[2] ECOCEM Materials Ltd., Paris, France

**Abstract.** Ground granulated blast-furnace slag (GGBS) is a common by-product used for decades in the cement and concrete industry, and having beneficial effects on environmental properties and durability of concretes. However, GGBS reacts less rapidly than cement and the short-term compressive strength of GGBS-concretes are usually lower than the ones of Portland cement concretes. The aim of this paper is to test the efficiency and evaluate the synergic effect of combining different activation routes (fineness of Portland cement and GGBS, use of chemical activation, and application of thermal cycles) on short-term compressive strength of GGBS-Portland cement-based materials. Results showed that the simultaneous use of all activation routes allowed blended cement with GGBS to achieve almost the same initial mechanical characteristics than Portland cement.

**Keywords:** Ground granulated blast-furnace slag · Activation · Temperature · Fineness

## 1 Introduction

Ground granulated blast-furnace slag (GGBS) is a common supplementary cementing material (SCM) used for decades in the cement and concrete industry. GGBS is a by-product of the steel industry, rapidly quenched with water and ground to a fineness similar to that of a Portland cement. The main components of GGBS are CaO (30–50%), $SiO_2$ (28–38%), $Al_2O_3$ (8–24%), and MgO (1–18%). GGBS has been recognized to have beneficial effects on environmental properties (lower $CO_2$ production than Portland cement) and durability of concretes. Examples of durability improvement of GGBS-based concretes are numerous and can be found easily in the literature (Juenger et al. 2011; Öner et al. 2003; Roy 1999).

However, GGBS reacts less rapidly than cement and the short-term compressive strengths of GGBS-concretes are usually lower than the ones of Portland cement concretes. This situation could be a problem in domain such as the precast industry, where the short-term strength (e.g. between 6 h and 24 h) must be high enough to maintain the rate of production of concrete elements.

© Springer Nature Singapore Pte Ltd. 2018
H. Tran-Nguyen et al. (eds.), *Proceedings of the 4th Congrès International de Géotechnique - Ouvrages -Structures*, Lecture Notes in Civil Engineering 8,
DOI 10.1007/978-981-10-6713-6_58

On the one hand, solutions exist to improve the short-term strength of GGBS concrete. They are based on mainly three approaches, most of the time used separately: increase the fineness of the GGBS, increase the temperature of curing by applying thermal cycles to the concrete, or use chemical activators to enhance the reactivity of the GGBS. On the other hand, it is well known that the increase of the cement fineness generally improves its reactivity, especially at short term.

The combination of all of these methods is not often found in the literature, but it could represent a real opportunity to counteract the limited reactivity of GGBS at young ages by exploiting the synergy between the different activation routes available. The use of higher amount of GGBS could thus improve the long term durability of the concretes, without the inconvenient of the lack of performance at very short term. The precast industry is well adapted to the combination of all these activation routes, especially because of the possibility to increase the temperature of concrete curing.

The aim of this paper is to test the efficiency and evaluate the synergic effect of combining different activation routes (fineness of Portland cement and GGBS, use of chemical activation, and application of thermal cycles) on short-term compressive strength of GGBS-Portland cement-based materials.

## 2 Materials and Methods

The Portland cement was a CEM I 52.5 N CE CP2 NF as specified in European Standard NF EN 197-1 (AFNOR 2012). Its chemical composition is given in Table 1 and its original fineness was 4000 $cm^2/g$ (Blaine specific surface). A highly amorphous industrial GGBS (chemical analysis in Table 1) was used at two finenesses: 4300 and 6800 $cm^2/g$. The aggregate used in mortar production was a normalized quartz sand conformed to NF EN 196-1 with particle size ranging between 0 and 2 mm (AFNOR 2006). The sodium sulfate used for the activation of the systems was from analytical grade.

**Table 1.** Properties of CEM I and GGBS

| | Oxides (%) | | | | | | | | | | |
|---|---|---|---|---|---|---|---|---|---|---|---|
| | CaO | $SiO_2$ | $Al_2O_3$ | $Fe_2O_3$ | $SO_3$ | $Na_2O$ | $K_2O$ | Loss on ignition | Specific gravity, $g/cm^3$ | D50, µm | Blaine ($cm^2/g$) |
| CEM I | 67.41 | 22.84 | 2.7 | 1.84 | 2.23 | 0.14 | 0.23 | 1.72 | 3.13 | 12.6 | 4000 |
| GGBS | 41.35 | 36.85 | 11.44 | 0.1 | 1.93 | 0.34 | 0.44 | – | 2.91 | 12.8 | 4300 |

The experimental program was carried out on pastes for the calorimetric study, and on mortars prepared according to NF EN 196-1 (AFNOR 2006) for the strength tests. The mass of binder (cement or cement+GGBS) was kept constant at 450 g. Granular-to-sand ratio and water-to-binder ratio were set at 3 and 0.50, respectively. A reference mortar composed of 100% of Portland cement was prepared and cured at

40 °C and 60 °C for 6 h. Sixteen mortars with GGBS were cast to evaluate the effect of the following parameters (illustrated in Fig. 1):

- GGBS content: 50% and 70%
- GGBS fineness: 4300 $cm^2/g$ and 6800 $cm^2/g$, two industrial grades available
- cement fineness: 4000 $cm^2/g$ and 7800 $cm^2/g$, the last one being obtained after a grinding of 10 min in a laboratory grinder.
- temperature of curing: 40 °C and 60 °C in climate chambers
- chemical activation: 0.8% $Na_2SO_4$

The samples were cast in 4 × 4 × 16 cm polystyrene molds, sealed in plastic bags and allowed to harden at two different temperatures: 40 °C for 6 h or 60 °C for 6 h (compressive strength test 1), followed by a cure at 20 °C until the age of test (compressive strength test 2). The compressive strength results were the mean of three values.

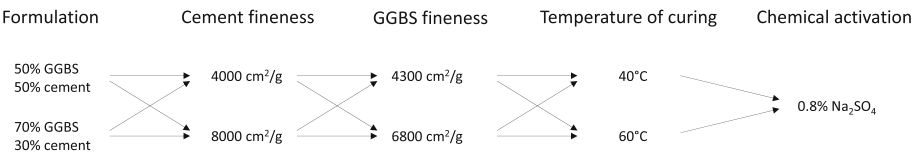


**Fig. 1.** Schematic representation of the 16 mortar mixtures containing GGBS

## 3 Isothermal Calorimetry

Figure 2 presents the cumulative heat of hydration after 6h and 24h of pastes cured at 40 °C or 60 °C, measured by isothermal calorimetry. Each paste was composed of 50 to 70% of GGBS (fineness 4300 or 6800 $cm^2/g$) and CEM I (4300 $cm^2/g$), and an addition of 0.8% $Na_2SO_4$ was added to half of them. Total heat released was calculated by normalizing the heat obtained with respect to the mass of paste.

It appears clearly that with a 6 h thermal curing, the addition of a chemical activator systematically led to a higher hydration heat, no matter what curing temperature, GGBS content or fineness chosen. The mixture which led to the higher 6 h heat released included 50% of finer GGBS, addition of $Na_2SO_4$ and 60 °C thermal curing.

Following this study, several points can be observed:

- The more GGBS, the lower hydration heat.
- Combining a finer GGBS with $Na_2SO_4$ as chemical activator, with a 40 °C thermal curing, led to the same heat released at 6 h (column L, 74 kJ/kg) as with a coarser GGBS, no chemical activation and a 60 °C thermal curing (column M, 74 kJ/kg). The comparison being done on 70% GGBS pastes.
- Enhance curing temperature by 20 °C allowed to obtain the same heat after 6 h on a mixture with 70% of GGBS 4300 $cm^2/g$ (column M, 74 kJ/kg), as with 50% of same GGBS cured at 40 °C (column A, 72 kJ/kg), without any chemical activation in both case.

– A special synergetic behavior appeared by combining chemical and thermal activations. The gain of hydration heat (at 6 h) obtained by enhancing curing temperature from 40 °C to 60 °C was higher in cases where $Na_2SO_4$ was present. This phenomenon is highlighted by comparing the gain of heat between columns A & B (B − A = 12 kJ/kg) and E & F (F − E = 21 kJ/kg).
– From 6 h to 24 h, the gain of heat was systematically lower, when $Na_2SO_4$ was added to the mixtures, than for pastes without chemical activation involved. This effect was particularly marked for pastes using a 60 °C thermal curing, and in most cases, 24 h heat of hydration was higher for mixtures which did not include chemical activation. For this reason, using a too long thermal curing coupled with a chemical activation based on $Na_2SO_4$ would not be recommended. Thus, the results of compressive strength of mortars presented in the next part, has been realized on mixtures with 0.8% $Na_2SO_4$ and not cured longer than 6 h.

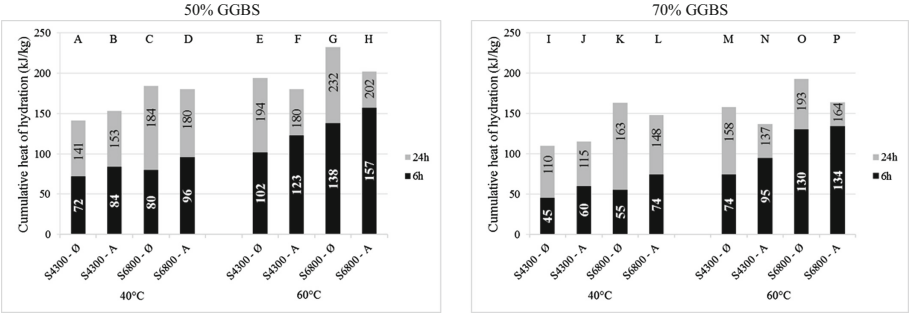


**Fig. 2.** Cumulative heat of hydration at 6 h and 24 h of paste cured 24 h at 40 °C or 60 °C. Paste contained 50% or 70% of GGBS (fineness 4300 or 6800 $cm^2/g$) and CEM I 4000 $cm^2/g$, 0.8% $Na_2SO_4$ (A) or not ($\phi$), and w/b = 0.4.

## 4 Compressive Strength Results

Figure 3 presents the strength activity index, defined as the ratio of compressive strength of GGBS mortar and reference mortar, at 6h and 24h. All mortars included 0.8% $Na_2SO_4$ per part of binder and were all cured 6h at 40°C or 60°C (followed by a cure at 20°C). Four activations routes were investigated: cement fineness, GGBS fineness, chemical activation (only at one level) and increase in the curing temperature.

It can be seen that some activation routes were better than others to improve the strength of GGBS-Portland cement mixtures. Individual activation route cannot alone allow the GGBS mixture to challenge the Portland cement. The only combination which led to the better results was the increase in the temperature to 60 °C, with fineness of cement and GGBS at their maximum levels.

Several observations can be made:

– When the curing temperature was set at 40° during 6 h, no combination of activation routes allowed us to reach, neither at 6 h nor 24 h, the reference mortar

composed of commercial CEM I. The better result at this curing temperature (SAI of 0.74) was obtained after 24 h for the mortar mixture with the finest cement and GGBS (8000 and 6800 $cm^2/g$, respectively).

– The curing temperature of 60 °C during 6 h led to much better results, as it was possible to reach or get close to the reference at 6 h and 24 h for 50% GGBS mortars made with the finest cement and GGBS (8000 and 6800 $cm^2/g$, respectively). When 70% of GGBS was used, the strength at 6 h approached 90% of the reference with the same combination of cement-GGBS fineness. However, the strength activity index decreased at 24 h (0.72), probably due to a blockage effect sometimes seen when the hydration is strongly activated (Marciano and Battagin 1997).
– When the cement fineness was kept at 4000 $cm^2/g$, and by combining fine GGBS (6800 $cm^2/g$) and high temperature (e.g. 60 °C), it was possible to almost reach the reference cured at 40 °C (for 50%-GGBS mixtures at 6 and 24 h, and 70%-GGBS mixture at 6 h). It means that it could be possible to avoid the cement grinding by combining high GGBS fineness and temperature of curing higher than the reference CEM I.

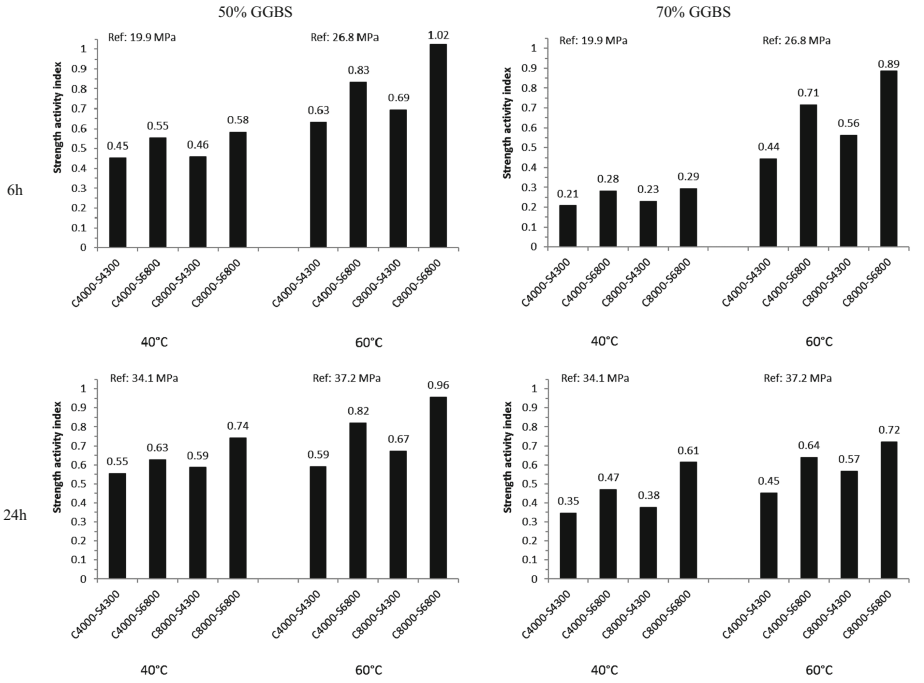


**Fig. 3.** Strength activity index (defined as the ratio of compressive strength of GGBS mortar and reference mortar) at 6 h and 24 h of mortars cured 6 h at 40 °C or 60 °C. Reference mortars contained 100% CEM I (4000 $cm^2/g$), while GGBS mixtures (50 and 70% of fineness: 4300 or 6800 $cm^2/g$) were made with cement of fineness 4000 or 8000 $cm^2/g$.

Figure 4 presents the increase in strength (in %) when a given parameter went from a minimum value to a maximum value. All the calculations were made by taking mortars 2 by 2 with only one parameter changing, all the others remaining equals. For example, when the GGBS fineness went from 4300 $cm^2/g$ to 6800 $cm^2/g$, several increases were calculated with constant values of cement content (30 or 50%), cement fineness (4000 or 8000 $cm^2/g$), and curing temperature (40 or 60 °C). Figure 4 gives the mean increase of the values, as well as the minimum and maximum increases obtained.

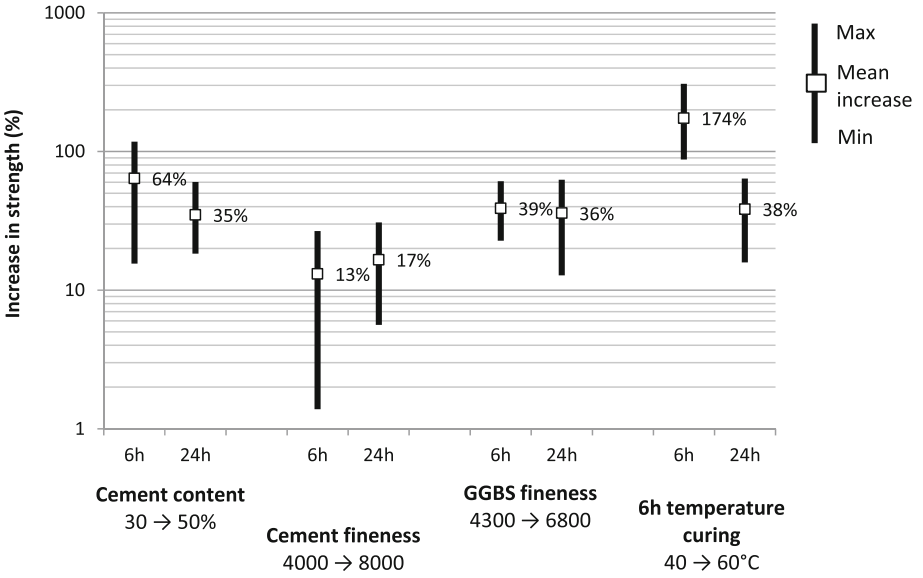


**Fig. 4.** Increase in strength (in %) when a given parameter went from a minimum value to a maximum value (example: GGBS fineness from 4300 $cm^2/g$ to 6800 $cm^2/g$)

It can be seen (inside the min and max values of each parameter chosen in this study) that all parameters did not have the same effect on the increase in strength at young ages:

- The curing temperature had a huge effect on the strength at 6 h, as passing from 40 °C to 60 °C led to a significant increase in strength between 90 and 300%, with a mean value of +174%.
- This effect was much less important at 24 h, the gain being at a mean value of +38%
- The effect of GGBS fineness was in the same order of magnitude at 6 h and 24 h, with mean increase values between +36 and +39% when the fineness of the GGBS went from 4300 to 6800 $cm^2/g$.
- The cement content fallowed a similar trend, meaning that 50% GGBS (i.e. 50% of cement) led logically to the better results.

– The increase of the cement fineness was the less significant parameter, as the mean increase in strength were at average values of +13–17%, although a significant effort to increase the fineness (4000 to 8000 $cm^2/g$). However, it should be kept in mind that the increase in cement fineness could help reaching the goal of approaching the reference mortar when it is combined to other activation routes (GGBS fineness and temperature).

## 5 Energy Consumption

An analysis based on a simple calculation of the energy demand when GGBS is used as cement replacement is presented. The calculation is based on the energy consumed for the production of cement and GGBS, which includes the manufacturing process (e.g. heating of cement raw meal) and the final grinding of the material (clinker, GGBS). It excludes the energy for thermal treatment at 40 and 60 °C since the comparisons are made here for mixtures cured at the same temperature.

The energy required ($E$, in kWh/t of binder) is given by Eq. 1, as a function of the binder composition, and of the energy needed for the manufacturing process and the grinding of cement and GGBS. A calculation of the performance energy $E_{performance}$ (in kWh/t/MPa) can also be proposed (Eq. 2), by dividing the required energy $E$ by the compressive strength of the mortar containing the binder under consideration. $E_{performance}$ gives the energy cost of each MPa of strength.

$$\mathrm{E}\ \{\text{in kWh/t}\} = \mathrm{C} \cdot \left(\mathrm{E}_{\text{cement}}^{\text{process}} + \mathrm{E}_{\text{cement}}^{\text{grinding}}\right) + \mathrm{GGBS} \cdot \left(\mathrm{E}_{\text{GGBS}}^{\text{process}} + \mathrm{E}_{\text{GGBS}}^{\text{grinding}}\right) \quad (1)$$

$$\mathrm{E}_{\text{performance}}\ \left\{\text{in kWh/t} \cdot \text{MPa}^{-1}\right\} = \frac{\mathrm{E}}{\text{Strength}} \quad (2)$$

where

- E is the energy consumption (in kWh) for the production of one ton of binder,
- C and GGBS are the proportions of cement and GGBS in the binder respectively,
- $\mathrm{E}_{\text{cement}}^{\text{process}}$ and $\mathrm{E}_{\text{cement}}^{\text{grinding}}$ are the energy consumption (in kWh/t) of the cement manufacturing process and the finish grinding of the material, respectively,
- $\mathrm{E}_{\text{GGBS}}^{\text{process}}$ and $\mathrm{E}_{\text{GGBS}}^{\text{grinding}}$ are the energy consumption (in kWh/t) for the GGBS process and the grinding of the material, respectively,
- $\mathrm{E}_{\text{performance}}$ is the energy consumption for the production of one ton of binder, relative to the compressive strength of the mortar containing the binder considered,
- Strength is the compressive strength of the mortar of composition C+GGBS

The data used for the calculations were taken from the literature and are reported in Table 2 (Bribián et al. 2011; Moya et al. 2011; Hosten and Fidan 2012; Touil et al. 2006; Snow et al. 1997; Vergne 2003). The total energy required to produce cement was evaluated to be in the range 800–1200 kWh per ton of cement, including around 50 kWh/t for the finish grinding of the clinker. In the case of GGBS, the process energy

was assumed to be 0 kWh/t (as it is a by-product). The energy for GGBS grinding is recognized to be higher than for clinker, due to the presence of hard glass. According to various authors (Snow et al. 1997; Vergne 2003), 50% more energy is necessary to reach the same fineness for GGBS as for clinker.

**Table 2.** Data used for the calculation of energy consumption

| | Energy consumption (kWh/t) | | |
|---|---|---|---|
| | Cement | GGBS | |
| Manufacturing process | $E_{GGBS}^{process} = 950$[a] | From the steel plant | $E_{GGBS}^{process} = 0$ |
| Ref. | (Bribián et al. 2011; Moya et al. 2011; Hosten and Fidan 2012) | | - |
| Finish grinding | $E_{cement}^{grinding} = 50$ or 125 | Grinding | $E_{GGBS}^{grinding} = 75$ or 125 |
| Ref. | (Hosten and Fidan 2012; Touil et al. 2006) | | (Snow et al. 1997; Vergne 2003) |

[a]Values in the literature between 800–1200 kWh/t for dry process (initial data in GJ/t, with 3.6 GJ = 1000 kWh)

The results of the calculations are given in Fig. 5(a) and (b) for all the composition studied.

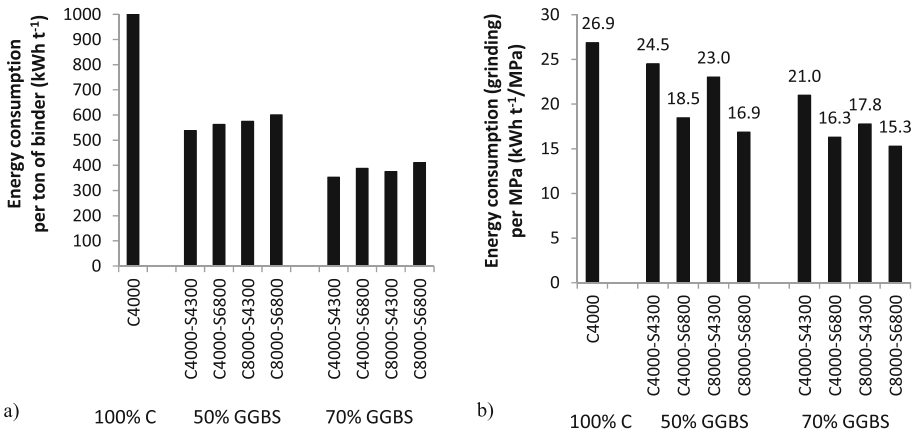


**Fig. 5.** (a) Energy consumption of mortars containing GGBS. Energy requirement of binder (E, in kWh/t of binder). (b) Energy consumption of mortars containing GGBS. Performance energy ($E_{performance}$, in kWh/t/MPa) for mortars cured at 60 °C (for 6 h), then tests for compressive strength at 24 h.

*(a) Energy requirement of binder E, in kWh/t of binder – Fig. 5(a)*

When 1 ton of binder was considered, the energy consumption with GGBS was always lower than for the reference with only cement (Fig. 5). This means that 1 ton

of binder with GGBS had a lower energy cost (almost proportional to the cement remaining in the system), although the grinding of GGBS required more energy than the grinding of clinker. GGBS remained less energy consuming because of the absence of energy demand of the manufacturing process.

*(b) Performance energy $E_{performance}$, in kWh/t/MPa – Fig. 5(b)*
When the energy consumption was considered relative to the performance of mortars (for instance compressive strength at 24 h for mortars cured at 60 °C), it can be seen that:

- The use of GGBS systematically (for these conditions) involved a decrease in the energy consumption per MPa, meaning a better energetic efficiency of the system.
- The best $E_{performance}$ were obtained for fine GGBS, whatever the fineness of the cement.
- It is possible to obtain good $E_{performance}$ with up to 70% of GGBS.

This means that, from a "performance energy" point of view, it is better to use fine GGBS without considering the fineness of the cement. These mixtures lead to the best efficiency of the GGBS, i.e. more performance (in terms of MPa) for a given energy: each MPa cost less kWh per ton of binder.

## 6 Conclusion

This paper aimed at evaluating the possibility of using GGBS blended cements in the precast industry as a challenger to Portland cement used alone. Combinations of four activation routes were tested on 50% and 70% GGBS mixtures. The following conclusions can be drawn:

- In heated systems (such as in precast industry), it is possible to challenge, in terms of compressive strength, Portland cement at 6 h and 24 h, when combining chemical activation, the fineness of the GGBS, the fineness of the cement and a curing temperature of 60 °C.
- The best activation route is the temperature, followed by the fineness of the GGBS.
- The cost of each MPa (per kWh per ton of binder) is lower with fine GGBS used in replacement of the cement.

A possible perspective to optimize the GGBS mixtures would be to add fine limestone filler (LF) to improve the packing, as GGBS and LF are known to work well together.

## References

AFNOR: EN 197-1 Cement - Part 1: composition, specifications and conformity criteria for common cements (2012)

AFNOR: EN 196-1 Methods of testing cement - Part 1: determination of strength (2006)

Bribián, I.Z., Capilla, A.V., Usón, A.A.: Life cycle assessment of building materials: Comparative analysis of energy and environmental impacts and evaluation of the eco-efficiency improvement potential. Build. Environ. **46**, 1133–1140 (2011)

Hosten, C., Fidan, B.: An industrial comparative study of cement clinker grinding systems regarding the specific energy consumption and cement properties. Powder Technol. **221**, 183–188 (2012)

Juenger, M.C.G., Winnefeld, F., Provis, J.L., Ideker, J.H.: Advances in alternative cementitious binders. Cem. Concr. Res. **41**, 1232–1243 (2011)

Marciano, E., Battagin, A.F.: The influence of alkali activator on the early hydration and performance of portland blast furnace slag cement. In: Proceedings of the 10th International Congress on the Chemistry of Cement, Gothenburg (1997)

Moya, J.A., Pardo, N., Mercier, A.: The potential for improvements in energy efficiency and $CO_2$ emissions in the EU27 cement industry and the relationship with the capital budgeting decision criteria. J. Clean. Prod. **19**, 1207–1215 (2011)

Öner, M., Erdoğdu, K., Günlü, A.: Effect of components fineness on strength of blast furnace slag cement. Cem. Concr. Res. **33**, 463–469 (2003)

Roy, D.M.: Alkali-activated cements opportunities and challenges. Cem. Concr. Res. **29**, 249–254 (1999)

Snow, R.H., Allen, T., Ennis, B.J., Litster, J.D.: Size reduction and size enlargement. In: Perry, R.H., Green, D.W. (eds.) Perry's Chemical Engineers' Handbook, 7th edn. McGraw-Hill, New York City (1997)

Touil, D., Belaadi, S., Frances, C.: Energy efficiency of cement finish grinding in a dry batch ball mill. Cem. Concr. Res. **36**, 416–421 (2006)

Vergne, J.N.: The Hard Rock Miner's Handbook, 3rd edn. McIntosh Engineering, North Bay (2003)

# The Flow Response of Reinforced Earth Structures Utilized Fine-Grained Poorly Draining Materials as Backfill

D. Bui Van[1(✉)], A. Chinkulkijniwat[1], S. Horpibulsuk[1], S. Yubonchit[1], A. Udomchai[2], I. Limrat[1], A. Le Tuan[3], H. Pham Tien[4], and O. Kennedy[5]

[1] School of Civil Engineering, Suranaree University of Technology, Nakhon Ratchasima 30000, Thailand
buivanduc@humg.edu.vn
[2] Center of Excellence in Civil Engineering, School of Civil Engineering, Suranaree University of Technology, Nakhon Ratchasima 30000, Thailand
[3] Faculty of Civil Engineering, Hanoi University of Mining and Geology, Hanoi, Vietnam
[4] Institute of Applied Geothermal Science and Technology, Technische Universität Darmstadt, Darmstadt, Germany
[5] Department Of Civil Engineering, Michael Okpara University Of Agriculture, Umudike, P.M.B.7267, Umuahia 440109, Abia State, Nigeria

**Abstract.** Reinforced earth structures, later known as Mechanically Stabilized Earth (MSE) walls, have been widely employed over four decades due to their ease of installation, quick construction compared to conventional reinforce concrete. Yet, numerous failures of MSE walls structure take place. Most of those failures are frequently attributed to the presence of water within or behind the reinforced zone, flow response inside reinforced earth structures as well. Recently, the use of "high fines" and/or "high plasticity" soils for reinforced fill has become more frequent due to the difficulties in finding an appropriate borrow pit. This paper utilized a well calibrated numerical model to perform series of parametric calculation of MSE incorporated with drainage composite, in which fine-grained poorly draining material was utilized as backfill. The experiments were conducted to investigate the influences of water retention characteristics of poorly draining materials utilized as backfills on the seepage response in MSE wall as subjected to rising of upstream water table. The flow response was examined in terms of effective saturation distribution, changes in phreatic surface as well. The calculated results show that the larger pore size yields the narrower zone of high saturation. The more uniform pore size yields narrower effective saturation profile in range of intermediate saturation zone. The moisture profile in reinforced soil mass is somewhat affected by flow properties of the soil placed next to reinforced part. The distribution of effective saturation at the interface between backfill and wall drainage composite is also governed by the capillary barrier which taken place at the interface between two materials having different pore size.

**Keywords:** Critical suction · Capillary barrier · Effective saturation · Water retention characteristic · Reinforced earth techniques

© Springer Nature Singapore Pte Ltd. 2018
H. Tran-Nguyen et al. (eds.), *Proceedings of the 4th Congrès International de Géotechnique - Ouvrages -Structures*, Lecture Notes in Civil Engineering 8,
DOI 10.1007/978-981-10-6713-6_59

## 1 Introduction

Reinforced earth techniques was first introduced by [1], later known as Mechanically Stabilized Earth (MSE) walls, have been widely employed over four decades due to their ease of installation, quick construction, appropriate for different site conditions; consequently more costly compared to conventional reinforce concrete walls. As a type of gravity structures, MSE wall, is usually made of unsaturated earthen soils and the performance of this kind of reinforced earth structure is primary governed by the interaction between fill material and reinforcements. The interaction of the backfill material and reinforcements forms a flexible, coherent block that is able to sustain significant loads and movements, be also able to tolerate much larger settlements than reinforced concrete retaining wall which is unable to accommodate significant differential settlements. The construction cost of reinforced earth structures is mainly controlled by transportation of backfill materials and reinforcement types [2] this implies that if the reinforcements are designed for a certain construction site, the former one would be a major aspect. In tropical climate countries, granular materials are not readily available in the vicinity of typical construction sites while the residual soils are often lateritic soils which cover large areas, as a result of this the consideration the use of recommended materials as backfill for reinforced earth structures becomes a challenging task. Moreover, when considering the need for reducing the construction cost, local government is often obliged to use local soils with low permeability and low friction angle in constructing reinforced earth structures. [3] Reported that the use of "high fines" and/or "high plasticity" soils for reinforced fill becomes more frequent. Cases studies and applications of reinforced soil structures with lateritic soil backfill were examined by [4, 5], in which the reinforced soil structures performance using fine-grained poorly draining materials is primary governed by the amount of moisture content held in itself. Further, when impermeable reinforcements are utilized in reinforced soil structures, the moisture content conditions should be monitored and considered, similarly applicable drainage systems need to be employed. Seventeen of twenty six failure cases of MSE wall in the United States were related to low permeability backfill materials [6]. It is thereby an assertion can be withdrawn is that if fine-grained soils are utilized as backfill material in MSE walls both seepage water and accumulation of water behind and under the reinforced system should be either prevented or properly collected or discharged, and drainage system should protect not only the wall but also the embankment behind the wall. The use of the latter techniques has been reported in some current works [7–9] in which the geocomposites comprise a core material of geonet covered between two nonwoven geotextile were used to replace the conventional drainage system which typically made of well-graded gravel material. This study considers a practical scenario of reinforced earth structures to investigate the flow response inside the reinforced earth structure utilized high fine-grained soils. The scenario was established by which lateritic soil was utilized for unreinforced zone and granular soil was used for reinforced zone.

## 2 Theoretical Background

### 2.1 Constituent of Water Retention Characteristic Model

Soil water retention characteristic (SWRC) is the fundamental soil properties [10, 11] which is widely used in many applications in geotechnical engineering field. It's generally recognized that both physical and engineering features of soil are mainly affected by the SWRC. SWRC is defined as the relationship between amount of water held in the soil and the combined effect of these forces (often expressed in term of potential head) holding it. The graph giving the relation between soil water retention and soil water content is known as water retention curve (Fig. 1). Higher capillary yields higher suction and lower moisture content. Moisture content is held in the soil by two primary forces: capillarity and adsorption, the former one holds moisture in the pores between soil particles or between aggregates of the particles while the latter one is responsible for water attracted to the surface of soil particles [12].

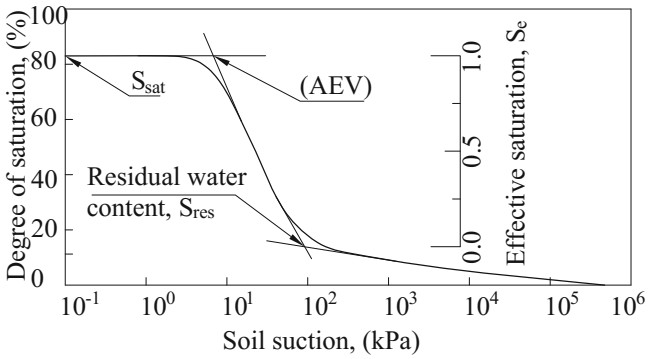


**Fig. 1.** Fundamental constituents of the SWRs

Four key constituents of the SWRC were introduced by [13] including maximum saturation $S_{sat}$, air entry value $AEV$, slope of SWRC, and residual saturation $S_{res}$. AEV is a point in the model where air begins to enter the soil pores (during drainage) or where all air is expelled (during wetting), the AEV is represented in term of $g_a$; maximum saturation, $S_{sat}$, is the amount of water held in the soil pores; residual saturation, $S_{res}$, is the amount of water held in the soil at high suction; the part of WRC curve between AEV and point of complete dryness is defined as slope of WRC curve depending on the range of pore sizes in the soil matrix (with assuming that other factors such as stress history are remained the same [14]). The term $g_n$ was designated to account for the slope of WRC curve, narrower pore-size distribution yield steeper slope and hence higher $g_n$ while in the broad pore-size distribution such as in clayey soil the rate of moisture discharge is very slow towards the end of completely dry soil, hence

the slope is very gentle for this section of WRC or lower $g_n$. It is, therefore, four these parameters need to be considered once examining the influences of soil water retention characteristics on hydrologic response.

### 2.2 Soil Water Flow Through Unsaturated Geo-Materials

The movement of water flows through unsaturated geo-materials (i.e., soils or geosynthetics) is more complex than those for water flow through saturated media [15]. This is partly because the most important variable that governs the rate of water flow through geo-materials (i.,e hydraulic conductivity) is not constant with varying water content. Instead, the hydraulic conductivity under unsaturated conditions varies with the level of water content or suction. Consequently, relative amounts of water and air in the geo-material highly influence its hydraulic behavior. [16] stated that the transient water flow in reinforced soil systems containing geotextiles whereby unsaturated soil conditions may dominate is predominantly governed by WRC. The transient water flow within an unsaturated porous medium is governed by the following equation:

$$\frac{\partial \theta}{\partial t} = k_x \frac{\partial^2 h}{\partial x^2} + k_y \frac{\partial^2 h}{\partial y^2} \tag{1}$$

where $\theta$ is volumetric water content, $h$ is the total head, $k_x$ and $k_y$ are the unsaturated coefficient of permeability in the x- and y- directions.

Along with WRC, the hydrologic response is also affected by k-function of the media through which water flows. After the first model was proposed by [17], several WRC models have been developed (Table 1). However, the continuous WRC model proposed by [18] fits degree of saturation versus soil suction data over the entire range of soil suction was then employed to represent the WRC, similarly the mathematic equation proposed by [19] used to present k-function, respectively. These models, termed as VG and VGM models are presented in Eqs. 2 and 3:

$$S_e = \frac{S - S_{res}}{S_{sat} - S_{res}} = \left[1 + \left(g_a \left| h_p \right|\right)^{g_n}\right]^{g_c} \tag{2}$$

$$k_r(S_e) = S_e^{0.5}\left[1 - \left(1 - S_e^{-1/g_c}\right)^{-g_c}\right]^2 \tag{3}$$

where $S_e$ is effective degree of saturation, $S$ is degree of saturation, $S_{res}$ is residual saturation at a very high value of suction, $S_{sat}$ is maximum saturation, $h_p$ [m] is matric suction head, $k_r$ is the relative permeability coefficient. $g_a[m^{-1}]$, $g_c$ and $g_n$ are fitting parameters, and according to [19], $g_c$ is assigned as $1/g_n - 1$ Among these parameters, $S_{res}$, $g_a$, and $g_n$ are parameters related to the type of porous media.

**Table 1.** Summary of several available soil water characteristic models

| Authors | SWCC model | Parameters | Time |
|---|---|---|---|
| Gardner | $\theta(h) = \theta_r + (\theta_s - \theta_r)[1 + (\alpha h)^n]^{-1}$ | $\theta_r, \theta_s$, α, n | 1958 |
| Brooks-Corey | $\theta(h) = \theta_r + (\theta_s - \theta_r)(\alpha h)^{-\lambda}$ | $\theta_r, \theta_s$, α, λ | 1964 |
| Brutsaert | $\theta(h) = \theta_r + (\theta_s - \theta_r)\left(1/\left(1 + \frac{\psi}{a}\right)^n\right)$ | $\theta_r, \theta_s$, α, n | 1966 |
| Campbell | $\theta(h) = \theta_s(\alpha h)^{\lambda}$ | $\theta_s$, α, λ | 1974 |
| Van Genuchten | $\theta(h) = \theta_r + (\theta_s - \theta_r)[1 + (\alpha h)^n]^{-m}$ | $\theta_r, \theta_s$, α, n, m | 1980 |
| Tani | $\theta(h) = \theta_r + (\theta_s - \theta_r)[1 + (\alpha h)e^{-\alpha h}]$ | $\theta_r, \theta_s$, α | 1982 |
| Mc Kee, C.R | $\theta = \theta_r + (\theta_s - \theta_r)\exp\left(\frac{\alpha - \psi}{n}\right)$ | $\theta_r, \theta_s$, α, n | 1984 |
| Fermi | $\theta = \theta_r + (\theta_s - \theta_r)(1/(1 + \exp\left(\frac{\alpha - \psi}{n}\right)))$ | $\theta_r, \theta_s$, α, n | 1987 |
| Fredlung-Xing | $\theta(h) = \theta_s + \frac{\theta_s - \theta_r}{[\ln(2.7183 + (\alpha h)^n]^m}$ | $\theta_r, \theta_s$, α, n, m | 1994 |
| Ruso | $\theta(h) = \theta_r + (\theta_s - \theta_r)\left[(1 + 0.5\alpha h)e^{0.5\alpha h}\right]^{\frac{2}{2+n}}$ | $\theta_r, \theta_s$, α, n | 1998 |
| Kosugi | $\theta(h) = \theta_r + \frac{1}{2}(\theta_s - \theta_r)erfc\left[\frac{\ln(h/h_m)}{\sigma\sqrt{2}}\right]$ | $\theta_r, \theta_s$, σ, $h_m$ | 1999 |
| Pereira | $\theta(h) = \theta_r + \frac{\theta_s - \theta_r}{\left[1 + (h/c)^b\right]^a}$ | $\theta_r, \theta_s$, a, b, c | 2000 |

a, b,c having meaning similar to the α, n, m. erfc: denotes the complementary error function (refer to [20])

## 3 Materials and Methods

Three types of materials were employed throughout this study, they were a sandy soil, a lateritic soil, and a geocomposites. The fundamental properties and WRC of the former and last one were utilized from [7, 21]. The lateritic soil was classified as SM-SC soil according to USCS, which consisted of 26% of fine particles with a plasticity index of 16%, saturated hydraulic conductivity of $4 \times 10^{-6}\ m/sec$, and the WRC of lateritic soil was determined using pressure extractor apparatus [22]. The grain size distribution of sandy soil and lateritic soil are shown in the Fig. 2a; the water retention characteristics of these three materials were summarized in the Fig. 2b. The fitting parameters are summarized in Table 2.

Parametric study method was chosen to carry out by varying the flow properties of high fine-grained soils. A well calibrated numerical model using the Plaxis 2D, 2011 finite element modelling software was proposed by [7] was used for the parametric study. The proposed model incorporated soil characteristics, soil reinforcement components, and drainage systems made of geotextile and geonet. The finite element mesh and boundary conditions assigned to the numerical model is depicted in the Fig. 3. The bottom boundary was assumed as an impervious boundary. In total, fifteen cases were performed to investigate the flow response in MSE walls. The set of parameters assigned to the scenarios was shown in the Table 3.

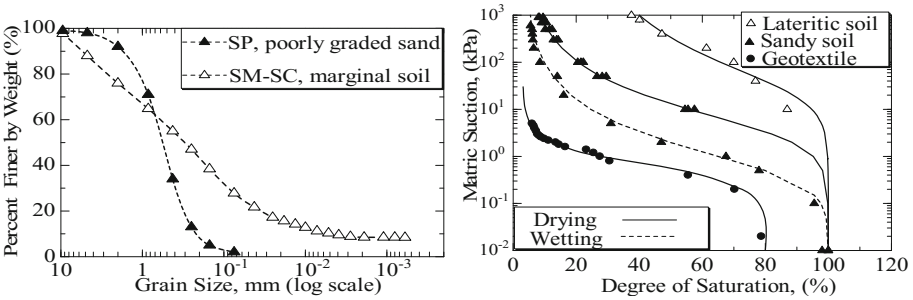


**Fig. 2.** Grained-size distribution of selected soils (a), and (b) WRC of three materials used in this study.

**Table 2.** van Genuchten parameters of materials

| Factors | Unit | Backfills | | Geotextile | Geonet |
|---|---|---|---|---|---|
| | | Sandy | Lateritic | | |
| $g_a$ | $m^{-1}$ | 20 | 0.8 | 20 | 600 |
| $g_n$ | – | 1.5 | 1.4 | 1.5 | 40 |
| $S_{res}$ | – | 0.03 | 0.2 | 0.03 | 0 |
| $S_{sat}$ | – | 1.0 | 1.0 | 0.8 | 1.0 |
| *Hydraulic properties* | | | | | |
| $K_{lateral}$ | m/day | 17 | 0.3456 | 320 | 69120 |
| $K_{long}$ | m/day | 17 | 0.3456 | 2000 | 69120 |

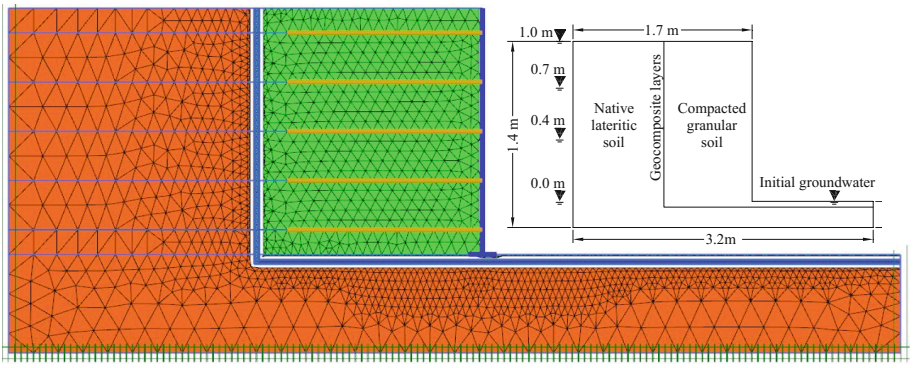


**Fig. 3.** Finite element mesh and boundary conditions assigned to the numerical model

**Table 3.** Set of unsaturated flow parameters of backfill materials assigned to considered scenario

| Scenario | Materials properties | | | | | | | | | | | Remarks |
|---|---|---|---|---|---|---|---|---|---|---|---|---|
| | Backfill materials | | | | | | | | | Geotextile | Geonet | |
| | Sandy soil | | | | | Lateritic soil | | | | n/a | n/a | |
| | $S_{res}$ (-) | $S_{sat}$ (-) | $g_n$ (-) | $g_a$ ($m^{-1}$) | k | $S_{res}$ (-) | $S_{sat}$ (-) | $g_n$ (-) | $g_a$ ($m^{-1}$) | k | | |
| Scenario: L-S | 0.03 | 1.0 | 1.5 | 20 | 17 | 0.1 | 1.0 | 1.4 | 0.8 | 0.3456 | | Case 1 |
| | | | | | | 0.3 | | | | | | Case 2 |
| | | | | | | 0.5 | | | | | | Case 3 |
| | | | | | | 0.2 | 0.7 | 1.4 | 0.8 | 0.3456 | | Case 4 |
| | | | | | | | 0.8 | | | | | Case 5 |
| | | | | | | | 0.9 | | | | | Case 6 |
| | | | | | | 0.2 | 1.0 | 1.1 | 1.4 | 0.3456 | | Case 7 |
| | | | | | | | | 1.2 | | | | Case 8 |
| | | | | | | | | 1.3 | | | | Case 9 |
| | | | | | | | | 1.4 | | | | Case 10 |
| | | | | | | | | 1.5 | | | | Case 11 |
| | | | | | | 0.2 | 1.0 | 1.4 | 0.5 | 0.3456 | | Case 12 |
| | | | | | | | | | 1.0 | | | Case 13 |
| | | | | | | | | | 3.0 | | | Case 14 |
| | | | | | | | | | 5.0 | | | Case 15 |

## 4 Parametric Study Results and Discussions

The scenario was considered to simulate a feasible case, in which the recommended backfill is not readily available for a huge amount of required backfill materials, the use of local soil with low hydraulic conductivity is then compelled for the unreinforced zone, whereas the reinforced zone was filled by good draining backfills. The effects of water retention characteristic of fine-grained soil utilized as backfill for unreinforced zone on moisture condition was evaluated by varying the constituent elements of WRC of lateritic soil while the properties of reinforced soil mass kept constant.

### 4.1 Effect of $g_a$

The changes in phreatic surface in unreinforced zone at different values of $g_a$ are shown in the Fig. 4. It is clearly exhibited that the higher $g_a$ value of outer soil yields genter phreatice surface, whereas the phreatic surface in reinforced soil mass are not changed regardless of changing in $g_a$. Figure 5 shows the profile of effective saturation along vertical sections located outside and inside protected zone, these sections is far 5 cm from the wall drainage geocomposite. The effective saturation profile in unreinforced soil mass is almost higher of 90% for the entire height of MSE wall in case low $g_a$ of 0.5, and 0.8. However, the magnitude of effective saturation is then notably decrease at ga of 3.0. In reinforced zone, the effect of $g_a$ of lateritic soil on moisture condition is not trivial. The variation of effective saturation is almost the same with different values of $g_a$.

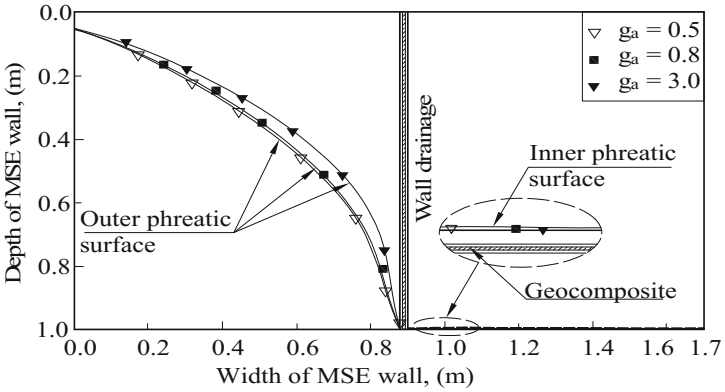


**Fig. 4.** Changes in phreatic surface with various values of $g_a$ of lateritic soil in in unreinforced soil mass.

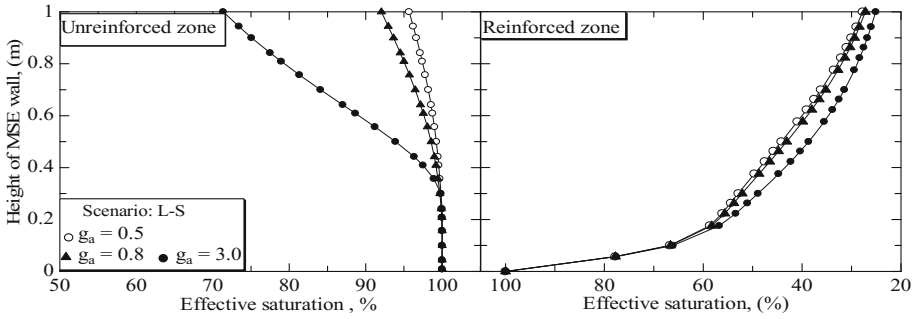


**Fig. 5.** Effective saturation profile the interface between wall drainage and soil for various magnitudes of $g_a$ of lateritic soil.

### 4.2 Effect of $g_n$

Figure 6 shows the phreatic surface and effective saturation at various values of $g_n$ of lateritic soil. The computed results show that the lower $g_n$ the gentler phreatic surface. The lower $g_n$ brings about the wider effective saturation distribution in the unreinforced soil mass. Inversely, the changes in the distribution of effective saturation in reinforced soil mass due to varying of $g_n$ of lateritic soil is insignificant.

### 4.3 Discussion on the Computed Results of Moisture Profile

#### 4.3.1 Effect of $g_a$

Since lateritic soil having low $g_a$, wider range of suction, hence the high saturation range become so wider that covers almost entire mass of lateritic soil. Due to this, the effect of $g_n$ on moisture profile could not recognizably exhibit. The effective saturation at the interface located in the unreinforced zone was found at a high values of around of

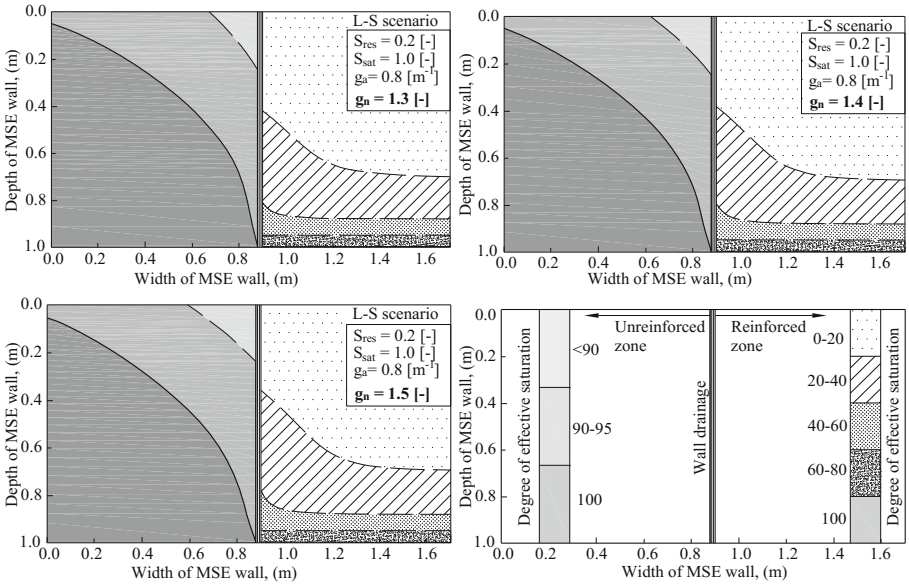


**Fig. 6.** Phreatic surface (solid lines) and effective saturation contour lines (dashed line) at various magnitudes of $g_n$ of lateritic soil

90% with respect to a low range of $g_a$ of (0.5−1.0). It was then significantly decreased as $g_a$ increased. The change in $g_a$ of outer soil somewhat causes a little effect on the effective saturation inside the reinforced zone. The $g_a$ value also affects the phreatic inside the unreinforced zone. The lower $g_a$ results in the lower height of phreatic surface. This is due to the capillary barrier occurred at the interface between two materials having different pore size. In other words, the interface between soil and geotextile may act as a capillary barrier which causes water being obstructed at the interface. This barrier is only broken when the value of suction at the interface decreases to a critical value or hydraulic conductivity of the two unsaturated materials are equal [23], consequently water from unreinforced zone is capable of "breaking" into wall drainage composite having large pore. The lower suction at critical point (lower $g_a$) the more difficult for water permeate through the interface. As a results of this phenomenon, the amount of water accumulated at the interface increased, hence the lower elevation of phreatic surface.

### 4.3.2 Effect of $g_n$

The fine-grained soil possessing so low value of $g_a$ that the effect of $g_n$ on moisture response could not clearly recognized. It was also found the lower $g_n$ (higher suction at critical point) caused the wider distribution of the effective saturation and higher phreatic surface in unreinforced zone while having a minor influence in the reinforced zone.

It is noted that the computed result in this research and that introduced in the [24] having the same finding of lower $g_a$ brings about lower phreatic surface whereas the effect of $g_n$ on phreatic surface was found to be different from this finding. [24] Stated that lower $g_n$ value the higher phreatic surface due to capillary effect as explained in the previous section. It is, however, in this scenario the value of suction at breakthrough point builds up with value of $g_a$, but decreases with $g_n$ value (Fig. 7), consequently higher phreatic obtained.

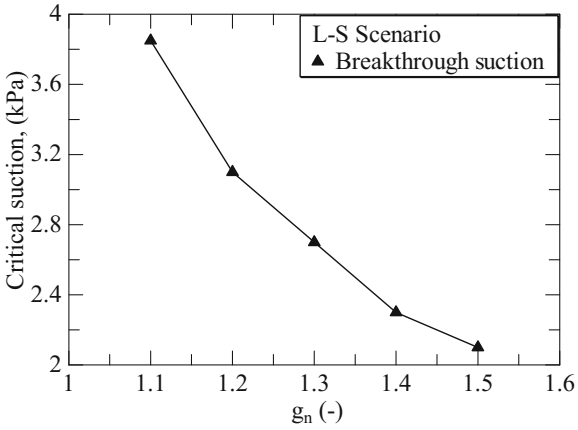


**Fig. 7.** Variation of critical suction at breakthrough point with $g_n$ of lateritic soil

## 5 Conclusions

The flow response of reinforced earth structures utilized high fine-grained soils as materials for reinforced earth were examined, the following findings can be drawn as follows:

(1) The moisture responses in reinforced soil mass is slightly affected by the flow properties of the high fine-grained soil placed next to reinforced part;
(2) The interface between soil and wall drainage composite may act as a hydraulic barrier, termed as capillary barrier, which occupies a function on the elevation of phreatic surface located in unreinforced zone.
(3) As poorly draining materials are utilized as backfill materials for reinforced soil structures, the moisture content should be monitored; further, the permeable reinforcements and adequate drainage systems need to be put into the reinforced earth structures.

The more investigation on the moisture response needs to be carried out to consider a feasible case that the reinforced earth structures are fully filled by high fine-grained soils. In addition, MSE walls are normally made of unsaturated soils so the load

deformation behavior of soil reinforcements embedded in unsaturated soil should be investigated in order to predict the bearing capacity of reinforcements under unsaturated condition.

**Acknowledgments.** The first author is grateful to the financial support from Suranaree University of Technology under SUT-Ph.D scholarship program for his Ph.D studies.

## References

1. Vidal, H.: The principle of reinforced earth. Highw. Res. Rec. No 282, Transp. Res. Board Washington, DC (1969)
2. Horpibulsuk, S., Niramitkornburee, A.: Pullout resistance of bearing reinforcement embedded in sand. Soils Found. **50**(2), 215–226 (2010)
3. Stulgis, R.: Selecting reinforced fill materials for mse retaining walls. In: Geosynthetics Research and Development in Progress, pp. 1–6. ASCE (2005)
4. Zornberg, J., Mitchell, J.: Reinforced soil structures with poorly draining backfills. Part I: reinforcement interactions and functions. Geosynth. Int. **1**(2), 103–147 (1994)
5. Mitchell, J.: Reinforced soil structures with poorly draining backfills part II: case histories and applications. Geosynth. Int. **2**(1), 265–307 (1995)
6. Koerner, R.M., Soong, T.-Y.: Geosynthetic reinforced segmental retaining walls. Geotext. Geomembr. **19**(6), 359–386 (2001)
7. Chinkulkijniwat, A., Horpibulsuk, S., Bui Van, D., Udomchai, A., Goodary, R., Arulrajah, A.: Influential factors affecting drainage design considerations for mechanical stabilised earth walls using geocomposites. Geosynthetics Int. 1–18 (2016)
8. McKean, J., Inouye, K.: Field evaluation of the long-term performance of geocomposite sheet drains. Geotext. Geomembr. **19**(4), 213–234 (2001)
9. Narejo, D., Ramsey, B.: MSE wall drainage alternatives careful drainage design can prevent costly retaining-wall failures. Geotech. Fabr. Rep. **19**(5), 26–29 (2001)
10. Leong, E.C., Rahardjo, H.: Review of soil-water characteristic curve equations. J. Geotech. Geoenviron. Eng. **123**(12), 1106–1117 (1997)
11. Too, V.K., Omuto, C.T., Biamah, E.K., Obiero, J.P.: Review of soil water retention characteristic (SWRC) models between saturation and oven dryness. Open J.Mod. Hydrol. **4**(4), 173 (2014)
12. Marshall, T.J., Holmes, J.W., Rose, C.W.: Soil Physics, Cambridge University Press (1996)
13. Fredlund, D.G., Xing, A.: Equations for the soil-water characteristic curve. Can. Geotech. J **31**(4), 521–532 (1994)
14. Omuto, C.: Biexponential model for water retention characteristics. Geoderma **149**(3), 235–242 (2009)
15. Bouazza, A., Zornberg, J., McCartney, J.S., Singh, R.M.: Unsaturated geotechnics applied to geoenvironmental engineering problems involving geosynthetics. Eng. Geol. **165**, 143–153 (2013)
16. Bouazza, A., Freund, M., Nahlawi, H.: Water retention of nonwoven polyester geotextiles. Polym. Test. **25**(8), 1038–1043 (2006)
17. Gardner, W.: Mathematics of isothermal water conduction in unsaturated soil. Highw. Res. Board Spec. Rep. (40) (1958)
18. van-Genuchten.: A closed-form equation for predicting the hydraulic conductivity of unsaturated soils. Soil Sci. Soc. Am. J. **44**(5), 892–898 (1980)

19. Mualem, Y.: A new model for predicting the hydraulic conductivity of unsaturated porous media. Water Resour. Res. **12**(3), 513–522 (1976)
20. Kosugi, K.: General model for unsaturated hydraulic conductivity for soils with lognormal pore-size distribution. Soil Sci. Soc. Am. J. **63**(2), 270–277 (1999)
21. Bui Van, D., Chinkulkijniwat, A., Horpibulsuk, S., et al.: Influence of nonwoven geotextile on the hydraulic response of mechanical stabilized earth wall. In: Proceeding of the sixth International Conference on Geotechnique, Construction Materials & Environment, Bangkok, Thailand November 2016. ISBN 978–49905958-6-9 C3051, 367-372
22. ASTM: 2008 Standard test methods for determination of the soil water chararcteristic curve for desorption using a hanging column, pressure extractor, chilled mirror hygrometer, and/or centrifuge, D6836. ASTM International
23. Iryo, T., Rowe, R.K.: On the hydraulic behavior of unsaturated nonwoven geotextiles. Geotext. Geomembr. **21**(6), 381–404 (2003)
24. Wise, W.R., Clement, T., Molz, F.J.: Variably saturated modeling of transient drainage: sensitivity to soil properties. J. Hydrol. **161**(1), 91–108 (1994)

# Using a Spray Test to Study the Surface Erosion of Geomaterials Application on Construction Material of Soil-Cement Mixtures in Le Havre, France

Van-Nghia Nguyen[1(✉)] and Said Taibi[2]

[1] Division of Hydropower and Renewable Energy, Thuy Loi University, Ha Noi City, Vietnam
nghia_nvn@tlu.edu.vn
[2] Laboratory of Waves and Complex Medium, Le Havre University, Le Havre, France

**Abstract.** A Spray Test and the first test results on soil-cement mixture in the laboratory were presented in this paper. This device simulates the impact of rains on the walls or earthen walls. The results show a resistance to erosion by a rain of the soil-cement mixture, while the other materials were eroded by rains under the same precipitations.

**Keywords:** Spray Test · Earth-wall · Resistance to erosion · CémaTerre · Microcracking

## 1 Introduction

Earth-wall constructions are always subjected to a natural condition that why they are influenced by rainfall over time. The resistance to erosion or durability by rains of these earth-walls depends not only on their properties but also on the precipitations. Numerous researchers showed the influence of the intensity of the rains, angle of rainfall, exceeding roofing, the roughness of wall (Eassey 1997; Heathcote 1995). In another hand, the properties of materials play an important role such as soil composition, dry density, compaction water content, cement content, clay percentage, etc. It found that the resistance to erosion of earth-wall increase with an increase of clay percentage (Reddy and Jagadish 1987), an increase of dry density of the material (Jagadish and Reddy 1984; Tannous 1995), an increase of cement percentage (Ngowi 1997; Walker 1995).

The erosion of the earth-wall by rains is a type of external erosion where the grain of wall material is pulled by the flash. To study the surface erosion of earthen wall, it exists numerous devices to study at laboratory and at field such as Spray Test (Schneider 1981; NZS-4298 1998; SAZS-724 2012), Rainfall Test (Ogunye and Boussabaine 2002), Drip Test (NZS-4298 1998; ASZS 724 2012), Climatic Simulation Chamber (Hall 2007), Climatic conditions exposure (Guettala et al. 2006).

© Springer Nature Singapore Pte Ltd. 2018
H. Tran-Nguyen et al. (eds.), *Proceedings of the 4th Congrès International de Géotechnique - Ouvrages -Structures*, Lecture Notes in Civil Engineering 8,
DOI 10.1007/978-981-10-6713-6_60

For the Spray Test, it did not accurately simulate the long-term effects of natural rainfall, as there appears to be little correlation with the actual weathering performance (Ogunye and Boussabaine 2002), but it was suitable for soil in the field but not for the earthen wall, mainly for the wall consisting of soil with a binder of cement and lime especially for the area having high precipitations and earth-wall having high resistance to erosion by rain. So the Spray Test is one suitable choice to study the surface erosion of soil-cement mixture.

In this paper, the authors use a Spray Test which was adapted from the one illustrated in NZS-4298 and SAZS-724 (NZS-4298 1998; SAZS-724 2012) to study the surface erosion of a CémaTerre, this material used in Le Havre is the mixture of soil and cement.

## 2 Materials and Experimental Apparatus

### 2.1 Material

In this work, two materials were used to erosion characterization. The Marne having 80% of the liquid limit, 27.5% of Standard Proctor Optimum (OPN) water content, 1.5 g/cm$^3$ of dry density. The soil-lime-cement named CémaTerre was a patented product of the CémaTerre society.

### 2.2 Experimental Apparatus

#### 2.2.1 Apparatus Description

A Spray Test was designed based on the one presented in NZS-4298 and SAZS-724 (NZS-4298 1998; SAZS-724 2012). This device (Fig. 1) consists of a reservoir with an electric submersible pump in which (3 bar of maximum pressure and 2560 l/min of maximum flow), a steel tube (500 mm in length, 12.2 mm in diameter) is fixed in horizontal position, a standard PVC nozzle consisting of 35 holes of 1.3 mm in diameter, a pressure regulator which allows changing the pressure from 0.5 bar to 15 bar, a valve to control the pressure and flow, a manometer for reading the pressure at the outlet of the valve, a wood plate with a hole 150 mm in diameter (Fig. 2) is placed on the sample to delimit the section of sample exposed to the spray. In respect the standard, the distance between nozzle and sample is fixed at 470 mm.

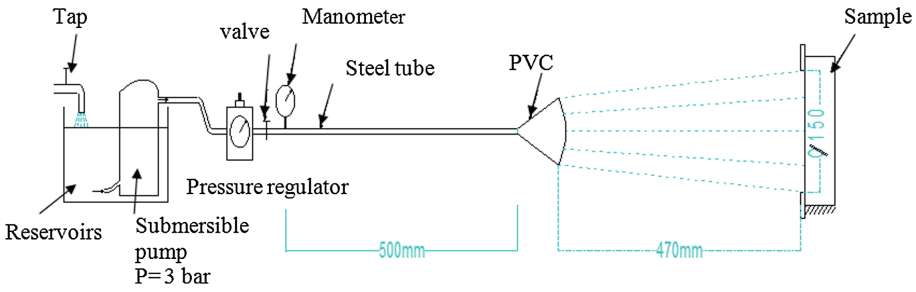


**Fig. 1.** Schema of the Spray Test

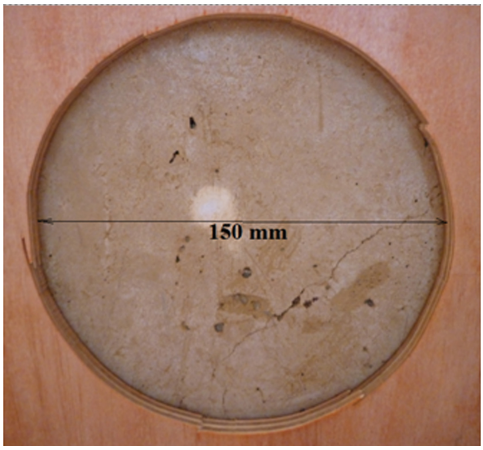


**Fig. 2.** Position of wood plate and sample

### 2.2.2 Apparatus Calibration

The objective is to verify the relation between the pressure in the tube and flow at the nozzle. Figure 3 shows the linear variation in flow and velocity at nozzle as a function of pressure respectively. Here, the velocity was calculated by the ratio of flow to a section of nozzles, at constant pressure the flow was measured manually in each five min for nine times.

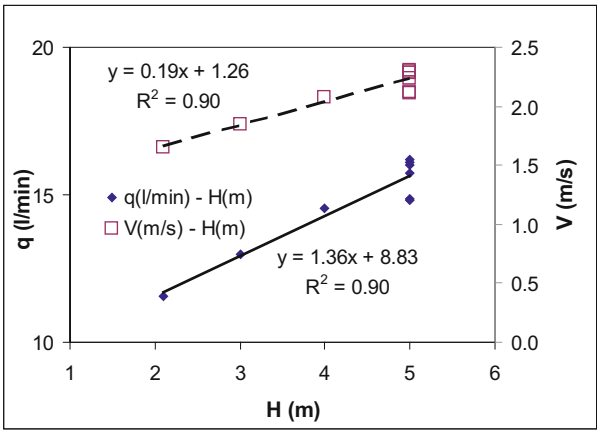


**Fig. 3.** Relationship between the flow, q (l/min), velocity, V (m/s) and pressure, H (m)

The volume of water projected at the surface of the sample during one hour corresponds to 77.5 years of rain in Le Havre, the annual rainfall being 709 mm (Blaizot 2010).

## 3 Results and Discussion

In the first step, five samples were carried out consecutively for one hour without interruption of the jets in according to the standards (NZS-4298 1998; SAZS-724 2012), the depth of the erosive cavities is measured at the end of the tests. The volume of water projected on the surface corresponds to 77.5 years of rain in Le Havre. The results show negligible erosion for this material. Only some thin layers of the surface were leached by the jet. According to the standards (NZS-4298 1998; SAZS-724 2012), the erodibility index of this material is in the rank 1, it means very resistance to erosion.

The tests were prolonged on the 6$^{th}$ sample beyond the standardized time of 60 min. Each time, the jet is stopped and pictures are taken at the same angle. Figure 4 shows these photos at different exposure times of the Spray Test.

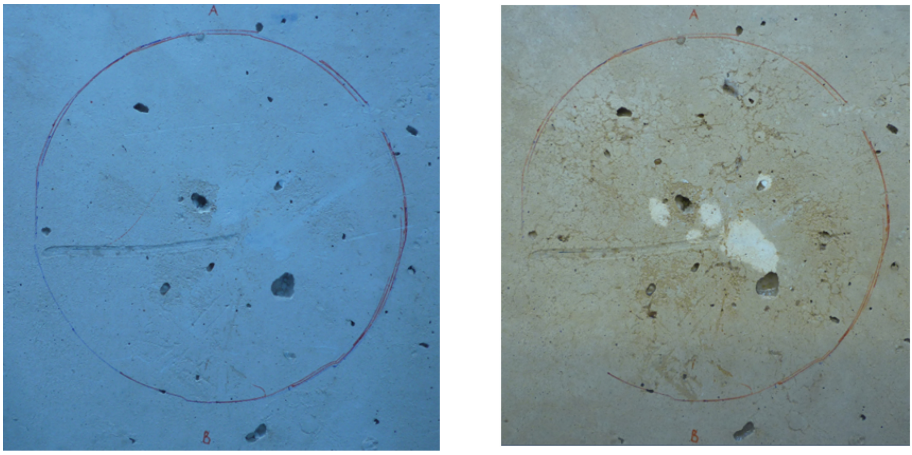

Initial state After 12 hours

**Fig. 4.** Surface state at different time under the jets of Spray Test

To analyze the surface state of the CémaTerre after exposures under the jets, an image analysis of exposed surface is then carried out using the "ImageJ" software. It is an open source software for image processing and analysis developed by the National Institute of Health. It is written in Java and allows the addition of new functionalities via plugins and macros.

The analysis using the software allows deducing the percentage of microcracking observed at the surface at different times of exposure to the jet. The results are shown in Fig. 5, the crack widening which is calculated by Eq. (1) increases slightly with an exposure time of jet, and stabilize after about 6 h. These microcracks were probably present initially on the surface of the material were hidden by the thin layer of "laitance" of the binder during the making of the sample by pouring the soil-cement and its vibration.

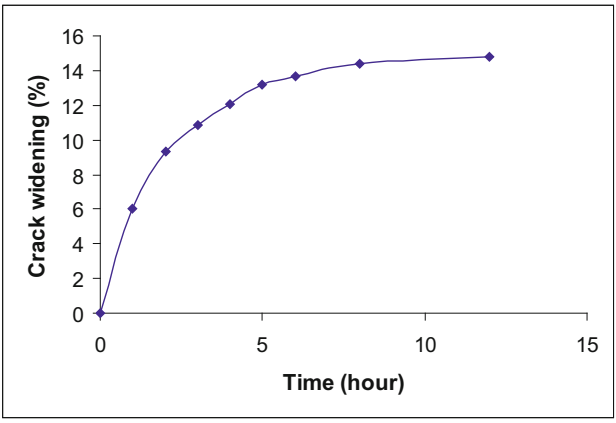


**Fig. 5.** Relationship between crack widening versus the time of jets.

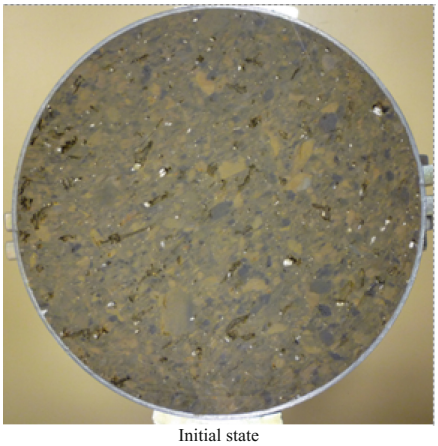
Initial state

After 15 min under the jets

After 30 min under the jets

After 45 min under the jets

**Fig. 6.** Photos of sample after different times under Spray Test

$$crack\ widening = \frac{crack\ surface - initial\ crack\ surface}{Total\ surface} \cdot 100\% \quad (1)$$

In order to locate these results in relation to other materials, "Spray Test" tests were carried out on Marne which compacted in the CBR mold (152 mm in diameter, 125 mm in height) in the OPN state. The results are shown in Figs. 6 and 7.

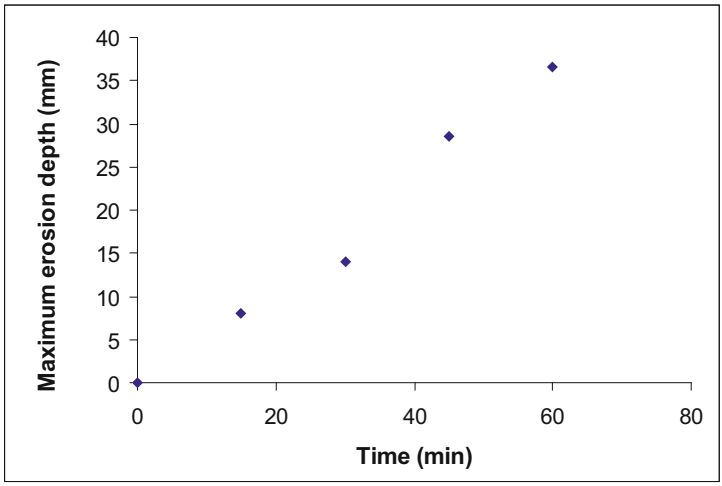


**Fig. 7.** Evolution of maximum erosion depth versus time

The evolution of the maximum depth of erosion created by the jets is quasi-linear with time (Fig. 7). The maximum erosion depth measured at the end of the test (after 60 min under the jets) is 36.5 mm. According to the classification proposed by the standards (NZS-4298 1998; SAZS-724 2012), the erodibility index is in rank 2. It's suitable with the result of a test using Drip Test (Nguyen and Taibi 2015).

## 4 Conclusion

In the case of "CémaTerre" which are soils treated with binders (lime and cement), they are very resistant to surface erosion according to the "Spray Test" standards.

The "Spray Test" seems well suited to test building materials based on raw earth such as clay or earthen concretes like CémaTerre.

The "Spray Test" should be suitable with the soil having a high liquid limit.

## References

Blaizot, D.: La pluie en France—Les villes où il pleut le plus et celles où il pleut le moins. Gloubik Sciences (2010). (http://sciences.gloubik.info/spip.php?article879)

Eassey, A.: The effect of the angle of raindrops on earth wall buildings. In: Construction Management Thesis, University of Technology, Sydney (1997)

Guettala, A., Abibsi, A., Houari, H.: Durability study of stabilized earth concrete under both laboratory and climatic conditions exposure. Constr. Build. Mater. **20**, 119–127 (2006). doi:10.1016/j.conbuildmat.2005.02.001

Hall, M.R.: Assessing the environmental performance of stabilised rammed earth walls using a climatic simulation chamber. Constr. Build. Mater. **42**, 139–145 (2007). doi:10.1016/j.buildenv.2005.08.017

Heathcote, K.A.: Durability of earthwall buildings. Constr. Build. Mater. **9**(3), 185–189 (1995). doi:10.1016/0950-0618(95)00035-E

Jagadish, K.S., Reddy, V.B.V.: The technology of pressed soil blocks for housing: problems and tasks. In: International Colloquium on Earth Construction for Developing Countries, Brussels, Belgium, 226–243 (1984)

Ngowi, A.B.: Improving the traditional earth construction: a case study of Botswana. Constr. Build. Mater. **11**(1), 1–7 (1997). doi:10.1016/S0950-0618(97)00006-8

Nguyen, V.N., Taibi, S.: Erosion de surface des Géo-matériaux, Application aux matériaux de Construction à base de Terre crue, p. 93. Projet CémaTerre (2015)

NZS-4298: 1998 Materials and Workmanship for Earth Buildings. Standards New Zealand (1998)

Ogunye, F.O., Boussabaine, H.: Development of a rainfall test rig as an aid in soil block weathering assessment. Constr. Build. Mater. **16**, 173–180 (2002). doi:10.1016/S0950-0618(02)00010-7

Reddy, B.V.V., Jagadish, K.S.: Spray Erosion studies on Pressed Soil Blocks. Build. Environ. **22**, 135–140 (1987). doi:10.1016/0360-1323(87)90033-3

SAZS-724: 2012 Rammed earth structures—Code of practice. Standard Zimbabwe (2002)

Schneider, L.M.: Bulletin 5 – Earth-wall Construction. National building Technology Centre, Chatswood (Original edition by Middleton JF) (1981)

Tannous, L.: The effect of density on the durability of stabilised soil blocks. In: Undergraduate Building Project, Faculty of Design Architecture and Building, University of Technology, Sydney (1995)

Walker, P.J.: Strength, durability and shrinkage characteristics of cement stabilised soil blocks. Cem. Concr. Compos. **17**, 301–310 (1995). doi:10.1016/0958-9465(95),00019-9

# Using Wastes from Thermal Power Plants for Manufacturing of Low Strength Construction Materials

Quoc-Bao Bui(✉), Minh-Tung Tran, and Duc-Hien Le

Faculty of Civil Engineering, Sustainable Developments in Civil Engineering Research Group, Ton Duc Thang University, Ho Chi Minh City, Vietnam
buiquocbao@tdt.edu.vn

**Abstract.** Thermal power plants (TPP) generates wastes (bottom and fly ashes) which become a serious environmental problem in Vietnam. Indeed, although in several countries fly ash can be used for cement industry, fly ash from actual TPP in Vietnam does not have enough good quality for cement production, because the fly ash treatment phase has not yet included in the generations of existing Vietnamese TPP. That is why bottom ash and fly ash purely become wastes and their evacuation is an urgent demand of the society. This paper presents an investigation using fly and bottom ashes in the manufacturing of construction materials. The aim of this study is to propose a possibility to reduce environmental impacts of fly and bottom ashes, and manufacture construction materials having low embodied energy by using less cement. Several proportions of fly ash, cement, gravel, sand and water are tried to manufacture low strength concretes which can be used for non-load-bearing walls. Specimens are tested in uniaxial compressions. Results show that with a reasonable cement amount (4–8% by weight), by replacing cement by fly ash or replacing sand by bottom ash at 10-30%, the obtained materials can be used for non-bearing materials or low strength structural materials.

**Keywords:** Industrial waste valorization · Low strength material · Low embodied energy · Fly ash · Bottom ash

## 1 Introduction

Thermal power plants (TPP) generates wastes (bottom and fly ashes) which become a serious environmental problem in Vietnam. Indeed, although in several countries fly ash can be used for cement industry, fly ash from actual TPP in Vietnam does not have enough good quality for cement production, because the fly ash treatment phase has not yet included in the generations of existing Vietnamese TPP. That is why bottom ash and fly ash purely become wastes and their evacuation is an urgent demand of the society.

On the other hand, to reduce environmental impacts in the construction factor, Vietnamese government has demanded to replace clayed burnt bricks by other more "green" materials and unburnt bricks are the current strategy adopted by construction companies. However, unburnt bricks still have several difficulties to find their places on

© Springer Nature Singapore Pte Ltd. 2018
H. Tran-Nguyen et al. (eds.), *Proceedings of the 4th Congrès International de Géotechnique - Ouvrages -Structures*, Lecture Notes in Civil Engineering 8,
DOI 10.1007/978-981-10-6713-6_61

the construction site in Vietnam, due to several reason: economic, environment, tradition. One of the main reasons is the use of important cement amount in the unburnt brick manufacturing (about 25% by weight), this increased both the manufacturing cost and the carbon footprint.

This paper presents an investigation using fly and bottom ashes in the manufacturing of construction materials. The aim of this study is to propose a possibility to reduce environmental impacts of fly ash which are actually considered as waste in Vietnam, and then formulate materials having low embodied energy by using less cement. Several proportions of fly ash, bottom ash, cement, gravel, sand and water are tried to manufacture low strength concretes which can be used for non-load-bearing walls. Specimens are tested in uniaxial compressions. Results show that with a reasonable cement amount (4-8% by weight), obtained compression strengths are about 4-8 MPa which is acceptable for non-structural materials.

## 2 Specimens Using Fly Ash

### 2.1 Materials Used

Gravels and sand are classical materials used for conventional concrete (Fig. 1). The maximal diameters for sand and gravels are of 4 mm and 20 mm, respectively. The optimum mix between Sand and Gravel was determined by using Dreux-Gorisse's method (Day 1999), which gave a ratio of Sand/Gravel = 2/3 (by weight and volume). The grain size distribution of the mixed aggregate (Sand + Gravel) is also illustrated in Fig. 1.

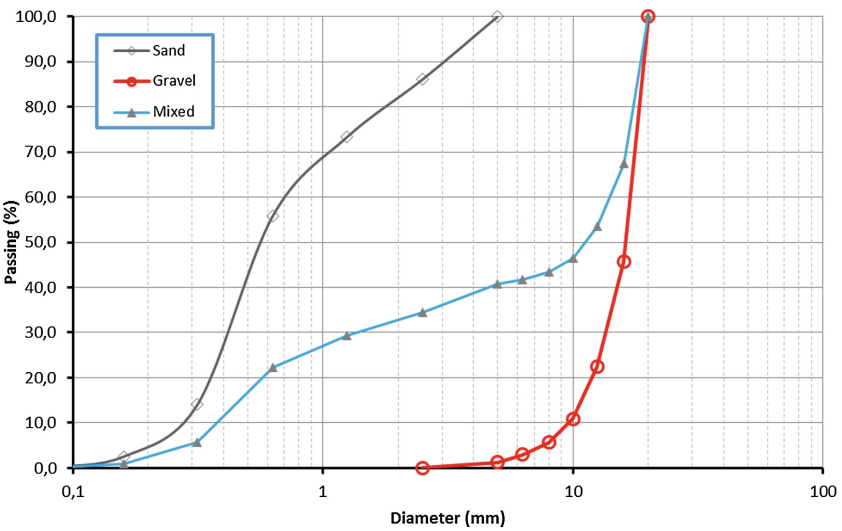


**Fig. 1.** Grain size distribution of the aggregate used.

The cement used was a current Porland cement, named PC 30, where a specified compressive strength at 28 days of the cement mortar (1 cement: 3 sand by weight) was 30 MPa. Because the scope of this study was to manufacture low-strength materials with reasonable costs, other higher quality cements were not tried.

Fly ash used was directly taken from a thermal power plants. The compositions of the used fly ash and bottom ash were analyzed following ASTM standard (2015) by a control company (Vinacontrol 2015), the results are presented in Tables 1 and 2.

The specified density of the fly and bottom ashes used was determined following Vietnamese standard. Results gave mean densities of 2.26 and 2.24 respectively for fly ash and bottom ash. The finesse modulus of bottom ash was also obtained from sieving analysis, giving a value of 2.73.

**Table 1.** Composition of fly ash studied, in %.

| Carbon | Hydro | Nitrogen | Sulfur | Oxygen | $SiO_2$ | $Al_2O_3$ | $Fe_2O_3$ | $TiO_2$ | CaO | MgO | $K_2O$ | $Na_2O$ | $P_2O_3$ | MnO | $SO_3$ | Other |
|---|---|---|---|---|---|---|---|---|---|---|---|---|---|---|---|---|
| 12.41 | 0.05 | 0.15 | 0.04 | 0.05 | 57.7 | 25.72 | 6.79 | 0.85 | 0.97 | 1.45 | 5.03 | 0.43 | 0.28 | 0.07 | 0.18 | 0.53 |

**Table 2.** Composition of bottom ash studied, in %.

| Carbon | Hydro | Nitrogen | Sulfur | Oxygen | $SiO_2$ | $Al_2O_3$ | $Fe_2O_3$ | $TiO_2$ | CaO | MgO | $K_2O$ | $Na_2O$ | $P_2O_5$ | MnO | $SO_3$ | Other |
|---|---|---|---|---|---|---|---|---|---|---|---|---|---|---|---|---|
| 10.44 | 0.09 | 0.14 | 0.05 | 0.07 | 57.54 | 23.47 | 8.76 | 0.70 | 1.57 | 1.27 | 5.12 | 0.21 | 0.20 | 0.11 | 0.12 | 0.93 |

## 2.2 Formulation of the Materials Investigated

First, a classical concrete was formulated, as a reference for the comparison. The referent concrete correspond to a 320 kg of cement in 1 $m^3$ concrete. The composition of this referent concrete was calculated following the well-known Dreux-Gorisse's method. The water was chosen (W/C = 0.7) to give a plastic concrete with a slump value of 7 ± 1 cm, which is the current value for current concretes. The result is detailed in Table 3. This referent case is named "14%C" (14% cement).

**Table 3.** Composition of the referent concrete, by weight.

| Gravel | Sand | Cement | Water |
|---|---|---|---|
| 45% | 30% | 14% | 10% |

Because the scope of the study was to manufacture low strength materials with low environmental impacts, another formulation using only 10% of cement was investigated. This case is called "10%C" (10% cement).

From this second "referent" case, other compositions were tested by replacing one part of cement by fly ash. Cement was respectively replaced at 10, 20, 40 and 60% by fly ash. The new formulations are called "9%C + 1%FA" (9% cement + 1% Fly Ash); "8%C + 2%FA" (8% cement + 2% Fly Ash); "6%C + 4%FA" (6% cement + 4% Fly Ash); "4%C + 6%FA" (4% cement + 6% Fly Ash).

### 2.3 Specimens Manufacturing

Specimens were manufactured in steel cubic 15 cm × 15 cm × 15 cm molds. It is well-known that cylinder specimens gave more realist results (see for example Bui et al. 2009) and compressive strength obtained on cubic specimens should be multiplied by a corrector factor (about 0.9) to obtain the corresponding strength on cylinder specimens. However, cubic specimens were chosen because of the simplicity in their manufacturing and testing (no need of surfacing).

For each composition studied, twelve specimens were manufactured: six specimens for compression tests at 14 days and six other for compression tests at 28 days. To investigate influence of the curing condition, a half of specimens were cured in water after the unmolding and the other half was cured in ambient air (about 28 °C and 75% RH).

### 2.4 Uniaxial Compression Tests

Cubic specimens was tested under loading rate of 0.1 mm/min (Fig. 2). The mean results obtained on three specimens of each composition are presented in Fig. 3 and Fig. 4, respectively for specimens cured in water and in ambient air.

**Fig. 2.** Uniaxial compression test on cubic specimens.

The mean compressive strength of the referent case (14% cement) after 28 days cured in water was about 22 MPa, which corresponded to a current concrete for constructions of "medium classes" in Vietnam. The compressive strength can be explained because no plasticizer was used and the water/cement ratio (of 0.7) was higher than a classical way (about 0.45-0.5).

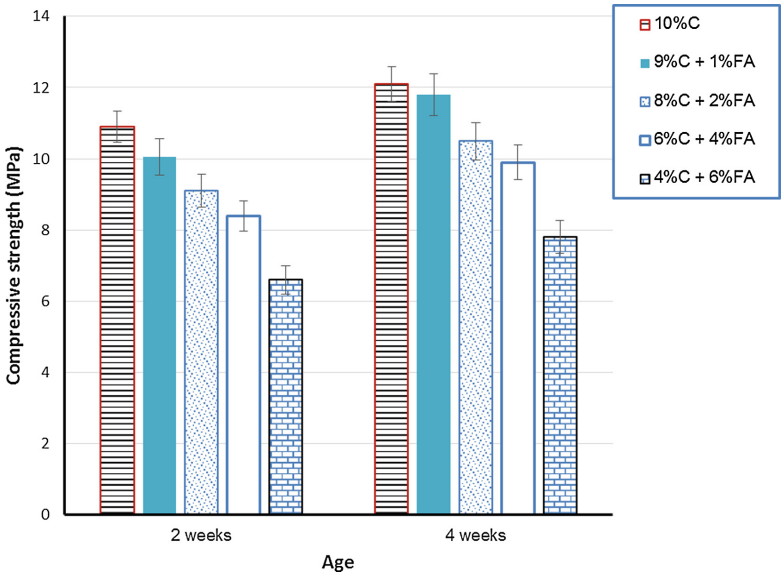


**Fig. 3.** Compressive strengths of different investigated compositions, replacing cement by fly ash and curing in water.

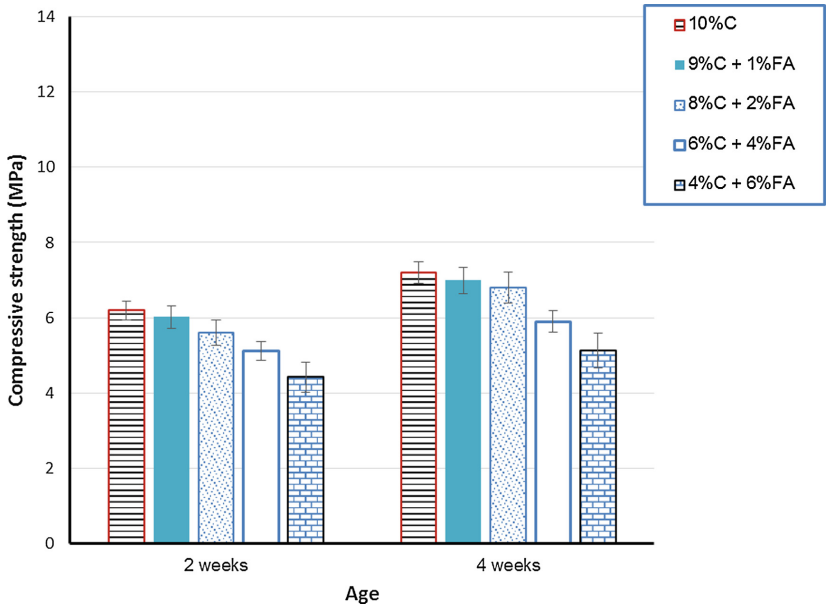


**Fig. 4.** Compressive strengths of different investigated compositions, replacing cement by fly ash and curing in ambient air.

Then, for the case of 10% cement without fly ash, the compressive strength decreased quickly and a mean compressive strength of 12 MPa was obtained at 28 days (cured in water). This result is comprehensive because the cement amount determined following Dreux-Gorisse's method (14%) corresponded to an empirical cement amount necessary to "cover" all aggregates. By decreasing this cement amount, several aggregates are not "covered" which leads to "weak points" in the microstructure of the concrete. The compressive strength is therefore decreased.

The present study concentrates to investigate the compressive strength evolution when fly ash is used. The results showed that, when cement is replaced by fly ash, the compressive strength decreased, but the compressive strengths obtained were in the range 4-10 MPa which is acceptable for non-load-bearing material or low-strength structural materials.

Results shows that curing conditions had significant influences on the results obtained. In the normalized curing condition, specimens could increase about 30-40% of their compressive strength.

Results from Figs. 3 and 4 also show that the strength evolutions from 14 days to 28 days was low (about 10%), this means that the hydrations were mainly occurred during the first two weeks.

## 3 Specimens Using Bottom Ash

In order to investigate the possibility to use bottom ash in the materials manufacturing, one part of sand was replaced by bottom ash, at amount of 5, 10 and 20% of sand, respectively. This corresponded to quantities of bottom ash of 1.5%, 3% and 6% on the entire mix, respectively. So three new compositions were investigated: "10%C + 1.5% BA" (10% cement + 1.5% bottom ash); "10%C + 3%BA" (10% cement + 3% bottom ash); "10%C + 6% BA" (10% cement + 6% bottom ash).

For each composition, six specimens were manufactured, three cured in water and three other cured in ambient air. They were tested under uniaxial compression at 28 days. The results are presented in Fig. 5 and Fig. 6, respectively for specimens cured in water and in ambient air. These figures confirm observations on specimens with fly ash: curing condition had important influences on the compressive strength (about 30%).

From these figures, it is observed that when sand is replaced by bottom ash at 5% and 10%, a slight increase in compressive strength can be noted. Then, when sand is substituted by bottom ash at 20%, the compressive strength trended to decrease. This can be suggested that first, there is some pozzolanic products in bottom ash which provide some supplementary reactions leading to slights increases in the compressive strength. Then, the used bottom ash has a finesse modulus lower than that of the used sand; this means that the used bottom ash is finer. This is why the bottom ash can better "fill" voids between gravels, compared to sand. However, after a certain level of bottom ash substitution, compressive strength decreases because the used bottom ash is finer than the used sand, so a more important cement mount should be needed to "cover" all bottom ash, compared to conventional sand. That is why for a same cement amount, specimens made with bottom ash can have more "weak points" than that made with conventional sand. These observations should be checked with higher number of specimens and by investigations at the micro-structure of the materials.

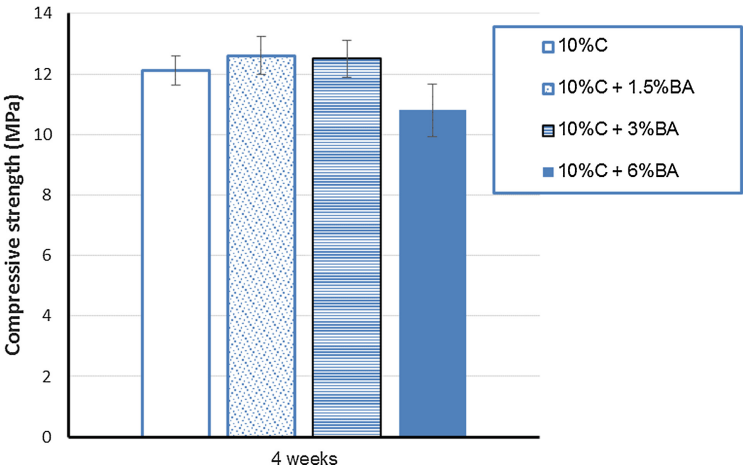


**Fig. 5.** Compressive strengths of different investigated compositions, replacing sand by bottom ash, curing in water.

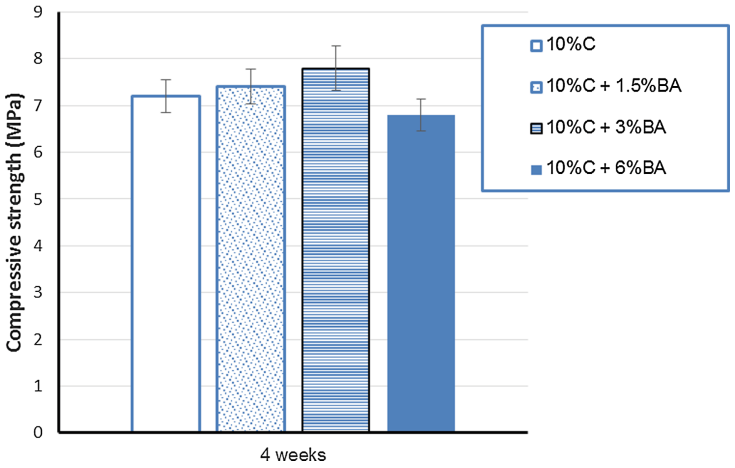


**Fig. 6.** Compressive strengths of different investigated compositions, replacing sand by bottom ash, curing in ambient air.

## 4 Conclusions and Outlook

This paper presents an investigation using fly ash and then bottom ash in the manufacturing of construction materials. The aim of this study is to propose a possibility to reduce environmental impacts of fly and bottom ashes which are actually considered as waste in Vietnam. So the main scope was to formulate non-conventional materials having low embodied energy by using less cement than current unburnt bricks. Several

proportions of fly ash, cement, gravel, sand and water were tried to manufacture low strength materials which can be used for non-load-bearing walls or individual houses where a high strength is not really necessary (Bui et al. 2016). Specimens were tested in uniaxial compressions which showed that with a reasonable cement amount (4-8% by weight) and acceptable quantities of fly and bottom ashes (cement substituted at 10, 20, 40 and 60% by fly ash; sand substituted at 5, 10 and 20% by bottom ash, respectively), the compression strengths obtained were about 4-12 MPa, depending on the composition and the curing condition. These results are acceptable for non-structural materials or for low strength structural materials.

Further studies will be carried out to study evolutions when fly ash and bottom are simultaneously used in the material. Further studies at the microscale of materials to investigate the potential reactions of fly and bottom ashes will also be interesting.

**Acknowledgement.** The authors wish to thanks students from Faculty of Civil Engineering of Ton Duc Thang University (Vietnam) for their assistance in the manufacturing and testing of specimens.

## References

ASTM D3176-15: Standard Practice for Ultimate Analysis of Coal and Coke, ASTM International, West Conshohocken, PA (2015)

Bui, Q.B., Morel, J.C., Hans, S., Meunier, N.: Compression behaviour of nonindustrial materials in civil engineering by three scale experiments: the case of rammed earth. Mater. Struct. **42**, 1101–1116 (2009)

Bui, Q.B., Morel, J.C., Tran, V.H., Hans, S., Oggero, M.: How to use in-situ soils as building materials. Procedia Eng. **145**, 1119–1126 (2016)

Day, K.W.: Concrete mix design, quality control and specification, 2nd edn. E & FN Spon, London (1999)

Vinacontrol HoChiMinh City (2015), Analysis results, 26 May 2015

# Geotechnics for Environment and Energy (GEE)

# 3D Electrical Resistivity Tomography of Karstified Formations Using Cross-Line Measurements

Maurits Van Horde[1], Thomas Hermans[2], Gael Dumont[3], and Frédéric Nguyen[4(✉)]

[1] Dredging International NV, DEME-Group, Zwijndrecht, Belgium
[2] Stanford University, Stanford, USA
[3] University of Liège, Liège, Belgium
[4] KU Leuven, Leuven, Belgium
f.nguyen@ulg.ac.be

**Abstract.** Limestone formations constitute a serious geological challenge for large building projects such as wind turbine farms. Indeed, limestone formations might be subject to karstic phenomena such as sinkholes or subsidence constituting a serious hazard for existing constructions and future civil engineering projects. In calcareous geological settings, a characterization of the subsurface to detect wealthy rocks is therefore mandatory. The classical approach consists in drilling boreholes and cone penetration tests to identify subsurface properties. However, they only provide punctual information whereas karstic environments show sharp variations with complex 3D geometry, making interpolation between boreholes relatively inefficient. In this context geophysical methods can provide spatially distributed information at a limited cost. In particular, surface electrical resistivity tomography (ERT) aims at mapping the distribution of electrical resistivity in the subsurface in a passive way using only surface sensors. The method is based on the measurement of electrical potential resulting from the injection of DC electrical current. In karstic contexts, weathered rocks generally show an increased porosity and water content compared to healthy limestones, leading to strong contrasts in their electrical resistivity. ERT is therefore particularly sound to investigate karstic phenomena. Most standard ERT applications use 2D profiles that are quick to acquire and interpret. However, in complex 3D geometries, the acquisition of 2D profiles is not sufficient to image correctly subsurface structures. 3D data sets require more efforts both for acquisition and interpretation, making their use more costly and therefore less common in practice. In this contribution, we propose an innovative 3D ERT acquisition procedure to reduce the field efforts and duration of the 3D acquisition procedure. The method is based on standard 2D parallel lines, but, in contrast with previous methodologies, we also acquire cross-line measurements in several directions to increase the ability of ERT to image 3D structures. To ensure a fast acquisition of large area, we limit the cross-line measurements to pre-defined line spacing and implement a roll-along technique moving previously acquired 2D lines in the perpendicular direction. The data can then be acquired with a standard 64 electrodes equipment. We first demonstrate the increased imaging capacities of our technique compared to standard acquisition methods with a numerical benchmark. Then, we validate it through a field application to detect the 3D geometry

© Springer Nature Singapore Pte Ltd. 2018
H. Tran-Nguyen et al. (eds.), *Proceedings of the 4th Congrès International de Géotechnique - Ouvrages -Structures*, Lecture Notes in Civil Engineering 8,
DOI 10.1007/978-981-10-6713-6_62

of karstic features and unaltered limestone formations. We analyze the minimum amount of cross-line measurements required for a proper imaging of the 3D structures. The proposed 3D survey induces extra costs of about 50% compared to a traditional 2D survey, but this extra cost is compensated by a largely better imaging of the subsurface. This cost will be reduced in the future by optimization of the survey to reduce acquisition time.

**Keywords:** 3D electrical resistivity tomography · Karstic environments · Cross-line measurements · Electrode configuration

## 1 Introduction

In the last two decades, electrical resistivity tomography (ERT) has been widely applied in many different contexts. The wide range of applications of ERT is a result of the large number of parameters influencing the electrical resistivity of the subsurface (porosity, fractures, rock/soil type, saturation, temperature, fluid electrical conductivity, etc.) and the robustness of the method. However, the standard use of ERT remains the collection of 2D subsurface profiles. Because of the simplicity of field implementation, requiring only one to two people for a couple of hours, 2D surveys are not time-consuming and relatively cost-effective. In addition, acquisition times have drastically decreased with the advent of multi-channel systems and automated switching systems [1]. Nevertheless, one of the major drawbacks of 2D survey is the underlying assumption that the subsurface is actually 2.5D, i.e. that electrical resistivity is constant in the direction perpendicular to the profile. This assumption enables to successfully reduce the complexity of forward modeling from 3D to 2D using a Fourier-cosine transformation [2]. Most interpretation software, commercial or academic, uses this assumption in the inversion of 2D data sets. This assumption can be valid for certain conditions (profile perpendicular to main geological structures, relatively homogeneous subsurface), but it can also lead to distorted and misleading results in strongly variable and heterogeneous environments [3], such as encountered in karstic settings. In such cases, or when a detailed mapping of the subsurface is required, 3D acquisition and inversion techniques must be considered. This is particularly true for karstic hazard, an engineering target suited for ERT given its sensitivity to electrical resistivity, where the 3D nature of the dissolution processes makes the 2.5D hypothesis of the subsurface much weaker than for fault imaging for example.

In this paper, we propose an innovative 3D acquisition procedure based on the roll-along technique of [4]. It makes use of 2D parallel lines with additional cross-line measurements. However, in order to increase the number of directions represented in the data, we propose to use cross-line measurements in several directions as proposed in [5] for imaging seepage in an embankment. Those cross-line measurements are based on dipole-dipole configurations as commonly used in cross-borehole surveys. We illustrate the method by investigating the subsurface geometry in a karstic environment for a future wind turbine project. We first describe the field site and the geological context. Then, the designed acquisition and processing procedure is described and assessed by numerical benchmark modeling, using a synthetic model. We applied our validated methodology to the field case to image the top of the

unaltered limestone formation and to characterize the 3D geometry of karst features. We then discuss the importance of cross-line measuring and analyze its capability and optimal setup for correct subsurface geometry imaging.

## 2 Site Description

The test site is located in the Couvin region, Belgium (Fig. 1). It is a large unbuilt area where a wind turbine construction project is ongoing. The survey site region is located at the southwestern edge of the synclinorium of Dinant. This geological structure composed of a succession of sedimentary rocks was folded during the Variscan orogeny. The succession of sedimentary formations is the result of the Devonian transgression towards the north which is actually made up of a succession of transgressive and regressive phases. This enables to observe the progression of terrigenous clastic sedimentation of the lower Devonian to carbonated sedimentation, which characterizes the Middle Devonian, to the Upper Devonian base including the establishment of reef systems built up by biostromes of the Eifelian (Couvinian) and bioherms of the Givetian [6]. These periods of carbonate production are interrupted by episodes of terrigenous sedimentation of various sizes. In the region of the survey site, limestone can be locally highly fractured and karstified. Karst features are generally filled with clayey sandstones of the Cenozoic and sediments of the Oligocene [7].

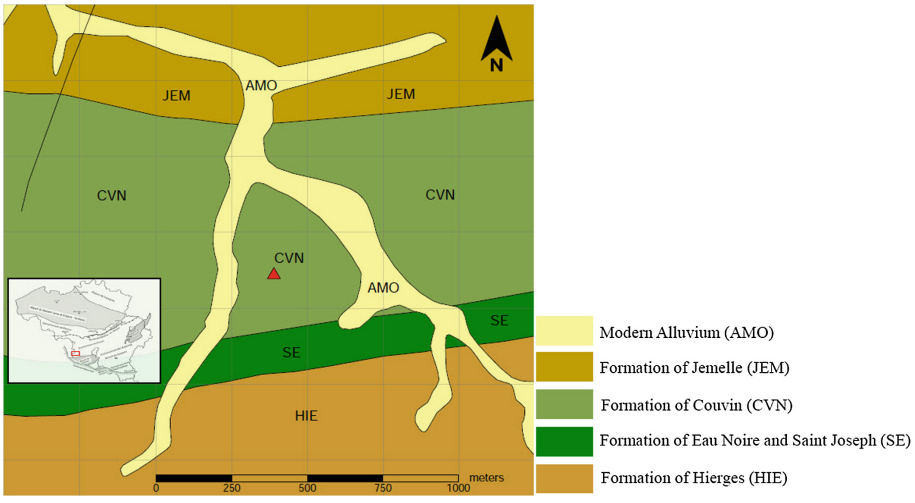


**Fig. 1.** Geological map of the site location. Red triangle represents the study area (modified after [6]).

In the study area, there are three major lithostratigraphic units (Fig. 1). The oldest is composed of the formations of Saint-Joseph and of Eau Noire, which are lower Devonian in age. It consists of layers of shale and thin limestone. The second oldest formation is the formation of Couvin, from the middle Devonian. It consists of very thick and compact succession of limestone layers. It was formerly used for production

of lime and stone used in the construction industry as well as for iron ore exploitation contained within karstic features filled with sediment. The youngest formation is the formation of Jemelle, also from the Middle Devonian. It mostly consists of shale layers.

Shallow karsts constitute a serious hazard to existing constructions and for civil engineering projects of all scales [8]. Constructions on top of paleokarst features may not be safe due to the risk of resurgence, subsurface sinkhole development and subsidence which can cause serious damage to infrastructures [9]. A karstic system can become unstable and severely compromise structural integrity and stability of the whole construction. This is why the subsurface geometry needs to be very well characterized in a systematic way when constructing in limestone settings [10]. In the study area, paleokarstic phenomena are present and may be reactivated due to the present hydrogeological setting.

## 3 Electrical Resistivity Tomography

### 3.1 Survey Design

The main objective of our survey design was to use the ABEM Terrameter LS (64 electrodes) equipment which is routinely used to execute 2D–ERT surveys. It was decided to use a set of 18 parallel profile lines of 32 electrodes in combination with cross-line electrical resistivity measuring (Fig. 2), applying the 3D roll along technique

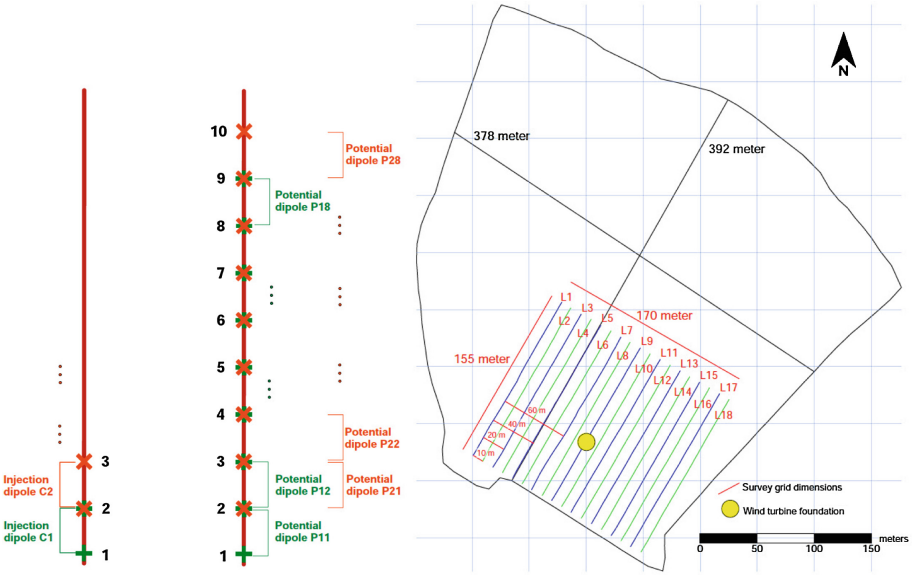


**Fig. 2.** Left: Cross-line measurement concept. Red lines indicate the electrode cables (2 per profile line). Electrode location for two different injection dipole are indicated with green and orange crosses respectively. Right: Survey site geometry is depicted by a dark grey line. Blue lines indicate lines of survey 1, green lines indicate lines of survey 2. Together they form the combined survey lay-out. The profile line ID number is indicated in red. The yellow dot is the location of the future wind turbine.

to progress laterally through the designed survey grid, connecting only 64 electrodes at a time. In-line measurements were performed along each line, and cross-line measurements were performed in between parallel profile lines with a certain offset with respect to a fixed chosen profile (Fig. 2 and Table 1). The latter contain 3D resistivity information on the subsoil in between parallel lines. The in-line electrode spacing is 5 m whereas the cross-line electrode spacing is 10 m. Since there are 18 profile lines in total, the combined survey grid consists of 576 electrodes. All electrodes were precisely positioned using a Trimble G8 GPS system. An in-line electrode spacing of 5 m was used to reach a sufficient depth of penetration for this site specific scenario since the pile foundations of the wind turbine will penetrate the surface up to 20 meters deep. Given the protocols used, this corresponds to a total number of 34644 measurements.

**Table 1.** Different dataset combinations made for three dimensional inversion with RES3Dinv®. ALL IL means all in line, ALL CL all cross-lines, CL # means that only the cross-line with # spacing has been used

| | Combination of datasets | Number of datapoints in protocol | Number of datapoints after processing |
|---|---|---|---|
| **Survey 1** | | | |
| All IL + All CL | 9 in-lines + 21 cross-lines | 17322 | 12239 |
| **Survey 1 + Survey 2** | | | |
| All IL | 18 in-lines | 7848 | 6721 |
| All IL + CL 40 | 18 in-lines + 14 cross-lines | 16780 | 12925 |
| All IL + CL 60 | 18 in-lines + 12 cross-lines | 15504 | 12264 |
| All IL + All CL | 18 in-lines + 42 cross-lines | 34644 | 25469 |

### 3.2 Inversion Parameters

All the inversions were carried out with the same inversion parameters in the software RES2DINV®. We use a L1 norm on the data to reduce the effect of possible outliers and a L1 norm on the model [11] to favor sharp contrasts of resistivity as expected in karstic formations. The inversion process made use of an incomplete Gauss-Newton scheme.

Despite, the low variance of the measured apparent resistivity, the final error of the inversion of the full data set was still relatively high (more than 13%). In consequence, the data set was further trimmed post-inversion based on the individual misfit of each simulated measurement versus the observed one. We removed data points with a misfit greater than 20% (5300 data). This reduced the RMS data misfit to about 6% for the full data sets (all in-line and all cross-line). For a fair comparison, other subsets were built based on this sorted/trimmed full data set. We stopped the inversions when the RMS data misfit reached a value between 5 and 6%.

### 3.3 Results for the Synthetic Benchmark

To validate if our designed survey method can solve and image an artificially pre-defined 3D geological structure, a numerical benchmark model is carried out and field resistivity measurements are numerically simulated. If the synthetic 3D resistivity model based on these numerically simulated resistivity data corresponds well to the initial defined geological structures, we can conclude that the designed survey methodology is capable of solving similar 3D-subsurface geometries. For synthetic modelling, a karstic environment was chosen similar to the environment expected at the site under investigation. The numerical geological structure consists of a central ridge of competent limestone bedrock with karstic features on the sides. The different geological units present are the sediment cover, 10 m thick (55 Ω.m), weathered limestone with debris (450 Ω.m), ghost rock and tertiary sandstone filling karstic features (250-300 Ω.m) and unaltered limestone bedrock (750-2500 Ω.m). RES3DMOD® is used to numerically simulate the apparent resistivity data corresponding to a pole-pole survey. The most important structure within the context of wind turbine project is to detect the position of the unaltered bedrock. We therefore use the detection of the shape and location of the central limestone ridge as an indicator of the performance of the survey. In the following figures, this characteristic of the model will be highlighted by the 600 Ω.m iso-surface.

The full data set contains all measurements, i.e. in-line and cross-line 20, 40 and 60 m for both surveys. It is expected than this brings the most valuable information on the 3D structure of the model. As it appears in Fig. 3, this data set enables to retrieve relatively accurately the location, depth and shape of the ridge in the middle of the model. This confirms the survey (in-line and cross-line spacing, number of parallel lines) was correctly designed. All the reduced data sets retrieve less accurately the ridge structure. First, it appears that that the use of a unique survey, i.e. an inter-line spacing of 20 m, is not able to image correctly the subsurface. The only feature that is adequately detected is the low resistive zone located at the origin of the grid. The reduction of acquisition time must not be done in detriment of the resolution of the survey. This is confirmed by the use of the in-line data from both surveys which already gives a better overview of the 3D structure. The reason of this relatively good performance lies in the orientation of 2D lines perpendicular to the geological structures. However, the width and depth of the ridge are not as accurate as with the full data set.

Adding cross-line measurements to 2D lines clearly improves the results. In this case, given the depth of the structure, cross-lines 40 m and 60 m are the most informative. They enable to refine imaging of the 3D structure. In this specific case, this is clearly the cross-line 40 that approaches the true model with most accuracy.

### 3.4 Results for the Field Data

In the inversion of the full data set (Fig. 4), a subsurface structure is recognizable with a central ridge of unaltered limestone bedrock at a depth between 225 m TAW and 195 m TAW. On its sides, two karstic features are clearly visible. The first is a large zone of low resistivity value between X = 0 and X = 50 m, the healthy bedrock being detected at a depth of 195 m TAW only. The second is a smallest low resistivity zone located between Y = 50 m and Y = 100 m and X = 75 m and X = 150 m.

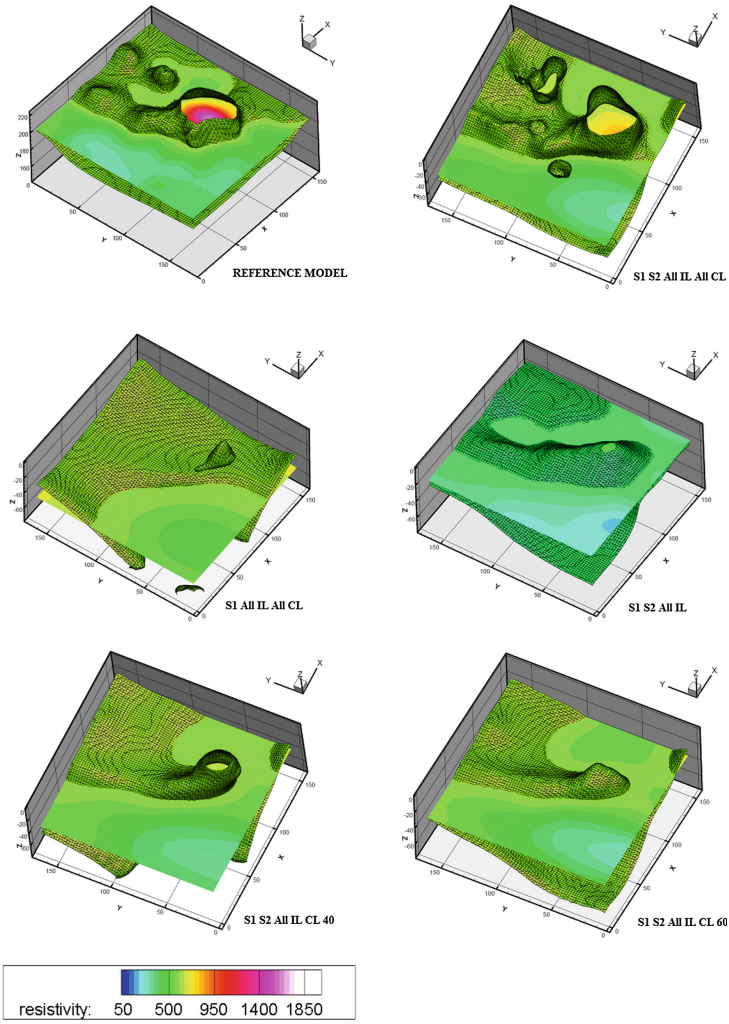


**Fig. 3.** Synthetic data inversion overview. Three dimensional block models of the subsurface resistivity distribution. The models show a resistivity iso-surface of 600 Ω.m representing the transition to altered limestone. The model annotation corresponds to the dataset combination overview provided in Table 1.

The inversion of reduced data sets confirms the observation made for the synthetic case. Clearly, the use of a spacing of 20 m between parallel lines is not sufficient to resolve the shape and location of the limestone ridge. This subset of data incorrectly locates the ridge as well as the second anomaly. The use of in-line data is sufficient to qualitatively detect most features of the subsurface geometry, but it is not accurate enough given the aim of the study. The depth of the unaltered bedrock seems to be found deeper down and the ridge does not appear as continuous. Also, due to a reduced

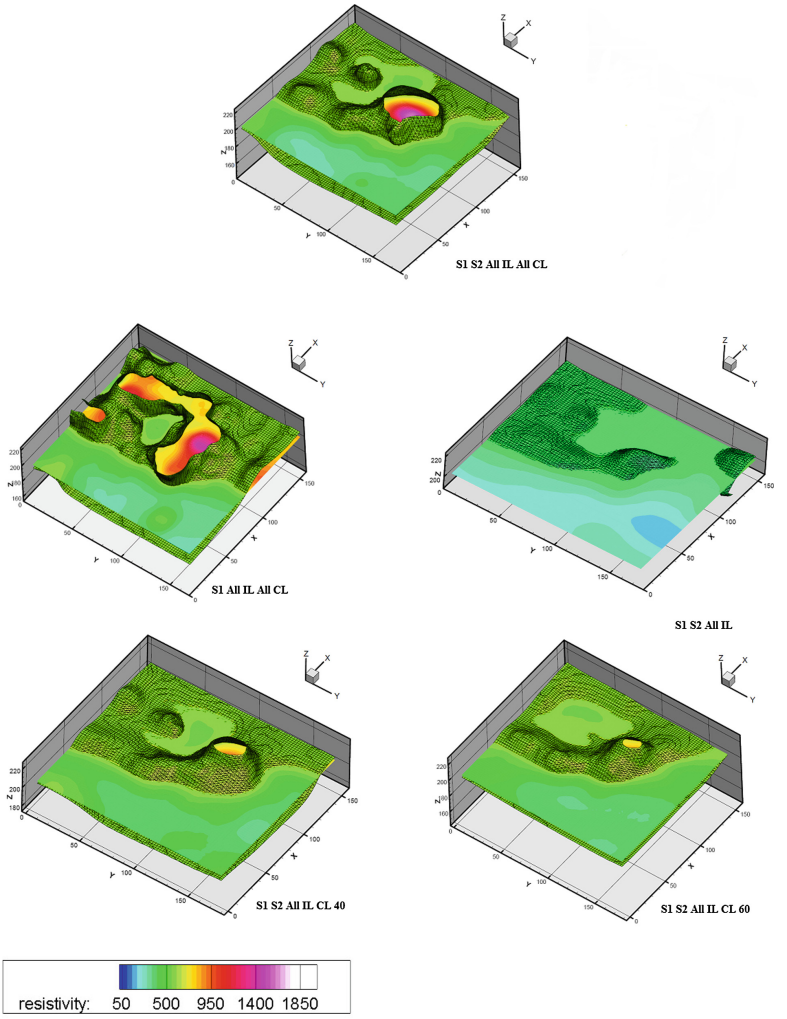


**Fig. 4.** Field data inversion overview: Three dimensional block models of the subsurface resistivity distribution. The models show a resistivity iso-surface of 600 Ω.m representing the transition to altered limestone. The model annotation corresponds to the dataset combination overview provided in Table 1.

depth of investigation and smaller coverage of the subsurface compared to cross-line data, this inversion images the first karstic anomaly as very low resistivity zone and is not able to detect the presence of healthy bedrock at depth.

Both inversions with additional cross-lines dipole (40 m and 60 m) manage to image the subsurface geometry as the full data set does. The data set with cross-line 40 m data seems to yield results the most similar to the reference, especially the second low resistivity anomaly is imaged with the same shape as in the reference. This is

probably linked to the depth of the targeted structures. Indeed, the cross-lines 20 m (not shown here), proved to be mainly helpful to image 3D structure in the first meters below the surface (surface deposits).

## 4 Conclusions

In this paper, we propose an innovative methodology to collect efficiently 3D electrical resistivity surveys. We combined the standard 2D parallel acquisition with cross-line measurement, using the roll-along technique in the perpendicular direction. In contrast to existing procedures, we include more than one direction in cross-line measurements using dipole-dipole configurations similar to what can be done in cross-borehole surveys.

We applied this methodology on a synthetic case. It proves that such a data set is informative to image the 3D resistivity structure of the subsurface. Especially, it is important to collect 3D measurements with a depth of investigation coherent with the expected structure of the subsurface. However, the collection of cross-line measurements must not be in detriment of a sufficiently small spacing between parallel lines.

Those results were validated by a field case study. We acquired on the field the proposed 3D in-line/cross-line surveys to image limestone formations subject to karstic features within the context of a wind turbine project. Our methodology enabled to successfully image the presence of a central unaltered limestone ridge surrounded by much less competent rock affected by karstic phenomena. The comparison with standard parallel 2D surveys clearly highlighted the added value of the cross-lines measurements to detect those structures. It provides crucial insight in subsurface geometry for the positioning of a future wind turbine foundation, to the best of our knowledge of the site. The developed method and its modeling results can provide a useful tool in pre-construction 3D subsurface characterization to gain in depth technical insight.

The acquisition of the 3D survey induces additional field and processing work, with an extra cost of about 50%, but those are compensated by the more accurate information brought by the survey. Future work should concentrate on the optimization of cross-line measurements in order to reduce the acquisition time of such surveys. Effort should be made to create an integrated site investigation framework for the characterization of geo-hazardous environments affected by karst features in the light of pre-construction risk analysis, combining geotechnical and geophysical survey methods such as cone penetration testing in combination with 3D ERT and seismic surveying.

**Acknowledgments.** We would like to thank the geophysical exploration company G-tec S.A. for giving us the opportunity to work on the field site, and for their help on the field for collecting the data. We would like to thank Windvision, for providing us the permission to work on their site and their interest in this work. We thank the Belgian American Educational Foundation and Wallonia-Brussels International for their financial support of T. Hermans.

## References


1. LaBrecque, D.J., Ramirez, A., Daily, W., Binley, A., Schima, S.A.: ERT monitoring of environmental remediation processes. Meas. Sci. Technol. **7**, 375–383 (1996)
2. Dey, A., Morrison, H.F.: Resistivity modeling for arbitrarily shaped two-dimensional structures. Geophys. Prospect. **27**, 106–136 (1979)
3. Nimmer, R.E., Osiensky, J.L., Binley, A.M., Williams, B.C.: Three-dimensional effects causing artifacts in two-dimensional, cross-borehole, electrical imaging. J. Hydrol. **359**, 59–70 (2008). doi:10.1016/j.jhydrol.2008.06.022
4. Dahlin, T., Bernstone, C., Loke, M.H.: A 3-D resistivity investigation of a contaminated site at Lernacken, Sweden. Geophysics **67**, 1692–1700 (2002). doi:10.1190/1.1527070
5. Cho, I.-K., Yeom, J.-Y.: Crossline resistivity tomography for the delineation of anomalous seepage pathways in an embankment dam. Geophysics **72**, G31–G38 (2007). doi:10.1190/1.2435200
6. Marion, J.-M., Barchy, L.: Carte géologique de Wallonie, Chimay-Couvin 57/7-8. Carte Géologique de Wallonie (1999a)
7. Marion, J.-M., Barchy, L.: Carte géologique de Wallonie, Chimay-Couvin 57/7-8. Notice Explicative. Carte Géologique de Wallonie (1999b)
8. Samyn, K., Mathieu, F., Bitri, A., Nachbaur, A., Closset, L.: Integrated geophysical approach in assessing karst presence and sinkhole susceptibility along flood-protection dykes of the Loire River, Orléans, France. Eng. Geol. **183**, 170–184 (2014). doi:10.1016/j.enggeo.2014.10.013
9. Sabbe, A.: Le risque karstique dans les constructions d'habitations-propositions de mitigation. In: Karst et Aménagements Du Territoire. Presented at the Karst et Aménagements du territoire (2005)
10. Alija, S., Torrijo, F.J., Quinta-Ferreira, M.: Geological engineering problems associated with tunnel construction in karst rock masses: the case of Gavarres tunnel (Spain). Eng. Geol. **157**, 103–111 (2013). doi:10.1016/j.enggeo.2013.02.010
11. Loke, M.H., Acworth, I., Dahlin, T.: A comparison of smooth and blocky inversion methods in 2D electrical imaging surveys. Explor. Geophys. **34**, 182–187 (2003). doi:10.1071/EG03182

# A Case Study of a Long-Duration Thermal Response Test in Borehole Heat Exchangers

Georgia Radioti(✉), Benjamin Cerfontaine, Robert Charlier, and Frederic Nguyen

University of Liege, Liege, Belgium
{gradioti, b.cerfontaine, robert.charlier, f.nguyen}@ulg.ac.be

**Abstract.** Shallow closed-loop geothermal systems are worldwide applied providing economical and environmental benefits. This paper presents an in-situ study of four Borehole Heat Exchangers of 100 m long, installed in an heterogeneous bedrock in the campus of the University of Liege (Liege, Belgium). A Thermal Response Test (TRT) of a heating phase of 7 months was conducted in one of the boreholes. During this test, temperature was measured at the pipe inlet and outlet, as well as along the four boreholes by the fiber optics. To further investigate the measured data, the test was simulated by 3D numerical modeling. The comparison of the measured data with the numerical results allowed to detect the critical parameters for the behavior of the BHE and for the temperature evolution in the surrounding rock mass. In this case study, the behavior of the BHE could be predicted based on the results of a typical-duration TRT (of a few days), considering the ground an homogenous and isotropic material. However, the thermal plume in the surrounding ground seems to be influenced by several factors, such as the bedrock heterogeneity, the distance to the heating source, air temperature variations and thermal effects at the borehole bottom end.

**Keywords:** Geothermal systems · High-resolution temperature profiles · Numerical modeling · Thermal response test

## 1 Site Set-up and Test Description

The site consists of four double-U BHEs (namely B1-B4), of about 100 m long, installed on the campus of the University of Liege (Liege, Belgium) (Fig. 1). During the pipes installation, fiber optic cables were attached along the outer surface of the pipe loops in the four borehole [1, 2]. Fiber optics allow to obtain continuous, high-resolution profiles, by applying the Distributed Temperature Sensing technique [3]. The boreholes were backfilled with the following grouting materials: B1 and B3 with a silica sand-based commercial material ($\lambda$ = 2.35 W/mK), B2 with a bentonite-based commercial material ($\lambda$ = 0.95 W/mK) and B4 with a homemade admixture with graphite ($\lambda$ = 2.5 W/mK) [4]. The bedrock consists mainly of siltstone and shale interbedded with sandstone layers [1].

© Springer Nature Singapore Pte Ltd. 2018
H. Tran-Nguyen et al. (eds.), *Proceedings of the 4th Congrès International de Géotechnique - Ouvrages -Structures*, Lecture Notes in Civil Engineering 8,
DOI 10.1007/978-981-10-6713-6_63

**Fig. 1.** Site location on the campus of the University of Liege (retrieved from Google Earth©) (left) and relative position of the four BHEs at the ground surface (right).

**Table 1.** Applied phases during the long-duration TRT in B2.

| Days | Water circulation | Heat injection | Configuration |
|---|---|---|---|
| 0-1.63 | √ | - | double-U |
| 1.63-95.18 | √ | √ | double-U |
| 95.18-95.61 | - | - | - |
| 95.61-96.67 | √ | - | double-U |
| 96.67-191.7 | √ | √ | double-U |
| 191.7-192.6 | - | - | - |
| 192.6-214.7 | √ | √ | single-U |
| 214.7-367 | - | - | - |

A long-duration Thermal Response Test (TRT) was conducted in B2. The geothermal pipes were connected to a test rig, enclosing a circulation pump, a heating wire element, water temperature sensors (pipe-inlet and outlet) and air temperature sensors. Water was circulated inside the pipe loops while heat was injected and temperature was recorded by the temperature sensors. The applied phases of the test are presented in Table 1. The heat injection was interrupted for short periods (<24 h), to study the influence of a short recovery on the thermal response of the system. Moreover, during the last 22 days, heat was injected only to the one U-pipe, resulting in decreasing the nominal power applied in the BHE in half. After the heating phase, a recovery phase without water circulation followed of a duration of 5 months. During the test, temperature was also measured by the fiber optics in the surrounding boreholes. The actually applied heating power during the test was calculated based on the pipe inlet and outlet water temperature measurements (Fig. 2). Oscillations in the heating power profile are mainly attributed to the insufficient test rig insulation, which allowed the thermal interaction between the circulating fluid and the ambient air.

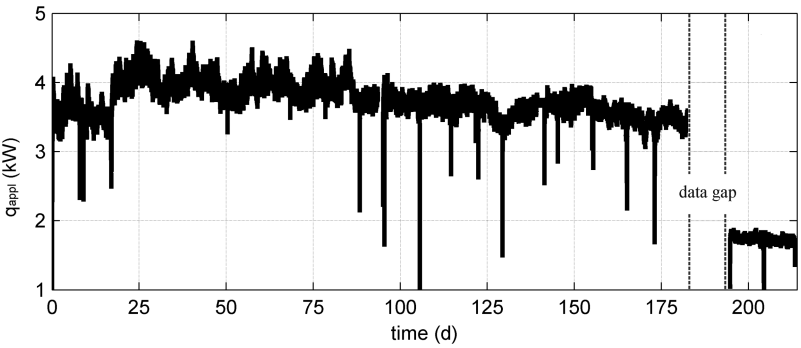


**Fig. 2.** Applied heating power during the long-duration TRT in B2.

## 2 3D Numerical Modeling

A 3D numerical model of the in-situ test was developed by using the finite element code LAGAMINE [5, 6]. This model includes an exact representation of the BHE geometry and materials (borehole, grouting, geothermal pipes), avoiding any hypothesis on the borehole thermal resistance. The flow along each pipe leg is represented by a 1D finite element. A fluid velocity and a convective heat transfer coefficient was imposed on each node of the 1D element, which interacts with a node at the center of the corresponding pipe leg of the 3D mesh [7].

All the materials, including the surrounding bedrock, are assumed homogenous media and a uniform initial temperature (11 °C) was assumed for the whole model domain. Table 2 presents the BHE geometry and the materials properties applied in the numerical model. A varying heat input was applied, following the main variations of the experimental applied heating power (Sect. 1).

**Table 2.** BHE geometry and materials properties for the numerical modeling in B2

| | |
|---|---|
| **$r_{bor}$ (m)** | 0.068 |
| **$r_{p,inner}$ (m)** | 0.0131 |
| **$r_{p,outer}$ (m)** | 0.016 |
| **d (m)** | 0.045 |
| **length (m)** | 95 |
| **$\lambda_{pipe}$ (W/mK)** | 0.42 |
| **$\rho c_{\rho,pipe}$ (kJ/m³K)** | 2083* |
| **$\lambda_{grout}$ (W/mK)** | 1.0 |
| **$\rho c_{\rho,grout}$ (kJ/m³K)** | 2500* |

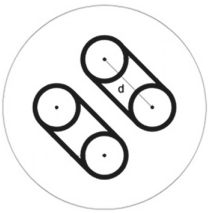


*handbooks

The applied ground thermal conductivity was estimated based on the data of only the first 60 h of the test (typical TRT duration) by applying the analytical solution of the Infinite Line Source model. The estimated value (2.90 W/mK) was in good agreement with the those of the 7-days TRTs conducted in-situ in the other 3 BHEs (B1, B3 and B4) [1].

# 3 Results

## 3.1 Water Temperature Evolution

The pipe inlet and outlet water temperature evolution is representative of the BHE behavior. Figure 3 compares the water measured and the numerical data for the heating and the recovery phase. The experimental results during the recovery phase in Fig. 3 correspond to the depth-average value of the fiber optic measurements along the borehole, assuming a uniform temperature distribution along the borehole cross-section. The numerical results are in good agreement with the measured temperature evolution during the heating as well as the recovery phase. This indicates that the effective ground thermal conductivity does not vary significantly with time and that in this case study a typical duration TRT can be representative of the BHE behavior for longer heating periods and different applied modes (heating/recovery).

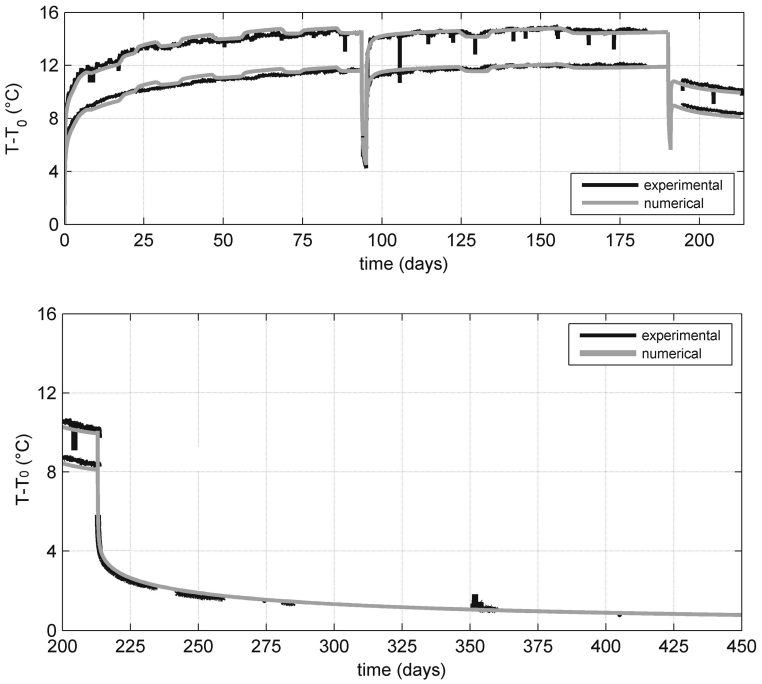


**Fig. 3.** Experimental and numerical water temperature evolution during the heating (top) and the recovery phase (bottom) in B2.

Figure 4 shows the water temperature distribution along the pipe loop during the first hours of the first heating phase ($t_0$ = 1.63 d) and of the second heating phase (i.e. after the first heat input interruption, $t_0$ = 95.61 d). For both phases, the temperature

profile develops gradually, obtaining the characteristic V-shape after approximately 12 min. Once it reaches the steady state, water temperature rises more quickly with time. This transition is also indicated in the water temperature evolution displayed in a semilog scale (Fig. 4 bottom). At steady state, the transferred heat decreases while water progressively advances along the pipe loop, indicated by the non-symmetrical obtained profiles. This is attributed to the lesser amount of heat subjected to each water section, starting with the maximum value at the ground level at the pipe inlet, and to the thermal interaction between the pipe legs. Approximately 65% of the injected heat is transferred in the downward pipe, while only 35% in the upward pipe, for this BHE geometry and for a flow rate of 9.5 l/min in each pipe loop.

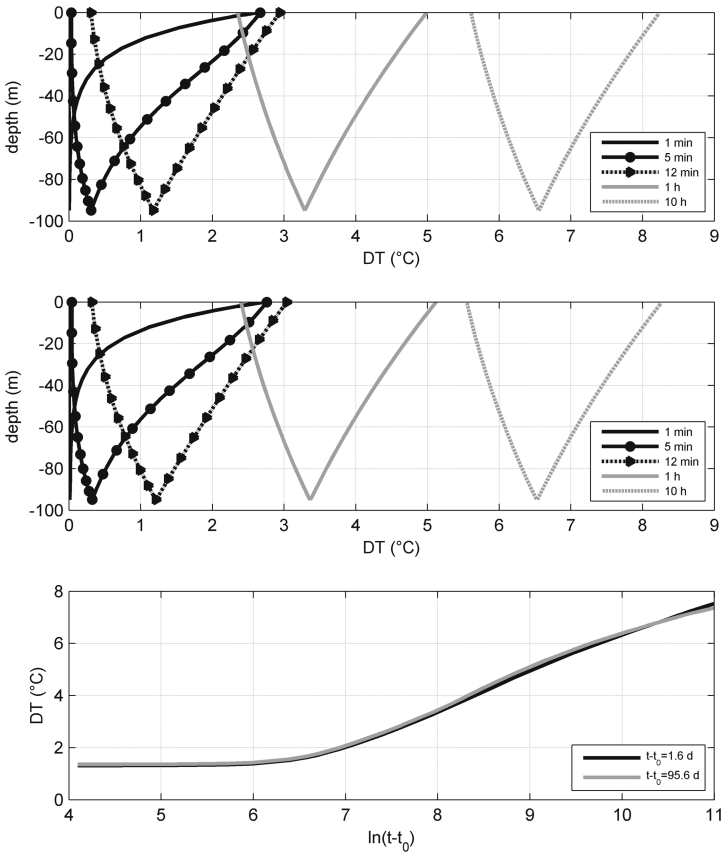


**Fig. 4.** Numerical water temperature profiles during the first heating phase ($t_0$ = 1.63 d, $T_0$ = 11 °C) (top), after the first heat input interruption ($t_0$ = 95.61 d, $T_0$ = 15.5 °C) (middle) and mean of pipe inlet and outlet numerical water temperature increase for both heating phases (bottom) in B2.

The steady-state heat transfer at the whole borehole cross section is achieved after approximately 10 h for both heating phases. This is included in the proposed range (1–12 h) for normal borehole sizes and ground conditions, according to [8].

### 3.2 Thermal Plume in the Surrounding Rock Mass

Figure 5 shows fiber optics temperature profiles along B3 (length of 100 m) during the heat injection in B2 (length of 95 m). The distance between B2 and B3, calculated based on measured azimuth and deviation data in both boreholes, is not constant with depth, becoming almost the half at the bottom of the boreholes.

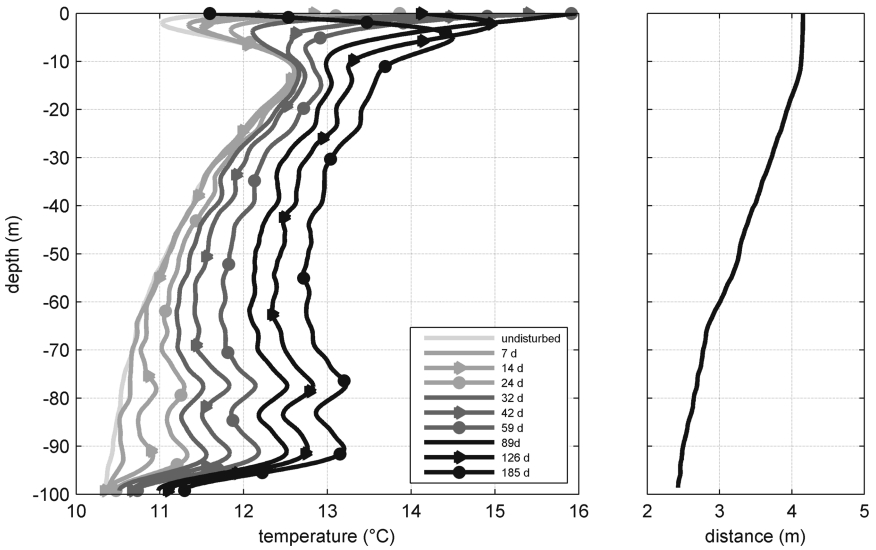


**Fig. 5.** Fiber optic temperature profiles in B3 during the heating of the double-U pipe in B2.

The negative temperature gradient of the undisturbed profile (before the heat injection) is attributed to the heating of the ground through structures surrounding the boreholes [9]. In the first approximately 18 m, ground temperature varies significantly with time, influenced by the ambient air temperature variations. Temperature starts to increase at the location of the sandstone layers in the lower part of the borehole, since this part is closer to B2 than the upper part and these layers are characterized by a higher thermal diffusivity compared to the shale/siltstone layers. Temperature increases progressively at higher depths, where the distance to B2 increases, while heating continues. The two thick sandstone layers at the bottom of the borehole are clearly detected as local maxima in the temperature profiles, indicating the higher heat transfer rate along them. Moreover, temperature decreases at high rate in the last 10 m (90 m-100 m depth), despite that a sandstone layer is located at this depth. This is attributed to the length of the heating BHE (B2, 95 m) and to the thermal effects at the borehole end that influence the temperature field at depths close to the bottom of the borehole.

## 4 Conclusions

This study presents numerical and experimental results of BHEs at the in-situ scale. The applied numerical formulation (1D finite element interacting with the 3D mesh) can reproduce transient and steady-state heat transfer phases, by taking into account an exact representation of the BHE geometry. The BHE behavior for long heating periods and different modes (heating/recovery) can be predicted based on a typical duration TRT (of a few days) by assuming homogeneous ground conditions, in this case study where groundwater effects are not dominant. However, the thermal plume in the surrounding ground seems to be influenced by several factors, such as the bedrock heterogeneity, the distance to the heating source, air temperature variations and thermal effects at the borehole bottom end.

**Acknowledgments.** The work undertaken in this paper is supported by the Walloon Region project Geotherwal n° 1117492 and the F.R.S.-FNRS F.R.I.A. fellowship of Georgia Radioti. We also would like to thank the University service ARI for their support in the installation of the BHEs as well as our partners in the project, the ULB (Université Libre de Bruxelles) and the companies OREX and Geolys. We thank the company REHAU for providing the pipes and the commercial grouting materials.

## References

1. Radioti, G., Delvoie, S., Charlier, R., Dumont, G., Nguyen, F.: Heterogeneous bedrock investigation for a closed-loop geothermal system: a case study. Geothermics **62**, 79–92 (2016)
2. Radioti, G., Charlier, R., Nguyen, F., Radu J.P.: Thermal response test in borehole heat exchangers equipped with fiber optics. In: Proceedings, International Workshop on Geomechanics and Energy: The Ground as Energy Source and Storage, pp. 96–100, EAGE, Lausanne, Switzerland (2013)
3. Hermans, T., Nguyen, F., Robert, T., Revil, A.: Geophysical methods for monitoring temperature changes in shallow low enthalpy geothermal systems. Energies **7**, 5083–5118 (2014)
4. Erol, S., François, B.: Efficiency of various grouting materials for borehole heat exchangers. Appl. Therm. Eng. **70**, 788–799 (2014)
5. Collin, F., Li, X.L., Radu, J.-P., Charlier, R.: Thermo-hydro-mechanical coupling in clay barriers. Eng. Geol. **64**, 179–193 (2002)
6. Charlier, R., Radu, J.P., Collin, F.: Numerical modelling of coupled transient phenomena. Revue Française de Génie Civil **5**(6), 719–741 (2001)
7. Cerfontaine, B., Radioti, G., Collin, F., Charlier, R.: Formulation of a 1D finite element of heat exchanger for accurate modelling of the grouting behaviour: application to cyclic thermal loading. Renew. Energy **96**, 65–79 (2016)
8. Spitler, J.D., Gehlin, S.: Thermal response testing for ground source heat pump systems-an historical review. Renew. Sustain. Energy Rev. **50**, 1125–1137 (2015)
9. Radioti, G., Delvoie, S., Sartor, K., Nguyen, F., Charlier, R.: Fiber-optic temperature measurements in closed-loop geothermal systems: a case study in heterogeneous bedrock. In: Proceedings of 1st International Conference on Energy Geotechnics ICEGT 2016, Kiel, Germany (2016)

# An Elastoplastic Model for Soils Exhibiting Particle Breakage

Vu P.Q. Nguyen(✉) and Mamoru Kikumoto

Department of Civil Engineering, Yokohama National University, Yokohama, Japan
nguyen-vu-hr@ynu.jp, kikumoto@ynu.ac.jp

**Abstract.** An elastoplastic constitutive model exhibiting particle crushing is developed based on the framework of continuum mechanics. The proposed model is formulated based on the extension of the critical state soil model [1, 2] to firstly incorporate the effect of packing density on the stress-strain characteristics by employing the concept of subloading surface [3]. Then, the effect of particle crushing is further implemented by incorporating the evolution of particle size distribution curve due to crushing stress and its effect on the constitutive behavior. Finally, the performance of the proposed model is validated with experimental test. The simulation results show that in spite of a simple formulation of the constitutive model, the behavior of crushable soils is well predicted.

**Keywords:** Elastoplastic · Constitutive model · Particle crushing · Critical state · Subloading · Particle size distribution · Grading index

## 1 Introduction

There are a number of geotechnical structures in which soil exhibits particle crushing, such as highway embankment, earth dams' embankment [4], or driven pile [5–7]. During their life of operation or during construction stages, soil's particles are broken into smaller ones due to large external forces or dynamic forces. Therefore, the initial physical properties of soil supporting these structures change significantly. The variation in the original engineering properties could put the stability of such structures in jeopardy. Hence, a proper consideration of particle crushing effect in soil' properties is vitally important to enable an economical safe design.

The particle size distribution (PSD), which is one of the most widely measured properties of soil in laboratory test, has been acknowledge to significantly control soil's stress-strain relationship [8, 9]. Although particle size evolution law can be implemented into a constitutive models using suitable particle crushing variables, very few models have incorporated the grain size evolution law to consider particle crushing phenomenon., Kikumoto [10] extended the Severn Trent sand model [11] with an additional grading index parameter $I_G$ (proposed by Wood [11]) taking into account the effect of particle breakage due to the evolutional of PSD. However, in particle crushing model of Kikumoto [10], the crushing behavior is implemented into the Severn Trent

© Springer Nature Singapore Pte Ltd. 2018
H. Tran-Nguyen et al. (eds.), *Proceedings of the 4th Congrès International de Géotechnique - Ouvrages -Structures*, Lecture Notes in Civil Engineering 8,
DOI 10.1007/978-981-10-6713-6_64

model by separately consider the effect of compression and shearing. This leads to the complication of the understanding of that Severn Trent crushing model.

The main objective of this study is to develop an innovative soil model considering particle crushing based on a critical state theory. The evolution of PSD due to crushing is utilized to formulate the crushing behavior of soil. The grading index $I_G$ which illustrates the crushing level, or the grading, of soil is necessary to fully determine this PSD equation. Consequently, the evolution law of PSD due to particle crushing is directly related to that of $I_G$. The advantage of the current model is that in spite of a simple formulation procedure, it can well describe stress-strain behavior of crushable soils.

## 2 Grading Index

The key purpose in the study of particle breakage is to determine the degree of crushing that the particles are exhibiting. Firstly, Hardin [12] proposed a relative breakage index $B_r$ which is described in Fig. 1b. The value of $B_r$ corresponding to the initial grading without any crushing (AC curve), and the critical state with the maximum crushing level (AD line) are set to be 0 and 1, respectively. The value of $B_r$ at any other soil state ($0 < B_r < 1$) is determined as follow:

$$B_r = \frac{S_{ABC}}{S_{ACD}} \tag{1}$$

Nevertheless, $B_r$ index is always equal to 0 for the initial soil state, regardless of different particle size distributions. This leads to the difficulty of observing the soil's state based on $B_r$ index. Thus, Wood [11] proposed a grading index $I_G$ whose definition is explained in Fig. 1a. For the single size grading $I_G$ (vertical line AB) and the critical grading (AE curve), $I_G$ is set to be 0 and 1, respectively. Then, the crushing index $I_G$ corresponding to any arbitrary soil state ($0 < I_G < 1$) is defined as:

$$I_G = \frac{S_{ABD}}{S_{ABE}} \tag{2}$$

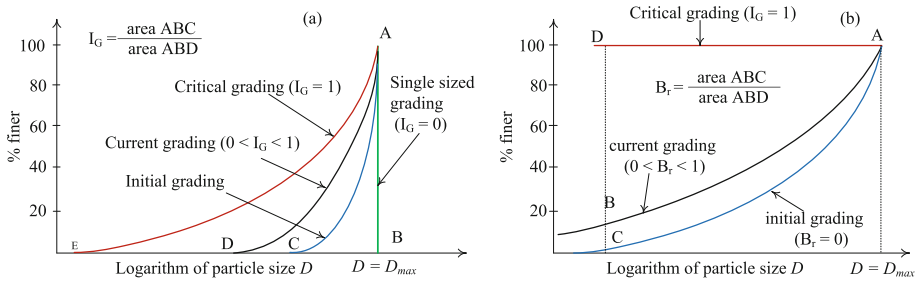


**Fig. 1.** (a) Definition of grading index $I_G$. (b) Definition of grading index $B_r$

According to this definition of $I_G$, the soil's state would be the same as long as they possess the same value of $I_G$, regardless of their initial gradings. Thus, it is possible to observe the soil's state based on $I_G$ value. Furthermore, $I_G$ is ranged from 0 to 1, which is useful for the formulation of constitutive model. Nevertheless, due to the fact that the calculation of $I_G$ depends on the critical grading, $I_G$ cannot be used when the critical grading curve is unknown.

## 3 Elastoplastic Model Considering Particle Crushing in Soils

An elastoplastic constitutive model considering crushing effect is developed based on continuum mechanics. The proposed model is formulated based on the extension of critical state model [1, 2] to incorporate the density effect on stress-strain characteristics by utilizing subloading surface concept [3]. Then, the effect of particle crushing is further implemented by considering the evolution of particle size distribution due to the change of crushing stress and its effect on the constitutive behavior.

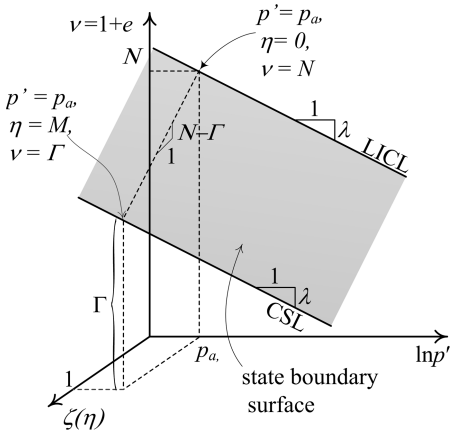


**Fig. 2.** Specific volume of soils in loosest state.

Critical state is an ultimate condition towards which all states of soil finally approach when the soil is sheared. The critical state line (*CSL*) has been chosen as linear in a semi logarithmic compression plane, which is the specific volume, $v$ (= 1 + $e$), versus the logarithm of mean effective stress, ln $p'$. Similar to *CSL*, limiting isotropic compression line (*LICL*) is a reference line in the $v$-ln $p'$ plane where any stress state finally approaches under isotropic compression. It is customary to utilize the State boundary surface containing *CSL* and *LICL* (Fig. 2) in the formation of critical state model [1]. Specific volume on the state boundary surface, $v_{sbs}$, which defines the loosest state of soil at the current stress ($p$, $\eta$) is given by considering the combined effects of compression and dilation as:

$$v_{\mathrm{sbs}} = N - \lambda \ln \frac{p'}{p_{\mathrm{a}}} + (\Gamma - \mathrm{N})\zeta(\eta) \tag{3}$$

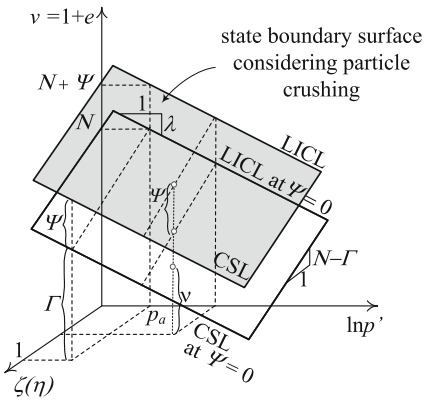


**Fig. 3.** State boundary surface considering crushing effect.

where $\eta$ (=$q/p'$) is stress ratio, $q$ is deviator stress, $p_a$ (=98 kPa) denotes atmospheric pressure, $\lambda$ is compression index, $\zeta(\eta)$ is a monotonic increasing function of stress ratio $\eta$ satisfying $\zeta(0) = 0$ on *NCL* and $\zeta(M) = 1$ on *CSL*. $N$ and $\Gamma$ represent specific volumes on *LICL* ($\eta = 0$) and *CSL* ($\eta = M$) at $p' = p_a$ respectively. It is postulated that different functions of $\zeta(\eta)$ are used for different versions of critical state models. In the current model, Eq. (4) is employed in accordance with the model of Roscoe and Burland [13] when $\alpha = 2$.

$$\zeta = \frac{\ln\left\{1 + \left(\frac{\eta}{M}\right)^{\alpha}\right\}}{\ln 2} \tag{4}$$

where $M$ is critical state stress ratio (=$\eta_{cs}$).

The particle crushing effect on soil behavior is then incorporated by extending the critical state concept. As noticed by a lot of researchers, breakage caused a downward parallel shift in the CSL in $e$ – log $p'$ space [14–16] and that the downward shift is a parallel shift of CSL in $e$ − log $p'$ space [16]. Therefore, our key concept in the formulation of the model for particle crushing is that the particle crushing effect of soils is considered by the downward parallel movement of the state boundary surface in the volumetric plane of $p'$ and $v$. For this purpose, a state variable $\Psi$ is newly introduced to represent the downward shift of the state boundary surface in the $p' - \zeta(\eta) - v$ space as indicated in Fig. 4. From this, the state parameter $\Psi$ is a non-negative variable defined as the volumetric distance between the state boundary surfaces for soil with and without density effect. $\Psi$ works as a state variable controlling the elastoplastic response in the constitutive model. The specific volume on the state boundary surface of crushed soil, $v_{sbs}^{crushed}$, is thus given in a similar way as Eq. (3).

$$v_{sbs}^{crushed} = v_{NC} + \psi = N - \lambda \ln\frac{p'}{p_a} + (\Gamma - N)\zeta(\eta) + \Psi \tag{5}$$

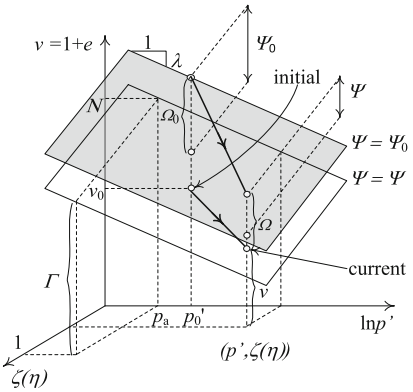


**Fig. 4.** Modeling of volumetric behavior of soil considering particle crushing and density effect

Due to the fact that the soil whose states lie under the state boundary surface do exhibit plastic strain together with elastic strain, subloading surface concept [3] is further introduced to portray this behavior. A state parameter $\Omega$, which is a combination of specific volume and mean effective stress to describe the changing strength and stiffness is incorporated in this model. As all states of soil locate on or below the state boundary surface in Fig. 1, the state boundary surface defines the loosest, upper limit of specific volume of soils. Consequently, the state parameter $\Omega(\geq 0)$ is thus defined as the specific volume difference between the current state and the loosest state under the same stress ($p$, $\eta$) on the state boundary surface as shown in Fig. 4.

According to this concept, soil exhibits irreversible deformation below the state boundary surface and gradually approaches the state boundary surface with loading. Taking a state variable $\Omega$ which is the difference between the specific volume of the current state and that on the state boundary surface under the same stress ($p'$, $\eta$ ), we can represent an arbitrary specific volume $v$ :

$$v = v_{\text{sbs}}^{\text{crushed}} - \Omega = N - \lambda \ln\frac{p'}{p_{\text{a}}} + (\Gamma - N)\zeta(\eta) + \Psi - \Omega. \tag{6}$$

During plastic flow, $\Omega$ decreases gradually with the development of plastic deformation and finally converges to zero. Therefore, an evolution law of $\Omega$ can be chosen as:

$$\frac{\dot{\Omega}}{v_0} = -Q(\Omega)\left\|\dot{\boldsymbol{\varepsilon}}^{\text{p}}\right\| \tag{7}$$

where $\dot{\boldsymbol{\varepsilon}}^{\text{p}}$ is plastic strain rate tensor and $Q(\Omega)$ is a function of $\Omega$ given as

$$Q(\Omega) = \omega\Omega|\Omega| \tag{8}$$

where $\omega$ is a parameter controlling the effect of density.

From the current specific volume $v$ by Eq. (6), and we can also calculate the initial specific volume $v_0$ by substituting the initial states: $v = v_0$, $\Psi = \Psi_0$, $\Omega = \Omega_0$, $p' = p'_0$ and $q = 0$ as:

$$v_0 = N - \lambda \ln \frac{p'_0}{p_a} + \Psi_0 - \Omega_0. \tag{9}$$

Total volumetric strain (compression is taken to be positive) generated from the initial state to the current state is given by:

$$\varepsilon_v = -\frac{dv}{v_0} = \frac{v_0 - v}{v_0}. \tag{10}$$

By substituting Eqs. (6) and (9) for Eq. (10), we get:

$$\varepsilon_v = \frac{1}{v_0}\left\{\lambda \ln \frac{p'}{p'_0} + (N - \Gamma)\zeta(\eta) - (\Psi - \Psi_0) + (\Omega - \Omega_0)\right\} \tag{11}$$

Then, the plastic volumetric strain can be determined by taking a difference between the total volumetric strain given by Eq. (11) and the elastic volumetric strain:

$$\varepsilon_v^p = \varepsilon_v - \varepsilon_v^e = \frac{1}{v_0}\left\{(\lambda - \kappa)\ln \frac{p'}{p'_0} + (N - \Gamma)\zeta(\eta) - (\Psi - \Psi_0) + (\Omega - \Omega_0)\right\} \tag{12}$$

From Eq. (12), yield function $f$ for soil considering the effect of crushing phenomenon can be written as follows:

$$f = \frac{1}{v_0}\left\{(\lambda - \kappa)\ln \frac{p'}{p'_0} + (N - \Gamma)\zeta(\eta) - (\Psi - \Psi_0) + (\Omega - \Omega_0)\right\} - \varepsilon_v^p \tag{13}$$

Assuming associated flow in the proposed model, plastic strain rate tensor is derived as:

$$\dot{\boldsymbol{\varepsilon}}^p = \langle \dot{\Lambda} \rangle \frac{\partial f}{\partial \boldsymbol{\sigma}'} \tag{14}$$

where $\dot{\Lambda}$ is the rate of the plastic multiplier. The loading criterion is thus given by $\dot{\Lambda} > 0$. As unlimited distortional strain is exhibited at critical state without any change in stress or volume, $\mathrm{tr}\left(\frac{\partial f}{\partial \boldsymbol{\sigma}}\right)$ becomes zero when $\eta$ is equal to $M$. $(N - \Gamma)$ is thus equal to $2\ln 2(\lambda - \kappa)\alpha$ case Eq. (4) is applied and the yield function is finally given as follows.

$$f = \frac{\lambda - \kappa}{v_0}\left[\ln \frac{p'}{p'_0} + \frac{2}{\alpha}\ln\left\{1 + \left(\frac{\eta}{M}\right)^{\alpha}\right\}\right] - \frac{\Psi - \Psi_0}{v_0} + \frac{\Omega - \Omega_0}{v_0} - \varepsilon_v^p \tag{15}$$

Now that we have known $I_G$ accounts for the level of particle crushing and $\psi$ is responsible for the packing & density effect on soil. Apparently, particle crushing will increase the soil's density, thus $I_G$ and $\psi$ has a close relationship. Therefore, it is possible to relate $I_G$ and $\psi$ as follow: (see Fig. 5)

$$\psi = \xi(1 - I_G) \tag{16}$$

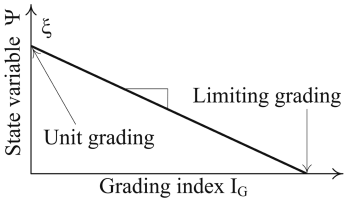


**Fig. 5.** Relationship between $I_G$ and $\psi$

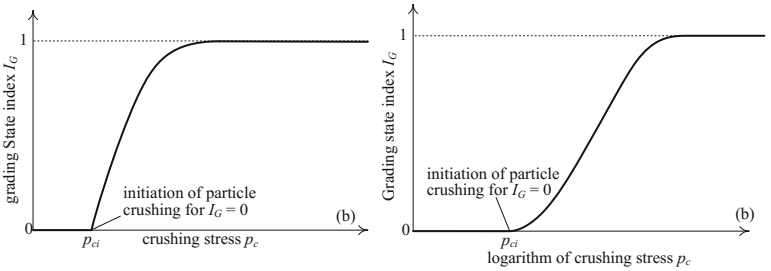


**Fig. 6.** Variation of the grading index $I_G$ with the increase of crushing

Now, the evolution law of $I_G$ is necessary. Thanks to the fact that $I_G$ has a direct relation to the evolution law of PSD due to the hardening parameter, crushing effect, it is natural to relate $I_G$ to the crushing stress that the soil is exhibited.

$$I_G = 1 - \exp\left(-\frac{p_c - p_{ci}}{p_r}\right) \tag{17}$$

in which $p_{ci}$ describe the initial size of the crushing surface. $p_r$ denotes a material constant property which controls the rate of particle crushing (see Fig. 6). $p_c$ is the mean stress at the time that particle crushing phenomenon occurs. The crushing behavior of soil particles obviously depends on properties of individual grains (such as mineralogy, hardness, shape and size) and environmental conditions (such as packing density, particle size distribution, stress level and mobilized friction), which would be reflected in soil parameters $p_r$ and $p_{ci}$. Equation (17) ensure that $I_G$ monotonically increases from 0 to 1 with the increase of $p_c$ to infinity (Fig. 6). Finally, $I_G$ is a stress dependent coefficient, and its evolution law can be derived as follow:

$$\dot{I}_G = \frac{1}{p_r}\exp\left(-\frac{p_c - p_{ci}}{p_r}\right)\dot{p}_c = \frac{1 - I_G}{p_r}\dot{p}_c \tag{18}$$

In case of isotropic consolidation, particle crushing happens when the soil's stress reaches $p_c$. On the other hand, when the soil exhibits shearing after isotropic consolidation, the combine effect of shearing and compressive stress will determine the occurrence of particle crushing. For the sake of simplicity, to judge the occurrence of particle crushing, we proposed the crushing surface $f_c$ with the same shape as yield surface:

$$f_c = \ln p + \frac{2}{\alpha}\ln\left\{1 + \left(\frac{\eta}{M_c}\right)^{\alpha}\right\} - \ln p'_c \tag{19}$$

where $M_c$ is a material parameter that controls the speed of crushing.

When particle crushing occurs, $f_c = 0, dp_c > 0$, and the consistency condition of $f_c$ requires that $df_c = 0$ which later leads to:

$$\dot{p}_c = p_c \frac{\partial f_c}{\partial \sigma_{ij}}\dot{\boldsymbol{\sigma}}_{ij} \tag{20}$$

From Eqs. (16, 18, 20), the time derivative of $\psi$ is derived:

$$\dot{\psi} = \frac{\partial \psi}{\partial I_G}\frac{\partial I_G}{\partial p_c}\frac{\partial p_c}{\partial \sigma_{ij}}\dot{\sigma}_{ij} = -\frac{\xi}{p_r}(1 - I_G)p_c\frac{\partial f_c}{\partial \sigma_{ij}}\dot{\sigma}_{ij}. \tag{21}$$

## 4 Simulation Results

### 4.1 Parametric Studies

a. *The parametric study of parameter $p_{ci}$*
A wide range of initial particle crushing $p_{ci}$ from 100 kPa to 10000 kPa has been utilized to study its effect on the grading index $I_G$ (Fig. 7a). According to the simulation results as well Eq. 17, the smaller $p_{ci}$ is, the faster $I_G$ will converge to 1 corresponding the assumed limiting crushing state. Thus, $p_{ci}$ is a material parameter representing the stress level that the soil exhibits crushing phenomenon (Table 1).
b. *The parametric study of parameter $p_r$*
Similarly, the dependence of $I_G$ on the material parameter $p_r$ in Eq. 17 is also clarified in Fig. 7b. The smaller the value of $p_r$, the faster $I_G$ will reach 1, its maximum value. Therefore, corresponding to each crushing stress, the speed of crushing of each kind of material can be adjusted by this material parameter.
c. *The parametric study of parameter $M_c$*:
The combination of effective mean stress and shearing stress will cause particle breakage. For the convenience in constitutive model, the crushing surface, which

possesses the same shape as Modified Cam Clay model, is the assumption for the combination of mean effective stress and deviator stress that causes breakage phenomenon. Compared with the large value of $M_c$, the small value of $M_c$ implies that under a certain effective mean stress, the magnitude of shearing stress required to initiate particle crushing is smaller (Fig. 7c). In other words, the crushing surface with a smaller $M_c$ is smaller in size in comparison to a larger $M_c$. Consequently, the soil's strength is smaller with a smaller value of $M_c$ as shown in Fig. 7(c).

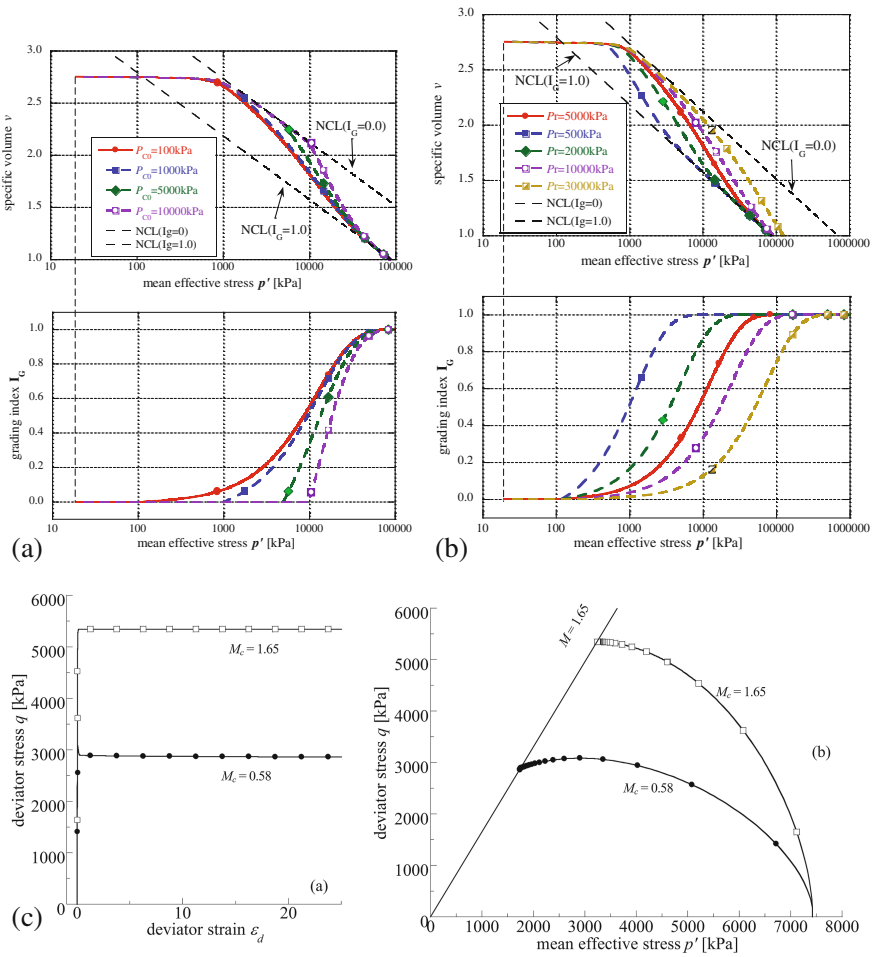


**Fig. 7.** Effect of material parameters on the model responses (a) crushing stress $p_{ci}$; (b) crushing resistance $p_r$; (c) $M_c$

**Table 1.** Material parameters

| | | | |
|---|---|---|---|
| $\lambda$ | 0.2650 | Parameters for Cam clay | Compression index |
| $\kappa$ | 0.0015 | | Swelling index |
| $M$ | 1.65 | | Critical state stress ratio $(= \eta cs)$ |
| $N$ | 2.80 | | Specific volume $v$ on $NCL$ at $p$ = 98 kPa |
| $v$ | 0.20 | | Poisson's ratio |
| $\alpha$ | 1.65 | | Shape of the yield surface |
| $a$ | 500 | Parameter for subloading surface | Effect of density |
| $P_{ci}$[kPa] | 100 | Parameters for particle crushing mechanism | Crushing strength for single sized grading |
| $P_r$[kPa] | 5000 | | Crushing resistance |
| $M_c$ | 0.58 | | Effect of shearing on crushing |
| $\xi$ | 0.55 | | Volumetric distance between state boundary surfaces for $I_G$ = 0 and 1 |

## 4.2 Validation of the Model

Figures 8 and 9 shows the simulation of experimental results by Coop and Lee [17] and their corresponding simulation results by our proposed model. These results showed the potential of the proposed model to depict well the stress-strain behavior of soil exhibiting crushing behavior under different initial confining stresses. An overall view of Figs. 8(a) and 9(a) reveals that the critical state of the consolidated undrained test was well observed by the proposed model both at standard test or at high pressure test with crushing behavior.

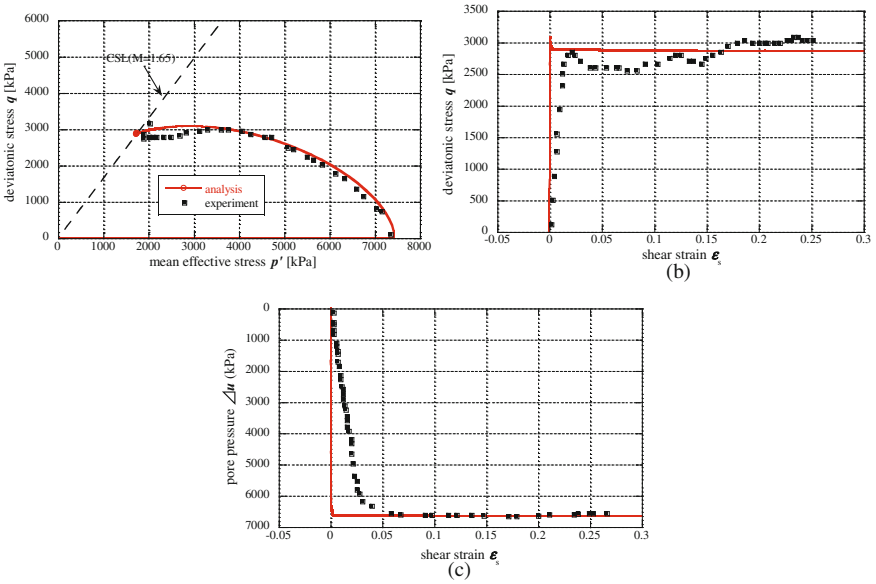


**Fig. 8.** Undrained shearing tests of crushable soil [17] and their simulations under high confining stress

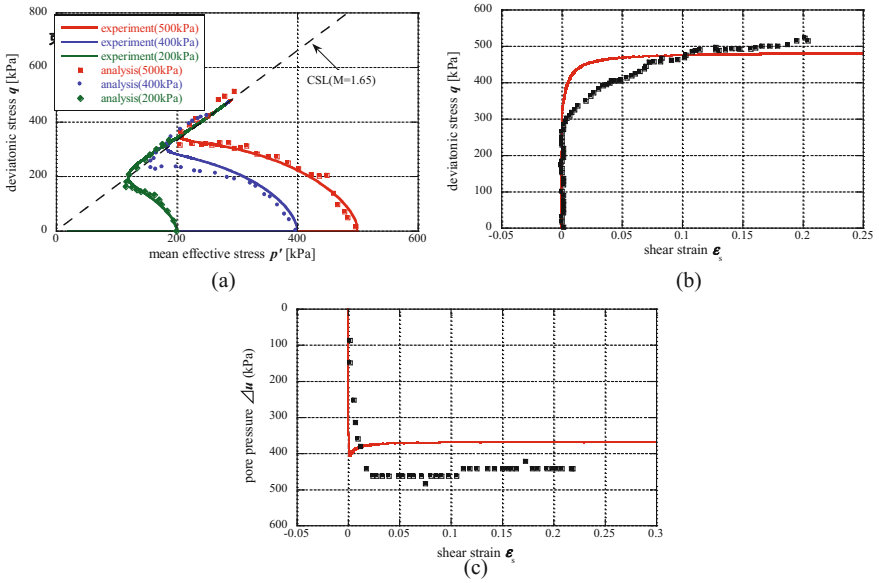


**Fig. 9.** Undrained shearing tests of crushable soil [17] and their simulations under relative low confining stress

## 5 Conclusion

A simple model considering the particle crushing phenomenon for soil has been developed in the framework of continuum mechanics. The model implemented the effect of crushing on consolidation and shearing in a unique manner. The evolution of the particle sized distribution due to particle crushing described through a single grading state index $I_G$. The downward shift of the CSL and the LICL in the compression plane due to crushing has been conducted. A number of validations of the proposed model via experimental tests have proved the potential of the model to well predict the crushing soil behavior. Also, the easy adaption of the model to FEM also reveals the large applicability of the model such as the analysis of strip footings' bearing capacity or the stability of earth dams on crushable soil.

## References

1. Rosco, K.H., Schofileld, A.N., Thurairajah, A.: Yielding of clays in states wetter than critical. Géotechnique **13**, 211–240 (1963)
2. Wood, D.M.: Soil behavior and critical state soil mechanics, Cambridge University Press (2007)
3. Hashiguchi, K., Ueno, M.: Elastoplastic constitutive laws of granular media. Proc. JSCE **227**, 45–60 (1977)

4. Al-Hattamleh, O.H., Al-deeky, H.H., Akhtar, M.N., Al, E.T.: The consequence of particle crushing in engineering properties of granular materials. Int. J. Geosci. **4**, 1055–1066 (2013)
5. Datta, M., Gulhati, S.K., Rao, G.V.: An appraisal of the existing practice of determining the axial capacity of deep penetration piles in calcareous soils. In: Proceedings of the 12th Annual Offshore Technology Conference, Houston, TX 4, pp. 119–130 (1980)
6. Polous, H.G., Chua, E.W.: Bearing capacity of foundations on calcareous sand. In: Proceedings of the 11th International Conference on Soil Mechanics and Foundation Engineering, San Franciso, AC 3, pp. 1619–1622 (1985)
7. Alba, J.L., Audibert, J.M.E.: Pile design in calcareous and carbonaceous granular material. In: Proceedings of the 2nd International Conference on Engineering for Calcareous Sediments, Bahrain, pp. 29–43 (1999)
8. Lade, P.V., Yamamoru, J.A., Bopp, P.A.: Significant of particle crushing in granular materials. J. Geotech. Eng. **122**(4), 309–316 (1996)
9. McDowell, G.R., Bolton, M.D.: Effect of particle size distribution on pile tip resistance in calcareous sand in the geotechnical centrifuge. Granul. Matter **2**(4), 179–187 (2000)
10. Kikumoto, M., Wood, D.M., Russell, A.: Particle crushing and deformation behaviour. Soils Found. **50**(4), 547–563 (2010)
11. Gajo, A., Wood, W.D.: A kinematic hardening constitutive model for sands: the multiaxial formulation. J. Numer. Anal. Methods Geomech. **23**(5), 925–965 (1999)
12. Hardin, B.O.: Crushing of soil particles. J. of Geotech. Eng., ASCE, 111(10), 1170–1192 (1985)
13. Roscoe, K.H., Burland, J.B.: On the generalized stress-strain behaviour of wet clay (1968)
14. Daouadji, A., Hicher, P.Y., Rahma, A.: Elastoplastic model for granular materials taking into account grain breakage. Eur. J. Mech. A/Solids **20**(1), 113–137 (2001)
15. Wood, D.M., Maeda K.: Changing grading of soil: effect on critical states. Acta Geotech., 3–14 (2008)
16. Ghafghazi, M., Shuttle, D.A., DeJong, J.T.: Particle breakage and the critical state of sand. Soils Found. **54**(3), 451–461 (2014)
17. Coop, M.R., Lee, I.K.: The behavior of granular soils at elevated stresses. In. Proceeding of. C. P. Worth Memorial Symposium Predictive Soil Mechanics, Thomas Telford, London, pp. 186–198 (1993)

# Application of a Cyclic Accumulation Model UDCAM to FE Analyses of Offshore Foundations

Huynh Dat Vu Khoa(✉) and Hans Petter Jostad

Norwegian Geotechnical Institute, Oslo, Norway
{Khoa.D.V.Huynh,Hans.Petter.Jostad}@ngi.no

**Abstract.** The Norwegian Geotechnical Institute (NGI) has developed several calculation procedures over the past few decades where effects of cyclic loading are taken into account. This paper presents an undrained cyclic accumulation procedure used for offshore foundation design. A constitutive model called UDCAM was developed based on the NGI's accumulation procedure and implemented into different finite element programs in order to better predict and optimize the offshore foundations. The UDCAM FE back-analysis of 1 g-model test of a gravity based structure in clay under cyclic loading was first performed for verifying the FE calculation procedure. The UDCAM model was then applied to analyze the undrained cyclic behavior of a large monopile to be installed at the potential offshore wind farm in the Korea Western Sea. The FE results were compared with the predictions obtained by the semi empirical (p-y) method recommended by API, which has been commonly used in the piled foundation design.

**Keywords:** Offshore engineering · Skirted foundations · Monopiles · Undrained cyclic degradation · Numerical modelling

## 1 Introduction

The effects of cyclic loading are for some structures very important and must therefore be carefully evaluated in the design process. The Norwegian Geotechnical Institute (NGI) has during the last 30 years developed several calculation procedures in order to characterize and predict these effects. Among them is the cyclic strain accumulation procedure described in Andersen (1976). The cyclic strength which is a function of the equivalent number of cycles, $N_{eq}$, and the average shear stress on the critical plane are then established from a case specific cyclic laboratory program. The effect of redistribution of stresses along the critical slip surface during cyclic loading is accounted by a strain compatibility approach. The design procedure has been verified by back-analyzing several model tests (Andersen et al. 1993; Keaveny et al. 1994) as well as applied to design a large number of offshore structures such as gravity based structures, e.g. Brent, Troll and Gullfaks, tension leg platforms, e.g. Heidrun and Snorre, and suction anchors for mooring of floating structures all around the world (Andersen et al. 2005).

© Springer Nature Singapore Pte Ltd. 2018
H. Tran-Nguyen et al. (eds.), *Proceedings of the 4th Congrès International de Géotechnique - Ouvrages -Structures*, Lecture Notes in Civil Engineering 8,
DOI 10.1007/978-981-10-6713-6_65

During the last decade, it has become more common to use the FE method in the design of offshore structures. Therefore, it is essential for NGI to establish a cyclic accumulation model using the same basis as the original design procedure. The first part of the paper briefly describes the soil behavior during cyclic loading. Special focus is put on the complexity of different failure mechanisms in soils underneath the offshore foundations. The second part introduces an UnDrained Cyclic Accumulation Model (UDCAM), which has been implemented into different finite element programs such as BIFURC (Jostad and Andresen 2009) and Plaxis (Jostad et al. 2014). This constitutive model accounts for soil degradation under undrained cyclic loading using the cyclic strain accumulation procedure. The main inputs to the model are cyclic contour diagrams established from a set of undrained static and cyclic triaxial and DSS tests valid for an equivalent number of cycles of the considered design storm load history. In the third part of the paper, the performance of UDCAM is verified by back-analyzing a physical model test of a gravity based structure in clay under static and cyclic loading conditions. These model tests were conducted by NGI (Dyvik et al. 1989). The last part is devoted to an application of the UDCAM model on the modelling of a more complex offshore foundation, which is a large diameter monopile subjected to cyclic loading at the potential offshore wind farm in the Korea Western Sea. The UDCAM FE-results are then compared with the predictions given by the semi empirical method recommended by the current industrial design guideline API (2011).

## 2 Undrained Cyclic Soil Behavior

Offshore foundations are generally subjected to a series of static and cyclic loads from both wind and waves. The loading conditions of the clays during a storm are usually considered as undrained. During undrained cyclic loading, the soil structure tends to be broken down and the soil volume tends to decrease, which can result in a cyclic soil strength smaller than the static soil strength (see for example Dyvik et al. 1989; Moses et al. 2003; Andersen 2009). Note that the soil volume is unchanged in the undrained condition due to the fact that the water is incompressible. Figure 1(a) illustrates an example of the soil strength degradation caused by cyclic loading. It is observed from the figure that when applying an undrained cyclic loading with a constant the maximum shear stress, $\tau$, the pore pressure, $u_p$, in the soil will accumulate and the effective stress decreases accordingly until the stress path has reached failure at cycle N. The same soil can thus fail at a lower shear stress in cyclic loading than in monotonic loading. Moreover, the evolution of cyclic stresses also indicates that the number of cycles to failure and the failure mode can depend strongly on the combination of average and cyclic shear stresses ($\tau_a$, $\tau_{cy}$).

Figure 1(b) presents the development of the shear stress, the pore pressure and the shear strain over time. Each of them consists of two components: an average component and a cyclic component. It is seen that without an increase of the cyclic shear stress, the pore pressures and the shear strains keep increasing during cyclic loading. The permanents pore pressure ($u_p$), and the cyclic, average and permanent shear strains ($\gamma_{cy}$, $\gamma_a$ and $\gamma_p$) are the most important components for design.

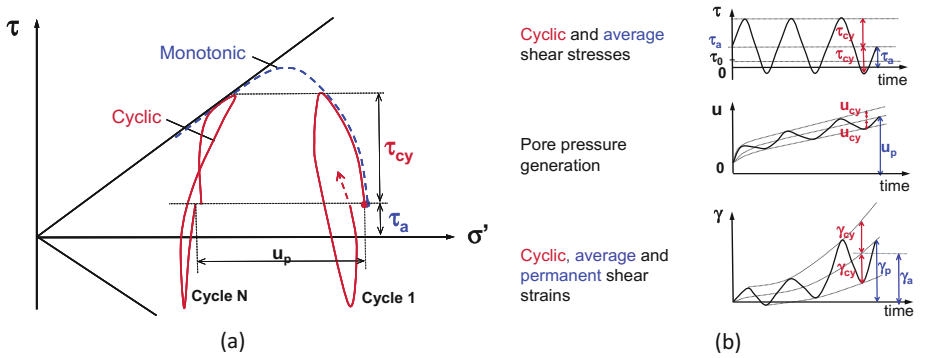


**Fig. 1.** Effective stress paths for undrained monotonic and cyclic tests (a) and development of shear stresses, pore pressure and shear strains during cyclic loading (b) (after Andersen 2009).

At NGI, the cyclic behavior of clays is described by using so-called cyclic contour diagrams, which are constructed from different undrained monotonic and cyclic laboratory tests, i.e. undrained triaxial compression (C) and extension (E) and direct simple shear (DSS) tests. Figure 2 shows an example of three dimensional contour diagrams for triaxial and DSS states for Moum clay reported by Jostad et al. (2014). The diagrams give relationships between normalized cyclic shear stress, $\tau_{cy}/\sigma_{vc}'$, cyclic shear strain, $\gamma_{cy}$, normalized average shear stress, $\tau_a/\sigma_{vc}'$, average shear strain, $\gamma_a$ and number of cycles, N. Note that the normalized (or reference) parameter of the shear stresses could be the static undrained compression strength, $s_u^C$, or the initial effective vertical consolidation stress, $\sigma_{vc}'$, as used for this case. The vertical contour lines represent the average strain while the horizontal lines are the cyclic strain. It is important to note that in offshore geotechnical engineering, failure for undrained clays is approximately defined at 15% average or cyclic shear strain. It is also observed from Fig. 2 that the cyclic soil behavior depends not only on the number of load cycles but also on the combination of the average and cyclic stresses as stated ealier.

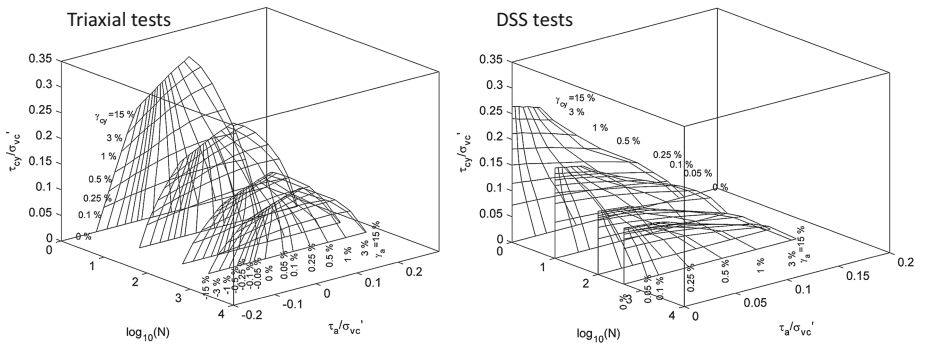


**Fig. 2.** Contour diagrams constructed from static and cyclic triaxial (left) and DSS (right) tests for Moum clay.

The stress conditions in the soil around a foundation subjected to cyclic loading are generally complicated. Figure 3(a) illustrates a simplified picture of the shear stresses along a potential failure surface in the soil beneath a shallow foundation. It is observed that the soil elements not only follow various characteristic stress paths (compression, DSS and extension) but also experience different combinations of average shear stress, $\tau_a$, and cyclic shear stress, $\tau_{cy}$. Moreover, for a monopile foundation shown in Fig. 3 (b), the characteristic stress paths in the soil could be even more complex due to the combination of different failure mechanisms such as wedge failure and flow-around failure. Jostad et al. (2014) state that the average stress over cyclic stress, $\tau_a/\tau_{cy}$, in the soil can be approximately assumed equal to the ratio of the average and cyclic loads, $F_a/F_{cy}$, from the structure if the average loads and cyclic loads act in the same direction. For an offshore gravity based foundation this is an acceptable assumption, as the average and cyclic loads are both induced by the wind and wave loads.

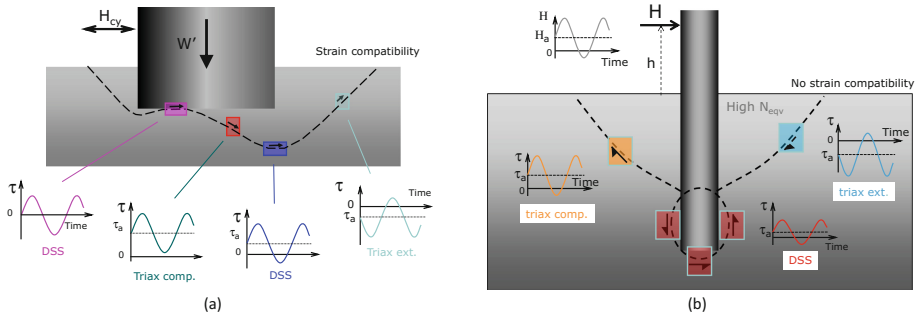


**Fig. 3.** Simplified loading conditions for some characteristic soil elements along potential failure surfaces for shallow foundation (a) and monopile foundation (b).

Several constitutive models have been developed to characterize and define the undrained cyclic behavior of soils. These models can be basically classified into two categories: implicit models (Mrŏz et al. 1978; Dafalias and Popov 1976; Ohno and Wang 1993) and semi-explicit models (Niemunis et al. 2005; Achmus et al. 2009). Although some constitutive models are able to predict well the soil behavior under cyclic loading, their application in the offshore foundation design is limited due to the fact that these models often require a significant number of input parameters. In addition, they can be computational costly and may struggle with accumulation of errors. Over several decades, NGI has accumulated significant experience on cyclic degradation of soils through a numerous experimental tests mainly conducted in-house. Rather than relying on prediction from mathematical or empirical formulations, NGI has developed a procedure for calculating the effect of undrained cyclic degradation in soils directly based on laboratory test data (Andersen 1976). This means the full set of the cyclic contour diagrams plotted in Fig. 2 is actually the direct input parameters into the calculation procedure. Thanks to high-performance computing, the NGI's strain accumulation procedure has been recently successfully implemented as a material model into several finite element programs such as BIFURC (Jostad and Andresen

2009) and PLAXIS (Jostad et al 2014). The material model is called UDCAM, which stands for UnDrained Cyclic Accumulation Model. The following section gives a brief description of UDCAM and the FE calculation procedure of the cyclic degradation in soils.

## 3 FE-Analysis with UDCAM Material Model

### 3.1 Brief Introduction of UDCAM Model

The UDCAM model is available as a user-defined material model in the commercial finite element program Plaxis. The model can account for soil degradation under undrained cyclic loading using the strain accumulation principle developed at NGI. In the UDCAM model, it is assumed that the soil is nearly perfectly undrained during at least one single load cycle. Instead of analyzing the cyclic load history in the time domain (implicit method), the model considers the behavior during application of the critical maximum load (explicit method). The effect of the cyclic loading prior to the peak load is then determined at soil element level by cyclic laboratory tests. An idealized storm loading composition where the design storm is divided into number of load cycles at different load levels, are transferred to an equivalent number of cycles, $N_{eq}$, of the maximum cyclic load that will give the same cyclic shear strain (Andersen 1976) as the real cyclic load composition. The measured responses (stress-strain relationships) in the laboratory tests (or interpolated between the different tests) for the actual $N_{eq}$ are then used directly in the analyses. The UDCAM model will find the reduced cyclic stiffnesses and accumulated permanent shear strains. At large strains, the calculated stresses are limited by anisotropic undrained cyclic shear strength.

The main input to the UDCAM material model are digitized data of cyclic contour diagrams described in Sect. 2 and three parameters given in Table 1. To model the stress-strain relationship under undrained condition the similar total stress based elasto-plastic model with anisotropic shear strengths and anisotropic hardening functions developed for the NGI-ADP material model (Grimstad et al. 2012) was applied. Note that the UDCAM model uses an elliptic interpolation function between the triaxial stress state and the DSS stress state, which is slightly different compared to the NGI-ADP model. More details of the interpolation function are reported by Jostad et al. (2014).

**Table 1.** Description of input parameters to UDCAM material model.

| Symbol | Unit | Description |
|---|---|---|
| $z_{ref}$ | L | Reference depth where the "denormalization" value $s_{u,ref}$ is given |
| $s_{u,ref}$ | $F/L^2$ | Value of the "denormalization" for strength at depth $z_{ref}$ |
| $s_{u,inc}$ | $F/L^2/L$ | Increase in the "denormailzation" with depth<br>$s_u = s_{u,ref} + (z_{ref} - z) \cdot s_{u,inc}$ |

### 3.2 Cyclic Loads in UDCAM FE-Analysis

A time load history considered in the offshore foundation design generally consists of a large number of load cycles. Modelling every load cycle individually would require enormous calculation times. For the sake of convenience the load time series applied in FE-analysis are usually analyzed by explicit methods, where so-called load parcels with constant cyclic amplitude, $F_{cy}$, and average loads, $F_a$, are applied instead of following the individual load cycle (implicit methods). The load parcels can be established by using the rainflow counting method (Matsuishi and Endo 1968) or NGI counting method (Norén-Cosgriff et al. 2015), which basically counts the number of cycles at different cyclic load levels around a continuously varying average load. Figure 4 shows an example of the counting results from a given time series.

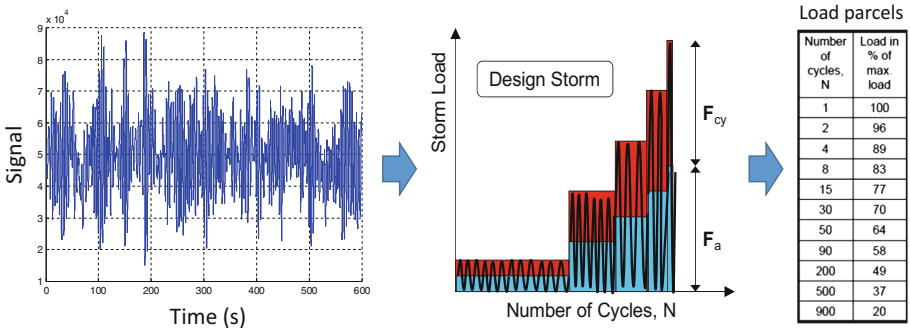


| Number of cycles, N | Load in % of max. load |
|---|---|
| 1 | 100 |
| 2 | 96 |
| 4 | 89 |
| 8 | 83 |
| 15 | 77 |
| 30 | 70 |
| 50 | 64 |
| 90 | 58 |
| 200 | 49 |
| 500 | 37 |
| 900 | 20 |

**Fig. 4.** Example of transformation from time series to idealized load composition with load parcels of constant cyclic load.

### 3.3 Loading Procedure in UDCAM FE-Analysis

Each load parcel consists of the average loads, $F_a$, the cyclic loads, $F_{cy}$ and the number of cycles, N. Due to the coupling between the average and the cyclic shear stress-shear strain relationships as shown by the cyclic contour diagrams (see Fig. 2), it is necessary to perform the analyses by a semi coupled procedure. Therefore, an analysis for a given load parcel (or part of a parcel) is divided into three phases as follows:

(i) Application of the average loads, $F_a$ (where also the soil weight is considered as an average load)
(ii) Application of the total loads, $F_a + F_{cy}$ (or alternatively only the cyclic loads, $F_{cy}$)
(iii) Input of the number of cycles at the given cyclic load level, $\Delta N$.

The average or cyclic material behavior is updated between each phase, since the average phase will produce output of $\tau_a$ and $\gamma_a$, in each integration point, as a function of $N_{eq}$, $\gamma_{cy}$ and $F_a$. The cyclic phase gives output of $\gamma_{cy}$, $\tau_{cy}$ and $N_{eq}$ as a function of $\gamma_a$ and $F_{cy}$ and $\Delta N$. The third phase is only used for specifying the number of cycles

without performing any calculations. Table 2 summarizes the iteration procedure schematically.

**Table 2.** Iteration procedure of UDCAM FE-analysis.

| | In | | Out |
|---|---|---|---|
| | Global level | Data from previous phase at each integration point | Data at each integration point |
| Average phase | Apply average load, $F_a$ | $\gamma_{cy}$ and N from previous cyclic phase<br>Average state variables (stresses etc.) from previous average phase | $\gamma_a$<br>$\tau_a$ |
| Cyclic phase | Apply cyclic load, $F_{cy}$ | $\gamma_a$ from previous average phase<br>Cyclic state variables (stresses etc.) from previous cyclic phase | $N_{eq}$<br>$\gamma_{cy}$<br>$\tau_{cy}$ |
| Neutral phase | Apply number of load cycles, $\Delta N$ | $N_{eq}$ from previous cyclic phase | $N = \Delta N + N_{eq}$ |

## 4 UDCAM FE Back-Analysis of Model Test of Shallow Foundation

NGI conducted a series of 1g-model tests to verify the procedure used for the design of foundations for deep-water gravity based structures (GBS) at the Troll field in the North Sea. The test program contained one static and four cyclic tests of a shallow skirted foundation on reconstituted Moum clay with an OCR of 3.4. The circular foundation had a 0.4 m diameter with 0.095 m skirt length and a submerged weight of 2825 N. Note that the cyclic tests were run with different moment arms and different cyclic load histories. Full details of the model tests were reported by Dyvik et al. (1989). Andersen et al. (1989); Jostad and Andresen (2009) performed back-calculations of one selected model test using the NGI's cyclic accumulation procedure. Their back-calculated results showed good agreement with the model test. Jostad et al. (2014) repeated the back-analysis of the same model test using both the Plaxis 2D and 3D FE-models in combination with the UDCAM material model described in Sect. 3. The full set of considered cyclic contour diagrams is previously plotted in Fig. 2. The cyclic load parcels are given in Table 3.

**Table 3.** Idealized cyclic load parcels for considered model test.

| Parcel | 1 | 2 | 3 | 4 | 5 | 6 | 7 | 8 | 9 | 10 | 11 |
|---|---|---|---|---|---|---|---|---|---|---|---|
| N (cycle) | 15 | 10 | 7 | 4 | 3 | 20 | 10 | 7 | 4 | 1 | 20 |
| $H_{cy}$ (N) | 240 | 480 | 510 | 537 | 575 | 601 | 660 | 709 | 761 | 808 | 719 |
| $V_a$ | W | W | W | W | W | W | W | W | W | W | W |

W = 2825 N

Figure 5 compares the failure mechanism observed from the model test and the 3D FE-analysis at the end of the cyclic loading. The deformed mesh and the shading plot of the calculated cyclic shear strains at the end of the FE analysis both indicate a rotational type of failure mode which agrees well with the model test result.

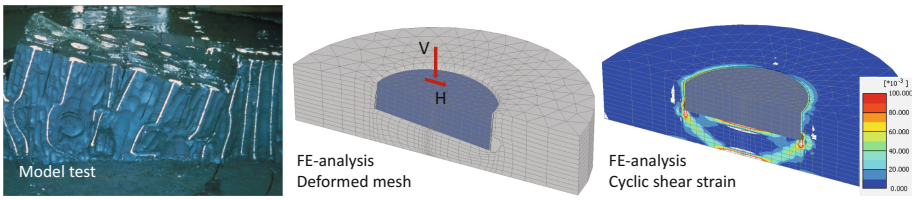


**Fig. 5.** Comparison of failure mechanism between model test and UDCAM FE-analysis.

A comparison of both the horizontal displacement at clay surface and the rotation of the foundation are also shown in Fig. 6. It is seen from the figure that the normalized horizontal load increases stepwise, which indicates that the FE-model reproduced well the variation of the applied loads from one parcel to another. The comparison shows that the FE-model combined with the UDCAM material model was able to successfully back-analyze the 1 g-model test of the shallow skirted foundation subjected to the cyclic loading. Further details of the FE back-analyses can be found in Jostad et al. (2014).

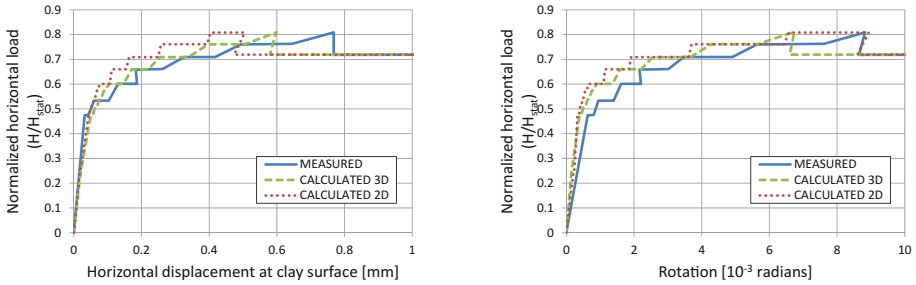


**Fig. 6.** Comparison of horizontal displacement (left) and rotation (right) of foundation obtained from model test and UDCAM FE-analysis.

**Table 4.** Idealized cyclic load parcels for monopile under ULS condition.

| Parcel | 1 | 2 | 3 | 4 | 5 | 6 | 7 | 8 | 9 | 10 | 11 |
|---|---|---|---|---|---|---|---|---|---|---|---|
| N (cycle) | 900 | 500 | 200 | 90 | 50 | 30 | 15 | 8 | 4 | 2 | 1 |
| $H_{tot}$ (MN) | 1.42 | 2.11 | 2.80 | 3.31 | 3.66 | 3.40 | 4.40 | 4.74 | 5.08 | 5.48 | 5.71 |
| $M_{tot}$ (MNm) | 42.98 | 79.51 | 105.29 | 124.63 | 137.53 | 150.42 | 165.46 | 178.36 | 191.25 | 206.29 | 214.89 |

Based on these results, it is concluded that the FE analysis with UDCAM can provide an efficient and reliable numerical tool for analyzing offshore foundations under undrained cyclic loading.

## 5 UDCAM FE-Analysis of Monopile Foundation

A three-dimensional FE analysis was performed to evaluate undrained cyclic responses of a monopile at the offshore wind farm in the Korea Western Sea. The Plaxis FE program with the UDCAM material model was used. The tubular steel pile has a 5.2 m diameter with a constant wall thickness of 0.054 m and a penetration depth of 45.0 m. The monopile supporting a 3 MW wind turbine was planned to be installed in the Korean Western Sea silty clay to silt. The full set of cyclic contour diagrams is illustrated in Fig. 7. The considered cyclic load parcels are given in Table 4.

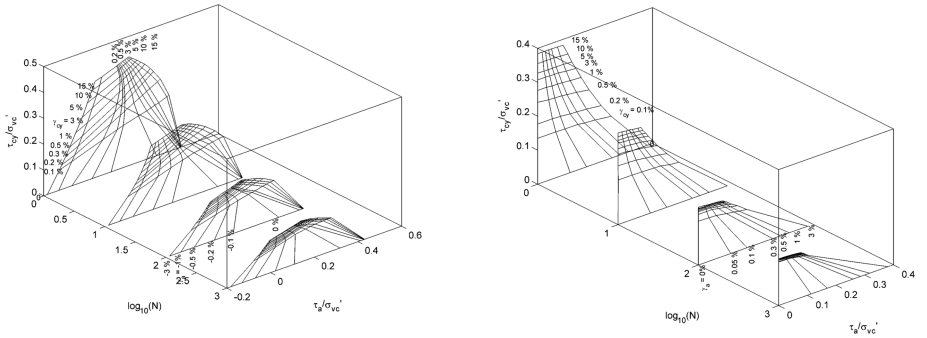


**Fig. 7.** Full set of contour diagrams constructed from static and cyclic triaxial tests (left) and DSS tests (right) for Korean Western Sea clay.

Figure 8 presents the deformed mesh and the soil failure mechanism depicted by the shading plot of the calculated cyclic shear strains at the end of the analysis. It can be seen that at the design load level, the soil is largely mobilized in the upper part around the monopile and forms a wedge type of failure mechanism.

Figure 9 shows a comparison of the pile responses calculated by the semi empirical (p-y) method recommended by American Petroleum Institute (API 2011) and by the UDCAM FE-analysis. The results obtained at the end of cyclic loading consist of the horizontal displacement, bending moment and shear force along the monopile. It is seen from Fig. 9 that the pile responses are different for the two calculation methods. In fact, the API method predicts larger horizontal displacement than the FE-analysis. In addition, the bending moments and shear forces in the monopile obtained from the API method are also larger and occur at greater depth, which may result in a too conservative design. Several reasons can be attributed to the difference between the API method and the FE-analysis. One obvious reason is that the API method was developed

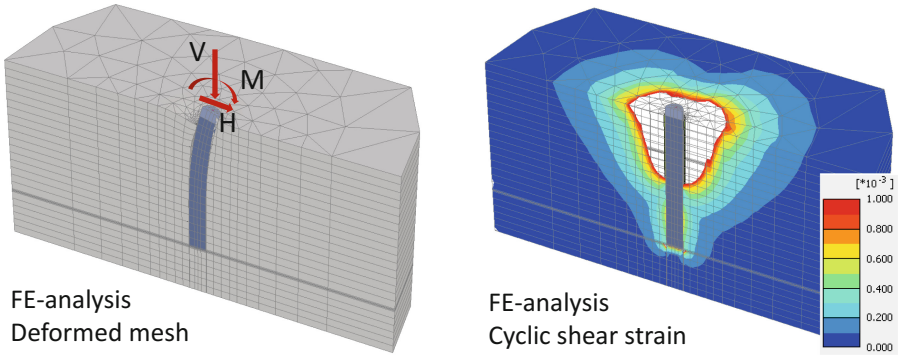


**Fig. 8.** FE-model of monopile: deformed mesh (a) and cyclic shear strains (b) calculated at end of analysis.

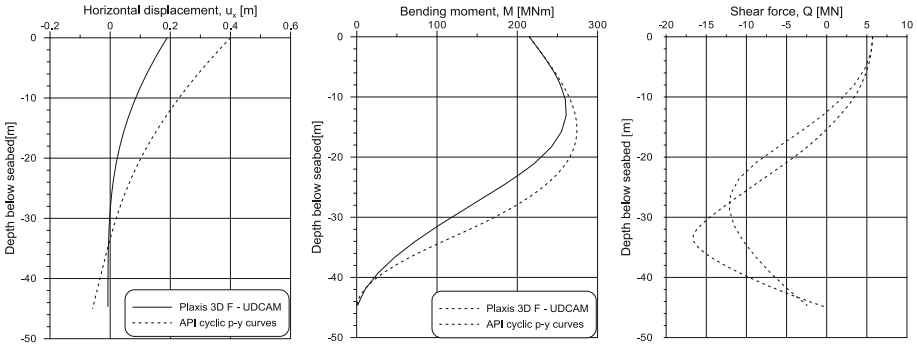


**Fig. 9.** Comparison of monopile responses calculated by UDCAM FE-analysis and semi empirical method recommended by API.

based on a limited amount of model tests on small (slender) piles in 1950s (Matlock 1970), therefore it is not suitable for large monopiles (slenderness) used in the offshore wind industry. Another reason is that the API method ignores coupling between the soil springs along the pile as well as the coupling between horizontal and vertical soil springs, which may be especially important for layered soils and short/large piles. So based on the above results, it is concluded that the UDCAM FE-analysis can provide a more realistic and optimized solution for the monopile design.

## 6 Conclusions

The paper describes the NGI's calculation procedure for taking into account the effect of undrained cyclic degradation in soils subjected to cyclic loading. This procedure has been recently developed into a material model called UDCAM of which the input

parameters are directly obtained from the laboratory tests. The implementation of the UDCAM model into different finite element programs provides a suitable numerical tool for analyzing complex undrained cyclic soil behavior in offshore foundation design. The UDCAM FE back-analysis of 1g-model test of a GBS in clay subjected to cyclic loading was carried out in order to validate the FE calculation procedure. It is observed from the back-calculated results that the FE-method with the UDCAM material model makes it possible to not only capture well the soil failure mechanism beneath the foundation but also reasonably predict the foundation responses in terms of displacement and rotation. The UDCAM FE-calculation procedure was further applied to monopile foundation design for offshore wind turbines, which is relatively more challenging problem due to both the combination of different soil failure mechanisms (wedge and flow-around failures) and the complex cyclic loading generated from wind, wave and wind-turbine loading. The comparison of the monopile responses obtained from the FE-analysis and the semi empirical (p-y) method recommended by API indicates that the UDCAM FE-analysis can give a more optimized solution for monopile design. Based on the results presented in the paper, it is concluded that the FE-method in combination with the UDCAM material model provides an efficient and robust numerical tool for analyzing offshore foundations subjected to cyclic loading.

**Acknowledgments.** The research work was carried out as a joint project between the GS E&C Research Institute in South Korea and the Norwegian Geotechnical Institute. The work was partially funded by this project, and partially supported by previous joint industry-sponsored research projects as well as the Norwegian Research Council. The authors would like to gratefully acknowledge all these supports.

## References

Achmus, M., Kuo, Y.S., Abdel-Rahman, K.: Behaviour of monopole foundations under cyclic lateral load. Comput. Geotech. **36**(5), 725–735 (2009)

Andersen, K.H.: Behaviour of clay subjected to undrained cyclic loading. In: Proceedings of the 1st International Conference on the Behaviour of Offshore Structures, BOSS 1976, Trondheim, vol. 1, pp. 392–403 (1976)

Andersen, K.H.: Bearing capacity under cyclic loading-offshore, along the coast, and on land. Can. Geotech. J. **46**(5), 513–535 (2009)

Andersen, K.H., Dyvik, R., Lauritzsen, R., Heien, D., Hårvik, L., Amundsen, T.: Model tests on gravity platforms. II: interpretation. J. Geotech. Eng. **115**, 1550–1568 (1989). ASCE

Andersen, K.H., Dyvik, R., Schrøder, K., Hansteen, O.E., Bysveen, S.: Field tests of anchors in clay II: predictions and interpretation. J. Geotech. Eng. **119**, 1532–1549 (1993). ASCE

Andersen, K.H., Murff, J.D., Randolph, M.F., Clukey, E., Erbrich, C., Jostad, H.P., Hansen, B., Aubeny, C., Sharma, P., Supachawarote, C.: Suction anchors for deepwater applications. In: Proceedings of International Symposium on Frontiers in Offshore Geotechniques, Perth, Western Australia, 19–21 September 2005 (2005)

API: Geotechnical and Foundation Design Considerations. ANSI/API RP 2GEO, 1st edn. American Petroleum Institute, Washington (2011)

Dafalias, Y.F., Popov, E.P.: Plastic internal variables formalism of cyclic plasticity. J. Appl. Mech. **43**(4), 645–651 (1976)

Dyvik, R., Andersen, K.H., Madshus, C., Amundsen, T.: Model tests on gravity platforms. I: description. J. Geotech. Eng. **115**, 1532–1549 (1989). ASCE

Grimstad, G., Andresen, L., Jostad, H.P.: NGI ADP: anisotropic shear strength model for clay. J. Numer. Anal. Methods Geomech. **36**(4), 483–497 (2012). doi:10.1002/nag.1016

Jostad, H.P., Andresen, L.: A FE procedure for calculation of displacements and capacity of foundations subjected to cyclic loading. In: Proceedings for COMGEO I, Juan-les-Pins, Cote d'Azur, France (2009)

Jostad, H.P., Grimstad, G., Andersen, K.H., Saue, M., Shin, Y., You, D.: A FE procedure for foundation design of offshore structures - applied to study a potential OWT monopile foundation in the Korean Western Sea. Geotech. Eng. **45**(4), 63–72 (2014)

Keaveny, J.M., Hansen, J.B., Madshus, C., Dyvik, R.: Horizontal capacity of large scale model anchors. In: Proceedings of the XIII ICSMFE, New Delhi, vol. 2, pp. 677–680 (1994)

Matlock, H.: Correlations for design of laterally loaded piles in soft clay. In: Proceedings of the 2nd Offshore Technology Conference, Houston, USA. Paper No. OTC 1204, pp. 577–594 (1970)

Matsuishi, M., Endo, T.: Fatigue of metals subjected to varying stress. Jpn. Soc. Mech. Eng. **68**, 37–40 (1968)

Moses, G.G., Rao, S.N., Rao, P.N.: Undrained strength behaviour of a cemented marine clay under monotonic and cyclic loading. Ocean Eng. **30**(14), 1765–1789 (2003)

Mrőz, Z., Norris, V.A., Zienkiewicz, O.C.: An anisotropic hardening model for soils and its application to cyclic loading. Int. J. Numer. Anal. Methods Geomech. **2**(3), 203–221 (1978)

Niemunis, A., Wichtmann, T., Triantafyllidis, T.: A high-cycle accumulation model for sand. Comput. Geotech. **32**(4), 245–263 (2005)

Norén-Cosgriff, K., Jostad, H.P., Madshus, C.: Idealized load composition for determination of cyclic undrained degradation of soils. In: Meyer, V. (ed.) Frontiers in Offshore Geotechnics III, pp. 1097–1101. Taylor & Francis Group, Oslo (2015)

Ohno, N., Wang, J.D.: Kinematic hardening rules with critical state of dynamic recovery, part I: formulation and basic features for ratchetting behavior. Int. J. Plast. **9**(3), 375–390 (1993)

# Assessment of Multiple Geophysical Techniques for the Characterization of Municipal Waste Deposit Sites

Gael Dumont[1], Tanguy Robert[2], Nicolas Mark[3], and Frédéric Nguyen[1(✉)]

[1] University of Liège, Liège, Belgium
f.nguyen@ulg.ac.be
[2] AQUALE sprl, Noville-les-Bois, Fernelmont, Belgium
[3] BOVA ENVIRO+, Namur, Belgium

**Abstract.** In this study, we tested the ability of geophysical methods to characterize a large technical landfill installed in a former sand quarry. The geophysical survey specifically aimed at delimitating the deposit site horizontal extension, at estimating its thickness and at characterizing the waste material composition (the moisture content in the present case). The site delimitation was conducted with electromagnetic (in-phase and out-of-phase) and magnetic (vertical gradient and total field) methods that clearly showed the transition between the waste deposit and the host formation. Regarding waste deposit thickness evaluation, electrical resistivity tomography appeared inefficient on this particularly thick deposit site. Thus, we propose a combination of horizontal to vertical noise spectral ratio (HVNSR) and multichannel analysis of the surface waves (MASW), which successfully determined the approximate waste deposit thickness in our test landfill. However, ERT appeared to be an appropriate tool to characterize the moisture content of the waste, which is of prior information for the organic waste biodegradation process. The global multi-scale and multi-method geophysical survey offers precious information for site rehabilitation studies, water content mitigation processes for enhanced biodegradation, or landfill mining operation planning.

**Keywords:** Solid waste · Applied geophysics · Landfill mining

## 1 Introduction

The characterization of former landfills is a major issue nowadays. Environmentally speaking, these sites represent a potential pollution for groundwater. Economically, waste recycling by landfill mining is more and more considered. Reactivating the biodigestion process is also used in order to enhance methane production and therfore, energy production. Finally, the rehabilitation of such sites represents an urban opportunity in densely populated area.

Landfill investigation primarily requires defining their exact location, which is achieved with remote sensing methods [1]. The site characterization includes the assessment of its horizontal extent and its thickness. Other parameters of interest are the

© Springer Nature Singapore Pte Ltd. 2018
H. Tran-Nguyen et al. (eds.), *Proceedings of the 4th Congrès International de Géotechnique - Ouvrages -Structures*, Lecture Notes in Civil Engineering 8,
DOI 10.1007/978-981-10-6713-6_66

state of digestion and the degree of humidity [2]. This information can be used to regulate the waste moisture and accelerate the stabilization process of the landfill, allowing a greater production and valorization of biogas when a power plant is associated with the landfill.

Currently, there is a need to find and develop cost-effective characterization methods that can complement the conventional "drilling – sampling – analysis" characterization methodology that provides analytical but sparse results at the scale of a site. Non-invasive geophysical methods could represent a pre-investigation strategy that would help designing the drilling grid and would provide indirect information on the waste material with a greater spatial coverage than boreholes.

In this work, we aimed at establishing an effective geophysical investigation strategy for the particular case of a large waste deposit site. We therefore used multiple geophysical techniques (ERT, EM, MAG, gravimetry, seismic and ambient noise) to characterize a known large landfill. We focused on (1) site boundary determination and site mapping, (2) waste material depth and (3) waste material characterization. We systematically compared all pieces of information obtained with each geophysical method to available historical and groundtruth data of the site. Finally, using all the geophysical methods applied, we propose an original integrated conceptual model of our test-landfill.

## 2 Site and Methods

### 2.1 Site Description

All field tests were performed on one of the largest engineered landfill of Belgium, located in a former sand quarry in Mont-Saint-Guibert (Fig. 1). The 26 ha wide and up to 60 m deep (5,3 million $m^3$ of waste) site is active since 1958. The deposit site is surrounded by multiple infrastructure elements. The present known site extension is represented by the black line (Fig. 1). The sand quarry (and therefore the waste deposit) used to extend beyond the present limits towards the S-W direction (black dotted line in Fig. 1). Around 11 million tons of wastes were landfilled. These are composed of municipal solid waste. Non-hazardous and non-toxic industrial waste and bulky waste were disposed in the current exploitation zone. Inert waste and clinker are mainly used for cover layers and dam and road stability. The site infrastructure includes a bottom leachate collection system and 200 vertical gas extraction wells. During the past 25 years, more than 1 billion $m^3$ of landfill gas have been produced. The waste is compacted with landfill compactors to conserve free space and maximize the landfill lifespan.

A part of the exploitation buildings is located in this older deposit zone. The landfill extension is limited by several roads that existed well before the sand quarry exploitation that do not allow geophysical survey far beyond the limit of the site.

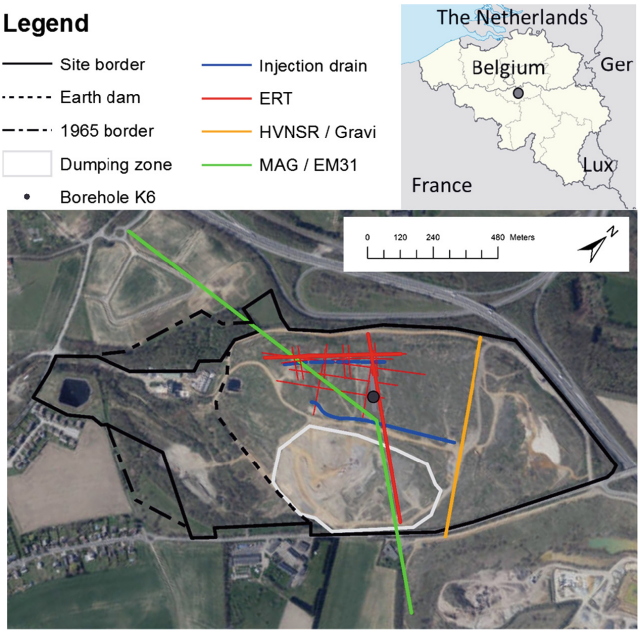


**Fig. 1.** The Mont-Saint-Guibert technical landfill site and location of the different geophysical surveys.

## 2.2 Methods

The geophysical campaigns were organized between 2012 and 2015. Some of these were designed to cover the full extent of the deposit (electromagnetic and magnetic mapping). Others provided linear or vertical profile information (electrical resistivity tomography, seismic methods). The geophysical surveys locations are found in Fig. 1.

The electromagnetic mapping were conducted with an EM31 (GEONICS) in vertical dipole mode on the former and new deposit. The device sensitivity peaks at 1.45 m depth (0.4 * intercoil spacing). The quadrature-phase component of the induced magnetic field is linearly related to the ground conductivity. However, the EM31 is characterized by some non-linearity for highly conductive media. The detection of large metallic objects can be done by measuring the in-phase component of the induced magnetic field. We refer to GEONICS technical note for more information [3–5].

The magnetic data were acquired with tree different magnetometers. A cesium vapor MAGMAPPER G-858 gradiometer (GEOMETRICS), with sensor located 0.4 and 1 m above the ground and sampling frequency of 0.5 s, and a GSM-19-GW Overhauser-effect gradiometer (GEM-Systems), with sensor are located 2 m and 2.6 m above de ground and a sampling frequency of 1 s, were used for the magnetic vertical gradient mapping. This parameter presents the advantage of minimizing the effect of temporal magnetic variations. A GSM-19-TW proton magnetometer (GEM-Systems) was used to assess the magnetic field stability on the site at a fixed location. Only a few

10 nT variation were recorded, two order of magnitude under the observed anomalies on the deposit site. We refer to [6] for more information on magnetometers.

Seismic data were acquired with the DacqLink2 logger and 24 4.5 Hz geophones. We used an 8 kg sledgehammer. Surface waves, that concentrate a large part of the tremor energy, were analyzed due to the inability to detect first arrivals. Multichannel analysis of the surface wave dispersive behavior (MASW) allows the estimation of the vertical shear-wave velocity (Vs) profile inside the waste dump. We refer to [7, 8] for more information on the MASW method and the inversion procedure.

The horizontal to vertical noise spectral ratios (HVNSR) were recorded with a CityShark microseismic station and a Lennartz Electronic LE-3Dlite sensor (1 Hz). The passive seismic method, introduced by [9, 10] and popularized by [11] measures the fundamental resonance frequency of soft sediment over a hard bedrock. For a 1D geology, the frequency of the fundamental mode resonance frequency depends on the soft layer average shear wave velocity (Vs) and thickness: f = Vs/4 h. The amplitude of the peak depends on the impedance (density * Vs) contrast between the soft sediment and the bedrock, but no direct correlation is established. Several measurements were performed outside the landfill, close to piezometers (where the depth to bedrock was known), in order to estimate the Vs vertical profile in the sand host formation. The 11 stations profile acquired across the waste deposit intended to calculate the landfill thickness. Both MASW and HVNSR data were analyzed with the GEOPSY software.

Several ERT profile were acquired on the landfill for characterization and for recirculation of leachate experiments monitoring. Investigation focused on the N-W zone of the present deposit site (Fig. 1). A long transversal profile completed the ERT data set. The electrode spacing varied with the targeted depth. A 2.5 m spacing was used for the cover layer and the vadose zone characterization. A 4 or 5 m spacing was used for deeper investigation and water level assessment. The multigradient protocol was used to take advantage of the multi-channel ability of the ABEM terrameter LS. Data were inverted using the CRTomo inversion code [12]. Parameters used for the inversion procedure are described in [2].

## 3 Results

### 3.1 Mapping

On the electrical resistivity map provided in Fig. 2, the waste deposit is divided into two main zones: the new deposit site and the former one, separated by an inert dam. The new deposit site is characterized by the lowest resistivity (about 5 Ωm). Flat areas along the landfill crest are generally more conductive, while steep areas close to the landfill N-W border are more resistive. Some specific sub-areas present different signatures. The N-E extent of the field presents higher values of resistivity. This zone was covered by two HDPE membrane cover layers (in 1990 and again in 2005 as a reaction to uneven settlement and surface water accumulation). Therefore, the shallow depth horizon is mainly composed of inert anti-punching material. The present deposit site also presents higher values of resistivity. This could be accounted for by the waste deposit of particular composition (organic wastes are forbidden since 2010). The

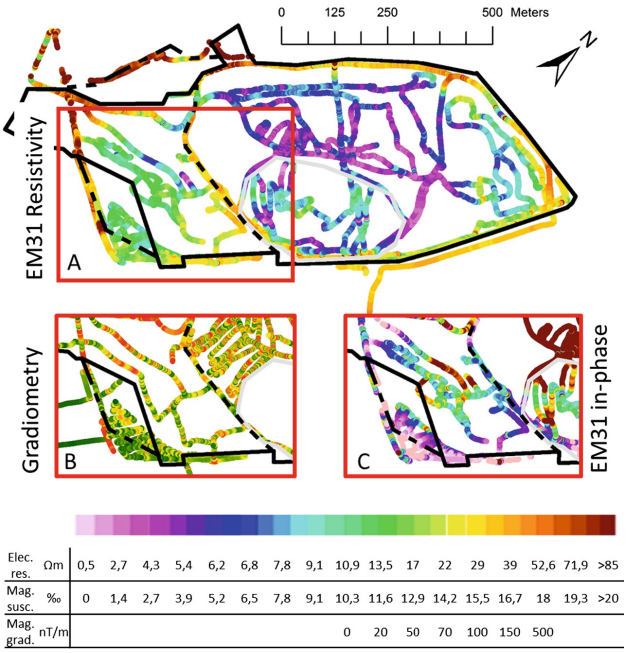


**Fig. 2.** Electromagnetic and magnetic mapping of the landfill: (a) Electrical resistivity (EM31 out-of-phase); (b) magnetic vertical gradient; (c) EM31 in-phase

different paths surrounding and crossing the waste deposit are characterized by low resistivity. The foundation layer is probably thin and lays directly on the waste material. These tracks were regularly moved during the landfill growth. At the contrary, the main entrance of the landfill (HVNSR profile northern extend, Fig. 1) has been unchanged since 1985 and presents high resistivity, more characteristic of sand deposit than waste material.

The former deposit site is characterized by much higher resistivity. A possible explanation for this might be a more mature waste (characterized by lower leachate salinity) and/or a thicker cover layer. The contrast between the former deposit and the host formation is unclear at the S-E border. A smaller zone of the former deposit site is characterized by resistivity close to these of the host loess formation (while waste material was apparently disposed in this area between 1985 and 1990).

The grass field outside of the landfill, in the S-E, was never excavated according to historical records and its resistivity is close the loess values. However, the grass field located at the Southern extremity of the landfill is characterized by slightly lower resistivity and a larger magnetic susceptibility (with both magnetometry and EM31 in-phase methods) than the host formation (Fig. 2a, b and c). Electromagnetic and magnetic mapping allowed us to detect a zone outside the present limit of the site but apparently excavated in the 60's and then backfilled with unknown material.

### 3.2 Thickness Estimation

The test-landfill, characterized by a known depth of up to around 60 m, represents a challenge for indirect depth estimation using geophysical methods, since surface surveys have generally limited depth of investigation and decreasing spatial resolution and sensitivity at increasing depth. We attempted to calculate the landfill depth using seismic methods. We combined MASW (single vertical profile) and HVNSR (Fig. 3). From the analysis of their dispersive behavior, we established that Vs varies from 100 m/s at the surface to 180 m/s at a 16 m depth (the average Vs over 16 m is 140 m/s). Vs increases by 5 (m/s)/m with depth and the average Vs increases by 2.5 (m/s)/m. Given the 4.5 Hz geophone and the light sledge hammer used, the Vs profile is not available for larger depth, as the investigation depth is generally considered equal to half the wavelength of the recorded lowest frequency surface wave. We then supposed that the Vs linearly increases with depth and reaches 400 m/s at 60 m depth (250 m/s mean Vs). The shear wave velocity of the sand host formation may also be estimated from several HVNSR data acquired close to piezometers, where the depth to bedrock is known from borehole data and varies from 20 to 54 m. There, the measured fundamental resonance frequency ranges from 1.7 to 3.4 Hz. The average Vs is 180 m/s at the surface and increases by 3.87 (m/s)/m when the depth increases. The coefficient of determination is rather low (0.63) but typical of such approaches (e.g. [13]).

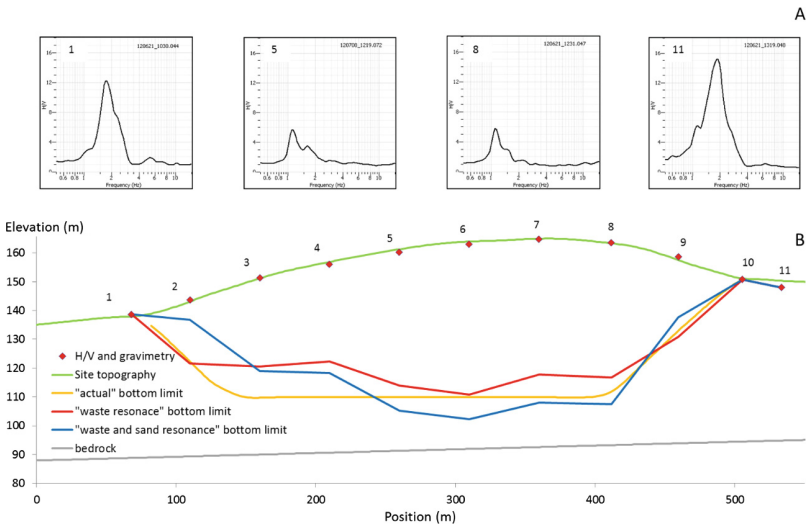


**Fig. 3.** (a) HVNSR resonance peaks; (b) HVNSR transversal profile. See location on Fig. 1

### 3.3 Water Content Estimation

Because of the high contrasts in electric resistivity provided by borehole investigation, we expected that geoelectrical methods might enable us to accurately image electric resistivity, and then water distribution inside the waste material.

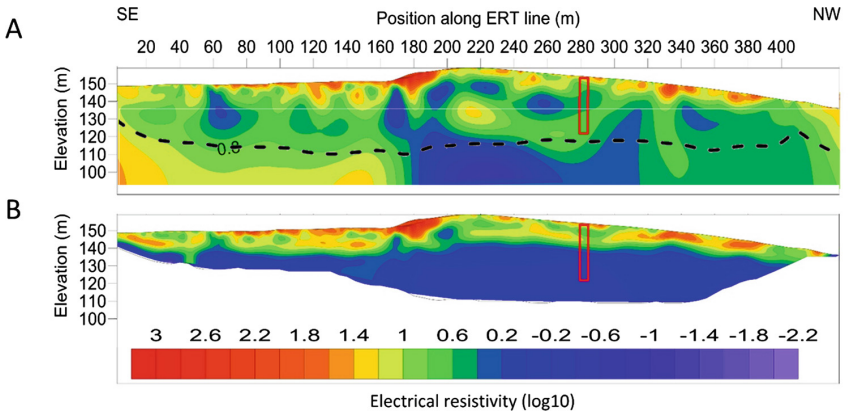


**Fig. 4.** ERT transversal profile inverted with (a) basic inversion process (DOI in dotted line); (b) advanced inversion process. The borehole location is the red rectangle

The transversal ERT profile was inverted with (1) a standard inversion procedure (robust norm on the data; see [12] for more details) and (2) a reference model to impose the depth and electrical resistivity of the saturated zone (see [2] for more details). We show here the importance of incorporating prior information in the inversion to achieve a coherent result. Both inversion processes converged and the error weighted $Chi^2$ of the data misfit reached 1 (i.e. the data set was fitted within its error level assessed with reciprocal measurements). The standard inversion is presented at Fig. 4a. The depth of investigation (DOI; as defined by [14], with 1 and 100 Ωm reference models, 0.05 reference model weight in the objective function and 0.1 DOI threshold for interpretation) was far too low to estimate the landfill depth. In the S-E area, the transition with the HDPE membrane was depicted at 40−50 m depth while it was actually at 20 m. In the N-W zone, the landfill was much deeper. The resistivity contrast with the HDPE bottom membrane was not detected. An inert dam separates the present dumping zone from the rest of the site. The depth to water table is overestimated with respect to borehole information.

The reference model inversion is presented at Fig. 4b. The electrical resistivity distribution was rather different than for the basic inversion procedure below elevation 135 m, while the error levels reached were identical. With the reference model process, the unsaturated zone was in agreement with borehole data as the depth to the water table was imposed [2]. The saturated zone appeared relatively homogeneous. This is also partially due to the lower spatial resolution and sensitivity of ERT profiles at depth. The transition between the unsaturated and the saturated zone appeared rather smooth, while it is known to be sharp from borehole EM investigation [2]. The thickness of the unsaturated zone was also overestimated. This could be explained by the limited depth of investigation of the ERT method but also the non-uniqueness of the inverse problem.

## 4 Conclusions

We here tested the ability of geophysical methods to characterize a large technical landfill installed in a former sand quarry. The geophysical surveys specifically aimed at delimitating the deposit site horizontal extension, at estimating its thickness and at characterizing the waste material composition (the moisture content in the present case).

The site delimitation was conducted with electromagnetic (in-phase and out-of-phase) and magnetic (vertical gradient and total field) methods. These cheap and quick methods are well suited to rapidly and precisely find the site extents. The combined use of EM and MAG mapping clearly showed the transition between the waste deposit, neighboring tracks and natural ground condition. Inside the landfill perimeter, the EM mapping also allowed the differentiation between the new and the old deposit area and the identification of zones characterized by specific electrical resistivity and magnetic susceptibility signatures. So, present dump zone, the N-E restored area and the entrance of the site are characterized by higher resistivity and lower magnetic susceptibility.

Regarding waste deposit thickness evaluation, traditional seismic reflection and refraction techniques were ineffective due to the restricted use of explosive sources (due to biogas hazard). Then we propose a combination of horizontal to vertical noise spectral ratio (HVNSR) and multichannel analysis of the surface waves (MASW), which successfully determined the approximate waste deposit thickness in our test landfill. Nonetheless, for this particular study, uncertainty remained on the origin of the resonance phenomenon due to a medium seismic impedance contrast between waste material and the host sand formation.

ERT appeared to be an appropriate tool to characterize the moisture content of the waste. When available, additional historical or drilling information (e.g. the location of the bottom HDPE geomembrane and the depth of the saturated zone in this case) can be used to constrain the inversion process and as a consequence, enhance the resolution in upper parts of inverted resistivity models.

Globally, the full geophysical campaign, which necessitated less than 2 weeks survey for a couple of technicians and one week data treatment for an engineer, offers a good understanding of the site extension, depth, volume and water content. This information acquired at low cost (compared to the "drilling-sampling-analyses" approach) offers precious information for site rehabilitation studies, water content mitigation processes for enhanced biodegradation or landfill mining operation planning.

**Acknowledgments.** The MINERVE project is a multidisciplinary research program financed by the Walloon Region (Plan Marshall2.vert, pôle GreenWin; http://greenwinminerve.com/). We are grateful to SHANKS, the leader of the research program for the access to the site and technical support.

## References

1. Beaumont, B., Radoux, J., Defourny, P.: Assessment of airborne and spaceborne thermal infrared remote sensing for detecting and characterizing landfills, pp. 237–248 (2014). doi:10.2495/WM140201

2. Dumont, G., Pilawski, T., Dzaomuho-Lenieregue, P., Hiligsmann, S., Delvigne, F., Thonart, P., Robert, T., Nguyen, F., Hermans, T.: Gravimetric water distribution assessment from geoelectrical methods (ERT and EMI) in municipal solid waste landfill. Waste Manag. (2016). doi:10.1016/j.wasman.2016.02.013
3. McNeill, J.D.: Use of EM31 inphase information (No. TN-11). Geonics Ltd., Ontario, Canada (1983)
4. McNeill, J.D.: Electrical conductivity of soils and rocks (No. TN-5). Geonics Ltd., Ontario, Canada (1980a)
5. McNeill, J.D.: Electromagnetic terrain conductivity measurment at low induction numbers (No. TN-11). Geonics Ltd., Ontario, Canada (1980b)
6. Hrvoic, I., Hollyer, G.M., Eng, P.: Brief review of quantum magnetometers. GEM Syst. Tech. Pap (2005)
7. Wathelet, M., Jongmans, D., Ohrnberger, M.: Surface-wave inversion using a direct search algorithm and its application to ambient vibration measurements. Surf. Geophys. **2**, 211–221 (2004)
8. Socco, L.V., Foti, S., Boiero, D.: Surface-wave analysis for building near-surface velocity models–established approaches and new perspectives. Geophysics **75**, 83–102 (2010)
9. Nogoshi, M., Igarashi, T.: On the propagation characteristics of microtremors. J. Seismol. Soc. Jpn. **23**, 264–280 (1970)
10. Nogoshi, M., Igarashi, T.: On the amplitude characteristics of microtremors. J. Seismol. Soc. Jpn. **24**, 24–40 (1971)
11. Nakamura, Y.: A method for dynamic characteristics estimation of subsurface using microtremor on the ground surface. Q. Rep. Railw. Tech. Res. Inst. **30**, 25–33 (1989)
12. Kemna, A.: Tomographic inversion of complex resistivity-theory and application. Ruhr-Universität, Bochum, Germany (2000)
13. Sauret, E.S.G., Beaujean, J., Nguyen, F., Wildemeersch, S., Brouyere, S.: Characterization of superficial deposits using electrical resistivity tomography (ERT) and horizontal-to-vertical spectral ratio (HVSR) geophysical methods: A case study. J. Appl. Geophys. **121**, 140–148 (2015). doi:10.1016/j.jappgeo.2015.07.012
14. Oldenburg, D.W., Li, Y.: Estimating depth of investigation in dc resistivity and IP surveys. Geophysics **64**, 403–416 (1999). doi:10.1190/1.1444545

# Seismic Cone Testing Using Seafloor Drill Technology

D.H. Doan[1(✉)], P. Looijen[2], and A.G. Cooper[3]

[1] Fugro GeoConsulting, 27, rue des Peupliers, 92752 Nanterre, France
h.doan@fugro.com
[2] Fugro Engineers, P.O. Box 130, 2630 AC Nootdorp, The Netherlands
[3] Fugro Marine GeoServices, 6100 Hillcroft Ave., Houston, TX 77081, USA

**Abstract.** Seafloor drilling systems are the latest innovative technology to explore the next frontier of ultra-deep water locations. Drilling, sampling and in situ testing (e.g., cone resistance and seismic velocities) are directly performed using the remotely operated seabed system. This paper provides a background of such seafloor drill technology and its benefits to the offshore industry. By reviewing an example from the field, the paper specifically discusses the performance of the system equipped with a dual-array cone for measuring in situ shear wave velocity in deep water sediments. These field measurements of shear wave velocity corresponded favourably with the advanced laboratory testing on intact, recovered samples. They also can be employed in conjunction with cone penetration testing in order to provide a high confidence shear wave velocity profile for deep water sediments for engineering purposes.

**Keywords:** Seafloor drilling systems · Cone resistance · Seismic cone · Shear wave velocity

## 1 Introduction

Seafloor drilling systems are the latest innovative technology to explore the next frontier of ultra-deep water locations (Cooper et al. 2015; Nguyen et al. 2013; Yetginer et al. 2012). They are sophisticated data gathering devices rather than simple coring tools and can operate in water depths up to 4,000 m and on seafloor slopes up to 25°. They are capable of performing rotary drilling, coring, sampling, and in situ testing including piezocone penetration tests, ball probe tests and seismic measurements with real-time observation to 150 m below the seafloor. This paper provides a background on such seafloor drill technology and its benefits to the offshore industry. Moreover, the performance of the system equipped with a dual-array cone was proven in the offshore environment for measuring in situ shear wave velocity in deep water sediments.

## 2 Description and Application of Equipment and Operational Details

The SFD Seafloor Drills combine proven drilling technology and remotely operated vehicle (ROV) telemetry. The spread consists of a seafloor drilling unit with a dedicated launch and recovery system (LARS). Additionally, there are ancillary containers

© Springer Nature Singapore Pte Ltd. 2018
H. Tran-Nguyen et al. (eds.), *Proceedings of the 4th Congrès International de Géotechnique - Ouvrages -Structures*, Lecture Notes in Civil Engineering 8,
DOI 10.1007/978-981-10-6713-6_67

including a control van that are mobilized onto the vessel of opportunity (VOO) as illustrated in Fig. 1.

**Fig. 1.** Mid-ship SFD deck layout

SFDs are controlled remotely (wireline mode) with a fiber optic umbilical that transmits data real-time back to the Control Van on-board the vessel as pictured in Fig. 2. They have thrusters on-board the units to maneuver and orient them subsea. There is also a polymer mud injection system, which is used to maintain a positive head through the drill string and to stabilize the boreholes. All of the ROV components are pressure-compensated to 4,000 m water depth.

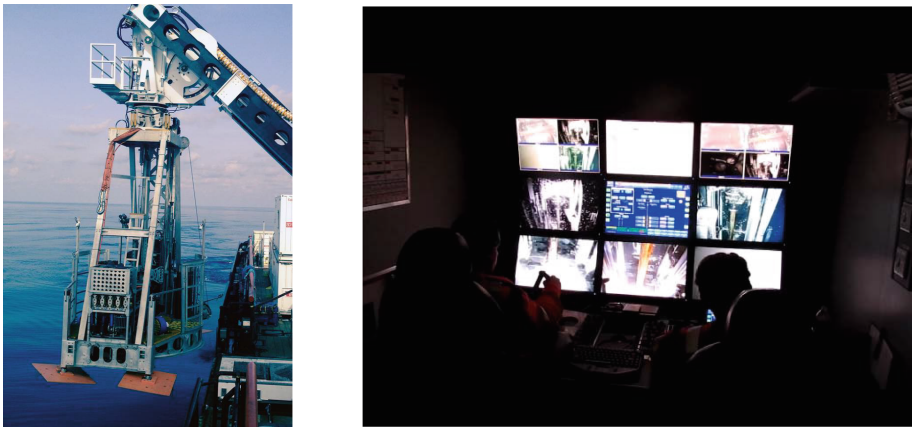

**Fig. 2.** Left: launch of a SFD; Right: inside the control van

The SFDs are designed for offshore geotechnical and geohazard investigations with the ability to collect data using Shelby tubes, liners, core barrels, and in situ testing tools, including:

- Piezocone Penetration Test (PCPT)
- Seismic Piezocone Penetration Test (SCPT)
- Vane Shear Test (VST)
- Ball Probe Test (BPT)
- T-Bar Test (T-Bar)
- Piezoprobe Test.

The above list is comprised of downhole tools except for the T-Bar, which is pushed from the seafloor to a maximum depth of 2.5 m without any drilling operations, specifically for pipeline route surveys.

Prior to a dive, the SFD Seafloor Drills are loaded with a selection of tooling for the soil conditions likely to be encountered in the borehole. The tooling includes casings, drill pipe, core barrels, Shelby tubes, liners and downhole in situ testing tools.

Once the dive commences, all drill pipes and geotechnical tools are handled by a robotic arm and twin tower-mounted retrieval systems. The operators have the flexibility to use any of the samplers or downhole in situ tools available on the rig at any time.

As the work progresses, retrieval of the samplers is done automatically. Drilling parameters (e.g., weight on bit, flow rate, and torque) are monitored and logged using the Graphical User Interface (GUI) software, and the samples are stored on-board the Seafloor Drills until the end of the dive. From start to finish of each dive, all necessary drill pipe and geotechnical tools are presented, used, and retrieved using the Seafloor Drills' robotic systems.

For downhole PCPT, the tool is passed into the borehole with the wireline, and the drill string is then retracted off bottom. The PCPT probe is locked into position in the Bottom Hole Assembly (BHA), and the drill string is advanced at a constant rate of penetration of 2 cm/s. The data is transmitted to the SFD' Control Van or auxiliary stations on-board the vessel in real-time.

Further details on the drilling, sampling and testing process can be found in Cooper et al. (2015).

## 3 Shear Wave Velocity Measurement

This section describes a case example in approximately 450 m of water where the SFD system was deployed for a geohazard and geotechnical survey for an important deep water offshore oil and gas development. The geotechnical borings were a combination of rotary drilling, sampling, and in-situ testing including cone penetration and ball probe tests. The intact, high quality samples were recovered and used for advanced laboratory testing. Soil conditions within the boreholes consisted of normally to slightly consolidated, highly plastic clays from very soft at the seafloor; then firm to stiff to approximately 60.0 m below seafloor (BSF); and finally very stiff down to 90.0 m BSF.

### 3.1 In Situ Seismic Measurements and Data Processing

Seismic measurements were performed in downhole mode in which the tool is lowered and latched into the drill string, as described Peuchen et al. (2002). These seismic measurements were conducted at CPT termination depths and, in most cases, every 2 m interval. Shear wave measurements were obtained by two sets of geophone arrays (dual geophone) as presented Fig. 3. The upper array (array of three perpendicular geophones x1-y1-z1) and the lower array (three perpendicular geophones x2-y2-z2) are 500 mm apart with the lower positioned 278 mm above the cone tip. The hydraulic underwater shear wave hammer (HUSH box), consisting of a spring-driven steel mass hammered to a steel striking plate was mounted on the seabed frame at a distance of 4.25 m from the boring location. The mass and spring were horizontally mounted, giving a single near-horizontal strike direction and tangential relative to the axis of the test location.

**Fig. 3.** Left: hydraulic underwater shear wave hammer; Right: dual-array cone

Seismic data were controlled and collected by SECAS, a PC-based 6 channel seismograph with digital storage facilities. They have been then analysed by using SC3-RAV$^{TM}$, a Windows program, which facilitates comprehensive downhole seismic testing data reduction, analysis, and display (SC3-RAV User's Manual 2011).

Shear wave velocity calculation was based on two methods: the cross correlation technique and the hand picking method. In general, cross correlations between the full wave channels provide the most reliable result for this site investigation. The cross correlation technique implements a patented mathematical algorithm to derive downhole seismic interval velocity profiles based on cross correlating the wave recorded at consecutive depth increments (Baziw 1993). The value of the time shift at the maximum cross correlation value is assumed to be the relative travel time difference for the wave to travel the depth increment. This technique has the following advantages:

- It minimizes the human bias associated with visually selecting a crossover point in deriving interval times
- It utilizes the full waveform in deriving interval travel times as opposed to a single point

- The correlation coefficient between the two waves can be used as a velocity accuracy estimate; this parameters gives the user an indication of the similarity between the two wave being correlated and the subsequent accuracy of the velocity estimate
- It obtains two independent velocity estimates for each depth increment by comparing source wave generated on both the right and left side of the seismic probe.

Figure 4 presents the recorded traces as function of penetration depth. X and Y axes represent the orientation of two horizontal perpendicular geophones. It is noted that the data stacking is often required for data processing, as this would reduce the noise, improve the signal-to-noise ratio, improve seismic data quality, and reduce errors in trigger timing.

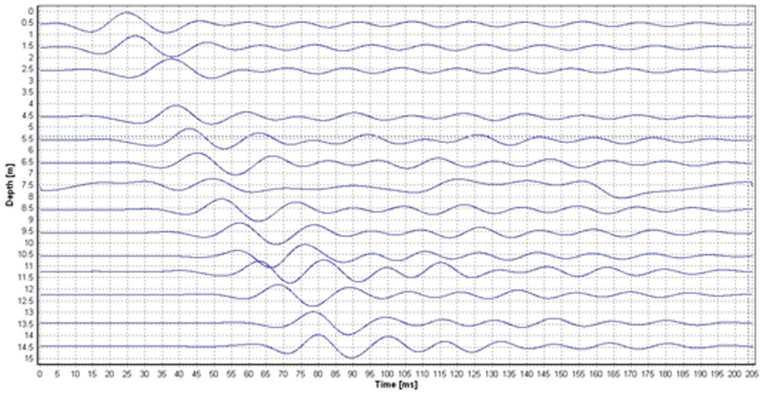


SCPT X-Traces at location BH1

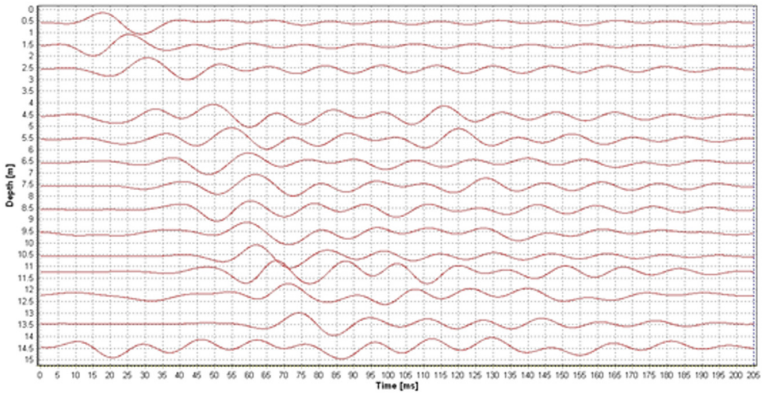


SCPT Y-Traces at location BH1

**Fig. 4.** Case example – data processing: recorded traces versus depth

### 3.2 Laboratory Seismic Measurements

The advanced laboratory testing program included the anisotropically consolidated undrained triaxial tests with measurement of shear wave velocity using the bender element (BE), and anisotropically consolidated resonant column (RC) tests.

BE tests were performed by triggering a shear wave through the samples at the end of anisotropic consolidation stages so as to determine the shear wave velocity of the specimen under a desired stress state. The measurement was part of anisotropically consolidated undrained triaxial compression/extension tests. During such these advanced laboratory tests, saturation was obtained by incrementing cell pressure and back pressure. The degree of saturation was checked by the pore water pressure response to small variations in cell pressure. Samples were consolidated to the estimated effective stress of the in situ conditions ($K_o$ stress path) in order to minimise the effects of sample disturbance.

RC tests were performed on specimens with a height to diameter ratio of approximately 2:1 under a fixed free test arrangement. In this arrangement the specimen is fully fixed at the bottom and an electrical oscillator applies torsional motion to the top. RC tests provided a determination of the shear wave velocity, hence a small strain shear modulus ($G_{max}$), and a determination of the rate of shear modulus degradation and damping ratio with increasing shear strain at small shear strain by torsional vibration. The samples were consolidated to estimated in situ stress state prior to all laboratory measurements.

### 3.3 Seismic Velocities from Cone Resistance

Shear wave velocity calculated from cone resistance is also presented for comparison against the measured values. The relationship proposed by Mayne and Rix (1995) for clay has been employed as follows: $V_s = 1.75\ (q_c)^{0.627}$, where $V_s$ is shear wave velocity (m/s) and $q_c$ is cone resistance (kPa).

### 3.4 Comparative Results

Figure 5 presents a comparison of shear velocities from various measurement methods. Generally, a positive correlation was found between the in situ measurement and advanced laboratory test results. For the first few meters, the results are scattered, which can be attributed to noises identified near surface. Wave interference effects can prevent accurate interpretation of test results obtained close to seafloor. Common interferences for S-waves are P-waves and surface waves. For some ground conditions, interference can also result from S-wave refraction and reflection.

It is appreciated that the system only provided useable wave signals down to approximately 65 m below seafloor during this site investigation.

Using a seafloor drill such SFD system to obtain field measurements of Vs combined with cone penetration testing should continue to be considered for offshore investigations as initially suggested Peuchen et al. (2002). Coupled with a well-defined advanced laboratory program, this solution would enable a best definition of the shear wave velocity profile for input into engineering assessments.

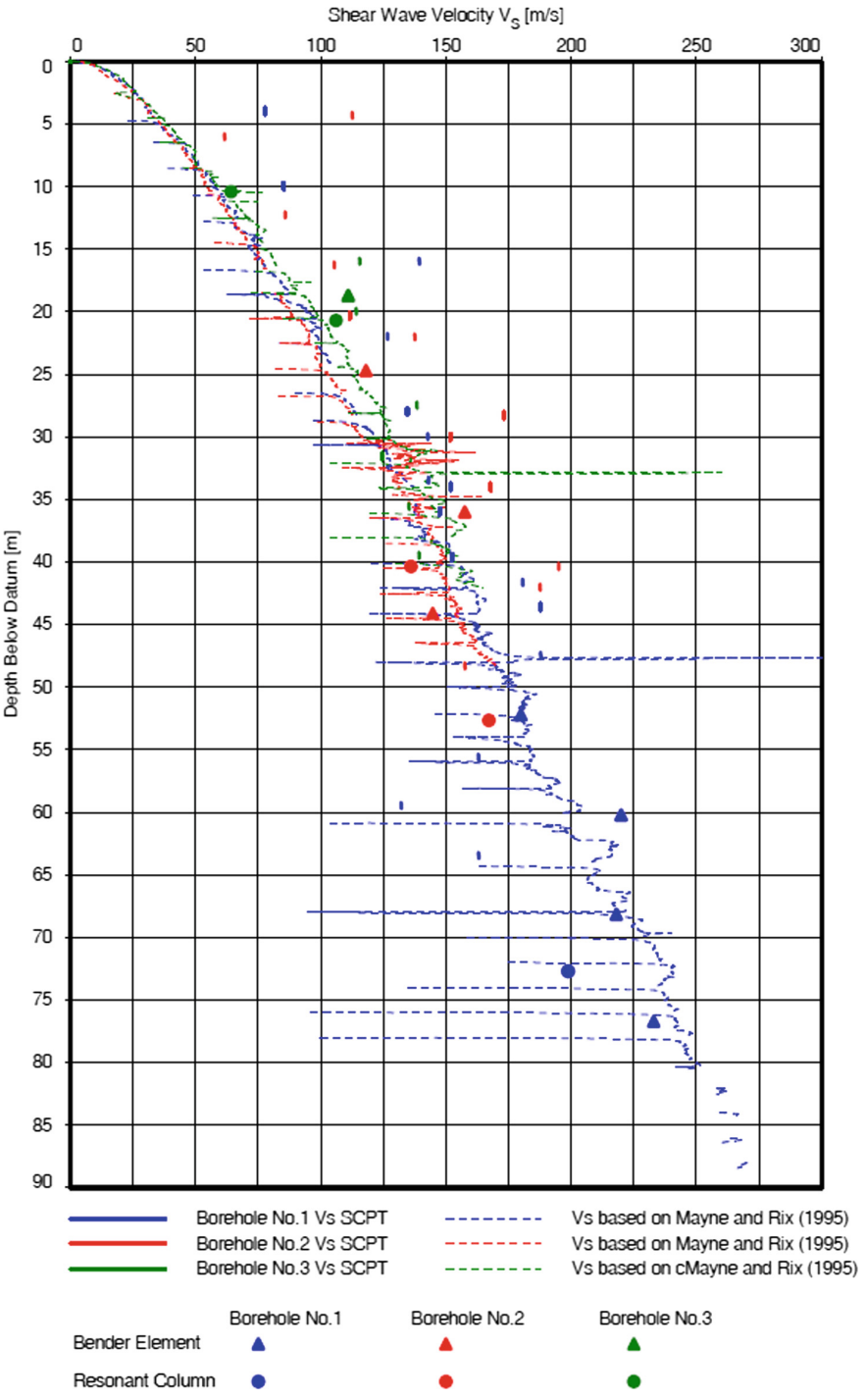


**Fig. 5.** Case example – shear wave velocity measurements at an offshore site

## 4 Conclusions

The in situ measurements of shear wave velocity obtained by a SFD corresponded favorably with the advanced laboratory testing on intact, recovered samples. This information can be used with the shear wave velocity derived from cone penetration resistance to provide a high confidence shear wave velocity profile for deep water sediments; a key soil parameter for a range of engineering applications such as static, dynamic and soil liquefaction analyses of foundation systems.

**Acknowledgments.** The authors would like to recognize Nico Parasie (Fugro) and Jean-Louis Colliat-Dangus (TOTAL) for information presented in this paper. We would also like to extend our thanks to others within the Fugro organization who contributed to this study.

## References

Baziw, E.J.: Digital filtering techniques for interpreting seismic cone data. J. Geotech. Eng. **119** (6), 98–1018 (1993). ASCE

Cooper, A.G., Gan, K.C., Hoare, S.D.: Seafloor drill technology - bearing capacity and breakout force analysis. In: OTC 26187 MS Offshore Technology Conference, 27–29 October, Rio de Janeiro, Brazil (2015)

Mayne, P.W., Rix, G.J.: Correlations between shear wave velocity and cone tip resistance in natural clays. Soils Found. **35**(2), 107–110 (1995)

Nguyen, H.Q., Kelleher, P., DeGroot, D.J., Lunne, T., Senders, M., Banimahd, M.: Offshore site characterization of small strain shear modulus using a seabed based drilling system. In: OTC 24124 MS Offshore Technology Conference, 6–9 May, Texas, USA (2013)

Peuchen, J., de Ruijter, M.R., Hospers, B., Assen, R.L.: Shear wave velocity integrated in offshore geotechnical practice. In: SUT-OSIG-02-379 Society of Underwater Technology Conference, 26–28 November, London, UK (2002)

SC3-RAV User's Manual: Processing of Seismic Cone Penetration Data (2011)

Yetginer, A.G., Tjelta, T.I., Yang, S., Lunne, T., Colliat-Dangus, J.L., Longuet, A.: Seafloor based drilling and sample quality at soft clay sites. In: Offshore Site Investigation and Geotechnics: Integrated Technologies - Present and Future, 12–14 September, London, UK (2012)

# Conductive Heat Transfer Analysis of Energy Pile

Tri Van Nguyen[1,2(✉)], Anh Minh Tang[1], and Jean-Michel Pereira[1]

[1] École des Ponts ParisTech, Marne-la-Vallée, France
{van-tri.nguyen, anhminh.tang, jean-michel.pereira}@enpc.fr
[2] Hanoi University of Mining and Geology, Hanoi, Vietnam

**Abstract.** In the range of vertical ground heat exchanger borehole and energy pile, heat is diffused from the heat pipes into the concrete and then to the surrounding soil. The heat transfer process usually follows three main mechanisms: conduction, convection and radiation. Among them, the heat conduction due to temperature gradient is the most relevant process associated with heat transfer in soil and pile. The review of conduction heat transfer models applied to vertical heat exchanger borehole and energy pile shows that the existing models can be classified into two groups, the first one is applied in homogeneous media and the second one is applied in composite media. Most of these models are generally suitable for the case of steady state conduction of heat exchanger boreholes. However, energy pile foundation has larger diameter and smaller length than that of the borehole. As a result, heat transfer inside the pile will take a longer time to reach the steady state. In this paper, a new solution of conductive heat transfer based on the transient heat model is presented. This solution is applied for energy pile and is validated by using the solution of finite element method.

**Keywords:** Heat conduction transfer · Energy pile foundation · Transient heat

## 1 Introduction

In the range of vertical heat exchanger borehole and energy pile, heat is diffused from the heat pipes into the concrete and then to the surrounding soil. If the materials are considered heterogeneous, the heat transfer process usually follows three main mechanisms: conduction, convection and radiation. Among them, the heat conduction due to temperature gradient is the most relevant process associated with heat transfer in soil and pile [1]. Therefore, analytical and numerical solutions tend to simulate the conductive heat transfer of heat exchanger pile. In addition, the heat diffusion is typically a three-dimensional transient process. However, considering the small ratio of the diameter to the length of heat exchanger borehole or energy pile, the vertical heat transfer effect can be neglected. Therefore, the existing models usually consider the heat source as an infinite line source, and thus are referred to as 1D heat transfer models. A literature review on the analytical conductive heat transfer models shows that the majority of the models are firstly developed for calculating heat transfer in the

© Springer Nature Singapore Pte Ltd. 2018
H. Tran-Nguyen et al. (eds.), *Proceedings of the 4th Congrès International de Géotechnique - Ouvrages -Structures*, Lecture Notes in Civil Engineering 8,
DOI 10.1007/978-981-10-6713-6_68

long term. In addition, the thermal properties of borehole ground heat exchanger are often assumed to be negligible [2–7]. In contrast to the borehole, as energy piles have a higher diameter, it may take a considerable period of time to achieve thermal steady state. Beside, as the energy demand of the building changes with hours, the problem of heat transfer in the short term is really needed [8–10].

In the majority of the existing models [8, 11–14], the solutions are usually represented in symbolic functions form and therefore solving them must be done by numerical integration methods. These models are then called semi-analytical solutions. Practically, the results obtained from analytical solutions have excellent accuracy but the existing heat transfer solutions, used for transient heat in heterogeneous medium, usually need a large amount of computation time. In the lack of a simplified theoretical model, the idea of developing an empirical model is considered. Actually, an empirical model is often expressed as simple mathematical forms and it only gives approximate results [9, 15].

In this paper, a simple analytical heat transfer solution for short term analyses is presented. The solution accounts for the difference in thermal properties between the concrete pile and the surrounding soil. By using this solution, the transient heat in both pile and soil can be identified simultaneously.

## 2 Background

Lamarche and Beauchamp [11] have developed an analytical solution for the short term heat transfer of geothermal vertical borehole based on the Kevil's line source theory. Two different cases have been mentioned: the first one relates to a given total heat per unit length and the second one relates to a given fluid temperature. For simplicity, heat pipes inside the borehole are represented equal to an equivalent pipe diameter. Heat transfer equation of pile and soil are determined independently based on the initial and boundary conditions, in which the temperature at the pile-soil interface is continuous and the temperature functions refer to thermal properties of both pile and soil. Only the heat transfer function inside the pile has been identified (Eq. 1) in their study.

$$\Delta T = \frac{\dot{q}}{\lambda_{soil}} \frac{4\tilde{\lambda}}{\pi^4 \delta^2} \int_0^\infty \left(1 - e^{-\alpha u^2 t}\right) \frac{Y_o(u\tilde{r})J_1(u) - J_o(u\tilde{r})Y_1(u)}{\phi^2 + \psi^2} \frac{du}{u^4} \tag{1}$$

where $\Delta T$ is the temperature change of borehole.

$$\phi = Y_1(\beta)\left[Y_0(\beta\delta\gamma)J_1(\beta\delta) - Y_1(\beta\delta\gamma)J_0(\beta\delta)\tilde{\lambda}\gamma\right] - J_1(\beta)\left[Y_0(\beta\delta\gamma)Y_1(\beta\delta) - Y_1(\beta\delta\gamma)Y_0(\beta\delta)\tilde{\lambda}\gamma\right]$$

$$\psi = J_1(\beta)\left[J_0(\beta\delta\gamma)Y_1(\beta\delta) - J_1(\beta\delta\gamma)Y_0(\beta\delta)\tilde{\lambda}\gamma\right] - Y_1(\beta)\left[J_0(\beta\delta\gamma)J_1(\beta\delta) - J_1(\beta\delta\gamma)J_0(\beta\delta)\tilde{\lambda}\gamma\right]$$

$$\tilde{\lambda} = \lambda_{soil}/\lambda_{pile};\ \tilde{r} = r/r_e;\ \delta = r_p/r_e$$

where $r$ is the distance from the heat source, $r_e$ is the pipe radius, and $r_p$ is the pile radius.

This solution is found by using the Laplace transform method and also using the contour integration method which was firstly introduced by Carslaw and Jaeger [16]. Practically, to increase the heat exchange capacity between pile and surrounding soil, multiple heat pipes will be incorporated into the pile thus temperature inside the pile at a given time can be considered relatively uniform. By considering this simple hypothesis and using classical technique of Lamarche and Beauchamp [11], the present paper introduces a new simplified function which allows determining the transient heat transfer in pile and surrounding soil simultaneously.

## 3 Proposed Analytical Model for Short-Time Heat Transfer Model

The heat source is supposed to be located at the center of the pile (Fig. 1). The pile temperature is considered uniform and it only depends on time. Thus, the pile temperature can be assumed equal to the soil temperature at the pile-soil interface. Thus, the problem is solved with the following assumptions:

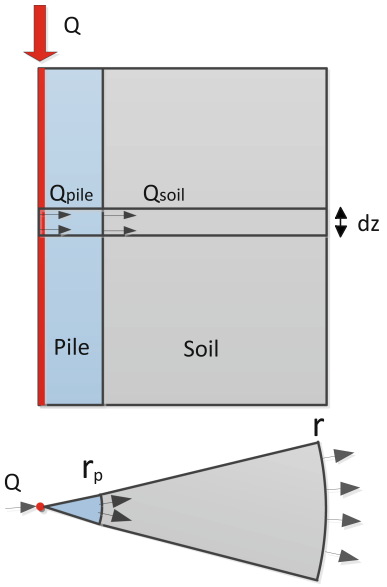


**Fig. 1.** Heat transfer model

- The heat source is an infinite line source;
- The heat transfer mechanism in pile and surrounding soil is purely conductive;
- The surrounding soil is a homogeneous and semi-infinite medium;
- Initial soil and pile temperature is homogenous ($T_o$), which corresponds to the case where the energy piles are installed below the building so that the effect of thermal radiation on the ground surface can be neglected.

- A constant heat flux is imposed to the heat source and heat transfer in the vertical direction is negligible.
- The pile has a very large thermal conductivity.

The initial temperature conditions read as follows:

$$\begin{cases} 0 < r \le r_p, \;\; T = T_{pile} \\ r_p \le r < \infty, \; T = T_{soil} \\ t = 0, \; T_{pile} = T_{soil} = T_0 \end{cases}$$

and the boundary conditions as follows:

$$\begin{cases} r = r_p, \; T_{soil}(r,t) = T_{pile}(r,t) \\ r = \infty, \; T_{soil}(r,t) = T_0 \\ -\lambda_{soil} A \left. \frac{dT_{soil}}{dr} \right|_{r=r_p} = \dot{Q}_{soil}, \; [W] \end{cases} \tag{2}$$

where $r_p$ is the radius of pile, $\lambda_{soil}$ is the thermal conductivity of soil ($Wm^{-1}$ $°C^{-1}$), and $A$ is the heat transfer area ($m^2$).

The heat transfer from the heat source to the surrounding soil can be solved by combining the heat energy balance and the heat conduction equations:

$$dQ = const, \; (J) \tag{3}$$

$$\frac{1}{\alpha}\frac{\partial T}{\partial t} = \frac{\partial^2 T}{\partial r^2} + \frac{1}{r}\frac{\partial T}{\partial r} \tag{4}$$

where, $\alpha$ is the thermal diffusion, ($m^2$/s).

By applying a constant heat flow along the entire length of the heat source, the energy balance can be expressed as follows:

$$\begin{aligned} \dot{Q} &= const, \; [W] \\ dQ &= dQ_{pile} + dQ_{soil}, \; [J] \end{aligned} \tag{5}$$

Combining the Eq. (2÷5) allows determining the temperature of surrounding soil. For simplicity, put $T(r, t) = T_{soil} - T_o$, where T(r, t) is the soil temperature, that depends on time and space.

The initial and boundary conditions for temperature of soil can be re-written as follows:

$$\begin{cases} t = 0 \Rightarrow T(r, t = 0) = 0 \\ r = r_p, \Rightarrow T(r,t)|_{soil} = T(r,t)|_{pile} \\ r = \infty \Rightarrow T(r = \infty, t) = 0 \\ -\lambda_{soil} A \left. \frac{dT(r,t)}{dr} \right|_{r=r_p} = \dot{Q}_{soil}, \; [W] \end{cases} \tag{6}$$

The Eq. (5) can be represented as follows:

$$\dot{Q} - \left| -\lambda_{soil} A \frac{dT_{soil}}{dr} \right| = m_{pile} c_{pile} \frac{dT_{soil}}{dt}, \left[ \frac{J}{s} \right] \tag{7}$$

Considering conduction only, the heat transfer equation in the soil can be written as follow:

$$\frac{1}{\alpha_{soil}} \frac{\partial T(r,t)}{\partial t} = \frac{\partial^2 T(r,t)}{\partial r^2} + \frac{1}{r} \frac{\partial T(r,t)}{\partial r} \tag{8}$$

where $\alpha_{soil}$ is the soil thermal diffusivity, $r$ is the distance from pile' surface

Rewriting the heat transfer equation in Laplace space:

$$\frac{1}{\alpha_{soil}} \frac{\partial T(r,t)}{\partial t} = \frac{\partial^2 T(r,t)}{\partial r^2} + \frac{1}{r} \frac{\partial T(r,t)}{\partial r} \tag{9}$$

where $q^2 = s\alpha^{-1}$ and $s$ is a complex variable. A general solution of soil temperature is expressed as follows:

$$\bar{T}(r,s) = a_1 K_0(qr) + a_2 I_0(qr) \tag{10}$$

where $I_o$ and $K_o$ are the modified Bessel functions of the first and the second kinds, respectively. $a_1$, $a_2$ are constants. From the temperature condition at the boundary, $a_2$ equals to zero. The equation thus simplifies as follows:

$$\bar{T}(r,s) = a_1 K_0(qr) \tag{11}$$

By using the boundary conditions, the constant $a_1$ of the equation can be found:

$$a_1 = \frac{\dot{Q}}{s} \frac{1}{m_{soil} c_{soil} s K_0(qr_p) + \lambda_{soil} A q K_1(qr_p)} \tag{12}$$

Thus

$$\bar{T}(r,s) = \frac{\dot{Q}}{s} \frac{K_0(qr)}{m_{soil} c_{soil} s K_0(qr_p) + \lambda_{soil} A q K_1(qr_p)} \tag{13}$$

The inverse Laplace transform of the solution is written as follows:

$$T(r,t) = \frac{1}{2\pi i} \int_{a-i\infty}^{a+i\infty} e^{st} \bar{T}(r,s) ds \tag{14}$$

This equation can be solved by the contour integration method. Details about this technique can be found in the studies by Carslaw and Jaeger [16] and Lamarche and Beauchamp [11]. The final solution for soil temperature is then:

$$T_{soil}(r,t) = T_0 + \frac{\dot{q}}{\lambda_{soil}} \frac{2}{\pi^2 r_p} \int_0^\infty \left(1 - e^{-\alpha u^2 t}\right) \frac{Y_0(ur)\phi - J_0(ur)\psi}{\phi^2 + \psi^2} \frac{du}{u^2} \tag{15}$$

where:

$$\phi = A_1 u J_0(ur_p) + A_2 J_1(ur_p);\ \psi = A_1 u Y_0(ur_p) + A_2 Y_1(ur_p);\ A_1 = -r_p \tilde{\rho}\tilde{c};\ A_2 = 2$$
$$\tilde{\rho} = \rho_{pile}/\rho_{soil};\ \tilde{c} = c_{pile}/c_{soil}$$

Using explicit integration method can solve this equation.

## 4 Validation of the Proposed Solution

In this section, the analytical results (using MATLAB) will be compared with the numerical calculation using the finite element method (Plaxis 2D Thermal, version 2016). A 2D axisymmetric model of unit length of pile and surrounding soil is modeled with the same boundary conditions and physical properties compared to the analytical model. Boundary of the semi-infinite surrounding soil is chosen large enough to neglect its impact on temperature changes. The finite element mesh is refined small enough until no variation is obtained for the results, in which the minimum size of the refined mesh is modeled for the soil and pile elements located near the heat source. The initial temperature of pile and soil is constant and homogeneous. The heat flow is null at the surface, bottom and vertical sides. Heat is not allowed to transfer through the axisymmetric side of the model. To avoid the effect of thermal expansion coefficient on the temperature, the very small thermal expansion coefficient is used in the numerical model. In addition, fully coupled analysis method is used in the numerical model (Plaxis), in which mechanisms of heat transfer in porous media (containing three phases: solid, moisture and gas) are calculated by using the average value of thermal properties of the media, therefore the thermal properties of the water are used similar to the soil's properties and the permeability value of water is chosen very small. The parameters, used for the numerical and the analytical calculations, are presented in the Table 1.

**Table 1.** Parameters used for the calculations

| Parameters | Pile | Soil |
|---|---|---|
| Dimensions: diameter × length (m) | 0.4 × 1.0 | 20.0 × 1.0 |
| Thermal conductivity λ (W/m/K) | 1.5 | 1.0 |
| Specific heat capacity c (KJ/kg/°C) | 1.1 | 1.0 |
| Density (kg/m) | 2500.0 | 1800.0 |
| Initial temperature $T_o$ (°C) | 13.0 | 13.0 |

To heat the pile, a constant heat flow (60 W/m) is imposed along the pile on a cylindrical-surface with 0.3 m diameter (Fig. 2). The results of numerical and analytical methods are represented in Figs. 3 and 4.

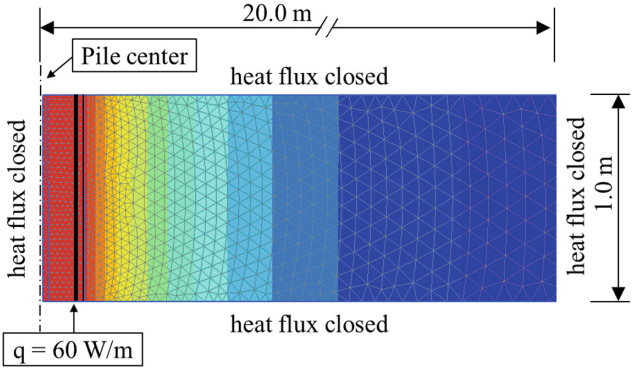


**Fig. 2.** Meshing, thermal boundary conditions and heat transfer modeling in pile and surrounding soil

Figure 3 show the temperature values obtained at the soil/pile surface (0.2 m) and at two distances from the pile axis (0.4 m and 0.6 m) versus elapsed time. The results show a good agreement between the numerical and analytical methods.

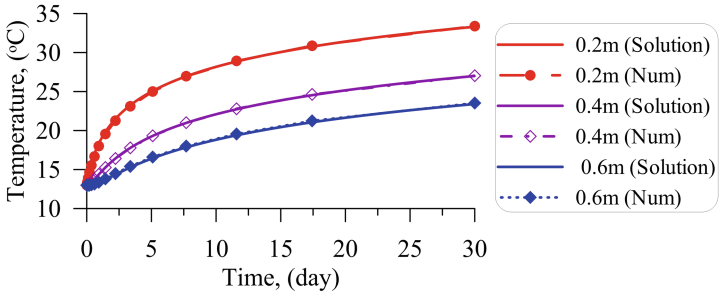


**Fig. 3.** Temperature of soil at different distances from the pile axis versus elapsed time

Figure 4 shows the temperature versus the distance from the pile's axis at 5 days and 30 days. It can be seen that the analytical solution slightly underestimates the results obtained by the numerical simulation and discrepancies between the two models are very small.

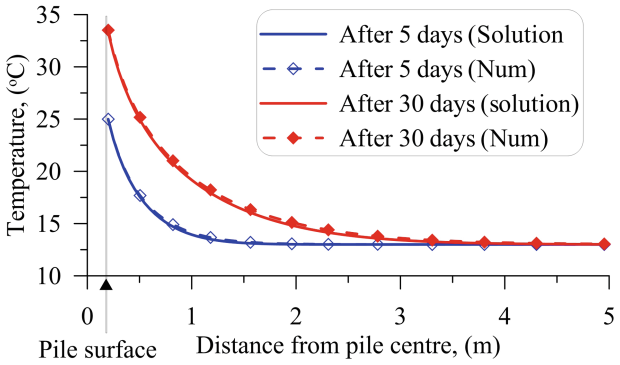


**Fig. 4.** Heat transfer in surrounding soil

## 5 Conclusions

In this work, based on the approach of Laplace transform method and also the contour integral method, an analytical solution of the short-term thermal response of energy pile and soil is proposed. Some conclusions can be drawn:

- The solution can be used to determine correctly the transient heat response of energy pile and surrounding soil at any given time. Especially, temperature response of pile and surrounding soil is determined simultaneously.
- Analytical solution shows a good agreement with the numerical model.

## References

1. GSHP Association: Thermal Pile Design, Installation & Materials Standards. Ground source Heat Pump Association National Energy Centre, no. 1 (2012)
2. Man, Y., Yang, H., Diao, N., Liu, J., Fang, Z.: A new model and analytical solutions for borehole and pile ground heat exchangers. Int. J. Heat Mass Transf. **53**(13–14), 2593–2601 (2010)
3. Bozis, D., Papakostas, K., Kyriakis, N.: On the evaluation of design parameters effects on the heat transfer efficiency of energy piles. Energy Build. **43**(4), 1020–1029 (2011)
4. Jaeger, J.G.: Some problems involving line sources in conduction of heat. Lond. Edinb. Dublin Philos. Mag. J. Sci. **35**(242), 169–179 (1944)
5. Bandos, T.V., Montero, Á., Fernández, E., Santander, J.L.G., Isidro, J.M., Pérez, J., De Córdoba, P.J.F., Urchueguía, J.F.: Finite line-source model for borehole heat exchangers: effect of vertical temperature variations. Geothermics **38**(2), 263–270 (2009)
6. Eskilson, P.: Thermal analysis of Heat Extraction System. Ph.D. thesis, Lund University, Sweden (1987)
7. Carslaw, H.S., Jaeger, J.C.: Conduction of Heat in Solids, 1st edn. Oxford Science Publications/Claremore Press, Oxford (1947)
8. Li, M., Lai, A.C.K.: New temperature response functions (G functions) for pile and borehole ground heat exchangers based on composite-medium line-source theory. Energy **38**(1), 255–263 (2012)

9. Yavuzturk, C., Spitler, J.D.: A short time step response factor model for vertical ground loop heat exchangers. ASHRAE Trans. **105**(2), 475–485 (1999)
10. Low, J.E., Loveridge, F.A., Powrie, W.: Measuring soil thermal properties for use in energy foundation design. In: 18th International Conference for Soil Mechanical and Geotechnical Engineering, pp. 3375–3378 (2013)
11. Lamarche, L., Beauchamp, B.: New solutions for the short-time analysis of geothermal vertical boreholes. Int. J. Heat Mass Transf. **50**(7–8), 1408–1419 (2007)
12. Li, M., Lai, A.C.K.: Heat-source solutions to heat conduction in anisotropic media with application to pile and borehole ground heat exchangers. Appl. Energy **96**, 451–458 (2012)
13. Zeng, H.Y., Diao, N.R., Fang, Z.H.: A finite line-source model for boreholes in geothermal heat exchangers. Heat Transf. Asian Res. **31**(7), 558–567 (2002)
14. Young, T.R.: Development, verification, and design analysis of the borehole fluid thermal mass model for approximating short term borehole thermal response (2001)
15. Loveridge, F., Powrie, W.: Temperature response functions (G -functions) for single pile heat exchangers. Energy **57**, 554–564 (2013)
16. Carslaw, H.S., Jaeger, J.C.: Some two-dimensional problems in conduction of heat with circular symmetry. Proc. Lond. Math. Soc. **15**(23), 361–388 (1940)

# Effect of Site Parameters on Dynamic Impedance of Bridge Piles Subjected to Seismic Loading

Muhammad Tariq A. Chaudhary(✉)

Department of Civil Engineering, Kuwait University, Kuwait City, Kuwait
mtariqch@hotmail.com

**Abstract.** Dynamic impedance of pile groups is dependent on soil parameters, i.e. soil unit weight ($\rho_s$), Poisson's ratio ($\nu$), shear modulus ($G_s$), shear wave velocity ($V_s$) and damping ratio ($\beta_s$). The last three soil parameters ($G_s$, $V_s$ & $\beta_s$) strongly depend on the strain level caused by propagating seismic waves. Near surface (30 m depth) values of soil design parameters ($G_s$, $V_s$ & $\beta_s$) are normally used in design and these are influenced by variation in soil properties like plasticity index (PI), over consolidation ratio (OCR), effective stress ($\sigma'$), depth of soil strata over bedrock ($H$) and impedance contrast ratio (ICR) between the strata and the bedrock. The aim of this study was to investigate the sensitivity of dynamic pile-group impedance to variation in soil design parameters ($G_s$, $V_s$ & $\beta_s$) caused by variation in soil properties for a typical bridge that was founded in site classes C and D according to the AASHTO Code and were subjected to a suite of actual earthquake ground motions.

**Keywords:** Pile group · Dynamic impedance · Bridge · Site parameters · Seismic loading · Shear wave velocity

## 1 Introduction

Bridges are vital links in a nation's infrastructure. Integrity and functionality of these structures is dependent on the performance of their foundations during a seismic event. Pile group foundations are commonly adopted in typical 'soil' sites. These foundations are designed based on the average soil properties of the top 30 m strata depth. Soil design properties are influenced by variation in site parameters like plasticity index (PI), over consolidation ratio (OCR), effective stress ($\sigma'$), depth of soil strata over bedrock ($H$) and impedance contrast ratio (ICR) between the strata and the bedrock (Anbazhagan et al. 2012; Pitilakis et al. 2013, Chaudhary 2016). The aim of this study was to quantify the effect of variation in site parameters on dynamic impedance of bridge piles founded in AASHTO site classes C and D subjected to a suite of actual seismic ground motions. The study comprised of the following steps: (1) design of pile group foundations based on AASHTO code and current design practice for the chosen bridge, (2) 1-D non-linear site response analysis of representative soil profiles for determining median design values of soil design parameters based on variation in site parameters (PI, OCR, σ', H and ICR), (3) computation of pile group impedance based

© Springer Nature Singapore Pte Ltd. 2018
H. Tran-Nguyen et al. (eds.), *Proceedings of the 4th Congrès International de Géotechnique - Ouvrages -Structures*, Lecture Notes in Civil Engineering 8,
DOI 10.1007/978-981-10-6713-6_69

on available theoretical formulations for soil design parameters determined in step 2 and (4) comparison of computed pile group impedance values to discern the effect of site parameters.

## 2 Bridge Layout and Pile Foundation Design

### 2.1 Bridge Layout

The bridge included in the study was a 4-span bridge with equal spans of 30 m and a total length of 120 m. The considered bridge represents the interior span of bridges typically used for urban elevated highways. Deck width of the selected bridge was 15.6 m representing a typical 4-lane highway bridge. Longitudinal elevation and bridge cross section are depicted in Fig. 1.

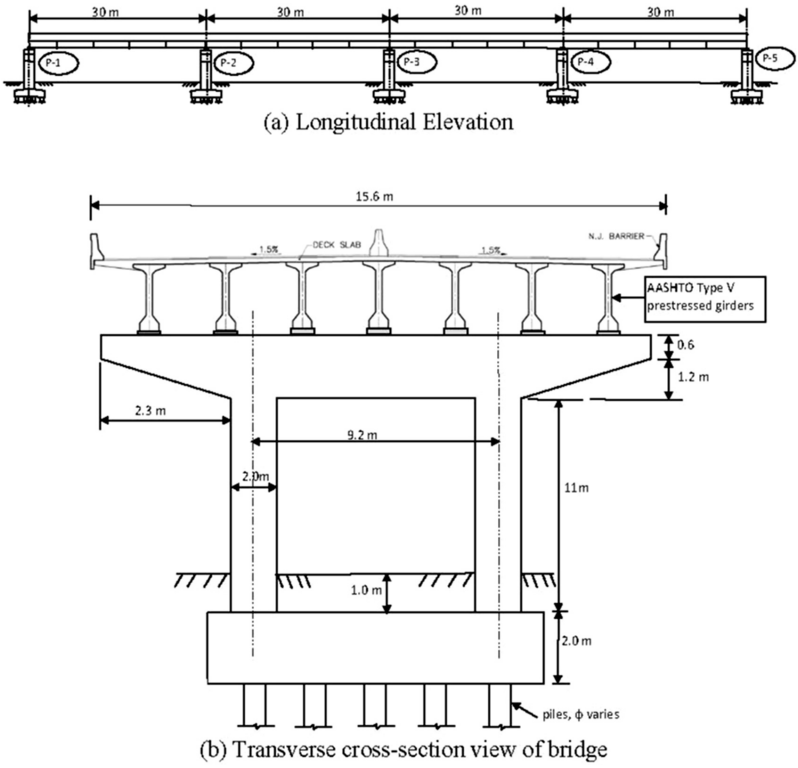


**Fig. 1.** Bridge layout and section

The bridge was designed for typical dead load of the materials used and live load consisting of AASHTO HL-93 loading (AASHTO 2010). The bridge sub-structure components were designed according to the single mode spectral method for a

moderate seismic zone with PGA of 0.2 g in two seismic site classes (i.e. C and D) according to the AASHTO code. Site class C represents very hard soil or soil-rock with $V_{s30}$ between 360 and 760 m/s. Shallow spread foundations are suitable in this site class for upper range of $V_{s30}$ while deep pile foundations are normally used for the lower values of $V_{s30}$. Site class D has $V_{s30}$ range of 175 m/s to 360 m/s and pile foundations are commonly used in this site class.

## 2.2 Pile Foundation Design

Solid reinforced concrete piles were designed as the foundation elements for the bridge using the applicable design codes and design practices for the mentioned site classes. These site classes were further subdivided based on $V_{s30}$ as listed in Table 1. Laterally loaded piles were designed for an allowable lateral displacement of 12 mm (Caltrans 2013). Lateral load analysis and design of piles were carried out using the procedure described in the technical manual for COM624 computer program (Reese et al. 1984). Group effect was taken into account by using an average p-multiplier of 0.5 (Peterson and Rollins 1996). Table 1 lists the soil parameters adopted in the design of piles for various soil types. Pile in a particular soil type was designed for three soil conditions: (a) sand (PI = 0), (b) medium clay (PI = 15) and (c) stiff clay (PI = 60). The condition that resulted in the strictest pile design was adopted for a particular soil type. A factor of safety of 2.5 was adopted for the vertical load design of piles. Table 2 summarizes pile design for all five soil profiles.

**Table 1.** Soil parameters used for pile design

| Soil type | *Vs* (m/s) | $\nu$ | $\gamma$ (kN/m$^3$) | $c_u$ (kPa) | | $\phi$ (degrees) | $\varepsilon_{50}$ | $k_i$ (kN/m$^3$) | |
|---|---|---|---|---|---|---|---|---|---|
| | | | | PI = 15 | PI = 60 | | | Clays | Sands |
| C_high | 600 | 0.35 | 20.21 | 70 | 90 | 35 | 0.007 | 120,000 | 60,000 |
| C_avg | 475 | 0.35 | 19.82 | 50 | 70 | 35 | 0.007 | 90,000 | 40,000 |
| D_high | 359 | 0.40 | 19.42 | 30 | 45 | 30 | 0.010 | 27,000 | 30,000 |
| D_avg | 275 | 0.40 | 18.64 | 20 | 30 | 30 | 0.015 | 18,000 | 17,000 |
| D_low | 173 | 0.40 | 18.15 | 15 | 25 | 30 | 0.020 | 8,500 | 8,000 |

**Table 2.** Pile design summary

| Soil type | No. of piles | Pile diameter (mm) | Pile length (m) |
|---|---|---|---|
| C_high | 9 | 900 | 22 |
| C_avg | 9 | 1000 | 25 |
| D_high | 12 | 900 | 30 |
| D_avg | 13 | 1000 | 32 |
| D_low | 16 | 1100 | 35 |

## 3 Effect of Variation in Site Parameters on Soil Design Parameters

In order to find out frequency dependent dynamic pile group impedance in different modes, the following information about soil is needed: (i) soil unit weight, $\gamma_s$; (ii) Poisson's ratio, ν; (iii) shear modulus, $G_s$; (iv) shear wave velocity, $V_s$ and (v) soil damping ratio $\beta_s$. The last three soil parameters ($G_s$, $V_s$ & $\beta_s$) strongly depend on the strain level caused by propagating shear waves. For calculating pile group impedance, it is therefore important to use representative values of these parameters taking in to account the site stratigraphy and the level of ground shaking. To achieve this objective, one dimensional non-linear site response analysis was conducted using STRATA (Kottke and Rathje 2008).

Seismic design parameters (β, $V_s$ and G) are sensitive to variation in $V_{s30}$, PI, OCR, σ', depth of soil strata and ratio of strata stiffness to bedrock stiffness; termed as impedance contrast ratio (ICR). Variations in PI, OCR, σ', strata depth and ICR considered in the study are summarized in Table 3. 1-D non-linear seismic site response analysis was performed for five generic soil profiles falling within the $V_{s30}$ range for the chosen soil classes from Douglas et al. (2009) and twenty actual far-field ground motions varying in PGA from 0.036 to 0.47 g were selected from ATC-63 (2008) and Chaudhary (2017). Acceleration response spectra of these strong motions is depicted in Fig. 2 in which the selected ground motions were grouped into three categories i.e., design basis earthquakes (DBE), functional evaluation earthquakes (FEE) and maximum credible earthquake (MCE) based on a design PGA of 0.2g.

**Table 3.** Variation in soil parameters

| Parameter | Range |
|---|---|
| $V_{s30}$ (m/s) | 600 (C_high) |
| | 475 (C_avg) |
| | 350 (D_high) |
| | 275 (D_avg) |
| | 175 (D_low) |
| PI | 0, 15, 60 |
| σ′ (atm) | 2, 4 |
| Strata depth (m) | 40, 110 |
| $V_{s\ bedrock}$ (m/s) | 600, 760, 1350, 2251, 3353 |
| ICR | 1 to 18 |

Variation in damping ratio, shear wave velocity and shear modulus along strata depth for analysis cases outlined in Table 3 was determined by conducting more than 2400 1-D site response analysis for the chosen ground motions. Soil parameters in the top 30 m depth are used for designing pile foundations. Therefore, weighted damping ratio in the top 30 m depth and travel time averaged $V_{s30}$ were computed for each soil type and their median values are listed in Tables 4 and 5 respectively for 110 m strata as an example.

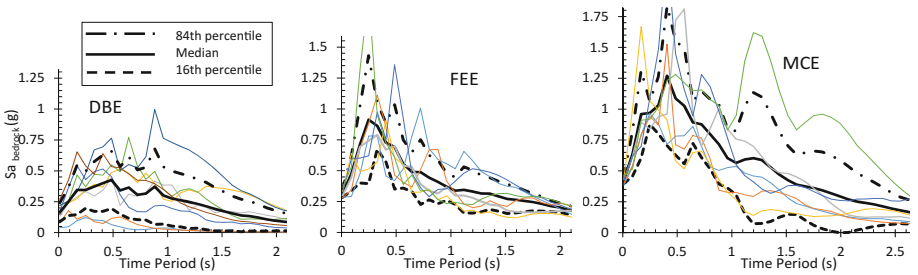


**Fig. 2.** Spectral acceleration of selected input ground motions for DBE (PGA < 0.27 g), FEE (0.27 g < PGA < 0.36 g) and MCE (0.38 g < PGA < 0.46 g)

**Table 4.** Median values of β (%) – 110 m strata

| Soil | DBE (PGA < 0.27 g) | | | FEE (0.27 g < PGA < 0.36 g) | | | MCE (0.38 g < PGA < 0.46 g) | | |
|---|---|---|---|---|---|---|---|---|---|
| | PI 0 | 15 | 60 | 0 | 15 | 60 | 0 | 15 | 60 |
| C_high | 2.44 | 1.63 | 1.57 | 4.31 | 2.63 | 2.07 | 5.42 | 3.17 | 2.29 |
| C_avg. | 4.34 | 2.66 | 2.10 | 6.17 | 3.86 | 2.73 | 8.56 | 5.18 | 3.44 |
| D_high | 7.68 | 4.27 | 2.91 | 9.21 | 7.14 | 4.88 | 11.46 | 8.46 | 6.08 |
| D_avg. | 10.92 | 6.72 | 4.28 | 12.68 | 8.97 | 5.77 | 15.01 | 12.43 | 8.21 |
| D_low | 11.50 | 9.42 | 6.63 | 11.80 | 9.58 | 7.10 | 13.71 | 12.07 | 9.52 |

**Table 5.** Median values of $V_{s30}$ (m/s) – 110 m strata

| Soil | DBE (PGA < 0.27 g) | | | FEE (0.27 g < PGA < 0.36 g) | | | MCE (0.38 g < PGA < 0.46 g | | |
|---|---|---|---|---|---|---|---|---|---|
| | PI 0 | 15 | 60 | 0 | 15 | 60 | 0 | 15 | 60 |
| C_high | 558.73 | 578.01 | 589.54 | 516.68 | 554.11 | 576.74 | 491.42 | 543.02 | 571.84 |
| C_avg. | 408.65 | 436.72 | 453.75 | 377.94 | 415.96 | 442.21 | 340.20 | 394.01 | 430.54 |
| D_high | 247.52 | 302.06 | 329.45 | 211.27 | 253.37 | 297.23 | 164.52 | 225.79 | 278.09 |
| D_avg. | 160.91 | 210.95 | 242.06 | 144.59 | 185.94 | 225.91 | 101.75 | 140.32 | 201.93 |
| D low | 103.46 | 116.60 | 136.79 | 100.36 | 115.77 | 133.89 | 84.10 | 98.31 | 118.58 |

## 4 Dynamic Pile-Group Impedance Computations

Variation of pile group impedance with the dimensionless frequency parameter, $a_0 = \omega d/Vs$, for translational ($K_H$), vertical ($K_V$) and rotational ($K_R$) modes in various soil profiles was computed for two strata depths i.e. 40 m and 110 m for the median values of soil damping ratio and time averaged shear wave velocity in the top 30 m

depth as described in Sect. 3. Real and imaginary parts of the pile group impedance represent stiffness and damping respectively.

Dynamic impedance of a pile groups in horizontal, vertical and rocking modes was computed using the dynamic stiffness of a single pile in conjunction with dynamic interaction factors (Gazetas 1984; Dobry and Gazetas 1988; Makris and Gazetas 1992). Variation in horizontal pile group impedance with $a_0$ in various soil profiles for different earthquake levels for 40 m deep strata is depicted in Fig. 3 while Fig. 4 depicts variation in vertical pile group impedance due to variation in PI for DBE.

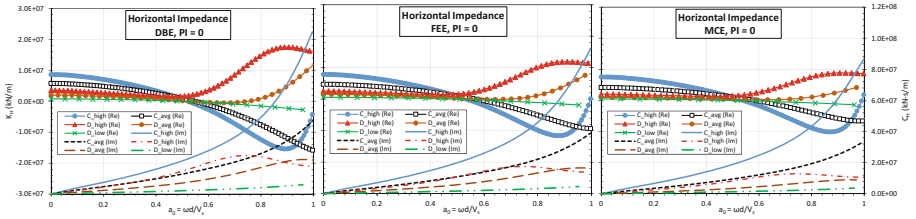


**Fig. 3.** Variation in horizontal impedance (40 m strata) with earthquake intensity

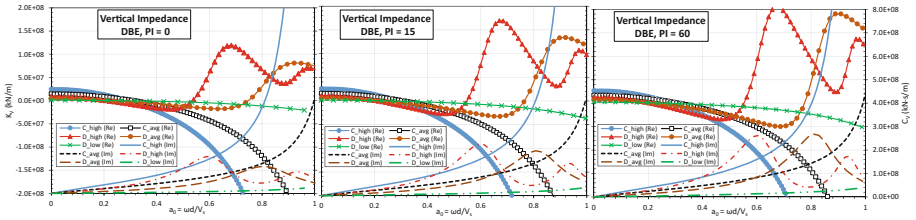


**Fig. 4.** Variation in vertical impedance (40 m strata) with PI

Frequency parameter, $a_0$, varied between 0.015 and 0.115 for the soil types considered in the study. It can be observed from Figs. 3 and 4 that the pile group stiffness values do not show appreciable variation with $a_0$. Maximum variation of pile group stiffness within the applicable range of $a_0$ was 6% for pile group in soil type D_high. It is therefore concluded that frequency dependence of pile group stiffness can be safely ignored for the pile groups presented herein. On the other hand, damping coefficient of the pile group increased with $a_0$ and a value corresponding to the fundamental period of pile-soil-bridge system can be used as the design value. Figure 5 depicts the median values of pile group stiffness in the horizontal and rocking modes for various soil types and earthquake levels corresponding to $a_0$ at the fundamental period for 40 m deep strata.

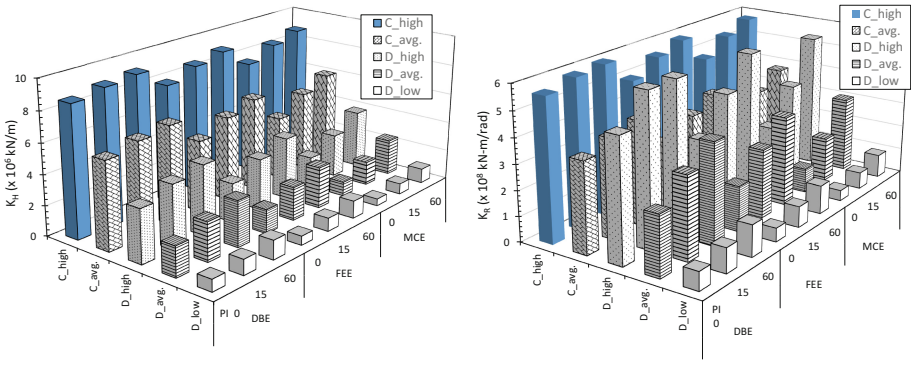


**Fig. 5.** Variation in median value of horizontal and rocking pile-group stiffness (40 m strata)

## 5 Comparison of Pile-Group Stiffness for 40 m and 110 m Strata Depths

Comparison of pile-group stiffness for soil design parameters computed with 40 m and 110 m strata depths was computed by the following expression:

$$\%diff. = \left| \frac{(K_{40m} - K_{110m})}{max(K_{40m}, K_{110m})} \right| \tag{1}$$

Percentage difference in horizontal, vertical and rocking pile-group stiffness for the two strata depths is presented in Fig. 6. Cases in which the percentage difference is more than 10% are considered critical based on commonly adopted engineering design practice. The following observations are made:

(i) The difference in pile-group stiffness for the two strata can be safely ignored for soil types C_high and C_avg. for all modes of pile-group stiffness.
(ii) The influence of variation in strata depth on pile-group stiffness is moderate for soil type D_low and can be ignored for plastic soils with confidence and for non-plastic soils with caution and engineering judgement.
(iii) The influence of variation in strata depth on pile-group stiffness is significant for soil types D_high and D_avg. and cannot be ignored for both plastic as well as non-plastic soils.
(iv) The number of cases in which pile-group stiffness is affected by strata depth increases with increasing earthquake intensity.
(v) Maximum number of cases in which pile-group stiffness is affected by strata depth is for non-plastic soils.

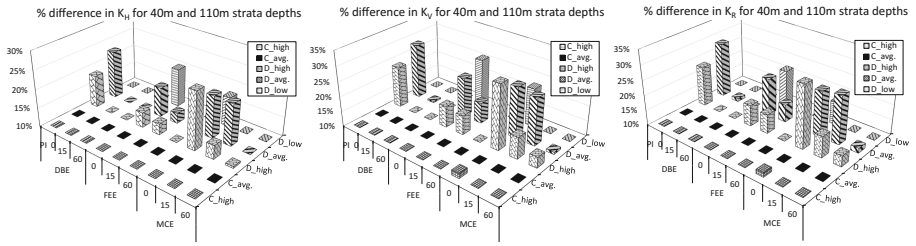


**Fig. 6.** Percentage difference in pile-group stiffness for two strata depths

# 6 Effect of ICR on Pile-Group Stiffness

## 6.1 Computation of Pile Group Impedance Taking into Account ICR

Effect of ICR on pile group stiffness was evaluated by computing pile group stiffness corresponding to soil design parameters determined for the following cases: (i) ICR_high corresponded to the analysis case with maximum spread in β and $V_s$, (ii) median value and (iii) ICR_low case corresponding to the least spread in β and $V_s$. Figure 7 depicts this variation for 40 m strata depth case as an example.

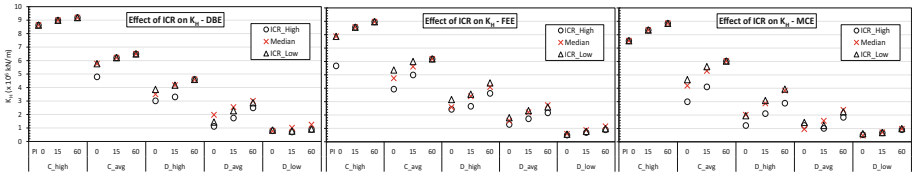


**Fig. 7.** Variation in horizontal pile group stiffness due to variation in ICR for various earthquake levels and soil types (40 m strata)

## 6.2 Error in Pile Group Stiffness Due to ICR

Percentage error in the design value of pile group stiffness due to ICR compared to the median value was computed as the maximum absolute error between the median value and the values corresponding to high and low ICR values. Mathematically, it can be expressed as:

$$Error = \max\left(\left|\frac{K_{median} - K_{ICR_low}}{K_{median}}\right|, \left|\frac{K_{median} - K_{ICR_high}}{K_{median}}\right|\right) \quad (2)$$

It was observed that the error ranged from 0% to more than 70% for various cases. Error values more than 10% were deemed to be critical and are plotted in Figs. 8 and 9 for 40 m and 110 m deep strata respectively.

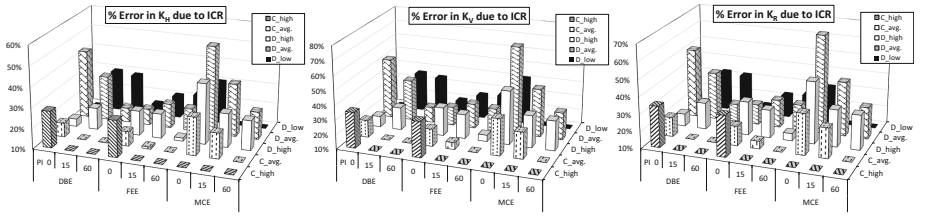


**Fig. 8.** Percentage error in pile-group stiffness due to ICR – 40 m strata

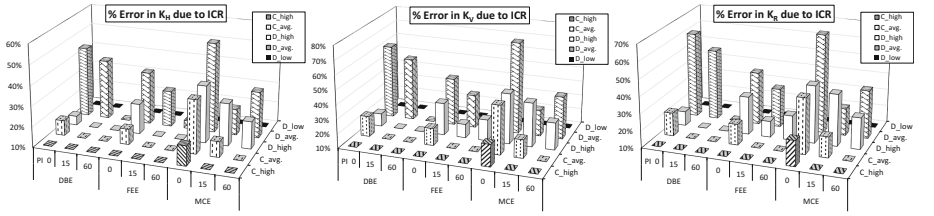


**Fig. 9.** Percentage error in pile-group stiffness due to ICR – 110 m strata

The following observations are made:

(i) The error ranged from 0% to more than 70% for various cases for both strata depths.
(ii) The most error was observed for soil type D_high and D_avg. for both strata depths. This means that ICR effect cannot be neglected for these soil types.
(iii) Soil classes C_high and C_avg. exhibited the least error for both strata depths and ICR effect can be ignored for these soil type based on engineering judgment.
(iv) Soil type D_low exhibited error comparable to class C soils for 40 m dep strata but had the least error for 110 m deep strata. This means behavior of this soil should be closely watched.
(v) Earthquake intensity did not have a significant impact on error in pile-group stiffness due to ICR.
(vi) Both plastic as well as non-plastic soils are affected by ICR with non-plastic soils being affected a little more than plastic soils.

## 7 Conclusions

The study revealed that the dynamic stiffness of pile groups studied herein did not significantly depend on applicable frequency range while damping coefficient increased with increasing frequency. It was also found that dynamic impedance of pile groups is moderately sensitive to the strata depth used in 1-D wave propagation analysis for soil type C but had a strong influence on impedance for pile groups in class D soils. Non-plastic soils (PI = 0) exhibited more variation in pile group impedance as

compared to plastic soils. Effect of ICR was found to be significant for pile groups in soil type D and to a lesser extent for soil type D in cohesionless soil only. The study pointed to the need of carrying out site specific investigations for determining dynamic soil design parameters for pile foundation design for soil types D and cohesionless soils in soil type C as the generic code-based vales can induce significant error in pile group impedance.

**Acknowledgement.** This work was supported by Kuwait University, Research Grant No. EV01/15.

## References

AASHTO: AASHTO LRFD Bridge Design Specifications. American Association of State Highway and Transportation Officials, Washington, D.C. (2010)

ATC-63: Quantification of building seismic performance factors. ATC-63 Project Report prepared by the Applied Technology Council for the Federal Emergency Management Agency, Washington, D.C. (2008)

Anbazhagan, P., Sheikh, M.N., Parihar, A.: Influence of rock depth on seismic site classification for shallow bedrock regions. Nat. Hazards Rev. **14**(2), 108–121 (2012)

Caltrans: Deep foundations. Memo to designers 3-1, Sacramento, CA (2013)

Chaudhary M.T.A.: Effect of ground conditions on design parameters for bridge foundations. In: Civil, Architectural and Environmental Engineering: Proceedings of the International Conference ICCAE, Taipei, 4–6 November 2016. CRC Press (2016). ISBN 9781138029859

Chaudhary, M.T.A.: Seismic response of bridges supported on shallow rock foundations considering SSI and pier column inelasticity. KSCE J. Civil Eng. **21**(1), 285–295 (2017)

Dobry, R., Gazetas, G.: Simple method for dynamic stiffness and damping of floating pile groups. Geotechnique **38**(4), 557–574 (1988)

Douglas, J., Gehl, P., Bonilla, L.F., Scotti, O., Régnier, J., Duval, A.M., Bertrand, E.: Making the most of available site information for empirical ground-motion prediction. Bull. Seismol. Soc. Am. **99**(3), 1502–1520 (2009)

Gazetas, G.: Seismic response of end-bearing piles. Soil Dyn. Earthq. Eng. **3**(2), 82–93 (1984)

Kottke, A.R., Rathje, E.M.: Technical Manual for Strata. PEER Report 2008/10. University of California, Berkeley, California (2008). http://nees.org/resources/strata

Makris, N., Gazetas, G.: Dynamic pile-soil-pile interaction. Part II: lateral and seismic response. Earthq. Eng. Struct. Dyn. **21**, 145–162 (1992)

Peterson, K., Rollins, K.M.: Static and dynamic lateral load testing of a full-scale pile group in clay. Research 60 Report CEG.96-02. Department of Civil Engineering, Brigham Young University (1996)

Pitilakis, K., Riga, E., Anastasiadis, A.: New code site classification, amplification factors and normalized response spectra based on a worldwide ground-motion database. Bull. Earthq. Eng. **11**(4), 925–966 (2013)

Reese, L.C., Cooley, L.A., Radhakrishnan, N.: Laterally loaded piles and computer program COM624G. University of Texas, Austin (1984)

# Effects of Operating Parameters of the NSV System on Field Soilcrete Characteristics in the Mekong Delta, Vietnam

Hoang-Hung Tran-Nguyen[1(✉)], Chau Dac Truong[1], and Khang Thien Truong[2]

[1] Department of Civil Engineering,
Ho Chi Minh City University of Technology, Ho Chi Minh, Vietnam
tnhhung@hcmut.edu.vn, chaubrdc@gmail.com
[2] Something Vietnam Co. Ltd., Ho Chi Minh, Vietnam
t_khang@stvn.vn

**Abstract.** Unconfined compressive strength (UCS) and uniformity of soilcrete are strongly influenced by deep mixing equipment and its operating parameters. Soil cement mixing was applied to reinforce the two sections of earth levees (1) 60 m long in An Giang and (2) 30 m long in Dong Thap using a mini light-weight soil-cement wet mixing system, named as a NSV system. Core boring was employed to take field soilcrete samples and UCS tests were conducted to investigate soilcrete characteristics. The operating parameters were save in the built-in memory of the NSV system during construction. This paper instigated the proper operating parameters such as mixing energy, penetrating/lifting speeds, rotation speed, and mixing duration to optimize the NSV system for the Mekong Delta conditions. The results indicate that the field soilcrete achieved high UCS and uniformity along soilcrete columns with the mixing time of 800 times/m, mixing duration of 2.5–3.5 min/m, rod rotations of 40–50 times/m (penetration) and 70–80 times/m (lift), penetrating speed of 0.5 m/min and lifting speed of 1.2 m/min.

**Keywords:** Soilcrete · Deep mixing method · NSV · Earth levee · Unconfined compressive strength · Operating parameter

## 1 Introduction

Earth levees broken have caused losses of lives and properties in the Mekong Delta, Vietnam. In general, earth levees have been constructed to protect paddies and local people during yearly flood seasons. Earth levees broken in the flood season 2011 submerged 1088 houses, damaged 10 km roads, destroyed 292 hectares of paddies, and caused the total loss of 70 billion VND (An Giang province's portal 2013).

Soil cement deep mixing technology (SCDM) can create soil mixed cement (or soilcrete) walls cutting seepage off and improving slope stability of earth levees (Tran-Nguyen et al. 2016; 2015c). However, the SCDM has limit applications for earth levee's reinforcement in the Mekong Delta due to narrow embankments and low bearing capacity of earth levees. A NSV system which is a light-weigh equipment

© Springer Nature Singapore Pte Ltd. 2018
H. Tran-Nguyen et al. (eds.), *Proceedings of the 4th Congrès International de Géotechnique - Ouvrages -Structures*, Lecture Notes in Civil Engineering 8,
DOI 10.1007/978-981-10-6713-6_70

system to create soilcrete columns was utilized to form soilcrete walls reinforcing earth levees in the Mekong Delta as pilot tests to investigate how feasible the SCDM is. This paper investigated effects of operating parameters of the NSV system such as rotation speed, penetrating speed, lifting speed of the mixing rod, and mixing time to field soilcrete characteristics. This study expects to optimize the operating parameters of the NSV system for the Mekong Delta conditions.

## 2 Methodology

Effects of operating parameters of the NSV system were investigated on the field data obtained from the built-in operation system of the NSV system and the field core borehole samples taken from the two research sites in the Mekong Delta.

### 2.1 Research Sites

A 60-m and a 30-m reinforced sections were chosen for this study in An Giang and Dong Thap provinces, respectively (Fig. 1). The two sections are the typical earth levees in the Mekong Delta with narrow surface width of 3–5 m and the embankment height of 2.5–3 m above the elevation of a paddy surface.

a) A research site in An Giang province

b) A research site in Dong Thap province

**Fig. 1.** The research sites selected in the Mekong Delta Vietnam

### 2.2 Geological Properties of the Research Sites

Three soil layers were found along a 25-m soil profile in the An Giang and Dong Thap sites, respectively. The key soil properties are given in Table 1. It is noted that the water table fluctuates by seasons which are from the paddy surface to the earth levee surfaces. The soil layers below the water table are believed to be fully saturated.

**Table 1.** Soil properties along the 25-m soil profiles at the two research sites

| Properties | An Giang province | | | Dong Thap province | | |
|---|---|---|---|---|---|---|
| | Medium clay | Soft clay | Stiff clay | Medium clay | Soft clay | Stiff clay |
| Thickness (m) | 4.1 | 6.4 | 14.5 | 4.6 | 2.9 | 17.5 |
| Unit weight, $\gamma_w$ (kN/m$^3$) | 17.95 | 15.64 | 19.36 | 19.4 | 16.03 | 20.26 |
| Moisture content, $W$ (%) | 37.7 | 65.6 | 27.6 | 27.6 | 61.5 | 22 |
| Void ratio, $e$ | 1.06 | 1.76 | 0.77 | 0.77 | 1.63 | 0.6 |
| Plasticity Index, $PI$ | 28 | 26.4 | 14.7 | 14.7 | 27.5 | 13 |
| Unconfined compressive strength, $q_u$ (kN/m$^2$) | 73.95 | 29.04 | 151.27 | 151.3 | 33.92 | 77.46 |
| SPT, $N$ (blows) | 7 | 1 | 9 | 12 | 1 | 14 |

### 2.3 Description of the NSV System

The NSV system modified partially to tolerate the Vietnam conditions was employed to create field soilcrete walls at the research sites (Fig. 1). The NSV system can move versatilely on the low capacity and narrow embankments of earth levees in the Mekong Delta. The NSV system can form soilcrete columns with the diameter of 600 mm, a maximum lifting and penetrating speeds of 9 m/min, a maximum rotation speed of 80 rpm, and a maximum length of 12 m.

The mixing blade of the NSV system was uniquely designed by Something Group (Kamimura and Khang 2013) and provides mixing energy or mixing times, $N$, defined by Eq. (1). $N$ is an average accumulated mixing times per meter depth of a soilcrete column for penetrating and lifting cycles.

$$N = n_p.\frac{\omega_p}{v_p} + n_l.\frac{\omega_l}{v_l} \tag{1}$$

where $N$ – mixing times or mixing energy (times/m), $n_p$ – Number of metal blades during penetrating, $\omega_p$ – rotation speed of the blades during penetrating (rpm), $v_p$ – penetrating speed (m/min), $n_l$ – Number of metal blades during lifting, $\omega_l$ – rotation speed of the blades during lifting (rpm), $v_l$ – lifting speed (m/min). The mixing blades of the NSV system are shown in Fig. 2. The Eq. (1) indicates that the NSV system can creative unlimited mixing times depending on the rotation speed and penetrating/lifting speeds.

**Fig. 2.** The detail mixing blades of the NSV system designed by Something Group

## 2.4 Testing Materials

A water and PCB40 ordinary Portland cement ratio of 0.7:1 was used (Tran-Nguyen et al. 2015a, b, c, 2016). Water in the rivers was utilized to mix with dry cement. The water in the rivers was tested to meet the requirements of the TCVN 3994-85.

## 2.5 Trial Constructions

Trial soilcrete walls were constructed at the two research sites: (1) a 60-m long in An Giang and a 30-m long in Dong Thap provinces. Double row and single row soilcrete columns were created using the NSV system with cement contents of 250 and 300 kg/m$^3$ (Fig. 3). The depths of the soilcrete columns were 10.5 m and 8 m for the An Giang and Dong Thap sites, respectively. In principle, the tips of soilcrete columns were designed to bear on higher strength layers (Table 1).

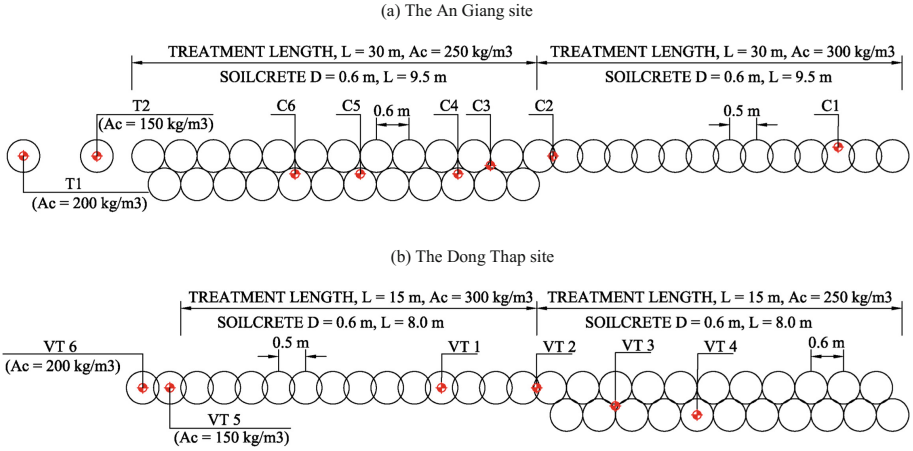


**Fig. 3.** Plan views of the reinforcements and the core samples' locations at the research sites

Each soilcrete column was formed by a V-shape mixing progress (Fig. 4). During creating a soilcrete column, cement slurry is injected during penetrating until the tip reaches a designed depth. The blades rotate at higher speed during lifting to mix soil-cement uniformly. According Kamimura and Khang (2013), soilcrete is uniform and high strength at a rotation speed of 240 times/m during penetrating, a rotation speed of 360 times/m during lifting, and a rotation speed of 600 times/m at the tip.

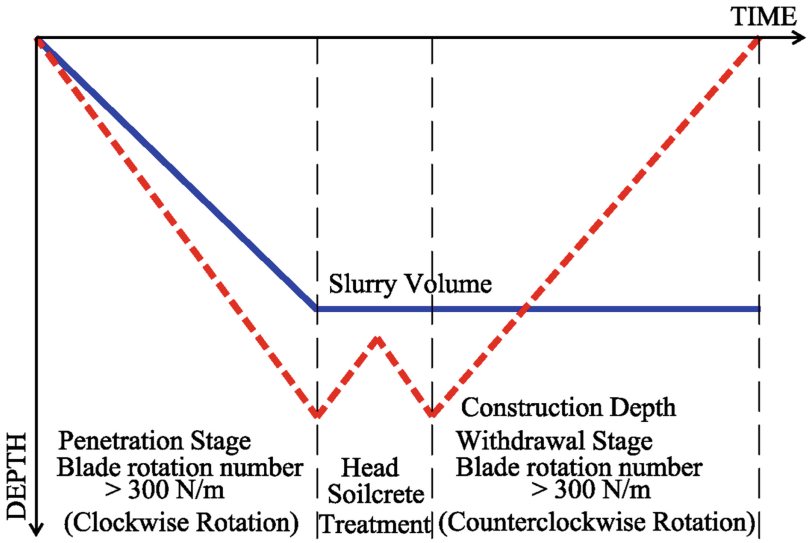


**Fig. 4.** A mixing progress of the NSV system (Kamimura and Khang 2013)

**Fig. 5.** Core drilling instrument and core samples

### 2.6 Quality Control for the Trial Constructions

Characteristics of field soilcrete were determined by core borehole samples. The core borehole locations were shown in Fig. 5. Unconfined compressive strength (UCS) test was employed to determine soilcrete strength and stiffness (ASTM D2166, ASTM D1633, TCVN 9403:2012). A TSZ30-2.0 instrument (Fig. 6) was utilized to conduct UCS tests at a maximum displacement speed of 1 mm/min.

**Fig. 6.** UCS test setup

## 3 Results and Discussion

About 56 and 61 UCS soilcrete specimens made from the field core samples at the Dong Thap and An Giang sites, respectively (Fig. 4). The UCS data combined with the operating parameters stored by the NSV system were analyzed. Effects of field soilcrete characteristics on the NSV operating parameters data saved in the NSV memory such as rotation speed, penetrating speed, lifting speed, and mixing duration per meter were discussed in detail.

### 3.1 Mixing Energy or the Total Mixing Times per Meter Length of a Soilcrete Column

UCS or $q_u$ increased in increasing the mixing energy (Figs. 7 and 8). $q_u$ of the soilcrete specimens at the An Giang site was lower than that of the soilcrete specimens at the Dong Thap site (Fig. 7). Average mixing times of 600–800 times/m (Eq. 1) at the An Giang site formed $q_u$ of 0.7–1.7 MPa, whereas $q_u$ of 1–2.5 MPa at the Dong Thap site for average mixing times of 800–1000 times/m. $q_u$ of soilcrete specimens taken at the overlapped locations (C2, VT2 in Fig. 3) (e.g., 1.5–2.7 MPa in Fig. 8) was greater than

that of soilcrete specimens taken inside the soilcrete columns (C1, VT1 in Fig. 3) (e.g., 0.8–1.7 MPa in Fig. 8). At the overlapped locations, the soilcrete was mixed at higher energy than that of the inside soilcrete columns. The results recommend that the mixing time of 800 times/m is the optimum mixing energy of the NSV system for the Mekong Delta soils.

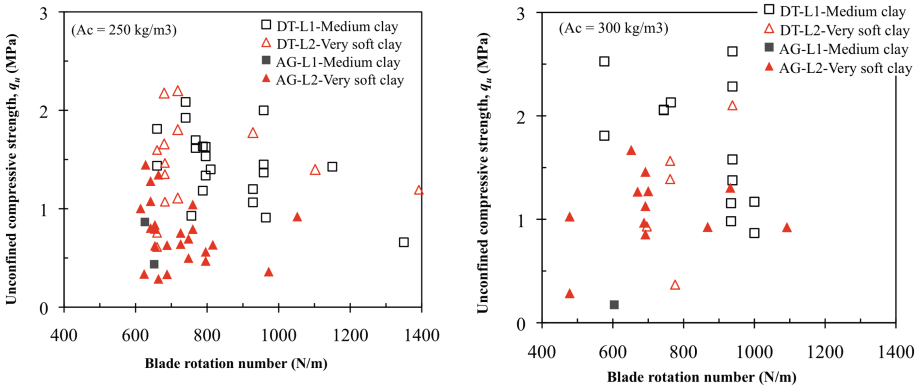


**Fig. 7.** Mixing energy versus $q_u$ varying with soil types and cement contents at the two sites

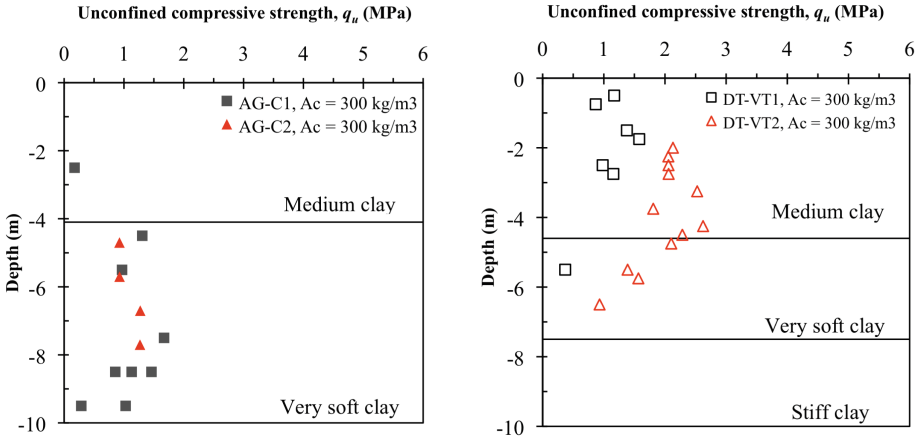


**Fig. 8.** $q_u$ of soilcrete at overlapped locations (C2, VT2) and at inside soilcrete columns (C1, VT1)

### 3.2 Mixing Times During Penetrating and Lifting Cycles

Figures 9 and 10 show the mixing times during penetrating and lifting cycles versus $q_u$ at the cement contents of 250 and 300 kg/m$^3$ at the Dong Thap and An Giang sites, respectively. With the mixing times of 300–500 times per meter depth for the both

penetrating and lifting cycles, $q_u$ was quite consistent from 1 to 2 MPa which are high enough to reinforce earth levees in the Mekong Delta. $q_u$ increased slightly in increasing the mixing times. Something Group reported that $q_u$ was consistent at the mixing times of 650–700 times/m (Kamimura and Khang 2013).

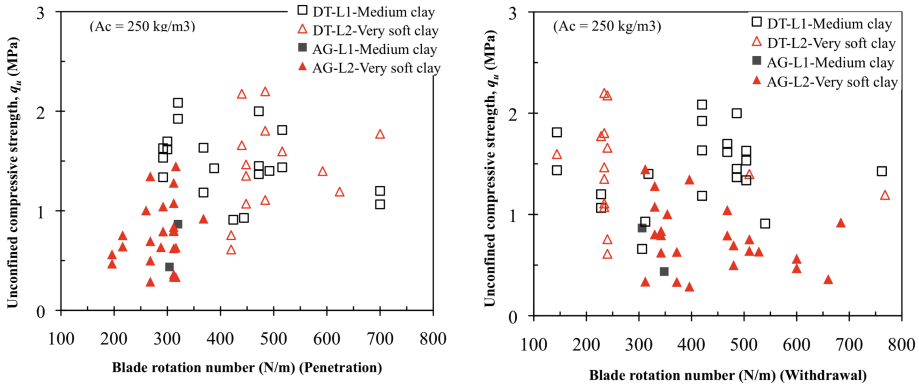


**Fig. 9.** Soilcrete strength versus the mixing times at a cement content of 250 kg/m$^3$

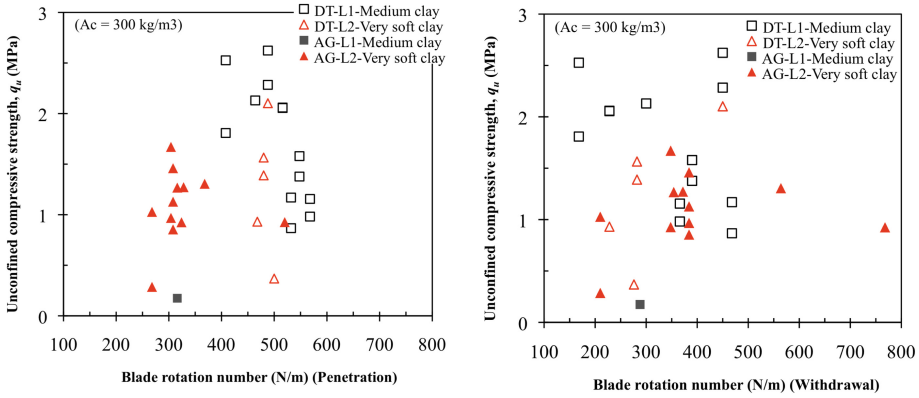


**Fig. 10.** Soilcrete strength versus the mixing times at a cement content of 300 kg/m$^3$

### 3.3 Rotation Speed of the Mixing Rod

Rotation speed of the mixing rod during penetrating and lifting cycles affects field soilcrete strength. Rotation speed of 40–60 rpm during penetrating and 60–80 rpm during lifting provided high $q_u$ (e.g., $\geq 1$ MPa) (Figs. 11 and 12). During penetration, the mixing blade needs high energy and low rotation speed to cut soils with high shear strength. During lifting, rotation speed was higher due to the soil inside a column

disturbed totally with low energy. Thus, lifting process was utilized to increase the uniformity of soilcrete columns (Larsson 2004). It is noted that cement slurry was injected into soil during penetration process only. Understanding relevant rotation speeds to form uniform field soilcrete is a key data to optimize the performance of the NSV system in the Mekong Delta.

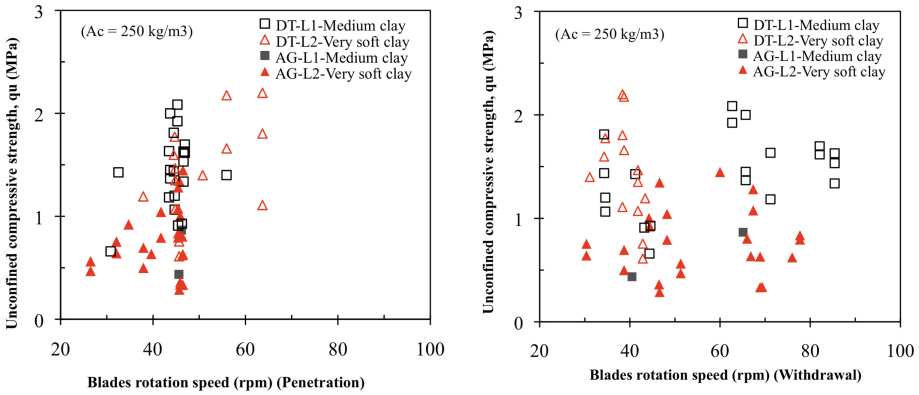


**Fig. 11.** Soilcrete strength versus rotation speed at a cement content of 250 kg/m$^3$

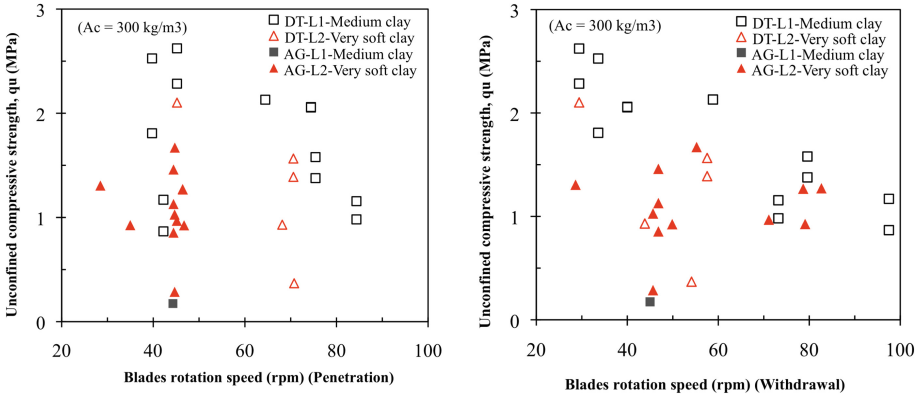


**Fig. 12.** Soilcrete strength versus rotation speed at a cement content of 300 kg/m$^3$

### 3.4 Penetrating and Lifting Speed of the Mixing Rod

Speeds of the mixing rod of 0.4–0.6 m/min during penetrating and 1–1.5 m/min during lifting provided high $q_u$ (Figs. 13 and 14). The typical speeds were also applied for other deep mixing technologies using metal blades (Tran-Nguyen 2016; Tran-Nguyen et al. 2016; Kitazume and Terashi 2013). For the NSV system, a penetrating speed of

0.5 m/min and a lifting speed of 1.2 m/min were relevant to create expected field soilcrete strength. Proper penetrating/lifting speeds data can be applied to enhance the execution of the NSV system for the Mekong Delta soils.

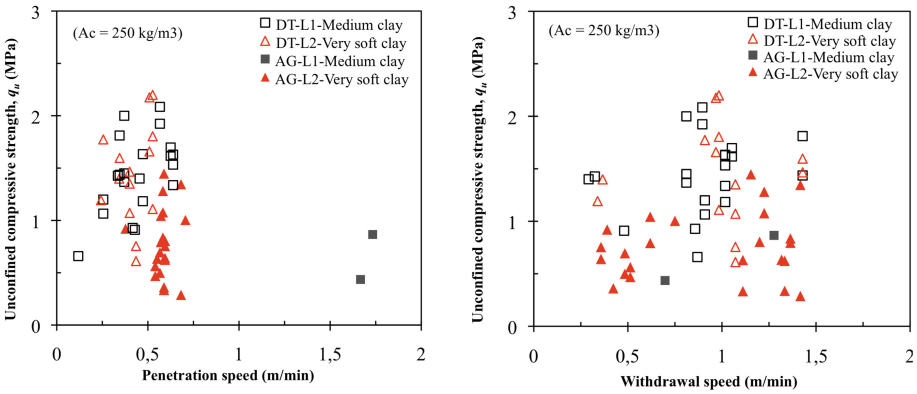


**Fig. 13.** Soilcrete strength versus penetrating/lifting speed at a cement content of 250 kg/m$^3$

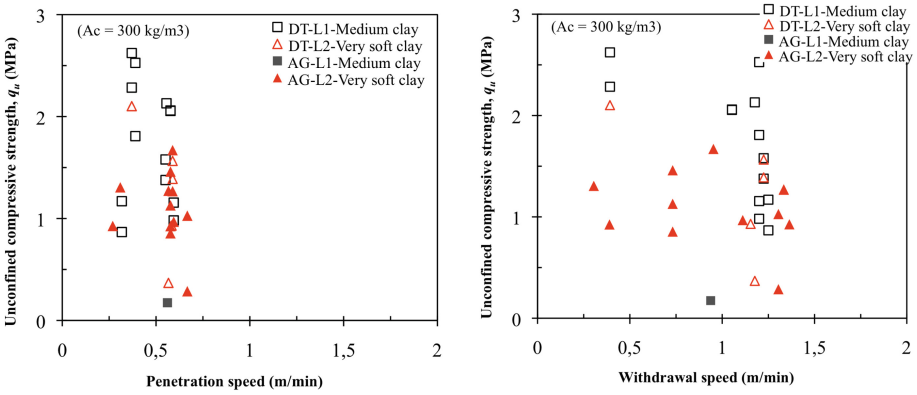


**Fig. 14.** Soilcrete strength versus penetrating/lifting speed at a cement content of 300 kg/m$^3$

### 3.5 The Total Mixing Duration per Meter Length of a Soilcrete Column

The total suitable mixing duration combining the appropriate rotation speed, penetrating speed, and lifting speed of the mixing rod creates expected soilcrete strength and uniformity. Figure 15 demonstrates the field soilcrete strength at the rotation speeds of 60–80 rpm and the penetrating speed of 0.5 m/min. The total mixing duration of 2.5–3.5 min provided high field soilcrete strength.

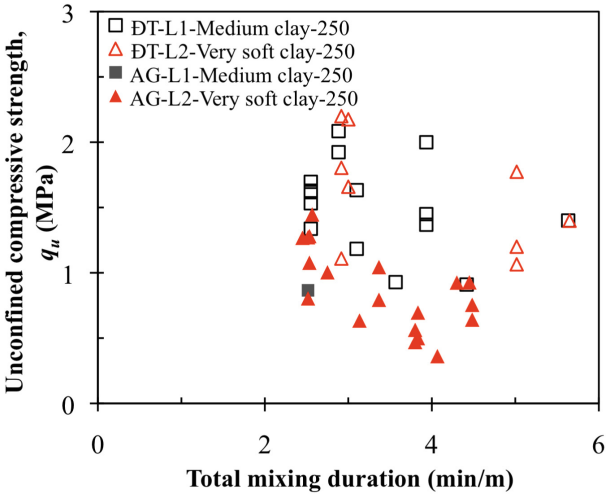


**Fig. 15.** Soilcrete strength vs. the total mixing duration at the penetrating speed of 0.5 m/min and the rotation speeds of 40–50 rpm

## 4 Conclusions

Effects of the NSV operating parameters were assessed basing on field data obtained from the field trials in An Giang and Dong Thap provinces. The field trial constructions consist of construction of soilcrete walls, field core samples, soilcrete properties obtained from the UCS tests, and analysis of effects of soilcrete characteristics on the NSV operating parameters. This study investigated the optimum parameters of the NSV system such as mixing energy, mixing duration, rotation speed, and penetrating/lifting speeds for the Mekong Delta soils with the minimal consumed energy of the equipment system. This investigation is used to modify the NSV system to meet the Mekong Delta conditions and to produce economic technology to reinforce earth levees. The results indicate the following findings:

(1) Field soilcrete columns created by the NSV system were uniform and high strength.
(2) A mixing time of 800 times/m is the appropriate mixing energy of the NSV system for the Mekong Delta.
(3) Rotation speeds of 40–50 rpm during penetrating and of 70–80 rpm during lifting can create uniform soilcrete.
(4) The mixing duration of 2.5–3.5 min/m can create quality field soilcrete with the suitable consumed energy of the NSV system.

## 5 Acknowledgement

The authors would like to thank the JICA for AUN/SEED-Net and An Giang provinces who funded for the research via the research contract of HCMUT CRI 1301 and 1401 and c/HD-KHCN-CCTL. The HCMUT supported the research team significantly during the research implementation.

## References

An Giang province's portal. Investigating earth levees frequently to protect rice fields in the Autumn-Winter season and educating farmers to protect their children during the flood season. http://www.angiang.gov.vn/. Accessed 15 Oct 2013. (in Vietnamese)

Kamimura, M., Khang, T.T.: Reinforcing housing foundations using soil cement deep mixing method in Ho Chi Minh City – The 1st field experiment. In: Proceedings of 13th Conference on Science and Technology, HCMUT, Vietnam, pp. 611–619 (2013). (in Vietnamese)

Kitazume, M., Terashi, M.: The Deep Mixing Method. CRC Press/Balkema, Leiden (2013). 405 p.

Larsson, S.: Mixing Processes for Ground Improvement by Deep Mixing. Swedish Deep Stabilization Research Centre, Report 12 (2004). 244 p.

Ministry of Construction. Stabilization of soft soil – The soil cement mixing method. TCVN 9403:2012, National Standard (2012) 42 p. (in Vietnamese)

Tran-Nguyen, H.-H.: The Jet Grouting Technology. HCMC: VNU-HCMC, HCMC, Vietnam (2016) 368 p. (in Vietnamese)

Tran-Nguyen, H.-H., Le, K.B., Le, P.L.: Behaviors of field soilcrete created by a light-weight equipment system to reinforce an earth levee in Vietnam. Malays. J. Civil Eng. **28**(1), 91–107 (2016)

Tran-Nguyen, H.-H., Le, B.K., Le, L.P., Do, C.M.T., Nguyen, T.B., Truong, C.D., Mai, P.A.: Laboratory investigation of soilcrete created from the Mekong Delta's soils mixed with cement. In: Proceedings of the Deep Mixing 2015, San Francisco, USA, 2–5 June 2005, pp. 725–734 (2015a)

Tran-Nguyen, H.-H., Kitazume, M., Tanaka, H., Kobayashi, T., Truong, K.T., Le, B.K., Le, L.P.: Effects of deep mixing method to reinforce earth levees in the Mekong Delta, Vietnam. In: Proceedings of the Deep Mixing 2015, San Francisco, USA, 2–5 June 2015, pp. 151–160 (2015b)

Tran-Nguyen, H.-H., Le, L.P., Le, B.K., Ly, H.M.T.: Field experiment study on deep mixing method to treat piping and sliding of earth levees in the Mekong Delta, Vietnam. In: Proceedings of Innovations in Construction, CIGOS 2015, Paris, France, 11–12 May 2015, 10 p. (2015c)

# Effects of Pore-Water Chemistry on the Behaviour of Unsatuarted Clays

X. Lei[1,4(✉)], H. Wong[1,4], A. Fabbri[2,4], A. Limam[3,4], and Y.M. Cheng[1,4]

[1] Key Lab Mt Hazards & Earth Surface Proc, Inst Mt Hazards & Environm, CAS, Chengdu, China
xiaoqin.lei@imde.ac.cn, kwaikwan.wong@entpe.fr, yung-ming.cheng@polyu.edu.hk
[2] Université de Lyon/ENTPE/LGCB-LTDS (UMR CNRS 5513), Vaulx en Velin, France
antonin.fabbri@entpe.fr
[3] Université de Lyon/INSA Lyon, Villeurbanne, France
ali.limam@insa-lyon.fr
[4] Department of Civil and Environmental Engineering, Hong Kong Polytechnic University, Hong Kong, Hong Kong

**Abstract.** Due to their various applications in geo-environmental engineering, such as in landfill and nuclear waste disposals, the coupled chemo-hydro-mechanical analysis of expansive soils has gained more and more attention recently. These expansive soils are usually unsaturated under field conditions; therefore the capillary effects need to be taken into account appropriately. For this purpose, based on a rigorous thermodynamic framework [2], the authors have extended the chemo-mechanical model of Loret el al. [5] for saturated homoionic expansive soils to the unsaturated case [3]. This chemo-mechanical unsaturated model is subsequently applied to simulate the behaviour of triaxial samples subject to combined chemo-mechanical loadings under laboratory conditions to investigate its precision and pertinence in view of future refinements.

**Keywords:** Chemo-mechanical coupling · Elasto-plasticity · Unsaturated soil · Expansive clay · Double structure · Thermodynamics principles · Multiphysics

## 1 Introduction

Due to their uncommon characteristics (extremely low hydraulic permeability, high swelling capacity, etc.), expansive clays are widely used as sealing materials in geotechnical and geo-environmental engineering. However these clays are sensitive to pore water chemical compositions and matric suction changes. Coupled chemo-hydro-mechanical analyses are therefore required to evaluate their mechanical stability and sealing performance. To address this complex problem, theoretical developments, based on the rigorous thermodynamic framework [1], were undertaken [2–4] to extend the chemomechanical model [5, 6] for saturated expansive clays to account for partial

© Springer Nature Singapore Pte Ltd. 2018
H. Tran-Nguyen et al. (eds.), *Proceedings of the 4th Congrès International de Géotechnique - Ouvrages -Structures*, Lecture Notes in Civil Engineering 8,
DOI 10.1007/978-981-10-6713-6_71

saturation and suction effects. There have been a few other attempts following different lines of reasoning to model chemomechanical couplings such as [7, 8], but due to limited space are not cited nor analysed here.

## 2 Soil Structure of Unsaturated Smectite

The properties of unsaturated expansive soils are strongly related to their special soil structures. A typical representative structure for these soils can be described at two structural levels as illustrated in Fig. 1. At the macroscopic level, the soil is considered as a complex of clay aggregates, separated by inter-aggregate pores filled by either gas or free water. Water in inter-aggregate pores is free to move (free water) and is dominated by capillary forces. Inside each aggregate, the microstructural system consists of several clay particles. Each particle contains several layers. Water can reside in the inter-layers or is attached to the surface of these clay particles. This absorbed water being strongly bonded to the clay particles, will not migrate nor evaporate except when subjected to very large forces and therefore will be considered as part of the solid phase. However, absorbed water and free water can exchange mass to maintain thermodynamic equilibrium. Here this phase change process is treated as a chemical reaction.

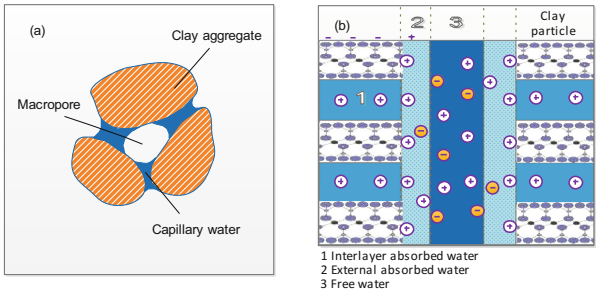


**Fig. 1.** Macro-structure (a) and microstructure (b) of an unsaturated smectite.

## 3 Theoretical Framework

Mathematically, the unsaturated expansive clay is treated as a three-phase multi-species porous medium, containing solid $\mathcal{S}$, liquid $\mathcal{L}$, and gaseous phase $\mathcal{G}$. The species contained in each of them can be summarised by the following sets:

$$\mathcal{S} = \left\{\mathrm{c}', \mathrm{w}', \mathrm{s}_i'\right\}; \mathcal{L} = \{\mathrm{w}, \mathrm{s}_i\}; \mathcal{G} = \{\mathrm{g}\}; \mathcal{F} = \mathcal{L} \cup \mathcal{G} \tag{1}$$

where "$\mathrm{c}'$" is the solid clay species, "w" is the water species, "$\mathrm{s}_i$" is the $i$-th salt species, and "g" is the air species. The superscript " ' " indicates species that are attached to the solid phase. For example, "w" refers to the free water in the liquid phase, and "$\mathrm{w}'$" refers to the absorbed water attached to the solid phase. "$\mathcal{F}$" is used to denote the set of species that compose the 2 fluid phases. To describe the preferential

exchange of species between solid and liquid phases that arises from the physical-chemical reactions, a fictitious semi-permeable membrane is assumed to surround the cluster of clay platelets, which is a priori impermeable to clay species $\mathrm{c}'$. To simplify, the exchange between liquid water and water vapour is neglected by assuming that dry air is the only species in the gaseous phase. To facilitate the frequent reference of the exchangeable species, we also introduced the following sets of exchangeable species are also introduced: $\mathcal{S}^{\leftrightarrow} = \left\{\mathrm{w}', \mathrm{s}_i'\right\}; \mathcal{C} = \left\{\mathrm{w}, \mathrm{s}_i\right\}$.This multi-species porous medium is treated as the superposition of several continua as described in great detail in Coussy [1]. Irreversible thermodynamics provides an efficient description of coupled physical processes. Based on energy and entropy balance, the Clausius-Duhem inequality associated with the above open thermodynamic tri-phasic clay system has been derived in Lei et al. [2], and is presented by Eq. (2). This inequality states that the overall dissipation $\Phi$ of a thermodynamically viable process must be non-negative. For our multi-physical problem, we assume that this dissipation can be decomposed into distinct components associated with mechanical work $\Phi_m$, phase change $\Phi_{pc}$, mass transport $\Phi_{tr}$, and thermal transport $\Phi_{th}$. Each contribution will be required to be non-negative.

$$\Phi = \Phi_m + \Phi_{pc} + \Phi_{tr} + \Phi_{th} \geq 0 \tag{2}$$

$$\Phi_m = \boldsymbol{\sigma} : \frac{d^s}{dt}\boldsymbol{\varepsilon} + \sum_{k\in \mathrm{F}} \mu_k \frac{d^s}{dt} m_k + \sum_{k'\in \mathrm{S}^{\leftrightarrow}} \mu_{k'} \frac{d^s}{dt} m_{k'} - \eta \frac{d^s}{dt} T - \frac{d^s}{dt}\Psi \geq 0 \tag{3}$$

$$\Phi_{pc} = - \sum_{\substack{k \in \mathrm{C} \\ k' \in \mathrm{S}^{\leftrightarrow}}} (\mu_k - \mu_{k'}) \hat{m}_k \geq 0 \tag{4}$$

$$\Phi_{tr} = - \sum_{k\in \mathrm{F}} \boldsymbol{I}^k \cdot [\nabla \mu_k + \eta_k \nabla T] \geq 0 \tag{5}$$

$$\Phi_{th} = - \frac{q \cdot \nabla T}{T} \geq 0 \tag{6}$$

In the above, $\boldsymbol{\sigma}$ and $\boldsymbol{\varepsilon}$ are respectively the stress and (linearized) strain tensors; $m_j$ and $\hat{m}_j$ are the mass content and the mass growth rate of species $j$ due to phase change per unit initial volume $d\Omega_0$; $\mu_j$ is the specific chemical potential of species $j$; $\eta$ is the total entropy per unit initial overall volume of porous medium, $T$ is the absolute temperature, $q$ is the heat flux vector, and $\Psi$ is the total Lagrangian free energy.

## 4 Chemo-Elastic-Plastic Model

In what follows, a set of constitutive relationships under isothermal conditions will be formulated. These include a chemo-elastic-plastic model for unsaturated soil skeleton, an unsaturated flow model, and a model of phase change kinematics.

### 4.1 Energy Distribution

The dissipation $\Phi_m$ is the mechanical dissipation from which constitutive models for solid skeleton deformations can be derived. To achieve this objective, we decompose the total free energy $\Psi$ and the total entropy $\eta$ into two parts, one associated with the apparent solid skeleton and the other with the bulk fluids. By subtraction, the corresponding parts concerning the apparent solid skeleton can be obtained.

$$\Psi_{\mathrm{S}} = \Psi - \sum_{\alpha=\mathcal{L},\mathcal{G}} \Psi_\alpha; \eta_{\mathrm{S}} = \eta - \sum_{\alpha=\mathcal{L},\mathcal{G}} \eta_\alpha \tag{7}$$

From the energy point of view, the apparent solid skeleton can be further viewed as comprising the solid skeleton and the interfaces. Each part has its own associated free energy [1]. To proceed, the solid skeleton (sol) is conceptually isolated from its attached interfaces (int) by assuming that each of them has its own associated dissipations and free energies:

$$\Phi_m = \Phi_{sol} + \Phi_{\mathrm{int}}; \Psi = \Psi_{sol} + \Psi_{\mathrm{int}} \tag{8}$$

In what follows, only the constitutive model for solid skeleton deformation will be presented. In addition, the free energy $\Psi$ may include an elastic component $\Psi^e$ (reversible) and a locked component $\Psi^p$ (stored during previous irreversible process). Recovery of the second component is necessarily accompanied by dissipative process). In consequence, we can write:

$$\Psi_{sol} = \Psi^e_{sol} + \Psi^p_{sol} \tag{9}$$

Based on the Clausius-Duhem inequality (2) and the above analysis, the elastic work input stored as elastic free energy for the solid skeleton can be rewritten as [3]:

$$d\Psi^e_{sol} = \bar{\sigma} : d\boldsymbol{\varepsilon}^e + \bar{\mu}_{w'} dm^e_{w'} \tag{10}$$

The generalized effective stresses $\bar{\sigma}$ and the effective chemical potential of absorbed water $\bar{\mu}_{w'}$ is defined as [2]:

$$\bar{\sigma} = \boldsymbol{\sigma} + p^* \mathbf{1}; \bar{\mu}_{w'} = \mu_{w'} - \frac{p^*}{\rho_{w'}} \tag{11}$$

The equivalent pore pressure $p^*$ is defined by $p^* = S_\mathcal{L} p_\mathcal{L} + (1 - S_\mathcal{L}) p_\mathcal{G}$. A few steps' of development lead to the following Clausius-Duhem inequality [3]:

$$\Phi_{sol} = \bar{\sigma} : d\boldsymbol{\varepsilon}^p + \bar{\mu}_{w'} dm^p_{w'} + \beta_{sol} d\xi_{sol} \geq 0 \tag{12}$$

Here, $\beta_{sol}$ is the conjugate of $\xi_{sol}$, defined by $\beta_{sol} = -\left(\frac{\partial \Psi^p_{sol}}{\partial \xi_{sol}}\right)_{S_\mathcal{L}}$.

### 4.2 Chemo-Hyperelastic Model

In tri-axial stress state, the strain work expression (10) can be recast to the following form:

$$d\Psi^e_{sol} = \bar{p}d\varepsilon^e_v + qd\varepsilon^e_s + \bar{\mu}_{w'}dm^e_{w'} \tag{13}$$

where the effective stresses $\bar{\sigma}$ and strains $\boldsymbol{\varepsilon}$ are replaced by the effective mean stress $\bar{p}$, the Mises equivalent stress $q$, the volumetric strain $\varepsilon^e_v$ and the equivalent deviatoric strain $\varepsilon^e_s$, It turns out more convenient to take the stress as independent variable rather than the strain. To this end, we apply a partial Legendre transform to define another thermodynamic potential $\bar{\Psi}^e_{sol}$:

$$d\bar{\Psi}^e_{sol}\left(\bar{p}, q, m^e_{w'}\right) = \varepsilon^e_v d\bar{p} + \varepsilon^e_s dq - \bar{\mu}_{w'}dm^e_{w'} \tag{14}$$

This potential allows to express the generalised strain variables $\left(\varepsilon^e_v, \varepsilon^e_s, m^e_{w'}\right)$ in terms of their work-conjugate, the generalised stress variables $(\bar{p}, q, \bar{\mu}_{w'})$. Now let $\bar{p}_0$ denote a small reference stress when the pore fluid is distilled water and is under purely mechanical loading during an elastic deformation, and the slope of an over consolidation line (OCL) is $\kappa^w$. After chemical loading, the slope of this OCL becomes $\kappa$, and it intersects the original OCL at the point corresponding to a particular effective stress $\bar{p}_\kappa$. Following Loret et al. [5], the expression of the skeleton free energy $\bar{\Psi}^e_{sol}$ is taken to be [2]:

$$\bar{\Psi}^e_{sol} = \bar{p}\kappa^w \ln\frac{\bar{p}_\kappa}{\bar{p}_0} + \kappa\bar{p}\left(\ln\frac{\bar{p}}{\bar{p}_\kappa} - 1\right) + \frac{q^2}{6G} - \mu^0_{w'}m^e_{w'} - \frac{RT}{d\Omega_0}\left(N_{w'}\ln N_{w'} - N_S \ln N_S\right) \tag{15}$$

In the above, $R$ is the universal gas constant, $\mu^0_{w'}$ is the reference chemical potential, $\mathcal{M}_{w'}$ is the molar mass of absorbed water, and $x_{w'} = N_{w'}/N_S$ is the molar fraction of the absorbed water species with $N_{w'}$ and $N_S$ denoting respectively the molar quantities of absorbed water and that of the entire solid phase within an elementary volume. Using this thermodynamic potential, an incremental chemo-hyperelastic constitutive model can be derived as:

$$\begin{bmatrix} d\varepsilon^e_v \\ d\varepsilon^e_s \\ -d\bar{\mu}_{w'} \end{bmatrix} = \begin{bmatrix} \frac{\partial^2\bar{\Psi}^e_{sol}}{\partial\bar{p}^2} & \frac{\partial^2\bar{\Psi}^e_{sol}}{\partial\bar{p}\partial q} & \frac{\partial^2\bar{\Psi}^e_{sol}}{\partial\bar{p}\partial m^e_{w'}} \\ \frac{\partial^2\bar{\Psi}^e_{sol}}{\partial q\partial\bar{p}} & \frac{\partial^2\bar{\Psi}^e_{sol}}{\partial q^2} & \frac{\partial^2\bar{\Psi}^e_{sol}}{\partial q\partial m^e_{w'}} \\ \frac{\partial^2\bar{\Psi}^e_{sol}}{\partial m^e_{w'}\partial\bar{p}} & \frac{\partial^2\bar{\Psi}^e_{sol}}{\partial m^e_{w'}\partial q} & \frac{\partial^2\bar{\Psi}^e_{sol}}{\partial m^{e\,2}_{w'}} \end{bmatrix} \begin{bmatrix} d\bar{p} \\ dq \\ dm^e_{w'} \end{bmatrix} \tag{16}$$

After a few steps of rearrangements, accounting for the dependence of the elastic coefficient $\kappa$ on the absorbed water mass content $m^e_{w'}$ while assuming a constant

Poisson's ratio, the generalised stress vector $\boldsymbol{\Sigma} = [\bar{p}, q, -\bar{\mu}_{w'}]^T$ is related to the generalised elastic strains vecor $\boldsymbol{E}^e = \left[\varepsilon_v^e, \varepsilon_s^e, m_{w'}^e\right]^T$ via a generalised elastic stiffness matrix:

$$\dot{\boldsymbol{\Sigma}} = \boldsymbol{D}^e \dot{\boldsymbol{E}}^e \tag{17}$$

with:

$$\mathbf{D}^e = \begin{bmatrix} D_{uu} & 0 & D_{um} \\ 0 & 3G & 0 \\ D_{mu} & 0 & D_{mm} \end{bmatrix};$$

$$D_{uu} = \frac{\bar{p}}{\kappa};\ D_{um} = -\frac{\bar{p}}{\kappa}\ln\frac{\bar{p}}{\bar{p}_\kappa}\frac{d\kappa}{dm_{w'}^e} = D_{mu};$$

$$D_{mm} = \frac{\bar{p}}{\kappa}\left(\ln\frac{\bar{p}}{\bar{p}_\kappa}\frac{d\kappa}{dm_{w'}^e}\right)^2 + \bar{p}\left(1 - \ln\frac{\bar{p}}{\bar{p}_\kappa}\right)\frac{d^2\kappa}{dm_{w'}^{e\,2}} + \frac{RT}{\mathrm{M}_{w'}}\frac{1}{x_{w'}}\frac{dx_{w'}}{dm_{w'}^e}$$

### 4.3 Elasto-Plastic Model

Using the Cam-Clay notation, the solid skeleton dissipation (15) can be rewritten as:

$$\Phi_{sol} = \bar{p}d\varepsilon_v^p + qd\varepsilon_s^p + \bar{\mu}_{w'}dm_{w'}^p + \beta_{sol}d\xi_{sol} \geq 0 \tag{18}$$

The principle of maximum plastic dissipation implies the following normality flow rule

$$d\varepsilon_v^p = d\lambda\frac{\partial g}{\partial \bar{p}};\ d\varepsilon_s^p = d\lambda\frac{\partial g}{\partial q};\ dm_{w'}^p = d\lambda\frac{\partial g}{\partial \bar{\mu}_{w'}} \tag{19}$$

where $d\lambda \geq 0$ is the plastic multiplier, and $g$ is the plastic potential. For simplicity, the plastic potential $g$ is set equal to the yield function $f$ introduced below. In addition, we also use the normality flow rule for the hardening variable:

$$d\xi_{sol} = d\lambda\frac{\partial g}{\partial \beta_{sol}} \tag{20}$$

Consistent with the classic plasticity theory, it is assumed that a yield surface exists for the unsaturated expansive soil representing the boundary of the elastic region:

$$f = f\left(\bar{p}, q, \bar{\mu}_{w'}, \beta_{sol}\right) = 0 \tag{21}$$

Following the usual procedure in classical plasticity [1], we obtain the elastoplastic tangent stiffness matrix relating the stress rate to the total strain rate:

$$\dot{\boldsymbol{\Sigma}} = (\boldsymbol{D}^e - \boldsymbol{D}^p)\dot{\boldsymbol{E}} \tag{22}$$

During plastic loading, the stress point is always on the yield surface ($f = 0$) and the consistency condition ($df = 0$) should be satisfied at all times. This allows to derive an explicit expression of the matrix $\mathbf{D}^p$ (see [3]):

The modified Cam-Clay model is adopted as the base model, with the yield surface:

$$f = \frac{q^2}{M^2 \bar{p}} + \bar{p} - \bar{p}_c = 0 \tag{23}$$

where $M$ is the slope of the critical state line, and $\bar{p}_c$ is the preconsolidation stress which classically depends on the volumetric plastic strain $\varepsilon_v^p$. To account for effects of suction and pore water chemistry, $\bar{p}_c$ now also depends on matric suction $s$ and pore water salt concentration $c_s$:

$$\bar{p}_c = \bar{p}_{co} \exp\left(\frac{\varepsilon_v^p}{\lambda - \kappa}\right) \left(\frac{\bar{p}_\lambda}{\bar{p}_{co}}\right)^{\left(1 - \frac{\lambda^w - \kappa^w}{\lambda - \kappa}\right)} \left(\frac{\bar{p}_\lambda}{\bar{p}_k}\right)^{\left(\frac{\kappa - \kappa^w}{\lambda - \kappa}\right)} \tag{24}$$

In the above hardening law, $\bar{p}_{co}$, $\bar{p}_k$, $\bar{p}_\lambda$, $\kappa^w$ and $\lambda^w$ are material constants, whereas $\kappa$ and $\lambda$ evolve with suction $s$ and pore water salinity $c_s$, and control the evolution of the preconsolidation pressure.

### 4.4 Diffusion and Mass Transfer Equations

To complete the theoretical model so that it can be applied to heterogeneous porous media, we also need to derive the transport equations of different species in the fluid phases. To do this, we need to invoke the non-negativity of the dissipations mentioned in the inequations (5) to (7). This would lead to the classic formulations of the generalised Darcy's law and Fick's law governing pore-water flow and salt diffusion, as well as to a phenomenological kinetic law governing the phase transformation between free and absorbed water. Due to space limit, these developments would not be shown here; they can be found in [2, 3].

## 5 Experimental Results and Simulations

A few numerical simulations have been performed to verify the consistency, pertinence and accuracy of the theoretical model developed [2]. Concerning the case of heterogeneous porous media, [3] analysed the progressive intrusion of salt into a soil layer and its consequences; its results were also compared to that of a previous publication. In this paper, we choose to present some simulations of the experimental data reported in [9, 10]. While results are available for both saturated and unsaturated samples, attention here will be uniquely focused on unsaturated ones. On the other hand, the parameters used in the simulations, as summarized in Tables 1 and 2, were calibrated using both data on saturated and unsaturated samples [3, 4].

**Table 1.** Parameters for interpolation of chemo-mechanical properties at saturated state

| | $m_{c'}$ [kg/m$^3$] | $m_{s'}$ [kg/m$^3$] | $m_{w'}$ [kg/m$^3$] | $x_{w'}$ | $\kappa^c$ | $\lambda^c$ |
|---|---|---|---|---|---|---|
| 0 M | 240 | 0 | 336 | 0.967 | 0.013 | 0.089 |
| 6.53 M | 240 | 0 | 65.573 | 0.853 | 0.007 | 0.080 |

**Table 2.** Parameters for chemo-mechanical model

| $\bar{p}_{co}$ [kPa] | $\bar{p}_{\kappa}$ [kPa] | $\bar{p}_{\lambda}$ [kPa] | $s_e$ [kPa] | $k_3$ | $\lambda_3$ | $\beta$ |
|---|---|---|---|---|---|---|
| 50 | 5000 | 1300 | 10 | 1 | 5 | 0.084 |

### 5.1 Test Series 1 (Oedometric) and Results of Simulation

Two series of oedometric tests on unsaturated samples were reported in [10]. In the first, samples were prepared by mixing Boom Clay powder with $NaNo_3$ solutions at 3 different concentrations: 0 M, 4 M and 5.4 M, and were brought to an initial suction of 500 kPa. They were then subject to a compression-decompression cycle at constant suction up to a maximum axial stress of 1000 kPa. Results are plotted in Fig. 2a. Similarly to the case of saturated samples, a salinity increase reduces slightly the virgin compressibility $\lambda$, while leaving more or less unaffected the compressibility at over-consolidated states $\kappa$. The numerical simulations presented in Fig. 2b also appear reasonably close to experimental results.

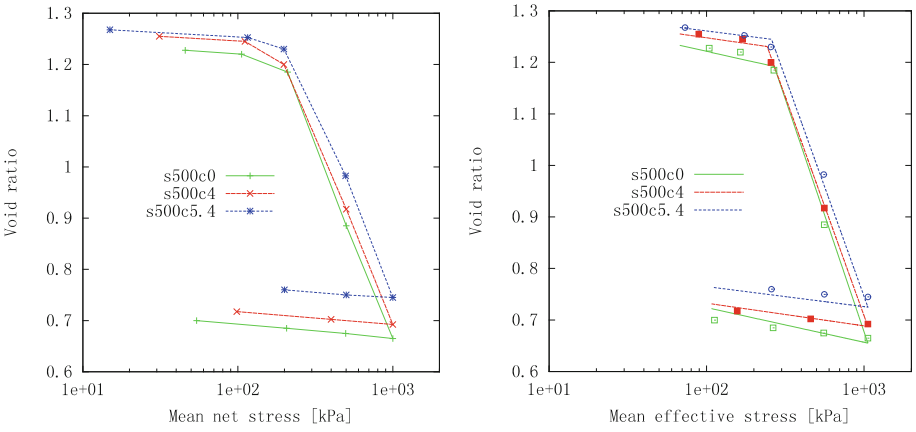


(a) Experimental results (b) Simulations

**Fig. 2.** Oedometric tests on unsaturated Boom Clay samples (a) experimental data (b) simulations.

### 5.2 Test Series 2 (Oedometric) and Results of Simulation

In the second series, 2 samples were prepared with distilled water and brought to an initial suction of 500 kPa and an initial stress of 40 kPa. From this initial state and keeping a constant suction and zero salinity, sample 1 was simply compressed to 1000 kPa then decompressed to around 50 kPa. By contrast, sample 2 was subject to a mixed chemo-mechanical loading path: (i) compressed to 100 kPa; (ii) exposed to 6.54 M $NaNo_3$ solution; (iii) further compressed to 1000 kPa; (iv) unloaded to 100 kPa; (v) exposed to distilled water. Experimental results are plotted in Fig. 3a while the simulation results are plotted in Fig. 3b. The tendencies observed are similar to the case of saturated samples [3, 4]. A normally consolidated or lowly overconsolidated clay is much more sensitive to salinity changes than a highly overconsolidated clay. This explains why exposure to 6.54 M solution during first compression (∼normal consolidation) induces a large volume contraction while exposure to distilled water at end of unloading (overconsolidated) has insignificant effects. Chemically-induced plastic collapse in the first case appears to be a logical explanation. Notice also in this regard that the first exposure to 6.54 M solution does induce consistently an increase in the preconsolidation pressure. The simulations globally capture the overall tendency with reasonable accuracy.

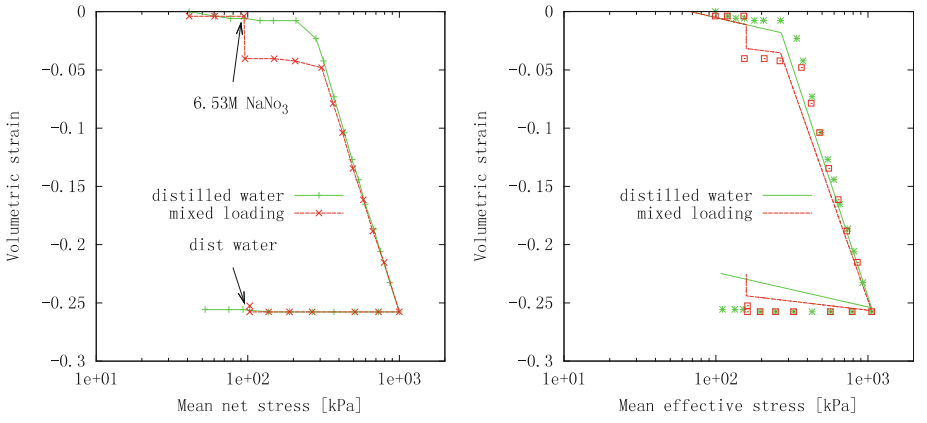


(a) Experimental results (b) Simulations

**Fig. 3.** Mixed chemical-mechanical loading on unsaturated samples: exposure to 6.53 M solution during loading and to distilled water during unloading, both at vertical stress 100 kPa.

At the present state, the extremely limited amount of experimental data on samples subject simultaneous to suction and chemical loadings does not allow an in-depth analysis of the model which would probably yield ideas on its possible refinements. Further experimentation appears necessary.

## 6 Conclusion

Based on the mixture theory and the theory of non-equilibrium thermodynamics, a theoretical chemo-mechanical model was developed. In this model, the governing equations for chemo-elastic-plastic deformations of unsaturated skeleton, fluid species diffusion and solid-liquid mass transfer have been systematically and rigorously derived. The model was then used to simulate the response of unsaturated soil samples observed during oedometric tests when subject to different chemo-mechanical loading paths. The comparisons globally do not invalidate the model construction while theory also pointed out the necessity for further studies.

## References

1. Coussy, O.: Poromechanics. Wiley, Hoboken (2004)
2. Lei, X., Wong, H., Fabbri, A., Limam, A., Cheng, Y.M.: A thermo-chemo-electro-mechanical framework of unsaturated expansive clays. Comput. Geotech. **62**, 175–192 (2014)
3. Lei, X.: Theoretical modelling of coupled chemo-hydro-mechanical behaviour of unsaturated expansive clays. Ph.D. thesis, INSA-Lyon/ENTPE (2015)
4. Lei, X., Wong, H., Fabbri, A., Limam, A., Cheng, Y.M.: A chemo-elastic-plastic model for unsaturated expansive clays. Int. J. Solids Struct. **62**, 175–192 (2016). doi:10.1016/j.ijsolstr.2016.01.008
5. Loret, B., Hueckel, T., Gajo, A.: Chemo-mechanical coupling in saturated porous media: elastic–plastic behaviour of homoionic expansive clays. Int. J. Solids Struct. **39**, 2773–2806 (2002)
6. Gajo, A., Loret, B.: Finite element simulations of chemo-mechanical coupling in elastic–plastic homoionic expansive clays. Comput. Methods Appl. Mech. Eng. **192**, 31–32 (2003)
7. Guimarães, L., Gens, A., Sanchez, M., Olivella, S.: A chemo-mechanical constitutive model accounting for cation exchange in expansive clays. Geotechique **63**, 2 (2013)
8. Liu, Z., Boukpeti, N., Li, X., Collin, F.: Modelling chemo-hydro-mechanical behaviour of unsaturated clays: a feasibility study. IJNAG **29**, 919–940 (2005)
9. Mokni, N., Romero, E., Olivella, S.: Chemo-hydro-mechanical behaviour of compacted Boom Clay: joint effects of osmotic and matric suctions. Geotechnique **64**, 681–693 (2014)
10. Mokni, N.: Ph.D. thesis. Universitat Politècnica de Catalunya (2014)

# Influence of Microcracking of Host Rock on the Hydromechanical Responses of Underground Structures: Constitutive Modeling and Numerical Simulations

T.A. Bui[1,2(✉)], H. Wong[2], and F. Deleruyelle[3]

[1] Université de Nantes, Institute GeM, Saint-Nazaire, France
tuan-anh.bui@univ-nantes.fr
[2] Université de Lyon, ENTPE/LGCB and LTDS UMR CNRS 5513, Vaulx-en-Velin, France
kwaikwan.wong@entpe.fr
[3] IRSN, PSE-ENV, SEDRE, UEMIS, Fontenay-aux-Roses, France
frederic.deleruyelle@irsn.fr

**Abstract.** This paper presents a numerical modeling accounting for the effect of cracking on both mechanical and hydraulic properties of unsaturated rocks. Firstly, the constitutive model developed by Bui, et al. [3], established in the framework of thermodynamics of porous media, is recalled. Its main feature is that damage intervenes on both mechanical behavior and hydraulic properties (water retention curve and hydraulic conductivity). Secondly, the model is validated against experimental data on an argillaceous rock. Finally, this constitutive model is implemented into a domestic finite element code to study numerically the evolution of hydromechanical responses of a radioactive waste underground gallery during a simplified life cycle. Numerical simulations demonstrate the consistency of the model and highlight the influence of desaturation on the hydromechanical behavior of the gallery.

**Keywords:** Poro-plasticity · Damage · Unsaturated rocks · Permeability · Finite element simulations · Radioactive waste disposal

## 1 Introduction

Studying the impact of microcracking of a rock medium is an important task for many engineering applications, such as seepage analysis in oil and gas extraction and reservoir engineering [1] or safety assessment of radioactive waste disposal [2, 3]. Damage induced by microcracking may decrease rock strength and increase rock deformation, which favors gallery convergences and implies additional stresses in the lining support of the structure. On one hand, microcracking could also enhance the permeability of the medium and modify pore pressure distribution, which may lead to mechanical instability as well as dissemination of confined materials (for instance $CO_2$ gas or radioelements in geologic disposal).

© Springer Nature Singapore Pte Ltd. 2018
H. Tran-Nguyen et al. (eds.), *Proceedings of the 4th Congrès International de Géotechnique - Ouvrages -Structures*, Lecture Notes in Civil Engineering 8,
DOI 10.1007/978-981-10-6713-6_72

In this context, Bui et al. [3] developed a constitutive model accounting for the effect of cracking on both mechanical and hydraulic properties of unsaturated rocks. The model is founded in the framework of thermodynamics of porous media using the concept of plastic effective stress and equivalent pore pressure. Using the concept of bundle cylindrical capillaries, damage effect on hydraulic behavior (water retention curve and hydraulic conductivity) is modelled using phenomenological functions. The intervention of damage on both mechanical and hydraulic parts enables this model to describe in a relevant manner bilateral couplings between these two parts. The model has been validated against experimental data on an argillaceous rock.

In this paper, this model [3] is exploited to study the evolution of hydromechanical responses of a radioactive waste underground gallery during a simplified life cycle. It is first implemented into a finite element computer code originally developed in LGCB (Laboratoire Génie Civil et Bâtiment, ENTPE, France). Numerical simulations in the general case of a lined tunnel demonstrate the consistency of the model and highlight the influence of desaturation on the gallery behavior. In this paper, the sign convention of continuum mechanics is adopted (expansive strain and tensile stress counted positively), except in Sect. 3 where numerical results are represented according to the sign convention of soil mechanics (expansive strain and tensile stress counted negatively) so as to be consistent with traditional interpretation of experimental results.

## 2 Constitutive Model

This section presents a constitutive model allowing to take into consideration the effect of microcracking on both mechanical and hydraulic properties of unsaturated rocks. The main theoretical framework of the model has been presented in [3] and will be briefly recalled hereafter.

Firstly, some basic assumptions are stated [3]. The rock is assumed to be isotropic and in an isothermal state. Displacements, strains and porosities are assumed to be infinitesimal. Only isotropic hardening, represented by a scalar $\gamma_p$, and isotropic damage, represented by a scalar internal variable $D$, are used to describe dissipative mechanisms (plasticity and damage). The total strain tensor $\boldsymbol{\varepsilon}$ and total porosity variation $\Delta\phi$ are classically supposed to be decomposable into elastic and plastic parts, which are respectively marked by superscripts $^{e}$ and $^{p}$:

$$\boldsymbol{\varepsilon} = \boldsymbol{\varepsilon}^{\boldsymbol{e}} + \boldsymbol{\varepsilon}^{\boldsymbol{p}}; \quad \Delta\phi = \phi - \phi_0 = \phi^e + \phi^p \tag{1}$$

where $\phi_0$ stands for the initial total porosity. Since it is generally difficult to evaluate the plastic porosity, the following assumption is adopted [4]:

$$\phi^p = b_{pl}\epsilon^p \tag{2}$$

where $b_{pl}$ is taken as a material parameter, representing the plastic hydro-mechanical coupling and $\epsilon^p = tr(\boldsymbol{\varepsilon}^{\boldsymbol{p}})$ is the plastic volumetric strain.

The free energy of skeleton $\Psi_s$ per unit overall volume is supposed to be decomposed into two parts, one emanating from the solid phase $\psi_s$, while another coming from the interfacial energy per unit volume of porous space $U$. Therefore the energy separation writes:

$$\Psi_s = \psi_s\left(\boldsymbol{\varepsilon}^{\boldsymbol{e}}, \phi^e, D, \gamma_p\right) + \phi U(\phi, S_w, D) \tag{3}$$

Noting that fully saturated state is used as the reference datum to define this interfacial energy, namely $U = 0$ at full saturation. This energy is linked to water retention mechanism and can be calculated via the water retention function,

$$U = \int_{S_w}^{1} p_c(\phi, \tilde{s}_w, D) d\tilde{s}_w \tag{4}$$

Following the approach of Coussy and Dangla [4], an equivalent pore pressure is postulated:

$$\pi_{eq} = p_w S_w + p_g S_g - \frac{2}{3} U \tag{5}$$

which accounts for not only different fluid pressures in the porous space, but also the interface effects through the interfacial energy.

The poroelastic equations are then extended from the classic saturated case by using this equivalent pressure:

$$\begin{aligned} \sigma - \sigma_0 &= K(D)\epsilon - b(D)\pi_{eq} + b_0\pi_{eq0} \\ \boldsymbol{s} - \boldsymbol{s}_0 &= 2G(D)\boldsymbol{e} \\ \phi - \phi_0 &= b(D)\epsilon + \beta(D)\pi_{eq} - \beta_0\pi_{eq0} \end{aligned} \tag{6}$$

where the subscript $_0$ stands for an initial value; $\sigma = \frac{1}{3}tr(\boldsymbol{\sigma})$ is the total mean stress; $\boldsymbol{s}$ the deviatoric total stress tensor and $\boldsymbol{e}$ the deviatoric strain tensor. In the above equations, the damage-dependent drained bulk and shear moduli $K(D)$ and $G(D)$, Biot's coefficient $b(D)$ and pore compressibility $\beta(D)$ are proposed based on [5, 6]:

$$\begin{aligned} K(D) = K_0(1-D); \quad G(D) = G_0(1-D) \\ b(D) = 1 - \tfrac{K(D)}{K_s} = 1 - \tfrac{K_0}{K_s}(1-D); \quad \beta(D) = \tfrac{b(D)-\phi_0}{K_s} \end{aligned} \tag{7}$$

For plastic evolution, the effective stress concept is adopted. A plastic effective stress is postulated based on Assumption (2) and thermodynamic analysis [3]:

$$\boldsymbol{\sigma}^{\boldsymbol{pl}} = \boldsymbol{\sigma} + b_{pl}\pi_{eq}\boldsymbol{\delta} \tag{8}$$

The plastic criterion function is then postulated in terms of this effective stress:

$$F_p\left(\boldsymbol{\sigma}^{\boldsymbol{pl}}, \alpha_p\right) = q^{pl} - \alpha_p R_c \sqrt{A_f\left(C_s - \frac{\sigma^{pl}}{R_c}\right)} \leq 0 \tag{9}$$

where $R_c$ and $C_s$ are respectively the unconfined compressive strength (UCS) and cohesion coefficient under saturated condition; $A_f$ related to the curvature of failure surface; $q^{pl} = \sqrt{\frac{3}{2}\boldsymbol{s}^{pl} : \boldsymbol{s}^{pl}}$ the Von Mises equivalent stress, with $\boldsymbol{s}^{pl}$ the deviatoric plastic effective stress tensor; and $\sigma^{pl} = \frac{1}{3}tr\left(\boldsymbol{\sigma}^{pl}\right)$ the plastic effective mean stress. The hardening function defined as a function of the hardening variable and damage as well:

$$\alpha_p\left(\gamma_p, D\right) = (1 - D)\frac{\gamma_p}{B_p + \gamma_p} \tag{10}$$

with $B_p$ a parameter controlling the hardening kinematics and the plastic hardening variable is chosen as plastic distortion:

$$\gamma_p = \int_o^t \sqrt{\frac{2}{3}\dot{\boldsymbol{e}}^p : \dot{\boldsymbol{e}}^p}\, d\tau \tag{11}$$

Consequently, damage is the unique mechanism responsible for the softening behaviour of the material. To describe the transition from plastic contractance to dilatancy, a non-associated flow rule is proposed:

$$\dot{\boldsymbol{\varepsilon}}^{\boldsymbol{p}} = \dot{\lambda}_p \frac{\partial G_p}{\partial \boldsymbol{\sigma}^{\boldsymbol{pl}}}; \quad G_p\left(\boldsymbol{\sigma}^{\boldsymbol{pl}}, \alpha_p; D\right) = q^{pl} - \left[\alpha_p - \alpha_p^{cd}(1 - D)\right]\left(C_s R_c - \sigma^{pl}\right) \tag{12}$$

where the plastic multiplier satisfies:

$$\dot{\lambda}_p \geq 0 \quad F_p \leq 0 \quad \dot{\lambda}_p F_p = 0 \tag{13}$$

To complete, damage evolution law must be specified. Based on experimental and physical observations that damage process is promoted by plastic sliding and limited by confining pressure, we define firstly a practical damage driving force:

$$Y_d = \int_o^t \frac{\sqrt{\frac{2}{3}\dot{\boldsymbol{e}}^p : \dot{\boldsymbol{e}}^p}}{\xi_d} d\tau; dY_d = \frac{\sqrt{\frac{2}{3}d\boldsymbol{e}^p : d\boldsymbol{e}^p}}{\xi_d}; \xi_d = \frac{\left\langle \sigma^{pl} \right\rangle + P_r}{P_r} \tag{14}$$

$\sigma^{pl}$ is the mean effective stress, $\langle . \rangle$ the Macaulay bracket, defined as $\langle x \rangle = \frac{1}{2}(x + |x|)$, and $P_r$ = 1 MPa the reference pressure. Inspired by plasticity theory, the damage evolution law writes,

$$\dot{D} = \dot{\lambda}_d \frac{\partial F_d}{\partial Y_d}; F_d(Y_d; D) = 1 - \frac{1}{e^{r_1 Y_d}} - r_0 D \tag{15}$$

where $F_d$ is the damage criterion function with $r_0$ and $r_1$ two model parameters.

The main feature of this model is that it takes into account the effect of damage on both mechanical and hydraulic properties. For the latter, a statistical approach [7, 8] is employed assuming that [9, 10] (i) created cracks are much bigger than natural pores and (ii) cracks and pores are connected and form a unique porous space with a *bimodal*

*pore size distribution*. Noting that the porosity change in rocks is generally small, this approach allows to calculate the degree of saturation of a cracked medium as follows:

$$S_w = S_w(\phi, p_c, D) = [1 - h_d(D)]S_{w1}(p_c) + h_d(D)S_{w2}(p_c) \tag{16}$$

in which the weighting function $h_d(D)$ is phenomenologically assumed to take the following form:

$$h_d(D) = \zeta D^2 \tag{17}$$

and the partial water retention for each mode (pores and fissures) are assumed to take the Van-Genuchten (V-G) form:

$$S_{w1}(p_c) = \left[\frac{1}{1 + (\alpha_1 p_c)^{n_1}}\right]^{1-\frac{1}{n_1}}; S_{w2}(p_c) = \left[\frac{1}{1 + (\alpha_2 p_c)^{n_2}}\right]^{1-\frac{1}{n_2}} \tag{18}$$

The permeability of a damaged unsaturated medium is then estimated from the water retention function (15) using the approach of Mualem [8]:

$$K_w(\phi, p_c, D) = F_S \phi^2 S_w^{h_t} \left(\int_{\infty}^{p_c} \frac{1}{p} \frac{\partial S_w}{\partial p} dp\right)^2 \tag{19}$$

where $h_t$ is introduced to take into account tortuosity effect of water-filled connected pores. To simplify, we take $h_t = -1$ as suggested by [11], while $F_S$ accounts for the shape, tortuosity and connectivity of pores and can be identified from the measured value of the saturated permeability.

## 3 Model Calibration and Validation

The model presented above is applied to simulate the behaviour of Callovo-Oxfordian argillite, the potential host rock considered for a radioactive waste disposal in France. The procedure for identification of model parameters was presented in [3]. The calibration procedure is performed according to the experimental results obtained from [12]. The main parameters are summarized in Table 1.

**Table 1.** Model parameters used for the simulations of triaxial tests (series for different water content) [12]

| |
|---|
| $E = 5000\ MPa;\ \ \nu = 0.18;\ \ b = 0.6;\ \ \phi_0 = 0.18;$ |
| $n_1 = 1.49; \alpha_1 = \frac{1}{15} MPa^{-1};\ n_2 = 4.2;\ \alpha_2 = 20.4\ MPa^{-1};\ \ \zeta = 1.5;$ |
| $A_f = 3.7\ ;\ C_s = 0.03\ ;\ \ R_c = 25\ MPa;\ \ B_p = 9.10^{-4};\ \ \alpha_p^{cd} = 0.7;\ b_{pl} = 0.3$ |
| $r_0 = 2.5;\ r_1 = 250;\ r_2 = 1;\ \beta_d = 1$ |

Using these parameters, we simulated some triaxial tests at different water content. Figure 1(a, b) show that the model is capable to reproduce the main features of the mechanical behaviour of this rock such as damage softening, plastic dilatancy and especially the hardening effect of suction.

**Fig. 1.** Triaxial test at different water content (continuous lines are numerical simulations) (a) Confining pressure 5 MPa (b) Confining pressure 2 MPa

Figure 2 shows the evolution of the intrinsic permeability during the test obtained from (19). It could be observed that the simulated intrinsic permeability increases significantly (up to four orders of magnitude) during the test, due to damage effect. Furthermore, the confining pressure tends to reduce the permeability alteration. These results are qualitatively in good agreement with experimental observations [14] and more realistic than the ones obtained by the classic Kozeny-Carman's model which predicts the permeability change only due to the change of the porosity.

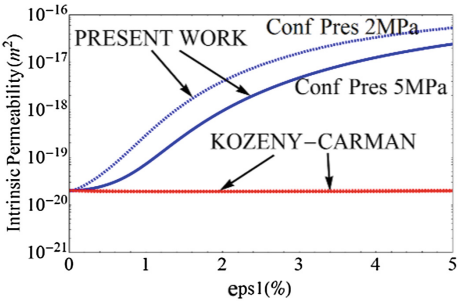


**Fig. 2.** Evolutions of intrinsic permeability during the tests. Continuous lines: 5 MPa; dashed lines 2 MPa. blue lines: this work; red lines: Kozeny-Carman model

## 4 Simulation of the Behavior of an Undergrounds Gallery

The developed model was implemented into a 1D domestic finite element code written in C++. The aim is to simulate the hydromechanical behavior of an underground radioactive waste gallery subjected to a ventilation after its excavation.

The rock mass, prior to excavation, is assumed to be in a hydromechanical equilibrium. The initial conditions write:

$$\boldsymbol{\sigma}(r,0) = -P_\infty \boldsymbol{\delta}; \quad \boldsymbol{u}(r,0) = 0; \quad \boldsymbol{\varepsilon}(r,0) = 0; \quad p_w(r,0) = p_{w0} \tag{20}$$

with $p_{w0}$ is the hydrostatic in-situ stress and $P_\infty$ is the geostatic overburden.

The excavation process is assumed to be very fast and occurs from $t_0 = 0$ to $t_1 = 1$ day. During this phase, the radial mechanical total stress and the water pressure at the gallery wall drop rapidly to zero (all the water entering the cavity is drained off). These boundary conditions last until $t_2 = 2$ months which marks the lining emplacement. From this moment, the physical domain is enlarged with a lining of thickness $e$. The geometry parameters and the main parameters for the lining, referred to [13] is summarized in Table 2. Note that $\alpha_L$ and $n_L$ are VG parameters for this material and $a$ is the radius of the gallery.

**Table 2.** Boundary conditions at different stages

| | | |
|---|---|---|
| $a = 3.6\,\text{m}$ | $\phi_L = 0.15$ | $e = 0.75\,\text{m}$ |
| $E_L = 30000\,\text{MPa}$ | $\alpha_L = 0.5\,\text{MPa}^{-1}$ | $n_L = 1.54$ |
| $\upsilon_L = 0.25$ | $b_L = 0.8$ | $K_{wSL} = 10^{-16} m^2$ |

Once the gallery is lined, a ventilation is immediately posed to ensure the working condition inside the gallery. This process leads to an imposed relative humidity at the gallery inner wall. We assume that the imposed relative humidity of 80%, corresponding to an imposed suction of 30.2 MPa. The mesh and boundary conditions are summarized in Table 3. Note that the mesh is refined near the gallery wall.

**Table 3.** Boundary conditions at different stages

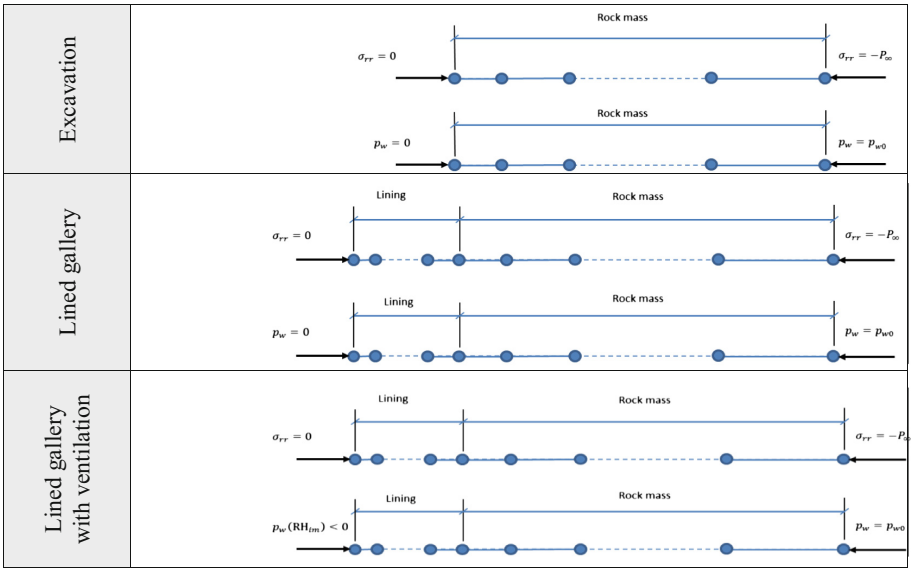

The excavation process is assumed to be very fast and occurs from $t_0 = 0$ to $t_1 = 1$ day. During this phase, the radial mechanical total stress and the water pressure at the gallery wall drop rapidly to zero (all the water entering the cavity is drained off). These boundary conditions last until $t_2 = 2$ months which marks the lining emplacement. From this moment, the physical domain is enlarged with a lining of thickness $e$. The geometry parameters and the main parameters for the lining, referred to [13] is summarized in Table 2. Note that $\alpha_L$ and $n_L$ are VG parameters for this material and $a$ is the radius of the gallery.

Figure 3a shows the profiles of the displacement in the rock mass. It is observed that due the evolution of the water pressure (ventilation process), the displacements continue to evolve even in absence of mechanical loading. The shrinkage at the gallery wall is less important than within the massif. This evolution of the displacement is accompanied with the evolution of the water pressure as shown in Fig. 3b. Before desaturation (prior to the lining emplacement), the water pressure is progressively dissipated, with nil value at the gallery wall. After desaturation, water pressure at the wall suddenly changes from zero to −30.2 MPa due to the imposed relative humidity. A depression front continues to penetrate into the lining and then the massif. Since the water permeability of the lining is higher than that of the host rock (5000 times greater at full saturation), the dissipation in the lining is much faster than in the massif. The greater saturation of the rock mass compared to that of the lining (which promotes hydraulic transport) cannot compensate this contrast. The evolution of the water pressure leads to the penetration of a desaturation front inside the massif. Furthermore, it is seen that the degree of saturation in the support (dashed lines) is actually smaller than that in the massif (continuous lines). Indeed, due to a greater permeability (and a rather small thickness), the saturation state of the lining quickly reaches a quasi-homogeneous state.

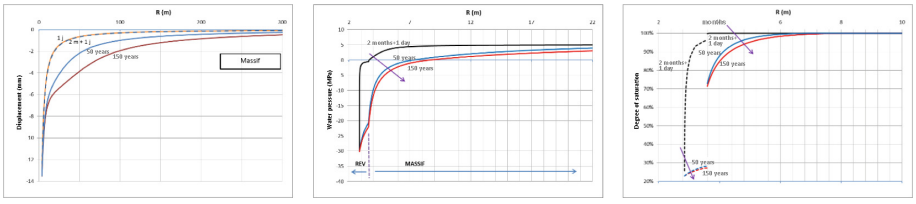


**Fig. 3.** Profiles in the massif at different times of (a) Radial displacements (b) Water pressures (c) Degree of saturation (arrows indicate time evolution)

Finally, the evolution of the saturated permeability is shown in Fig. 4. After excavation, the massif remains saturated and the permeability increases in the vicinity of the gallery (red arrow), due to damage then decreases thereafter (direction of evolution according to the green arrow). The latter phenomenon may be explained by a decrease of the porosity due to the recompression of the rock mass.

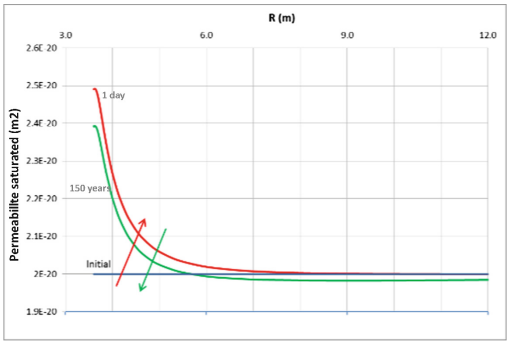


**Fig. 4.** Profiles of intrinsic permeability in the rock mass (the red arrow indicates the evolution from intial state to 1 day, while the other one indicates the evolution from 1day to 150 years)

## 5 Conclusion

A previously developed model [3], which accounts for the damage effect on both mechanical and hydraulic responses of unsaturated rocks, has been recalled. This model has been used to study the hydromechanical response of a lined tunnel subjected to desaturation. It is shown that damage and desaturation induce not only convergent displacements but also a change of the rock permeability. The consistency of the numerical model has been illustrated.

## References

1. Maleki, K., Pouya, A.: Numerical simulation of damage–permeability relationship in brittle geomaterials. Comput. Geotech. **37**, 619–628 (2010)
2. Souley, M., Homand, F., Pepa, S., Hoxha, D.: Damage-induced permeability changes in granite: a case example at the URL in Canada. Int. J. Rock Mech. Min. Sci. **38**, 297–310 (2001)
3. Bui, T., Wong, H., Deleruyelle, F., Zhou, A., Lei, X.: A coupled poroplastic damage model accounting for cracking effects on both hydraulic and mechanical properties of unsaturated media. Int. J. Numer. Anal. Methods Geomech. **40**, 625–650 (2016)
4. Coussy, O.: Poromechanics. Wiley, Chichester (2004)
5. Ju, J.W.: On energy-based coupled elastoplastic damage theories : constitutive modeling and computational aspects. Inter. J. Solids Strucut. **25**(7), 803–833 (1989)
6. Shao, J.F.: Poroelastic behaviour of brittle rock materials with anisotropic damage. Mech. Mater. **30**, 41–53 (1998)
7. Durner, W.: Hydraulic conductivity estimation for soils with heterogenous pore structure. Water Resour. Res. **30**(2), 211–223 (1994)
8. Mualem, Y.: A new model for predicting the hydraulic conductivity of unsaturated porous media. Water Resour. Res. **12**, 513–522 (1976)
9. Maleki, K.: Modélisation numérique du couplage entre l'endommagement et la perméabilité des roches. Application à l'étude des ouvrages de stockage souterrain, Thèse de Doctorat, ENPC, Paris, France (2004)

10. Arson, C., Pereira, J.M.: Influence of damage on pore size distribution and permeability of rocks. Int. J. Numer. Anal. Methods Geomech. **37**(8), 810–831 (2013)
11. Schaap, M., Leij, F.: Improved prediction of unsaturated hydraulic conductivity with the mualem-van genuchten model. Soil Sci. Soc. Am. J. **64**, 843–851 (2000)
12. Chiarelli, A.S.: Etude expérimentale et modélisation du comportement mécanique de l'argilite de l'est, Thèse de doctorat, Université Lille I, Lille (2000)
13. Gerard, P., Charlier, R., Barnichon, J.D., Su, K., Shao, J.F., Duveau, G., Giot, R., Collin, F.: Numerical modelling of coupled mechanics and gaz transfer around radioactive waste in long-term storage. J. Theor. Appl. Mech. **38**(1–2), 25–44 (2008)

# Jet Grouting Mitigating Settlement of Bridge Approaching Embankments of Tam Bang and Vam Dinh Bridges

Hoang-Hung Tran-Nguyen and Chuong Hong Quach(✉)

Department of Bridge and Highway Engineering, Faculty of Civil Engineering, Ho Chi Minh City University of Technology, Ho Chi Minh, Vietnam
tnhhung@hcmut.edu.vn, bachlong20062003@yahoo.com

**Abstract.** Large differential settlement (e.g., >30 mm) of bridge approaching embankments behind abutments in service has caused difficult travel for vehicles. The current techniques to reduce large settlements such as pavement refilled are still ineffective and less sustainable. Jet Grouting has high potential application to treat large settlements but has limit applications. This paper attempted applying the Jet Grouting to reinforce bridge approaching embankments in Vietnam. The Tam Bang and Vam Dinh bridges on the DT852 highway in Dong Thap province were investigated and reinforced using the Jet Grouting technology. The primary consolidation settlement analysis indicates that (1) the Jet Grouting technology has full capacity of mitigating large differential settlements of the Tam Bang and Vam Dinh bridges, (2) The proposed solutions can gain public trust, (3) Jet Grouting technology has high potential applications to reinforce differential settlement of bridge abutments in the Mekong Delta.

**Keywords:** Soilcrete · Jet Grouting · Deep mixing method · Settlement · Ground improvement · Bridge embankment · Abutment

## 1 Introduction

Bridge approaching embankments serve smooth travel between a road and a bridge. A 5-m area of a bridge abutment has often occurred large differential settlements such as 30 mm or more in Vietnam, particularly in the Mekong Delta – the Southern Vietnam which rests on thick soft ground layers. Large differential settlements of bridge abutments have caused difficult travel for vehicles (Phan 2015). A survey of almost all bridges in Dong Thap province which is one of thirteen provinces in the Mekong Delta showed that large differential settlements have taken place. Differential settlements were also observed at bridges in other provinces in the Mekong Delta. Large differential settlements have produced negative reactions from the community.

Several research (Phan 2015) reported that many reasons have caused large differential settlements in the Mekong Delta. The key factor is a thick soft clay layer (e.g., >=10 m) underneath bridge approaching embankments. Almost all soft ground layers beneath bridge approaching embankments on highways connecting districts of a

© Springer Nature Singapore Pte Ltd. 2018
H. Tran-Nguyen et al. (eds.), *Proceedings of the 4th Congrès International de Géotechnique - Ouvrages -Structures*, Lecture Notes in Civil Engineering 8,
DOI 10.1007/978-981-10-6713-6_73

province in the Mekong Delta have not been often reinforced. Approaching slabs have not been often installed behind bridge abutments.

The local authorities have tried to apply various techniques such as pavement refill or reconstruction to treat large differential settlements but the current techniques are still temporary and ineffective. Jet Grouting technology has high potential application to treat large differential settlements of bridge approaching embankments. Jet Grouting which is one of the soil cement deep mixing technologies can create soil-cement columns or soilcrete columns using high pressure beams (20–60 MPa) to cut, to erode the in-situ soils, and to mix the disturbed soils with cement slurry. The Jet Grouting can reinforce soil layers below the ground surface and preserve the surface layer. The Jet Grouting is not widely used for highway projects even thought the Jet Grouting was first applied in Vietnam in 1999 (Tran Nguyen 2016). Tran-Nguyen et al. (2016, 2014, 2013) conducted a research of modifying a used Jet Grouting system and performed several field pilot tests in Ho Chi Minh City (HCM). Soilcrete diameters varied from 0.8 m to 1.7 m for the HCM's geological conditions (Tran-Nguyen et al. 2013).

This paper proposed to apply the Jet Grouting technology to reinforce bridge approaching embankments in service to mitigate large differential settlement. Applying Jet Grouting to treat large differential settlement is still a new idea in Vietnam. Therefore, the two solutions were proposed and designed to treat the approaching embankments of Vam Dinh and Tam Bang bridges in service in Dong Thap province. The Vam Dinh and Tam Bang bridges have been in service over 6 years, and large differential settlements have been in progress. The local authority refilled the pavement periodically which is every 8–12 weeks. Thus, the local authority has search for new innovative technologies to treat the settlement effectively and sustainably. The recommending solutions were based on the laboratory study (Quach 2016). The solutions are expected that the large differential settlements at the Vam Dinh and Tam Bang bridges will be less than 30 mm after 5 years treated, or the pavement only refilled in every 5-year period during next 15 years in service. This study is the basics for field experiments.

## 2 Implementation

### 2.1 Methods

Consolidation settlement and settlement at time before and after reinforcement were analyzed (22TCN262-2000 and Das 2011). Several bridge embankment cross-sections behind an abutment were used to model for settlement analysis. Settlement was investigated along the profile of the road surface.

### 2.2 Settlement Analysis

(a) Primary consolidation settlement before reinforcement

Primary consolidation settlement before reinforcement was analyzed using Eqs. (1) and (2) (22TCN262-2000; Das 2011).

For OCR = 1:

$$S_c = \sum_{i=1}^{n} \frac{H_i}{1+e_0^i}\left[C_c^i \log\frac{\Delta\sigma^i + \sigma_0^i}{\sigma_0^i}\right] \quad (1)$$

For OCR > 1:

$$S_c = \sum_{i=1}^{n} \frac{H_i}{1+e_0^i}\left[C_c^i \log\frac{\Delta\sigma^i + \sigma_0^i}{\sigma_0^i} + C_r \log\frac{\sigma_c^i}{\sigma_0^i}\right] \quad (2)$$

where OCR – over-consolidation ratio of a soil layer $i$, $S_c$ – primary consolidation settlement (m), $H_i$, $e_0^i$, $C_c^i$, $C_r^i$ - thickness each soil layer (e.g., <=2 m), initial void ratio, compression index, swell index of layer $i$, $\sigma_0^i$, $\Delta\sigma^i$, $\sigma_c^i$ - overburden stress, increase pressure, preconsolidation pressure of a soil layer $i$, respectively.

(b) Primary consolidation settlement after reinforcement

After reinforced, a soft clay layer is separated into two layers: a reinforced layer with soilcrete columns above and a unimproved layer beneath (Kitazume and Terashi 2013; Tran Nguyen Hoang Hung 2016). The strain at failure of soilcrete material is small and varies from 1% to 3%. Soilcrete secant modulus of elasticity is usually higher 100 times than that of the soft clay (Tran-Nguyen et al. 2014). In addition, soilcrete permeability is low and around $10^{-9}$ m/s (Kitazume and Terashi 2013). In other word, primary consolidation settlement of the reinforced layer is believed to be insignificant or negligible. On the other hand, primary consolidation settlement of unimproved soft clay layer underneath is considered main factor to cause the settlement of an embankment after the reinforcement. The consolidation settlement can be determined using on the linear or elastic stress distribution theory (Tran Nguyen 2016). The embankment pressure is totally transferred to the unimproved soft clay layer and the primary consolidation settlement was analyzed using Eqs. (1) and (2).

(c) Settlement at time

According the Vietnam Code, the asphalt pavement of a highway has a 15-year life cycle, and the pavement will be replaced. Thus, settlement at the road surface is mainly primary consolidation settlement and it is important to observe time rate of settlement of the road surface during the first 15 years in service. The time settlement of primary consolidation is computed using Eq. (3):

$$S_t = U \,.\, S_c \quad (3)$$

where $S_t$ - settlement at time, $S_c$ – the total settlement of primary consolidation, $U$ – average degree of consolidation, $T_v$ - Time factor determined by (Das 2011 or 22TCN262-2000).

(d) Scale of differential settlement of bridge approaching embankment, $\Delta S$

Degree of differential settlement may cause uneven travel for vehicles on a highway. Phan (2015) proposed the three scales of differential settlements as following:

- Normal for $\Delta S \leq 30$ mm: vehicles can travel smoothly for a maximum speed of 60 km/h.
- Warning for $30 < \Delta S < 70$ mm: all vehicles can travel at a speed of 60 km/h with strong shock.
- Impact for $\Delta S \geq 70$ mm: all vehicles have to slow down at a maximum speed of 30 km/h with strong shock.

The 22TCN262-2000 requires that the total accumulated settlement of bridge approaching embankments shall be less than 0.2 m after 15 years in service for highways with an allowance speed of 60 km/h.

### 2.3 Parameters for Reinforcement Design

The soilcrete properties created by the Jet Grouting technology need to design to mitigate differential settlement appropriately. The designed soilcrete parameters consist of diameter $D$, column spacing $S$, required strength $q_{uyc}$, and reinforced depth $H_r$.

(e) Required soilcrete strength, $q_{uyc}$

Required soilcrete strength has to tolerate directly the embankment pressure (Eq. 4) (Kitazume and Terashi 2013).

$$q_{uyc} \geq F_s \frac{\gamma_e H_e}{as} \tag{4}$$

where $q_{uyc}$ (kN/m$^2$) – required soilcrete strength, $FS$ – factor of safety, $FS$ = 1–1.2, $H_e$ – embankment height (m), $\gamma_e$ – unit weight of embankment fill (kN/m$^3$), $as$ – replacement ratio by Eq. (5)

$$as = \frac{n \times A_c}{B \times L} \tag{5}$$

where: $n$ – total soilcrete columns in a reinforced area, $A_c$ (m$^2$) – Area of a soilcrete column, $B$ and $L$ (m) – dimensions of a reinforced area.

(f) Soilcrete column depth, $H_r$

$H_r$ is determined to meet the requirement of the total differential settlement of bridge approaching embankment of 0.2 m after the first 15 years in service (22TCN262-2000). Thus, $H_r$ may less than the thickness of a soft clay layer below an embankment, and maintains differential settlements of 30–50 mm per every 5-year period.

## 3 Research Site

Tam Bang bridge (km 10 + 891) and Vam Dinh bridge (km 10 + 620) on the DT852 highway in Dong Thap province were chosen for this study (Fig. 1). The Tam Bang bridge has the backfill height of 3.2 m at the abutments and the backfill height of 2.8 m at the Vam Dinh abutments. The bridges have been in service for 6 years and large differential settlements of 50–100 mm have taken place about every 12-week period. The authority has to refill pavement to maintain the normal service of the highway.

**Fig. 1.** The Tam Bang and Vam Ding bridges in Dong Thap province (Google maps)

The two 30-m boreholes were drilled to investigate geological conditions at the Tam Bang and Vam Dinh bridges, respectively. The soil properties along the soil profiles were given in Table 1.

**Table 1.** The soil properties along the 30-m soil profiles at the Tam Bang and Vam Dinh bridges (LAS XD475 2016)

| | Soil layer | Thickness (m) | Unit weight $\gamma_w$ (kN/m$^3$) | Initial Void ratio $e_0$ | Compression index $C_c$ | Swell index $C_r$ | Coefficient of consolidation $c_v$ (m$^2$/s) | Preconsolidation pressure $\sigma_p$ (kPa) |
|---|---|---|---|---|---|---|---|---|
| Tam Bang bridge | Surface layer | 1 | - | - | - | - | - | - |
| | Very soft clay | 10 | 16.5 | 1.42 | 0.426 | 0.144 | $1.9 \times 10^{-12}$ | 80 |
| | Soft clay | 12 | 16.8 | 1.29 | 0.349 | 0.140 | $2.1 \times 10^{-12}$ | 87 |
| | Medium stiff clay | >7 | 17.6 | 1.02 | 0.231 | 0.105 | $1.8 \times 10^{-12}$ | 90.6 |
| Vam Dinh bridge | Surface layer | 3.6 | 20.4 | - | - | - | - | - |
| | Medium still clay | 3.6 | 18.4 | 0.98 | - | - | - | - |
| | Very soft clay | 6 | 16.2 | 0.15 | 0.533 | 0.170 | $2.4 \times 10^{-12}$ | 68 |
| | Soft clay | 7.8 | 16.2 | 0.15 | 0.527 | 0.152 | $1.9 \times 10^{-12}$ | 102.8 |
| | Fine sand | >9 | 19 | 0.75 | - | - | - | - |

# 4 Results

## 4.1 Primary Consolidation Settlement Before Reinforcement

Over 10 embankment cross-sections behind the abutments of the Tam Bang and Vam Dinh bridges were used to analyze the primary consolidation settlements without reinforcement. Figure 2 shows variations of the total primary consolidation settlements and the 15-year primary consolidation settlements with heights of the embankments. The results display that differential settlements behind the abutments were higher than the allowance settlement (22TCN262-2000).

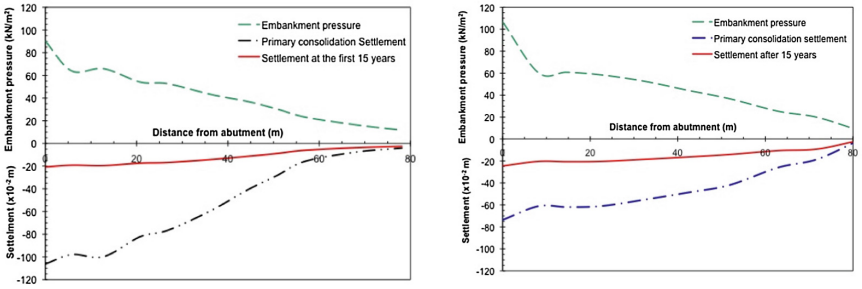


(a). Tam Bang bridge (b). Vam Dinh bridge

**Fig. 2.** The analyzed primary consolidation settlements without reinforcement at the Tam Bang and Vam Dinh bridges

Figure 3 demonstrates the measured elevations of the embankments behind the abutments of the Tam Bang and Vam Dinh bridges in 2015 and the original designed elevations (2009) of the embankments at the centerline. The pavements of the bridge approach embankments were refilled before the measurements.

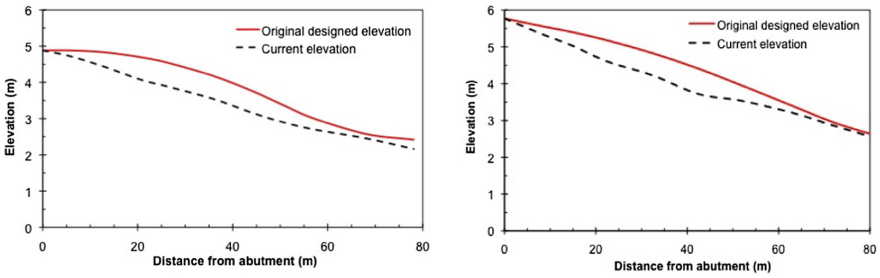


(a). Tam Bang bridge (b). Vam Dinh bridge

**Fig. 3.** The measured elevations (2015) and the original designed elevations (2009) of the embankments of the bridges

### 4.2 The Proposed Reinforcement Solutions

(a) The lengths of the reinforcement sections

Based on the field observation and survey, a length of 15 m behind an abutment has occurred large settlements. In addition, Fig. 2 exhibits the settlements of this 15-m section were significantly higher than the requirement. Therefore, the proposed reinforcement was designed for the first 15 m long sections behind abutments.

(b) Designed soilcrete parameters

Based on the field measurement, large differential settlements of 5-m areas of bridge embankments behind abutments have often developed with time and caused difficult travel. Therefore, reinforcement sections are mainly performed in the 5-m areas behind abutments. The soilcrete parameters were designed using a trial-and-error procedure until large differential settlements meet the requirement during the first 15 years in service. According to the previous research (Tran Nguyen 2016; Tran-Nguyen et al. 2016, 2014, 2013; Tran-Nguyen and Nguyen 2013), the soil properties, the embankment pressure, and the settlement analysis, the reinforced parameters were proposed to be a column diameter of 1 m, strength of 0.5 MPa, an average reinforced depth of 10 m, a replacement ratio of 0.2, and a reinforced width of 9 m. Figures 3, 4 show the detail design reinforcement plans for the Tam Bang and Vam Dinh bridges, respectively (Fig. 5).

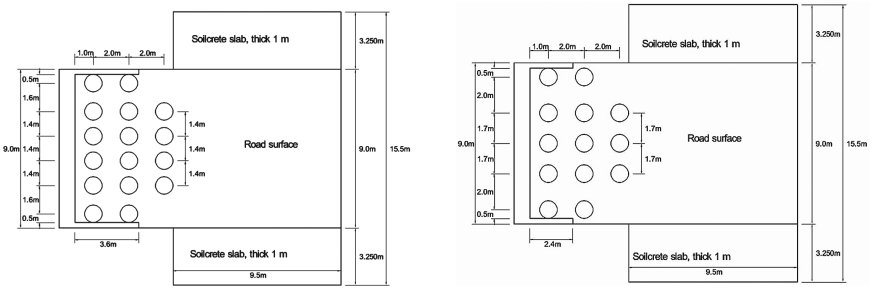


(a). Tam Bang bridge (b). Vam Dinh bridge

**Fig. 4.** The plan views of the reinforcements of Tam Bang and Vam Dinh bridges

### 4.3 Primary Consolidation Settlements After Reinforced

Figure 6 presents the reinforcements reduced the settlements at the both bridges. The results indicate that the designed reinforcements using the Jet Grouting technology diminished the primary consolidation settlements of the bridge embankments meeting the requirement of the 22TCN262-2000 which is less than 0.2 m.

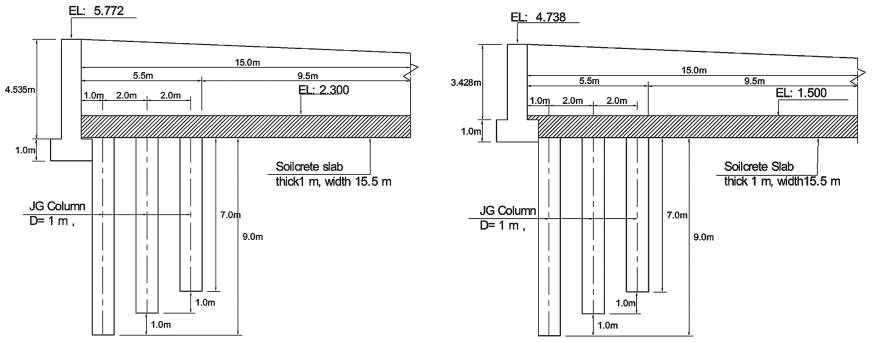


(a). Tam Bang bridge (b). Vam Dinh bridge

**Fig. 5.** The profiles of the reinforcements of Tam Bang and Vam Dinh bridges

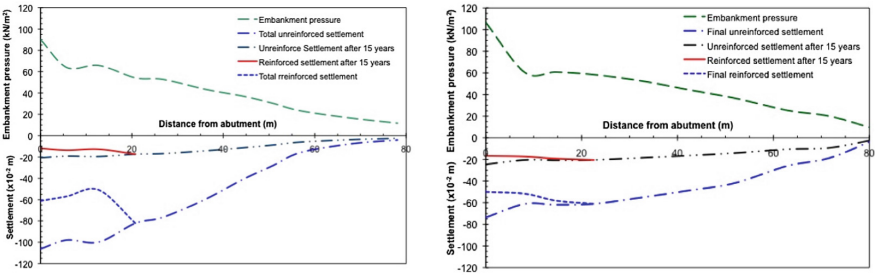


(a). Tam Bang bridge (b). Vam Dinh bridge

**Fig. 6.** The settlements after the bridge approaching embankments reinforced using the Jet Grouting technology

## 4.4 Time Rate Settlement

Figure 7 exhibits the results of the time rate of primary consolidation settlement analysis after the reinforcement using the Jet Grouting technology. It is noted that the total settlement of bridge abutments shall be less than 0.2 m for the first 15 years in service (22TCN262-2000).

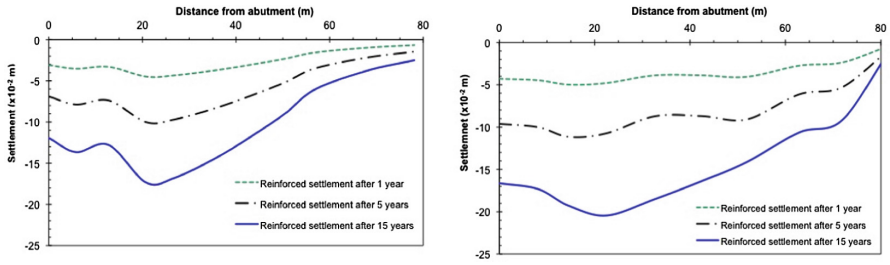


(a). Tam Bang bridge (b). Vam Dinh bridge

**Fig. 7.** The time rate of primary consolidation settlement after the both bridges reinforced

# 5 Discussions

## 5.1 Settlement Versus Reinforcement

The target of the reinforcement was the differential settlements within 0.2 m for the 15 years in service (22TCN262-2000). The proposed solutions have just met the requirement for the Tam Bang bridge and reduced the settlement significantly for the Vam Dinh bridge (Figs. 6, 7). The results indicate that the Jet Grouting technology can reinforce the bridge approaching embankments successfully.

## 5.2 Time Rate of Primary Consolidation Settlement

Accumulated differential settlements of 30 mm or more occurring only in every 5-year period have proved the effectiveness of the reinforcement solutions. Without the reinforcements, large differential settlements of 50 mm have taken place in every 3-month period. The authority has to refilled pavement every 3 months to maintain the normal service for the highway. After the reinforcements, the authority only refills the pavement every 5 years. The 5-year period of maintenance lessens negative reactions from the community and reduces the maintenance cost.

## 5.3 Smooth Travel After the Reinforcements

After the reinforcements, the reinforced sections retain differential settlements of 30 mm or less in every 5-year period. The adjacent unreinforced sections still settle due to consolidation but settlement is uniform along the road and the settlement transfers smoothly in the longitudinal direction. In other word, the bridge differential settlement is maintained at the scale “Normal”. For highways connecting areas within a province with the allowance speed of 60 km/h, differential settlement of 30 mm or less keeps a highway serving properly.

## 5.4 Potential Practical Applications

An investigation on large differential settlements of bridge approaching embankments at the 135 bridges in the Southern Vietnam from 2002 to 2011 reported that almost all bridges have occurred large differential settlements behind abutments (Phan 2015). The refilling pavement technique is widely applied to treat large settlements. This study recommends that the Jet Grouting technology has high practical applications to diminish large differential settlements in Vietnam.

# 6 Conclusions

The over 10 bridge embankment cross-sections of the Tam Bang and Vam Dinh bridges were used to analyze primary consolidation settlement and time rate of primary consolidation without and with the reinforcements using the Jet Grouting technology. The soilcrete properties have the designed strength of 0.5 MPa, the diameter of 1 m,

the replacement ratio of 0.2, the average depth of 10 m, and the reinforced length of 5 m. The results suggest that (1) the large differential settlements were successfully treated for the first year. (2) The pavement is refilled in every 5-year period instead every 3 months. (3) The total settlements meet the 22TCN262-2000's requirement during the first 15 years in service. (4) The Jet Grouting technology can apply massively to mitigate large differential settlements of bridge embankments in the Mekong Delta.

**Acknowledgement.** The authors acknowledge Dong Thap Department of Science and Technology funding for the research and Ho Chi Minh City University of Technology has supported significantly during the research implementation.

## References

Phan, B.Q: Some techniques to treat difficult travel for vehicles due to large differential settlements of bridge approaching embankments in the Mekong Delta. Ph.D. dissertation, Institute of Science and Technology for Transport, Hanoi, Vietnam, 126 p. (2015). (in Vietnamese)

Das, B.M.: Principles of Geotechnical Engineering. Cengage Learning, Boston (2011). 666 p.

Kitazume, M., Terashi, M.: The Deep Mixing Method. Taylor & Francis Group, London (2013). 405 p.

Las XD475: Report on soil investigation for the Jet Grouting research project in Dong Thap province, 60 p. (2016). (in Vietnamese)

Quach, C.H., Tran Nguyen, H.H.: Mechanical behaviors of soilcrete created from soils of Tam Bang and Vam Dinh bridges simulating jet grouting technology. Geotech. J. **2**, 42–51 (2016). (in Vietnamese)

Ministry of Construction: Soft ground improvement – Soil cement mixing technology. Vietnam Code: TCVN 9403:2012, 42 p. (2012). (in Vietnamese)

Ministry of Transport: Survey and design of highway embankments on soft ground. Vietnam Code: 22TCN262-2000, 45 p. (2000). (in Vietnamese)

Tran Nguyen, H.H.: Jet Grouting Technology. Vietnam National University in Ho Chi Minh City, Ho Chi Minh City (2016). 368 p. (in Vietnamese)

Tran-Nguyen, H.H., Le, K.B., Le, P.L.: Behaviors of field soilcrete created by a light-weight equipment system to reinforce an earth levee in Vietnam. Malays. J. Civ. Eng. **28**(1), 91–107 (2016)

Tran-Nguyen, H.H., Le, T.T., Ly, T.H.: A field trial study on jet grouting to improve the subsoil in HCM City in Vietnam. J. Teknol.: Sci. Eng. **69**, 23–29 (2014)

Tran-Nguyen, H.H., Le, T.T., Ly, T.H.: Soilcrete characteristics created by a single jet grouting system in Ho Chi Minh City. In: Proceedings of the 2nd International Conference on Geotechnics for Sustainable Development, pp. 465–474, Hanoi, 28–29 November 2013 (2013)

Tran-Nguyen, H.H., Nguyen T.T.B.: Effect of soilcrete characteristics on surface settlement during tunneling in Vietnam. Malays. J. Civ. Eng. **25** Special Issue (1), 25–39 (2013)

# Laboratory Study of Local Clay-Pile Friction Evolution for Large Numbers of Cycles

Rawaz Dlawar Muhammed[1,2,3(✉)], Jean Canou[1], Jean-Claude Dupla[1], and Alain Tabbagh[2]

[1] Ecole Des Ponts ParisTech, Laboratoire Navier, Université Paris-Est, Champs-Sur-Marne, Ile-de-France, France
{rawaz.muhammed, jean.canou, jean-claude.dupla}@enpc.fr
[2] Université Pierre et Marie Curie, Paris, Ile-de-France, France
alain.tabbagh@upmc.fr
[3] Koya University, Koya, Erbil, Iraq

**Abstract.** This work aims at investigating the evolution of local friction mobilized at the pile-soil interface, focusing on small amplitude and large number of displacement controlled cycles, corresponding to fatigue behaviour (10^5 cycles). An experimental program has been conducted in a calibration chamber with an instrumented pile-probe installed and loaded in reconstituted specimens of saturated clay.

After describing the testing setup and the experimental procedure, a typical test is presented, carried out on a reference French kaolinite to evaluate the local friction mobilized upon different monotonic loadings and its evolution during the application of displacement-controlled cyclic loading. Quasi-static displacement-controlled compression tests are carried out before and after the cyclic sequence in order to evaluate the influence of the cyclic sequence on the mobilized static local friction after cycles, as compared to the initial friction mobilized. The displacement-controlled cyclic test allows to observe an initial phase of friction degradation which starts progressively from the very beginning of the cyclic sequence (cyclic softening), followed by a stabilization phase until the end of the test. The evolution of mobilized friction during the application of the cycles is quantified by introducing a coefficient of evolution which allows to clearly visualize the degradation and reinforcement phases. The local shaft friction evolution, upon the cyclic loading, is interpreted in terms of the combination of excess pore water pressure generation and dissipation which develops during the cyclic sequence and controls the evolution of effective normal stress acting on the soil-pile interface. A comparison is made between maximum static shear mobilized before the cycles and after the cycles, showing a clear influence of the cyclic sequence on this quantity. Finally, the repeatability of the test is checked, showing a fairly good level of repeatability.

**Keywords:** Pile · Local shaft friction · Cyclic loading · Saturated clay · Physical modelling · Calibration chamber · Instrumented pile-probe · Excess pore water pressure

© Springer Nature Singapore Pte Ltd. 2018
H. Tran-Nguyen et al. (eds.), *Proceedings of the 4th Congrès International de Géotechnique - Ouvrages -Structures*, Lecture Notes in Civil Engineering 8,
DOI 10.1007/978-981-10-6713-6_74

# 1 Introduction

The study of the local soil-pile friction constitutes an important issue in geotechnical engineering related to the improvement in the design of piles. Despite the progress that has been made in the last decades, the friction behaviour still remains complex, particularly in the case of cyclic loadings, and still requires additional theoretical and experimental researches.

In the experimental point of view, the physical modelling approach, based on the use of calibration chambers, seems to be particularly interesting to better understand, under well-controlled laboratory conditions, the mechanisms of interface friction mobilization under static and cyclic axial loading. Since the early 1980s, an important number of experimental researches has been developed in this field, often in relation to the offshore petroleum industry and a significant number of results, have been presented by using of different types of probes tested in different types of soil specimens. Most of previous researchers (e.g., [1, 3–7, 9, 10]) studied friction mobilization only for small to medium number of loading cycles and observed a degradation of this last throughout laboratory and in-situ experiments. However the real solicitations acting on a pile can reach several hundred thousand of repeated cycles. One can give foundations of offshore structures, railway bridges …etc. as an example, hence the need to study friction mobilization for large number of loading cycles. In the case of coarse grained soils, Bekki [2] have presented results concerning the evolution of local friction along an instrumented pile-probe jacked into a sand specimen reconstituted in a calibration chamber, for large numbers of displacement-controlled cycles ($10^5$ cycles). The auteur showed that after an initial degradation phase of the local skin friction a reinforcement phase develops up to very high number of cycles. However, for the case of fine-grained soils, typically saturated clays, no publication has been found on the subject in the literature.

The present work therefore describes a complete laboratory prototype setup and a specific experimental procedure, of physical modelling approach, which have been developed to study the local friction behaviour of soil-pile interface submitted to very large numbers of axial loading cycles, in the case of reconstituted saturated clay.

# 2 Used Material, Testing Equipment and Procedure

## 2.1 Kaolinite Speswhite

The material used throughout this study was a specific kaolinite clay called Speswhite. It has a white color and is considered as a reference clay in France, especially, for testing reconstituted specimens in centrifuges and calibration chambers. Table 1 lists some of the geotechnical properties of this clay.

**Table 1.** Physical properties of Speswhite kaolinite

| Mineralogy | Liquid limit (%) | Plastic limit (%) | Plasticity index (%) | Soil particle density (t/m$^3$) | Percent. finer than 10 μm (%) |
|---|---|---|---|---|---|
| kaolinite | 58 | 28 | 30 | 2,64 | 98 |

## 2.2 Testing Equipment and Procedure

Loading tests were performed in the calibration chamber of Navier laboratory (Fig. 1) which can hold soil specimens of 524 mm in diameter and 700 mm high. Independent vertical and horizontal stresses may be applied to the specimens, allowing to generate isotropic or anisotropic initial states of stress, $K_0$ conditions, etc. The chamber itself is incorporated in a guiding and loading mechanical framework allowing the chamber to be moved and adjusted in translation and rotation on a rail track system, as shown in the Fig. 1. The four columns loading frame is equipped with two hydraulic jacks:

- a long stroke (1 m) 100 kN standard jack, equipped with a force transducer and a "wire" displacement transducer, of displacement-controlled type (displacement range 0.1 to 100 mm/s), used typically for installation of probes, penetrometer testing, etc.;
- a servocontrolled hydraulic actuator, equipped with a ± 100 kN precision force transducer and integrated precision LVDT (± 75 mm displacement range) for vertical displacement measurement, which allows to perform precise monotonic and cyclic tests of force or displacement-controlled type.

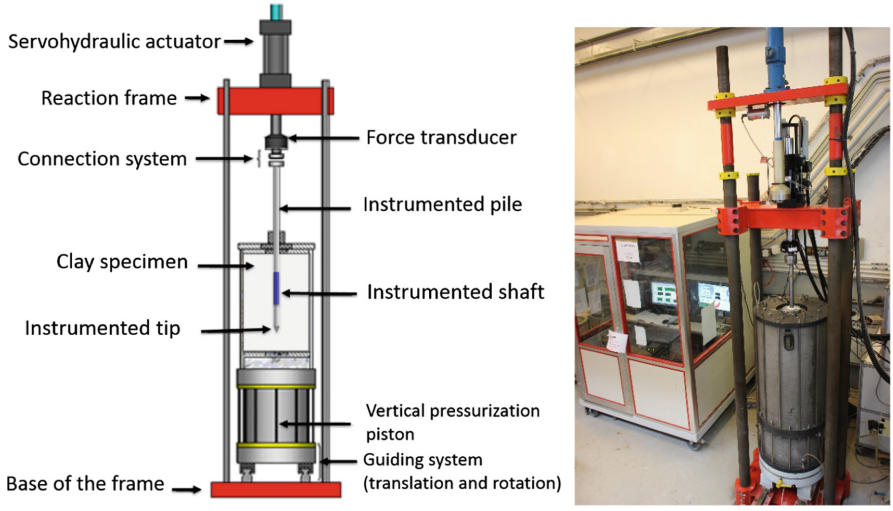


**Fig. 1.** Functional scheme and overall view of the experimental setup including the control and data acquisition booth

For the specimen reconstitution, a big size consolidometer is developed which allows to reconstitute, starting from a soil slurry, saturated clay specimens of 524 mm diameter and 600 to 800 mm high under $K_0$ conditions (no lateral deformation during the consolidation process). The consolidometer is composed of two adjustable halves of Plexiglas tube and equipped with a top and bottom draining plates. A loading frame

composed of double-action hydraulic jack allows to consolidate the specimen by application of constant force increments to the top plate (Fig. 2a and b). The hydraulic jack is powered by a hydro-pneumatic pump which allows to apply controlled pressure steps to the jack. Figure 2 shows an overall view of the consolidation set-up. Once the targeted consolidation value of the clay massif is achieved, the specimen is unmolded and placed in the calibration chamber and re-subjected to stress by means of the horizontal and vertical pressurization systems of the device. It is then possible to install and load the pile probe.

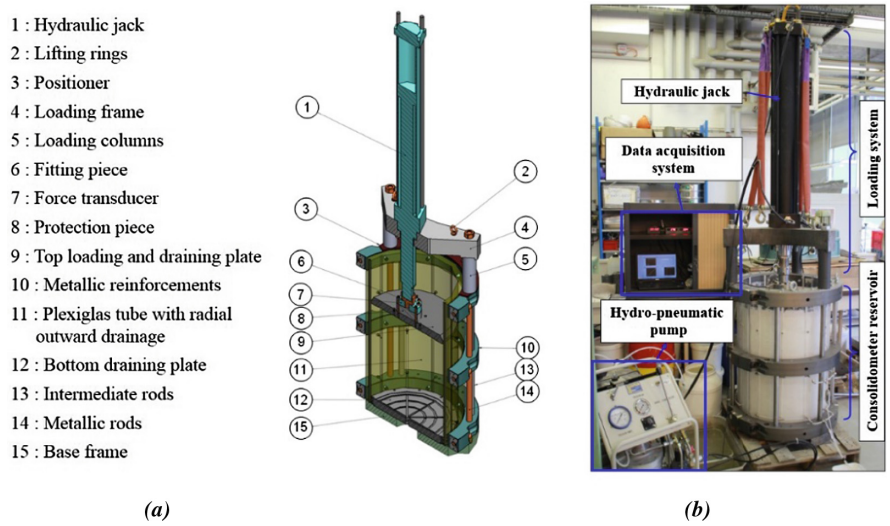


**Fig. 2.** Consolidometer set up and ancillary equipment: (a) 3-D drawing showing one half of the consolidometer, (b) Overall view of the consolidometer set up and ancillary equipment

The used probe is a prototype type that has been developed to make direct and independent measurements of tip resistance and local shaft friction representative of values occurring along a pile shaft. Figure 3 shows a simplified cross section together with a view of the probe. The probe has a cross section of 10 $cm^2$ (diameter of 36 mm), similar to standard penetrometers.

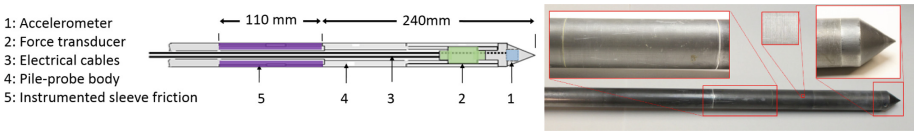


**Fig. 3.** Simplified cross-section and view of the instrumented pile-probe

# 3 Typical Results

## 3.1 Clay Specimen Characteristics

The initial consolidation of the specimen has been achieved in five steps, by using the developed consolidometer, corresponding to successive vertical stresses of 5, 15, 45, 125 and 250 kPa. The clay specimen has been then placed in the calibration chamber and submitted to a final vertical effective stress $\sigma'_{v0}$ of 250 kPa and a final effective horizontal stress $\sigma'_{h0}$ of 150 kPa corresponding to an estimated value of $K_0$ equal to 0.6. The permeability and consolidation coefficient of the clay under this state of stress have been determined based on oedometer tests, giving $k = 2.7*10^{-9}$ m/s and $c_v = 3.0*10^{-7}$ m$^2$/s.

## 3.2 Installation Phase of the Probe

The probe is installed displacement-controlled with a constant penetration rate of 1 mm/s. Results of tip résistance and local skin friction versus penetration depth of the tip are shown in the Fig. 4a and b. The tip résistance starts to mobilize rapidly and reaches a stabilized value after 140 mm of pile head penetration. The local friction, for its part, starts to mobilize once the sleeve friction gets into the soil specimen at about 250 mm of penetration depth after which it increases progressively and reaches an almost stabilized value. This stabilization of tip resistance and local skin friction values accounts for the soil homogeneity within the reconstituted specimen and thus validates the preparation method.

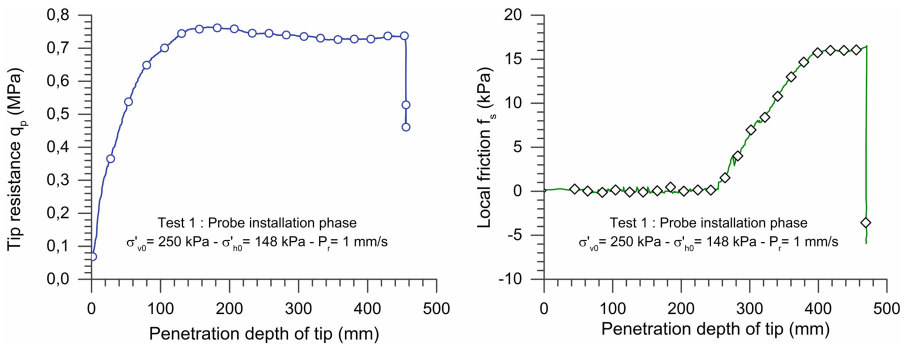


**Fig. 4.** Installation phase: (a) tip resistance versus penetration depth, (b) local friction versus penetration depth

During different loading stages of the test, results of tip resistance, local friction and total head load are recovered continuously. Only the results of local friction evolution, upon different static and cyclic displacement-controlled tests, are discussed in this paper.

### 3.3 Pre-cyclic Static Tests

Once the installation stage of the probe has been achieved, the probe is completely unloaded and left for about 12 h. This time is of great importance for the dissipation of the excess pore-water pressures, generated within the soil around the face and shoulder of the cone during the installation phase. Two pre-cyclic static compression tests were then performed at two different rates. The first static test being performed at 30 μm/min and the second one at 300 μm/min. A very rapid mobilization of local friction, followed by a plateau was obtained in both cases (about 34 kPa). It is interesting to note that the results obtained in terms of failure characteristics are very similar for both tests and that the second loading is not significantly affected by the first one (Fig. 5).

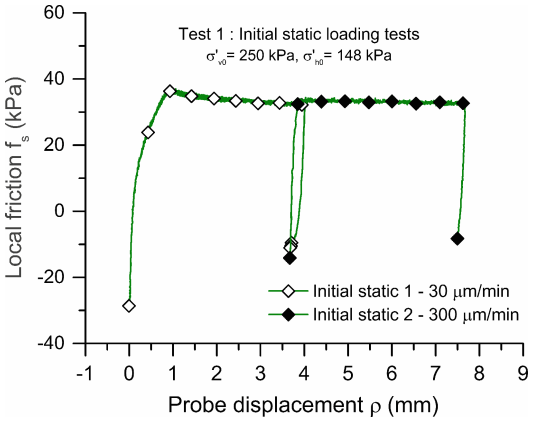


**Fig. 5.** Evolution of local friction upon initial static loading tests

### 3.4 Displacement Controlled Cyclic Sequence

In order to study the local friction mobilization during the application large number of cycles, displacement-controlled cyclic loading has to be realized. The key parameters of this type of cyclic tests are the displacement amplitude (alternated or non-alternated signal), the signal shape, the frequency of the signal and the number of cycles. Figure 6 presents the results corresponding to this cyclic test in which $10^5$ cycles have been applied with a cyclic displacement amplitude $\rho_c$ equal to ± 250 μm (alternated signal) and a frequency of 1 Hz. The shape of the signal is sinusoidal (Fig. 6a). A degradation process is observed from the very first cycle, which keeps going progressively for about $10^4$ cycles, corresponding to cyclic strain-softening of the probe-soil interface. Then, a quasi-stabilization of mobilized friction is observed up to the end of the cyclic sequence.

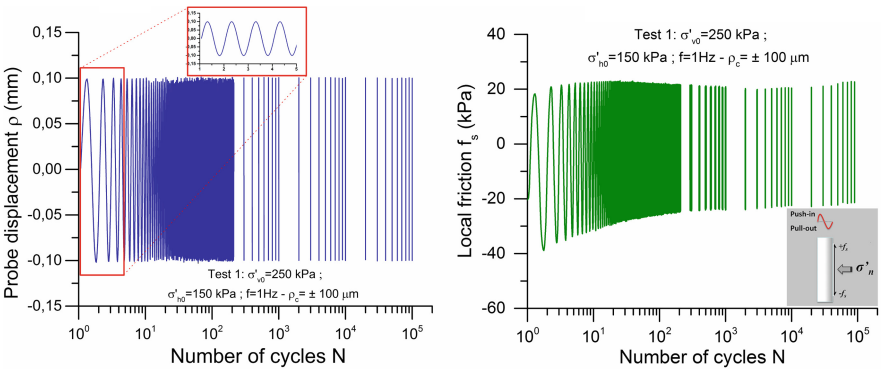


**Fig. 6.** Cyclic loading phase: (a) displacement-controlled loading signal versus number of cycles, (b) tip resistance versus number of cycles, (c) local friction versus number of cycles

In order to better visualize the evolution of local friction mobilization during cyclic loading, a coefficient called coefficient of friction evolution $C_{e,fs}$ (Bekki et al. 2013), has been defined as follows:

$$C_{e,fs} = \frac{f_{s,\max(i)} - f_{s,\min(i)}}{f_{s,\max(1)} - f_{s,\min(1)}} \tag{1}$$

where $f_{s,max(1)}$ and $f_{s,max(i)}$ are the maximum skin friction measured on first cycle and cycle i respectively (push-in phases), $f_{s,min(1)}$ and $f_{s,min(i)}$ being the values of minimum skin friction measured on first cycle and on cycle i respectively (pull-out phases).

This coefficient can easily make a distinction between degradation phases corresponding to a decrease of $C_{e,\,fs}$ and reinforcement phases, corresponding to an increase of this coefficient and to quantify the importance of the degradation or reinforcement with respect to the initial mobilization observed on the first cycle. Figure 7 shows a plot of this coefficient versus number of cycles, which clearly accounts for the progressive degradation phase observed up to cycle n° $10^4$, followed by the stabilization phase toward the end of the cyclic sequence. The minimum value reached is about 0.79 corresponding to a non-negligible degradation (about 21%). This results can be interpreted by the evolution of the effective normal stress acting on the probe shaft, $\sigma'_n$, the local friction mobilized being equal to $f_s = \sigma'_n\ tg\ \delta_{mob}$, $\delta_{mob}$ being the mobilized friction coefficient. During the degradation phase, it's supposed that the excess pore water pressure around the sleeve will progressively increase which results in a progressive decrease in the normal effective stress and corresponding decrease of mobilized friction. It will be of great importance to have direct measurements of the pore water pressure around the probe to further validate this hypothesis.

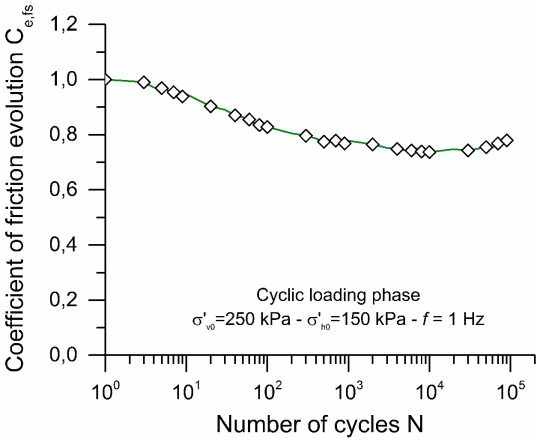


**Fig. 7.** Coefficient of evolution $C_{e,\,fs}$ versus number of cycles for the test presented

### 3.5 Post-cyclic Static Tests

Two post-cyclic tests were conducted to quantify the influence of the cyclic sequence on the static response of the interface. The two final static tests were performed at the same displacement rate of 300 μm/min up to failure (4 mm vertical displacement). The first static test was performed directly after the end of the cyclic sequence while the second one was performed after a resting period of 2 h after the first static test allowing for full drainage of the soil around the probe. A significant difference may be observed between the two loadings. A sharp peak of friction (of about 43 kPa) is obtained for a low displacement (about 250 μm) upon the first loading, followed by a rapid strain softening and a stabilization at an ultimate value of about 29 kPa. For the second loading, no peak is observed and full mobilization of friction is obtained for a very small displacement (about 170 μm) followed by a constant friction plateau of about 29 kPa. This second response is qualitatively very similar to the initial static response observed before the cyclic sequence. It is also interesting to note that the ultimate value of friction obtained at large displacements is very similar for both loadings.

In order to quantify the influence of the cycles on the post-cyclic static response, a skin friction degradation coefficient $D_\tau$ [8], has been defined as follows:

$$D_\tau = \frac{\text{property after cyclic loading}}{\text{property for initial static loading}} \tag{2}$$

It's interesting to note that the calculated value of skin friction degradation $D_\tau(D_\tau = 0.85)$ is relatively close to the value of coefficient of evolution $C_{e,\,fs}$ ($C_{e,\,fs}$ = 0.81) at the end of the cyclic sequence (cycle n° $10_5$) (Fig. 8).

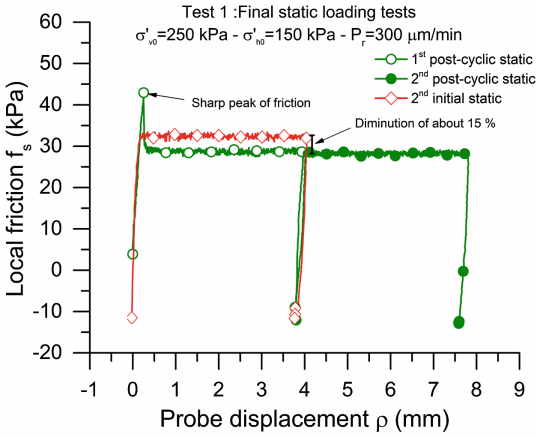


**Fig. 8.** Comparison between the initial and final static load tests in terms of local friction

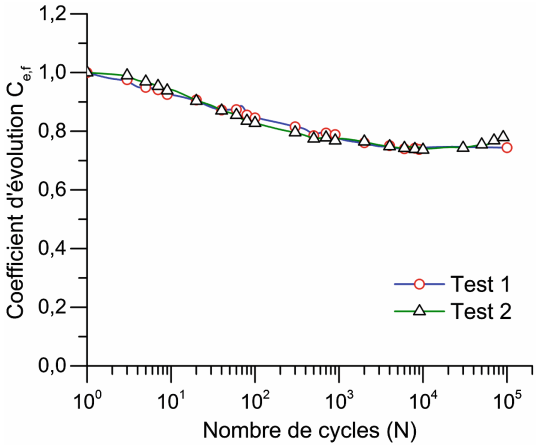


**Fig. 9.** Evaluation of test repeatability in terms of $C_{e,fs}$ coefficient versus number of cycles

### 3.6 Repeatability of the Test

Repeatability of the test was verified by conducting another test (named Test 2) with same testing conditions and parameters as the ones implemented for Test 1. Only results of the cyclic sequence is presented here. Figure 9 shows a comparison of the results obtained in terms of friction evolution coefficient. It may be observed that the trends obtained are qualitatively and quantitatively fairly similar for both tests, accounting for a good level of repeatability of the test in terms of friction evolution.

## 4 Conclusions

A testing setup associated to a specific experimental procedure, corresponding to a physical modelling type of approach, have been presented, in order to study the evolution of mobilized local friction along a pile-probe submitted to large numbers of axial cycles in a saturated clay. The results show, upon the cyclic loading sequence, a progressive phase of degradation of local friction (cyclic strain-softening), which keeps going up to large numbers of cycles, followed by a stabilization phase of the latter until the end of the test. The results also show, in terms of post-cyclic static response, that the application of the cycles will result, with respect to the value obtained before the cycles, in a significant increase of static friction (peak value), however followed by rapid strain-softening. Finally, repeatability tests have been carried out, accounting for a good level of repeatability of the results obtained, therefore validating the testing setup and the experimental procedure developed.

**Acknowledgments.** This work was partly funded by the national French research program SOLCYP, which help is greatly aknowledged.

## References

1. Al-Douri, R.H., Poulos, H.G.: Predicted and observed cyclic performance of piles in calcareous sand. J. Geotech. Eng. ASCE **121**(1), 1–16 (1995)
2. Bekki, H., Canou, J., Tali, B., Dupla, J.-C., Bouafia, A.: Evolution of local friction along a model pile shaft in a calibration chamber for a large number of loading cycles. C. R. Mec. **341**(6), 499–507 (2013)
3. Chan, S.F., Hanna, T.H.: Repeated loading on single piles in sand. J. Geotech. Eng. **106**(2), 171–188 (1980)
4. Chin, J.T., Poulos, H.G.: Tests on model jacked piles in calcareous sand. Geotech. Test. J. **19** (2), 164–180 (1996)
5. Goulois, A., Whitman, R.V., Høeg, K.: Effects of sustained shear stresses on the cyclic degradation of clay. In: Chaney, R.C., Demars, K.R. (eds.) Strength Testing of Marine Sediments: Laboratory and In-situ Measurements. ASTM STP, vol. 883, pp. 336–351. American Society for testing and Materials, Philadelphia (1985)
6. Matlock, H., Bogard, D., Cheang, L.: A laboratory study of axially loaded piles and pile groups including pore pressure measurements. In: Proceeding of the Third International Conference on the Behavior of Offshore Structure (BOSS), vol. 1, pp. 105–121 (1982)
7. Poulos, H.G.: Some aspects of skin friction of piles in clay under cyclic loading. Geotech. Eng. **12**(1), 1–17 (1981)
8. Poulos, H.G.: Cyclic axial loading analysis of piles in sand. J. Geotech. Geoenviron. Eng. **115**(6), 836–851 (1989)
9. Poulos, H.G.: Cyclic axial response of single pile. J. Geotech. Eng. Div. **107**(1), 41–58 (1981)
10. Procter, D.C., Khaffaf, J.H.: Cyclic axial displacement tests on model piles in clay. Géotechnique **37**(4), 505–509 (1987)

# Numerical Modelling of Desiccation Cracking of Clayey Soil by Using Cohesive Fracture Method

Thi Dong Vo[1,2(✉)], Amade Pouya[1], Sahar Hemmati[2], and Anh Minh Tang[1]

[1] Laboratoire Navier (UMR8205), Université Paris Est, Marne-La-Vallée, France
{thi-dong.vo,amade.pouya,anhminh.tang}@enpc.fr
[2] IFSTTAR GERS/SRO, Université Paris Est, Marne-La-Vallée, France
sahar.hemmati@ifsttar.fr

**Abstract.** This paper presents a numerical study on the desiccation cracking process of clayey soils. The initiation and propagation of cracks are investigated using a finite element code including damage-elastic cohesive fracture law to describe the behaviour of cracks. The coupling between the hydraulic behaviour (moisture transfers in the soil matrix and in the cracks) and the mechanical behaviour (volume change of the soil matrix and development of cracks) is also considered in the code. The results of laboratory test performed on a clay soil, taken from the literature review, are used to evaluate the numerical modelling. The results show that the code is able to reproduce the main trends observed experimentally (*i.e.* the shrinkage related to drying, cracks development).

**Keywords:** Unsaturated soil · Evaporation · Desiccation cracking · Cohesive fracture · Damage

## 1 Introduction

Desiccation cracking is a common phenomenon in soils and rocks. It involves a gradual moisture content reduction induced by evaporation from geo-material surface. The reduction of moisture content is accompanied by invading of air in the soil pores, increasing of suction and effective stress, and soil shrinkage. Shrinkage due to the desiccation from the soil surface in restrained condition (by frictional boundary condition, concentration of stress or heterogeneity of soil, *etc.*) induces an increase of tensile stress which generates the formation of cracks network when this stress reaches the tensile strength [1–3]. Due to the hydro-mechanical nature of formation and propagation of desiccation cracks, this process influences various soil properties: changes the permeability of soil, as well as the soil compressibility and decreases the mechanical strength. That could be one of the reasons for the instability of earth structure and becomes now a great challenge in engineering geotechnical domain. The hydro-mechanical coupling is one of the difficulties in the modelling of desiccation cracks that was neglected in various works.

© Springer Nature Singapore Pte Ltd. 2018
H. Tran-Nguyen et al. (eds.), *Proceedings of the 4th Congrès International de Géotechnique - Ouvrages -Structures*, Lecture Notes in Civil Engineering 8,
DOI 10.1007/978-981-10-6713-6_75

In the present work, a hydro-mechanical model is developed to simulate the desiccation cracking of a clayey soil using cohesive fracture method. Damage-elastic behaviour of cohesive fracture [4] was used to model the initiation and propagation of cracks. The FEM code Porofis [5], for POROus FISsured media, is used to simulate the laboratory desiccation tests reported by Sanchez et al. [6]. The results allow investigating not only the evolution of stress, strain and hydric state (suction, degree of saturation) at different locations in the soil specimen, but also the development of cracks during desiccation.

## 2 Gouverning Equations

This section presents briefly the governing equations of hydraulic and mechanical problems, more details can be found in [5, 7]. In the present model, the soil is represented as a homogenous porous medium containing a family of cohesive cracks. The volumetric forces and gravity effects are not considered in this study.

### 2.1 Cohesive Crack Representation

In the Finite Elements Method enriched by Joint elements (JFEM) used here, the cohesive crack elements are represented by 4-nodes interface elements. The joint elements are placed in the mesh on predetermined paths corresponding to potential crack propagation. For the mechanical problem, it is necessary to split the nodes on discontinuity lines and create joint elements in order to allow displacement discontinuities across fractures. But, in the hydraulic problem, at least for the fractures considered here with infinite transversal conductivity, and consequently with continuous pressure across the fracture, there is no need to split the nodes because the pressure has the same value on the two sides of the fracture. The specific mesh for this purpose is prepared with commercial tools GID and DISROC dedicated for meshing fractured media. One of the limitations of cohesive crack method is that the crack locations and pathways need to be predefined. However, this limitation can be addressed by proving a multiple unbiased potential crack with a high density and therefore the spacing between cracks will be minimised. This latter approach is chosen in the current work.

### 2.2 Hydraulic Behaviour

The hydraulic diffusion process in a homogeneous unsaturated porous material representing the soil is simulated. The flow in the soil around the cracks is governed by Darcy's law while the flow in the cracks is governed by the cubic law [8] and they satisfy the mass conservation condition. During desiccation, the suction evolution is related to the degree of saturation by the Van Genuchten model. The equation that allows determining the flow in the soil matrix with an assumption of incompressible fluid can be then written as follows:

$$div\left(\frac{k}{\rho g}\nabla p\right) = C_M \frac{\partial p}{\partial t} + r \tag{1}$$

with $C_M = S\left(\frac{1}{N} + \frac{\phi S'}{S}\right)$, $r = S\frac{\partial \varepsilon_v}{\partial t}$, $k$ is the soil hydraulic conductivity, $g$ is the gravity acceleration, $N$ is the Biot modulus, $S'$ is the derivative $dS/dp$ calculated from the water retention curve.

For the cracks, the transversal conductivity between two crack walls is infinitely high. This implies that the pressure is continuous between two opposite faces of the crack and the pressure takes the same value $p$ for a given point along the crack line. The equation, which allows calculating the pressure for every location $\underline{s}$ along the crack surface, can be written as below:

$$\nabla_s.(c\partial_s p) = r^{mf} + r^f \tag{2}$$

where $r^{mf} = \|\underline{v}\|.\underline{n}$; $r^f = \frac{\partial e}{\partial t}$,

In this equation, $\nabla_s.()$ designates the divergence in the crack. The fluid-crack mass exchanges are taken into account by the jump of fluid velocity across the crack $\|\underline{v}\|$ by presenting the discontinuity with values $\underline{v}^+$ and $\underline{v}^-$ for two faces of the crack. $\underline{n}$ is the normal unit vector to the fracture surface.

### 2.3 Mechanical Behaviour

For the mechanical problem, the initiation and the propagation of crack are modeled by placing the cohesive cracks represented by joint elements. The effective stress is formulated to describe the mechanical behavior of the soil matrix while the failure criterion of the cohesive cracks is based on total stress. In fact, if the cracks are considered as very big size pores, suction in these pores would be negligible, thus it is reasonable to consider their failure in terms of total stress. The continuity of total stress is ensured at the interface between the matrix element and the joint element.

The soil matrix is assumed to be an isotropic elastic linear material governing by the following equation:

$$\underline{\underline{\sigma}} + (Sp)\underline{\underline{\delta}} = \mathrm{C} : \underline{\underline{\varepsilon}} \tag{3}$$

The elastic damage of cohesive crack law [4] is used to describe the initiation and the propagation of cracks. In this model, a damage variable $d$ is added in order to represent the process of damage through the decrease of crack stiffness and the evolution of yield surface. Under the effect of evaporation, the tensile stress increases with suction corresponding the increase of normal stress of cohesive cracks. The initiation of cracks could be considered as the breakage of bonds by degradation of the crack stiffness when the tensile stress reaches the tensile strength. The following equation is used to simulate the cohesive damage crack behavior:

$$\underline{\sigma} = (1 - d)\underline{\underline{R}}\underline{u} \tag{4}$$

where $\underline{\sigma}$ is the stress vector on the matrix/crack interface surface, $\underline{n}$ is the normal unit vector on this surface, $\underline{\underline{R}}$ is the crack stiffness tensor. The crack opening ($e$) changes

with the deformation from the initial value $e_0$ to: $e = e_0 + u_n$ with $u_n$ is the normal component of the displacement discontinuity $u$ through two crack's wall.

### 2.4 Coupling Hydro-Mechanical

The coupling between the mechanical and the hydraulic problems is performed by a sequential resolution of both of the problems and the interactions between them. For each time increment, the hydraulic problem is calculated by solving the Eq. (1) and Eq. (2). The outputs correspond to the soil suction, degree of saturation and hydraulic conductivity of soil. These values are then used as inputs for the mechanical problem. For the matrix, the hydro-mechanical coupling Eq. (3) allows updating the effective stress in the soil matrix. For the cracks, the fluid pressure resulting from the resolution of the hydraulic problem is introduced in the mechanical problem Eq. (4) for calculating the crack opening. Reciprocally, the matrix and the cracks deformations resulting from the resolution of the mechanical problem are then introduced into the hydraulic problem through the source term $r$ related to the volumetric strain of the matrix in Eq. (1) and $r^f$ in Eq. (2) representing the crack opening evolution. Besides, the crack opening $e$ is used to update the hydraulic conductivity of crack following the cubic law [8] which implies that when the crack is mechanically opened, its hydraulic conductivity increases quickly and potentially conducts more fluid through it.

## 3 Numerical Simulation

### 3.1 Geometry and Model Parameters

The hydro-mechanical finite element code presented above is used to simulate the desiccation experiments reported by Sanchez et al. [6]. In this test, a circular plate of organic silt (30% sand, 57% silt and 13% clay) of 100 mm in diameter and 13 mm in thickness was first prepared at the slurry state and then air-dried. By using the 2D profile laser technique, various soil characteristics (volume change, water loss, crack development, *etc.*) were observed during drying in that work.

In order to simulate this test, a 2D mesh with plane strain condition shown in Fig. 1 is used. Its width is equal to the diameter of the sample (100 mm) and its height is equal to the initial height of the sample (13 mm). The experimental observation showed that there are 4 cracks (for a typical cross section) after 24 h of drying and these cracks are propagated vertically in depth. As mentioned above, a great unbiased number of cracks and pathways can be introduced in FEM. The crack development will be dictated by the behaviour of the model. In the present work, in order to optimize the calculation cost while ensuring an adequate mesh density, 100 vertically oriented cohesive cracks were distributed regularly with a distance of *1* mm in the mesh (see Fig. 1). For the mechanical boundary conditions, the displacements at the bottom, the right and left sides are fixed while the top of the mesh (representing the soil surface) is free to move. For the hydraulic boundary conditions, no flux was allowed at the bottom, the right and left sides of the mesh. On the top of the mesh, a homogenous flux, calculated from the evaporation rate estimated from the test was imposed. This applied

evaporation isn't constant and changes with the suction on the top surface as the following function:

$$\begin{cases} E_a = E_p & \text{if } |s| \le |s_0| \\ E_a = E_p \exp[-\alpha(s - s_0)] & \text{if } |s| > |s_0| \end{cases} \quad (5)$$

where $E_a$ is the actual applied evaporation; $E_p$ is the potential evaporation rate which represents the evaporation capacity of the soil in a completely saturated condition, $s$ is the actual suction at the surface and $s_0$ is a suction of the onset of the second phase in the evaporation process where the evaporation rate decreases quickly, $\alpha$ is a curve coefficient. The Table 1 presents the soil properties, cohesive crack parameters and evaporation condition used in the model.

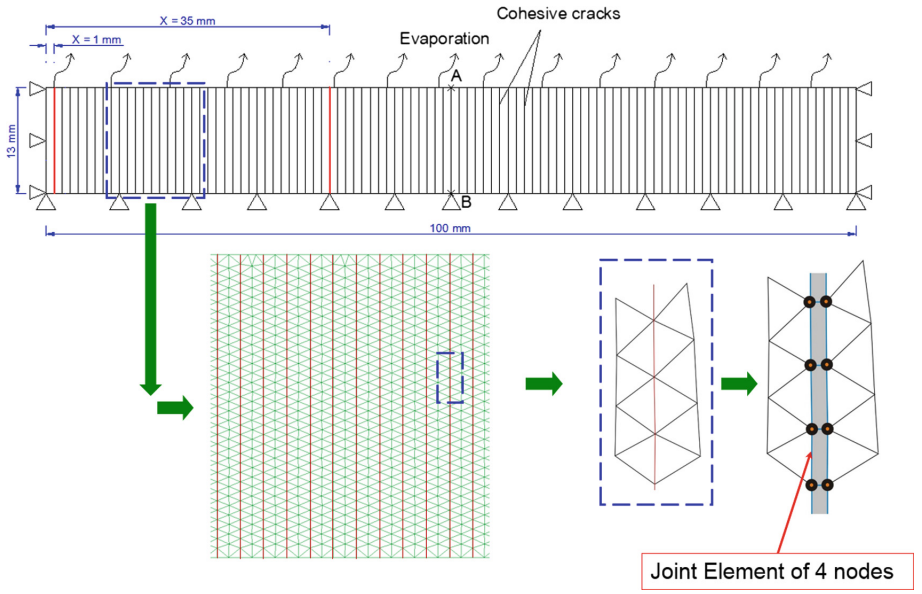


**Fig. 1.** Geometry and boundary condition

**Table 1.** Model parameters

| Soil | $E$ (MPa) | $\nu$ (−) | $k_s$ (m/s) | Water retention curve (Van Genuchten model) | | | |
|---|---|---|---|---|---|---|---|
| | | | | $\alpha$ (MPa$^{-1}$) | $n$ (−) | $m$ (−) | $S_r$ (−) |
| | 1 | 0.3 | $10^{-8}$ | 9.81 | 1.60 | 0.375 | 0.02 |

| Crack | $R_{tt}$ (MPa/mm) | $R_{nn}$ (MPa/mm) | $R_{tn} = R_{nt}$ (MPa/mm) | $\sigma_R$ (MPa) | $C_{coh}$ (MPa) | $\varphi$ (°) | $\beta$ (−) | $e_0$ (mm) |
|---|---|---|---|---|---|---|---|---|
| | 1 | 10000 | 0 | 0.09 | 0.08 | 30 | 1 | $10^{-3}$ |

| Desiccation rate | $E_p$ (mm/h) | $\alpha$ (−) | $s_0$ (MPa) |
|---|---|---|---|
| | 0.3 | 1.857 | 0.3 |

### 3.2 Results

The Fig. 2 presents the morphology evolution of the specimen during drying. It can be observed that the proposed model could reproduce two main phases observed in the experimental test. At the beginning of the test, only the settlement at the soil surface was observed without cracking (*i.e.* with t = 3 h). The two first cracks appeared close to the two lateral walls at t = 4 h. During the next 4 h, the opening of these cracks increased and no more cracks appeared. After t = 8 h, the crack network develops very quickly and, the cracks appear with the same spacing of around 6–10 mm (t = 9 and 10 h). At t = 12 h, the specimen presents 17 cracks while 100 cohesive joints were placed in the model.

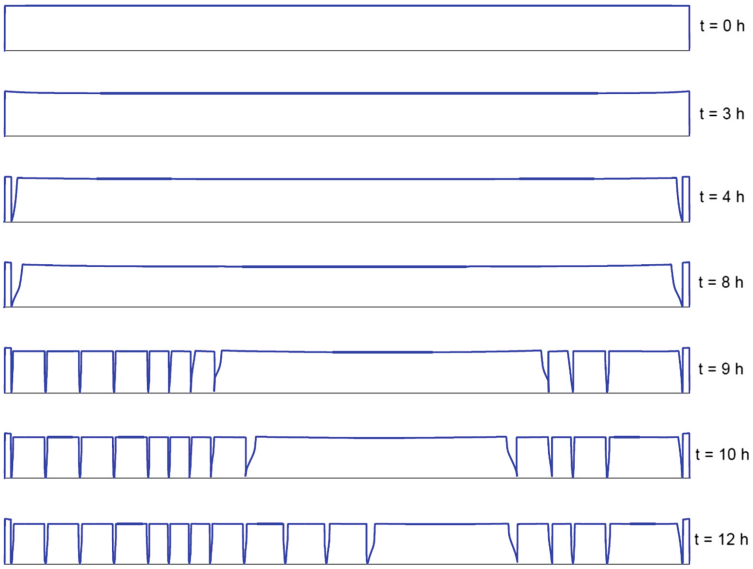


**Fig. 2.** Description of the cracks observed at various moments

The evolutions of suction measured at the top and at the bottom of the specimen (point A and point B in Fig. 1) are shown in Fig. 3*a*. It can be seen that the suctions at these two points are similar, showing that the suction is homogenous in the specimen during the drying test. After 12 h of drying, the soil suction reaches approximately to 0.3 MPa. The degrees of saturation calculated at these two points are also plotted in the Fig. 3*b*. It can be observed that these values are slightly lower than the average degree of saturation measured in the experiment. However, the trend observed on the numerical simulation is similar to the one observed in the experiment: a progressive decrease of degree of saturation during drying and the degree of saturation remains high after 12 h of drying.

Two families of cracks can be identified: (*i*) the two first cracks appear close to the boundary of the soil specimen in contact with the rigid mould, which is defined as lateral gap in the experimental work; (*ii*) the cracks develop in the middle of soil

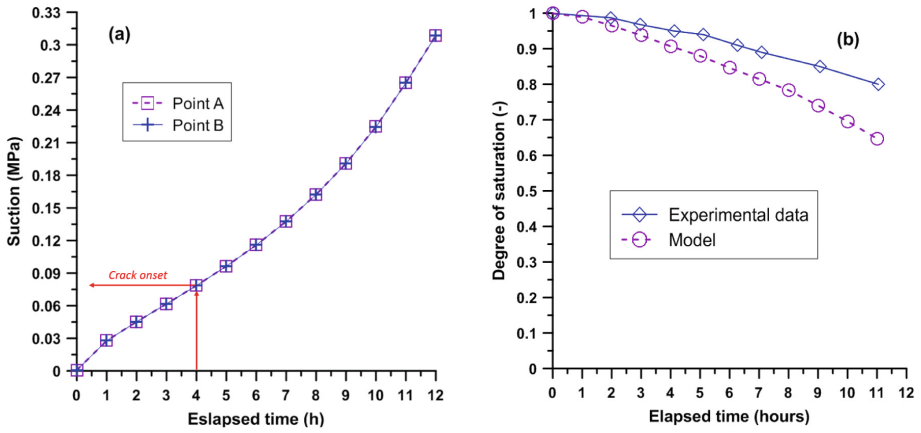


**Fig. 3.** (a) Suction and (b) Degree of saturation versus elapsed time. (Experimental data taken from [6])

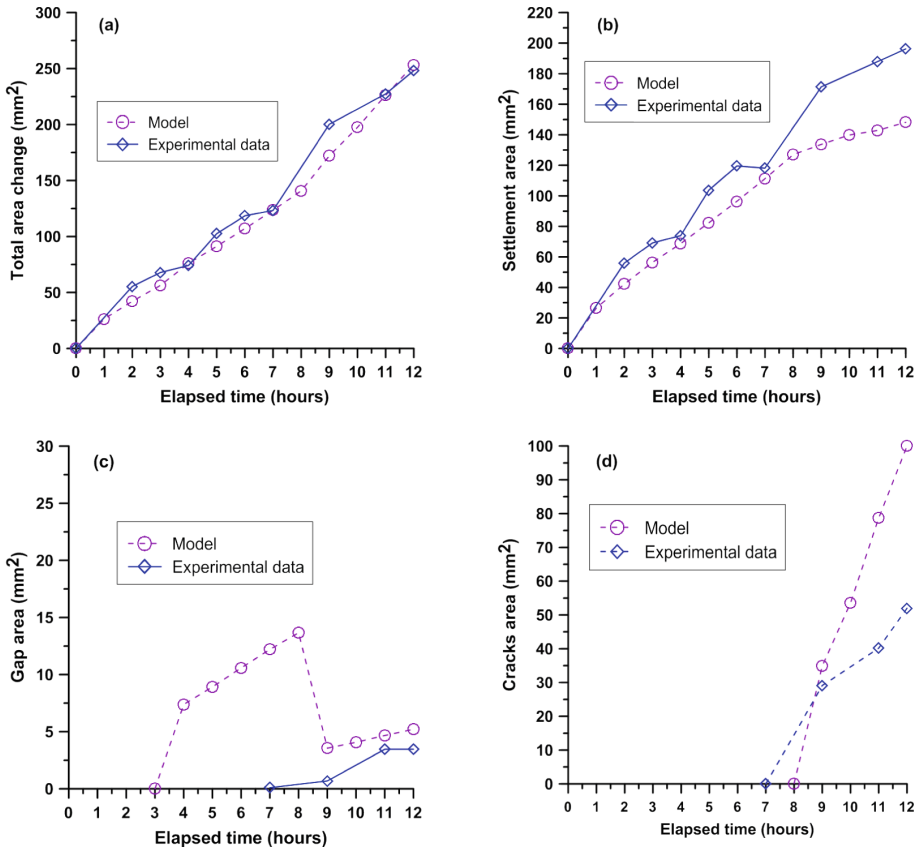


**Fig. 4.** Time evolution of different components of soil shrinkage: (a) Total; (b) Settlement; (c) Gap; (d) Cracks

sample, which is defined as "cracks" in the experimental work. In the experimental work, the 2D measured profiles were used to calculate the three components of soil shrinkage for a generic cross section: vertical displacement of the top surface (settlement), lateral shrinkage (gap), and cracks. These three components of the deformation mentioned above can be also determined in the simulation. The Fig. 4 presents the comparison between the numerical simulation and the experimental work for each shrinkage component. It can be seen that the results obtained by the model are in good agreement with the experimental data. In addition, it can be observed that at the beginning (t = 0–3 h), the shrinkage corresponds only to the settlement. For t = 3–8 h, the gap appears but its area remains small, and the total shrinkage area is still associated with the settlement. From t = 8 h, cracks appears quickly and there are an abrupt increase of cracks area. It can be concluded that the increase of crack area is the main cause of the total shrinkage area in this phase. Note that, in the experiment, drying was performed for 24 h while in the present work the simulation was stopped after 12 h. In the present work, a linear elastic mechanical behaviour of soil matrix is considered but this assumption is reasonable only when the soil strain remains small.

## 4 Discussion and Conclusions

In this study, a desiccation cracking experiment is simulated using a hydro-mechanical model where (*i*) the hydraulic diffusion under evaporation effect, (*ii*) the shrinkage of a soil sample and (*iii*) the initiation and the propagation of desiccation cracks, among others couplings, are considered. The diffusion equation includes the evolution of soil and crack hydraulic properties (degree of saturation, soil hydraulic conductivity and crack hydraulic conductivity, the mass exchange between soil matrix/cracks) and the deformation processes of the soil and the crack are equally taken into account. A finite element model, including cohesive fractures model, is used to simulate the development of cracks. The coupling between hydraulic and mechanical phenomena is performed by an iterative process passing from the hydraulic problem resolution to the mechanical problem resolution and vice versa.

A 2D plane strain model is used in the present work while the experiment was performed with a cylindrical specimen. The prime interest of this work is not a quantitative prediction of the experimental results, but a qualitative reproduction of the main trends and the crack development during drying. Various experimental studies in the literature show that the crack network would be different for the two cases: (*i*) for the case of a long bar (similar to the model in the present work) the cracks are formed successively and perpendicular to the long side of the specimen; (*ii*) for the case of a circular sample or a rectangular slab, the cracks can appear simultaneously or successively in order to create a cracks network. In the experimental work used to justify the present work, the evolution of a typical section is analysed. A 3D mesh would be then necessary to reproduce exactly the cracks pattern in this case. Even if the 3D crack pattern is not simulated in the present work, the result obtained in the 2D study allows improving the understanding on the shrinkage cracking mechanisms.

The model is able to reproduce correctly the main phases of the desiccation and the development of soil shrinkage versus elapsed time (Figs. 2, 4). At the beginning, the

shrinkage is associated with settlement only. In the model, the settlement without cracking corresponds to the elastic phase of cohesive cracks in which the tensile stress increases with drying but remains smaller than the tensile strength. The damage phase begins when the tensile stress of cohesive cracks reaches the soil tensile strength and the crack is initiated. In the present work, the crack network appears quickly at t = 8.3 h. This time can be observed as the critical time in the development process of cracking. Li et al. [9] studied the desiccation cracks initiation and development at ground surface and showed that the desiccation cracks development in three stages: initial, primary and steady states. In the first stage, few cracks developed with gradually decreasing water content and a critical suction value exists for crack initiation, after which cracks appear and propagate quickly.

Despite some limitations, the results of numerical simulation show good agreement with the experimental data in terms of the hydraulic diffusion, the crack initiation, the shrinkage evolution and mostly the chronology of desiccation phases (settlement without cracking and then formation and propagation of cracks). The results of the present work indicate that the proposed hydro-mechanical coupled model using the cohesive fracture law for modelling of crack propagation can reproduce correctly the hydro-mechanical coupled phenomena related to shrinkage and crack formation during drying of clayey soils.

## References

1. Kindle, E.M.: Some factors affecting the development of mud-cracks. J. Geol. **25**(2), 135–144 (1917)
2. Towner, : The mechanics of cracking of drying. J. Agric. Eng. Res. **36**, 115–124 (1987)
3. Peron, H., Hueckel, T., Laloui, L., Hu, L.B.: Fundamentals of desiccation cracking of fine-grained soils: experimental characterisation and mechanisms identification. Can. Geotech. J. **46**, 1177–1201 (2009)
4. Pouya, A., Bemani, P.: A damage-plasticity model for cohesive fractures. Int. J. Rock Mech. Min. Sci. **73**, 194–202 (2015)
5. Pouya, A.: A finite element method for medeling coupled flow and deformation in porous fractured media. Int. J. Numer. Anal. Methods Geomech.vol. 32 (2015)
6. Sanchez, M., Atique, A., Kim, S., Romero, E., Zielinski, M.: Exploring desiccation cracks in soils using a 2D profile laser device. Acta Geotech. **8**(6), 583–596 (2013)
7. Vo, T.D., Pouya, A., Hemmati, S., Tang, A.M.: Numerical modelling of desiccation cracking of clayey soil using a cohesive fracture method. Comput. Geotech. **85**, 15–27 (2017)
8. Zimmerman, R.W., Bodvarsson, G.S.: Hydraulic conductivity of rock fractures (1994)
9. Li, J.H., Zhang, L.M.: Study of desiccation crack initiation and development at ground surface. Eng. Geol. **123**, 347–358 (2011)

# Pneumatic Flow Mixing Method for Beneficial Use of Dredged Soil

M. Kitazume(✉)

Tokyo Institute of Technology, Meguro, Tokyo, Japan
kitazume@cv.titech.ac.jp

**Abstract.** A huge amount of soft soil is dredged by grab dredger or pump dredger at many ports every year to maintain enough sea route and sea berth. These soft soils used to be transported and dumped out to a disposal site or land reclamation site. It is becoming more difficult to construct any disposal area for dredged soil and subsoil. In order to prolong the service life of the sites, beneficial use and volume reduction of the dredged soil are desirable. The pneumatic flow mixing method was developed in Japan for beneficial use of dredged soil, land reclamation and land development, in which dredged soil is mixed with relatively small amount of cement in a transporting pipeline. The soil mixture forms several separated mud plugs in the pipeline, and is thoroughly mixed during the transporting. The mixture transported and deposited at reclamation site gains relatively large strength rapidly so that no additional soil improvement is required. This method is expected to promote the beneficial use of dredged soil and to provide an economical and rapid construction for land reclamation, and was applied to the Central Japan International Airport and Tokyo/Haneda International Airport. In this article is described briefly the development of pneumatic flow mixing method and its two large scale applications as well as the mechanical properties of the stabilized soil.

**Keywords:** Pneumatic flow mixing method · Stabilized soil · Beneficial use · Dredges soil · Land reclamation

## 1 Introduction

Many man-made islands have been constructed to obtain enough plain land area for airport, electric power plant, manufacture plant, residential area and so on. These islands require huge amount of soil with relatively high quality soil properties for land reclamation, which is used to obtain in mountain, river and seabed. Recently it becomes more difficult to obtain such a soil with reasonable expense because of restrict environmental protection, which requires use of less quality soil as a reclamation material. A huge amount of soft soil is dredged at many ports every year to maintain enough sea route and sea berth. These soft soils are used to dump at disposal sites constructed at coast area. It becomes more difficult to construct the disposal area for dredged soil and subsoil, because of restrict environmental restriction and economical reason. As the dredged soil usually has a high water content of the order of a hundred percent, man-made islands constructed with it are so week and high compressible that no structure can be

© Springer Nature Singapore Pte Ltd. 2018
H. Tran-Nguyen et al. (eds.), *Proceedings of the 4th Congrès International de Géotechnique - Ouvrages -Structures*, Lecture Notes in Civil Engineering 8,
DOI 10.1007/978-981-10-6713-6_76

constructed without any soil improvement. Vertical drain method is one of the most frequently used soil improvement techniques to improve such a clayey deposit. However the method requires relatively long period to complete the consolidation. In order to prolong the service life of the sites, beneficial use and volume reduction of the dredged soil are desirable. These circumstances promote beneficial use of dredged soft soils as a reclamation material, and many studies and researches have been carried out to investigate stabilizing methods for the soil and to establish recycling system for the soil.

The pneumatic flow mixing method [1, 2], one of the admixture stabilization techniques, was developed to make dredges soil beneficial use for land reclamation and land development, in which dredged soil is mixed with relatively small amount of cement in a transporting pipeline. When relatively large amount of compressed air is injected into the pipeline, the soft soil is separated into small blocks by the injected air. The soil plug and injected binder are thoroughly mixed by means of turbulent flow during transporting. The mixture transported and placed at reclamation site gains relatively high strength rapidly so that no additional soil improvement is required. In this article is described briefly the development of Pneumatic Flow Mixing Method and its two large scale applications as well as the mechanical properties of the stabilized soil.

## 2 Pneumatic Flow Mixing Method

### 2.1 Development of the Method

The pneumatic flow mixing method is one of the soil admixture stabilization techniques, in which dredged soil or surplus soil is mixed with a relatively small amount of cement in a pipeline. The development of the method has been initiated by the Ministry of Transport, the Fifth District Port Construction Bureau, where many laboratory tests were carried out to investigate the mechanical properties of stabilized soil, and many full-scale land reclamation and backfill were also carried out at Nagoya Port to investigate the mechanical properties of field stabilized soil and to develop construction procedures and quality control and assurance [1]. The method was applied to construct a huge scale man-made island for the Central Japan International Airport at Nagoya in 2001 [3, 4]. After the construction of the airport, the method has been applied to many marine construction and on land construction projects in Japan and in USA [5–9]. In 2008, the method was applied to the expansion project of the Tokyo Haneda International Airport [10].

### 2.2 Mechanism of the Method

Transporting soil in a pipeline without any air requires high pressure due to the friction generated on the inner surface of pipeline. When a relatively large amount of compressed air is injected into the pipeline, however, soil can be separated into small blocks, as schematically shown in Fig. 1 [1]. The separated soil block, called as ‘plug’, is forwarded to an outlet with the help of compressed air. The forming plug and air block functions to reduce the friction and in turn can reduce the required air pressure considerably for transporting. The formation of the plug is dependent upon the ratio of

soil and air in the mix, and the pile diameter [11]. When binder is injected into the pipeline, the soil plug and binder are thoroughly mixed by the help of the turbulent flow generated in the plug during transporting. The soil and binder mixture, transported and placed at the designated reclamation site, gains high strength rapidly so that no additional soil improvement is necessary for assuring the successful performance of superstructures on the stabilized soil ground [3, 12].

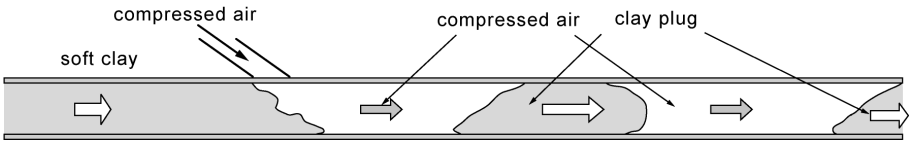


**Fig. 1.** Schematic view of plug flow [1].

### 2.3 Facility

Figure 2 shows a group of barges for one kind of the Pneumatic Flow Mixing Method available in Japan, which consists of a pneumatic barge, a cement supplier barge and a placement barge. In the figure, the dredged soil in the soil transport barge is loaded into the hopper on the pneumatic barge at first, and is transported to the reclamation site by the compressed air. Cement is then injected to the soil on the cement supplier barge and they are thoroughly mixed during transporting in the pipeline. Cement in the slurry or dry form is added to the soil while the slurry form is common. The soil mixture is allowed to place to reclamation site through a cyclone on the placement barge, which functions to release the air pressure transporting soil plugs. A tremie pipe is usually used to place the soil mixture under seawater to minimize the entrapping seawater within the soil, which can cause considerably decrease of the stabilized soil. There are several variations available in the cement injection techniques and transporting techniques by various construction firms to improve the degree of mixing of clay and binder [2, 13, 14].

**Fig. 2.** Group of barges for pneumatic flow mixing method.

# 3 Application of the Method

## 3.1 Land Reclamation for Central Japan Japan International Airport

(1) Outline of project

A man-made island was constructed for Central Japan International Airport in Nagoya, as shown in Fig. 3 [3, 4, 15, 16]. The plane area of the man-made island was about 5.8 million $m^2$, and the total amount of reclamation was about 70 million $m^3$. The 8.6 million $m^3$ of dredged soil excavated at Nagoya Port was used as a reclamation material after stabilization by the pneumatic flow mixing method in order to reduce the amount of mountain soil needed for the land reclamation and to promote the recycling of dredged soil. It was the first huge scale application of the method, and a lot of laboratory and field tests were carried out to investigate the physical and mechanical properties of stabilized soil, to develop construction machinery and procedure, and to develop quality control and assurance. These investigations were summarized and published by the Ministry of Transport in 1999 [1].

**Fig. 3.** Aerial view of Central Japan International Airport.

(2) Design and stabilization work

The designed field strength of the stabilized soil was determined as 120 $kN/m^2$ based on two criteria: (a) minimum *CBR* value of 3% was assured for the basement layer, and (b) no consolidation settlement was allowed. The average strength for the field stabilized soil, $q_{uf}$, was determined as 157 $kN/m^2$ by assuming the probability of 75%, and the average strength of laboratory stabilized soil, $q_{ul}$, was determined 314 $kN/m^2$ by assuming the strength ratio, $q_{uf}/q_{ul}$, of 0.5. The total of 8.6 million $m^3$ of the dredged soil was excavated at 12 sites in Nagoya Port. The properties of the dredged soils from the different sites varies significantly. For ease of quality control of the stabilized soil, a quality control system by water/cement ratio, *W/C*, was introduced

in the project. The target flow value of the stabilized soil mixture was determined as 95 mm, based on the previous case histories of the method [1]. According to these considerations and procedures, the detail mixing conditions of stabilized soil were determined for each expected dredged soil.

The sea revetment was constructed in advance along all the periphery of the land reclamation area to prevent any adverse environmental impact to the surrounding seawater. Three sets of the pneumatic system were operated at the construction site to complete constructing the man-made island within about 18 months. The dredged soft soil was mixed with blast furnace slag cement along the 1,500 m long pipeline and placed at the construction site by the cyclone method. The placement of stabilized soil was carried out in two stages: placement under the sea water level and above the sea water level, as shown in Fig. 4. The stabilized soil layer was soon covered by the mountain soil to start the construction of airport facilities. The land reclamation with the stabilized soil commenced in June 2001 and was completed in October 2002.

**Fig. 4.** Pneumatic flow mixing method at the Central Japan International Airport.

(3) Strength of the stabilized soil ground

Figure 5(a) shows measured unconfined compressive strength profile along the depth [4]. Though there was a lot of scatter in the measured data, the mean strength of stabilized soil was 296 kN/m$^2$, which was higher than the target value of 157 kN/m$^2$. The mean strength and the coefficient of variation of the stabilized soil placed above the sea water level were 364 kN/m$^2$ and 28%, respectively. Those for soil placed under the sea water level were 282 kN/m$^2$ and 38%, respectively, which were of smaller strength and larger variation compared to those above the sea water level. Figure 5(b) shows the water content profile of the stabilized soil along the depth. Also there was a lot of scatter in the measured data, but the mean was 105.3%. The water contents of the stabilized soils placed above and below the sea water level were 96.9% and 107%, respectively, which confirms the phenomenon that seawater are entrapped during the placement underwater.

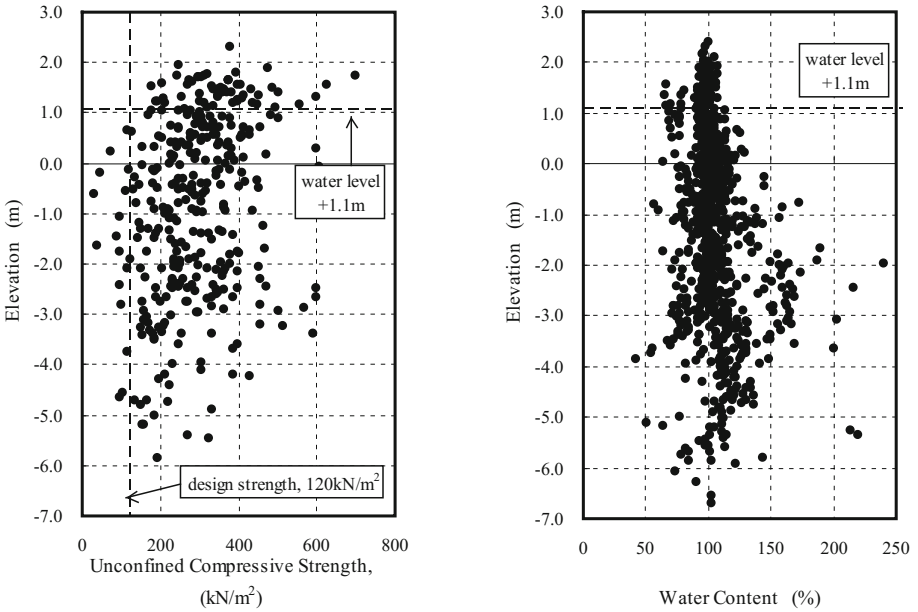


(a) Unconfined compressive strength (b) Water content distribution.

**Fig. 5.** Unconfined compressive strength and water content distribution of stabilized soil along depth [4].

### 3.2 Land Reclamation for Tokyo/Haneda International Airport

(1) Outline of project

The construction of a fourth runway of Tokyo/Haneda International Airport was planned in 2001 and commenced in 2006 in order to cope with recent, and expected future increases in air transportation (Fig. 6). The man-made island was located between the mouth of the Tama River and the main sea route to Tokyo Port. In order to minimize any adverse influence to the water flow of the Tama River, the west part of the island was a steel-jacket-platform structure while the other was reclamation land. The east part of the island was constructed with cement stabilized dredged soil and mountain soil. The soft soil was excavated at the front of the island and the sea route of Tokyo Port, and was stabilized with cement and backfilled behind the revetment and the steel wall revetment [10].

(2) Design and stabilization work

The design strength was determined as 300 kN/m$^2$ by considering that no soil failure was allowed by the overburden pressure. The coefficient of variation and the probability of field stabilized soil were assumed as 0.35 and 75%, respectively. In order to incorporate the possibility of failure of the stabilized soil due to differential settlement, the design strength was determined as the residual strength of the stabilized soil. As the strength ratio of $q_{uf}/q_{ul}$ was assumed at 0.5, and the average strength of the

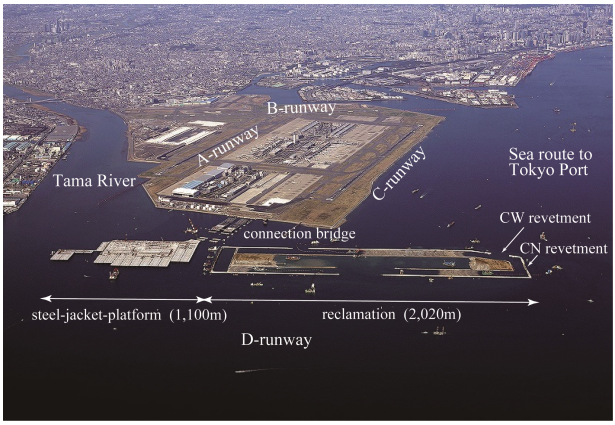


**Fig. 6.** Aerial view of construction site and existing airfield on March 15th, 2009 (by courtesy of the Tokyo/Haneda International Airport Construction Office).

laboratory stabilized soil was 942 kN/m$^2$. The soil used in the method was excavated at three sites in the Tokyo Bay area. According to the $q_u$ and *W/C* relationships which were obtained in the laboratory mix tests, the mix condition for each soil were determined for assuring the design strength.

In the project, about 4.8 million m$^3$ of dredged soil was stabilized from autumn 2008 to the end of 2009 (Fig. 7). The stabilization work was conducted using a three sets of the system. In order to minimize the water entrapment into the stabilized soil, placement was conducted by a pump system and a tremie pipe was kept within the stabilized soil at the construction site.

(a) cement supplier barge.

(b) Placement barge.

**Fig. 7.** Pneumatic flow mixing execution in Tokyo/Haneda International Airport construction.

The stabilized soil was sampled at the outlet of the placement machine and put into a plastic mold and cured in a laboratory. The stabilized soil in the field was also sampled by the rotary double core cube. The unconfined compression tests were carried

out in November 2008 [17]. The mean strength of the mold stabilized soil, $q_{um91}$, was 1,046 kN/m$^2$, which was 111% of the target strength. The coefficient of variation of the stabilized soil and probability were 0.265 and 88.0%, respectively. The mean strength, $q_{uf91}$, and the coefficient of variation of the field sample were 645 kN/m$^2$ and 0.376. The strength ratio, $q_{uf91}/q_{um91}$, was 0.62, which was larger than the design assumed value of 0.5, and the probability of the field stabilized soil was about 85%, which was higher than the design. According to the test results on the strength ratio, the mixing condition was modified to achieve the target laboratory strength of 785 kN/m$^2$ for further stabilization work. After modifying the mixing condition, the strength of stabilized soil was investigated again on the mold and field stabilized soils in February 2009.

Figures 8(a) and (b) show the strength of the mold and field stabilized soils at 28 days' curing [17]. The average strength, $q_{um28}$, the coefficient of variation, and the probability of the mold stabilized soil were 956 kN/m$^2$, 0.21, and 100%, respectively. On the field stabilized soil, the average strength, $q_{uf28}$, and the coefficient of variation were 672 kN/m$^2$ and 0.35, respectively, and the probability was estimated at 92.8% by incorporating the strength increase from 28 days' curing and 91 days' curing of 1.10. The strength ratio, $q_{uf}/q_{um}$, was 0.70, which was larger than the design, and the probability was 93%; that was also larger than the design value of 25%. Based on them, the mixing condition was modified again based on the strength ratio of 0.7. The construction of land reclamation by the pneumatic flow mixing method was successfully completed in August 2010, and the new run way began operating in October 2010.

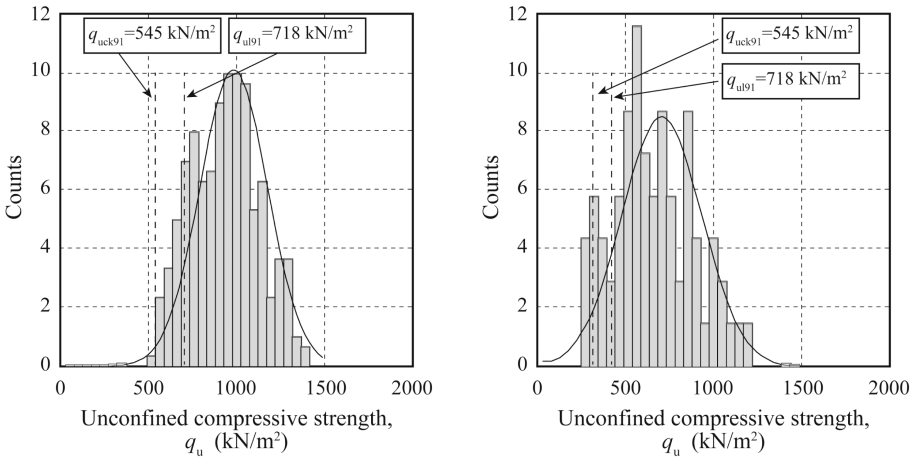


(a) Mold stabilized soil.

(b) Field sampled stabilized soil.

**Fig. 8.** Unconfined compressive strength of field stabilized soil after modifying the mixing condition [17].

## 4 Concluding Remarks

In this manuscript, the development of the pneumatic flow mixing method and its two applications are briefly introduced for beneficial use of dredged soft soil. This manuscript at first emphasizes the necessity and importance of beneficial use of dredged soil as a land reclamation material. The pneumatic flow mixing method is one of the admixture stabilization techniques, in which dredged soil or surplus soil is mixed with a relatively small amount of cement without any mixing paddles and blades in a pipeline. As the mixing and transporting soil and binder can be conducted in a pipeline continuously, the methods is suitable and efficient for large scale project such as the Central Japan International Airport and the Tokyo/Haneda International Airport projects. The applications introduced in the manuscript clearly reveals the high applicability and efficiency of the method for beneficial use of dredged soil. The author hopes that this manuscript will be helpful and useful for promoting the pneumatic flow mixing method.

## References

1. Ministry of Transport: The Fifth District Port Construction Bureau. Pneumatic Flow Mixing Method, 157 p. Yasuki Publishers (1999). (in Japanese)
2. Kitazume, M.: The Pneumatic Flow Mixing Method, 233 p. CRC Press, Taylor & Francis Group (2016)
3. Kitazume, M., Satoh, T.: Development of pneumatic flow mixing method and its application to Central Japan International Airport construction. J. Ground Improv. **7**(3), 139–148 (2003)
4. Kitazume, M., Satoh, T.: Quality control in Central Japan International Airport construction. J. Ground Improv. **9**(2), 59–66 (2005)
5. Kobayashi, K., Yoshida, G., Sato, H.: "Quality assurance of pneumatic flow mixing method: Snake mixer method". In: Proceedings of the Annual Research Conference, Civil Engineering Research Institute for Cold Region, Ministry of Ministry of Land, Infrastructure, Transport and Tourism, pp. 393–400 (2000). (in Japanese)
6. Yamauchi, H., Ishiyama, Y., Oonishi, F.: "Study for beneficial use of soft dredged soil: case history of backfill behind the breakwater at Kushiro Port". In: Proceedings of the Annual Technical Meeting, Civil Engineering Research Institute for Cold Region (2011). (in Japanese)
7. Yamagoshi, Y., Akashi, Y., Nakagawa, M., Kanno, H., Tanaka, Y., Tsuji, T., Imamura, T., Shibuya, T.: "Reclamation of the artificial ground made of dredged soil and converter slag by using pipe mixing method". J. Geotech. Eng. Jpn. Soc. Civ. Eng. **69**(2), 952–957 (2013). (in Japanese)
8. Watanabe, A.: "Challenge to soft soil: Pneumatic flow mixing method for dredged soil". In: Proceedings of the Annual Research Conference, Ministry of Ministry of Land, Infrastructure, Transport and Tourism (2005). (in Japanese)
9. Maher, A., Kitazume, M., Janbaz, M., Miskewitz, R., Douglas, S., Yang, D.: "Utlization of Pneumatic Floe Tube Mixing technique (PFTM) for processing and stabilization of contaminated soft sediments in the NY/NJ harbor". Mar. Georesour. Geotechnol (2016)
10. Mizukami, J., Matsunaga, Y.: "Construction of D - Runway at Tokyo International Airport". In: Proceedings. of the 15th Asian Regional Conference on Soil Mechanics and Geotechnical Engineering, CD-ROM (2015)

11. Akagawa, K.: Gas-liquid two-phase flow. Mech. Eng. **11**, 15 (1980). (in Japanese)
12. Coastal Development Institute of Technology: Technical Manual of Pneumatic Flow Mixing Method Revised Version, Daikousha Publishers, 188 p. (2008). (in Japanese)
13. Horii, R., Shinsha, H., Fujio, Y.: "Plant for the pneumatic flow mixing method". J. Kensetsu Kikaika 30–35 (1999). (in Japanese)
14. Yamane, N., Taguchi, H., Fukaya, T., Dam, K.L., Kishida, T., Iwatsuki, T.: "Strength characteristics of cement-treated soil using compressed air-mixture pipeline". In: Proceedings of 34th Annual Conference of Japanese Geotechnical Society, pp. 2253–2254. (in Japanese) (1998)
15. Satoh, T.: "Application of pneumatic flow mixing method to Central Japan International Airport construction". J. Jpn. Soc. Civ. Eng. 749/6-61, 33–47 (2003). (in Japanese)
16. Satoh, T.: Development and application of pneumatic flow mixing method to reclamation for offshore airport. Tech. Note Port Harbour Res. Inst. **1076**, 81 (2004). (in Japanese)
17. Yamatoya, T., Mitarai, Y., Iba, H., Watanabe, M.: "Attempt of quality control of treated soil by pneumatic flow mixing method in the construction of D runway". In: Technical Meeting of Construction of Tokyo/Haneda International Airport, Ministry of Land, Infrastructure, Transport and Tourism (2009). (in Japanese)

# Rigid Retaining Walls Interacting with Unsaturated Soils in Axial Symmetry

Thanh Vo(✉) and Adrian Russell

School of Civil and Environmental Engineering, Centre for Infrastructure Engineering and Safety, The University of New South Wales, Sydney, NSW, Australia
{thanh.vo,a.russell}@unsw.edu.au

**Abstract.** The slip line theory is applied to the problem of an axisymmetric retaining wall interacting with unsaturated soil. Active and passive failures of a rigid vertical wall are considered. The slip line governing equations assume the limiting equilibrium state of a Mohr-Coulomb soil. A linear variation of the contribution of suction to the effective stress with depth is assumed. A standard finite difference method is used to solve the governing equations. The finite difference procedures were validated with recently published literature on axisymmetric retaining walls retaining dry soils. It is shown that adopting the effective stress concept enables the influence of suction in unsaturated soils to be considered in a simple way. An example of analysis is presented to illustrate this. Moreover, the paper shows significant influence of the length scale and the magnitude of the circumferential stress on computed earth pressures.

## 1 Introduction

Retaining walls are used by engineers to resist lateral earth pressure. They often interact with compacted and natural soils above the ground water table. These soils are mostly unsaturated meaning they contain a significant amount of both water and air.

Retaining wall-unsaturated soil interactions have been investigated by some researchers in experiments and theories [1–6]. It has been shown that unsaturated soils are stronger and stiffer than saturated and dry soils. They are also more brittle and prone to shear band formation at a low confining pressure [7].

The slip line theory underpins many design charts used in foundation engineering. The effective stress concept for unsaturated soils [8] when combined with the slip line theory has been shown to capture major features of retaining wall-unsaturated soil interactions [6, 7].

The majority of previous researches on retaining wall-unsaturated soil interaction analysis is limited to a plane strain idealisation. There have been some studies applying the slip line theory to axisymmetric retaining walls interacting with dry soils [9–12]. This paper presents research applying the slip line theory to axisymmetric retaining walls interacting with unsaturated soils. Both active failure and passive failure mechanisms are considered. It is shown that the influence of suction in unsaturated soil, the influence of length scale and the influence of the magnitude of the circumferential stress on computed earth pressures are significant.

© Springer Nature Singapore Pte Ltd. 2018
H. Tran-Nguyen et al. (eds.), *Proceedings of the 4th Congrès International de Géotechnique - Ouvrages -Structures*, Lecture Notes in Civil Engineering 8,
DOI 10.1007/978-981-10-6713-6_77

## 2 Slip Line Governing Equations

### 2.1 Effective Stress and Failure Criterion

It is assumed that soil shear strength is governed by the Mohr-Coulomb failure criterion:

$$\tau = c' + \sigma' \tan \varphi' \tag{1}$$

in which $c'$ is soil cohesion and $\varphi'$ is soil friction. $\sigma'$ is effective stress and for an unsaturated soil is defined as [8]:

$$\sigma' = \sigma - u_a + \chi(u_a - u_w) \tag{2}$$

where $\sigma$ is total stress, $u_a$ is pore air pressure, $u_w$ is pore water pressure and $\chi$ is effective stress parameter. When pore air pressure is equal to atmospheric pressure and is taken as the pressure datum, Eq. (2) can be written as:

$$\sigma' = \sigma + \chi s \tag{3}$$

where $s = u_a - u_w$ is soil suction. $\chi s$ is the contribution of suction to the effective stress. It is assumed that $\varphi'$ is constant in this paper.

### 2.2 Cohesion and Contribution of Suction to the Effective Stress

Unsaturated frictional soils are treated as non-homogeneous soils in this paper. The non-homogeneity may occur in the soil cohesion ($c'$) and the contribution of suction to the effective stress ($\chi s$). For simplicity, it is assumed that $c'$ is constant and $\chi s$ varies linearly with depth by the function:

$$\chi s = (\chi s)_0 + k_{\chi s} z \tag{4}$$

where $(\chi s)_0$ is contribution of suction to the effective stress at $z = 0$ and $k_{\chi s}$ is a constant. Non-homogeneity in the soil cohesion has been treated by several authors [13–15]. This paper focuses on the non-homogeneity occurring in the contribution of suction to the effective stress.

### 2.3 Stress Equations

With reference to the coordinates system shown in Fig. 1, the static equilibrium equations are expressed as:

$$\frac{\partial \sigma_{rr}}{\partial r} + \frac{\partial \sigma_{rz}}{\partial z} + \frac{\sigma_{rr} - \sigma_{\theta\theta}}{r} = 0 \tag{5}$$

$$\frac{\partial \sigma_{rz}}{\partial r} + \frac{\partial \sigma_{zz}}{\partial z} + \frac{\sigma_{rz}}{r} = \gamma_t \tag{6}$$

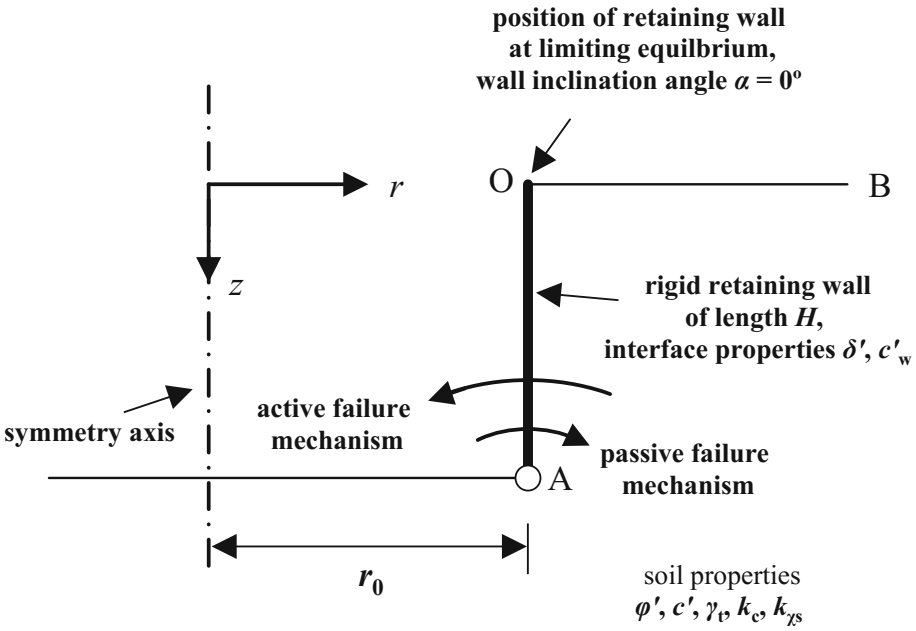


**Fig. 1.** Coordinates system and problem geometry.

where $\sigma_{zz}$, $\sigma_{rr}$ are normal stresses in the z and r directions, respectively, $\sigma_{\theta\theta}$ is the orthogonal circumferential stress, $\sigma_{zr}$ is shear stress and $\gamma_t$ is soil unit weight. The other shear stresses, $\sigma_{z\theta}$ and $\sigma_{r\theta}$, are always zero.

At the onset of failure, the stress components $\sigma_{zz}$, $\sigma_{rr}$, $\sigma_{zr}$ satisfy:

$$\sigma_{zz} = \left[(1 + \sin\varphi' \cos 2\psi)\sigma'_m - c' \cot\varphi'\right] - \chi s \tag{7}$$

$$\sigma_{rr} = \left[(1 - \sin\varphi' \cos 2\psi)\sigma'_m - c' \cot\varphi'\right] - \chi s \tag{8}$$

$$\sigma_{zr} = \sigma' \sin\varphi' \sin 2\psi \tag{9}$$

where $\sigma'_m$ is effective mean stress, and $\psi$ is angle between the vertical axis and the major principal stress direction. The circumferential stress $\sigma_{\theta\theta}$ is assumed smaller than or equal to the major principal stress in active failure, and greater than or equal to the minor principal stress in passive failure:

$$\sigma_{\theta\theta} = \left[k_{\theta\theta}(1 \pm \sin\varphi')\sigma'_m - c' \cot\varphi'\right] - \chi s \tag{10}$$

where $k_{\theta\theta}$ is a constant, the (+) sign in Eq. (10) applies to an active failure mode and the (−) sign in Eq. (10) applies to a passive failure mode. In this paper, the constant $k_{\theta\theta}$ will be varied to investigate the influence of the magnitude of the circumferential stress.

$k_{\theta\theta}$ is varied such that the magnitude of $\sigma_{\theta\theta}$ is always between the minor principal stress and the major principal stress.

The stress components in Eqs. (7) to (10) are substituted into Eqs. (5) and (6) and solved to obtain two families of stress slip lines ($\xi$, $\eta$):

$$\langle \xi \rangle \equiv \begin{cases} \mathrm{d}r = \tan(\psi - \mu)\mathrm{d}z \\ -\mathrm{d}\sigma_{\mathrm{m}}' + 2\tan\varphi'\sigma_{\mathrm{m}}'\mathrm{d}\psi = A\left[-\frac{\sin(\psi+\mu)}{\cos^2\varphi'}\mathrm{d}z + \frac{\cos(\psi+\mu)}{\cos^2\varphi'}\mathrm{d}r\right] \end{cases} \tag{11}$$

$$\langle \eta \rangle \equiv \begin{cases} \mathrm{d}r = \tan(\psi + \mu)\mathrm{d}z \\ \mathrm{d}\sigma_{\mathrm{m}}' + 2\tan\varphi'\sigma_{\mathrm{m}}'\mathrm{d}\psi = B\left[\frac{\sin(\psi-\mu)}{\cos^2\varphi'}\mathrm{d}z - \frac{\cos(\psi-\mu)}{\cos^2\varphi'}\mathrm{d}r\right] \end{cases} \tag{12}$$

where

$$\begin{aligned} A = {} & \sin(\psi+\mu)\left[\gamma_{\mathrm{t}} + \frac{\partial(c'\cot\varphi' + \chi s)}{\partial z} - \frac{\sigma_{\mathrm{m}}'\sin\varphi'\sin 2\psi}{r}\right] \\ & + \cos(\psi+\mu)\left[\frac{\sigma_{\mathrm{m}}'(1-\sin\varphi'\cos 2\psi) - \sigma_{\mathrm{m}}'k_{\theta\theta}(1\pm\sin\varphi')}{r}\right] \end{aligned} \tag{13}$$

and

$$\begin{aligned} B = {} & \sin(\psi-\mu)\left[\gamma_{\mathrm{t}} + \frac{\partial(c'\cot\varphi' + \chi s)}{\partial z} - \frac{\sigma_{\mathrm{m}}'\sin\varphi'\sin 2\psi}{r}\right] \\ & + \cos(\psi-\mu)\left[\frac{\sigma_{\mathrm{m}}'(1-\sin\varphi'\cos 2\psi) - \sigma_{\mathrm{m}}'k_{\theta\theta}(1\pm\sin\varphi')}{r}\right] \end{aligned} \tag{14}$$

and $\mu = \pi/4 - \varphi'/2$.

## 3 The Axisymmetric Retaining Wall Problem

### 3.1 Problem Definition

A typical axisymmetric retaining wall interacting with unsaturated frictional soil is shown in Fig. 1. The vertical wall OA is at a distance $r_0$ from the axis of symmetry. An active and passive failure corresponds to the soil below OB reaching a minimal and a maximal stress state, respectively [16]. The soil-wall interface friction angle is negative in active failure and positive in passive failure.

### 3.2 Boundary Conditions

Boundary conditions of this problem include the soil surface OB, the singular point O and the retaining wall-soil interface OA (Fig. 1). At the soil surface OB, $\psi$ = 0, $\sigma' = [q + c'\cot\varphi' + (\chi s)_0]/(1+\sin\varphi')$, $z$ = 0, $r = r_0$ + [0, distance OB] in active

failure and $\psi = \pi/2$, $\sigma' = [q + c' \cot \varphi' + (\chi s)_0]/(1 - \sin \varphi')$, $z = 0$, $r = r_0 +$ [0, distance OB] in passive failure where $r_0$ is the distance between the symmetry axis and $q$ is the surcharge applied on OB. At the soil-wall interface OA, $\psi = (\Delta'/2 - \delta'/2) + \alpha$, $z/(r_0 - r) = \tan(\pi/2 - \alpha)$ in active failure and $\psi = \pi/2 - (\Delta'/2 + \delta'/2) - \alpha$, $z/(r_0 - r) = \tan(\pi/2 - \alpha)$ in passive failure where $\Delta' = \sin^{-1}(\sin \delta' / \sin \varphi')$ and $\alpha$ is the wall inclination angle. The singular point O is treated as a slip line in the limit so the variables $\psi$, $\sigma'$ transit from their values on OB to their values on OA.

### 3.3 Solution Procedures

The governing equations and boundary conditions were solved using a finite difference procedure similar to Sokolovski [16]. The numerical procedures were verified by reproducing the results of Liu and Wang [17] (an active failure) and Keshavarz and Ebrahimi [12] (a passive failure). Using only 100 characteristic pairs, exact agreements are achieved as shown in Figs. 2 and 3. Adaptive remeshing can be used to obtain even more accurate results [18, 19] but they are not needed in these validations.

It is noted that when the total normal stress ($\sigma_{nn}$) is smaller than zero in an active failure (Fig. 2), the soil separates from the retaining wall and changes the boundary conditions of the problem. The authors will address this issue in a future paper.

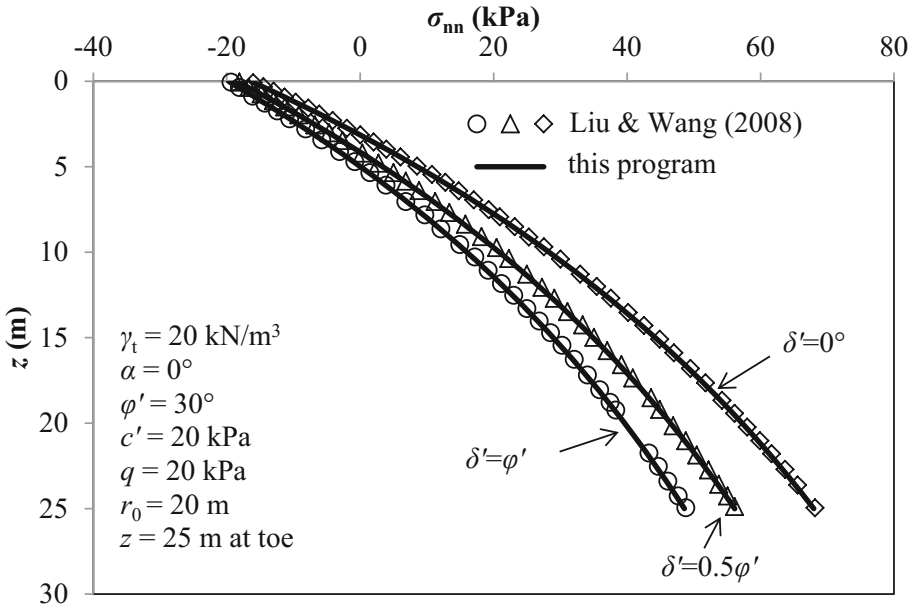


**Fig. 2.** Validation against Liu and Wang [17] (an active failure).

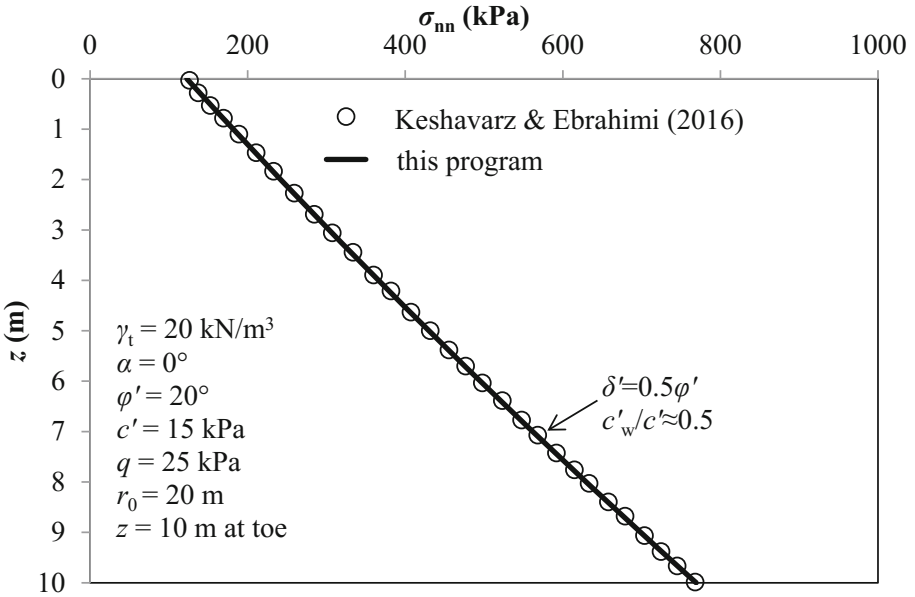


**Fig. 3.** Validation against Keshavarz and Ebrahimi [12] (a passive failure).

## 4 Result of Slip Line Analyses

Results are presented for a typical silt ($\varphi' = 25$, $c' = 17.5\,\text{kPa}$) in Figs. 4, 5 and 6. Parameters which are different in cases 1.1–3.12 are shown in Table 1. Parameters which are constant in the cases are:

$$\gamma_t = 20\,\text{kN/m}^3$$

$$\alpha = 0^\circ$$

$$\varphi' = 25^\circ$$

$$\delta' = 12.5^\circ$$

$$c' = 17.5\,\text{kPa}$$

$$c'_w/c' \approx 0.5$$

$$q = 22.5\,\text{kPa}$$

$$z = 17.5\,\text{m at toe}$$

The influence of the contribution of suction to the effective stress is investigated in cases 1.1–1.3. The influence of the length scale is investigated in cases 2.4–2.6. The influence of the magnitude of the circumferential stress is investigated in cases 3.7–3.12.

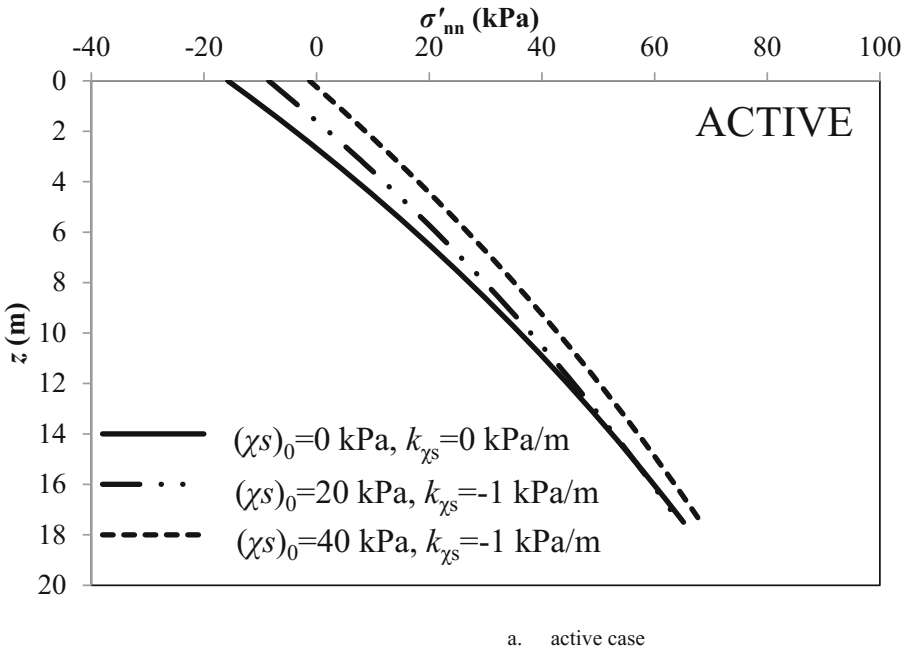


a. active case

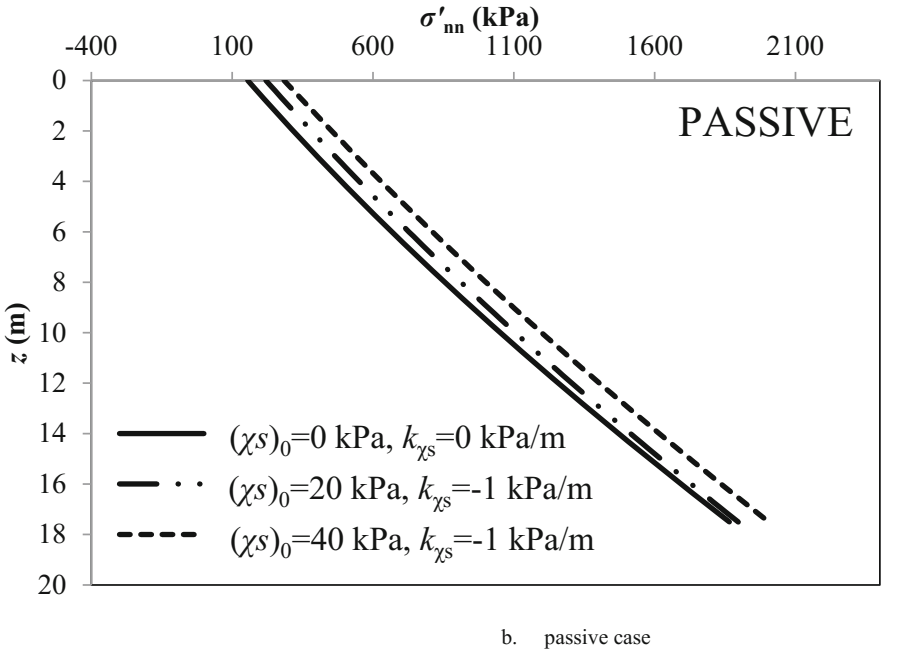


b. passive case

**Fig. 4.** Influence of the contribution of suction to the effective stress on computed earth pressures.

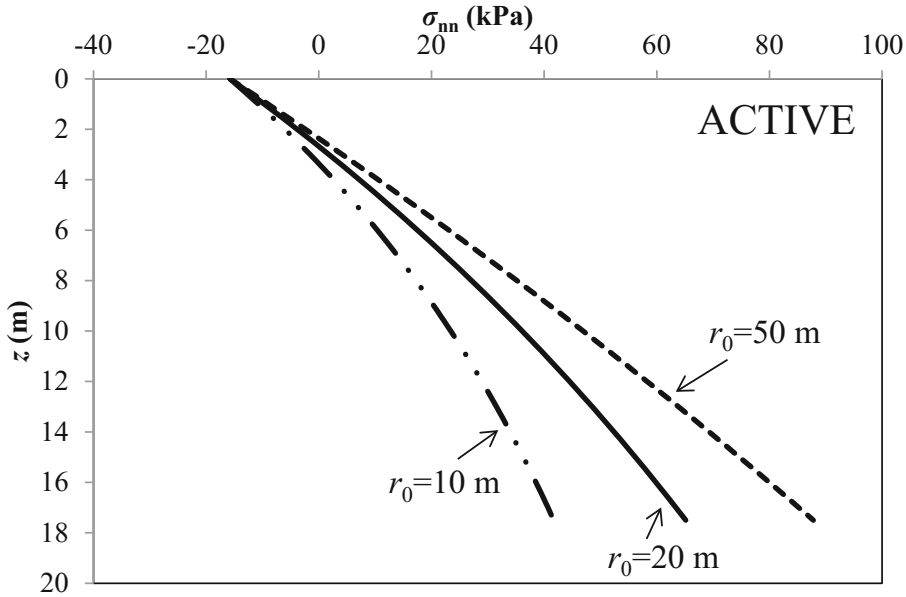


a. active case

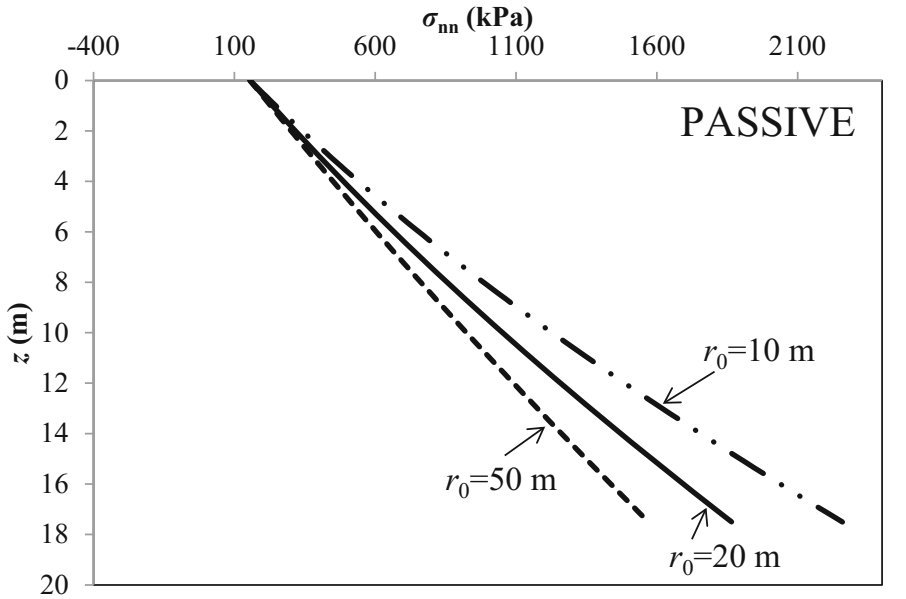


b. passive case

**Fig. 5.** Influence of the length scale on computed earth pressures.

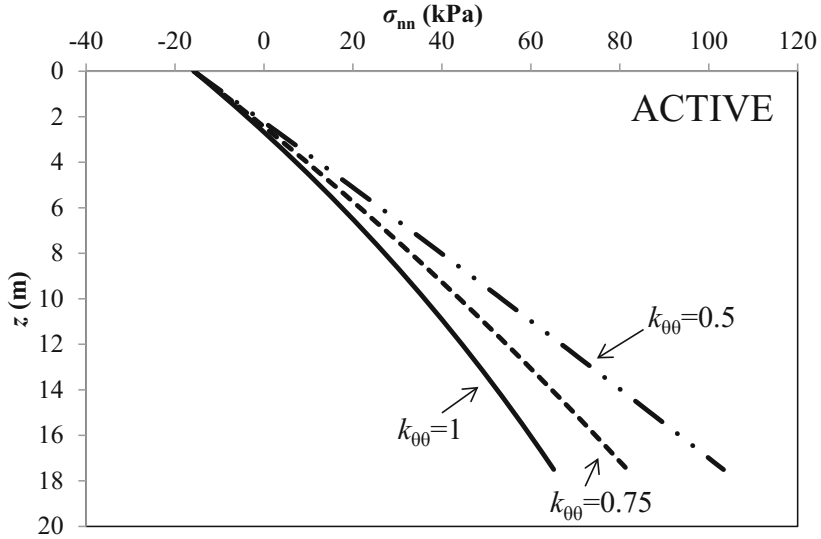


a. active case ($k_{\theta\theta}$=1 here means the circumferential stress is equal to the major principal stress)

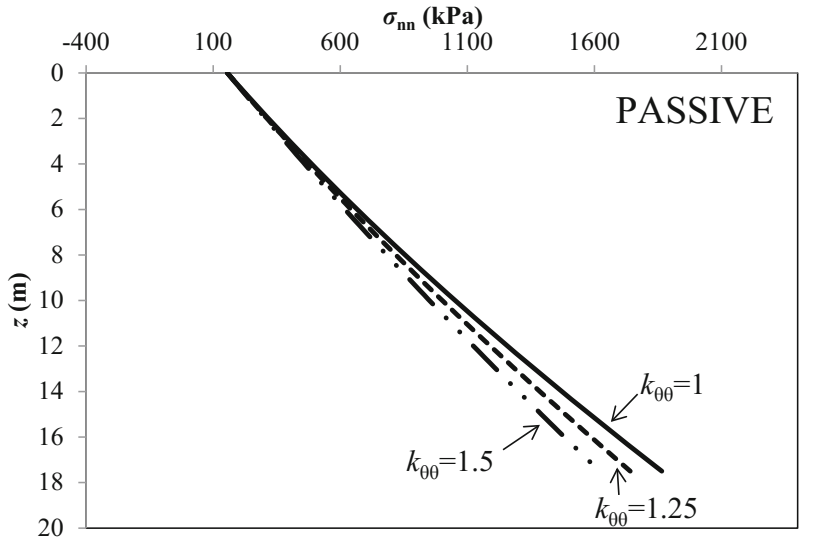


b. passive case ($k_{\theta\theta}$=1 here means the circumferential stress is equal to the minor principal stress)

**Fig. 6.** Influence of the magnitude of the circumferential stress on computed earth pressures.

**Table 1.** Parameters adopted in analyses.

| Case no. | $(\chi s)_0$ [kPa] | $k_{\chi s}$ [kPa/m] | $r_0$ [m] | $k_{\theta\theta}$ [-] |
|---|---|---|---|---|
| 1.1 | 0 | 0 | 20 | 1 |
| 1.2 | 20 | −1 | 20 | 1 |
| 1.3 | 40 | −1 | 20 | 1 |
| 2.4 | 0 | 0 | 10 | 1 |
| 2.5 | 0 | 0 | 20 | 1 |
| 2.6 | 0 | 0 | 50 | 1 |
| 3.7 | 0 | 0 | 20 | 0.5 (active) |
| 3.8 | 0 | 0 | 20 | 0.75 (active) |
| 3.9 | 0 | 0 | 20 | 1 (active) |
| 3.10 | 0 | 0 | 20 | 1.5 (passive) |
| 3.11 | 0 | 0 | 20 | 1.25 (passive) |
| 3.12 | 0 | 0 | 20 | 1 (passive) |

### 4.1 Influence of the Contribution of Suction to the Effective Stress

The influence of the contribution of suction to the effective stress profile is shown in Figs. 4a–b. The effective stresses $\sigma'_{nn}$ normal to the wall are plotted against $z$ in these figures. The contribution of suction to the effective stress increases the lateral earth pressure in active and passive failures.

### 4.2 Influence of the Length Scale

The influence of the length scale is shown in Figs. 5a–b. As $r_0$ increases, the lateral earth pressure becomes higher in active failure and becomes lower in passive failure. These results imply that the axisymmetric retaining wall problem cannot be made completely independent of the length dimension. In particular, design charts for axisymmetric retaining wall problem e.g. Liu et al. [10] and Keshavarz and Ebrahimi [12] must contain $r_0$.

### 4.3 Influence of the Magnitude of the Circumferential Stress

The influence of circumferential stress is shown in Figs. 6a–b. When the circumferential stress becomes smaller than the major principal stress in active failure, the lateral earth pressure increases (Fig. 6a). When the circumferential stress becomes greater than the minor principal stress in passive failure, the lateral earth pressure reduces (Fig. 6b).

## 5 Conclusions

The slip line theory has been applied to a retaining wall-unsaturated soil interaction problem. The retaining wall is vertical and axisymmetric. Assuming the wall reaching active and passive failures, the governing equations are presented and solved iteratively using the finite difference method. An example of analysis shows that limiting lateral

earth pressures are higher in unsaturated soil. This is due to the contribution of suction to the effective stress. Moreover, the length scale and the magnitude of the circumferential stress are shown to influence the lateral earth pressure significantly.

## References


1. Fredlund, D.: Second Canadian geotechnical colloquium appropriate concepts and technology for unsaturated soils. Can. Geotech. J. **16**, 121–139 (1979)
2. Pufahl, D.E., Fredlund, D., Rahardjo, H.: Lateral earth pressure in expansive clay soils. Can. Geotech. J. **20**, 228–241 (1983)
3. Lu, N., Likos, W.J.: Unsaturated Soil Mechanics, 1st edn. Wiley, Hoboken (2004)
4. Vo, T., Russell, A.R.: Slip line theory applied to a retaining wall–unsaturated soil interaction problem. Comput. Geotech. **55**, 412–428 (2014)
5. Vahedifard, F., Leshchinsky, B.A., Mortezaei, K., Lu, N.: Active earth pressures for unsaturated retaining structures. J. Geotech. Geoenvironmental Eng. **141**(11) (2015)
6. Vo, T., Taiebat, H., Russell, A.R.: Interaction of a rotating rigid retaining wall with unsaturated soil in experiments. Géotechnique **66**, 366–377 (2016)
7. Vo, T., Russell, A.R.: Interaction between retaining walls and unsaturated soils in experiments and using slip line theory. J. Eng. Mech. **143**(4) (2017)
8. Bishop, A.W.: The principle of effective stress. Teknisk Ukeblad **106**, 859–863 (1959)
9. Cheng, Y.M., Hu, Y.Y., Wei, W.B.: General axisymmetric active earth pressure by method of characteristics: theory and numerical formulation. Int. J. Geomech. **7**, 1–15 (2007)
10. Liu, F-q., Wang, J-h., Zhang, L-l.: Axi-symmetric active earth pressure for layered backfills obtained by the slip line method. J. Shanghai Jiaotong Univ. (Sci.). **13**, 579–584 (2008)
11. Liu, F.Q., Wang, J.H., Zhang, L.L.: Discussion of "General axisymmetric active earth pressure by method of characteristic - theory and numerical formulation" by Y.M. Cheng, Y. Y. Hu, and W.B. Wei. Int. J. Geomech. **8**, 325–326 (2008)
12. Keshavarz, A., Ebrahimi, M.: Axisymmetric passive lateral earth pressure of retaining walls. KSCE J. Civ. Eng. **21**(5), 1706–1716 (2016)
13. Davis, E.H., Booker, J.R.: The effect of increasing strength with depth on the bearing capacity of clays. Géotechnique **23**, 551–563 (1973)
14. Tani, K., Craig, W.H.: Bearing capacity of circular foundations on soft clay of strength increasing with depth. Soils Found. **35**, 21–35 (1995)
15. Hu, Y., Randolph, M.F.: Deep penetration of shallow foundations on non-homogeneous soil. Soils Found. **38**, 241–246 (1998)
16. Sokolovski, W.V.: Statics of Soil Media, 2nd edn. Butterworths, London (1954)
17. Liu, F., Wang, J.: A generalized slip line solution to the active earth pressure on circular retaining walls. Comput. Geotech. **35**, 155–164 (2008)
18. Martin, C.M.: User guide for ABC - analysis of bearing capacity version 1.0. University of Oxford, UK (2004)
19. Vo, T., Russell, A.R.: Bearing capacity of strip footing on unsaturated soils by the slip line theory. Comput. Geotech. **74**, 122–131 (2016)

# Sanding Onset for Offshore Depleted Using Critical Drawdown Pressure: A Case Study for Well X Cuulong Basin in Vietnam

Tu An Bui[1], Van Hung Nguyen[1(✉)], Tien Trung Duong[1], Hai Linh Duong[1], Huu Truong Nguyen[1], and Minh Hoang Truong[2]

[1] Petrovietnam University, Baria, Vung Tau, Vietnam
{anbt, hungnv, trungdt, linhlh, truongnh}@pvu.edu.vn
[2] Ho Chi Minh City University of Science, Ho Chi Minh City, Vietnam
tmhoang@hcmus.edu.vn

**Abstract.** This paper presents the reservoir pressure depletion will cause rock stress changes, which results in an increasing likelihood of serious sand production in the unconsolidated sandstone reservoir. This paper aims at offshore unconsolidated sandstone oil reservoir, analyzes rock stresses of the borehole wall with impact of reservoir pressure depletion on in-situ stresses on rock strength. A full review basic theory in geomechanics will be presented, such as: rock failure criterions, sanding critical drawdown pressure calculating model and a numerical calculating method for the model are developed. Furthermore, a case study sanding prediction method for pressure depletion of offshore oil reservoir in Cuulong Basin, Vietnam also is presented. Using the model analysis, on the other hand the chart of sanding onset is relatively large with the high formation pressure depletion. On the other hand, the sand will be appeared no matter how small the drawdown is.

**Keywords:** Sanding · Drawdown pressure · Geomechanics model

## 1 Introduction

Currently, there are many studies about geological structure and oil and gas exploration in some different regions in Cuu Long basin using various methods and research materials. Many discoveries have been put into production such as Bach Ho, Rang Dong and Rong. Oil and gas in Cuu Long basin are produced from three targets: fractured granite basement, Oligocene and Miocene sandstone, in which Miocene sandstone is usually unconsolidated or weakly consolidated. Therefore, in production stage, when pore pressure declines, increase of formation stresses causes formation failure so sanding occurs. Sanding normally involves with pressure depletion, mechanical characteristics of rock and production rate. If an oil well is completed without sand control equipment, cohesionles sand particles could be transported from the reservoir to the wellbore by the flow of fluid and cause reduction in production rate. Sand accumulation in wellbore restricts fluid flow from reservoir to wellhead. Sand also causes erosion of downhole and surface facilities. Thus, it is necessary to limit sanding

© Springer Nature Singapore Pte Ltd. 2018
H. Tran-Nguyen et al. (eds.), *Proceedings of the 4th Congrès International de Géotechnique - Ouvrages -Structures*, Lecture Notes in Civil Engineering 8,
DOI 10.1007/978-981-10-6713-6_78

impacts in production stage by selecting an appropriate sanding onset prediction model for forecasting sanding potential of oil wells, which is absolutely necessary.

Many sand production prediction models have been developed in oil and gas industry. One of them is technical method and logging to determine maximum production rate in sandstone reservoir without sand control so that sanding does not occur. Core experiments are conducted at reservoir conditions to determine failure states due to stress variation, perforation conditions, etc.

In this paper, the authors present the sanding onset prediction model for wells in sandstone reservoir in Cuu Long basin. This model introduces a relationship to calculate critical bottom hole pressure corresponding to a known value of reservoir pressure from core data, in-situ stresses, depth, inclination angle and azimuth of well. An excel spreadsheet is also presented to calculate from input data available.

## 2 Geology Data

The geological structure of Cuu Long basin is very complex. The basin was formed as a result of collision of three tectonic plates: the Eurasian plate from the North, the Indo-Australian plate from the West and South; the Pacific plate from the East [Nguyen et al. 2014]. During pre-Tertiary, entire Southeast Asian continental shelf is influenced by the folding and magmatic processes many times. Therefore, most of the Pre-Cenozoic sedimentary areas, basements were crinkled and became heterogeneous in age and material content.

During the early period of Early Miocene, starting of folding, strong subsidence took place in the central of the basin, subsidence rate increased, marine flooded into this area and the egde zones were deltaic. Therefore, a specific system created in this period were characterized by the coastal-deltaic sediments. Along the way to the center of the basin, clay and silt content rose. In deep axial zone, material content was mainly coastal fluvial clay and silt. During the late period of Early Miocene, Rotalia shale section appeared with the thickness of about 200–250 m, covered almost the entire basin and acted as a regional seal. During Middle Miocene, the basin continued subsiding, marine incursion flooded into a large area and formed Con Son sediment including sandstone formations alternating thin siltstone layers and shale. In the late period of Middle Miocene, the basin was lifted up.

In conslusion, Cuu Long basin experienced various development stages, such as foreland basin (before Oligocene), rift basin (in the Oligocene), folding basins (in the Miocene), and continental shelf basin (from Pliocene to present). Sediment supply sources were mainly from Cuu Long delta in the northwest and Corat – Con son uplift in the southwest. In the initial stage, in Eocene-Oligocene, Con Son uplift acted as submarine basis separating between the basin and South China Sea. However, since the late Miocene, the area involved in the process of subsidence and expansion. This process still continues, marine floods to the entire basin, while continental shelf materials are deposited. This basin forms were related to the tensile stresses so faults in the basin were mainly normal and horsts, grabens were formed: this is the main focus of upward movement of oil from the deep reservoirs.

# 3 Theory

## 3.1 Overview

Sanding is the appearance of small to large amount of solid particles flowing with reservoir fluid. Solid content varies from several grams per a ton of fluid. When the amount of sand produced is larger than a certain limit value (this limit depends on the conditions of specified fields, such as the limit in Gulf Coast field is 0.1% of total volume), sand control must be applied. The consequence of sanding is enormous, sand accumulation in production well can cause well abandonment, formation collapse so that the well can not be produced, sand rise in well while drilling…

## 3.2 Rock Mechanics

Changes in status of rock are important to determine failure mechanism. Failure can be seen on the curve (Fig. 1), the figure illustrates the change of the rock's status when pressure changes. Rock has three states: elastic, plastic and failure state. This curve consists of four regions. The Fig. 1 shows rock mechanics hebaviour under a loading. From the point O to A: elastic deformation, if there is force conducted on the object, it causes deformation and then the object returns to its original position when stopping conducting the force. From A to B: strain changes with stress. From O to B: the elasticity region. Point B is ultimate strength. From B to C: when force is applied, deformation changes and the object can not return to its original position when stopping conducting the force. BC is the plasticity region, state starts changing at point B. From C to D: rupture.

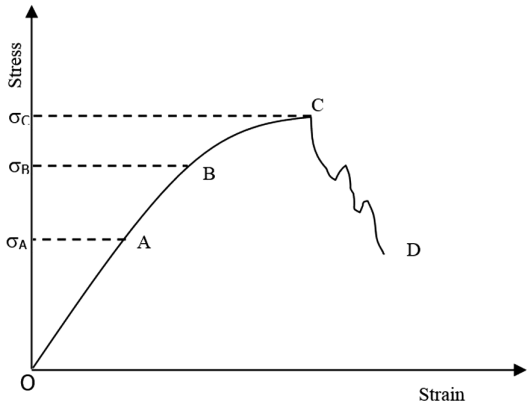


**Fig. 1.** Stress and strain relationship

## 3.3 Wellbore Bore Stability

In order to determine the stress state of the formation at a certain depth, we consider an infinitesimal element at that depth. Meanwhile, the element is subjected to forces, as shown below (Fig. 2).

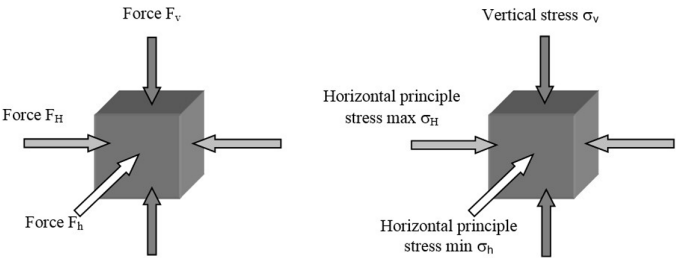


**Fig. 2.** Stress state of formation

a. Determination of formation stress

The stresses of the formation are always in equilibrium or steady state. If there is any change of forces, there will be a stress concentration and a new equilibrium will be established. The stress state of the formation is represented by three principal stresses: overburden stress ($\sigma_v$), minimum horizontal stress ($\sigma_h$) and maximum horizontal stress ($\sigma_H$). The methods to determine the magnitude and direction of the stress are microfrac testing, determination of deformation and record of elastic deformation. In addition, methods for determining the stress related to the destruction of formation such as: Kaiser's effect, bottom hole illustration tools and sonic logging tools. However, stress is also determined through density log by correlations.

In fact, overburden stress ($\sigma_v$), minimum horizontal stress ($\sigma_h$) and maximum horizontal stress($\sigma_H$) are determined through stress gradient values from the researches and measures, these values will be compared with the values calculated from formulas or core experiments.

b. Formation failure mechanism

When the formation is drilled through the new stress state is set around the well. The magnitude of this new state of stress can be large enough to cause failure to the formation. Any impact of the stress state can cause sand appearance. If bottom hole pressure increases, normal stress increases and tangential stress decreases. When tangential stress

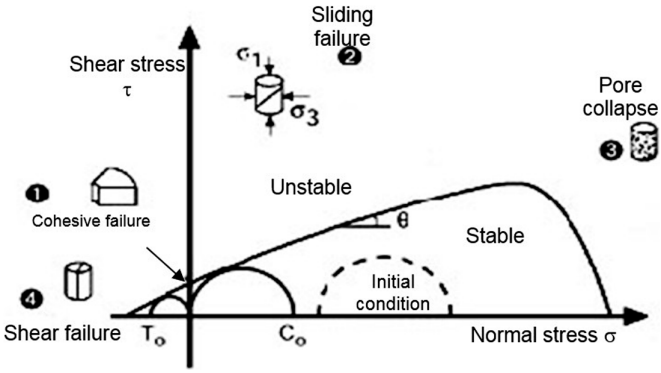


**Fig. 3.** Mohr's failure mechanism

falls to a small enough value, it will change from shear state to tensile state. Most of formation can remain stable against tensile force, but will fail due to shear force. If bottom hole pressure drops, tangential stress will increase and normal stress will decrease. Large pressure reduction in the wellbore can cause normal stress greater than formation strength. Sand particles begins to flow into the well. Formation failure mechanism includes: tensile failure, shear failure, cohesive failure and pore collapse (Fig. 3).

## 4 Building Model

### 4.1 Studying Some Models for Predicting Sand Production

a. Field data method

Morita (1989) et al., 1989 study sand production from field data. In this study, five sand types from five different formations are experimented: sand production from weak formations (Alaska region); sand production due to water influx in formations of weak to moderate strength (North Sea region); sand production due to reservoir pressure reduction in strong formations, abnormal tectonic forces (Saint Andreas – California) and sand production due to dramatic change of flow or excessive production rate.

b. Core experiment

Study of perforation stability based on numerical and physical model is presented by Somerville and Bin Samsuri (1991). Physical model consists of two types: block model and cylinder model. Uniaxial compression test is conducted on a block model with length of 457 mm, width of 305 mm, 127 mm diameter dril hole, 12-mm-diameter perforation tunnel and alternate perforation density and angle. Triaxial compression test is conducted on cylinder model with length of 110 mm, 55 mm diameter, 25 mm diameter drill hole and alternate perforation density and angle. Wellbore failure occurs at the perforation entrance and propagates along the wellbore. An observation is drawn that: the influence of geometric parameters of perforation such as diameter and length of shot hole to perforation stability and sand production is less strong than influence of structural parameters such as perforation density, perforation angle and shape of perforation hole. Spiral perforation tunnel is more stable and produces less sand than other shapes such as linear and plain shape. The perforation stability decreases and amount of produced sand increases when the perforation density increases.

c. Numerical model method

In this method, mechanical characteristics of field are dertermined in laboratory by using finite element method to predict affected formation based on principle stresses at failure position. Young's modulus and Poisson's ratio are determined in stress and strain laboratory. The fine grain and coarse grain models are used to determine their sanding potential. The results show that the amount of fine grains produced increases after limit point and extends when reaching equilibrium. The amount of solid particles produced may involve with the volume and ares of rock limit surface. Therefore, the amount of sand produced can be estimated by defining limit of the rock surfaces around the perforation hole.

d. Welltest method

Welltest process designed properly with efficient operation of surface equipment, bottom-hole tools and sand detection devices is the best method to verify sand production at initial reservoir pressure. However, testing equipment and well completion must be compatible with critical pressure drawdown and flow rate. The process must also be operated continuously under the original sand production points to check whether the sand amount of the flow rate decreases fast, otherwise an intermittent sand production does not take place. Sand checking process should include repeat of flow checking steps and the expansion of flow under lightly sand production conditions.

### 4.2 Sand Production Prediction Model Applied to Cuu Long Basin

a. Basis of model

Many authors have studied the stress distribution near the wellbore, but mainly focused on the assumption that the vicinity of wellbore is homogeneous, near-wellbore stress zones are poroelastic. Considering a well in space, the stress distribution around the well are determined through the Kirsch's equation, in this case well model is assumed to be linear elastic and homogenous.

Let consider the coordinate system where the z axis coincides with the axis of the well and angle θ from the x-axis to a certain direction (Fig. 4). So Kirsch's equations for stress calculation are as follow Eqs. (1)–(3):

$$\sigma_x = (\sigma_H \cos^2 a + \sigma_h \sin^2 a)\cos^2 i + \sigma_v \sin^2 i \tag{1}$$

$$\sigma_y = (\sigma_H \sin^2 a + \sigma_h \cos^2 a)\sin^2 i \tag{2}$$

$$\sigma_z = (\sigma_H \cos^2 a + \sigma_h \sin^2 a)\sin^2 i + \sigma_v \cos^2 i \tag{3}$$

b. Calculation model

From the theoretical basis of formation failure, a sand production prediction model is commonly used today in the oil and gas exploration companies. This model [Edson et al. 2014] predicts the shear stress around the open hole, or cased hole completion (with perforation). Sand production is considered to occur when the maximum effective tangential stress around the wellbore exceeds the apparent axial compressive stress (Fig. 5).

In this model, formation stresses are considered to be perpendicular to the axis of the well, while tangential stresses on the surface of the wellbore are given by Eqs. (4) and (5):

$$\sigma_{\theta 1} = 3\sigma_y - \sigma_x - p_w(1 - A) - Ap_r \tag{4}$$

$$\sigma_{\theta 2} = 3\sigma_x - \sigma_y - p_w(1 - A) - Ap_r \tag{5}$$

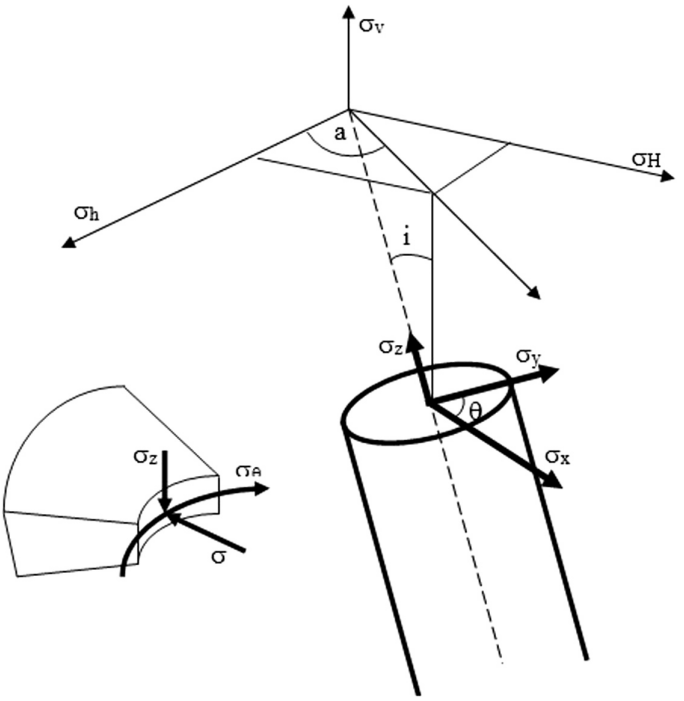


**Fig. 4.** Stress distribution at wellbore

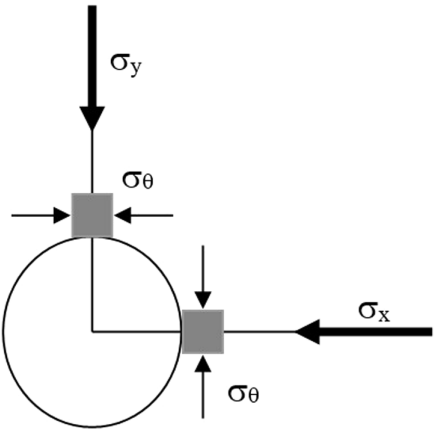


**Fig. 5.** Tangential stresses at wellbore

To prevent sand production, the maximum effective tangential stress, $\sigma_{\theta 2} - p_w$, must be smaller than effective formation strength, U: $\sigma_{\theta 2} - p_w \leq U$

Solving this inequation for bottom hole pressure, $p_w$ in Eq. (6):

$$p_w \geq \text{CBHFP} = \frac{3\sigma_1 - \sigma_3 - U}{2 - A} - p_r \frac{A}{2 - A} \tag{6}$$

Critical Drawdown Pressure (CDP) is defined as the pressure reduction from the reservoir pressure to a pressure value at which formation failure occurs, Eq. (7).

$$\text{CDP} = \frac{1}{2 - A}[2p_r - (3\sigma_1 - \sigma_3 - U)] \tag{7}$$

Critical reservoir pressure (CRP) is defined as the reservoir pressure reduction corresponding to the CDP = 0. Therefore, we have Eq. (8):

$$\text{CRP} = \frac{3\sigma_1 - \sigma_3 - U}{2} \tag{8}$$

Formation strength, U is determined from thick wall cylincder model experiments with outer diameter-inner diameter ration ranging from 6 to 8. Thus:

- U = 3.1TWC - for cased and perforated completion.
- U = 2.5TWC- for open-hole completion.

where TWC: is determined from experiment. In addition, TWC is also determined from the empirical formulas $\text{TWC} = 9.1\text{UCS}^{0.61}$ or correlations.

$\sigma_1$ and $\sigma_3$ are linearly dependent on reservoir pressure $p_r$. In production stage, reservoir pressure declines and then in-situ stress and formation stress change as a result of reservoir pressure depletion. Therefore, a sand-free producing well can

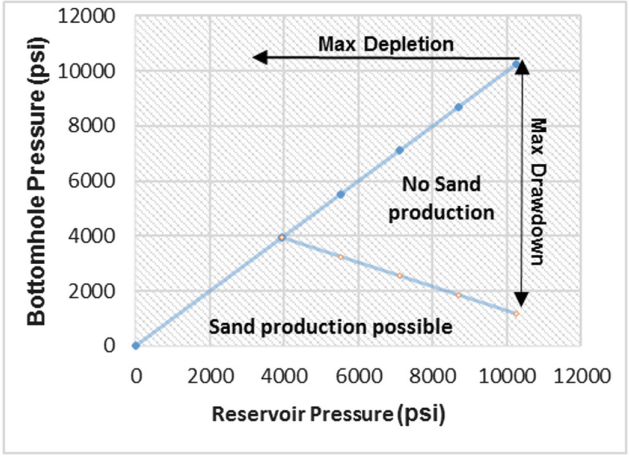


**Fig. 6.** Predicting sanding potential by shear failure stress model

produce sand after a period of time. To study the effect of reservoir pressure depletion on sanding potential, the model is conducted at the different reservoir pressure. In Fig. 6, the triangular graph is built to identify no-sanding regions and sanding regions based on the relationship between depletion of reservoir pressure and critical bottom hole pressure. Thus, there is a critical bottom-hole pressure corresponding to a reservoir pressure, if bottom hole pressure is smaller than this critical bottom-hole pressure the formation will fail and sand will be produced.

## 5 Results and Discussion

### 5.1 Mechanical Characteristics of Miocene Sandstone

From the theory above, the sanding mechanisms due to shear forces involve directly with the reservoir pressure depletion. Therefore, to prevent sand production during production stage, fields must be produced at minimum (critical) bottom-hole pressure while reservoir pressure declines. To produce above this level, it is necessary to use mechanical sand control and water and gas injection for reservoir pressure maintainance.

From core analysis results of some fields such as Bach Ho, Rong, Rang Dong, Su Tu Den, compressive strength changes from 638 to 3,075 psi, average value is 1,407 psi. According to the classification of Deere and Miller, compressive strength of Miocene sandstone in Cuu Long basin are generally very weak. Poisson's ratio changes from 0.22 to 0.37 and average value is 0.29. Young's modulus varies from 377,098 – 1,363,354 psi and average value is 681,677 psi. Permeability varies from 390–4,402 mD and average value is 2,199 mD. Porosity varies from 14.8–31.7% and average value is 26.4%. Overall, permeability and pororsity of Miocene sandstone in Cuu Long basin are quite high, so this is a good reservoir. However, sand production occurs easily due to very weak mechanical characteristics.

### 5.2 Results of Model Application

The production wells X1, X2, X3, X4 are designed to be drilled in Miocene sandstone, initial information shown in Table 1, sanding potential are analyzed with azimuth and inclination of well or perforation angle for open hole and/or cased – perforated wells during reservoir pressure depletion.

a. X1 well

Sanding potential is analyzed for open hole completion. Results (Fig. 7) shows that with the initial reservoir pressure of 9,836 psi, the maximum allowable drawdown pressure is 6,913 psi corresponding to allowable critical bottom-hole pressure of 2,923 psi. No-sanding zone expressed by triangular graph describes the relationship between the reservoir pressure and bottom hole pressure. Considering well inclination angle, with constant azimuth, the Fig. 8 shows that the greater the angle is the bigger the sanding zone is and vice versa. Considering well azimuth, with constant inclination angle, the Fig. 9 shows that the smaller the azimuth is the smaller the sanding zone is and vice versa.

**Table 1.** Wells information

| Parameters | Unit | X1 | X2 | X3 | X4 |
|---|---|---|---|---|---|
| Well diameter | in | 8.5 | 8.5 | 8.5 | 8.5 |
| TVD | m | 3,442 | 3,045 | 3,000 | 2,705 |
| Inclination angle (i) | degree | 65 | 6 | 10 | 90 |
| Azimuth (a) | degree | 80 | 70 | 60 | 60 |
| Poisson's ration | | 0.29 | 0.28 | 0.15 | 0.28 |
| Biot's constant | | 1 | 1 | 1 | 1 |
| Reservoir pressure | psi | 9,836 | 9,131 | 8,000 | 3,916 |
| UCS | psi | 1,500 | 1,800 | 1,500 | 2,093 |
| Overburden stress | psi | 11,150 | 9,100 | 9,100 | 8,509 |
| Minimum horizontal stress | psi | 9,100 | 9,050 | 9,050 | 5,297 |
| Maximum horizontal stress | psi | 10,500 | 10,500 | 10,500 | 6,078 |

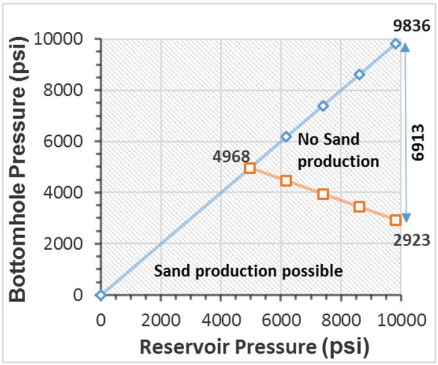


**Fig. 7.** Sand production prediction for X1 well

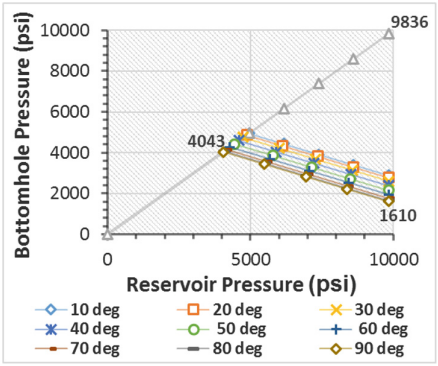


**Fig. 8.** Sand production analysis of inclination for X1 well

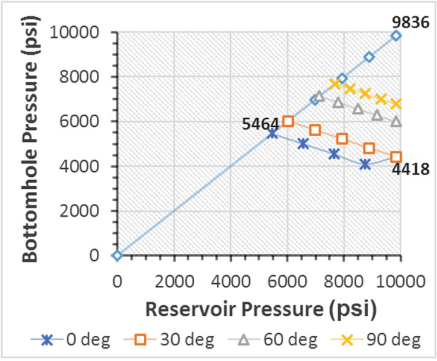


**Fig. 9.** Sand production analysis of azimuth for X1 well

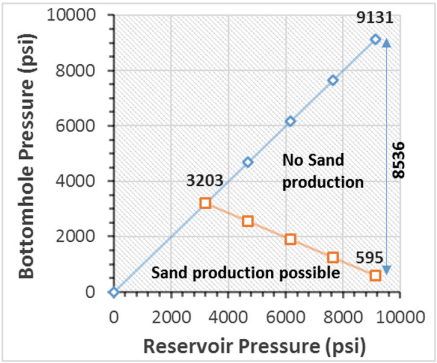


**Fig. 10.** Sand production prediction for X2 well

The results show that: when drilling a production well, it is necessary to consider the angle of inclination and the azimuth of wellbore in producing formation to determine the maximum value of bottom-hole drawdown pressure without sand production.

b. X2 well

Sanding potential is analyzed for open hole completion. Results (Fig. 10) shows that with the initial reservoir pressure of 9,131 psi, the maximum allowable drawdown pressure is 8,536 psi corresponding to allowable critical bottom-hole pressure of 595 psi. If differential pressure exists at bottom-hole when reservoir pressure declines to 3,203 psi, the formation fails and sand production occurs. The Fig. 11 shows that the no-sanding zone is very stable inspire of an increase in inclination angle. Sanding potential is independent on inclination angle when azimuth remains constant (Fig. 12).

c. X3 well

Sanding potential is analyzed for open-hole and cased - perforated completion. Calculation results are shown in Fig. 13. The result above shows that sanding potential in open hole completion is very high with critical reservoir pressure of 4,988 psi,

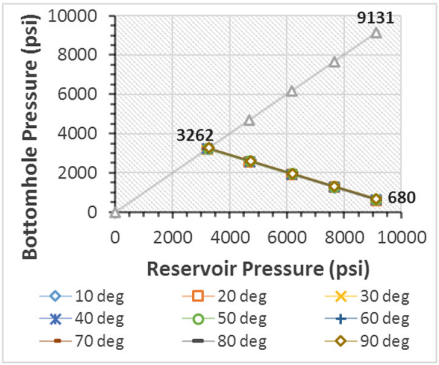


**Fig. 11.** Sand production analysis of inclination for X2 well

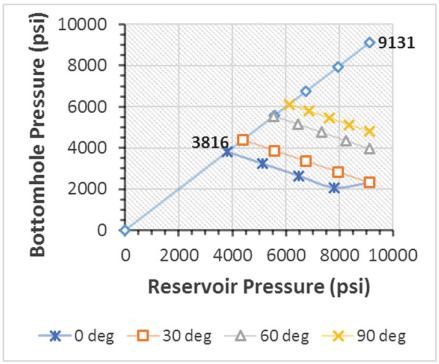


**Fig. 12.** Sand production analysis of azimuth for X2 well

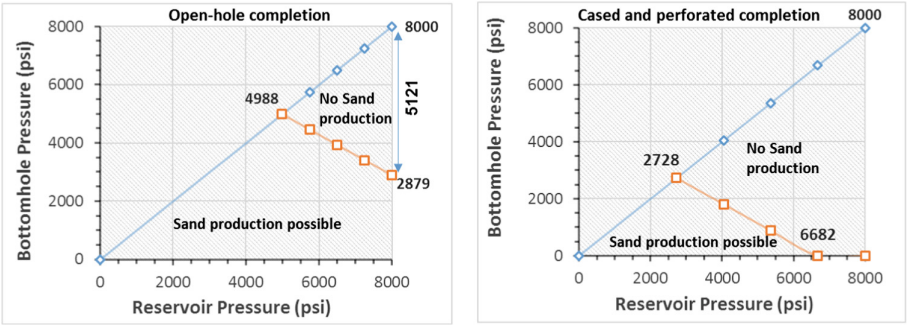


**Fig. 13.** Sand production prediction for X3 well

maximum differential pressure of 5,121 psi, minimum bottom hole pressure of 2,879 psi. In the other hand, for cased and perforated completion well the differential between reservoir pressure and bottom hole pressure could be equal to reservoir pressure until

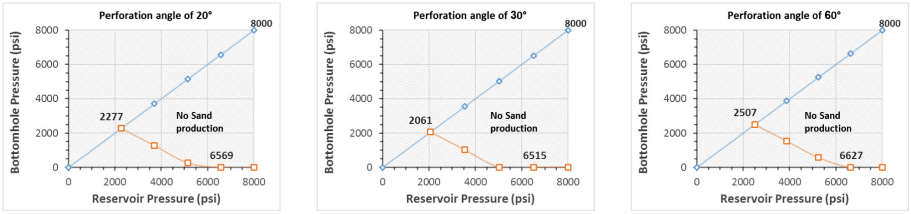


**Fig. 14.** Sand production analyses with respect to inclination for X3 well

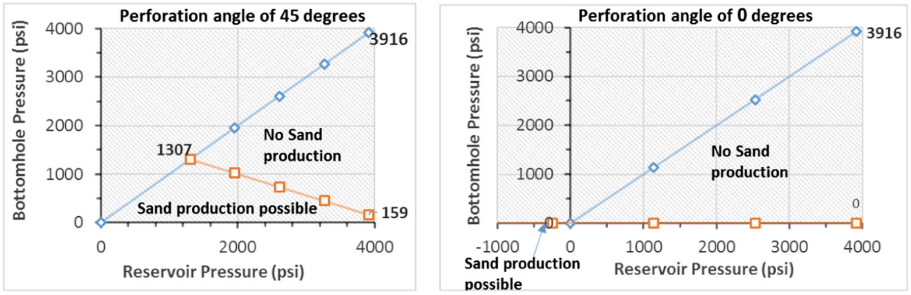


**Fig. 15.** Sand production analyses with respect to perforation angle for X4 well

reservoir pressure reachs 6,682 psi, critical reservoir pressure is 2,728 psi, no-sanding zone is very large, so production stage is efficient. In cased and perforatied completion, Fig. 14 illustrates the result of considering effect of perforation angle to no-sanding zone when perforation angle varies from 20 to 60°. The result shows that the optimum perforation angle is approximately 30° therefore no-sanding zone is largest.

d. X4 well

Sanding potential is analyzed with perforation angle for cased completion. The result in the Fig. 15 indicates that cased and perforated completion is optimum for this horizontal well, when perforation angle is 45° sand production phenomenon will occur at the end of life cycle of the field. However, when the perforation angle is 0° (perforations are parallel to the vertical line), sand production phenomenon will not occur.

## 6 Conclusion

Sand production prediction model studied in this paper could be applied when production wells in the Miocene sandstone in Cuu Long Basin. This model predicts the failure shear stress around openhole wells, or cased and perforated completion wells. Sand production problem occurs when the maximum value of the effective tangential stress around wellbore exceeds the effective formation strength. From the theory studied above, the sanding mechanism due to shear forces directly involves with the reduction of the reservoir pressure. Therefore, to prevent sanding during production

stage, bottom hole pressure must be greater than critical pressure (CBHFP) during reservoir pressure depletion. The methodology to determine CBHFP could be divided into three steps:

1. Determine stress along the well axe (UCS log-derived) in the producing wellbore section from sonic log data, uniaxial compression test of core sample and mechanical formation.
2. From the value of UCS, estimate effective formation strength U from correlation between UCS and TWC, TWC could be estimated by empirical formulas.
3. Estimate overburden stress, reservoir pressure and in-situ stresses ($\sigma_1$ and $\sigma_2$) along the productive section of wellbore. From the values of $\sigma_1$ and $\sigma_2$ and the values determined in the first step, calculate CBHFB using the formula below:

$$p_w \geq \text{CBHFP} = \frac{3\sigma_1 - \sigma_2 - U - Ap_r}{2 - A}$$

Calculation results and analysis show that sanding potential of a well depends on effective formation strength, in-situ stress states, azimuth and inclination angles of the wells, perfpration direction, the azimuth of the principal stresses. To produce at high flow rate and optimum pressure without sanding, production well in sandstone reservoir must be completed with casing and perforation. Declination angle, azimuth and perforation angle should be analyzed such that sanding zone is smallest and drawdown pressure is maximum.

**Acknowledgments.** This work is funded by Petrovietnam University under grant code GV1501, we would like to thank to the board of manager of PVU for the support.

## References

Nguyen, B.T.T., Tokanaga, T., Okui, A.: In Situ Stress and Pore Pressure Fields in the North Cuu Long Basin, Offshore Vietnam. SPE 87055 (2014)

Araujo, E.F., et al.: Analytical Prediction Model of Sand Production Integrating Geomechanics for Open Hole and Cased – Perforated Wells. SPE-171107-MS (2014)

Morita, N., Whitfill, D.L., Massie, I., Knudsen, T.W.: Realistic Sand Production Prediction: Numerical Approach. SPE Production Engineer (1989)

Somerville, J.M., Bin Samsuri, A.: Perforation stability: physical and numerical modellin, pp. 91–763. ARMA (1991)

# Soil Stabilization by Using Alkaline-Activated Ground Bottom Ash Coupled with Red Mud

My Quoc Dang[1], Young-sang Kim[2(✉)], and Tan Manh Do[2]

[1] Department of Civil Engineering, Nha Trang University, Nha Trang, Khanh Hoa, Vietnam
quocmy89@gmail.com
[2] Department of Civil and Environment Engineering, Chonnam National University, Yeosu, South Korea
geoyskim@chonnam.ac.kr, geotmdo@gmail.com

**Abstract.** This study evaluates the feasibility of incorporating bottom ash and red mud into a binder to stabilize soil. In this study, the bottom ash collected from Honam Thermal Power Plant in South Korea was ground to decrease particle size. It was then coupled with red mud to form a new binder based on the geopolymer synthesis theory. Sodium silicate solution ($Na_2SiO_3$) in terms of alkaline-activator was added into mixture to enhance the activity of binder. Weathered granite soil which is classified as SM in USCS is the target of stabilization. Unconfined compressive strength of stabilized soil and heavy metal content of leachate were examined. Experimental results showed that ground bottom ash coupled with red mud can be used to stabilize weathered granite soil at the ambient curing condition. The highest compressive strength of stabilized soil was 4.1 MPa. Red mud in certain limits has contributed to the increment of soil strength, however, the long-term strength decreased with the increase of red mud content. In addition, based on the results obtained with leaching test, it can be concluded that leachate from the stabilized soil is not harmful to the environment.

**Keywords:** Soil stabilization · Ground bottom ash · Red mud

## 1 Introduction

With urbanization, more and more residences, high-rise buildings, and transport systems (e.g. highways, parking lots, railways, stations) have been constructed. As a result, the demand of land for infrastructure construction increases rapidly. Nevertheless, the construction sites with favorable geotechnical conditions become less available. This makes soil stabilization become an important part of geotechnical practice.

Currently, Portland cement is being widely used as a stabilizer to improve the engineering properties of soil. According to statistics, the global cement production increased from 3310 million to 4100 million tons in the period from 2010 to 2015 (Kim et al. 2016). However, the production of cement raises some environmental issues especially $CO_2$ emissions causing the greenhouse effects. It is estimated that corresponding to one ton of cement produced, one ton of $CO_2$ is emitted into the atmosphere

© Springer Nature Singapore Pte Ltd. 2018
H. Tran-Nguyen et al. (eds.), *Proceedings of the 4th Congrès International de Géotechnique - Ouvrages -Structures*, Lecture Notes in Civil Engineering 8,
DOI 10.1007/978-981-10-6713-6_79

(Daviddovits 2002). The cement production contributes about 7% of the total greenhouse gas emissions on over the world (Shi et al. 2012). In the efforts to solve these issues, many studies that try to find out the alternative material to substitute cement have been published (Higgins 2005; Chindaprasirt et al. 2009). One of the new alternative materials which can be used to replace cement is geopolymer based material.

The term "geopolymer" was first introduced by Joseph Davidovits in 1978 (Davidovits et al. 1990). Geopolymers are formed by reaction between aluminosilicate materials (contain a high amount of silica and alumina) with alkaline solutions, resulting in a mixture of gels and crystalline compounds that ultimately harden into a new strong matrix (Verdolotti et al. 2008). Using geopolymer materials has great significance for the environment. It not only reduces greenhouse gas emissions but also consumes vast volumes of industrial wastes (Majidi 2009). A source of aluminosilicate binder is coal ash - a waste material generated from coal-fired thermal power plants. The main components of coal ash are fly ash (65–95%) and bottom ash (5–35%) (Wang et al. 2005). According to American Coal Ash Association, around 83% of recycling coal ash in U.S is fly ash (ACAA 2016). It has been an effective material successfully used in many projects to improve the strength characteristics of soils. Opposed to fly ash, only a small amount of bottom ash has been recycled. Most of it has been discharged into the environment by mixing with water and pumping to the ash pond or compacting into landfill (Asokan et al. 2005). Coal ash disposal is a big problem of the world due to its possible adverse environmental impacts as well as due to its high volume of the generation which requires a large land area for disposal. Coal ash contains heavy metals and metalloids, these elements can be leached out under acidic conditions and can contaminate the surrounding soils, surface water, and groundwater sources. In recent years, a new approach to the recycling of the bottom ash has been pointed out in some studies of Cheriaf et al. (1999), and Jaturapitakkul and Cheerarot (2003). In that, bottom ash was ground to be used as a partial replacement of cement due to its pozzolanic reaction.

Red mud is a solid waste material produced during the physical and chemical processing of bauxite (Bayer process) in the industrial production of aluminum. The disposal of red mud is nearly similar with coal ash. It is usually disposed in mud impoundment (for slurry state) or heap in the pond (for dry state). The disposal of massive amount of red mud with high alkalinity (pH 10–12.5) has caused serious environmental issues such as groundwater pollution, soil contamination. Furthermore, due to its fine particle, red mud stored in the pond can emit dust into the air and threaten the health of people living around that area (Liu and Zhang 2011). To recycle red mud, there are some studies have succeeded in improving the compressive strength of concrete by using red mud to substitute a part of cement (Ashok and Sureshkumar 2014; Metilda et al. 2015).

This study proposes a new binder that can be used to replace cement in soil stabilization. Herein, ground bottom ash and red mud were activated by alkaline activator to form a binder based on geopolymer synthesis. The specimen was cured at the ambient curing condition which makes it possible to apply in the field. This can turn the bottom ash and red mud into a valuable resource for sustainable infrastructure construction instead of treating it as a waste material.

## 2 Experimental Program

### 2.1 Materials

In the present study, bottom ash was collected from Honam Thermal Power Plant in South Korea. The particles of collected bottom ash were angular, amorphous, irregular and had high porosity with a lot of craters and pores on the surface. In order to be used as a binder, bottom ash was dried at a temperature of 105 °C for 2 days to ensure that moisture content was completely evaporated. Subsequently, a laboratory ball mill machine (UBM-100L, RAMT) was used. After grinding, fineness of ground bottom ash (GBA) was checked complying with standard ASTM C204-16, the test methods for the fineness of hydraulic cement by air-permeability apparatus. The test result indicated that after 3 h of grinding the fineness of ground bottom ash was 2,000 $cm^2/g$. Figure 1 shows the particle size distribution of bottom ash before and after grinding. It can be observed that the particle size of raw bottom ash ranges from 0.075 mm to 10 mm, whereas that of ground bottom ash varies from 0.004 mm to 0.25 mm. In order to determine the chemical compositions of bottom ash, the X-ray Fluorescence test (XRF) was performed. The analyzing result was given in Table 1.

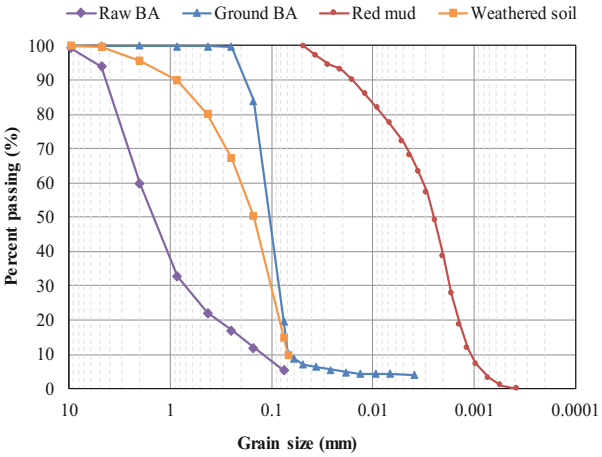


**Fig. 1.** Particle size distributions of materials

**Table 1.** Chemical composition of ground bottom ash and red mud (% by weight)

| | $SiO_2$ | $Al_2O_3$ | CaO | MgO | $Fe_2O_3$ | $TiO_2$ | $K_2O$ | $Na_2O$ | LOI |
|---|---|---|---|---|---|---|---|---|---|
| GBA | 62.53 | 20.91 | 1.80 | 0.69 | 8.70 | 1.28 | 1.44 | 0.39 | 1.85 |
| RM | 15.12 | 19.87 | 7.10 | 0.37 | 22.21 | 5.24 | 0.11 | 14.92 | 13.68 |

Red mud (RM) was collected from an alumina plant in Naju, South Korea, which was dried and pulverized to obtain fine powders. Thereafter, the particle size analysis

and XRF were performed. The test results of the red mud were shown in Fig. 1 and Table 1 along with those of ground bottom ash for comparison. It can be observed that red mud has particle size ranges from 0.0004 mm to 0.05 mm which is much smaller than that of ground bottom ash. In addition, it contains 15.12% of $SiO_2$, 19.87% of $Al_2O_3$ which have a major role in forming geopolymer.

To activate ground bottom ash sodium silicate solution ($Na_2SiO_3$) were used. Sodium silicate solution known as water glass was purchased directly from the company with a $SiO_2/Na_2O$ molar ratio of 3.1 and the percentages by weight are 10% of $Na_2O$, 30% of $SiO_2$ and 60% of water. The other characteristics of the sodium silicate solution are specific gravity = 1.41, viscosity at 20 °C = 400 cp.

Weathered soil was the object of stabilization. After being collected from the field, some components in soil such as roots, leaves were discarded. Thereafter, the soil was dried in the oven to remove the water content. Geotechnical properties of soils including specific gravity, liquid limit, plastic limit, plasticity index, particle size were determined complying to the procedure of American Society of Testing and Materials (ASTM). Test results were summarized in Table 2.

**Table 2.** Geotechnical properties of materials

| Type of materials | $G_s$ | % passing No. 200 | $C_u$ | $C_c$ | LL | PL | PI | USCS |
|---|---|---|---|---|---|---|---|---|
| Weathered soil | 2.62 | 15.05 | 3.22 | 0.86 | 27.8 | NP | – | SM |
| GBA | 2.50 | 19.77 | 1.81 | 0.92 | – | – | – | – |
| RM | 3.15 | 100 | 2.98 | 0.89 | – | – | – | – |
| Remark: NP (Non-plastic) | | | | | | | | |

## 2.2 Sample Preparation and Test Procedure

The mixture proportion was designed to evaluate the effects of red mud content and the amount of $Na_2SiO_3$ on compressive strength of stabilized soil. Herein, the ratio of water/binder and binder/soil were selected as 1.2 and 0.33, respectively. To evaluate the effects of red mud content, the ratio of RM/GBA was varied from 0 to 0.4 and $Na_2SiO_3$/binder was kept at 0.5. To evaluate the effect of activator content, the ratio of $Na_2SiO_3$/binder was varied from 0.3 to 0.6, whereas, RM/GBA ratio was kept at 0.2.

The mixing of mixtures was performed by using a 10-litres mixer. At first, soil and binder were mixed at the setting of 150 rpm for 3 min. Subsequently, alkaline-activators and extra water were slowly added to the mixture and mixed for 10 min. The mixture was then cast into the plastic cylindrical molds (50 mm in diameter and 100 mm in height) by dividing into three layers and tamping 25 times for each layer. For each case study, 10 specimens were prepared to measure unconfined compressive strength as well as the concertation of toxic heavy metals. The specimen was kept in the molds for 3 days, thereafter, it was demolded and cured at the ambient condition with the temperature of 25 °C and 50% of humidity.

The unconfined compressive strength of stabilized soil was determined at 7, 14 and 28 days of curing age and complied a procedure of standard ASTM D2166-16.

Moreover, in order to measure the toxic heavy metal content of leachate, a procedure based on a research of Razak et al. (2009) on industrial waste bottom ash has been applied. At the age of 7 days, the specimen was immersed in a tank filled with distilled water. The amount water filled in the tank was eight times the volume of the specimen (liquid/solid = 8:1). The tank was kept closed at room temperature. At 28 days, water in the tank was collected to determine the toxic heavy metal content. The experiment was performed by using inductively coupled plasma mass spectrometer (ICP-MS) and complied standard ASTM D5673-16.

## 3 Experimental Results

### 3.1 Unconfined Compressive Strength

The effects of RM/GBA ratio on the unconfined compressive strength of stabilized soil is shown in Fig. 2. For the first case that without using of red mud, the compressive strengths obtained at 7, 14, and 28 days are 0.5, 2.4 and 3.1 MPa, respectively. The replacement of ground bottom ash by red mud in certain limit has a positive influence on the development of soil strength. In particular, the compressive strengths increase and get maximum value at the RM/GBA ratio of 0.1 for all curing times. After that point, the compressive strength continuously decreases with the addition of red mud into mixture. This indicates that 0.1 is the optimum RM/GBA ratio for compressive strengths in soil stabilized with ground bottom ash and red mud. This result is consistent with some previous studies (Ashok and Sureshkumar 2014; Metilda et al. 2015). The compressive strength of stabilized soil increases to a certain limit with the use of red mud in the mixture can be explained by the characteristics of red mud. Firstly, red mud has high alkalinity (pH = 11.6) so it can accelerate the dissolve of ions from aluminosilicate materials. Secondly, red mud has fine particles that make specimens become denser and low porosity (Liu and Zhang 2011). Finally, as can be seen in Table 1, red mud contains 35% of $SiO_2$ and $Al_2O_3$. It can offset a part of reactants which were lost when ground bottom ash is replaced. However, when the amount of red mud exceeds the optimal value, the compressive strength decreases due to the

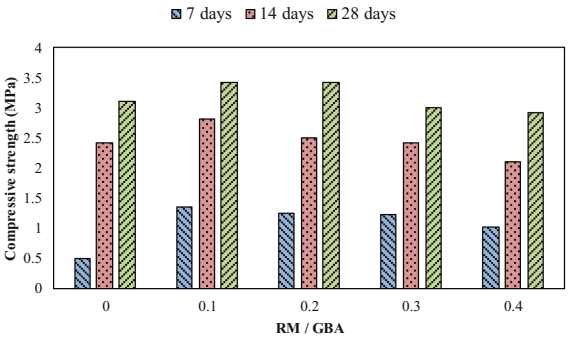


**Fig. 2.** Effects of RM/GBA ratio on unconfined compressive strength of stabilized soil

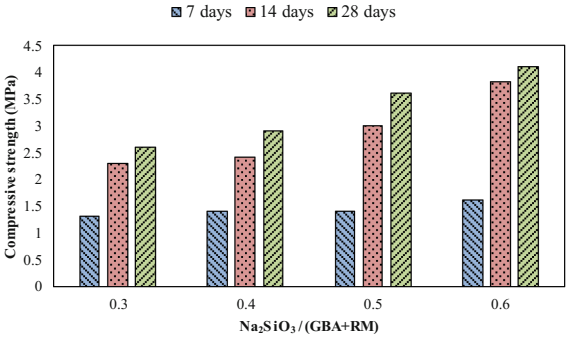


**Fig. 3.** Effects of $Na_2SiO_3$/(GBA + RM) ratio on unconfined compressive strength of stabilized soil

reduction of ground bottom ash amount – the main ingredient which provides Al and Si for geopolymerization.

Figure 3 shows the effect of $Na_2SiO_3$/(GBA + RM) ratio on the unconfined compressive strength of the stabilized. It can be seen that the 7-day compressive strengths of all cases are almost the same. However, the 14-day and 28-day compressive strength show a rapid increase with the increase of $Na_2SiO_3$ amount. In particular, strength increases 1.2 times for case of $Na_2SiO_3$/binder ratio of 0.3 and 1.6 times for final case which the ratio of $Na_2SiO_3$/binder is 0.6. The reason for this phenomenon is that a higher $Na_2SiO_3$/binder ratio provides more reactive silica and hence promotes a larger extent of geopolymerization of the soil mixture. The higher concentration of soluble silica in the mixture induces an increase of silicon in the structure of geopolymer which typically leads to higher compressive strength (Duxson et al. 2007).

### 3.2 Concentration of Toxic Heavy Metals

The term toxic heavy metal is generally used to refer to a group of metals and metalloids that have a relatively high density (>5 g/cm$^3$) and potential toxicity (Alloway 1995). The most common contaminants of toxic heavy metal are arsenic (As), cadmium (Cd), chromium (Cr), copper (Cu), nickel (Ni), lead (Pb), and zinc (Zn) (Lambert et al. 2000). The accumulation of large amounts of toxic heavy metals in soil reduces the number and activity of soil microorganisms that conducive to the development of the plants. Moreover, toxic heavy metals can enter food chains from polluted soil and water, consequently, cause food contamination threatening human and animal health.

In this study, the toxicity of the stabilized soils was studied by measuring the concentration of toxic heavy metals in the leachate. The results were compared with contamination levels suggested by the United States Environmental Protection Agency (CFR 2016) and the Ministry of Environment – South Korea (MOE 2010). As can be observed from Table 3, the concentrations of toxic heavy metals are below the limitation. Therefore, soils stabilized by ground bottom ash are non-hazardous. The toxic heavy metals arranged in descending order of concentration are Cu, As, Cr, Zn, Ni, Pb, and Cd.

**Table 3.** Concentration of toxic heavy metals in leachate of stabilized soil (mg/L)

| Case | As | Cd | Ni | Cu | Pb | Zn | Cr | Remarks |
|---|---|---|---|---|---|---|---|---|
| R0.0-Si0.5 | 0.0080 | 0.0000 | 0.0024 | 0.1068 | 0.0036 | 0.0245 | 0.0012 | - R0.0 represents for the RM/GBA of 0.0.<br>- Si0.5 represents for the $Na_2SiO_3$/(RM + GBA) of 0.5 |
| R0.1-Si0.5 | 0.0428 | 0.0002 | 0.0059 | 0.1989 | 0.0050 | 0.0121 | 0.0094 | |
| R0.2-Si0.5 | 0.0599 | 0.0000 | 0.0060 | 0.2131 | 0.0018 | 0.0083 | 0.0149 | |
| R0.3-Si0.5 | 0.0725 | 0.0000 | 0.0060 | 0.2090 | 0.0014 | 0.0073 | 0.0207 | |
| R0.4-Si0.5 | 0.0869 | 0.0001 | 0.0066 | 0.2556 | 0.0016 | 0.0088 | 0.0306 | |
| R0.2-Si0.3 | 0.0662 | 0.0000 | 0.0060 | 0.2110 | 0.0016 | 0.0078 | 0.0178 | |
| R0.2-Si0.4 | 0.0797 | 0.0000 | 0.0063 | 0.2323 | 0.0015 | 0.0080 | 0.0257 | |
| R0.2-Si0.5 | 0.0599 | 0.0000 | 0.0060 | 0.2131 | 0.0018 | 0.0083 | 0.0149 | |
| R0.2-Si0.6 | 0.0825 | 0.0000 | 0.0068 | 0.2696 | 0.0017 | 0.0087 | 0.0269 | |
| Contamination levels | | | | | | | | |
| - U.S. | 5 | 1 | – | – | 5 | – | 5 | |
| - South Korea | 75 | 12 | 300 | 450 | 700 | 900 | 15 | |

## 4 Conclusions

This study evaluates the feasibility of utilization of ground bottom ash and red mud as a binder for soil stabilization. A series of experiment has been performed on various mixtures to find out the element affecting the compressive strength of stabilized soils and the impacts of binder to the environment. Based on the obtained data, the following conclusions could be derived.

1. Ground bottom ash and red mud activated by $Na_2SiO_3$ solution can be used as a binder to stabilize soil. The compressive strength of soil increase with the activator content.
2. The presence of red mud in the mixture has contributed to the development of strength at early-age as well as later-age. At all curing time, the optimum RM/GBA ratio is 0.1.
3. Soil stabilized by ground bottom ash and red mud is non-hazardous. The concentration of toxic heavy metals is within the allowable ranges.

**Acknowledgments.** This research was supported by a grant (No. 16-RDRP-B076564-03) from Regional Development Research Program funded by Ministry of Land, Infrastructure, and Transport of Korean government.

## References

ACAA: American Coal Ash Association (2016). https://www.acaa-usa.org/Publications/Production-Use-Reports. Accessed 01 Nov 2016

Alloway, B.J.: Heavy Metals in Soils, 3rd edn. Springer, Netherlands (1995)

Ashok, P., Sureshkumar, M.P.: Experimental studies on concrete utilising red mud as a partial replacement of cement with hydrated lime. J. Mech. Civil Eng. 1–10 (2014)

Asokan, P., Saxena, M., Asolekar, S.R.: Coal combustion residues - environmental implications and recycling potentials. Resour. Conserv. Recycl. **43**(3), 239–262 (2005)

CFR: U.S. Government Publishing Office (2016). https://www.gpo.gov/fdsys/pkg/CFR-2016-title40-vol28/xml/CFR-2016-title40-vol28-part261-subpartC.xml. Accessed 01 Jan 2017

Cheriaf, M., Cavalcante Rocha, J., Péra, J.: Pozzolanic properties of pulverized coal combustion bottom ash. Cem. Concr. Res. **29**(9), 1387–1391 (1999)

Chindaprasirt, P., Jaturapitakkul, C., Chalee, W., Rattanasak, U.: Comparative study on the characteristics of fly ash and bottom ash geopolymers. Waste Manage. **29**(2), 539–543 (2009)

Daviddovits, J.: Environmentally driven geopolymer cement applications. In: Geopolymer 2002 Conference, Melbourne, Australia (2002)

Davidovits, J., Comrie, D.C., Paterson, J.H., Ritcey, D.J.: Geopolymeric concretes for environmental protection. Concr. Int. **12**(7), 30–40 (1990)

Duxson, P., et al.: Geopolymer technology: the current state of the art. J. Mater. Sci. **42**(9), 2917–2933 (2007)

Higgins, D.D.: Soil stabilisation with ground granulated blast furnace slag. UK Cementitious Slag Makers Association (2005)

Jaturapitakkul, C., Cheerarot, R.: Development of bottom ash as pozzolanic material. J. Mater. Civil Eng. **15**(1), 48–53 (2003)

Kim, Y.S., Dang, M.Q., Do, T.M.: Studies on compressive strength of sand stabilized by alkali-activated ground bottom ash and cured at the ambient conditions. Int. J. Geo-Eng. **7**(1), 15 (2016)

Lambert, M., Leven, B.A., Green, R.M.: New methods of cleaning up heavy metal in soils and water. Environmental Science and Technology Briefs for Citizens, pp. 1–3 (2000)

Liu, X., Zhang, N.: Utilization of red mud in cement production: a review. Waste Manage. Res. **29**(10), 1053–1063 (2011)

Majidi, B.: Geopolymer technology, from fundamentals to advanced applications: a review. Mater. Technol. **24**(2), 79–87 (2009)

Metilda, D.L., Selvamony, C., Anandakumar, R., Seeni, A.: Investigations on optimum possibility of replacing cement partially by red mud in concrete. Sci. Res. Essays **10**(4), 137–143 (2015)

MOE: Ministry of Environment (2010). http://stat.me.go.kr/nesis/mesp2/webStatistics/stat_main.jsp?tblID=DT_106N_ZZZ_003184&inq_gubun=1. Accessed 01 Jan 2016

Razak, H.A., Naganathan, S., Hamid, S.N.A.: Performance appraisal of industrial waste incineration bottom ash as controlled low-strength material. J. Hazard. Mater. **172**(2–3), 862–867 (2009)

Shi, X.S., Collins, F.G., Zhao, X.L., Wang, Q.T.: Mechanical properties and microstructure analysis of fly ash geopolymeric recycled concrete. J. Hazard. Mater. **237–238**, 20–29 (2012)

Verdolotti, L., Iannace, S., Lavorgna, M., Lamanna, R.: Geopolymerization reaction to consolidate incoherent pozzolanic soil. J. Mater. Sci. **43**(3), 865–873 (2008)

Wang, S., Boyjoo, Y., Choueib, A., Zhu, Z.H.: Removal of dyes from aqueous solution using fly ash and red mud. Water Res. **39**(1), 129–138 (2005)

# Thermal Conductivity of Controlled Low Strength Material (CLSM) Made with Excavated Soil and Coal Ash

Tan Manh Do[1,2], Young-sang Kim[1(✉)], My Quoc Dang[3], and Ngan Thi Tuyet Vu[1]

[1] Department of Civil and Environmental Engineering, Chonnam National University, Yeosu Campus, Korea
geoyskim@chonnam.ac.kr
[2] Department of Civil Engineering, Hanoi University of Mining and Geology, Hanoi, Vietnam
[3] Department of Civil Engineering, Nha Trang University, Nha Trang, Vietnam

**Abstract.** This paper focused on the quantitative evaluation of thermal conductivity of CLSM made with excavated soil and coal ash for a possible use as thermal grout for borehole heat exchangers. In a preliminary study, control mixtures were produced with Portland cement or cementless binder, Class F fly ash, and ponded ash. Then, for other mixtures, excavated soil substituted for ponded ash in amounts of 10, 20, 30, and 40% by weight. A series of laboratory tests including bleeding, flowability, initial setting time, and unconfined compressive strength were carried out in accordance with applicable ASTM Standard. Afterward, thermal conductivity was measured by using thermal needle probe, conforming ASTM D 5334 to verify the feasibiliy as thermal grout for borehole heat exchangers. The test results presented herein showed that the engineering properties of CLSM with excavated soil, possibly up to 30%, satisfied the specifications of ACI 229R. Moreover, an increase of excavated soil amount in CLSM could lead an improvement in thermal conductivity.

**Keywords:** Thermal conductivity · CLSM · Excavated soil · Ponded ash

## 1 Introduction

Ground-Source Heat Pump (GSHP) systems exchange heat with the ground by using the ground as a heat source and sink, either with vertical or horizontal ground heat exchangers. In this system, thermal grout in boreholes is used to fill up as well as provide heat transfer medium between the heat exchanger and surrounding ground (e.g., soils or rocks) and also control groundwater movement to prevent contamination of water supply. Enhanced heat pump coefficient of performance (COP) and reduced up-front loop installation costs can be achieved through optimization of the grout thermal conductivity. From the outset, conventional bentonite based grouts are used as the thermal grout for borehole heat exchangers (Eckhart 1991). However, these bentonite based grouts had relatively low thermal conductivity and subjected to shrinkage, desiccation, cracking. Due to the reasons mentioned above, there have been a number

© Springer Nature Singapore Pte Ltd. 2018
H. Tran-Nguyen et al. (eds.), *Proceedings of the 4th Congrès International de Géotechnique - Ouvrages -Structures*, Lecture Notes in Civil Engineering 8,
DOI 10.1007/978-981-10-6713-6_80

of studies developing new cementitious grouts for borehole heat exchangers in GSHP systems. Interestingly, controlled low strength materials (CLSM) has very good workability and low shrinkage as reported in ACI 229R (1999). However, research on a feasible use of CLSM as the thermal grout for borehole heat exchangers has not been closely evaluated. It is, therefore, ideal to apply CLSM as a thermal grout for borehole heat exchangers to replace the use of conventional grouts. American Concrete Institute (ACI) defines CLSM as a self-leveling, self-compacting, and cementitious material primarily used to replace conventional backfill soil and structural fillings that result in unconfined compressive strengths of 8.3 MPa or less (ACI 229R 1999). There are various inherent advantages of using CLSM instead of compacted fill in the applications mentioned. These benefits include reduced labor and equipment costs, faster construction, and the ability to be deposited in confined spaces (ACI 229R 1999). Another advantage of CLSM is the possibility that it can be produced using by-products that may otherwise be dumped, thus reducing the demand on landfills and contributing toward sustainable development (ACI 229R 1999). Meanwhile, large amounts of coal ash are produced annually from the combustion process of thermal power plants. The disposal of these wastes will be a big challenge in the near future for Korea because of the harmful environmental effects. In addition, in the area of construction, a considerable amount of soil is excavated and removed from construction sites. Finding an alternative use of these construction wastes will be an effective way to reduce the cost of their disposal and treatment, and finally reduce environmental pollution. For that purpose, the CLSM mixture made with excavated soil and coal ash was proposed considered to its thermal property for borehole heat exchangers.

## 2 Experimental Techniques

In the present study, ponded ash originating from cogeneration plants and excavated soil from construction sites in Jeolla Province (South Korea) were used as fine aggregates in the production of CLSM. Ponded ash (PA) was used as the main fine aggregate, while excavated soil (ES) was used as a substitute for PA in CLSM mixtures. The particle size distribution curves of ponded ash, excavated soil, and their different combinations are compared in Fig. 1. Soil classification parameters based on Unified Soil Classification System (USCS) are summarized in Table 1. Herein, "PA" and "ES" indicate ponded ash and excavated soil, respectively. The numbers "91," "82," "73," and "64," signify the ratios of ponded ash to excavated soil in combinations of 9:1, 8:2, 7:3, and 6:4, respectively. The fineness modulus (FM) of ponded ash and PA-ES combinations varied in range of 2.25–3.37. Fineness modulus mentioned is an empirical figure obtained by adding the total percentage of the sample of an aggregate retained on each of a specified series of sieves, and dividing the sum by 100. In general, a smaller value indicates a finer aggregate. In addition, a cementless binder (CB) was feasibly evaluated and compared with cement for the production of CLSM. Ordinary Type I Portland cement conforming to ASTM C150 was employed. A cementless binder used in this investigation is a nonsintering cement manufactured by adding phosphogypsum and waste lime to granulated blast furnace slag as sulfate and alkali activators (Kim et al. 2016; Mun et al. 2007). The reactions of pozzolanic

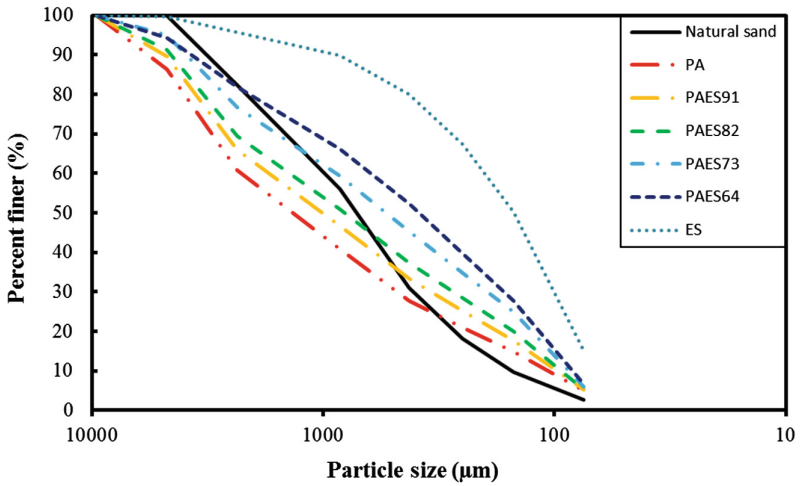


**Fig. 1.** Particle size distributions of ponded ash, excavated soil, and PA-ES combinations

**Table 1.** Soil classification parameters

| Case studies | Soil classification parameters | | | | | | |
|---|---|---|---|---|---|---|---|
| | $D_{10}$ (mm) | $D_{30}$ (mm) | $D_{60}$ (mm) | $C_u$ | $C_c$ | Fineness modulus | USCS |
| PA | 0.11 | 0.49 | 2.30 | 20.25 | 0.94 | 3.37 | SP |
| PAES91 | 0.10 | 0.35 | 1.89 | 18.13 | 0.63 | 3.09 | SP-SM |
| PAES82 | 0.10 | 0.28 | 1.60 | 16.05 | 0.50 | 2.91 | SP-SM |
| PAES73 | 0.09 | 0.20 | 0.91 | 9.99 | 0.49 | 2.51 | SP-SM |
| PAES64 | 0.09 | 0.17 | 0.66 | 7.63 | 0.49 | 2.25 | SP-SM |
| ES | – | 0.11 | 0.21 | – | – | 1.08 | SM |

Note: $D_{10}$, $D_{60}$, $D_{30}$ refer particle diameter such that 10%, 60% and 30% correspdingly of the soil grain are smaller than this size; $C_u$ refers the coefficient of uniformity; $C_c$ refers the coefficient of curvature; SP refers a poorly graded sand; SM refers a silty sand.

materials (e.g., fly ash and ponded ash in CLSM mixture) and slag coupled with some activators in CB are believed to help in hardening and strength development of CLSM. Fly ash used in CLSM can improve the fluidity or flowability of mixtures with its spherical shaped particles (Fig. 2). In this study, Class F Fly ash with a specific gravity of 2.3 produced from a cogeneration plant in Jeolla-do Province (South Korea) conforming to ASTM C618 was used.

First, control mixtures were produced with Portland cement or cementless binder, Class F fly ash, ponded ash. Subsequently, excavated soil was substituted for ponded ash in amounts of 10, 20, 30, and 40% replacement by weight (i.e., the ratio of water per binder was fixed as 1.37). The properties of the fresh mix, such as bleeding, flowability, and setting time were tested immediately after mixing in accordance with

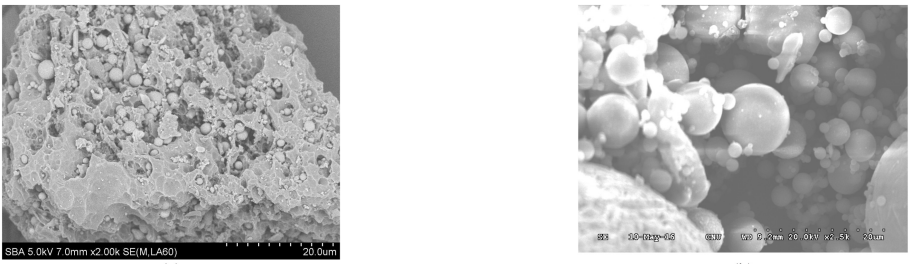


(a) (b)

**Fig. 2.** SEM image of particle surfaces of Ponded ash (a), Fly ash (b)

applicable ASTM Standards (2004): C 940, D 6103, C 403, respectively. Bleeding is commonly used to quantify the degree of subsidence for CLSM. Flowability is a measurement of the spread of a predetermined volume of CLSM achieved by removal of the flow cylinder within a specified time. Further, unconfined compressive strength test was performed with 50 × 100 mm cylindrical specimens cast in plastic molds and then stored inside a wet chamber curing condition that maintained a temperature of 25° and 100% relative humidity until desirable testing times of 3, 7, and 28 days as presented in ASTM D 4832. Finally, thermal conductivity test conforming to ASTM D5334 was also conducted simultaneously with unconfined compressive strength test to verify the feasibility of CLSM the thermal grout for borehole heat exchangers. Two sets of CLSM specimens were prepared for the thermal conductivity test: one set was soaked into water for a saturated curing condition (SC) and the other set was cured in a room temperature condition (RT). For a thermal conductivity test, the thermal needle probe used consists of a heating element and a temperature measuring element and is inserted into the specimen (see Fig. 3). A known current and voltage are applied to the probe and the temperature rise with time is recorded over a period of time. The temperature decay with time after the cessation of heating can also be included in the analysis to minimize effects of temperature drift during measurement. The thermal conductivity is obtained from an analysis of the time series temperature data during the heating cycle and cooling cycle. In this study, thermal conductivity test conforming to

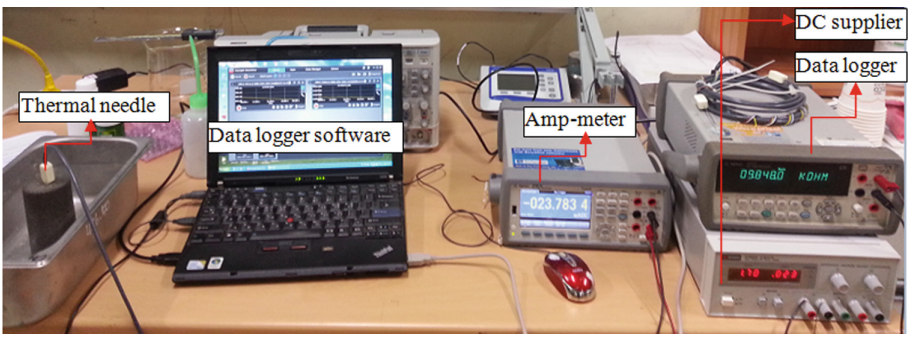


**Fig. 3.** Thermal conductivity devices setup (ASTM D5334)

ASTM D5334 was performed to verify the feasibility of CLSM as the thermal grout for borehole heat exchangers. The thermal conductivity is obtained from an analysis of the time series temperature data during the heating cycle and cooling cycle. For calculation of thermal conductivity through the sensor (thermal needle), the resistance versus temperature relationship for each sensor should be known. In order to obtain that relationship, the resistance values were measured from specific temperatures (10–60 degree Celsius) matching to the temperature range of CLSM specimens.

## 3 Results and Discussion

### 3.1 General Properties of CLSM Made with Excavated Soil and Coal Ash

Test results of flowability, bleeding, initial setting time and compressive strength of coal ash and excavated soil based CLSM are summarized in Table 2. As expected, the good flowability of higher than 200 mm (ACI 229R 1999) was achieved consistently at the ES content of 30%, regardless of binders used. In addition, it was found that the flowability decreased with a corresponding increase in the ES content (i.e., the amount of ES replacement to ponded ash in fine aggregate). The excess water added to maintain the required flowability of CLSM comes out as bleed. The bleeding values of all prepared mixtures varied in the range of 1.54–5.94%, all of which conformed to the bleeding requirement of CLSM of less than 5% at 2 h except for the mixture Control-CB (5.94%). More importantly, an increase in ES content could lead to a decrease in bleeding of CLSM in comparison with the control mixtures, regardless of binders used. Initial setting time was found in the range of 9.53–23.46 h, which was all below the maximum allowable limit of 36 h as required for general CLSM. Table 2 also shows the unconfined compressive strengths in average for various CLSM

**Table 2.** All general properties of CLSM mixtures made with excavated soil and coal ash

| Mix code | Proportion of PA and ES (%) | | Compressive strength (kPa) | | | Bleeding (%) | Flow (cm) | Initial set (hours) |
|---|---|---|---|---|---|---|---|---|
| | PA | ES | 3 days | 7 days | 28 days | | | |
| Control-C | 100 | 0 | 295.8 | 429.8 | 794.7 | 5.00 | 29 | 9.53 |
| PAES91-C | 90 | 10 | 250.2 | 380.8 | 743.9 | 3.13 | 28 | 10.66 |
| PAES82-C | 80 | 20 | 211.8 | 323.1 | 650.5 | 2.37 | 25 | 11.69 |
| PAES73-C | 70 | 30 | 175.7 | 282.2 | 538.2 | 1.78 | 21 | 12.66 |
| PAES64-C | 60 | 40 | 163.5 | 264.5 | 528.7 | 1.54 | 16 | 13.79 |
| Control-CB | 100 | 0 | 378.3 | 500.1 | 888.0 | 5.94 | 31.0 | 19.26 |
| PAES91-CB | 90 | 10 | 309.5 | 399.1 | 636.5 | 4.90 | 28 | 20.73 |
| PAES82-CB | 80 | 20 | 277.4 | 349.6 | 499.1 | 4.04 | 26 | 21.69 |
| PAES73-CB | 70 | 30 | 259.8 | 290.2 | 473.8 | 3.43 | 23 | 22.68 |
| PAES64-CB | 60 | 40 | 219.0 | 259.8 | 413.6 | 2.18 | 17 | 23.46 |

PA: Ponded ash; ES: Excavated soil

mixtures in experimental program. There were increments in compressive strength of all CLSM mixtures due to the hydration process of cementitious materials which gradually completed with curing ages. The 3-day strength and 7-day strength varied in ranges of 0.16–0.38 MPa and 0.26–0.5 MPa, respectively. At 28 days age, the strength was 0.42 to 0.89 MPa, conforming to strength requirement of CLSM in ACI 229.

### 3.2 Thermal Conductivity of CLSM Made with Excavated Soil and Coal Ash

The thermal conductivity of the various fully saturated CLSM made with ES and PA is shown in Table 3. The thermal conductivity of the proposed CLSM mixtures ranged from 0.90 to 1.28 W/mK, which was higher than one of conventional grout (i.e., neat cement grouts and high solids bentonite). It was found that the replacement of ES tends to improve the thermal conductivity of CLSM mixtures. The thermal conductivity of control mixtures, Control-C and Control-CB, were 0.93 and 0.9 W/mK, respectively. These values increased by 37.63% (1.28 W/mK) and 22.2% (1.1 W/mK) at the ES replacement of 40%. The increase in the thermal conductivity with the increase of ES content is observed. The reason is that the small particles of ES help to make more contact points and then specific surface increase and eventually induces better contact between neighboring solid particles for heat transfer. This tendency is primarily due to the decrease in the fineness modulus (FM) of fine aggregate after the combinations as detailed in Table 1. The 3.37 fineness modulus of PA was much higher than that of ES (FM = 1.08). The FM of PA-ES combinations decreased when the ES content increased.

Table 3 also compares the thermal conductivity of all CLSM mixtures with two different curing methods at 28 days. As a result, thermal conductivity ranged from 0.4 to 0.68 and 0.9 to 1.28 W/mK for the mixtures cured with RT and SC conditions, respectively. Considering the influence of these curing conditions it was expected that the higher results would correspond to the curing method that provides more humidity surrounding specimen. In particular, thermal conductivity showed large enough values as CLSM specimens under SC condition (i.e., up to 1.28 W/mK). Then, there were decreases in thermal conductivity values in comparison to the ones of CLSM under RT condition. This observation might be explained by the different moisture contents of CLSM mixtures under the two different curing conditions. Under SC condition, thermal conductivity showed highest values since the pores would be fully filled with water. Under RT curing conditions, that water might be partially replaced by air. Since the thermal conductivity of water (0.6 W/mK) is much greater than that of air (0.024 W/mK), the decreases in total thermal conductivity of CLSM mixtures in these cases are expected. The same finding can be observed from the thermal conductivity of CLSM made with CB. However, these thermal conductivity values were slightly lower than those of CLSM made with cement.

**Table 3.** Thermal conductivity of CLSM mixtures made with excavated soil and coal ash

| Mix code | Proportion of PA and ES (%) | | Thermal conductivity (W/mK) | |
|---|---|---|---|---|
| | PA | ES | Saturated condition (SC) | Room temperature (RT) |
| Control-C | 100 | 0 | 0.93 | 0.58 |
| PAES91-C | 90 | 10 | 0.95 | 0.57 |
| PAES82-C | 80 | 20 | 1.06 | 0.62 |
| PAES73-C | 70 | 30 | 1.16 | 0.67 |
| PAES64-C | 60 | 40 | 1.28 | 0.68 |
| Control-CB | 100 | 0 | 0.9 | 0.4 |
| PAES91-CB | 90 | 10 | 0.91 | 0.47 |
| PAES82-CB | 80 | 20 | 0.97 | 0.52 |
| PAES73-CB | 70 | 30 | 1 | 0.54 |
| PAES64-CB | 60 | 40 | 1.1 | 0.65 |
| Neat cement grouts | – | – | 0.8 | – |
| High solids bentonite | – | – | 0.87 | – |
| Thermally enhanced bentonite | – | – | 1.46 | – |

PA: Ponded ash; ES: Excavated soil

## 4 Conclusions

All of the CLSM mixtures made with excavated soil and coal ash performed well and conformed to the requirements of CLSM in ACI with regard to all general properties including bleeding, flowability, setting time, unconfined compressive strength. In addition, it was found that the thermal conductivity of the proposed CLSM mixtures ranged from 0.90 to 1.28 W/mK, which was higher than one of conventional grout. More importantly, the thermal conductivity increased with a corresponding increase in the ES content, regardless of binders used. The reason is that the small particles of ES help to make more contact points and then specific surface increase and eventually induces better contact between neighboring solid particles for heat. Regarding the effect of curing condition, it was expected that the thermal conductivity of CLSM mixtures under SC condition was higher than that obtained under the RT condition.

**Acknowledgments.** This research was supported by a grant (No 17-RDRP-B076564-04) from Regional Development Research Program funded by Ministry of Land, Infrastructure and Transport-South Korean.

## References

ACI Committee 229: Controlled low strength materials (ACI 229R-99). American Concrete Institute, Farmington Hill (1999)

Eckhart, F.: Grouting Procedures of Ground-Source Heat Pump Systems, Oklahoma State University. Ground Source Heat Pump Publications, Tulsa (1991)

Kim, Y.S., Do, T.M., Kim, H.K., Kang, G.O.: Utilization of excavated soil in coal ash-based controlled low-strength material (CLSM). Constr. Build. Mater. **124**, 598–605 (2016)

Mun, K.J., Hyoung, W.K., Lee, C.W., So, S.Y., Soh, Y.S.: Basic properties of non-sintering cement using phosphogypsum and waste lime as activator. Constr. Build. Mater. **21**, 1342–1350 (2007)

# Undrained Behavior of Macau Marine Clay with Various Strain Rates and Different Stress Histories

Shengshen Wu[1,2(✉)], Thomas Lok[1], and Annan Zhou[2]

[1] University of Macau, Macau, China
s3479492@student.rmit.edu.au, mhlok@umac.mo
[2] RMIT University, Melbourne, Australia
annan.zhou@rmit.edu.au

**Abstract.** Hydro-mechanical behaviors of a saturated clay with various strain-rate and different stress histories are investigated through a series of consolidated-undrained and $K_0$ consolidated undrained ($K_0$CU) tests which were conducted on reconstituted specimens. The samples were taken from an excavation site in Macau and reconstituted in the laboratory to provide homogenous specimens. A total of four CU tests and four $K_0$CU tests were undertaken on 38 mm diameter samples. The samples were saturated first by use back pressure saturation method (back pressure 200 kPa), after saturation, they were loaded to a confining stress 400 kPa and then unload to 50 kPa, 100 kPa, 200 kPa, 400 kPa (OCR = 8, 4, 2, 1) and finally were sheared at constant shear rate (0.1%/h, 1%/h, 10%/h) to failure. In this research the responses of marine clay under various strain rates under different OCRs on the strain-rate effects will be discussed, parameters for accounting the strain-rate effects on undrained shear strength will be proposed.

**Keywords:** Triaxial · Over-consolidation ratios · Strain rate · Shear strength

## 1 Introduction

In Macau, soft marine deposits are usually referred to as Macau marine clay (MMC), the stress-strain-strength behavior of which is important for the design of many infrastructures constructed in this coastal area. In particular, MMC has caused many problems due to its high compressibility and low shear strength. However, only a few systematic studies were found in the literature regarding the behavior of MMC. Yeung and So [1] described the general properties of Hong Kong and Macau marine clays. Recently, Yan and Ma [2] provided geotechnical characterization of MMC from oedometer and $K_0$ triaxial tests.

When a clayey soil is subjected to shearing, it was generally observed (e.g. [3]) that the undrained shear strength increases with increasing strain rate. For heavily over consolidated clay, Whitman [4] found the strain-rate effects on strength appeared to be greater for over consolidated specimens (Over-consolidation ratio (OCR) = 16) than for normally consolidated specimens. Graham et al. [5] found that the OCR has no appreciable influence on the strain-rate effects in conventional triaxial compression

© Springer Nature Singapore Pte Ltd. 2018
H. Tran-Nguyen et al. (eds.), *Proceedings of the 4th Congrès International de Géotechnique - Ouvrages -Structures*, Lecture Notes in Civil Engineering 8,
DOI 10.1007/978-981-10-6713-6_81

tests. However, Sheahan et al. [6] found that the effects decrease with the increase of OCR. From those studies, it may be concluded that the influence of OCR on strain-rate effects is still unclear.

Furthermore, the undrained shear strength ($S_u$) of clay is not a constant value, which depends on several environment factors such as stress state, stress history, strain rate, among others. Kulhawy and Mayne [7] attempted to estimate the normalized undrained shear strength in a unified way as follows:

$$\frac{S_u}{\sigma_{v'}} = a_{test} \times b_{OCR} \times C_{rate} \times \frac{S_{u,CIUC,NC,1\%}}{\sigma_{v'}} \quad (1)$$

$\sigma'_v$ is the effective stress.$S_{u,CIUC,NC,1\%}$ is the undrained shear strength under isotropic consolidated-undrained (ICU) test with a strain rate of 1%/h on normal consolidated clay. $a_{test}$ $b_{OCR}$ $C_{rate}$ are factors that quantify the effect of test type, over consolidated ratio and strain rate.

The focus of this study is to investigate the influence of strain-rate and OCR on undrained shear strength of MMC. Uniform reconstituted samples were obtained by reconsolidating disturbed samples taken from an excavation site at the northern part of Macau. A series of isotropic consolidated-undrained (ICU) and $K_0$ consolidated-undrained ($K_0$CU) tests were conducted on normal consolidated and over consolidated specimens. The objectives are to provide a better understanding of the undrained shear strength of MMC.

## 2 Physical Properties of Tested Soils and Test Procedures

Disturbed samples of marine clay were retrieved from an excavation site at the northern part of Macau. Because of some coarse particles such as gravels or shells must be eliminated from the sample, the sample was first prepared in slurry form before passing through a 0.425 mm sieve. The slurry of MMC with water content around 2 times of the liquid limit was then reconsolidated in a consolidometer [8] under a pressure of about 100 kPa to prepare consistent remolded samples for following tests. The comparison of Atterberg limits from different sources is shown in Fig. 1. MMC can be classified as high plasticity silt clay, although it is very close to the A-line.

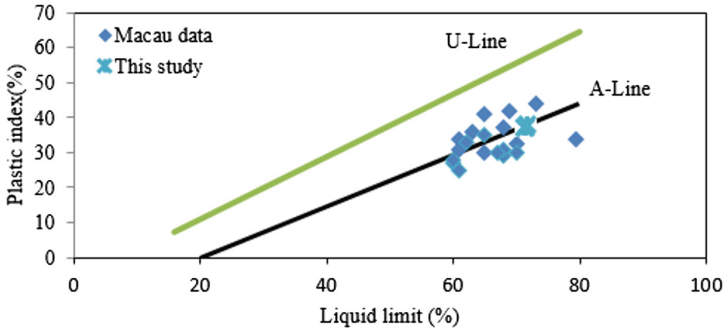


**Fig. 1.** Plasticity Chart

**Fig. 2.** Triaxial testing system.

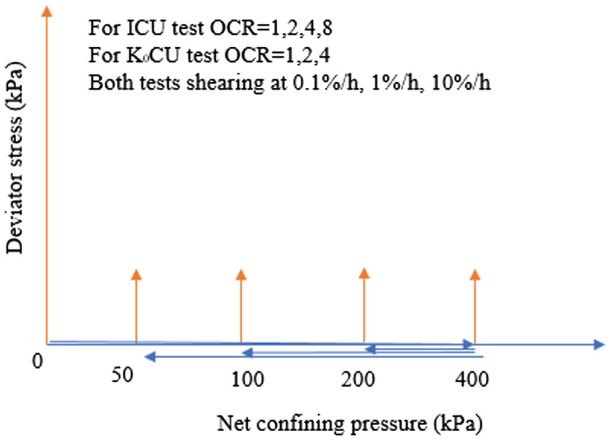


**Fig. 3.** Test procedures

In this research, a Triaxial Testing system (Fig. 2) was used to perform the tests. The instrument is designed is only for saturated soils. The instrument is consisting of pressure transducers for the pore air pressure, pore water pressure and confining pressure measurement. LVDT is attached to the loading ram to measure the axial displacement. Cell volume, back volume also can be recorded by different pressure volume controllers.

Moreover, the test procedures shows in the Fig. 3, before the consolidation stage, back pressure saturation method and flushing water method were used to saturate the samples. After the saturation, a series of ICU tests (with 5 different stress stages) and $K_0$CU tests (with 4 different stress stages) were performed. the saturated samples were first consolidated under an isotropical confining pressure (400 kPa), when the specimen

reach to the end of the primary consolidation (this may need 1-2 days), the specimens unload to different stress conditions for ICU tests (400 kPa, 200 kPa, 100 kPa, 50 kPa) and for $K_0$CU tests (400 kPa, 200 kPa, 100 kPa), and when the specimen reach to the stable state (this need 0.5-1 day), the shearing process happens. During the shearing process, the pore pressure valve is closed; the strain rate for the ICU tests and $K_0$CU tests is 0.1%/h, 1%/h and 10%/h.

## 3 Test Results and Discussion

### 3.1 Isotropic Consolidation Undrained Shearing Tests

In order to investigate the effects of OCR and shearing strain rate on the behavior of MMC, in isotropic condition, a series of ICU tests were conducted on several specimens, with axial strain rates of 10%/h, 1%/h and 0.1%/h. The test results are shown in Table 1. Figure 4 presents the relationship between OCR and $S_u/\sigma_v'$, which shows that

**Table 1.** Summary of the ICU test

| | OCR = 1 | | | OCR = 2 | | |
|---|---|---|---|---|---|---|
| ε (%/h) | 0.1 | 1 | 10 | 0.1 | 1 | 10 |
| $\sigma_0'$ (kPa) | 400 | 400 | 400 | 200 | 200 | 200 |
| $S_u$ (kPa) | 273 | 285 | 295 | 240 | 250 | 255 |
| | OCR = 4 | | | OCR = 8 | | |
| ε (%/h) | 0.1 | 1 | 10 | 0.1 | 1 | 10 |
| $\sigma_0'$ (kPa) | 100 | 100 | 100 | 50 | 50 | 50 |
| $S_u$ (kPa) | 180 | 192 | 198 | 159 | 173 | 178 |

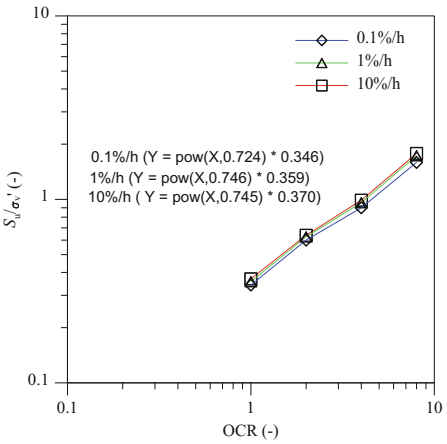


**Fig. 4.** $S_u/\sigma_v'$ vs. OCR (ICU)

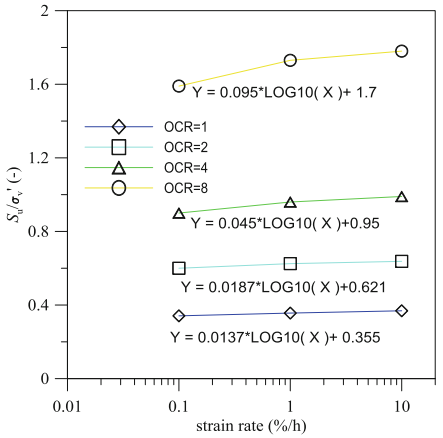


**Fig. 5.** $S_u/\sigma_v'$ vs. $\log \dot{\varepsilon}(\%/\mathrm{h})$ (ICU)

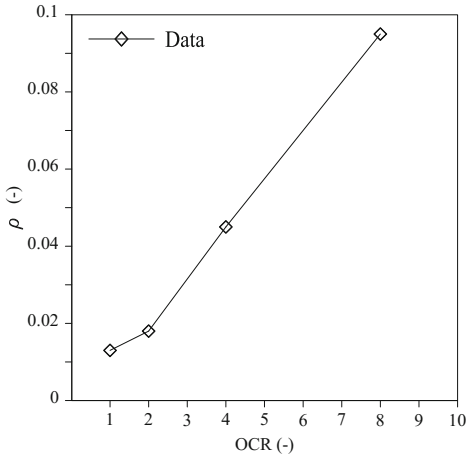


**Fig. 6.** $\rho_q$ vs. OCR

the shear strength generally increases with the OCR value and the following correlation [7] can be established:

$$\frac{S_u}{\sigma_{v'}} = \mathrm{OCR}^n \frac{S_{u,CIUC,NC,1\%}}{\sigma_{v'}} \tag{2}$$

where: n = 0.738. Moreover, the change in undrained shear strength with strain rate can be described by parameters $\rho_q$ as follows:

$$\rho_q = \frac{\Delta\left(\frac{S_u}{\sigma_{v'}}\right)}{\Delta\log(\dot{\varepsilon})} \tag{3}$$

where $\sigma_{v'}$ is current effective stress, $\dot{\varepsilon}$ is axial strain rate, the results are in Fig. 5, it also can be seen from the graph that the $S_u/\sigma_v^{'}$ increase with the shearing strain rate. Furthermore, According to Fig. 6, the effect of OCR on $\rho_q$ is obvious. The value of $\rho_q$ increases monotonically with increasing OCR

### 3.2 $K_0$ Consolidation Undrained Shearing Tests

In order to compare the results with ICU tests, $K_0$ consolidation was carried out before shearing. It was achieved by increasing the vertical pressure and horizontal pressure proportionally. The axial strain and volume change of the specimen were monitored during the process to ensure approximately zero radial strain. For $K_0$ unloading, due to the limitation of the equipment, a step decreasing procedure (manually control) was used. Kulhawy and Mayne [7] was used to determine $K_0$ along the stress path:

$$K_0 = \left(1 - \sin\phi^{'}\right)\left[\left(\frac{OCR}{OCR_{MAX}^{1-\sin\phi^{'}}}\right) + \frac{3}{4}\left(1 - \frac{OCR}{OCR_{MAX}}\right)\right] \tag{4}$$

(where $OCR_{MAX}$ is the maximum value of the over consolidation ratio which soil already experienced). The probable bounds of $K_0$ in soil with more complex unload-reload histories can be determined using this equation, which requires stress history and angle for a particular soil be known. The unloading procedure was carried as follows: First, Decrease the vertical stress by 10 kPa/h each time. Second, calculate the new OCR, and then calculate $K_0$ from the new OCR using the previous equation. Third, adjust the required horizontal stress for the new OCR as $\sigma_{h'} = K_0\sigma_v'$. The process is repeated until the required stresses for the corresponding OCR is reached. Adjustment of the stresses is made to ensure the change of radial strain in the unloading process to be less than 0.1%.

After $K_0$ consolidation, undrained shearing was carried out with axial strain rates of 10%/h, 1%/h and 0.1%/h. In these tests, average $K_0$ value was found to be about 0.528. The test results are shown in Table 2. Figure 7 presents the relationship between OCR and $S_u/\sigma_v^{'}$, which shows the shear strength increases with increasing OCR values and average value of n = 0.827 for Eq. (1). was obtained from $K_0$ condition. Figure 8 shows that the undrained shear strength increases generally with the strain rate. The monotonically increasing of value of $\rho_q$ with OCR is observed in Fig. 9.

**Table 2.** Summary of the $K_0$ CU test

| | OCR = 1 | | | OCR = 2 | | | | OCR = 4 | | |
|---|---|---|---|---|---|---|---|---|---|---|
| ε (%/h) | 0.1 | 1 | 10 | 0.1 | 1 | 10 | ε (%/h) | 0.1 | 1 | 10 |
| $K_0$ | 0.524 | 0.53 | 0.527 | 0.543 | 0.527 | 0.537 | $\sigma_0'$ (kPa) | 100 | 100 | 100 |
| $\sigma_0'$ (kPa) | 400 | 400 | 400 | 200 | 200 | 200 | $K_0$ | 0.5236 | 0.53 | 0.513 |
| $S_u$ (kPa) | 270 | 275 | 288 | 248 | 252 | 262 | $S_u$ (kPa) | 210 | 216 | 229 |

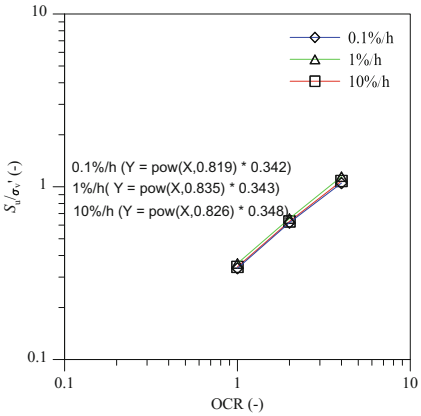


**Fig. 7.** $S_u/\sigma_v'$ vs. OCR ($K_0$)

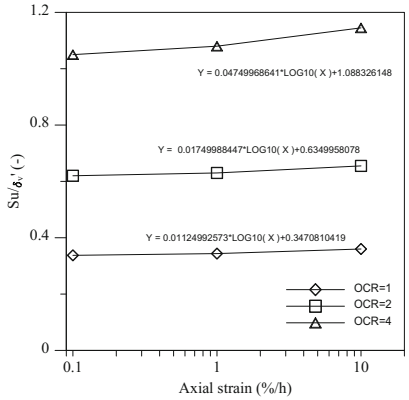


**Fig. 8.** $S_u/\sigma_v'$ vs. $\log \dot{\varepsilon}(\%/\mathrm{h})$ ($K_0$)

### 3.3 Compare Interpretation Factors

Moreover, there are some other definitions to describe the relationship between shear strength and shearing strain rate.

The first definition is according to Zhu [9]

$$\rho_q = \frac{\Delta\left(\frac{S_u}{\sigma_0'}\right)}{\Delta\log(\dot{\varepsilon}_a)} \tag{5}$$

where $\sigma_0'$ is the current effective stress, $S_u$ is the shear strength and $\dot{\varepsilon}_a$ is shearing rate. The results of $\rho_q$ for the ICU and $K_0$ CU tests are shown in Figs. 10 and 11, respectively. In general, the shear strength increases with OCR value at different shearing

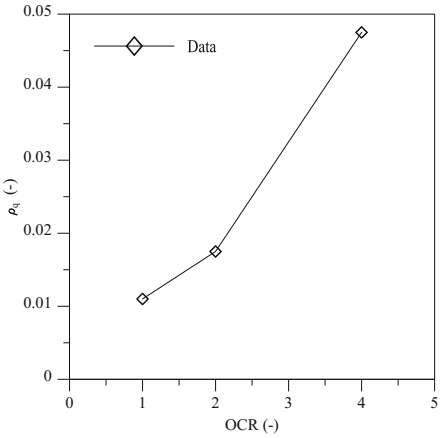


**Fig. 9.** $\rho_q$ vs. OCR ($K_0$)

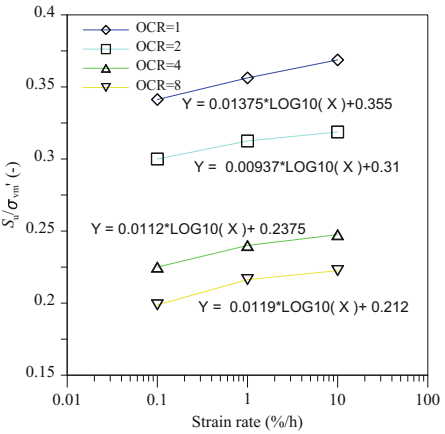


**Fig. 10.** $\overline{\rho_q}$ for ICU test

strain rate. From Figs. 4 and 7, $\rho_q$ can be determined by the variation of shear strength with strain rate for different OCR values. This definition is equivalent to the definition of $\rho_q$ in this study as shown in Eq. (3). $\rho_q$ can be clearly determined by the variation of shear strength with strain rate for different OCR values.

The second definition is form Sheahan et al. [6]:

$$\overline{\rho_q} = \frac{\Delta\left(\frac{S_u}{\sigma_{vm'}}\right)}{\Delta\log(\dot{\varepsilon}_a)} \tag{6}$$

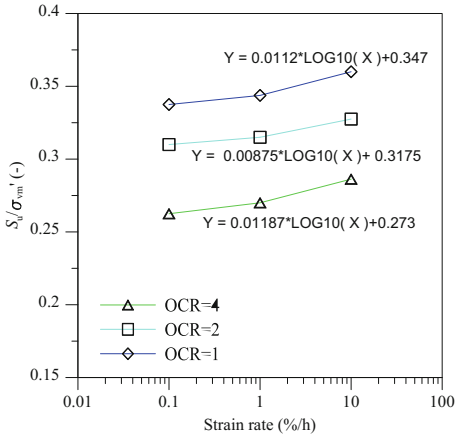


**Fig. 11.** $\overline{\rho_q}$ for $K_0$ CU test

From first and second definition, it is easy to show that:

$$\overline{\rho}_q = \frac{\Delta\left(\frac{S_u}{OCR\sigma_0'}\right)}{\Delta\log(\dot{\varepsilon}_a)} \tag{7}$$

The factor $\sigma_{0'}$ is constant, but $\overline{\rho_q}$ is influenced by both $S_u$ and OCR. Since $S_u/\sigma_0'$ also increases with OCR, consequently, $\overline{\rho_q}$ may increase or decrease with OCR depending on the ratio of $\Delta\left(\frac{S_u}{OCR\sigma_0'}\right)$. It is also proved by experiment result above that $\overline{\rho_q}$ does not increase monotonically with OCR.

The results of $\overline{\rho_q}$ for the ICU and $K_0$CU tests are shown in Figs. 10 and 11, respectively. The $\overline{\rho_q}$ value first decreases (from OCR = 1 to OCR = 2) and then increases (OCR >= 2) with increasing OCR values. The variation of $\overline{\rho_q}$ with OCR is more complicate than the monotonically increasing $\rho$ with OCR.

Furthermore, From the definition of $\rho_q$ in Eq. (3),

$$\left(\frac{S_u}{\sigma_{v'}}\right)_{\dot{\varepsilon}} = \left(\frac{S_u}{\sigma_{v'}}\right)_{\dot{\varepsilon}_{ref}} + \rho_q \Delta\log(\dot{\varepsilon}) \tag{8}$$

Also, from Eq. (1), the factor, $C_{rate}$, is given as:

$$C_{rate} = 1 + A\log_{10}(\dot{\varepsilon}/1\%) \tag{9}$$

Where A = 0.1 by Kulhawy and Mayne [7]. Comparing to Eq. (3), the relationship between A and $\rho$ is as follows:

$$\rho_q = A\left(\frac{S_u}{\sigma_{v'}}\right)_{\dot{\varepsilon}_{ref}} \tag{10}$$

However, according to the experimental data, the value of A is not a constant and varies with OCR and stress conditions. The value of A is summarized in Table 3. From the comparison, this study gives a prediction range from experiment results comparing to Kulhawy and Mayne's [7] constant value.

**Table 3.** The value of A

| | ICU (OCR = 1–8) | $K_0$ CU (OCR = 1–4) |
|---|---|---|
| This study | 0.039–0.055 | 0.032–0.044 |
| (Kulhawy) | 0.1 | 0.1 |

## 4 Conclusion

In this study, a series of tests was conducted to investigate the effects of strain rate and OCR on the undrained shear strength of MMC. Both ICU and $K_0$CU tests were performed with three different axial strain rates under different OCR. The effects of strain rate on undrained shear strength and the influence of OCR on the strain rate effects were investigated. The following conclusions are drawn:

(I) Higher strain rates result in higher undrained shear strength for different OCRs in both ICU and $K_0$ CU conditions.
(II) Higher OCR result in higher shear strength for all strain rates in both ICU and $K_0$CU conditions.
(III) For ICU specimens, the shear strength for OCR = 1 is larger than the shear strength in $K_0$CU test for different strain rates. But for OCR >= 2, the shear strength for the ICU specimens is smaller than the shear strength in $K_0$CU test for different strain rates.
(IV) $\rho_q$ is the best parameter to describe the strain rate effect since $\rho_q$ is monotonically increasing with OCR but the other parameters, such as $\overline{\rho}_q$, do not show such simple relationship.

The test results and analysis data of the mechanical behavior of saturated MMC under different OCR is shown above. However, the numerical model and experiments related to the unsaturated soil are ignored in this research, and it can be investigated in the future.

## References

1. Yeung, A., So, S.: Geotechnical engineering properties of Hong Kong marine clays. In: Lee, C.F., et al. (eds.) Soft Soil Engineering, pp. 695–700. CRC Press, Boca Raton (2001)
2. Yan, W., Ma, Y.: Geotechnical characterization of Macau marine deposits. Eng. Geol. **113**(1), 62–69 (2010)

3. Yin, J.-H., Graham, J.: Elastic viscoplastic modelling of the time-dependent stress-strain behaviour of soils. Can. Geotech. J. **36**(4), 736–745 (1999)
4. Whitman, R.V.: Stress-strain-time behavior of soil in one dimensional compression. DTIC Document (1963)
5. Graham, J., et al.: Time effects on the stress-strain behaviour of natural soft clays. Géotechnique **33**(3), 327–340 (1983)
6. Sheahan, T.C., et al.: Rate-dependent undrained shear behavior of saturated clay. J. Geotech. Eng. **122**(2), 99–108 (1996)
7. Kulhawy, F.H., Mayne, P.W.: Manual on estimating soil properties for foundation design. Electric Power Research Institude, Palo Alto, CA, USA; Cornell University, Ithaca, NY, USA. Geotechnical Engineering Group (1990)
8. Xuantao, S.: Experimental investigation on the consolidation and very small-strian stiffness properties of macau marine clay. University of Macau (2008)
9. Zhu, J.G.: Experimental study and elastic viscous-plastic modeling of the time-dependent stress-strain behavior of Hong Kong marine deposits. Ph.D. thesis. The Hong Kong Polytechnic University, Hong Kong (1999)

# Innovative Design and Methods (IDM)

# A New Formula for the Shear Strength of Exterior RC Beam-Column Joints Using Headed Bars

Minh Tung Tran, Minh Tien Nguyen, and Quoc Bao Bui(✉)

Sustainable Developments in Civil Engineering Research Group,
Faculty of Civil Engineering, Ton Duc Thang University,
Ho Chi Minh City, Vietnam
buiquocbao@tdt.edu.vn

**Abstract.** In several cases where high quantities of steel reinforcements are needed at reinforced concrete (RC) beam-column joints, headed bars are employed as a solution to facilitate the placing of reinforcement bars. This paper establishes a new formula for the prediction of the shear strength of exterior RC beam-column joints where beam longitudinal reinforcements use headed bars. A database was collected, which contains most of available test data of exterior beam-column connections using headed bars and subject to quasi-static cyclic loading. First, influences of the key parameters for the joint shear strength of the connections were evaluated by using the collected database. Then, three most important parameters were chosen to develop a formula for the prediction of the joint shear strength. The accuracy of the proposed formula was evaluated by comparing the predicted joint shear strength using the proposed formula and that of 30 experimental exterior connections collected from different sources, and also with predicted values using two existing analytical models. This evaluation showed a better relevancy of the proposed model in predicting exterior joint shear strength, compared to the existing formulas

**Keywords:** RC beam-column frame · Headed bars · Exterior joints · Shear strength

## 1 Introduction

Beam-column joints are critical regions of RC frame structures. Beam-column joints are usually solicited when a RC structure undergoes a seismic loading and their failures can lead to severe damages of the whole structure. Therefore, to improve the safety of the whole structures under seismic loading, the shear strength and ductility of beam-column connections in general and of exterior connections in particular, must be carefully examined. To avoid brittle joint shear failure, it is required that plastic hinges should appear in beams before in joints. This design strategy is called "strong column-weak beam" philosophy. In practice, the prediction of the beam bending moment capacity is relatively relevant, while the prediction of the joint shear strength is still to be investigated. That is the reason why numerous attempts have been paid to analyze the behavior of the beam-column joints.

© Springer Nature Singapore Pte Ltd. 2018
H. Tran-Nguyen et al. (eds.), *Proceedings of the 4th Congrès International de Géotechnique - Ouvrages -Structures*, Lecture Notes in Civil Engineering 8,
DOI 10.1007/978-981-10-6713-6_82

In order to meet the ductility requirements, the details of the reinforcement at the beam-column connection are carefully required by the standard codes, for example ACI 352R-02 [1], AIJ-1999 [2], Eurocode8-2004 [3]. The two most important requirements are the anchored length of the beam reinforcement bars into the joint and the amount of the horizontal stirrups detailed at the joint. To meet these two requirements, the beam bars are conventionally bended on 90° hook in to the joint and a relatively large amount of the horizontal stirrups are put at a small volume of the joint core. The placement of this reinforcement with large development length is a challenge as it makes steel congestion which hinders concrete placement and compaction inside the joint core during the casting whereas the concrete compressive strength is the crucial for the joint shear strength. To overcome this difficulty many attempts have been made to minimize the reinforcement congestion at exterior beam-column joints and using headed bars (Fig. 1) is considered as a potential solution for these problems [4].

**Fig. 1.** Example of a headed bar.

However, the researches about the joint shear strength of the exterior beam-column connections in general and of the exterior beam-column connections with headed bars in particular are still incomplete. The recent studies showed that the shear strength of exterior RC beam-column joints is influenced by the concrete strength, joint panel geometry, reinforcement confinement, column axial load, and reinforcement details at the joint location [5–8]. Lim et al. [9] used numerical method to analyze the influence of reinforcing details on the performance of beam-column connections under blast load and the amount of the diagonal reinforcement at the joint core was considered as the crucial factors. The influencing factors of the joint shear strength of beam-column joints with beam reinforcement bars anchored into the joint core by the conventional 90° hook have been analyzed by Tran et al. 2014 [5], while similar considerations for the exterior beam-column joints with headed bars have not yet been analyzed. Kang and Mitra [10] used binomial logistic regression methodology to establish a statistical model for predicting the performance of beam-column connections with headed bars but the factors of joint shear strength and the joint shear strength prediction were not thoroughly considered. The research community has not yet understood the full behavior of RC beam-column connections because of the large variations in both the geometry and the distribution of forces that occur in a relatively small volume at the joint region [11]. The inconsistencies in the existing design standards [2, 3, 12, 13] for predicting the shear strength of RC beam-column connections clearly displayed this point of view.

It can be concluded that although many efforts have been paid, the research communities still have some inconsistency views about the behavior of beam-column

joints especially the joints with headed bars. To bridge this gap, in this paper a database of exterior beam-column connections with headed bars is assembled. The database contains 30 tested specimens which had failures of brittle joint shear. Using this database, key factors of the joint shear strength for this kind of connections are examined and the joint shear strength of beam-column joints with headed bars is evaluated. Based on these analyses, a formula for predicting the joint shear strength of beam-column joints with headed bars is proposed.

## 2 The Collected Database

From the published literature [4, 14–20], a total of 30 experimental RC beam-column connections with headed bars have been collected. All of the specimens were subjected to quasi-static cyclic lateral loading and were at least one-third scale. The final failure modes of the collected specimens were either joint shear (J) or joint shear with yielding of beam reinforcement (BJ). All of the specimens had no out-of-plane members (slabs and/or transverse beams) and no eccentricity between beams and columns. Specimens that failed in terms of weak column-strong beam and weak beam-strong joint were excluded from the collected data because in these cases, the column or beam flexural capacity is relatively low and thus failure of the column or beam caused by flexural moment can occur before the shear strength of the connection is reached. Only specimens with beam bars anchored into the joint by headed nut were included in the database. In the collected results, the experimental shear forces, $V_{test}$, were either collected from the reported values or calculated using the maximum applied load measured from the tests. In this calculation, the effective height of the beam cross section is assumed to be 85% of the total beam height, $h_b$. This value is acceptable for the configurations where a high quantity of steel reinforcement is present, which is usually the case when headed bars are employed.

The collected database covers a broad range of various parameters including joint reinforcement ratio, reinforcement yielding stress, concrete strength, and beam height to column height ratio hb/hc, as summarized in Table 1. In this table $b_b$, $h_b$ are the width and the height of the beam section, respectively; $b_c$, $h_c$ are the width and the height of the column section, respectively; fc' is the concrete compressive strength; fyb is the yield stress of headed bars; $d_b$ is the diameter of the beam bar; $l_p$ is the provided development length of the beam bars; $\frac{A_{brg}}{A_b}$ is the net bearing area of head to sectional area of the beam bar ratio. Among 30 connections studied, 17 specimens failed in J mode, while 13 specimens failed in BJ mode.

The definitions and the ranges of some main parameters in the collected database are summarized in Table 2. In this table, the index of the beam bars details, $\lambda_b$ is a new parameter and this is a function of the provided development length ($l_p$), the bar diameter ($d_b$), the clear bar spacing ($c_s$) and the clear cover to bar ($c_{cb}$) of the beam longitudinal bar. The influence of $\lambda_b$ on the joint shear strength will be discussed in the following section. It can be seen in Table 2 that the concrete compressive strength fc' ranges from 28.3 to 138.6 MPa, while the yield stress of headed bars ranges from 524 to 1034 MPa. These data show that in most of the collected specimens, high strength

**Table 1.** The collected database of exterior RC beam-column with headed bars.

| Authors | I.D | $b_b$ (mm) | $h_b$ (mm) | $b_c$ (mm) | $h_c$ (mm) | $f_c^{'}$ (MPa) | $f_{yb}$ (MPa) | $d_b$ (mm) | $l_p$ (mm) | $\frac{A_{brg}}{A_b}$ | $V_{test}$ (kN) | Failure mode |
|---|---|---|---|---|---|---|---|---|---|---|---|---|
| Kiyohara et al. (2005) [15] | No.1 | 450 | 600 | 500 | 550 | 95.1 | 710 | 29 | 365 | 5.7 | 1913.6 | BJ |
| | No.2 | 450 | 600 | 500 | 550 | 95.1 | 710 | 29 | 365 | 5.7 | 2285.9 | BJ |
| | No.5 | 450 | 600 | 500 | 550 | 95.1 | 710 | 29 | 276 | 5.7 | 1727.2 | BJ |
| Kiyohara et al. (2004) [16] | No.6 | 450 | 600 | 500 | 550 | 106.2 | 1034 | 29 | 365 | 5.7 | 2842.8 | J |
| | No.7 | 450 | 600 | 500 | 550 | 138.6 | 1034 | 29 | 365 | 5.7 | 2957.6 | J |
| | No.8 | 450 | 600 | 500 | 550 | 47.6 | 1034 | 29 | 365 | 5.7 | 1988.3 | J |
| | No.9 | 450 | 600 | 500 | 550 | 106.2 | 1034 | 29 | 365 | 5.7 | 3352.2 | J |
| | No.10 | 450 | 600 | 500 | 550 | 108.2 | 1034 | 29 | 461 | 5.7 | 2645.3 | J |
| | No.11 | 450 | 600 | 500 | 550 | 103.4 | 689 | 29 | 276 | 5.7 | 2022.2 | BJ |
| Adachi and Masuo (2007) [17] | J30-12-0 | 350 | 450 | 400 | 450 | 31.0 | 524 | 25 | 315 | 5.4 | 1151.2 | BJ |
| | J60-12-0 | 350 | 450 | 400 | 450 | 62.7 | 524 | 25 | 300 | 5.4 | 1229.5 | BJ |
| | J60-12-P1 | 350 | 450 | 400 | 450 | 62.7 | 524 | 25 | 300 | 5.4 | 1304.2 | BJ |
| Masuo et al. (2006) [14] | AH12-2-45 | 300 | 450 | 325 | 450 | 129.6 | 1020 | 25 | 300 | 5.8 | 1002.6 | BJ |
| | AH12-2-40 | 300 | 450 | 325 | 400 | 129.6 | 1020 | 25 | 300 | 5.8 | 938.1 | BJ |
| | AH12-2-45A | 300 | 450 | 325 | 450 | 129.6 | 1020 | 25 | 300 | 5.8 | 994.2 | BJ |
| | AH8-2-45 | 300 | 450 | 325 | 450 | 90.3 | 1020 | 25 | 300 | 5.8 | 895.9 | BJ |
| Tasai et al. (2000) [18] | No.6 | 350 | 450 | 375 | 400 | 51.7 | 724 | 25 | 300 | 8 | 997.3 | J |
| | No.7 | 350 | 450 | 375 | 400 | 51.7 | 724 | 25 | 300 | 8 | 609.8 | BJ |
| Takeuchi et al. (2001) [19] | 0-2 | 350 | 450 | 375 | 400 | 60.7 | 586 | 25 | 268 | 5.8 | 694.8 | BJ |
| | 0-6 | 350 | 450 | 375 | 400 | 44.1 | 717 | 25 | 268 | 5.8 | 835.4 | J |
| | 0-7 | 350 | 450 | 375 | 400 | 62.1 | 717 | 25 | 268 | 5.8 | 984.8 | J |
| Murakami et al. (1998) [20] | No.102 | 300 | 300 | 300 | 300 | 39.3 | 945 | 19 | 224 | 2.1 | 534.2 | J |
| | No.103 | 300 | 300 | 300 | 300 | 39.3 | 945 | 19 | 224 | 5.8 | 415.9 | J |
| | No.104 | 300 | 300 | 300 | 300 | 39.3 | 945 | 19 | 224 | 13.4 | 489.3 | J |
| | M8D16 | 300 | 300 | 300 | 300 | 28.3 | 1000 | 16 | 226 | 6 | 486.6 | J |
| | M4D19 | 300 | 300 | 300 | 300 | 28.3 | 1000 | 19 | 224 | 6 | 460.4 | J |
| | M3D19 | 300 | 300 | 300 | 300 | 28.3 | 1000 | 19 | 224 | 6 | 457.3 | J |
| | M2D22 | 300 | 300 | 300 | 300 | 28.3 | 972 | 22 | 224 | 6 | 459.9 | J |
| Dhake et al. (2015) [4] | J4 | 150 | 180 | 150 | 200 | 30.0 | 525 | 12 | 132 | 4 | 99.8 | J |
| | J5 | 150 | 180 | 150 | 200 | 30.0 | 525 | 12 | 84 | 4 | 86.6 | J |

concrete and high strength steel were used which were popular in the practical application of headed bars.

The normalized horizontal joint shear reinforcement, $\chi_{jh} = \frac{A_{sjh}f_{jhy}}{b_j h_c \sqrt{f_c'}}$, (where $A_{sjh}$, $f_{jhy}$ are the total sectional area and the yield stress of the stirrups, respectively, placed at the joint core; $b_j = (b_c + b_b)/2$ is the effective joint width), ranging from 0 to 0.24.

The normalized vertical joint shear reinforcement, $\chi_{jv} = \frac{A_{sjv}f_{jvy}}{b_j h_c \sqrt{f_c'}}$, (where $A_{sjv}$, $f_{jvy}$ are the area and yield strength of the intermediate vertical reinforcement passing through the joint, respectively), ranges from 0 to 1.47.

These values, especially the normalized horizontal joint shear reinforcement $\chi_{jh}$, are relatively small, compared to the amount of reinforcement required by ACI 352R-02 [1].

Table 2 shows that the development length ($l_p$) of the beam bars ranging from 7 to 24.3$d_b$, is also short compared to the requirement in ACI 318-08 [12]. A comparison between the provided and the development lengths of the beam bars of all the collected samples and that required in ACI 318-08 [12] is shown in Fig. 2. From this figure, it can be seen that all specimens did not meet the required development length of the beam bars, following ACI 318-08. From the above discussions about the variation

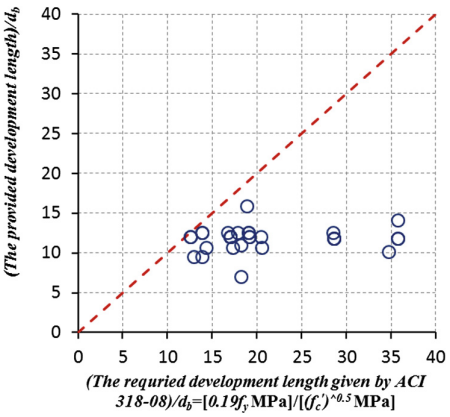


**Fig. 2.** Comparison between the provided and the required beam bar development length

**Table 2.** Definitions and ranges of parameters in the collected database.

| Parameters | Symbol (unit) | Range of the parameters | |
|---|---|---|---|
| | | Min. | Max. |
| Concrete compressive strength | $f_c^{'}$(MPa) | 28.3 | 138.6 |
| Specified yield stress of headed bars | $f_y$ (MPa) | 524 | 1034 |
| Normalized horizontal joint shear reinforcement | $\chi_{jh} = \frac{A_{sjh} f_{jhy}}{b_j h_c \sqrt{f_c'}}$ | 0.0 | 0.24 |
| Normalized vertical joint shear reinforcement | $\chi_{jv} = \frac{A_{sjv} f_{jvy}}{b_j h_c \sqrt{f_c'}}$ | 0.0 | 1.47 |
| Normalized joint shear reinforcement | $\chi_j = \chi_{jh} + \chi_{jv}$ | 0.0 | 1.65 |
| Column depth to beam height ratio | $h_c/h_b$ | 0.89 | 1.11 |
| Column depth to beam bar diameter ratio | $h_c/d_b$ | 13.6 | 19.0 |
| Development length of the beam bars | $l_p$ ($d_b$) | 7.0 | 15.9 |
| The index of the beam bars details | $\lambda_b = \frac{l_p c_{cb}}{d_b c_s}$ | 1.9 | 24.3 |

intervals of the key parameters of the beam-column joints, it can be concluded that most of the specimens in the database did not meet the requirements imposed by the standard. It is the reason why all specimens had failures in either J or BJ mode, and their joint shear strength need to be evaluated.

## 3 Influencing Parameters of Beam-Column Joint Using Headed Bars

The main influencing parameters for the joint shear behavior of the conventional beam-column connections have been examined by Kim and LaFave [21]. From their study, concrete compressive strength fc′, in-plane geometry (interior, exterior or knee

connections), dimensions of the beams and columns (hb, bb, hc, bc), joint transverse reinforcement and beam reinforcement are among the influencing parameters for shear strength of the conventional beam-column joint. Furthermore, the bond condition which is strongly influenced by the development length and the details of the beam reinforcement bars, are also known as the influencing parameters for the shear strength of the conventional joint [5]. In the following part, the influencing parameters for the joint shear strength of connections with headed bars are evaluated by using the collected database.

To evaluate the importance of the keys parameters on the contribution to the joint shear strength, the dependence of the joint shear stress, vtest on the examined parameters is studied on the collected database. The dependence level of these relationships is quantified by the correlation coefficient (CC). The CC of two quantities X and Y is calculated using following equation:

$$CC(X,Y) = \frac{\sum_{i=1}^{n}(x_i - \overline{x})(y_i - \overline{y})}{\sqrt{\sum_{i=1}^{n}(x_i - \overline{x})^2 (y_i - \overline{y})^2}} \quad (1)$$

where $x_i$, $y_i$, i = 1, …, n are the available data of parameters X and Y, respectively; $\overline{x}$ and $\overline{y}$ are the average values of the parameters X and Y, respectively. The CC of two parameters can vary from −1.0 to +1.0. A CC near ±1.0 indicates a strong positive or negative relationship between the two examined quantities, respectively, while a near 0.0 coefficient indicates a weak relationship.

For the collected database, the three most important parameters include the concrete compressive strength, $f_c'$ with CC = 0.71, the index of the beam bars details, $\lambda_b$ with CC = 0.58 and the normalzed joint shear reinforcement, $\chi_j$ with CC = 0.52. The relationship between the maximum tested joint shear stress and these three parameters are shown in Fig. 3. From this figure, it can be seen that beside the concrete compressive strength and the joint shear reinforcement which are usually considered as the important factors of the joint performance, the index of the beam bars details, $\lambda_b$ is a new important parameter. The important level of this parameter is even higher than the

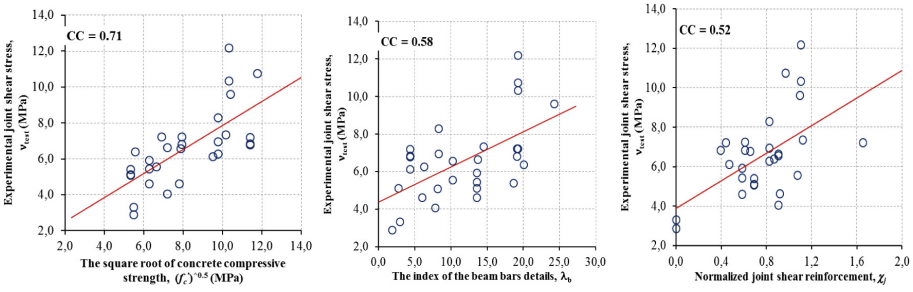


**Fig. 3.** The relationship between the tested joint shear stress and the concrete compressive strength, the index of the beam bars details and the normalized joint shear reinforcement.

joint shear reinforcement. That is why, it is necessary to take into account the index of the beam bars details ($\lambda_b$) and the normalized joint shear reinforcement ($\chi_j$) in the shear strength evaluation of exterior RC beam-column joints, with beam longitudinal reinforcements anchored into the joint by headed bars.

## 4 Models for Shear Strength of Beam – Column Connections

### 4.1 Previous Models

To resist a joint shear force, both strut and truss mechanisms are developed, thus the joint shear strength $V_j$ is usually composed of two components as follows:

$$V_j = V_{ch} + V_{sh} \tag{2}$$

where Vch, Vsh are the shear strengths come from the concrete strut and truss mechanisms, respectively. The first component depends mostly on the concrete strength and the second term mainly depends on the horizontal and vertical joint shear reinforcements. However, in ACI 352R-02 [1] the second term is ignored and the joint shear connection is expressed by a function of the concrete compressive strength as following:

$$V_{ACI} = vb_jh_c = \gamma_{ACI}\sqrt{f_c'}b_jh_c \tag{3}$$

where ν is the joint shear stress and γACI is the joint shear factor given by the code.

In AJIs-1999 [2] the contribution of the joint shear reinforcement is also ignored and the joint shear strength is defined as a function of the concrete compressive strength as follows:

$$V_{AJI} = vb_jh_c = k\phi\left(f_c'\right)^{0.7}b_jh_c \tag{4}$$

where k and ϕ are the joint shear strength factors defined by the code.

The above equations proved that the concrete compressive strength is the crucial parameter.

### 4.2 Model Proposed by the Present Study

In the proposed model, the universal form of the joint shear strength is expected as the sum of all key influencing parameters, as illustrated in following equation:

$$V_j = b_jh_c\sqrt{f_c'}\left(\sum_{i=1}^{n} a_ix_i + c\right) \tag{5}$$

where xi represents the input influencing parameters; n is the number of influencing parameters; ai are coefficients and c is the intercept. The ai and c can be identified by basing on a regression analysis from the experimental data.

The existing models mentioned above focused only on the concrete compressive strength while effects of the index of the beam bars details ($\lambda_b$) and the normalized joint shear reinforcement ($\chi_j$) have not been taken into account. However, significant correlations between the joint shear strength and those two parameters have been showed in the present study. By using a regression analysis (by Microsoft Excel) with experimental data collected, the coefficients ai and c are identified and a new empirical formula can be suggested as following:

$$V_j = b_j h_c \sqrt{f_c'}(0.02\lambda_b + 0.06\chi_j + 0.55) \tag{6}$$

The relevancy of this formula will be verified in the next section.

### 4.3 Assessing the Robustness of the Proposed Model

The experimental results from the database were used to verify the proposed model. A comparison between the tested joint shear strength ($V_{test}$) and the predicted joint shear strength ($V_{model}$) calculated from Eq. (6) is shown in Fig. 4a. The figure shows that the predicted joint shear strengths are close to that of the tested values. The proposed model predicts the joint shear strengths of 30 collected specimens with an average test-to-model shear strength ratio (AVG) of 1.00, a coefficient of variation (COV) of 15.2% and an average error (AVE) of 12.2%. The similar comparisons between the experimental results and that of the existing formulas mentioned in the regulations ACI (Eq. (3)) and AJI (Eq. (4)), are illustrated in Figs. 4b and c, respectively. The model from ACI predicted the joint shear strengths of the collected specimens with an AVG of 0.82, a COV of 21.9% and an AVE of 29.7%. These values for the prediction of the AJI model are AVG = 0.77, COV = 26.9 and AVE = 41.7%. The above figures show that the results predicted by using the model proposed in the present study (Vmodel) are clearly more accurate than that predicted by the empirical formulas suggested by ACI and AJI, on the database of 30 specimens studied in this paper.

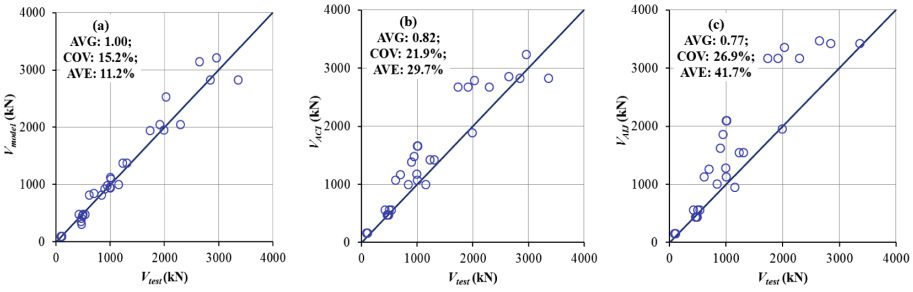


**Fig. 4.** Comparison of the experimental results ($V_{test}$) with that obtained by the proposed model ($V_{model}$), ACI ($V_{ACI}$) and AIJ ($V_{AIJ}$).

The proposed model considers three key parameters including the concrete compressive strength fc′, the index of the beam bars details $\lambda_b$ and the normalized joint shear reinforcement $\chi_j$. Among three parameters, the concrete compressive strength is the conventional parameter, so the influence of this parameter on the shear strength of beam-column connections with headed bars is visible. The influence of the two remaining parameters are double checked to evaluate the suitability of these parameters as well as the accuracy of the model. Figure 5 demonstrates the variation of the test-to-predicted joint shear strength ratio with the index of the beam bars details and the normalized joint shear reinforcement, respectively. The linear regression lines are illustrated on the figures to show the dependence of the joint shear strength on the considered parameters. This figures show that when $\lambda_b$ and $\chi_j$ vary in a wide interval (from 0 to 25 for $\lambda_b$ and from 0 to 2 for $\chi_j$, respectively), the joint shear strength ratio has no clear dependence on these parameters. These figures also show that the test-to-predicted joint shear strength ratio of the proposed model varies around 1.00 in a small range from 0.74 to 1.48 despite the large range variation of the considered parameters. These figures proved that the influencing parameters have been rationally considered in the proposed model and thus the model can appropriately predict the joint shear strength of beam-column joints with headed bars.

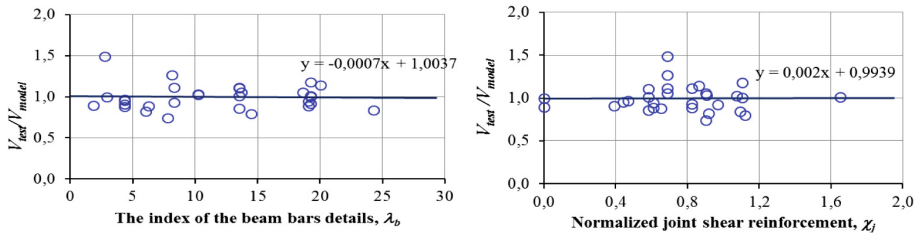


**Fig. 5.** Sensibility of the model results in function of $\lambda_b$ and $\chi_j$.

## 5 Conclusions

The present study seeks a new formulation to predict the shear strength of exterior RC beam-column connections with beam longitudinal reinforcement anchored into the joint by headed bars. The model was developed based on regression analysis using the database collected from the literature. Influences of the most important parameters were analyzed. It is showed that, beside the well-known concrete compressive strength, the index of the beam bars details and the normalized joint shear reinforcement had also vital roles in the joint shear strength. That was why finally these three parameters were chosen to generate the new model, in which the index of the beam bars details was a new parameter comparing to existing models. The regression analysis was used to identify the coefficients of the new model. The results showed that the proposed model had higher accuracy in the prediction of the joint shear strength, compared to formulas mentioned in the regulations (ACI and AJI).

The new model provided satisfying results in the case of experimental results collected from the literature (30 specimens), further investigations with a larger number of specimens will be interesting to verify the relevancy of the proposed model.

## References


1. ACI 352R-02: Recommendations for design of beam-column joints in monolithic reinforced concrete structures. In: ACI 352R-02, ACI-ASCE Joint Committee 352. American Concrete Institute, Farmington Hills, MI (2002)
2. AIJ: Design guideline for earthquake resistance reinforced concrete buildings based on inelastic displacement concept. Tokyo, Japan (1999)
3. Eurocode8-2004: Design of structures for earthquake resistance. part 1: general rules, seismic actions and rules for buildings, London (2004)
4. Dhake, P.D., Patil, H.S., Patil, Y.D.: Anchorage behaviour and development length of headed bars in exterior beam-column joints. Mag. Concr. Res. **67**, 53–62 (2015)
5. Tran, T.M., Hadi, M.N.S., Pham, T.M.: A new empirical model for shear strength of reinforced concrete beam-column connections. Mag. Concr. Res. **66**, 514–530 (2014)
6. Hadi, M.N.S., Tran, T.M.: Retrofitting nonseismically detailed exterior beam-column joints using concrete covers together with CFRP jacket. Constr. Build. Mater. **63**, 161–173 (2014)
7. Lima, C., Martinelli, E., Faella, C.: Capacity models for shear strength of exterior joints in RC frames: state-of-the-art and synoptic examination. Bull. Earthquake Eng. **10**, 967–983 (2012)
8. Park, S., Mosalam, K.M.: Parameters for shear strength prediction of exterior beam–column joints without transverse reinforcement. Eng. Struct. **36**, 198–209 (2012)
9. Lim, K.-M., Shin, H.-O., Kim, D.-J., Yoon, Y.-S., Lee, J.-H.: Numerical assessment of reinforcing details in beam-column joints on blast resistance. Int. J. Concr. Struct. Mater. **10**, 87–96 (2016)
10. Kang, T.H.K., Mitra, N.: Prediction of performance of exterior beam-column connections with headed bars subject to load reversal. Eng. Struct. **41**, 209–217 (2012)
11. Pantazopoulou, S., Bonacci, J.: Consideration of questions about beam-column joints. ACI Struct. J. **89**, 27–36 (1992)
12. ACI318R: Building code requirements for structural concrete and commentary. American Concrete Institute, Farmington Hills (2008)
13. NZS-3101: Concrete structures standard. part 1: the design of concrete structures. Standards Association of New Zealand, Wellington (1995)
14. Masuo, K., Adachi, M., Imanishi, T.: Ultimate strength of R/C exterior beam-column joint using mechanical anchorage for beam reinforcement USD590. In: Proceedings of the Architectural Institute of Japan, September 2006, pp. 25–28 (2006). (in Japanese)
15. Kiyohara, T., Hasegawa, Y., Fujimoto, T., Akane, M., Amemiya, A.T., et al.: Seismic performance of high strength RC exterior beam column joint with beam main bars anchored. In: Proceedings of the Architectural Institute of Japan, September 2005, pp. 33–42 (2005). (in Japanese)
16. Kiyohara, T., Tasai, A., Watanabe, K., Hasegawa, Y., Fujimoto, T.: Seismic capacity of high strength RC exterior beam column joint with beam main bars anchored mechanically. In: Proceedings of Architectural Institute of Japan, August 2004, pp. 27–34 (2004). (in Japanese)

17. Adachi, M., Masuo, K.: The effect of orthogonal beams on ultimate strength of R/C exterior beam-column joint using mechanical anchorages. In: Proceedings of the Architectural Institute of Japan, August 2007, pp. 633–634 (2007). (in Japanese)
18. Tasai, A., Kawakatsu, T.K., Murakami, M.: Shear performance of exterior beam column joint with beam main bars anchored mechanically. In: Proceedings of the Architectural Institute of Japan, September 2000, pp. 857–860 (2000). (in Japanese)
19. Takeuchi, H., Kishimoto, T., Hattori, S., Nakamura, K., Hosoya, H., Ichikawa, M.: Development of mechanical anchorage used circular anchor plate. In: Proceedings of the Architectural Institute of Japan, September 2001, pp. 111–114 (2001). (in Japanese)
20. Murakami, M., Fuji, T., Kubota, T.: Failure behavior of beam-column joints with mechanical anchorage in Subassemblage frames. Concr. Res. Technol. **8**(1), 1–9 (1998)
21. Kim, J., LaFave, J.M.: Key influence parameters for the joint shear behaviour of reinforced concrete (RC) beam-column connections. Eng. Struct. **29**, 2523–2539 (2007)

# A Probabilistic Explicit Cracking Model for Steel Fibres Reinforced Concretes (SFRC)

Pierre Rossi(✉) and Jean-Louis Tailhan

IFSTTAR-Université Paris-Est, Marne-La-Vallée, France
{pierre.rossi,jean-louis.tailhan}@ifsttar.fr

**Abstract.** SFRC is increasingly used for structural applications. The present paper is devoted to a probabilistic explicit cracking model developed since 1985. It is used to analyze the cracking behaviour of different SFRC beams submitted to different loading conditions: bending and shear. It is demonstrated that this numerical model is fully capable to provide precise information about the cracking process related to this types of structural behaviour, especially concerning the cracks opening evolution.

**Keywords:** Cracking · Numerical model · Probabilistic approach · Serviceability state · Steel fibre reinforced concrete · Structures

## 1 Introduction

Crack control is very important for durability aspects and is certainly a major advantage of SFRC compared to structures using traditional reinforcement bars. Nowadays, existing design recommendations are not able to provide sufficient relevant information regarding cracking in the serviceability limit state (i.e. with regard to cracks opening and spacing). In this way, the best approach for designing structures with respect to both safety and sustainable development is the use of finite element analysis.

IFSTTAR has been developing a probabilistic explicit cracking model since 1985 (first publication in materials and structures in 1987 [1]). The numerical model, originally developed to analyze cracking of structures made of ordinary concrete, has been enhanced to take into consideration cracking of fibre reinforced concrete structures [2]. In this paper, an improvement of the probabilistic explicit cracking model devoted to the analysis of fibre reinforced concrete cracking is proposed. The improved numerical model is used to analyze the cracking behaviour of different SFRC beams submitted to different loading conditions: bending, and shear. The main objective of this presentation is to demonstrate the capability of this numerical model to provide precise information about the cracking process related to these types of structural behaviour, especially concerning the opening and the spacing of the cracks.

## 2 Probabilistic Explicit Cracking Model of SFRC

This improved model (yet published [3, 4]) is based on three main physical evidences that have been observed experimentally:

© Springer Nature Singapore Pte Ltd. 2018
H. Tran-Nguyen et al. (eds.), *Proceedings of the 4th Congrès International de Géotechnique - Ouvrages -Structures*, Lecture Notes in Civil Engineering 8,
DOI 10.1007/978-981-10-6713-6_83

- Concrete is a heterogeneous material in which the heterogeneities can be modeled through a random spatial distribution of a mechanical property considered as dominant in the cracking process, namely the tensile strength [1].
- Scale effects of concrete cracking are taken into account by the fact that the tensile strength depend on the size of the mesh elements chosen for the finite element analysis [1, 5]. In contrast, the average post-cracking energy is considered independent of scale effects [6].
- Cracking is explicitly treated through the creation of random kinematic discontinuities, which provides access to quantitative information on the cracking state (number of cracks, opening and spacing of these cracks). Numerically speaking, these cracks are represented by interface elements.

The crack initiation criterion may be summarized as following: the interface element opens when the normal tensile stress at the centre of the interface element reaches a critical value. The critical value corresponds to the tensile strength of the material (a Weibull random distribution function [7] is used concerning this material parameter). This critical value depends on the total volume of the two volumetric elements interfaced by the considered interface element. This means that the stress and the rigidity of the interface element briefly become equal to zero until the bridging effect of the fibres takes over. The criterion of crack creation is schematically presented in Fig. 1. Therefore, the creation of cracks in the cement matrix is represented by an elastic perfectly brittle behaviour, whereas the bridging effect of the fibres is described by the following modelling approach: Normal and tangential stresses in the interface element linearly increase with normal and tangential displacements when a "broken" interface element re-opens to take into account the elastic effect of the fibres inside the crack. Physically speaking, the rigidity of the fibres (inside the cracks) is more important in tension than in shear. Thus, the interface element rigidity is considered different for normal and tangential displacements. In 2D, normal and tangential rigidities of the interface element are $K'_n$ and $K'_t$ respectively. The post-cracking elastic behaviour exists until it reaches a threshold value, $\zeta_0$, related to the normal displacement (Fig. 1). From this limit value, the mechanical behaviour of the interface element changes. The normal stress is considered as linearly decreasing with the normal displacement in order to take into account the damage of the bond between the concrete and the fibre, and fibre pullout. The decreasing evolution is obtained by using a damage model. Finally, the interface element is considered definitively broken when the normal displacement reaches a threshold value, $\zeta_c$ (Fig. 1). This value corresponds to the state where the effect of fibres is considered negligible. It is determined from a uniaxial tensile test. At this point, its normal and tangential rigidities are set to zero.

The post-cracking energy dissipated by the bridging effect of the fibres is considered randomly distributed on the mesh elements. The random distribution is a log-normal distribution function with a mean value independent of the mesh elements size and a standard deviation that is due to the heterogeneity of the material increasing as the mesh elements size decreases [6]. To model a given structural element, the random distribution function is determined in the following manner:

- The mean value is directly obtained by performing a certain number of uniaxial tensile tests on notched specimens (the post-cracking energy is classically determined from the load-crack opening curve) or indirectly by performing an inverse approach based on numerical simulations of bending test.
- The standard deviation, which depends on the mesh elements size, is determined by an inverse analysis approach that consists of simulating uniaxial tests (on notched specimens) or bending tests with different element mesh sizes. As a matter of fact, knowing from the mean value of the post-cracking energy, several numerical simulations are realized for each mesh size and the standard deviation related to each mesh size is obtained by fitting the experimental results (in terms of mean and standard deviation of the numerical responses compared to their corresponding experimental values). By this way, it is possible to find a relation between the standard deviation and the finite element mesh size.

The threshold parameters $\zeta_0$ and $\zeta_c$ are determined by an inverse analysis approach to best fit the simplified triangular stress-displacement curve representing the post-cracking energy (Fig. 1) to the experimental tensile softening curve.

Figure 1 presents the numerical mechanical behaviour adopted to represent the experimental post-cracking behaviour. Only the normal stress - normal displacement curve is considered in this figure.

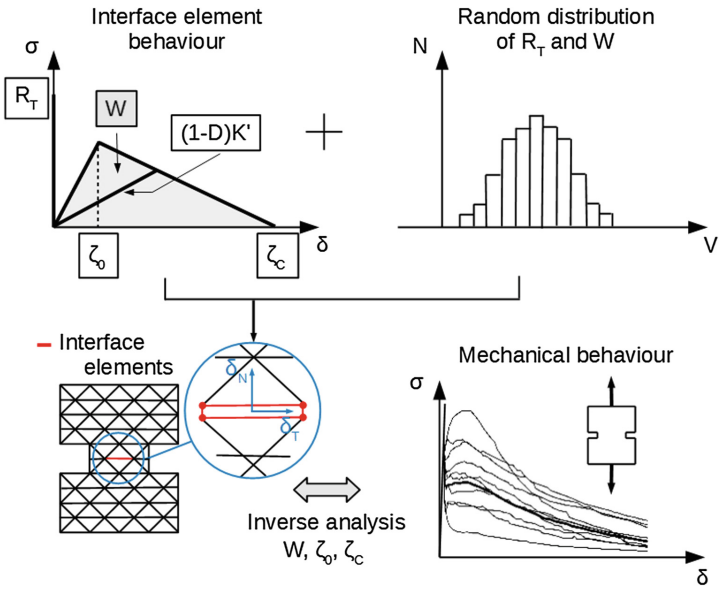


**Fig. 1.** Principles of the explicit probabilistic cracking model of SFRC

## 3 Examples of Application of the Numerical Model

Two types of structural application are proposed: the first one about the bending behaviour of a beam and the second one about the shear behaviour of another beam. The two examples have been yet published [3, 4].

### 3.1 Bending Behaviour of a SFRC Beam

The SFRC beam was submitted to 4-point bending. The experimental campaign that allows the comparison of experimental and numerical results was conducted at Ecole Polytechnique de Montréal, Canada [8]. The dimensions (length, width, height) of the beam were the following: 2600 × 400 × 300 mm$^3$. The testing apparatus used for this experimental campaign is presented in Fig. 2.

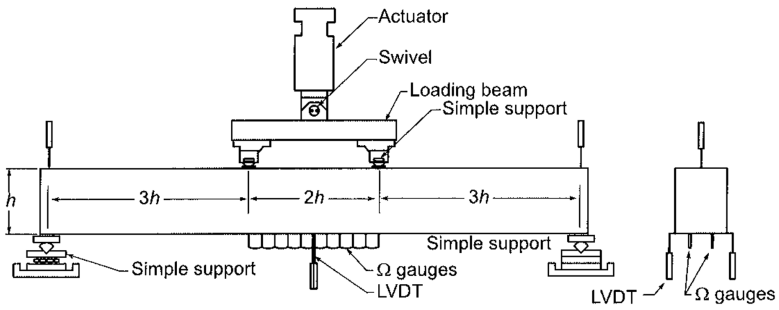


**Fig. 2.** Beams' dimensions, testing apparatus and instrumentation the experimental tests

The SFRC used was a self-compacting one containing 78 kg/m$^3$ of hooked-end steel fibres. These fibers were 35 mm long and had a diameter of 0.55 mm. This SFRC achieved an average compressive strength of approximately 60 MPa at 28 days.

In order to characterize the tensile behavior, uniaxial tension tests were performed on this SFRC. The uniaxial tension test was conducted on notched core-cylinders (h = 100 mm and ø = 85 mm). Six specimens for each mix were cored horizontally from a 500 × 600 × 400 mm$^3$ block casted in addition to the beams.

These tensile tests were performed to determinate, by inverse approach, the parameters of tensile behaviour model of the SFRC.

The numerical simulations were performed in 2D in plane stresses conditions.

The finite elements mesh used to simulate the beam behaviour is presented in Fig. 3.

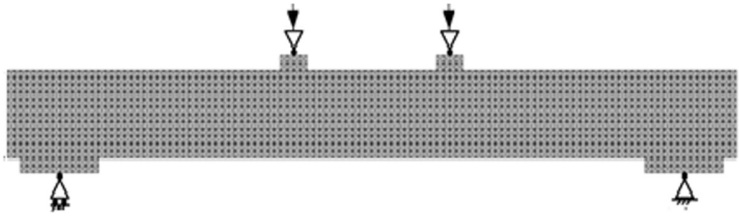

**Fig. 3.** Finite elements mesh of the SFRC beam.

The parameters of the tensile behaviour model related to the studied SFRC were the following:

- Average tensile strength: 2.46 MPa,
- Tensile strength standard deviation: 0.34 MPa,
- Average post-cracking energy: 4.26 MPa.mm,
- Post-cracking energy standard deviation: 0.88 MPa.mm,
- $\delta_0$: 0.05 mm,
- $\delta_C$: 4 mm.

Figure 4 presents a comparison between the global behaviour of the SFRC beam obtained with the experience and with the numerical simulation. This global behaviour is considered in the frame of the Load-deflection curve of the beam.

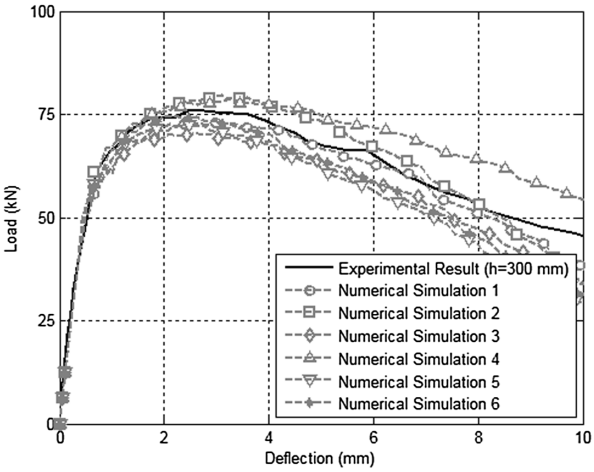


**Fig. 4.** Load-deflection curve - comparison between experience and numerical simulation.

Figure 5 presents an example of cracking pattern obtained with the numerical simulation.

Figure 6 proposes a comparison between the evolutions (with the loading moment) of the maximum crack opening displacement obtained experimentally with the one obtained numerically.

Considering Figs. 4 and 6, it appears clearly that the numerical model is capable to give good information about the global behaviour of the SFRC beam and about its cracking process in bending conditions.

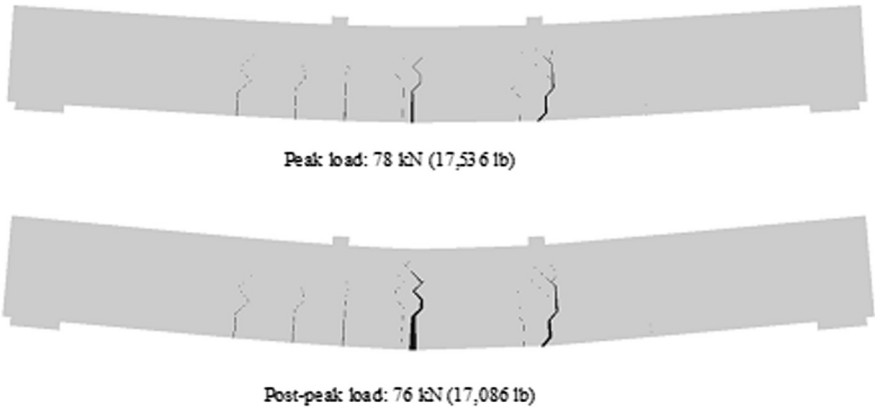


**Fig. 5.** Example of cracking pattern obtained with the numerical simulation

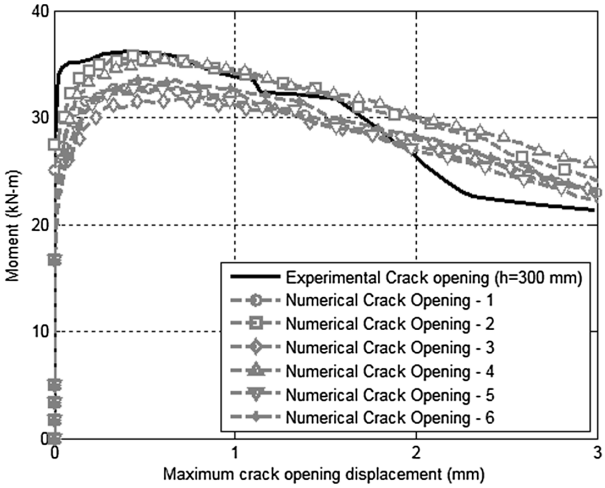


**Fig. 6.** Maximum crack opening displacement versus loading moment - comparison between experience and numerical simulation

### 3.2 Shear Behaviour of a SFRC Beam

The beam was designed to fail in shear. It means that bending reinforcement (rebars) was designed to avoid bending failure due to the appearance of a bending cracking mechanism.

The beam geometry and its reinforcement are presented in Fig. 7.

The concrete that was used was a high-strength SFRC (compressive strength around 90 MPa) containing 100 kg/m$^3$ of steel fibres with a length of 30 mm and a diameter of 0.5 mm.

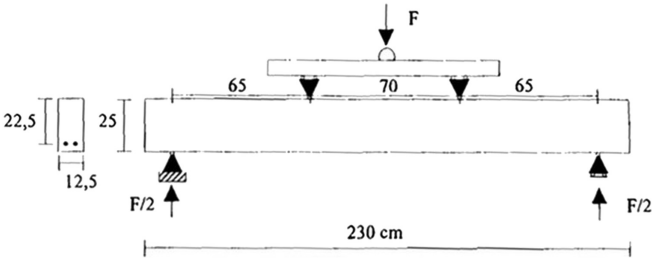


**Fig. 7.** Beam geometry and test set-up

Two types of measurement were recorded: the evolution of the central beam deflection and shear cracks openings using LVDTs. The test set-up related to the cracks opening is presented in Fig. 8.

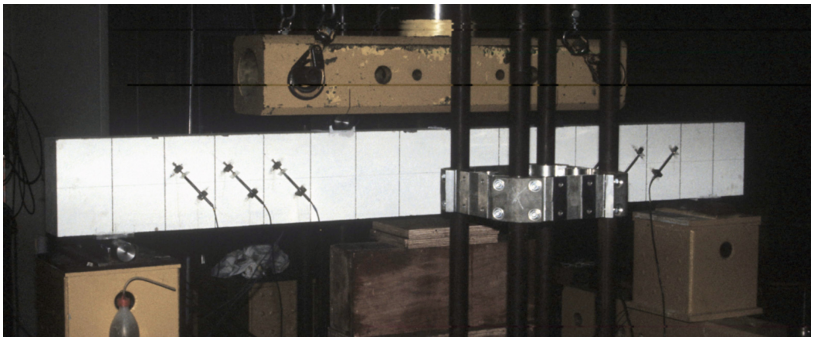

**Fig. 8.** Measurement test set-up of the cracks openings

Two beams were tested during this experimental study.

The finite element mesh and the boundary conditions adopted for the numerical simulation are presented in Fig. 9.

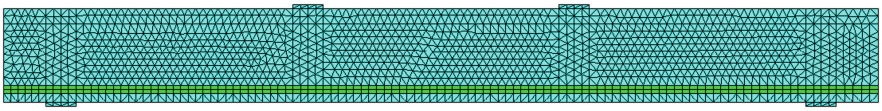

**Fig. 9.** Finite elements mesh of the high performance SFRC beam.

The parameters of the tensile behaviour model related to the studied SFRC were the following:

- Average tensile strength: 5.7 MPa,
- Tensile strength standard deviation: 0.5 MPa,

– Average post-cracking energy: 2.9 MPa.mm,
– Post-cracking energy standard deviation: 2.9 MPa.mm,
– $\delta_0$: 0.1 mm,
– $\delta_C$: 1.5 mm.

These parameters were determined by performing an inverse analysis of uniaxial tensile tests results obtained on notched cylindrical specimens (these specimens were cored in a SFRC beam casted only for this purpose).

Load-deflection curves representing the global behaviour of the beam for both experimental tests and numerical simulations are presented in Fig. 10.

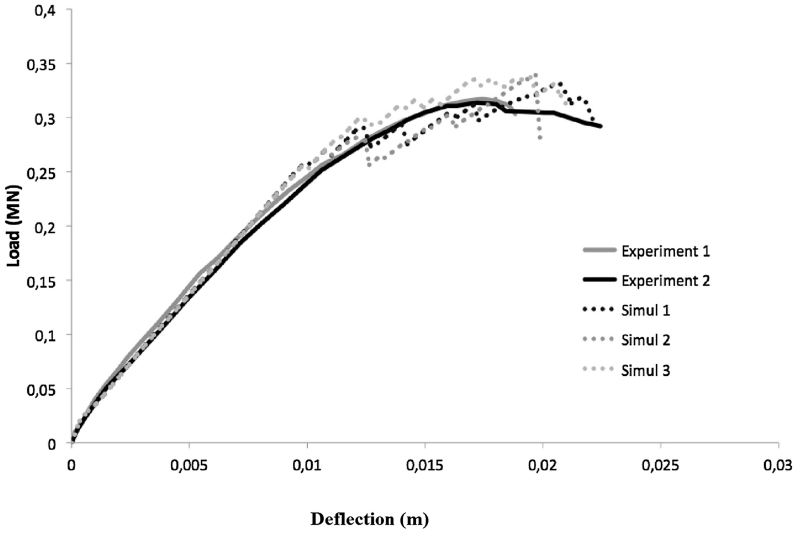


**Fig. 10.** Load-deflection curves related to the experimental tests and the numerical simulations of the beam behaviour

An example of the evolution of the cracking process of the beam given by the numerical simulation is presented in Fig. 11.

A comparison between experience and numerical simulations concerning the cracks opening evolution with the load is presented in Fig. 12.

As shown in Figs. 10, 11 and 12, the proposed numerical model is capable to give relevant results related to the global beam behaviour (*load-deflection* curve) of the beam, its mechanism of rupture and related to the cracks opening evolution.

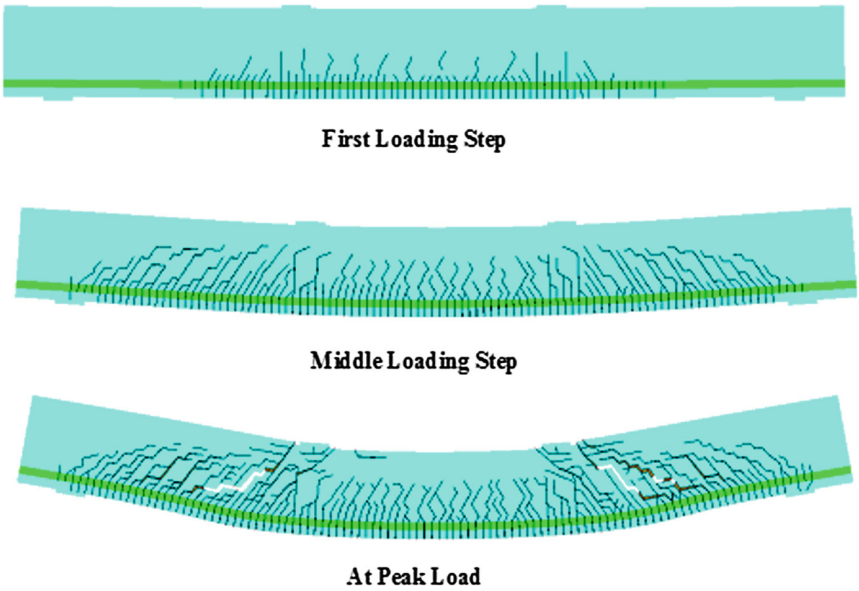


**Fig. 11.** Example of evolution of the cracking process of the beam given by the numerical simulation

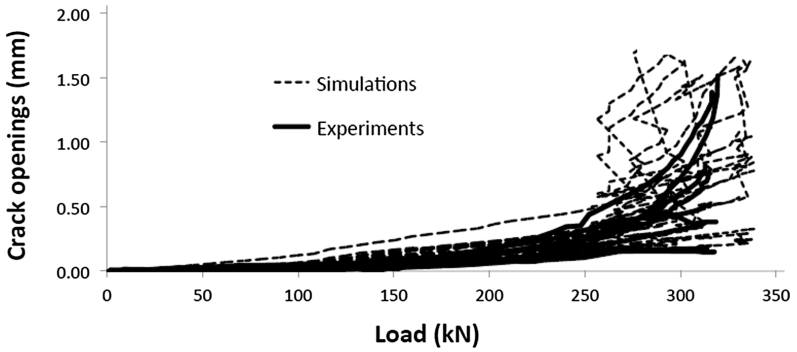


**Fig. 12.** Cracks opening versus load: comparison between experience and numerical simulations

## 4 Conclusions

This paper presents a probabilistic explicit cracking model for SFRC using interface elements.

The physical bases of this model are the following:

– The creation of microcracks is the consequence of the matrix heterogeneity. The heterogeneity is taken into account by a perfect-brittle model in which the tensile strength is probabilized through a Weibull random distribution function.

– The propagation of macrocracks is controlled by the effect of fibres (post-cracking behaviour). The effect of fibres is taken into account by a damage model in which the tensile stress at the level of an interface element is a linear decreasing function of the opening displacement related to this element. The post-cracking energy is considered as a probabilized parameter following a log-normal random distribution function.

This model has been used to simulate the bending and the shear behaviour of SFRC beams.

The comparison between experimental and numerical results shows clearly that the present numerical model is capable to give interesting information of both at the global level (structural behaviour) and at the local level (evolution of the cracks opening with the load).

This relevancy of the numerical model to get good prediction of the cracking process is mainly the consequence of two choices:

– an explicit description of the cracks through the use of interface elements;
– the use of probabilistic approaches for the cracks creation and the post-cracking fibres acting.

## References

1. Rossi, P., Richer, S.: Numerical modelling of concrete cracking based on a stochastic approach. Mater. Struct. **20**(119), 334–337 (1987)
2. Rossi, P., Wu, X.: A probabilistic model for material behaviour analysis and appraisement of the concrete structures. Mag. Concr. Res. **44**(161), 271–280 (1992)
3. Tailhan, J.L., Rossi, P., Daviau-Desnoyers, D.: Numerical modelling of cracking in Steel Fibre Reinforced Concrete (SFRC) structures. Cem. Concr. Compos. **15**, 315–321 (2015)
4. Rossi, P., Daviau-Desnoyers, D., Tailhan, J.-L.: Analysis of cracking in Steel Fibre Reinforced Concrete (SFRC) structures in bending using probabilistic modelling. Struct. Concr. **16**(3), 381–388 (2015)
5. Rossi, P., Wu, X., Le Maou, F., Belloc, A.: Scale effect on concrete in tension. Mater. Struct. **27**, 437–444 (1994)
6. Rossi, P.: Experimental study of scaling effect related to post-cracking behaviours of metal fibres reinforced concretes. Eur. J. Environ. Civil Eng. **16**(10), 1261–1268 (2012)
7. Tailhan, J.L., Dal Pont, S., Rossi, P.: From local to global probabilistic modelling of concrete cracking. Ann. Solid. Struct. Mech. **1**, 103–115 (2010)
8. de Montaignac de Chauvance, R.: Analyse du comportement d'éléments fléchis en béton renforcé de fibes métalliques. Du matériau à la structure. Ph.D. thesis of Ecole Polytechnique de Montréal, Canada, p. 258 (2011). (in french)

# Achieving Robustness of Structures Is Key to Resilience

Paul Smith(✉)

Arup, London, UK
paul-c.smith@arup.com

**Abstract.** Man-made structures are erected according to a requirement to serve a useful purpose, either to an individual, organization or society as a whole. If we take the example of a building structure, it protects its occupants from the environment. The first set functional requirements will be to keep out annoyances like noise, rain, cold, ice, snow and heat. In our radically changing world, new and more onerous requirements need to be considered, ranging from noxious pollution to the possibility of the structure having to withstand an extreme natural hazard, like with an earthquake or tornado. The fact is that structures, whether making up the fabric of our habitable buildings or supply infrastructure, need to be robust against the various annoyances and accidental situations that the structures will be exposed to. The generic damage-effect of climate change will likely make "natural" hazards much more extreme and potentially dangerous in the future. Climate change effects have the likelihood of radically degrading and bypassing the safety barriers of previously engineered design bases. In addition, due to the way in which our civilisation has evolved to the present day, with its commodity trade and service networks, our society more exposed and vulnerable to severe and potentially extreme shock-hazard scenarios. People and organisations implicitly depend on their structural fabric to be functional and safe. Regardless of the great diversity of structures, the one unvarying expectation is that they are robust enough to safely protect the structure's users throughout their intended life period. However, judgements by structural engineers allied with interpretation of design codes and standards can vary greatly. There being a difficult balance between economy of construction and the ultimate robustness of the structural design solution.

This study paper investigates the relationship between robustness of our structural fabric and how important it is to achieving a resilient society, where people are safe, organisations are stable and the economy is sustainable. Essentially we will outline the key quantities that link structural robustness to societal resilience, and whether this crucial relationship is adequately reflected in application of structural design code and standards practice. The thinking logic and methodology provided in this CIGOS 2017 paper will take these key considerations and factors related structural robustness and resilience, the two principal parts of this paper encompass:-

- Risk Analysis in relation to Robustness.
  - Qualitative - Holistic Systems Thinking;
  - Quantitative - Risk Analysis (QRA);
  - Reasons for Poor Structural Robustness.

© Springer Nature Singapore Pte Ltd. 2018
H. Tran-Nguyen et al. (eds.), *Proceedings of the 4th Congrès International de Géotechnique - Ouvrages -Structures*, Lecture Notes in Civil Engineering 8,
DOI 10.1007/978-981-10-6713-6_84

- Future Coping and Adaptability.
- Structural robustness and resultant resilience;
- Future design objectives;
- Specific design principles and options.

**Keywords:** Risk analysis · EuroCode EN 1991-1-7 · Coping · Adaptability · Structures · Robustness · Resilience

## 1 Hard Times to Come

Our world is changing. Our more intertwined and denser society faces an enormous challenge for ourselves, and future generations. And our world is likely to change to even greater extent, the key reason being climate change that is happening now. Future mitigation of climate change will involve various new technology initiatives and political will that shall have to be developed and actually implemented, including:-

- To develop and use carbon-free energy-power generation – nuclear, solar and wind;
- To develop and use by carbon-neutral energy-power generation – biofuels;
- To position power generation plant facilities in low-hazard zones;
- To establish governance policies for system-integrated energy-power generation that accounts for climate change amplified risk-hazards;
- To use power with greater efficiency;
- Lessen power transmission-distribution losses;
- Building more robust, efficient and sustainable structures (like buildings and infrastructure);
- To more wisely locate and re-locate urban and rural populous.

The generic damage-effect of climate change will likely make “natural” hazards much more extreme and potentially dangerous in the future. Climate change effects have the likelihood of radically degrading and bypassing the safety barriers of previously engineered design bases, well inside the expected service life that will likely equate beyond 100 years; equivalent to the life time of a nuclear power station that represents critical energy supply infrastructure. The risk from more extreme storms and their destructive waves will be arguably greater, coming with a higher chance of existing sea defences being breached and possibly failing completely. Storm waves are much harder to predict if you are guarding against one particular extreme wave that has enough force and energy to destroy previously sound sea defences. In essence, it is one thing to limit flooding from wave overtopping to restrict flooding, but quite another to protect against the most extreme wave possible, with many variables to consider, such as the fetch, angle to the shore, wind and basic still sea water level.

It is likely that past design margins that were previously adequate shall diminish to such an extent such that existing defences like sea walls and levees shall be totally

bypassed, allowing spatially expansive inundation of seawater with enormous energy and unlimited wavelength. The risk to coastal facing regions from extreme storms shall increase significantly over the next few decades, more than past experience would suggest, yet so extreme the damage may become that communities and infrastructure shall no other alternative but to recede back inland. A major problem arises for coastal-facing structures, as planning to move big engineering facilities together with their necessary infrastructure network introduces profound political, economic and logistical challenges. Civil and structural designers and engineers will be obligated to demonstrate withstand and resilience against more extreme natural external hazards aggravated by climate change.

The reality is that natural disasters and the man-made technological dangers which may accompany them are not linear problems that can be solved in isolation; is not achieved by just addressing individual components parts of an interactive and dynamically changing damage-loss sequence that kills people, destroys the structural fabric of the infrastructure and dictates complete dislocation of communities away from their once-homes. The newly emerging technology for improved robustness with integral resilient technology will enable our energy infrastructure to stay intact with future severe and extreme hazards or shocks beyond the original design capacity and manage emergencies using well founded coping strategies.

Therefore, our past approach and methodology used to analyse risk should be revisited to achieve the robustness and resilience needs when accounting for future hazards aggravated by climate change amplification. It is advocate that the approach to risk reduction into the future should utilise a much more holistic approach assessing if we can cope with severe and extreme hazards, while accounting for the temporal-dynamic impact effects that our critical infrastructure and the diverse fabric that the urban and rural socio-technical systems will be exposed to.

It is advised that a much more holistic approach is taken to analyse the significance of future emerging risks. Future risk assessment logic should encompass a much broader perspective of the hazard withstand and risk assessment, including an enhanced understanding as to whether the likely future hazard-event scenarios that will critical buildings and infrastructure, their sites and the adjacent urban or rural regions can actually cope with the hazards as they unfold, as well as conceptually testing whether the proposed response and recovery actions will actually be feasible. In addition, there will be the need to ascertain if safety-critical facilities and their adjacent emergency services can cope with distributed severe hazards.

## 2 Risk Analysis in Relation to Robustness

### 2.1 A Basis for Robustness, Accident Situations and the Consequences

The European Standard EN 1991-1-7 [1], defines robustness as:-

> "*the ability of a structure to withstand events like fire, explosions, impact or the consequences of human error, without being damaged to an extent disproportionate to the original cause*."

European Standard EN 1991-1-7
Figure 3.1 – Strategies for Accidental Design Situations

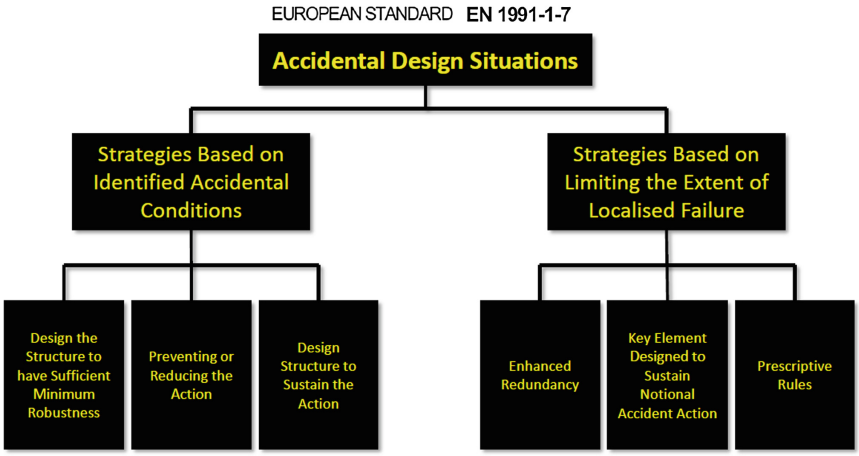


Basic Types of 'Accident Situations' that Buildings Need to Resist:-

- Natural Hazards;
- Fire;
- Explosion;
- Impacts;
- Rail;
- Aircraft (Helicopter);
- Criminality;
- Terrorist Threat;
- Other types of shocks and threats; as well as,
- Accounting for Inadequacies in the Design and Construction processes.

Coping Strategies for Accidental Design Situations with Climate Change

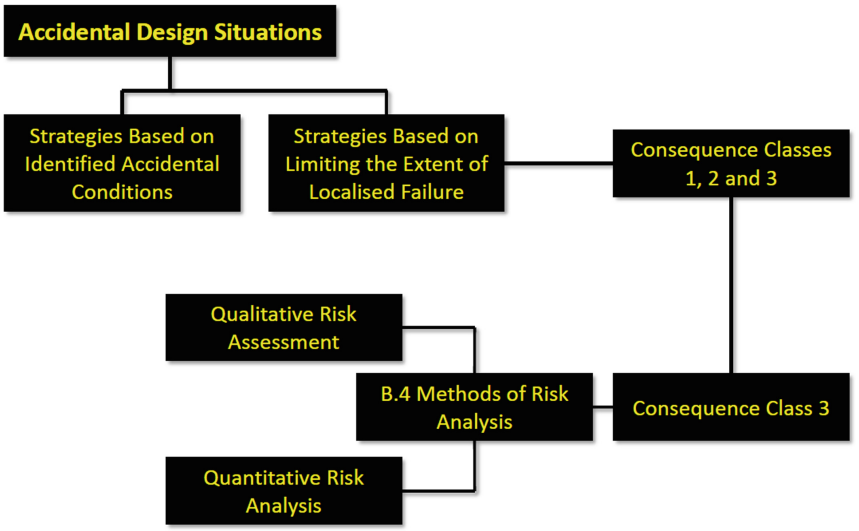

Consequences of Single Building Failure due to Poor Robustness:-

- Occupant's Direct Losses.
  - Dead and Maimed Victims;
  - Physical Health Impairment;
  - Mental Health Impairment;
  - Unavailable to Community;
  - Undermines Resilience;
  - Inhibits Ability to Cope.
- Owner, Designer and Builder Indirect Losses.
  - Business and Economic;
  - Professionalism;
  - Criminal or Civil Prosecution;
  - Industry Public Image.

### 2.2 Reasons for Poor Structural Robustness

Supplemental to the broadly generic accident situations mentioned above, is a much broader spectrum of factors that need to be accounted for by the structural design and construction professions, taking due cognizance of the present day circumstance and future uncertain changes yet to come; including:

- Poor design process;
- Poor awareness of shock-threat risks;
- Poor awareness of need to better response and recovery capability;
- Poor planning to cope with shock-threats;
- Poor system integrity {like obsolescent and vulnerable infrastructure};
- Poor account of social factors;
- Poor technical substantiation;
- Poor specification;
- Poor construction technique and methods;
- Poor risk management;
- Poor risk analysis;
- Aged and obsolescence in critical parts of the socio-technical system;
- Foolish occupancy by bad industrial and domestic placement;
- Local vulnerability against shock-threat risks;
- Structural and system weaknesses;
- Material imperfections and degradation;
- Unrevealed construction and build faults;
- Unexpected conditions;
- Unusual conditions;
- Ignorance now and in future;
- Water-ocean hazards;
- Wind-atmosphere hazards;
- Fire-atmosphere hazards;
- Land-earthquake hazards;

- Land-slide hazards;
- Man-made pollution and chemo-toxic hazards;
- Population growth as a risk amplifier;
- Climate change amplification {from severe to extreme magnitudes and durations not experienced before}.

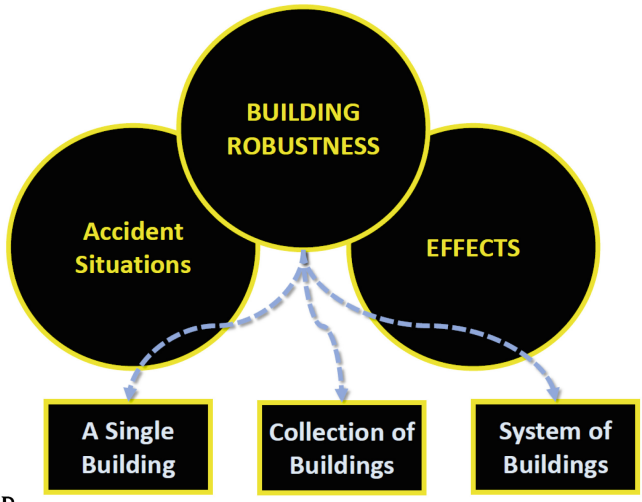


ARUP

# 3 Future Coping and Adaptability

## 3.1 Structural Robustness and Resultant Resilience

Building and Infrastructure System Robustness

- Strength;
- Stability;
- Resilience.

System Resilience Encompasses:-

- Robustness;
- Awareness;
- Forewarning;
- Preparedness;
- Response;
- Recovery;
- Resources;
- Coping;
- Adaptability;
- Surveillance.

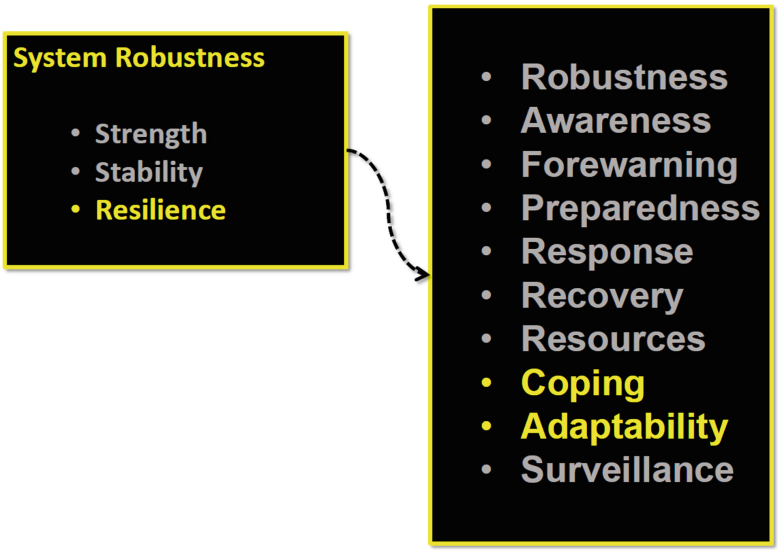


## 3.2 Design Objectives to Achieve Robustness and Resilience

- Future Design Objectives that may be applied in order to Cope and Adapt to future shocks we will need to develop and have:-
  - Sustainable basis to design;
  - Low energy construction methods;

- Minimal carbon footprint;
- Use low carbon-input materials;
- Use low carbon-input systems;
- Utilise local materials and products;
- Buildings are for people;
- Account for the populous and its demography;
- Consider the people under stress;
- Account for socio-technical needs;
- Low external energy feed;
- Low external services provision;
- Plan for long period "islanding";
- Plan for peak habitation islanding;
- Optimum natural day lighting;
- Adequate night lighting during emergencies;
- Integral renewable energy;
- Stored energy for night periods;
- Ensure personal dignity;
- Ensure social solidarity and help;
- Provide medical capability;
- Intuitive medical equipment;
- Apply a "Holistic Integrity" mindset.

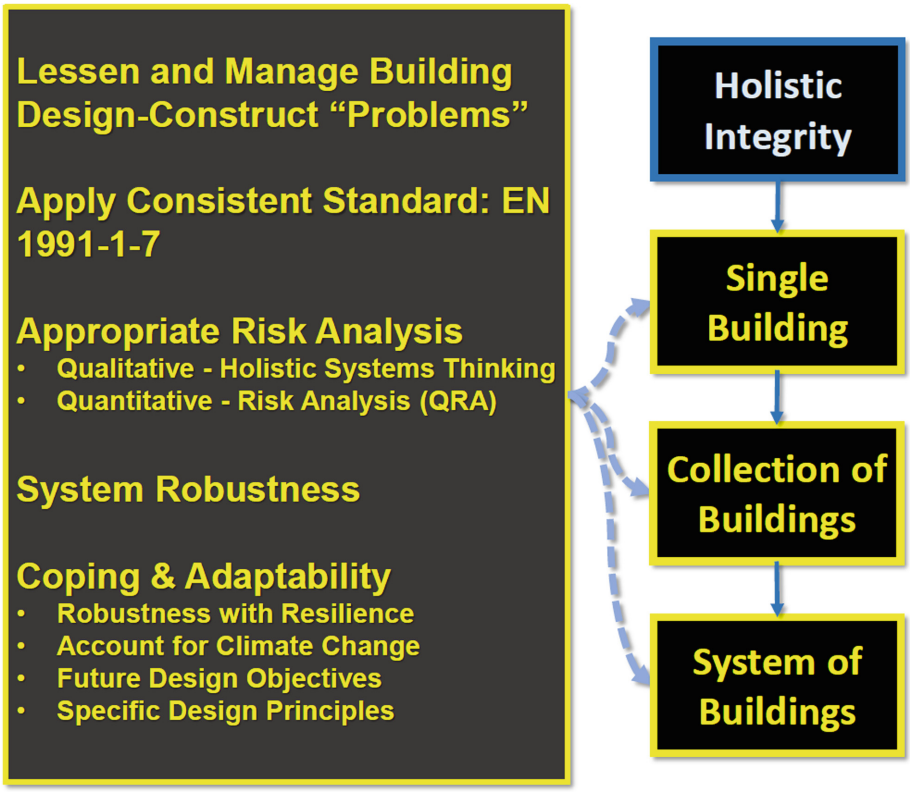

### 3.3 Specific Design Principles and Options

- Specific Design Principles:-
  - To fit with the coping strategy;
  - Effective shock and hazard monitoring capability and stations;
  - Efficient forewarning alarms;
  - Emergency communications;
  - Emergency air, water & food;
  - Fast evacuation routes;
  - Integral safe havens;
  - Access to safety equipment;
  - Hand-lift safety equipment;
  - Retains intrinsic flexibility;
  - Wise location;
  - Lessen vulnerability;
  - Minimise weaknesses;
  - Increase strength margins;
  - Eradicate catastrophic failure modes;
  - Prevent dynamic fluid peaks;
  - Minimisation presence and production of debris;
  - Optimise debris buoyancy (against flood water scenarios);
  - Ensure response success;
  - Ensure recovery success;
  - Carry out actual “Stress Tests” on the engineered systems.

- Resilient Design Options:-
  - Proven coping strategies;
  - Real condition stress tested;
  - Regular practical exercises;
  - Adequate response time;
  - Adequate scale;
  - Adequate capability;
  - Trained operatives;
  - Intuitive design and use;
  - Intuitive direction;
  - No single point failures;
  - No common cause failures;
  - No common mode failures;
  - Diversity of systems;
  - Stress-tested system backups;
  - Independent networks;
  - Redundancy of components;
  - Modular-standard configuration;
  - Failure zone separation;
  - Debris zone free.

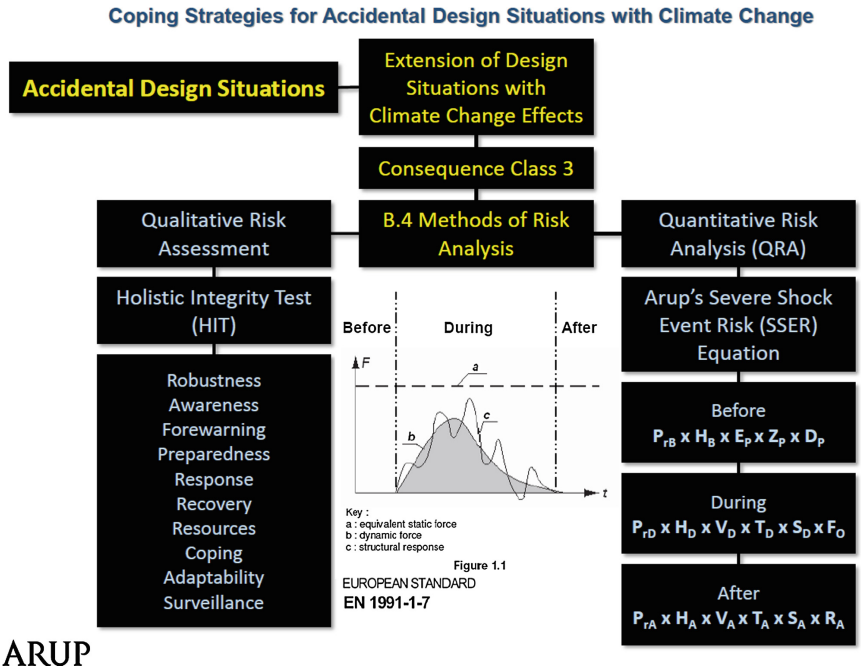


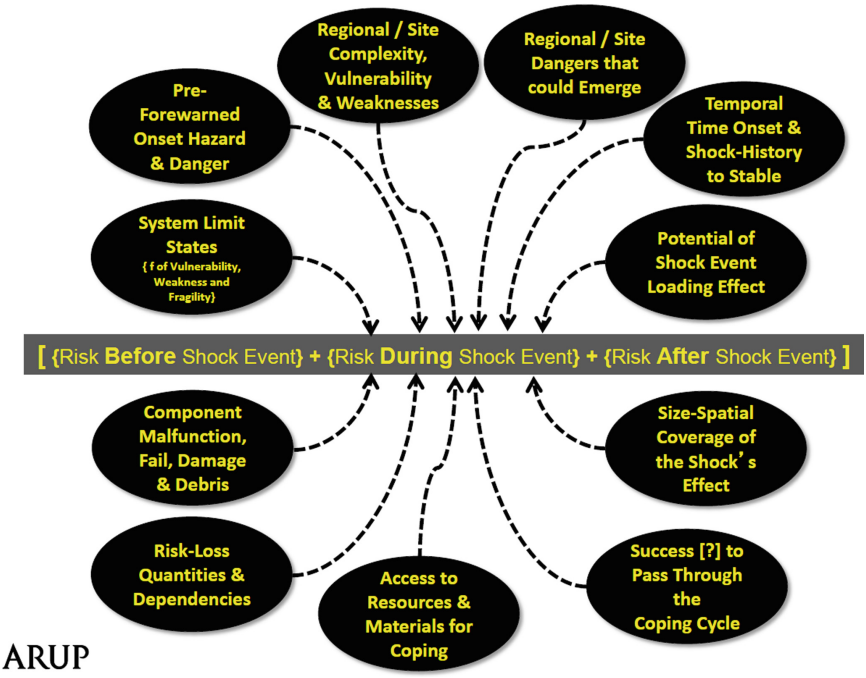


## Reference

1. EuroCode EN 1991-1-7

# BATIPACK®: An Innovative and Ecologic Building Process

N. Matiere and Q.H. Ung(✉)

MATIERE SAS, Rue Louis MATIERE, Arpajon sur Cère, France
{n.matiere,uqh}@matiere.fr

**Abstract.** The BatiPack® process is an innovative system for the construction of load-bearing walls with controlled costs and delays. The wood brick, hollow, contains isolating within it, are maneuverable and designed to be assembled quickly and easily without any special skill and without lifting equipment. By its mechanical, ecologic characteristics, the process thus perfectly substitutes for traditional masonry materials. It can be adapted to any type of project and size of building.

Delivered on pallets, it is easily transportable and can be stored anywhere. The assembly is made by nesting and gluing in a groove. The prestressing put in place by a cable positioned on each side of each block gives the system lightness, minimal consumption of raw material and above all flexibility combined with high strength.

All types of coatings can also be placed on the BatiPack which also offers maximum thermal resistance, thanks to insulated materials which are integrated inside of the blocks. The customer has the choice between wood fiber, wool of rock, of cotton or of soil.

This process has various mechanical properties and has a high seismic resistance.

**Keywords:** Timber structure · Modular building · Prefabrication · Wood brick

## 1 Introduction

BATIPACK is an innovative load-bearing wall system. The process consists in assembling composite wood hollow bricks by nesting and gluing. The pre-stressing put in place by a cable vertically positioned on each side of each block gives the system lightness, minimal consumption of raw material and above all flexibility combined with high strength.

The 6 faces of the hollow block are made with OSB 4 panels (panels working under high stress used in humid environment). The boxes are completely filled with rock wool insulation, varying in thickness depending on the desired thermal performance. The upper side and the male side face are coated with a band of compressible rockwool. The blocks are thus highly insulating, and designed to be assembled quickly and easily.

The process is thus perfectly substituted for traditional masonry materials and is provided for the realization of bearing walls or separation wall for individual or collective housing.

© Springer Nature Singapore Pte Ltd. 2018
H. Tran-Nguyen et al. (eds.), *Proceedings of the 4th Congrès International de Géotechnique - Ouvrages -Structures*, Lecture Notes in Civil Engineering 8,
DOI 10.1007/978-981-10-6713-6_85

## 2 Description

See Fig. 1.

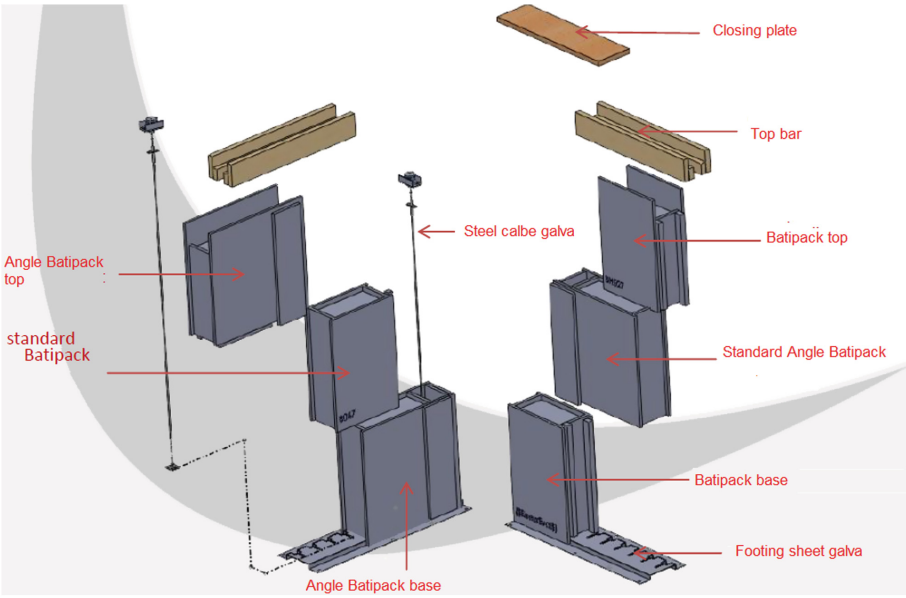


**Fig. 1.** Batipack conception

### 2.1 Composition of Batipack Block

The 6 faces of the hollow block are made of OSB 4 panels (high-stress panels used in humid environments), in respect with NF EN 300/4, label CE according to NF EN 13986 and certified by CTB-OSB 4.

The thicknesses are 15 mm for the large vertical faces, 18 mm for the small vertical faces and 9 mm for the horizontal faces.

The edges of the facings are covered with a PVC tape.

The box is completely filled with a wool insulation of density 70 kg/m and thermal conductivity 0.037 W/m.K of thickness variable according to the thickness of the box and the desired thermal performance.

The upper side and the male side face are covered with a band of ROCKMUR compressible rock wool of ROCKWOOL with a density of 50 kg/m$^3$.

There are several types of bricks, including (Fig. 2):

- Current part bricks with a base model (BB), a standard model (B) and a top model (BH).
- The angle bricks with a base model (BAB), a standard model (BA) and a top model (BAH).

**Fig. 2.** Batipack blocks

The geometrical characteristics of the Batipack caissons may vary and are given below:

- Thickness: 200 to 400 mm
- Width: from 300 to 600 mm with step of 100 m
- Height: from 350 to 600 mm with step of 50 mm.

The dimensional variations of the bricks previously described make it possible to adapt to each building project according to the facade dimensions desired by the client.

### 2.2 Connection to the Foundation

The Batipact base boxes are supported on a 3 mm thick metallic plate. In this metallic footing, fences are disposed to provide the fixation with the boxes of the first row as well as the positioning and the anchoring of the prestressed cable.

The metallic footing, in direct contact with the masonry, must be covered by a Z350 hot dip galvanized coating in accordance with NF EN 10346.

Other types of connection to the foundation can be considered (Fig. 3).

A specific component of footing is necessary for the building corners; it is made by reconstituting of the linear part and welding.

The protective coating of the areas affected by welding is recovered with a painting riche in zinc.

### 2.3 Prestressing System

The BatiPack system stability is based on the continuous vertical compression which is achieved by a prestressed cable positioned on each side of each block (Fig. 4).

**Fig. 3.** Connections to the foundation

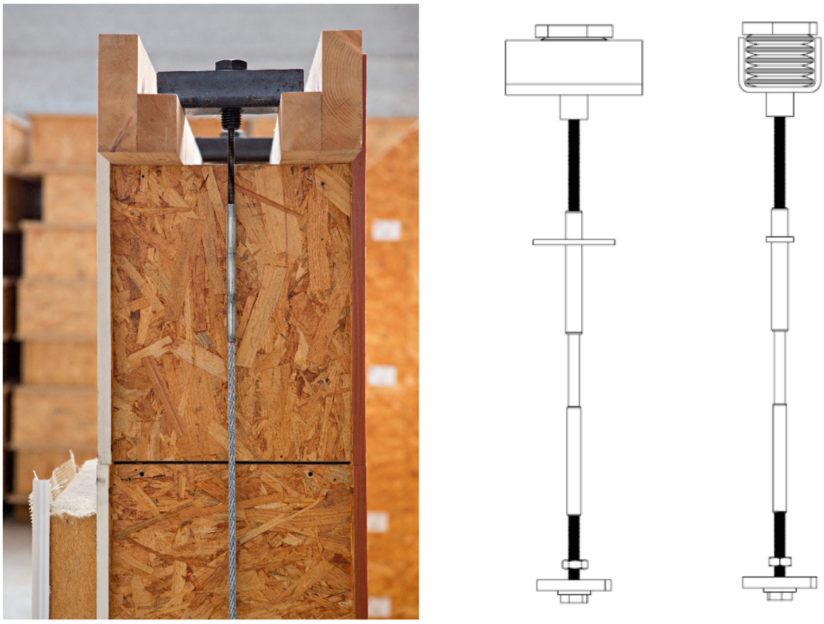

**Fig. 4.** Prestressing cable installation.

Each cable is made of galvanized steel with a diameter of 8 mm. It is dotted with a threaded sleeve at each end. Prestressed cables are connected in the base with the metallic footing, on the top with a double top bar in L shape.

The structures are self-stable by connecting blocks by cables, without any direct rigid connection between blocks.

The prestressing, maintaining a constant pressure from the bottom to the top of walls, gives some advantages:

- Lightness of the structure.
- Minimal consumption of raw materials.
- Flexibility combined with high solidity.

### 2.4 Pre-frames for Doors or Windows

The pre-frame is surmounted by a hollow block forming a lintel. This element is supplied and dimensioned in the way that no load is applied to the doors or windows carpentry.

## 3 Performance

### 3.1 Mechanical Performance

The walls of the Batipack system are used as load-bearing elements. They are then exposed in their plane by horizontal forces which are transmitted to the foundations of the structure. We can consider Batipack walls as a Bracing system which is a static system designed to ensure the overall stability of a structure with respect to horizontal effects resulting from possible actions on its plane (e.g. wind, earthquake, shock, braking, etc.). Studies carried out by the FCBA (French Institute of Technology for Forest-based and Furniture Sectors), a partner of the CSTB (Scientific and Technical Center for Buildings), determined the modification coefficient (Kmod), for a permanent load, equal to 0.42, for a live load, equal to 0.79 [1].

With respect to the horizontal loads perpendicular to the plane, under the wind load according to Eurocode, the Batipack system has an deflection lower than H/500 for H = 3.00 m [1].

The behavior of the walls of the Batipack system with regard to soft body shocks is satisfied. The wall elements are not damaged and retain their bearing function.

### 3.2 Earthquake Resistance

According to NF EN 1998-1, the walls of the Batipack system have a limited degree of ductility (class L), i.e. the seismic behavior factor "q" to be used for earthquake design is: q = 1.5 [1].

This seismic behavior factor "q" is defined by Eurocode 8 (Design of structures for earthquake resistance). In practice, the q-factor is used for structural design: the seismic actions are determined by an equivalent linear calculation where the elastic forces obtained are divided by q, which limits the resistance of the structure.

The studies carried out by the FCBA (French Institute of Technology for Forest-based and Furniture Sectors) validated the performance of the BatiPack under seismic loading.

### 3.3 Insulation Performance, Safety and Durability

The Batipack construction brick is wrapped by a vapor barrier film. This disposition offers to the product a good water vapor permeability and a satisfied humidity resistance.

The waterproof of the construction is ensured by the use of a water-tight film, according to DTU 31.2. The waterproofing is then reinforced by the installation of a traditional exterior coating defined and implemented in accordance with DTU 31.2.

The batipack system configuration composed by the assembly of the hollow blocks behaves like a double wall with connections. This shows a notable improvement in acoustic performance.

The tests with respect to the insulation to the outside air noise have been carried out. The results show that the product matches the existing norms concerning decibels reductions imposed by DTU 31.2.

Thermal insulation is ensured on the one hand by rockwool insulation, with a certified thermal conductivity of 0.037 W/(m.K), and on the other hand by the internal and external coatings. The heating measuring index can be up to 2.5 times higher than the other materials [1].

The massive wood used for the manufacture of the caissons and the assembly of the walls receive a treatment allowing classifying in Use class 2, including in termite zone, according to Eurocode 5 (Design of timber structures).

The materials used in the manufacturing of the BatiPack system (OSB 4 and rock wool) are completely free of formaldehyde, unlike most materials used in the construction field.

It is importance to note that OSB material is not attacked by common wood-boring insects such as termites, ants, bees, or wood weevils. The material is certificated Anti-termite.

The OSB 4 product is 100% PEFC (Program of the Endorsement of Forest Certification) certified by the FCBA (French Institute of Technology for Forest-based and Furniture Sectors).

## 4 Implementation

Batipack block is designed to be palletized and film-wrapped immediately. Easy and fast delivery thanks to the palletised-packaging processed at the factory, each Batipack® brick has its own serial number and is assembled in an ascending order following the erection notice that comes with the invoice.

The Batipack process provide composite wood bricks which are designed to be hand-manipulated, an assembling methodology that do not require any particular skill or special equipment. The insertion of frame during the construction period is also simplified.

## 5 Some Achievements with the Batipack® Brick

Apart France, the BatiPack® product has already been exported and set up in Guinea, Senegal, the Philippines, Argentina, Irak. Batipack system can be applied on many types of building project, for example [2]:

- Houses and chalets (Fig. 5)

**Fig. 5.** Houses and chalets.

- Extension (Fig. 6)

**Fig. 6.** Extension.

- Technical and industrial building (Fig. 7)
- …

**Fig. 7.** Industrial building.

## 6 Conclusions

Due to its innovative concept, the Batipack® presents various advantages:

- Optimized logistic
- A short erection delay thanks to its hand-manipulating conception.

Its multiples performances also position it as a serious alternative to classic construction materials and technologies, mainly because of:

- Its thermic, acoustic characteristics
- Its seismic resistance
- Its mechanical performances.

## References

1. FCBA (French Institute of Technology for Forest-Based and Furniture Sectors): Dossier technique, Reference 2010.347.0356 (2010)
2. MATIERE SAS: Batipack-La performance du bois: the heating, phonic and seismic hight performances load-bearing walls (2017)

# Experimental Investigation of Bond-Dependent Coefficient of Glass Fiber Reinforced Polymer Bars

Thuy Duong Tran[1], Manh Hung Nguyen[2], and Trung Hieu Nguyen[1(✉)]

[1] Department of Civil Engineering, National University of Civil Engineering, Hanoi, Vietnam
{duongtt,hieunt}@nuce.edu.vn
[2] Department of Civil Engineering, Vinh University, Vinh, Vietnam
hungmanh.dhxd@gmail.com

**Abstract.** In recent years, Glass Fiber Reinforced Polymer (GFRP) bars have become an alternative to steel reinforcement in concrete structures. Due to the relatively low modulus of elasticity and the different surface treatment, the problems of bond between the GFRP bars and the concrete should be carefully considered. This paper focus on the experimental evaluation of the bond–dependent coefficient ($k_b$) of GFRP bars according to the ACI 440.1R-06. This coefficient takes into account the degree of bond between the GFRP bar and the surrounding concrete and was used in calculating of serviceability limited state of concrete structures.

**Keywords:** Glass fiber reinforced polymer · Bond · Crack width · Serviceability

## 1 Introduction

Commercially available GFRP reinforcement bars are made of continuous Glass fibers embedded in a resin matrix (e.g. ACI 440.1R-03 [1]). GFRP bars have various types of cross-sectional shapes (square. round. hollow). In recent years, GFRP bars are increasingly being used as alternative reinforcement for buildings and bridges, especially in corrosive environments. Compared to steel bars, GFRP bars have several advantages such as corrosion resistance, high strength, lightweight, and high thermal resistance. Beside these advantages, GFRP bars have also inconveniences: lower modulus of elasticity and the different surface treatment which leads to higher reinforcement strains, wider cracks and larger deflections. Therefore, the design of reinforced concrete members with GFRP bars is often governed by the serviceability limited state (deflection and crack width). Crack width calculations include the effect of bond between FRP bars and surrounding concrete. This is normally taken into account in FRP design codes and guides through the so called bond dependent coefficient ($k_b$) (El-Nemr et al. [5]). Literature shown that $k_b$ value depends on many parameters, for example concrete cross section, GFRP bar manufacturers, fiber types, resin

© Springer Nature Singapore Pte Ltd. 2018
H. Tran-Nguyen et al. (eds.), *Proceedings of the 4th Congrès International de Géotechnique - Ouvrages -Structures*, Lecture Notes in Civil Engineering 8,
DOI 10.1007/978-981-10-6713-6_86

formulations and surface treatments. According to ACI 440.1R-06 [2], for GFRP bars having bond behavior similar to steel bars, $k_b$ is assumed equal to 1 and for GFRP bars having bond behavior inferior to steel, $k_b$ is larger than 1.0 and vice versa.

The determination of $k_b$ was introduced in ACI 440.1R-03 [1] by modifying the Gergely-Lutz [7] equation to account for FRP instead of steel bars. Some typical $k_b$ values for GFRP reinforcing bars cited in [1] are between 0.71 and 1.83. ACI440.1R-03 [1] advised that designers used a value of 1.2 for deformed GFRP bars unless more specific information were available for a particular bar. Later, ACI.440.1R-06 [2] adopted a modified version of the crack width equation proposed by Frosch [6]. It was reported that $k_b$ values ranged from 0.60 to 1.72, with a mean of 1.10.

According to ACI.440.1R-06 [2] and CSA S806-12 [4], $k_b$ should be determined from the measured crack widths and strains in FRP bars during testing and using Eq. (1):

$$w = 2\frac{f_f}{E_f}\beta k_b\sqrt{\left(\frac{s}{2}\right)^2 + d_c^2} \tag{1}$$

where:
$w$ is the maximum crack width. CSA S806-12 [4] implicitly allows crack width of 0.5 mm for exterior exposure and 0.7 mm for interior exposure. ACI 440.1R-06 [2] does not address the maximum allowable crack width of FRP-reinforced members. It recommends that the CSA S806-12 [4] limits be used for most cases.
$f_f$ is the stress in FRP reinforcement in tension (MPa);
$E_f$ is the modulus of elasticity of GFRP bar (MPa);
$\beta$ is the ration of distance from neutral axis to extreme tension fiber to distance from neutral axis to center of GFRP tensile reinforcement;
$k_b$ is the bond-dependent coefficient;
$d_c$ is the thickness of concrete cover from extreme tension fiber to center of GFRP bar (mm);
$s$ is the longitudinal GFRP bar spacing (mm).

This article presents an investigation to determine the $k_b$ coefficient of different diameters of GFRP bars in normal strength concrete. This works has been performed at Laboratory of Testing and Construction Inspection, National University of Civil Engineering (NUCE), Vietnam.

## 2 Experimental Research

### 2.1 Test Specimens and Materials

The details of testing specimens are shown in Fig. 1. Six rectangular beam specimens having a cross section of 200 × 300 mm and 3000 mm of length were fabricated and tested under flexion at NUCE. All beams were reinforced in the bottom with two longitudinal GFRP bars and in the top with 2D14 steel bars. The transversal reinforcement steels were D8 with the space of 100 mm. Six beams were divided into three

group (2 beams in each group) based n the diameter of longitudinal GFRP bars in the bottom and the concrete cover as follows:

- Group 1 (beams 2D14-1 and 2D14-2): 2∅14 GFRP bars and concrete cover c = 40 mm;
- Group 2 (beam 2D16-1 and 2D16-2): 2∅16 GFRP bars and concrete cover c = 40 mm;
- Group 3 (beam 2D20-1 and 2D20-2): 2∅20 GFRP bars and concrete cover c = 50 mm.

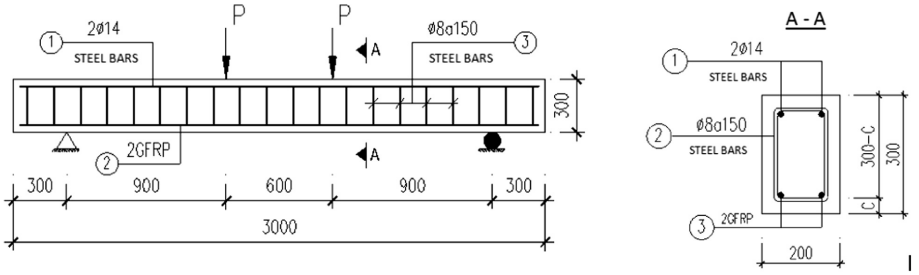


**Fig. 1.** Details of test specimens

The mix proportion of concrete was presented in Table 1. To determine the concrete strength and modulus of elasticity, six 150 × 300 mm concrete cylinder specimens were cast and tested in compression after 28 days of curing. The 28-day compressive strength and modulus of elasticity of concrete were determined according to the average test results of three specimens and their value were also tabulated in Table 1. The yield strengths of the transverse and longitudinal steel bar obtained from tensile tests were 240 MPa and 320 MPa, respectively (Fig. 2).

**Table 1.** Mixture proportions for 1 $m^3$ of concrete ($kg/m^3$)

| Cement PCB30 | Fine aggregate | Coarse aggregate | Water | The 28-day compressive strength (MPa) | Modulus of elasticity (GPa) |
|---|---|---|---|---|---|
| 480 | 595 | 1250 | 180 | 40.8 | 39.20 |

The GFRP reinforcing bars were manufactured by FRP Vietnam JSC. They had a helical wrapping surface. Normalized measurements were conducted to determine the cross-section areas of the re-bars according to ACI 440.3R-04 [3]. The mechanical properties of GFRP bars are shown in Table 2.

In Fig. 3 presents images of the details of reinforcements and concreting process. All specimens were preserved and tested in flexion after 28 days of curing.

*a- Compressive Strength Test*

*b- Modulus of Elasticity Test*

**Fig. 2.** Testing for mechanical properties of concrete

**Table 2.** Mechanical properties of GFRP bar

| FRP bar designation | Experimental bar diameter db (mm) | Ultimate tensile strength (MPa) | Modulus of elasticity (GPa) | Ultimate elongation (%) |
|---|---|---|---|---|
| Ø14 | 12.37 | 928.34 | 46.0 | 2.018 |
| Ø16 | 14.78 | 938.50 | 46.0 | 2.086 |
| Ø20 | 18.30 | 973.70 | 46.0 | 2.117 |

a- Details of reinforcements

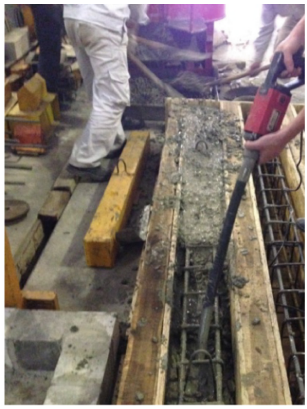

b- Concrete casting

**Fig. 3.** Fabrication of reinforced concrete beams

## 2.2 Test Setup and Instrumentation

Details of the setup are shown in Fig. 4. All specimens were tested in four-point bending. The span length of all tested beams was 2400 mm. The loads were applied using one hydraulic jack and a steel spreader beam. The loading process was carried out as stress control with a constant rate of 0.25 MPa/s. The applied load was measured

using a load cell. Longitudinal GFRP bars strains were measured by two strain gages (called T1 and T2). Their locations in the specimens can be seen in Fig. 5a. Each monitored GFRP bar had one strain gage at the center of the bars. The displacement at the mid-span and the two supports were measured using Linear Variable Differential Transformers (LVDTs). To measure the initial crack width of the first crack (N1) and second crack (N2) of tested beam, a microscope with precision of 0.01 mm was used. The widths of these cracks were monitored by extensometers at the level of the reinforcing bars until the end of testing.

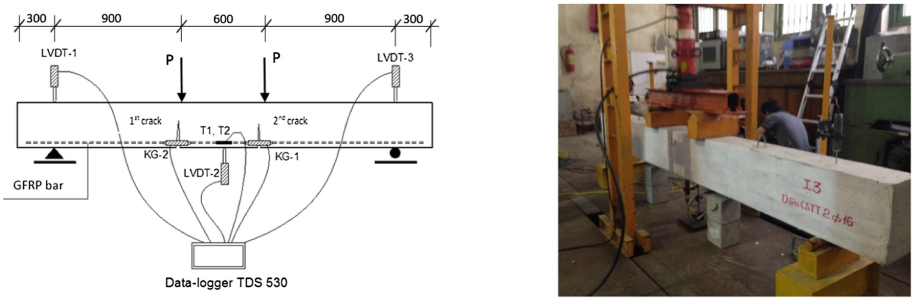


**Fig. 4.** Test setup

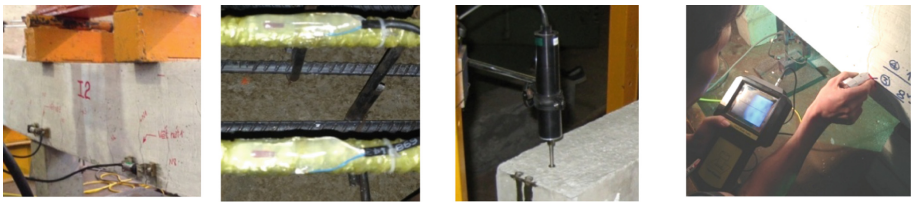

a- Extensometers KG-1 and KG-2 b- Strain gages c- LVDTs d- Microscope

**Fig. 5.** Images of Instruments

## 2.3 Test Procedure

During the test, loads, displacements and crack widths of the first and second cracks were recorded through a computerized data-logger system. The test procedure is described as follows:

a. Setup the test specimen;
b. Load the beam until the first flexural crack appears. At that stage; loading is held constant to measure the initial crack width with a microscope;
c. Placing the first extensometer at the level of GFRP bars to monitor the width of the first crack;
d. Repeat the b and c stages for the second crack of beam.

## 3 Test Results and Discussions

Figure 6 shows the experimental force versus mid-span deflection curves for the six specimens. Concrete cracking was identified in all tested beams at a load level of about 10 kN. After that all beams showed strictly increasing load-deflection behaviour until the beam failed. It can be to seem that the main parameter controlling the behavior of reinforced concrete beams is the longitudinal reinforcement stiffness, EA. Furthermore, the diagram of load-deflection in the reinforced concrete beams with FRP almost like a straight line with light slope until the failure of beams. Concerning the failure mode, all beam specimens failure was due to concrete compressive crushing.

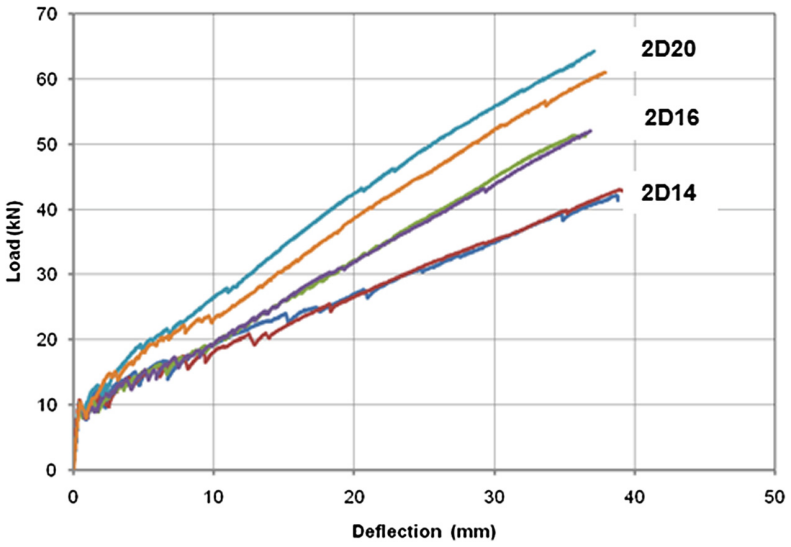


**Fig. 6.** Load-mid span deflection of all tested beam.

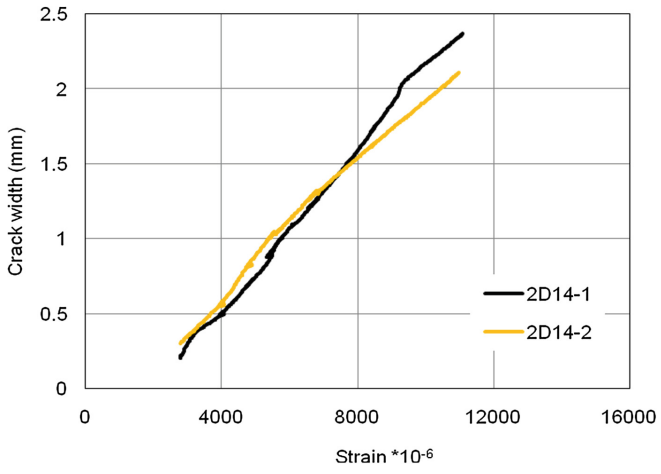


**Fig. 7.** Crack width – strain in FRP reinforcing bar relationship of 2D14 beams

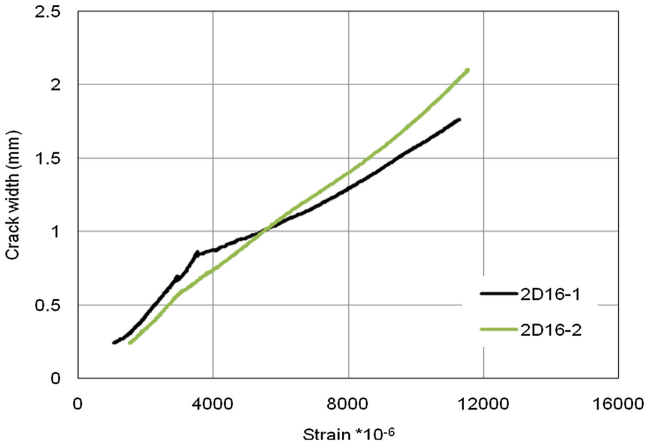


**Fig. 8.** Crack width – strain in FRP reinforcing bar relationship of 2D16 beams

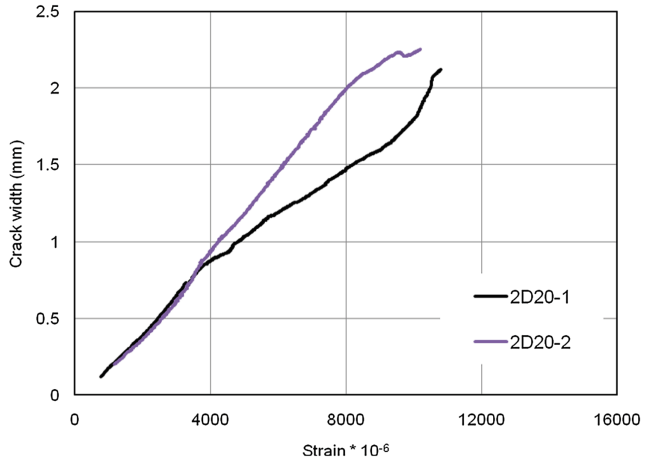


**Fig. 9.** Crack width – strain in FRP reinforcing bar relationship of 2D20 beams

Figures 7, 8 and 9 show the relationships between the crack width of the first crack (N1) with the strain in FRP reinforcing bars at mid-span of tested beams, where each curve represents the average of the two strain readings. It can be seen that these relationships were shaped linear in all tested beams. Figure 10 presents these relationships of all beams. The obtained results show that the influence of the diameter of FRP reinforcing bars on the crack width was not significant.

Table 3 shows the $k_b$ values of each tested beam calculated at crack width 0.7 mm according to Eq. (1). The $k_b$ values were varied with GFRP bar diameters but the results did not show a consistent trend of relationship. According to [2, 5], this inconsistent

**Table 3.** Caculation of $k_b$ values according to Eq. (1)

| Tested beam | Crack | $w$ (mm) | Strain $\varepsilon * 10^{-6}$ | $E_f$ (MPa) | $f_f$ (MPa) | $\beta$ | $s$ (mm) | $d_c$ (mm) | $K_b$ |
|---|---|---|---|---|---|---|---|---|---|
| 2D14-1 | $N_1$ | 0.7 | 3295 | 46000 | 151.57 | 1.269 | 106 | 47 | 1.181 |
| | $N_2$ | 0.7 | 3867 | 46000 | 177.88 | 1.269 | 106 | 47 | 1.007 |
| 2D14-2 | $N_1$ | 0.7 | 4827 | 46000 | 222.02 | 1.269 | 106 | 47 | 0.807 |
| | $N_2$ | 0.7 | 4441 | 46000 | 204.26 | 1.269 | 106 | 47 | 0.877 |
| 2D16-1 | $N_1$ | 0.7 | 3021 | 46000 | 139.01 | 1.218 | 104 | 48 | 1.315 |
| | $N_2$ | 0.7 | 3520 | 46000 | 162.04 | 1.218 | 104 | 48 | 1.125 |
| 2D16-2 | $N_1$ | 0.7 | 3630 | 46000 | 167.15 | 1.218 | 104 | 48 | 1.094 |
| | $N_2$ | 0.7 | 3717 | 46000 | 171.00 | 1.218 | 104 | 48 | 1.068 |
| 2D20-1 | $N_1$ | 0.7 | 3203 | 46000 | 147.33 | 1.300 | 80 | 60 | 1.165 |
| | $N_2$ | 0.7 | 3905 | 46000 | 179.63 | 1.300 | 80 | 60 | 0.956 |
| 2D20-2 | $N_1$ | 0.7 | 3308 | 46000 | 152.17 | 1.300 | 80 | 60 | 1.128 |
| | $N_2$ | 0.7 | 3454 | 46000 | 158.88 | 1.300 | 80 | 60 | 1.079 |

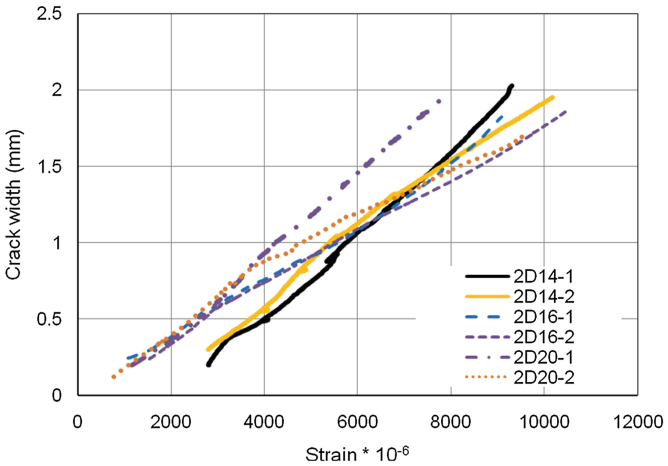


**Fig. 10.** Crack width – strain in FRP reinforcing bar relationship of all tested beams

trend can be explained by the complex bond behavior of GFRP bar with helical wrapping surface. Figure 11 presents the histogram of $k_b$ coefficients. The results of the analysis showed that for all tested beams, the average or mean value of $k_b$ coefficient is 1.067 with a coefficient of variation of 12.9%. This experimental result was suitable with recommendation of ACI 440.1R-06 [2].

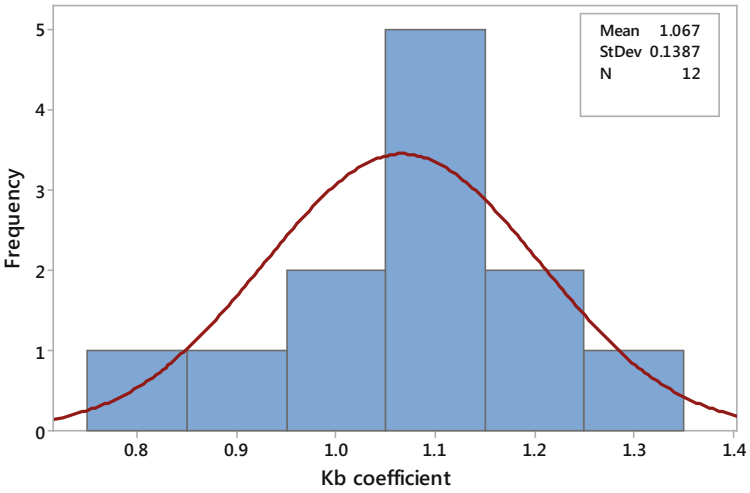


**Fig. 11.** Histogram of $k_b$ coefficient

## 4 Conclusions

This study aimed at investigating the bond-dependent coefficient of GFRP reinforcing bars. Based on the test results of this study, the following conclusions are drawn:

- The GFRP bar diameters influence the bond-dependent coefficient ($k_b$) value but yet no trend or clear relationship was observed.
- The mean calculated values of $k_b$ base on experimental results at crack width 0.7 mm was suitable with recommendation of ACI 440.1R-06 and can use in calculating of serviceability limited state of concrete structures.

**Acknowledgements.** The authors are grateful to FRP Vietnam JSC for providing the FRP bars. This study was conducted at Laboratory of Testing and Construction Inspection (LCTI), Faculty of Building and Industrial Construction, National University of Civil Engineering, Vietnam and the authors would like to thank the technicians in the laboratory for providing assistance in specimen fabrication and testing.

## References

1. ACI 440.1R-03: Guide for Design and Construction of Concrete Reinforced with FRP Bars. American Concrete Institute, Farmington Hills (2003)
2. ACI 440.1R-06: Guide for Design and Construction of Concrete Reinforced with FRP Bars. American Concrete Institute, Farmington Hills (2006)
3. ACI 440.3R-12: Guide Test Methods for Fiber-Reinforced Polymer (FRPs) for Reinforcing or Strengthening Concrete Structures. American Concrete Institute, Farmington Hills (2012)
4. CSA S806-12: Design and Construction of Building Components with Fiber Reinforced Polymers, CAN/CSA S806-12, Rexdale, ON (2012)

5. El-Nemr, A., Ahmed, E., Benmokrane, B.: Bond-dependent coefficient of glass and carbon FRP bars in normal and high-strength concretes. J. Constr. Build. Mater. **01**(01), 21–38 (2016)
6. Frosh, R.J.: Another look at cracking and crack control in reinforced concrete. ACI Struct. J. **96**(3), 437–442 (1999)
7. Gergely, P., Lutz, L.A.: Maximum Crack Width in Reinforced Concrete Flexural Members, ACI SP-20, pp. 87–117. American Concrete Institute, Detroit (1968)
8. Kassem, C., Farghaly, A.S., Benmokrane, B.: Evaluation of flexural behavior and serviceability performance of concrete beams reinforced with FRP bars. J. Compos. Constr. **15**(5), 682–695 (2011)

# Experimental Research on Flexural Strengthening of Two-Way Reinforced Concrete Slabs Using Carbon Fiber Reinforced Polymer Sheets

Manh Hung Nguyen[1], Thuy Duong Tran[2], and Trung Hieu Nguyen[2(✉)]

[1] Department of Civil Engineering, Vinh University, Vinh, Vietnam
hungmanh.dhxd@gmail.com
[2] Department of Civil Engineering, National University of Civil Engineering, Hanoi, Vietnam
{duongtt,hieunt}@nuce.edu.vn

**Abstract.** In this paper, the strengthening of two-way reinforced concrete (R/C) slabs using Carbon Fiber Reinforced Polymer (CFRP) sheets is evaluated experimentally. Five identical square R/C slabs with 1200 mm side length and 60 mm thickness were constructed and tested to failure under a monotonic central loading point. One un-strengthened slab was used as reference slab while four slabs were strengthened with CFRP sheets. The obtained results of this experimental research have shown the flexural behavior of strengthened slab by CFRP materials and the strengthening effectiveness for moment resist of R/C slab using this material.

**Keywords:** Strengthening · Carbon fiber reinforced polymer · Two-way slab · Flexural strength

## 1 Introduction

Fiber Reinforced Polymer (FRP) is a composite made of high strength fibers and a matrix for binding these fibers to fabricate structural shapes (e.g. ACI 440.2R-02 [1]). Common fiber types include aramid, carbon and glass; common matrices are epoxies. FRP materials can be used to rehabilitate or restore the strength of deteriorated structural member, retrofit or strengthen a sound structural member to resist increased loads due to changes in use of the structure or address design or construction errors (e.g. ACI 440.2R-02 [1], CEB-FIP 2001 [3]). The effectiveness of the FRP materials for concrete is attributed to its unique mechanical and chemical properties such as superior strength to weight ratio, high tensile strength and modulus, corrosion resistance and durability. The use of FRP also shows the convenience of construction process such as quick, simple and not required much machinery. Due to the advantages, many research works have been carried out throughout on the use of FRP for externally strengthening concrete structures. Figure 1 shown example of the strengthening of R/C structures using FRP. Composite materials for strengthening

© Springer Nature Singapore Pte Ltd. 2018
H. Tran-Nguyen et al. (eds.), *Proceedings of the 4th Congrès International de Géotechnique - Ouvrages -Structures*, Lecture Notes in Civil Engineering 8,
DOI 10.1007/978-981-10-6713-6_87

structures are available in the form of one direction thin strips made by pultrison or sheets or fabrics made of fibers one or at least two directions.

a- Strengthening of R/C column

b- Strengthening of R/C beam

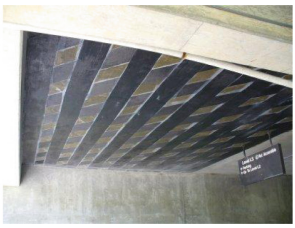

c- Strengthening of R/C slab

**Fig. 1.** Example of strengthening of R/C structures using CFRP sheets in Vietnam

In Vietnam, FRP materials have been used to reinforce a number of bridges and buildings. However, the application is still limited. The main reason is the cost and technical standard applicable to this type of reinforcement material. Currently in Vietnam there is no standard design of reinforced concrete structures strengthened with FRP materials.

This paper presents an experimental study on flexural strengthening of two-way R/C slabs using CFRP sheets. Experimental research works were carried out at Laboratory of Testing and Construction Inspection, National University of Civil Engineering, Vietnam.

## 2 Experimental Research

### 2.1 Test Specimens and Materials

Five square R/C slabs with 1200 mm length and 60 mm thickness were cast in this research. The details of testing specimens are shown in Fig. 2. The reinforcing steel bars were arranged according to the design provisions of ACI 318-05 [2] and consisted of 6 mm diameter spaced at 150 mm. The selected reinforcement ratio aims to obtain flexural failure mode in all slabs. One un-strengthened slab was used as reference specimen, named M-01. For the strengthening, the CFRP sheets (125 mm-width) were applied in one layer and externally bonded to the tension face of the slab. The strengthened specimens M-11 and M-12 were strengthened using CFRP sheets in two perpendicular directions, parallel to the tension reinforcement. Two slabs, M-21 and M-22 were strengthened using the same CFRP sheets areas as the specimens M-11, M-12 and inclined 45° compared to horizontal.

Concerning to materials properties, the mix proportions of concrete was presented in Table 1. To determine the concrete strength, three 150 × 300 mm concrete cylinders specimens were cast. The 28 day compressive strength of concrete was determined according to the average test results of three specimens and its value was 21.8 MPa. The yield strengths of the reinforcing steel bars obtained from tensile tests was

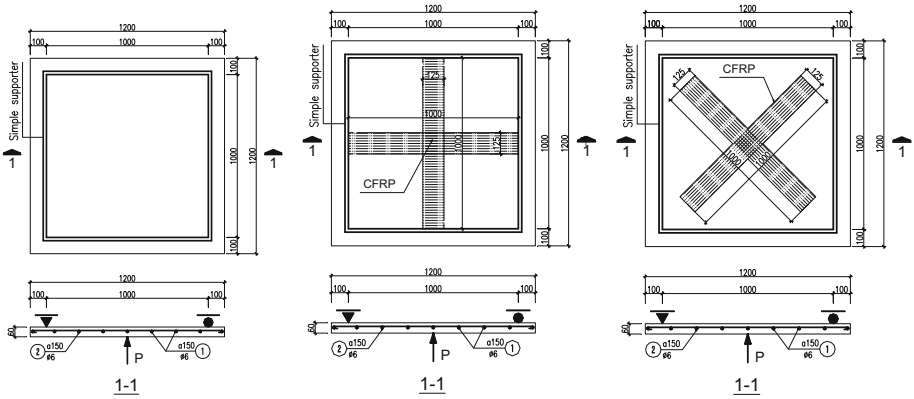


**Fig. 2.** Details of test specimens

285 MPa. The CFPR sheets used in this study were unidirectional and manufactured by Fyfe Company (USA). Table 2 presents the mechanical properties of the CFRP as provided by the manufacturers.

**Table 1.** Mixture proportions for 1 $m^3$ of concrete ($kg/m^3$)

| Cement | Fine aggregate | Coarse aggregate | Water |
|---|---|---|---|
| 420 | 600 | 1160 | 180 |

**Table 2.** Mechanical properties for CFRP sheets

| Material | Thickness (mm) | Modulus of elasticity (MPa) | Ultimate tensile strength (MPa) | Ultimate tensile elongation (%) |
|---|---|---|---|---|
| CFRP | 1.0 | 95800 | 986 | 0.85 |

As regards to the strengthening procedure, the concrete surface to be strengthened was roughened carefully to improve the bond characteristics between concrete and the

**Fig. 3.** Installation of FRP sheets on tested R/C slabs

CFRP sheets. The epoxy resin was applied on both the concrete surfaces and the strengthening materials. Afterward, the CFRP sheets were bonded to the concrete surface according to the type of strengthening (Fig. 3).

### 2.2 Test Setup and Instrumentation

Details of the test setup are shown in Fig. 4. All slabs were tested under a monotonic central loading point and were simply supported over the four edges, thereby permitting the corner to lift when load was applied. Load was applied monotonically at the mid-span of the slab using a hydraulic jack. A load cell was used to measure the applied load. Five Linear Variable Differential Transducers (LVDTs) were placed under the center-point of the slab and at four edges to measure the deflection of tested slab. The LVDTs, load cell were connected through a Data acquisition system. The analog electrical signals of loads, deflections were converted through the data acquisition system to digital signals and were stored in computer.

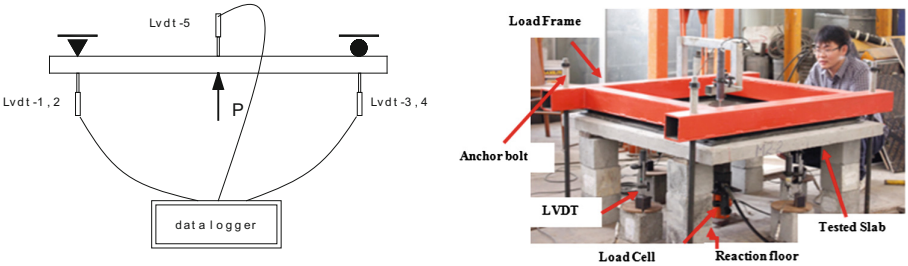


**Fig. 4.** Test setup

During the test, loads and displacements were recorded through a computerized data-logger system. Before testing, the ultimate strengths of the reference and strengthened slabs were approximately estimated using the available analytical method of ACI 318-05 [1]. Prior to the failure of the slab, data were recorded at a prescribed load increment. In order to accurately measure the cracking load and the corresponding deflection, smaller increments were applied around the cracking state.

## 3 Test Results and Discussions

### 3.1 Load-Deflection Relationships

Figure 5 shows the central load-deflection relationships of all tested specimens while Table 3 presents the ultimate capacities and deflection characteristics of all tested slabs. It can be seen that there are three different behavioral zones on each curve. The first zone represents the stiffness of the uncracked slab. The first visible crack loads were determined based on a first change in slope of the load–deflection curve. The stiffness of a slab at any loading point is the slope of the load-deflection curve at that point.

It can see that in this initial stage of loading, all specimens show almost the same stiffness. The reference specimen M-01 indicated the lowest first crack load but it can be seen that a minor differences in the stiffness of the reference slab and the strengthened slabs. The strengthened slabs behave like the reference slab with internal steel reinforcing bars carrying the majority of tension force in the section.

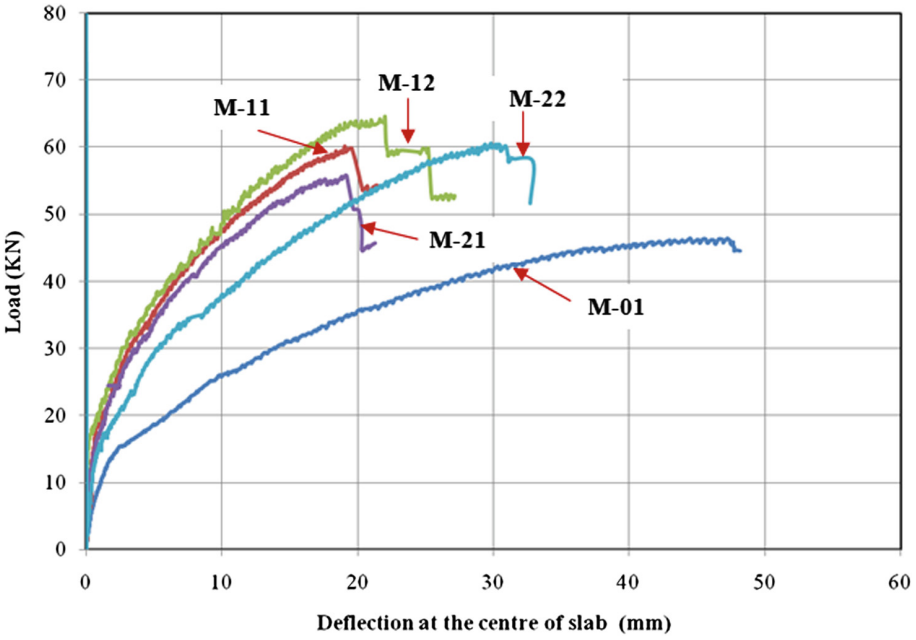


**Fig. 5.** Load-deflection curves of all tested specimens

The second zone represents the stiffness of the cracked section. For the flexural strengthening specimens, the slope of the load-deflection curve was higher than that of the corresponding reference specimen M-01. The specimen M-22 exhibited the lowest stiffness among all strengthened slabs, which could possibly due to its highest concrete cover thickness. As a result, at the same loading level, specimen M22 has the highest deflection value. For any give value of load, the deflections of strengthened slabs were lower than that of the control slab. The results show that the contribution of CFRP layer to the structural stiffness was found to be significant. The obtained results presented in Fig. 5 that the yield loads (generally seen as a second change in slope of the load–deflection curve) of strengthened slabs were higher than that of the control slab. It can be seen that, in the cracking stage, the external CFRP sheets reduced the stress in the tensile steel reinforcement and hence increased the yield load of the strengthened slabs. The third zone corresponds to a damaged slab with wide crack, yielding reinforcement and debonding or rupturing the FRP material. As shown in Fig. 5 and Table 3, the ultimate load carrying capacity of strengthened slabs was significantly higher than that of the control slab. This result again shows the effectiveness of the FRP material for

**Table 3.** Ultimate capacities and deflection characteristics of all tested slabs

| Slab | Cracking load $P_{cr}$ (kN) | Deflection at cracking load, $\delta_{cr}$ (mm) | Ultimate load $P_u$ (kN) | % increase in ultimate load | Deflection at ultimate load, $\delta_u$ (mm) |
|---|---|---|---|---|---|
| M-01 | 1.5 | 2.8 | 46.0 | - | 48.0 |
| M-11 | 1.8 | 1.1 | 60.0 | 30.4 | 19.5 |
| M-12 | 1.8 | 1.2 | 65.0 | 41.3 | 22.1 |
| M-21 | 1.7 | 1.4 | 60.0 | 30.4 | 19.3 |
| M-22 | 1.7 | 1.3 | 59.0 | 28.3 | 31.0 |

strengthening of R/C structures. Regarding the influence of the direction of CFRP sheets on the behavior of the flexural strengthening slab, the obtained results showed this influence was negligible.

### 3.2 Mode of Failure

The typical mode of failure of the control slab and the strengthened slabs were presented in Figs. 6, 7 and 8, respectively. The control slab failed by yielding of steel reinforcement followed by crushing of concrete. All strengthened specimens failed prematurely without warning by delamination of the CFRP sheets after yielding of steel reinforcement.

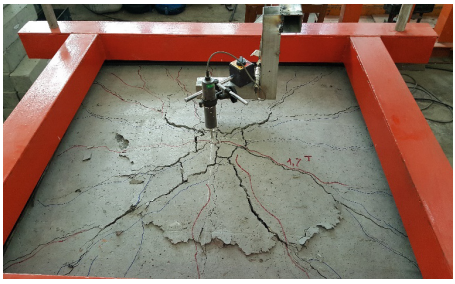

**Fig. 6.** Diagonal yield lines failures of the un-strengthened slab

**Fig. 7.** De-ponding failure of strengthened specimen M-11

**Fig. 8.** De-ponding failure of strengthened specimen M-21

## 4 Conclusion

The results of the above-mentioned experimental program have improved the understanding of the behavior of flexural strengthening of Two-way reinforced concrete slab using CFRP sheets. Based on the test results of this study, the following conclusions are drawn:

- Externally bonded CFRP sheet is an effective method to strengthen the reinforced concrete slabs at cracking stage. FRP composite improve the structural stiffness and the structural load carrying capacity. The flexural strengthening specimens using CFRP sheets showed an average gain in the load capacity of approximately 33% over that of the control (unstrengthened) specimen.
- For the flexural strengthening technique, debonding between FRP materials and concrete was the main cause of failure. Therefore, to use the full potential of FRP composite and to avoid flexural sudden failure due to deponding of FRP, it is necessary to improve the adhesion between the FRP and the concrete surface.

## References

1. ACI 440.2R-02: Guide for the Design and Construction of Externally Bonded FRP Systems for Strengthening Concrete Structures, Reported by ACI Committee 440 (2002)
2. ACI 318-05: Building Code Requirements for Structural Concrete and Commentary. American Concrete Institute (2005)
3. CEB-FIP: Externally bonded FRP reinforcement for RC concretes, FIR Bulletin 14. FIB-Int. Fed. Struct. Concr, Lausanne, pp. 59–68 (2001)
4. Ebead, U., Marzouk, H.: Fiber-reinforced polymer strengthening of two-way slabs. ACI Struct. J. **101**(5), 650–659 (2004)
5. Lawrence, C.B.: Composites for Construction: Structural Design with FRP Materials. Wiley, Hoboken (2006)
6. ISIS M04: Externally Bonded FRP for Strengthening Reinforced Concrete Structures. The Canadian Network of Centres of Excellence on Intelligent Sensing for Innovative Structures, Winnipeg (2001)
7. Nguyen, M.H., Tran, T.D.: Experimental study on flexural strengthening of one-way reinforced concrete slabs using carbon and glass fiber reinforced polymer sheets. In: The 7th International Conference of Asia Concrete Federation, Hanoi, Vietnam (2016)

# Image Processing in the Characterization of Crack Propagation in Cold-Formed Steel Samples

Daniel Dias-da-Costa[1,2], Cao Hung Pham[1(✉)], and Gregory J. Hancock[1]

[1] School of Civil Engineering, The University of Sydney, 2006 Sydney, NSW, Australia
{daniel.diasdacosta, caohung.pham, gregory.hancock}@sydney.edu.au
[2] ISISE, Department of Civil Engineering, University of Coimbra, Coimbra, Portugal

**Abstract.** This paper focuses on a technique developed to monitor and track automatically the crack propagation at two sides of the corner of a coupon to investigate the corner effect on the fracture toughness of the high strength cold-formed steel channel sections. The coupons taken longitudinally along the corners of channel sections were initially pre-cracked at both sides under fatigue loading and then loaded monotonically under tension until failure. When assessing the fracture toughness, it was particularly important to identify the precise moment of initiation and propagation of the pre-existing cracks. The technique was based on image processing with a grid of circular targets attached on the surface prior to the monotonic test and used for scaling and orientating all acquired images. A digital correlation procedure was applied to track both edges of the notch of each crack and quantify its opening during the test. By correlating the changes in the rate of crack mouth opening, the different stages of propagation could be identified together with the corresponding critical loads. The fracture toughness is determined based on these critical loads which could not be captured directly from the load versus axial displacement curves.

**Keywords:** Image processing · Cold-formed steel · Coupon test · Fracture toughness · Corner area

## 1 Introduction

The use of cold-formed steel construction has accelerated dramatically with advantages such as high strength-to-weight ratio, ease of prefabrication and installation, versatility and high structural efficiency. Due to the small difference between the yield point and tensile strength, fracture toughness becomes an important parameter in ultimate strength analysis as cold-reduced steels are more brittle compared with hot-rolled steels. An experimental program (Dias-da-Costa et al. 2017) has been performed recently at the University of Sydney to investigate the corner effect on the fracture toughness of high strength steel channel sections. The specimens were initially

© Springer Nature Singapore Pte Ltd. 2018
H. Tran-Nguyen et al. (eds.), *Proceedings of the 4th Congrès International de Géotechnique - Ouvrages -Structures*, Lecture Notes in Civil Engineering 8,
DOI 10.1007/978-981-10-6713-6_88

pre-cracked on both sides under fatigue loading and then loaded monotonically under tension until failure. Given the existence of damage before the monotonic loading, it was particularly important to identify the precise moment of initiation and propagation of pre-existing fatigue cracks for the assessment of the fracture toughness.

Previous works from Pham et al. (2016) at the University of Sydney have tried to investigate experimentally and numerically the fracture toughness of G450 sheet steels at ambient temperature. From the experimental investigation, identifying the stages of propagation can be very difficult from load versus displacement curves given by the loading machine, and the use of gauges or extensometers to measure the crack opening may be limited due to the size of the pre-existing notch. In order to identify the critical load at crack initiation in Pham et al. (2016), the load-deflection response was simulated and compared with that from the test using the FEM package ABAQUS/CAE 6.14 (2014). After confirmation of the FEM results, the fracture toughness was only computed at crack initiation in the elastic range by using the FEM model.

This paper therefore presents a technique based on image processing that can be used to monitor fracture toughness tests in cold-formed steel and characterize the process of crack propagation by quantifying the crack mouth opening (CMOD) during the test. In the following sections, the technique is presented and demonstrated in the testing of a cold-formed steel coupon.

## 2 Image Processing Technique

The image processing technique herein adopted uses a grid of circular targets attached to the surface of the specimen prior to the test. These targets allow scaling and orienting all the images acquired during a test. A digital correlation method is then applied to measure the opening of the crack by tracking the position of each vertex of the crack mouth. In the following section, more details are given.

### 2.1 Target Detection and Procedure for Scaling

The procedure for target detection and scaling is described in (Criminisi et al. 2000 and Dias-da-Costa et al. 2014) and, for this reason, only the main aspects are recovered in the following sections. In addition, the camera is assumed to be calibrated regarding the intrinsic parameters (optical, geometric and digital characteristics of the camera). Toolboxes available for this purpose can be found in Bouquet (2010).

During the test, the displacements are assumed to occur within the same plane. This allows using a single camera model, in which world plane targets can be assumed to be projected into the image place by the following Eq. (1):

$$\mathbf{X} = \omega \mathbf{H} \mathbf{x} \Leftrightarrow \begin{Bmatrix} X \\ Y \\ T \end{Bmatrix} = \omega \begin{bmatrix} h_1 & h_2 & h_3 \\ h_4 & h_5 & h_6 \\ h_7 & h_8 & h_9 \end{bmatrix} \begin{Bmatrix} x \\ y \\ 1 \end{Bmatrix} \tag{1}$$

where $\mathbf{X} = (X, Y, T)^T$ and $\mathbf{x} = (x, y, 1)^T$ are, respectively the world and image coordinates, $\omega$ is a scale factor and $\mathbf{H}$ is a $3 \times 3$ matrix containing the homographic

parameters. Any target located in the same projective ray is mapped into the same point, which position can be represented using the third component 'T' in the vector of real coordinates. Also, the third component of the image plane can indeed have any coordinate (all targets are assumed to remain inside that plane, although not necessarily in the same positions during the test). In the following derivations, '1' is assumed for this third component, without loss of generality.

Equation (1) can be recast to relate explicitly world and image coordinates, by replacing the scale factor and parameter 'T', as follows:

$$\begin{cases} \frac{\omega}{T} = \frac{1}{h_7 x + h_8 y + h_9} \\ h_1 x + h_2 y + h_3 - X(h_7 x + h_8 y + h_9) = 0 \\ h_4 x + h_5 y + h_6 - Y(h_7 x + h_8 y + h_9) = 0 \end{cases} \tag{2}$$

The last two expressions in Eq. (2) can be applied to the grid of targets before starting the test, such that the homographic parameters can be obtained. The grid spacing is used to obtain the world coordinates for each target before the test, whereas the coordinates in the image are computed by applying the Hough transform algorithm to calculate the center for each circular target (Ballard 1981). The system of equations is given by:

$$\mathbf{Wh} = \begin{pmatrix} x_1 & y_1 & 1 & 0 & 0 & 0 & -x_1X_1 & -y_1X_1 & -X_1 \\ 0 & 0 & 0 & x_1 & y_1 & 1 & -x_1Y_1 & -y_1Y_1 & -Y_1 \\ x_2 & y_2 & 1 & 0 & 0 & 0 & -x_2X_2 & -y_2X_2 & -X_2 \\ 0 & 0 & 0 & x_2 & y_2 & 1 & -x_2Y_2 & -y_2Y_2 & -Y_2 \\ \vdots & \vdots & \vdots & \vdots & \vdots & \vdots & \vdots & \vdots & \vdots \\ x_n & y_n & 1 & 0 & 0 & 0 & -x_nX_n & -y_nX_n & -X_n \\ 0 & 0 & 0 & x_n & y_n & 1 & -x_nY_n & -y_nY_n & -Y_n \end{pmatrix} \begin{pmatrix} h_1 \\ h_2 \\ h_3 \\ h_4 \\ h_5 \\ h_6 \\ h_7 \\ h_8 \\ h_9 \end{pmatrix} = \mathbf{0} \tag{3}$$

where 'n' is the number of targets.

The system in Eq. (3) is overdetermined when more than four targets are available and can be solved adopting a least-squares approach, which is equivalent to extracting the eigenvector for the smallest eigenvalue of $\mathbf{W}^T\mathbf{W}$ (Criminisi et al. 2000). It is worth mentioning that the number of unknowns homographic parameters is eight, provided that any world distance (e.g. grid spacing) for scaling is known.

The homographic parameters are solved before starting each test and then used to recover the world coordinates for any target in the image plane during the test. This is done by assuming that the camera remains stable during the test, and that all displacements of interest occur within the initial plane.

### 2.2 Digital Image Correlation

The fact that the CMOD is defined by the distance between two vertices (e.g. tips of the notch) and that these vertices present distinctive geometrical features, a digital image correlation procedure can efficiently track their position during the test. Since the

relation between world coordinates and image coordinates are given by Eq. (1), then the CMOD can be directly computed. In the tracking of the displacement/coordinates of each vertex, a small region of interest is initially defined and searched for in subsequent images by maximizing the following correlation coefficient:

$$r = \frac{\sum_m \sum_n \left(I_{mn} - \overline{I}\right)\left(F_{mn} - \overline{F}\right)}{\sqrt{\left[\sum_m \sum_n \left(I_{mn} - \overline{I}\right)^2\right]\left[\sum_m \sum_n \left(F_{mn} - \overline{F}\right)^2\right]}} \tag{4}$$

where $I$ and $F$ contain values for each pixel inside the region of interest in the initial and final images (in grey scale), respectively, and $\overline{I}$ and $\overline{F}$ are the mean values.

The use of the vertices as distinctive geometrical features is an efficient way of avoiding the need for marking the surface of the specimen using random speckle patterns, which can be difficult especially in small areas (Abanto-Bueno and Lambros 2002, Nunes and Reis 2012).

## 3 Experimental Program

### 3.1 Test Set-up and Data

Fracture toughness tests (Dias-da-Costa et al. 2017) were performed in the Structures Laboratory at School of Civil Engineering, the University of Sydney using the Material Test System (MTS) 810 servo-hydraulic dynamic tester and the MTS Sintech 65G electromechanical testing machines. Six specimens of varying thicknesses: 1.9, 2.4 and 3.0 mm were designed in accordance to ASTM E399 (American Society for Testing and Materials E 399 2013) to ensure the validity of the results. All specimens were subjected to a cyclic tensile load in the MTS 810 machine to create an initial fatigue crack towards the corners. This was followed by a monotonically increasing tension load, applied by moving the crosshead at a constant velocity in the MTS Sintech 65G testing machine. Using photogrammetry and image processing techniques, the load required to cause the initial crack propagation was determined. Coupon specimens were cut using a wire electrical discharge machining (EDM) process from the corner section of cold-formed steel cee-section as shown below in Fig. 1. Following this process, the above specimens were then further cut to form the shape of a tensile coupon in accordance with ASTM E338 (American Society for Testing and Materials E 338 2003). The specimen consisted of two shoulders for gripping and a reduced gauge section in between for testing the corner properties. The reduced section is essential to allow the deformation and failure to occur within this region. The gauge section must be of sufficient length, such that deformation will not be experienced by the shoulder sections.

To ensure that fracture occurs at the desired location, it is imperative to create two notches at the middle of the reduced gauge section to reduce the cross-sectional area, allowing the initial fatigue crack to form in this region of higher stress concentrations. The notch has a total depth of 3 mm, with a further 0.5 mm of V-section cut out to

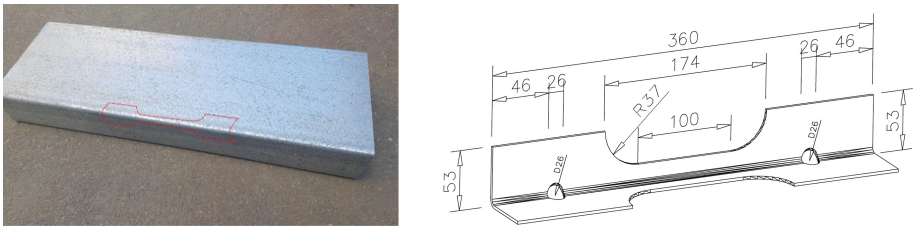


**Fig. 1.** Coupon specimen

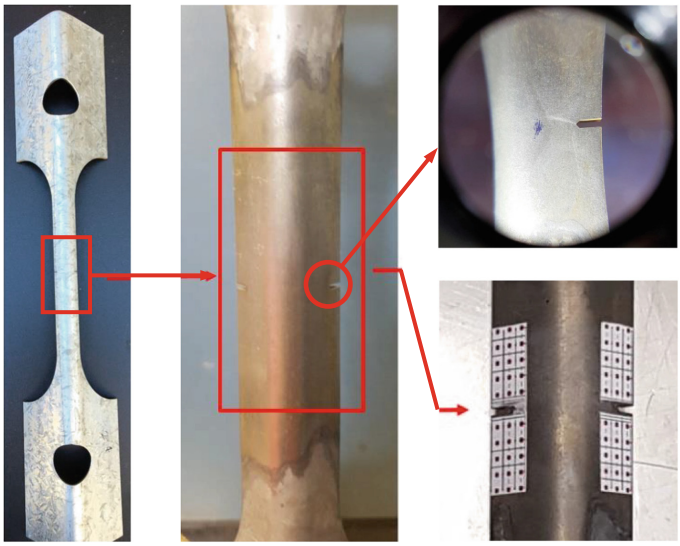

**Fig. 2.** V-shape notch, removal of zinc coating and grids attached for image processing

allow for the stress concentration to develop at the tip. After removing the galvanized zinc coatings, special target stickers were attached to the specimen around the notch section as shown in Fig. 2.

### 3.2 Experimental Procedure

The fracture toughness test was conducted in two stages in accordance with ASTM E338 (American Society for Testing and Materials E 338 2003) and ASTM E399 (American Society for Testing and Materials E 399 2013). The initial test required the specimen to be subjected to a tensile cyclic load (fatigue loading) to create initial crack propagation at the end of the V-shaped notch due to the reduced cross sectional area. The second stage of the test involved subjecting the specimen to a tensile monotonic loading until fracture failure occurred. This stage was set-up as shown below in Fig. 3. Since the specimen has a notch and a fatigue crack prepared at the middle of the gauge section, the fracture was expected to initiate and propagate from this point onwards as it

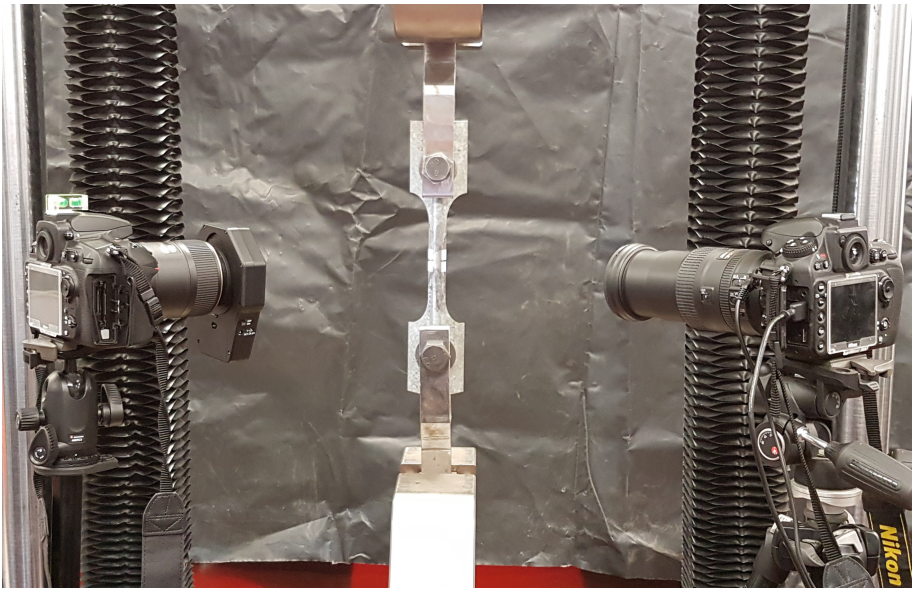


**Fig. 3.** Monotonic loading experimental setup

was the location with highest stress concentration and lowest cross sectional area. This second stage was conducted in the MTS Sintech 65G electromechanical testing machine at constant displacement of 0.4 mm/min. During each test, digital cameras were used to monitor the process of crack localization and propagation according to the procedure described in the following section. The D800 Nikon cameras were placed on tripods to provide stability and minimize vibration and were remotely triggered to maintain a fixed position locked onto the specimen. One camera was equipped with a 105 mm lens and the other with a 28–300 mm lens.

The load vs. displacement curve for the monotonic tensile test of a 1.9 mm thickness coupon until failure is shown in Fig. 4a. There, it can be seen the initial load applied to the specimen and the subsequent axial displacement until failure, which

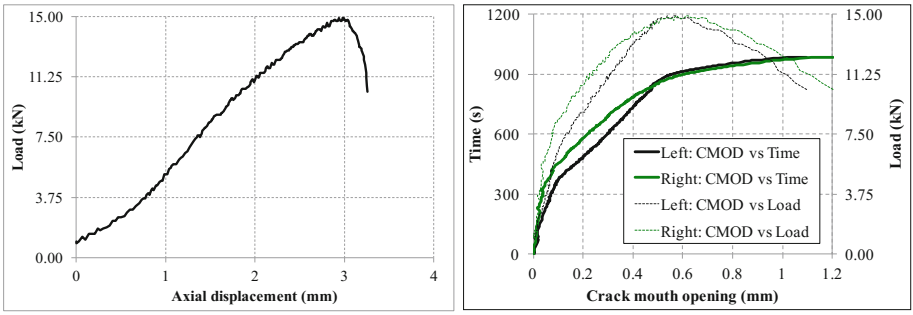


**Fig. 4.** (a) load vs. axial displacement (testing machine); (b) CMOD vs. load and time

occurs after the propagation of the crack through the specimen. No significant changes are noticeable in the specimen response from this figure before the peak load, with the load vs. axial displacement progressing almost linearly up to that point.

The image processing technique described in Sect. 2 was applied to the specimen during the test. Figure 4b shows the CMOD vs. load and time. By comparing Figs. 4a and b, three distinct stages are easily identified in the latter figure by significant changes in the slope. Such changes are related with the process of localization and propagation. The first stage, corresponds to the opening of the fatigue cracks introduced before the test, and is almost linear. Figures 5a and b show the crack opening before the test and at the end of the first linear branch. The second branch (or stage) is associated with the process of propagation, with the crack progressively widening and causing yielding and necking to develop at the tip of the pre-existing crack. The crack remains almost unchanged in length – see Fig. 5c. This stage starts at 33% to 45% of the capacity of the specimen and progresses until approaching the maximum strength of the specimen.

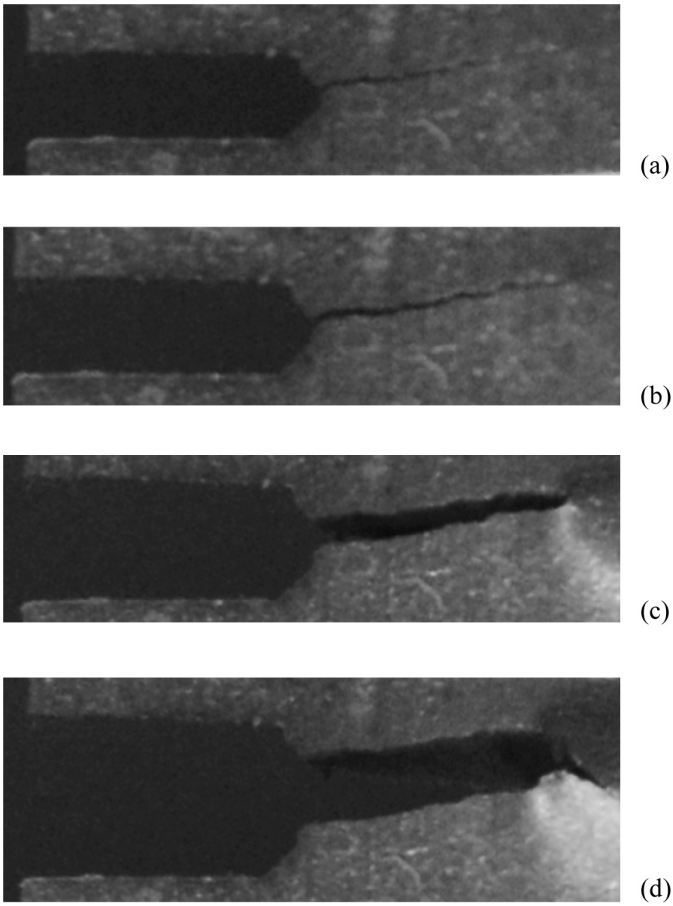


**Fig. 5.** (a)–(d) different stages of crack propagation for crack 1

After this stage the rate of crack opening increases quickly and a new crack front propagates through the yielded/necked region, with the loss of load capacity (see Fig. 5d) and subsequent failure.

The three stages of propagation cannot be easily identified from the load vs. axial displacement provided by the testing machine (Fig. 4a). The rate of opening combined with the CMOD provides the necessary data to pinpoint the mechanisms controlling damage propagation. Without analyzing the rate of opening for each crack and the changes in deformation, it is very difficult to experimentally identify the loads associated with the stages of propagation.

## 4 Conclusion

The main purpose of this work is to show the application of an image processing technique to identify the stages of fracture propagation in fracture toughness tensile tests. The technique is based on the determination of homographic parameters relating world and image coordinates for a single camera, upon which a digital image correlation is applied to track the crack opening during the test. The definition of a region of interest around each vertex of the crack mouth allows avoiding the need for special speckles applied in the surface. Other than attaching an initial grid of targets, no further preparations are needed. The technique allows determining the different stages of propagation in pre-cracked specimens under monotonic tensile loading, which is critical to the evaluation of the fracture toughness. By correlating the changes in the rate of crack mouth opening, the different stages of propagation could be identified together with the corresponding critical loads.

The tested specimen showed three stages of propagation for each pre-crack. The first stage progressed from the beginning of loading and progressed until a third of the capacity of the specimen. It was characterized by a linear opening of the pre-existing crack. For higher loads, the behavior changes and the crack opens faster and a process of necking and yielding progressively develops at the tip. This continues until approaching the maximum capacity of the specimen, where the rate of opening increases even further with a new crack front propagating through the specimen. This phenomenon is accompanied by the softening of applied load.

Following this preliminary work, it should be highlighted the advantage of using the proposed image processing technique for characterization and identification of propagation, and associated loads, which are relevant for fracture toughness and that could not be identified from load versus axial displacement curves.

**Acknowledgments.** The authors would like to thank Fielders for the supply of the test specimens for the project performed at the University of Sydney. Thanks are also extended to all technicians at the J.W. Roderick Laboratory for Materials and Structures at the University of Sydney.

## References

Abanto-Bueno, J., Lambros, J.: Investigation of crack growth in functionally graded materials using digital image correlation. Eng. Fract. Mech. **69**(14–16), 1695–1711 (2002)

ABAQUS/Standard: ABAQUS/CAE User's Manual. Dassault Systèmes Simulia Corp., Providence (2014)

American Society for Testing and Materials E 338: Standard Method of Sharp-Notch Tension Testing of High-Strength Sheet Materials, Philadelphia, USA (2003)

American Society for Testing and Materials E 399: Standard Test Method for Linear-Elastic Plane-Strain Fracture Toughness $K_{IC}$ of Metallic Materials, Philadelphia, USA (2013)

Ballard, D.H.: Generalizing the Hough transform to detect arbitrary shapes. Pattern Recogn. **13**(2), 111–122 (1981)

Bouquet, J.: Camera calibration toolbox for Matlab (2010). http://www.vision.caltech.edu/bouguetj/calib_doc/

Criminisi, A., Reid, I., Zisserman, A.: Single view metrology. Int. J. Comput. Vis. **40**(2), l23–148 (2000)

Dias-da-Costa, D., Pham, T.D., Tu, J., Pham, C.H., Hancock, G.J., Proust, G.: Observations on fracture toughness measurement at the corners of G450 cold-formed steel channel sections subject to tension. Paper presented at the 8th European conference on steel and composite structures, Eurosteel, 13–17 September 2017, Copenhagen Denmark (2017)

Dias-da-Costa, D., Valença, J., do Carmo, R.: Curvature assessment of reinforced concrete beams using photogrammetric techniques. Mater. Struct. **47**(10), 1745–1760 (2014)

Nunes, L., Reis, J.: Estimation of crack-tip-opening displacement and crack extension of glass fiber reinforced polymer mortars using digital image correlation method. Mater. Des. **33**, 248–253 (2012)

Pham, C.H., Phan, D.K., Huynh, M.T., Hancock, G.J.: Fracture of G450 sheet steels at ambient temperature subjected to tension. Structures **8**, 310–317 (2016)

# Impact of Measurement Errors in Inverse Analysis

Jun Lei[1], Jose-Antonio Lozano-Galant[2], Maria Nogal[3], Dong Xu[1(✉)], and Jose Turmo[4]

[1] Tongji University, Shanghai, China
{13l0269, xu_dong}@tongji.edu.cn
[2] University of Castilla-La Mancha, Ciudad Real, Spain
joseantonio.lozano@uclm.es
[3] Trinity College Dublin, Dublin, Ireland
nogalm@tcd.ie
[4] Universitat Politècnica de Catalunya BarcelonaTech, Barcelona, Spain
jose.turmo@upc.edu

**Abstract.** During the first step in the development of any structural system identification method, the method should be validated by noise-free measurements in the first place. Nevertheless, this assumption is far from reality as the measurements in these tests are always subjected to the errors of measurement devices. To fill this gap, this paper analyzes the effects of measurement errors in a parametric structural system identification method: the observability method. To illustrate the symbolic approach of this method a simply supported beam is first analyzed in detail. This simulation provides the parametric equations of the estimates. Then, the effects of errors in a particular measurement, errors in all measurements, load locations are studied in this structure. Two additional examples of increasing complexity are also analyzed to show the effect of modelling errors on the estimates. A fluctuation of the observed parameters around the real values is proved a characteristic of this method. The results of these structures illustrate how important the effects of modelling errors are especially in areas with low curvatures.

**Keywords:** Inverse analysis · Observability method · Structural system identification · Measurement errors · Modelling errors

## 1 Introduction

Structural health monitoring has been increasingly important in the life-cycle management of structures. One of the key component of structural health monitoring is the structural system identification (SSI). The objective of any SSI method is to estimate the structural parameters of the structure [1]. In direct analysis, the parameters of the parameterized model are known and the structural response is to be solved. However, in the case of SSI, aka inverse analysis, the estimation of the unknown parameters is based on the observed structural response. Depending on the external excitations, SSI can be categorized as static and dynamic. Compared to static SSI, dynamic SSI has been developed extensively in the past decades. However, the application of static SSI

© Springer Nature Singapore Pte Ltd. 2018
H. Tran-Nguyen et al. (eds.), *Proceedings of the 4th Congrès International de Géotechnique - Ouvrages -Structures*, Lecture Notes in Civil Engineering 8,
DOI 10.1007/978-981-10-6713-6_89

does not need the information of the structural mass and damping. Also, the accuracy of the static measurements (static strains, deflections or rotations) is higher than that of dynamic measurements. Hence, in some cases, static SSI might be preferred [2]. If the parameters in the parameterized model for a specific SSI method represent the physical quantities (i.e. elastic moduli, cross-sectional area or inertia), then this method is regarded as a parametric method. If no physical meaning exists in these parameters, the method will be categorized as nonparametric method.

SSI by observability method (OM) was proposed as a parametric static SSI method by [3]. This method transforms the system of equilibrium equations at the nodes in the finite element model (FEM) by a series of algebraic operations and applies the observability method on the resulting coefficient matrix [4]. Based on the characteristic of the null space of the symbolical coefficient matrix, the observability of the parameters, i.e. whether all or a subset of the parameters can be identified or not given a particular measurement set, can be obtained. The strategy to ensure the identifiability of structural parameters was investigated in [5]. This method was also applied in cable-stayed bridge, which is highly statically redundant [6]. A numerical approach was combined with the symbolical approach to provide the numerical estimation of the parameters [7].

SSI can be interpreted as the estimation of structural parameters using collected measurements. Hence, two types of errors might be introduced in SSI. The first type of errors might occur during the process of collecting data, i.e. measurement errors, while the second type of errors might occur in the process of parameter estimation, i.e. modelling errors. In this paper, the impact of measurement errors on the inverse analysis via SSI by OM is studied. The effect of modelling errors inherent to this method is also discussed.

The remaining part of this paper is organized as follows. In Sect. 2, the implementation of SSI by OM is demonstrated first and exemplified by a simply supported beam. The parametric equations of the structural parameters are derived explicitly. In the next section, the effect of a specific noisy measurement on the estimation is studied first. The effects of load cases and different types of measurements are also studied. Then, the performance of the proposed method using noisy measurements are evaluated. In Sect. 4, the modelling errors in the proposed method is studied through two examples. Some conclusions are drawn in the end.

## 2 Structural System Identification by Observability Method

### 2.1 Observability Method

OM has been applied in many areas of engineering (e.g. transportation, hydraulic problem and power system). It is related to the ability of identifying the parameters in the parametric system with a given set of input. One way to check the observability of the parameters is to analyze the null space of the coefficient matrix of the linear system of equations, as described in [8].

### 2.2 Structural System Identification by Observability Method

For structural system, using the theory of strength, the equilibrium equations can be given as follows:

$$\left[K(A_j, E_j, I_j, L_j)\right] \cdot \{\delta\} = \{f\} \tag{1}$$

in which $[K]$ is the stiffness matrix of the structure, $\{\delta\}$, is a vector of nodal displacements and $\{f\}$ is a vector of nodal forces. For 2D analysis, $[K]$ includes the geometrical and mechanical properties of the elements of the structure, such as length, $L_j$, shear modulus, $G_j$, Young's modulus, $E_j$, area, $A_j$, inertia, $I_j$, and torsional stiffness, $J_j$, associated with the j-element. Detailed form of the matrix $[K]$ can be found in many textbooks on finite element method for structures of beam elements. Such an example can be found in [3].

When the SSI is introduced in the stiffness matrix method, the matrix $[K]$ is partially unknown. Usually, $L_j$ is assumed known while the stiffnesses are traditionally assumed as unknown. The determination of the unknown parameters in $[K]$ leads to a nonlinear problem as these parameters are multiplied by the displacements of the nodes (in 2D, horizontal and vertical deflection and rotation associated with the k-node $u_k$, $v_k$ and $w_k$ respectively). This implies that non-linear products of variables, e.g. $E_jA_ju_k$, $E_jA_jv_k$, $E_jI_ju_k$, might appear, leading to a polynomial system of equations.

To solve these equations in a linear-form, system (1) can be rewritten as:

$$[K^*] \cdot \{\delta^*\} = \{f\} \tag{2}$$

in which the products of variables are located in the modified vector of displacements $\{\delta^*\}$ and the modified stiffness matrix $[K^*]$ is a matrix of coefficients with different dimensions from the initial stiffness matrix $[K]$ (see [3] for more details). Depending on the known information, the unknown variables of vector $\{\delta^*\}$ may be the non-linear products presented above, as well as other factors of single variables, e.g. $E_jI_j$, $E_jA_j$, $E_j$, $A_j$, $I_j$ or nodal deflections.

Once the boundary conditions and the applied forces are introduced into Eq. (2), it can be assumed that a subset of deflections $\{\delta_1^*\}$ of $\{\delta^*\}$ and a subset of forces $\{f_1\}$ of $\{f\}$ are known and the remaining subset $\{\delta_0^*\}$ of $\{\delta^*\}$ and $f_o$ of $\{f\}$ are not. By static condensation, the system in (2) can be partitioned as follows:

$$[K^*] \cdot \{\delta^*\} = \begin{pmatrix} K_{00}^* & K_{01}^* \\ K_{10}^* & K_{11}^* \end{pmatrix} \begin{Bmatrix} \delta_0^* \\ \delta_1^* \end{Bmatrix} = \begin{Bmatrix} f_0 \\ f_1 \end{Bmatrix} = \{f\} \tag{3}$$

where $K_{00}^*, K_{01}^*, K_{10}^*$ and $K_{11}^*$ are partitioned matrices of $[K^*]$ and $\delta_1^*$, $\delta_0^*, f_o$ and $f_1$ are partitioned vectors of $\{\delta^*\}$ and $\{f\}$.

Equation (3) can be transformed such that all the unknowns, $\{\delta_0^*\}$ and $\{f_0\}$, are collected in the unknown variables $\{z\}$, and the coefficient matrix and the right-hand side vector are known, as depicted in Eq. (4).

$$[B] \cdot \{z\} = \begin{pmatrix} K_{10}^* & 0 \\ K_{00}^* & -I \end{pmatrix} \begin{Bmatrix} \delta_0^* \\ f_0 \end{Bmatrix} = \begin{Bmatrix} f_1 - K_{11}^* \delta_1^* \\ -K_{01}^* \delta_1^* \end{Bmatrix} = \{D\} \tag{4}$$

where 0 and $I$ are the null and the identity matrices, respectively. For Eq. (4) to have a solution, it is sufficient to calculate the null space $[V]$ of $[B]$ and checking that $[V]$ $[D] = 0$. Examination of matrix $[V]$ and identification of its null rows leads to identification of the observable variables (subset of variables with a unique solution) of vector $\{z\}$. The solution of Eq. (4) should have the structure indicated in Eq. (5).

$$z_g = z_p + V \cdot p \tag{5}$$

The particular solution $z_p$ and the null space $V$ can be obtained in many software, e.g. Matlab and Maple. In SSI by OM, the parameters are identified in a recursive way. This is to say, if any unknown variable is observed in current recursive step, these variables will be successively introduced in the next recursive step. For more technical details, it is strongly recommended to read [3].

### 2.3 An Example of Structural System Identification by Observability Method

The procedure of the algorithm combining the symbolical and the numerical approach is exemplified by the simply supported beam depicted in Fig. 1a. This structure is simulated by a FEM with three elements each of the length $L$. Since the axial behavior of this structure is not interested, the FEM can be parameterized by three bending stiffnesses, $EI_1$, $EI_2$ and $EI_3$. The measurement set used here includes one rotation, $w_1$, and two deflections, $v_2$ and $v_3$.

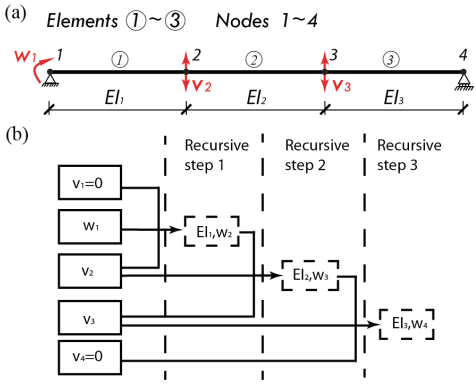


**Fig. 1.** (a) FEM of the simply supported beam; (b) recursive steps for the identification of the simply supported beam

The equilibrium equations related with moments and vertical forces are established first and then rearranged by algebraic operations such that all the unknown physical quantities are clustered in the variables, as depicted in Eq. (6).

$$\begin{pmatrix} \frac{4w_1}{3L}-\frac{2v_2}{3L^2} & \frac{2}{3L} & 0 & 0 & 0 & 0 & 0 & 0 & 0 & 0 \\ \frac{4v_2}{9L^3}-\frac{2w_1}{3L^2} & -\frac{2}{3L^2} & \frac{4v_3}{9L^3}-\frac{4v_3}{9L^3} & \frac{2}{3L^2} & \frac{2}{3L^2} & 0 & 0 & 0 & 0 & 0 \\ \frac{2w_1}{3L}-\frac{2v_2}{3L^2} & \frac{4}{3L} & \frac{2v_2}{3L^2}-\frac{2v_3}{3L^2} & \frac{4}{3L} & \frac{2}{3L} & 0 & 0 & 0 & 0 & 0 \\ 0 & 0 & \frac{4v_3}{9L^3}-\frac{4v_2}{9L^3} & -\frac{2}{3L^2} & -\frac{2}{3L^2} & \frac{4v_3}{9L^3} & \frac{2}{3L^2} & \frac{2}{3L^2} & 0 & 0 \\ 0 & 0 & \frac{2v_2}{3L^2}-\frac{2v_3}{3L^2} & \frac{2}{3L} & \frac{4}{3L} & \frac{2v_3}{3L^2} & \frac{4}{3L} & \frac{2}{3L} & 0 & 0 \\ 0 & 0 & 0 & 0 & 0 & \frac{2v_3}{3L^2} & \frac{2}{3L} & \frac{4}{3L} & 0 & 0 \\ \frac{2w_1}{3L^2}-\frac{4v_2}{9L^3} & \frac{2}{3L^2} & 0 & 0 & 0 & 0 & 0 & 0 & -1 & 0 \\ 0 & 0 & 0 & 0 & 0 & -\frac{4v_3}{9L^3} & -\frac{2}{3L^2} & -\frac{2}{3L^2} & 0 & -1 \end{pmatrix} \begin{pmatrix} EI_1 \\ EI_1w_2 \\ EI_2 \\ EI_2w_2 \\ EI_2w_3 \\ EI_3 \\ EI_3w_3 \\ EI_3w_4 \\ V_1 \\ V_4 \end{pmatrix} = \begin{pmatrix} M_1 \\ V_2 \\ M_2 \\ V_3 \\ M_3 \\ M_4 \\ 0 \\ 0 \end{pmatrix} \tag{6}$$

In Eq. (6), the unknown variables include the three bending stiffnesses, $EI_1$–$EI_3$, reactions, $V_1$ and $V_4$, and coupled terms (e.g. $EI_3w_4$). All the measured displacements, i.e. $w_1$, $v_2$ and $v_3$, are absorbed in the coefficient matrix of Eq. (6). According to Eq. (5), the general solution of Eq. (6) is given as:

$$\begin{Bmatrix} EI_1 \\ EI_1w_2 \\ EI_2 \\ EI_2w_2 \\ EI_2w_3 \\ EI_3 \\ EI_3w_3 \\ EI_3w_4 \\ V_1 \\ V_4 \end{Bmatrix}_g = \begin{Bmatrix} EI_1 \\ EI_1w_2 \\ EI_2 \\ EI_2w_2 \\ EI_2w_3 \\ EI_3 \\ EI_3w_3 \\ EI_3w_4 \\ V_1 \\ V_4 \end{Bmatrix}_p + \begin{Bmatrix} 0 & 0 \\ 0 & 0 \\ -\frac{L}{v_2-v_3} & 0 \\ 1 & 0 \\ 1 & 0 \\ 0 & -\frac{L}{v_3} \\ 0 & 1 \\ 0 & 1 \\ 0 & 0 \\ 0 & 0 \end{Bmatrix} \cdot \{p_1\} \tag{7}$$

Note that the null space of the coefficient matrix in Eq. (6) should be obtained symbolically. This is because in the numerical calculation, infinitesimal non-zero values might be obtained instead of zeros values. This is undesirable since it will wrongly reduce the number of observable variables. In the null space, the rows related with the unknown variables $EI_1$, $EI_1w_2$, $V_1$ and $V_4$ are all zeros. Consequently, the values of the vector $p_1$ will not affect the values of these unknown variables. The values of these variables in the general solution are the same as those in the particular solution. Hence, they are determined, unique and observable. Obviously, when $EI_1$ and $EI_1w_2$ are determined, $w_2$ can be also determined. The particular solution of these parameters can be symbolically obtained by the left divide, \, in Matlab. Hence, the parametric equation for $EI_1$ is provided in Eq. (8):

$$EI_1 = \frac{-(8M_1 - M_2 - M_3 - M_4 + 2V_2L + V_3L)L^2}{18(v_2 - w_1L)} \tag{8}$$

in which $M_i$ and $V_i$ are the bending moments and the vertical forces (external loads) applied at the i$^{th}$ node of the structure, and $L$ is the length of the beam elements in the model. It should be noted that the parametric Eq. (8) might lead to unrealistic estimation if the denominator tends to zero or is negative when errors are introduced. The parametric equations for $EI_2$ and $EI_3$ can be obtained in the same way. The analysis of Eq. (6) shows that $EI_1$ depends on the nodal forces applied at the load case ($M_1$–$M_4$, $V_2$ and $V_3$), the length of the element, $L$, and the measured deflection $v_2$ and rotation $w_1$.

Once the observable parameters are identified, their values can be numerically calculated. To illustrate the results of the method, a concrete beam of 0.3 m height and 0.2 m width is considered. The inertia and the Young's modulus are 4.5e−4 m$^4$ and 3.5e7 kN/m$^2$. The total length (3·L) of the beam is 3 m. A concentrated load of −55 kN is applied at node 2. This load case is represented by the following nodal forces: $M_1 = M_2 = M_3 = M_4 = V_3 = 0$ and $V_2 = -55$ kN.

In SSI by OM, parameters observed in previous steps are introduced into the next step in a recursive way, which enables the identification of new parameters and displacements. These recursive steps are finished when all unknowns are observed or no more unknown can be observed. The recursive steps for this simply supported beam with measurement set {$w_1$, $v_2$ and $v_3$} are depicted in Fig. 1b. In recursive step 1, $EI_1$ and $w_2$ are identified. Then, {$EI_2$, $w_3$} and {$EI_3$, $w_4$} are identified respectively in recursive step 2 and 3. When no error is introduced in the measurements, the estimations of $EI_1$, $EI_2$ and $EI_3$ are the same as the real values.

A flow chart of the algorithm of SSI by OM is provided in Fig. 2. Detailed description of this chart can be found in [9].

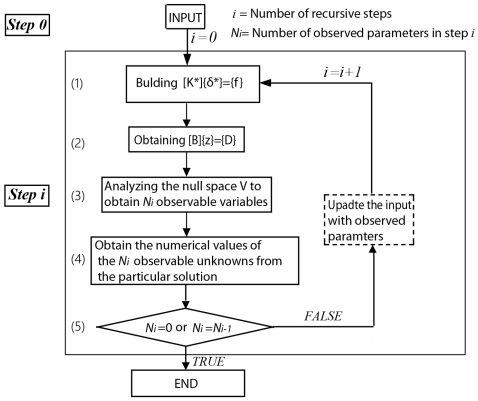


**Fig. 2.** Flow chart of the algorithm of SSI by OM

## 3 Measurement Errors

With the parametric equations for $EI_1$–$EI_3$, sensitivity analysis is carried out for the structure in Fig. 1a. The effects of errors in one measurement, load locations are considered. Also, random errors in all measurements are investigated.

### 3.1 Errors in One Measurement

With the specified values of $w_1$, $v_2$, $v_3$, the estimated values of $EI_1$–$EI_3$ can be determined by the parametric equations. The Young's modulus of the three beam elements is assumed as known (2.5e7 kN/m$^2$). Errors from −5% to 5% are introduced in $w_1$ and $v_3$. The estimated values of the parameters are normalized by associated real values. In Fig. 3, it is seen that the deviation between the estimated inertia and the actual one for an error of −5% in $w_1$ changes from 23.5% in $EI_1$ to −18% in $EI_2$, and 68.2% in $EI_3$. Errors in $v_3$ have no impact on the estimation of $EI_1$ and $EI_2$. The deviation in $EI_3$ due to −5% errors in $v_3$ is an overestimation of almost 100%. Generally, the system is more sensitive to errors in deflections than in rotations.

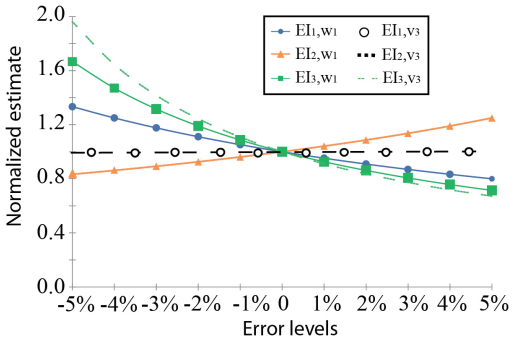


**Fig. 3.** Normalized estimation for bending stiffnesses, for different error levels in each measurement $v_3$, $w_1$

### 3.2 Effect of Load Locations

In this section, a bending moment, $M$, is applied at different locations of the structure. The first location is at the left end, i.e. x = 0, and the other location is at the right end, i.e. x = 3L. In Fig. 4, it can be seen that the closer the load to the measurements, the smaller the effect of errors. For example, for an error of −5% in $v_2$, the deviation of $EI_1$

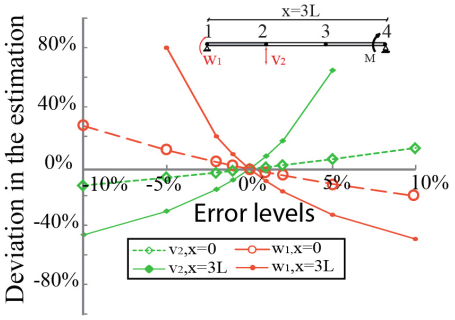


**Fig. 4.** Deviation in the estimations for bending stiffnesses, for different error levels in $v_2$, $w_1$ with a bending moment applied at different locations

increases from −5.8% to −28.6% when $M$ is moved from x = 0 to x = 3L. For the same error level in $w_1$, moving M from x = 0 to x = 3L increases the deviation of $EI_1$ from 12.7% to 81.2%.

### 3.3 Random Errors in All Measurements

Errors are introduced in all measurements by adding a proportion of associated error-free displacements $v_i$, as indicated in Eq. (9).

$$ve_i = v_i(1 + r \cdot e) \tag{9}$$

Two measurement sets are used here. Set 1 {$w_1$, $v_2$ and $v_3$} include one rotation and two deflections. Set 2 {$w_1$, $w_2$, $w_3$} is only composed of rotations. In the generation of the noisy measurements, some geometric conditions, i.e. $ve_2 > ve_3$ and $we_1 < we_2 < we_3$, are imposed. 200 admissible deformed shapes are obtained in this way. The deviation in the estimations with 5% measurement errors (i.e. e = 5%) are presented in Fig. 5. Different bounds of the estimations are considered: the 0 and 2 times the original inertia, 0.5 and 1.5 times the original inertia and 0.75 and 1.25 times the original inertia.

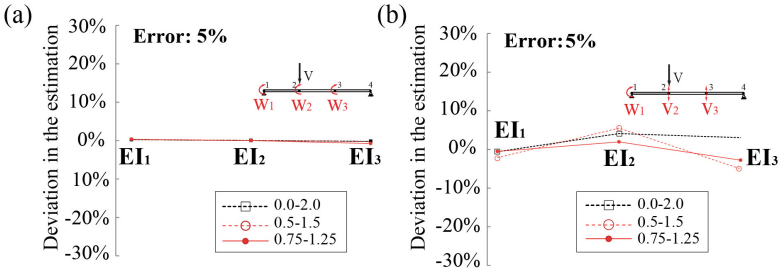


**Fig. 5.** Percentage deviations in the estimations using (a) $w_1$–$w_3$; (b) $w_1$, $v_2$ and $v_3$ with 5% measurement errors

It is seen that when only rotations are used, the estimations are unbiased. However, when deflections are used in the estimation, the deviations in the estimations are higher. The biggest deviation is seen in $EI_3$ with an underestimation of 5%.

## 4 Errors in Parameter Estimation

To clarify the effects of different modelling errors, two examples of increasing complexity are analyzed in this section.

### 4.1 Analysis of the Recursive Process

This is a cantilever beam with the length of 30 m. Young's modulus E is 210 GN/m$^2$. The area and the inertia of the girder are 0.07 m$^2$ and 0.04 m$^4$. The loading case is a bending moment with the magnitude of 100 kN•m applied at the free end, which will

induce a uniform curvature in the structure. This structure is modelled by a FEM of 30 beam elements each with the length of 1 m. The inertias of each element are assumed unknown. The deviation in the estimation using measurement Set 1 $\{v_2–v_{31}\}$ and Set 2 $\{v_3–v_{31}, w_{31}\}$ are presented in Fig. 6. The precision in the measurements are 1e−5 m in v and 1e−5 rad in w.

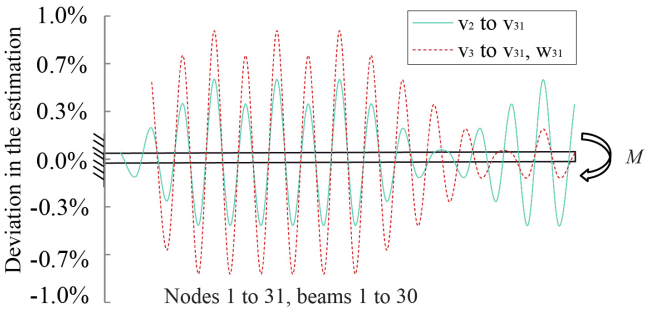


**Fig. 6.** Percentage deviation in the estimations

Counterintuitively, the errors in the estimation obtained in previous steps do not propagate during the recursive steps. For Set1, the initial error of −0.01% is increased to 0.04% at the end of the beam. This is similar in the case of set 2. This is because the inertia of the current element has to be underestimated to compensate the impact of overestimating the inertia of adjacent elements, which leads to the fluctuation in the estimations.

### 4.2 Analysis of the Effect of Curvature

A 60 m two-span continuous beam is analyzed here. This SSI problem was presented in [10]. The FEM is composed of 60 elements. The material and mechanical properties are the same as those used in the preceding section. This analysis aims at providing a better understanding of the modelling errors in SSI by OM.

A concentrated vertical load V = −100 kN is applied at mid-span of span 1. This loading produces a maximum positive bending moment of 500 kN•m at the mid-span of span 1 and a maximum negative moment of −250 kN•m at the section above the

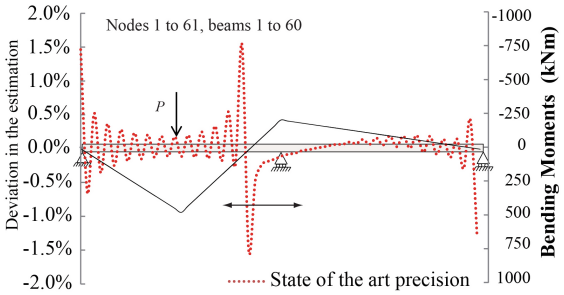


**Fig. 7.** Percentage deviation in the estimations

middle support. The precision of measurements is the same as previous section. The measurement set include 58 deflections, $v_2$–$v_{30}$, $v_{32}$–$v_{60}$, and two rotations, $w_{29}$ and $w_{30}$. The accuracy of the estimation and the moment diagram are provided in Fig. 7.

In this figure, the largest deviation of the estimations is seen at the null curvature zone, i.e. at x = 0, x = 27 and x = 60 m. Due to the inaccuracy of the estimation in null curvature zone, adequate load cases are recommended in SSI by OM.

## 5 Conclusions

The effects of measurement errors and modelling errors in SSI by OM are studied in this paper. A simply supported beam is used to exemplify the characteristic of the method and the parametric equations of the parameters are provided. It is showed that the estimations are more sensitive to the error in deflections than in rotations. This effect is significantly mitigated when errors in all measurements are considered. For the same load case, it is recommended to use measurements closer to the load location to reduce the effect of errors. Due to the modelling errors, the deviation of previous estimation in adjacent elements will be rectified by adjusting the current estimation. This is presented as the fluctuation in the estimations. Also, the curvature of the beam plays an important role in the accuracy of the estimations. Higher deviations are observed in low curvature zones. It is recommended to select sufficient loading cases to avoid the adverse effect of null curvatures in SSI by OM.

**Acknowledgments.** This work was partially funded by the Spanish Ministry of Economy and Competitiveness and the FEDER fund through the grant project (BIA2013-47290-R) directed by Jose Turmo. It is also to be noted that part of this work was done through a collaborative agreement between Tongji University (China) and Technical University of Catalonia, UPC, BarcelonaTech. This included an exchange of faculty financed by the Chinese government. The financial support from the High End Foreign Experts program (GDW20143100115) from the Chinese government is greatly appreciated. Funding for this research has been provided to Mr. Jose Antonio Lozano-Galant by the Spanish Ministry of Education through its program (CAS14/00994) for postdoctoral stays and to Mr. LEI Jun by the Chinese Scholarship Council through its program (No. 201506260116) and by the Ministerio de Economia y Competitividad through its program (BES-2014-07022) for his Ph.D. stays.

## References

1. Castillo, E., Lozano-Galant, J.A., Nogal, M., Turmo, J.: New tool to help decision making in civil engineering. J. Civil Eng. Manage. **21**(6), 689–697 (2015)
2. Sanayei, M., Imbaro, G., McClain, J., Brown, L.: Structural model updating using experimental static measurements. J. Struct. Eng. **123**(6), 792–798 (1997)
3. Lozano-Galant, J.A., Nogal, M., Castillo, E., Turmo, J.: Application of observability techniques to structural system identification. Comput. Aided Civil Infrastruct. Eng. **28**(6), 434–450 (2013)

4. Castillo, E., Nogal, M., Lozano-Galant, J.-G., Turmo, J.: Solving some special cases of monomial-ratio equations appearing frequently in physical and engineering problems. Math. Prob. Eng. **2016**, 25 (2016)
5. Lozano-Galant, J.A., Nogal, M., Turmo, J., Castillo, E.: Selection of measurement sets in static structural identification of bridges using observability trees. Comput. Concr. **15**(5), 771–794 (2015)
6. Lozano-Galant, J.A., Nogal, M., Paya-Zaforteza, I., Turmo, J.: Structural system identification of cable-stayed bridges with observability techniques. Struct. Infrastruct. Eng. **10**(11), 1331–1344 (2014)
7. Nogal, M., Lozano-Galant, J.A., Turmo, J., Castillo, E.: Numerical damage identification of structures by observability techniques based on static loading tests. Struct. Infrastruct. Eng. **12**(9), 1216–1227 (2015)
8. Castillo, E., Conejo, A.J., Eva Pruneda, R., Solares, C.: Observability in linear systems of equations and inequalities: applications. Comput. Oper. Res. **34**(6 Spec. Iss.), 1708–1720 (2007)
9. Lei, J., Lozano-Galant, J.A., Nogal, M., Xu, D., Turmo, J.: Analysis of measurement and modelling errors in structural system identification by observability techniques. Struct. Control Health Monit. (2016). doi:10.1002/stc.1923
10. Abdo, M.A.-B.: Parametric study of using only static response in structural damage detection. Eng. Struct. **34**, 124–131 (2012)

# Improving the Understanding of Tunnel Excavation Under Pressure Using a Small-Scale EPBS Model

N. Berthoz[1(✉)], D. Branque[2], and D. Subrin[1]

[1] Centre d'Etudes des Tunnels, Bron, France
{nicolas.berthoz, didier.subrin}
@developpement-durable.gouv.fr
[2] Ecole Nationale des Travaux Publics de l'Etat, LTDS, UMR CNRS5513, Lyon, France
denis.branque@entpe.fr

**Abstract.** This article presents the main results of an extensive series of tests on a small-scale earth pressure balance tunnel boring machine. The results concern the soil/machine interaction behaviours during excavation. Some analysis performed at a small scale is compared to data from work to extend Paris metro line 12.

**Keywords:** Tunnel · EPBS · Physical modeling

## 1 Introduction

Minimising impacts on neighbouring structures is a major concern for the designers of tunnels in urban areas, in which the soil is generally soft and water-bearing, and there are a large number of sensitive neighbouring surface structures and underground networks.

Tunnel boring machines with a pressurised shield offer an attractive technical solution to this challenge. With the exception of air pressure balance TBMs, whose use is reserved for small diameter tunnels, two main types of TBM may be used: earth pressure balance TBMs and slurry pressure balance TBMs. These two technologies have different scopes of application, but are tending to converge due to regular innovations implemented by manufacturers and contractors.

While there has been considerable progress in recent decades, prediction of how soil will respond to excavation with this type of machine remains difficult due to the three-dimensional nature of the phenomena, the large number of sources of displacement around the machine, and the complexity of soil behaviour. In this context, large quantities of experimental data are required to validate the models developed.

Physical modelling therefore emerges as a significant source of knowledge. Indeed, in modelling there are fewer uncertainties as to the geotechnical context than on-site. Furthermore, machine operating conditions can easily be adjusted without any external consideration, such as interruptions in works, disrupting the results obtained. Lastly, using a scale model offers far greater possibilities for instrumenting the soil and the machine.

© Springer Nature Singapore Pte Ltd. 2018
H. Tran-Nguyen et al. (eds.), *Proceedings of the 4th Congrès International de Géotechnique - Ouvrages -Structures*, Lecture Notes in Civil Engineering 8,
DOI 10.1007/978-981-10-6713-6_90

Three broad categories of physical models may be distinguished:

- two-dimensional standard section models (Atkinson and Potts 1977; Lee and Chiang 2007…)
- three-dimensional models in which excavation is modelled by static unloading of the cutting face (Mair 1979; Messerli et al. 2010…),
- three-dimensional models reproducing the progress of the TBM through the soil. There are only three experimental systems in this category: Nomoto et al. (1999), Xu et al. (2011) and the earth pressure balance tunnel boring machine model at the French State School of Public Works (ENTPE), to which this article is devoted. Only the ENTPE's scale model has an independent cutting wheel and extraction screw, replicating real-life tunnel boring machines.

After a presentation of the scale model, this article is structured in the form of answers to different questions concerning the soil/machine interaction behaviour. Note that this research has been the subject of several publications, to which readers may refer (Berthoz et al. 2012, 2013, 2017).

## 2 Presentation of the Scale Model

The ENTPE's scale model of an earth pressure balance TBM is presented in Fig. 1. This model, on a scale of between 1/4 and 1/25 compared to actual TBM diameters, comprises a cutting wheel with a diameter (D) of 55 cm, a conical cutting chamber, an extraction screw inclined at 10° to the horizontal, a cylindrical tail seal and four thrust jacks. Excavation takes place in a reconstituted 2.0 × 1.3 × 1.3 m formation. Pressure, $\sigma_s$, may be applied at the surface using air chambers, in order to model the load of an infinitely flexible built structure. Two cutting wheels with different opening ratios (35 or 80%) are used, depending on the mechanical characteristics of the soil passed through. These cutting wheels entail overcutting of 3 mm (0.4% of the diameter). At the time of writing, watertightness of the scale model is not sufficient to allow tests in groundwater to be performed.

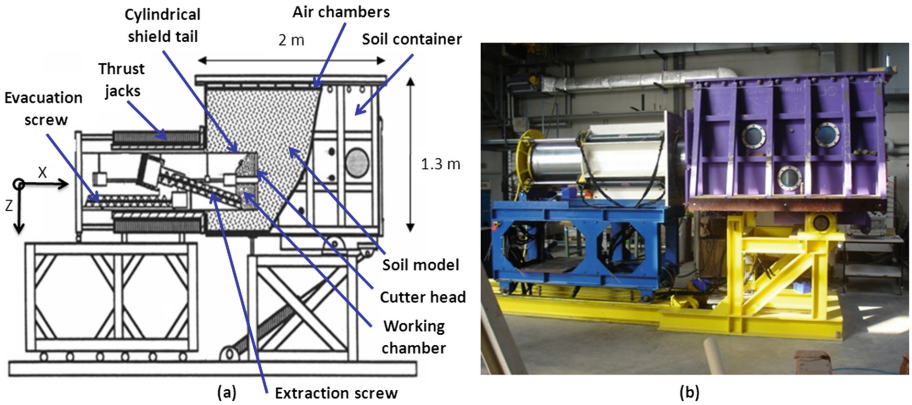


**Fig. 1.** Cross-sectional view (a) and photograph (b) of the ENTPE's model EPB TBM.

Tests comprise two phases: An excavation phase over a distance of one metre, followed by a failure phase with collapse or compression of the cutting face. During tests, machine and soil behaviour values are analysed in real time. The TBM values measured are similar to those for actual TBMs: cutting chamber pressure, cutting wheel torque, extraction screw torque, horizontal thrust, speed of progress and the extracted mass. Soil behaviour is interpreted using the following:

- 18 total stress sensors, allowing monitoring, in various locations, of stress values horizontally ($\sigma_x$ and $\sigma_y$) and vertically ($\sigma_z$), with the reference points (x, y, z) defined as shown in Fig. 1,
- 18 vertical displacement sensors on the surface,
- 15 horizontal or vertical displacement sensors within the soil formation.

As shown in Fig. 2, this instrumentation is located on the surface (P1), around a standard section of the tunnel (P2), ahead of the cutting face (P3) and in the overburden (P4). Location of the sensors is optimised in such a way as to minimise both reinforcement of the soil and interactions between sensors.

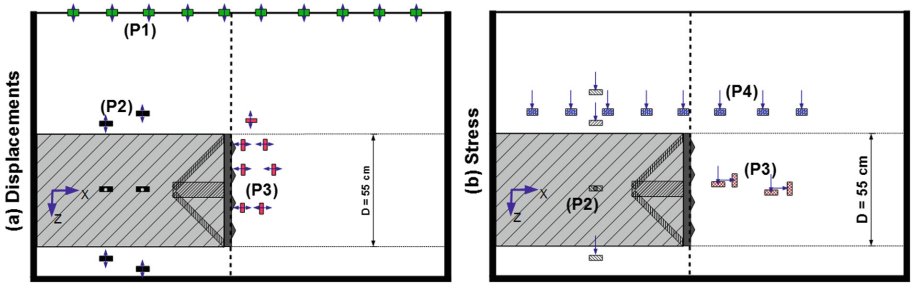


**Fig. 2.** Cross location of sensors during scale model testing.

Prior to each test, all sensors are calibrated in the planned test conditions (soil type, density and stress conditions). In addition, the extensive calibration campaign has allowed the influence of soil density, water content and grain size on stress measurements to be quantified. Details of these findings can be found in Berthoz et al. (2013). In summary, the degree of uncertainty for the stress measurements performed is approximately ±10% during scale model testing.

Tests are performed using Hostun S28 sand ($d_{50}$ = 0.35 mm) that is dry (purely frictional material) or slightly damp (cohesive-frictional material). The mechanical characteristics of these materials are estimated by means of triaxial rotational shear and trench stability tests. Young's modulus values range from 5 to 10 MPa and cohesion values range from 0 to 2.5 kPa. The materials are deposited in a loose state.

The choice of these modelling materials and their installation is designed in line with similarity laws (Mandel 1962), an essential condition for the observed phenomena to be representative. In practical terms, these laws dictate relationships between different scale factors, U*: quotients in which the scale model value is divided by the worksite value. In this instance, the tunnel diameter ratio is considered as the scale ratio for lengths, L*.

| Test | Young modulus $E_{50}$ (MPa) | Effective cohesion c' (kPa) | Cutting Wheel Open Ratio | Surface pressure $\sigma_s$ (kPa) | Face pressure over initial horizontal stress |
|---|---|---|---|---|---|
| MF9 | 5 | 0.0 | 35% | 17 | 3.5 |
| MF10 | 5 | 0.0 | 35% | 17 | 2; 1.3 |
| MF11 | 5 | 0.0 | 35% | 0 | 4.5 |
| MF13 | 5 | 0.0 | 35% | 0 | 1.6 |
| MC1 | 10 | 2.5 | 80% | 0 | n/a |
| MC2 | 10 | 2.0 | 80% | 0 | 3.3 |
| MC3 | 10 | 2.0 | 80% | 0 | 2.8 |
| MC4 | 10 | 1.5 | 80% | 0 | 0.6 |
| MC5 | 10 | 0.5 | 80% | 0 | 3.8; 2.6 |
| MC6 | 10 | 0.5 | 80% | 50 | 0.3 |
| MC7 | 10 | 0.5 | 80% | 50 | 0.5 |
| MC8 | 10 | 0.5 | 80% | 0 | 6.5; 3.5; 5.1 |
| MS1 | 5 ; 10 | 0 ; 3 | 35% | 0 | 11.6; 4.8 |
| MS2 | 5 ; 10 | 0 ; 3 | 35% | 0 | 3.4 |
| MS3 | 10 ; 5 ; 10 | 0.5 ; 0 ; 3 | 35% | 0 | 0.7 |

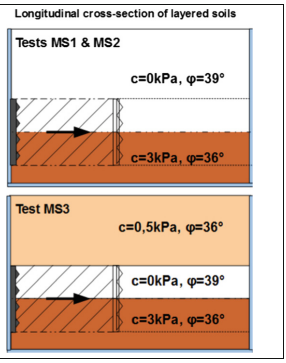


**Fig. 3.** Summary of scale model test conditions

Four tests in purely frictional soil (MF), eight tests in cohesive-frictional soil (MC) and three tests in layered soil (MS) are analysed in this article. The mechanical characteristics of the soils reproduced, and the mean face pressure during a balance regime $P_f$ applied during excavations, are summarised in Fig. 3.

## 3 Is the Physical Modelling Representative of Reality?

Observing similarity laws is a necessary but insufficient condition for there being no scale effects during scale model testing. Comparison with measurements performed at full scale is essential. The relevant analysis has been conducted here for TBM values and transverse settlement curves.

For TBM values, the mean operating and control parameter values measured for the scale model are consistent with those measured during works to extend Paris metro line 12 (Moyal et al. 2011) once scale factors have been taken into account (Table 1). Indeed, for an identical geotechnical context (in terms of cohesion, Young's modulus and overburden thickness), and applying scale ratios, it is interesting to note that the TBM control parameters (cutting wheel torque, thrust and pressure values in the cutting chamber) present similar values. In terms of driving parameters, the fact that the forward speed of the machine, and consequently the cutting wheel and extraction screw rotation speeds, are lower on the scale model than *in situ* does not invalidate the analysis, since the observed phenomena are stationary.

Concerning transverse settlement curves, scale model tests reveal Gaussian profiles (Berthoz et al. 2017), in line with the well-known observations of Peck (1969). In cohesive-frictional soils, the position of the inflection point i normalised by the tunnel diameter D, characterising the transverse extension of these curves, is in the neighbourhood of 0.6 (= 0.37 H/D where H is the depth of the tunnel axis); this is consistent with measurements performed on worksites in coarse-grained soil (0.25 to 0.45 H/D according to Mair and Taylor (1997)).

These two findings suggest that the phenomena observed with the scale model are indeed suitably representative.

**Table 1.** Average TBM values for the scale model and from Paris metro line 12 extension works.

| | | Scale factor (Sf) | Measured on L12 | L12 * Sf | Measured on ENTPE | Accordance |
|---|---|---|---|---|---|---|
| Geometry and soil | Diameter D (m) | L* = 0.06 | 9.17 | 0.55 | 0.55 | – |
| | Extraction screw diameter (m) | $L_{screw}$* | 0.9 | 0.054 | 0.08 | Yes |
| | Overburden C (m) | = L* | 13 | 0.8 | 0.60 | Yes |
| | E (MPa) | = L* | 120 | 7.2 | 5 to 10 | Yes |
| | c (kPa) | = L* | 30 | 1.8 | 0 to 2 | Yes |
| Driving parameters | Average forward speed (mm/min) | $= \sqrt{L^*}$ | 31 | 7.6 | 1.8–5.0 | Yes |
| | Cutting wheel rotational speed (rpm) | $= 1/\sqrt{L^*}$ | 1.4 | 5.7 | 1.3–5.0 | Yes |
| | Extraction screw rotational speed (rpm) | $= 1/\sqrt{L^*_{vis}}$ | 8.6 | 28.7 | 8–15 | NO |
| Control parameters | Torque on the cutting wheel (daN.m) | $= (L^*)^4$ | 700000–1200000 | 9–16 | 12–33 | Yes |
| | Total advancement thrust (daN) | $= (L^*)^3$ | 2535000 | 550 | 300–700 | Yes |
| | Average pressure in working chamber (kPa) | = L* | 175 | 10 | 3–20 | Yes |

## 4 Which Measures Should Be Favoured to Drive the Machine?

Proper operation of the TBM is essential to maintain suitable pressure at the cutting face and allow a 'balanced' regime (*i.e.* one resulting in limited, controlled soil deformation) to be achieved. Three conditions are required for this regime to be established:

- applying initial face pressure that is appropriate for the geotechnical context,
- maintaining a constant quantity of materials in the cutting chamber,
- applying a cutting wheel rotation speed that is enough to prevent the solid parts of the cutting wheel abutting the face.

Tests on scale models revealed that cutting wheel torque, hydraulic jack thrust and mean pressure values in the cutting chamber offer three relevant indicators with regard to the second condition specified above. Indeed, these parameters appear to be highly sensitive to variations in the cutting chamber fill level. The increase in cutting wheel torque in the event of under-extraction ($R < 1$, where R is the quotient of incoming and outgoing flow rates in the cutting chamber) shown in Fig. 4 is one example of this.

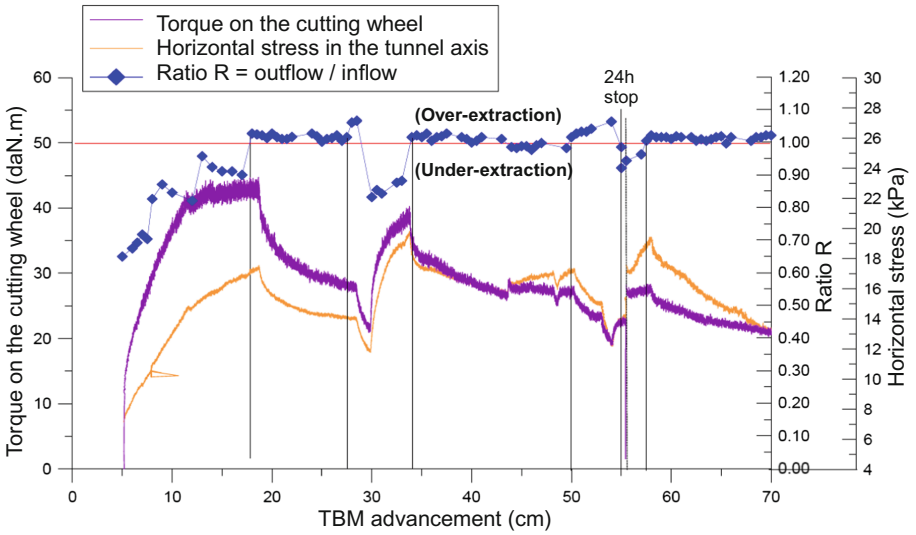


**Fig. 4.** Sensitivity of cutting wheel torque to the quantity of material in the cutting chamber.

## 5 What Is the Magnitude of the Impact of Mechanical Soil Properties and Face Pressure on Surface Settlement?

Estimation of surface displacement as a result of TBM excavation is a difficult but necessary stage if the corrective measures required for the preservation of neighbouring structures are to be implemented.

The first step is to identify the shape of the three-dimensional settlement curve generated. Scale model testing has confirmed that settlement curves follow a Gaussian distribution transversely (Peck 1969), and a cumulative Gaussian distribution longitudinally (Attewell and Woodman 1982).

The wide range of tests performed has also allowed settlement curve sensitivity to soil mechanical characteristics and to face pressure exercised by the TBM to be quantified (Fig. 5). The curves shown are "master" curves. Indeed, in view of the stationary nature of the phenomena observed, a single settlement curve plotted against distance from the machine may be drawn by taking the means of the measurements made by each sensor (Berthoz et al. 2017).

Other things being equal, increase in face pressure (a), and/or soil mechanical characteristics (b), therefore reduces the extent of the settlement generated. For instance, dividing by three the face pressure exercised between tests MF11 and MF13 for a purely frictional soil doubles surface settlement at a distance of one diameter from the rear of the face. This data will be useful when configuring specific digital models.

However, excessive face pressure results in increased settlement after the shield has passed (as in tests MC5 and MC8 in Fig. 5a). This observation may be explained by the stress release generated by face pressure in the overburden above the TBM crown, in similar fashion to the cutting face compression failure mechanisms presented above.

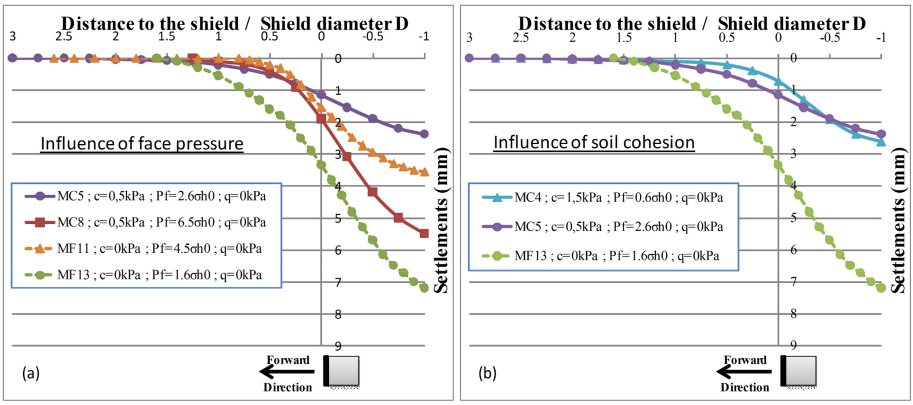


**Fig. 5.** Influence of the face pressure exercised by the TBM (a) and soil cohesion (b) on surface settlements.

## 6 What Is the TBM Zone of Influence?

Identifying the zone of influence of a tunnel boring machine is important in built-up areas, particularly in order to preserve neighbouring underground structures (tunnels, piles, networks, *etc.*). It was partly to address this issue that significant instrumentation was set up inside the reconstituted soils used for scale modelling.

The measurements carried out showed that horizontal displacement at the front and on either side of the TBM may be significant, and extend to a distance of up to one machine diameter during 'ideal' excavation regimes. For instance, Fig. 6 illustrates this for the longitudinal direction. On this illustration, it is also worth noting that the direction of the resulting displacements correlates closely with the face pressure exercised: if the latter is higher (or, contrariwise, lower) than the initial horizontal stress in the soil, compression (or, contrariwise, extrusion) is observed. The extent of these displacements also increases as the TBM approaches. However, the influence of soil mechanical characteristics on the extent of horizontal displacement at the face appears to be secondary compared to that of face pressure.

Vertical stress measurements ahead of the cutting face and within the tunnel overburden offer a second lesson about events adjacent to the TBM. Indeed, these measures reveal the existence of a decompressed area ahead of and above the cutting face, with the weight of the adjacent soil distributed longitudinally and transversely in an arch effect. This stress redistribution may have an impact on neighbouring underground structures and machine guiding.

These arch effects have been observed irrespective of the nature of the soil (*i.e.* even in dry sand soil), and irrespective of the face pressure exercised. This is shown by the progression of vertical stress measured 0.2 D above the tunnel axis in a range of scale model tests (Fig. 7). What is more, the greater the potential shear stress in the soil, the larger the extent of the decompressed area appears to be (Fig. 7a compared to b).

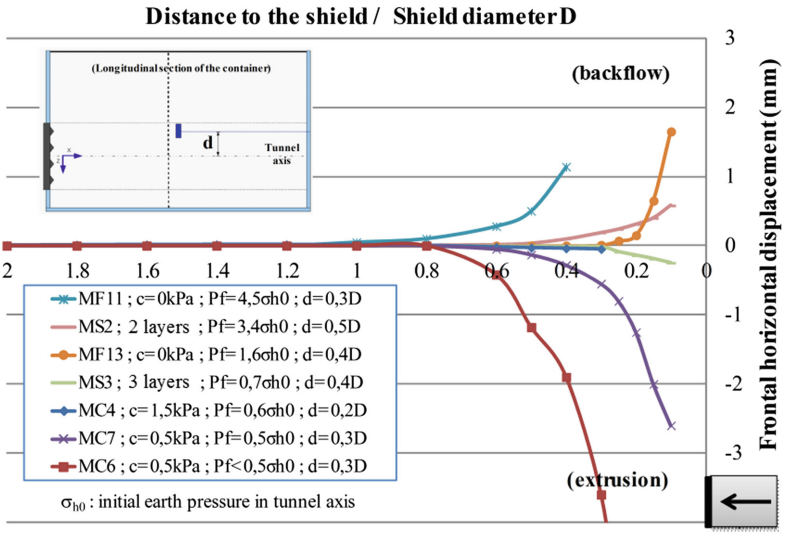


**Fig. 6.** Horizontal displacement values measured at the top of the cutting face.

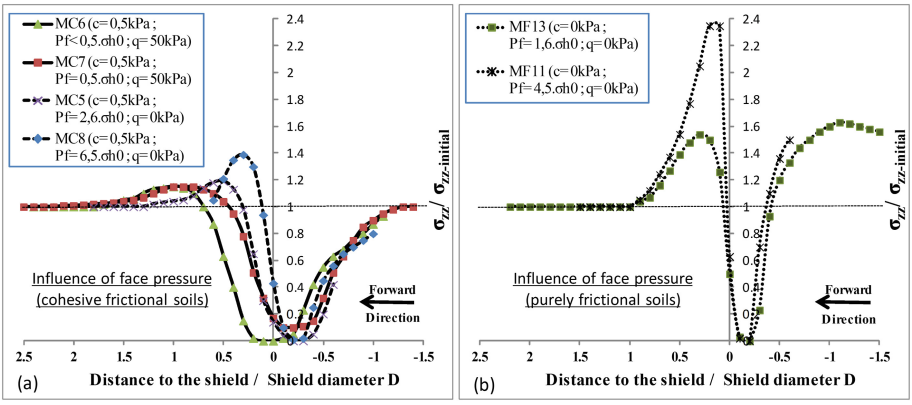


**Fig. 7.** Changes in vertical stress 0.2 D above the tunnel crown.

## 7 Conclusion

Physical modelling is a significant source of knowledge about the complex procedure of pressurised tunnel excavation. Several results obtained using a scale model of an earth pressure balance tunnel boring machine have been presented in this article. These results relate to soil/machine interaction behaviour during excavation.

The development of predictive digital models of the impacts generated by excavation using pressurised face tunnel boring machines may be pursued on the basis of the extensive databases established by means of physical modelling. In addition, these

developments should be compared with data from worksites. The authors thank RATP, XELIS and Chantiers Modernes BTP for sharing the data collected during Paris metro line 12 extension works. The French Tunnels Study Unit (CETU) and ENTPE will continue to collect and analyse such data during future worksites, in order to consolidate these approaches.

## References

Atkinson, J.H., Potts, D.M.: Subsidence above shallow tunnels in soft ground. JGED, ASCE GT4, pp. 307–325 (1977)

Attewell, P.B., Woodman, J.P.: Predicting the dynamics of ground settlement and its derivatives caused by tunneling in soil. Ground Eng. **15**(8), 13–22 (1982). London

Berthoz, N., Branque, D., Subrin, D., Wong, H., Humbert, E.: Face failure in homogeneous and stratified soft ground: theoretical and experimental approaches on 1 g EPBS reduced scale model. TUST **30**, 25–37 (2012)

Berthoz, N., Branque, D., Wong, H., Subrin, D., Humbert, E.: Stress measurement in partially saturated soils and its application to physical modeling of tunnel excavation. CGJ **50**, 1077–1087 (2013)

Berthoz, N., Branque, D., Wong, H., Subrin, D.: TMB-soft ground interaction: experimental study on 1 g EPBS reduced scale model. TUST (under review) (2017)

Lee, C., Chiang, K.: Responses of single piles to tunnelling-induced soil movements in sandy ground. CGJ **44**, 1224–1241 (2007)

Mair, R.J.: Centrifugal modelling of tunnel construction in soft clay. Ph.D. thesis, Cambridge University (1979)

Mair, R.J., Taylor, R.N.: Bored tunneling in the urban environment: State-of-the-art report and theme lecture. In: 14th ICSMGE, pp. 2353–2385 (1997)

Mandel, J.: Scale model testing of soil mechanics – similarity study. Revue d'industrie minérale **9**, 611–620 (1962)

Messerli, J., Pimentel, E., Anagnostou, G.: Experimental study into tunnel face collapse in sand. In: 7th ICPMG, Zurich, Switzerland (2010)

Moyal, P., Beaugendre, N., Piljan, J.L., Lechantre, G., Gauthier, P.: Extension of Paris metro line 12 from Porte de la Chapelle to Mairie d'Aubervilliers). In: Proceedings of AFTES International Congress, Lyon, France (2011)

Nomoto, T., Imamura, S., Hagiwara, T., Kusakabe, O., Fujii, N.: Shield tunnel construction in centrifuge. JGGE **125**(4), 289–300 (1999)

Peck, R.B.: Deep excavations and tunneling in soft ground. In: Proceedings of the 7th International Conference on Soil Mechanics and Foundation Engineering, Mexico City, State of the Art Volume, pp. 225–290 (1969)

Xu, Q., Zhu, H., Ding, W., Ge, X.: Laboratory model tests and field investigations of EPB shield machine tunneling in soft ground in Shanghai. Tunn. Undergr. Space Technol. **26**, 1–14 (2011)

# Influence of Boundary Conditions on the Behavior of Infilled Frames

Quoc Khanh Le Dinh(✉) and Thanh Cong Bui

Faculty of Civil Engineering, Ho Chi Minh City University of Technology, Ho Chi Minh City, Vietnam
dlkquoc@yahoo.com, bcthanh@yahoo.com

**Abstract.** This paper focuses on the influence of the contact surfaces between autoclaved aerated concrete blocks (AAC) and the surrounding reinforced concrete frame. From the experimental results and from the model proposed by the authors, different behaviors between ideal and real models have been analyzed and compared given a variety of aspects: the stiffness degradation, the drift, the cracking peak, the strength, the ductility and the energy dissipation. The research aims to provide parameters for calculating work approaching the actual behavior to obtain safer and cost-saving construction.

**Keywords:** Infilled frames · Infilled masonry wall · Ideal model · Real model

## 1 Introduction

In recent years, traditional clay bricks have been proposed to be replaced by AAC blocks in Vietnam. Despite the instructions outlined in Vietnam Standards (2011), there are many defects with respect to their application in infilled frames where cracks form (Fig. 1) and affect the structure's aesthetics. In addition to the AAC block properties, such as the elastic modulus or the compression capacity, the boundary condition between the infilled masonry wall and the surrounding frames (Fig. 2), which affects the frame behavior, needs to be thoroughly investigated.

**Fig. 1.** The cracks of infilled AAC masonry wall

According to Fig. 3, which shows the stages of constructing a masonry wall, deflection Δ is noted to occur due to the floor-beam self-weight after the formworks are removed (Fig. 3b). Therefore, no load is imposed on the infilled masonry wall when it is installed.

© Springer Nature Singapore Pte Ltd. 2018
H. Tran-Nguyen et al. (eds.), *Proceedings of the 4th Congrès International de Géotechnique - Ouvrages -Structures*, Lecture Notes in Civil Engineering 8,
DOI 10.1007/978-981-10-6713-6_91

**Fig. 2.** The gaps between the infilled AAC masonry wall and the upper beam

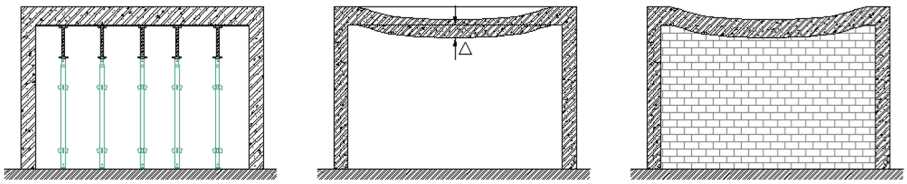

**(a).** Before removing the formworks **(b).** After removing the formworks **(c).** Installing the infilled masonry wall

**Fig. 3.** The stages of the infilled masonry wall construction

Additionally, to prevent failure due to stability when the mortar does not achieve sufficient strength, at least two stages are required when constructing an infilled masonry wall. Therefore, only half the wall's weight is acting on the beam in the first stage; then, the weight is transferred to the constructed wall in the lower story (Fig. 4a). In the second stage, part of the wall built in the first stage achieves its strength and takes the weight of the wall, which is then transferred to the two ends of the beam, as they have a greater stiffness than the middle section, and finally to the columns (Fig. 4c). Therefore, if the construction of the infilled masonry wall begins from the top story and then proceeds to a lower story; the loads transferred to the beam from the stories above are negligible.

Therefore, there is little self-weight acting vertically from the upper beam on the masonry wall. Conversely, the main forces acting on the frame include lateral wind and earthquake forces (Fig. 5), which govern the infilled frame behavior.

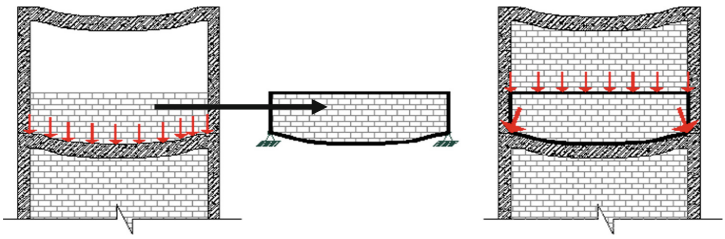

**(a).** Stage 1 of infilled masonry wall construction **b).** The constructed wall has achieved its strength **(c).** Stage 2 of infilled masonry wall construction

**Fig. 4.** The stages of constructing an infilled masonry wall and the load imposed upon the beam

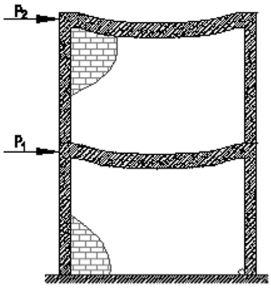


**Fig. 5.** Infilled frame under lateral actions

Structurally, the infilled frame can be considered a composite structure consisting of the masonry wall and the surrounding frame where dowel bars are installed to ensure the wall lies within the vertical frame plane. According to the experiment by Kwan and Liauw (1984), the dowel bars have little influence on the structure behavior, and the contact surfaces between the masonry wall and frames govern the infilled frame behavior.

## 2 The Analytical Model

Some ideal models have been proposed by Holmes (1962), Smith (1969), Mainstone (1971) and Kappos et al. (1998) that assume perfect contact surfaces between the infilled masonry wall and the frame by inserting an equivalent single strut model to replace the infilled masonry wall. Quoc et al. (2016) addressed this problem using a multi-strut model with a gap-element to consider the gap's effect on infilled masonry behavior. The equivalent width and location of the struts in the multi-strut model are determined by formulas (1) to (7) as follow:

$$W_{mlt} = 0,5(W_{e,icm} + W_{m,icm}) \tag{1}$$

$$W_{e,icm} = \frac{\alpha_h.l'}{\sqrt{(h' - \alpha_h)^2 + l'^2}} \tag{2}$$

$$W_{m,icm} = \frac{3\alpha_h l' + 2.tg\varphi\left((h' - \alpha_h)^2 + l'^2\right)}{3\sqrt{(h' - \alpha_h)^2 + l'^2}} \tag{3}$$

$$\alpha_h = \arccos(\frac{C}{m}) \tag{4}$$

$$C = \frac{1}{\sqrt{\left(\frac{2(lJ_c + 6hJ_d)}{3mh^2J_d} - 1\right)^2 + 1}} \tag{5}$$

$$m = \sqrt[4]{\frac{t.k_0}{4EJ_c}} \tag{6}$$

$$\begin{cases} X_n = n.\frac{W_{mlt}}{\sin\theta} \\ X_n < l \end{cases} \text{ and } \begin{cases} Y_m = m.\frac{W_{mlt}}{\cos\theta} \\ Y_m < h \end{cases} \tag{7}$$

where

$W_{e,icm}$ and $W_{m,icm}$ are the equivalent widths at the end and middle of the strut, as shown in Fig. 6; $\alpha_h$ is the vertical contact length between the frame column and the infilled masonry wall; $\alpha$ is the force transfer angle of the AAC (masonry wall material property); h' and l' are the height and width of the infilled masonry wall; h and l are the story length and span of the reinforced concrete frame; $J_c$ and $J_d$ are the moment of inertia of the column and beam; t is the thickness of the infilled masonry wall; E is the elastic modulus of the reinforced concrete frame; $k_0$ is the Winkler constant of the infilled masonry wall; $X_n$ is the location of the struts in the multi-strut model in the x-direction; and $Y_m$ is location of the struts in the multi-strut model in the y-direction (Fig. 7).

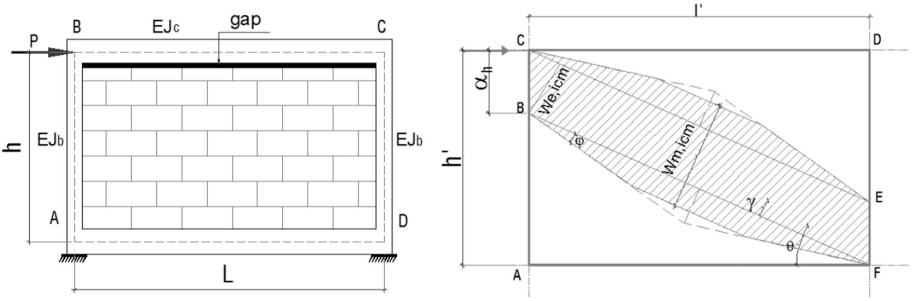


**Fig. 6.** The equivalent single strut model (Quoc et al. 2016)

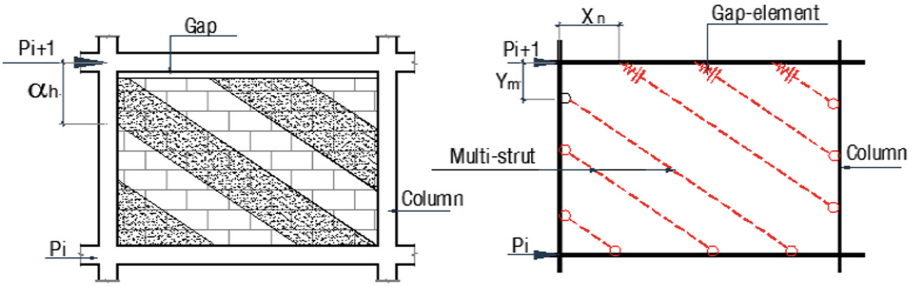


**Fig. 7.** The multi-strut model (Quoc et al. 2016)

## 3 The Experimental Model

The tested models were reinforced concrete infilled frames with a scale ratio of 1:2. The masonry wall on the upper beam was replaced by the precast concrete block with an equivalent weight (Fig. 8c).

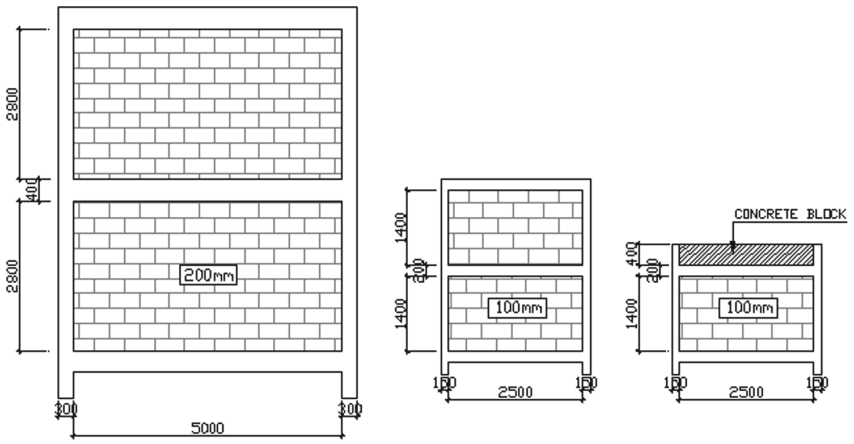


**(a).** The real model **(b).** The scale model **(c).** The testing model

**Fig. 8.** The experimental model

Three specimens of the infilled frame were considered:

Model $K_1$ – An ideal model with tightly filled mortar where no gap at the top surface of the frame was allowed (Fig. 9a).

**(a).** The ideal model **(b).** The real model

**Fig. 9.** The boundary between the upper beam and the infilled masonry wall

Model $K_2$ – A real model where the gap at the top was 10 mm (Fig. 9b).
Model $K_3$ – A bare frame.

The properties of the reinforced concrete infilled frame are as follows:

The concrete's aggregate was 1 × 2 mm in size with a mean compressive strength of $f'_c$ = 42.1 MPa;
Long rebar 4D12 (beam) with a yield strength of $f_y$ = 454 MPa and an ultimate strength of $f_u$ = 632 MPa;
Long rebar 4D10 (column) with a yield strength of $f_y$ = 489 MPa and an ultimate strength of $f_u$ = 586 MPa;
Stirup D4@75 for the beam and D4@50 for the column with a yield strength of $f_y$ = 333 MPa;
AAC blocks with a unit weight of $g_{AAC}$ = 7.5 kN/m3 and a unit compressive strength of $f_{AAC}$ = 3.5 MPa; the prism compressive strength is $f_{p,m}$ = 3.15 MPa;
Mortar with compressive strength of $f_{cm}$ = 11.9 MPa.

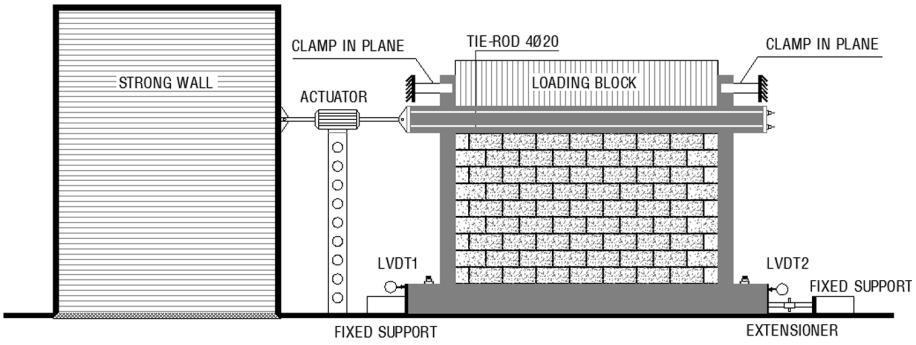


**Fig. 10.** The setup of test model

The setup of the test model is illustrated in Fig. 10, and the cyclic loads used were taken from American Concrete Institute Standards ACI 374.2R-13 (Fig. 11).

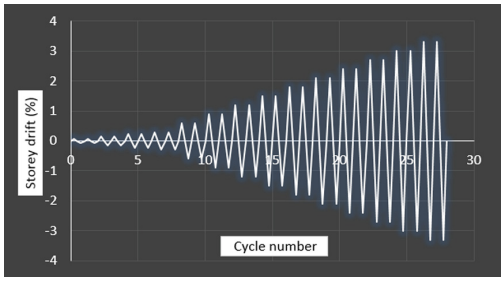


**Fig. 11.** Loading cycles in accordance with ACI 374.2R – 13 Quoc et al. (2016)

The summary of the experimental results is included in Table 1, and the lateral displacement and ductility are in Table 2, whereas Figs. 12(a, b, c) and 13 show the load-lateral displacement curve, the failure patterns of the infilled masonry walls (IMWs), and the energy dissipation capacity due to the hysteretic behavior.

**Table 1.** Summary of experimental results

| Model | Cracking load of IMWs (kN) | Drift at cracking of IMWs (%) | Cracking load of frame (kN) | Drift at cracking of frame (%) | Maximum load (kN) | Drift at maximum load (%) | Initial stiffness (kN/mm) | Failure pattern |
|---|---|---|---|---|---|---|---|---|
| $K_1$ | 39.95 | 0.23 | 75.1 | 0.72 | 90.38 | 1.96 | 12.08 | Crushing at the corners |
| $K_2$ | 40.2 | 0.37 | 55.5 | 0.78 | 74.64 | 1.91 | 9.96 | Crushing at the corners |
| $K_3$ | | | 14.2 | 0.64 | 26.59 | 2.70 | 2.43 | |

**Table 2.** Lateral displacement and ductility

| Frame model | Displacement (mm) | | Ductility |
|---|---|---|---|
| | At yield | At 80% Pmax | |
| K1 | 6.67 | 48.13 | 7.21 |
| K2 | 12.34 | 53.90 | 4.37 |
| K3 | 10.40 | 55.04 | 5.29 |

### 3.1 Discussion

$K_1$'s (ideal model) initial stiffness was 1.21 times greater than $K_2$ (real model) because of the perfect contact surface between the wall and the frame. However, while having only 3 contact surfaces, $K_2$'s stiffness was much greater (4.1 times) than $K_3$'s stiffness (bare frame).

The horizontal stiffness of the frames is governed by the infilled masonry wall (IMW) stiffness. Therefore, the cracking of the IMW in $K_1$ occurred earlier than $K_2$'s because $K_1$'s load adsorption was much more than $K_2$.

The horizontal load-bearing capacity of frame $K_2$ (74.64 kN) was 1.21 times less than $K_1$'s (90.38 kN) meaning that the influence of the contact surface (good or lack fit) on the load-bearing capacity was significant.

The displacement ductility of $K_2$ compared to $K_1$ was 1.65 times smaller, and the energy dissipation capacity of $K_2$ was less than $K_1$'s (Fig. 13); thus, an infilled masonry wall with good contact boundaries would have a greater energy dissipation capacity (Fig. 14).

## 4 Comparision Between the Ideal and Real Model

The parameters of the multi-strut model for the infilled masonry wall models $K_1$ and $K_2$ are listed in Table 3 according to Quoc et al. (2016) and consist of 3 struts with an equivalent width $W_{mlt}$. The nonlinear static analysis results (push-over) from SAP2000 V15 are presented in Fig. 15.

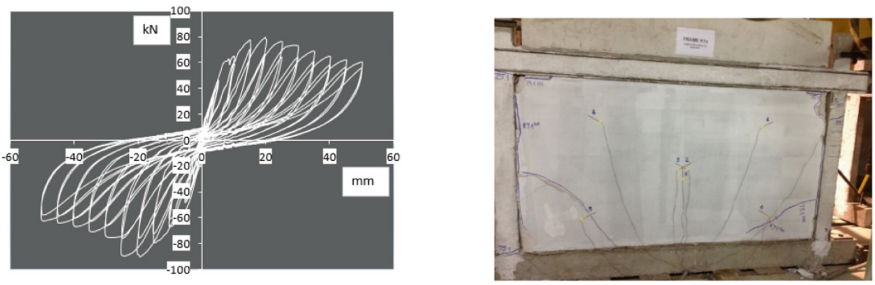


**(a).** Infilled frame $K_1$ without any gap

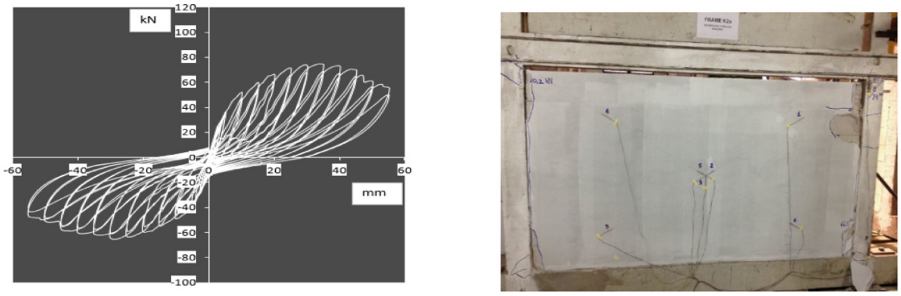


**(b).** Infilled frame $K_2$ with the gap at the top

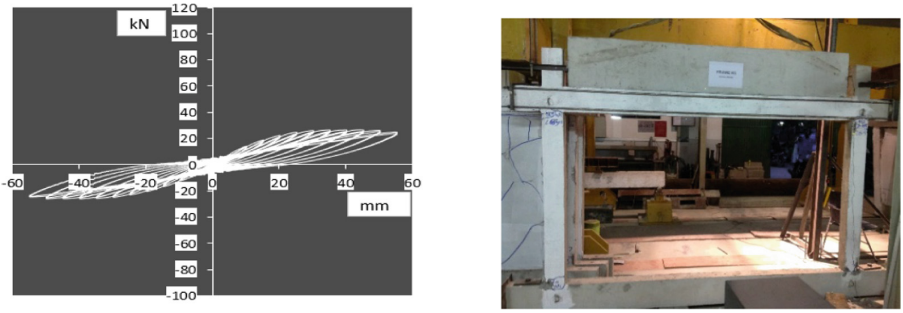


**(c).** Bare frame $K_3$

**Fig. 12.** Load-lateral deflection curves under cyclic loading and the failure patterns of the experimental models

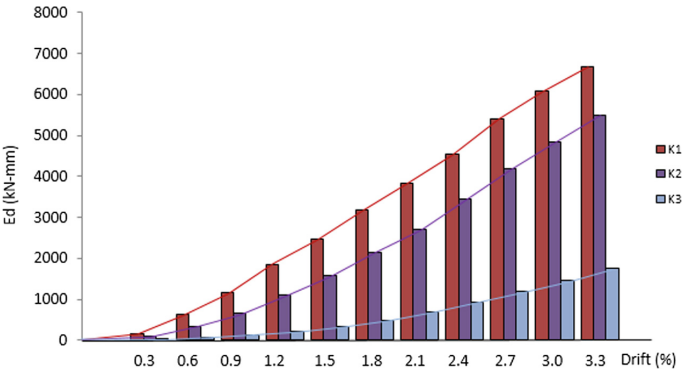


**Fig. 13.** Cumulative energy dissipation diagram

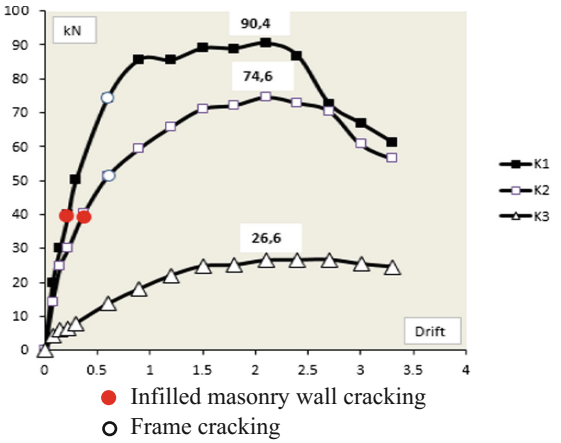


**Fig. 14.** Horizontal loading versus drift of the experimental models

**Table 3.** Parameters equivalent multi-strut

| Model | n | $\alpha_h$ | $\alpha_l$ | $W_e$ | $W_m$ | $W_{mlt}$ |
|---|---|---|---|---|---|---|
| K1 | 3 | 1.168 | 0.382 | 0.58 | 0.78 | 0.68 |
| K2 | 3 | 1.168 | 0 | 0.56 | 0.69 | 0.62 |

## 4.1 Discussion

For $K_1$'s ideal model, the analytical results of the multi-strut model (Quoc et al. 2015) corresponded to the test results in both the elastic and inelastic stage compared with the other models from Ibarra et al. (2005), Smith (1969) and Mainstone (1971). Moreover, the errors in the horizontal load-bearing capacity $P_{max}$ between the multi-strut model

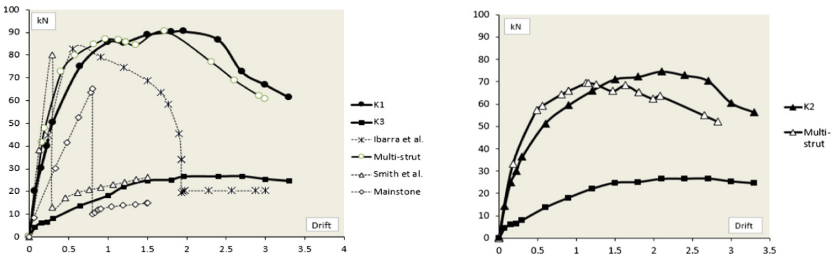


**(a).** Frame $K_1$: Multi-strut model versus other models and experimental results **(b).** Frame $K_2$: Multi-strut model versus experimental results

**Fig. 15.** Horizontal loading versus drift in the models and the experimental results

and test result was 0.1% (90.43 kN as opposed to 90.38 kN), which demonstrates excellent agreement.

For $K_2$'s real model, the errors in $P_{max}$ between the multi-strut model and the test result was 9.1% (68.41 kN as opposed to 74.64 kN), which is within the acceptable range. The advantage of the multi-strut model is its ability to describe real-life behavior, which includes the presence of the gap at the top of the frame, whereas other models are limited in this respect.

The horizontal load-bearing capacity $P_{max}$ of $K_1$ and $K_2$ was 3.4 times and 2.8 times greater than $K_3$'s capacity (bare frame), respectively, confirming that the stiffness of the infilled masonry wall should be included in the calculation and design.

## 5 Conclusion

In reality, it is almost impossible for an ideal condition such as frame $K_1$ to exist, demonstrating the importance of studying the behavior of a real system, i.e., frame $K_2$, to provide precise calculations and predictions. The frame cracking load and maximum horizontal load of the real model ($K_2$) are much smaller than in the ideal model ($K_1$). Evidently, the boundaries between the frame and the infilled masonry wall plays a critical role.

The multi-strut model, which transforms an infilled masonry wall into diagonal struts with a gap-element connection, demonstrated the interaction between the frame and the infilled masonry wall, resulting in similar calculations and the determination of a horizontal load-bearing capacity (peak value) that can be used during the design process.

## References

ACI 374.2R-13: Guide for testing reinforced concrete structure elements under slowly applied simulated seismic loads, Farmington Hills, MI, USA (2013)

CSI (Computer and Structure, Inc.): Analysis Reference Manual for SAP2000, Berkeley, CA, USA (2013)

Holmes, M.: Steel frames with brickwork and concrete infilling. Proc. Inst. Civ. Eng. **19**(4), 473–478 (1961)

Ibarra, L.F., Medina, R.A., Krawinkler, H.: Hysteretic models that incorporate strength and stiffness deterioration. Earthq. Eng. Struct. Dyn. **34**(12), 1489–1511 (2005)

Kappos, A.J., Stylianidis, K.C., Michailidis, C.N.: Analytical models for brick masonry infilled R/C frames under lateral loading. J. Earthq. Eng. **2**(1), 59–88 (1998)

Kwan, K.H., Liauw, T.C.: Non-linear analysis of integral infilled frames. J. Struct. Eng. **6**(3), 223–231 (1984)

Mainstone, R.J.: On the stiffnesses and strengths of infilled frames. Proc. Inst. Civ. Eng. **9**(2), 57–90 (1971)

Quoc, D.L.K., Thanh, B.C., Yen, N.V.: A macro-element model for masonry-infilled structural frames. Struct. Build. **169**(2), 108–120 (2016)

Smith, B.S., Carter, C.A.: Method of analysis for infilled frames. Proc. Inst. Civ. Eng. **44**(4), 31–48 (1969)

TCVN 7959-2011: Lightweight concrete, autoclaved aerated concrete block (AAC), Hanoi, VN (2011)

# In-Plane Behavior of Seismically Damaged Clay Masonry Walls Repaired with External TRC

Thi-Loan Bui[1], Xuan-Huy Nguyen[1(✉)], and A. Si Larbi[2]

[1] Department of Construction Engineering, University of Transport and Communications, 3 Cau Giay, Lang Thuong, Dong Da, Ha Noi, Vietnam
Nguyenxuanhuy@utc.edu.vn

[2] Laboratoire de Tribologie et de Dynamique des Systèmes (LTDS), UMR 5513, Université de Lyon, Ecole Nationale d'Ingénieurs de Saint-Etienne (ENISE), 58 Rue Jean Parot, 42023 Saint-Etienne Cedex 2, France

**Abstract.** Recently earthquakes with quite high magnitude have continuously occurred in the Vietnam territory which cause the dangerous to masonry buildings. The stringent seismic design requirements for masonry structure will be therefore considered in the construction field of Vietnam. The paper, which an exploratory study, focuses on the behavior of clay solid brick masonry walls, especially walls repaired on both sides with TRC (Textile Reinforced Concrete) composite under cyclic in-plane loading condition. This work is the first step towards defining the potentiality including both technical and scientific aspects of using TRC in seismic strengthening and repairing the masonry structure in Vietnam. Thus, an experimental program has been performed at laboratory scale. Two walls have been submitted for cyclic shear-compression tests in-plane solicitation: the first one (unreinforced wall) is tested to the pre-defined damage level and failure mode, and then repaired with TRC strips as the second one. A comparative study on global behavior and on mechanism of failure is performed and, although the limited number tests, highlights that, thanks to the contribution of TRC strips, the wall's residual strength and deformation ability are upgraded. In addition, compared to the unreinforced specimen, the repaired one is more stable strength and stiffness change at later stages. Furthermore, the TRC strips help to reduce the risk of out-of plane failure. However, it seems to be that, the low reinforcement ratio and (or) the relatively unsuitable formulation of mortar, especially the grain size, in TRC limit its efficiency in reinforcing solutions.

**Keywords:** Earthquake · Masonry wall · Strengthening · TRC · In-plane behavior

## 1 Introduction

In Vietnam, the clay solid brick masonry structure is widely used for the construction. However, this type of structure can suffer extensive damage under seismic loading [1, 2]. Solutions for repairing or strengthening masonry structures are necessary due to

© Springer Nature Singapore Pte Ltd. 2018
H. Tran-Nguyen et al. (eds.), *Proceedings of the 4th Congrès International de Géotechnique - Ouvrages -Structures*, Lecture Notes in Civil Engineering 8,
DOI 10.1007/978-981-10-6713-6_92

several recent earthquakes in this country. FRP materials have emerged as promising alternative materials for strengthening and rehabilitation of structures. On the other hand, FRP can be potentially damaged while used improperly in a number of harmful environments. The use of FRP reinforcement is also not recommended for structures in which fire resistance is essential to maintain structural integrity. These limitations are related to the epoxy matrix used to embed and bond the fibers. Substituting the epoxy matrix with a cementitious matrix appeared to be the most reasonable solution to improve the overall performance of externally-bonded composite systems.

The textile reinforced concrete (TRC) composites, which combine a suitable fine-grained mortar with the latest generation of textile fabrics, would benefit from promotion. The efficiency of TRC for strengthening masonry structures has recently been investigated [3–9]. However, the research of TRC in the repairing of clay solid brick masonry structure is limited. This paper focuses on the behavior of clay solid brick masonry walls, especially walls repaired on both sides with TRC composite under cyclic in-plane loading condition. The experimental study has been performed at laboratory in University of Transport and Communications, Vietnam. Two walls have been submitted for cyclic shear-compression tests in-plane solicitation: the first one (unreinforced wall) is tested to the pre-defined damage level and failure mode, and then repaired with TRC strips as the second one. A comparative study on global behavior and on mechanism of failure is performed and, although the limited number tests, highlights that, thanks to the contribution of TRC strips, the wall's residual strength and deformation ability are upgraded. In addition, compared to the unreinforced specimen, the repaired one is more stable strength and stiffness change at later stages.

## 2 Experimental Program

### 2.1 Masonry Wall

The dimensions of the masonry wall are 1160 mm long, 1275 mm high and 105 mm thick. The specimens have been built from clay block units. These blocks (220 mm × 105 mm × 55 mm) are assembled with a mortar composed of Portland cement M75. This 1 $m^3$ mortar composed of Portland is composed by 320 kg of cement PCB30, 106 $m^3$ sand and 260 L of water. The masonry wall was cast with the reinforced concrete block of 300 mm thickness at the base. A reinforced concrete beam on top of the wall was used to apply the horizontal and vertical loading, Fig. 2.

### 2.2 Reinforcement

#### 2.2.1 Strengthening Material TRC

TRC consists of fabrics made of single continuous fibres- the so-called filaments. For TRC, currently carbon or alkaline resistant (AR) glass fibres are used. In the course of works performed by Contamine et al. [10], it has been possible to select a composite, whose components are listed in Table 1, that results from a compromise between all of the aforementioned parameters, including workability and thixo-tropy (to apply strengthening materials more easily).

**Table 1.** Mix design for TRC composite

| Textile | | Mortar** | |
|---|---|---|---|
| Nature of fibres | Verre-AR | Grain size | <1 mm* |
| TEX | 1200* | Silica-fume | Sika PP1* |
| Fibre diameter | 19 μm* | Fly-ash | Pha lai * |
| Number of filament/yarn | 1600* | Additive | Sika viscocrete 3000-20 M |
| Knitted grid size | 3 mm × 5 mm* | Ciment PC40 | But son |
| Tensile strength (yarn) | 1102 MPa* | Compressive strength | 60 MPa* |
| Young modulus | 74000 MPa* | Young modulus | 1700 MPa* |

* Provided properties; ** Laboratory characterisation

### 2.2.2 Anchorages

To reduce or ideally remove the premature failure by overturning effects due to lateral loads on walls and to best maximize the potential of each reinforcement solution by a priori improving its efficiency, a connector, in the form of an anchorage (see Fig. 1), has been introduced between walls (on their lower part, on both sides) and their foundation footings. Given the existing solutions and their well-established performances (easy application and high strength), only connection solutions based on carbon fibres and an epoxy resin have been considered. The anchorage system (MAPEI) is an anchor made from monodirectional carbon fibres with at least 36 yarns, each including 12,000 fibres. The anchorage strength given by the manufacturer is 30 kN at the ultimate limit state.

**Fig. 1.** Description of a MAPEI anchor

### 2.2.3 Strengthening Configurations

The strengthening configurations have been proposed taking into account the failure mode. It was observed that the flexural horizontal cracks located at two faces of the wall. However, it is the first time we work with this type of reinforcing composite material (TRC) with limited experiences, especially about the technic of production the mortar in TRC. We decided therefore to test only one strengthening configuration in this study.

According to this objective, the masonry wall has been reinforced by a TRC layer over a width of 200 mm along the entire height of the masonry on each side of both faces (Fig. 2). The anchorage system (MAPEI) is an anchor made from monodirectional carbon fibres with at least 36 yarns, each including 12,000 fibres. The anchorage strength given by the manufacturer is 30 kN at the ultimate limit state.

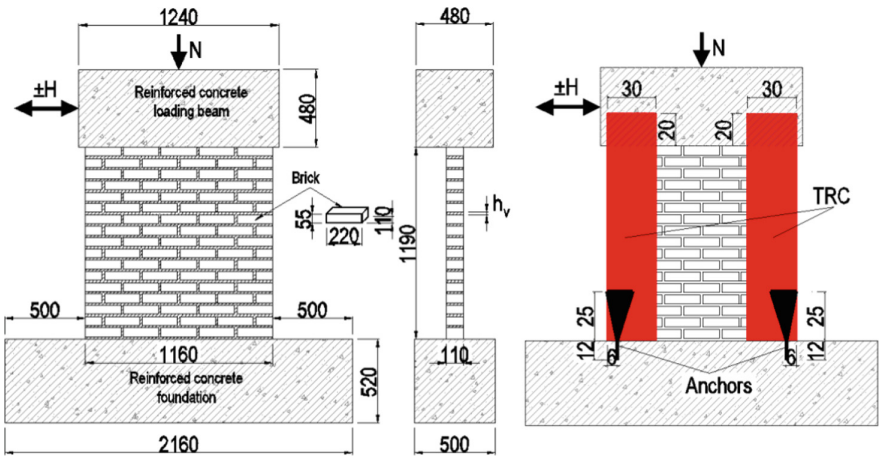


**Fig. 2.** Unreinforced masonry wall (URW) and TRC-repaired wall (TRCRW)

### 2.2.4 Application of Strengthening Systems and Anchorages Placement

TRC reinforcements have been laid up. First of all, wall surfaces have been cleaned to remove dust and loose materials, which could disturb the bond between the masonry wall and its reinforcements. The application of a strengthening system first involves covering the wall with a layer of mortar. Then, the textile is placed along the wall and is pressed against the resin or mortar. A second layer of resin or mortar is eventually applied to ensure fabric impregnation. For walls reinforced with several layers, the last two steps are repeated as necessary. These reinforcements are anchored to the foundation because of the CFRP structural connections. An anchorage anchor is composed of two parts: the anchorage strictly speaking and the "whip". The anchorage that is first impregnated with epoxy-resin is inserted into holes that have been drilled before in the reinforced concrete footing and is filled with resin. The remaining part of the anchor (the whip) is deployed similar to a fan on the wall, and resin is again applied so that the adhesive completely penetrates into the fibres. This splayed part ensures the connection of strengthening materials with the masonry wall.

## 2.3 Testing Procedure

Specimens have been subjected to a combination of cyclic shear-compression tests in-plane solicitation. The vertical loading is centered and applied by means of a hydraulic actuator. This actuator is combined with a force sensor that is placed on the reinforced concrete beam. These devices are held by a steel profile connected to the strong floor through steel rods, which allows us to control the applied vertical load (Fig. 3).

The vertical load is should represent the weight of the upper floors. In literature, this value varies greatly and depends on the masonry compression strength (with large ranges from 2.5% to 25% of the masonry compression strength). In this study, a value of approximately 10% of the masonry compression strength has been adopted. It corresponds to a mean vertical stress of 0.25 MPa.

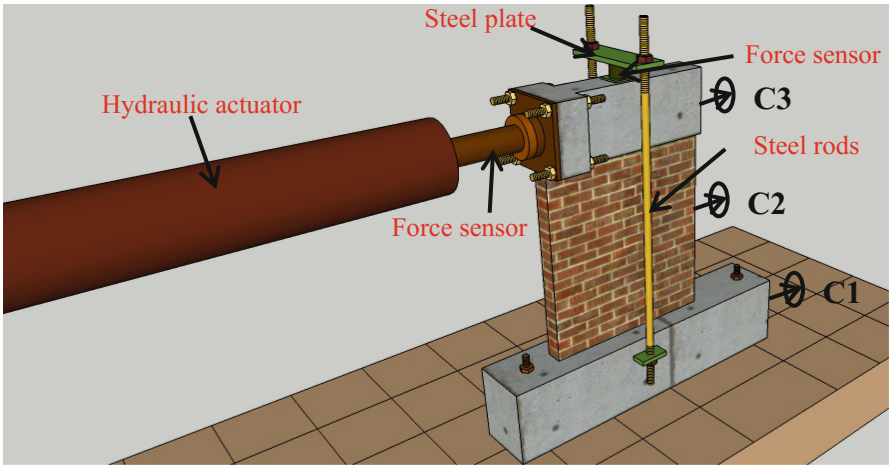


**Fig. 3.** Test set-up

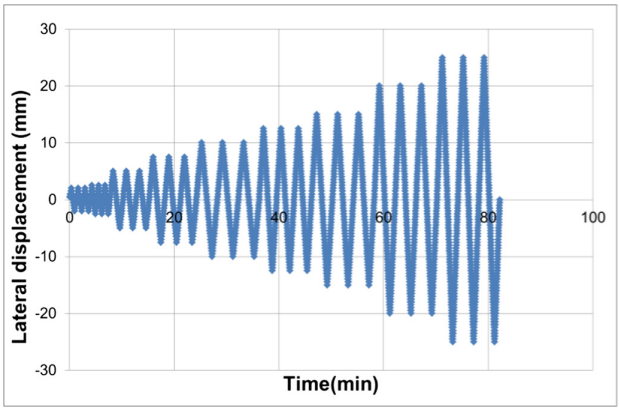


**Fig. 4.** Loading scheme

According to Tomazevic [11], failure is ascertained when horizontal load falls by 20%. The horizontal forces were applied under controlled cyclic displacement until horizontal load falls by 20%. The actuator is operated in displacement control to apply quasi-static, reserved cyclic loading to the specimen using incremental displacement amplitude. To reflect the cumulative damage, 3 cycles are repeated at each displacement amplitude. Figure 4 presents the loading sequence adopted for the test.

In addition to the force sensors that have been presented before in the description of the test set-up, for the sake of clarity, several displacement transducers complete the instrumentation. The displacement transducer (LVDT) C1 assumes that the reinforced concrete block at the base has no slips. To have more information of the displacement of the wall, the LVDTs C2 and C3 was placed at the middle and at the top of this wall, respectively.

## 2.4 Experimental Results

### 2.4.1 Hysteretic Response Curves

The hysteretic responses of all the tested specimens are shown in Fig. 5. These responses reflect the detailed relation of corresponding displacement and lateral force at the head of wall throughout the loading process. During the initial loading stage, the deformation of the specimens is small and the stiffness keeps constant. The hysteretic curves are approximately in a linear elastic state. After cracking occurs, the loop turns into an inverse "S" shape and gradually tilts to the horizontal axis.

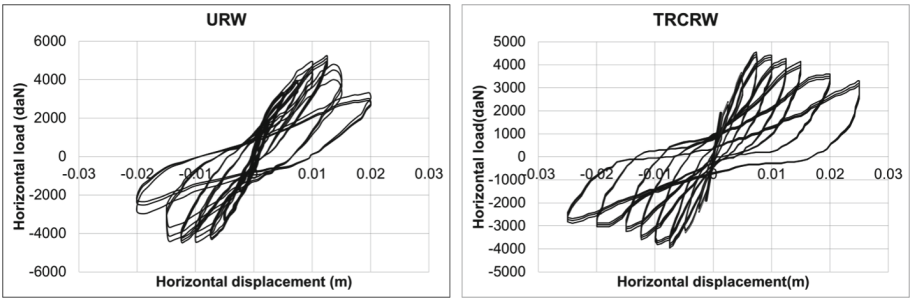


**Fig. 5.** Hysteresis loops of reference and repaired walls

### 2.4.2 Envelope Curves

The envelope curve was obtained from these hysteretic response curves. In Fig. 6, the specimens' envelope curves for the first loading cycle are presented. The unbalanced damage of the specimens during the tests (see below) is indicated by these unsymmetrical curves.

It must be noted that, compared to the repaired specimen (TRCRW), the reference one (URW) has unstable deformation and less loops with a relatively steep decline of

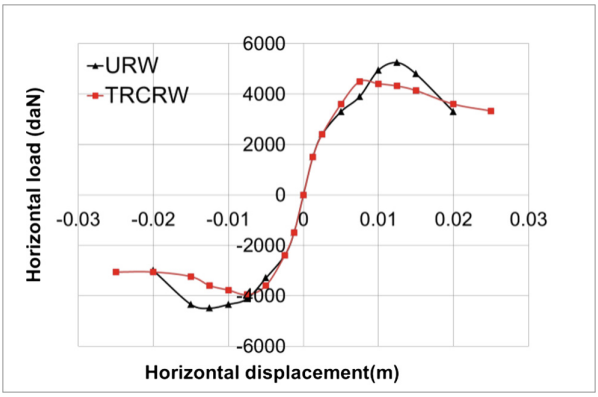


**Fig. 6.** Envelope curves for reference and retrofitted walls

strength at later stages. Thanks to the contribution of TRC strips, the repaired wall show a relatively stable strength change.

On the other hand, in comparison of two envelope curves (see Fig. 6) it is found that thanks to this strengthening configuration, the wall's residual strength is upgrade (36%) and the deformation ability is also increased (25%).

However, the strength capacity of the reference one is still not completely restored with this repairing solution (the TRCRW's strength maximum is still 15% smaller than that of the reference one). This undesirable result should be explained by two reasons: the first one is related to the low reinforcement ratio (only one layer of TRC for each strip is applied) and; the second one seems come from the relatively unsuitable formulation of mortar (produced in Vietnam) for this textile type, especially the grain size. This last reason will be reinforced with the analysis of failure mode bellow.

### 2.4.3 Stiffness Degradation

Stiffness degradation usually occurs during the reversed cyclic loading. Under different displacement levels, the lateral secant stiffness can be determined by:

$$K_i = \left(\left|+F_{max,i}\right| + \left|-F_{max,i}\right|\right) / \left(\left|+X_{max,i}\right| + \left|-X_{max,i}\right|\right) \quad (1)$$

Here, $\left|\pm F_{max,i}\right|$ = positive and negative peak lateral loads of the $i$th cycle, $\left|\pm X_{max,i}\right|$ = displacements corresponding to the peak lateral loads of the $i$th cycle. Figure 7 shows the stiffness degradation of the first cycle at each displacement level.

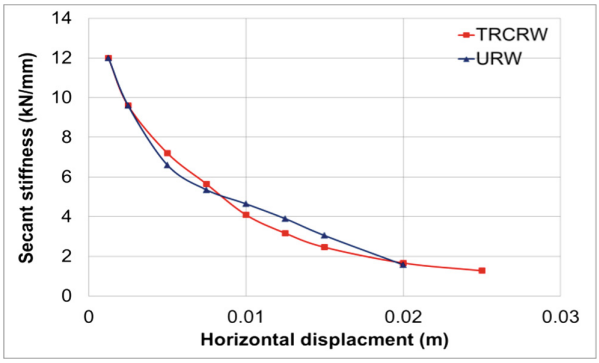


**Fig. 7.** Lateral secant stiffness for reference and repaired walls

According to this figure; the stiffness of URW decreases more rapidly than that of TRCRW at later stage. This observation shows that, thanks to the contribution of TRC strips, the repaired wall has a relatively stable stiffness change in compare to the reference wall.

### 2.4.4 Failure Modes

This section is devoted to providing information regarding failure modes, so that the efficiency of strengthening material in the global lateral behavior and their impact on damage mechanisms can be precise.

- Unreinforced wall (URW)

An unreinforced wall exhibits a flexural failure mode (Fig. 8) characterized by horizontal cracks on the left and right parts of the wall (on two sides where lateral load is applied) due to tensile stresses in bed mortar joints.

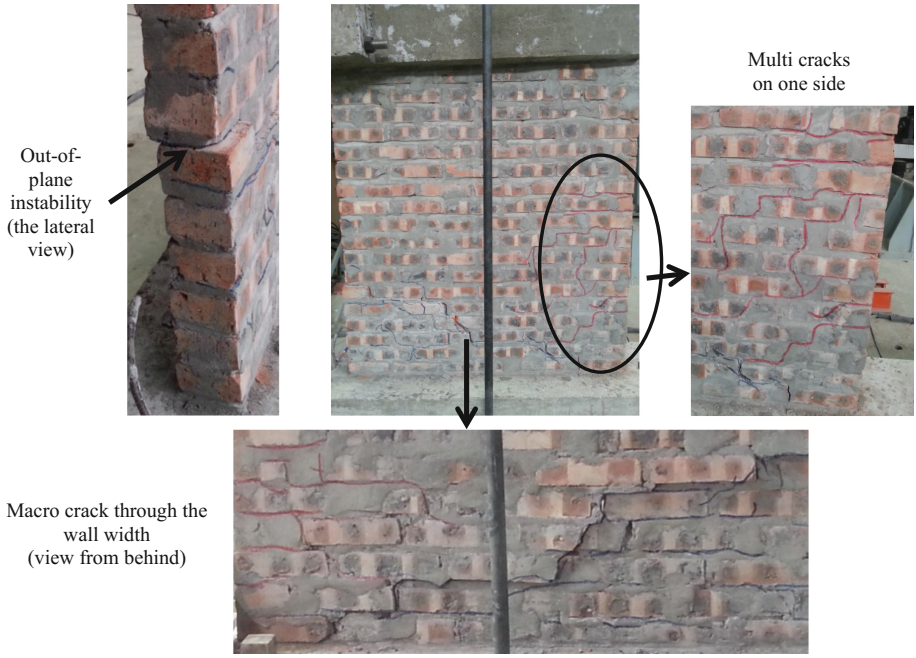


**Fig. 8.** Failure mode of reference wall URW

To better understand the failure process, the order in which damage has been visually detected is as follows. Horizontal cracks start to open on the toe of two sides probably because the tensile bond strength is exceeded and gradually develops as the crack opening grows. The increasing lateral displacements induce others cracks along the wall height. Also, the cracks on the wall's toes grow and spread through the wall width (through horizontal and vertical mortar joints). At the ultimate limit state, a macro crack along the wall width (created by the meeting of cracks on two sides) has been observed and causes an out-of-plane instability that corresponds to a significantly fall of horizontal load (see Fig. 6). At this state, it is considered that the wall is completely collapsed.

It is worth noting that observation of this failure mode has given valuable information for designing strengthening configurations as mentioned above.

- TRC Reinforced wall (TRCRW)

The failure mode of reinforced wall is presented in Fig. 9. It must be noted that this wall still exhibits a flexural failure mode (as the URW wall) which is characterized by horizontal cracks on the left and right parts of the wall, but the damage mechanism of this wall is different from that of the reference one.

**Fig. 9.** Failure mode of TRC-repaired wall (TRCRW)

First, one can see in the failure mode of TRCRW, the TRC strips show their efficiency in bridging micro cracks distributed along the wall height so these cracks are disappeared in the repaired wall. In contrast, the macro crack along wall width observed in the reference one is reappeared in this repairing wall. This result shows that the TRC strips bring a low effect in changing the failure mechanism. However, at the ultimate limit state, there is no out-of-plane instability observed as in the unreinforced wall. So, it is clearly to say that the contribution of TRC strips helps to reduce the risk of out-of-plane failure of reinforced wall.

In addition, another damage mechanism is also observed. That is the debonding of mortar in TRC, especially at places near to the anchors. It is found that the penetration of mortar into textile, the most important key decides the working efficiency of TRC, is not really good. This phenomenon should be explained by the unsuitable formulation of mortar in TRC, especially the grain size. This reason and (or) the low reinforcement ratio (only one layer of TRC for each strip) limit its efficiency in improving the strength capacity and the failure mechanism of repaired wall as mentioned above.

## 2.5 Conclusions

In conclusion, the present exploratory experimental study has focused on clay masonry walls repaired by TRC composites that are subject to cyclic in-plane combined shear-compression tests. This is the first step towards defining the potentiality including

both technical and scientific aspects of using TRC in seismic strengthening and repairing the masonry structure in Vietnam. Although the limited number tests, the main findings are as follows:

- The solution of using TRC in repairing masonry wall helps to upgrade the residual strength and deformation capacity.
- Thanks to the contribution of TRC strip, the repaired wall is more stable strength and stiffness change; especially for the post-pic phrase,
- The using of TRC strips helps to reduce the risk of out-of-plane failure,
- A low strengthening ratio of TRC brings a not very high efficiency,
- The relatively unsuitable formulation of mortar in TRC, especially the grain size, limits its efficiency in reinforcing solutions.

These two last found limited efficiencies propose others study in the future where the formulation of mortar in TRC should be further studied at material scale and more strengthening configurations will be considered at structure scale.

## References

1. Fallahi, A., Alaghebadian, R., Miyajima, M.: Microtremor measurements and building damage during the Changureh-Avaj, Iran earthquake of June 2002. J. Nat. Disaster. Sci. **25** (3), 37–46 (2003)
2. Klingner, R.: Behavior of masonry in the Northridge (US) and Tecoman-Colima (Mexico) earthquakes: lessons learned, and changes in design provisions. 6_Congresso Nacional de Sismologia e Engenharia Sismica, Guimaraes, Portugal (2004)
3. Bernat, E., Gil, L., Roca, P., Escrig, C.: Experimental and analytical study of TRM strengthened brickwork walls under eccentric compressive loading. Constr. Build. Mater. **44**, 35–47 (2013)
4. Carozzi, F.G., Milani, G., Poggi, C.: Mechanical properties and numerical modeling of fabric reinforced cementitious matrix (FRCM) systems for strengthening of masonry structures. Compos. Struct. **107**, 711–725 (2014)
5. Papanicolaou, C.G., Triantafillou, T.C., Karlos, K., Papathanasiou, M.: Textilereinforced mortar (TRM) versus FRP as strengthening material of URM walls: in-plane cyclic loading. Mater. Struct. **40**, 1081–1097 (2007)
6. Papanicolaou, C., Triantafillou, T., Lekka, M.: Externally bonded grids as strengthening and seismic retrofitting materials of masonry panels. Constr. Build. Mater. **25**, 504–514 (2011)
7. Da Porto, F., Mosele, F., Modena, C.: In-plane cyclic behaviour of a new reinforced masonry system: experimental results. Eng. Struct. **33**, 2584–2596 (2011)
8. Prota, A., Marcari, G., Fabbrocino, G., Manfredi, G., Aldea, C.: Experimental in-plane behavior of tuff masonry strengthened with cementitious matrix-grid composites. J. Compos. Constr. ASCE **10**(3), 223–233 (2006)
9. Bui, T.-L., Si Larbi, A., Reboul, N., Ferrier, E.: Shear behaviour of masonry walls strengthened by external bonded FRP and TRC. Compos. Struct. **132**, 923–932 (2015)
10. Contamine, R., Si Larbi, A., Hamelin, P.: Contribution to direct tensile testing of textile reinforced concrete (TRC) composites. Mater. Sci. Eng., A **528**, 8589–8598 (2011)
11. Tomazevic, M., Lutman, M., Petkovic, L.: Seismic behavior of masonry walls: experimental simulation. J. Struct. Eng. ASCE **122**(9), 1040–1047 (1996)

# Potential of Periodic Networks for Seismic Isolation of Sites

Ali Bougressi, Nouredine Bourahla(✉), and Mohamed Anis Doufene

Department of Civil Engineering, University Saad Dahleb, Blida, Algeria
abougressi@yahoo.fr, nbourahla@univ-blida.dz,
ma.doufene@yahoo.fr

**Abstract.** The concept of frequency band gaps that has been widely used in many disciplines of physics and semiconductors is extended to other phenomena such as seismic vibrations. This paper presents the potential of an approach based on periodic arrays to protect a site from seismic effects. The scheme consists of a periodic arrangement of inclusions that act as a barrier to divert or attenuate the propagation of the seismic waves. The aim is to seek large low frequency gaps within the range of the earthquake ground motion frequency content. To this end a numerical study of two periodic arrays (1D and 2D) has been conducted to bring out the potential to block the propagation of seismic surface waves. The obtained numerical results show that under certain conditions, a band gap can be shifted to the low frequency range (7.91 to 21.13 Hz) which is suitable for application in seismic engineering. It is recognized that the models used in this study are very simplistic compared to reality, and therefore more research work is needed to corroborate these results by investigating the transmissibility of the system with different materials and configurations.

**Keywords:** Periodic arrays · Bands of frequency gap · Seismic isolation of a site · Seismic waves

## 1 Introduction

Phononic crystals are macroscopic materials with spatial periodicity in one or more directions of space. As such, they are capable of blocking acoustic or elastic propagation in certain directions and frequency ranges. This is known as a band of frequencies gap, which is most often abbreviated as a "band gap" [13]. This concept is widely used in a variety of applications, including physical, chemical, and biological sensors in the field of nano and micro structures. Potential of this concept to mirror, guide, filter and stop acoustic or elastic waves has been extensively investigated recently [8, 9, 11, 12], which opened possibilities of use as energy dissipater in micromechanical resonators at high frequency ranges. Still however, that the Bragg diffraction in the field of civil engineering is a challenging task because the structures are flexible (very low frequency range) and the seismic waves are very long. Several attempts have been made to apply the concept efficiently and overcome this obstacle. In this context, two perspectives were addressed, the first approach rely on isolating a structure using meta-material foundations [14, 16–18], where most of the authors

© Springer Nature Singapore Pte Ltd. 2018
H. Tran-Nguyen et al. (eds.), *Proceedings of the 4th Congrès International de Géotechnique - Ouvrages -Structures*, Lecture Notes in Civil Engineering 8,
DOI 10.1007/978-981-10-6713-6_93

showed experimentally and numerically that the foundation system can efficiently isolate the super-structures; and the second acts directly on the site to divert or stop ground vibration to propagate into a site by implementing periodic networks on the ground [1, 5, 10], in which some large-scale experiment showed that a periodic array of boreholes embedded in the soil can deflect the energy of an incoming seismic wave [3]. The aim of the work presented is to explore the limits of using ordinary materials and dimensions compatible with full scale sites in different periodical schemes to obtain band gaps in the low frequency range [0.1 to 20 Hz]. To this purpose two periodic arrays with one and two-dimensional periodicities are presented. A study of the effect of certain parameters of the elementary cell constituting the periodic network on the band frequency gap is presented, namely the influence of the density of the core, the modulus of elasticity of the polymer and that of the matrix as well as the filling fraction of the components.

## 2 Basic Principles and Assumptions for this Study

Before introducing the models, the underlying theory and assumptions are first presented together with the main terms used in this study.

In a periodic network, the passage from one point to another spaced by a period L results in a phase shift of $e^{i\vec{k}_B L}$. The calculation of the band gaps of a periodic network is limited to the study of an elementary cell by applying periodic boundary conditions given by Eq. (2) below.

According to Bloch's theory [7], solutions of the wave equation with Floquet-Bloch nature can be written as:

$$u(r,t) = e^{i(K.r-\omega t)} \cdot u_k(\vec{r}) \tag{1}$$

where k denotes the wave vector in the reciprocal space, ω the angular frequency; and $u_k(\vec{r})$ has the same periodicity as elastic parameters and satisfies $u_k(r) = u_k(r + 1)$. Then, the following expression can be derived:

$$\begin{aligned} u_k(r+L,t) &= e^{i(K(r+L)-\omega t)} \cdot u_k(r+L) \\ &= e^{iK.L} \cdot e^{i(K.r-\omega t)} \cdot u_k(r) = u(r,t) \cdot e^{iK.L} \end{aligned} \tag{2}$$

Thus an equation with eigenvalues can be obtained. To each wave vector $\vec{k}$ corresponds a set of eigenvalues, whose solutions ω(k) constitute the dispersion curves in the network. The solutions being themselves periodic, it is possible to represent the totality of the solutions on a graph reduced to the zone of Brillouin in the reciprocal space [6]. The Brillouin zone is the equivalent of the elementary cell in real space, it is the smallest cell to describe this reciprocal network where the knowledge of the band structure in this reduced Brillouin zone is sufficient to know the set of the propagation modes in the network. For each of these directions, there are frequencies f authorized which are solution of the problem to the eigenvalues.

The main property offered by periodic arrays is the possibility of creating bands gap at the band structure. A band gap occurs in this case as a frequency interval where no link is defined between the frequency and the wave vector (it is the unauthorized frequencies) and therefore a wave at these frequencies cannot spread in the middle. The mechanism governing the band gap contitution is based on two phenomena: Bragg reflections due to the periodicity of the network whose waves lengths of the elastic waves, $\lambda$ propagating in the medium, are on the order of periodicity of the network **a** or, on the local resonance phenomenon of the elements placed in networks whose waves lengths exceed by far the periodicity of the network $\lambda >> a$ [2], this is the case for simsic waves.

The main idea is to introduce into each cell a local resonator, the interaction between the modes of vibrations of the resonator and those of the matrix can give rise to band gaps, it is therefore possible to place singular elements possessing resonance properties rather than simple diffusing elements. The appearance of the band of frequency gap is related to the fact that each resonator will trap a part of the energy of the transmitted wave, however the wave interacts with all the resonant elements coupled to each other and also coupled to the host matrix. It is really this association that plays a key role in the presence or not of such a band gap.

## 3 Numerical Models and Band Calculation

### 3.1 Periodic Array 1D

The first model is a one-dimensional periodic lattice, the elementary cell of this model (Fig. 1(b)) consists of three layers: clay, rubber and steel having thicknesses $e_1$, $e_2$ and $e_3$ respectively. This cell is arranged periodically (constant period a = 1 m) in the direction x, as shown in Fig. 1(a). The elastic properties of the materials used are given in Table 1.

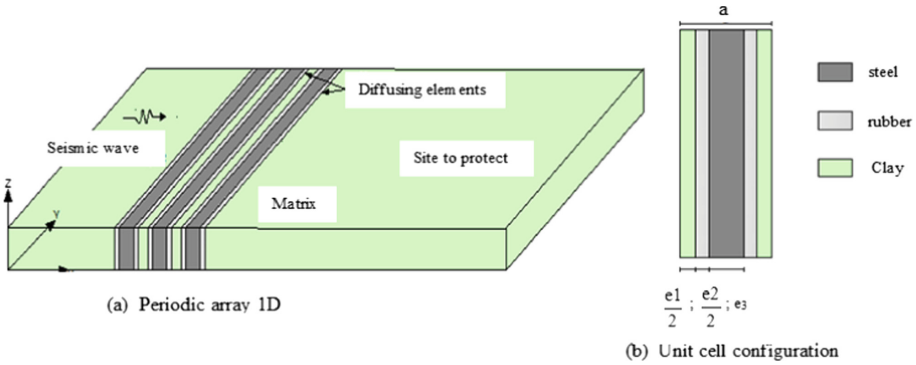


**Fig. 1.** Periodic array 1D.

**Table 1.** Properties of used materials

| Matériaux | Density ρ (Kg/m$^3$) | Elastic modulus E (Gpa) | Poisson's ratio ν |
|---|---|---|---|
| Clay | 1,500 | 3.9 | 0.3 |
| Rubber | 1,300 | $1.37 \times 10^{-4}$ | 0.463 |
| Steel | 7,850 | 210 | 0.3 |

This is a one dimensional structure because the periodicity exists only for one direction of space and consequently, kx is the only component of the wave vector k.

With the configuration mentioned above, a 2D plane strain model is elaborated on COMSOL Multiphysics software [4] to solve for the eigenfrequencies and construct the dispersion curves.

The mesh of the elementary cell and the periodic boundary conditions imposed in the x direction are shown in Fig. 2, where the right boundary conditions $U_i^k(r)$ are related to those at the left $U_i^k(l)$. Moreover, for a problem of plane deformations, the components of the displacement vector are $U_i^k(i = u, v)$ (Fig. 3 and Table 2).

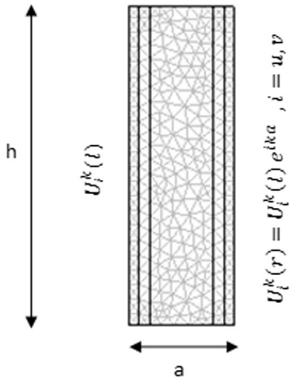


**Fig. 2.** Discretized mesh and periodic boundary conditions.

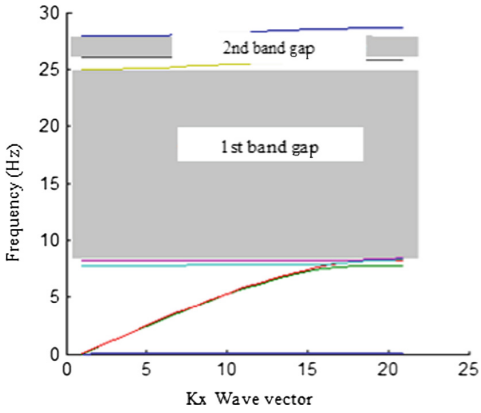


**Fig. 3.** Dispersion Curves of Model 1 (1D).

**Table 2.** Band gaps obtained for model 1

| a(m) | $e_1$(m) | $e_2$(m) | $e_3$(m) | h(m) | Band gap (Hz) |
|---|---|---|---|---|---|
| 1 | 0.2 | 0.2 | 0.6 | 10 | [8.4–25]; [26.05–27.89] |

### 3.2 Periodic Array 2D

In fact, the one-dimensional periodic structures have limited interest for seismic protection applications, hence periodic two-dimensional structures are then produced. The second model studied is a square periodic array, the structural units of this model is made of a clay matrix containing steel circular cylinders inclusions (0.39 m radius) with rubber coating (0.10 m thick). These units are arranged periodically in a square lattice (1 m of lattice constant), as shown in Fig. 4(a).

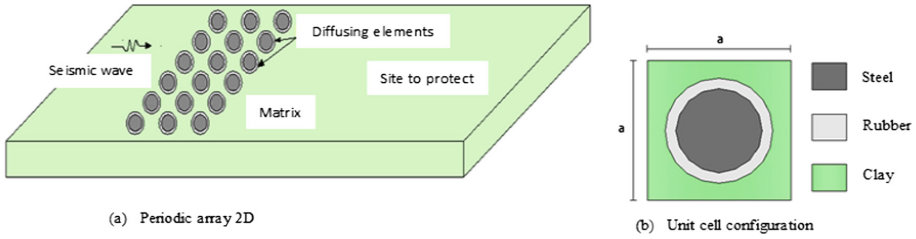


**Fig. 4.** Periodic array 2D.

The mesh results and boundary condition are shown in Fig. 5, where the right and top boundary conditions $U_i^k(r)$ and $U_i^k(t)$ are related to the left and bottom boundary conditions $U_i^k(l)$ and $U_i^k(b)$ through two-phase coefficients $e^{ikxa}$ and $e^{ikya}$, respectively.

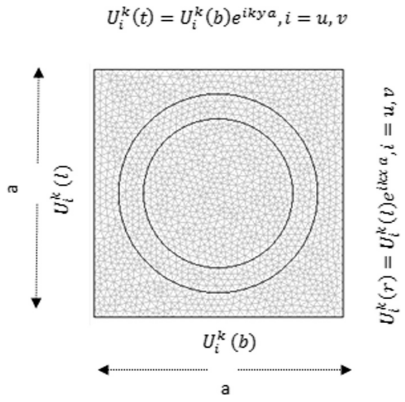


**Fig. 5.** Discretized mesh and periodic boundary conditions

The band of frequency gap of in-plane mode waves is obtained the COMSOL software. The corresponding dispersion curve is shown in Fig. 6, where the segments ΓX, XM, MΓ on the abscissa represent waves traveling along the direction of 0°, 0°–45°, 45° respectively, and the vertical coordinate represents the frequency of the wave.

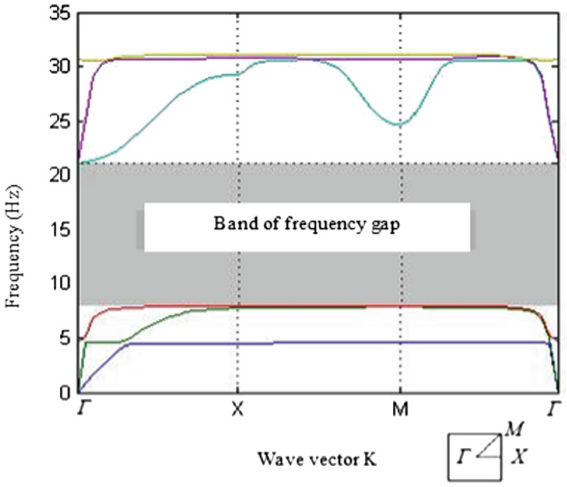


**Fig. 6.** Dispersion curve of model 2 (Two-dimensional periodicity).

The obtained band gap ranges from 7.91 to 21.13 Hz, which is wide and low enough to prevent the propagation of the surface seismic waves (in the two directions x and y) having frequencies which coincide with the band gap frequencies.

## 4 Identification and Study of Parameters Influencing the Band Gaps Characteristics

A parametric study on the elementary cell of the second model is presented based on the three characteristics: the lower frequency of the band (LFB), the upper frequency of the band (UFB) and the width of the frequency band (WFB). The factors studied are: the properties of the materials (elastic modulus E, density ρ and Poisson's ν) and geometric configuration including filling fraction F (representing the ratio of the area occupied by the elementary particle and the area of the elementary cell) and core radius to coating thickness ratio α. The calculation was performed under the same lattice constant.

### 4.1 Influence of the Core Density

Different densities of materials such as clay, concrete, aluminum, steel and lead were used for the core. Figure 7 shows that the LFB decreases rapidly as the core density increases. Thus, for a density value of $\rho = 11{,}600\ kg/m^3$, LFB reaches the lowest frequency 5.04 Hz, which is appropriate for seismic isolation.

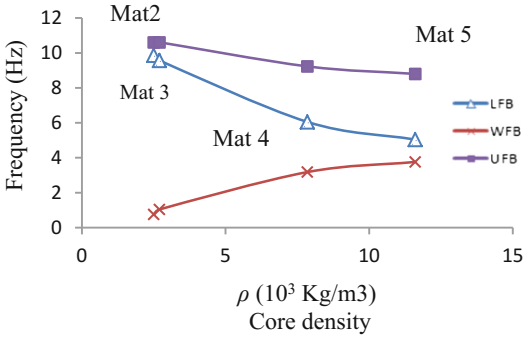


**Fig. 7.** Influence of core density on band of frequency gap.

### 4.2 Influence of the Coating Elastic Modulus

The main characteristic of the coating materials is its elastic modulus which controls the resonator frequency. It acts as a mass-spring oscillator with the coating soft rubber as spring. This has been reported by a recent study [15] which explains why it is necessary to maintain a low elastic modulus for the coating. Figure 8 shows the trend in variation for different elastic modulus in the range of rubber characteristics.

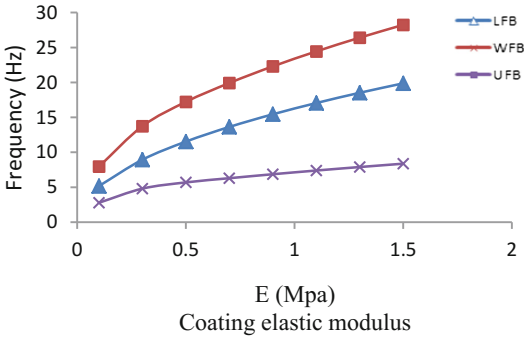


**Fig. 8.** Influence of coating elastic modulus on band of frequency gap.

### 4.3 Influence of Matrix Elastic Modulus

Figure 9 shows that the variation in the elastic modulus of the matrix does not entail any modification on the band of frequency gap because the elastic modulus of the matrix is much higher than the coating. As a consequence, a broad field can be used to choose the matrix material, which also makes it possible to select the various materials used in the field of civil engineering for the design of periodic networks.

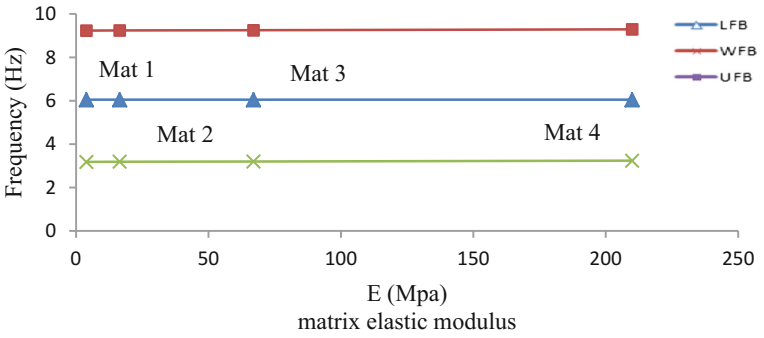


**Fig. 9.** Influence of matrix elastic modulus on the band of frequency gap.

### 4.4 Influence of Filling Fraction and Parameter α

The filling fraction is defined as: $F = \pi R_{ext}^2/a^2$ and $R_{ext} = R_{int} + \mathrm{e}$, where $R_{int}$ denotes the core radius and e denotes the coating thickness. A parameter $\alpha = R_{int}/e$ is defined to assess the contribution of this factor on the band of frequency gap. Figures 10 and 11 respectively show the influence of the filling fraction F and the ratio α on the position and the width of the band frequency gap. An opposite trend can be noticed, because the increase of F factor tend to increase the mass of the resonator which decrease its frequency, however when increasing the values of α, the spring rigidity tends to increase and thus the resonator frequency increases.

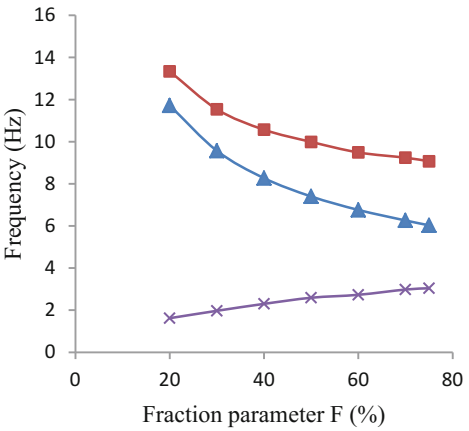


**Fig. 10.** Influence of filling fraction on band of frequency gap.

This is illustrated in Fig. 11 where the value of the fill fraction F was maintained at 75.43%, the LFB varies slightly with increasing values of α. The UFB, however, grows rapidly. Because the rate of the UFB is higher than the LFB, the WFB increases substantially.

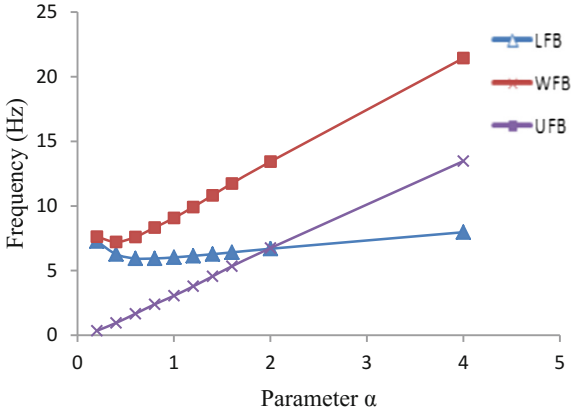


**Fig. 11.** Influence of parameter α on the band of frequency gap.

## 5 Conclusion

Application of periodic networks to mitigate earthquake induced vibration is still a challenging task due to the very low frequency range of interest. The main concern of the present work is to explore the reachable limits of frequency gaps for material properties and network dimensions close to full scale sites implementing civil engineering structures. The numerical results obtained from 1-D and 2-D models showed that for characteristics of real materials it is possible to produce a low frequency gap from 7.91 to 21.13 Hz. Parameters characterizing the material properties and the geometric configuration of the cells have been varied within the range of common materials to identify the trend and the limits of variation of the Low Frequency Band, the Upper Frequency Band and the Width of the Frequency Band. It has been found that an elementary cell consisting of a high density core coated with a soft material having a low elastic modulus and a maximum filling fraction has a wider band gap in the low frequency range.

## References

1. Algoz, B.B., Algoz, S.: Towards earthquake shields: a numerical investigation of earthquake shielding with seismic crystals. Open J. Acoust. **1**, 63–69 (2011)
2. Bernier, D.: Propriétés de super-prisme des cristaux photoniques sur substrats SOI pour le démultiplexage en longueur d'onde. Thèse de doctorat, Université de Paris-Sud XI, Orsay (2008)
3. Brûlé, S., Javelaud, E.H., Enoch, S., Guenneau, S.: Experiments on seismic metamaterials: molding surface waves. Phys. Rev. Lett. **112**, 133901 (2014)
4. COMSOL Multiphysics Reference Guide ©1998–2012 COMSOL
5. Finocchio, G., Casablanca, O., Ricciardi, G., Alibrandi, U., Garesc, F., Chiappini, M., Azzerboni, B.: Seismic metamaterials based on isochronous mechanical oscillators. Appl. Phys. Lett. **104**, 191903 (2014)

6. Hofman, M.: Composants optiques a base de cristaux photoniques pour applications a l'imagerie infrarouge. Thèse de doctorat, Université des sciences et technologies de Lille (2011)
7. Jia, G., Shi, Z.: A new seismic isolation system and its feasibility study. Earthq. Eng. Eng. Vib. **9**(1), 75–82 (2010)
8. Khelif, A., Achaoui, Y., Benchabane, S., Laude, V., Aoubiza, B.: Locally resonant surface acoustic wave band gaps in a two-dimensional phononic crystal of pillars on a surface. Phys. Rev. B **81**, 214303 (2010)
9. Khales, H., Hassein-Bey, A., Serhane, R., Khelif, A.: Evidence of complete elastic band gap in phononic strip waveguides. In: 2013 Proceedings of the 2nd International Conference on Phononic Crystals/Metamaterials, Phonon Transport and Optomechanics, Egypt (2013)
10. Meseguer, F., Holgado, M., Caballero, D., Benaches, N., Sánchez-Dehesa, J., López, C., Llinares, J.: Rayleigh-wave attenuation by a semi-infnite two-dimensional elastic-band-gap crystal. Phys. Rev. B **59**, 12169 (1999)
11. Mohammadi, S., Eftekhar, A.A., Khelif, A., Hunt, W.D., Adibi, A.: Evidence of large high frequency complete phononic band gaps in silicon phononic crystal plates. Appl. Phys. Lett. **92**, 221905 (2008)
12. Oudich, M., Assouar, M.B., Hou, Z.: Propagation of acoustic waves and wave guiding in a two-dimensional locally resonant phononic crystal plate. Appl. Phys. Lett. **97**, 193503 (2010)
13. Van Der Biest, F.: Diffusion multiple et renversement du temps ultrasonore dans des milieux périodiques et désordonnés. Thèse de doctorat, Université de Paris 7 (2006)
14. Wagner, P.R., Dertimanis, V.K., Chatzi, E.N., Antoniadis, I.A.: Design of metamaterials for seismic isolation. In: Proceedings of the 34th IMAC, A Conference and Exposition on Structural Dynamics of Civil Structures, Vol. 2, pp. 275–287 (2016)
15. Xiao, W., Zeng, G.W., Cheng, Y.S.: Flexural vibration band gaps in a thin plate containing a periodic array of hemmed discs. Appl. Acoust. **69**, 255–261 (2006)
16. Xiang, H.J., Shi, Z.F., Wang, S.J., Mo, Y.L.: Vibration attenuation and frequency band gaps in layered periodic foundation: theory and experiment. In: 2012 Proceedings of the 15WCEE, Lisboa, Portugal (2012)
17. Xiongyan, L., Suduo, X., Yancheng, C.: Three-dimensional seismic isolation bearing and its application in long span hangars. Earthq. Eng. Eng. Vib. **12**, 55–65 (2013)
18. Yan, Y., Laskar, A., Cheng, Z., Menq, F., Tang, Y., Mo, Y.L., Shi, Z.: Seismic isolation of two dimensional periodic foundations. J. Appl. Phys. **116**, 044908 (2014)

# Quantitatively Analysing Holistic Risk and Testing the Accident Coping Strategies

Paul Smith(✉)

Arup, London, UK
paul-c.smith@arup.com

**Abstract.** Climate change hazards and malicious attack threats are major problems that the world must start to mitigate, prepare for, cope with and adapt to. A more holistic approach to severe event-hazard/threat risk assessment thereby accounts for the infrastructure's damage, the scale and capability of preparedness, the success of response and final recovery actions, investigating the complete coping cycle for the particular socio-technical system of interest. A holistically based coping test method has been developed by Arup, called the "Holistic Integrity Test" (HIT). In broad terms for application, there are 10 key risk-related socio-technical system integrity factors that will advise governing authorities of their region's coping capability against natural geo-hazards, including the effects of climate change, but also malicious attack threats.

**Keywords:** Climate change · Coping ability · Coping cycle · Temporal-dynamic risk analysis · TDRA · Holistic integrity test · HIT

## 1 Accounting for Future Event-Hazards in Terms of Coping Ability

Climate change and malicious attack threats are major problems that the world must start to mitigate, prepare for, cope with and adapt to. To assure Management of Safety there is a need for a more holistic approach to risk and hazard assessment, considering how safety-critical infrastructure like nuclear power plants, their site and regional location can effectively cope with future extreme hazards. Focused on nuclear power here, the need for a more holistic approach to risk applies across the whole of our interdependent society and the intertwined buildings, infrastructure, facilities, communication and data networks, supplies and services (our "structural-fabric") that enable our civilisation to be maintained and develop. The energy facilities and infrastructure are vulnerable to 'natural' hazards and malicious threats related to criminal, anti-political and terrorist attacks.

We cannot ignore that fact that carbon-free nuclear power generation gives the promise for mitigation of climate change caused by $CO_2$ emission, and yet our nuclear plant designs will need to tolerate and withstand many forms of hazard events, including the need for adapting to more extreme natural hazards amplified by climate change. In addition, owner/operator organisations that run the future nuclear power plants that are needed to mitigate climate change shall have to persuade governments

© Springer Nature Singapore Pte Ltd. 2018
H. Tran-Nguyen et al. (eds.), *Proceedings of the 4th Congrès International de Géotechnique - Ouvrages -Structures*, Lecture Notes in Civil Engineering 8,
DOI 10.1007/978-981-10-6713-6_94

and the public as a whole that their plants are safe and can cope against the shock from extreme hazards like earthquake, worse storms, worse floods and other natural hazards that will become ever increasingly onerous due to climate change amplification. The coping strategies that are implemented in order to recover back to a safe and stable state after an extreme event-hazard scenario need to be tested in terms of their scale and capability. There is a fundamental need to better understand what it means to be able to cope with and adapt to extreme hazards into the future, while taking account of climate change, [1]. The ability to recover after a severe or extreme hazard-shock depends on the extent of the infrastructure and the safety-critical facilities, while also accounting for the functional failure of essential system, permanent structural damage and residual debris that remains.

Modelling of the event-hazard's shock impact to determine the risk and loss consequences requires a progressive temporal-dynamic time-history analysis, merging both deterministic and probabilistic techniques. This implies account of the impact damage and loss incurred by the socio-technical fabric, analysed in terms of certain non-linear factors through a dynamic timeline that depicts the whole event scenario from start to end Whether the region impacted has a more developed infrastructure or not, its resilience essentially depends the ease and success for passing through the "coping cycle"; before, during and after the severe-extreme hazard impact events [2].

The principal risk modelling factors to be considered are (i) the character of the socio-technical system itself, (ii) the potential loss sensitivity of the intrinsic demography, (iii) the type of economy and business base, (iv) the key dependencies that have evolved within our complex and intertwined society (whether located in more or less developed regions), together with (v) the exposure vulnerability and likely weaknesses that will lead to failure and loss of the structural-fabric; (vi) the region's incident/disaster preparedness also need to be appropriately scaled and capable, (vii) with due awareness of the likely duration of the impact, (viii) the spatial distribution of the hazard events impact in terms of area affected, (ix) whether any forewarning is feasible, (x) the ability to evacuate prior to the event, and (xi) what support resources will ultimately be available to enable the coping strategy to be successfully completed. This gives a general indication of the range of risk modelling factors that need to be considered and accounted for in a more holistic approach to risk. Using this type of holistic logic, we effectively progress the hazard and the shock through the complete coping cycle, from beginning of the hazard load build-up through to the individual stages of response and then recovery back to previously "normal" conditions.

The intent of this initiative towards a more holistic approach to risk analysis is not to replace the type of techniques developed some forty years ago with WASH-1400, [3], but to supplement and consolidate the fault and event tree logic approach, merging the dimensions of space and time with a more holistic and temporal perspective of the hazard's impact effect and how good our coping strategies actually are. In essence, we are merging three fundamental methodologies of using:

- established risk analysis modelling that has been applied across the nuclear industry for PSA/PRA modelling, while including the hazard event's space and time parameters;

- assessing the potential fragility and failure modes of the structural fabric through the timeline of the hazard event; and then,
- investigating the ability of the plant, site and region to cope with the distributed damage and loss that will likely result if and when the severe to extreme hazard conditions arise in the future – testing the coping strategies and the (in effect) the existing coping-resilience governance being advocated by the responsible owner-operator organisations.

A more holistic approach to severe event-hazard risk assessment thereby accounts for the infrastructure's damage, the scale and capability of preparedness, the success of response and final recovery actions, investigating the complete coping cycle for the particular socio-technical system of interest, [2]. The benefit of applying a holistic approach to hazard-risk assessment can better indicate potential improvements in system robustness, enhanced resilience measures, practical adaptation and realistic emergency response and recovery actions in terms of their scale and capability needs. Meanwhile, the coping cycle as the infrastructure and/or region passes through the event-hazard shock scenario is best described and analysed by a systems thinking logic. The individual parts of the cycle progress from response actually during the hazard or shock scenario, subsequently to recovery from severe events; then possibly including the need for regional reconstruction, remediation, rehabilitation (after forced evacuation) after an extreme hazard, to eventually attain a completely recovered state which will be further sustained for a long period yet to come.

The individual parts of the cycle progress from response actually during the hazard or shock scenario, subsequently to recovery from severe events; then possibly including the need for regional reconstruction, remediation, rehabilitation (after forced evacuation) after an extreme hazard, to eventually attain a completely recovered state which will be further sustained for a long period yet to come.

## 2 Quantitative Hazard-Risk Analysis Using a Holistic Approach

In the future, designers and builders shall be aggressively asked to demonstrate the robustness, resilience and coping strategies that are able to withstand severe to extreme event-hazard shocks that can catastrophically damage future structural fabric, like with society's critical infrastructure networks and power generation systems. If such events are not defended against in order to minimize the potential damage that can happen, then they can progress into severe accident and disaster scenarios, thereby threatening to human welfare and to the environment. This raises the need for risk analysis tools that are able to model the temporal-dynamic interrelationships as they progress through the various scenario combinations that will have to be analysed.

A newly developed Severe Shock Event Risk (SSER) modelling approach has been formulated in order to quantitatively indicate the risk reduction options and optimum coping strategies that may be deemed as best practice solutions for a given region and its infrastructure, [2].

The Severe Shock Event Risk (or SSER) methodology has been developed (by Arup) so it can cater for the temporal-dynamic modelling of a severe hazard/shock event causing an accident or disaster scenario, within a much broader holistic context of the power plant's site and regional location, together with the failure mechanisms and resultant damage effect on the impacted socio-technical system when an extreme hazard hits.

SSER equation has been holistically derived by considering the actual temporal sequence of a severe or extreme shock event and its spatial effect. The temporal basis of the SSER matrix equation essentially considers the damage-loss and the eventual recovery sequence, effectively as a success sequence that may be represented by probabilistic success tree modelling, taking due cognisance of the region's exposure vulnerability, the infrastructure's fragility and the success of recovery. The challenge to this approach is that the analysis processing has to be non-linear in order to capture that numerous interactions and inter-dependencies that result in a complex analysis.

This holistic approach allows us to gain confidence that we may be able to cope with future geo-hazards, from severe, to climate change amplified extreme magnitudes and their longer impact periods, thereby increasing the possible loss consequences.

The SSER method is demarcated out into three risk modelling parts that account for:

- the hazard exposure and loss potential before any hazard-shock impact occurs;
- screening of the region's vulnerability, its weakness by reference to damage fragility, together with what the integrated losses would be across the time and space dimenions; then,
- the response and recovery demand in terms of the effort that is needed to cope with the predicted socio-technical system's damage, while taking due cognisance of inhibitors caused by structural-fabric damage that introduces important functional failures, including hazard inundation and debris fields etc.,

The quantitative basis to the SSER method is expressed in three partitioned data-matrices for modelling the various data inputs, symbolically considers the principal risk and coping factors that need to be accounted for as an accident or regional disaster scenario is played out, broken out into three progressive stages:

- Before the Shock Event, BSE;
- During the Shock Event, DSE;
- After the Shock Event, ASE.

The specific algorithm being expressed as:-

$$\begin{aligned}\text{SSER} &= \text{f}\{\text{Exposure Potential Before} + \text{Fragile Damage During} + \text{Ability to Recover After}\}\\ &= \{[\text{P}_{\text{rB}}].[\text{H}_{\text{B}}].[\text{E}_{\text{P}}].[\text{Z}_{\text{P}}].[\text{D}_{\text{P}}]\}^{\text{BSE}} + \{[\text{P}_{\text{rD}}].[\text{H}_{\text{D}}].[\text{V}_{\text{D}}].[\text{T}_{\text{D}}].[\text{S}_{\text{D}}].[\text{F}_{\text{O}}]\}^{\text{DSE}}\\ &+ \{[\text{P}_{\text{rA}}].[\text{H}_{\text{A}}].[\text{V}_{\text{A}}].[\text{T}_{\text{A}}].[\text{S}_{\text{A}}].[\text{R}_{\text{A}}]\}^{\text{ASE}}\end{aligned}$$

The respective factors, parameters and criteria of the SSER temporal-risk matrix equation are outlined in Table 1. Also, please view Fig. 1. It is advocated that the SSER methodology enhances the way that we carry out quantified risk analysis using a

**Table 1.** The SSER temporal-risk analysis data and information, [2].

| BSE of the SSER | $\{P_{rB} \times H_B \times E_P \times Z_P \times D_P\}^{BSE}$ |
|---|---|
| $P_{rB}$ Range of severe shock events | Range of possibility to shock event-hazards the integrity of the socio-technical system |
| $H_B$ Possible shock/geo-hazard events | Possible Worst Case with Uncertainty of Hazard (Shock) to possibly failure, damage and destruct the system's parts and components, accounting for the possible: \| Magnitude \| Hazard Event Duration \| Scale of Hazard \| Rate of Hazard Impact |
| $E_P$ Exposure potential of the region | The Exposure Potential recognises the projected point in time when the shock event occurs, taking due cognisance of the temporal character of the socio-technical system:- time of day, demography, location LDC/MDC, interdependencies, physical robustness etc. |
| $Z_P$ Technical system properties | Socio-technical system characteristic properties; utilising the SERT (Arup) Categorisation of System, Expanse, Rate and Time sensitivity characteristics |
| $D_P$ Potential emergent danger | Process and energy industries sometimes contain highly dangerous substances that are harmful as sewage waste, chemo-toxic, carcinogenic and radiological consequences if uncontrolled release |
| DSE of the SSER | $\{P_{rD} \times H_D \times T_D \times S_D \times F_O\}^{DSE}$ |
| $P_{rD}$, Probability of damage | Derived from the Fragility Curves that are characteristic of the structural fabric in the socio-technical region's system |
| $P_{rD}$, Probability of response success | Using "Success Trees" we can ascertain the probability of success of the coping strategy, while accounting for the region's fragility that will put more demand on response actions |
| $H_D$ Hazard characteristic matrix | Hazard Magnitude \| Hazard Event Duration \| Scale of Hazard \| Rate of Hazard Impact |
| $V_D$ Vulnerability/ weakness matrix | Physical \| Natural \| Human \| Economic \| Social \| Political \| Security \| {Akin to "Circle of Capacities"} |
| $T_D$ Event's time duration | The Severe Shock Event Duration (TD) is a shorter period than the Hazard Event Duration, since system is only affected and potentially "damaged" when magnitude is severe |
| $S_D$ Size and bounds of the S-T system | Size of the socio-technical system over which the Hazard causes an impact, with the socio-technical system including human demography and economics |
| $F_O$ Likelihood of forewarning | $F_O$ is an 'Onset Factor' (related to success of response during the shock event). The event may be too quick for a commensurate response, whereas if there is ample forewarning |
| ASE of the SSER | $\{P_{rA} \times H_A \times V_A \times T_A \times S_A \times R_A\}^{ASE}$ |
| $P_{rA}$ Probability of recovery success | Ascertain the probability of success of the coping strategy, while accounting for the region's damaged and debris that will inhibit the recovery actions |
| $H_A$ Hazards to recovery matrix | Hazards from the Effect of the Shock Event that Inhibit the Recovery Phase, considering factors like:- \| Functional Failure \| Damage \| Debris \| Victims \| |
| $V_A$ Vulnerabilities to recovery | \| Recovery \| Reconstruction \| Remediation \| Rehabilitation \| Sustainability \|. Equivalent to the vulnerability in not being able to successfully go through the Coping Cycle as a complete process, getting back to stability and a new form of economic sustainability |

(*continued*)

**Table 1.** (*continued*)

| ASE of the SSER | $\{P_{rA} \times H_A \times V_A \times T_A \times S_A \times R_A\}^{ASE}$ |
|---|---|
| $T_A$ Impact time on the region | Impact time after event duration is effectively the total period from Recovery back to a Sustainable economic region |
| $S_A$ Size and bounds of the S-T system for recovery actions | Size of the socio-technical system over which the Coping Cycle needs to progress back to a sustainable economic region; accounting for the resources ($R_A$) needed for recovery |
| $R_A$ Resources for recovery actions | Since the damaged socio-technical system across the region affected by the severe and/or extreme hazard will be damaged with losses, then the remaining resources in the affected region and beyond are crucial in order to supply equipment/supplies etc., for the coping strategy, through response to recovery as the coping cycle progresses |

holistic approach, modelling the damage incurred on a socio-technical system when exposed to an extreme event-hazard, then accounting for the necessary response and recovery actions through the time-history of the impacting hazard-shock scenarios; thereby simulating the entire cause and effect in the temporal-dynamic time domain.

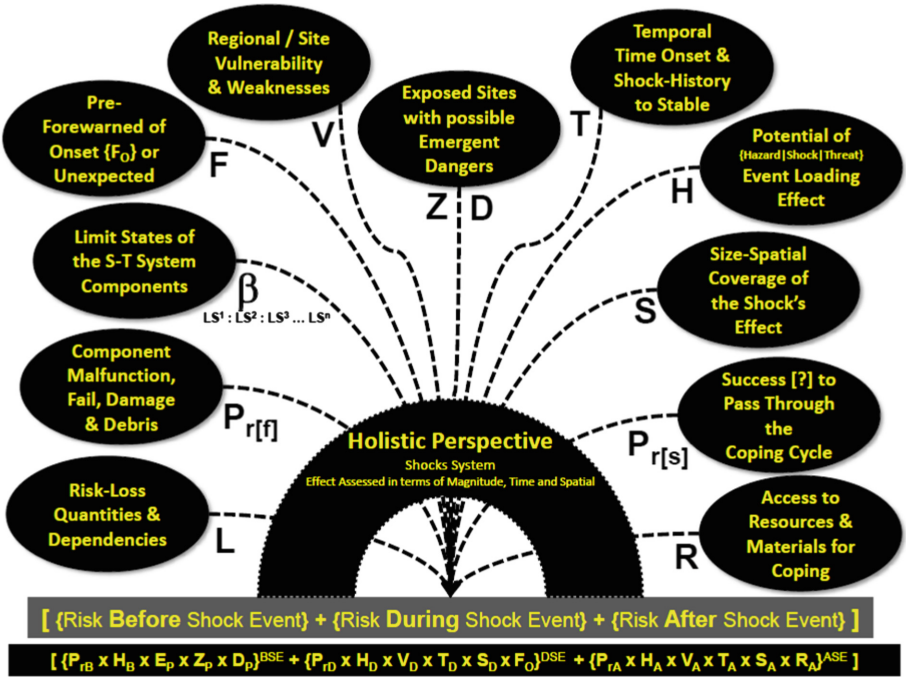


**Fig. 1.** The logic of the SSER is based on a holistic approach [2].

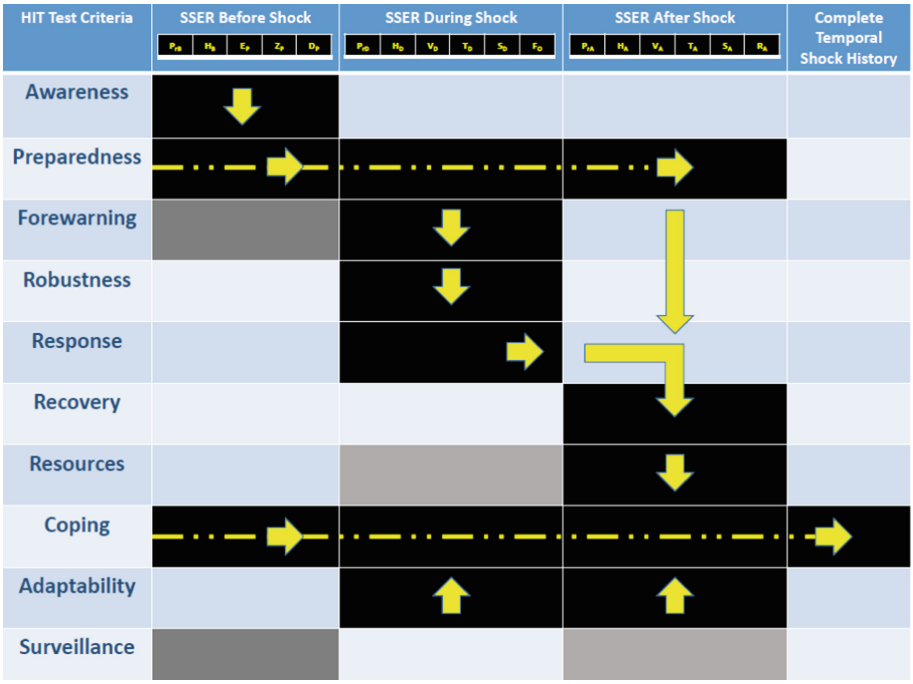


**Fig. 2.** HIT test items against the SSER matrix equation [2].

The socio-technical risk profile encompasses a wide gamut of any event or situation that threatens damage to human safety and welfare, including:

- Loss of human life in general;
- Human illness, disease, injury and world pandemic threats;
- Denser populous, human migration and homelessness;
- Damage to property and essential services;
- Disruption of production and supply of money, food, water, energy or fuel;
- Disruption of communication networks;
- Disruption of infrastructure and the facilities for transport; or,
- Disruption of services relating to health, policing and security.
- In addition, any event or situation that threatens damage to the environment involves:
- Contamination to land, water or air with biological, chemical or radioactive matter; or,
- Disruption or destruction of plant life or animal life.

In simple terms, this technique is identified as "Temporal-Dynamic Risk Analysis", abbreviated to TDRA, [2]. TDRA analysis tools that utilise matrix equations like the SSER will need to perform iterative non-linear dynamic analyses as it tries to solve the hazard's damage effect through the temporal and space domains, the TDRA will need to perform numerous non-linear iterations with time-step and spatial-step increments,

depending on the rate sensitivity of the component sub-systems being damaged by the hazard-shock load function, [2].

In simple terms, two hierarchical system levels will need to be modelled using the TDRA technique, these being that the:-

- the first set of iterations will need to simulate the wide and dispersed socio-technical system in terms of its macro-structure, together with adjacent interfaces; and then,
- a micro-structure iteration loop that models particular component parts of the socio-technical system's fabric that could cause failure or destruction of the region's particularly important buildings, its specific facilities, networks, detailed infrastructure, connected services, then its access to supplies and resources.

A TDRA software's non-linear time-step period and its spatial-step space for the micro-structure will be dictated by the level of accuracy judged necessary to inform the emergency response and recovery management, while the socio-technical system's coupling, interaction and rate sensitivity will have to be considered. For example, the more complex and rate sensitive the system is, then more iterations will be required with a small time-step period. The TDRA tools will be able to produce a breakdown report for executive review, providing actual quantitative and dimensionless comparisons of socio-technical systems and their ability to cope with hazard-shock events. The TDRA tools will help regional planning and emergency services to optimise and enhance their coping ability and societal resilience for the various hazard-shock scenarios identified to be significant for their locality. It is also important to take due cognizance of the debris that results from the damage, being very important, as remnant debris acts as a major inhibitor to response and recovery actions. This type of temporal-dynamic hazard modelling technique using the SSER can be quite informative about the vulnerability, fragility and overall weaknesses of the region's structural fabric, as well as integrating the consequential economic loss, thereafter economy being re-established over an elongated impact period, how to improve robustness, reduce risk, enhance coping resilience, better response and recovery capability.

Applying a holistic mind-set by using the SSER, we open up a broader spectrum of important hazard and risk parameters than is available with the past legacy risk assessment measure of just "probability x consequence". As well as the non-linear simulation capability that a TDRA analysis tool could offer, another very important advantage will be the ability to calculate the probability of success of the response, recovery and overall coping strategies, iterating to the optimised routes and actions.

## 3 Means to Test the Hazard Coping Strategies – Holistic Integrity Test (HIT)

The coping capability can then be indicated in terms of the region's awareness, its robustness, the feasible forewarning, their preparedness, the success of the response, the success and time to recovery, the necessary resources needed and the supply chain routes available, the people's and business's adaptability and the goodness of the surveillance to keep a look out for vulnerabilities and weaknesses. It is informative to initially represent the coping cycle in the form of a simplified damage effect on the system during the hazard,

then the system's recovering out of the damaged state. Here the SSER matrix equation is overlaid with the basic model idealisation of hazard induced damage during the emergency response phase, through to the recovery phase. This approach takes the thinking of Casti, [5], supplemented by considering the spatial and time domains in combination, while also accounting for Perrow's theory, [4], regarding the interaction and coupling relationship that are intrinsic of "normal accidents".

A holistically based coping test method has been developed by Arup, called the "Holistic Integrity Test" (or simply HIT test). In broad terms for application, there are 10 key risk-related socio-technical system integrity factors that will advise governing authorities of their region's coping capability against natural geo-hazards and the effects of climate change, being:

- **Awareness;**
- **Robustness;**
- **Forewarning;**
- **Preparedness;**
- **Response;**
- **Recovery;**
- **Resources;**
- **Coping;**
- **Adaptability; and,**
- **Surveillance.**

The resulting assessment output from the HIT test extracts the soundness and completeness of the risk management and coping strategy, questioning the practitioners, but another dimension is also provided by the HIT's more in-depth test methodology uses an objective quantitative temporal-risk analysis modelling and the holistic SSER matrix equation. The HIT test method investigates the goodness of the coping strategies, while taking advantage of the new TDRA quantitative modelling tools to account for the damaged/disrupted system resulting from the socio-technical system's intrinsic vulnerability and weaknesses that exist could allow initiating events to progress to accidents or disasters [2]. This holistic approach using the HIT with the SSER risk matrix essentially interrogates the quality of a socio-technical system and its ability to survive and cope against severe (and extreme by the climate change amplifier), measured in terms of its human habitation, demography, structural-fabric and the essential functions, together with the region's resources and economic situation, see Fig. 2. It is advocated that such an approach will likely become very important into the future as the deleterious effects of climate change really do happen to cause extreme damage and losses to our socio-technical systems.

## References

1. IPCC, 5th Climate Change Synthesis Report (2014)
2. Hazard Design and Assessment, TINCE Paris, Smith (2016)
3. Reactor Safety Study, WASH – 1400, USNRC, NUREG-75/014, October 1975
4. Normal Accidents: Living with High-Risk Technologies, Perrow (1984)
5. X-Events - The Collapse of Everything, Casti (2012)

# Review of Direct Strength Method of Design for Cold-Formed Steel Structures with Holes with a Focus on Shear

Song Hong Pham(✉), Cao Hung Pham(✉), and Gregory J. Hancock(✉)

School of Civil Engineering, The University of Sydney, Sydney, NSW, Australia
{songhong.pham, caohung.pham, gregory.hancock}@sydney.edu.au

**Abstract.** The Direct Strength Method (DSM) design rules for cold-formed steel members have been incorporated recently into the North American specification for the design of cold-formed steel structural members (AISI S100-12) and the Australian cold- formed steel structures standard (AS/NZS 4600:2005). The method covers the design of structures with and without holes subjected to compression and bending and without holes for shear. Recent research has extended the DSM to the design of beams with holes predominantly in shear. This paper reviews the DSM design guidelines for perforated members in compression and bending and the latest research on the DSM for perforated beams in shear.

**Keywords:** Direct Strength Method · Cold-formed steel · Web opening · Shear

## 1 Introduction

The DSM of design for cold-formed steel structures has been developed recently (Schafer 2006a) as an alternative to the traditional effective width method. The DSM significantly reduces the design effort by directly computing the strength of thin-walled members based solely on the elastic buckling load/moment of cross-section and the yield load/moment. The strength curves were established to fit a wide range of experimental data on members experiencing different instability modes, including local, distortional or global buckling. Figure 1 shows the DSM strength curves for local and distortional buckling together with corresponding test data depicted by the red and blue colors, respectively. Equations (1) and (2) are the DSM design equations, which describe the red curve in Fig. 1, for column local buckling strength. The blue curve for distortional buckling is described by other set of equations given in the AISI S100-12 (AISI 2012) and the AS/NZS 4600:2005 (Standards Australia 2005).

A thin-walled member may buckle in either local, distortional or global mode or a combination of those modes. Local buckling involves distortion of the individual plate components while the junction lines remain straight, as seen in Fig. 2a. Distortional buckling is characterized by the distortion of one portion of cross-section and the junction lines are not straight as demonstrated in Fig. 2b. Global buckling including flexural, torsional or flexural - torsional buckling involves translation and/or rotation of

© Springer Nature Singapore Pte Ltd. 2018
H. Tran-Nguyen et al. (eds.), *Proceedings of the 4th Congrès International de Géotechnique - Ouvrages -Structures*, Lecture Notes in Civil Engineering 8,
DOI 10.1007/978-981-10-6713-6_95

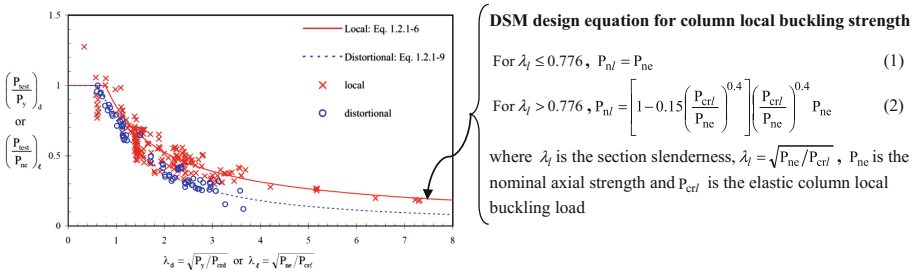


**Fig. 1.** Column buckling tests (Schafer 2006b)

the entire cross-section. Figure 2c shows an example of column buckling under flexural – torsional mode. The traditional Finite Element Method (FEM) using such commercial packages as Abaqus (Dassault Systèmes Simulia Corp. 2014) and Ansys (ANSYS Inc. 2016) is a powerful tool to predict the buckling behavior of plate assemblages. Recent development of free, open source computer programs using the Finite Strip Method (FSM) such as CUFSM (Li and Schafer 2010), THIN-WALL-2 (Nguyen et al. 2015) allows the buckling analysis to be very simple and convenient. The Semi-Analytical Finite Strip Method (SAFSM) developed by Hancock and Pham (2013) has been encoded into the THIN-WALL-2 program which supports 2D, 3D buckling mode views.

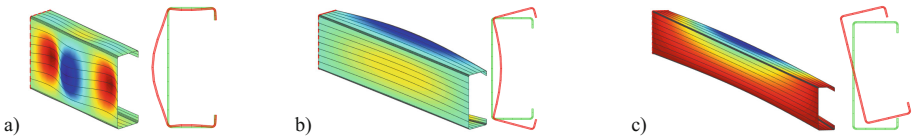


**Fig. 2.** (a) Local, (b) distortional and (c) global buckling of channel section column by THIN-WALL-2

The local and distortional buckling modes occur at different half-wavelengths with critical values at the minima in a "signature curve", pioneered by Hancock (1978) that relates the buckling loads/moments and the buckling half-wavelengths as illustrated in Fig. 3. For most of standard commercial cold-formed sections, these minima are distinct and the buckling stresses at those points can be used as input to the DSM design equations.

The load/moment that causes a section to yield can be determined directly on the basis of cross-section properties and the yield stress. For instance, the yield load of a column is computed as $P_y = A_g f_y$ where $A_g$ is the gross area of cross-section and $f_y$ is the yield stress. For perforated sections, the application of the DSM is not straight forward since other different buckling or failure modes may occur and therefore the buckling and yielding loads/moment need to be re-formulated.

The DSM has substantial advantages over the traditional effective width design method. Besides the capacity to produce member strength quickly and simply, it

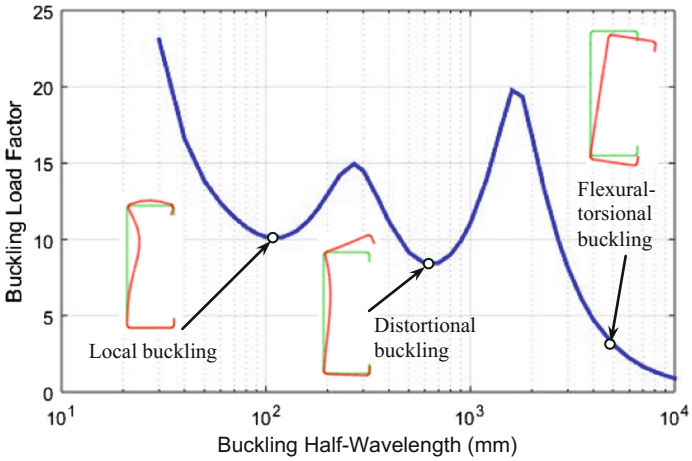


**Fig. 3.** A signature curve and buckling modes (Schafer 2006b) of a beam under bending about major axis, reproduced by THIN-WALL-2 for a 200 mm deep, 1.5 mm thick channel section

naturally accounts for material non-linearity, imperfections, and residual stresses in the design equations. Further, the interaction between local and global buckling modes is also included. The DSM also serves as a great tool for section optimization. Owing to its simplicity and with the powerful aids of numerical buckling solutions, the strength of complex thin-walled section members can be computed easily. This empowers engineers, practitioners and students to enhance and optimize thin-walled sections. For instance, originating from standard plain sections, more advanced sections have been engineered and commercialized as shown in Fig. 4. They require little extra material and effort to be manufactured but their strength is enhanced significantly.

**Fig. 4.** Stiffened thin-walled sections in Australian market (Lysaght)

## 2 DSM of Design of Perforated Members in Compression and Bending

This section summarizes the recent development of the DSM design rules for thin-walled structural members with holes. One of the significant outcomes is the format of the original DSM equations for beams and columns without holes has been retained. Only the buckling and yield load/moment were modified to include web holes.

### 2.1 Buckling Solutions

It was found that web openings can change the buckling mode shapes of cold-formed steel members (Moen and Schafer 2009). Therefore, the method to determine buckling load/moment of perforated beams and columns has to be revised. FEM is still a useful tool but it requires manual inspection to identify the correct mode shapes. In most cases, this is a daunting task. Moen and Schafer (2009) provided an alternative approach to approximate the local buckling load and moment for a column ($P_{crl}$) and a beam ($M_{crl}$). The method assumes that local buckling occurs as either buckling of the unstiffened strip(s) adjacent to a hole at the net section or as local buckling of the gross section between holes. This approach is an improvement over element-based methods because the interaction between the unstiffened strip and the connected cross-section is explicitly considered (AISI 2012). For a column with holes, the local buckling load is determined as:

$$P_{crl} = \min(P_{crlnh}, P_{crlh}) \tag{3}$$

where $P_{crlnh}$ is the local buckling load of the gross section by a finite strip analysis, $P_{crlh}$ is the local buckling load of the net section by a finite strip analysis, but restraining the deformations to local buckling and examining only those buckling half-wavelengths shorter than the length of the hole. Both of the $P_{crlnh}$ and $P_{crlh}$ can be determined using the public domain finite strip program CUFSM as illustrated in Fig. 5. The same approach is applicable to determine the local buckling moment ($M_{crl}$) for beams.

For distortional buckling, the presence of the web openings reduces the rotational restraint provided by the web to the flanges, thus decreasing the distortional buckling load. To account for the stiffness reduction because of the holes, Moen and Schafer (2009) developed an approximate method to compute $P_{crd}$ and $M_{crd}$ by reducing the web thickness by:

$$t_r = \left(1 - \frac{L_h}{L_{crd}}\right)^{1/3} t \tag{4}$$

where $L_{crd}$ is the distortional buckling half-wavelength, determined by analyzing gross cross-section using FSM, $L_h$ is the length of the hole. Once the reduced web thickness is computed, finite strip analysis is performed again with the new web thickness and at the length $L_{crd}$. This approach relies on the fact that distortional buckling occurs at intermediate half-wavelengths, thus the local effect of the web holes is not as critical as in the case of local buckling.

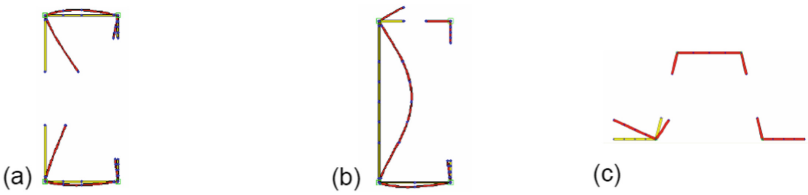


**Fig. 5.** Buckling of column net cross-sections using CUFSM (AISI 2012)

For global buckling, Moen and Schafer (2009) proposed a weighted average approximation to estimate the buckling load and moment to account for the presence of web holes. The quantities to be averaged include the second moment of area $I$ and the St. Venant torsional constant $J$ as following:

$$I_{avg} = \frac{I_g L_g + I_{net} L_{net}}{L} \tag{5}$$

$$J_{avg} = \frac{J_g L_g + J_{net} L_{net}}{L} \tag{6}$$

where $L_{net}$ is the total length of the regions containing holes, $L_g$ is the length of the regions without holes. The weighted average warping torsion constant $C_{w,avg}$ is not able to be computed using preceding average expression because of the occurrence of a localized shear stress adjacent to the hole. Therefore, $C_{w,avg}$ is determined on the basis of net section with the depth of the hole extended to $h^*_{hole}$:

$$h^*_{hole} = h_{hole} + \frac{1}{2}(H - h_{hole}) \left(\frac{h_{hole}}{H}\right)^{0.2} \tag{7}$$

where $h_{hole}$ is the depth of the hole and $H$ is the web depth. THIN-WALL-2 and CUFSM can be used to determine $C_{w,avg}$ by setting the section thickness to be zero over $h^*_{hole}$.

### 2.2 Strength

From the experiments and the FE simulations, it has been observed (Moen and Schafer 2010) that for low slenderness members experiencing local buckling, yielding and collapse of the net section governs the beam and column behavior. As a result, the local buckling strength $P_{nl}$ and $M_{nl}$ are capped to not exceed the yielding strength of the net section, as following:

$P_{nl} \leq P_{ynet}$ where $P_{ynet} = A_{net} f_y$, and $A_{net}$ is the net area of cross-section at the location of a hole

$M_{nl} \leq M_{ynet}$ where $M_{ynet} = Z_{fnet} f_y$, and $Z_{fnet}$ is the net section modulus referenced to the extreme fiber at first yield

When distortional buckling is of interest, for structures with low slenderness, inelastic buckling and yielding at the net section also occur, enforcing the strength to not exceed the yield values of sections at the location of the hole. Further, for an intermediate range of the slenderness, there is a transition zone from the capped yielding value to an elastic buckling-dominated strength.

## 3 DSM of Design for Perforated Sections in Shear

For cold-formed steel channel members subjected to shear, it is widely accepted that the shear force is resisted by the vertical beam webs alone. As a result, the presence of web openings reduces the shear buckling and shear strength considerably. To design

these perforated beams, both the AISI S100-12 (AISI 2012) and the AS/NZS 4600:2005 (Standards Australia 2005) adopt an empirical approach in which the shear strength of a member with holes is determined as a fraction of the strength of the unperforated member. This is reflected by using a reduction factor $q_s$, as following:

$$V_{perforated} = q_s V_{unperforated} \tag{8}$$

where $V_{unperforated}$ is the shear strength of beam without holes, which can be determined by the DSM design rules for shear developed by Pham and Hancock (2012) for beams with web stiffener spacing not exceeding twice the web depth. Recent research at the University of Sydney (Pham et al. 2017a) has shown that the DSM design rules for beams without holes can be used to design beams with holes by modifying the buckling force and the shear load at yielding.

### 3.1 Buckling Solutions

The shear buckling force $(V_{cr})$ can be determined directly from a buckling analysis or it can be computed on the basis of the shear buckling coefficient $(k_v)$ using the following expression:

$$V_{cr} = k_v \frac{\pi^2 E A_w}{12(1-\mu^2)\ (b/t)^2} \tag{9}$$

where $E$ is the modulus of elasticity; $\mu$ is the Poisson's ratio; $b$ is the depth of the flat portion of the web; $t$ is the thickness of section, $A_w$ is the cross-sectional area of the web. To determine the shear buckling force for thin-walled structures, FEM using shell elements is a powerful tool even though it is not always available for engineers to use such FE packages as Abaqus and Ansys because of the high cost. Figure 6 shows a buckling mode shape produced by Abaqus of a C-section beam with web hole, subjected to shear.

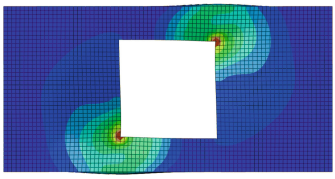

**Fig. 6.** Buckling of a perforated channel member using FEM

Freely available finite strip programs including THIN-WALL-2 and CUFSM are currently not able to analyze members with holes subjected to shear. In fact, a computer program named Isoparametric Spline Finite Strip Method (ISFSM) (Eccher 2007) developed at Sydney University can perform the task but it has not been freely available for public use. Instead, researchers have proposed several methods to determine $k_v$. Pham (2016, 2017) employed the ISFSM program and the FEM to study the buckling capacity of lipped channel section members with central square and

circular holes. The relationship between the shear buckling coefficients ($k_v$) and the ratios of opening sizes to the web depths (*d/b*) was graphed and approximated by a set of design equations. Pham et al. (2017b) extended the buckling analysis using FEM to beams with holes with various aspect ratios (AR = shear span /web depth). The results are shown in Fig. 7 where Case B and Case C refer to the methods to apply shear forces. In Case B, a couple consisting of shear forces (*V*) parallel to the web is applied at the two end sections and a bending moment (*M* = *Va*, where *a* is the shear span) at one end to balance the coupled shear action. In Case C, a pair of bending moments with half value (*M* = *Va/2*) acting at both end sections in the same direction is applied to balance with the longitudinal shear stresses caused by the two coupling shear forces.

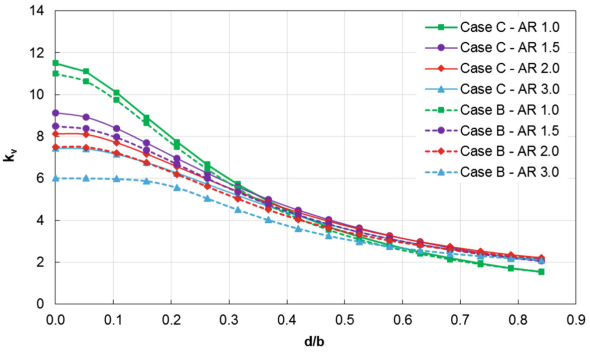


**Fig. 7.** Variation of shear buckling coefficients in relation to hole sizes (Pham et al. 2017b)

On the basis of the buckling analysis database, Pham et al. (2017b) applied an Artificial Neural Network (ANN) to approximate the shear buckling coefficients of beams with central web openings. The ANN is a computational model that acquires all the necessary inputs, which are non-dimensional section and hole size parameters to establish a relationship among these inputs in order to produce answers as close as possible to the expected output provided. The network allows the shear buckling coefficients of the perforated members to be estimated by the following equation:

$$k_v = 5.39\frac{b}{L} - 3.33\frac{d}{b} - 17.7\frac{w}{L} + 11.9\frac{A_0}{A} + 5.37$$

where $L$ is the shear span; $b$ is the web depth; $w$ is the width of web opening; $d$ is the depth of web opening; $A_0$ is the area of web opening; $A$ is the surface area of web plate. This provides a simple and powerful tool to approximate the shear buckling coefficients for beams with various aspect ratios and central hole sizes. For beams with circular web holes, Pham et al. (2017a) proposed a simple approach to convert the circular opening shapes to square ones by using the relation $d = 0.85D$ where $d$ is the square size and $D$ is the circular diameter. This transformation allows the buckling coefficients of members with circular web openings to be determined based on the values for members with square openings.

### 3.2 Shear Strength of Beams with Holes Using the DSM

As mentioned previously, the DSM requires two inputs to compute the member strength directly, including the shear buckling force and the shear yield load. The buckling force is available on the basis of the preceding approaches. The shear load at yielding, conventionally, is determined by the formula $V_y = 0.6A_w f_y$ where $A_w$ is the cross-sectional web area and $f_y$ is the yield stress. Pham et al. (2017a) showed that this expression is not accurate to predict shear strength using the DSM regardless of whether the gross or net area of the web cross-section is used. In other words, the expression to determine $V_y$ needs to be re-formulated to include the web hole. Once stability issues are excluded, as a primary assumption to determine shear yield load $V_y$, FE simulations have shown that the beam with a small web hole subjected predominantly to shear fails by traditional web shear yielding as shown in Fig. 8a. In contrast, the beam with a substantially large hole fails by a Vierendeel mechanism. This type of failure is characterized by a yielding pattern at the four corners of the opening, followed by the formation of the plastic hinges at those locations which triggers the failure mechanism as seen in Fig. 8b. This suggests that the shear load at yielding carried over the large hole is determined as $V_{vrd} = 4M_{pv}/d$ where $M_{pv}$ is the plastic bending moment of the top or bottom segment at the location of the hole and $d$ is the width of the web opening.

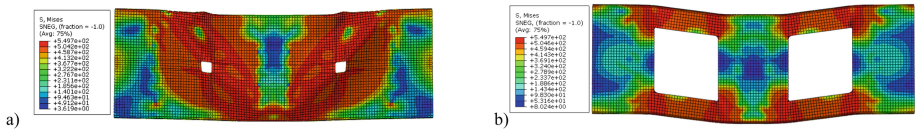


**Fig. 8.** Shear failure modes of 200-mm-deep beam with (a) 20 mm and (b) 120 mm square holes (Pham et al. 2017a)

As a result, a practical model has been developed to describe the transition of failure modes from traditional web shear for beams with small holes to the Vierendeel mechanism for beams with substantially large web holes, shown as the red curve in Fig. 10a. A linear transition has been suggested for beams with intermediate hole sizes. In the case of $d/b = 1.0$, the shear yielding load vanishes when computed on the basis of the net section $V_{y,net}$, but it is still captured well by the proposed method because of the inclusion of the flanges. The new proposal does not require a reduction in the shear capacity until $d/b = 0.1$ by comparison with the net section approach, which requires an immediate reduction. The proposed shear yield load and the buckling loads of beam with holes are used in the DSM design equations for shear to verify the predominantly shear tests conducted by Pham et al. (2014, 2016), as shown in Fig. 9.

The experiments were performed on 200-mm-deep channel members with the thicknesses of 1.5, 1.9 and 2.4 mm and with square hole sizes of 0 (no hole), 40, 80 and 120 mm. The results in Fig. 10b shows that the DSM is able to predict shear strength of beams with holes very well.

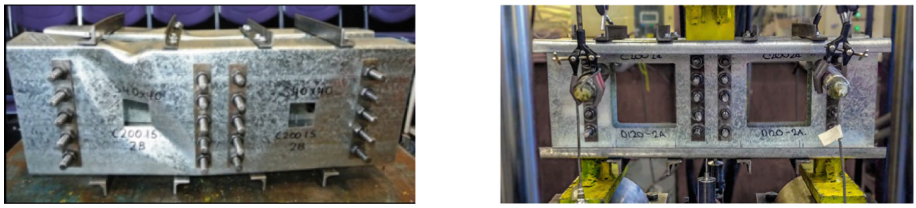

**Fig. 9.** Shear tests on beams with holes (Pham et al. 2014, 2016)

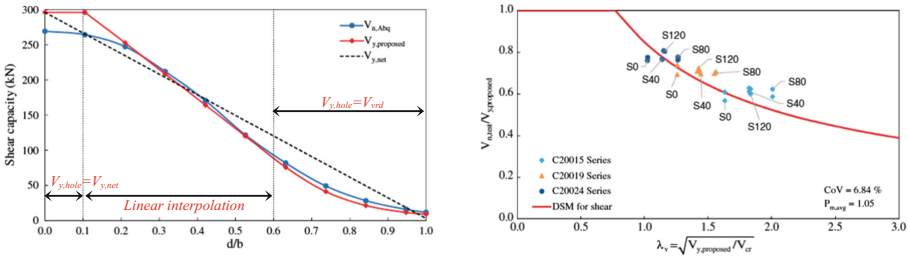


**Fig. 10.** (a) Proposed design model for $V_y$ and (b) its performance (Pham et al. 2017a)

## 4 Conclusion

The DSM of design of thin-walled members has been widely accepted as an alternative to the traditional effective width design approach. The method has been well developed for structures without holes and been available in both the North American specification and the Australian standard. For members with holes, the guidelines for beams and columns have been incorporated recently into the North American specification. The DSM for beams with holes subjected to shear has been developed and is being extended to beams with larger aspect ratios.

**Acknowledgments.** Funding provided by a University of Sydney International Scholarship for the first author is appreciated.

## References

AISI: North American specification for the design of cold-formed steel structural members. In: S100-12th edn. Washington, D.C, U.S.A. (2012)

ANSYS Inc.: Ansys. PA, U.S.A. (2016)

Dassault Systèmes Simulia Corp.: Abaqus/CAE. Providence, RI, U.S.A. (2014)

Eccher, G.: Isoparametric spline finite strip analysis of perforated thin-walled steel structures. The University of Sydney, Australia; University of Trento, Italy (2007)

Hancock, G.J.: Local, distortional and lateral buckling of I-beams. J. Struct. Div. **104**, 1787–1798 (1978)

Hancock, G.J., Pham, C.H.: Shear buckling of channel sections with simply supported ends using the Semi-Analytical Finite Strip Method (2013)

Li, Z., Schafer, B.W.: Buckling analysis of cold-formed steel members with general boundary conditions using CUFSM : conventional and constrained finite strip methods. In: Twentieth International Specialty Conference on Cold-Formed Steel Structures. Missouri Univ. of Science and Technology, Saint Louis, Missouri, U.S.A. (2010)

Lysaght B Structural Products. http://www.lysaght.com/product-applications/structural-products. Accessed 2 Mar 2017

Moen, C.D., Schafer, B.W.: Direct strength method for design of cold-formed steel columns with holes. J. Struct. Eng. **137**, 559–570 (2010)

Moen, C.D., Schafer, B.W.: Elastic buckling of cold-formed steel columns and beams with holes. Eng. Struct. **31**, 2812–2824 (2009)

Nguyen, V.V., Hancock, G.J., Pham, C.H.: Development of the thin-wall-2 program for buckling analysis of thin-walled sections under generalised loading. In: Eighth International Conference on Advances in Steel Structures, Lisbon, Portugal (2015)

Pham, C.H.: Shear buckling of plates and thin-walled channel sections with holes. J. Constr. Steel Res. **108**, 800–811 (2017)

Pham, C.H.: Elastic shear buckling of plates and thin-walled channel sections with centrally located holes. In: Proceedings of the 7th International Conference on Coupled Instabilities in Metal Structures, Baltimore, Maryland, U.S.A. (2016)

Pham, C.H., Chin, Y.H., Boutros, P., Hancock, G.J.: The behaviour of cold-formed C-sections with square holes in shear. In: 22nd International Specialty Conference on Cold-Formed Steel Structures. St. Louis, Missouri, U.S.A., pp. 311–327 (2014)

Pham, C.H., Hancock, G.J.: Direct strength design of cold-formed C-sections for shear and combined actions. J. Struct. Eng. ASCE **138**, 759–768 (2012)

Pham, C.H., Pelosi, A., Earls, T., Hancock, G.J.: Experimental and numerical investigations of cold-formed C-sections with square holes in shear. In: 23rd International Specialty Conference on Cold-Formed Steel Structures, Baltimore, U.S.A. (2016)

Pham, S.H., Pham, C.H., Hancock, G.J.: Direct strength method of design for channel sections in shear with square and circular web holes. J. Struct. Eng. **4017017**, 1–8 (2017)

Pham, S.H., Pham, C.H., Hancock, G.J.: On the design of cold-formed steel beams with holes in shear using the direct strength method. In: The 8th European Conference on Steel and Composite Structures, Copenhagen, Denmark (2017b)

Schafer, B.W.: Designing cold-formed steel using the direct strength method. In: 18th International Specialty Conference on Cold-Formed Steel Structures, Orlando, Florida, U.S.A. (2006a)

Schafer, B.W.: Review: the direct strength method of cold-formed steel member design. In: Stability and Ductility of Steel Structures, Lisbon, Portugal (2006b)

Standards Australia: Cold-formed steel structures. Australian/New Zealand Standard, Sydney, Australia (2005)

# The Need for a Holistic Approach to Address Future Emerging Risks

Paul Smith(✉)

Arup, London, UK
paul-c.smith@arup.com

**Abstract.** In the future, the world and civilised society with its complex infrastructure shall be exposed to more severe and potentially risky hazard and shock scenarios. Climate change will amplify severe hazards into extreme conditions never before experienced. Climate change is an emerging reality in a much more complex and interwoven set of considerations encompassing economic development, population growth and the need for political awareness and real action to be taken. We are also becoming more vulnerable to malicious shock attacks caused by criminal, anti-political and terrorist activities, including situations that involve physical damage, but also "soft-transmitted" cyber-attack aimed at our densely coupled communication and data networks. As scientists, engineers and managers in the carbon-free nuclear industry, it is judged that we need more holistic approaches to risk and hazard assessment that are able to substantiate that the infrastructure is not only robust and resilient enough to withstand the impact, but also to test the capability and effectiveness of the overall 'wider-field' coping strategies; including not only the plant itself, but also the site, the adjacent region and the resident country-wide infrastructure and resource capability. Resilience essentially depends the ease and success for passing through the "coping cycle".

**Keywords:** Holistic approach · Risk · Resilience · Coping strategies · Coping cycle · Coping test

## 1 Hard Times to Come

Our world is changing. Our more intertwined and denser society faces an enormous challenge for ourselves, and future generations. And our world is likely to change to even greater extent, one of the key reasons being climate change that is happening now. Future mitigation of climate change will involve various new technology initiatives and political will that shall have to be developed and actually implemented, including:

- To develop and use carbon-free energy-power generation – nuclear, solar and wind.
- To develop and use by carbon-neutral energy-power generation – biofuels.
- To position power generation plant facilities in low-hazard zones.
- To establish governance policies for system-integrated energy-power generation that accounts for climate change amplified risk-hazards.
- To use power with greater efficiency.
- Lessen power transmission-distribution losses.

© Springer Nature Singapore Pte Ltd. 2018
H. Tran-Nguyen et al. (eds.), *Proceedings of the 4th Congrès International de Géotechnique - Ouvrages -Structures*, Lecture Notes in Civil Engineering 8,
DOI 10.1007/978-981-10-6713-6_96

- Develop more efficient and sustainable buildings and infrastructure.
- To more wisely locate and re-locate urban and rural populous.

Let's try to understand what current and future generations over the next 100 years are likely to be exposed to in terms of climate change effects. This seems too far ahead to comprehend and with gross uncertainty, but that is precisely what the Intergovernmental Panel on Climate Change (or IPCC), in their 5th assessment report of 2014 have done [1]. The most recent information on climate change provided by the findings in the IPCC [1] covers:

- Observed changes in the world's climate and their causes;
- Future climate changes, risks and impacts;
- Future pathways for adaptation, mitigation and sustainable development; and,
- Mitigation and adaptation.

The IPCC identified concern for hidden tipping points in the climatic system of our planet, while the 2014 happened to be the warmest year on record. It is anticipated that this year, 2016, will be even warmer still. And other critical concerns have also been cited, with acidification of the ocean, and loss of oxygen from the ocean's coastal regions and interior. These and many other key topics and events were explained like never before in the IPCC's history since 1988. The future of nuclear power generation and climate change is intertwined. Lurking beneath the "facts" about climate change is a vexing uncertainty related to how human society with its governmental policies and economic growth needs provide energy in the future. In 2014 the IPCC established four graded $CO_2$ emission equivalent scenarios in their 5th assessment report [1], called "Representative Concentration Pathways" (RCPs).

Considerable evidence is now available that shows substantial melting of continental ice that resides on land, including the Greenland and Antarctica ice sheets is occurring earlier than had been originally expected. When adding a storm surge transient condition at vulnerable coastal regions, this implies that the serious flooding experienced today in 2016 that would still allow people and businesses to recover, will be extremely difficult and likely impossible in the next 100 years – so we must start to not assess just "risk", but assess our ability to "cope" with extreme hazards amplified by climate change. In vulnerable regions, any existing nuclear power plants would be inundated and could credible experience what happened in Japan at the Fukushima Daiichi on the 11th March 2011.

Energy and infrastructure designers of the future shall have to consider more carefully and with greater intention to achieve less vulnerability and enhance defensive measures that are robust and ultimately resilient. In particular is the weakness against cyber-attack aimed at our densely coupled communication and data networks, introduced by criminal, anti-political and terrorist groups. And the sophistication of such threats shall become more and more demanding as become highly dependent on our densely coupled and highly interactive communication and data networks. The physical infrastructure that enables conveyance of the communications and data will need to be robust, yet also the transmitted software information shall be vulnerable to malicious cyber-attack.

## 2 Making Nuclear Power Viable for Mitigation of Climate Change

Of the principal forms of carbon-free power generation that presently give the promise for mitigation of climate change caused by $CO_2$ emission, it becomes apparent that the future feasibility and overall goodness of nuclear power generation should be aggressively investigated and potentially actioned, especially taking account of the knowledge and experience that exists in the industry. However, there are fundamental challenges and inhibitions that need to be addressed before the world's governments and public will accept new nuclear power plants as part of the energy-mix that includes wind and solar sources. It is advocated that there are sub-issues that also need to be addressed, specifically the approach we use to persuade the public of nuclear power's safety, together with how we explain risk, and our strategy for adapting to climate change itself, being able to withstand, tolerate and cope with the effects of climate change causing global sea rise, more severe storms, greater demands on infrastructure and many other factors yet to be accounted for.

Nuclear power generation is a carbon-free energy technology that needs to be seriously considered for its ability to mitigate the adverse effects of climate change, but also to give operational robust in power supply with ultimate safety that the public can believe in as we adapt to the actual pathway of climate change that shall show its hand as the decades go by. The generic damage-effect of climate change will likely make "natural" hazards much more extreme and potentially dangerous in the future. Climate change effects have the likelihood of radically degrading and bypassing the safety barriers of previously engineered design bases, well inside the expected service life that will likely equate beyond 100 years – effectively the life time of a nuclear power station.

The risk from more extreme storms and their destructive waves will be arguably greater, coming with a higher chance of existing sea defences being breached and possibly failing completely. Storm waves are much harder to predict if you are guarding against one particular extreme wave that has enough force and energy to destroy previously sound sea defences. It is therefore highly likely that past design margins that were previously adequate shall diminish to such an extent such that existing defences like sea walls and levees shall be totally bypassed, allowing spatially expansive inundation of seawater with enormous energy and unlimited wavelength. The risk to coastal facing regions from extreme storms shall increase significantly over the next few decades, more than past experience would suggest, yet so extreme the damage may become that communities and infrastructure shall no other alternative but to recede back inland.

A major problem arises for coastal-facing nuclear power plants, as planning to move big engineering facilities together with their necessary transmission network introduces profound political, economic and logistical challenges. The practice of nuclear design must now promote innovative thinking so that nuclear plants and their sites can be made resilient to withstand and tolerate an expanded range of expected, probable, possible and even unexpected hazard/shock scenarios that are indicated by the ICPP modelling.

Designers and engineers will be obligated to demonstrate withstand and resilience against more extreme natural external hazards aggravated by climate change. There can be no doubt that designers of the future nuclear power generation technology shall have a unique and highly demanding challenge. This challenge also applies to existing nuclear installations where highly hazardous source terms will be stored, prior and during decommissioning. The reality is that natural disasters and the man-made technological dangers which may accompany them are not linear problems that can be solved in isolation; is not achieved by just addressing individual components parts of an interactive and dynamically changing damage-loss sequence that kills people, destroys the structural fabric of the infrastructure and dictates complete dislocation of communities away from their once-homes. The newly emerging technology for improved robustness with integral resilient technology will enable our energy infrastructure to stay intact with future severe and extreme hazards or shocks beyond the original design capacity and manage emergencies using well founded coping strategies.

Therefore, our past approach and methodology used to analyse risk should be revisited to achieve the robustness and resilience needs when accounting for future hazards aggravated by climate change amplification. It is advocate that the approach to risk reduction into the future should utilise a much more holistic approach assessing if we can cope with severe and extreme hazards, while accounting for the temporal-dynamic impact effects that our critical infrastructure (like nuclear power plants) and the diverse fabric that the urban and rural socio-technical systems will be exposed to. As an innovative and highly technological society, have to develop new forms of risk-coping modelling tools that are better able to account for climate change and extreme hazard events, and especially whether we can actually cope with the hazard scenarios in terms of robustness and resilience. When considering climate change we can no longer just presume the validity and broad utility of previously established quantified risk analysis, simply perceiving risk as predicted probability of occurrence times the estimated unmitigated consequence upon total failure of all the engineered protection and safety measures.

## 3 Future Needs of Risk Assessment with a Holistic Approach

The IPCC introduced a reasonable range of $CO_2$ emission "pathways" that we can benchmark against. The "Representative Concentration Pathways" (RCPs) scenarios help to indicate the severe to extreme climate variations. However, we should be aware that they are simply "projections" that is all too often under question in one way or another because of contradictory business or political (and with usually selfish inward looking) views. These RCPs can be used as benchmarks for future risk assessment and to test the hazard coping strategies, especially if we assume that new nuclear powers plants designed and built over the next decade will likely operate for at least 80 to 100 years, taking the risk assessment benchmark projections to $2026 + 100 = 2126$. Therefore, we need to be confident that the new nuclear power plants that give us carbon-free energy-power shall be safe and the plant, site and region able to cope with any possible severe or extreme hazard conditions. Accounting for the future severe to extreme hazard conditions, and benchmarking to the IPCC's pathways [1] only

applying quantified risk assessment logic purely based on the 'probability times consequence' principle isn't very informative and too blunt an analysis tool.

It is advised that a much more holistic approach is taken to analyse the significance of future emerging risks. Future risk assessment logic should encompass a much broader perspective of the hazard withstand and risk assessment, including an enhanced understanding as to whether the likely future hazard-event scenarios that will impact nuclear power plants, their sites and the adjacent urban or rural regions can actually cope with the hazards as they unfold, as well as conceptually testing whether the proposed response and recovery actions will actually be feasible. In addition, there will be the need to ascertain if safety-critical facilities and their adjacent emergency services can cope with distributed severe hazards.

As scientists, engineers and managers in the carbon-free nuclear industry, it is judged that we need more holistic approaches to risk and hazard assessment that are able to substantiate that the infrastructure is not only robust and resilient enough to withstand the impact, but also to test the capability and effectiveness of the overall 'wider-field' coping strategies; including not only the plant itself, but also the site, the adjacent region and the resident country-wide infrastructure and resource capability. It is suggested the basic "how much should I worry" measure of just probability of occurrence times the unmitigated consequence is too blunt a measure to satisfy society's future needs, especially when needing to account for climate change, as benchmarked to future projections like those provided by the IPCC's RCPs [1].

A much more holistic approach to assess risk and hazards that will impact nuclear power plants is quite important when we consider that nuclear power generation is both (i) part of the carbon-free mitigation agenda, and (ii) when nuclear power plant designers, builders and operators shall have to adapt to the deleterious effects of climate change like with global sea rise. Fundamental difficulties need to be addressed if we are to better cope with accidents and disasters with our increasingly uncertain future, while using nuclear power as a mitigator of climate change while our engineering must be able to adapt in order to withstand and tolerate more problematical event-hazard scenarios. And from the IPCC work, we know that climate change amplified hazards will become more frequent, have greater magnitude, longer impact periods and wider distributed consequential effect.

The following fundamental deficiencies are judged be present with the current approach 'probability + consequence' risk logic that only indicates the chance for things to go wrong and the associated unmitigated consequence, without an understanding of how we should and can cope with future accidents and disasters that will happen:-

- The risk assessment measure of probability and consequence cannot resolve the necessary risk reduction information that shall be needed when modelling severe to extreme natural hazards and climate change effects.
- There is no insight on how accidents and disasters progress through time in real terms.
- The actual damage caused to crucial systems (like energy, transportation, networks, services and supplies) is not fully taken into account.

- There is a gross lack of understanding on whether regional systems and organisations can cope with future unanticipated hazards and shocks; as is expected with climate change causing global sea rise and super storms.
- There needs to be a better understanding of whether regional systems and organisations could survive severe hazard and shock scenarios, especially testing for the capability to recover back to normality.
- No information is provided about the response and recovery needs during a severe hazard and shock scenario, no insight about the scale capability that would be needed to effectively cope with evolving accident or disaster situations.
- The system and/or organisation that needs to be assessed for its exposure to future risk and whether it can cope should be quantitatively modelled. The analysis technique should be verified, validated and subjected to peer review and audit.
- There needs to be an expanded risk assessment logic which considers time on spatial domains using a more holistic perspective, while able to analyse the exposure potential and consequent risk that needs to be prepared for into the future.
- There needs to be an objective test as to whether a particular societal system and/or organisation can actually cope and survive a severe hazard or shock scenario, dependent on the overall integrity of the system or organisation and its ability to withstand extremely severe events.
- No longer is it viable (or commercially wise) for governments or businesses to screen out low probability high impact events, as emphasised by numerous lessons learnt, together with the advent of climate change effects that are projected to exhibit increased wild weather and damaging impacts two coastal regions.

Taking a look at flood risk, the design standard of protection is generally quoted as the "return exceedance" probability of the design flood event, quoted as an annual chance (1 in 100), probability of occurrence (1%) or as a return period (1 in 100 years). In the UK, implemented measures to reduce probability typically protect against floods with annual chance in the range 1 in 75 to 1 in 200, with some large tidal barriers up to 1 in 1000. However, climate change and sea level rise can have a dramatic effect on the return exceedance probability; some high end sea level rise scenarios can turn a present day 1 in 1000 event into a 1 in 150 by 2050, and can become an event occurring more than once a year by 2100. Using this thinking, a present day 1 in 10,000 year return exceedance sea level hazard event could become a 1 in 5 by 2100, as a result of climate change. Thinly spread public budgets in an austere time does not allow us to build defences specified to the worst/highest predictions. The point here is that there is an increasing chance that hazard defences, like with flood risk management measures, will be exceeded over their lifetime. Current risk management tends to focus on setting the optimum economic standard of protection based on risk reduction (prevention of flooding). We have to be aware of the known limitations of designs, testing coping when design standards are exceeded.

Hence, we have to holistically test our protection systems and ensure that our coping strategies actually work. Not only that, but we must also ensure that the previously designed and installed protection systems do not act as inhibitors, or at worst amplifiers of the loss consequences, while hampering the response and recovery countermeasures. Therefore, in addition to the earlier mentioned key analysis principles

that encompass the consideration of the holistic context, the system being affected, the exposure potential, and the system's probable loss of its functional integrity, but also to properly account for the limit states and behaviour of the impacted system, and to better work out what the needed coping strategies should be; for example, by introducing enhanced system robustness, preparedness and resilience. Hurricanes Katrina and Sandy in the USA were conceptual warnings that we must test our ability to cope with severe to extreme transient conditions, checking for how much damage of our complex networks, services and supplies can happen.

All infrastructure and safety-critical industries should re-think how to carry out risk/hazard withstand assessments; the authors strongly advise that there needs to be a more holistic approach, together with particular testing of the coping strategies, their scale, capability and likelihood of success in terms of response and recovery actions. Governments around the world have to understand what specific demands shall come when making ready for population growth, food and water supplies, financing and taxation, economic inputs and outputs needs, public housing, social services, essential services (like electricity and wastewater treatment). Three profound questions become apparent for local and centralized governments in their search for answers:-

- How can the region and its society maintain its coping capability and general wellbeing, knowing that initially severe hazard conditions will gradually lead to more extreme severity of the hazard-shock scenarios more frequently, with greater risk and consequential losses, further aggravated by uncertain rate of climate change and malicious threats in different parts of the world?
- What is the lead time needed to completely relocate a city to a safer locality?
- Where and who do governments, insurers and the emergency services go to for objective insight on what can be done, how to plan ahead, and ultimately how best to reduce the risk posed – which can only be driven by local and central government policy, funded across the tax paying population and business?

"Management of Safety" will require advance in risk analysis software tools taking into account numerous non-linear and dynamic factors when modelling a severe-extreme shock event and/or severe nuclear accident; the range complicating factors include:-

- System representation as a socio-technical system, both human and engineering;
- Temporal time-history of the hazard and damage to the failure event scenarios;
- Scale in term of the direct and indirect spatial impact of the accident/disaster;
- Temporal impact duration both during and after the hazard-shock has impacted;
- Damage to the system, including faulted states and the formation of debris;
- Accounting for malicious cyber-attack, even during hazard and accident scenarios;
- General randomness and gross uncertainty of what's happening;
- Fast rate sensitivity of any critical process or safety protection;
- Time-dependent and interactive cascade and domino effects;
- Complicated change in the dynamic consequences as more damage occurs;
- A-causal situations not accounted for or ever considered need to be accounted;
- Unrevealed states and conditions that could "bias" or "warp" the event sequences;
- Emergency response capability and reliability upon demand;

- Post-event recovery and stabilization, including the probability of success;
- Working out what scale of resources are needed for the response and recovery etc.,

Hazards research now encompasses disciplines such as climatology, economics, engineering, geography, geology, law, meteorology, planning, seismology, and sociology. Professionals, in those and other fields, have continued to investigate how engineering projects, warnings, land use management, planning for response and recovery, insurance, and building codes can help individuals and groups adapt to natural hazards, as well as reduce the resulting deaths, injuries, costs, and social, environmental, and economic disruption. There is a general tendency that the development of coping strategies for managing hazards follow a traditional planning process like:- (a) study the problem, (b) implement one solution, and (c) move on to the next problem. This approach casts hazards as static and mitigation as an upward, positive, linear trend. However, the reality is that coping with severe hazard events is an extremely complex, non-linear and highly dynamic set of circumstances.

Coping resilience is effectively the ability to recover back to a safe and stable state after hazard and/or shock scenarios. It is therefore very important for us to understand what it means to be able to cope with and adapt to extreme hazards into the future, but also to gain insight of when and how certain regions will eventually be unable to cope. The degree of impact from severe to extreme hazards depends on many factors, and varies greatly between less and more developed regional countries. Whether the region impacted has a more developed infrastructure or not, its resilience essentially depends the ease and success to cope, as the region at risk passes through the severe-extreme hazard impact events [2]; temporally defined as before, during and after the severe-extreme event.

## References

1. 5th Assessment Report, Intergovernmental Panel on Climate Change (2014)
2. Smith, P.: Design and Hazard Assessment, TINCE, Paris (2016)

# Transmissibility Based Operational Modal Analysis in Presence of Harmonics

Van-Dong Do[1], Thien-Phu Le[2(✉)], and Alexis Beakou[1]

[1] Université Clermont Auvergne, CNRS, SIGMA Clermont, Institut Pascal, 63000 Clermont-Ferrand, France
{van_dong.do,alexis.beakou}@sigma-clermont.fr
[2] LMEE, Université d'Evry Val-d'Essonne, 40 rue du Pelvoux, 91020 Evry Cedex, France
thienphu.le@univ-evry.fr

**Abstract.** A modal model comprising natural frequencies, damping ratios and mode shapes called modal parameters, is always appreciated due to its appropriate interpretation for physical phenomenon. For real structures, the modal parameters can be obtained from an operational modal analysis that offers several advantages: simple equipment thus low cost, continuous use, real boundary conditions. However, the excitation not controlled and not measured is always assumed as white noise in the operational modal analysis. In presence of harmonics on excitation, the white noise assumption is not verified and that makes the modal identification process difficult, even leading to biased results. A transmissibility function defined by ratio in frequency domain between two responses, is known as independent of excitation nature. This study proposes therefore to apply the transmissibly functions for modal identification in presence of harmonics. The proposition is validated by numerical examples and an experimental test.

**Keywords:** Modal identification · Transmissibility function · Harmonic component · Operational modal analysis

## 1 Introduction

A linear structure in vibrational behavior can be modelled by a spatial model or a modal model. The later one comprising natural frequencies, damping ratios and mode shapes called modal parameters, is always preferred due to its appropriate interpretation for physical phenomenon. The knowledge of modal parameters allows several applications such as: health monitoring of structures, updating finite element models [1]. Classically, modal parameters are obtained from an experimental modal analysis where both artificial excitation by a hammer/shaker, and its structural responses are measured. These dynamic tests are convenient in laboratory conditions. For real structures, an operational vibration testing is more adequate because of several advantages: simple equipment thus low cost, continuous use, real boundary conditions. However, excitation of natural form such as wind, noise, operational loadings, is not measured and hence the name "unknown input" or "response only" dynamic tests. The excitation not controlled and not measured is always assumed as white noise in operational modal analysis [2].

© Springer Nature Singapore Pte Ltd. 2018
H. Tran-Nguyen et al. (eds.), *Proceedings of the 4th Congrès International de Géotechnique - Ouvrages -Structures*, Lecture Notes in Civil Engineering 8,
DOI 10.1007/978-981-10-6713-6_97

In presence of harmonics on excitation for instance structures having rotating components such buildings with fans/air-conditioners, high speed machining machines, the white noise assumption is not verified and that makes the modal identification process difficult, even leading to biased results. To distinguish natural frequencies and harmonic components, several indicators have been proposed using damping ratio, mode shape, and histogram and kurtosis value [3–5].

In order to palliate the white noise assumption, Devriendt and Guillaume [6] proposed to use transmissibility functions defined by ratio in frequency domain between measured responses as primary data. The authors showed that this technique is (i) independent of excitation nature in the neighborhood of a system's pole [6] and (ii) able to identify natural frequencies in presence of harmonics when different load conditions are considered [7]. Araújo and Laier [8] proposed to use only one load condition to identify modal parameters. The authors obtained good results when excitation is of colored noise and singular value decomposition is applied to power spectral density transmissibility matrices.

The aim of this paper is to assess the performance of the modal identification techniques based on transmissibility functions in presence of harmonics. For the sake of completeness, Sect. 2 presents briefly definitions and most relevant properties of transmissibility functions/matrices. The procedure to obtain modal parameters from singular values is also explained. Section 3 is devoted to applications with a numerical example and a laboratory test. The performance of the methods is finally commented in the conclusions section.

## 2 Modal Identification Based on Transmissibility Functions

This section gives a short description of the modal identification method based on transmissibility functions. Interested readers can find a complete presentation of the method and its demonstrations in references [6–8].

### 2.1 Definitions

Vibration responses of a $N$ degree-of-freedom linear structure are noted by vector $\mathbf{x}(t)$ in time domain and in frequency domain by $\hat{\mathbf{x}}(\omega)$. A transmissibility function $T_{ij}(\omega)$ is defined in frequency domain by

$$T_{ij}(\omega) = \frac{\hat{x}_i(\omega)}{\hat{x}_j(\omega)} \tag{1}$$

where $\hat{x}_i(\omega)$ and $\hat{x}_j(\omega)$ are respectively responses in degree-of-freedom (DoF) $i$ and $j$. The transmissibility function depends in general on excitation (location, direction and amplitude) and it is therefore not possible to use it in a direct way to identify modal parameters. Devriendt and Guillaume [6] noted however that at a system's pole, transmissibility functions are independent of excitation and equal to ratio of the mode shape. Let's consider two loading cases $k$ and $l$, the corresponding transmissibility functions are respectively $T_{ij}^k(\omega)$ and $T_{ij}^l(\omega)$. They proposed therefore a new function

$$\Delta_{ij}^{kl}(\omega) = T_{ij}^{k}(\omega) - T_{ij}^{l}(\omega) \tag{2}$$

and noted that the system's poles were also the poles of functions $\Delta_{ij}^{-1\,kl}(\omega) = \frac{1}{\Delta_{ij}^{kl}(\omega)}$. Using $\Delta_{ij}^{-1\,kl}(\omega)$ as primary data, it is possible to apply classical modal identification methods in frequency domain for instance the LSCF method or the PolyMAX method to extract modal parameters. As $\Delta_{ij}^{-1\,kl}(\omega)$ can contain more than the system's poles, the choice of physical poles are performed via the rank of a matrix of transmissibility functions composed from three loading cases

$$T(\omega) = \begin{bmatrix} T_{1r}^{1}(\omega) & T_{1r}^{2}(\omega) & T_{1r}^{3}(\omega) \\ T_{2r}^{1}(\omega) & T_{2r}^{2}(\omega) & T_{2r}^{3}(\omega) \\ \vdots & \vdots & \vdots \\ 1 & 1 & 1 \end{bmatrix} \tag{3}$$

At the system's poles, the second singular value $\sigma_2(\omega)$ of $T(\omega)$ tends toward zeros. The curve $\frac{1}{\sigma_2(\omega)}$ shows hence pics at natural frequencies of the mechanical system.

### 2.2 Method PSDTM-SVD

The application of the previous technique needs three independent loading cases. In practice, it is not simple although a loading case can be different from another by either location or direction or amplitude. Araujo and Laier [8] proposed an alternative method using responses of only one loading case. The method denoted by PSDTM-SVD, is based on the singular value decomposition of power spectrum density transmissibility matrices with different references. From operational responses, a transmissibility function between two responses $x_i(t)$ and $x_j(t)$ with reference to response $x_k(t)$ is estimated by

$$T_{ij}^{k}(\omega) = \frac{S_{x_i x_k}(\omega)}{S_{x_j x_k}(\omega)} \tag{4}$$

where $S_{x_i x_k}(\omega)$ is the cross power spectrum density function of $x_i(t)$ and $x_k(t)$. Assume that responses are measured at $L$ sensors; it is thus possible to establish $L$ matrices $T^{(j)}(\omega)$ by

$$T^{(j)}(\omega) = \begin{bmatrix} T_{1j}^{1}(\omega) & T_{1j}^{2}(\omega) & \dots & T_{1j}^{L}(\omega) \\ T_{2j}^{1}(\omega) & T_{2j}^{2}(\omega) & \dots & T_{2j}^{L}(\omega) \\ \vdots & \vdots & \vdots & \vdots \\ T_{Lj}^{1}(\omega) & T_{Lj}^{2}(\omega) & \dots & T_{Lj}^{L}(\omega) \end{bmatrix}, j = 1 \cdots L \tag{5}$$

Araujo and Laier [8] showed that at a natural frequency $\omega_m$, the columns of $T^{(j)}(\omega_m)$ are linearly dependent. That is equivalent with the rank of the matrix is equal

to one. Using singular value decomposition of $T^{(j)}(\omega)$, singular values from second to $L^{\text{th}}$ tend toward zero. The inverse of these singular values can be used to assess the natural frequencies of the system. The authors proposed a global curve via two stages of average. The first stage is to take average of singular values from second obtained with $L$ matrices $T^{(j)}(\omega)$

$$\hat{\sum}^{-1}(\omega) = \frac{1}{L}\sum_{j=1}^{L}\left[\frac{1}{\sigma_2^{(j)}(\omega)} \quad \frac{1}{\sigma_3^{(j)}(\omega)} \quad \cdots \quad \frac{1}{\sigma_L^{(j)}(\omega)}\right] = \left[\frac{1}{\hat{\sigma}_2(\omega)} \quad \frac{1}{\hat{\sigma}_3(\omega)} \quad \cdots \quad \frac{1}{\hat{\sigma}_L(\omega)}\right] \tag{6}$$

In the second stage, the global curve $\pi(\omega)$ is obtained by the product of the averaged singular values as

$$\pi(\omega) = \prod_{k=2}^{L}\frac{1}{\hat{\sigma}_k(\omega)} \tag{7}$$

The natural frequencies are indicated in the curve $\pi(\omega)$ by peaks.

## 3 Applications

### 3.1 Numerical Example

A two-Degree-of-Freedom (DoF) system was used for numerical validation. It is illustrated in Fig. 1a with its mechanical properties. The excitation force is generated using a combination between a white-noise excitation and harmonic excitation, located at the second DoF $(f_1(t) = 0, f_2(t) \neq 0)$. The harmonic excitation has the form of $A\sin(2\pi f_0 t)$ and the Gaussian white-noise excitation has zero mean and standard deviation $\sigma_w$. The relative weight of the white noise and the harmonic excitation is measured by the signal to noise ratio (SNR) in dB, defined by

$$SNR = 20\log_{10}\left(\frac{\sigma_w}{\sigma_h}\right) \tag{8}$$

where $\sigma_h = \frac{A}{\sqrt{2}}$ is standard deviation of the harmonic excitation. In this example, harmonic component was kept constant with $A = 10$ and $f_0 = 50\,(\text{Hz})$ while the white noise was taken with different values of $\sigma_w$ to simulate different SNR levels. Figure 1b presents responses in displacement corresponding to SNR $= 8$ dB. They were obtained by the Runge-Kutta algorithm, with $50,000$ points and sampling period $\Delta t = 0.002(\text{s})$.

The PSDTM-SVD method was applied to identify the modal parameters of the system. The power spectral density functions were estimated with Hamming windows of 2048 points and 75% overlapping. The Frequency Domain Decomposition (FDD) method [3, 4] was also used for comparison purpose.

The performance of the PSDTM-SVD method was checked with different values of SNR. It can be noted that when SNR $\geq 8$ dB, two structural modes are easily identified from the $\pi(.)$ curve and the peak of 50 Hz is almost reduced. Figure 2 shows $\pi(.)$ curve

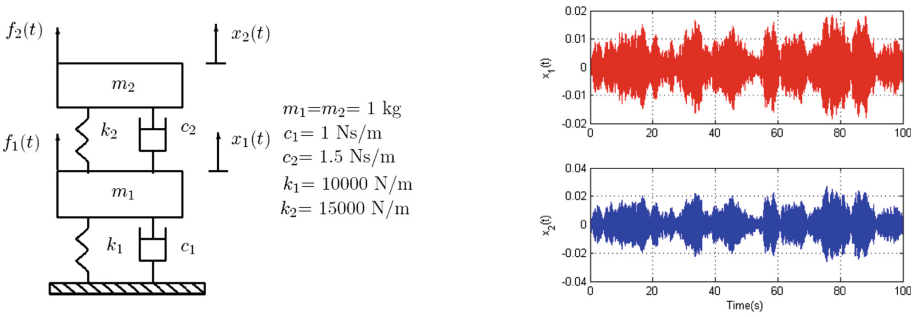


(a) (b)

**Fig. 1.** (a) 2 DoFs system, (b) simulated responses for SNR = 8 dB.

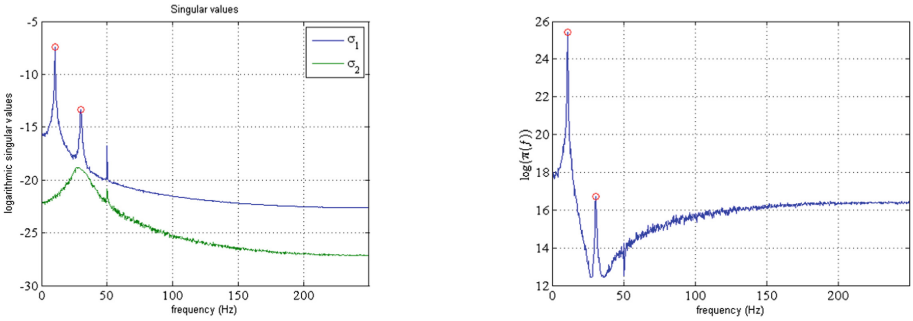


(a) (b)

**Fig. 2.** SNR = 8 dB: (a) FDD method; (b) PSDTM-SVD method.

and singular curves when SNR = 8 dB. The peak corresponding to the harmonic frequency in the PSDTM-SVD method is quite eliminated while its peak is still well visible in the FDD method. Table 1 presents identified modal parameters. They are in good agreement with their exact values.

When harmonic component becomes more important, i.e. SNR decreases, the peak of 50 Hz is more visible in the $\pi(.)$ curve and it makes the identification process

**Table 1.** Exact values and identified values of modal parameters of the 2 DOFs system

| Modal parameters | Exact | FDD | PSDTM-SVD |
|---|---|---|---|
| $f_1$ (Hz) | 10.3004 | 10.2539 | 10.2539 |
| $f_2$ (Hz) | 30.1183 | 30.0293 | 30.0293 |
| Mode 1 | 1.0000 | 1.0000 | 1.0000 |
| | 1.3874 | 1.3880 | 1.3878 |
| Mode 2 | 1.0000 | 1.0000 | 1.0000 |
| | −0.7208 | −0.6981 | −0.7200 |

more complex. Figure 3 presents curves for the case SNR = 0 dB. One notes the presence of the harmonic frequency in both the PSDTM-SVD method and the FDD method.

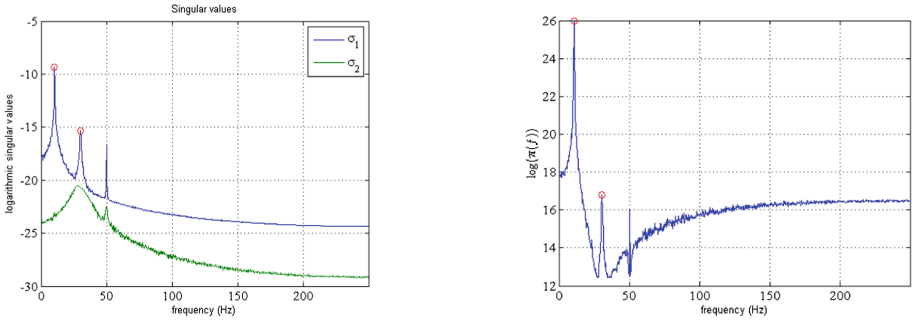


(a) (b)

**Fig. 3.** SNR = 0 dB: (a) FDD method; (b) PSDTM-SVD method.

### 3.2 Laboratory Experimental Test

In order to investigate the efficiency of the transmissibility functions based approach, an experimental test was carried out for a beam of Dural material. The beam is of 850 mm in length and has a rectangular cross-section of 40 mm × 4.5 mm. The Dural material has a Young modulus of 74 GPa and a density of 2790 kg/m$^3$. The beam was clamped at its left side and connected at 700 mm to LSD 201 shaker which was suspended by steel cables with a support. Time responses were recorded at three points by accelerometers with 192,000 points and a sampling period of 0.0025 s. The signals were divided into 75% overlapping segments of 2048 points for PSD estimate. Two load conditions were considered. Load case 1 denotes the case when there is only white noise excitation generated by the shaker. Load case 2 indicates the case when the white noise is added by the excitation generated by a rotating mass on a motor located at 315 mm from the left boundary. The experimental test configuration is presented in Fig. 4.

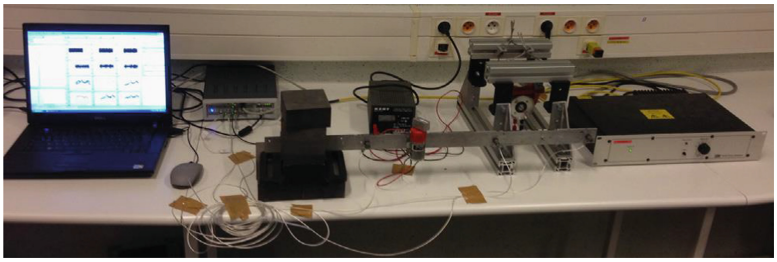

**Fig. 4.** Laboratory test: instrumented beam.

Three first modes of the beam were easily identified by the PSDTM-SVD method from the load case 1. Figure 5a shows clearly three peaks of these modes in the $\pi(.)$ curve. The identified frequencies and mode shapes from the load case 1 are given in Table 2.

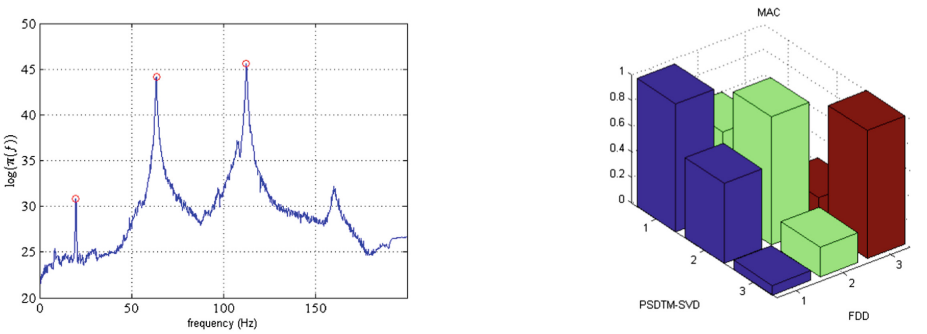


(a) (b)

**Fig. 5.** Load case 1: (a) PSDTM-SVD method, (b) MAC matrix between modes shapes

They are quite identical for the PSDTM-SVD method and the FDD method. Figure 5b shows the correlation of identified mode shapes through the modal assurance criterion (MAC) matrix.

**Table 2.** Laboratory test: Identified modal parameters from load case1.

| Modal parameters | FDD | PSDTM-SVD |
|---|---|---|
| $f_1$ (Hz) | 19.7266 | 19.7266 |
| $f_2$ (Hz) | 63.4766 | 63.4766 |
| $f_3$ (Hz) | 112.5000 | 112.5000 |
| Mode 1 | 1.0000 | 1.0000 |
| | 2.0022 | 1.9609 |
| | −2.0401 | −1.9598 |
| Mode 2 | 1.0000 | 1.0000 |
| | −2.2233 | −2.2225 |
| | 6.0712 | 6.0802 |
| Mode 3 | 1.0000 | 1.0000 |
| | −1.5406 | −1.5418 |
| | −2.2172 | −2.2146 |

For the load case 2, in the $\pi(.)$ curve of the PSDTM-SVD method in Fig. 6a, there are additional peaks; especially the predominance of the first peak at 13.33 Hz. It comes from the rotating eccentric mass of 800 rpm. Among the three structural modes

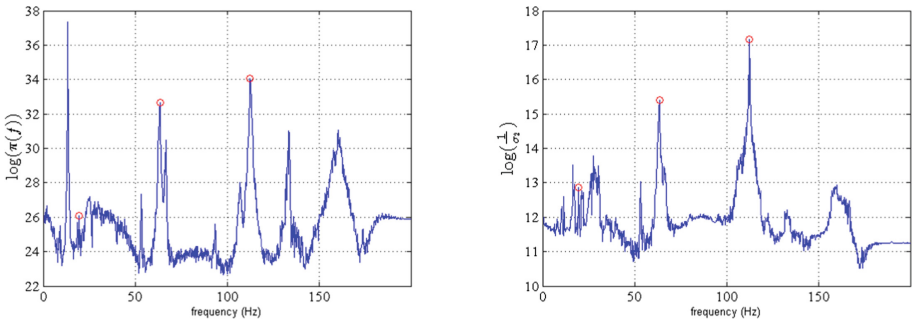


(a) (b)

**Fig. 6.** Load case 2: (a) PSDTM-SVD method, (b) transmissibility method with load cases 1 and 2.

previously identified with the load case 1 and indicated by circle markers in Fig. 6a, the first mode is almost hidden by the harmonic of the rotating mass.

In order to reduce the influence of the harmonic component, both load cases were together used. The matrix $T(\omega)$ given in Eq. (3) was established with two load cases instead of three. The inverse of its second singular values is presented in Fig. 6b. The peak of the harmonic component is much reduced and the peaks of second and third structural modes become the most dominant. The first structural mode is however still difficult to identify.

## 4 Conclusions

The operational vibration testing is the most convenient for real structures. However, its common assumption of white noise excitation is rarely verified in real conditions, particularly when harmonic components are inside excitation due to rotating part of mechanical systems and structures.

Transmissibility functions and matrix used as primary data are recognized as independent of nature of excitation. They can thus alleviate the assumption of the white noise excitation. The performance of this approach through the PSDTM-SVD method is studied in this work when both harmonic excitation and white noise excitation exist together.

The results of the two degree-of-freedom numerical example show that the PSDTM-SVD method is performant and structural frequencies are well identified when white noise excitation is more dominant than harmonic component $(\text{SNR} \geq 8\ \text{dB})$. If they are of same order $(\text{SNR} = 0\ \text{dB})$, the peak of the harmonic component cohabits with structural modes. It makes the modal identification process difficult.

For the laboratory experimental test, the PSDTM-SVD method gives good results if there is only white noise excitation. When harmonic excitation is added to the white noise excitation, the predominance of the harmonic component among the peaks complicates the distinction between the harmonic and structural frequencies. The predominance is

reduced when both available load conditions are used together. The sharpness of the first structural mode close to the harmonic component is however also reduced.

**Acknowledgments.** This work is funded by the European Union and by the Auvergne-Rhône-Alpes region through the CPER 2015-2020 program. Europe is committed to Auvergne with the European Regional Development Fund (FEDER).

## References

1. Maia, M.N., Silva, J.M.: Theoretical and Experimental Modal Analysis. Research Studies Press, Baldock (2003)
2. Le, T.-P., Paultre, P., Weber, B., Proulx, J., Argoul, P.: Modal identification based on ambient excitation tests. In: Proceedings of 24th IMAC conference (2006)
3. Brincker, R., Andersen, P., Moller, N.: An indicator for separation of structural and harmonic modes in output-only modal testing. In: Proceedings of IMAC XVIII (2000)
4. Jacobsen, N.-J.: Separating structural modes and harmonic components in operational modal analysis. In: Proceedings of IMAC XXIV (2006)
5. Le, T.-P., Argoul, P.: Distinction between harmonic and structural components in ambient excitation tests using the time–frequency domain decomposition technique. Mech. Syst. Signal Process. **52–53**, 29–45 (2015)
6. Devriendt, C., Guillaume, P.: Identification of modal parameters from transmissibility measurements. J. Sound Vib. **314**, 343–356 (2008)
7. Devriendt, C., De Sitter, G., Vanlanduit, S., Guillaume, P.: Operational modal analysis in the presence of harmonic excitations by the use of transmissibility measurements. Mech. Syst. Signal Process. **23**, 621–635 (2009)
8. Araújo, I.G., Laier, J.E.: Operational modal analysis using SVD of power spectral density transmissibility matrices. Mech. Syst. Signal Process. **46**, 129–145 (2014)

# Unibridge®: A New Concept in Prefabricated Modular Bridge

N. Matiere, Q.H. Ung(✉), and P.A. Nicolaudie

MATIERE SAS, Rue Louis MATIERE, Arpajon sur Cère, France
{n.matiere,uqh,pa.nicolaudie}@matiere.fr

**Abstract.** Unibridge® is a pre-designed and prefabricated modular steel bridge system. It is a simple, robust and durable structure suitable for use in emergency situations and as a permanent bridge. Unibridge® is a modular predesigned and prefabricated steel bridge system. It has been designed for international load classes and can be built in single lane or multi-lane road width. It uses either a steel deck system with anti-skid coating or concrete deck.

Unibridge® is constructed from prefabricated girders either 11.4 m or 6 m length. They are pinned end to end and connected transversely with spacers which allows for the installation of a steel deck with anti-skid coating or a concrete deck in-situ. The prefabricated girders are provided in three different heights (1 m, 1.25 m and 1.6 m) and the span of the bridge dictates which girder to use.

Multi-span bridges can be built to achieve bridge lengths up to 57 m. As with single span bridges, Unibridge® multi-span bridges can be cantilever launched from the home bank to the far bank.

**Keywords:** Bridge · Steel · Modular structure · Prefabrication

## 1 Introduction

The first portable metallic bridges were invented during WWII. The heaviest parts could be carried by teams of 4 or 6 men. The elements could be assembled on site by a section of the Army Corps of Engineers.

Allied Armed Forces made ample use of this lateral beams' type of bridge to replace structures destroyed by the occupying Army. "Without these, we couldn't have won the war", asserted General Montgomery. During the 60 following years, the lateral beams bridges have been used extensively, as temporary structures, on worksites, following natural disasters or in war zones.

But in 2003, a whole new concept changed everything: more engineered to suit modern vehicles and yet more modular, easier to assemble as well as more aesthetic, UNIBRIDGE® by Matière® has revolutionized the metallic bridge market.

Multiple panels and parts have been replaced by 11.4 m long watertight box girders, prefabricated in factory conditions and assembled on site.

The process has been approved by the Committee IVOR (Group of independent Experts examining innovations, Direction of Research, and Technical Scientific Animation, Ministry of Transport, of Equipment, of Tourism and of the Sea-France), who

© Springer Nature Singapore Pte Ltd. 2018
H. Tran-Nguyen et al. (eds.), *Proceedings of the 4th Congrès International de Géotechnique - Ouvrages -Structures*, Lecture Notes in Civil Engineering 8,
DOI 10.1007/978-981-10-6713-6_98

found it to be “original in its functionalities (modular geometry, scalability over time) and in the assembly methods implemented” and has won some awards [1, 2].

## 2 Basic Concept

Made of beam elements 11.40 m and 6.10 m long, assembled lengthwise by pins and transversally by spacers, the UNIBRIDGE® is entirely modular (Fig. 1).

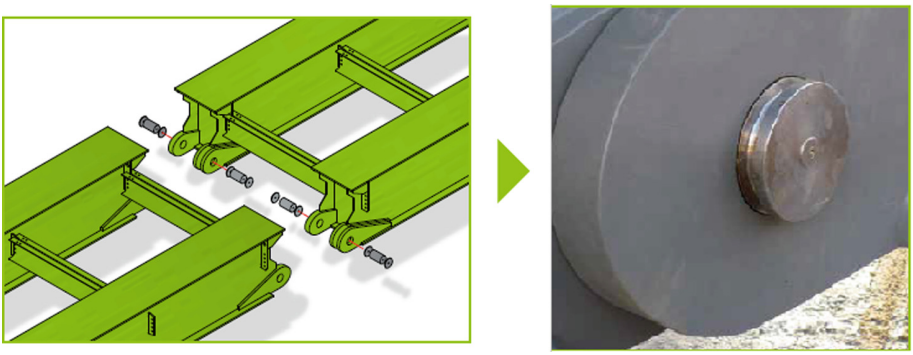

**Fig. 1.** Lengthwise connexion by pins principle.

It is possible to construct bridges with multiple spans. At this time, the maximum length between two bridge bearings is approximately 57 m (Fig. 2).

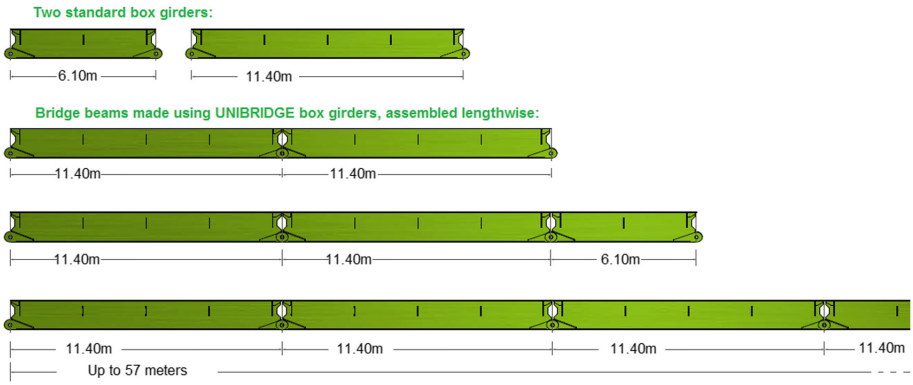


**Fig. 2.** Longitudinal modularity.

Its transversal modularity allows the UNIBRIDGE® to increase its carriageway’s width, anytime during the structure’s lifetime, by adding extra beams. It may also be dismantled and reassembled elsewhere if the user wishes (Fig. 3).

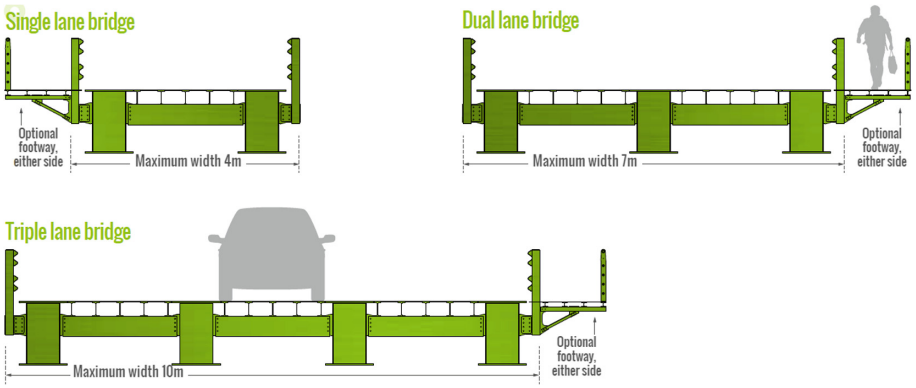


**Fig. 3.** Transversal modularity.

The UNIBRIDGE® structures are extremely robust and durable. They are calculated according to the standards in effect within the country where they are to be implemented (Eurocodes, AASHTO, British Standards, Australian Standards, SATCC, etc.). Accepted load specifications are therefore those defined by the selected standards.

## 3 Manufacturing Process

All steel used in UNIBRIDGE® is of the same grade and origin as those used on major metallic art structures. It originates from European factories and is subject to permanent traceability standards throughout the manufacturing process.

The European NF EN1090-2 manufacturing standard is applied to all manufacturing operations of girders, decking and accessories (from flame-cutting to final machining, including fabrication by means of welding robots).

Particular care is given in applying the anticorrosive agent: after going through the shot-blasting unit, components are painted in compliance with ACQPA specifications, or galvanized.

Ongoing audits are performed throughout the manufacturing chain, from steel traceability to pre-painting coarseness control, from welding verification to checking the adhesive properties of the anti-skid coating. Once they are completed and recorded, these audit files represent a valuable set of references for the bridge, prior to commissioning.

## 4 Implementation

Made of beam elements 11.40 m and 6.10 m long, the modules are easy to transport. By road, a semi-trailer lorry is sufficient. By sea, all components fit into 40-foot containers.

The UNIBRIDGE® is designed to be installed quickly and easily using minimal equipment. It can be erected within very short notice using small erection teams: 6 staff members assemble a 45 m span in 12 h.

The type of installation is based on the aspects of the bridge site, which determine the bridge's implementation method: height, location of the water, launching means available. We can use one of two classical methods:

Crane installation: Crane installation involves assembling the principal beams (UNIBRIDGE® box girders) on the ground. With minimal preparation and faster installation, craning is a rapid solution, and can be adapted to the equipment and tools available on-site. The crane then lifts them individually onto their permanent bearings before they are linked together by spacers (Fig. 4a).

Launching: The beams are positioned on frames or rollers, in a straight line along the axis of the gap to be spanned. In the event of a long or wide bridge, lines of beams are launched one after the other. A launching nose is installed on the leading beam. The line of beams are then either pulled into place using a winch, or pushed using an excavator or other common construction machinery. This operation is repeated for each beam before they are linked together by spacers (Fig. 4b).

**Fig. 4.** (**a**) Crane installation method; (**b**) Launching method

As well as a metallic or wooden deck, the UNIBRIDGE® can be fitted with a composite (metal-concrete) deck.

Classical steel deck: The use of a steel deck with anti-skid coating allows the bridge to be opened to traffic immediately after installation. Deck components can be also provided as prefabricated elements.

Concrete deck: Once the steel beams are installed by launching or by crane, a lost formwork (galvanized cladding) is installed, the reinforcing bars are then put in place and the concrete is poured directly. The concrete is waterproof-tested and the footways are installed. Lastly, the roadway surface is completed. The process of concrete pouring, drying and application of roadway surface takes approximately 2 weeks.

## 5 Applications

A permanent bridge, adapted to every situation that can also be temporarily installed, then dismantled and replaced. The UNIBRIDGE® can either be temporary or permanent, and is therefore relevant to many situations (road structures, railway structure, mining works, worksites, natural disasters zones, etc.).

**Fig. 5.** Some applications of UNIBRIDGE® structures.

It is also adapted to maritime needs and may be used for military operations such as: emergency bridges, access restoration, civil-military operations, humanitarian operations.

It may be sold or rented for the duration of a worksite or reconstruction.

For example, the Unibridge® system can be used for the following applications;

- Shared pathway pedestrian bridges for pedestrians and bicycles using one single box girder.
- Single lane road bridges with individual spans up to 50.8 m using two box girders and a load capacity to meet most civil requirements.
- Double lane or triple lane road bridges with individual spans up to 44.8 m using three box girders and a load capacity to meet most civil requirements.

- Flyover/overpass applications.
- Military applications (military load MC80 or equivalent up to 72 tonnes e.g. Abrams tanks).
- Mining applications up to 200 tonnes capacity.
- Railway applications with spans up to 22 m with one single track and one or two pedestrian walkways.
- Marine applications using modules which form the key components of the access pier connecting the lifting bridge/ramp to the terminal building of a modular RO-RO (Roll-On, Roll-Off) maritime port.

To date, UNIBRIDGE® structures have been built in Oceania, South East Asia, Africa, Indian Ocean, Middle East, Caribbean and Central America (Fig. 5).

## 6 Conclusions

The UNIBRIDGE® system is a new and innovative steel bridge concept which eliminates individual design time and cost. It allows the rapid construction of bridges for a wide variety of uses thank to its modular standardized elements. Such a structure has the following features:

- All bridge connections are made with either pins or bolts and there is no need for any specialist tools such as pneumatic or electric powered tools. All tools are hand operated. There is no on-site welding.
- Unibridge® is routinely launched across gaps using a launching nose and equipment without the need for temporary supports.
- Unibridge® has been designed to accommodate a range of live loads e.g. AASHTO, Eurocode, British Standards and all Unibridge® structures are capable of carrying these loads.
- The bridge is designed for 100 year design life with a fatigue life of more than 1,000,000 cycles of the appropriate Eurocode vehicle.
- Unibridge® is capable of accommodating abnormal loads, both oversized and overweight vehicles, and the structural members are underneath the deck level with no chance of vehicle collision or damage.
- Unibridge® does not require the addition of reinforcement members depending on the span and load configuration.
- The installation of modular steel deck system with anti-skid system or concrete deck in-situ or concrete desk pre-cast.

With regard to sustainable development, Unibridge® fits with all criteria [3]:

- Re-use: The product is reusable. Since it is easy to dismantle, easy to transport, easy to reassemble, the metallic bridge may have several lives. The material, steel, has almost unlimited recycling potential.
- Industrialization: The standardized product is manufactured according to methods that allow industrialization of tasks, an optimal process and a minimum laboriousness.

- Zero defects: The quality control process runs throughout the entire manufacturing cycle: origin and traceability of steel, welding, anti-corrosion coating checked at the factory. The components are produced in series, they are identical and interchangeable.
- Carbon emission limitation: Container shipment from the plant promotes loading/unloading operations during shipments and lower carbon emissions.
- Modularity: A highly reduced number of industrial components thank to the extreme longitudinal and transversal modularity.
- Sustainability: One lane bridge at the first time, then one can add/remove lanes afterwards if traffic demands.
- Respect for the environment: The wide range authorized by the process allows respecting the aquatic environment and the biodiversity by limiting or suppressing the supports in river.
- Easy implementation: Assembly is facilitated for local labor; no welding is required on site.

## References

1. Beideler, J.: Jean-Piere Lamoure, FNTP "Assister les entreprises dans l'innovation" Moniteur N° 5296 (2005). http://www.lemoniteur.fr/articles/jean-pierre-lamoure-fntp-assister-les-entreprises-dans-l-innovation-182803
2. Sas, M.: Somerset Council's excellent engineers awarded (2011). http://www.unibridge.net.au/en/view/somerset_councils_excellent_engineers_awarded/default.aspx
3. Eiffage Construction durable – Pratiques et Procédés-Savoir-faire exclusifs-CD-BM01 – UNIBRIDGE (2012)

# Water Treatment and Environment (WTE)

# A Modified Model for the Prediction of Bioclogging in Saturated Porous Media

Hoang Lam Pham(✉), Philippe Sechet, and Zhujun Huang

Laboratoire des Ecoulements Geophysiques et Industriels,
CNRS/UJF/G-INP, UMR5519, Grenoble, France
{Hoang-Lam.Pham, Philippe.Sechet,
Zhujun.Huang}@legi.grenoble-inp.fr

**Abstract.** Bioclogging or the process that biofilm is conditioned for the development in porous media, leading the biomass accumulation in pore spaces and reducing the permeability of porous media that impedes fluid flow. Numerous research has focused on the study of bioclogging, but the process is very complicated and still poorly understood. This results in various permeability models that are only capable of predicting under certain conditions. In the study, we aim to mathematically develop a macroscopic model to predict permeability reduction in the saturated biofilter. The model adopts the concept that permeability reduction results from two mechanisms: pore radius reduction and pore plugging by mass accumulation. In the former, porosity, grain sizes, tortuosity and bulk factor determine the magnitude of permeability reduction. The pore plugging, in the other hand, interprets recent experimental findings of straining process in deep bed filtration that clogging in pore throat can be induced by deposited particles with the diameter many times smaller than that of pore throat. The model proves its capacity by obtaining a good match to a wide range of experimental data in predicting: permeability of clean porous media and magnitude of bioclogging in the biofilter.

**Keywords:** Permeability reduction · Biofilter · Biofilm · Porous media

## 1 Introduction

Knowledge of bioclogging of porous media is crucial to many engineering processes: in situ bioremediation of soil and groundwater, biofilter wastewater and air pollutant treatment, geological carbon sequestration, microbial enhanced oil recovery. In the study concerning microbial process in porous media, along with the effort to solve advection-diffusion-reaction equations that represent the mass balance of solutes, one must deal with the momentum conservation that characterizes fluid pattern in porous media (Kildsgaard and Engesgaard 2001; Seifert and Engesgaard 2007; Karrabi et al. 2011). Many permeability models have been developed to predict permeability reduction in porous media. The models root from the process that mass accumulation leads to the decrease of pore space, resulting in permeability reduction. Therefore, the connection between permeability and porosity is the objectives of many studies for the development of permeability models.

© Springer Nature Singapore Pte Ltd. 2018
H. Tran-Nguyen et al. (eds.), *Proceedings of the 4th Congrès International de Géotechnique - Ouvrages -Structures*, Lecture Notes in Civil Engineering 8,
DOI 10.1007/978-981-10-6713-6_99

The most popular permeability model was proposed by Carman (1937). The model stated that the magnitude of permeability reduction depends on the third power of porosity:

$$\frac{K}{K_0} = \left(\frac{n}{n_0}\right)^3 \frac{(1-n)^2}{(1-n_0)^2} \left(\frac{d_G}{d_{G,0}}\right)^2 \tag{1}$$

Where $K_0$, $n_0$,$d_{G,0}$ are permeability ($m^2$), porosity (-) and grain diameter (m) of the clean bed, without the effect of mass deposit, respectively. Similarly, K, n,$d_G$ are permeability ($m^2$), porosity (-) and grain diameter (m), respectively at time t when geometric of porous media is affected by mass accumulation.

The term of grain size on the right-hand side of Eq. (1) can be mathematically interpreted as a function of porosity, the relative permeability is found to have the power relationship with relative porosity, and this feature receives consensus of many studies about permeability reduction in porous media. Clement et al. (1996) developed a macroscopic model connecting permeability and porosity, and found that power number of 19/6 obtained the good match to the biofilm-based model proposed by Taylor et al. (1990) and was referenced in some macroscopic models to predict permeability change in porous media (Ham et al. 2007; Kildsgaard and Engesgaard 2001).

A similar form of the power relationship between permeability and porosity was reported by Verma and Pruess (1988). In this model, a new definition of critical porosity was introduced, which was based on the observation that when porosity is less than critical porosity, permeability is approximately equal to zero (Verma and Pruess 1988). Ebigbo et al. (2010) used the critical porosity of 0.6 in modeling permeability reduction in porous media. Its value was based on experiments conducted by Cunningham et al. (1991). In the columns conditioned for biofilm growth of Pseudomonas aeruginosa, the relative permeability (defined as the ratio $K/K_0$) was closed to $10^{-4}$ when the volumetric fraction of biofilm reached 0.4.

Other studies attributed the possibility that a portion of the pore is plugged by mass deposition which induces permeability reduction (Thullner et al. 2002; Vandevivere 1995). In the mathematical derivation, the permeability of plugged areas is characterized by a minimum permeability $K_{min}$. In this approach, the biofilm was considered as porous materials that can convey fluid at very low rate. The total permeability of porous media assuming that permeability reduction is caused by only plugging is approximately represented by an harmonic relationship function of initial permeability $K_0$ and biofilm permeability $K_{min}$. The value of $K_{min}$ can be approximately with the magnitude of permeability of clean bed: $K_0/K_{min}$ = 2500–10000 (Vandevivere 1995).

$$\frac{K}{K_0} = \frac{K_{min}/K_0}{1 - \frac{n}{n_0} + \left(\frac{n}{n_0}\right)\left(\frac{K_{min}}{K_0}\right)} \tag{2}$$

Vandevivere (1995) combined the two concepts to explain of bioclogging. Porous media is treated as bundles of capillary tubes which shelter for biofilm development. In the feedback, biofilm alters tube in both patterns: tube diameter reduction and a portion

of the tube plugging. The biomass that contributes to each pattern is characterized by F ($n_M$) which is dependent on mass concentration.

$$F(n_M) = \exp\left(-0.5\left(\frac{n_{M,rel}}{n_{M,c}}\right)^2\right) \tag{3}$$

where $n_{M,rel}$ is the relative volumetric fraction of mass deposition, equal to the ratio of the volumetric fraction of mass deposition ($n_M$) to the maximum porosity of porous media ($n_0$). $n_{M,c}$ is the value which indicates how fast mass aggregates are formed and plug pore space.

As we have seen above, many permeability models have been developed and used to study the microbial processes in porous media. However, the existing models include empirical parameters that are originated from experimental conditions or model assumptions. Carman (1937) introduced a constant, which its value along with the effect of tortuosity was approximated to 5. Vandervivere (1995) assumed that biomass distribution for each pattern of clogging followed the normal distribution and reported that the critical parameter which determines the distribution is not available or difficult for experimental measurement. Thullner et al. (2002) included empirical parameters that correlate to numerical results in an interconnected network of capillaries. In the estimating permeability reduction, one may cope with the problem of the discrepancy in the predicted results compared to the existing models. In the study, we aim to develop a permeability model for saturated porous media. The important goal of the work is to provide a macroscopic model that can be used to predict a wide range of experimental bioclogging data. Specifically, the model is mathematically derived from the Hagen–Poiseuille equation that characterizes the laminar flow rate in the capillary tube and Darcy's law that defines fluid flow in porous media at macroscopic scale. The model also mathematically interprets two possible mechanisms that result in permeability reduction: pore radius reduction and pore plugging for the best presentation of bioclogging in porous media.

## 2 Model Development

Porous media can be represented by many conceptual models: sphere-in-shell (Happel 1958), capillary tube (Tien 1989), and constricted tube (Payatakes et al. 1973). In this study, porous media is treated as bundles of capillary tubes and Fig. 1. presents the possible mechanisms that reduce pore space of porous media. Biomass covers the inner

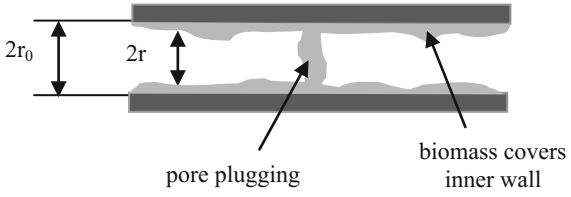


**Fig. 1.** Schematic representation of mechanisms that results in permeability reduction.

wall, leading to the decrease of pore radius from $r_o$ to r. Biomass also plugs the portion of capillary tubes, impeding fluid flow. In recent studies of the retention of bacteria, colloid or nanoparticles in packed column, straining has been reported as an important mechanism contributes to the removal of suspended particles (Bradford et al. 2002). This process was showed to occur at the early stage (time scale of seconds) and the very low ratio of particle diameter and grain diameter of 0.002 (Bradford et al. 2002). Motivated by the recent findings of straining, our work adopts the concept that permeability reduction by the decrease of pore radius ($K_R$) and permeability reduction by pore plugging ($K_P$) contribute to the overall permeability reduction of porous media (K).

For laminar flow through the tortuous capillary with radius r, Hagen–Poiseuille equation can be used to characterize the flow rate:

$$u = \frac{1}{8}\frac{\Delta P}{L\tau}\frac{r^2}{\mu} \tag{4}$$

Where u is the flow velocity in the capillary tube ($ms^{-1}$).μ is the dynamic viscosity ($kgm^{-1}s^{-1}$). r is the radius of the capillary tube (m). L is the strength line distance of capillary tube (m), ΔP is the pressure loss (pa) and τ is tortuosity of the capillary tube (-). The value of τ implies the level of tortuosity of the capillary tube. In this work the tortuosity model proposed by Yu and Li (2004), which the description of flow path is based on grain geometry is used:

$$\tau = \frac{1}{2}\left[1 + \frac{1}{2}\sqrt{1-n} + \sqrt{1-n} \times \frac{\sqrt{\left(\frac{1}{\sqrt{1-n}} - 1\right)^2 + \frac{1}{4}}}{1 - \sqrt{1-n}}\right] \tag{5}$$

On the other hand, laminar flow in porous media can be described by Darcy's law that permeability is explicitly expressed:

$$u = \frac{U}{n} = \frac{K_R}{n}\frac{\Delta P}{L} \tag{6}$$

Where U is Darcy or approach velocity ($ms^{-1}$). $K_R$ is the permeability of capillary tube ($m^2$) or the permeability caused by the reduction of tube radius. Comparing Eqs. (6) and (4), the expression for permeability is obtained:

$$K_R = \frac{n}{8}\frac{r^2}{\tau} \tag{7}$$

In Eq. (7), the pore radius can be related to porosity and specific surface area $S_{sf}$ (as $m^{-1}$):

$$r = \frac{2n}{S_{sf}(1-n)} \tag{8}$$

In the case of high biomass accumulation in porous media, thick biofilm covers grain surface and modifies the grain with the tendency of increasing the radius of grains. With the assumption that biofilm is homogeneous and uniformly distributed on spherical grain, the specific surface area can be calculated as the function of grain size:

$$S_{sf} = \frac{6}{d_G} \tag{9}$$

and the grain diameter is determined through the relation with porosity:

$$\frac{d_G}{d_{G,0}} = \sqrt[3]{\frac{1-n}{1-n_0}} \tag{10}$$

where $d_G$ is the diameter of grain at time t. The minimum value of $d_G$ is the diameter of clean grain ($d_{G,0}$), without the effect of mass deposition. Substituting Eqs. (10), (9) and (8) into Eq. (7), the permeability $K_R$ can be estimated:

$$K_R = \frac{n^3}{72\tau} \frac{d_{G,0}^2}{(1-n)^{4/3}} \frac{1}{(1-n_0)^{2/3}} \tag{11}$$

Equation (11) indicates that porosity, tortuosity, grain size determine the magnitude of permeability. Equation (11) can be used to estimate the permeability of clean bed packed with spherical grains by returning all the variables into initial ones ($n \rightarrow n_0$ and $\tau \rightarrow \tau_0$):

$$K_0 = \frac{n_0^3}{72\tau_0} \frac{d_{G,0}^2}{(1-n_0)^2} \tag{12}$$

For an convenient monitoring, the evolution of permeability is usually presented in term of relative permeability, which is defined as the ratio of permeability at time t to clean bed permeability.

$$\frac{K_R}{K_0} = \left(\frac{n}{n_0}\right)^3 \frac{\tau_0}{\tau} \frac{(1-n_0)^{4/3}}{(1-n)^{4/3}} \tag{13}$$

To obtain the satisfactory when compared to experimental data, the model should include all the parameters that influence the fluid moving in porous media such as biofilm components and morphology (Veerapaneni and Wiesner 1997). To our best knowledge, there is no universal model to characterize these effects. A bulk factor $\beta_B$ was usually used to correct theoretical models (Mays and Hunt 2005), which defines the effective porosity: $n = n_0 - \beta_B n_M$ with $n_M$ is the volumetric fraction of mass deposition.

Thus, Eq. (13) is transformed to new formula:

$$\frac{K_R}{K_0} = \left(\frac{n_0 - \beta_B n_M}{n_0}\right)^3 \frac{\tau_0}{\tau} \frac{(1-n_0)^{4/3}}{(1-n_0+\beta_B n_M)^{4/3}} \tag{14}$$

It is noted that specific surface area that is modeled by Eq. (9) may underestimate the surface modification by deposition of fine particles with very high specific surface area. Veerapaneni and Wiesner (1997) conducted the experiment of the deposition of nano particles in packed column and obtained the severe permeability reduction in order of three at very small volumetric fraction of mass accumulation of 0.001. In such conditions, specific surface area was the main parameter driving clogging in packed column and specific surface area can be calculated by the following equation:

$$S_{sf} = S_{sf,0} + N_e S_p n_M \tag{15}$$

Where $S_{sf,0}$ and $S_p$ are the specific surface area of clean bed ($m^{-1}$) and fine particle ($m^{-1}$). For the simple, the grain and fine particle are assumed spherical forms, and specific surface area can be calculated: $S_{sf,0} = 6/d_{G,0}$ and $S_p = 6/d_P$, with $d_P$ is the diameter of fine particle. $N_e$ is the fraction of surface area of deposited particles contributing to the modification of surface area of grain and always less than 1. In the case that mass deposition is very small compared to clean bed porosity, by combining Eqs. (8) and (15) and bulk factor, the modified model has a simple form which is similar to published result (Mays and Hunt 2005) that was derived in the different approach:

$$\frac{K_R}{K_0} = \left(\frac{1}{1+\gamma n_M}\right)^2 \tag{16}$$

with $\gamma = \beta_B N_e \frac{d_{G,0}}{d_p}$ Finally, the modified model for permeability reduction is developed. The permeability of clean bed porous media can be estimated by Eq. (12). To account for the effect of biomass accumulation, Eq. (14) is proposed to predict permeability evolution in porous media. However, the predicted permeability is not representative for overall permeability. As mentioned above, two mechanisms (i) mass accumulation and cover the inner wall of pore, leading the reduction of pore radius, and (ii) mass deposition forms aggregation and plugs a portion of the pore result in permeability reduction contribute to the overall permeability of porous media. Following Vandervivere 's approach (Vandevivere 1995), the total permeability reduction is expressed:

$$K = F(n_M)K_R + (1 - F(n_M))K_P \tag{17}$$

where $K_R$ and $K_P$ are computed from the Eqs. (14) and (2), respectively and F(M) is defined from Eq. (3).

## 3 Result and Discussion

A wide range of experimental bioclogging data (Kildsgaard and Engesgaard 2001; Seifert and Engesgaard 2007; Karrabi et al. 2011; Cunningham et al. 1991; Vandevivere and Baveye 1992) is used to validate the modified model in two aspects: estimating the clean bed permeability and predicting permeability evolution in porous media. In the experiment, permeability can be measured indirectly through pressure gradient governed by Darcy's law. The results of the comparison of experimental data and predicted one by Eq. (12) is showed in Fig. 2. To provide the more convenient viewing for readers, the figure is presented in log-scale with the unit of $10^{-9}$ $m^2$. It is observed from the figure that the predicted values are very similar to experimental ones. These values present linear relationship with the slope of 0.972, which indicates the good agreement between the compared values. Specifically, In cases of grain size of 0.54 mm and 4 mm, the predicted permeability is very closed to obtained permeability measured in experiment.

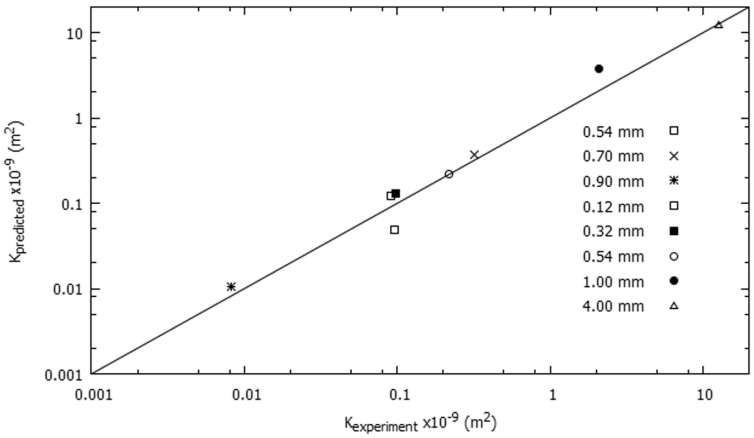


**Fig. 2.** The comparison of experimental $K_0$ and predicted $K_0$ from modified model

For the permeability evolution in porous media, the validity of the modified model is examined by the reproduction of the novel data sets of biofilter with various grain size from 0.09 mm to 1 mm (Cunningham et al. 1991; Vandevivere and Baveye 1992). Equation (17) is used to estimate permeability reduction. Figure 3. presents the good results of the predicting capacity of modified model. Experimental and predicted data show the good match in both decline tendency and magnitude of permeability reduction.

In term of clean bed permeability and permeability evolution, the modified model proves its validity by qualitatively and quantitatively predicting bioclogging in porous media. However, there is still differences in simulated and measured data. It may be explained by the drawback of the model assumptions. Tortuosity in Eq. (13) is calculated by the simple assumptions of grain geometry and flow route that may be not appropriate for the description of a real porous media (Ghanbarian et al. 2013) It is

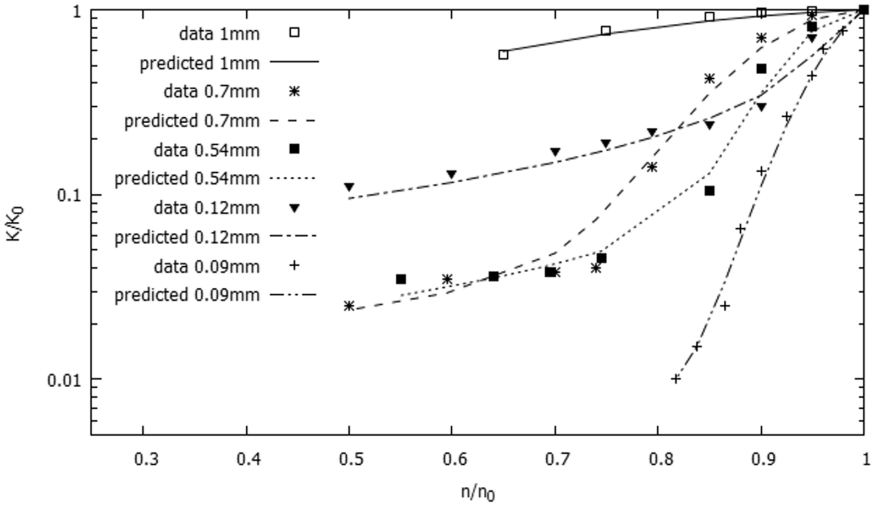


**Fig. 3.** Profile of permeability evolution versus relative porosity obtained from bioclogging experiments (points) and calculation from modified model (lines).

worth noting that biofilm is heterogeneous and stratified (Lewandowski 2000) The voids and channels in the biofilm can convey fluid and contribute to global permeability (Pintelon et al. 2012). Although this contribution of biofilm is implicitly included through the term of minimum permeability but the biofilm permeability is not systematically incorporated in the modified model. The bulk factor characterizes the biofilm component and morphology. In consequence, the bulk factor is temporal variables that is dependent on biofilm strain, nutrient concentration, hydrodynamic condition. By treating bulk factor as the fitting parameter or in correlation with only approaching velocity (Krauss and May 2014) the output from the permeability model maybe different from measured data.

**Acknowledgments.** This study has been conducted under the framework of CARE-RESCIF initiatives.

## References

Bradford, S.A., Yates, S.R., Bettahar, M., Simunek, J.: Physical factors affecting the transport and fate of colloids in saturated porous media. Water Resour. Res. **38** (2002). doi:10.1029/2002WR001340

Carman, P.C.: Fluid flow through granular beds. Trans. Inst. Chem. Eng. **15**, 150–166 (1937)

Clement, T., Hooker, B., Skeen, R.: Macroscopic models for predicting changes in saturated porous media properties caused by microbial growth. Groundwater **34**(5), 934–942 (1996)

Cunningham, A.B., Characklis, W.G., Abedeen, F., Crawford, D.: Influence of biofilm accumulation on porous media hydrodynamics. Environ. Sci. Technol. **25**(7), 1305–1311 (1991). doi:10.1021/es00019a013

Ebigbo, A., Helmig, R., Cunningham, A.B., Class, H., Gerlach, R.: Modelling biofilm growth in the presence of carbon dioxide and water flow in the subsurface. Adv. Water Resour. **33**, 762–781 (2010). doi:10.1016/j.advwatres.2010.04.004

Ghanbarian, B., Hunt, A.G., Ewing, R.P., Sahimi, M.: Tortuosity in porous media: a critical review. Soil Sci. Soc. Am. J. **77**, 1461–1477 (2013). doi:10.2136/sssaj2012.0435

Ham, Y.J., Kim, S.B., Park, S.J.: Numerical experiments for bioclogging in porous media. Environ. Technol. **28**(10), 1079–1089 (2007). doi:10.1080/09593332808618871

Happel, J.: Viscous flow in multiparticle systems: slow motion of fluids relative to beds of spherical particles. Am. Inst. Chem. Eng. J. **4**, 197–201 (1958). doi:10.1002/aic.690040214

Karrabi, M., Sechet, P., Morra, C., Cartellier, A., Geindreau, C., Martins, J.M.F.: Investigation of hydrodynamic/biomass growth coupling in a pilot scale granular bioreactor at low pore Reynolds number. Chem. Eng. Sci. **66**, 1765–1782 (2011). doi:10.1016/j.ces.2011.01.010

Kildsgaard, J., Engesgaard, P.: Numerical analysis of biological clogging in two-dimensional sand box experiments. J. Contam. Hydrol. **50**, 261–285 (2001). doi:10.1016/S0169-7722(01)00109-7

Krauss, E.D., Mays, D.C.: Modification of the Kozeny-Carman equation to quantify formation damage by fines in clean, unconsolidated porous media. SPE Reserv. Eval. Eng. **17**(4), 466–472 (2014). doi:10.2118/165148-PA

Lewandowski, Z.: Notes on biofilm porosity. Wat. Res. **34**(9), 2620–2624 (2000). doi:10.1016/S0043-1354(00)00186-X

Mays, D.C., Hunt, J.R.: Hydrodynamic Aspects of Particle Clogging in Porous Media. Environ. Sci. Technol. **39**, 577–584 (2005). doi:10.1021/es049367k

Payatakes, A.C., Tien, C., Turian, R.M.: A new model for granular porous media: Part I: model formulation. Am. Inst. Chem. Eng. J. **19**, 58–66 (1973). doi:10.1002/aic.690190110

Pintelon, T.R.R., Picioreanu, C., van Loosdrecht, M.C.M., Johns, M.L.: The effect of biofilm permeability on bio-clogging of porous media. Biotechnol. Bioeng. **109**(4), 1031–1042 (2012). doi:10.1002/bit.24381

Seifert, D., Engesgaard, P.: Use of tracer tests to investigate changes in flow and transport properties due to bioclogging of porous media. J. Contam. Hydrol. **93**(1), 58–71 (2007). doi:10.1016/j.jconhyd.2007.01.014

Taylor, S.W., Milly, P.C.D., Jaffé, P.R.: Biofilm growth and the related changes in the physical properties of a porous medium: 2: permeability. Water Resour. Res. **26**(9), 2161–2169 (1990). doi:10.1111/j.1745-6584.1996.tb02088.x

Thullner, M., Zeyer, J., Kinzelbach, W.: Influence of microbial growth on hydraulic properties of pore networks. Transp. Porous Med. **49**(1), 99–122 (2002). doi:10.1023/A:1016030112089

Tien, C.: In Granular Filtration of Aerosols and Hydrosols, 1st edn. Butterworth, Boston (1989)

Vandevivere, P.: Bacterial clogging of porous media: a new modeling approach. Biofouling **8**, 281–291 (1995). doi:10.1080/08927019509378281

Vandevivere, P., Baveye, P.: Relationship between transport of bacteria and their clogging efficiency in sand columns. Appl. Environ. Microbiol. **58**, 2523–2530 (1992)

Veerapaneni, S., Wiesner, M.R.: Deposit morphology and head loss development in porous media. Environ. Sci. Technol. **31**, 2738–2744 (1997). doi:10.1021/es960979h

Verma, A., Pruess, K.: Thermohydrological conditions and silica redistribution near high-level nuclear wastes emplaced in saturated geological formations. J. Geophys. Res. **93**, 1159–1173 (1988). doi:10.1029/JB093iB02p01159

Yu, B.M., Li, J.H.: A geometry model for tortuosity of flow path in porous media. Chin. Phys. Lett. **21**, 1569–1571 (2004). doi:10.1088/0256-307X/21/8/044

# Modelling of Pollutant Diffusion in Unsaturated Double-Porosity Medium by a Multiscale Method

T.D. Tran Ngoc[1(✉)], Q. Pham Minh[1], H. Ly Minh[1], T. Tran Van[2], and Thong Nguyen[3]

[1] CARE Center – Faculty of Environment and Natural Resources, Ho Chi Minh City University of Technology – Vietnam National University, Ho Chi Minh City, Viet Nam
tntdung@hcmut.edu.vn
[2] Faculty of Civil Engineering, Ho Chi Minh City University of Technology and Education, Ho Chi Minh City, Viet Nam
[3] CARE Center – Faculty of Civil Engineering, Ho Chi Minh City University of Technology – Vietnam National University, Ho Chi Minh City, Viet Nam

**Abstract.** Diffusion mechanism study of mass transport has received much attention in geo-environment domain, especially in waste containment applications. Diffusion of a substance in a homogeneous porous medium is traditionally modeled by Fick's law. However, natural geology environments are often heterogeneous and thus that requires advanced models enabling to capture diffusion behavior in such media. "Double-porosity" medium concept can be replaced a class of heterogeneous media in which there exists two macro- and micro-porosity domains with very contrasted hydraulic properties, fractured rocks or aggregated soils, for example. In this paper, the development of a macroscopic model for pollutant diffusion in unsaturated double-porosity medium is presented, applying a multiscale method. The resulting model consists of coupled two equations for the diffusion in the macro- and micro-porosity domains. The effective diffusion tensor representing for the double-porosity medium is also obtained. The developed model is verified by comparing with the reference solution of the fine scale model through a numerical example of hydrogeology problem.

**Keywords:** Diffusion · Mass transport · Double-porosity medium · Multiscale method · Homogenization

## 1 Introduction

The diffusion mechanism proposed by Fick (1855) occurs when existing a concentration difference in media. This mechanism is widely applied in many areas such as waste containment, polluted soil remediation, catalytic packed-bed reactors, degradation of building materials, etc. It has really received much attention of environmental geotechnical engineering since the 1970s, in order to tackle civil problems of burial

© Springer Nature Singapore Pte Ltd. 2018
H. Tran-Nguyen et al. (eds.), *Proceedings of the 4th Congrès International de Géotechnique - Ouvrages -Structures*, Lecture Notes in Civil Engineering 8,
DOI 10.1007/978-981-10-6713-6_100

domestic and hazardous waste works (Shackelford 2014). Permeability coefficient of geological medium (soil, fractured rock) is always required small for containment. That is only a necessary condition, but not sufficient to ensure a safe leakage. In this case, diffusion is predominant for pollutant transport processes, compared with other mechanisms. The pollutant leakage is accelerated by the diffusion, whereas the prediction results with the pure convection or convection-diffusion or diffusion-dispersion mechanisms are not satisfactory (Shackelford and Redmond 1995).

Diffusive transport in an unsaturated homogeneous medium is also modelled by Fick's law (Rowe 2001) with the diffusion coefficient depending on the porosity and saturation of the medium. This coefficient can be estimated by using Millington and Quirk (1961) empirical formulas. However, it is needed to modify the conventional Fick's law (Auriault and Lewandowska 1995) for transport in a heterogeneous medium. Indeed, natural geological formation is often heterogeneously structured due to superposed chemical-physical-biological effects. For a class of heterogeneous media which is characterized by two porosity domains (micro-porosity and macro-porosity) with contrasted hydraulic and diffusive properties, such as aggregated soil or fractured rock, we can use the concept of "double-porosity medium" (Barenblatt et al. 1960; Beckner et al. 1988) to represent them. A diffusive mathematical model in a composite medium under saturated condition was presented in Auriault and Lewandowska (1995). It is necessary to determine the Laplace transform in this model.

The purpose of this paper is to present a modelling for pollutant diffusion in an unsaturated double-porosity medium, by using asymptotic homogeneous method and a numerical implementation to verify the obtained model.

## 2 Homogenization and Problem Formulation

### 2.1 Method

The homogenization method allows to describe behavior of a heterogeneous medium by replacing it with an equivalent homogeneous medium. This process is called scale passage with the principle based on asymptotic developments. From this mathematical method, Auriault (1991) proposed an approach called physical homogenization with non-dimensional numbers that involve physical processes. Auriault's approach is used in this article (for more details in Auriault et al. 2009).

Homogenization begins with the description of physical phenomena on a heterogeneous material scale, which is very small compared with the scale of the work we perform. The basis of the homogeneous method is to satisfy the separation of scales for geometric and physical quantities:

$$\varepsilon = \frac{\ell}{L} \ll 1, \tag{1}$$

where $\ell$ and $L$ [L] are the characteristic lengths at the micro- and macro-scale, respectively. Equation (1) is equivalent to the presence of a REV (representative elementary volume). In the presence of two scales, we can introduce two non-dimensional spatial variables $\boldsymbol{x} = \boldsymbol{x}$ $(x_1, x_2, x_3)$ and $\boldsymbol{y} = \boldsymbol{y}$ $(y_1, y_2, y_3)$ [-] are macro variable ($\boldsymbol{x} = \boldsymbol{X}/L$,

slow variable) and micro variable ($\boldsymbol{y} = \boldsymbol{X}/\ell$, quick variable), respectively. $\boldsymbol{X} = \boldsymbol{X}$ ($X_1$, $X_2$, $X_3$) [L] is space variable. Thus, the derivation operator can be written:

$$\nabla_y \rightarrow \nabla_y + \varepsilon \nabla_x \tag{2}$$

The physical quantities of the considered problem are postulated in the expression of the asymptotic expansion form:

$$\psi^*(\boldsymbol{x}, \boldsymbol{y}, t^*) = \psi^{(0)}(\boldsymbol{x}, \boldsymbol{y}, t^*) + \varepsilon\psi^{(1)}(\boldsymbol{x}, \boldsymbol{y}, t^*) + \varepsilon^2\psi^{(2)}(\boldsymbol{x}, \boldsymbol{y}, t^*) + \ldots \tag{3}$$

where "*" designs for non-dimensional quantities.

To achieve a model at the macro-scale, the homogenization process respects the steps in the methodology proposed by Auriault (1991).

## 2.2 Assumptions

We consider the diffusion phenomenon of a small concentration in an unsaturated double-porosity medium of size ($L$) without deformation (solid). This periodic medium consists of the same REVs with size $\ell$, containing two porous materials and satisfying Eq. (1) (Fig. 1). These two porous materials have very different hydraulic and diffusive characteristics:

$$D_2/D_1 = O(\varepsilon^2), \tag{4}$$

with $D_1$ and $D_2$ [$L^2T^{-1}$] are the diffusion coefficients of the porous domain 1 and porous domain 2, respectively. In each porous materials, Fick's law is applied to calculate average flux. No flow occurs in the environment, due to very small Peclet number. Adsorption, as well as bio-chemical reactions are not considered here.

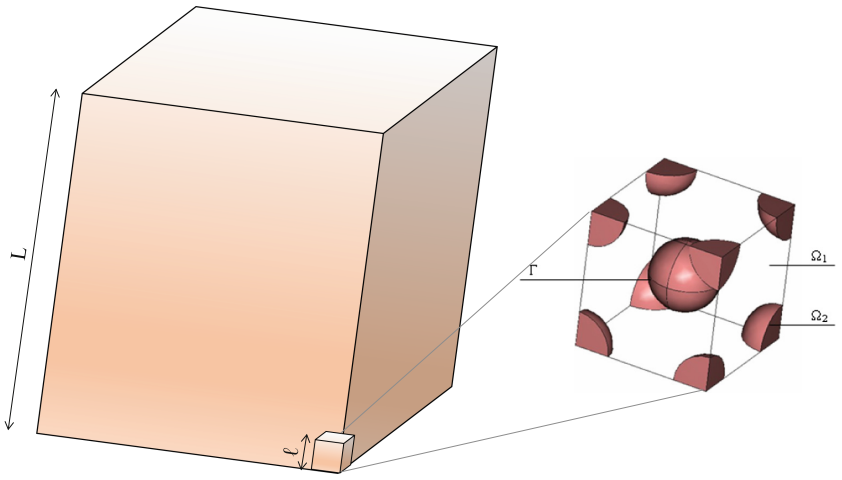


**Fig. 1.** Periodic double-porosity medium: porous domain $\Omega_1$ with continuity and high-permeability, porous domain $\Omega_2$ with low-permeability and interface $\Gamma$.

### 2.3 Description of Diffusion Problem at the Local-Scale

The governing equation of the solute diffusion in each porous domain of the unsaturated double-porosity medium is as follows:

$$\frac{\partial(\theta_1 C_1)}{\partial t} = \nabla_X \cdot (\boldsymbol{D}_1(\theta_1) \cdot \nabla_X C_1) \text{ in } \Omega_1, \tag{5}$$

$$\frac{\partial(\theta_2 C_2)}{\partial t} = \nabla_X \cdot (\boldsymbol{D}_2(\theta_2) \cdot \nabla_X C_2) \text{ in } \Omega_2, \tag{6}$$

with the continuous condition at the interface:

$$(\boldsymbol{D}_1(\theta_1) \cdot \nabla_X C_1) \cdot \boldsymbol{N} = (\boldsymbol{D}_2(\theta_2) \cdot \nabla_X C_2) \cdot \boldsymbol{N} \text{ on } \Gamma, \tag{7}$$

$$C_1 = C_2 \text{ on } \Gamma, \tag{8}$$

where $C$ [$\mathrm{ML}^{-3}$] is solute concentration; $\boldsymbol{D}$ [$\mathrm{L}^2\mathrm{T}^{-1}$] is diffusion tensor; $\theta$ [$\mathrm{L}^3\mathrm{L}^{-3}$] is water content; $t$ [T] is time; và $\boldsymbol{N}$ [-] is the unit vector normal to $\Gamma$ and exterior to $\Omega_1$. "1" and "2" are the indices denoting the macro- and micro-porosity domain, respectively.

### 2.4 Normalization of Governing Equations

The diffusion problem at the above local-scale will be expressed in terms of non-dimensional quantities:

$$C_1^* = \frac{C_1}{C_c};\ C_2^* = \frac{C_2}{C_c};\ \boldsymbol{D}_1^* = \frac{\boldsymbol{D}_1}{D_{1c}};\ \boldsymbol{D}_2^* = \frac{\boldsymbol{D}_2}{D_{2c}};\ \theta_1^* = \frac{\theta_1}{\theta_c};\ \theta_2^* = \frac{\theta_2}{\theta_c} \text{ và } t^* = \frac{t}{t_c}, \tag{9}$$

with "$c$" subscript indicates the characteristic quantities that we can observe.

From Eq. (9), Eqs. (5)–(8) are normalized for micro-length $\ell$:

$$\frac{\ell^2 \theta_{1c}}{D_{1c} t_c} \frac{\partial(\theta_1^* C_1)}{\partial t^*} = \nabla_y \cdot (\boldsymbol{D}_1^* \cdot \nabla_y C_1^*) \text{ in } \Omega_1, \tag{10}$$

$$\frac{\ell^2 \theta_{2c}}{D_{2c} t_c} \frac{\partial(\theta_2^* C_2)}{\partial t^*} = \nabla_y \cdot (\boldsymbol{D}_2^* \cdot \nabla_y C_2^*) \text{ in } \Omega_2, \tag{11}$$

$$(\boldsymbol{D}_1^* \cdot \nabla_y C_1^*) \cdot \boldsymbol{N} = \frac{D_{2c}}{D_{1c}} \cdot (\boldsymbol{D}_2^* \cdot \nabla_y C_2^*) \cdot \boldsymbol{N} \text{ on } \Gamma, \tag{12}$$

$$C_1^* = C_2^* \text{ on } \Gamma, \tag{13}$$

### 2.5 Estimation of Non-dimensional Numbers

We consider the time characteristic $t_c = \frac{L^2 \theta_{1c}}{D_{1c}}$. So $P_{1l} = \frac{\ell^2 \theta_{1c}}{D_{1c} t_c} = O(\varepsilon^2)$ and Eq. (4), we have:

$$P_{2l} = \frac{\ell^2 \theta_{2c}}{D_{2c} t_c} = O(1) \text{ with } \frac{\theta_{2c}}{\theta_{1c}} O(1) \tag{14}$$

By means of the above estimations, the local problem (10)–(13) can be reformulated as follows:

$$\varepsilon^2 \frac{\partial(\theta_1^* C_1)}{\partial t^*} = \nabla_y \cdot (\boldsymbol{D}_1^* \cdot \nabla_y C_1^*) \text{ in } \Omega_1, \tag{15}$$

$$\frac{\partial(\theta_2^* C_2)}{\partial t^*} = \nabla_y \cdot (\boldsymbol{D}_2^* \cdot \nabla_y C_2^*) \text{ in } \Omega_2, \tag{16}$$

$$(\boldsymbol{D}_1^* \cdot \nabla_y C_1^*) \cdot \boldsymbol{N} = \varepsilon^2 \cdot (\boldsymbol{D}_2^* \cdot \nabla_y C_2^*) \cdot \boldsymbol{N} \text{ on } \Gamma, \tag{17}$$

$$C_1^* = C_2^* \text{ on } \Gamma, \tag{18}$$

## 3 Homogenization Analysis

The purpose of the analysis is to provide the governing equation of the macroscopic model containing the parameter describing effective diffusion for a continuous medium from the real double-porosity medium.

Introducing asymptote developments of Eq. (3) into Eqs. (15)–(18) and grouping the numbers with the same order $\varepsilon$ lead to the adimensional equations with asymptotic developments. Performing homogenization for these equations with the $\varepsilon$ successive orders, we receive the interesting results. Details of the mathematical transformation process of the problems are presented in Tran Ngoc (2008). Here, we present the boundary local value problem and macroscopic model obtained from the homogenization analysis.

### 3.1 Local Boundary Value Problem

At the order $\varepsilon^1$, we obtain:

$$\nabla_y \cdot \left[\boldsymbol{D}_1^* \cdot \left(\nabla_y \chi + \boldsymbol{I}\right)\right] = 0 \text{ in } \Omega_1, \tag{19}$$

$$\left[\boldsymbol{D}_1^* \cdot \left(\nabla_y \chi + \boldsymbol{I}\right)\right] \cdot \boldsymbol{N} = 0 \text{ in } \Gamma, \tag{20}$$

$$\langle \chi \rangle = \frac{1}{|\Omega|} \int_{\Omega_1} \chi d\Omega = 0 \, (\Omega = \Omega_1 + \Omega_2) \tag{21}$$

with $\chi(\boldsymbol{y})$ is $\boldsymbol{y}$-periodic vector function. Vector $\chi(\boldsymbol{y})$ is solved from the above boundary local value problem. $\boldsymbol{I}$ is the unit matrix. "$\langle\ \rangle$" signifies a volume average.

### 3.2 Diffusion Model in Double-Porosity Medium

To determine the macro-scale model, we analyze at the order $\varepsilon^2$ and coming back to the dimensional problem, we obtain a macro-diffusion model with $C_1$ and $C_2$ non-equilibrium at the local scale and an effective diffusion coefficient $\boldsymbol{D}_{\text{eff}}$ of medium:

$$\phi_1 \frac{\partial(\theta_1 C_1)}{\partial t} = \nabla_X \cdot (\boldsymbol{D}_{\boldsymbol{eff}} \cdot \nabla_x C_1) - \frac{\partial \langle \theta_2 C_2 \rangle}{\partial t}, \tag{22}$$

$$\frac{\partial(\theta_2 C_2)}{\partial t} = \nabla_X \cdot (\boldsymbol{D_2} \cdot \nabla_X C_2), \tag{23}$$

$$C_1 = C_2 \text{ on } \Gamma, \tag{24}$$

$$\text{with } \boldsymbol{D}_{\boldsymbol{eff}}(\theta) = \frac{1}{|\Omega|} \int_{\Omega_1} \boldsymbol{D}_1(\theta) \cdot (\nabla \chi + \boldsymbol{I}) d\Omega \quad \text{and } \phi_1 = \frac{|\Omega_1|}{|\Omega|}. \tag{25}$$

## 4 Numerical Example

The diffusion model in the double-porosity medium developed above is numerically implemented through an example. To verify this model, we will compare its solution (two-scale) with the reference solution (fine scale). Both problems of fine-scale and homogenized models are implemented by a finite elementary commercial software developed with MATLAB.

### 4.1 Description of Example Problem

The 2D double-porosity medium consists of spheres of $R$ radius arranged in the sandy matrix (Fig. 2). The boundary and initial conditions are summarized in Fig. 2. The geometrical and physical parameters of the two materials are shown in Table 1. The effective diffusion of the double-porosity medium is $D_{\text{eff}} = 6.37 \times 10^{-10}$ m$^2$/s calculated from the local boundary value problem (19)–(21). (Not presented in detail here).

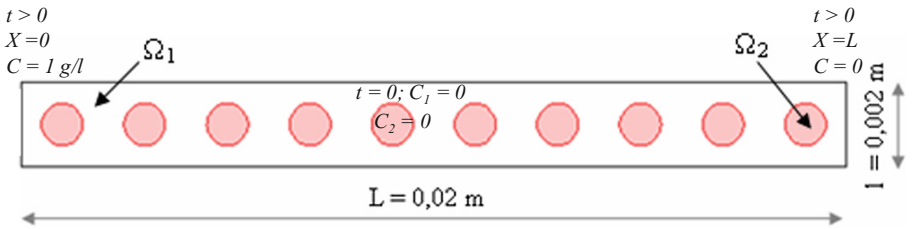


**Fig. 2.** Geometrical dimensions and conditions of the example problem.

**Table 1.** Geometric and physical parameters of the two materials in the double-porosity medium of the example problem.

| Parameter | L | $\ell$ | R | $\phi_1$ | $\phi_2$ | $\theta_1$ | $\theta_2$ | $D_1$ | $D_2$ |
|---|---|---|---|---|---|---|---|---|---|
| Unit | m | m | m | – | – | $m^3/m^3$ | $m^3/m^3$ | $m^2/s$ | $m^2/s$ |
| Value | 0.02 | 0.002 | 0.0005 | 0.804 | 0.196 | 0.5 | 0.3 | $1\times10^{-13}$ | $1\times10^{-9}$ |

## 4.2 Results

The numerical implementation strategy of the homogenized model can be referred to Tran Ngoc et al. (2011). The macro- and micro-domain of the homogenized model were discritized into ~1200 elements, while the reference model is run at a fine scale by discretizing the problem domain into about 1500 triangle elements. The solution time of the homegenized and reference model were at the order of 1 s and of 1 min, respectively, by using a computer with 1.99 GHz/RAM 1.99 Go. Results of the solute concentration at some selected times are presented in Fig. 3. The average diffusive flux at cross sections of X different locations are in agreement between the two models, Fig. 4 for X = L = 0.02 m, at the outlet of the medium.

Figure 5 shows that the oscillated concentration profiles are observed in the fine scale model, because the solute travels by diffusion from the macro domain 1 (sand, for example) to the micro domain 2 (clay, for example) and go-on. The result of the homogenized model provides the macro- and mico-concentration curves in accordance with the results of the fine scale model in the domain 1 and 2.

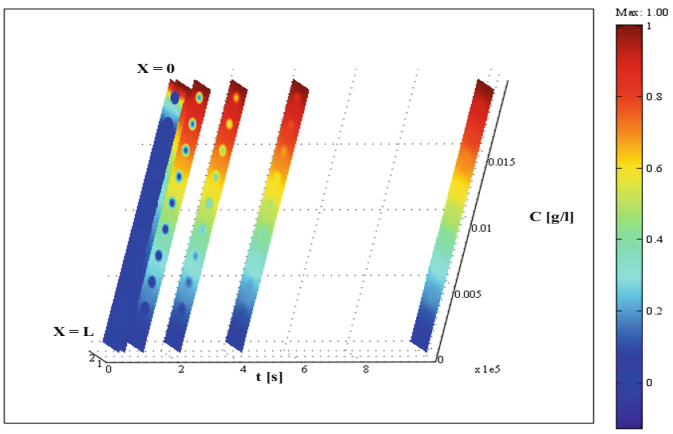


**Fig. 3.** Solute concentration in the medium at different times obtained from the reference (fine scale) model.

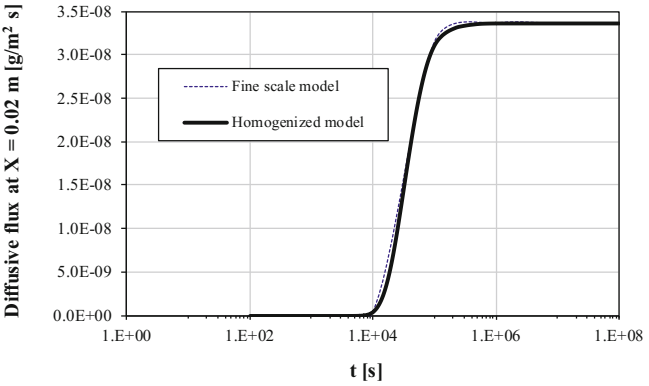


**Fig. 4.** Comparison of the diffuse flux at the outlet of the medium between the reference (fine scale) and homogenized models.

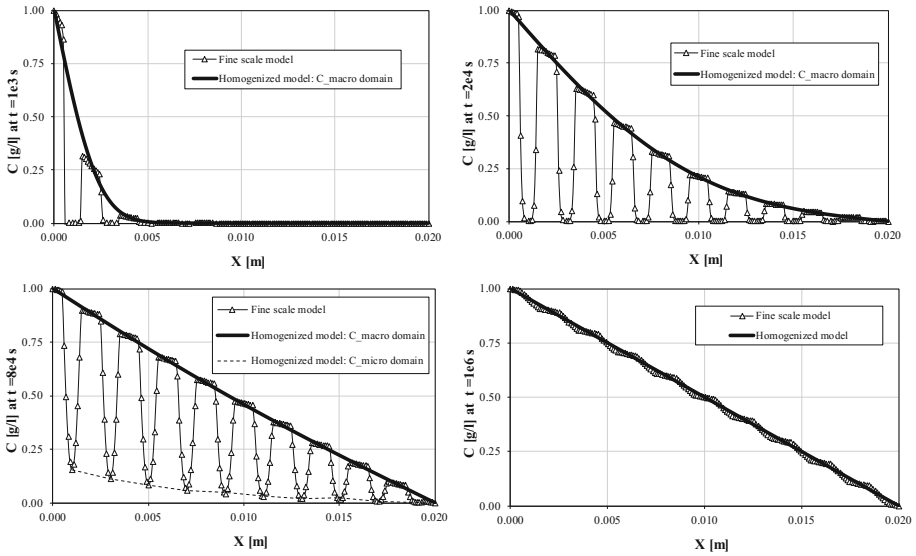


**Fig. 5.** Solute concentration profiles at different times calculated from the reference model and the homogenized model for the concentration in the macro domaine (1) and micro domain (2). (The solute concentrations in the micro domain only presented at t = 8e4 s, are very small ($\sim 0$) at t = 1e3 s or 2e4 s, and at t = 1e6 s the concentrations are approximately equal at two domains (equilibrium state).)

## 5 Conclusion

The diffusion transport model in the unsaturated double-porosity medium was developed by applying the homogenization method. The obtained model is a system of two-equation that allows to describe the diffusion at both micro- and macro-scale. The

concentrations in the two domains interact with each other on their interface. The diffusion transport between the two domains and the effective diffusion coefficient representing the entire medium were derived without imposing *a priori* any conditions. The proposed model is capable to simulate the diffusion in the double-porosity medium, by verifying the concentration results of the homogenized and reference model.

Finally, the multiscale method presented in this paper can be used to model other transport processes including the bio-chemical changes of pollutants, as well as the hydro-chemico-mechanical couplings in multi-physics, multi-phase and multi-component problems.

**Acknowledgments.** This research is funded by Vietnam National Foundation for Science and Technology Development (NAFOSTED) under grant number 107.01-2015.25.

## References

Auriault, J.L.: Heterogeneous medium. Is an equivalent macroscopic description possible? Int. J. Engg. Sci. **29**(7), 785–795 (1991)

Auriault, J.L., Boutin, C., Geindreau, C.: Homogenization of coupled phenomena in heterogenous media. Wiley-ISTE, Hoboken (2009)

Auriault, J., Lewandowska, J.: Non-gaussian diffusion modeling in composite porous medium by homogenization: tail effect. Transp. Porous Med. **21**, 47–74 (1995)

Barenblatt, G., Zheltov, I., Kochina, I.: Basic concepts in the theory of seepage of homogeneous liquids in the fissured rocks. J. Appl. Math. **24**(5), 1286–1303 (1960)

Beckner, B.L., Firoozabadi, A., Aziz, K.: Modeling transverse imbibition in double-porosity simulators. In: SPE California Regional Meeting, Long Beach, California, 23–25 March 1988 (1988)

Fick, A.: Ueber diffusion. Ann. Phys. **170**, 59–86 (1855)

Millington, R.J., Quirk, J.M.: Permeability of porous solids. Trans. Faraday Soc. **57**, 1200–1207 (1961)

Rowe, R.K.: Geotechnical and Geoenvironmental Engineering Handbook. Springer, New York (2001)

Shackelford, C.D.: The ISSMGE Kerry Rowe lecture: the role of diffusion in environmental geotechnics. Can. Geotech. J. **51**, 1219–1242 (2014)

Shackelford, C.D., Redmond, P.L.: Solute breakthrough curves for processed kaolin at low flow rates. J. Geotech. Eng. **121**(1), 17–32 (1995)

Tran Ngoc, T.D.: Transport de solutés dans un milieu à double-porosité non saturé. Modélisation par homogénéisation et application, Thèse doctorale, Université Joseph Fourier, Grenoble (in French) (2008)

Tran Ngoc, T.D., Lewandowska, J., Vauclin, M., Bertin, H.: Two-scale modeling of solute dispersion in unsaturated double-porosity media: Homogenization and experimental validation. Int. J. Numer. Anal. Meth. Geomech. **35**(14), 1536–1559 (2011)

# On the Use of Foam for the in Situ Remediation of Polluted Heterogeneous Soils

H. Bertin[1(✉)], E. Del Campo Estrada[1], and O. Atteia[2]

[1] I2M, UMR CNRS 5295, Université de Bordeaux, Talence, France
henri.bertin@u-bordeaux.fr
[2] ENSEGID, Bordeaux INP, Pessac, France
Olivier.atteia@ensegid.fr

**Abstract.** In this paper we present an experimental study of foam flow in porous media dealing with 1D sandpacks columns and 2D laboratory pilot. 1D porous column were dedicated to the study of foam generation and propagation in porous media of different permeabilities. We show that the resistance factor (RF) to flow, that is the ratio between pressure drop in presence of foam and pressure drop in absence of foam, is a non-monotonous function of permeability. A 2D transparent laboratory pilot ($1 \times 0.5 \times 0.02$ m$^3$), made of two water saturated sand layers of different permeabilities has been used to visualize foam flow. We clearly see that foam remains in high permeability layer and does not enter in the low permeability one. Moreover when we inject a liquid tracer we see that fluid velocities are quite similar in both layers showing the front straightened up.

**Keywords:** Foam · Porous media · Soil remediation · Experiments

## 1 Introduction

Remediation of polluted soils is an important concern in civil engineering especially for industrial wastelands. Several remediation techniques can be used, they can be ex situ (excavation) or in situ (sparging, oxidation, bioremediation, use of surfactants …) [1]. When the soil is heterogeneous, in situ remediation is complicated because trapped pollutants in low permeability zones are very difficult to displace due to preferential flow in high permeability zones. Therefore it is important to find a practical way to ensure a complete sweep of the different permeability zones. The objective of our study is to show that foam can be used for that purpose.

Foam that is a dispersion of gas bubbles in a surfactant laden solution can be generated inside porous media by co injecting gas and a foaming solution. It has been shown that foam stability in porous media depends on capillary pressure and that foam is stronger in high permeability porous media than in low permeability ones [2, 3]. This particular foam property can be used in the field as a blocking effect. Foam generation in a high permeability zone can block the flow of fluids and divert it towards the low permeability zone [4–6]. In this paper we will present an experimental study performed on 1D sand columns of different permeabilities and a 2D heterogeneous pilot made of two layers of different characteristics.

© Springer Nature Singapore Pte Ltd. 2018
H. Tran-Nguyen et al. (eds.), *Proceedings of the 4th Congrès International de Géotechnique - Ouvrages -Structures*, Lecture Notes in Civil Engineering 8,
DOI 10.1007/978-981-10-6713-6_101

## 2 Experimental Study

### 2.1 Surfactant Choice

First step is to choose surfactant that present good foaming property, that does not adsorb too much on the solid matrix and that is "green", i.e. biodegradable and biocompatible. Among all the available products we selected three products; a commercial one (Triton X-100), a biosurfactant (Rhamnolipid) and a sucro ester (sucrose Laurate). The foaming solution is prepared by dissolution of the surfactant in pure water.

Characterization of the surfactant consists in measuring the Interfacial Tension as a function of the surfactant concentration and to determine the Critical Micellar Concentration (CMC). Then, following the procedures described in [7] we measured the foam stability (half life time) through the drainage of a foam column (Table 1).

**Table 1.** Porous media characteristics

| Surfactant | CMC (mg/L) | Half life time (min.) |
|---|---|---|
| Sucroester | 250 | 250 |
| Rhamnolipid | 40 | 50 |
| Triton X-100 | 150 | 25 |

In the following we use the sucroester due to its interesting properties and the Triton® X-100, as it has been used in lab studies and field tests for soil remediation [8].

### 2.2 1D Porous Columns

The porous media are made of calibrated glass beads or sand grains (Table 2) of different grain diameter (dg) packed in a cylindrical column (L = 40 cm; inner diameter = 4 cm) with two pierced plugs allowing the flow of the fluids and the pressure measurement.

**Table 2.** Porous media characteristics

| Porous media | Dg (µm) | Porosity | k (Darcy) |
|---|---|---|---|
| Glass beads | 30 | 0.42 | 0.25 |
| Sand 1 | 141 | 0.39 | 8 |
| Sand 2 | 209 | 0.39 | 17 |
| Sand 3 | 452 | 0.39 | 75 |

### 2.3 Experimental Setup (1D)

The experimental setup used for the column experiments is presented in Fig. 1.

The porous column is connected to the air cylinder through a gas mass flow controller and a liquid pump. This setup allows the co-injection of gas and liquid foaming solution in the porous column described in Sect. 2.2. Pressure drop is

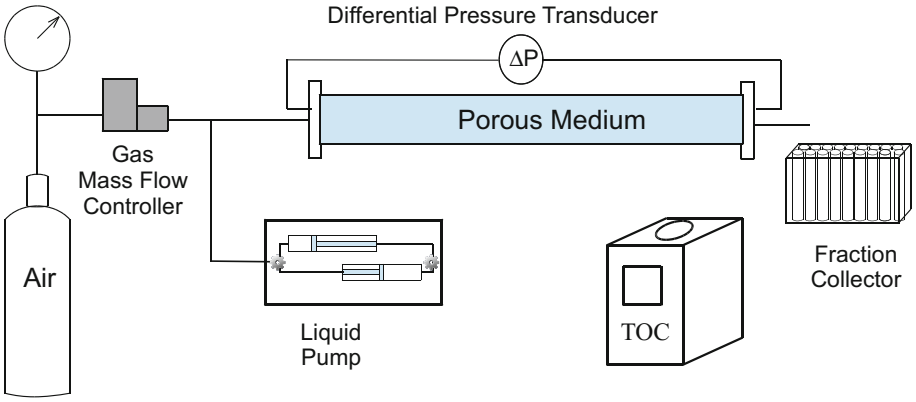


**Fig. 1.** Experimental setup for 1D column

measured continuously during the experiment and the effluents are collected at the column outlet to measure the liquid recovery and the surfactant adsorption using a Total organic Carbon measurement device (TOC).

### 2.4 Experimental Procedure (1D)

After packing the porous media is water saturated under vacuum and porosity is measured by weighting. Water is injected at different values of the flow rate, pressure drop is measured and permeability is determined through the application of the Darcy' law;

$$\frac{Q}{A} = \frac{k}{\mu}\frac{\Delta P}{L} \tag{1}$$

where Q is the water flow rate, A the column section area, μ the viscosity, L the column length, ΔP the pressure drop and k the permeability expressed in Darcy (1 Darcy $\approx 1.10^{-12}$ $m^2$).

Three pore volume of surfactant solution are then injected to complete the adsorption of the surfactant. Gas and surfactant solution are co-injected at a constant total flow rate of 3 mL/min for different gas/liquid ratio (85%, 95% and 99%).

### 2.5 2D Heterogeneous Pilot

The pilot is made of two glass plates mounted in a metallic frame pierced with small holes; 8 on each side, allowing injection and aspiration of the fluids. The high permeability layer, made of coarse sand (k ≈ 61.6 Darcy), is on the bottom and the low permeability layer, made of fine sand (k ≈ 13.3 Darcy), is on the top of the pilot. The two layers are in direct capillary contact and the top of the pilot is filled with clay (Fig. 2).

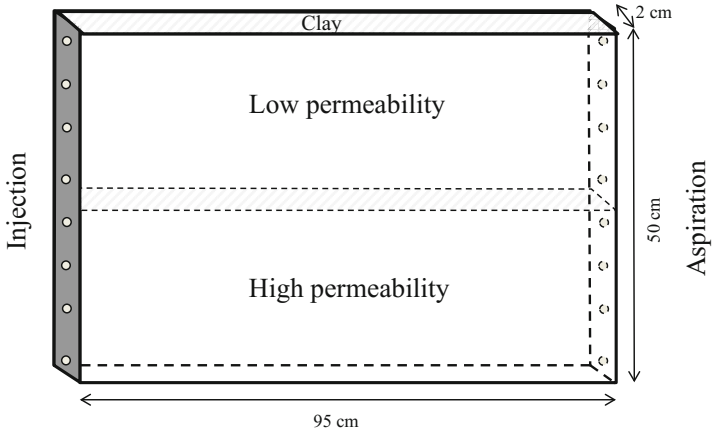


**Fig. 2.** Experimental 2D heterogeneous pilot

The experimental setup is completed by a peristaltic pump for the liquid injection and a mass flow controller for the gas.

The change of color between the wetted sand and the sand containing foam, that is mostly gas, allows a direct visualization of the gas and liquid flows.

### 2.6 Experimental Procedure (2D)

- The sand is deposited as the water is filling up the cell. When the two layers are carried out the top of the pilot is covered by a clay layer which role is to ensure imperviousness of the pilot ceiling.
- A colored tracer, Erioglaucine Disodium Salt, is injected in the pilot to visualize the flow path and determine the layers permeability.
- The foaming solution (Triton X-100, C = 10 × CMC) is injected in the pilot until all the water initially in place is displaced.
- Foam is generated in the high permeability layer by co-injection of gas (90%) and foaming solution (10%). The foam front propagation is controlled visually.
- The colored tracer is injected in the pilot from the 8 injector plots and the displacement is followed visually.

## 3 Experimental Results and Discussion

### 3.1 1D Porous Columns

Our attention is focused on the ability of foam to reduce the gas flow in the zone where it has been generated. For that we define a resistance factor to flow (RF) as follows;

$$RF_{gas} = \left.\frac{\Delta P_{foam}}{\Delta P_{gas}}\right|_{Q} \tag{2}$$

where $\Delta P_{foam}$ and $\Delta P_{gas}$ are the pressure drop measured when foam is flowing and the pressure drop when gas is flowing alone at the same value of flow rate, Q.

Experimental results are presented in Fig. 3 where we see a weak dependence of the Resistance Factor on the surfactant type and foam quality but a strong dependence on the core permeability. These observations are commented here below.

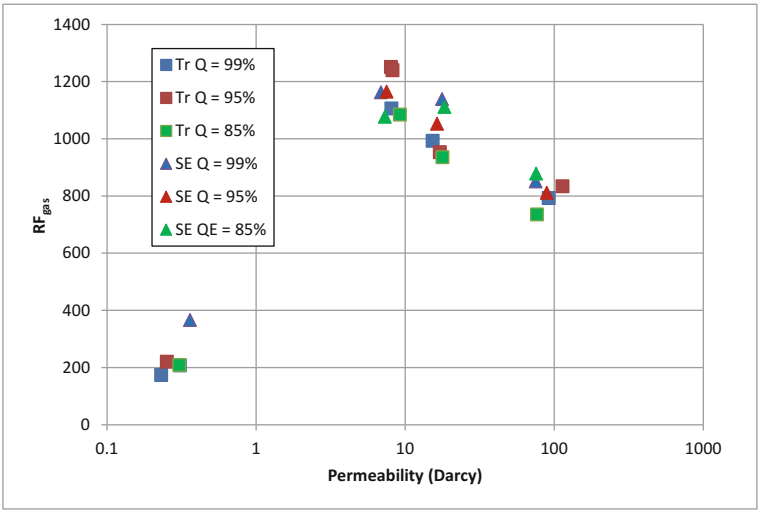


**Fig. 3.** Resistance factor (Eq. 1) vs core permeability for different surfactants (Tr = Triton X-100; SE = Sucroester) and different foam qualities (85, 95 and 99%).

- Influence of surfactant
  The results obtained with the two surfactants are very close as long as the concentration is similar (in our case we used a surfactant concentration equal to ten times the CMC).
- Influence of foam quality
  Foam quality which is the ratio between the gas volume and the liquid volume shows a weak influence on the Resistance Factor as long as this foam quality is greater than 85%.
- Influence of permeability
  The permeability plays a key role on foam formation and propagation in porous media. This result confirms previous experimental observations published in the literature [9]. Explanation is that the key parameter is capillary pressure that will control the foam stability in porous media through the stability of the liquid films separating the gas bubbles. The higher the capillary pressure the more unstable are the liquid films. In Fig. 3 we clearly see two zones, when permeability is lower than 1 Darcy we have a weak foam and, when permeability is greater than 1 Darcy we have a strong foam [10].

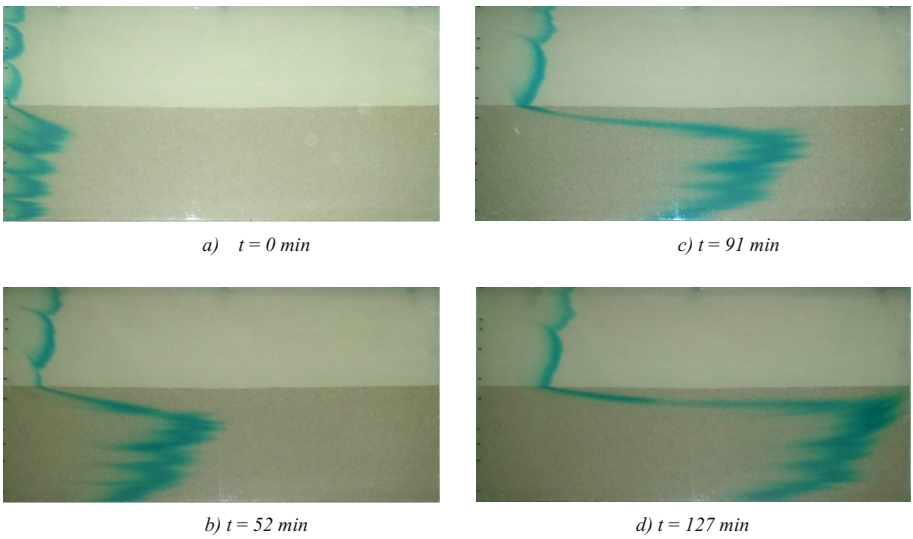


**Fig. 4.** Tracer flow in the experimental 2D heterogeneous pilot

From these observations we can confirm that foam in porous media depends strongly on the porous medium where it is generated as long as the foaming solution concentration and the foam quality are sufficient to generate foam.

The experimental data have been analyzed considering the capillary pressure of each porous medium and compared to data and correlations published in the literature [3].

### 3.2 2D Heterogeneous Pilot

- Tracer flow
  When the died tracer is injected in the heterogeneous system we clearly see that it flows preferentially in the high permeability layer, where resistance to flow is low, compared to the low permeability layer where the resistance to flow is high. This expected behavior leads to a low sweep efficiency in the low permeability layer.
- Foam placement
  The gas and the foaming solution are co-injected at the 4 injector plots located in front of the high permeability layer. Foam is generated in the porous medium, as seen by the change of color of the lower layer, in a triangular shape due to gravity effect (Fig. 5).
- Tracer flow
  When the tracer is injected from the 8 injector plots we see that the colored front is slowed down in the region where foam is present allowing a better sweep of the upper zone. A comparison between the displacement fronts visualized in Figs. 4 and 6 shows the foam blockage efficiency. However, we also notice the colored front is flowing also in the high permeability layer where foam is not present.

*a) t = 13 min*

*c) t = 38 min*

*b) t = 28 min*

*d) t = 139 min*

**Fig. 5.** Foam placement in the experimental 2D heterogeneous pilot

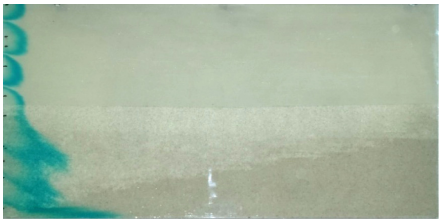

*a) t = 06min*

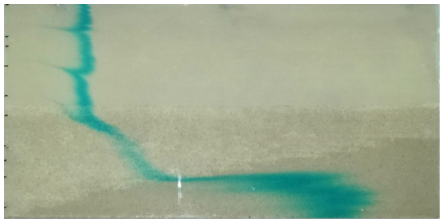

*c) t = 94 min*

*b) t = 35 min*

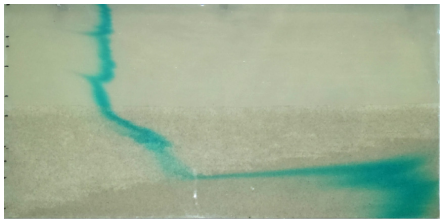

*d) t = 115 min*

**Fig. 6.** Tracer flow after foam placement in the experimental 2D heterogeneous pilot

## 4 Conclusion

We presented an experimental study dealing with foam flow in porous media of different permeabilities and heterogeneity.

The data obtained with the 1D column show that foam can be generated and propagated in porous columns as long as enough surfactant is available, meaning that the surfactant concentration should be higher than the Critical Micellar Concentration, and as long as the foam quality is close to 90%. The key parameter appears to be permeability. There are two regimes, weak and strong foam, that depend on permeability.

The 2D heterogeneous pilot, which is a prospective topic, shows that it is possible to generate foam in a selective way in the high permeability layer in order to divert the flow towards the low permeability layer. Even if he high permeability zone is not entirely blocked due to gravity segregation, it appears that flow in the high permeability layer is slowed down and the low permeability zone is better swept than when foam was not present.

The next studies must deal with the injection process, to minimize gravity effects, and consider the presence of pollutant in the porous media.

**Acknowledgments.** The authors acknowledge INNOVASOL Foundation who supported this study.

## References

1. Atteia, O., Del Campo Estrada, E., Bertin, H.J.: Soil flushing: a review of the origin of efficiency variability. Rev. Environ. Sci. Biotechnol. **12**(4), 379–389 (2013)
2. Lee, H.O., Heller, J.P., Hoefer, A.M.W.: Change in apparent viscosity of $CO_2$ foam with rock permeability. SPE Res. Eng. **6**(4), 421–428 (1991)
3. Del Campo Estrada, E., Bertin, H., Atteia, O.: Experimental study of foam flow in sand columns: surfactant choice and resistance factor measurement. Transp. Porous Media **108**, 335–354 (2015)
4. Kovscek, A.R., Bertin, H.J.: Foam mobility in heterogeneous porous media (II. Experimental Observations). Transp. Porous Media **52**, 37–49 (2003)
5. Siddiqui, S., Talabani, S., Saleh, S.T., Islam, M.R.: Foam flow in low-permeability Berea sandstone cores: a laboratory investigation. J. Pet. Sci. Eng. **36**, 133–148 (2002)
6. Pang, Z.: The blocking ability and flowing characteristics of steady foams in porous media. Transp. Porous Media **85**, 299–316 (2010)
7. Salager, J.-L., Choplin, L.: Mousses. Formation, formulation et propriétés. Techniques de l'Ingénieur, Génie des Procédés **J2–200**, 1–14 (2008)
8. Mulligan, C.N., Eftekhari, F.: Remediation with surfactant foam of PCP-contaminated soil. Eng. Geol. **70**, 269–279 (2003)
9. Khatib, Z.I., Hirasaki, G.J., Falls, A.H.: Effects of capillary pressure on coalescence and phase mobilities in foams flowing through porous media. SPE Res. Eng. **3**, 919–926 (1988)
10. Lee, S., Kam, S.I.: Enhanced oil recovery by using $CO_2$ foams. In: Sheng, J.J. (ed.) Fundamentals and Field Applications. Enhanced Oil Recovery Field Case Studies. Elsevier (2013)

# Optimization of Decolorization and COD Removal from Textile Wastewater Using Electro Fenton Process

Duc Dat Duc Nguyen[1,2(✉)], Thi Thuy Nguyen[2], and Tan Phong Nguyen[1]

[1] Ho Chi Minh City University of Technology, Ho Chi Minh City, Viet Nam
nguyendatduc@cntp.edu.vn, ntphong@hcmut.edu.vn
[2] Ho Chi Minh City University of Food Industry, Ho Chi Minh City, Viet Nam
thuyng3@gmail.com

**Abstract.** Synthetic dye is a widely used product, but dyeing industrial effluents have adversely impacted environment. During dyeing processes, 12% of dye input is wasted, and approximately 20% of this amount is discharged to the environment. In this study, Electro Fenton (EF) system was applied to treat a textile wastewater. $H_2O_2$ forming was accelerated by aeration at 1 $l_{air}/l_{sample}$/min and graphite electrode was used to reduce investment cost. Response surface methodology - Central composite Design (CCF) was used to investigate the effects of pH, $Fe^{2+}$ concentration, and voltage on the removal efficiency. At pH 2.78, $Fe^{2+}$ concentration of 2.0 mMol/l, and voltage of 16 V, the treatment system reached its optimum operating condition. Under this condition, color and COD (Chemical oxygen demand) in the effluent were 57 ± 2 Pt-Co and 56 ± 1 mg/l, respectively, after 30 min of treatment which met the national standard (QCVN 13:2015/BTNMT, column A).

**Keywords:** Electro Fenton · Textile wastewater · Synthetic dye · Response surface methodology · CCF

## 1 Introduction

The wastewater from dyes and dye manufacturing industry causes serious impact on natural water bodies and land in the surrounding area. This wastewater contains high organic loading and may have the presence of toxic or presence of bio-recalcitrant compounds, hence the application of biological treatment is not feasible (Azbar 2004). The structure of dye molecules is generally complex and stable to heat and light. Furthermore, synthetic dyes usually contain aromatic rings which are harmful and non-biodegradable. As a result, textile wastewater exhibits low BOD to COD ratios (<0.1). Even at a low concentration of dyes, it still a source of turbidity and non-aesthetic pollution, hence the discharging of such wastewater to the environment is troublesome (Nidheesh et al. 2014).

The drawbacks of traditional physico-chemical processes, such as adsorption, coagulation and filtration for the treatment of dyeing wastewater are related to cost and the generation of large volume of sludge (Ahmad 2010). On the other hand, advanced

© Springer Nature Singapore Pte Ltd. 2018
H. Tran-Nguyen et al. (eds.), *Proceedings of the 4th Congrès International de Géotechnique - Ouvrages -Structures*, Lecture Notes in Civil Engineering 8,
DOI 10.1007/978-981-10-6713-6_102

oxidation processes (AOPs) offer effective and rapid alternative treatments for various persistent contaminants until their overall mineralization, base on the in situ generation of hydroxyl radicals (OH*), a highly powerful oxidizing agent (Panizza et al. 2011).

Among these advanced processes, Electro Fenton (EF) process is the treatment based on the continuous supply of $H_2O_2$ which is electrochemically generated (Eq. 2) in the wastewater containing $Fe^{2+}$ or $Fe^{3+}$ as catalyst (Boye et al. 2002; Brillas et al. 2004). At the optimal pH $\sim$ 3, the ferric ion generated by Fenton reaction (Eq. 3) is mainly found in the form of $Fe(OH)^{2+}$. At the cathode, $Fe(OH)^{2+}$ was reduced to form again $Fe^{2+}$ (Eq. 4) which then serves as catalyst for the Fenton reaction (Eq. 3). As a result, homogeneous $OH^*$ radicals was continuously generated (Guivarch et al. 2003). Since $O_2$ formed at the anode electrode (Eq. 1) is not enough to generate a high amount of $H_2O_2$ (Eq. 2), air should be supplied at the cathode to accelerate the generation of $H_2O_2$ (Su et al. 2012).

$$2\ H_2O \rightarrow O_2 + 4H^+ + 4e^- \quad (1)$$

$$O_2 + 2H^+ + 2e^- \rightarrow H_2O_2 \quad (2)$$

$$Fe^{2+} + H_2O_2 \rightarrow Fe(OH)^{2+} + OH^* \quad (3)$$

$$Fe(OH)^{2+} + e^- \rightarrow Fe^{2+} + OH^- \quad (4)$$

There are various parameters which affected EF process such as electrode materials, pH, catalyst loading, applied current density or voltage, oxygen sparging rate, temperature, catalyst species and form, distance between the electrodes (Nidheesh and Gandhimathi 2012). Thought Platin and Boron-Doped Diamond (BDD) have been frequently used as the anode material for the degradation of various pollutants in EF process (Nidheesh and Gandhimathi 2012), they may induce a high cost. To lower the investment cost, carbonaceous materials such as graphite electrodes would be a good option (Nidheesh et al. 2014). Among operational parameters, pH, $Fe^{2+}$ concentration, voltage strongly affected the EF efficiency.

Response surface methodology – central composite design (CCF) has been widely used to optimize for the treatment of wastewater. To the best of our knowledge, the optimization of decolorization and COD removal from real textile wastewater using Electro Fenton process has not reported previously. The aim of this study was to achieve optimal operating condition of various parameters, including the amount of $Fe^{2+}$ used, pH, applied voltage, for the removal of color and COD from a real textile wastewater. In final step, validation test was carried out with application these optimum conditions for real textile wastewater to compare the result between predicted values and experimental values.

## 2 Experimental

### 2.1 Wastewater Sampling

Wastewater was collected from the equalization tank of THANHCONG textile garment investment trading joint stock company wastewater treatment plan. The textile

wastewater was pre-treated by coagulation/flocculation method with $FeCl_3$ 1% w/w in order to eliminate Total suspended solid (TSS). Wastewater characteristics after pre-treatment are shown in Table 1.

**Table 1.** Textile wastewater characteristics

| Parameter | Unit | Value (n = 3) |
|---|---|---|
| pH | – | 8.6 ± 0.2 |
| TSS | mg/l | 12 ± 4 |
| COD | $mgO_2/l$ | 785 ± 2 |
| Color | Pt-Co | 725 ± 2 |

## 2.2 Materials and Apparatus

$K_2CrO_7$ (Merck, Germany), $FeSO_4.7H_2O$ (Merck, Germany), and $Fe(NH_4)_2(SO_4)_2.6H_2O$ (Merck, Germany) were purchased to analyze COD. An UV–VIS spectrometer was used to measure color of the wastewater. pH was measured using a pH meter (WTW Inolab 7110, Germany). Graphite electrodes with 40 $cm^2$ areas were supplied by Dry Cell & Storage Battery Joint Stock Company.

## 2.3 Textile Wastewater Treatment by EF Process

Figure 1 shows the experimental setup for the treatment of textile wastewater by EF process. The reactor was made by a 500 ml glass beaker. Graphite electrodes were connected to the direct current power supply (MATRIX MPS-3005S) which provided constant voltage. The distance between electrodes was kept 2 cm in all experiments. The air was pumped at 1 $l_{air}/l_{sample}$/min near the cathode and $Fe^{2+}$ was added at different concentrations for each experiment. Magnetic stirring was used to avoid concentration gradients. Before and after each experiment, the electrodes were washed properly using HCl acid solution followed by distilled water. Electro Fenton was then performed for 30 min under differential dosages of $Fe^{2+}$, and HCl which were adjusted for each set experiment. Next, the pH of solution was adjusted to 7 using 1 N NaOH and water sample was taken to centrifuge. The supernatant was then taken for COD and color analyses.

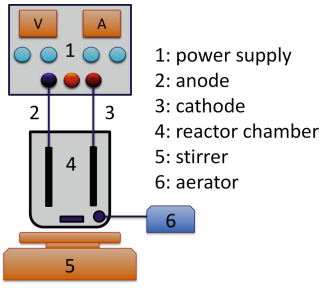


**Fig. 1.** Schema of the reactor

### 2.4 Response Surface Analysis

Experimental designs were made by using Modde 5.0 (Umetrics, Umea, Sweden). Based on Central composite Design (CCF), 17 experiments were designed for 3 factors at three levels, included $Fe^{2+}$ concentration ($x_1$; 1, 2, 3 mMol/l), pH ($x_2$; 2, 3, 4), and voltage ($x_3$; 10, 15, 20 V). The polynomial models for the output of COD and color with respect to the Electro Fenton variables were expressed as follows (Box and Draper 1987):

$$Y = \beta_0 + \sum_{i=1}^{3} \beta_i x_i + \sum_{i=1}^{3} \beta_{ii} x_i^2 + \sum_{i=1}^{3} \sum_{j=1}^{3} \beta_{ij} x_i x_j + \varepsilon \quad (5)$$

where Y is the predicted response by the model $\beta_0$, $\beta_i$, $\beta_{ii}$, $\beta_{ij}$, are the constant regression coefficients of the model. $x_i$, $x_i^2$ and $x_i x_j$ represent the linear, quadratic and interactive in terms of the uncoded independent variables, respectively, $\varepsilon$ is the random error. The coefficient of determination ($R^2$) was used to evaluate the accuracy of the full quadratic equation. The experimental design and results of outputs of COD and color during EF process are presented in Table 2.

**Table 2.** The experimental design and results

| Exp. No. | Experimental design matrix | | | Reaction conditions | | | Color, Pt-Co | | COD, mg/l | |
|---|---|---|---|---|---|---|---|---|---|---|
| | ($X_1$) $Fe^{2+}$, mMol/l | ($X_2$) pH | ($X_3$) U, V | $Fe^{2+}$, mMol/l | pH | U, V | Observed | Predicted | Observed | Predicted |
| 1 | −1 | −1 | −1 | 1 | 2 | 10 | 96 | 97.2 | 97 | 96.3 |
| 2 | 1 | −1 | −1 | 3 | 2 | 10 | 102 | 102.1 | 84 | 86.8 |
| 3 | −1 | 1 | −1 | 1 | 4 | 10 | 86 | 86.3 | 137 | 135.1 |
| 4 | 1 | 1 | −1 | 3 | 4 | 10 | 102 | 102.7 | 137 | 135.6 |
| 5 | −1 | −1 | 1 | 1 | 2 | 20 | 96 | 95.9 | 81 | 82.8 |
| 6 | 1 | −1 | 1 | 3 | 2 | 20 | 64 | 64.3 | 104 | 106.3 |
| 7 | −1 | 1 | 1 | 1 | 4 | 20 | 96 | 96.5 | 84 | 81.6 |
| 8 | 1 | 1 | 1 | 3 | 4 | 20 | 77 | 76.4 | 114 | 115.1 |
| 9 | −1 | 0 | 0 | 1 | 3 | 15 | 80 | 78.1 | 54 | 57.2 |
| 10 | 1 | 0 | 0 | 3 | 3 | 15 | 71 | 70.5 | 74 | 69.2 |
| 11 | 0 | −1 | 0 | 2 | 2 | 15 | 64 | 62.5 | 71 | 64.8 |
| 12 | 0 | 1 | 0 | 2 | 4 | 15 | 64 | 63.1 | 84 | 88.6 |
| 13 | 0 | 0 | −1 | 2 | 3 | 10 | 80 | 77.7 | 87 | 88.2 |
| 14 | 0 | 0 | 1 | 2 | 3 | 20 | 64 | 63.9 | 74 | 71.2 |
| 15 | 0 | 0 | 0 | 2 | 3 | 15 | 58 | 58.9 | 56 | 57.4 |
| 16 | 0 | 0 | 0 | 2 | 3 | 15 | 56 | 58.9 | 58 | 57.4 |
| 17 | 0 | 0 | 0 | 2 | 3 | 15 | 58 | 58.9 | 55 | 57.4 |

### 2.5 Parameter Analysis

Measurements of sample parameters was analyzed based on national technical regulation: pH (TCVN 6492:2011 with SevenCompact S220 pH meter); Color (TCVN 6185:2008 with Photolab 6100 VIS spectrophotometer); COD (TCVN 6491:1999); TSS (TCVN 6625:2000).

## 3 Results and Discussion

### 3.1 Fitting of Second-Order Polynomial Equation and Statistical Analysis

Analysis of variance (ANOVA) is a statistical technique that subdivides the total variation in a set of data into component parts associated with specific sources of variation for the purpose of testing hypotheses on the parameters of the model (Li et al. 2007). The Fisher distribution (F-test) from ANOVA was used to statistically validate the significance of regressions and the lack of fit for the quadratic models. The ANOVA for the fitted quadratic polynomial models of EF process is shown in Table 3. The quadratic regression models showed the determination coefficient ($R^2$) values were 0.994 and 0.987 for $Y_1$ (Color) and $Y_2$ (COD), which were higher than 0.97 and considered as realizable model, as suggested by Prakash Maran et al. (2013). Similarly, $R^2_{adj}$ were greater than 0.95 for both responses, indicated that there was less than 5.0% of the all variations, which could not be explained by the developed mathematical models (Thirugnanasambandham and Sivakumar 2015). The F values calculated for the regressions were 135.16 for $Y_1$ and 58.7 for $Y_2$. All these values were greater than 3.29 as theoretically calculated for 95% confidence level by Neto et al. (2005), corroborating that the developed models are statistically significant. In addition, the F values calculated for the lack of fit of the above models were 3.295 for $Y_1$ and 11.528 for $Y_2$, which were both lower than 19.30 tabulated for 95% confidence level as given by Neto et al. (2005).

**Table 3.** ANOVA results for the experimental response of COD and color outputs

| DF = 7 | $Y_1 - R^2 = 0.994$; $R^2_{Adj.} = 0.987$ | | | | | $Y_2 - R^2 = 0.987$; $R^2_{Adj.} = 0.97$ | | | | |
|---|---|---|---|---|---|---|---|---|---|---|
| | SS | MS | F | p | SD | SS | MS | F | p | SD |
| Total | 105870 | 6227.65 | | | | 134491 | 7911.24 | | | |
| Constant | 101564 | 101564 | | | | 123847 | 123847 | | | |
| Corrected | 4305.52 | 269.09 | | | 16.4041 | 10643.9 | 665.24 | | | 25.79 |
| Regression | 4280.89 | 475.65 | 135.16 | 0 | 21.8095 | 10504.7 | 1167.19 | 58.708 | 0 | 34.16 |
| Residual | 24.6334 | 3.52 | | | 1.87592 | 139.16 | 19.88 | | | 4.459 |
| Lack of fit | 21.97 | 4.39 | 3.29 | 0.249 | 2.09603 | 134.50 | 26.9 | 11.528 | 0.082 | 5.19 |
| Pure error | 2.67 | 1.33 | | | 1.1547 | 4.66 | 2.33 | | | 1.53 |

Note: SS: Sum of square; MS: Mean of square; F: Fisher value; p: p values; SD: Standard deviation; DF: Degree of freedom

An empirical relationship expressed by a second-order polynomial equation was fitted between the experimental and input variables, as shown in following equations:

$$Y_1 = 58.901 - 3.8x_1 + 0.299x_2 - 6.9x_3 + 15.422x_1^2 + 3.922x_2^2 + 11.922x_3^2 + 2.875x_1x_2 - 9.125x_1x_3 + 2.875x_2x_3 \quad (6)$$

$$Y_2 = 57.366 + 6x_1 + 11.900x_2 - 8.500x_3 + 5.859x_1^2 + 19.359x_2^2 + 22.359x_3^2 + 2.500x_1x_2 + 8.250x_1x_3 - 9.999x_2x_3 \quad (7)$$

Figure 2(a), (b) show that the residuals for $Y_1$ and $Y_2$ are randomly distributed around the mean in front of predicted values due to the good agreement of the models, thereby discarding systematic errors (Ghenymy et al. 2012). Moreover, good linear correlations were found between the predicted (calculated according to Eqs. (6) and (7)) and observed values the for $Y_1$ and $Y_2$, with respective $R^2$ values of 0.994 and 0.987. A normal probability plot of these residuals is shown in Fig. 2(c), (d). The data points on this plot lied reasonably close to a straight line, supporting for the conclusion that all variations in the polynomial equations are the significant factors and that the underlying assumptions of the analysis are satisfied.

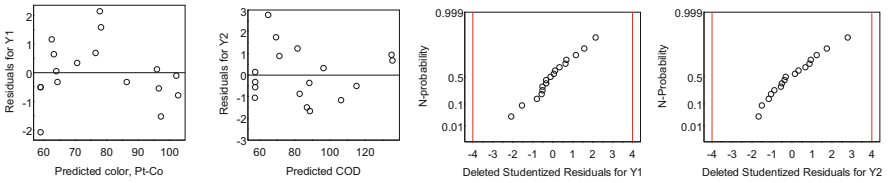


a. Residual - predicted plots for $Y_1$ b. Residual - predicted plots for $Y_2$ c. N-probability - residual error plots for $Y_1$ d. N- probability - residual error plots for $Y_2$

**Fig. 2.** Statistical analysis plots

The ANOVA for the second-order equation is presented in Table 4. This analysis was used to check whether the equations adequately represented the actual relationship between the responses and variables. As can be seen, almost p values were less than 0.05, indicated that the model terms were significant at 95% of probability level (Neto et al. 2005), except some cases where p values were higher than 0.05 (i.e. pH ($Y_1$); $Fe^{2+}$*$Fe^{2+}$, $Fe^{2+}$*pH ($Y_2$)).

### 3.2 Determination and Application of Optimum Condition of Treatment

Application of Modde 5.0 provided us the minimal point which represented the optimum condition for the treatment, as can be seen from Fig. 3. Accordingly, the optimal condition was at pH = 2.78, $Fe^{2+}$ concentration of 2.0 mMol/l, and voltage of 16 V. Operating at this condition resulted in the predicted color and COD of effluent of 58.0 Pt-Co and 55.3 mg/l, respectively.

**Table 4.** ANOVA of the second-order polynomial equation

| Model terms | Color | | | COD | | |
|---|---|---|---|---|---|---|
| | Coefficients | Standard error | p | Coefficients | Standard error | p |
| Constant | 58.901 | 0.802 | 2.30E-11 | 57.366 | 1.907 | 1.16E-08 |
| $Fe^{2+}$ | −3.800 | 0.593 | 0.000365 | 6.000 | 1.410 | 0.003768 |
| pH | 0.2999 | 0.593 | **0.628** | 11.900 | 1.410 | 6.47E-05 |
| U | −6.900 | 0.593 | 7.84E-06 | −8.500 | 1.410 | 0.000527 |
| $Fe^{2+}$*$Fe^{2+}$ | 15.422 | 1.146 | 2.94E-06 | 5.859 | 2.724 | **0.068** |
| pH*pH | 3.922 | 1.146 | 0.011096 | 19.359 | 2.724 | 0.00019 |
| U*U | 11.922 | 1.146 | 1.65E-05 | 22.359 | 2.724 | 7.73E-05 |
| $Fe^{2+}$*pH | 2.875 | 0.663 | 0.003418 | 2.500 | 1.576 | **0.156** |
| $Fe^{2+}$*U | −9.125 | 0.663 | 2.53E-06 | 8.250 | 1.576 | 0.0012 |
| pH*U | 2.875 | 0.663 | 0.003418 | −9.999 | 1.576 | 0.00038 |
| Confident level = 0.95 | | | | Confident level = 0.95 | | |

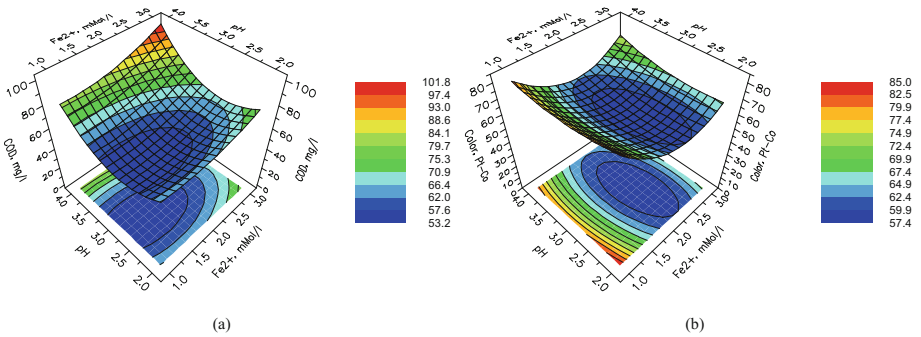


**Fig. 3.** Contour plots of output of color and COD at voltage of 16 V

To evaluate the prediction quantities from the polynomial equations, a real test was carried out for the treatment of real textile wastewater operated at the optimum condition. As can be seen from Table 5, COD in the effluent was 56 ± 1 mg/l and the color was 57 ± 2 Pt-Co, indicating that the actual values of color and COD in the effluent were very similar to their predicted values. Moreover, color and COD in the effluent met well the QCVN 13:2015/BTNMT (Column A). This high removal efficiency can be explained due to following reasons: (i) OH* forming in this condition was extremely high, (ii) OH* scavenger such as $HCO_3^-$ was eliminated because of the low pH (Nidheesh and Gandhimathi 2012).

**Table 5.** Treatment of real textile wastewater under optimum condition

| No. | Parameters | Influent (n = 3) (Average ± Standard deviation) | Effluent (n = 3) (Average ± Standard deviation) | QCVN 13:2015/BTNMT, Column A |
|---|---|---|---|---|
| 1 | Color, Pt-Co | 725 ± 4 | 57 ± 2 | 75 |
| 2 | COD, mg/l | 785 ± 2 | 56 ± 1 | 100 |

### 3.3 Assessment of Effect of Various Parameters on the Removal Efficiency

#### 3.3.1 Effect of $Fe^{2+}$ Concentration

From the Figs. 4a and 5a, it is observed that the Color and COD in the effluent were decreased with the increasing $Fe^{2+}$ concentration up to 2 mMol, which would be due to the formation of highly OH* radical. This radical has strong affinity to the toxic matters presented in the wastewater and oxidize them which resulted in higher removal efficiency. However, there were drastic increase values of color and COD in the effluent when $Fe^{2+}$ concentration continued increasing, which may be due to the change in Fenton's reaction mechanism. Because of the excessive hydrogen peroxide formation (8) which worked as a scavenger of hydroxyl radicals, leading to the production of hydroperoxyl radical (Eq. 8). This new forming radical is much weaker in oxidizing ability compared to hydroxyl radical (Bautistaa et al. 2007).

$$H_2O_2 + OH^* \rightarrow HO_2^* + H_2O \tag{8}$$

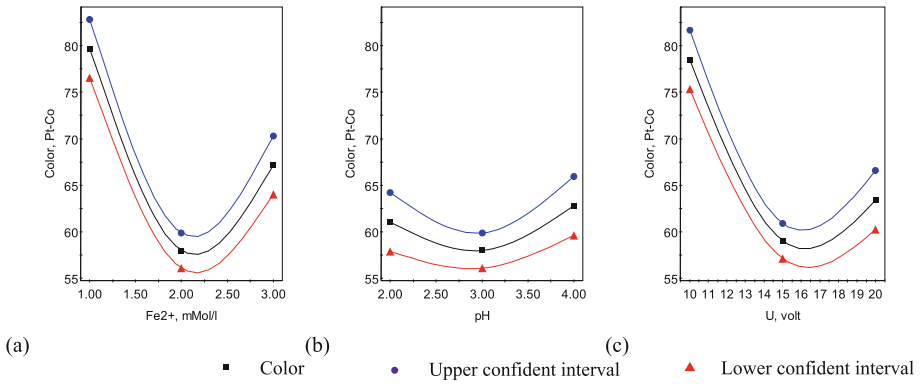


**Fig. 4.** Prediction plots of variables to output of color

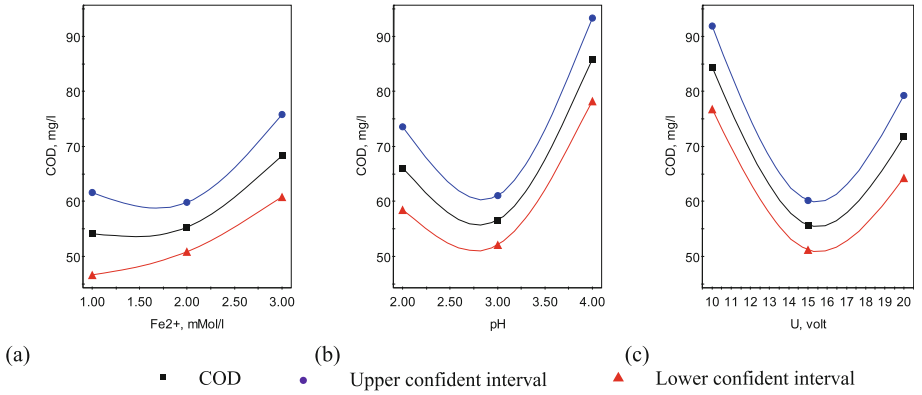


**Fig. 5.** Prediction plots of variables to output of COD

### 3.3.2 Effect of Initial pH

From Figs. 4b and 5b, the outputs of color and COD were decreased with the increasing of pH up to 2.78. Thereafter, there was a drastic increase in output values when pH kept increasing. This can be explained by the fact that when pH < 2.78, instead of decomposing $H_2O_2$ to OH* radical by $Fe^{2+}$, $H_2O_2$ turned into $H_3O_2^+$ by capturing one proton. As $H_3O_2^+$ is electrophilic, leading to the lower rate of reaction between $H_2O_2$ and $Fe^{2+}$, thereby reducing the removal efficiency of color and COD (Deng 2007).

### 3.3.3 Effect of Applied Voltage

The formation the $OH^*$ rate is mainly controlled by the applied voltage during electrolysis. According to Figs. 4c and 5c, outputs of color and COD strongly decreased with the increasing voltage up to 16 V. This could assign for the formation of large amount of highly reactive $OH^*$ radical. Further increase of voltage beyond 16 V would discharge oxygen at the anode via reaction (1) and the evolution of hydrogen at the cathode via reaction (9). These species inhibit the formation of $OH^*$ radical (Zhang et al. 2006).

$$2H^+ + 2e^- \rightarrow H_2 \tag{9}$$

## 4 Conclusions

The Electro Fenton process was successfully optimized for decolorization and COD removal from real textile wastewater using Response surface methodology - Central composite Design (CCF). The regression polynomial equations were formulated for the relations between variables ($Fe^{2+}$ concentration, pH, voltage) and responses (color and COD) with coefficient of determination ($R^2$) value of 0.994 (for color) and 0.987 (for COD). At pH = 2.78, $Fe^{2+}$ concentration of 2.0 mMol/l, and voltage of 16 V, the treatment system reached its optimum operating condition, resulted in the predicted color output of 57 ± 2 Pt-Co and COD output of 56 ± 1 mg/l. Testing for output validation was performed by the treatment of real textile wastewater under the optimum condition which proved the consistency between the observed and predicted values of color and COD. Extended discussion about the effect of $Fe^{2+}$ concentration, pH and voltage on color and COD removal was given based on the results from the developed model. Finally, the results from this study confirmed that Electro Fenton process is a promising solution to treat textile wastewater since the color and COD effluent from this process met well the national standard, QCVN 13:2015/BTNMT.

## References

Ahmad, A.: Effect of preparation conditions of activated carbon from bamboo waste for real textile wastewater. J. Hazard. Mater. **173**, 487–493 (2010)

Azbar, N.: Comparison of various advanced oxidation processes and chemical treatment methods for COD and color removal from a polyester and acetate fiber dyeing effluent. Chemosphere **55**, 35–43 (2004)

Bautistaa, P., Mohedanoa, P., Gilarranza, M., Casasa, J., Rodriguez, J.: Application of Fenton oxidation to cosmetic wastewaters treatment. J. Hazard. Mater. **143**, 128–134 (2007)

Box, G., Draper, N.: Empirical Model-Building and Response Surfaces. Wiley, New York (1987)

Boye, B., Dieng, M., Brillas, E.: Degradation of herbicide 4-chlorophenoxyacetic acid by advanced electrochemical oxidation methods. Environ. Sci. Technol. **36**(13), 3030–3035 (2002)

Brillas, E., Boye, B., Sires, I., Garrido, J., Rodrıguez, R., Arias, C., Cabot, P., Comninellis, C.: Electrochemical destruction of chlorophenoxy herbicides by anodic oxidation and electro-Fenton using a boron-doped diamond electrode. Electrochim. Acta **49**(25), 4487–4496 (2004)

Deng, Y.: Physical and oxidative removal of organics during Fenton treatment of mature municipal landfill leachate. J. Hazard. Mater. **146**, 334–340 (2007)

Ghenymy, A., Segura, S., Rodríguez, R., Brillas, E., Begrani, M., Abdelouahid, B.: Optimization of the electro-Fenton and solar photoelectro-Fenton treatments of sulfanilic acid solutions using a pre-pilot flow plant by response surface methodology. J. Hazard. Mater. **221**(2012), 288–297 (2012)

Guivarch, E., Trevin, S., Lahitte, C., Oturan, M.: Degradation of azo dyes in water by electro-Fenton process. Environ. Chem. Lett. **1**(1), 38–44 (2003)

Li, H., Zhao, G., Niu, S., Luan, Y.: Technologic parameter optimization of gas quenching process using response surface method. Comput. Mater. Sci. **38**(4), 561–570 (2007)

Neto, B., Scarminio, I., Bruns, R.: Statistical Design - Chemometrics (Data Handling in Science and Technology). Elsevier (2005)

Nidheesh, P., Gandhimathi, R.: Trends in electro-Fenton process for water and wastewater treatment: an overview. Desalination **299**, 1–15 (2012)

Nidheesh, P., Gandhimathi, R., Sanjini, N.: $NaHCO_3$ enhanced Rhodamine B removal from aqueous solution by graphite–graphite electro Fenton system. Sep. Purif. Technol. **132**(2014), 568–576 (2014)

Panizza, M., Asadi, M., Mahvi, A.: Evaluation of Electro-Fenton process performance for COD and Reactive Blue 19 removal from aqueous solution. Iran. J. Health Environ. **5**(4), 433–444 (2011)

Prakash Maran, J., Sivakumar, V., Thirugnanasambandham, K., Sridhar, R.: Response surface modeling and analysis of barrier and optical properties of maize starch based edible films. Int. J. Biol. Macromol. **60**, 412–421 (2013)

Su, C., Chang, A., Bellotindos, L., Lu, M.: Degradation of acetaminophen by Fenton and electro-Fenton processes in aerator reactor. Sep. Purif. Technol. **99**, 8–13 (2012)

Thirugnanasambandham, K., Sivakumar, V.: Optimization of treatment of grey wastewater using Electro-Fenton technique – Modeling and validation. Process Saf. Environ. Prot. **95**, 60–68 (2015)

Zhang, H., Zhang, D., Zhou, J.: Removal of COD from landfill leachate by electroFenton method. J. Hazard. Mater. **135**, 106–111 (2006)

# Parameter Study on Remediating Cr(VI) in Water Using Activated Charcoal

Alfa-Sika Mande Seyf-Laye[1,2,3(✉)], Tchakala Ibrahim[2], Djaneye-Boundjou Gbandi[2], and Chen Honghan[1]

[1] Beijing Key Laboratory of Water Resources and Environmental Engineering, China University of Geosciences (Beijing), Beijing 100083, People's Republic of China
seyf009@yahoo.ca

[2] Water Chemistry Laboratory, Faculty of Science, University of Lomé, BP. 1515, Lomé, Togo
bigtchak73@yahoo.fr, adjaneye@yahoo.fr

[3] Faculty of Science and Technology, University of Kara, BP. 404, Kara, Togo

**Abstract.** Commercial activated charcoal was investigated for removal of Cr(VI) from aqueous solutions. The effects of altering the initial Cr(VI) concentration, pH, contact time and amount of activated charcoal were studied. Maximum adsorption of Cr(VI) was achieved between pH 1–3 and after a contact time of 120 min. The percentage of Cr(VI) removed decreased from 99.99–90.83% when the initial Cr(VI) concentration was increased from 0.05–0.5 mg $ml^{-1}$ at pH 2 and 26 ± 2 °C. Various kinetic models such as pseudo first-order and pseudo second-order models were used to evaluate the mechanism of Cr(VI) adsorption on activated charcoal. The Cr(VI) removal process was found to be governed by second-order kinetics and the rate constant of the adsorption ($k_2$) was 0.1800 g $kg^{-1}$ $min^{-1}$ for an initial Cr(VI) concentration of 0.1 mg $ml^{-1}$. The adsorption of Cr(VI) was evaluated using Langmuir, Freundlich, and Temkin isotherms and their constants were determined. The maximum adsorption capacity obtained using the Langmuir isotherm model was 45.24 g $kg^{-1}$ at pH 2.

**Keywords:** Parameter · Activated charcoal · Adsorption · Water · Cr(VI)

## 1 Introduction

All over the world industry is forced to diminish down to acceptable level contents of heavy metal in water and industrial waste waters. Conventional methods like precipitation are a favorable especially when dealing with large volume of matter which contains heavy metal ions in low concentration. Typically these ions are precipitated as hydrated metal oxides or hydroxides using calcium oxide. Precipitation is accompanied by flocculation or coagulation, and one major problem is the formation of large amounts of sediments containing heavy metal ions. In recent years, considerable attention has been devoted to fine new adsorbents. One of the suitable methods for removing heavy metals from water and waste water is using surface adsorption process.

© Springer Nature Singapore Pte Ltd. 2018
H. Tran-Nguyen et al. (eds.), *Proceedings of the 4th Congrès International de Géotechnique - Ouvrages -Structures*, Lecture Notes in Civil Engineering 8,
DOI 10.1007/978-981-10-6713-6_103

Activated carbon is the most widely used adsorbent for this purpose because it has a high capacity for adsorption of organic matter, but its use is limited because of its high cost (Battacharya and Venkobachar 1984; Khare et al. 1987). This has led to search for cheaper substitutes. Coal, fly ash, wood, silica gel, clay materials (bentonite, montmorillonite, etc.), agricultural wastes (bagasse pith, maize cob, coconut shell, rice husk, etc.), and cotton wastes have been tried with varying success for metal ions removal (Mande Seyf-Laye et al. 2009; Singh and Rawat 1994; Theng and Wells 1995).

The objective of this study was to investigate the use of activated charcoal as an adsorbent material for removing Cr(VI) from wastewater.

Batch experiments were carried out for kinetic studies on the removal of Cr(VI) from aqueous solutions. The influence of various important parameters such as the pH, contact time, adsorbent amount, and initial Cr(VI) concentration were investigated by varying any one of the process parameters and holding the other parameters constant. The Langmuir and Freundlich equations were used to fit the equilibrium isotherm models. Pseudo first-order and second-order kinetic models were used to evaluate the mechanism of adsorption.

## 2 Experimental

Commercial activated carbon in granular form (CAC) (Table 1) was obtained from Sinopharm Chemical Reagent Co. Ltd (Beijing, China) and crushed and sieved to a particle size of 450 μm. A Cr(VI) stock solution (1 $mg.ml^{-1}$) was prepared by dissolving 99.9% $K_2Cr_2O_7$ (2.8287 g) in distilled water (1 L). This solution was diluted as required to obtain 0.05–0.5 $mg.ml^{-1}$ Cr(VI) standard solutions. The initial pH of the solution was adjusted using either 0.5 M NaOH or 0.5 M $H_2SO_4$. The batch experiments were carried out in 100 ml conical flasks by agitating a pre-weighed amount of the activated charcoal with 50 ml of the aqueous Cr(VI) solution for a predetermined period of time (based on prior kinetic studies) at 26 ± 2 °C on a water bath-mechanical shaker (198 rpm). The effect of altering the initial pH was studied with 0.05 $mg.ml^{-1}$ Cr(VI). The effect of altering the contact time was studied with 0.1–0.4 $mg.ml^{-1}$ Cr(VI) solutions at pH 2. Experiments were also conducted to investigate the effect of varying the amount of activated charcoal from 2–24 $g.L^{-1}$ with a Cr(VI) concentration of 0.250 $mg.ml^{-1}$ at pH 2. Adsorption isotherm studies were carried out with the different standard solutions (0.05–0.5 $mg.ml^{-1}$ Cr(VI)) while maintaining the adsorbent dosage at 10 $g.L^{-1}$ and the pH at 2. An UV-visible spectrophotometer was employed with 1,5-diphenylcarbazide in acid medium to determine the concentrations of Cr(VI) remaining in the sample. The absorbance of the purple-violet colored solution was recorded at 540 nm. The filtrate was analyzed for the remaining Cr(VI) concentration. The amount of Cr(VI) adsorbed (g $kg^{-1}$) at time $t$ was calculated using Eq. (1):

$$q_t = \frac{C_0 - C_t}{m_s} \times V \tag{1}$$

**Table 1.** Linear regression equations, coefficients of determination ($R^2$) and isotherm constants for the Freundlich and Langmuir isotherm models for adsorption of Cr(VI) by activated charcoal.

| *Langmuir isotherm* | | | |
|---|---|---|---|
| Linear regression equation | $q_m$ | b | $R^2$ |
| Ce = 0.0221Ce + 0.0727 | 45.25 | 0.3039 | 0.9800 |
| *Freundlich isotherm* | | | |
| Linear regression equation | $K_f$ | $n_f$ | $R^2$ |
| $\log q_e$ = 0.2259 logCe + 1.2139 | 16,364 | 0.2259 | 0.9886 |

Where $C_0$ and $C_t$ are the Cr(VI) concentrations in g $L^{-1}$ at time 0 and time $t$, respectively, $V$ is the volume of the Cr(VI) solutions in $L$, and $m_s$ is the weight of activated charcoal in kg.

## 3 Results and Discussion

### 3.1 Effect of Initial PH

The percentage of Cr(VI) adsorbed by activated charcoal decreased from 99.9–39.54% when the pH was increased from 1–7 (Fig. 1). The maximum percent removal of Cr (VI) was obtained between pH 1–3, and therefore pH 2 was selected for the rest of the experiments. Chromium exists mostly in two oxidation states which are Cr(VI) and Cr(III) and the stability of these forms is dependent on the pH of the system (Cimino et al. 2000; Selomulya et al. 1999; Shama and Forster 1994). It is well known that the dominant form of Cr(VI) at pH 2 is $HCrO_4^-$. Increasing the pH will shift the concentration of $HCrO_4^-$ to other forms; $CrO_4^{2-}$ and $Cr_2O_7^{2-}$. Maximum adsorption at pH 1.0 indicates that it is the $HCrO_4^-$ form of Cr(VI), which is the predominant species between pH 1 and 4, which is adsorbed preferentially on the activated charcoal.

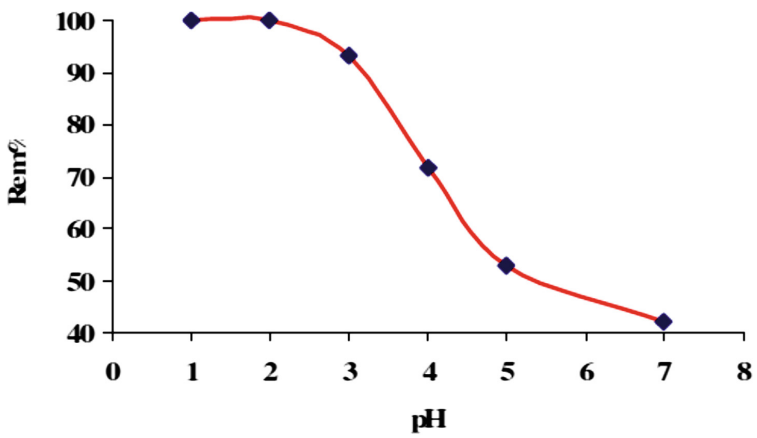


**Fig. 1.** Effect of initial pH on the percentage of Cr(VI) adsorbed by activated charcoal (10 g $L^{-1}$) at a Cr(VI) concentration of 0.05 mg $ml^{-1}$.

### 3.2 Effect of Contact Time

The contact time was found to be an important parameter for the adsorption of Cr(VI) on activated charcoal (Fig. 2). Over the first 20 min the percent removal of Cr(VI) from the aqueous solution increased rapidly and reached 60.21–97.43% (for 0.4–0.1 mg. $ml^{-1}$ Cr(VI) solutions. After this the percent removal tapered off until at 120 min it reached 99.76% and 90.83% for solutions containing 0.1 and 0.4 $mg.ml^{-1}$ of Cr(VI), respectively. Further increase in the contact time had a negligible effect on the percent removal. Therefore, a contact time of 120 min was used for Cr(VI) adsorption on activated charcoal in all the batch studies.

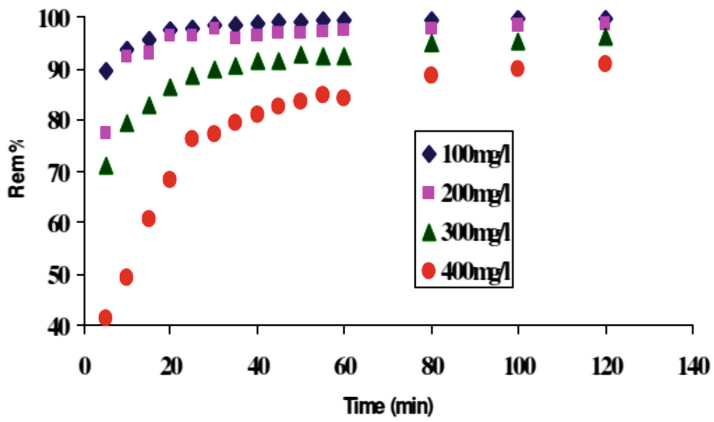


**Fig. 2.** Effect of contact time on the percentage of Cr(VI) adsorbed by activated charcoal (10 g $L^{-1}$) at pH 2 for solutions with different initial Cr(VI) concentrations (0.1–0.4 $mg.ml^{-1}$).

### 3.3 Effect of Initial Cr(VI) Concentration

When the initial Cr(VI) concentration was varied from 0.05–0.5 $mg.ml^{-1}$, the percentage of Cr(VI) removed decreased from 99.99–88.21% (Fig. 3). However, the absolute amount of Cr(VI) removed per unit mass of activated charcoal (or absorption capacity) significantly increased from 4.99–44.10 $g.kg^{-1}$ with the increase in initial Cr (VI) concentration.

### 3.4 Effect of Adsorbent Amount on Cr(VI) Removal

When the amount of activated charcoal was increased from 2–24 g $L^{-1}$, the percentage of Cr(VI) removed increased from 56–99.44% (Fig. 4). The amount of activated charcoal selected for subsequent experiments was 10.0 g $L^{-1}$ as above this amount the removal of Cr(VI) remained stable.

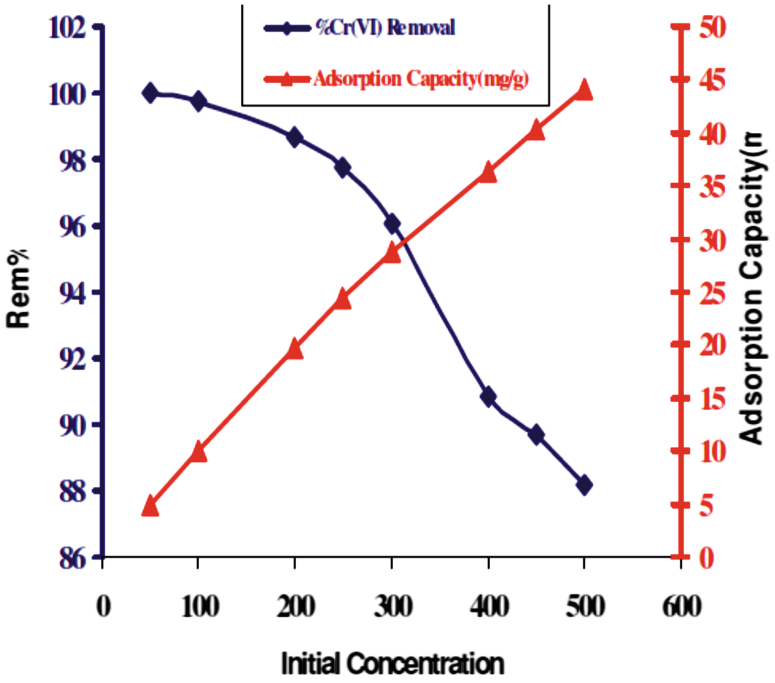


**Fig. 3.** Effect of initial Cr(VI) concentration (0.05–0.5 $mg.ml^{-1}$) on the absorption capacity and percentage of Cr(VI) adsorbed by activated charcoal (10 g $L^{-1}$) at pH 2 with a contact time of 120 min.

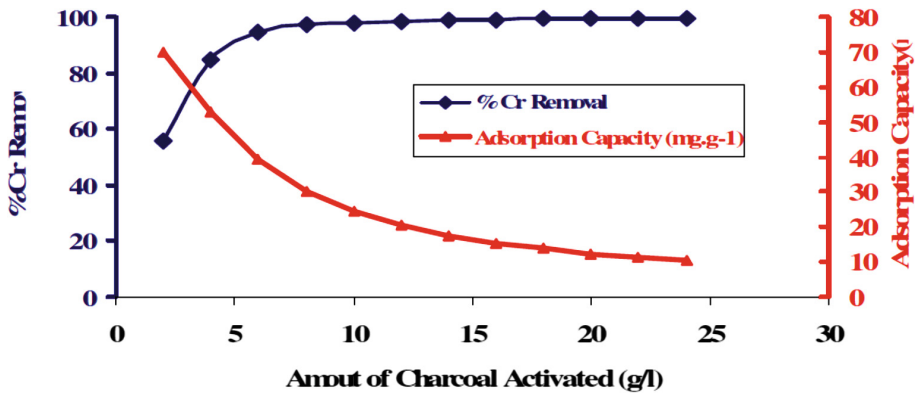


**Fig. 4.** Effect of the amount of activated charcoal on the percentage of Cr(VI) adsorbed at an initial Cr(VI) concentration of 0.250 $mg.ml^{-1}$, a contact time of 120 min, and pH 2.

### 3.5 Adsorption Isotherm

The equilibrium of adsorption is an important physicochemical parameter for evaluation of the adsorption process. The adsorption isotherm ($q_e$ versus $C_e$) obtained in this study showed that the adsorption capacity (g $kg^{-1}$) increased with increasing equilibrium Cr(VI) concentrations ($C_e$) and eventually attained a constant value (Fig. 5).

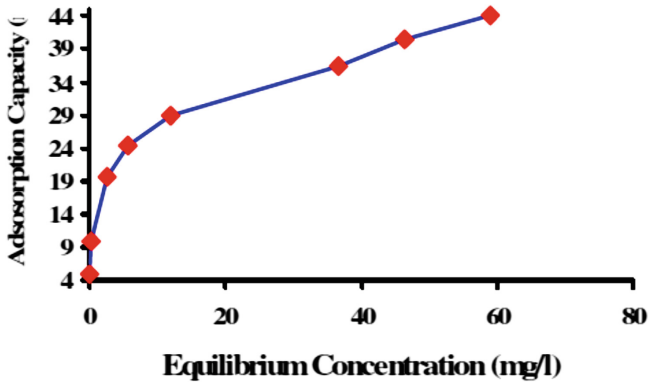


**Fig. 5.** Adsorption isotherm obtained for Cr(VI) absorption by activated charcoal (10 g/l) at initial concentrations (0.05, 0.1, 0.2, 0.25, 0.3, 0.4, 0.45, 0.5 mg ml), pH 2 and contact time 120 min.

To model the adsorption behavior, three adsorption isotherms were studied and their correlation with the experimental data was assessed. These included the Freundlich and Langmuir isotherms, which are the earliest and simplest known relationships describing the adsorption equation (Muhamad et al. 1998; Jalali et al. 2002). Table 1 shows the adsorption capacities of various adsorbents. It is clear from this table that the adsorption capacity of the commercial activated carbon used in this study far exceeded that of other activated carbons prepared from different materials.

- *Langmuir isotherm*

The linear form of the Langmuir equation is shown in Eq. (2) (Bulut and Aydin 2006; Langmuir 1996; Ravikumar et al. 2007).

$$\frac{C_e}{q_e} = \frac{1}{bq_m} + \frac{C_e}{q_m} \tag{2}$$

Where $b$ and $q_m$ are constants related to the apparent energy of adsorption and the adsorption capacity, respectively; and $q_e$ is the amount adsorbed per unit mass of the adsorbent (g $kg^{-1}$) with an equilibrium concentration of $C_e$ (mg $ml^{-1}$). A plot of ($C_e/q_e$) vs. $C_e$ was linear and the constants $q_m$ and $b$ were determined from the slope and intercept of the plot (Table 3). The correlation coefficient obtained with the Langmuir equation was high ($R^2$ = 0.98), which indicated a good fit between the

parameters. The dimensionless parameter ($R_L = 1/1 + bC_0$), which is a measure of adsorption favorability, was found to be in the range of 0.00653–0.06174 ($0 < R_L < 1$) and confirmed that Cr(VI) removal using activated charcoal at pH 2 and 26 ± 2 °C was a favorable adsorption process.

- *Freundlich isotherm*

The Freundlich isotherm is expressed by Eq. (3) (Freundlich 1906)

$$q_e = K_f C_e^{n_f} \tag{3}$$

Where $K_f$ ($g^{1-1/n}\ l^{1/n}\ kg^{-1}$) is the Freundlich constant, which indicates the relative adsorption capacity of the adsorbent related to the bonding energy, and $n_f$ is the heterogeneity factor representing how the absorption deviates from linearity. Values of $n_f$ less than one are an indication that significant adsorption takes place at low concentration, while high $K_f$ values indicate greater adsorption intensity. The linear form of the Freundlich isotherm is Eq. (4):

$$\boldsymbol{log q_e} = logK_f + n_f log C_e \tag{4}$$

The Freundlich coefficients were determined from a plot of log $\boldsymbol{q_e}$ versus log ($\boldsymbol{C_e}$) and are given in Table 2. The Freundlich model clearly agreed very well with the experimental data.

**Table 2.** Kinetic constants for pseudo first-order and pseudo second-order models of the Cr(VI) adsorption by activated charcoal.

| Co (mg/L) | qe ($g\ kg^{-1}$) | Pseudo first-order kinetics model | | | Pseudo second-order kinetics model | | |
|---|---|---|---|---|---|---|---|
| | (Experimental) | $k_1$ | $q_e$ | $R^2$ | $k_2$ | $q_e$ | $R^2$ |
| 100 | 9.97 | 0.0199 | 0.77 | 0.9652 | 0.1800 | 10.02 | 1.000 |
| 200 | 19.73 | 0.0159 | 2.23 | 0.8456 | 0.0451 | 19.88 | 1.000 |
| 300 | 28.81 | 0.0155 | 7.06 | 0.9751 | 0.0141 | 29.32 | 0.9999 |
| 400 | 36.33 | 0.0172 | 21.2 | 0.9815 | 0.0032 | 38.75 | 0.9998 |

### 3.6 Adsorption Kinetics

- *Pseudo first-order kinetics*

Kinetic modeling of the removal of Cr(VI) by activated charcoal was carried out using the well-known Lagergren model (Hameed 2009; Tabak et al. 2009).

$$\log(q_e - q_t) = \log q_e - k_{ad} t/2.303 \tag{5}$$

Where $q_e$ and $q_t$ are the amounts of Cr(VI) adsorbed (g $kg^{-1}$) at equilibrium and time $t$, respectively, and $k_{ad}$ (L $min^{-1}$) is the rate constant of the pseudo first-order adsorption operation.

A plot of log $(q_e - q_t)$ versus t was linear and represents the pseudo first-order kinetics for the removal of Cr(VI) using activated charcoal. The first-order rate constants $k_1$ and $q_e$ were calculated for a range of initial Cr(VI) concentrations (0.1–0.4 mg $L^{-1}$) with a constant amount of activated charcoal (10 g $L^{-1}$) (Table 2). The regression correlation coefficient was in the range 0.97–0.982, which is good and shows the applicability of the pseudo first-order kinetic model to the removal of Cr(VI) using activated charcoal. The experimental values of $q_e$ obtained using initial Cr(VI) concentrations of 100, 200, 300, and 400 mg $L^{-1}$ were 9.97, 19.73, 28.81, and 36.33 g $kg^{-1}$, respectively, which do not agree with the values predicted by the pseudo first-order model.

- *Pseudo second-order kinetics*

The pseudo second-order adsorption kinetic rate equation is expressed as Eq. (6) (Ho et al. 2000):

$$\frac{1}{(q_e - q_t)} = \frac{1}{q_e} + k_2 t \tag{6}$$

Where $k_2$ is the rate constant of pseudo second-order adsorption ($g\,kg^{-1}\,min^{-1}$). Equation (6) can be rearranged to obtain Eq. (7), which has the linear form:

$$\frac{t}{q_t} = \frac{1}{h} + \frac{1}{q_e} t \tag{7}$$

With $h$ ($g\,kg^{-1}\,min^{-1}$), the initial adsorption rate, expressed by: Eq. (8)

$$h = k_2 q_e^2 \tag{8}$$

The plot of $(t/q_t)$ and $t$ of Eq. (9) was linear (Fig. 10), and $q_e$ and $k_2$ were determined from the slope and intercept, respectively. Because pseudo first-order kinetics were not applicable to the adsorption of Cr(VI) on activated charcoal, the second-order kinetic model was evaluated. The calculated $q_e$ values agreed with the experimental values, and the values obtained for the regression correlation coefficients were more than 0.9998. These results indicate that the kinetics of Cr(VI) adsorption using activated charcoal are explained better by a second-order kinetic model than a first-order one.

### 3.7 Comparison of Cr(VI) Removal with Different Adsorbents Reported in Literature

The adsorption capacities of the adsorbents for the removal of Cr(VI) have been compared with those of others reported in literature and the values of adsorption capacities have been presented in Table 3. The values reported ares in the form of

**Table 3.** Comparison of adsorption capacities (g $kg^{-1}$) of the adsorbents for the removal of Cr(VI) with those of other adsorbents

| Absorbent | Adsorption capacities (g $kg^{-1}$) | Reference |
|---|---|---|
| Coconut tree sawdust | 3.46 | Selvi et al. 2001 |
| Rind of orange (Citrus sinensis), (L.) Osbeck | 10.74 | Poojari et al. 2015 |
| Sawdust | 20.70 | Bhattacharya et al. 2006 |
| Banana peels | 24.61 | Mande Seyf-Laye et al. 2009 |
| Rice husk ash | 25.64 | Bhattacharya et al. 2006 |
| Clarified sludge | 26.31 | Bhattacharya et al. 2006 |
| Maize cob | 28.57 | Mande Seyf-Laye et al. 2009 |
| Leaf mould | 43 | Sharma and Forster 1994 |
| Commercial activated charcoal | 45.24 | Present work |

monolayer adsorption capacity. The experimental data of the present investigations are comparable with the reported values.

## 4 Conclusion

Activated charcoal has been successfully used to remove Cr(VI) from aqueous solution. The adsorption of Cr(VI) fitted well at low pH values, and the removal of Cr(VI) depended on the initial concentration, contact time and amount of activated charcoal. The Freundlich and Langmuir isotherm models agreed with the experimental data. Cr(VI) adsorption obeyed a second order rate equation, and the rate constant was found to be 0.0032 $kg.g^{-1}$ $min^{-1}$ with an initial Cr(VI) concentration 0.4 $mg.ml^{-1}$.

**Acknowledgments.** This work was supported by 863 Program (2007AA06A410) from the Chinese Ministry of Science and Technology. The analytical data were supplied by the Lab of Water Resources and Environmental Engineering in the China University of Geosciences, Beijing.

## References

Mande Seyf-Laye, A.-S., Liu, M., Liu, F., Chen, H.: Kinetics of the adsorption of chromium (VI) ions from water by vegetable precursors treated with sulphuric acid. Adsorp. Sci. Technol **27**(10), 965–974 (2009)

Poojari, A.C., Maind, S.D., Bhalerao, S.A.: Effective removal of Cr(VI) from aqueous solutions using rind of Orange (Citrus sinensis), (L.) Osbeck. Int. J. Curr. Microbiol. App. Sci. **4**(4), 653–671 (2015)

Battacharya, A., Venkobachar, C.: Removal of cadmium (II) by low cost adsorbents. J. Environ. Eng. ASCE **110**, 110–122 (1984)

Bhattacharya, A.K., Mandal, S.N., Das, S.K.: Removal of Cr(VI) from aqueous solution by adsorption onto low cost non-conventional adsorbents. Indian J. Chem. Technol. **13**, 576–583 (2006)

Bulut, Y., Aydin, H.: A kinetics and thermodynamics study of methylene blue adsorption on wheat shells. Desalination **194**, 259–267 (2006)

Cimino, G., Passerini, A., Toscano, G.: Removal of toxic cations and Cr(VI) from aqueous solution by hazelnut shell. Water Res. **34**, 2955–2962 (2000)

Freundlich, H.M.F.: Uber die adsorption in losungen. Zeitschrift fur Physikalische Chemie (Leipzig) **57A**, 385–470 (1906)

Hameed, B.H.: Spent tea leaves: a new non-conventional and lowcost adsorbent for removal of basic dye from aqueous solutions. J. Hazard. Mater. **161**, 753–759 (2009)

Ho, Y., Mckay, G., Wase, D., Foster, C.F.: Study of the sorption of divalent metal ions on to peat. Adsorp. Sci. Technol. **18**, 639–650 (2000)

Jalali, R., Ghafourian, H., Aself, Z., Davarpanah, S.J., Sepehr, S.: Removal and recovery of lead using nonliving biomass of marine algae. J. Harzard. Mater. **92**(3), 253–262 (2002)

Khare, S.K., Panday, K.K., Srivastava, R.M., Singh, V.N.: Removal of victoria blue from aqueous solution by fly ash. J. Chem. Technol. Biotechnol. **38**, 99–104 (1987)

Langmuir, I.: The constitution and fundamental properties of solids and liquids. Am. J. Chem. Soc. **38**, 2221–2295 (1996)

Muhamad, N., Parr, J., Smith, D.M., Wheatley, D.A.: Adsorption of heavy metals in slow sand filters. In: Proceeding of the WEDC Conference on Sanitation and Water for all Islamabad, Pakistan, pp. 346–349 (1998)

Ravikumar, K., Krishnan, S., Ramalingnam, S., Balu, K.: Optimization of process variables by the application of response surface methodology for dye removal using a novel adsorbent. Dyes Pigm. **72**, 66–69 (2007)

Selomulya, C., Meeyoo, V., Amal, R.: Mechanisms of Cr(VI) removal from water by various types of activated carbons. J. Chem. Technol. Biotechnol. **74**, 111–122 (1999)

Selvi, K., Pattabhi, S., Kadirvelu, K.: Removal of Cr(VI) from aqueous solution by adsorption onto activated carbon. Bioresour. Technol. **80**, 87–89 (2001)

Sharma, D.C., Forster, C.F.: The treatment of chromium wastewaters using the sorptive potential of leaf mould. Bioresour. Technol. **49**, 31–40 (1994)

Singh, B.K., Rawat, N.S.: Comparative sorption equilibrium studies of toxic phenols on fly ash and impregnated fly ash. J. Chem. Technol. Biotechnol. **61**, 307–317 (1994)

Tabak, A., Eren, E., Afsin, B., Caglar, B.: Determination of adsorptive properties of a Turkish sepiolite for removal of reactive blue 15 anionic dye from aqueous solutions. J. Hazard. Mater. **161**, 1087–1094 (2009)

Theng, B.K.G., Wells, N.: Assessing the capacity of some New Zealand clays for decolourizing vegetable oil and butter. Appl. Clay Sci. **9**, 321–326 (1995)

# Processes Causing Strong Acidic Groundwaters in and Around the Mekong Delta Area

Quang-Khai Ha, Seunghyun Choi, and Kangjoo Kim(✉)

Department of Environmental Engineering, Kunsan National University, Gunsan, Jeonbuk 573-701, Republic of Korea
quangkhai02@gmail.com, kangjoo@kunsan.ac.kr

**Abstract.** Extremely acidic groundwaters (EAG; pH < 3) are frequently observed in the Mekong Delta area. This study geochemically investigates the processes for this phenomenon. Forty-two groundwater and eight sediment samples were collected and performed chemical/mineralogical analyses and leaching experiments. Long-term data from 178 wells of National Groundwater Monitoring Network of the Southern Vietnam (NGMS) were also inspected. In the study area, groundwaters are characterized by increasing concentrations of various species such as $SO_4$, Fe, Mn, Al, Pb, Cr, Zn and U at low pH. $SO_4$ (up to 2959 mg/L) and Fe (up to 1679 mg/L) concentrations in the EAG are generally very high. Framboidal pyrite grains are typically observed in the sediment samples taken from the sites where acidic groundwaters were observed. The leaching experiments with those sediments using deionized water derived pH as low as 2.7 and high metal concentrations in the extractants. Heavy metal concentrations were also high in the extractants of pyrite-free sediments when the pH was adjusted to acidic range. Our results suggest that the high metal concentration in the acidic groundwater are closely related with the low pH induced by the pyrite oxidation. This study also shows that the acidic pH of groundwater is in part related with the well installation; that is, well installation chemically disturbs the confined aquifer, which was originally under reducing environments, and triggers the pyrite oxidation.

**Keywords:** Acidic groundwater · Heavy metal contamination · Mekong delta

## 1 Introduction

Extremely acidic groundwaters (EAG; pH < 3) are widely observed in many countries around the world such as Australia (Appleyard et al. 2004; Benison and Bowen 2015), Netherlands (Fest et al. 2007), and America (Verplanck et al. 2009). Previous studies have demonstrated that low pH is the frequent cause of serious environmental problems such as heavy metal contamination, infrastructure corrosion, inhibition of plant growth, and fish kills. It is well known that pH is a mater variable controlling behaviors of heavy metals. Low pH promotes dissolution of various minerals and increases

© Springer Nature Singapore Pte Ltd. 2018
H. Tran-Nguyen et al. (eds.), *Proceedings of the 4th Congrès International de Géotechnique - Ouvrages -Structures*, Lecture Notes in Civil Engineering 8,
DOI 10.1007/978-981-10-6713-6_104

concentrations of heavy metals in natural waters. EAG sometimes show extremely high concentrations of Al (~8000 mg/L), Fe (~1300 mg/L), Mn (~46 mg/L) and As (~7 mg/L) EAG (Appleyard et al. 2004; Benison and Bowen 2015), bringing risks for human health and ecological systems at the same time.

Earlier studies proposed several processes such nitrification and pyrite oxidation as causes deriving EAG. Pyrite oxidation generates sulfuric acids, thus, the groundwater can show very low pH. Pyrite oxidation is frequently triggered by human activities: for example, groundwater level decline by over-abstraction (Appleyard et al. 2004), nitrate supplied from fertilizers (Zhang et al. 2009), artificial injection of aerated surface waters (Seibert et al. 2016), canal digging, and so on. Nitrification can also low the pH of dilute groundwaters to a very low level. Even though it has been reported that well installation can disturb groundwater quality (Kim 2003), its role has not been evaluated from the perspective of EAG generation.

In the Mekong delta area, heavy metal concentrations in groundwater have been a big issue and many studies have been performed to investigate the origin of heavy metals (Buschmann et al. 2008; Nguyen and Itoi 2009; Hoang et al. 2010). The paper demonstrates that acidified groundwaters by well installation induced pyrite oxidation is the main cause of the heavy metals contamination in groundwater.

For the study, groundwater monitoring data and mineralogical characteristics of the Mekong delta sediments were investigated. Leaching experiments of the sediment are also performed to support our explanation.

## 2 Study Area

Mekong Delta Vietnam (MDV) (Fig. 1) covers an area of 39,000 $km^2$. According to the geologic unit, sediment in the area can be distinguished into eight confined aquifers: Holocene (qh), Upper Pleistocene (qp3), Upper- Middle Pleistocene (qp2-3), Lower Pleistocene (qp1), Middle Pliocene (n22), Lower Pliocene (n21), Upper Miocene (n13) and Upper Middle Miocene (n123), in ascending order (Nguyen et al. 2004).

Acid sulfate soil (ASS) is commonly observed in the area (Gröger et al. 2011; Husson et al. 2000) and masks 40% of Holocene surface (Fig. 1). In the older sediment, pyrite has been observed in the samples 100 and 125 m depth in upper-middle Pleistocene aquifers and 265 m in Miocene aquifers (Nguyen and Itoi 2009).

Water resources in this area include rainfall, surface water, and groundwater. The groundwater is the most important sources of water supply and occupies 62% of domestic water supply. Groundwater abstraction rate has increased from 0.14 to 0.28 million $m^3$/day during periods 2001–2004. In 2010, the total amount of groundwater usage was around 2 million $m^3$/day (Bui 2014). As a result, groundwater level in the area was decreasing with a rate ranging from 0.5 (qp3) to 2.85 m/year (n13) during 2000–2010.

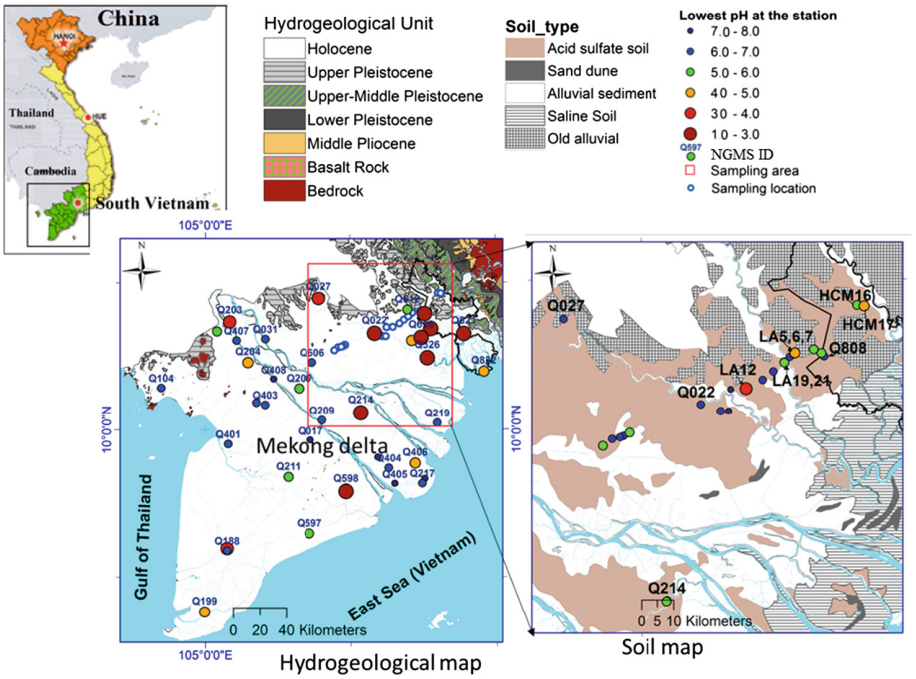


**Fig. 1.** Study area. Distribution of the lowest pH values at monitoring stations (NGMS) plotted on the hydrogeological map (modified from Nguyen et al. 2004) and the pH data of the study plotted on the soil map.

## 3 Methodology

### 3.1 Groundwater Data

Long-term groundwater monitoring data obtained from 178 wells in 39 stations of National Groundwater Monitoring Network of southern Vietnam (NGMS) was investigated. Forty-two groundwater wells in Acid Sulfate Soil (ASS) area were additionally sampled and analyzed as a part of this study.

### 3.2 Sediment Data

Four soil samples (0.5–1 m in depth) were collected from the ASS area (Fig. 1). A 54 m long core sample was retrieved in the station Q808 and near the NGMS well Q808010 (Fig. 1). Selected sediment samples were analyzed for X-ray fluorescence (XRF), X-ray diffraction (XRD) and Scanning Electron Microscope (SEM). Leaching experiments was also conducted at laboratory conditions in a 250-mL glass bottles with a solution/sediment ratio of 10 mL/g dry weight (Exp. 1). Additional experiments were performed by controlling pH (Exp. 2).

# 4 Result and Discussion

## 4.1 Occurrences of Acidic Groundwaters

The groundwater pH of NGMS ranges from 1.4 to 9. Twelve out of 178 wells showed pH less than 3 at least once during their monitoring periods (Fig. 1). These 12 wells are characterized by elevated Fe, $SO_4$, Al, and Mn concentrations, which are up to 1700 mg/L, 3000 mg/L, 2 mg/L and 25 mg/L, respectively. Figure 2 show groundwater time series data from the well Q808010 in the NGMS reflecting that low pH (less than 3) was observed at the beginning (15 years) of well installation and the pH is recovered after that. High $SO_4$, Fe, Al, and Si was observed at the same time with low pH.

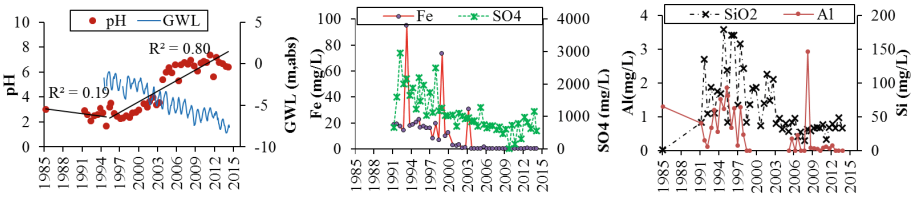


**Fig. 2.** Long-term monitoring data of groundwater level (GWL), pH, Fe (total), $SO_4$, Al and Si from the well name Q808010 in NGMS

High Fe and Mn concentrations are widely observed in the area (Buschmann et al. 2008; Hoang et al. 2010). The observation reveals that many of the groundwater samples are not suitable for drinking.

High $SO_4$ concentration is likely to be associated with seawater intrusion (Ngo et al. 2015; Bui 2014) or pyrite oxidation. However, long-term monitoring data from the 12 acidic NGMS wells show elevated $SO_4$ and Fe concentration in low pH (Fig. 2). Acidic groundwaters typically show pH values negatively correlated with $SO_4$ and Fe when they are associated with pyrite oxidation (Appleyard et al. 2004; Benison and Bowen 2015; Zhang et al. 2009).

Lowed pH induced by pyrite oxidation increase the solubility of heavy metals. pH is the master variable controlling mobilization of the most of heavy metals (Kjøller et al. 2004).

## 4.2 Soil/Sediment Characteristic and Leaching Experiments

Soil sample LA12 was obtained at the location where pH 3.7 were observed in the nearby wells. Four sediment samples were selected from the core drilled during this study. Pyrite framboids are commonly observed in the core samples of gray sediments (K10 and K19) (Fig. 3). Pyrite minerals also observed at the sample LA12. These observations indicate pyrite oxidation as the cause of the EAG.

One type of leaching experiments was conducted using deionized water without adjusting pH of the solution during the reaction. The solutions showed acidic pH as low as 2.7 after the experiments and very high $SO_4$ and Fe concentrations when the

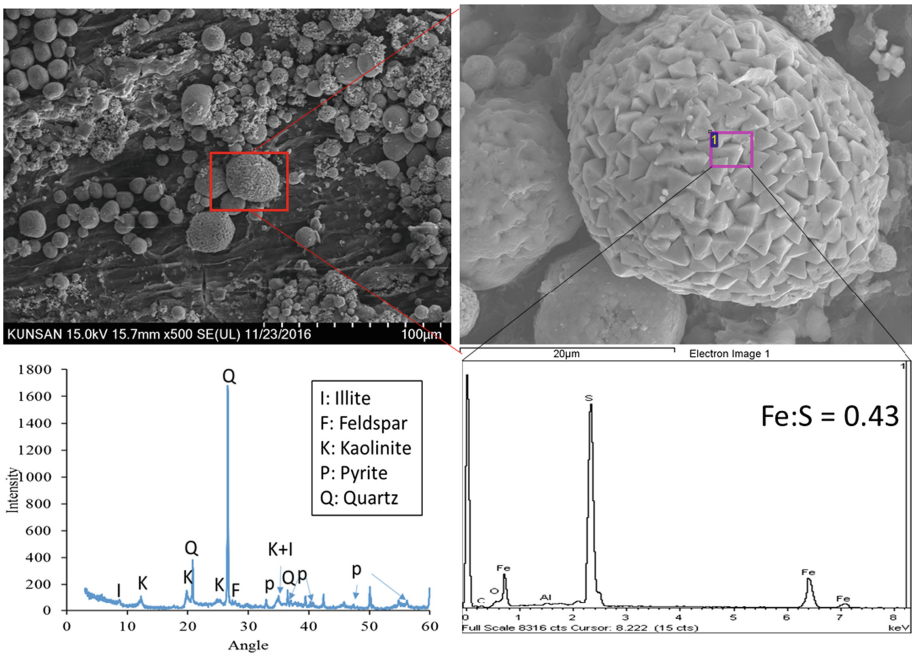


**Fig. 3.** Pyrite minerals (Framboidal structure), EDS data and XRD results from the sample K10 (10.5 m depth)

experiments were performed using pyrite-bearing samples. However, $SO_4$ and Fe concentrations were very low when the sample is free from sulfide (K25).

To verify the influence of pH on the mobilization of heavy metals, the leaching experiment of sediment samples were conducted under pH-constant conditions. Regardless of the presence of pyrite in the sediments used for the experiments, similar patterns of metals concentration (Fe, Mn, Al, Pb, Cr, Ni, and Zn) were derived as a function of pH. Generally, the concentrations of metals were high in acidic pH. Higher concentrations of Si and Al at low pH are likely the results of mineral dissolution.

### 4.3 The Cause of Pyrite Oxidation

The 12 NGMS wells, which showed pH less than 3 at least once after the well installation, do not indicate any significant relation between groundwater level and pH, suggesting that groundwater level decline is not the major cause for the acidic groundwaters in the study area. Kim (2003) has reported that water chemistry in aquifer can be disturbed for several years after well installation. The data for 12 NGMS wells also indicate that the acidic groundwaters are partly associated with the aquifer disturbance by well installation. In other words, some wells show features that the pyrite oxidation is triggered by well installation and have caused the acidification of groundwaters. When the pyrite around the well is depleted by oxidation, the wells show the trend recovering pH.

## 5 Conclusion

It was revealed that the extremely acidic groundwaters occurring in the plain area within and around the Mekong delta are associated with oxidation of pyrite in the sediment. The groundwater data also strongly suggest that the pyrite oxidation is triggered in part by groundwater development. In other words, well installation has oxidized the aquifer around the well and have caused the acidic groundwaters. Our finding suggests that groundwater should be prudently developed from the aquifers that have been under strong reducing environments.

## References

Appleyard, S., Wong, S., Willis-Jones, B., Angeloni, J., Watkins, R.: Groundwater acidification caused by urban development in Perth, Western Australia: source, distribution, and implications for management. Soil Res. **42**(6), 579–585 (2004). doi:10.1071/SR03074

Benison, K.C., Bowen, B.B.: The evolution of end-member continental waters: the origin of acidity in southern Western Australia. GSA Today **25**(6), 4–10 (2015). doi:10.1130/GSATG231A.1

Bui, T.-V.: Report on Assessment of Climate Change on Groundwater Resources in Mekong Delta, Proposal of Adaptation Measures. Division for Water Resources Planning and Investigation for the South of Vietnam (DWRPIS) (2014). (in Vietnamese)

Buschmann, J., Berg, M., Stengel, C., Winkel, L., Sampson, M.L., Trang, P.T.K., Viet, P.H.: Contamination of drinking water resources in the Mekong delta floodplains: arsenic and other trace metals pose serious health risks to population. Environ. Int. **34**(6), 756–764 (2008). doi:10.1016/j.envint.2007.12.025

Fest, E.P., Temminghoff, E.J., Griffioen, J., Van Der Grift, B., Van Riemsdijk, W.H.: Groundwater chemistry of Al under Dutch sandy soils: effects of land use and depth. Appl. Geochem. **22**(7), 1427–1438 (2007). doi:10.1016/j.apgeochem.2007.02.002

Gröger, J., Proske, U., Hanebuth, T.J., Hamer, K.: Cycling of trace metals and rare earth elements (REE) in acid sulfate soils in the Plain of Reeds, Vietnam. Chem. Geol. **288**(3), 162–177 (2011). doi:10.1016/j.chemgeo.2011.07.018

Hoang, T.H., Bang, S., Kim, K.W., Nguyen, M.H., Dang, D.M.: Arsenic in groundwater and sediment in the Mekong River delta, Vietnam. Environ. Pollut. **158**(8), 2648–2658 (2010). doi:10.1016/j.envpol.2010.05.001

Husson, O., Verburg, P.H., Phung, M.T., Van Mensvoort, M.E.F.: Spatial variability of acid sulphate soils in the Plain of Reeds, Mekong delta, Vietnam. Geoderma **97**(1), 1–19 (2000)

Kjøller, C., Postma, D., Larsen, F.: Groundwater acidification and the mobilization of trace metals in a sandy aquifer. Environ. Sci. Technol. **38**(10), 2829–2835 (2004). doi:10.1021/es030133v

Kim, K.: Long-term disturbance of ground water chemistry following well installation. Gr. Water **41**(6), 780–789 (2003). doi:10.1111/j.1745-6584.2003.tb02419.x

Ngo, M.T., Lee, J.M., Lee, H.A., Woo, N.C.: The sustainability risk of Ho Chi Minh City, Vietnam, due to saltwater intrusion. Geosci. J. **19**(3), 547–560 (2015). doi:10.1007/s12303-014-0052-4

Nguyen, H.D., Vu, B.M., Nguyen, H.D.: Hydrogeological map. Identification of Geological units from Neogene to Quaternary and structural geological study in southern plain of Vietnam. Division for Water Resources Planning and Investigation for the South of Vietnam (DWRPIS) (2004). (in Vietnamese)

Nguyen, K.P., Itoi, R.: Source and release mechanism of arsenic in aquifers of the Mekong Delta, Vietnam. J. Contam. Hydrol. **103**(1), 58–69 (2009). doi:10.1016/j.jconhyd.2008.09.005

Seibert, S., Atteia, O., Ursula Salmon, S., Siade, A., Douglas, G., Prommer, H.: Identification and quantification of redox and pH buffering processes in a heterogeneous, low carbonate aquifer during managed aquifer recharge. Water Resour. Res. **52**(5), 4003–4025 (2016). doi:10.1002/2015WR017802

Verplanck, P.L., Nordstrom, D.K., Bove, D.J., Plumlee, G.S., Runkel, R.L.: Naturally acidic surface and ground waters draining porphyry-related mineralized areas of the Southern Rocky Mountains, Colorado and New Mexico. Appl. Geochem. **24**(2), 255–267 (2009). doi:10.1016/j.apgeochem.2008.11.014

Zhang, Y.C., Slomp, C.P., Broers, H.P., Passier, H.F., Van Cappellen, P.: Denitrification coupled to pyrite oxidation and changes in groundwater quality in a shallow sandy aquifer. Geochim. Cosmochim. Acta **73**(22), 6716–6726 (2009). doi:10.1016/j.gca.2009.08.026

# Removal of Cd(II) from Aqueous Solutions Using Red Mud/Graphene Composite

Xuan Linh Ha[1], Ngan Hanh Hoang[1], Thi Trang Nhung Nguyen[1], Thi Thuy Nguyen[2], Thanh Hai Nguyen[3], Van Thanh Dang[3,4(✉)], and Nhat Huy Nguyen[5(✉)]

[1] Department of Administrative Affairs, Thai Nguyen University, Thai Nguyen, Vietnam
[2] Faculty of Biotechnology and Environmental Engineering, HCMC University of Food Industry, Ho Chi Minh City, Vietnam
[3] Research and Development Center for Advanced Technology, Hanoi, Vietnam
thanhdv@tnmc.edu.vn
[4] TNU-University of Medicine and Pharmacy, Thai Nguyen, Vietnam
[5] Faculty of Environment and Natural Resources, Bach Khoa University, VNU-HCM, Ho Chi Minh City, Vietnam
nnhuy@hcmut.edu.vn

**Abstract.** In this study, we developed a simple and convenient one-step method for activation of graphite using high basic red mud slurry to produce a mixture of red mud/graphene (REEG) under mild reaction conditions. The wet red mud was mixed up with graphene by direct electrochemical exfoliation of graphite in its solution. The REEG obtained was characterized and applied for removal of Cadmium (Cd(II)) from aqueous solutions. The effects of pH, contact time, and initial concentrations on the removal of Cd(II) were investigated. A removal efficiency of 98.95% at pH 6 was obtained after 60 min of adsorption, via the dispersion of 0.1 g of REEG in Cd(II) stock solutions (50 mL, 1 ppm). The maximum adsorption capacity ($q_{max}$) was calculated to be 12.598 mg/g. Results showed that REEG is effective for removal of Cd(II) from aqueous environment, which could also act as an effective adsorbent for the removal of other heavy metals from polluted water.

**Keywords:** Red mud · Graphene · Cadmium · Adsorption

## 1 Introduction

Cadmium compounds (Cd(II)) are very toxic chemicals and human carcinogens as proven by epidemiological and mechanistic studies (Gupta and Sharma 2002). Therefore, it is necessary to study on the removal of Cd(II) from the wastewater before discharge in to the water sources. Among various methods for Cd(II) removal, adsorption using nanomaterials fabricated from abundant wastes of agriculture (Garg et al. 2008) and industry (Gupta and Sharma 2002) is attracted and feasible. Recently, red mud waste from aluminum production has been successfully utilized for adsorption of heavy metals in wastewater such as Pb, Ni, Zn, Cd, Cu, Cr, and Hg. The main

© Springer Nature Singapore Pte Ltd. 2018
H. Tran-Nguyen et al. (eds.), *Proceedings of the 4th Congrès International de Géotechnique - Ouvrages -Structures*, Lecture Notes in Civil Engineering 8,
DOI 10.1007/978-981-10-6713-6_105

components of red mud are $Fe_2O_3$, $SiO_2$, $Al_2O_3$, CaO, $Na_2O$ (Balakrishnan et al. 2011; Genç-Fuhrman et al. 2004; Gräfe et al. 2011; Klauber et al. 2011; Tran et al. 2015) and this mixture exists at high pH values over 12 (Gräfe et al. 2011). Therefore, red mud needs to be treated and neutralized before using as an adsorbent via activation at high temperature (Palmer et al. 2010), under acidic condition (Wang et al. 2005), or combination with other materials (Klauber et al. 2011). Recently, modification of graphene under basic condition has showed that the modified graphene materials have higher surface area and surface reactivity (Li et al. 2011; Wang and Kaskel 2012; Zhang and Zhao 2009). Moreover, the combination of graphene with other metal oxides showed a great potential for removal of heavy metal ions in water (Guo et al. 2015). However, there has not been any study reporting the utilization of basic condition of red mud for activation of graphite to produce a red mud/graphene composite adsorbent.

In this study, we activated graphite using basic red mud slurry to produce a mixture of red mud/graphene. This material was then employed as an adsorbent for removal of Cd(II) in water.

## 2 Experimental and Methods

### 2.1 Material Synthesis and Characterization

Red mud (RM) slurry was taken at Tan Binh Chemical Factory, Ho Chi Minh City. The raw RM material was mixed with 300 ml of $(NH_4)_2SO_4$ 2.5% and further added with KOH solution to form an electrolytic solution at pH 14. Graphene was then prepared by electrochemical exfoliation process (EEP) using two high-purity graphite rods (HG) with the bias voltage increased gradually to 10 V, temperature of 70–80 °C, mixing at 400 rpm using a magnetic stirrer for 120 min. After cooling to room temperature, the resulting composite of graphene and red mud was collected by vacuum filtration, washed with DI water, and dried at 150 °C under vacuum for 24 h. The obtained powder (denoted as REEG) was stored in a drying box at 50 °C. For comparison, the electrolytic solution (mixed of KOH (10%, 100 mL) and $(NH_4)_2SO_4$ (2.5%, 300 mL) at a pH 14) was used for the electrochemical exfoliation of graphite, and the powder prepared from this EEP was named as electrochemically exfoliated graphene sheets (EEG).

The structures of the RM, EEG, REEG powders were examined using a D2 X-ray diffractometer equipped with a Cu $K_\alpha$ tube and a Ni filter ($\lambda$ = 0.1542 nm). Raman spectra of these samples were recorded using a high-resolution confocal Raman microscope (HORIBA, Lab RAM HR 800) and a 514.5 nm Ar laser source. High-resolution transmission electron microscopy (HRTEM) images were taken using a JEOL 2100F apparatus operated at 200 kV. Scanning electron microscopy (SEM) was performed using a JEOL JSM-6500F scanning electron microscope operated at 15 kV.

### 2.2 Adsorption Study

The Cd(II) removal tests were conducted in batch adsorption experiments at room temperature for Cd(II) solution prepared from stock solution (1000 ppm, Sigma Aldrich Dilutions). Investigated influence factors included contact time (0 to 300 min), initial Cd(II) concentration (1, 5, 10, 20, and 25 mg/l), and initial pH of solution (from 1.0 to 12). Equilibrium isotherms were determined with different initial concentrations of Cd(II) (1, 5, 10, 20, and 25 mg/L) at room temperature and pH 6. After these test periods, the samples were centrifuged at the speed of 4000 rpm for 30 min and the supernatant was used to determine the concentration of Cd(II) by inductively coupled plasma optical emission spectrometry (ICP - OES).

The adsorption capacity was calculated as following equation:

$$q = \frac{(c_0 - c_{cb})v}{M} \quad (1)$$

Where:
V: the volume of the solution (l),
M: the adsorbent amount (g),
$c_0$: the initial concentration (mg/l),
$c_{cb}$: the equilibrium concentration (mg/l),
q: the adsorption capacity at equilibrium time (mg/g).

$pH_{pzc}$ for the REEG was determined according to the method published in the literature (Faria et al. 2004). 25 mL of 0.01 M NaCl solution were added to a series of 250 mL conical flask, and the initial pH was adjusted to between 2 and 12 using 0.1 M NaOH or HCl. Then, 0.1 g of the REEG was added to each flask and the final pH was measured after shaking for 48 h at room temperature. Concomitantly, the difference between the initial pH and final pH (initial pH – final pH) was plotted against the initial pH. The point at which the resulting curve intersected with abscissa gave $pH_{pzc}$ of the REEG.

In this study, the equilibrium data were calculated using the Freundlich and Langmuir isotherm expressions given by the following equations, respectively,

$$\text{Freundlich: } q_e = K_f.C_e^{\frac{1}{n}} \quad (2)$$

$$\text{Langmuir: } q_e = \frac{q_0 b c_e}{1 + b c_e} \quad (3)$$

Where $K_f$ and n are Freundlich constants related to sorption capacity and sorption intensity of adsorbents; the value of n falling in the range of 1–10 indicates favorable sorption; $q_e$ is the adsorption capacity at equilibrium condition; $C_e$ is the equilibrium concentration of Cd(II) in solution; $q_0$ is the monolayer adsorption capacity; b is the Langmuir constant related to the free energy of adsorption.

## 3 Results and Discussion

### 3.1 Material Synthesis and Characterization

Figure 1 presents the SEM images of red mud (RM was collected by filtration of the slurry and dried at 110 °C overnight), electrochemically exfoliated graphene (EEG), and electrochemically exfoliated Red Mud/Graphene (REEG). These images revealed significant differences between the RM, EEG and REEG. RM contained various fine particles with average size of about 50 nm while EEG had flattened sheet morphology.

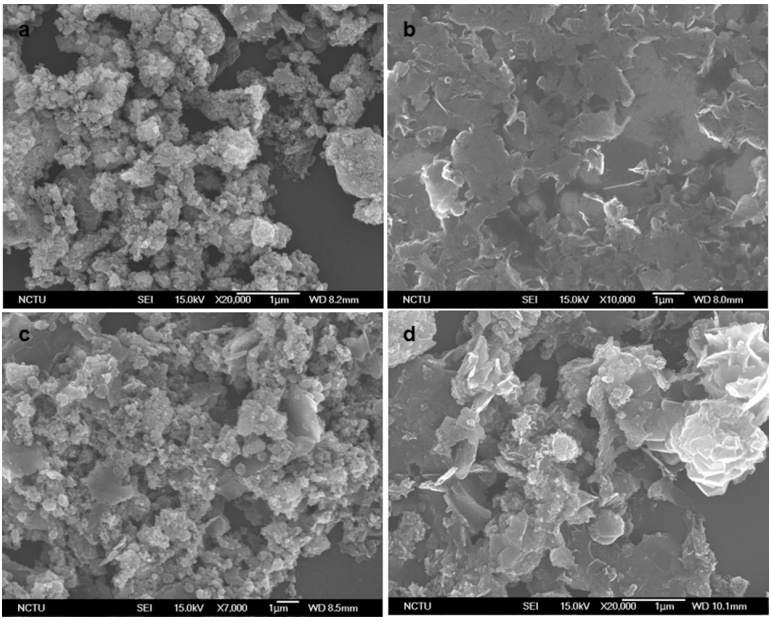


**Fig. 1.** SEM images of (a) RM, (b) EEG, (c) low and (d) high magnification REEG

Through exfoliating, flattened graphene sheets (Fig. 1b) were surrounded by RM nanoparticles with microporous multi-layer structure (Fig. 2c), which can have good adsorption activity, as clearly observed in TEM image (Fig. 2). The aggregation of activated red mud particles and graphene sheets formed irregular cluster containing both nanosheet and nanoparticle, which formed microporous structure in REEG material. The chemical composition of REEG was further determined by energy dispersive x-ray (EDS), as shown in inset of Fig. 2a. One can observe that Fe was the dominant component in red mud with 29.3% in mass, and the other principal components were C, O, and oxides of Al and Si. Figure 2b displays X-ray diffraction (XRD) patterns of the RM, EEG and REEG. XRD pattern of EEG showed a characteristic sharp with high-intensity (002) peak at a $2\theta$ value of 26.6° and three other small peaks at $2\theta$ values of 42.8°, 21.6°, and 34.6°, corresponding to the 100, 101, and 004 reflections, respectively. After modification with red mud, these peaks were still

observed while new small peaks appeared at $2\theta$ values of 18.1°, 21.3°, 29.6°, 33.1°, 35.6°, 37.1°, 54.2°, 62.2°, and 64.3°. These new peaks can be assignable to the phases of quartz (Qz = $SiO_2$), gibbsite (Gb = ɣ-$Al(OH)_3$), goethite (Gt = α-FeOOH), and hematite (Hm = ($Fe_2O_3$) (Tran et al. 2015; Cristina de Resende et al. 2014) with dominant hematite phase, which could facilitate the adsorption of Cd(II) on the surface of REEG. Additionally, the position of G peak in REEG (Fig. 2c) had shifted to a lower frequency (from 1583 $cm^{-1}$ to 1573 $cm^{-1}$) with an increase in $I_D/I_G$ (0.91) as compared to that of EEE (0.80), indicating an enhancement in disorder or structural defect of graphene after EEP.

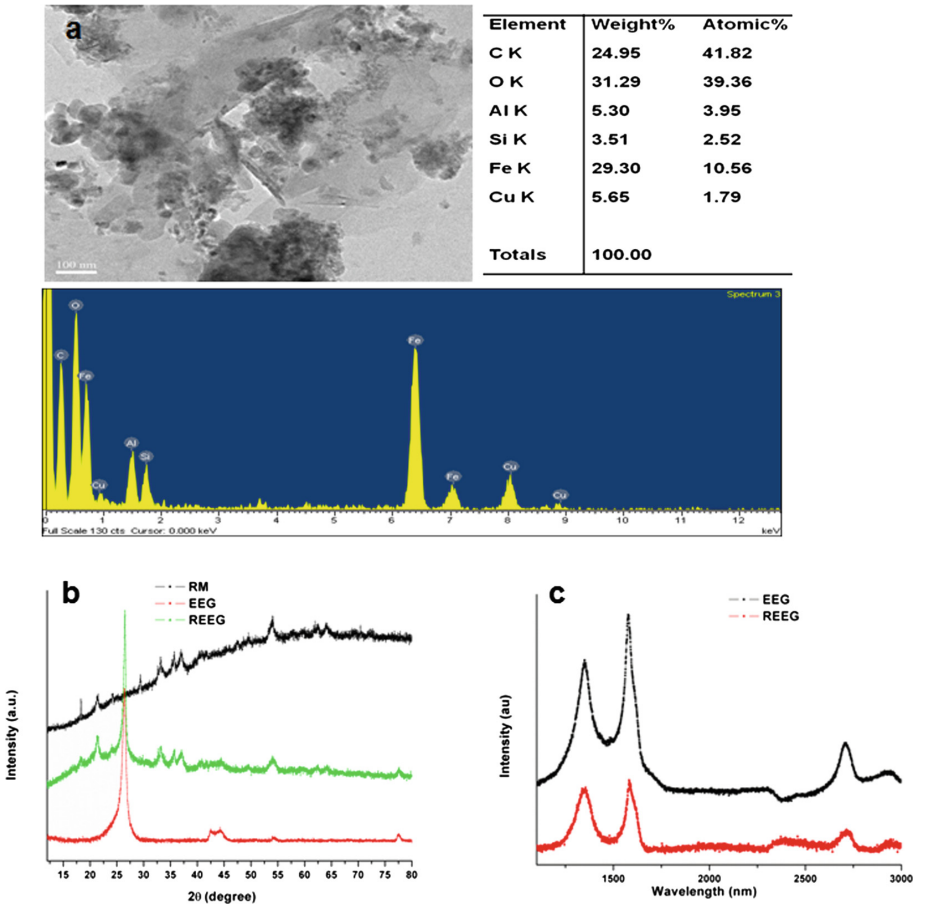


**Fig. 2.** (a) TEM image of the REEG sample; inset: EDS spectrum of the in situ–recorded area and chemical composition of REEG. The Cu signal arose from the TEM support grid; (b) X-ray diffraction patterns of the RM, EEG and REEG; (c) Raman spectra of the EEG and REEG

### 3.2 Cd(II) Adsorption Results

Figure 3a presents isoelectric point ($pH_{pzc}$) with the change of solution pH of the REEG. The result revealed that the $pH_{pzc}$ of REEG was 8.1, which is similar to the previous result (Atun and Hisarli 2000). Figure 3b shows the effect of pH on the adsorption efficiency of Cd(II) on the REEG with Cd(II) concentration of 1 mg/l, adsorbent dosage of 0.1 g, temperature of 25 °C, and contact time of 60 min. It can be observed that the adsorption of Cd(II) increased with increasing pH for experiments with pH < 6. This phenomenon can be explained as follows: at pH < $pH_{pzc}$, the surface charge of REEG is positive because of the protonation reaction ($\equiv SOH + H^+ \rightarrow \equiv SOH_2^+$, where $\equiv$ S represents the surface of REEG, and –OH represents the oxygen-containing functional groups). The positive metal ions are difficult to adsorb on the positively charged surface of REEG due to the electrostatic repulsion. At pH > $pH_{pzc}$, the surface charge of REEG is negative because of the deprotonation reaction ($\equiv SOH \rightarrow \equiv SO^- + H^+$). The sorption of Cd(II) on REEG could be expressed by the following reaction (Zhao et al. 2011):

$$\equiv SO^-_{(s)} + Cd^{2+}_{(aq)} \rightarrow \left[(\equiv SO^-)_2 Cd^{2+}\right]$$

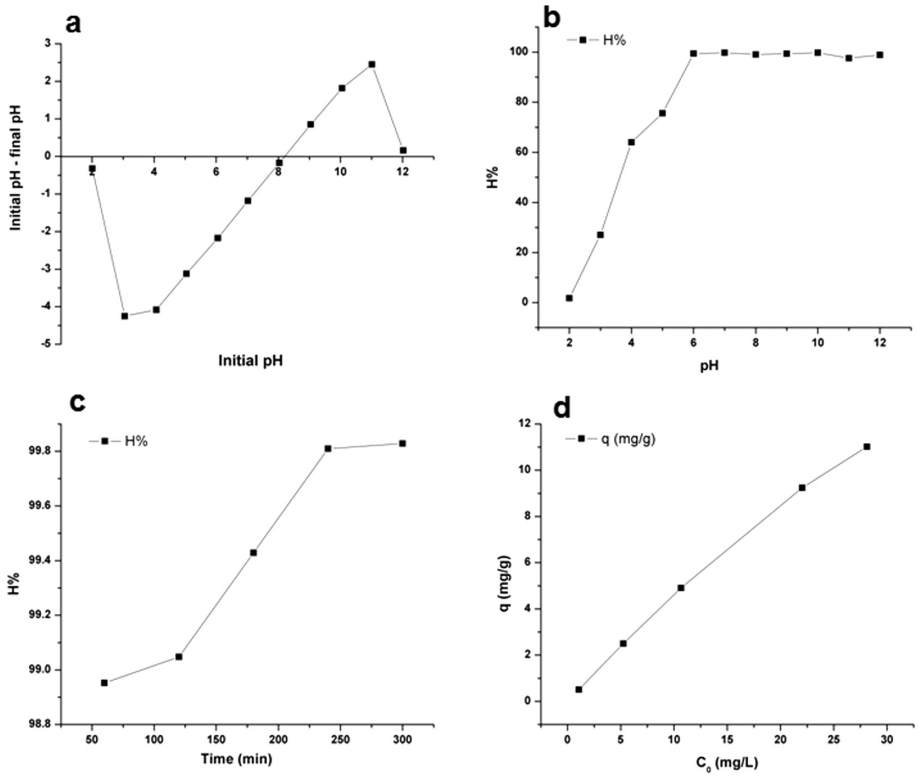


**Fig. 3.** The isoelectric point of REEG (a) and the effect of pH (b), contact time (c), initial Cd(II) concentration (d) on the adsorption efficiency of Cd(II) on the REEG.

The solution pH affects the degree of deprotonation and the speciation of the surface functional groups. With increasing pH, the surface charge is more negative and the electrostatic interactions between the metal ions and REEG become stronger, and thereby resulted in the increase of metal ion adsorption. Notably, at pH = 6, about 98% Cd(II) was adsorbed on REEG. Therefore, pH 6, which generally occurs in actual environments, was chosen as the optimum value for further experiments.

Figure 3c shows the effect of contact time on the amount of Cd(II) adsorbed on the REEG, in which the adsorption efficiency increased during 300 min experiment. Clearly, Cd(II) was quickly removed after 60 min with adsorption efficiency of 98.95% and remained nearly constant afterwards. The equilibrium time was then chosen at 60 min for further experiments.

Figure 3d displays the influence of initial metal concentration on the adsorption capacity of Cd(II) on the REEG (adsorbent dosage of 0.1 g, pH 6, temperature of 25 °C, contact time of 60 min). When the initial concentration of Cd(II) increased, the adsorption efficiency decreased but the adsorption capacity increased. The isotherm parameters and correlation coefficient ($R^2$) values are shown in Table 1. Results indicated that Langmuir model fits better than Freundlich model for expressing the adsorption of Cd(II), since its $R^2$ value was higher. This confirmed that the Cd(II) adsorption was monolayer adsorption and the interaction between the adsorbed metal ions was negligible. Additionally, the $q_{max}$ of Cd(II) was predicted as 12.598 mg/g, which compares favorably with previous results (Atun and Hisarli 2000; Garg et al. 2008; Kanu et al. 2014). Furthermore, the adsorption efficiency of Cd(II) were both investigated using RM and EEG (Fig. 4). This results showed that red mud/graphene composite (REEG) is comparable with the pure graphene (EEG) for adsorption of Cd (II). The preparation and application of REEG is more environmental friendly than that of EEG since the waste red mud was employed both as a precursor and an activating agent for producing of adsorbent without the use of KOH. These suggested that REEG is a low-cost but effective and environmental friendly adsorbent for the removal of Cd(II), which could be a promising adsorbent for wastewater treatment applications.

**Table 1.** Adsorption isotherm constants for the adsorption of Cd(II) by the REEG

| Model | Parameters | Cd(II) |
|---|---|---|
| Langmuir | $q_{max}$ (mg/g) | 12.598 |
| | b | 0.9553 |
| | $R^2$ | 0.9883 |
| Freundlich | n | 1.7170 |
| | $K_f$ | 1.9320 |
| | $R^2$ | 0.9644 |

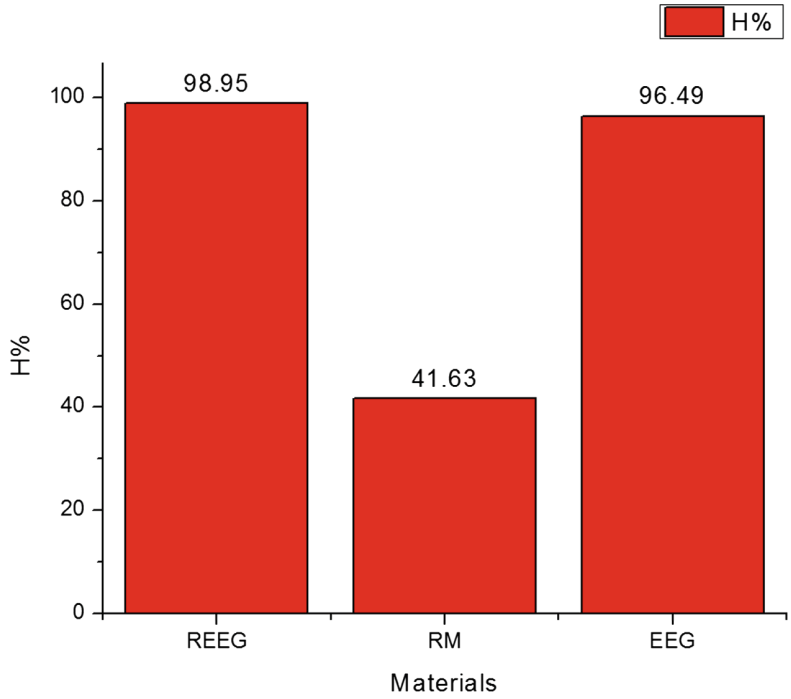


**Fig. 4.** Comparison of adsorption efficiency of REEG with RM and EEG (adsorbent dosage of 0.1 g, pH 6, temperature of 25 °C, contact time of 60 min, Cd(II) concentration of 1 mg/l)

## 4 Conclusions

An adsorbent from red mud/graphene composite (REEG) was successfully prepared and applied for Cd(II) adsorption in wastewater. A removal efficiency of 98.95% at pH ~ 6 was obtained after 60 min by using of 0.1 g of REEG for 50 ml of 1 ppm Cd (II) solutions. The maximum adsorption capacity ($q_{max}$) was calculated by applying the Langmuir equation for Cd(II) adsorption in the adsorption isotherm and was found to be 12.598 mg/g. The REEG material has proven to be an effective but low-cost adsorbent for the removal of Cd(II), which could be promising for wastewater treatment applications.

**Acknowledgments.** This research is funded by grant number B2017 - TNA – 29 and DH2017-TN01-04. We would also thank Dr. Le Huu Phuoc at Department of Electrophysics, National Chiao Tung University, Hsinchu, Taiwan for his help in SEM imaging.

## References

Atun, G., Hisarli, G.: A study of surface properties of red mud by potentiometric method. J. Colloid Interface Sci. **228**(1), 40–45 (2000). doi:10.1006/jcis.2000.6926

Balakrishnan, M., Batra, V.S., Hargreaves, J.S.J., Pulford, I.D.: Waste materials - catalytic opportunities: an overview of the application of large scale waste materials as resources for catalytic applications. Green Chem. **13**(1), 16–24 (2011). doi:10.1039/c0gc00685h

de Resende, E.C., do Rosário Guimarães Carvalho, I., Schlaf, M., Guerreiro, M.C.: Red mud waste from the Bayer process as a catalyst for the desulfurization of hydrocarbon fuels. RSC Adv. **4**(88), 47287–47296 (2014). doi:10.1039/c4ra07635d

Faria, P., Orfao, J., Pereira, M.: Adsorption of anionic and cationic dyes on activated carbons with different surface chemistries. Water Res. **38**(8), 2043–2052 (2004). doi:10.1016/j.watres.2004.01.034

Garg, U., Kaur, M.P., Jawa, G.K., Sud, D., Garg, V.K.: Removal of cadmium (II) from aqueous solutions by adsorption on agricultural waste biomass. J. Hazard. Mater. **154**(1–3), 1149–1157 (2008). doi:10.1016/j.jhazmat.2007.11.040

Genç-Fuhrman, H., Tjell, J.C., McConchie, D.: Adsorption of arsenic from water using activated neutralized red mud. Environ. Sci. Technol. **38**(8), 2428–2434 (2004). doi:10.1021/es035207h

Gräfe, M., Power, G., Klauber, C.: Bauxite residue issues: III. Alkalinity and associated chemistry. Hydrometallurgy **108**(1–2), 60–79 (2011). doi:10.1016/j.hydromet.2011.02.004

Guo, L., Ye, P., Wang, J., Fu, F., Wu, Z.: Three-dimensional Fe3O4-graphene macroscopic composites for arsenic and arsenate removal. J. Hazard. Mater. **298**, 28–35 (2015). doi:10.1016/j.jhazmat.2015.05.011

Gupta, V.K., Sharma, S.: Removal of cadmium and zinc from aqueous solutions using red mud. Environ. Sci. Technol. **36**(16), 3612–3617 (2002). doi:10.1021/es020010v

Kanu, S.A., Moyo, M., Khamlich, S., Okonkwo, J.O.: Adsorption of cadmium from aqueous solution using Rooibos shoots as adsorbent. Toxicol. Environ. Chem. **96**(10), 1452–1462 (2014). doi:10.1080/02772248.2015.1030666

Klauber, C., Gräfe, M., Power, G.: Bauxite residue issues: II. Options for residue utilization. Hydrometallurgy **108**(1–2), 11–32 (2011). doi:10.1016/j.hydromet.2011.02.007

Li, Y., van Zijll, M., Chiang, S., Pan, N.: KOH modified graphene nanosheets for supercapacitor electrodes. J. Power Sources **196**(14), 6003–6006 (2011). doi:10.1016/j.jpowsour.2011.02.092

Palmer, S.J., Nothling, M., Bakon, K.H., Frost, R.L.: Thermally activated seawater neutralised red mud used for the removal of arsenate, vanadate and molybdate from aqueous solutions. J. Colloid Interface Sci. **342**(1), 147–154 (2010). doi:10.1016/j.jcis.2009.10.010

Tran, D.N.H., Kabiri, S., Wang, L., Losic, D.: Engineered graphene-nanoparticle aerogel composites for efficient removal of phosphate from water. J. Mater. Chem. A **3**(13), 6844-6852 (2015). doi:10.1039/c4ta06308b

Wang, J., Kaskel, S.: KOH activation of carbon-based materials for energy storage. J. Mater. Chem. **22**(45), 23710–23725 (2012). doi:10.1039/c2jm34066f

Wang, S., Boyjoo, Y., Choueib, A., Zhu, Z.H.: Removal of dyes from aqueous solution using fly ash and red mud. Water Res. **39**(1), 129–138 (2005). doi:10.1016/j.watres.2004.09.011

Zhang, L.L., Zhao, X.S.: Carbon-based materials as supercapacitor electrodes. Chem. Soc. Rev. **38**(9), 2520–2531 (2009). doi:10.1039/b813846j

Zhao, G., Li, J., Ren, X., Chen, C., Wang, X.: Few-layered graphene oxide nanosheets as superior sorbents for heavy metal ion pollution management. Environ. Sci. Technol. **45**(24), 10454–10462 (2011). doi:10.1021/es203439v

# Studies on the Photocatalytic Activity of Metal Oxide and Their Composite for Dye Degradation Application

Tchakala Ibrahim[1(✉)], Kodom Tomkouani[1], M. Vedhanayagam[2], Alfa-Sika Mande Seyf-Laye[3], K.J. Sreeram[2], Bawa L. Moctar[1], and Djaneye-Boundjou Gbandi[1]

[1] Laboratory of Water Chemistry, Faculty of Sciences, University of Lome, Lomé, Togo
ibrahimtchakala@gmail.com
[2] Chemical Laboratory, Central Leather Research Institute (CLRI), Adyar, Chennai 600 020, India
[3] Faculty of Science and Technology, University of Kara, BP 404, Kara, Togo

**Abstract.** In this work, ZnO nanorods and Graphene-ZnO-PdO nanocomposite was synthesized through hydrothermal method. Crystallinity of the materials has been studied using X-ray diffraction (XRD) and morphology was analysed through Field Emission Scanning Electron Microscopy (FE-SEM) and Transmission electron microscopy (TEM) techniques. The synthesized nanomaterials are used for the photocatalytic degradation of Methylene Blue (MB) under UV-light illumination (365 nm) and the results were compared with commercial ZnO material. Graphene-ZnO-PdO nanocomposite exhibits higher degradation of MB under UV-light illumination than ZnO nanorods and commercial ZnO material. These nanocomposite materials can so be used for methylene blue MB photodegradation as for textile wastewater treatment.

**Keywords:** Methylene blue · Metal oxide · Nanoparticles · Photocatalytic degradation

## 1 Introduction

Zinc oxide (ZnO) is a wide bandgap ( ~ 3.37 eV) and n-type semiconductor [1], which has achieved application in many fields such as photocatalysis, solar cells, gas sensors and photodetectors [2, 3]. In general, small size ZnO nanoparticles have increased specific surface area and more numbers of active sites where the photo generated charge carriers are able to react with absorbed molecules to form hydroxyl and superoxide radicals [4]. However, small ZnO nanoparticles without capping agents can easily form aggregations, leading to the loss of its active sites and photocatalytic efficiency. Moreover, the high electron-hole recombination rate also limits the photo-oxidation rate of organic compounds on ZnO surface, and also aggravates its photo-corrosion in photocatalysis process [5]. Therefore, it is highly desirable to develop a simple and effective technique to overcome the drawbacks of ZnO by improving its photocatalytic efficiency while deterring the formation of aggregations. Graphene oxide (GO) is a

© Springer Nature Singapore Pte Ltd. 2018
H. Tran-Nguyen et al. (eds.), *Proceedings of the 4th Congrès International de Géotechnique - Ouvrages -Structures*, Lecture Notes in Civil Engineering 8,
DOI 10.1007/978-981-10-6713-6_106

chemically functionalized graphene with hydroxyl and carboxyl groups, which possesses excellent solubility in solvents and thus provides various opportunities for the construction of GO-based hybrid composites [6]. The new GO-based hybrid with metal and metal oxide nanoparticles such as Pt, Au, Ag, $TiO_2$, ZnO, $Fe_3O_4$ have shown potential application in the areas of optics, electronics, catalysts and sensors [7–9]. Among these, the fabrication of GO-based hybrid catalysts, especially those for the photodegradation of organic pollutants, is of the utmost concern at current stage. Moreover, GO shows strong positive effect in the dispersion and stabilization of the photocatalytic nanocrystals without the introduction of organic surfactants. All these illustrate the unique electronic properties, extremely high specific surface area and locally conjugated aromatic system of GO, making it ideal candidates for catalyst carrier or promoter. Several reduced GO (RGO)/ZnO hybridized composites for the enhanced photocatalytic activity in the removal of organic dye have been reported. However, during the reduction process, GO is easy to be aggregated even with the addition of polymer or surfactants, which limited the production and quality of RGO-ZnO composite. It is interesting to produce GO-ZnO composite by simple blending. And then during the photocatalytic process, GO will be reduced into RGO, which can easily produce RGO-ZnO composite with high photocatalytic activity in the degradation of organic dye. Moreover, there are still no reports in the long-term stability of ZnO and graphene based ZnO composite. Recently, Liu *et al.* [10] fabricated ZnO-Graphene nanocomposite for photocatalytic reduction of Cr (IV). Zhang Chen *et al.* [11] have reported the synthesis of Graphene-ZnO nanocomposites for application in anti-photocorrosion and with improved photoactivity. Silver modification significantly improved the photocatalytic Rhodamine B degradation capability of the Graphene-ZnO quasi-shell-core composite. In this work, a facile method was applied for the preparation of high-quality ZnO and GO-ZnO-PdO composite materials by simply mixing the solution of GO sheets, ZnO and PdO nanoparticles. It is worth to be highlighted that this method can successfully anchor uniform size ZnO and PdO nanoparticles on GO sheets. Assembling the ZnO nanoparticles on large GO sheets can remarkably enhance its photocatalytic activity of dye degradation both under UV light irradiation. Moreover, involving GO sheets into the system could effectively prevent the ZnO nanoparticle aggregation without additional capping agents. As a result, this high-quality GO-ZnO-PdO nanocomposite is beneficial for the applications in environmental engineering and other fields. From the detailed literature survey, the scope of metal oxide as well as Graphene-metal oxide nanocomposites and their application in the field of photocatalytic reactivity was well understood. To the best of our knowledge, there is no report on the using Graphene-ZnO-PdO NCs for Photodegradation of Methylene Blue under UV light illumination. In the present work, we are going to synthesis ZnO nanoparticles and Graphene-ZnO-PdO nanocomposite through hydrothermal method [11, 12] and used for Methylene Blue dye degradation application. The results were compared with standard commercial ZnO particles. The objective of the work is the synthesis of ZnO nanoparticles and Graphene-ZnO-PdO nanocomposites through hydrothermal method, study the characteristics of the nanocomposites through XRD, FE-SEM, TEM techniques, and used of synthesized nanoparticles/nanocomposites for degradation of Methylene Blue under UV light illumination.

## 2 Materials and Methods

Zinc acetate dihydrate ($Zn(Ac)_2 2H_2O$) ($\geq 98\%$), Pottassium hydroxide (KOH), ($\geq 98\%$), Ethanol ($\geq 99.9\%$), Sodium hydroxide ($\geq 92\%$), Palladium Chloride, Isopropanol, Ammonium Hydroxide were purchased from Sigma Aldrich Pvt. Ltd and Graphite powder(50 nm Mesh) and Commercial Zinc Oxide (ZnO) were purchased from German Merck. The methylene blue was purchased from SD fine chemical limited, Mumbai. These chemicals were used without further purification. The Milli-Q-water (18 Ω) was used for throughout the experiment.

### 2.1 Synthesis of ZnO Nanorods

In a typical procedure, $Zn(CH_3COO)_2.2H_2O$ (18.2 mmol, 5 g) was dissolved in a beaker with 60 mL absolute methanol under magnetic stirring at cooling condition for 90 min. At the same time, powdered LiOH (364 mmol, 1.087 g) was dissolved in another beaker with 60 mL of absolute methanol and magnetic stirring at room temperature for 45 min. Then, this basic solution was dropped into the zinc acetate solution for few minutes. The mixture was stirred slowly for 30 min at room temperature and dry at 120 °C for 10 h. After cooling to room temperature for 30 min, the solution was centrifuged at 7500 rpm during 15 min and the obtained material was dried in an vacuum at 60 °C for 12 h.

### 2.2 Preparation of Graphene Oxide (GO) Using Hummer Methods

Graphite oxide was synthesized from natural graphite powder by a modified Hummer's method []. Graphite powder (3 g) was put into solution of concentrated $H_2SO_4$ (12 ml), $K_2S_2O_8$ (2.5 g) and $P_2O_5$ (2.5 g). The mixture was kept at 80 °C for 4.5 h using a hot plate. Successively, the mixture was cooled to room temperature and diluted with 0.5 L of de-ionized (DI) water and left overnight. Then, the mixture was filtered and washed with de-ionized water using 0.2 micron Nylon Millipore filter to remove the residual acid. The product was dried under ambient condition overnight. This pre-oxidized graphite was then subjected to oxidation by Hummer's method described as follows. Pre-treated graphite powder was put into cold (0 °C) concentrated $H_2SO_4$ (120 ml). Then, $KMnO_4$ (15 g) was added gradually under stirring and the temperature of the mixture was kept to be below 20 °C by cooling. Successively, the mixture was stirred at 35 °C for 2 h, and then diluted with DI water (250 ml). Because the addition of water in concentrated sulphuric acid medium released a large amount of heat, the addition of water was carried out in an ice bath to keep the temperature below 50 °C. After adding all of the 250 ml of DI water, the mixture was stirred for 2 h and then 0.7 L of DI was added. Shortly after the dilution with 0.7 L of $H_2O$, 20 ml of 30% $H_2O_2$ was added to the mixture, the colour of mixture changed into brilliant yellow along with bubbling. The mixture was filtered and washed with 1:10 HCl aqueous solution (1 L) to remove metal ions followed by 1 L of DI water to remove the acid. The resulting solid was dried in air and diluted to make a GO dispersion (0.5% W/W). Finally, it was purified by dialysis for one week to remove the remaining metal species. Exfoliation was carried out by sonicating 0.1 mg/ml GO dispersion under ambient

condition for 20 min. The resulting homogeneous yellow-brown dispersion was tested to be stable for several months and used for further characterization.

### 2.3 Synthesis of Graphene Oxide-Zinc Oxide-Palladium Oxide (GO-ZnO-PdO) Nanocomposite by Hydrothermal Method

5 g of Zinc Acetate di-hydrate was dissolved in 50 mL pure ethanol and kept in stirrer for 30 min. After the duration of 30 min solution of 1 g Lithium Hydroxide and 50 mL Ethanol is added drop wise to the above solution. The overall solution is left to stir for another 30 min. The pH of the solution was adjusted to 9 using sodium hydroxide (3 M). 1 mL of PEG was added to the solution after 15 min. In another beaker separate solution was prepared by dissolving 100 mg of Palladium Chloride in 40 mL iso-propanol. The pH of the solution prepared in this second beaker was adjusted to 9 using ammonium hydroxide. Then the two solutions prepared were mixed and kept for 30 min. 100 mg of graphene oxide was added to mixed solution and then stirred continuously for 6 h. Later solution prepared is kept in heating mantle at 80 °C for 1 h and cooled to get powder. The powder obtained is transferred to Teflon lined autoclave and treated in box furnace at 400 °C for 2 h. Finally, powder sample was used for further characterization.

### 2.4 X-Ray Diffraction Method (XRD)

The structure and crystallinity of the synthesized nanoparticles were analysed by using X-ray Diffractometer, XRD (Miniflux11, Rigaku diffractometer, CuK$\alpha$ radiation ($\lambda$ = 0.1548), Japan. The samples were scanned from 0 to 80$^{o}$ with scan speed of 1 $^{o}$/min.

### 2.5 Field Emission Scanning Electron Microscopy (FE-SEM)

The FE-SEM image was carried out on a Hitachi (SU6600), Japan. Sample was dissolved in ethanol and then sonicated for 10 min. After samples for FE-SEM were prepared by drop casting 100 μL of solution dropped on an aluminium foil and dried by keeping an overnight at ambient conditions before taking the FE-SEM images.

### 2.6 Transmission Electron Microscopy (TEM)

Transmission electron microscope (TEM) and Energy dispersive X-ray analysis (EDAX) spectrum were carried out on a HRTEM (JEOL 3010; 300 kV) or Hitachi (H-7650; 80 kV). Sample was dissolved in ethanol and then sonicated for 10 min. After samples for TEM were prepared by drop casting 100 μL of solution dropped on a carbon coated Cu grid and dried by keeping an overnight at ambient conditions before taking the TEM images.

## 2.7 Molecule Model Used in the Study for Photodegradation: Methylene Blue

Methylene blue (MB) is the most common dye used in the dyeing of cotton, wood and silk. It can cause eye burns responsible for permanent damage to the eyes of man and animals. Inhalation can lead to breathing difficulties and oral ingestion produces a burning sensation, causes nausea, vomiting, sweating and abundant cold sweats. Treatment of industrial wastewater containing the dye turns of great interest nowadays to due environmental concerns.

## 2.8 Photocatalytic Degradation

**Procedure:** Photocatalytic studies were carried out in a multilamp photoreactor (HML MP88, supplied by Heber Scientific, India) fitted with eight 8 W medium pressure mercury vapor lamps set in parallel and have emission maximum at 365 nm. It has a reaction chamber with specially designed reflector made of highly polished aluminium and built in cooling fan. The volume of the reaction solution was maintained as 50 mL. Air was bubbled through the reaction solution for effective stirring. The light exposure length is 330 mm.

**Analysis:** the photocatalytic activity of the catalysts was evaluated by monitoring the degradation of methylene blue (MB) in an aqueous solution under UV-light irradiation with continuous stirring. Methylene blue solution in concentration 1 g/L was prepared by dissolving 100 mg of methylene blue powders ($C_{16}H_{18}ClN_3S$) in 100 mL of double deionized water. This solution was then used to prepared MB solutions in concentrations varied from 20 to 100 mg/L (namely 20, 40, 60, 80 and 100). The concentration of MB solution was determined by measuring the value at approximately 664 nm using a UV-Vis spectrophotometer. In all cases 50 mL of the MB solution containing appropriate quantity of the semiconductor powder was magnetically stirred in dark for 40 min to ensure an adsorption/desorption equilibrium. The reaction suspensions containing MB and ZnO photocatalyst were irradiated by four parallel 8 W medium pressure mercury lamps with continuous stirring. At specific time intervals, 2 mL of sample was withdrawn and nanoparticles were removed by centrifugation. Absorbance measurements were also recorded in the range of 200–800 nm, using a UV-vis spectrophotometer. The photocatalytic degradation efficiency of the MB solutions was calculated with the following equation:

$$\phi_t = \frac{(Ce - Ct)}{Ce} \times 100 \quad (\%) \tag{1}$$

where $Ce$ is the concentration of MB dye solution before the illumination, $Ct$ is the concentration of MB solutions in suspension after time $t$.

# 3 Result and Discussion

## 3.1 Nanoparticle Characterization

### 3.1.1 X-Ray Diffraction Pattern (XRD)

Powder X-ray diffraction study was carried out on commercial ZnO particles and prepared ZnO nanorod, GO-ZnO-PdO nanocomposite. From XRD it is very clear that the commercial ZnO peaks can be exactly indexed to a hexagonal ZnO phase (wurzite structure, space group (SG):- $p6_3mc$) with lattice constants a = 3.2508 Å and c = 5.2069 Å (c/a = 1.60), well matched with the standard card (JCPDS-36-1451) [14]. The diffraction peaks are intense and very sharp indicated that the material is highly crystalline. According to diffraction peaks, no impurities were detected in this sample. The ZnO nanorods exhibit similar peaks of commercial ZnO along with greater intensity of (002) plane than (001) shows that the formation of nanorods is along the C-axis. GO-ZnO-PdO nanocomposites shows XRD spectrum comparable to the ZnO nanoparticle together with additional new peaks. The additional peaks are corresponds to GO and PdO nanoparticles. PdO diffraction peaks marked in Fig. 1 indicating the separate phases of PdO as tetragonal (space group D4h9 – P44/mmc), which matches with the standard card (JCPDS 41-1107) [15]. For Graphene, diffraction peaks is also observed at about $2\theta = 26.15°$ which is well correlated with the hexagonal structure with p63/mmc (194) space group (JCPDS 411487) [16]. No other impurities peaks were observed. The [001] reflections of GO are not observed in the XRD pattern of GO-ZnO as a result of the intercalation of ZnO and PdO nanoparticles which destroyed the regular stack of GO. The XRD analysis further confirms that ZnO and PdO nanoparticles have been effectively intercalated into the GO sheets. The crystalline size of nanoparticle was manipulated by using Debye-Scherrer formula [17] (Fig. 2).

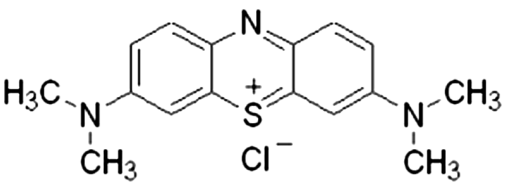


**Fig. 1.** Molecular structure of methylene blue

$$D = 0.9\,\lambda/\beta\cos\theta \tag{2}$$

where, D is the crystal size (in nm), λ is the X-ray wavelength of source Cu-Kα ($1.5418 \times 10^{-10}$ m), β is the full width at half maximum intensity of the diffraction peak located at 2θ and θ is the Bragg's diffraction angle. The crystal size of the nanocomposite is calculated it is found to be 50 nm for commercial ZnO and 55 nm × 23 nm for ZnO nanorods and 27 nm (GO), 40 nm (ZnO), 18 nm (PdO) respectively.

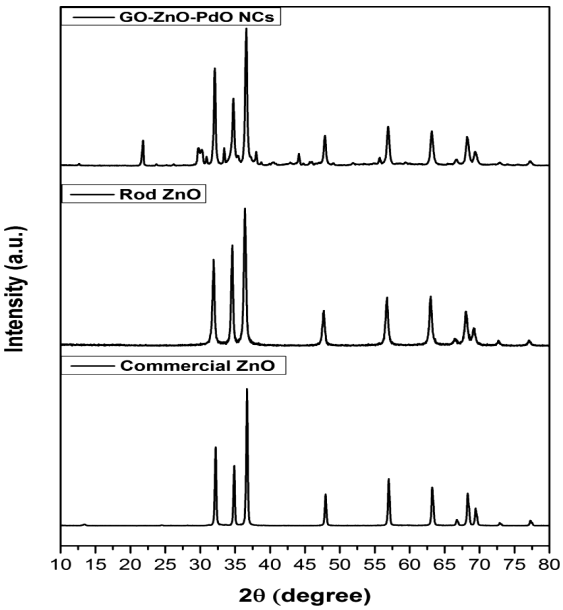


**Fig. 2.** Shows that the XRD spectrum of ZnO commercial, ZnO nanorods and GO-ZnO-PdO nanocomposites

### 3.1.2 FE-SEM and TEM Analysis

The morphology of ZnO nanorods and GO-ZnO-PdO nanocomposites were investigated by TEM and FE-SEM analysis respectively. The morphologies of ZnO nanomaterial exhibit the rods shape structure. ZnO nanorods have a length and diameter in the range of 50 × 19 nm. Figure 3(b) shows that layer of Graphene oxide sheets are whole covered by ZnO and PdO nanoparticles. ZnO and PdO nanoparticle are uniformly dispersed on the graphene oxide layer and most of the nanoparticles are round

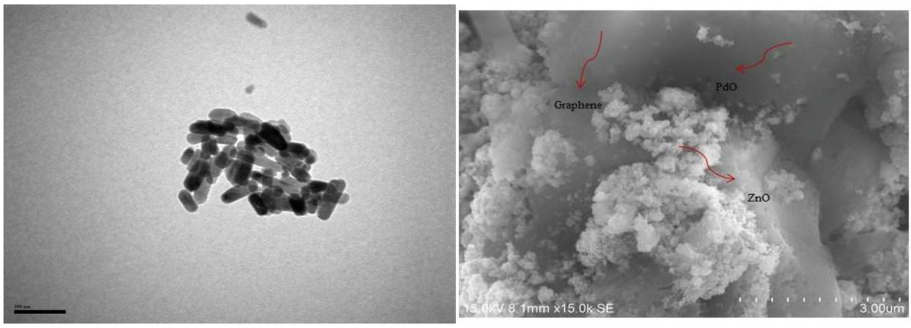


(a) (b)

**Fig. 3.** Shows that the TEM image of (a) ZnO nanorods and (b) GO-ZnO-PdO nanocomposites

in shape with only few nanoparticles with irregular shapes. The size of GO sheets is over several microns. FE-SEM image clearly indicate that the ZnO and PdO nanoparticles were successfully anchored onto the GO sheets.

## 3.2 Photocatalytic Degradation of Methylene Blue

### 3.2.1 Adsorption Isotherm

The adsorption isotherms of MB were carried out under without UV light illumination for the all the sample. The Fig. 4 shows that when the initial concentration of MB increases, the adsorbed amount increases to reach a limit value corresponding to the maximum quantity adsorbed. The commercial ZnO material follows the Langmuir type (L-type) whereas GO-ZnO-PdO nanocomposite exhibit both Langmuir and Freundlich isotherm according to the classification of Giles and Smith [18]. For the commercial ZnO material the time required to reach the adsorption equilibrium state of MB is 40 min while in the case of GO-ZnO-PdO nanocomposite the equilibrium state is reached at 30 min probably due to large surface area (data not shown here).

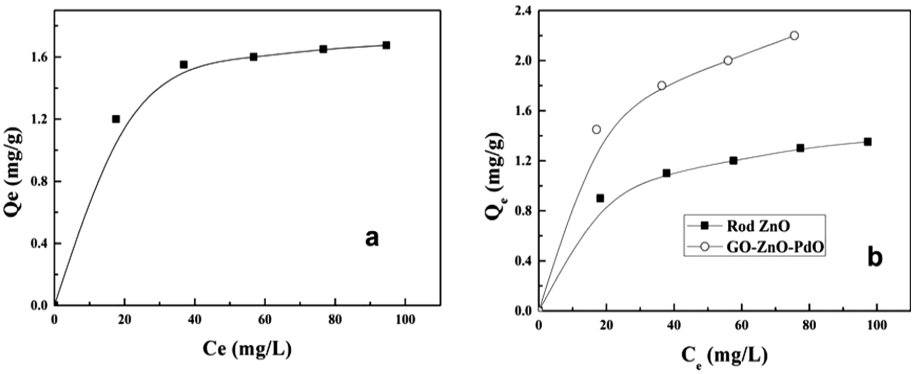


**Fig. 4.** Adsorption isotherm of MB (a) commercial ZnO (b) rod ZnO and GO-ZnO without UV light

### 3.2.2 Effect of Nanoparticles on Photocatalytic Reaction

Before photodegradation studies, adsorption amount of Methylene Blue and it photolysis were evaluated. The Fig. 5 shows MB removal kinetics in dark with photocatalyst, under UV without photocatalyst and under UV with photocatalyst. In dark with photocatalyst and under UV light illumination without photocatalyst, the maximum amount of MB disappearance was about 5% after 60 min.

Regarding photocatalysis (photocatalyst under illumination) efficiency, there was a complete disappearance of MB after 40 min of irradiation. This result shows clearly that ZnO material can be efficiently used for the photocatalytic degradation of methylene blue in aqueous media.

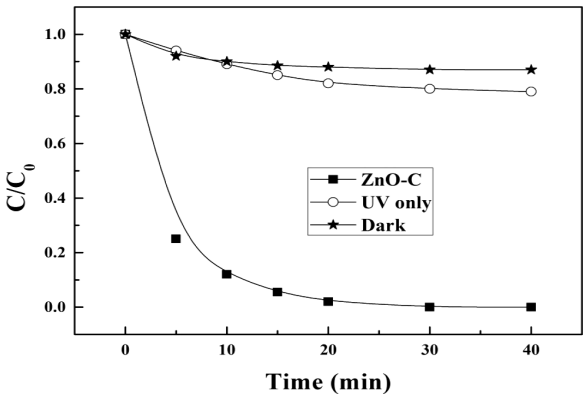


**Fig. 5.** Shows that the Photodegradation of MB (20 mg/L) versus photolysis and adsorption using ZnO-C (2 g/L), free pH

### 3.2.3 Effect of Initial Dye Concentration

The influence of initial concentration of the dye solution on the photocatalytic degradation is an important aspect of the study. The kinetic study of the photocatalytic reaction of the dye as a function of the initial concentration was achieved by varying the initial concentration of methylene blue 20 to 100 mg/L (Fig. 6). According this graph, we noted that more time is required for MB removal at higher initial concentration. The photocatalytic degradation decreased with increasing initial concentration of MB. Indeed, for a MB concentration of 20 mg/L, total photodegradation is observed at 40 min, whereas with a concentration of 80 mg/L and 100 mg/L the total elimination is after 100 and 120 min of irradiation respectively for commercial ZnO material. The photoactivity studies of synthesized nanomaterial such as ZnO nanorods and GO-ZnO-PdO nanocomposite show that these material were more efficiency regarding MB removal. 100% MB removal was observed within 20 min for GO-ZnO-PdO nanocomposite, whereas for ZnO nanorods, 100% of MB removal was achieved in 30 min (20 mg/L of dye). For the two last photocatalysts, 100 min were necessary to remove Methylene blue from water when concentration do not exceed 40 mg/L. More time is needed for the target dye removal when the concentration is over 40 mg/L. Indeed, we note that ZnO nanorods exhibit 90% and 50% of degradation for 80 mg/L and 100 mg/L of MB, while for GO-ZnO-PdO nanocomposites only 70% was achieved for 80 mg/L of MB. This result clearly reveals that at lower concentration of methylene blue, GO-ZnO-PdO nanocomposite are more efficient whereas at high concentration ZnO nanorods become more efficient photocatalyst. Nevertheless, increasing in the substrate concentration leads to decrease in the degradation rate of the dye. The presumed reason is that when the initial concentration of dye is increased, more and more dye molecules are adsorbed on the surface of photocatalyst. The large amount of adsorbed dye is thought to have an inhibitive effect on the reaction of dye molecules with photogenerated holes or hydroxyl radicals, because of the lack of any direct contact between them. Once the concentration of dye is increased, it also causes the dye molecules to adsorb light and the photons never reach the photocatalyst surface, thus the

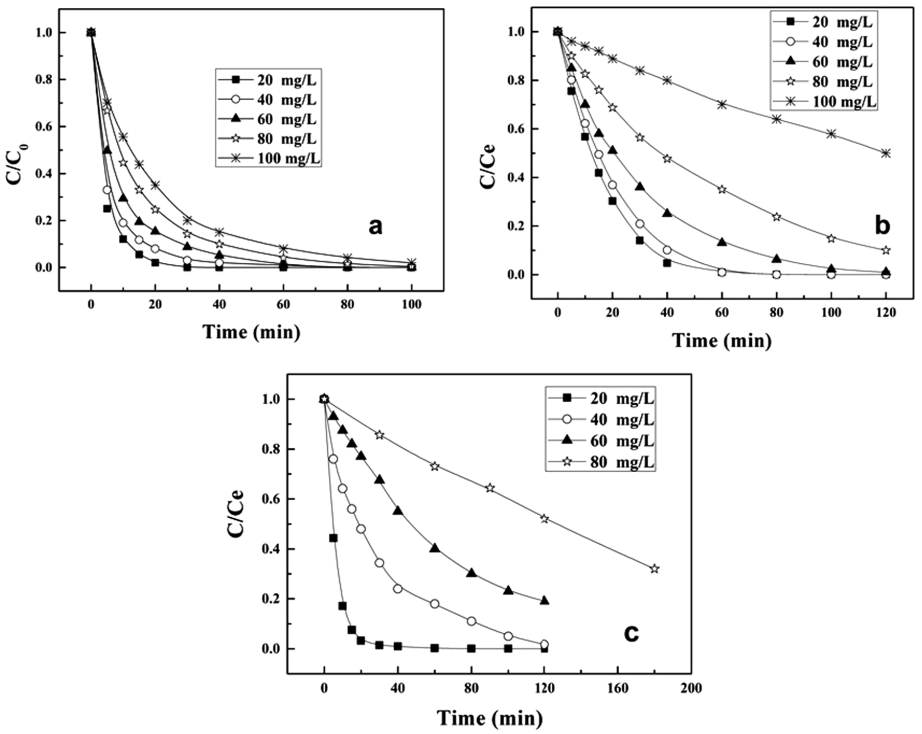


**Fig. 6.** Effect of initial concentration on the photodegradation efficiency of MB solutions on (a) commercial ZnO (b) Rod ZnO (c) GO-ZnO-PdO nanocomposites

photodegradation efficiency decreases [19]. In addition to this at higher concentration of nanoparticles GO-ZnO-PdO tend to aggregated more than ZnO nanorods leads to reduce the active surface area of the photocatalyst. There should be an optimum value of catalyst amount and the substrate concentration leading to maximum efficiency of MB degradation. Indeed an increased opacity of the suspension, brought about as a result of excess of photocatalyst particles, would lead to UV absorption decrease.

### 3.2.4 Kinetics of Photodegradation of MB on (a) ZnO Commercial, (b) Rod ZnO, (c) GO-ZnO-PdO

To analyze degradation kinetics, simplified apparent pseudo first-order kinetics rates were used for MB degradation:

$$\ln\left(\frac{C_e}{C}\right) = k_{ap} \cdot t \tag{3}$$

where, $k_{ap}$ was the apparent pseudo-first-order rate constant of initial degradation ($min^{-1}$), C and $C_e$ represents transient and initial concentrations of MB, respectively. The rate constant $k_{ap}$ was calculated from the slope of theln Ce/C versus t. As theses curves are linear, the degradation kinetic of MB follows well Langmuir kinetic model. The value of initial rate of photocatalytic degradation of MB is calculated using the equation:

**Table 1.** Shows that initial rate and rate constant at different initials concentrations dye

| Nanoparticles | Constants | MB concentration | | | |
|---|---|---|---|---|---|
| ZnO commercial | $k_{ap}$ ($min^{-1}$) | 0.1866 | 0.12190 | 0.0939 | 0.0716 |
| | $r_0$ (mg/L/min) | 3.7336 | 4.8760 | 5.6320 | 5.7290 |
| Rod ZnO | $k_{ap}$ ($min^{-1}$) | 0.0646 | 0.0521 | 0.0338 | 0.0187 |
| | $r_0$ (mg/L/min) | 1.292 | 2.084 | 2.028 | 1.496 |
| GO-ZnO-PdO | $k_{ap}$ ($min^{-1}$) | 0.14676 | 0.03381 | 0.01311 | 0.00492 |
| | $r_0$ (mg/L/min) | 2.935 | 1.3524 | 0.7866 | 0.3936 |

$$r_0 = k_{ap}.C_e \tag{4}$$

The results indicate that the initial rate ($r_0$) increases gradually with increase the initial concentration of dye (Table 1). We note that at low initial concentration of MB solution (20 mg/L) the photocatalyst GO-ZnO (kap = 0.14676 $min^{-1}$) is more active than rod ZnO (kap = 0.646 $min^{-1}$), while for the initial concentration high o or equal to 40 mg/L, rod ZnO is efficient than GO-ZnO (Fig. 7).

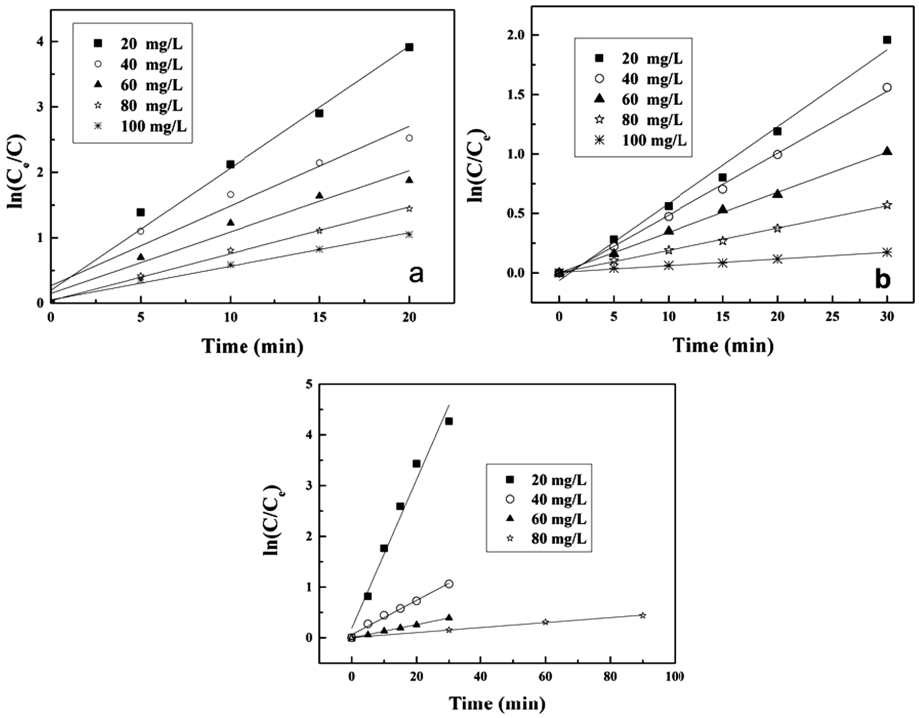


**Fig. 7.** Kinetics of photodegradation of MB on (a) ZnO commercial, (b) Rod ZnO, (c) GO-ZnO-PdO

## 4 Conclusion

We have successfully synthesised high quality of ZnO nanorods and GO-ZnO-PdO nanocomposites through hydrothermal method. The degradation of Methylene blue by commercial ZnO, ZnO nanorods and GO-ZnO-PdO nanocomposite exhibits the first order reaction kinetics. The order of photocatalytic activity of nanomaterials is estimated as GO-ZnO-PdO > ZnO nanorods > commercial ZnO materials for MB concentration not exceeding 40 mg/L. GO-ZnO-PdO exhibits more efficiency probably due to larger surface area and extended pi-electron conjugation of GO. Synthesized ZnO nanorods as well as GO-ZnO-PdO nanocomposite material are good candidate for photocatalytic removal of dye from water.

**Acknowledgments.** We express our sincere thanks to DAAD and the EXCEED SWINDON project for the financial support to attend the Expert Workshop on "Sustainable Use of Water Resources" in Mekelle (Ethiopia) May 15-20, 2017.

## References

1. Wang, Z.L.: Splendid one-dimensional nanostructures of zinc oxide: a new nanomaterial family for nanotechnology. ACS Nano **2**, 1987–1992 (2008)
2. Kim, H., Jeong, H., An, T.K., Park, C.E., Yong, K.: Hybrid-type quantum-dot cosensitized ZnO nanowire solar cell with enhanced visible-light harvesting. ACS Appl. Mater. Interfaces. **5**, 268–275 (2012)
3. Park, S., An, S., Ko, H., Jin, C., Lee, C.: Synthesis of nanograined ZnO nanowires and their enchanced gas sensing properties. ACS Appl. Mater. Interfaces. **4**, 3650–3656 (2012)
4. Kumar, R., Anandan, S., Hembram, K., Narasinga Rao, T.: Efficient ZnO-based visible-light-driven photocatalyst for antibacterial applications. ACS Appl. Mater. Interfaces. **6**, 13138–13148 (2014)
5. Wang, Y., Shi, R., Lin, J., Zhu, Y.: Enhancement of photocurrent and photocatalytic activity of ZnO hybridized with graphite-like C3N4. Energy Environ. Sci. **4**, 2922–2929 (2011)
6. Dikin, D.A.L., Stankovich, S., Zimney, E.J., Piner, R.D., Dommett, G.H.B., Evmeneko, G., Nguyen, S.T., Ruoff, R.S.: Preparation and characterization of graphene oxide paper. Nature **448**, 457–460 (2007)
7. Xu, C., Wang, X.: Fabrication of flexible metal-nanoparticle films using graphene oxyde sheets as substrates. Small **5**, 457–460 (2009)
8. Lightcap, I.V., Kosel, T.H., Kamat, P.V.: Anchoring semiconductor and metal nanoparticles on a two-dimensional catalyst mat. storing and shuttling electrons with reduced graphene oxide. Nano Lett. **10**, 577–583 (2010)
9. Liu, J., Bai, H., Wang, Y., Liu, Z., Zhang, X., Sun, D.D.: Self-assembling $TiO_2$ nanorods on large graphene oxide sheets at a two-phase interface and their anti-recombination in photo catalytic applications. Adv. Func. Mater. **20**, 4175–4181 (2010)
10. Liu, X., Pan, L., Zaho, Q., Lv, T., Zhu, G., Chen, T., Lu, T., Sun, Z., Sun, C.: UV-assisted photocatalytic synthesis of ZnO-reduced graphene oxide composites with enhanced photocatalytic activity in reduction of Cr(VI). Chem. Eng. J. **183**, 238–243 (2012)

11. Chen, Z., Zhang, N., Xu, Y.-J.: Synthesis of graphene – ZnO nanorod nanocomposites with improved photoactivity and anti-photocorrosion. CrystEngComm **15**, 3022–3030 (2013)
12. Baruwati, B., Kumar, D.K., Manorama, S.V.: Hydrothermal synthesis of highly crystalline ZnO nanoparticles: a competitive sensor for LPG and EtOH. Sens. Actuators B Chem. **119**, 676–682 (2006)
13. Zhang, Y., Tang, Z.-R., Fu, X., Sun, J.: $TiO_2$-graphene nanocomposites for gasphase photocatalytic degradation of volatile aromatic pollutant: is $TiO_2$-graphene truly different from other $TiO_2$-carbon composite materials? ACS Nano **4**, 7303–7314 (2010)
14. Yang, Q., Cai, H., Hu, Z., Duan, Z., Yang, X., Sun, J., Xu, N., Wu, J.: Extended photoresponse and multi-band luminescence of ZnO/ZnSe Core/shell nanorods. Nanoscale Res. Lett. **9**, 31 (2014)
15. Brantley, W.A., Cai, Z., Papazoglou, E., Mitchell, J.C., Kerber, S.J., Mann, G.P., Barr, T.: X-ray diffraction studies of oxidized high-palladium: alloys. Dent. Mater. Off. Publ. Acad. Dent. Mater. **12**, 333–341 (1996)
16. Frusteri, L., Cannilla, C., Brbera, K., Parathoner, S., Centi, G., Frusteri, F.: Carbon growth evidences as a result of benzene pyrolysis. Carbon **59**, 296–307 (2013)
17. Holzwarth, U., Gibson, N.: The Scherrer equation versus the 'Debeye-Scherrer equation'. Nat. Nano **6**, 534 (2011)
18. Giles, C.H., Smith, D.: A general treatment and classification of the solute adsorption isotherm. J. Colloid Interf. Sci. **47**, 755–765 (1974)
19. Daneshvar, N., Salari, D., Khataee, A.R.: J. Photochem. Photobiol. A **157**, 111–116 (2003)

# Treatment of Domestic Wastewater from Small Cities on Vertical Flow Constructed Wetlands (VFCWs)

R. Gourdon[1(✉)], M. Kania[1,2], M. Gautier[1], B. Kim[1], and P. Michel[2]

[1] Univ Lyon, INSA Lyon, DEEP, 20 av. Albert Einstein, 69621 Villeurbanne Cedex, France
{remy.gourdon, manon.kania, mathieu.gautier, boram.kim}@insa-lyon.fr
[2] SCIRPE, 5 Allée Alban Vistel, 69110 Sainte-Foy-Lès-Lyon, France
pmi@scirpe.fr

**Abstract.** To improve denitrification and phosphorus removal in VFCWs, the French company SCIRPE has developed a patented process called Azoé® which comprises biological pre-treatment on a trickling filter followed by two stages of partially saturated vertical flow filters planted with reeds. Phosphorus removal is carried out by addition of $FeCl_3$ at the outlet of the biological trickling filter. Phosphorus thus precipitated accumulates mainly on the surface of the first filter in the form of a sludge layer. After several years of operation, this surface layer represents a stock of phosphorus potentially mobilizable as a function of the biophysicochemical conditions of the environment. However the fate of organic and mineral micropollutants, (pharmaceutical residues, pesticides, metals, etc.) in the system is poorly known. In the present study, the performance of these systems was studied by monitoring an Azoé® plant in operation. The results confirmed the very good efficiency in carbon and nitrogen treatment, the good stability of phosphorus retention, and a high rate of removal or retention of most micropollutants analyzed.

**Keywords:** Vertical flow constructed wetland · Wastewater treatment · Extensive process · Low energy · Nitrification · Denitrification · Phosphorus removal · Micropollutants

## 1 Introduction

Stormwater and domestic wastewaters carry a large variety of dissolved and particulate constituents. Proper treatments are necessary to allow (i) water reuse, (ii) discharge to the environment, or (iii) recovery of potentially valuable nutrients. Constructed wetlands are considered amongst the technologies best adapted to extensive treatment. Their development in Europe has been considerable since the end of the 90s, making them today the number one treatment process used at small community scale with more than 3500 plants in operation in France.

Vertical-flow constructed wetlands (VFCWs) are predominant in France. They are characterized by the formation of a layer of sludge deposits at the surface of the filters

© Springer Nature Singapore Pte Ltd. 2018
H. Tran-Nguyen et al. (eds.), *Proceedings of the 4th Congrès International de Géotechnique - Ouvrages -Structures*, Lecture Notes in Civil Engineering 8,
DOI 10.1007/978-981-10-6713-6_107

originating from the percolation of raw wastewater (Molle 2014; Kim et al. 2013). VFCWs have been mainly developed to treat organic matter and nitrogen. Phosphorus removal has become however a challenging issue since its uncontrolled discharge into water bodies may result in their eutrophication, whereas phosphorus is at the same time a non-renewable resource of great value as a fertilizer component. While agriculture demands phosphorus inputs, wastewaters are a good source of phosphorus if properly treated (Bellier et al. 2006; Kim et al. 2014; Caravelli et al. 2010). A diversity of organic and metallic pollutants are however present in domestic wastewater and runoff stormwater. They may accumulate in the sludge layer via complexation or adsorption mechanisms onto particulate organic matter (OM) and/or mineral phases. These retention phenomena have positive incidences on the treatment performance but also bear risks of adverse effects.

This study reports field investigations of the performance of the first Azoe® VFCW plant in operation for close to 15 years with respect to several parameters.

## 2 Materials and Methods

### 2.1 Site of Investigation

An AZOE® plant of 1100 inhabitant equivalents, in operation since 2004 in Jura, France, and regularly monitored, was used as a study site. This plant, whose operating principle is shown in Fig. 1, was described in details in previous articles (Kim et al. 2013, 2014). The first stage of planted filters comprises three hydraulically independent cells in parallel. Each cell is fed over a period of 7 days and then put to rest for 14 days. The 2$^{nd}$ stage operates on the same principle as the 1$^{st}$ stage but comprises two cells.

### 2.2 Description of Field Monitoring Campaigns

Several campaigns were conducted. Sampling was carried out at four different points on the processing line to determine the efficiency of each stage of the treatment chain. A 24 h time-proportional inflow/outflow sampling method was used. The following points were sampled (Fig. 1): raw wastewater (inflow); trickling filter effluent after ferric chloride injection (PS1); effluent from the first filter stage (PS2); and treated water at the output of the second filter (outflow). Refrigerated auto-samplers were used to store the samples at a temperature of about 4 °C before being analyzed within 24 h. Micropollutants were only analyzed at the inlet and outlet over a period of 24 h of regular operation. The selection of target micropollutants to be analyzed was carried out on the basis of literature data. Metallic or metalloid trace elements (Al, Mn, Si, Zn, As, Cd, Cr, Cu, Ni, Pb) and more than one hundred organic micropollutants were analyzed, among which:

- priority substances and pollutants regulated by the WFD;
- pesticides, including glyphosate and its degradation products;
- pharmaceutical substances.

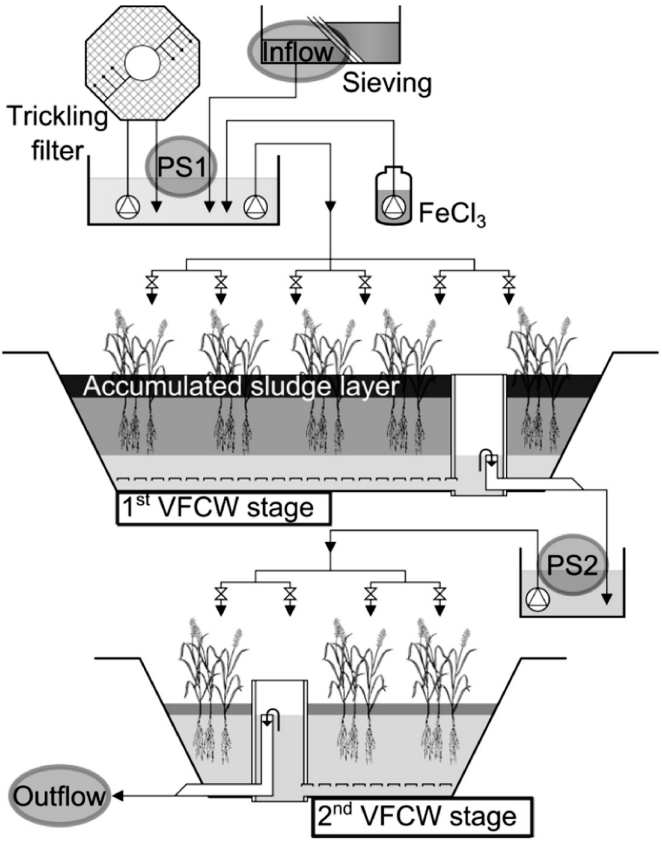


**Fig. 1.** Simplified diagram of the VFCW plant selected for the study

### 2.3 Analytical Procedures

The following parameters were analyzed following French standard methods (Kock-Schulmeyer et al. 2013): total suspended solids (TSS), five-day biochemical oxygen demand ($BOD_5$), chemical oxygen demand (COD), total Kjeldahl nitrogen (TKN), nitrate ($NO_3$–N), total nitrogen (TN) and total phosphorus (TP) concentrations. The treatment performance with respect to each parameter was calculated as a 24-h input-output balance of the considered parameter expressed as a percentage. The 95% confidence interval was determined by ± mean standard deviation (SEM), which was calculated as the standard deviation (SD) divided by the square root of the number of samples.

Regarding micropollutants, samples of 2.5 L were taken in brown glass flasks and analyzed within 48 h by a specialized analytical laboratory. GC-MS techniques were used for volatile compounds, HPLC-MS techniques for pesticides and polar pharmaceutical substances. A fluorescence-coupled HPLC technique was used for the analysis of glyphosate and its degradation products. Metals and metalloids (Al, Mn, Si, Zn, As,

Cd, Cr, Cu, Ni, Pb) were analyzed by ICP-OES on an Ultima 2, Horiba Jobin Yvon system.

## 3 Results and Discussion

### 3.1 Treatment of Carbon, Nitrogen and Phosphate Loads

Results given in Table 1 showed a very good efficiency of carbon and nitrogen removal. The removal rates of suspended solids (99%), $BOD_5$ (98%) and COD (94%) were excellent. TKN removal (97%) was even higher than the average performance recorded on French VFCWs, (average of 85%, Thistleton et al. 2002). This good performance can probably be explained by the nitrification activity of the biological trickling filter. Furthermore, the plant was very efficient in total nitrogen removal, probably due to the denitrification phenomenon favored by the anoxic conditions in the saturated zone of VFCWs stages (Kim et al. 2013). Phosphorus removal was not as good as for the other parameters, and the outflow concentration was more variable, with an average of 2.8 mg. $L^{-1}$. A molar ratio of Fe/P greater than 1.5 is generally recommended (Caravelli et al. 2010; Szabo et al. 2008; Thistleton et al. 2002 whereas it was less than 1.5 in almost half of the campaigns. This may explain the observed variability in phosphorus removal (Kim et al. 2014).

**Table 1.** Average values ± SEM (number of data) for selected parameters in inflow and outflow of the monitored plant

| Variable | Inflow (mg/L) | Outflow (mg/L) | Removal (%) |
|---|---|---|---|
| TSS | 450 ± 104 (44) | 3.4 ± 0.7 (44) | 98.8 ± 0.5 (39) |
| $BOD_5$ | 286 ± 65 (43) | 3.2 ± 0.6 (43) | 97.9 ± 1.1 (38) |
| COD | 794 ± 179 (44) | 25 ± 3 (44) | 94.4 ± 2.5 (39) |
| TP | 9.5 ± 1.6 (40) | 2.8 ± 0.4 (40) | 59.6 ± 12 (35) |
| TN | 71 ± 10 (40) | 17 ± 3 (39) | 70.9 ± 6.2 (35) |
| TKN | 70 ± 9 (42) | 1.6 ± 0.3 (43) | 97.2 ± 1.0 (37) |

Figure 2 shows the evolution of various parameters along the treatment line. Most of COD load was in suspended solids (>0.45 µm). The trickling filter showed good efficiency in COD removal. After the first stage of planted filter, COD was almost exclusively soluble due to the excellent removal of suspended solids.

### 3.2 Monitoring of Micropollutants

Figure 3 shows the concentrations of the micropollutants analyzed at the inlet and outlet of the plant on a 24-h monitoring campaign. Although more than 100 compounds were analyzed, only 7 pesticides and 7 pharmaceutical substances were detected in the inflow.

Chlortoluron, isoproturon and diruon, which are urea-type herbicides, were found at very low concentrations (0.03, 0.06 and 0.02 µg $L^{-1}$ respectively) in the inflow

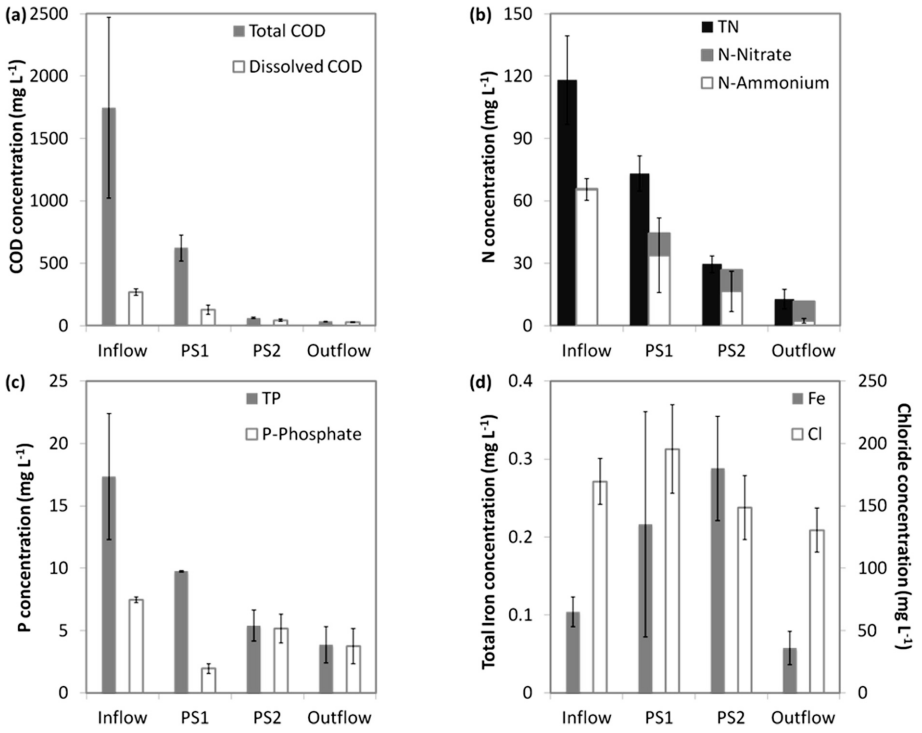


**Fig. 2.** Average concentrations along the treatment line: (a) total and dissolved COD, (b); Total Nitrogen (TN), $NH_4$-N et $NO_3$-N, (c) total phosphorus (TP) and P-phosphate ($PO_4$-P); Total dissolved iron and chloride (d)

wastewater. Their use is strictly restricted or even banned in the case of Diuron (Kock-Schulmeyer et al. 2013). Glyphosate and its degradation product AMPA are the pesticides detected at the highest concentration in the inflow of the plant and in the outflow as well (1.34 µg $L^{-1}$ inlet and 1.56 µg $L^{-1}$ at the outflow for glyphosate, 1.25 µg $L^{-1}$ and 3.90 µg $L^{-1}$ for its degradation product). The pharmaceutical products detected in this study are the most frequently detected in the environment. They were found at higher concentrations than pesticides, which can be explained by the respective origins of these molecules (leaching of agricultural soils for pesticides, direct discharges into wastewater for pharmaceutical substances).

Figure 3 showed that metrafenon, chlortoluron, isoproturon and diuron were detected at very low concentrations in the inflow wastewater and were below the detection limit at the outlet of the system. On the contrary, nicosulfuron, glyphosate and its major metabolite AMPA exhibited higher concentrations in the outflow than the inflow. These results suggest a partial biodegradation of glyphosate in the plant. However, monitoring was done over a single day and therefore the variations of inlet concentrations in time were not evaluated. These variations may explain the higher concentrations of glyphosate and nicosulfuron in the outlet. The planted filters and more specifically the surface sludge deposits, have the capacity to sorb micropollutants.

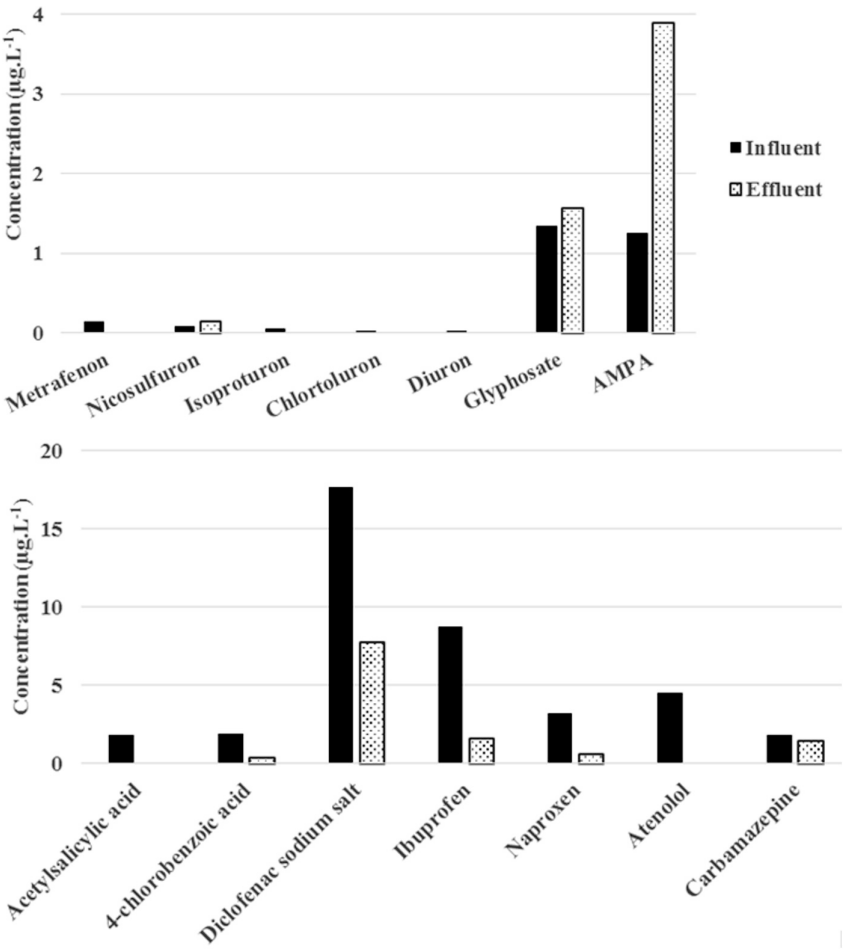


**Fig. 3.** Pesticides (top) and pharmaceutical (bottom) micropolluants concentrations analyzed at inlet and outlet of the plant

If limited (bio)degradation occurs, the micropollutants accumulate within the surface sludge layer. According to possible variations in physicochemical conditions (pH, ionic charge, temperature, etc.), accumulated micropollutants may then be partially released, which may explain higher concentrations at the outlet.

All of pharmaceutical micropollutants detected in the monitoring campaign revealed a decrease of their concentrations from inlet to outlet (Fig. 3), suggesting a good retention (sorption) and/or (bio)degradation in the system. However the performance was low for carbamazepine and to a lesser extent diclofenac. These results are consistent with those from other studies on VFCWs plants (Avila et al. 2015; Verlicchi and Zambello 2014). Carbamazepine appears to be poorly degraded or removed in many wastewater treatment systems (Kock-Schulmeyer et al. 2013).

Figure 4 showed that all metals except manganese were very well removed by the system. Sorption onto organic matter within the surface sludge layer was probably the mechanisms of retention. Arsenic exhibited a higher concentration at the outlet. This might be explained, as for glyphosate above, by the variation in time of inlet concentration.

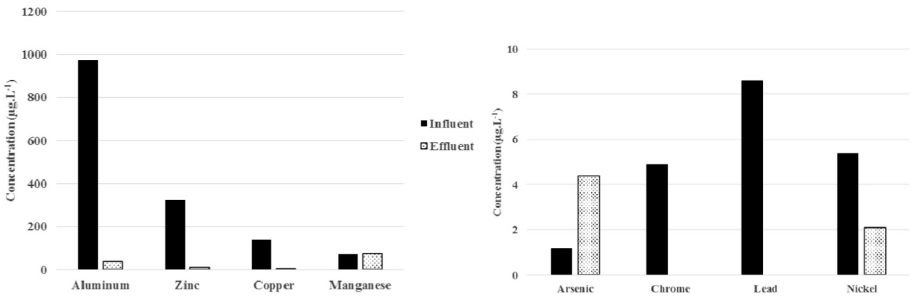


**Fig. 4.** Monitoring of major (left) and trace (right) metals and metalloïds

## 4 Conclusion

Results from this study confirmed the very good efficiency of the monitored Azoe® VFCW plant. Performance in the removal of suspended solids, carbon and nitrogen were excellent. The trickling filter was shown to provide a significant contribution. The retention/degradation or (bio)degradation of trace organic micropollutants (pesticides or pharmaceutical substances) was observed within the system, most probably occurring by sorption, photolysis, hydrolysis and biodegradation within the surface sludge layer. These processes are governed by the physicochemical properties of the molecules (solubility, hydrophobicity, biodegradability, etc.) and the characteristics of the treatment system. Further studies are needed to better characterize the influence of operating conditions on the retention/degradation of micropollutants. Regarding the process studied here, pre-treatment on a bacterial trickling filter and the addition of ferric chloride probably played a role in these processes.

**Acknowledgments.** The authors wish to thank SCIRPE Company and French CIFRE (Conventions Industrielles de Formation par la REcherche) for funding this research project.

## References

Ávila, C., et al.: Emerging organic contaminant removal in a full-scale hybrid constructed wetland system for wastewater treatment and reuse. Ecol. Eng. **80**, 108–116 (2015)

Bellier, N., Chazarenc, F., Comeau, Y.: Phosphorus removal from wastewater by mineral apatite. Water Res. **40**(15), 2965–2971 (2006)

Caravelli, A.H., Contreras, E.M., Zaritzky, N.E.: Phosphorous removal in batch systems using ferric chloride in the presence of activated sludges. J. Hazard. Mater. **177**(1–3), 199–208 (2010)

Kim, B., Gautier, M., Gourdon, R.: Physical-chemical characterization of solid materials sampled from a partially flooded vertical flow constructed wetland. Water Sci. Technol. **68**(10), 2257–2263 (2013)

Kim, B., Gautier, M., Prost-Boucle, S., Molle, P., Michel, P., Gourdon, R.: Performance evaluation of partially saturated vertical-flow constructed wetland with trickling filter and chemical precipitation: a field study. Ecological Engg. **71**, 41–47 (2014)

Kock-Schulmeyer, M., et al.: Occurrence and behavior of pesticides in wastewater treatment plants and their environmental impact. Sci. Total Environ. **458–460**, 466–476 (2013)

Molle, P.: French vertical flow constructed wetlands: a need of a better understanding of the role of the deposit layer. Water Sci. Technol. **69**(1), 106–112 (2014)

Szabo, A., Takacs, I., Murthy, S., Daigger, G.T., Licsko, I., Smith, S.: Significance of design and operational variables in chemical phosphorus removal. Water Environ. Res. **80**(5), 407–416 (2008)

Thistleton, J., Berry, T.A., Pearce, P., Parsons, S.A.: Mechanisms of chemical phosphorus removal II: iron (III) salts. Process Saf. Environ. Prot. **80**(5), 265–269 (2002)

Verlicchi, P., Zambello, E.: How efficient are constructed wetlands in removing pharmaceuticals from untreated and treated urban wastewaters? A review. Sci. Total Environ. **470–471**, 1281–1306 (2014)

# Treatment of Slaughterhouse Wastewater by Intermittent Cycle Extended Aeration System (ICEAS)

Duc Tiep Nguyen and Tan Phong Nguyen(✉)

Faculty of Environment and Natural Resources,
Ho Chi Minh City University of Technology, Ho Chi Minh City, Vietnam
ductiepnguyen.vn@gmail.com, ntphong@hcmut.edu.vn

**Abstract.** This research conducts a slaughterhouse wastewater study with high nitrogen concentration by applying intermittent cycle extended aeration system (ICEAS) model combined with and without Mutag BioChip media to assessing the efficiency of this treatment. A model made from poly acrylic with a capacity of 18 L was utilized to evaluate COD and nitrogen removal efficiency for different organic loading rate (OLR). The results showed that removal efficiency of the ICEAS model combined with Mutag BioChip media was higher than one of the ICEAS model without Mutag BioChip media in terms of COD; $NH_4^+$-N and TN parameters. At the OLR of 0.5 kg COD/$m^3$.day, the corresponding treatment efficiency of these parameters was of 91.48%; 87.08% and 83.59%, respectively. In the case that the OLR increased up to 2.0 kg COD/$m^3$.day, the corresponding treatment efficiency only decreases slightly. It proves that the use of Mutag BioChip media allowed to increase the removal efficiency for slaughterhouse wastewater treatment.

**Keywords:** Slaughterhouse wastewater · Mutag BioChip · ICEAS

## 1 Introduction

Slaughterhouse wastewater (SWW) is considered detrimental worldwide due to its complex composition of fats, proteins, and fibers from the slaughtering process (Johns 1995; Ruiz et al. 1997; Wu and Mittal 2011; Bustillo-Lecompte et al. 2014). The major part of the contamination is caused by blood and by stomach and intestinal mucus (Tritt and Schuchardt 1992). Furthermore, slaughterhouse wastewater contains high levels of organics, pathogenic and non-pathogenic microorganisms, detergents and disinfectants used for cleaning activities (Masse and Masse 2000; Debik and Coskun 2009). Slaughterhouse wastewater samples also include nutrients, heavy metals, color, and turbidity, among others. It is also important to note that disinfectant, cleaning agents, and pharmaceuticals for veterinary purposes can be present in the SWW (Tritt and Schuchardt 1992). Slaughterhouses are part of a large industry, which is common to numerous countries worldwide where meat is an important part of their diet. Therefore, slaughterhouse wastewater requires significant treatment for a safe and sustainable release to the environment (Johns 1995).

© Springer Nature Singapore Pte Ltd. 2018
H. Tran-Nguyen et al. (eds.), *Proceedings of the 4th Congrès International de Géotechnique - Ouvrages -Structures*, Lecture Notes in Civil Engineering 8,
DOI 10.1007/978-981-10-6713-6_108

A modification of the sequencing batch reactor (SBR) process is the intermittent cycle extended aeration system – sequencing batch reactor (ICEAS – SBR), which is operated on the principle of continuous influent as in the conventional activated sludge process, but has intermittent effluent withdrawing which is similar to the SBR system. ICEAS – SBR offers the advantages of easy operation and flexibility (Bustillo-Lecompte et al. 2014). Many researches proved that ICEAS – SBR having high removal efficient in sewage wastewater (Tritt and Schuchardt 1992; Debik and Coskun 2009), but its treatment ability in high nitrogen concentration wastewater is not studied thoroughly. On the other hand, the moving bed is usually used in order to enhance treatability of the system. The moving bed sequencing biofilm batch reactor (MBSBBR) is a combination of the SBR process and the moving bed batch reactor (MBBR) process. Some studies pointed that MBSBBR had higher treatability than SBR (Khararjian et al. 1990; Chen et al. 2001). This process is proved flexible, reliable and easy to operating (no clogging problems, little suspended solid in the reactor, easy to settle or decant (Lee et al. 2001). Similarly, the combination of ICEAS – SBR and MBBR, intermittent cycle extended aeration system – moving bed sequencing batch reactor (ICEAS – MBSBR), would have these advantages too. In this study Mutag BioChip media was used to the increase microbial density and the efficiency of COD, $NH_4^+$, and TN.

## 2 Materials and Methods

### 2.1 Raw Wastewater, Seed Sludge

Slaughterhouse wastewater was collected at the collection tank after through grit chamber of wastewater treatment plant of VISSAN Joint Stock Company, located in 420 No Trang Long Street, Ward 13, Binh Thanh District, Ho Chi Minh City. Compositions and properties of wastewater were represented as pH: 6–7.5; COD: 813–1,219 mg/l; TSS: 950–1,100 mg/l; TN: 71–102 mg/l. The ICEAS influent was used at the suitable dilution ratio raw tannery wastewater. Seed sludge was taken from wastewater treatment plant of VISSAN Company, Binh Thanh District, Ho Chi Minh City. Seed sludge was light brown, well-settled with SVI being 97 and MLVSS/MLSS ratio being 0.8.

### 2.2 Reactor and Operation

ICEAS – MBSBR used to test and ICEAS – SBR used to the control. Each polyacrylic reactor was manufactured with dimensions 300 × 150 × 450 (L × W × H) (mm). The model was completely automatically controlled by a timer. Mutag Biochip media was used in ICEAS - MBSBR with surface area of 3000 $m^2/m^3$, dimension 22 mm diameter × 0.8 mm height, and specific weight of 170 $kg/m^3$. Mutag Biochip was added to 10% reactor volume (1.8 L).

A baffle was installed to split the reactor into 2 parts: the pre reactor and the main reactor with the ratio 1:4 (Fig. 1). As the wastewater continued to flow in settle phase, the partition helped to prevent turbulence in the tank, without obstructing the

sedimentation. In addition, in the decanting phase, the baffle helped to retain the water input long enough in the pre-reactor. This would not create disturbances in the main reactor and increase the concentration of the substance's output. An air pump and diffusers were placed at the bottom of the ICEAS tank which kept DO remaining 3–4 mg/l in the aeration phase. A mixing was used to create the anoxic condition with DO <0.5 mg/L. The mixed liquor suspended solid (MLSS) concentration of the seed sludge was approximately 3,000 mg/l; pH in the tank varied from 6.5 to 7.5.

The reactor was operated at a hydraulic retention time (HRT) of 12 h with 40 L/day continuous flow. The cycle time was 9 h including 8 h for reacting, 0.4 h for settling and 0.2 h for the decanting phase. The reacting phase consisted 1 h of aeration and 1 h of stirring alternately. All items in the process operated automatically and were controlled by timer.

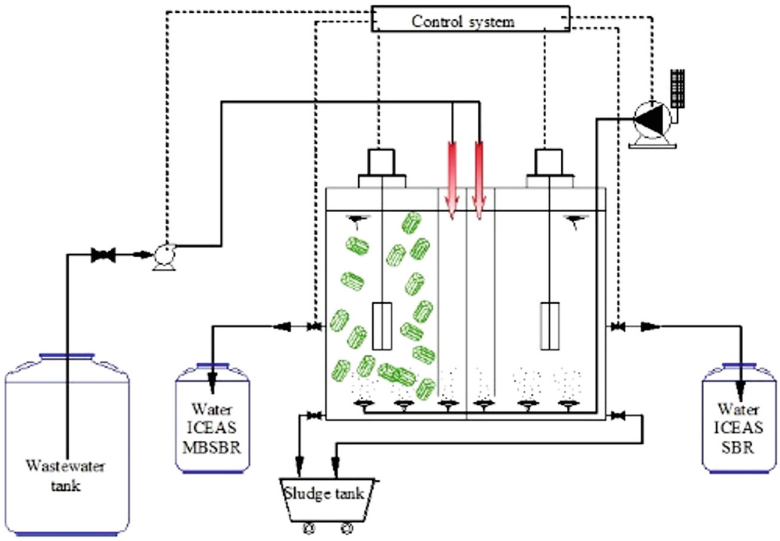


**Fig. 1.** Schematic structure of ICEAS – SBR and ICEAS – MBSBR

## 2.3 Analytical Methods

The samples were collected at the influent and effluent positions of the reactor. The parameters of wastewater such as pH, COD, SS, TKN, $NH_4^+$-N, $NO_2^-$-N, $NO_3^-$-N, TN were analyzed according to Vietnam National Standards and Standard Methods for the Examination of Water and Wastewater (APHA, Eaton DA, and AWWA) at the Laboratory of Environmental Engineering, Faculty of Environment and Natural Resources, Ho Chi Minh City University of Technology (HCMUT). Biomass concentration was assessed at the last days of each organic loading rate (OLR).

# 3 Results and Discussion

## 3.1 COD Removal

The results obtained show that the treatment effect decreased when increasing organic loading rate (OLR). When operating with the OLR at 1.0 kg COD/$m^3$.day, COD removal efficiency of two models were the highest. In the case of increased OLR under 2.0 kg COD/$m^3$.day both models remained stable and efficient removal reached column B QCVN 40: 2011/BTNMT. It is also implied that the using of Mutag Biochip$^{TM}$ could be applied to systems ICEAS - SBR when COD concentration exceeded allowable output at a low level (Table 1 and Fig. 2).

**Table 1.** COD removal results in the organic loading rate

| Organic loading rate, kg COD/$m^3$.day | COD influent, mg/l | COD effluent, mg/l (ICEAS-SBR) | COD effluent, mg/l (ICEAS-MBSBR) | Efficient, % (ICEAS-SBR) | Efficient, % (ICEAS-MBSBR) |
|---|---|---|---|---|---|
| 0.5 | 335.6 ± 5.2 | 53.6 ± 30.7 | 43.6 ± 25.9 | 84.13 ± 8.94 | 87.07 ± 7.58 |
| 1.0 | 495.1 ± 14.9 | 38.3 ± 5.7 | 34.5 ± 7.2 | 92.26 ± 1.08 | 93.04 ± 1.33 |
| 1.5 | 719.5 ± 13.6 | 76.7 ± 3.0 | 74.4 ± 3.0 | 89.34 ± 0.43 | 89.65 ± 0.46 |
| 2.0 | 802.0 ± 16.3 | 90.5 ± 3.9 | 85.0 ± 2.5 | 88.72 ± 0.47 | 89.39 ± 0.42 |
| 2.5 | 937.7 ± 22.7 | 167.0 ± 17.4 | 143.7 ± 14.2 | 82.20 ± 1.74 | 84.70 ± 1.32 |

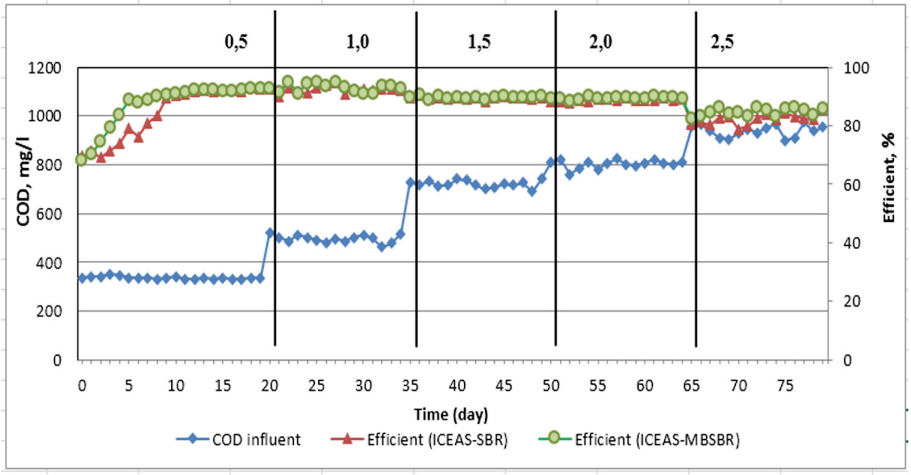


**Fig. 2.** The transformation inlet COD, COD removal efficiency of the model ICEAS - SBR and ICEAS - MBSBR through each organic loading rate

Overall, removal efficiency of the model ICEAS - MBSBR always reached higher than ICEAS - SBR during operation. At organic loading rates 1.0; 1.5; 2.0 kg COD/$m^3$.day, the difference removal efficiency between ICEAS - MBSBR and ICEAS - SBR was not much. In the contract, the organic loading rate at 2.5 kg COD/$m^3$.day, removal effectively of the model ICEAS - MBSBR greater than the model ICEAS - SBR.

From here shows, the ability to remove of the ICEAS - MBSBR was more efficient than ICEAS – SBR. We could say that the intermittent aeration mode was more important than the process of biological growth to COD removal.

### 3.2 Ammonia Nitrogen Removal

After 80 days of operation, effectively remove ammonia in wastewater input of model ICEAS - SBR and ICEAS - MBSBR at different organic loading rate were shown in Fig. 3. The results showed that the model was capable handling high ammonia effectively. This could be explained by the intermittent aeration which increased ammonia oxidizing bacteria group.

At the organic loading rate 0.5 kg COD/$m^3$.day, effective treatment ammonia both models obtained ammonia approximately equal at the end of the period were 88.46% and operator 88.59%. Overall, the efficiency treatment ammonia of the model ICEAS - MBSBR better than model ICEAS - SBR. In the first days of operation, mud is well adapted and efficiency treatment ammonia increased stable at the end of the period. Last ammonia output of this stage is 3.6 - 3.5 mg/l.

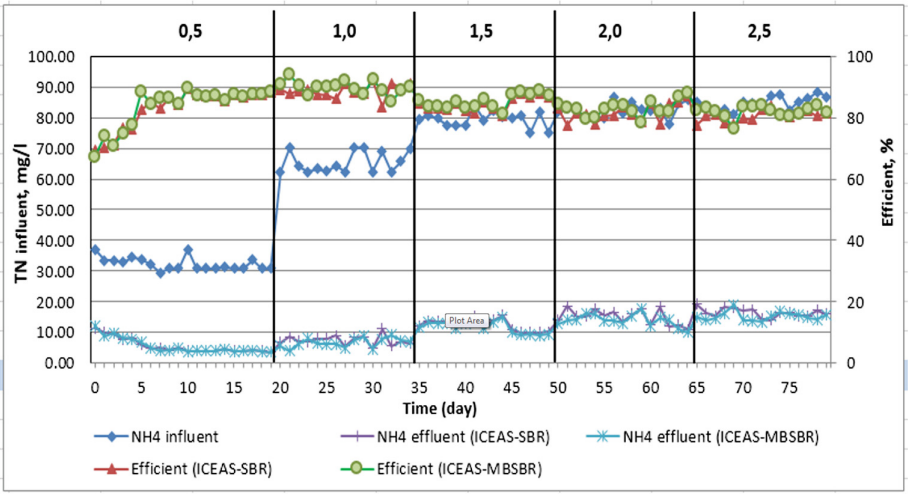


**Fig. 3.** The concentration change input, output and efficiency of removing ammonia both models

At the organic loading rate 1.0 kg COD/$m^3$.day, ammonia treatment efficiency increased slightly compared to the last days of operation in the first load. At this stage, the mud has good growth rates on Mutag Biochip$^{TM}$, that can help ammonia treatment efficiency of the model ICEAS - MBSBR better than model ICEAS - SBR. Ammonia removal performance average of each model is 89.93-88.74%. Ammonia concentrations obtained are 9.1 and 15 mg/l in both models.

At the organic loading rate 1.5 kg COD/$m^3$.day, ammonia treatment efficiency begun to decrease compared with the previous loading. For model ICEAS - SBR ammonia treatment efficiency decreased 4.31%. For model ICEAS - MBSBR ammonia treatment efficiency decreased 4.58%. In this loading, we observed high nitrogen concentrations input led to higher output levels. The average ammonia concentration output 12.4 mg/l. Model ICEAS - MBSBR was still better.

In the organic loading rate 2.0 kg COD/$m^3$.day, ammonia treatment efficiency continued to decline compared to the previous loading. For model ICEAS - SBR ammonia treatment efficiency decreased 2.69%. For model ICEAS - MBSBR ammonia treatment efficiency decreased 2.25%. Model ICEAS - MBSBR was still for the performance of the process better. During this period the ammonia concentration was 14.5 mg/l.

In the organic loading rate 2.5 kg COD/m3.day, ammonia treatment efficiency at this loading went down compared to previous loading. For model ICEAS - SBR ammonia treatment efficiency fell 2.77%. For model ICEAS - MBSBR ammonia treatment efficiency decreased by 1.11%. Model ICEAS - MBSBR was still for performance of the process better than the model ICEAS - SBR. During this period the ammonia concentration was 15.8 mg/l (Table 2).

**Table 2.** Results $NH4^+$-N removal in each loading rate

| Organic loading rate, kg COD/m3.day | $NH_4^+$ influent, mg/l | $NH_4^+$ effluent, mg/l (ICEAS-SBR) | $NH_4^+$ effluent, mg/l (ICEAS-MBSBR) | Efficient, % (ICEAS-SBR) | Efficient, % (ICEAS-MBSBR) |
|---|---|---|---|---|---|
| 0.5 | 32.3 ± 2.1 | 5.6 ± 2.3 | 5.5 ± 2.4 | 83.00 ± 6.33 | 83.55 ± 6.49 |
| 1.0 | 65.4 ± 3.4 | 7.4 ± 1.6 | 6.6 ± 1.4 | 88.74 ± 2.12 | 89.93 ± 2.14 |
| 1.5 | 79.4 ± 2.4 | 12.4 ± 1.9 | 11.6 ± 1.9 | 84.43 ± 2.24 | 85.34 ± 2.23 |
| 2.0 | 82.5 ± 2.4 | 15.1 ± 2.3 | 13.9 ± 1.9 | 81.73 ± 2.82 | 83.10 ± 2.49 |
| 2.5 | 84.8 ± 2.1 | 16.4 ± 1.4 | 15.2 ± 1.4 | 80.62 ± 1.77 | 82.04 ± 1.86 |

### 3.3 Nitrate and Nitrite Concentration of ICEAS – SBR and ICEAS – MBSBR

Figure 4 shown nitrate and nitrite concentration effluent of ICEAS – SBR and ICEAS – MBSBR. Nitrite concentration influent was low. When the OLR increased, nitrite concentration also increased from 0.71 mg/l to 3.0 mg/l in OLR 2.5 kg COD/$m^3$.day. Similar, nitrate concentration increased from 1.31 to 4.51 mg/L in OLR 2.5 kg COD/$m^3$.day.

On the whole, nitrate removal efficient at ICEAS – MBSBR was higher than ICEAS – SBR. This result shown Mutag Biochip was good condition for nitrate removal efficient, so denitrification removal efficient also increased. Bioflim in Mutag Biochip carried out two process: nitration and denitrification.

ICEAS – MBSBR, both process: interrupted aeration and bioflim attachment were enhanced nitration and denitrification. But ICEAS – SBR only have interrupted aeration process enhanced nitration and denitrification. However, the difference between the ICEAS - MBSBR and ICEAS - SBR is about 3%.

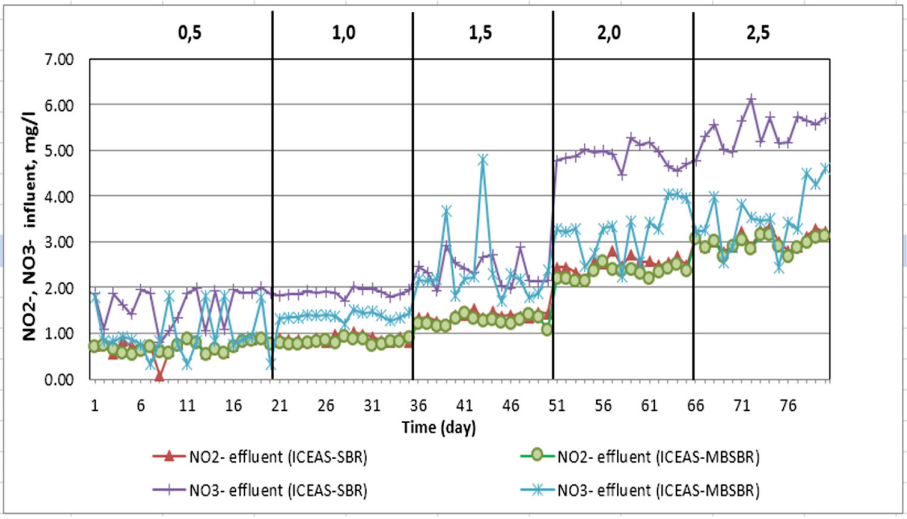


**Fig. 4.** Nitrate and nitrite concentration effluent of ICEAS – SBR and ICEAS – MBSBR

### 3.4 Organic Nitrogen Removal

Figure 5 shown organic nitrogen concentration inffluent so low, organic nitrogen removal efficient no stabilization. On the whole, organic nitrogen removal in ICEAS – MBSBR was higher than ICEAS – SBR equivalent 64.74 and 71.79%. The organic nitrogen degradation not high and do not affect to nitrogen removal efficient.

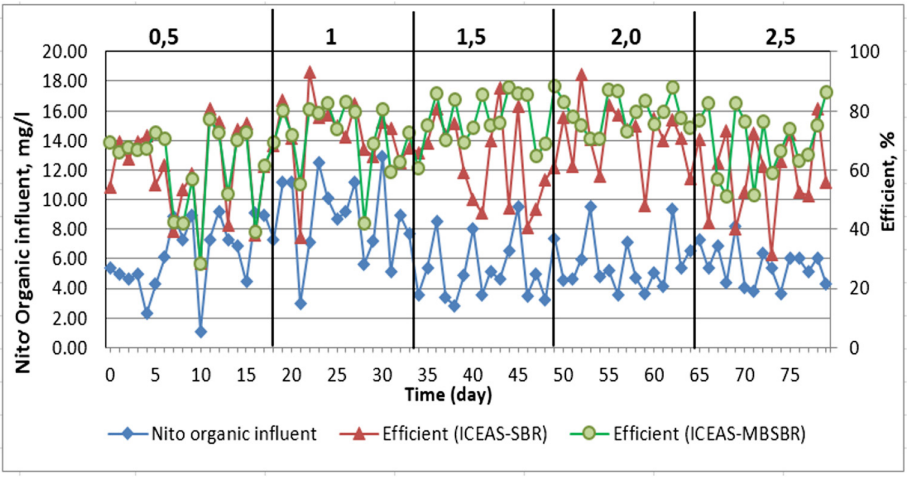


**Fig. 5.** TN removal efficient in different OLRs

### 3.5 Total Nitrogen Removal

Total nitrogen in wastewater include ammonia, nitrite, nitrate and organic nitrogen. In the metabolism process, organic nitrogen was decomposed into ammonia. Part of the ammonia would be involved in the construction process of microbial cells. However, most of nitrite and nitrate were used by the facultative anaerobic bacteria as electron acceptors in reaction energy harvesting. nitrogen gas is simultaneously formed and get out of the water environment. Research results showed that the model was capable of nitrogen removal efficiency. This could be explained the ammonia oxidizing bacteria and denitrification bacteria were increased by the intermittent aeration. Figures 3 and 6 shows ammonia removal efficiency of ICEAS – SBR model and ICEAS – MBSBR model. TN removal efficiency of ICEAS – MBSBR was always higher than ICEAS – SBR during operation. This showed that the ammonia metabolism in the model was occurred negligible and nitrate effluent because decreasing of nitrogen removal efficiency was increased by the nitrification (Table 3).

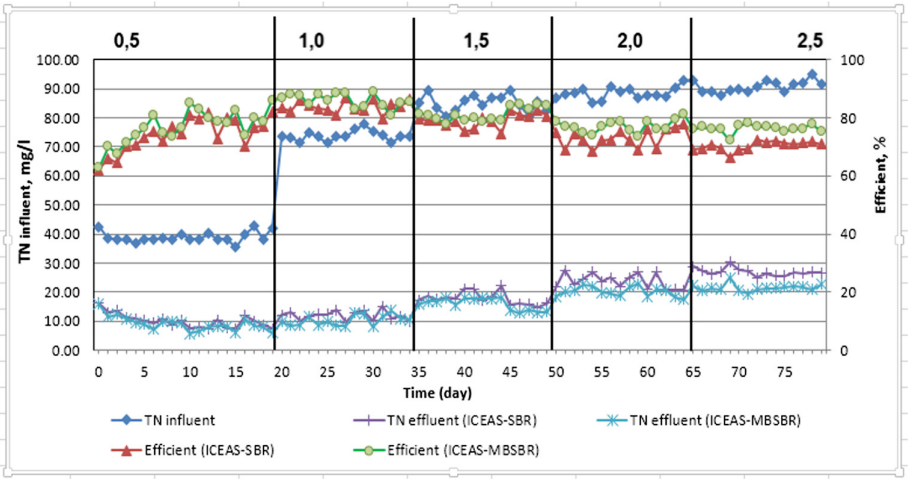


**Fig. 6.** Daily changes in TN removal efficiency at different OLRs of ICEAS – SBR and ICEAS – MBSBR

**Table 3.** TN removal efficiency at different OLRs

| Organic loading rate, kg COD/m3.day | TN influent, mg/l | TN effluent, mg/l (ICEAS-SBR) | TN effluent, mg/l (ICEAS-MBSBR) | Efficient, % (ICEAS-SBR) | Efficient, % (ICEAS-MBSBR) |
|---|---|---|---|---|---|
| 0.5 | 38.9 ± 1.8 | 10.0 ± 2.3 | 9.1 ± 2.4 | 74.28 ± 5.62 | 76.77 ± 5.73 |
| 1.0 | 73.8 ± 1.7 | 12.0 ± 1.5 | 10.3 ± 1.8 | 83.79 ± 2.00 | 86.11 ± 2.34 |
| 1.5 | 85.1 ± 2.7 | 17.8 ± 2.1 | 15.9 ± 2.0 | 79.07 ± 2.34 | 81.27 ± 2.34 |
| 2.0 | 88.5 ± 2.0 | 23.8 ± 2.4 | 20.2 ± 1.6 | 73.11 ± 2.98 | 77.15 ± 2.03 |

### 3.6 Biomass Concentration

Figure 7 illustrates MLSS in the end of each loading rate 0.5 – 2.5 kg COD/$m^3$.day of ICEAS – SBR and ICEAS – MBSBR with the seed MLSS being 2,200 mg/l. The formation of the biofilm on the surface and inside of Mutag Biochip$^{TM}$ media of ICEAS – MBSBR was observed. Generally, total biomass of ICEAS – MBSBR was always higher than ICEAS – SBR. In the beginning, biofilm formed slowly because it was very slight and easy to be broken by the media collision during aeration and stirring phase. The attached biomass in the end of 0.5 kg COD/$m^3$.day loading rate was 365 mg/l. In next period, attached biomass became subtain and developed while the loading rate increased. However, in 1.5; 2.0 and 2.5 kg COD/$m^3$.day loading rate, non-attached biomass of both systems increased slightly and the differences were small. Reversely, attached biomass of ICEAS – MBSBR in 3 last loading rate increased dramatically. MLSS in the end of each loading rate of ICEAS – SBR was 2,800, 3,320, 3,480, 3,800 mg/l, respectively; non-attached biomass of ICEAS – MBSBR was 2,650, 3,350, 3,500, 3,790, 4,050 mg/l and attached biomass was 365, 560, 875, 1,020, and 1,125 mg/l.

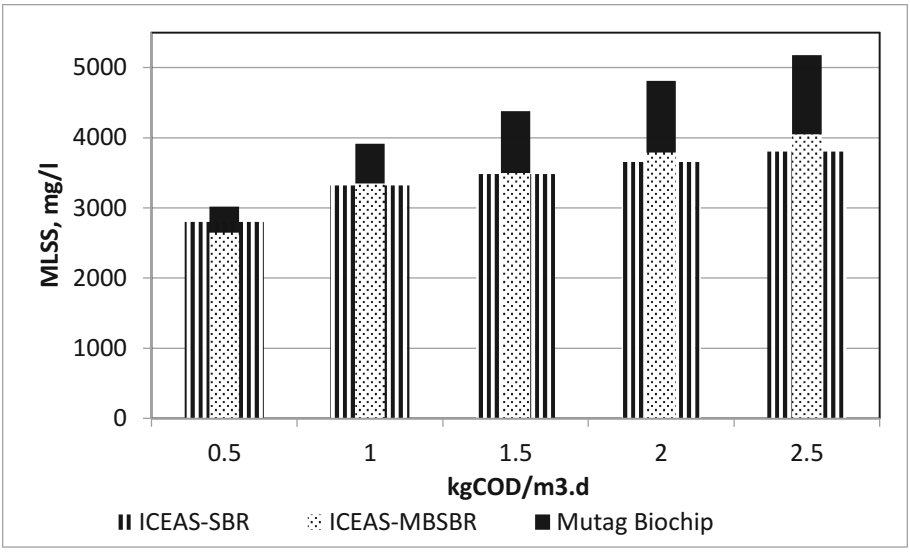


**Fig. 7.** Biomass concentration in ICEAS – SBR and suspended, adhesive biomass in ICEAS – MBSBR

## 4 Conclusions

Experimental study indicates that efficient treatment of ICEAS – MBSBR model is higher than ICEAS – SBR in term of COD and nitrogen removal when organic loading rate (OLR) at 0.5; 1.0; 1.5; 2.0; and 2.5 kg COD/$m^3$.day. Study also shows that

aeration and anoxic phase are suitable to treat wastewater with high nitrogen concentration. Biomass concentration attached on the surface of Mutag BiochipTM in ICEAS – MBSBR increased since organic loading rate increased. However, it was revealed that Mutag Biochip helped increasing COD and nitrogen removal efficient, but the difference between 2 conditions was not large.

## References

Johns, M.: Developments in wastewater treatment in the meat processing industry: a review. Bioresour. Technol. **54**, 203–216 (1995)

Ruiz, I., Veiga, M.C., De Santiago, P., Blazquez, R.: Treatment of slaughterhouse wastewater in a UASB reactor and an anaerobic filter. Bioresour. Technol. **60**(3), 251–258 (1997)

Wu, P., Mittal, G.: Characterization of provincially inspected slaughterhouse wastewater in Ontario. Canada. Can. Biosyst. Eng. **53**, 6.9–6.18 (2011)

Bustillo-Lecompte, C.F., Mehrvar, M., Quinones-Bolanos, E.: Cost-effectiveness analysis of TOC removal from slaughterhouse wastewater using combined anaerobic-aerobic and UV/H2O2 processes. J. Environ. Manag. **134**, 145–152 (2014)

Tritt, W.P., Schuchardt, F.: Materials flow and possibilities of treating liquid and solid wastes from slaughterhouses in Germany. A review. Bioresour. Technol. **41**(3), 235–245 (1992)

Masse, D.I., Masse, L.: Characterization of wastewater from hog slaughter-houses in Eastern Canada and evaluation of their in-plant wastewater treatment systems. Can. Agric. Eng. **42**(3), 139–146 (2000)

Debik, E., Coskun, T.: Use of the static granular bed reactor (SGBR) with anaerobic sludge to treat poultry slaughterhouse wastewater and kinetic modeling. Bioresour. Technol. **100**(11), 2777–2782 (2009)

Khararjian, H.A., Callaway, W.H., Cardinal, P., Meany, J.: Intermittent cycle extended aeration system (ICEAS R) for small wastewater treatment plants. Water Sci. Technol. **22**(3–4), 323–330 (1990)

Chen, A.C., Chang, J.S., Yang, L., Yang, Y.H.: Nitrogen removal from sewage by continuous flow SBR system with intermittent aeration. Environ. Technol. **22**(5), 553–559 (2001)

Lee, H., Brereton, J.A., Mavinic, D.S., Fiorante, R.A., Oldham, W.K., Paisley, J.K.: Nutrient removal with methanol as a carbon source full-scale continuous inflow SBR application. Environ. Technol. **22**(10), 1223–1235 (2001)

Li, H., Chen, Y., Gu, G., Liu, Y.: Phosphorous removal in intermittent cycle extended aeration system wastewater treatment plant - effect of temperature. In: Proceedings of the 2nd International Conference, Shanghai, pp. 2970–2973 (2008)

Sombatsompop, K., Songpim, A., Reabroi, S., Inkongngam, P.: A comparative study of sequencing batch reactor and moving-bed sequencing batch reactor for piggery wastewater treatment. Maejo Int. J. Sci. Technol. **5**(02), 191–203 (2011)

Lim, P.-E., Lim, J.-W., Seng, C.-E.: Enhancement of nitrogen removal in moving bed sequencing batch reactor with intermittent aeration during REACT period. J. Chem. Eng. **197**, 199–203 (2012)

Pastorelli, G., Canziani, R., Pedrazzi, L., Rozzi, A.: Phosphorus and nitrogen removal in moving-bed sequencing batch biofilm reactors. Water Sci. Technol. **40**(4–5), 169–176 (1999)

# Urban Stormwater Management by Green Infrastructure: Design and Comparison of Three Scenarios

Jean-Luc Bertrand-Krajewski[1(✉)] and Pauline Herrero[1,2]

[1] University of Lyon, INSA Lyon, Villeurbanne, France
jean-luc.bertrand-krajewski@insa-lyon.fr,
pauline.herrero.insa@gmail.com
[2] GRAIE, Villeurbanne, France

**Abstract.** Three scenarios for stormwater management in a 6.5 ha industrial area are investigated: (S1) separate stormwater pipe system with a downstream infiltration tank, (S2) succession of infiltration swales along roads and (S3) vegetated roofs and infiltration swales. Long-term simulations of the three scenarios are carried out with 6 min time step rainfall and evapotranspiration time series over 21 years (1992–2012). The model combines the Canoé® software for sewers and Matlab® codes for infiltration tank, infiltration swales and vegetated roofs. In scenario S1, the separate stormwater network includes 535 m of pipes and a 1600 $m^3$ downstream infiltration tank. In scenario S3, all roofs are vegetated, with a storage capacity of 32 $mm/m^2$, allowing to divide by two the total length of swales compared to scenario S2 (408 m and 203 m respectively) with impervious roofs. Vegetated roofs allow a mean decrease of 42% of the annual runoff volume. Continuous simulations allow to study in detail the hydrological behavior of the infrastructures at all time scales (from the time step to multi-year scales) and analyze statistically the results.

**Keywords:** Urban stormwater · Infiltration · Evapotranspiration · Modelling · Design · Green roofs · Swales

## 1 Introduction

Traditional sewer pipe systems (i.e. grey infrastructure) are no longer the single approach to manage urban stormwater. Green infrastructures (e.g. green roofs, swales, raingardens, etc.), among other Sustainable Urban Drainage Systems (SUDS) (Fletcher et al. 2015), offer better options for integrated approaches combining stormwater management, pollutant control, landscaping, biodiversity, liveability in cities, etc. (Dover 2015). Their comparative advantage and their possible combination with grey infrastructure has been investigated by several authors, with a diversity of approaches (e.g. De Sousa et al. 2012; Wang et al. 2013; Casal Campos et al. 2015). Modelling green infrastructure, especially green roofs, is an active field, from empirical to physically based models (e.g. Zimmer and Geiger 1997; Palla et al. 2012; Loc et al. 2015).

In this paper, three scenarios for stormwater management in a densely urbanized 6.5 ha industrial area are investigated:

© Springer Nature Singapore Pte Ltd. 2018
H. Tran-Nguyen et al. (eds.), *Proceedings of the 4th Congrès International de Géotechnique - Ouvrages -Structures*, Lecture Notes in Civil Engineering 8,
DOI 10.1007/978-981-10-6713-6_109

- Scenario S1: a separate stormwater pipe system with a downstream infiltration tank
- Scenario S2: a succession of infiltration swales along roads
- Scenario S3: vegetated roofs and infiltration swales.

The conditions and aims of the study were the following ones:

- Use a real case as a basis for scenario comparison
- Design the infrastructures of the three scenarios with the same design rainfall
- Simulate the behavior of the infrastructures for the three scenarios over a long period
- Compare the results according to a set of evaluation criteria.

The following sections present successively the case study site, the data, the methods and the models used, and some of the main results obtained.

## 2 Data and Methods

### 2.1 Case Study Site

The case study site is a flat 6.5 ha area, located 34 km north-east of Lyon, France, progressively urbanized since 2006, with various light industry and workshops activities including carpentry, public works company, car repair, metal working, hardware store, retail stores, swimming pool equipment, offices for tertiary activities (informatics, consulting, etc.). It is almost entirely impervious (roads, parking lots, handling and storage areas, and roofs). The soil is composed of sandy gravels fluvio-glacial alluvium. *In situ* field measurements by means of Porchet tests indicate a high soil hydraulic conductivity from $0.6 \times 10^{-3}$ m/s to $1 \times 10^{-3}$ m/s (Lozano and Landry 2005). The thickness of the non-saturated layer of soil above the local groundwater is 5–6 m. Both hydraulic conductivity and non-saturated zone allow rapid and efficient stormwater infiltration. The main characteristics of the catchment are summarized in Table 1 (the total surface is 5.85 ha, which is less than 6.5 ha as some surfaces are not connected to the stormwater system).

**Table 1.** Main characteristics of the catchment

| Type of surface | Surface (ha) | Runoff coefficient (-) |
|---|---|---|
| Roads | 1.23 | 0.95 |
| Roofs | 3.23 | 0.95 |
| Parking and other impervious areas | 1.39 | 0.70 |
| Total | 5.85 | – |

In scenario S1, the runoff from all roofs, roads, parking and other impervious surfaces (handling and storage areas) is collected in a separate stormwater network of circular pipes. The catchment is divided in 13 sub-catchments, according to the initial design of the industrial area in 2006. An infiltration tank is located at the outlet of the network.

In scenario S2, all pipes are replaced by a succession of infiltration swales built along the roads. The swales collect the runoff from all roofs, roads, parking and other impervious surfaces. There is one swale per sub-catchment. The last swale may overflow into a downstream infiltration tank.

In scenario S3, all roofs are replaced by vegetated roofs which store and evapotranspirate the rainwater. In case the vegetated roofs are saturated, they discharge into the nearest infiltration swales which also collect the runoff from all roads, parking and other impervious surfaces. In case of saturation of both roofs and swales, the excess runoff is discharged into a downstream infiltration tank.

The site is used as a real basis for this case study. However, as none of the above scenarios is implemented in reality, there are no field data to verify the modelling results. The real system includes pipes with a downstream infiltration tank, runoff from impervious roofs is infiltrated locally, and no monitoring data exist.

### 2.2 Models

For S1, the rainfall runoff process in the 13 sub-catchments and the runoff transfer in the pipes are simulated with the Canoé® commercial software (Chocat 2014). As the network is a simple converging structure without backwater effect, the simple Muskingum model is used to simulate the hydraulics in the sewer system. Main parameters of the model (imperviousness, sub-catchment runoff coefficient and Muskingum parameters) are set to the previous values used by the consulting company SEDic in 2006 when they designed the sewer system.

For S2 and S3, the authors developed a specific Matlab® code to simulate infiltration swales. The model includes inflows, outflows and storage in swales, coupled to infiltration and evaporation processes. Infiltration is represented by the simplified Darcy equation where infiltration per unit length is proportional to the swale wet perimeter and to the hydraulic conductivity. Hydraulic conductivity has been set to the lowest measured value $0.6 \times 10^{-3}$ m/s (Lozano and Landry 2005). Evaporation is calculated according to Horton and Magnus equations (Llamas 1993), where input data have been given by the local Météo France station. Details of the model are given in Bertrand-Krajewski and Herrero (2016). The same code is used to simulate the downstream infiltration tank for all three scenarios. The swales are described in a simple way: they have a constant rectangular cross section, a width of 2.5 m and a maximum depth of 0.5 m before overflow can start. A swale starts to discharge into the downstream swale when the water depth reaches 0.4 m. The discharge is calculated with a standard broadcrested weir equation. Evapotranspiration in swales is neglected.

For S3, the vegetated roofs are assumed to be built with standard Hydropack® units (http://www.vegetalid.us/green-roof-solutions/green-roofs.html). A Hydropack® unit is a pre-vegetated tray with a 60 mm thick artificial substrate with additional cells under the substrate layer to increase the water storage. The cells contain clay pellets to allow the stored water to be lifted back to the substrate by the vegetation roots (sedum) for evapotranspiration. A Matlab® code has been developed to simulate Hydropack® vegetated roofs. It includes the following processes: interception by vegetation, evaporation and evapotranspiration, gravity flow through the substrate, storage in the substrate and in the underlying cells, backflow from cells for evapotranspiration. It has

been previously tested and calibrated with 50 rainfall events monitored at 1 min time step on a pilot scale vegetated roof (Principato 2015; Principato et al. 2015). For 39 events among 50, calibration Nash-Sutcliffe coefficients are above 0.6, and above 0.97 for 23 events. This indicates the ability of the model to simulate Hydropack® green roofs. For the continuous simulation of this case study, mean values of the parameters calibrated for the pilot scale vegetated roof are used.

### 2.3 Data for Design and Simulation

For S1, all pipes have been designed with the symmetric double triangular design rainfall used for the initial project in 2006. The design rainfall has a duration of 2.5 h, a total depth of 39.2 mm and a maximum intensity of 115 mm/h. The central intense period has a duration of 18 min and a depth of 20.5 mm. The return period is 7 years for the entire duration of 2.5 h and 10 years for the intense period of 18 min.

The same design rainfall has also been used to design the swales for S2 and S3. The length of the swales is calculated to have no overflow from any swale for the design rainfall, with the assumption that all swales are empty when the rainfall starts. The volume of the downstream infiltration tank is designed to correspond to a maximum water depth of 1.5 m before overflow can start.

Contrarily to swales, the vegetated roofs are not designed with the design rainfall in S3. Standard Hydropack® units with a maximum storage capacity of 32 mm are assumed to be installed on the roofs. This is close to but lower than the design rainfall depth (39.2 mm), which means that green roofs in S3 may discharge into the swales before the design rainfall depth is reached.

Data from the nearest Météo France station in Lyon, France have been used to build three continuous 21 years long times series with a 6 min time step for the period 1992–2012, for rainfall, potential evapotranspiration and evaporation respectively. The annual rainfall depth varies from 722 mm (in 2011) to 1,168 mm (in 1993), with a mean value of 886 mm. Two events are considered as separate events if the dry period is longer than 2 h. With this separation criterion, the rainfall series contains 5,031 events, 2,432 of them with a rainfall depth greater than 1 mm and 1,739 events with a depth higher than 2 mm. Potential evapotranspiration is calculated with the standard Penman-Monteith equation (Zotarelli et al. 2014).

### 2.4 Evaluation Criteria

To compare the three scenarios in terms of design (size of the facilities) and annual hydrological performance, a set of evaluation criteria is defined, with the following elements: length of sewer pipes, length of infiltration swales, volume of the downstream infiltration tank, amount of land needed for infiltration tank and swales, and annual hydrological mass balance.

# 3 Results and Discussion

## 3.1 Design

The design of all infrastructures for the three scenarios is given in Table 2. The length of underground public sewer pipes is 535 m (diameters from 400 to 600 mm) for S1, and zero for S2 and S3. This length of public sewer pipes does not include the length of the private pipes to transfer the water from each impervious surface to the public sewer system. The length of infiltration swales is 408 m and 203 m for S2 and S3 respectively, and zero for S1. Replacing traditional impervious roofs by vegetated roofs (32,300 $m^2$) leads to a 50% decrease of the length of swales. This significant decrease corresponds to the roof ratio (total surface of roofs divided by the catchment surface) which is approximately 50% in this case (see Table 1). The benefit of vegetated roofs is reduced if the roof ratio decreases. But in most urbanized areas the roof ratio ranges from 40% to 60%. This case study is therefore representative.

**Table 2.** Infrastructures design for the three scenarios

| | Scenario 1 | Scenario 2 | Scenario 3 |
|---|---|---|---|
| Length of pipes (m) | 535 | 0 | 0 |
| Length of infiltration swales (m) | 0 | 408 | 203 |
| Surface of vegetated roofs ($m^2$) | 0 | 0 | 32,300 |
| Volume of downstream infiltration tank ($m^3$) | 1,600 | 30 | 20 |
| Amount of land for infiltration tank and swales ($m^2$) | 1,067 | 1,040 | 521 |

The volume of the downstream infiltration tank is large for S1 (1,600 $m^3$) as it receives all runoff from the entire catchment. It dramatically decreases for S2 and S3 (30 $m^3$ and 20 $m^3$ respectively). A modified design of the most downstream swale would allow to completely eliminate the need of the infiltration tank for S2 and S3. The amount of land for infrastructures is similar for S1 (1,067 $m^2$) and S2 (1,040 $m^2$): the amount of land required by the downstream tank in S1 is equivalent to the amount of land required by the swales in S2. The decrease is approximately 50% for S3 (521 $m^2$), as swales are replaced by the vegetated roof surfaces. Vegetated roofs make more surface available in the catchment for other land uses (additional business plots, landscaping and recreational areas, etc.) which may partly compensate for the additional costs of vegetated roofs compared to traditional impervious roofs.

## 3.2 Hydrological Mass Balance

The annual hydrological mass balances are shown in Fig. 1. For S1 (graph 1a), the annual volume *VinfB* infiltrated by the downstream infiltration tank corresponds to the total annual runoff volume, which itself closely corresponds to the annual rainfall depth. It ranges from 38,260 $m^3$ (year 2011) to 61,890 $m^3$ (year 1993), with a mean value of 46,940 $m^3$.

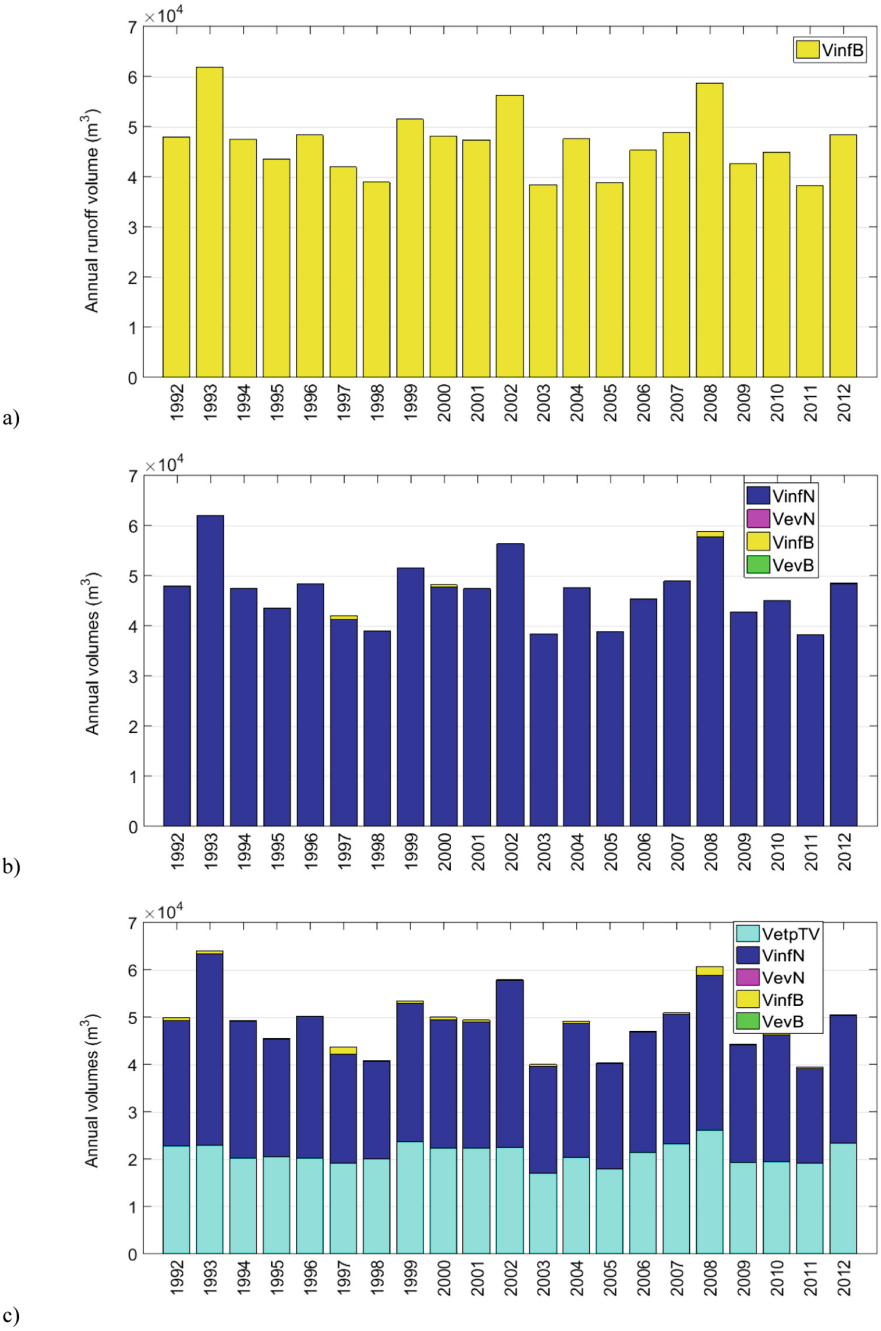


**Fig. 1.** Annual hydrological mass balance, from a to c for scenarios 1 to 3 respectively. *VinfB*: volume infiltrated in downstream tank, *VinfN*: volume infiltrated in swales, *VevN*: volume evaporated in swales, *VevB*: volume evaporated in downstream tank and *VetpTV*: volume evapotranspirated by vegetated roofs.

For S2 (graph 1b), the annual volume has four components: *VinfN* and *VevN* are the volumes respectively infiltrated and evaporated by the swales; *VinfB* and *VevB* are the volumes respectively infiltrated and evaporated by the downstream tank. The total annual volume ranges from 38,330 $m^3$ (year 2011) to 62,010 $m^3$ (year 1993), with a mean value of 47,000 $m^3$. The minor differences (mean relative difference is +0.13% of annual total volume) compared to S1 are due to minor differences in rainfall loss processes between Canoé® and the Matlab® code: they are negligible. *VinfN* is clearly the predominant component in S2 and is close to *VinfB* in S1. For three years only (1997, 2000 and 2008), *VinfB* is not negligible and respectively equal to 791, 386 and 971 $m^3$. (i.e. 1.9, 0.8 and 1.7% of the annual total volume). Over 21 years, *VinfB* ranges from 15 to 971 $m^3$, with a mean value of 118 $m^3$. It corresponds to the volume discharged from the last swale into the downstream tank. An adaptation of the last swale would allow to eliminate the need for the downstream tank. *VevN* and *VevB* are negligible components compared to infiltrated volumes. In this case, the model could be simplified and the evaporation process could be neglected, as in S1.

For S3, a fifth component is added: *VetpTV* is the volume evapotranspirated by the vegetated roofs. The total annual volumes are larger (min = 39,430 $m^3$, max = 64,050 $m^3$, mean = 48,740 $m^3$) than in S1 and S2: this difference (mean value is +3.7%) is due to the fact that in S1 and S2, the runoff over the impervious roofs is affected by a runoff coefficient of 0.95 (see Table 1) in Canoé®, while in the Matlab® code for the vegetated roofs all the rainfall is accounted for in the calculation (which is equivalent to a virtual runoff coefficient of 1). *VinfN* ranges from 19,970 $m^3$ in 2011 to 40,410 $m^3$, which corresponds to a decrease of respectively 48% and 32% compared to S2. Over the 21 years, the mean *VinfN* is equal to 27,170 $m^3$, i.e. a mean 42% decrease compared to S2, provided by the vegetated roofs. Indeed, *VetpTV* varies from 17,020 $m^3$ in 2003 to 26,130 $m^3$ in 2008 (mean value = 21,160 $m^3$). Clearly, storage in and evapotranspiration by vegetated roofs is a significant component in the annual mass balance for S3.

In S2, the swales receive runoff from all impervious surfaces, including roofs. In S3, roofs are vegetated and swales receives only runoff from other impervious surfaces (roads, parking lots, handling and storage areas). As the vegetated roofs in S3 have a maximum storage capacity of 32 mm, i.e. 7.2 mm less than the swales they replace (design rainfall depth for swales is 39.2 mm), they discharge into the swales when they are saturated for a variable few number of events each year. Consequently, as the swales in S3 have not been designed to account for this additional volume discharged by the vegetated roofs, they overflow more into the downstream tank: *VinfB* is not negligible for 13 years among 21 (from 38 $m^3$ in 2005 to 760 $m^3$ in 2008, mean value is 420 $m^3$) in S3, compared to only 3 years among 21 in S2.

### 3.3 Event Scale Analysis of Vegetated Roofs

For most of the 5,031 rainfall events in the period 1992–2012 in S3, the total rainfall depth is stored in and evapotranspirated by the vegetated roofs, with no outflow into the swales. There is a roof outflow only when the vegetated roof is saturated. The water content of the vegetated roofs varies at the beginning of each rainfall event, as it depends on the succession of antecedent dry periods and previous events.

Evapotranspiration is mainly observed during dry periods after and between rainfall events. This is why continuous modelling is necessary to account for these processes and why traditional event scale modelling is not appropriate for green infrastructures. As a consequence, it is not possible to define a unique rainfall depth threshold ensuring no outflow from the vegetated roofs (Bertrand-Krajewski and Vacherie 2014).

Figure 2 illustrates the behavior of both the impervious roof (scenario S1) and the vegetated roof (scenario S3) of the sub-catchment n° 1 (area = 3,834 $m^2$) in case of the strong rainfall event dated 5–6 December 2006. This event has the following characteristics: beginning on 5 Dec. at 23:24, end on 6 Dec. at 11:54, duration 12.6 h, depth 48 mm, return period less than 2 years.

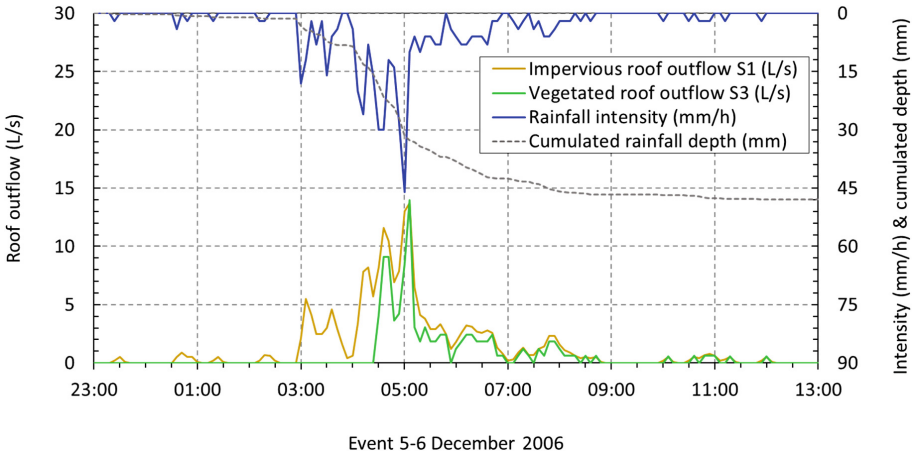


**Fig. 2.** Outflow from the roof of sub-catchment n° 1, event 5–6 December 2006, scenarios S1 and S3.

For S1, the impervious roof outflow closely reflects the rainfall intensity. For S3, the vegetated roof outflow is zero until 04:24: the first 15.6 mm of rain are entirely stored in the vegetated roof. From 04:30, the vegetated roof discharges into the swale n° 1, with an outflow close to the outflow from the impervious roof in S1 as the saturated vegetated roof behaves like an impervious roof. However, the vegetated roof outflow is lower than the outflow from the impervious roof because the water needs to percolate by gravity through the substrate before being discharged into the roof gutter. This leads to lower peak values and some delay in the outflow in S3 compared to S1.

## 4 Conclusion

Three scenarios for stormwater management in a 6.5 ha industrial are compared: one scenario with standard grey infrastructure (S1: sewer pipes), two scenarios with green infrastructures (S2: infiltration swales, S3: infiltration swales and vegetated roofs). They are simulated with rainfall and evapotranspiration continuous times series over a

period of 21 years (1992–2012) with a 6 min time step. The pre-design of the infrastructures (except vegetated roofs) is done with a standard double triangular design storm with a 7 to 10 years return period.

The three scenarios correspond to very different sizes of infrastructures: 535 m of public sewer pipes in S1, 408 m and 203 m of swales in S2 and S3 respectively, 32,300 $m^2$ of vegetated roofs in S3. The downstream infiltration tank for scenarios S1 to S3 has a volume of 1,600 $m^3$, 30 $m^3$ and 20 $m^3$ respectively. The vegetated roofs in S3 allow to divide by two the length of infiltration swales compared to S2. In addition, the vegetated roofs lead to a mean 42% decrease of the annual runoff volume to be infiltrated by the swales in S2. They have a significant positive effect on the annual hydrological mass balance.

Long term continuous simulation at short time steps allows to analyze in detail the behavior of all infrastructures, and especially the vegetated roofs which have a 32 mm storage capacity and a high potential of evapotranspiration, which significantly reduces the runoff to be dealt with in swales. Detailed analyses at all time scales from a few minutes to decades are possible, contrarily to standard design with a single non-realistic design rainfall event. In scenarios 2 and 3, green infrastructures (swales, vegetated roofs) appear as efficient to manage stormwater at the catchment scale in a highly impervious area. In addition, they offer added values (less pollutant transfers, interception of pollutants, higher landscape quality, increased building quality with green roofs, etc.) compared to grey infrastructure.

**Acknowledgements.** The authors thank the consulting company SEDic for having provided the case study data set. The meteorological data have been provided by Météo France as part of an agreement with the laboratory DEEP at INSA Lyon for education and research purposes.

## References

Bertrand-Krajewski, J.-L., Herrero, P.: Comparaison de différentes solutions de gestion des eaux pluviales dans un projet d'aménagement. TSM **4**, 28–41 (2016). (in French)

Bertrand-Krajewski, J.-L., Vacherie, S.: Projet ECCLAIRA – Rapport de fin de contrat – Partie INSA Lyon LGCIE-DEEP: suivi expérimental de la toiture végétalisée du Centre de Congrès de Lyon, LGCIE-DEEP, Version finale révisée et actualisée. INSA Lyon, Villeurbanne (2014). 24 pages (in French)

Casal Campos, A., Fu, G., Butler, D., Moore, A.: An integrated environmental assessment of green and gray infrastructure strategies for robust decision making. Environ. Sci. Technol. **49** (14), 8307–8314 (2015)

Chocat, B.: Notice Canoé – Version 3. Villeurbanne (France): INSA Lyon – Sogreah – Alison (2014). 477 pages (in French). http://www.canoe-hydro.com/public/archives/notice_canoe_v3.pdf. Accessed 27 Mar 2017

De Sousa, M.R.C., Montalto, F.A., Spatari, S.: Using life cycle assessment to evaluate green and grey combined sewer overflow control strategies. J. Ind. Ecol. **16**(6), 901–913 (2012)

Dover, J.W.: Green Infrastructure. Routledge, Oxon (2015)

Fletcher, T.D., Shuster, W., Hunt, W.F., Ashley, R., Butler, D., Arthur, S., Trowsdale, S., Barraud, S., Semadeni-Davies, A., Bertrand-Krajewski, J.-L., Mikkelsen, P.S., Rivard, G., Uhl, M., Dagenais, D., Viklander, M.: SUDS, LID, BMPs, WSUD and more - the evolution and application of terminology surrounding urban drainage. Urban Water J. **12**(7), 525–542 (2015)

Llamas, J.: Hydrologie générale: principes et applications. Gaëtan Morin Editeur, Boucherville (1993)

Loc, H.H., Babel, M.S., Weesakul, S., Irvine, K.N., Duyen, P.M.: Exploratory assessment of SUDS feasibility in Nhieu Loc-Thi Nghe basin, Ho Chi Minh City, Vietnam. Br. J. Environ. Clim. Change **5**(2), 91–103 (2015)

Lozano, C., Landry, P.: Aménagement d'une zone d'activités Route de Charmoz, commune de Meximieux (01) - Etude de faisabilité géotechnique, missions géotechniques normalisées type G0 – G11. Ain Géotechnique, rapport technique, Oyonnax (2005). 12 pages (in French)

Palla, A., Gnecco, I., Lanza, L.G.: Compared performance of a conceptual and a mechanistic hydrologic models of a green roof. Hydrol. Process. **26**(1), 73–84 (2012)

Principato, F.: Vegetated roofs as a Low Impact Development (LID) approach: hydrologic and hydraulic modelling for stormwater runoff mitigation in urban environment. Ph.D. thesis, Universita della Calabria, Rende, Italy (2015). 160 pages

Principato, F., Piro, P., Grimard, J.-C., Bertrand-Krajewski, J.-L.: Test of a vegetated roof hydrological model with two experimental data sets. In: Proceedings of the 10th UDM - International Conference on Urban Drainage Modelling, Mont Sainte Anne, Quebec, Canada, Oral Presentations I, 20–23 September 2015, pp. 207–210 (2015)

Wang, R., Eckelman, M.J., Zimmerman, J.B.: Consequential environmental and economic life cycle assessment of green and gray stormwater infrastructures for combined sewer systems. Environ. Sci. Technol. **47**(19), 11189–11198 (2013)

Zimmer, U., Geiger, W.F.: Model for the design of multi-layered infiltration systems. Water Sci. Technol. **36**(8–9), 301–306 (1997)

Zotarelli, L., Dukes, M.D., Romero, C.C., Migliaccio, K.W., Morgan, K.T.: Step by step calculation of the Penman-Monteith evapotranspiration (FAO-56 method). Institute of Food and Agricultural Sciences, University of Florida, USA, document AE459 (2014). 10 pages. https://edis.ifas.ufl.edu/pdffiles/AE/AE45900.pdf. Accessed 27 Mar 2017

# Case Studies (CS)

# Behavior of Prestressed Concrete Self-stabilizing Floating Fuel Storage Tanks

D. Jiang(✉), K.H. Tan, K.C.G. Ong, S. Heng, J. Dai, B.K. Lim, and K.K. Ang

Department of Civil and Environmental Engineering, National University of Singapore, Singapore, Singapore
{ceejd, tankh, ceeongkc, sonalheng, ceelbk, kk_ang}@nus.edu.sg

**Abstract.** Prestressed concrete (PC) cylindrical tanks are used in industrial applications as liquid containing facilities, and are commonly constructed as base-supported structures with their associated foundations poured in place. In land-space constrained countries, however, it becomes viable to construct such facilities on sea as floating structures. This study deals with the design of an innovative self-stabilizing floating fuel storage tank. For this new type of fuel storage facility, the self-weight of the tank and the in-fill fuel are automatically balanced by the buoyancy force, and there is no need for vertical supporting foundations. Furthermore, the hydrostatic pressures on the tank wall due to outside sea water and in-fill fuel balance each other to a great extent, leading to significant reduction in material consumption and construction costs. Due to the absence of specific guidelines and engineering practices, it remains unknown whether PC floating self-stabilizing fuel storage tanks are applicable in the offshore environment. In this study, a comprehensive stability analysis was first carried out to determine the geometrical dimensions for tanks of different capacities varying from 5,000 $m^3$ to 15,000 $m^3$ in order to meet the operational requirements. Finite element (FE) models were then developed to assess the structural performance of a selected tank of 12,500 $m^3$ capacity when subjected to self-weight and hydrostatic pressure. Based on the analytical results, potential technical challenges were identified and design recommendations were further provided.

**Keywords:** Design · Floating structures · Fuel storage tanks · Prestressed concrete · Stability analysis · Structural analysis

## 1 Introduction

For many metropolis in coastal areas, there is an increasing need for space development to accommodate excessive industry facilities, such as fuel storage tanks, power stations, wind turbines and others. In order to address the issue of land scarcity, it becomes preferable to construct these facilities in seawater areas as floating structures. Two notable floating hydrocarbon storage facilities, the Kamigoto Oil Storage Base and the Shirashima Oil Storage Base, are located in Japan. They are composed of several huge steel oil reservoirs, each measuring up to 397 m in length. In the deep seawater area of

© Springer Nature Singapore Pte Ltd. 2018
H. Tran-Nguyen et al. (eds.), *Proceedings of the 4th Congrès International de Géotechnique - Ouvrages -Structures*, Lecture Notes in Civil Engineering 8,
DOI 10.1007/978-981-10-6713-6_110

the North Sea, many concrete floating structures, such as the Heidrun Platform and the Troll Oje's Platform, for oil exploration and production have been implemented in the past forty years. However, up to the present, no operational concrete floating platforms for fuel storage in shallow waters have been constructed.

In this study, an innovative self-stabilizing floating storage tank was proposed for use in shallow waters. A comprehensive stability analysis was carried out to determine geometrical parameters applicable for tank designs with different fuel capacities. Finite element (FE) models were then developed to assess the structural performance of a selected tank when subjected to self-weight and hydrostatic pressure. Based on the analytical results, potential technical challenges were identified and design recommendations were further provided.

## 2 Design Concepts of Self-stabilizing Fuel Storage Tanks

Unlike the monolithic oil reservoirs employed in the Kamigoto and Shirashima Oil Bases, the proposed Floating Hydrocarbon Storage/Bunker Facility (FHSBF) comprises an arrangement of free floating tanks enclosed by spacers and barges which are in turn laterally restrained by mooring rubber-fender-dolphin systems. In this case, the space for water ballasting can be saved and FHSBF is more easily assembled and disassembled. The individual tanks are to be designed to be self-stabilizing and the maximum tilt angle under environmental loads does not exceed allowable limits. In order to achieve larger buoyancy and better stability performance, two different tank design concepts, either double-hull or single-hull structure, were developed, as shown in Fig. 1.

(a) Square-circular double-hull structure

(b) Circular sing-hull with floaters

**Fig. 1.** Design concepts of self-stabilizing fuel storage tanks.

The idea of a square-circular double-hull structure has reference or makes reference to the design of ship structures. The void between inner and outer walls provides not only extra buoyancy force but space to house operation facilities, such as manifolds, control center, pump rooms and others. An alternative option is to utilize single-hull structure, which enjoys the advantages of easy construction and smaller hydrostatic pressure differences on both sides of the tank wall. Four floaters are attached to the single-hull cylindrical tank at the four corners, which can improve stability performance and be used to interact with rubber fenders installed on the sides of floating barges. The performance of the two design concepts are evaluated by further stability and structural analyses, as described in the next two sections.

# 3 Stability Analysis

## 3.1 Design Criteria

The floating self-stabilizing fuel storage tanks should be designed to satisfy displacement limitations. Since no codes or standards are available for the stability analysis of floating tanks, design guidelines and specifications for offshore vessels are referred to identify critical limiting values of tank motions (Jensen et al. 1991; Veritas 2001). Established design criteria are listed as follows and will be used to evaluate the stability performance of tank designs with different geometric dimensions.

(i) The initial metacentric height ($GM_0$) of moored tanks shall not be smaller than 0.15 m;
(ii) Rotational (roll/pitch/yaw) motions of moored tanks shall not exceed 2° under working environmental conditions;
(iii) Rotational (roll/pitch/yaw) movements of moored floating tanks shall not exceed 5° under extreme environmental conditions.

## 3.2 Methodology and Formulation

Figure 2 shows the locations of the tank's center of gravity ($\overline{CG}$), center of buoyancy ($\overline{CB}$) and metacenter at upright and tilted position. The initial metacentric height can be determined from Eq. (1).

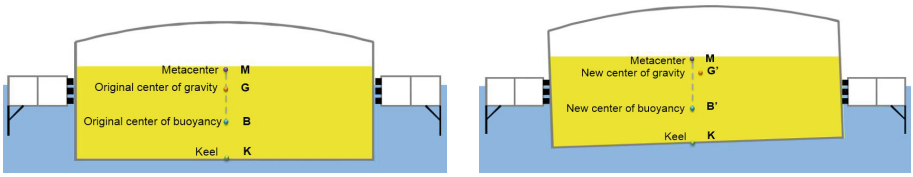


(a) Floating tank at the upright position (b) Floating tank at the tilted position

**Fig. 2.** Self-stabilizing floating tank at upright and tilted positions.

$$\overline{GM_0} = \overline{KB} + \overline{BM} - \overline{KG} \tag{1}$$

where $\overline{KB}$ is the height of the buoyancy center, $\overline{KG}$ is the center of gravity, $\overline{BM}$ is the metacentric radius which is given by Eq. (2).

$$\overline{BM} = \frac{I_O}{V} \tag{2}$$

where $I_O$ is the second moment of area of the water plane, and $V$ is the displaced water volume. When the tank is filled with hydrocarbon products, the free surface of the

stored find tends to raise the gravity center as shown in Fig. 2(b). The virtual rise in $\overline{CG}$ due to free surface effects may be expressed as Eq. (3).

$$\overline{GG'} = \frac{\rho_{fuel}}{\rho_{water}} \frac{I_i}{V} \tag{3}$$

where $\rho_{fuel}$ and $\rho_{water}$ denote the densities of fuel and water, respectively; and $I_i$ is the second moment of area of the fuel plane. The metacentric height shall then be replaced with $\overline{G'M_0}$.

Since incoming wave loads are resisted by the surrounding floating barges, only wind and water current loads are taken into consideration in the stability analysis. According to DNV standards (Veritas 2011, 2013), wind and current loads can be assumed as uniform pressures on the tank wall. Note that rubber fenders on floating barges are designed to restrain the horizontal motion within prescribed limits. Thus only angular movement, i.e. tilting motion, will be studied herein.

Figure 3 shows the forces acting on the floating storage tank. Point A denotes the intersection between the resultant rubber fender reaction force and the metacentric radius ($\overline{BM}$). Static equilibrium of moments is expressed in Eq. (4).

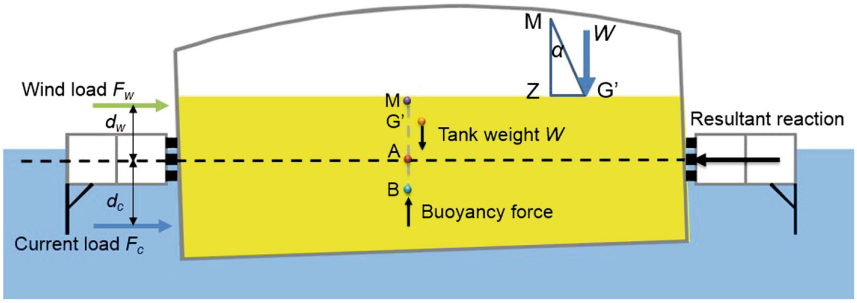


**Fig. 3.** Forces acting on floating fuel storage tanks.

$$W \times \overline{GM} \tan \alpha = |F_w d_w| + |F_c d_c| \tag{4}$$

where $W$ is the weight of the tank, $\alpha$ is the tilt angle due to sustained wind and current loads, $d_w$ and $d_c$ are the lever arms from the wind/current load center to point A, $F_w$ and $F_c$ are the resultant wind and current load actions on the tank, respectively; $F_c = \frac{1}{2}\rho_{water} v_c^2 A_c C_{DS}$ and $F_w = \frac{1}{2}\rho_{air} v_w^2 A_w C_S C_h$, are parameters defined in the DNV codes of practice (Veritas 2011, 2013).

### 3.3 Hydrostatic Analysis of Floating Storage Tanks Under Wind and Current Loads

Table 1 lists the material properties and basic geometric information adopted in the stability analysis, which are determined on the basis of clients' inputs and engineering judgement. In the analysis, two load combinations, wind and current loads in the same and opposite directions, are considered to achieve the most adverse load effects. Wind speeds with 1-year and 100-year return periods are taken as 15.9 m/s and 24.0 m/s, respectively. As for the current speed, 1-year and 100-year values are 1.46 m/s and 1.90 m/s.

**Table 1.** Material and geometric properties of individual fuel storage tanks

| Material Properties | | Geometric properties (Double-hull) | | Geometric properties (Single-hull) | |
|---|---|---|---|---|---|
| Parameter | Value | Parameter | Value | Parameter | Value |
| Concrete density | 1800 kg/m$^3$ | Outer wall thickness | 450 mm | Wall thickness | 450 mm |
| Seawater density | 1025 kg/m$^3$ | Inner wall thickness | 450 mm | Floater thickness | 500 mm |
| Fuel density | 870 kg/m$^3$ | Dome roof thickness | 200 mm | Dome roof thickness | 200 mm |
| Air density | 1.25 kg/m$^3$ | Base slab thickness | 750 mm | Base slab thickness | 750 mm |
| | | Stiffener thickness | 350 mm | | |

**Square-Circular Double-Hull Structures**

A wide range of tank dimensions was studied and results were categorized with different *L/D* & *D/H* ratios, where *L* is the length of the outer wall, *D* is the diameter of the inner wall, and *H* the total height of the tank. Figure 4 shows the maximum tilting angles of various fuel storage tanks with *L/D* = 1.05 and 1.10. It is seen that the tilting motion decreases with respect to both *D/H* ratios and storage capacity of tanks. For the same *D/H* value, larger L/D ratios improve the stability of the storage tanks. For the case with *L/D* = 1.05, tanks with *D/H* $\geq$ 1.4 fulfill the design criteria specified in Sect. 3.1. Tanks with *D/H* = 1.3 are operationally stable for storage capacities above 7,500 m$^3$ under working environmental condition whereas tanks with *D/H* $\leq$ 1.2 are unstable for all storage capacities. When *L/D* value increases to 1.10, tanks with *D/H* $\geq$ 1.2 fulfill the stability requirements when the storage capacity is greater than 6,500 m$^3$.

**Circular Single-Hull Structures**

Figure 5(a) shows the maximum tilting angle of single-wall cylindrical tanks without floaters under wind and current loads at their 1-year return period. It is seen that tanks with a minimum *D/H* ratio of 1.8 can fulfill the stability design criteria. Comparing with double-hull structures, it is important to recognize that a single-hull tank design

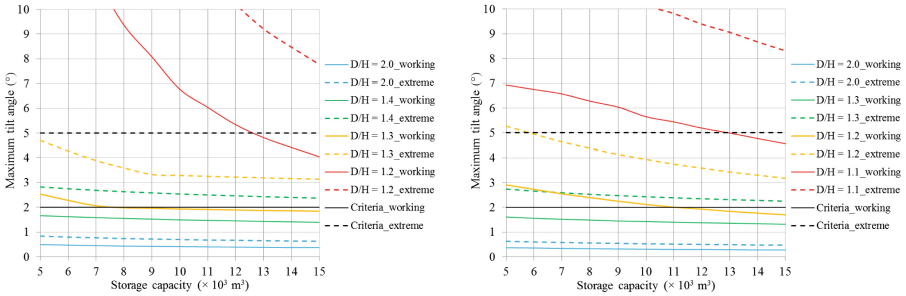


(a) L/D = 1.05 (b) L/D = 1.10

**Fig. 4.** Maximum tilting angle of double-hull fuel storage tanks.

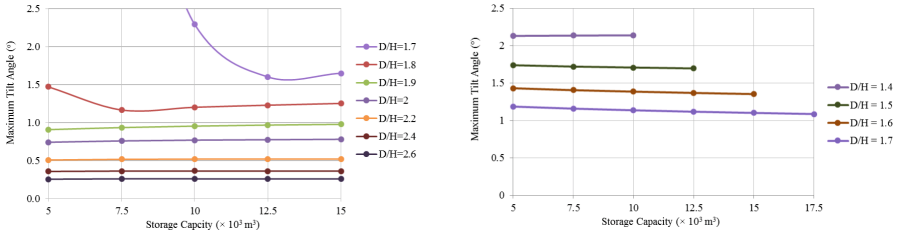


(a) tanks without floaters (b) tanks with four floaters

**Fig. 5.** Maximum tilting angle of single-hull fuel storage tanks.

does not provide satisfactory stability under environmental loads, and also result in a larger use of sea space.

To improve this design concept, an innovative design in which four hollow cylinders are attached to the single-hull structure at the corners, as shown in Fig. 1(b), is proposed. Figure 5(b) represents the maximum tilting angle of the tank under working conditions. It is observed that tanks with $D/H \geq 1.6$ are operationally stable since the tilt angles are below $2^{o}$ under working environmental condition, which implies that the sea space can be significantly reduced by about 20% by this novel design. When tank storage capacity is smaller than 15,000 $m^3$, a smaller $D/H$ ratio can be used because the design requirement on the draft is satisfied.

## 4 Structural Analysis

Two self-stabilizing fuel storage tanks with practical geometric dimensions are selected on the basis of stability analysis results to conduct further analysis work, which helps to evaluate the structural performance of both double-hull and single-hull structures. Table 2 lists the geometric information of individual fuel storage tanks investigated using finite element (FE) analysis techniques.

**Table 2.** Geometric information of individual fuel storage tanks

| Item | Square-circular double-hull | Single hull with floaters |
|---|---|---|
| Capacity | 12,500 $m^3$ | 12,500 $m^3$ |
| Size | 35 m/ 32 m × 16.5 m (L/D × $H_w$) | 32 m × 16.5 m (D × $H_w$) |
| Wall | Inner/Outer wall thickness: 450 mm | Circular wall thickness: 450 mm |
| | Rib stiffener thickness: 350 mm | Floater thickness: 500 mm |
| Base | 750 mm | 750 mm |

### 4.1 Linear Finite Element Modelling

The floating fuel storage tanks are subjected to various actions at service, e.g. self-weight, hydrostatic pressures, wind load, current load, and others. Previous experience indicates that hydrostatic pressures takes up a major proportion of all the load effects. Therefore, only self-weight and hydrostatic pressures are taken into consideration in the linear FE analysis to evaluate the structural performance of both single-hull and double-hull structures. The hydrostatic pressures due to fuel and sea-water are shown in Fig. 6. Linear springs are attached beneath the base slab in the FE models to simulate the effects of buoyancy forces.

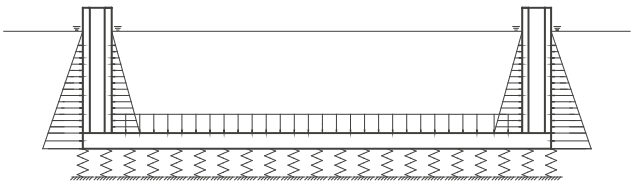

**Fig. 6.** Hydrostatic pressures applied on the inner and outer walls.

Figure 7 shows the FE models for double-hull and single-hull tanks developed with commercial software ABAQUS (Simulia 2015). Since prestressed concrete is utilized in the structure, fuel storage tanks are supposed to perform within the elastic range at the service limit state. In that case, a linear elastic model was defined and the density of lightweight concrete is taken as 2000 kg/$m^3$.

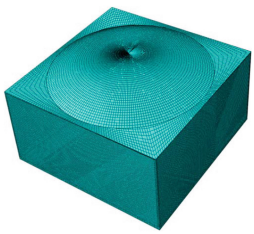

(a) double-hull tank structure

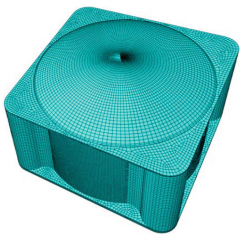

(b) single-hull tank structure with four floaters

**Fig. 7.** Finite element models of double-hull and single-hull structures.

### 4.2 Analysis Results

In the FE analysis, five different fuel level load cases (empty, 25%, 50%, 75% and full) were considered and the stress distribution in both the circumferential/tangential and vertical directions were investigated. Figures 8 and 9 depict the critical stress distribution along the wall height at the section between the side rib and corner rib. It can be seen that the outer side of the circular wall is in tension because of the outward fuel pressure, while the square wall is bending in the opposite direction. Besides, the fully loaded tank is the most adverse load case for both circular and square walls as the tensile stress value increases with respect to the fuel level for the double-hull structure. It is inferred from the stress distribution curves that both circumferential and vertical prestressing tendons (P.T.) are necessary to balance the tensile stress induced by hydrostatic pressures.

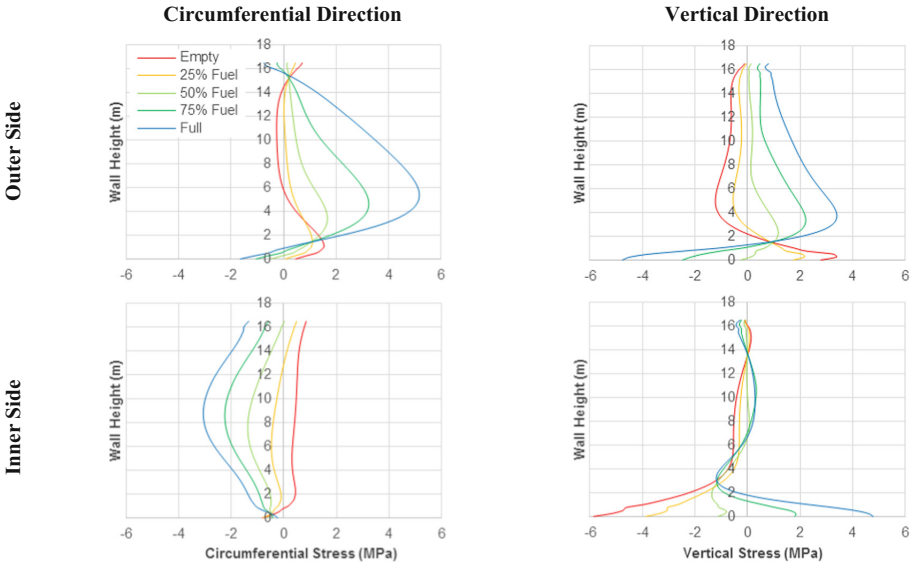


**Fig. 8.** Stress distribution along circular wall height (double-hull structure).

Figure 10 shows the stress distribution along the circular wall height for the single-hull fuel storage tank with four floaters. As compared to the circular-square double-hull structure, the tensile stress values are much lower for the single-hull circular wall because the hydrostatic pressures induced by seawater and fuel at both sides can be balanced to some extent. Furthermore, high tensile stress values are mainly located in the bottom portion. Therefore, with using a bottom-tapered wall, it is viable to avoid the use of P.T. in one, or even two, orthogonal? directions, which can significantly reduce material consumption and construction costs.

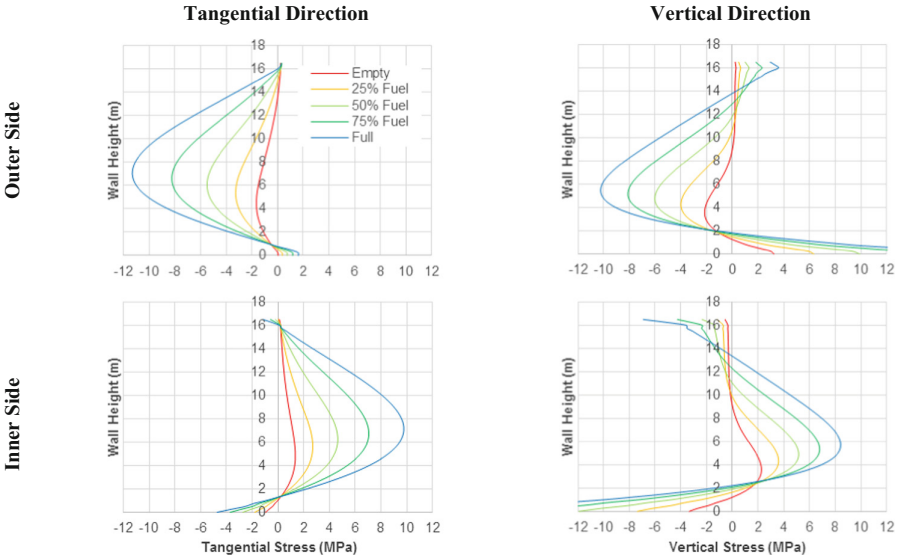


**Fig. 9.** Stress distribution along square wall height (double-hull structure).

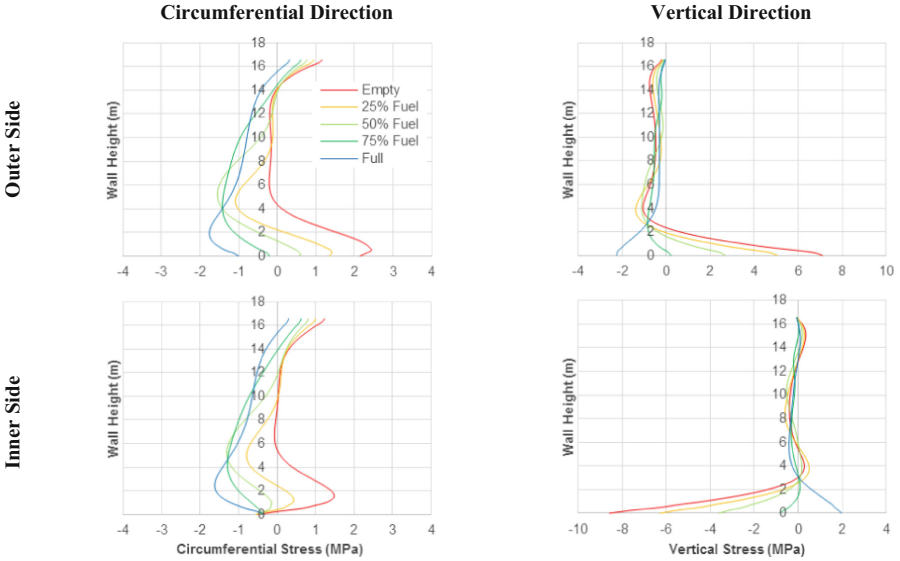


**Fig. 10.** Stress distribution along circular wall height (single-hull structure).

## 5 Summary and Recommendations

Two self-stabilizing floating tank configurations were proposed in this study. The stability and structural performances of the innovative design concepts were conducted. Based on the results of the present analysis, potential technical challenges and key design recommendations are summarized as follows:

- For double-hull tank structure, the stability performance improves with larger *L/D* and *D/H* ratios. The *D/H* design values are suggested to be greater than 1.4 and 1.2 for tanks with *L/D* ratios of 1.05 and 1.10, respectively.
- The single-hull structure does not generally provide satisfactory stability under environmental loads, however, a minimum *D/H* ratio of 1.8 can fulfill the stability design criteria. When floaters are attached to the wall, the tank with $D/H \geq 1.6$ are operationally stable, which can significantly decrease the required sea space.
- The outer and inner walls in the double-hull structure work separately to resist the hydrostatic pressures, and P.T. are necessary in both circumferential/tangential and vertical directions to balance the tensile stresses.
- As compared to double-hull structure, the circular single-hull structure shows better structural performance because the outer/inner hydrostatic pressures can be balanced to some extent. With a bottom-tapered wall, it is possible to avoid the use of P.T.
- When both stability and structural performances are taken into consideration, it is suggested that the single-hull tank with four floaters be adopted for the proposed self-stabilizing floating fuel storage tank.

**Acknowledgments.** The authors are grateful to the Singapore Land and Liveability National Innovation Challenge Directorate, Ministry of National Development, National Research Foundation and JTC Corporation for providing the research grant to conduct this research on concrete materials for large floating structures on the sea.

## References

Jensen, O.J., Viggosson, G., Thomsen, J., Bjordal, S., Lundgren, J.: Criteria for ship movements in harbours. Coast. Eng. **1990**, 3074–3087 (1991)

Simulia, D.S.: Abaqus 6.13 documentation Providence, Rhode Island, US (2015)

Veritas, D.N.: Rules for Classification of Ships, Part 3. Det Norske Veritas AS, Nøvik, Norway (2001)

Veritas, D.N.: DNV-RP-H103 Modelling and Analysis of Marine Operations, April (2011)

Veritas, D.N.: DNV-OS-C301: Stability and Watertight Integrity. Det Norske Veritas AS, Nøvik, Norway (2013)

# Current Concerns on Durability of Concrete Used in Nuclear Power Plants and Radioactive Waste Repositories

Quoc Tri Phung(✉), Norbert Maes, and Diederik Jacques

Institute for Environment, Health, and Safety,
Belgian Nuclear Research Centre (SCK•CEN), 2400 Mol, Belgium
{quoc.tri.phung, norbert.maes,
diederik.jacques}@sckcen.be

**Abstract.** Nuclear power, to most of us, is mystic and somehow scary, and despite its drawbacks, is still playing an important role in the world wide energy supply. However concrete, without mystery as the most widely used materials in construction, is used as a major constituent for nuclear facilities such as radioactive waste repositories and nuclear power plants. Concrete is the only practical material offering a number of advantages including sufficient shielding against the dangers of radiation, good compressive strength, low cost, easy building, and retention of radionuclides limiting their dissipation. The assessment of the long-term durability of such concrete structures is of utmost importance and urgently needed as our knowledge on concrete durability beyond the basis of an expected several decade service life is limited. Within its service environment, these structures undergo chemical degradation processes which are very slow but they significantly change the physical integrity and the chemical conditions of the structures with the passage of time. Current issues on durability of these concrete structures include alkali-silica reaction, delayed ettringite formation, leaching, carbonation, etc. which might be magnified under severe/accelerated conditions (high temperature, radiation, moisture, cyclic loading, and acidic environments). These degradations induce an evolution of the microstructure, cracking and changes in transport properties of concrete which are still unclear due to the limited experimental timeframe available to capture these processes. This paper presents an overview on these concerns with the focus on the long-term chemical degradation aspect and presenting a case study on Ca-leaching.

**Keywords:** Concrete durability · Radioactive waste · Nuclear power plant · Chemical degradation · Alkali silica reaction · Leaching

## 1 Introduction

Despite that renewable energy is steadily going up (e.g. biogas, municipal waste, solar, wind, hydro), nuclear power still has an important role in the energy supply worldwide and contributes almost 12% electricity of the world (Pomaro 2016). Nuclear energy is used by more than 30 countries. More than 25% of the electricity of Europe is nuclear

© Springer Nature Singapore Pte Ltd. 2018
H. Tran-Nguyen et al. (eds.), *Proceedings of the 4th Congrès International de Géotechnique - Ouvrages -Structures*, Lecture Notes in Civil Engineering 8,
DOI 10.1007/978-981-10-6713-6_111

power and is generated from 186 nuclear power plants (NPPs) as of 2016. In the United States 61 NPPs provide about 20% of the electricity supply (Naus 2009). Asia is the main region in the world where nuclear power is growing significantly. There are 128 operable nuclear power reactors, among them Japan contributes 43 reactors. The increase of NPPs also entails that considerable amounts of radioactive waste need to be managed for very long time periods.

In the case of nuclear wastes storage and disposal, a multi-barrier principle is adopted in order to ensure the safety of people working or living near storage facilities. Different types of confinement elements, often made from cementitious materials, are used so that optimal storage conditions are satisfied. These cementitious materials are envisaged for use both for encapsulation of radioactive waste and as engineered barriers for disposal of radioactive waste, both in near-surface repositories for low/intermediate active waste and geological/deep repositories for high level long-lived radioactive waste (see Fig. 1a, b). The role of cement-based materials in these applications is not only focused on the retention of radionuclides (attributed to its low transport properties) but also in helping creating beneficial conditions for the waste package integrity (steel corrosion) because of its high-pH buffering capacity for a very long period. Concrete is also the first choice for isolation the radioactive materials when a nuclear disaster happens. Following the 1986 Chernobyl disaster, the whole site of Chernobyl NPP was encased inside a vast structure known as the sarcophagus made from 400,000 $m^3$ of concrete to limit radioactive contamination of the environment. And recently, after the 2011 Fukushima accidence, Japanese engineers was thinking to burry NPP in thick concrete layers as done at Chernobyl.

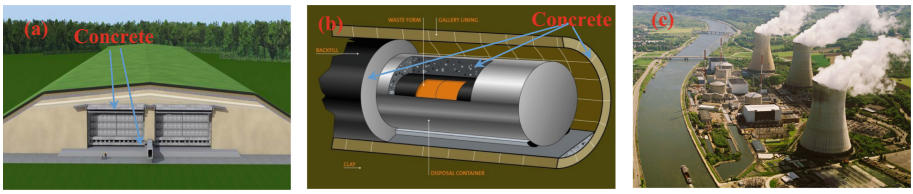


**Fig. 1.** Concrete used for (a) encapsulation, backfill and construction in low level waste facility, (b) disposal gallery lining, buffer, end-plug of gallery and backfill in high level waste facility – Belgian Supercontainer concept (examples of current proposed concepts by ONDRAF/NIRAS for Belgium, pictures taken from NIRAS (2012) and NIRAS (2011)) and (c) cooling towers in Tihange-Belgium NPP.

A typical NPP uses a number of concrete-based structures to provide foundation support and shielding as well as containment functions. Concrete structures also function as spent and new-fuel storage pools and cooling towers (Fig. 1c). Under its service environment, these concrete structures undergo chemical degradation processes which are usually very slow but important for the long-term durability assessment. Chemical degradation is typically the result of alteration of the cement matrix mineralogy caused by interaction with its environment. The interaction disturbs the equilibrium between the pore solution of the cementitious materials and the solid phases of

the cement matrix which results in dissolution and/or precipitation of minerals. The degradation is a function of many factors including the constituent materials, its location (e.g. coastal, inland or underground for waste disposal), climatic conditions (e.g. temperature and moisture), and the presence of external agents (e.g. sulfates and chemicals). The chemical degradation of cementitious materials is mostly followed by alteration of the microstructure and, thereby, its transport properties. The most common chemical degradation processes include chloride ingress, sulphate attack, alkali-silica reactions, carbonation and Ca-leaching. The operating licenses for commercial NPPs are typically issued for 40 years and can be renewed for additional 20 years with no limit to the number of renewals. Therefore, the concrete structures in NPPs need to be reliably designed for ages longer than 60 years. For waste disposal facilities, the service life of concrete structures is directly related to the time necessary for the waste's radioactivity to decay, which typically exceeds hundreds or thousands of years (Jacques et al. 2013). It is, therefore, necessary to explain how concrete will degrade, and how the properties evolve in the long-term. With this research, we aim at giving an overview on these concerns with the focus on the long-term chemical degradation aspect and presenting a case study on Ca-leaching in accelerated conditions.

## 2 Concrete Degradation in Nuclear Related Structures

### 2.1 Road Ahead to Ensure Concrete to be a Durable Material for Nuclear Related Structures

Many environments are highly aggressive due to various chemical components. In such environments, concrete is subjected to processes of chemical degradation. Common chemical degradation processes are sulfate and chloride attacks, alkali silica reaction (ASR), leaching and carbonation (Fig. **2**a). Depending on the roles of structures, the expected life span and the environments to which the concrete structures are exposed, different chemical degradation processes are considered. For concrete used in containment buildings of NPPs designed as the physical barrier against radioactive material release to the outside environment, potential degradation is reinforced corrosion and nuclear radiation induced cracking which breaks down its function to ensure the leak tightness and structural integrity. Other concrete structures (e.g. the reactor building, spent fuel pools, cooling towers) provide support and shielding functions and they undergo chemical degradation under different mechanisms depending on its surrounding working environments. For example, the spent fuel pools are exposed to "aggressive" water (e.g. borated or demineralized water), elevated temperatures and radiation, while the cooling towers may be susceptible to ageing due to their specific service conditions (e.g. freeze-thaw action, carbonation). Degradation surely affects the ability of these concrete structures to meet functional and performance requirements and reduce its expected service life.

Concrete degradation can be caused by external or internal attacks. The external attack can be reduced by designing thick cover, elements which allows ensuring a relative long expected life span of 100 years. However, the internal attack can cause destruction in short time scales regardless of structure thickness. The internal attack

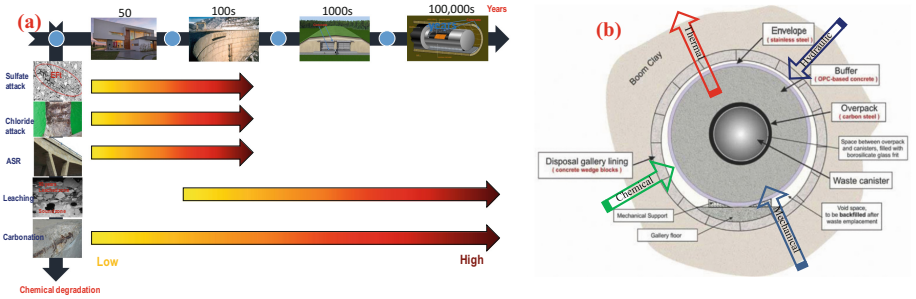


**Fig. 2.** Typical concrete degradation in relation to roles of concrete structures (a) and proposed Belgian repository concrete structure under coupled effects by chemical, physical and mechanical degradation processes (b) (NIRAS 2007)

commonly causes ASR cracking and internal sulfate attack induced delayed ettringite formation (DEF). To ensure durability and avoid internal attack, the selection of concrete constituents is essential. More care in the selection and characterization of aggregates will help to avoid ASR which can cause important degradation decades after construction is completed. Some structures (e.g. cooling towers) are subjected to degradation due to their relatively thin covers and severe environments (e.g. high humidity, freeze-thaw cycling and varying temperatures). Common external degradation mechanisms for these concrete structures are freeze-thaw, ice formation, carbonation and corrosion due to acidic water chemistry and corrosion from aggressive marine environments. Freezing and thawing of water in concrete causes extensive cracking and/or spalling resulting in loss of concrete integrity and an increase of permeability that allows water to reach and corrode rebar while chloride attack because vicinity of a marine environment or using municipal water (high chloride content) for cooling can seriously corrode the rebar and generate cracks. In general, the safety-related concrete structures in NPPs are designed to be robust enough to bear both internal and external attacks. However, as the nuclear power plants age, degradation incidences are starting to occur at an increasing rate, primarily due to environmental-related factors, which causes one-fourth of all containments to experience corrosion (IAEA 2016). This is perhaps due to the fact that there is only a little or no data on long-term concrete performance for concrete in NPPs, even though they are largely built of concrete!

Operations in the nuclear power industry certainly produce a wide variety of radioactive wastes. Over the last 60 years, more than 350,000 tons of high-level nuclear waste has been produced over the world and must be deposited for thousands of years in a safe place. And on the journey to find a suitable solution, underground repositories have been chosen by many countries, in which concrete is considered as a useful material (see Figs. 1a, b and **2**b) for these repositories with extremely long-term service life. Therefore, the assessment of the long-term performance of such concrete structures is of utmost importance. The role of cement-based materials in these applications is not only focused on the retention of radionuclides (attributed to its low transport properties) but also in helping creating beneficial conditions for the waste package integrity (steel corrosion) because of its high-pH buffering capacity for a very long period. Within its

service environment, these structures undergo coupled degradation processes (Fig. 2b) which might significantly change the physical integrity (e.g. transport and mechanical properties) and the chemical condition (e.g. pH) of the structures in the long-term. In many cases, the disposal facility is attacked by aggressive water, which will induce chemical disequilibrium and dissolution of cementitious solid phases by processes such as Ca-leaching and carbonation. The chemical degradation of cementitious materials is mostly followed by alteration of the microstructure and, thereby, transport properties. The transport properties such as permeability and diffusivity are the key parameters to evaluate whether the concrete still retains its function as a barrier against the transport of radionuclides and other hazardous products out of the disposal system. Moreover, the heat generated during the repository life may accelerate the chemical processes. The alteration of chemical properties will in turn induce changes in the cement microstructure and consequently changes in mechanical performance and transport properties (permeability, diffusion (Patel et al. 2016)) of concrete structures. Therefore, a systematic approach is needed to establish the relationship between multiple processes at multiple scales, which would provide knowledge of long-term safety of radioactive waste disposal and suggestions on how safety functions of the repository components can be improved in terms of material and structure designs. Although a lot of effort has been spent on studies concerning the use of cement-based materials in such structures, the evolution of the microstructure and transport properties under chemical degradation over long time periods (up to thousands of years) is still unclear due to the limited experimental timeframe available to capture these processes.

The predisposal waste management is to produce waste packages suitable for storage, transportation and final disposal. For decades, the nuclear industry has used cement-based materials (CBM) to immobilize low- and intermediate-level short-lived and long-lived radioactive waste originating from the operation of nuclear power plants and from the chemical reprocessing of spent fuel. Compared with other solidification techniques, the cementation technique is relatively simple and inexpensive. Moreover, CBM shows many advantages such as easy supply, good self-shielding and high alkalinity, which allow to precipitate and thus confine many radionuclides. One could expect that this practice would result in a stable waste form that is well compatible with the final disposal site, there are, however, many examples that show that this is not always the case. Specific issues have been addressed, such as the gel-formation attributed to ASR in the concrete operational waste of the nuclear power plant of Doel, Belgium (Federal Agency for Nuclear Control (FANC) 2014), the limitation of adverse cement–waste interactions which may affect the quality of the resulting solidified waste form, or the understanding and prediction of long-term properties of the waste packages and cement barriers. There is also a need for safe processes minimizing the production of secondary wastes.

In the following sub-sections, the authors will briefly address some current concerned degradation mechanisms of CBM in nuclear related structures.

### 2.2 Alkali Silica Reaction and Delayed Ettringite Formation

ASR is a deleterious reaction between the silica (from aggregates) and alkalis in pore solution or portlandite (CH) (solid phase) in the presence of water to form ASR gel

(e.g., calcium potassium silicate hydrate, calcium sodium silicate hydrate). The amount of ASR gel varies depending on the reaction temperature, type and proportions of the reacting materials, gel composition, gradation of aggregates, and other factors, among them silica content and the internal structure of aggregate are the most important. Swelling of this gel leads to stress development and potentially, cracking of concrete. ASR is a major durability problem of concrete including dams and hydraulic structures, pavements, bridges, and recently NPP concrete structures, while there is no feasible method available to stop the reaction. It has long been known that irradiation affects concrete properties. Nuclear irradiation (especially neutron irradiation presented later in Sect. 2.3) can significantly increase the reactivity of silica-rich aggregates. DEF is a special case of internal sulfate attack. It occurs when internal or external sulfates react with anhydrous or hydrated calcium aluminates after hardening inducing cracking in hardened concrete. DEF is a result of high early temperatures (above 70–80°C) in concrete which prevents the normal formation of ettringite or the decomposition of ettringite that has already formed. Use of cements having high sulfate from gypsum) and aluminate ($C_3A$) content can highly lead to DEF. The extent of DEF development is also dependent on water presence in concrete and the temperature. Elevated temperature, which is the case for concrete in nuclear related structures, increases potential for damage due to DEF.

During in-service inspection of the concrete engineered structures, extended degradations by ASR (Fig. 3a) of concrete apparent on the external surface of the secondary containment building of the Tihange 2 reactor were observed (Federal Agency for Nuclear Control (FANC) 2013). Typical degradation depths were 3 to 5 cm. DEF was also sometimes observed in association with ASR. DEF is also a high risk for cemented wastes containing high sulfate content. Seabrook NPP in the U.S. also appears to be significantly suffering from ASR in localized zone of its subbasement (Saouma and Hariri-Ardebili 2014) (Fig. 3b). Some NPPs in Japan, France and Canada also reported ASR related degradation.

### 2.3 Nuclear Radiation Damage

Concrete structures used as biological shields in NPPs and radioactive waste storage facilities are subjected to two types of radiation, gamma and neutron (William et al. 2013). Neutron radiation is the emission of neutrons; gamma rays are a special form of photon radiation. There are two types of interactions between nuclear radiation and the internal structure of concrete: geometric changes of solid phases and phase transformations resulting in changes in properties of concrete. Gamma rays have an insignificant effect on hydrated phases and aggregates of concrete but significantly influence the pore solution (Kontani et al. 2014). Water in the concrete can be decomposed by gamma rays by a process called radiolysis and can be converted to hydrogen, oxygen, and hydrogen peroxide which may react with the cement paste. Water can also be removed from the concrete by evaporation due to heat generated by gamma radiation resulting in shrinkage of cement paste (Fig. 3d). Neutron and gamma radiation can lead to an increase in concrete temperature up to 250°C (Fillmore 2004) inducing significant impacts on the mechanical and radiation-shielding properties of concrete. It also has been shown that as the gamma radiation dose increases the concentration of calcite

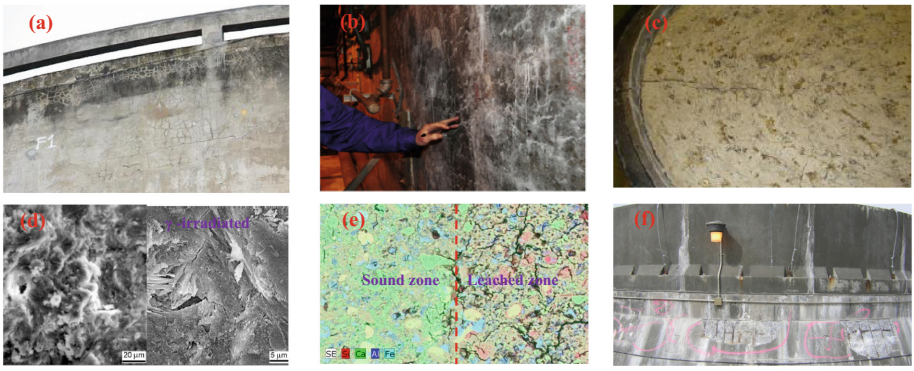


**Fig. 3.** ASR at containment building of Tihange NPP (a) (Federal Agency for Nuclear Control (FANC) 2013), Seabrook NPP (b) (Saouma and Hariri-Ardebili 2014) and cemented waste drum from Doel NPP (c) (Federal Agency for Nuclear Control (FANC) 2014); Effect of γ-radiation of dose 290 MGy on microstructure cement paste (d) (Lowinska-Kluge and Piszora 2008); Changes in microstructure and mineralogy due to leaching (e); Carbonation of a concrete cooling tower at a coal-fired electrical generation plant in the southwest U.S. (f).

increases resulting in carbonation of the concrete (Vodák et al. 2011). For neutron irradiation, the neutrons have more influence on the solid phase by scattering or ejecting neutrons than on the water phase. Under neutron radiation, the internal structure of some aggregates can be converted from an ordered crystalline structure to a disordered structure, resulting in a decrease in specific gravity and an increase in volume. Experimental studies have shown that the reactivity of silica-rich quartz can be significantly increased by exposure to nuclear radiation. As a result, irradiation can produce ASR in concretes containing aggregates that are typically nonreactive.

### 2.4 Ca-Leaching

Leaching (Phung et al. 2014) is a process of ion extraction from solid compounds by dissolution. In cement based-materials, leaching of calcium, also called decalcification, is of utmost importance because of the high calcium (Ca) content in cement compared to other potentially leachable ions ($Fe^{2+}$, $Al^{3+}$, $Mg^{2+}$, etc.) and the high solubility of the aqueous Ca-controlling phase portlandite. Ca-leaching is one of the most serious degradation processes in concrete and reinforced concrete structures for the very long-term (nuclear waste disposal system) or in hydro structures (dam, bridge, water tank) but it has only been studied since the 1980s despite the long history of concrete. The reason is that leaching of concrete is an extremely slow process under normal conditions (few mm leaching front in a hundred years). However, the lifetime of civil concrete structures is normally under one hundred years and that is too short to see the effects of leaching degradation. Leaching of concrete structures in NPPs have been observed even on dry surfaces of structures (Tcherner et al. 2017) which cause local reduction in alkalinity of concrete leading to corrosion of reinforcement and embedded parts. Leaching of cement-based materials also changes its properties such as an

increase in porosity (see Fig. 3e) and transport properties and detrimental effects on properties related to long-term durability. One might intuitively presume that leaching alters the cementitious materials to a material with coarser microstructure and higher transport properties. And this presumption is confirmed by literature. However, to what extent the microstructure and transport properties are modified, is still questionable, especially on the long-term.

### 2.5 Carbonation

Carbonation (Phung et al. 2015a) is a chemical degradation process through the reaction between $Ca^{2+}$ and $CO_3^{2-}$ ions. In most cases, it is believed that the driving force behind the carbonation is diffusion of $CO_2$. However, it depends on the conditions of carbonation, in the case of concrete used for underground waste disposal purposes, concrete is almost fully saturated and subjected to a high hydrostatic pressure and the surrounding environment may contain a high dissolved $CO_2$, a combination of diffusion and advection should be taken into account. Carbonation results in a pH decrease which accelerates the corrosion of reinforcing bars in concrete (Fig. 3f) because of dissolution of the thin oxide passive layer protecting the steel bars from corrosion. On the other hand, carbonation also results in beneficial effects. It is generally believed that carbonation decreases transport properties and refines pore structure and increase strength of Portland cement-based materials. Furthermore, in recent years, there is considerable interest in applying carbonation of cement-based materials for solidification and stabilization of radioactive waste. There are many factors influencing carbonation: chemistry of hydration products, free water content, internal relative humidity, pore structure, $CO_2$ partial pressure and external conditions where carbonation occurs (e.g. ambient relative humidity, temperature, $CO_2$ concentration and applied pressure). In general, the higher the $CO_2$ concentration, the quicker the carbonation proceeds. However, up to a certain concentration, the carbonation may not increase because the retention process resulting from porosity reduction and releasing water overwhelms the effect of higher concentration. Increasing temperature will speed up the carbonation process because the reaction and penetration of $CO_2$ occurs faster. The core reaction in carbonation is the reaction between dissolved $CO_2$ and portlandite. Therefore, the more portlandite is present in the hydration products, the higher the degree of carbonation. Water plays an important role in the carbonation process. Carbonation does not occur without water. It is a catalyst in carbonation reaction even though this reaction releases water. However, water can fill the pores and prevent $CO_2$ gas to penetrate into the concrete pore network. In fact, carbonation reaches the highest efficiency at an internal relative humidity between 50–70%.

Under irradiation conditions, carbonation of concrete can be accelerated due to elevated temperature, this phenomenon is known as radiation-induced carbonation (Vodák et al. 2011). The phase transformation in this type of carbonation is similar to the natural carbonation reaction in concrete. However, the natural carbonation reaction takes place at the surface layer of concrete, where $CO_2$ comes from the environment and penetrates into the concrete through diffusion, whereas the radiation-induced carbonation occurs in the concrete that has been irradiated and thus is not a diffusion-limiting reaction. Another major difference between the two types of

carbonation reaction is that the natural carbonation reaction can produce an increase in concrete strength as mentioned above, whereas the radiation-induced carbonation produces a decrease in the strength of the concrete as the result of a succession of chemical reactions, starting with radiolysis of water and terminating in the formation of calcite crystals (William et al. 2013). It is evidenced during repairing of concrete structure of secondary containment of reactor building of Tihange 2 reactor that a deeper than expected and extended carbonation front was developing on the whole structure (Federal Agency for Nuclear Control (FANC) 2013).

## 3 Case Study on Leaching

### 3.1 Experiments

Experiments were performed on cement pastes made from cement, tap water and limestone fillers (LS). Type I OPC cement (CEM I 52.5 N) was used. LS used had a $CaCO_3$ content of 98.30%. Superplasticizer Glenium 27 was added to the mix with content of 0.5% w.r.t. mass of cement. In order to investigate the effects of LS, three sets of cement pastes were cast in a temperature-controlled room of 21 ± 1°C: sample C0 with w/p ratio of 0.425, 0% of LS replacement; C10 with w/p ratio of 0.375 and 10% of LS replacement, and C20 with w/p ratio of 0.325 and 20% of LS replacement. The material compositions used in this study are relevant (but without coarse aggregates) for the composition used within the Belgian Supercontainer concept which is a proposed reference design for disposal of high-level waste and spent fuel (Bel et al. 2006). Note that all samples had quite similar w/c ratios of 0.415 ± 0.01. The leached samples are named C0-L, C10-L, C20-L, respectively. Cement pastes were cured for 28 days under sealed conditions then sawn into 25 mm thick slices. In order to accelerate the leaching, the saturated cement slices were immersed in 6 M ammonium nitrate solution. After leaching, a number of post-analysis techniques including scanning electron microscopy (SEM), XRD/QXRD, mercury intrusion porosimetry (MIP), and $N_2$-adsorption were used to characterize the microstructural and mineralogical changes. The leached depth was determined by phenolphthalein spraying. The effect of leaching on permeability was quantified with the permeability setup as discussed in (Phung et al. 2013).

### 3.2 Modelling

A one-dimensional diffusion-based transport model (Phung 2015; Phung et al. 2016) was developed to simulate leaching of saturated hardened cement paste in contact with an aggressive $NH_4NO_3$ solution with a concentration of 6 mol/l. The model was based on a macroscopic mass balance for Ca in aqueous and solid phases and the changes of Ca equilibrium with different $NH_4NO_3$ concentrations were taken into account. The proposed model only considered the degradation of portlandite and calcium silicate hydrates (C-S-H) which are the main hydrated phases in typical CEM I Ordinary Portlandite cement. The hydration during leaching was not taken into account in the model because of the short experimental duration.

### 3.3 Selected Results and Discussion

We only presents some selected results, the reader is referred to (Phung 2015) for more experimental and modelling details/results. Figure 4a shows a good agreement between the predicted leached depths with the measured ones. The modelling results show that within the investigated duration (28 days), the propagation rates of degraded depth and Ca-leached amount were almost in direct proportion to the square root of time. Higher LS addition resulted in slower degradation rate. Figure 4b compares the porosity of leached and reference samples determined by the combined MIP and $N_2$-adsorption method (Phung et al. 2015b). In the range of 3 nm–100 µm, the porosity of leached samples hugely increased, from 68% up to 159% compared to the porosity of reference samples. Despite different initial porosities, the porosities of all leached samples were quite similar. The higher LS replacement, the larger porosity increases. Such a large porosity increase is not only due to the decalcification of CH but also due to partial decalcification of the C-S-H system. In all leached samples, the cumulative pore volume curves exhibited two ranges of significant porosity increase. The first range was situated in the 60 nm – 500 nm pore sizes corresponding to CH dissolution. The second ranges was smaller than 10 nm corresponding to C-S-H (and other phases) dissolution. In contrast, reference samples exhibited only one significant pore volume increase stage. Portlandite profiles (normalized to the initial content) after 28-day immersion in $NH_4NO_3$ solution are shown in Fig. 4c. The CH content suddenly increased after the degraded front. Sample with higher LS replacement exhibits a steeper jump of CH content at the front. Figure 4c also shows that the predicted portlandite profile for samples C0 and C20 are in line with the profiles determined with quantitative X-ray diffraction measurements on powder, especially for sample without limestone fillers.

The specific surface areas (SSA) determined by the BET method of the leached samples significantly increased (Table 1). The SSA of samples C0 and C10 increased with a factor of 5 after 28-day of leaching. For the samples with the highest LS

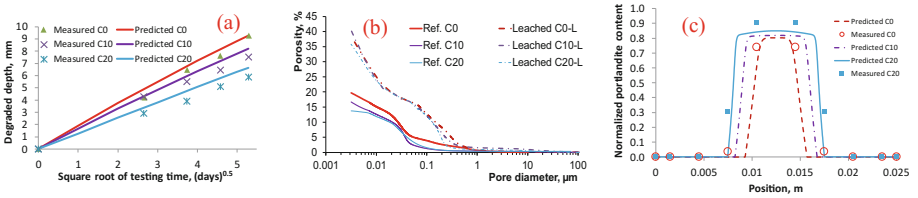


**Fig. 4.** Leached depth (a), porosity increase (b) and portlandite content of leached samples (c)

replacement C20, the SSA increased up to 15 times. Such an huge increase cannot only be attributed to portlandite dissolution but also to dissolution of C-S-H. The gel pores of C-S-H which have a higher SSA compared to micro/mesopores became more easily accessible by nitrogen after leaching. Leaching seriously increased the porosity in the mesopore region for all leached samples as shown in Table 1. The largest increase in porosity was for sample C10 of which the porosity increased almost 3 times.

Interestingly, the average pore diameter determined by BJH method decreased after leaching for all compositions. Rather than a refinement of the pore structure of the leached materials, this reduction indicates an opening of initially inaccessible gel pores. Sample S5L (the highest LS replacement) exhibited the largest decrease in average pore diameter, which could be the reason for obtaining the highest SSA increase (relative values) due to leaching.

Figure 5 shows the XRD patterns for leached and reference samples. It is clearly observable that CH was completely dissolved in all leached samples. There are two intense peaks of CH for the reference samples which totally disappear after leaching.

**Table 1.** $N_2$-adsorption results of leached and reference samples – "L" denotes leached sample

| | C0 | C0-L | C10 | C10-L | C20 | C20-L |
|---|---|---|---|---|---|---|
| BET surface area, $m^2/g$ | 30.6 | 145.8 | 34.8 | 182.3 | 5.5 | 86.7 |
| Porosity (BJH), % | 13.0 | 23.8 | 9.2 | 26.1 | 5.4 | 21.2 |
| BJH adsorption average pore diameter (4 V/A), nm | 11.6 | 7.8 | 9.5 | 7.3 | 15.8 | 6.8 |

Except for C-S-H, which cannot be detected, the most visible phases in the XRD patterns of the leached samples are calcite, ettringite and unhydrated cement which indicate that they are hardly degraded by the $NH_4NO_3$ solution. No new crystalline phases were observed as for leaching in deionized water. This underpins the statement that leaching in $NH_4NO_3$ results in same end-products, as obtained for "natural" leaching.

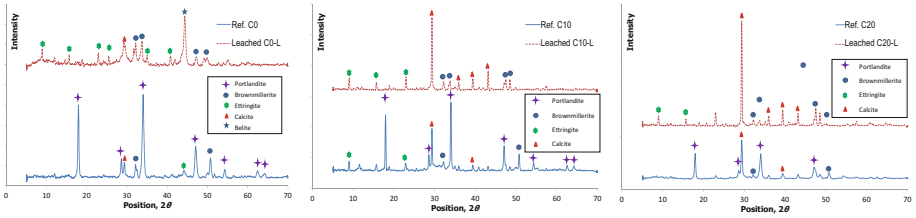


**Fig. 5.** XRD patterns of reference and leached samples taken in the first 3 mm depth from the exposed surface

SEM images (Fig. 6) show, similar to the MIP and $N_2$ adsorption measurements, an increase in pore sizes and porosity after leaching. Some big pores with diameter up to about 10 µm were observed in most of the leached samples which can be attributed to the portlandite dissolution. The dissolution of C-S-H mainly contributes to the increase of pore volume in the micropore to low mesopore range which is difficult to detect by SEM. Micro cracks were observed in all leached samples. Decalcification of C-S-H induces polymerization shrinkage, especially when the Ca/Si ratio is lower than 1.2. In addition, leaching induces a significant loss of mechanical properties. As a

consequence, decalcification shrinkage could generate tensile stresses around rigid particles (e.g. limestone fillers, unhydrated cements) which results in cracking.

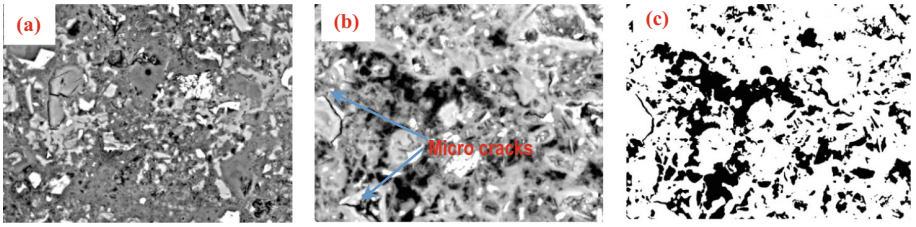


**Fig. 6.** SEM images of reference (a) and leached (b) samples C0 - field width of 128 μm, and segmented image showing the increases in porosity (in black) of leached sample C0 (c)

The evolution of composite permeability during leaching is shown in Fig. 7a. Longer immersion time in ammonium nitrate solution results in larger permeability coefficient. The change in composite permeability is larger during the first leaching stage when portlandite is still present in the sample. In the second leaching stage, the rate of permeability increase is slower because C-S-H decalcification has a smaller effect on the porosity increase. The intrinsic permeability of samples leached during 28 days increased around one order of magnitude depending on LS replacement as shown in Fig. 7a. Sample C0 without LS exhibited the largest increase in permeability, while sample S2L with the highest LS replacement exhibited the smallest increase. The extent of permeability increase is correlated with the porosity and PSD after leaching (Fig. 4b). Permeability change over the depth is shown in Fig. 7b. After 28 days of $NH_4NO_3$ immersion, the permeability increases for more than 2 orders of magnitudes near the exposed surface which is much higher than the increase of composite permeability because it is controlled by the permeability of "sound" zone.

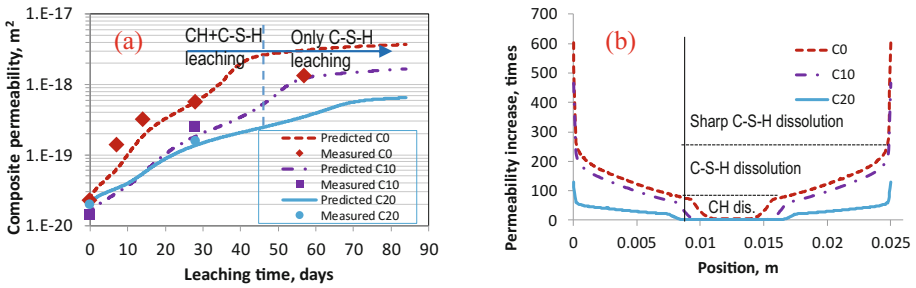


**Fig. 7.** Increase of composite permeability over time (a) and predicted permeability profile after 28-day immersion in $NH_4NO_3$ (b)

In general, mass transport properties are mainly affected by capillary and large pores. As such, an increase in permeability after leaching is linked to an increase in capillary pores resulting from portlandite dissolution. In addition, it is hypothesised here that C-S-H decalcification under accelerated leaching conditions is also an important factor because it increases the connectivity of different types of pores (gel, micro and mesopores). Furthermore, the decalcification shrinkage originating from a polymerization of C-S-H due to lower Ca/Si ratio induces micro cracks as seen in SEM images.

## 4 Conclusions and Perspective

In general, majority of concrete structures in NPPs meet their functional and performance requirements during their service period However, there are evidences of concrete degradation where the structures may not exhibit the desired durability without some forms of intervention. Periodic maintenance, and retrofitting are key elements to ensure the functions of concrete structures. It is indeed much better if concrete is well-designed in the beginning with a completely characterized material property data for long-term performance assessment. In this way, by considering the time evolution of environmental effects, elevated temperature and radiation, damage models and acceptance criteria can be developed to assess the current as well as predict the performance of concrete structures in the long-term. In any cases, the analysis and modelling of transport properties evolution due to degradation is a vital task as these properties govern the penetration of aggressive substances responsible for degradation and the transport of radionuclides transport.

The possibility to assess the service life of structures made of CBM for radioactive waste facilities is of great practical importance but raises new challenges. Unlike classical structures, the durability of waste disposal facilities needs to be predicted over hundreds up to thousands of years because of the long-lived activity of radioactive waste. Under service conditions, the disposal facility is attacked by aggressive water, which will induce chemical disequilibrium and dissolution of cementitious solid phases by processes such as Ca-leaching and carbonation. Moreover, the heat generated during the repository life may accelerate the chemical processes. The alteration of chemical properties will in turn induce changes in the cement microstructure and consequently changes in mechanical performance and transport properties of concrete structures. Therefore, a systematic approach is needed to establish the relationship between multiple processes at multiple scales, which would provide knowledge of long-term safety of radioactive waste disposal and suggestions on how safety functions of the repository components can be improved in terms of material and structure designs. Despite advances in this area, a significant amount of work is still needed due to limited experimental timeframe available to capture these long-term processes. There is still a long journey to reach the safest but economical solution for radioactive waste storage, but certainly CBM can be a reasonable choice on that journey.

As most of chemical degradation processes are very slow, accelerated tests are needed, and which in turn arises a question how to interpret and apply the accelerated results to the real concrete structures. Accelerated test results might be extrapolated to

the natural environments in which concretes undergo degradation by defining the degradation stages in terms of the changes in mineralogy (portlandite content, Ca/Si ratio) or microstructure (porosity, pore size distribution). It is then possible to predict the other properties (diffusivity, permeability, pH) at the same or similar degradation stages for leaching under normal conditions. In this sense, the combination of accelerated experiments and phenomenological model, for which inputs are obtained from accelerated tests, could be very useful to identify the comparative parameters and to predict the long-term behaviour of degraded materials. In this way, it is possible to imitate long-term naturally degraded cementitious materials in waste disposal by accelerated experiments. As an example, we have performed an accelerated leaching to understand the alteration degree of transport properties by establishing the links between mineralogy, microstructure and transport properties; and clearly describing the degradation processes/mechanisms by the combination of experiments and modelling. Results showed that the cement mixture had a significant impact on leaching; a higher limestone filler replacement resulted in an decreased rate of leaching propagation. The accelerated leaching highly altered the microstructure of the cement paste to a more porous material which is evidenced by the increases of specific surface area and total porosity and by the creation of a coarser pore size. Beside the increase in mesopore volumes, it is interesting to observe that the micropore volume was altered much more than the mesopore volume. Probably the leaching of C-S-H with a larger volume fraction than portlandite, results in a significant modification of the micropore structure. The changes in microstructures and mineralogy led to a significant increase in transport properties. The composite permeability increased by one order of magnitude, but the permeability of degraded zone could increase up to 3 orders of magnitude, which is much larger compared to the one order of magnitude often considered.

## References

Bel, J.J.P., Wickham, S.M., Gens, R.M.F.: Development of the supercontainer design for deep geological disposal of high-level heat emitting radioactive waste in Belgium. MRS Online Proc. Libr. **932**, 23–32 (2006). doi:10.1557/PROC-932-122.1

Federal Agency for Nuclear Control (FANC): B Sixth Meeting of the Contracting Parties to the Convention on Nuclear Safety (2013)

Federal Agency for Nuclear Control (FANC): B Fifth meeting of the Contracting Parties to the Joint Convention on the Safety of Spent Fuel Management and on the Safety of Radioactive Waste Management (2014)

Fillmore, D.: Literature Review of the Effects of Radiation and Temperature on the Aging of Concrete. United States. Department of Energy (2004)

IAEA: Ageing Management of Concrete Structures in Nuclear Power Plants. IAEA Nuclear Energy Series, vol NP-T-3.5. International Atomic Energy Agency, Vienna (2016)

Jacques, D., Maes, N., Perko, J., Seetharam, S.C., Phung, Q.T., Patel, R., Soto, A., Liu, S., Wang, L., Schutter, G.D., Ye, G., Breugel, K.: Concrete in engineered barriers for radioactive waste disposal facilities - phenomenological study and assessment of long term performance. In: Paper presented at the 15th International Conference on Environmental Remediation and Radioactive Waste Management - ICEM2013, Brussels, Belgium (2013)

Kontani, O., Ichikawa, Y., Ishizawa, A., Takizawa, M., Sato, O.: Irradiation effects on concrete structures. In: Infrastructure Systems for Nuclear Energy, pp 459–473. Wiley (2014). doi:10.1002/9781118536254.ch27

Lowinska-Kluge, A., Piszora, P.: Effect of gamma irradiation on cement composites observed with XRD and SEM methods in the range of radiation dose 0-1409 MGy. Acta Phys. Pol.-Ser. A Gen. Phys. **114**(2), 399 (2008)

Naus, D.: The management of aging in nuclear power plant concrete structures. Jom-Us **61**(7), 35–41 (2009)

NIRAS: Evolution of the Near-Field of the ONDRAF/NIRAS Repository Concept for category B and C wastes. NIROND-TR 2007-07 E (2007)

NIRAS: Afvalplan voor het langetermijnbeheer van geconditioneerd hoogradioactief en/of langlevend afval en overzicht van verwante vragen. NIROND 2011-02 N (2011)

NIRAS: Synthese van het veiligheidsrapport voor de oppervlaktebergingsinrichting van categorie A-afval in Dessel. NIROND-TR 2012–17 N (2012)

Patel, R.A., Phung, Q.T., Seetharam, S.C., Perko, J., Jacques, D., Maes, N., De Schutter, G., Ye, G., Van Breugel, K.: Diffusivity of saturated ordinary Portland cement-based materials: A critical review of experimental and analytical modelling approaches. Cem. Concr. Res. **90**, 52–72 (2016). doi:10.1016/j.cemconres.2016.09.015

Phung, Q.T.: Effects of Carbonation and Calcium Leaching on Microstructure and Transport Properties of Cement Pastes. Ph.D. thesis, Ghent University, Belgium (2015)

Phung, Q.T., Maes, N., De Schutter, G., Jacques, D., Ye, G.: Determination of water permeability of cementitious materials using a controlled constant flow method. Constr. Build. Mater. **47**, 1488–1496 (2013). doi:10.1016/j.conbuildmat.2013.06.074

Phung, Q.T., Maes, N., Jacques, D., Bruneel, E., Van Driessche, I., Ye, G., De Schutter, G.: Effect of limestone fillers on microstructure and permeability due to carbonation of cement pastes under controlled CO2 pressure conditions. Constr. Build. Mater. **82**, 376–390 (2015a). doi:10.1016/j.conbuildmat.2015.02.093

Phung, Q.T., Maes, N., Jacques, D., De Schutter, G., Ye, G.: Investigation of the changes in microstructure and transport properties of leached cement pastes accounting for mix composition. Cem. Concr. Res. **79**, 217–234 (2015b). doi:10.1016/j.cemconres.2015.09.017

Phung, Q.T., Maes, N., Jacques, D., Perko, J., De Schutter, G., Ye, G.: Modelling the evolution of microstructure and transport properties of cement pastes under conditions of accelerated leaching. Constr. Build. Mater. **115**, 179–192 (2016). doi:10.1016/j.conbuildmat.2016.04.049

Phung, Q.T., Maes, N., Jacques, D., Schutter, G.D., Ye, G.: Decalcification of cement paste in $NH_4NO_3$ solution: Microstructural alterations and its influence on the transport properties. In: Bastien, J., Rouleau, N., Fiset, M., Thomassin, M. (eds) 10th fib International PhD Symposium in Civil Engineering, Québec, Canada, pp 179–187 (2014)

Pomaro, B.: A review on radiation damage in concrete for nuclear facilities: from experiments to modeling. Model. Simul. Eng. **2016**, 10 (2016). doi:10.1155/2016/4165746

Saouma, V.E., Hariri-Ardebili, M.A.: A proposed aging management program for alkali silica reactions in a nuclear power plant. Nucl. Eng. Des. **277**, 248–264 (2014). doi:10.1016/j.nucengdes.2014.06.012

Tcherner, J., Vaithilingam, L., Han, M.: Effective aging management of NPP concrete structures. J. Adv. Concr. Technol. **15**(1), 1–9 (2017)

Vodák, F., Vydra, V., Trtík, K., Kapičková, O.: Effect of gamma irradiation on properties of hardened cement paste. Mater. Struct. **44**(1), 101–107 (2011). doi:10.1617/s11527-010-9612-x

William, K., Xi, Y., Naus, D.: A review of the effects of radiation on microstructure and properties of concretes used in nuclear power plants (2013)

# Innovating a New Kind of Modular Reactor Power Station Design

Paul Smith(✉)

Arup, London, UK
paul-c.smith@arup.com

**Abstract.** Our world is radically changing. We have will have to mitigate and adapt to the impact of climate change, while supporting a growing population in denser localities, all being vulnerable to increasingly severe climate and weather extremes, with many coastal regions becoming defenseless against global and local sea rise. The area of useable land for habitation and supply infrastructure will diminish as the years continue into the future; this especially being a critical problem for low lying islands, but also for highly developed countries where there exists complex and tightly coupled infrastructure close to sea level. Accepting that nuclear power generation is important for our future, the reality of whether countries can afford the considerable capital cost of providing safe nuclear power is presently questionable. The practice of design for new kinds of nuclear power should apply completely new and innovative thinking that enables lower capital cost, more efficient power generation and highly robust and ultimately resilient civil containment and support structures. Allied design considerations will be reducing the time for carrying out the build and construction process, reduced operating cost, improved through-life operability with less dose risk etc. Of major concern is a new kind of NPP that is efficient, but also robust and resilient in the face of climate change and sea rise.

## 1 The Need for Nuclear Power

Our world is radically changing. We have to mitigate and adapt to the impact of climate change, while supporting a growing population in denser localities, all being vulnerable to increasingly severe climate and weather extremes, with many coastal regions becoming defenseless against global and local sea rise. And the area of useable land for habitation and supply infrastructure will diminish as the years continue into the future; this especially being a critical problem for low lying islands, but also for highly developed countries where there exists complex and tightly coupled infrastructure. An integral part of our society's infrastructure is the dependence on reliable energy supply for social habitation, food and water supplies, transportation and our expanding economies across the world. In addition, proactive mitigation of future climate change shall involve various new technology innovations, together with the political will, enabling the reality for carbon-free energy supply sources from solar, wind and nuclear power generation.

Nuclear power generation is a carbon-free energy technology that needs to be seriously considered for its ability to mitigate the adverse effects of climate change, but

© Springer Nature Singapore Pte Ltd. 2018
H. Tran-Nguyen et al. (eds.), *Proceedings of the 4th Congrès International de Géotechnique - Ouvrages -Structures*, Lecture Notes in Civil Engineering 8,
DOI 10.1007/978-981-10-6713-6_112

also to give operational robustness in power supply with ultimate safety that the public can believe in as we adapt to the actual pathway of climate change that will show its hand as the decades go by. Future-proof design innovation must wisely consider the range of potential power station sites and their regional localities across the world, always considering the possible emerging hazards, threats and shocks – even the ones that may previously have been perceived as "unexpected" and therefore screened out. The power station sites will need to be justified for their benefit, balanced between the wellbeing and economic advantage provided, and the local risk exposure potential stemming from the varied shock scenarios that could arise. There are fundamental technical challenges and social inhibitions that need to be addressed before the world's governments and public will accept new nuclear power plants as part of the world's energy-mix, inclusive of renewables like wind and solar sources. Accepting that nuclear power generation is important for our future, the stark reality of whether countries can afford the considerable capital cost of providing safe nuclear power drives the economic argument, especially for countries that could greatly benefit from regional nuclear power plants. Other key decision factors that will drive the attractiveness of new nuclear power plants (NPPs) are:-

- Optimisation of power level and more efficient power generation;
- Less time of the build and construction process;
- More efficient supply chain engagement;
- Making use of new technology and materials;
- Attaining the necessary safety and security objectives;
- Reduced operating cost and manning requirements;
- Improved through-life operability;
- Reduced radiological dose burden to operators;
- Inclusion of passive reactor plant safety systems;
- Enhanced robustness of support and protection structures;
- Excellent seismic and mass-flood inundation withstand;
- Enhanced resilience capability with self-capable for 72+ hours;
- Comprehensive incident and accident coping strategies;
- Adaptability to adjust and be tolerant of climate change and its effects; and,
- Eradication of resistive energy loss in transmission networks.

It is also important to recognise that some of the external and internal hazards may be aggravated by the impact of climate change, while terrorist attack against nuclear power plants is now a very real and difficult challenge that shall need to be taken into account when designing new NPPs and their sites plus adjacent infrastructure. A common denominator to all these factors is the need for energy to provide power generation technology that mitigates carbon emissions causing climate change, then the structural fabric of the infrastructure itself needs to have adaptability intrinsically designed in, able to cope with and withstand the projected climate change variances yet to come in the decades and century to come.

Once a large and complex NPP facility has been constructed and commissioned, it is then financially expensive and logistically difficult to make any major modifications to its structure and engineered systems. Premature closure of any prime power supply

infrastructure is intensely problematical, simply because society depends upon its availability while the power plant becomes integral to the rest of a country's infrastructure needs. Nuclear power technology will usually have been chosen by a country to compensate for a lack of naturally occurring fuel resource. And power for already advanced and developing countries is fundamental to political stability, people's habitation, health and economic development. In more general terms, loss of domestic power supply for long periods jeopardises people's physiological wellbeing, as identified by Maslow in 1943, and undermines a country's ability to maintain its business and commerce. People's safety needs, again advocated by Maslow (1943), are obviously also important, but people have a tendency to retain little awareness of their safety and security needs except in times of emergency during natural disasters, or during periods of disorganisation in the social structure and its stability (like rioting or terrorism).

The fundamental problem is that no one has a crystal ball that can exactly tell us what the future has in store! As has been experienced across world politics in 2017, amplified yet further in June 2017 by the US President's decision to take the USA out of the Paris climate change agreement, the future is far from certain. Consequently, even though this paper is based on the most recent scientific evidence that climate change is likely, it is apparent that there exists diverse political opinion and unequal action among the world's member states to mitigate and adapt to it. For nuclear power to be a credible part of our world's energy mix, merged with renewable sources, recognised as a low carbon energy source, and accepted that they can be located in reasonable proximity to major population centres, then the nuclear power stations will have to be perceived by both governments and the public as safe, secure, robust and resilient against all forms of hazards and shock events. Protection and containment of the nuclear reactor plants will therefore be a key requirement, presuming that climate change will add to and amplify future atmospheric and coastal sea hazards, we will have to adapt to such impacts. The range of risk issues to be addressed in order to become "future proof" therefore includes global sea rise, terrorism, criminality, cyber-attack, political instability and other modern day shock conditions that are real and shall likely get worse into the future.

Mitigation of future climate change will involve various new technology innovations, together with the political will, enabling the reality for carbon-free sources from solar, wind and nuclear power generation. But our society, with its complex and tightly coupled infrastructure, will continue to be exposed and vulnerable to severe and potentially extreme shock-hazard scenarios. Accepting that nuclear power generation is important for our future, other key considerations are the capital cost, optimum time to build, security, safety, operating cost and through-life operability, of any new power stations. Accepting that our world is radically changing, and that nuclear power is part of the energy mix to mitigate climate change, and we need to adapt to the effects of climate change like with global sea rise increasing the risk of flood inundation, Arup has been investigating new kinds of power station design and construction methodology.

## 2 Expectations for a New Kind of Nuclear Power Plant

The design and engineering challenge is formidable for the new kinds of nuclear power stations into the future. As mentioned earlier, the future engineers and scientists need to find better engineering solutions that:-

- Fundamentally reduces the Nuclear Power Plant's (NPP's) initial capital expenditure;
- Lessens the duration of the build and construction process on site;
- Reduces the NPP's operating expenditure;
- Achieving improved through-life operability with less dose risk;
- Allows operation with reduced manning levels; and yet,
- Also achieves the strict quality, safety and security objectives that both government and the public will expect.

In order to attract significant investment for concentrated design and development of future NPP designs, it is obvious that many design and engineering challenges need to be solved, and may very well be overcome by applying diverse ideas and methods. However, from a generic perspective, Arup have identified eight key drivers that will dictate the configuration of new kinds of NPPs:-

- **Lower Capital Cost** to the owner/operator organisation;
- **Short Time for Build & Construction** on site;
- **Operational Flexibility** to meet future transmission supply systems;
- **Modularised Nuclear Assemblies** – mechanical, civil and EC&I;
- **Independent Parallel Sequencing** {IPS} of the NPP Build;
- Application of **New Technology and Materials**;
- Intrinsic **Seismic Isolation** of the most vulnerable reactor systems; and,
- Highly **Resilient Protection** with the ability to effectively respond and recover shock events.

The basis of this approach is depicted in Figs. 1, 2 and 3 that is at the end of this sub-section.

It is advocated that there are sub-issues that also need to be addressed, in particular:-

- the approach we use to persuade governments and the public of nuclear power's safety;
- better ways to explain an NPP's safety risk – balanced with its advantage in mitigating climate change;
- the strategy for adapting to climate change itself when the NPP has been built and is operating;
- rigorous substantiation of how the future NPPs will be able to withstand, tolerate and cope with the effects of climate change – which by its "nature" is an uncertain science;

and specifically:-

- how the NPP's design and engineering will actually be able to adapt to global/local sea rise;
- how the NPPs will safely cope with more severe storms, floods, droughts etc., and,
- how readily will the NPPs cater for more onerous demands in the future, especially related to the intrinsic region's infrastructure vulnerability to loss of services and supplies – like total Site Black Out and extended period power loss (as what happened at the Japanese Fukushima Daiichi plants in March 2011).

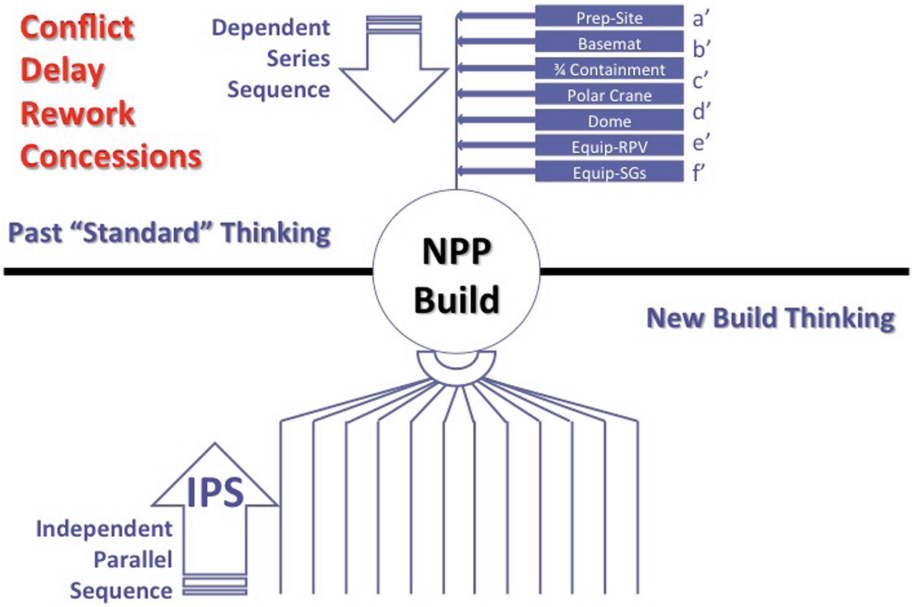


**Fig. 1.** Comparison of past "standard" and new NPP build thinking.

Cost benefit analysis of NPP designs is an established technique, trying to balance the factors for plant availability against the obligations for sustaining public and environmental safety. Inputs into the cost benefit analysis will require valid data that is fed into a logical algorithm for analysis. If done effectively, the cost benefit analysis will be able to discriminate between the benefits and dis-benefits. The substantive conclusion should in concept indicate that the power plant facility is feasible and is actually the right thing to do. The cost benefit algorithm that looks at capital and operating costs will normally be some form of probabilistic risk-based modeling, especially in the case of safety-critical infrastructure development. The justification that the power plant is the right thing to do will usually be documented in the plant's safety analysis report, while taking account of stochastic data and other empirical information that will have been specific to the nuclear plant technology and the site chosen for its placement.

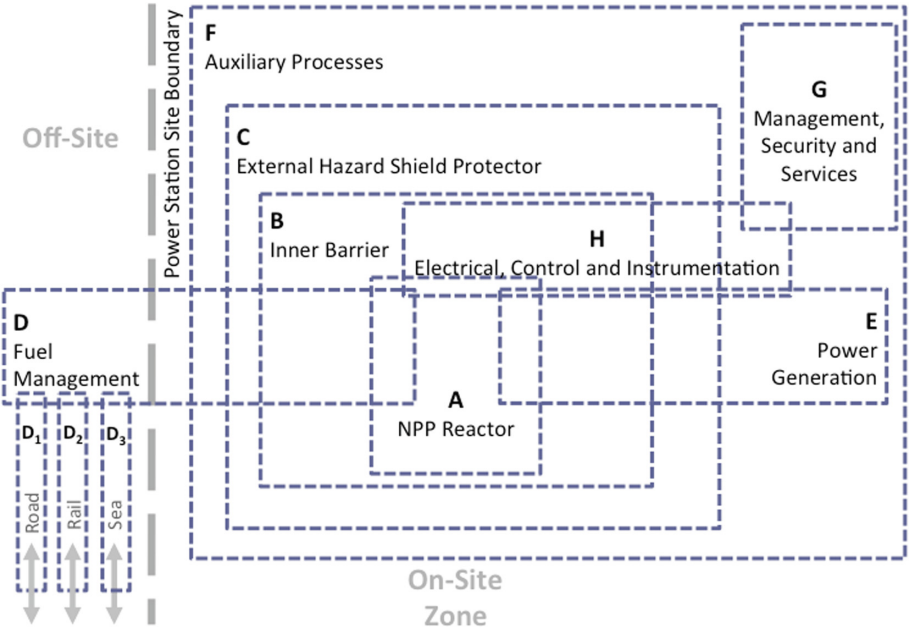


**Fig. 2.** Concept demarcation of the principal NPP system-architecture.

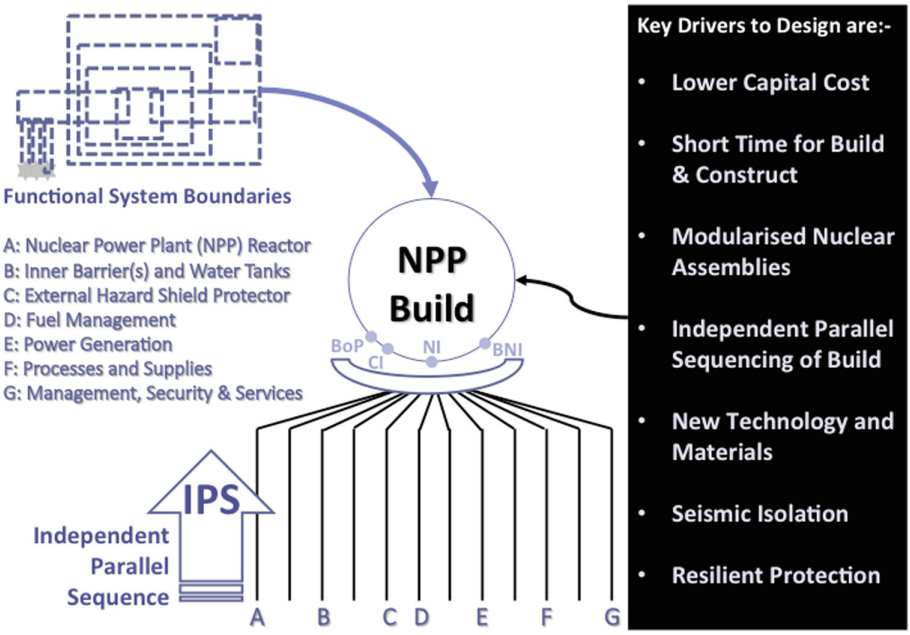


**Fig. 3.** Key drivers to design of a new kind of modularised build NPP.

## 3 Evolution of a Resilient Modular Containment – The "Protective Shield"

If we were now to follow a "no accident is tolerable" approach, Visser (1991), we should take a more holistic approach when designing new kinds NPPs by ensuring their overall robustness, resilience and the capability to cope with extreme hazards and potentially unexpected shock; not screening off high impact, low probability events, as has been past risk assessment practice. In the search for a "no accident is tolerable" approach, Visser (1991), we will need to be holistically wiser, while opening our minds to both the tangible 'facts' (that we have addressed as a norm in the past), but also accounting for other intangible possibilities that could evolve through an event sequence to a severe accident scenario, potentially amplified in its consequence by climate change.

In essence, it means that when we next formulate the engineering configuration and carry out our design code analyses of the future nuclear power plants, our final designs must be able to tolerate and withstand the range of the tangible/probables and the intangible/possibles. In addition, our safety-led defence in depth methodology will also need to be extended for post-event protection, mitigation and intervention strategies.

As discussed earlier, a crucial structure of the NPP design is the civil containment and the plant's internal support structures. From the lessons learnt experience of the Fukushima Daiichi accident in 2011, the civil containment design and its engineering needs to be improved in the following key areas:-

- Ultimate loading capacity with leak-tightness;
- Operability and reliability of the emergency relief and vent systems;
- Performance and reliability of the accident cooling systems and the coping strategy;
- Beyond design capacity and ultimate behavior of the containment;
- Reducing containment failure mechanisms and the formation of leakage paths;
- Improved management and control of severe accident corium scenarios;
- Better coping and resilience to multiple event sequences that arise during extreme hazards and severe accidents; and,
- Better response and recovery capability after possible extreme hazards and severe accidents.

Overall, there needs to be a more holistic acceptance that we need to design and build our infrastructure to be more robust against natural hazards like earthquake, storm, flood and tsunami; even tornadoes. If we presume global warming to be a growing reality, climate change and rising sea level is highly likely, then most certainly storms, cyclones and floods will return with greater regularity and that has greater destructive potential. The more of these events that occur, the more chance people shall be made homeless with the possibility for harm. More severe natural hazards like the mega-tsunami may seem a remote chance, so the timeliness of adequate up front warning for intervention measures should allow people to evacuate the vulnerable regions and avoid loss of life, but governments need to be ready and able with disaster plans that can work effectively. In addition to "conventional" habitation and transport infrastructure, there is a higher imperative that "critical and strategic" infrastructure is

both robust and resilient against future extreme hazards and shocks – this group includes fuel and power supply networks, power stations and emergency services. New NPPs will be identified to be of a critical category.

For the onset of extreme hazards when forewarning is impossible and people will not be able to evacuate quickly enough, and where safety-critical infrastructure like coastal sited nuclear plants could be endangered by mass-flood inundation, we need to identify these possible sites and enhance the design of their hydro-dynamic defences. Future hydro-dynamic design withstand of nuclear sites and their plant's civil containment design is a key imperative, therefore we have to apply a more holistic design approach than has been practiced in the past.

Arup is proactive to the reality of climate change, although much more needs to be done. The engineers and designers of today, and especially tomorrow, have a profound obligation to provide future-proof energy infrastructure that is robust, reliable and efficient source of energy in tune with the surrounding location and infrastructure. But the nuclear rector needs to be contained and be protected against external hazards, including earthquake and (in particular) mass-flood inundation, together with the associated safety, security, emergency response, recovery and monitoring data systems.

In simple terms, we may outline the function of a nuclear power plant containment to act as a biological shield against gamma-ray radiation, while further protecting the reactor internals against damage from the effects of a hurricane, tornado, flood or large aircraft impact. The present civil containment designs use a shell configuration that is strong at its outer curvature, yet weaker at its inside curvature, reflecting the inherent characteristic of shell structures. In addition, a single containment civil structure cannot act as a totally reliable protection against the release of radioactive fission products in the case of a severe accident because any containment structure can ultimately be made to fail if sufficiently high loadings are applied. This is an precisely why a pressure relief valve mechanism is provided in order to lessen excessive containment internal pressure build-up, and is therefore a very important integrity safeguard that makes up the containment system engineering design.

The very nature of a nuclear containment structure implies that its function is to "contain" whatever lies inside, with a further sub-implication that the internals inside the containment will also be protected. The ultimate integrity and reliability of the containment will be dictated by things like the:

- Design basis of the containment accounting for all the initiating events and subsequent secondary events;
- Conditions of loading against the structures resistance to loading;
- Internal loading parameters (primarily temperature and pressure); and,
- External loading parameters will be the energy of the impact force, together with the fluid/solid velocity.

The techniques used to design and analyse safety-critical structures like nuclear containments has developed since the early 1960's as light water reactor plants evolved particularly in the USA by companies like Westinghouse and Bechtel. Two main types of structural material have been used, steel and concrete, with composites of both in various geometric configurations. The standard nuclear secondary containment and building designs that used thinking some 50 years before climate change was accepted

as a real concern, must now apply a much more holistic view to design that needs to account for effects of climate change.

With this in mind, Arup is actively developing a new kind of modular civil "containment" that both protects against release of dangerous fission products in the event of a reactor accident, and is able to withstand extreme natural hazards that shall be amplified decade upon decade as a consequence of climate change effects. This new kind of nuclear power plant secondary containment, called the Protective Shield Concept (or abbreviated to the "PSC design" in Arup), is being developed to be very robust and resilient. The PSC is envisaged to be a composite assembly with pre- and post-stressed concrete parts that locate together, then fixed by compression-stiffening. It is anticipated that the PSC could be built and constructed on a power station site in a much shorter time than has existed in the past. See Figs. 4, 5, 6 and 7, below.

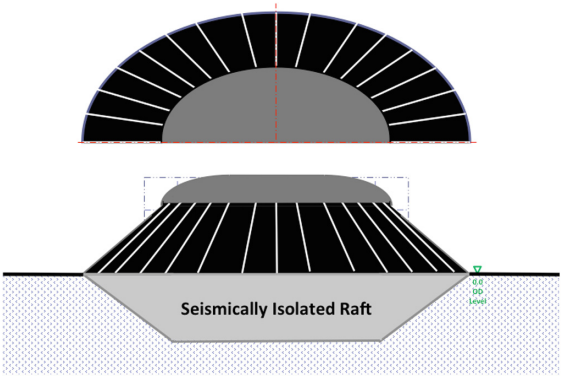


**Fig. 4.** Modularised build external hazard shield protector concept.

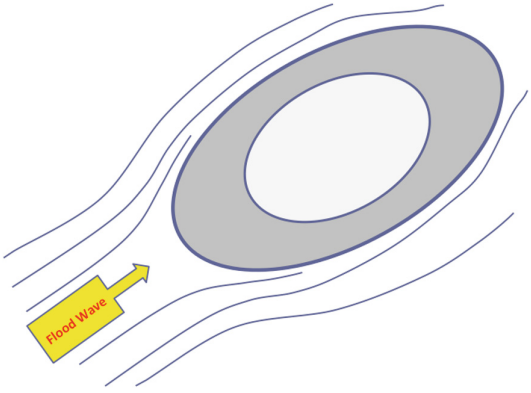


**Fig. 5.** Macro configuration of the hazard shield protector against flood.

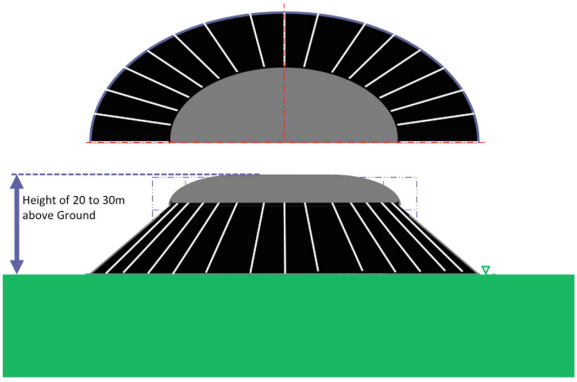


**Fig. 6.** Public view of new concept – visually smaller than past NPPs.

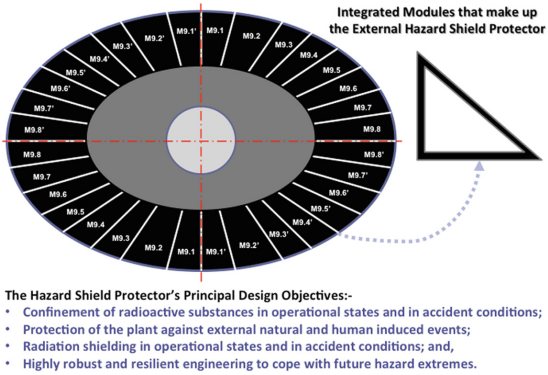


**Fig. 7.** Design objectives & build assembly of the shield protector.

## 4 A New Kind of NPP – It's a Management Challenge Too!

The established nuclear industry tends to have a conservative and unchanging mindset, so it was recognised as crucial to instigate an "ice-breaking" philosophy, structured with a broad set of design objectives at generic and specific levels, together with key design aims that try to eradicate past problems and inhibiting constraints. It will be necessary to establish completely new approaches to design, while at the same time the imperatives for good project management that can actually deliver systematic, safe and secure engineering solutions that can be readily built and work well in practice.

Establishing a completely new type of industrial process or energy conversion plant requires a mixture of creative ideas evolved through to ground-breaking innovation. But the ideas and innovation should be founded on sound thinking and pragmatic applicability that is feasible. Ground-breaking designs and their engineering further need to be wisely underpinned with a systematic design logic and progressive

development process, together with a keen eye on practical implementation in cooperation with existing supply chains to develop their existing technological capability and established design codes and standards. See Figs. 8 and 9 that follow.

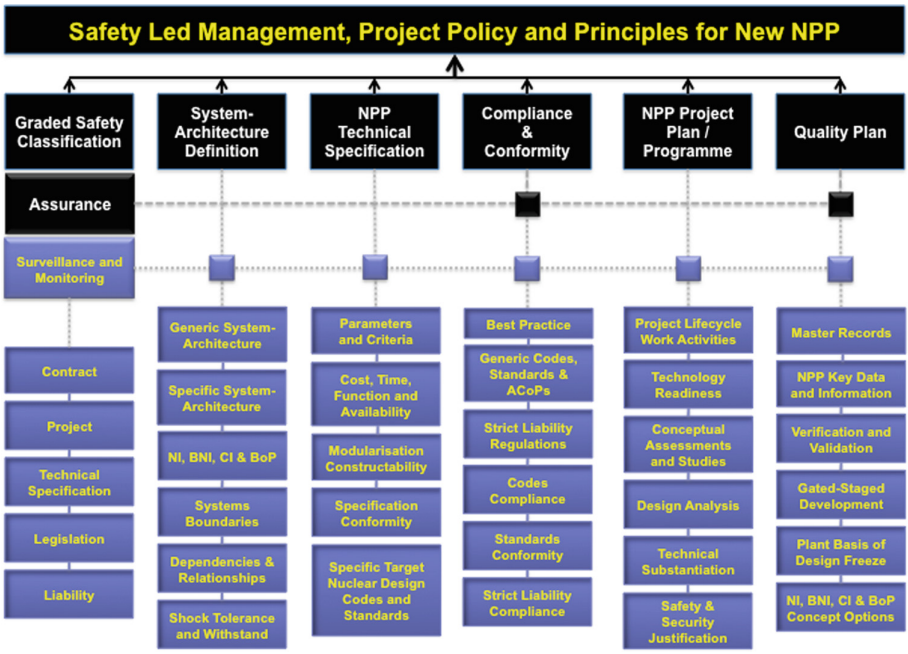


**Fig. 8.** Skeletal framework of the safety led management obligations.

It is recommended that the design and management process used for new kinds of NPPs (as for the next Generation IV technology), should take a more holistic approach. Not only considering compact and modular reactor circuits integrated with highly efficient nuclear fuel cycles, but also considering more robust and resilient system-architecture that includes the civil containment structure as a "protective shield", as introduced in this paper. This approach will better ensure the overall robustness, resilience and the capability of the NPP to cope with extreme hazards, the likes of which will be amplified due to the impact of climate change. It is advocated that this approach will provide for new kinds of nuclear power stations to be part of the world's energy mix, accepted as a low carbon energy source; in addition to offering a more favourable case for new NPPs to be located in reasonable proximity to major population centres, while also recognising the reality of population growth in developing countries.

| Region | Compliance and Conformity to Particular Nuclear Related Standards and Guidance that will relate to the Hazard Shield Protector. |
|---|---|
| UK | ONR Safety Assessment Principles (SAPs) 2014.<br><br>ONR Guidance to Inspectors for the Assessment of Licensee Submissions Covering Capable Faulting Hazard – Draft. |
| Worldwide – International Atomic Energy Agency (IAEA) | IAEA Specific Safety Guide SSG-9 on Seismic Hazard in Site Evaluation for Nuclear Installations.<br><br>IAEA Safety Standards: NS-G-1.6 on Seismic Design and Qualification for Nuclear Power Plants.<br><br>IAEA Safety Standards: NS-R-3 on Site Evaluations for Nuclear Installations.<br><br>IAEA Safety Publication: NS-G-3.5 on Flood Hazard for Nuclear Power Plants on Coastal and River Sites. |
| USA<br><br>NUREG | NUREG/CR-5503: Techniques for Identifying Faults and Determining Their Origins.<br><br>NUREG/CR-6966: Tsunami Hazard Assessment at Nuclear Power Plants Sites in the United States of America. |
| European | EUR. European Utility Requirements for LWR Nuclear Power Plants. |

**Fig. 9.** Specifically targeted nuclear design codes and standards.

## References

Maslow, A.H.: A theory of human motivation. Psychol. Rev. **50**, 370–396 (1943)

Visser, J.P.: Development of safety management in shell exploration and production. Contribution to 1991 Bad Homburg Workshop on Risk Management. In: Brehmer, B., Reason, J.T. (eds.) In Search of Safety. Lawrence Erlbaum, Hove (1991)

# Nuclear Civil Engineering Towards the Simplification and Digitalisation

Nguyen-Hoang Bui(✉), Pascal Charles, and Hervé Blieck

EDF/DIPNN/CNEN, Montrouge, France
{nguyen-hoang.bui, pascal-emmanuel.charles, herve.blieck}@edf.fr

**Abstract.** Further to the climate change summit COP21 organized in Paris, France in December 2015, nearly 200 governments have committed to cut the emission of greenhouse gases and to limit global warming to well below 2 °C by the end of the Century. Nuclear, low-carbon energy, is perfectly integrated within the universal energy mix plan. It is one of best solutions for guaranteeing energy production increases to meet growing demand and protection of the environment. In order to sustainably develop nuclear energy industry, the challenges of new build nuclear power plants (NPP) are to permanently ensure the highest levels of quality, security and safety as well as to optimize the project planning and economy. Therefore, it is important to study and to develop innovative concepts, technologies and methodologies, and to improve the process for the nuclear civil engineering.

Based on the simplification and the digitalisation, numerous important measures have been undertaken throughout the design of Hinkley Point C (HPC) NNP in Sumerset, UK. The paper consists of reviewing and analyzing some of them such as: the simplification of structural construction, the balance of use of pre-cast structures, the 3D reinforcement modeling method, the 4D modeling for project management and the improving of design processes. They allow optimizing the design, facilitating the calculations and analysis, and reinforcing the design robustness, anticipating any execution difficulties, minimising the interfaces and reducing the overall design time. A simple, quality and robust design contributes to shorten the construction period, to optimise the time-schedule and to improve the quality, security and safety of the construction as well as significantly reduce the cost and the impacts of construction to the environment. As a result, several perspectives of innovations for the future such as improvement of Building Information Modeling (BIM) applications for the project management will be also introduced.

**Keywords:** Nuclear civil engineering · Simplification · Digitalisation

## 1 Introduction

Currently four third generation European Pressure Reactors (EPR) are under construction in Europe (Finland, France) and in China. EDF has decided to build two new EPR reactors in Somerset, UK. EPR advanced technology guarantees the highest level of safety thanks to the robustness of its barrier design and its active and passive

© Springer Nature Singapore Pte Ltd. 2018
H. Tran-Nguyen et al. (eds.), *Proceedings of the 4th Congrès International de Géotechnique - Ouvrages -Structures*, Lecture Notes in Civil Engineering 8,
DOI 10.1007/978-981-10-6713-6_113

protection systems. The civil structures ensure safeguards against external and internal hazards. The construction is completed to the highest quality and security level. However, to improve the competitiveness of nuclear energy, EDF has launched the CAP 2030 fostering simplification and digitalisation. This is with the objective to reduce costs, to construct plants more rapidly by continually ensuring the highest level of quality, security, safety and minimising the impacts to the environment.

Regarding the civil design and construction, much optimisation has been carried out. In this paper, the authors review and analyse several measures undertaken for the HPC project, and focus on the simplification and digitalisation aspects.

## 2 Civil Design and Construction Simplification

Civil design and construction simplification consists firstly of defining the adequate design requirements by eliminating the conservative safety classification of structures and using available and appropriate hypothesis. The simplification can also be explored in conceptual design and the calculation methodologies. In addition, the use of pre-fabricated structures, the optimisation of processes and interfaces, the application of the advanced technologies for the design and construction, etc. will increase the productivity and the competitiveness. This section will concentrate on the conceptual design and improvements to the design process. For the conceptual design, various optimisations are possible i.e. alignment of superposed walls, elimination of angular elements and structures, standardisation of design, consideration of construction methodology and dismantling issues and so on. The optimisation of the gusset shape at the base of the inner containment as well as the use of pre-fabricated structures will be studied in detail. Regarding the design process optimisation, the steel structure design shall be analysed as an example of reducing the interfaces and of optimising the work chain.

### 2.1 Optimisation of the Gusset Shape at the Base of the Inner Containment in the Reactor Building

The reactor building civil structures are composed of inner and outer containment walls and of internal structures that are separated from the common raft and the containment walls by the steel liner and joint shown in red on Fig. 1. In the Flamanville 3 EPR NPP (FA3), difficulties were met during the construction of the gusset including the liner assembling and welding, the concreting, the removal of formwork and installation of the joint between gusset and the internal structure's raft. Following the evaluation of several options to simplify the gusset shape, the solution illustrated below was chosen.

According to feasibility studies, the horizontal reinforcement ratios are quite similar between both designs. The vertical reinforcement ratios are slightly higher due to the increase of internal efforts with the new shape of gusset. Despite the increase of reinforcements, the new shape of gusset offers design and construction advantages. Firstly, various studies showed few benefits of a wide gusset on the shear resistance. Additionally the new shape of the gusset simplification leads to an optimisation of the concrete volume, making the calculations and analysis easier and faster, thus

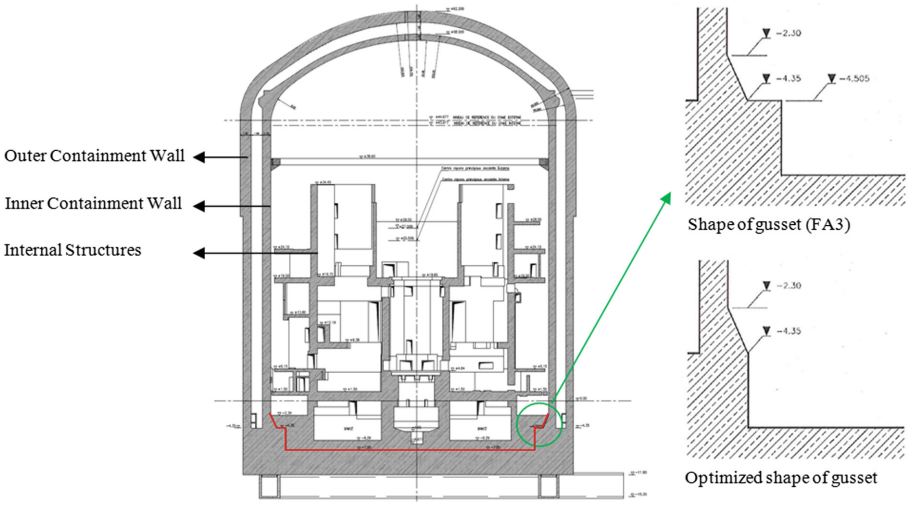


**Fig. 1.** Location and shapes of gusset of the reactor building.

eliminating the calculation uncertainties. Secondly, it reduces significantly the construction planning by reducing the liner welding works, avoiding the difficulties of pouring for the gusset's rectangular corner and simplifying reinforcement and formworks.

## 2.2 Use of Pre-fabricated Structures

The choice of pre-fabricated or on-site poured structures is based on a balance of the four following factors: (a) Adequacy between the element's weight and the capacity and the location of the crane; (b) Technical feasibility and the know-how of the civil works contractor, mainly on the connection details with other structures; (c) Planning of studies, especially the anticipation of design input data and (d) Planning of construction and the need to optimise some critical tasks.

Based on feedback from previous projects, the optimisation of the construction sequence and time-schedule by using pre-fabricated structures has been applied for the HPC project. For example, the fuel treatment and cooling (PTR) pool, the east and west parts of the central slab at +1.50 m, parts of south and north steam generator bunkers' walls, etc. in the reactor building are precast.

In particular, the construction of the PTR pool is on the critical path of the project planning due to large metal liner works (welding of equipment anchor plates and piping sleeves, interfaces with doors, etc.) and inspections. The liners are prefabricated in the workshop. They are transported and pre-assembled on site. There will be two precast packages for the cavity reactor and internal storage compartments as well as the transfer and instrumentation lance storage compartments. They will be composed of concrete slabs at +7.30 m/+ 6.30 m, full height wall liners, full height internal formwork and supporting steel structures, first lift of reinforcements and of formwork. Each package will weigh up to 700 t. Figure 2 provides details on the PTR pool and the two

packages. As a result of prefabrication of the pool, approximately 12 months could be saved in the overall construction planning with the reduction of 55% to 80% of welding works inside the building. This also means significant reduction in costs related to the on-site quality execution issues and the time-schedule saving.

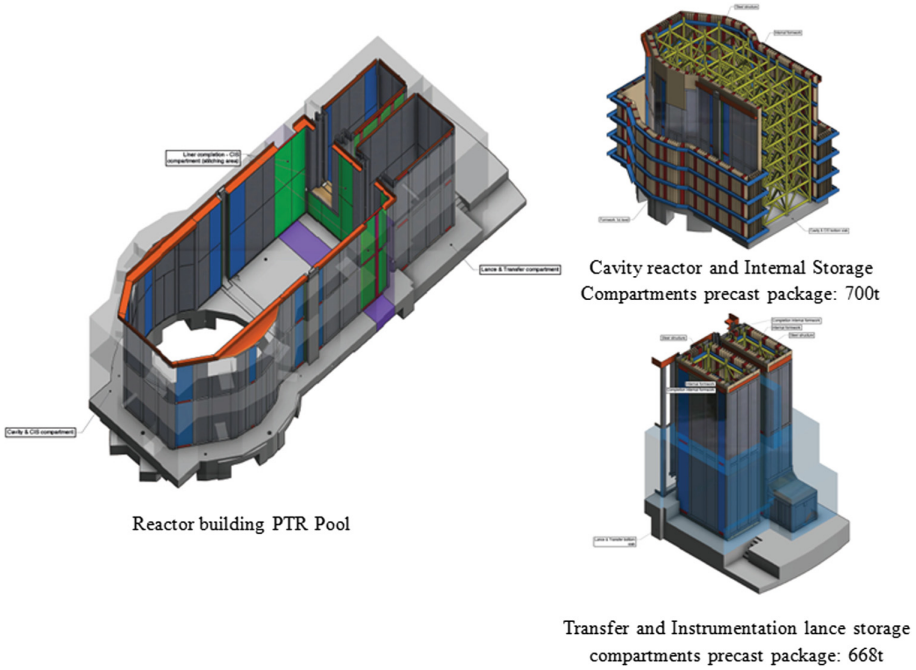


**Fig. 2.** Overview of the reactor building PTR pool and of the 2 packages of precast structures.

### 2.3 Secondary Steel Structure Design Process

Similarly for other civil structures studies, the detailed design of the secondary steel structures was performed by the steel structure supplier (EPR Flamanville 3 NPP) or by civil design offices (EPR Taishan 1&2 NPP).

Due to the interfaces with other disciplines inside the buildings (equipments, piping - electrical cable trays - HVAC ducts and their supports, etc.), the basic design (sizing, beam location) of steel structures were performed internally by EDF engineering teams. This design process leads to additional costs and delays in engineering time-schedule. Firstly, this is due to the repeated modeling works for basic and detail designs phases. Moreover, there are a lot of interactions between the steel designer and EDF for the validation of complex structural design with regards to layout requirements. Furthermore any modifications could lead to risks of additional works and therefore delays.

An integrated design process is under implementation. It covers both basic and detail designs that will be completed by EDF. The process is characterised by a

common team applying standards and using common guides and software. The same design procedures will be applied for all the design steps. This allows a uniform design and optimised work-flow. The input data, models, calculations, documents, drawings, catalogues, etc. are standardised for the automation of the design calculation chain and a uniform and harmonised design for all the structures. Within this design process, specialised design partners and civil works contractor are involved in the preparation of design procedures in order to benefit from their know-how and feedback as well as to implement construction methods and sequences early in the design chain. This process significantly reduces the cost and schedule and it reinforces the quality, the robustness, the safety, the flexibility and efficiency of the steelwork design.

As shown in the Fig. 3, the steel structure is defined in the 3D project master model (PDMS software) based on the layout requirements and previous projects' feedback and/or pre-sizing if relevant. The structural geometry is extracted and implemented in the RSTAB calculation software through a standardised structure calculation template (load cases, loads combinations, materials' characteristics, etc.). Following calculations and analysis, the frame and support efforts are extracted as an input for the design of anchor plates and of connections. On another hand, the detailed steel structure model is built from the PDMS geometry data and the detail design of connections. The drawings and manufacturing details are automatically generated respecting the agreed template. The structure design data prepared using BOCAD software can be directly used for the manufacturing process.

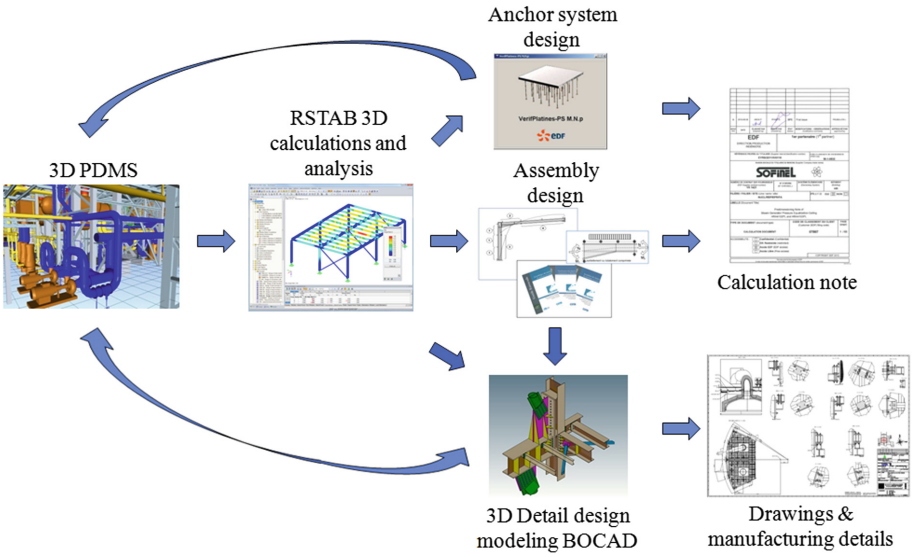


**Fig. 3.** Steel structure design chain

## 3 Digitalisation

The management of the design data from the PDMS project master model to the BOCAD detailed steel structure modeling and to the cutting, welding machines within the manufacturing process illustrates digitalisation in the nuclear civil engineering sector. For decades, digitalisation and management of documents and projects' data (models, calculation notes, drawings, etc.) were a part of quality management process in nuclear power plant projects. Whatever the field, digitalisation is applied for optimisation of the project management process to reinforce the quality and safety design by ensuring the highest level of data sharing and analysis and to reduce considerably the cost and planning by optimising the interfaces, accelerating the calculation process, detecting and anticipating any difficulties on site. Examples of two innovations, 3D reinforcement design method and 4D modeling will be detailed and analysed hereafter.

### 3.1 3D Reinforcement Design

By traditional methods, the standard 2D method is used for producing reinforcement drawings. For a large, complex project such as the construction of a nuclear power plant, clashes (rebar/rebar, rebar/embedded pieces) are often managed on site, that can introduce disruptions to the construction. That could lead to extra-costs due to modifications and additional studies as well as to delays to concrete pouring.

3D reinforcement modeling is an innovative method for producing civil execution drawings, enabling clash detection and clash resolution. Based on civil detail design calculations and reinforcement sketches, the reinforcements are modeled by TEKLA software. The clashes control is performed in order to detect any conflicts between reinforcement rebar, mainly in complex areas and between reinforcement rebar and embedded pipes, anchor plates, etc. (see Fig. 4a). The clashes will be jointly resolved by civil and layout designers. 2D drawings are generated once there are no longer any clashes present (see Fig. 4b).

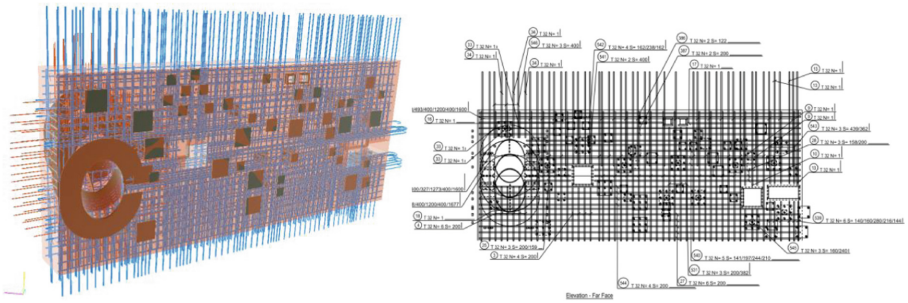

a) 3D reinforcement model b) 2D reinforcement drawings generated from the 3D model

**Fig. 4.** 3D and 2D reinforcement layout

This method requires more engineering time for the production of reinforcement drawings and the resolution of clashes. Furthermore, it requires additional work related to TEKLA tool development. Despite the additional costs for undertaking studies and the delay of 1.5 months for validating the reinforcement drawings, 3D reinforcement method presents numerous advantages. It reduces and eliminates clashes and undetected errors, therefore increases quality and design compliance. This could lead to an improvement in nuclear safety and regulatory confidence. Less design change is also a major factor for improvement of nuclear safety compliance and reduction of risks. In addition, it significantly improves the conditions for the reinforcement work and the installation of embedded parts on site since the clashes have already been resolved at the design stage and will not have to be treated during construction. Finally, it has notable benefits to the construction work and time-schedule.

### 3.2 4D Modeling

The 3D master model is composed of data (volume geometry, attributes including materials specifications, guide and detailed design drawings, specifications and design assumptions, etc.) from all disciplines and structures (civil and steel structures, piping – HVAC - electrical cable trays and their supports, cabinets, equipments, etc.). This has been widely used in the previous EPR projects.

A fourth dimension – the time has been introduced recently. 4D modeling enables the simulation of virtual construction. It has several beneficial uses: work preparation for facilitating the on-site construction, identification and resolution of clashes of planning especially for co-activities, demonstration of adequacy of construction and erection sequences, combination of stakeholders' information and data, etc. Finally, 4D modeling reinforces the constructability and the security on site. It also facilitates establishing a realistic time-schedule and avoiding any planning clashes.

## 4 Conclusion and Developments

Further to above reviewed measures, several innovations are under perspective such as: 5D and 6D modeling with the implementation of cost and association of all aspects of project life-cycle management information; automation of structural calculations, anchor plate and assembly design-flow until the generation of calculation note for the secondary steelworks, etc.

In conclusion, the simplification and the digitalisation are considered as performance levers for the nuclear energy. They promote the improvement of civil design quality and robustness, to optimise the time-schedule in particular during the construction, to facilitate the design and construction works, then to reinforce the security on the site. They contribute towards the improvement of safety and the reduction of overall costs. The optimisation of materials' uses, the guarantee of high security levels and the shortening of construction duration reduce in fact the impacts of construction on the environment. Every stakeholder and project member becomes a contributor towards simplification and digitalisation. They will firstly improve their work efficiency

and life quality. On the collective plan, this could improve the performance and competitiveness of the nuclear energy industry.

**Acknowleadgement.** The authors would like to express our gratitude to colleagues at EDF/CNEN and EDF/SOFINEL, especially Jean-Sébastien VAAST, Edouard MACHADO, Andres HALBRITTER, Julien MENACHE, Frédéric RICHARD, Vincent LIONNETON, who introduced and implemented the above innovations that have contributed significantly to the success of the HPC project.

# Soil-Structure Interaction Under Multiple Static Loads Using a Flexibility Matrix of Soil: Case Study of a Nuclear Power Plant

V.-N. Nguyen[1(✉)], P.-L. Regazzoni[2], D. Pham Thi Anh[1], S. Erlicher[1], S. Reynaud[2], and D. Allagnat[2]

[1] Egis Industries, Montreuil, France
{van-ngan.nguyen, dao.phamthianh, silvano.erlicher}@egis.fr
[2] Egis Géotechnique, Seyssins, France
{pierre-louis.regazzoni, sebastien.reynaud, dominique.allagnat}@egis.fr

**Abstract.** The purpose of this article is to present the methodology used to define the soil-structure interaction under multiple static loads of a nuclear power plant. Nuclear facilities are characterized by their geometrical complexity and by the large size of the buildings. This has induced the need for robust numerical tools and the need to develop a specific methodology. Actually, in structural calculations the soil is usually represented by linear springs defined at each node of the model by iterative process. When the stiffness computed at two subsequent iterations are almost identical, iteration is stopped. The obtained stiffness values depend on the load case. To simplify this process, and under condition of linearity of the soil behavior, it is proposed to compute the soil flexibility matrix which is finally integrated as a "superelement" within the software ANSYS for the structural computation. The soil flexibility matrix is an intrinsic representation of the soil, which is totally independent from the stiffness, loading, geometry of structures. Then, any modification of structures does not require the reconsideration of the boundary condition (soil). The effectiveness and accuracy of this procedure is discussed with reference to the case study of a nuclear power plant

**Keywords:** Substructure method · Flexibility matrix · Soil · Superelement · Nuclear island

## 1 Introduction

The purpose of this article is to present the methodology used to define the soil-structure interaction under static loads and accounting for the effect of adjacent buildings of a nuclear power plant. Nuclear facilities are characterized by their geometrical complexity and by the large size of the buildings. This has induced the need for robust numerical tools and the need to develop a specific three-step methodology.

The first phase was the implementation of the soil geometry, taking into account the different states of alteration, the fault network, the accurate lithology and the exact

© Springer Nature Singapore Pte Ltd. 2018
H. Tran-Nguyen et al. (eds.), *Proceedings of the 4th Congrès International de Géotechnique - Ouvrages -Structures*, Lecture Notes in Civil Engineering 8,
DOI 10.1007/978-981-10-6713-6_114

geometry of building foundations. This was achieved using specific tools like GDM and AutoCAD (Autodesk 2011). The second analysis step was the implementation of the soil model (lithology and mechanical parameters) in the software FLAC3D (ITASCA 2013) used for the soil mechanical computations and soil-structure interaction (SSI). The third phase was the SSI conducted to compute the soil flexibility matrix. This matrix is then used to represent the soil in the building FE model used for the design calculations.

Actually, in structural calculations the soil is usually represented by linear springs defined at each node of the model on the underside of the raft. For the definition of their stiffness, an iterative process is used, a first guess is made on spring stiffness in the building model; this gives the nodal reactions under the foundation, which are applied on the soil model. Then, the loading is applied and a first couple force/displacement on each node of the model is calculated. This allows defining a new set of stiffness which is implemented for the structural computation. A new set of force applied to the soil is calculated and the previous process is renewed. After several iterations, a convergence criterion is reached.

To simplify this process, and under condition of linearity of the soil behavior, it is proposed to compute the soil flexibility matrix. The main advantage is to facilitate the integration of the soil stiffness in the software used for the structural calculations.

## 2 The Geological 3D Model

### 2.1 Geological Context of the Studied Site

The layers of soil encountered are the following, from the most recent to the older deposits:

- "Made ground" (anthropic deposits): clay and sandy clay (thickness: 1–2 m);
- Over burden deposits: clay less or more gravely (thickness: $\sim$1 m);
- Blue Lias formation: alternation of mudstones and limestones (thickness: 75 m);
- Lilstock formation: limestones and mudstones (thickness: 1.3–3.4 m);
- Westbury formation: black shales with limestones beds (thickness: 7–11.5 m);
- Blue Anchor formation: grey to green mudstones and siltstones, with anhydrite-gypsum levels (thickness: 26–36 m);
- Red Mudstones formation: red and green mudstones and siltstones with nodules and levels of anhydrite -gypsum.

The foundation raft level is mainly in the lower part of the Blue Lias formation (mudstones and sandstones).

Three different water levels are taken into account for design computations: (i) the natural water level, (ii) the level for the construction period, 21 m below the natural water level (after drawdown), (iii) the level for the exploitation period, at 2 m below the natural water level (permanent water level drawdown).

## 2.2 Numerical Tool and Model Construction Method

The software used to build the geological model is the geo-modeler GDM (BRGM 2014). It allows building a geological model based on the interpolation of data between boreholes. A computer-aided design (CAD) with AutoCAD software allowed supplementing and correcting strata calculated with the software "GDM".

In order to build a geometrical model of the geological layers (3D geo-modeler), the synthesis of the factual data (boreholes data) and the interpreted data (geological map) is required.

All factual data and geological rules are captured in the GDM software (BRGM 2014). Some complementary assumptions are done in order to complete the data-set. These assumptions concerned mainly the layer thickness. Moreover, some conditions are imposed on the model. These conditions arise from geological processes applied by the software on the geometry of the strata. Data complements are done essentially in the South-West and Northern part of the model.

For interpolating the data, a grid of 2 m × 2 m is used. This grid size allows a sufficient detail in the numerical model of the soil for a reasonable computation times. For the interpolation computations of the DTM (Digital Terrain Model) of the site topography, we use the ordinary kriging (or linear kriging without derivative). For the computations of the geological surfaces, we use the universal kriging (or kriging with trend). This choice is justified by the dip of the layers in the Northern part of the model.

Due to numerical difficulties (spatial scattering of the geological data), it was not possible to build the fault model with GDM. Consequently, the GDM model has been computed without faults. Based on the analysis of a geologist, the faults are represented into surface object with software AutoCAD and Covadis.

The GDM model and the faults are then integrated into AutoCAD. This ensures the continuity between the lithological model and the faults system. To fit the geometrical model to our geological analysis, some redrawn work has been done with AutoCAD.

The AutoCAD files include all the geometrical information concerning the geological layers and the fault system of the site. An example of cross-section is given in Fig. 1 on the right. On the left of Fig. 1 also presents an extract of the geological map at the natural ground.

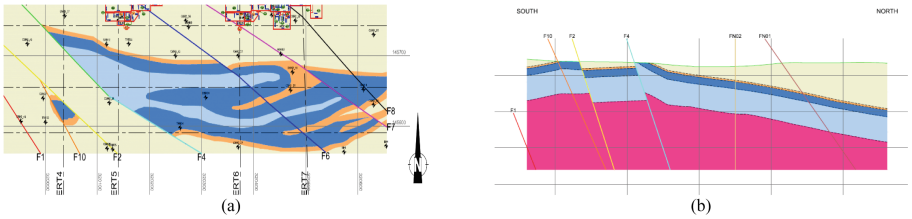


(a) (b)

**Fig. 1.** Example of cross-section of the numerical geological model (right) and extract of the geological map from the numerical geological model (left)

The geological model (essentially lithology and faults geometry) does not include all the information on the soil behavior. Thus, several additions have been made on the geological model to prepare the geotechnical model (essentially mechanical behavior, and additional layers):

- The layers of earth-fills and the surface soil layers, their base are defined as geometrical surface. This two layers have specific mechanical properties.
- The states of alteration of the rock that apply from the surface until deep, regardless of the nature of the rock: the parameters are defined according to the depth.

Geotechnically, the mechanical parameters are given by the point position compared to the geological layer and the alteration degrees.

In summary, in the numerical model, it is set 7 geotechnical layers: 5 rocky layers and 2 soil layers. The rocky layer is divided in to 4 sub-layers according to degree of alteration. Model size is about 1 000 000 soil volume element (800 m $\times$ 500 m $\times$ 100 m thick).

## 3 The Soil Mechanical 3D Model

### 3.1 Aim of Soil Mechanical Model and Numerical Tool

The soil mechanical model must allow representing the correct behavior of soil under the structure static loads accounting for the interaction effects due to neighboring buildings. This model should allow an accurate representation of the soil structure interaction (SSI) which is considered as an input data for the structural models.

The lithology and the geo-mechanical parameters are implemented in FLAC 3D code. This code allows the modeling of faults system and the use of a wide choice of constitutive laws, particularly the anisotropy of the rock formations. This model takes into account the phasing of construction and the corresponding water levels.

### 3.2 Soil Constitutive Laws and Parameters

As mentioned above, two types of mechanical behavior are possible: rock behavior or loose soil behavior. The mechanical parameters are defined for the different layers. In order to analyse the impact of non-linearity on the global ground behavior, two set of parameters are defined: one set defines the behavior without failure (linear elastic constitutive laws), another set defines the failure criteria. The non-linearity comes from the failure model. Consequently, for each type of mechanical behavior, two set of parameters are used:

(i) Soil:
  (a) 1st set: elasto-plastic behavior with isotropic behavior (2 parameters) and a Mohr-Coulomb criterion (3 parameters)
  (b) 2nd set: elastic behavior, isotropic behavior;

(ii) Rock:
  (a) 1st set: elasto-plastic behavior with isotropic elasticity and a Hoek-Brown criterion (3 parameters)
  (b) 2nd set: elastic behavior, transversely isotropic model (5 parameters).

The value of elastic modulus ranges from roughly 10 MPa for the soils to 1.000–10.000 MPa for the rocks. The mechanical parameters (modulus, Poisson's ratio, friction angle) were adjusted according to the in-situ tests (dilatometer, pressuremeter) and laboratory data (triaxial test, oedometer tests).

Concerning the fault system, the geometry of each principal fault is represented accurately. The mechanical law considered for faults is an elastic law, tangent and normal to the surface, and a Mohr-Coulomb criterion.

The "base" of the foundation rafts is modelled with CAD software in three dimensions. Then, the model is implemented in the soil computation software (Fig. 2).

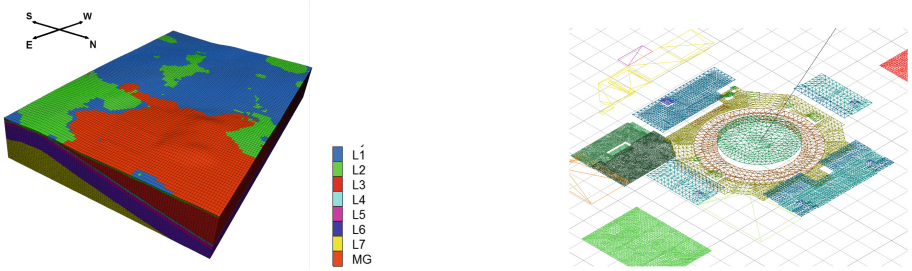


**Fig. 2.** (left) View of the initial soil computational model (FLAC 3D) with the different geotechnical layers without alteration layer and faults; (right) View of the slab geometry with the CAD software

### 3.3 Assessment of Non-linearity Effects

The soil mechanical 3D model was used to assess the overall behavior of ground under the dead weight of all buildings (long term behavior). Several tests were performed to check the model robustness. In particular, the comparison between the displacements calculated with FLAC 3D and those calculated with another simple computation method showed good compliance. This model enables, firstly, to know the details of the soil behavior under each building and, secondly, to calculate the soil structure interaction comprehensively (stress, strain, displacement…).

The effect of non-linearity is assessed by analyzing the occurrence of plasticity zones and by comparing the displacement obtained by the elasto-plastic model, with that obtained by the elastic model. Plastic zones appear at the last load step; nevertheless the movements obtained with both models (elastic and elasto-plastic model) are almost identical. It is then concluded that the soil behaves linearly under the operating

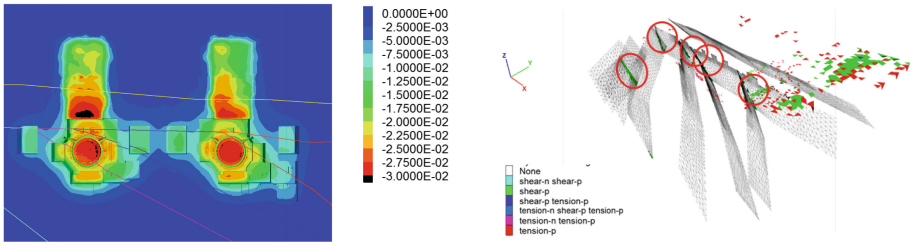


**Fig. 3.** On the left, map of Z-displacement of the soil surface under the deadweight (color-scale is in meter); on the right, view of plastic volumes of soil and representation of the fault system (color-scale shows the occurrence of plasticity)

loads. Thus the computation of the flexibility matrix can be performed. The following section explains the methodology (Fig. 3).

## 4 Computation of the Flexibility Matrix from Flac 3D Soil Model

Since the soil behavior is supposed linear, the force-displacement relationship is described by the following equation:

$$\{\delta\} = [S] \times \{F\} \tag{1}$$

The displacement vector $\{\delta\}$ at each point is obtained by the multiplication of the force vector $\{F\}$ by a flexibility matrix $[S]$.

In order to compute the flexibility matrix from the FLAC 3D model, a unitary force is applied at each point under the buildings according to one spatial direction (X, Y or Z). During the process, the three spatial directions are swept. The result of one computation is the displacement field under the buildings for one unit load. This vector is recorded as a structured text file which is easily readable by computer language. So, based on the text file, the flexibility matrix may be built and formatted to be read by another computer program, like the ANSYS software.

The main advantages of this method with respect to more commonly used on independent Winkler springs, are that the computed solution is accurate (taking into account the 3D effect), the effect of loads between different buildings and directions are taken into account at each point of the model and the answer takes into account the terms of coupling xz and yz (non-diagonal terms).

The flexibility matrix [S] generated by FLAC 3D software is a square matrix of size "3n × 3n", where n is the number of nodes of solid soil model in FLAC 3D at the interface with the foundation raft of the structure (see Eq. (2)). The matrix is composed by 9 sub-matrices:

- [Sxx], [Sxy], [Sxz]: corresponding to the displacement of each node in the respective directions X, Y, Z under the unit force of X direction,

- [Syx], [Syy], [Syz]: idem under the unit force of Y direction,
- [Sxz], [Syz], [Szz]: idem under the unit force of Z direction.

$$\begin{Bmatrix} \delta_{x,1} \\ \vdots \\ \delta_{x,n} \\ \delta_{y,1} \\ \vdots \\ \delta_{y,n} \\ \delta_{z,1} \\ \vdots \\ \delta_{z,n} \end{Bmatrix} = \begin{bmatrix} s_{xx,1,1} & \cdots & s_{xx,1,n} & & \\ \vdots & \ddots & \vdots & [S_{xy}] & [S_{xz}] \\ s_{xx,n,1} & \cdots & s_{xx,n,n} & & \\ s_{yx,1,1} & \cdots & s_{yx,1,n} & & \\ \vdots & \ddots & \vdots & [S_{yy}] & [S_{yz}] \\ s_{yx,n,1} & \cdots & s_{yx,n,n} & & \\ & [S_{zx}] & & [S_{zy}] & [S_{zz}] \end{bmatrix} \begin{Bmatrix} F_{x,1} \\ \vdots \\ F_{x,n} \\ F_{y,1} \\ \vdots \\ F_{y,n} \\ F_{z,1} \\ \vdots \\ F_{z,n} \end{Bmatrix} \tag{2}$$

## 5 Modelling the SSI Based on the Substructuring Method

The substructuring method for static analysis consists on condensing a group of finite elements into one reduced stiffness matrix called *superelement* (reduced model). This section presents the construction of the reduced stiffness matrix representing the soil (Fig. 4).

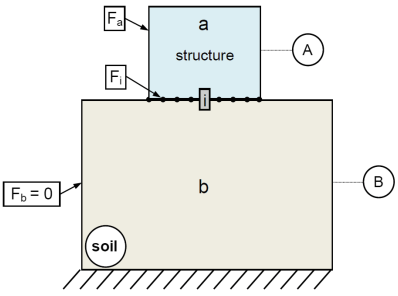


**Fig. 4.** Structure and soil models

Consider the finite element model G constitutes by the two substructures: A (structure model) and B (solid soil model) as shown in the figure below. The finite element model G (A + B) can be subdivided in the following Degrees of Freedom (DOF's) sets:

- a: internal DOF's of structure model (A),
- b: internal DOF's of soil model (B),
- i: interface DOF's between soil and structure.

The construction of the reduced stiffness matrix of the soil model (B) at the interface DOF's "i" is totally independent from the structural model (A) (AJA 2000). Thus, this task can be performed using a separate soil model.

Consider the finite element solid soil model as shown in figure above. After applying constraint conditions, static analysis equations become in flexibility submatrices form as follows:

$$\begin{bmatrix} S_{ii} & S_{ib} \\ S_{bi} & S_{bb} \end{bmatrix} \begin{Bmatrix} F_i \\ F_b \end{Bmatrix} = \begin{Bmatrix} \delta_i \\ \delta_b \end{Bmatrix} \tag{3}$$

In soil model, only interface surface (i) of soil with the structure is the loaded area ($F_i \neq 0$). All the other parts of soil model are considered as unloaded ($F_b = 0$). Thus, the Eq. (3) can be simplified:

$$[S_{ii}]\{F_i\} = \{\delta_i\} \tag{4}$$

$$\Leftrightarrow \{F_i\} = [S_{ii}]^{-1}\{\delta_i\} \tag{5}$$

Thus, the reduced stiffness matrix is the inverse of flexibility matrix at interfaces DOF's:

$$\left[K_{ii}^{red}\right] = [S_{ii}]^{-1} \tag{6}$$

- $[S_{ii}]$ is computed as explained in the previous section

To resume, in order to perform a static analysis of structures by substructuring method, the following items are needed (see Fig. 5):

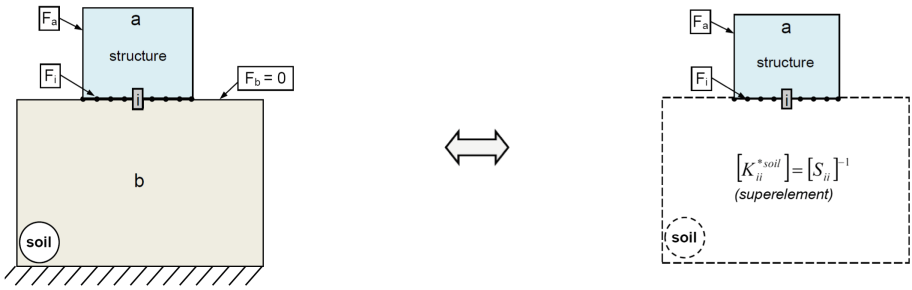


**Fig. 5.** Substructure method for SSI: Structure and full model of soil (left) is equivalent with structure and reduced soil model (right)

- finite element model of structures (A),
- reduced stiffness matrix of soil to interface DOF's calculated as the inverse of the flexibility matrix at the interface DOF's between structure and soil.

## 6 Case Study of a Nuclear Island

In this section, the results of SSI study of a nuclear facility using substructuring method are presented. These results are compared with the traditional method using independent Winkler soil-springs system:

- for substructuring method: a reduced stiffness matrix of soil $\left[K_{soil,A}^{i,red}\right]$ at interface DOF's between soil and structure is calculated and then integrated in ANSYS model as a *superelement*. This matrix is applied for all static loads;
- for Winkler soil-springs method: iterative process is required for each load case basing on the flexibility matrix of soil or directly on 3D model of soil.

Two representative load cases in vertical and horizontal directions are to be performed for the comparison and the results are shown in the Figs. 6 and 7:

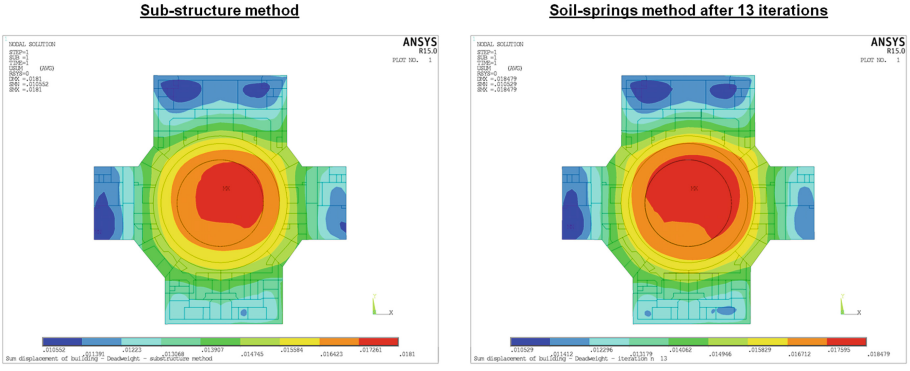


**Fig. 6.** Total displacement of raft under dead weight of structure: with substructure method (left) with soil-springs after 13 iterations (right)

- Dead weight of building (Fig. 6)
- Thermal load case (Fig. 7).

It is noticed that the settlement obtained with the substructure method (no need of any iteration process) is almost the same with the one obtained with independent Winkler soil-springs for a certain number of iterations: 13 iterations required for dead load and also 13 iterations needed for thermal load.

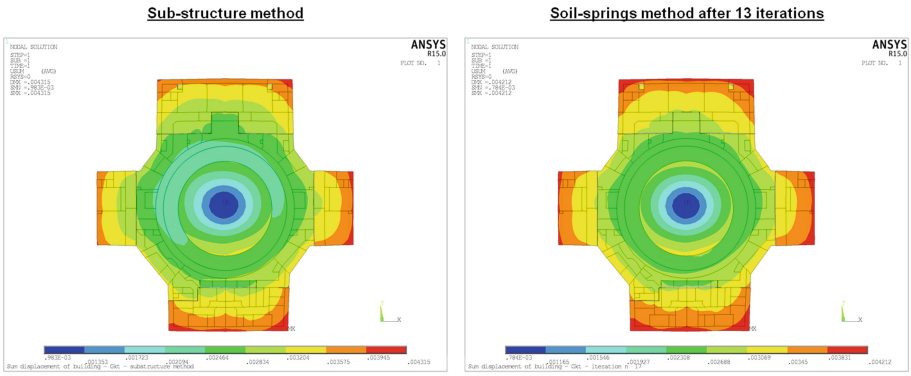


**Fig. 7.** Total displacement of raft under thermal load of structure: with substructure method (left) with soil-springs after 13 iterations (right)

## 7 Conclusion

In this paper, a methodology has been presented for the accurate representation of the soil by a flexibility matrix into a finite element model for static structural calculations. The main assumption is that the soil behavior is linear under the considered loads.

In detail, for the analyzed case study, the soil mechanical 3D model was built with several numerical tools: GDM and Autocad for the geological model, which has been implemented in FLAC3D with the suitable mechanical laws of soil. This model was used to assess the overall behavior of ground under the effect of the full structure deadweight. The effect of non-linearity is assessed by analyzing the occurrence of plasticity zones and it was concluded that the soil behaves linearly. Thus the computation of the soil flexibility matrix has been performed.

We recall that the soil flexibility matrix is an intrinsic representation of the soil, which is totally independent from the stiffness, loading, geometry of structures. Then, any modification of structures does not require the reconsideration of the boundary condition (soil) and the results are the same than the ones obtained with the complete model. This considerably improves the usual methodology based on the use of independent soil springs whose load dependent stiffness is obtained by an expensive iterative process.

**Acknowledgments.** We would like to thank EDF and TEGG for financial support and also the technical comments concerning these developments

## References

Aja, A.M.: Sub-modelling techniques for static analysis. In: MSC Software First South European Technology Conference, Principauté de Monaco, 7–9 June 2000 (2000)

AutoDesk: AutoCAD 2011, (2011) http://www.autodesk.fr/products/autodesk-autocad/overview

BRGM: Bureau des recherches géologiques et minières, GDM version 7.0 (2014). http://www.brgm.fr/production-scientifique/logiciels-scientifiques/gdm-standard-representation-modelisation-donnees

ITASCA: Finite Lagrangian Approach of Continua (F.L.A.C.3D) version 5.0 (2013). http://www.itascacg.com/software/flac

# Tunnel Muck Recycling for Road Construction – A Case Study in Vietnam

Thu-Hang Tran[1,2(✉)] and Minh-Long Le[3]

[1] Faculty of Civil Engineering, University of Transport and Communications, Hanoi, Vietnam
tranthuhang.utc@gmail.com
[2] Deo-Ca Investment Joint Stock Company, Hanoi, Vietnam
[3] Quang-Tri Department of Construction, Dong-Ha City, Quang-Tri Province, Vietnam
longbkxd@gmail.com

**Abstract.** In rock tunnel construction projects, the big volume of blasted rock muck gives burdens to the cost estimate and the environmental impacts. Tunnel muck recycling is an effort toward the sustainable development when replacing partly a non-renewable resource by a solid waste. In Deo-Ca road tunnel construction project located between Phu-Yen and Tuy-Hoa province (Vietnam), blasted rock was manufactured to become the recycled graded aggregates for constructing the road pavement and the tunnel lining. After recalling some fundamentals of the tunnel muck recycling, the paper introduced the case study on a recycled muck aggregate manufactured from Deo-Ca tunnel excavation. The possibility of utilizing the aggregate for the road base, sub-base and embankment were evaluated through the grain composition analysis. Based on the results of the trial road embankment construction, two mechanical characteristics were examined and the recommended construction parameters were proposed as the prototype for the large scale execution in some segments of the southern approach road of Deo-Ca tunnel.

**Keywords:** Tunnel muck · Recycling · Road construction material · Deo-Ca tunnel

## 1 Introduction

Towards a green planet, the 3R (Reduce – Reuse – Recycle) solution have been launched worldwide and has archived profits for the sustainable development. In the field of tunnel and mining engineering, the huge amount of rock muck created by the excavation phase threatens the limited capacity of waste dumps, and brings along many difficulties to the environment on the site. Meanwhile, the non-renewable resources for the construction have been shortened and become more costly by the time. Ideas and related studies on the tunnel rock muck reuse first appeared in 1990s (Bellopede et al. 2011). In general, there are two types of rock muck: (a) excavated by explosive; (b) excavated by TBM. While the former is coarser with smaller uniformity, the latter are finer sized with more flat grains in the shape of the flake (chip) (Girmscheid 2008).

© Springer Nature Singapore Pte Ltd. 2018
H. Tran-Nguyen et al. (eds.), *Proceedings of the 4th Congrès International de Géotechnique - Ouvrages -Structures*, Lecture Notes in Civil Engineering 8,
DOI 10.1007/978-981-10-6713-6_115

The rock muck quality depends on the characteristics of: the original rock, the original rock mass and the excavation technique (Bellopede et al. 2011). Mills, crushers and screenings are used for muck manufacture in order to obtain the objective rock aggregates that meet the utilization requirements. The most conventional usage of tunnel wasted rock is backfill material for land reclamation. Besides, other options have been proposed and applied in practice (Karlsson and Kauppila 2015). However, since hardly specific technical specifications for recycled rock can be found, recycled tunnel muck has to reach all requirements as traditional raw materials.

In this paper, the case study in Vietnam at Deo-Ca road tunnel construction project was presented. Located between Phu-Yen and Khanh-Hoa province in the middle of Vietnam, the project consists of two tunnels: (a) Deo-Ca road tunnel is 4.125 m long, two parallel tubes of which the interval spacing is 30 m; (b) Co-Ma road tunnel is 500 m long, two parallel tubes with the same interval spacing. Distanced three kilometers and a half, two tunnels have been both constructed by the NATM technology. Started from November 2013, the former's construction was scheduled to finish in July 2017 while the latter were technical opened in September 2015. The granular material used for road construction in the project was manufactured in several nearby quarries in Phu-Yen and Khanh-Hoa province (rock from Phu-Thanh and Ho-Sau quarry; soil from Van-Thang, Dai-Lanh and Hai-Thach quarry; etc.). However, when the demand had surpassed the supply capacity, another material source was in search. The ideal of blasted rock muck recycling for in-project demand was a practical action that lightened the environmental burden, solved the material crisis that bring economic and management benefits. After the manufacture in crushing screen plants, the recycled rock aggregate was obtained with an objective grain size distribution limit and a fixed nominal maximum grain diameter. Three types of muck reuse had been executed: (a) backfill materials for road embankment; (b) graded aggregates for road sub-base courses; (c) shotcrete graded aggregates for tunnel lining. In the scope of this research, the available technical data related to the tunnel muck recycling for road construction in Deo-Ca road tunnel construction project were collected, and then analyzed in order to understand the prospect of using tailings as a possible rock resource for road construction. All technical standards and specifications which were mentioned without any specific note were the current regulations of Vietnam.

## 2 Geotechnical Characteristics of the Original Rock

A granite zone of early and late Paleozoic era with different weathering levels forms the bedrock of Deo-Ca tunnel in its whole alignment (Service Geographique du Vietnam 1962). According to the geotechnical investigation carried out by the tunnel design consultant, the dominant rock type in the excavation zone of the tunnel is fractured low-weathered granite of which some geotechnical parameters are shown in Table 1 (CPRTDD 2014a, b; Công ty cổ phần Tư vấn xây dựng Hoàng Long 2011).

Based on the compression strength of the original rock, which had been determined following TCVN 7572-10:2006 standard (Bộ Khoa học và Công nghệ 2006), the

**Table 1.** Geotechnical parameters of rock in the excavation zone of Deo-Ca tunnel (CPRTDD 2014a, b; Công ty cổ phần Tư vấn xây dựng Hoàng Long 2011)

| Parameter | Value | Unit |
|---|---|---|
| Hardness | Medium | – |
| Unit weight | 2.4 | $T/m^3$ |
| Cohesion | 4.0 | MPa |
| Friction angle | 0 | Degree |
| Uni-axial compression strength (*) | >90.0 | MPa |
| Tensile strength (**) | >4.9 | MPa |
| Water absorption | 0.6 | % |
| Porosity | 1.0 | % |
| Compaction | 99.0 | % |
| Softening coefficient | 0.96 | – |

(*): Average value of the uni-axial compression strength in the saturated and unconfined condition.
(**): Average value of the splitting tensile strength in the saturated condition.

recycled crushed stone was classified in "hard" category (Tổng Công ty Tư vấn xây dựng Thủy lợi Việt Nam 2015) and was satisfied the rock type regulation of the required aggregates for the road sub-base and base courses (Bộ Khoa học và Công nghệ 2011a). The quality of the original rock was considered to be good. The high strength, the low water absorption and the small porosity of the original rock are favorable characteristics of the granite for using in road construction (Egesi and Tse 2012). The small porosity (1%) shows the high amount of silica ($SiO_2$) in the granite, which leads to the lower adhesive capacity with the asphalt when using as the crushed stone in asphalt concrete (Nguyễn 2014). Since the current Vietnamese specifications for the highway design and construction do not mention the requirement of the chemical content of the road material, no chemical content analysis of the tunnel tailings was executed in the scope of this study. With the average temperature in Phu-Yen and Khanh-Hoa province of around 26.5 °C and a slight variation within a year, the frost susceptibility of the tunnel muck was ignored.

After the excavation phase of the NATM tunneling, the blasted rock was gathered at waste dumps. Because the new graded aggregates supplied for Deo-Ca project had been exploited from some nearby quarries, manufactured from the same rock as the bedrock of Deo-Ca tunnel, the tailings were considered to be in the same quality as the raw material. However, the tunnel muck had to experience the same verification and selection as the raw rock material before passing the manufacture in crushing screen plants to become the graded aggregates. That was the excuse for the neglect of investigation into the tailings pollution in this study. With the same manufacturing process and the same original rock, the quality of the recycled and the new graded aggregate were expected to be similar. The graded aggregate which had been manufactured from Deo-Ca muck with the nominal maximum grain size $D_{max}$ = 150 mm (hereinafter called as Deo-Ca 1 aggregate) was become the subject of this study.

## 3 Grain Composition Analysis on the Graded Aggregated Made from Tunnel Muck

Seeing that the grain composition is one of the most important characteristics of the highway granular material following the current Vietnamese technical regulations, the paper focused on the grain size analysis of the recycled rock muck. The experiment for determining the grain composition of the manufactured rock muck had been carried out conforming to TCVN 4198:2014 standard (Bộ Khoa học và Công nghệ 2014) at the site laboratory Las-XD 1229. The aggregate grain composition was obtained and the analysis on the grain size distribution was executed. The result details are presented in the following sub-sections.

### 3.1 Graded Aggregate for Road Embankment

Deo-Ca 1 aggregate was aimed at replacing a part of backfill material for the road embankment. The grain size distribution curve of the aggregate is shown in Fig. 1 and its typical parameters are presented in Table 2.

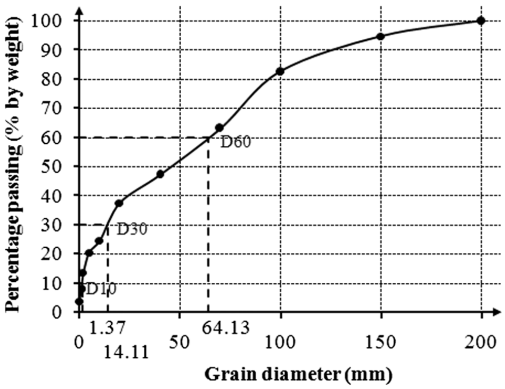


**Fig. 1.** Grain size distribution curve of Deo-Ca 1 aggregate

**Table 2.** Grain composition typical parameters of Deo-Ca 1 aggregate

| Parameter | Value | Unit |
|---|---|---|
| D60 | 64.13 | mm |
| D30 | 14.10 | mm |
| D10 | 1.37 | mm |
| $D_{max}$ | 150 | mm |
| Retained percentage on sieves $\geq$ 37.5 mm | 54.02 | % |
| Uniformity coefficient $C_U$ | 46.96 | – |
| Curvature coefficient $C_C$ | 2.27 | – |

Commentary on the obtained results:

- Since the uniformity coefficient $C_U$ was larger than 5.00 and the curvature coefficient value fell in the range $1 \leq C_C \leq 3$, the aggregate was evaluated to be well graded and good continuity (Land Transport New Zealand 2007; Department of the US Army 2001). The crushed rock mass which consisted of different size particles with a strong dissimilarity was predicted to ensure a good compaction to the road embankment.
- The percentage of the mass retained on sieves larger than 37.5 mm was 54.02%, which was smaller than the minimum required value (70%) in TCVN 9436:2012 standard (Bộ Khoa học và Công nghệ 2012) for rock - fill embankments. It was understood that the aggregate did not meet the regulation for that type of embankment.
- With the nominal maximum grain size $D_{max}$ = 150 mm, the aggregate agreed with the regulation for rock muck embankments for the layers beneath the effect zone of road surfacing in TCVN 4054:2005 standard (Bộ Khoa học và Công nghệ 2005). It was also satisfied the requirement for earth-rock embankment in the previous specification.

Deo-Ca 1 aggregate was concluded to have an appropriate grain composition for road embankment in the layers beneath the effect zone of the road surfacing.

### 3.2 Graded Aggregate for Road Sub-base Courses

Aimed at utilizing Deo-Ca 1 aggregate as a suitable material for road sub-base construction following the current Vietnamese standard, its grain composition was modified by suppressing all grains of which diameter was larger than 50 mm. To this end, the new aggregate (hereinafter called as Deo-Ca 2 aggregate) was formed. The grain composition typical parameters of Deo-Ca 2 aggregate are listed in Table 3.

**Table 3.** Grain composition typical parameters of Deo-Ca 2 aggregate

| Parameter | Value | Unit |
|---|---|---|
| D60 | 15.28 | mm |
| D30 | 2.92 | mm |
| D10 | 0.40 | mm |
| $D_{max}$ | 40.00 | mm |
| Uniformity coefficient $C_U$ | 38.61 | – |
| Curvature coefficient $C_C$ | 1.40 | – |

The grain size distribution was compared with the standard distribution boundary of the recommended graded aggregate for sub-base courses according to TCVN 8859:2011 standard (Bộ Khoa học và Công nghệ 2011a) (see Fig. 2).

Commentary on the obtained results:

- With the uniformity coefficient $C_U > 5.00$ and curvature coefficient $1 \leq C_C \leq 3$, the aggregate was found to be well graded and good continuity (Land Transport New Zealand 2007; Department of the US Army 2001).

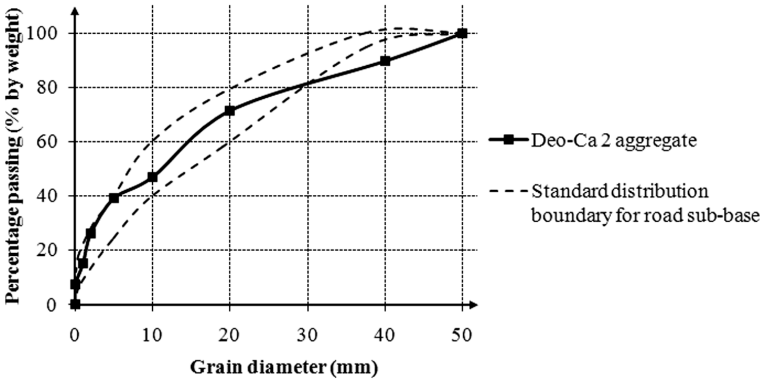


**Fig. 2.** Grain size distribution curve of Deo-Ca 2 and the standard distribution boundary

- The $D_{max}$ of Deo-Ca 2 aggregate was 40 mm and the grain size distribution curve did not stay completely in the standard distribution boundary of the standard $D_{max}$ = 37.5 mm graded aggregate.
- It was suggested to re-crush Deo-Ca 1 aggregate with the nominal maximum grain size $D_{max}$ = 37.5 mm and to reduce the grains of which diameter was larger than 30 mm to obtain a suitable material for road sub-base courses according to the mentioned standard.

### 3.3 Graded Aggregate for Road Base Courses

To learn whether Deo-Ca 1 aggregate can be put to use for road base construction following the current Vietnamese standard, a modification in Deo-Ca 1 aggregate had been tried by eliminating all grains of which diameter was larger than 40 mm. The new grain size distribution was recalculated and the new aggregate (hereinafter called as Deo-Ca 3 aggregate) was established. The grain composition typical parameters of Deo-Ca 3 aggregate are listed in Table 4.

**Table 4.** Grain composition typical parameters of Deo-Ca 3 aggregate

| Parameter | Value | Unit |
|---|---|---|
| D60 | 12.80 | mm |
| D30 | 2.22 | mm |
| D10 | 0.27 | mm |
| $D_{max}$ | 20.00 | mm |
| Uniformity coefficient $C_U$ | 46.77 | – |
| Curvature coefficient $C_C$ | 1.40 | – |

The grain size distribution curve of Deo-Ca 3 aggregate and the standard distribution boundary of the recommended graded aggregate for road base following TCVN 8859:2011 standard (Bộ Khoa học và Công nghệ 2011a) was sketched together in Fig. 3.

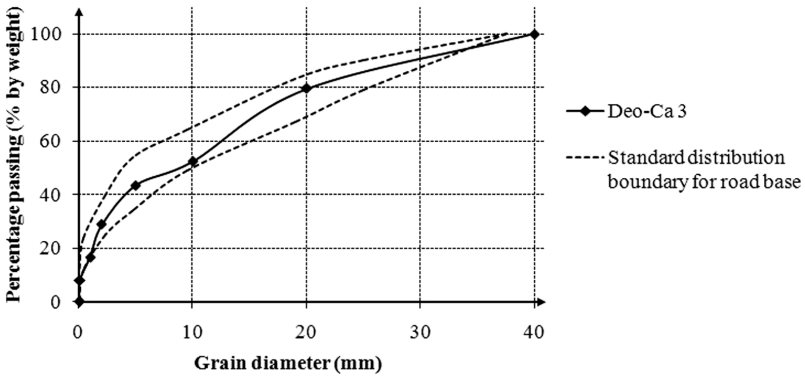


**Fig. 3.** Grain size distribution curve of Deo-Ca 3 aggregate and the standard distribution boundary

Even Deo-Ca 3 aggregate was found to be well graded thanked to the conformed value of the uniformity coefficient and the curvature coefficient, the aggregate was discovered to be not suitable for road base construction according to the mentioned specification due to the following matters:

- The size of nominal maximum grain size and the grain size distribution curve was not satisfied the regulation of grain composition of the standard graded aggregate recommended in TCVN 8859:2011 standard (Bộ Khoa học và Công nghệ 2011a).
- Since only the last segment of the grain size distribution curve where grain size was larger than 34 mm fell out of the required distribution boundary, it was suggested to re-crush Deo-Ca 1 aggregate with the nominal maximum grain size $D_{max}$ = 25 mm to obtain an appropriate material for road base courses according to the mentioned standard.

## 4 Construction Practice of the Road Embankment Using Recycled Rock Muck

Before the large-scale application of the blasted rock for road embankment in Deo-Ca road tunnel construction project, the trial work had been executed in order to investigate if it obeyed all requirements of the current technical construction standards. The experiment had been carried out at the 100 m road segment from KM8+300 to KM8 +400 of the southern approach road of Deo-Ca tunnel. Deo-Ca 1 aggregate was used as granular backfill material for an embankment portion that stayed beneath the effect zone of the road surfacing. The embankment portion was structured so that the crushed stone sizes were grown with the embankment's depth. It was covered by a 0.3 m intermediate rock layer of which the outer faces were sealed by small sized grains. The spacing between the top of recycled rock portion and the K98 portion (which stayed within the effect zone and directly above the top of muck portion) was 1.5 m. The compaction sequence for one point in the recycled rock portion included: (1) the

preliminary phase by 8T static compactors; (2) the main phase by 25T and 16T vibration compactors with different compacting scenarios; (3) the finish phase by 8T static compactors. The standard of trial recycled rock embankment portion was evaluated through these following parameters: (a) Density compaction of the embankment; (b) California bearing ratio (CBR).

### 4.1 Density Compaction of the Recycled Muck Embankment Portion

The density compaction of the trial recycled rock embankment portion was determined by the water replacement method following the American ASTM D5030-04 standard (ASTM 2004) at 8 points on the experiment road segment. The number of testing points was conformed to the regulation of TCVN 9436:2012 standard (Bộ Khoa học và Công nghệ 2012) (at least 2 points on the area of 1000 $m^2$). The obtained data were analyzed and the distribution of the empirical results was found to fit well the normal law with the mean $\mu = 77.86$, the standard deviation $\sigma = 5.01$, and the standard error SE = 1.77 (see Fig. 4).

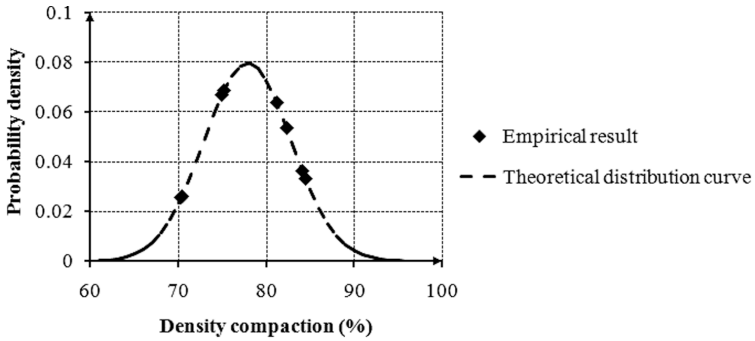


**Fig. 4.** Probability density of the empirical density compaction results and the equivalent theoretical distribution curve

It proved the reliability of the density compaction results and even if the sampling size is enlarged, the mean density compaction values from samplings will be almost certainly (99.7% of chance) within the range of $\mu \pm 3SE = 77.86 \pm 5.31$ (%). To this end, the mean porosity values from samplings will be almost certainly within the range of $16.83 \leq R \leq 27.46$ (%).

### 4.2 California Bearing Ratio of the Constructed Muck Embankment Portion

The California bearing ratio (CBR) of the embankment portion was determined through the correlation between CBR and the elastic modulus in an empirical function given in the 22TCN 211:2006 standard (Bộ Giao thông vận tải 2006):

$$E_0 = 7.93 \times CBR^{0.85} \quad (1)$$

With:
$E_0$: Elastic modulus determined using static plate load method, MPa.
CBR: California bearing ratio, %

The elastic modulus of several points on the trial construction segment had been measured by the static plate load method following TCVN 8861:2011 standard (Bộ Khoa học và Công nghệ 2011b). With the average value of the elastic modulus $E_0$ = 58.81 MPa, the deduced CBR value was 8.11%. Checking the required minimum CBR = 3 in TCVN 9436:2012 standard (Bộ Khoa học và Công nghệ 2012) for the embankment of Class 1 and express road, the obtained value was said to be satisfied.

## 5 Conclusion

In Vietnam, the number of road tunnels has been increased quickly from the 50 m pilot one, which was constructed in 1999 at the connection between Ninh-Binh and Thanh-Hoa province, to the total of 20.250 km in March 2017. In road tunnel construction projects, it is normally faced with a conflict when blasted rock muck is wasted at dumping areas, but rock material is in short supply, especially for the high embanked approach roads and the tunnel lining. However, the study on muck recycling in road tunnel projects in Vietnam is limited and keeps privately in each project, if any. At Deo-Ca road tunnel construction project, the blasted rock muck had been recycled to become the granular backfill material for the road structure. In the scope of this paper, the research was made on a $D_{max}$ = 150 mm recycled aggregate from Deo-Ca tunnel excavation for understanding the utilization possibility for road pavement. With the grain composition analysis, the proposed aggregate shown the adaptability for the earth – rock embankment while it needed to modify the crush screen process for the quest of a road foundation application (for base and sub-base courses). Based on the trial embankment construction of a 100 m road segment, the recommended construction parameters were proposed as the prototype for the large scale construction (Liên danh nhà thầu: Miền Tây - Hải Thạch - 492 2015) (see Table 5).

**Table 5.** Recommended construction parameters for large-scale embankment work using Deo-Ca 1 aggregate (Liên danh nhà thầu: Miền Tây - Hải Thạch - 492 2015)

| Parameter | Value | Unit |
|---|---|---|
| Compacting execution on one point | 12 | Time |
| Average porosity | 18.26 | % |
| Elastic modulus | 58.81 | MPa |
| Compactness ratio | K95 | – |
| Spraying factor | 1.28 | – |
| Standard reduction depth after compacting of each layer | 7 | cm |
| Maximum depth of a compacted layer | 300 | mm |

The construction sequence outline and the technical guide for the road embankment by the recycled material were also compiled. Finally, the utilization of the proposed aggregate was reached the approval of the state authorities for the standard road embankment phase of the road segment from KM8+250.77 to KM9+350 of the southern approach road construction package. It was considered as a favorable achievement for the 3R spread in tunnel engineering toward a better sustainable development in Vietnam.

**Acknowledgments.** Deep gratitude is expressed to Deo-Ca Investment joint stock company (Vietnam) – the owner of Deo-Ca road tunnel construction project for giving us the permission of access to all the technical documents related to the tunnel muck reclamation in the project for research purposes.

## References

ASTM: ASTM D5030-04 Standard Test Method for Density of Soil and Rock in Place by the Water Replacement. Method in a Test Pit. ASTM International (2004)

Bellopede, R., et al.: Main aspects of tunnel muck recycling. Am. J. Environ Sci. **9**(4), 338–347 (2011)

Bộ Giao thông vận tải: 22TCN 211:2006 Áo đường mềm – Các yêu cầu và chỉ dẫn thiết kế. Hà Nội (2006)

Bộ Khoa học và Công nghệ: TCVN 4054: 2005 Đường ô tô - Yêu cầu thiết kế. Hà Nội (2005)

Bộ Khoa học và Công nghệ: TCVN 7572-10: 2006 Cốt liệu cho bê tông và vữa - Phương pháp thử - Phần 10: Xác định cường độ và hệ số hóa mềm của đá gốc. Hà Nội (2006)

Bộ Khoa học và Công nghệ: TCVN 8859:2011 Lớp móng cấp phối đá dăm trong kết cấu áo đường ô tô - Vật liệu, thi công và nghiệm thu. Hà Nội (2011a)

Bộ Khoa học và Công nghệ: TCVN 8861-2011 Xác định mô đun đàn hồi nền, mặt đường bằng tấm ép cứng. Hà Nội (2011b)

Bộ Khoa học và Công nghệ: TCVN 9436:2012 Nền đường ô tô - Thi công và ng hiệm thu. Hà Nội (2012)

Bộ Khoa học và Công nghệ: TCVN 4198:2014 – Xác định thành phần hạt. Hà Nội (2014)

Công ty cổ phần Tư vấn xây dựng Hoàng Long: Tập IV: Hồ sơ khảo sát. Báo cáo khảo sát địa chất công trình. Công ty Cổ phần Đầu tư Đèo Cả, Hà Nội (2011)

CPRTDD: Detailed design report for north part of Deo-Ca tunnel construction. Deo-Ca joint stock company. Joint ventre of Nippon Koei Co., Ltd. and Nippon Koei Vietnam International Co., Ltd. (2014a)

CPRTDD: Detailed design report for south part of Deo-Ca tunnel construction. Deo-Ca joint stock company. Joint ventre of Nippon Koei Co., Ltd. and Nippon Koei Vietnam International Co., Ltd. (2014b)

Department of the US Army: FM 5-472/NAVFAC MO 330AFJMAN 32-1221(I). Materials testing. Washington, DC, Field Manual (2001)

Egesi, N., Tse, A.C.: Engineering-geological evaluation of rock materials from Bansara, Bamenda Massif Southeastern Nigeria, as aggregates for pavement construction. Geosciences **2**(5), 107–111 (2012). doi:10.5923/j.geo.20120205.01

Girmscheid, G.: Baubetrieb und Bauverfahren im Tunnelbau. Verlag Ernst and Sohn, Berlin (2008)

Karlsson, T., Kauppila, P.: Utilisation of mine waste, September 2015. http://wiki.gtk.fi/web/mine-closedure/wiki/-/wiki/Wiki/Utilisation+of+mine+waste/pop_up;jsessionid=07e8d620a1a619229bfc537b19c4. Accessed 24 Feb 2017

Land Transport New Zealand: Research Report 325: The effect of grading on the performance of basecourse aggregate. Land Transport New Zealand (2007)

Liên danh nhà thầu: Miền Tây - Hải Thạch – 492: Báo cáo thi công đắp thử đắp nền đường bằng đá hỗn hợp (đá nổ mìn chế biến qua trạm nghiền). Công ty Cổ phần Đầu tư Đèo Cả, Việt Nam (2015)

Nguyễn, V.T.: Tìm giải pháp tăng khả năng bám dính nhựa đường. Paper presented at the Conference "Tăng khả năng dính bám ổn định nhiệt cho kết dính nhựa đường", Đà Nẵng, 24 November 2014 (2014)

National Geographic Service of Vietnam: Nha Trang [cartographic material]: carte geologique 1:500,000, Vietnam (1962)

Tổng công ty Tư vấn xây dựng Thủy lợi Việt Nam: TCVN Công trình thủy lợi: Phân cấp đất đá (Dự thảo lần 1). Cục Quản lý xây dựng công trình (Bộ Nông nghiệp và Phát triển nông thôn), Hà Nội (2015)

# Author Index


**A**
Abdulazeez, Mohanad M., 346, 544
Aït Oumeziane, Y., 533
Allagnat, D., 1142
Andre, Ludovic, 588
Ang, K.K., 1097
Atteia, O., 1009

**B**
Ba, Makhaly, 377
Bach, Quoc Si, 354
Bart, M., 533
Beakou, Alexis, 972
Benabou, Lahouari, 172
Berthoz, N., 905
Bertin, H., 1009
Bertrand-Krajewski, Jean-Luc, 1084
Blieck, Hervé, 1134
Bougressi, Ali, 935
Bourahla, Nouredine, 935
Branque, D., 905
Bui Van, D., 598
Bui, Duc Vinh, 68, 243
Bui, Ha H., 288
Bui, Nguyen-Hoang, 1134
Bui, Q.-B., 59, 233, 319
Bui, Quoc Bao, 829
Bui, Quoc-Bao, 617
Bui, T.A., 726
Bui, Thanh Cong, 914
Bui, Thi-Loan, 925
Bui, Tu An, 786

**C**
Canou, Jean, 746
Cao, Minh Quyen, 254
Cerfontaine, Benjamin, 637
Charles, Pascal, 1134
Charlier, Robert, 637
Chaudhary, Muhammad Tariq A., 694
Chemrouk, Mohamed, 560
Cheng, Y.M., 716
Chijiwa, Nobuhiro, 367
Chinkulkijniwat, A., 598
Choi, Seunghyun, 1037
Chu, Thi Binh, 213
Chu, Thi Hai Vinh, 68, 243
Collet, F., 533
Cooper, A.G., 677
Cyr, Martin, 588

**D**
Dai, J., 1097
Dang, My Quoc, 800, 808
Dang, Van Thanh, 1044
Dao, Duy Kien, 68, 243
Del Campo Estrada, E., 1009
Deleruyelle, F., 726
Dias-da-Costa, Daniel, 885
Diep, Thi My Hanh, 508
Do, Quang Minh, 523
Do, Tan Manh, 800, 808
Do, Thi Vi Vi, 508
Do, Van-Dong, 972
Doan, D.H., 677
Doufene, Mohamed Anis, 935
Dumont, Gael, 627, 668
Duong, T.-H., 59
Duong, Thanh Nga, 580
Dupla, Jean-Claude, 746

**E**
Edil, Tuncer B., 3
ElGawady, Mohamed A., 346, 392, 544


© Springer Nature Singapore Pte Ltd. 2018

H. Tran-Nguyen et al. (eds.), *Proceedings of the 4th Congrès International de Géotechnique - Ouvrages -Structures*, Lecture Notes in Civil Engineering 8,
DOI 10.1007/978-981-10-6713-6

ElGawady, Mohamed, 426, 497
Erlicher, S., 1142

**F**
Fabbri, A., 716
Ferrier, Emmanuel, 471, 484

**G**
Gautier, M., 1066
Gbandi, Djaneye-Boundjou, 1027, 1053
Gheni, Ahmed A., 392
Gomaa, Eslam, 497
Gourdon, R., 1066
Grillet, A.-C., 319
Grillet, Anne-Cécile, 508
Gupta, Varun, 459

**H**
Ha, Quang-Khai, 1037
Ha, Xuan Linh, 1044
Hancock, Gregory J., 41, 78, 131, 224, 885, 954
Hemmati, Sahar, 756
Heng, S., 1097
Hermans, Thomas, 627
Herrero, Pauline, 1084
Hervé, Guillaume, 273
Hirose, Toshiharu, 263
Hjiaj, Mohammed, 30, 142
Ho, Duc-Duy, 100
Ho, Thanh Tri, 367
Ho, Xuan Ba, 442
Hoang, Ngan Hanh, 1044
Hoang, Trong-Quang, 329
Hoang, Truong Minh, 786
Honghan, Chen, 1027
Horpibulsuk, S., 598
Huang, Zhujun, 991
Huynh, Le Anh Thi, 202
Huynh, Minh Toan, 224

**I**
Ibrahim, Tchakala, 1027, 1053
Ichikawa, Kazuomi, 411

**J**
Jacques, Diederik, 1107
Jiang, D., 1097
Jostad, Hans Petter, 656

**K**
Kabeyasawa, Toshikazu, 15
Kabeyasawa, Toshimi, 15
Kaci, Abdelhak, 338
Kadri, El-Hadj, 338
Kania, M., 1066
Kashosi, Cedric, 497
Kawai, Marina, 411
Khoa, Huynh Dat Vu, 656
Kennedy, O., 598
Khoa, Huynh Dat Vu, 656
Kikumoto, Mamoru, 644
Kim, B., 1066
Kim, Kangjoo, 1037
Kim, Young-sang, 800, 808
Kimura, Yoshihiro, 263
Kitazume, M., 765
Kono, Kenji, 411
Kurar, Ritesh, 459

**L**
Labbé, Pierre, 273
Lanos, C., 533
Le Dinh, Quoc Khanh, 914
Le, Duc-Hien, 617
Le Nguyen, Khuong, 254
Le Tuan, A., 598
Le, Anh-Thang, 329
Le, Hong Thai, 367
Le, Minh-Long, 1153
Le, Quang-Huy, 100
Le, Thien-Phu, 972
Le, Tuan Nghia, 523
Le, Van Phuoc Nhan, 68, 243
Le, Van-Nhat, 172
Le, Xuan Huynh, 152
Lecompte, Thibaut, 560
Lei, Jun, 894
Lei, X., 716
Lim, B.K., 1097
Limam, A., 716
Limrat, I., 598
Linh, Luong Hai, 786
Lok, Thomas, 816
Looijen, P., 677
Lozano-Galant, Jose-Antonio, 283, 894
Ly Minh, H., 1000

**M**
Maes, Norbert, 1107
Mai, Bac V., 131
Mai, Chanh-Trung, 338
Mande Seyf-Laye, Alfa-Sika, 1027
Mark, Nicolas, 668
Matiere, N., 860, 981
Matoba, Moeko, 263
Michel, P., 1066
Moctar, Bawa L., 1053

Moissette, S., 533
Mudgal, Ankur, 459
Muhammed, Rawaz Dlawar, 746

**N**
Nain, Monika, 346
Ngo, Tien-Tung, 338
Nguyen Vo, Trong, 111
Nguyen, Dang Mao, 508
Nguyen, Duc Dat Duc, 1017
Nguyen, Duc Tiep, 1074
Nguyen, Duy-Liem, 89, 310
Nguyen, Frédéric, 627, 637, 668
Nguyen, Giang D., 131, 288
Nguyen, H.T. Tai, 181, 552
Nguyen, Hoc Thang, 402
Nguyen, Khanh Son, 367, 523, 552
Nguyen, Manh Hung, 868, 878
Nguyen, Minh Tien, 829
Nguyen, N. Hung, 181
Nguyen, Nhat Huy, 1044
Nguyen, N.T. Huynh, 552
Nguyen, Phi Long, 484
Nguyen, Quang Huy, 120
Nguyen, T. Hang, 181
Nguyen, Tan Phong, 1017, 1074
Nguyen, Tat-Thanh, 329
Nguyen, Thanh Hai, 243
Nguyen, Thi Thuy, 1017, 1044
Nguyen, Thi Trang Nhung, 1044
Nguyen, Thong, 1000
Nguyen, Thuong Anh, 273
Nguyen, Tien Long, 30, 142
Nguyen, Tri-Thong, 310
Nguyen, Trung Hieu, 100, 868, 878
Nguyen, Van Vinh, 78
Nguyen, Van-Nghia, 610, 1142
Nguyen, Vu P.Q., 644
Nguyen, Xuan-Huy, 925
Nguyen, Xuan Tung, 442
Nguyen-Ngoc, Tri Huynh, 367, 523
Nguyen-Phung, Anh Toan, 367, 523
Nguyen-Thi, Anh Quyen, 523
Nicolaudie, P.A., 981
Nogal, Maria, 894

**O**
Ong, K.C.G., 1097
Otsuki, Nobuaki, 367

**P**
Pereira, Jean-Michel, 685
Perrotin, P., 233
Pham Minh, Q., 1000
Pham Thi Anh, D., 1142
Pham, Cao Hung, 78, 131, 161, 202, 224, 434, 885, 954
Pham, Hoang Lam, 991
Pham, Ngoc Hieu, 161
Pham, Song Hong, 954
Pham, Trung Kien, 402
Phung, Quoc Tri, 1107
Plassiard, J.-P., 233
Plé, O., 233
Pouya, Amade, 756
Prétot, S., 533
Prime, N., 319
Promentilla, Michael A.B., 402
Proust, Gwénaëlle, 434
Prud'homme, E., 319
Purnomo, H., 233

**Q**
Quach, Chuong Hong, 736

**R**
Radioti, Georgia, 637
Rasmussen, Kim J.R., 161, 202
Regazzoni, P.-L., 1142
Reynaud, S., 1142
Robert, Tanguy, 668
Rossi, Pierre, 840
Russell, Adrian, 775

**S**
Sansour, Carlo, 30, 142
Sargon, Simon, 497
Sarkar, Raju, 459
Sato, Mutsuki, 263
Satomi, Tomoaki, 571, 580
Sawangsuriya, Auckpath, 385
Sechet, Philippe, 991
Semblat, Jean-François, 273
Sentosa, B., 59, 233
Seyf-Laye, Alfa-Sika Mande, 1053
Si Larbi, Amir, 471, 925
Smith, Paul, 850, 945, 964, 1122
Sramoon, Wilailak, 385
Sreeram, K.J., 1053
Subrin, D., 905

**T**
Tabbagh, Alain, 746
Tahenni, Touhami, 560
Taibi, Said, 610
Tailhan, Jean-Louis, 840
Takahashi, Hiroshi, 571, 580
Tan, K.H., 1097
Tang, Anh Minh, 685, 756
Tao, Quang-Bang, 172
Thuc, Chi Nhan Ha, 508
Tien, H. Pham, 598
Tlaiji, Tala, 471
Tomkouani, Kodom, 1053
Tong, Duy-Ngo, 89
Tran Ngoc, T.D., 1000
Tran Van, T., 1000
Tran, Dong Viet Phuong, 448
Tran, Khiem Quang, 571
Tran, Minh-Tung, 617
Tran, Truyen The, 442
Tran, Mien Van, 299
Tran, T. Nhan, 552
Tran, Minh Tung, 829
Tran, Thanh Viet, 152
Tran, Thu-Hang, 1153
Tran, Thuy Duong, 868, 878
Tran, Van Mein, 448
Tran, Van Toan, 120, 191
Tran-Nguyen, Hoang-Hung, 704, 736
Trinh, Huu Nam, 434
Trung, Duong Tien, 786
Truong, Ba Tam, 254
Truong, Chau Dac, 704
Truong, Khang Thien, 704
Truong, Nguyen Huu, 786
Truong, Quang Vinh, 213
Turmo, Jose, 283, 894

**U**
Udomchai, A., 598
Ung, Q.H., 860, 981

**V**
Van Horde, Maurits, 627
Van Hung, Nguyen, 786
Van Nguyen, Tri, 685
Vedhanayagam, M., 1053
Vo Thi Tuyet, Giang, 111
Vo, Thanh, 775
Vo, Thi Dong, 756
Vu, Ngan Thi Tuyet, 808
Vu, Quoc Anh, 152
Vu, Tran Huyen, 299
Vu, Xuan Hong, 471, 484
Vuong, Thi-Ngoc-Han, 310

**W**
Wachiraporn, Suppakorn, 385
Wang, Song, 426
Woloszyn, Monika, 508
Wong, H., 716, 726
Wu, Shengshen, 816

**X**
Xu, Dong, 283, 894

**Y**
Yap, Soon Poh, 367
Yubonchit, S., 598

**Z**
Zhou, Annan, 816